JUN 1 1 1991

0830-11-10
0309

NAS 1.55:3078

NASA Conference Publication 3078

Computational Fluid Dynamics Symposium on Aeropropulsion

Proceedings of a symposium held at
NASA Lewis Research Center
Cleveland, Ohio
April 24–26, 1990

NASA

HGW

NASA Conference Publication 3078

Computational Fluid Dynamics Symposium on Aeropropulsion

Proceedings of a symposium sponsored by
NASA Lewis Research Center and held at
Lewis Research Center
Cleveland, Ohio
April 24–26, 1990

NASA

National Aeronautics and
Space Administration

Office of Management

Scientific and Technical
Information Division

1991

I

PREFACE

Recognizing the considerable advances that have been made in computational fluid dynamics (CFD) and the impact that CFD has had on aeropropulsion research, the Internal Fluid Mechanics Division of NASA Lewis Research Center sponsored the Computational Fluid Dynamics Symposium on Aeropropulsion.

The objective of the symposium was to provide a forum for exchanging information regarding recent developments in numerical methods, physical and chemical modeling, and applications. It was also our objective to identify key issues and problem areas of CFD, specifically those affecting propulsion systems. Thus, a synergy could be developed among the government laboratories, universities, and industries.

The symposium included 4 invited and 34 contributed papers, covering such topics as numerical methods, grid generation (including structured and unstructured grids), turbomachinery, turbulence modeling (including pdf methods), high speed flows, chemically reacting flows, propulsion components (including the inlet nozzle), and combustors.

This publication supercedes the previous version (NASA CP-10045). It contains six papers that were not included in the preprint. In our opinion, the collected papers represent the current capability of CFD for propulsion applications.

Meng-Sing Liou
Louis A. Povinelli
Symposium Organizers
NASA Lewis Research Center

CONTENTS

ALGORITHMS I

Thoughts on the Chimera Method of Simulation of Three-Dimensional Viscous Flow (invited paper)
Joseph L. Steger, University of California at Davis **1**

Generation and Use of Unstructured Grids for Turbomachinery Calculations
Dana R. Lindquist and Michael B. Giles,
Massachusetts Institute of Technology **11**

Unstructured Grid Generation Using the Distance Function
Barna L. Bihari and Sukumar R. Chakravarthy,
Rockwell International Science Center **29**

Computational Study of Three Dimensional Viscous Flow Through a Turbine Cascade Using Multi-Domain Spectral Technique
Earl W. Renaud and Choon S. Tan,
Massachusetts Institute of Technology **41**

A Finite-Difference, Frequency-Domain Numerical Scheme for the Solution of the Linearized Unsteady Euler Equations
James R. Scott, NASA Lewis Research Center;
and Hafiz M. Atassi, University of Notre Dame **55**

A Pressure Flux-Split Technique for Computation of Inlet Flow Behaviour
H.S. Pordal, P.K. Khosla, and S.G. Rubin, University of Cincinnati . . **105**

TURBOMACHINERY

Simulation of Turbomachinery Flows (invited paper)
John J. Adamczyk, NASA Lewis Research Center **119**

Numerical Solutions of 2-D Multi-Stage Rotor/Stator Unsteady Flow Interactions
R.-J. Yang and S.-J. Lin, Rocketdyne Division,
Rockwell International **127**

Transonic Cascade Flow Calculations Using Non-Periodic C-Type Grids
Andrea Arnone, Institute for Computational Mechanics in Propulsion; and
Meng-Sing Liou and Louis A. Povinelli, NASA Lewis Research Center . . **143**

Computation of Supersonic and Low Subsonic Cascade Flows Using an Explicit Navier-Stokes Technique and the k-ε Turbulence Model
R.F. Kunz and B. Lakshminarayana, Pennsylvania State University . . . **163**

ALGORITHMS II

Flux-Vector Splitting for the 1990s (invited paper)
Bram van Leer, The University of Michigan 203

On the Application of ENO Scheme With Subcell Resolution to Conservation Laws With Stiff Source Terms
Shih-Hung Chang, Cleveland State University 215

Cost-Effective Accurate Coarse-Grid Method for Highly Convective Multidimensional Unsteady Flows
B.P. Leonard and H.S. Niknafs, The University of Akron 227

Choice of Velocity Variables for Complex Flow Computation
W. Shyy, University of Florida;
and G.C. Chang, Chung Shan Institute of Science and Technology 241

Distributed Minimal Residual (DMR) Method for Acceleration of Iterative Algorithms
Seungsoo Lee and George S. Dulikravich,
Pennsylvania State University 259

A Pressure Based Method for the Solution of Viscous Incompressible Turbomachinery Flows
G.V. Hobson and B. Lakshminarayana, Pennsylvania State University . . 281

A Multidimensional Finite Element Method for CFD
Darrell W. Pepper and Joseph W. Humphrey,
Advanced Projects Research, Inc. 311

TURBULENCE

The PDF Method for Turbulent Combustion (invited paper)
S.B. Pope, Cornell University 335

Pressure Algorithm for Elliptic Flow Calculations With the PDF Method
M.S. Anand, Allison Gas Turbine; S.B. Pope, Cornell University;
and H.C. Mongia, Allison Gas Turbine 347

Implicit Solution of Three-Dimensional Internal Turbulent Flows
V. Michelassi, Institute for Computational Mechanics in Propulsion;
M.-S. Liou and L.A. Povinelli, NASA Lewis Research Center;
and F. Martelli, University of Florence 363

Numerical Investigation of an Internal Layer in Turbulent Flow Over a Curved Hill
S.-W. Kim, Institute for Computational Mechanics in Propulsion 393

Computation of Turbulent High Speed Mixing Layers Using a Two-Equation Turbulent Model
J.R. Narayanan, Analytical Services and Materials, Inc.;
and B. Sekar, Vigyan Research Associates, Inc. 409

Heat Transfer, Velocity-Temperature Correlation, and Turbulent Shear Stress From Navier-Stokes Computations of Shock Wave/Turbulent Boundary Layer Interaction Flows
C.R. Wang, W.R. Hingst, and A.R. Porro, NASA Lewis Research Center . . 429

Wave Models for Turbulent Free Shear Flows
W.W. Liou and P.J. Morris, Pennsylvania State University 457

Computation of Laminar Viscous-Inviscid Interactions in High-Speed Internal Flows
David H. Rudy, James L. Thomas, and Ajay Kumar,
NASA Langley Research Center 473

Two and Three-Dimensional Shock-Shock Interactions on the Blunt Leading Edges of the Hypersonic Inlets
D.J. Singh, Old Dominion University;
A. Kumar, NASA Langley Research Center;
and S.N. Tiwari, Old Dominion University 487

Zonal Analysis of Two High-Speed Inlets
A.D. Dilley, G.F. Switzer, and W.M. Eppard,
Analytical Services and Materials, Inc. 507

Dynamics of Local Grid Manipulations for Internal Flow Problems
Peter R. Eiseman, Program Development Corporation;
and Aaron Snyder and Yung K. Choo, NASA Lewis Research Center 521

Grid Generation Strategies for Turbomachinery Configurations
K.D. Lee and T.L. Henderson, University of Illinois 547

3D Computation of Single-Expansion-Ramp and Scramjet Nozzles
H.T. Lai, Sverdrup Technology, Inc. 559

Solution of Three-Dimensional Afterbody Flow Using Reduced Navier-Stokes Equations
H.M.H. Almahroos, P.K. Khosla, and S.G. Rubin,
University of Cincinnati 583

COMBUSTORS

Recent Update of the RPLUS2D/3D Codes
Y-L Peter Tsai, Sverdrup Technology, Inc. 593

The Direct Simulation of High-Speed Mixing-Layers Without and With Chemical Heat Release
B. Sekar, Vigyan Research Associates;
H.S. Mukunda, Indian Institute of Science;
and M.H. Carpenter, NASA Langley Research Center 609

Computational Modelling of Dump Combustors Flowfield
D. Lentini, Universita' degli Studi di Roma "La Sapienza;" and
W.P. Jones, Imperial College of Science, Technology and Medicine . . . 623

Numerical Simulation of Transverse Fuel Injection
Marlon Mao and David W. Riggins,
Analytical Services and Materials, Inc.; and
Charles R. McClinton, NASA Langley Research Center **635**

A Highly Efficient Engineering Tool for Three-Dimensional Scramjet Flowfield and Heat Transfer Computations
Pradeep S. Kamath and Richard W. Hawkins,
Analytical Services and Materials, Inc.; Nathaniel R. Baker,
Lockheed Engineering and Sciences Company; and Charles R. McClinton,
NASA Langley Research Center **669**

THOUGHTS ON THE CHIMERA METHOD OF SIMULATION OF THREE-DIMENSIONAL VISCOUS FLOW

Joseph L. Steger

Department of Mechanical, Aeronautical, and Materials Engineering
University of California at Davis
Davis, California 95616

ABSTRACT

The chimera overset grid method is reviewed and discussed relative to other procedures for simulating flow about complex configurations. It is argued that while more refinement of the technique is needed, current schemes are competitive to unstructured grid schemes and should ultimately prove more useful.

INTRODUCTION AND OVERVIEW

There are currently two mainstream approaches for computing flow fields in which geometry imposes complex boundary conditons – composite structured grid schemes and unstructured grid schemes. In my assessment of the literature, unstructured grid methods are generally considered to be more versatile and easier to adapt to complex geometry while composite structured grid methods are generally considered to use more efficient numerical algorithms and require less computer memory. But with either composite-structured or unstructured grids, the capability to solve flow about complex configurations has been suitably demonstrated. Both pure-strain approaches have their strengths and weaknesses. Hybrid schemes which incorporate the best features of both have already appeared[1-3] and will likely become more important in treating flow about complex geometries.

The chimera[4] and similar methods which use overset grids[5-29] are generally classed into the composite structured grid catagory, because these approaches clearly grew out of an attempt to generalize body conforming structured grid schemes to treat more complex situations. The chimera approach uses a composite of overset structured grids to resolve geometry, flow features, or permit more efficient flow solvers. While chimera generally employs composite structured grids, the connectivity of the overset structured grids is itself unstructured.

The chimera approach has been used to compute inviscid and high Reynolds flow about complex configurations(c.f.[7,8,14-19,24-26]), and it has even been demonstrated for unsteady three dimensional viscous flow problems in which one body moves with respect to another[26]. The viability of this approach is perhaps best illustrated by the fact that this progress has been made by a relatively small group of researchers. Nevertheless, chimera is sometimes viewed as an intermediate solution approach, one which will ultimately be replaced by the unstructured grid method. With further examination, however, the chimera approach may be found to have more versatility than current unstructured schemes because, while grids can be abutted together like patches, they can also be overset. Oversetting can be somewhat foreign to finite volume and finite element methods, but oversetting can be useful. In overset schemes, intermediate boundary curves can be placed arbitrarilly. In overset regions, the possibility also exists of impressing solutions from one domain onto another via forcing functions rather than only through boundary interfaces. These features can and have been exploited in several ways.

Overset grids allow structured grids to be used without excessive distortion or inefficient use of grid density. Consequently, efficient numerical methods can be used which depend on structured grids such as alternating direction implicit schemes and parabolized Navier Stokes procedures. Moreover, numerical schemes that use structured-grids generally require less computer storage and are better suited to vectorizated computers. Arbitrary placement of intermediate boundaries can greatly simplify the task of structured grid generation. It allows, for example, the use of hyperbolic grid generation procedures[30,31] which do not conform to boundary value constraints but which generate nearly orthogonal grids with excellent mesh spacing control. Overset structured grids have also been used as a solution adaption procedure[21,22], and overset grids can be positioned in the field simply to implement a special solver, most of which require some kind of coordinate alignment, (usually to streamlines in flow field simulation). Overset grids allow one body to move with respect to another without regriding[10,26] or placement of new bodies into the domain without regenerating the entire mesh.

As noted earlier, the chimera method is an outgrowth of trying to generalize a powerful solution approach, the body conforming structured grid method, to more complex situations. The method is proven, but far from mature. There are weaknesses which must be removed if chimera is to remain competitve with unstructured grids.

There are two main criticisms leveled against the current implementations of the chimera method. One is the bookkeeping-like complexities associated with connecting overset grids together. In fact, the bookkeeping with a chimera scheme is similar to that associated with an unstructured grid – easier because the connectivities can be made using structured grid data but more difficult because of multiple oversetting. However, only a few reseachers have worked on this problem as opposed to the myriad that have worked on unstructured grids. Consequently, there is is less available software for overset structured grids.

The other criticism is that in most simulations of complex flows the solutions on the overset grids are merged using simple interpolation. The fact that interpolation is generally used to connect grids implies that conservation is not strictly enforced. For most practical applications it is difficult to devise a situation where this error is overall-significant since conservation is strictly maintained at all points in the domain (assuming the solver is a conservative one) except at a small number of interface boundaries. Nevertheless, this source of error has to be eliminated, and conservative interface schemes for overset grids have been devised[23,27]. Refinement and simplification of these techniques are still warranted for use with three dimensional flow solvers, however.

In the remainder of this paper, a brief review of the chimera scheme is given, and a few results from previously presented space shuttle flow field simulations are used to indicate current status. Some possible future directions for the chimera scheme are then indicted, followed by concluding remarks.

BACKGROUND AND PROGRESS

The chimera composite grid discretization method is a domain decomposition approach which uses overset body-conforming grids. In this approach, each component of a configuration is grided separately and is overset onto a major grid to form the complete model. The major grid is stretched over the entire field, and is often generated about a dominant boundary or body surface. Minor grids are used to resolve features of the geometry or flow that are not adequately resolved by the major grid, and are overset on the major grid without requiring mesh boundaries to join regularly.

For example, Fig. 1 shows surface grids generated for the integrated space shuttle configuration in its ascent mode. The configuration shown has simplified attach hardware, and various protuberances such as the external fuel lines and even the orbiter vertical tail have been neglected. A grid is then independently generated about each component. A composite grid is then formed by superimposing all grids together. The body-conforming grids used for each component are shown in Fig. 2 at their respective planes of symmetry. Here the external tank (ET) grid is treated as the major grid and is extended to the far field. Figure 3 shows nearby ξ = constant planes for the orbiter and ET projected onto an x=constant plane. Whenever points of a grid, say grid 1, fall within the body-boundary of another grid, say grid 2, the points of grid 1 are cut out forming a hole in grid 1. The hole-boundary data of grid 1 are then supplied from grid 2. Hole grid points have been removed from view in Fig. 3.

Software to interconnect the grids is needed to ascertain when points of one grid fall within a body boundary of another (grid hole points) and to supply pointers so that one grid can provide boundary data to another. Various algorithms have been devised for performing these tasks automatically [4,8,14-16,20,29]. For the illustrated shuttle grids, the code Pegasus [8,14,16,29] (provided and maintained by CALSPAN of AEDC) has been used. General software for this problem has also been developed in [20] and includes an interactive workstation demonstrator for two dimensional grids.

A flow simulation code developed for a single general curvilinear grid can be readily adapted for composite overset grids. One simply sets flags to blank out hole points and supplies a control program that calls in grids and interface routines. For example, the structured-grid, implicit, approximately-factored F3D scheme [32,33] for the thin-layer Navier-Stokes equations

$$\partial_\tau \hat{Q} + \partial_\xi \hat{F} + \partial_\eta \hat{G} + \partial_\zeta \hat{H} = Re^{-1} \partial_\zeta \hat{S} \tag{1}$$

was easily modified for chimera overset grids as

$$\begin{aligned} &\left[I + i_b h \delta_\xi^b (\hat{A}^+)^n + i_b h \delta_\zeta \hat{C}^n - i_b h Re^{-1} \bar{\delta}_\zeta J^{-1} \hat{M}^n J - i_b h D_i|_\zeta\right] \\ &\times \left[I + i_b h \delta_\xi^f (\hat{A}^-)^n + i_b h \delta_\eta \hat{B}^n - i_b h D_i|_\eta\right] \Delta \hat{Q}^n = \\ &- i_b \Delta t \{\delta_\xi^b (\hat{F}^+)^n + \delta_\xi^f (\hat{F}^-)^n + \delta_\eta \hat{G}^n + \delta_\zeta \hat{H}^n - Re^{-1} \bar{\delta}_\zeta \hat{S}^n + (D_e|_\eta + D_e|_\zeta) \hat{Q}^n\} \end{aligned} \tag{2}$$

Here introduction of the flag i_b accommodates the possibility of having arbitrary holes in the grid. (The hole includes hole-boundary points which are later updated by interpolating the solution from the overset grid which created the hole.) The array of values i_b is defined such that $i_b = 1$ at normal grid points and $i_b = 0$ at hole points. Thus, in Eq. (2) when $i_b = 1$ the normal scheme

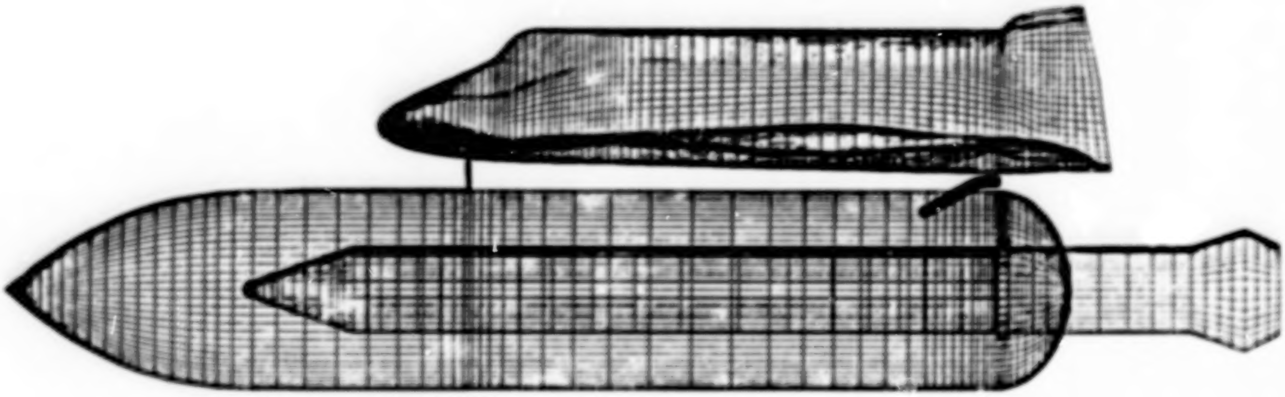

Fig. 1 Simplified configuration and surface grid point distributions for the integrated space shuttle.

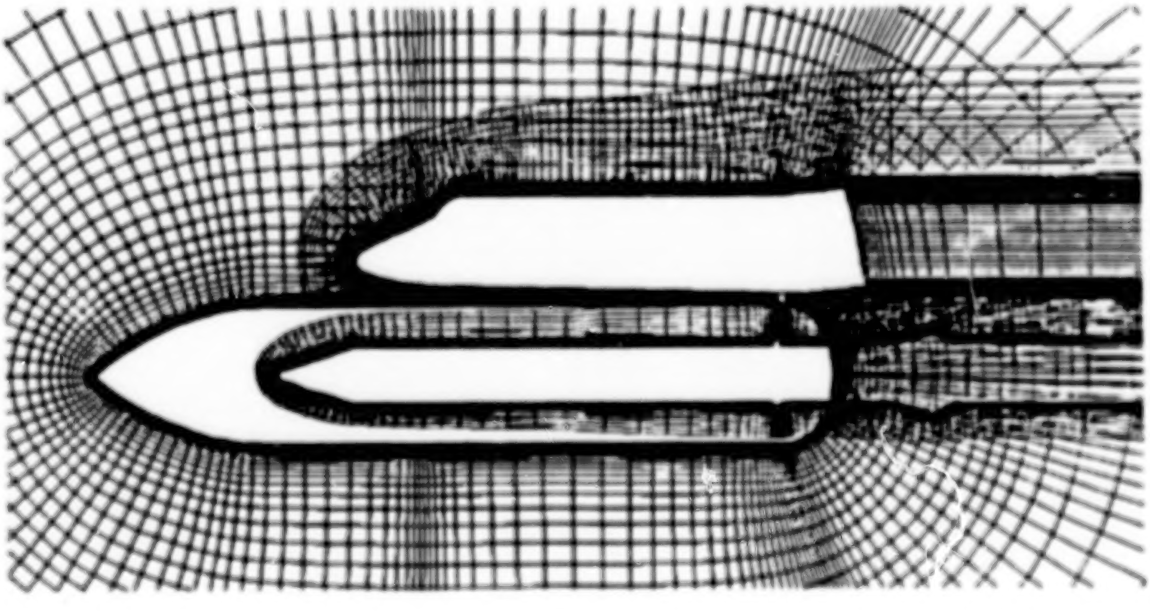

Fig. 2 Symmetry planes of all grids.

is maintained, but when $i_b = 0$ the scheme reduces to $\Delta\hat{Q}^n = 0$ or $\hat{Q}^{n+1} = \hat{Q}^n$ and thus $\hat{Q}$ is not changed at a hole point. For the most part i_b is coupled to the time step ($h = \Delta t$ or $(\Delta t)/2$) and is trivial to implement into the coding. (Difference operators that use more than one point to either side require some additional coding modification, see Ref. [24]) By using the i_b array it is not necessary to provide branching logic to avoid hole points, and computer vectorization is not inhibited.

The F3D algorithm was implemented on composite grids by writing a control program which at each "time step" fetched a grid and its data from an isolated large memory into a working memory. Boundary interface arrays that store grid interconnect data, Q_{BC}, are also fetched. The Q_{BC} array holds overset-grid boundary values for the current grid which are supplied from the other grids and is a relatively small array. Because the hole boundaries are arbitrarily located, the Q_{BC} array has pointers much like those used with unstructured grids. The solution on the current grid is then updated or advanced in time. Overset boundary data that the current grid sends to other grids are then found by interpolation and loaded into Q_{BC}, and all arrays are sent back to the isolated large memory. The next grid is then fetched, and so on.

To illustrate this capability, calculated results for the integrated space shuttle vehicle are taken from Refs. [24,25] and are reproduced in Figs. 4 and 5. These figures show comparisons between computational and experimental data for $M_\infty = 1.05$ at an angle of attack, $\alpha = -3°$, and using the wind tunnel Reynolds number $Re = 4.0 \times 10^6$/ft for the computations. Shaded surface pressure coefficient comparisons between the computation and wind tunnel data [34] are shown by Fig. 4. This kind of comparison is possible because the 3% scale wind tunnel model was instrumented with 1538 pressure taps. Mach contours in planes of symmetry of the ET and solid rocket booster (SRB) are also shown in Fig. 4, and are used to highlight the SRB plume which was modeled as a hot-air jet. A limited amount of flight test data [35] are also available for comparison, and Fig. 5 shows pressure comparisons between computation, flight, and wind tunnel data taken along the side of the fuselage. This computation required about 15 hours of computer time using a single processor of the CRAY 2, and employed a composite grid containing one million points distributed over seven distinct grids. Additional details of the experimental comparisons (and some disclaimers) are given in Refs.[24,25].

With the composite overset grid approach it is possible to move one body with respect to another without regriding at each time step advance of the flow field. Demonstration of this capability for SRB staging from the shuttle is presented in Ref. [26] .

FUTURE DIRECTIONS

As noted previously, two main criticisms can be leveled against the chimera approach: 1) the complexity of the interconnectivity is perhaps as difficult as dealing with an unstructured grid, and 2) nonconservative interpolations to update interface boundaries are often used in practical three dimensional computations. To indicate the complexity of the interconnectivity, it should be remarked that some of the attach-hardware used in the space shuttle simulations is not actually attached. The attach-hardware was floated between the body elements. This is because the algorithms devised to impose grid connectivity are not accurate enough when the refined grids used for

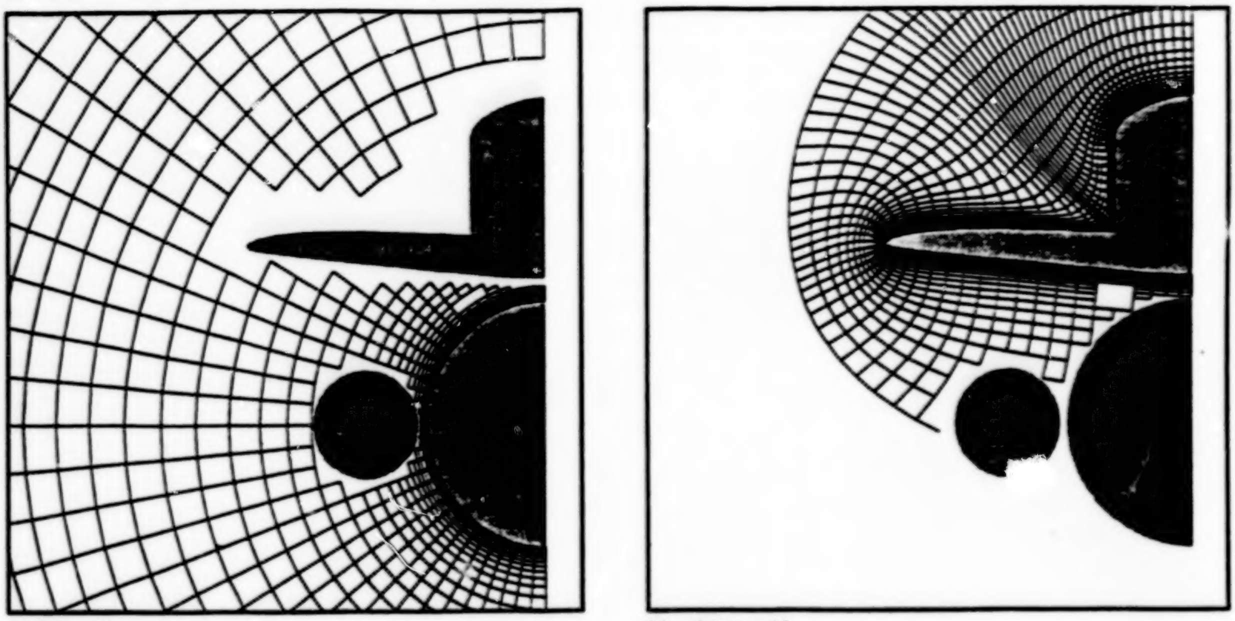

a) ET grid

b) orbiter grid

Fig. 3 Cross-section of grids showing holes, a)ET grid, b)Orbiter grid.

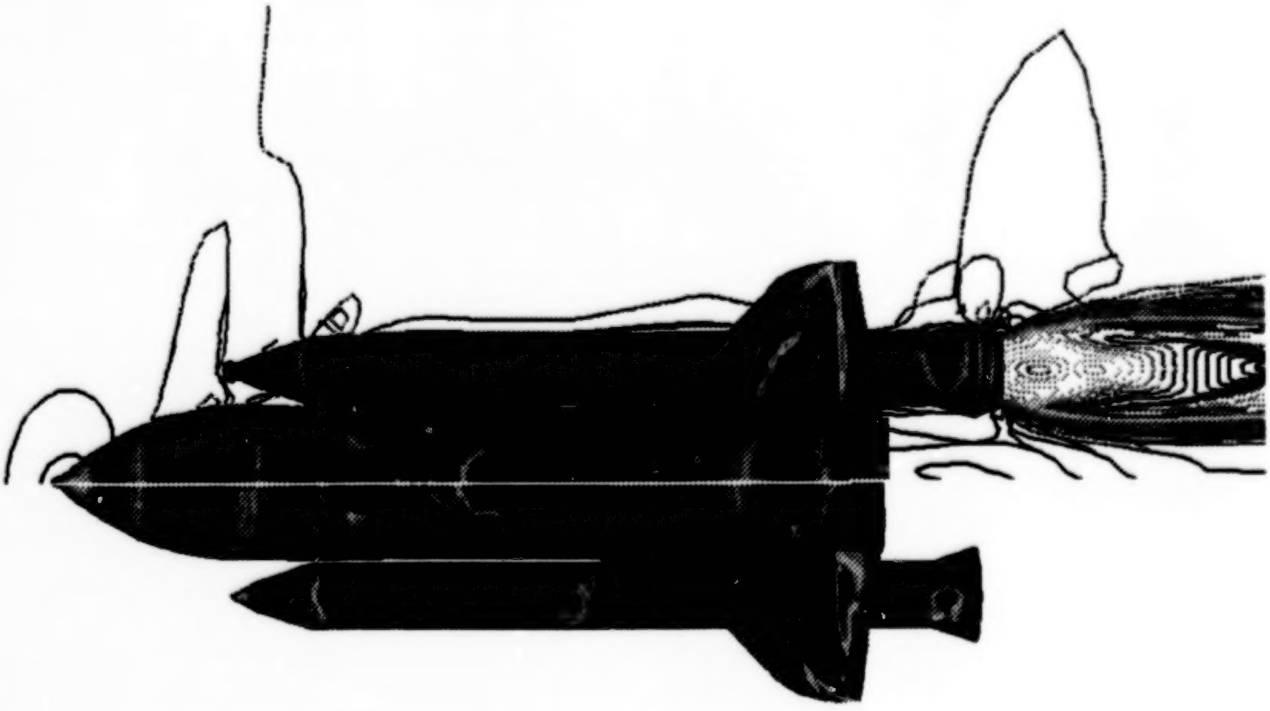

Fig. 4 Comparison of pressure coefficient between computation (top) and wind tunnel (bottom), $M_\infty = 1.05$, $\alpha = -3°$, and $Re = 4.0 \times 10^6/ft$ (3% model).

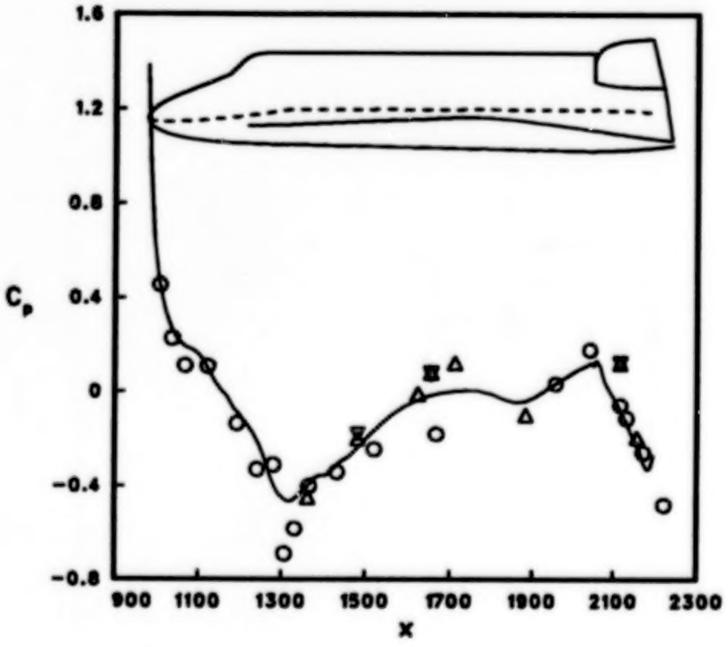

Fig. 5 Comparison of C_p from computation (–), wind tunnel (o), and flight test (∇ right side, Δ left side) along the $\phi = 70°$ line of the orbiter fuselage, $M_\infty = 1.05$ and $\alpha = -3°$, $Re = 4.0 \times 10^6/ft$, and 10°/9° elevon deflection.

high Reynolds number viscous flow simulation are encountered. Because the normal grid spacing is so fine, small errors in interpolation for the body surface can cause the test which identifies when points lie inside a another body surface to fail. Specifically, two viscous boundary layer grids emanating off the same surface cannot fall within that surface, yet due to the fineness of the grids, a viscous flow field point above the surface of one grid may be judged to be inside the same body surface of another grid because of interpolation error. Special logic can be used to exclude this case, and the problem is not encountered for inviscid simulations. There are a variety of ways to deal with this problem, they include more consistent interpolation schemes, introducing special viscous surface grids, alternate tests, and so on, but current software is inadequate and needs refinement.

Several approaches have been proposed to treat the problem of nonconservative interfaces, but they have not been implemented into the F3D code. It should be remarked that while the space shuttle simulations have used simple interpolation procedures because of their robustness, CALSPAN simulations for the last several years[16-18,28,29] have implemented an unpublished idea of Benek and use interpolants of delta quantities, specifically, $\hat{Q}^{n+1} - \hat{Q}^n$. Interpolating this quantity on interface boundaries ensures space-time conservation over the global field, but the ultility (or penalty) of this approach has not yet been rigourously examined.

A fairly obvious way to ensure interface conservation would be to introduce an unstructured flow solver in the vicinity of the interface boundaries. Already in chimera, primitive elements of an unstructured grid solver exist in the form of pointers and grid interfacing arrays which transfer interpolated values of the solution from one grid to the next. Some care would have to be taken, but an explicit differencing of the governing equations using unstructured data could substitute for the interpolation process. The chimera would then mimick a hybrid structure-unstructured approach much as in Refs. [1-3].

Finally, the chimera framework lends itself to the construction of a general-purpose flow code that can optionally take advantage of approximate solution methods, and some preliminary work has been carried out in this area. For example, the F3D flow simulation code used for the previously described shuttle work already has options (at various levels of maturity) to use either explicit or implicit solution algorithms as well as a semimarching scheme for predominately steady supersonic flow. In addition, a fortified option [36] of the basic algorithm is available. To support this option and to provide diagnostics of Navier-Stokes solution accuracy, a three-dimensional boundary-layer code in arbitrary general coordinates has also been included.

CONCLUDING REMARKS

Overset grid schemes such as chimera grew out of efforts to adapt body conforming structured grid methods to more complex boundaries. Although these schemes have not received the attention that unstructured (or patched) grid methods have received, they have proven to be competitive, and are likely to prove to be more powerful. Incorporation of unstructured grids into the overall chimera framework is quite feasible, and offers a relatively low risk route to a hybrid structured-unstructured simulation code as well as a fall back position in the (unlikely) event that chimera does not live up to its expectations.

REFERENCES

1. Nakahashi, K., " FDM-FEM Zonal Approach for Computations of Compressible Viscous Flows". 10th International Conference on Numerical Methods in Fluid Dynamics. Beijing, China, June, (1986).

2. Nakahashi, K. and Obayashi, S., "Viscous Flow Computations Using a Composite Grid", AIAA Paper No. 87-1128-CP, AIAA 8th Computational Fluid Dynamics Conference, (1987).

3. Weatherill, N. P., "On the Combination of Structured-Unstructured Meshes", in *Numerical Grid Generation in Computational Fluid Dynamics*, S. Sengupta, ed., Pineridge Press, (1988).

4. Steger, J. L., Dougherty, F. C., and Benek, J. A., "A Chimera Grid Scheme", in Advances in Grid Generation, K.N. Ghia and U. Chia, eds., ASME FED-5, 59-69, (1983).

5. Starius, G., "Composite Mesh Difference Methods for Elliptic and Boundary Value Problems", Numeri. Math. Vol. 28, (1977).

6. Atta, E. H., "Component Adaptive Grid Interfacing". AIAA Paper 81-0382, (1981).

7. Atta, E. H. and Vadyak, J. A., "A Grid Interfacing Zonal Algorithm for Three-Dimensional Transonic Flows about Aircraft Configurations". AIAA Paper 82-1017, (1982).

8. Benek, J. A., Buning, P. G., and Steger, J. L., "A 3-D Grid Embedding Technique", AIAA Paper No. 85-1523, (1985).

9. Eberhardt, D. S., "Overset Grids in Compressible Flow", AIAA Paper 81-0382, (1985).

10. Dougherty, F. C., Benek, J. A., and Steger, J. L., "On Application of Chimera Grid Scheme to Store Separation", NASA TM 88193, (1985).

11. Henshaw, W. D., "Part I: The Numerical Solution of Hyperbolic Systems of Conservation Laws; Part II: Composite Overlapping Grid Techniques", Ph.D. thesis, California Institute of Technology, (1985).

12. Chesshire, G., "Composite Grid Construction and Applications", Ph.D. thesis, California Institute of Technology, (1986).

13. Lombard, C.K.; and Venkatapathy, E., "Implicit Boundary Treatment for Joined and Disjoint Patched Mesh Systems". AIAA Paper 85-1503-CP, (1985).

14. Benek, J. A., Steger, J. L., Dougherty, F. C. and Buning P. G., "Chimera: A Grid Embedding Technique", AEDC-TR-85-64, Arnold Air Force Station, TN, (1986).

15. Steger, J. L. and Benek, J. A., "On the Use of Composite Grid Schemes in Computational Aerodynamics", Comp. Methods Appl. Mech. and Eng., vol. 64, nos. 1-3, (1987).

16. Benek, J. A., Donegan, T. L., and Suhs, N. E., "Extended Chimera Grid Embedding Scheme with Application to Viscous Flows'. AIAA-87-1126-CP, (1987).

17. Suhs, N. E., "Computations of Three-Dimensional Cavity Flow at Subsonic and Supersonic Mach Numbers", AIAA 87-1208, (1987).

18. Donegan, T. L., Benek, J. A., and Erickson, J. C., "Calculation of Transonic Wall Interference", AIAA 87-1432, (1987).

19. Van Dalsem, W. R., Panaras, A. G., and Steger, J. L., "Numerical Investigation of a Jet in Ground Effect with a Crossflow", SAE 872344, from P-203 – Proceedings of the International Powered Lift Conference, Santa Clara, CA. (1987).

20. Brown, D. L., Chesshire, G., and Henshaw, W. D., "Getting Started With CMPGRD", Center for Computational Mathematics and Mechanics, The Royal Institute of Technology, S-100 44 Stockholm, Sweden, (1988).

21. Berger, M.J., "Adaptive Mesh Refinements for Hyperbolic Partial Differential Equations", STAN-CS-82-924, Stanford University, (1982).
22. Berger, M.J. and Oliger, J., "Adaptive Mesh Refinements for Hyperbolic Partial Differential Equations", J. Comp. Physics, Vol. 53, (1987).
23. Berger, M.J., "On Conservation at Grid Interfaces", ICASE Report 84-43, NASA Langley Research Center, Hampton, Virginia, (1984).
24. NASA Ames Space Shuttle Flow Simulation Group: P. G. Buning, I. T. Chiu, S. Obayashi, Y. M. Rizk, and J. L. Steger, "Numerical Simulation of the Integrated Space Shuttle Vehicle in Ascent", AIAA Atmospheric Flight Mechanics Conference, Minneapolis, (1988).
25. NASA Ames Space Shuttle Flow Simulation Group: P. G. Buning, I. T. Chiu, F. W. Martin Jr., R. L. Meakin, S. Obayashi, Y. M. Rizk, J. L. Steger, and M. Yarrow, "Flowfield Simulation of the Space Shuttle Vehicle in Ascent", Proceedings of the Fourth International Conference on Supercomputing, Santa Clara, CA, (1989).
26. Meakin, R. L. and Suhs, N., "Unsteady Aerodynamic Simulation of Multiple Bodies in Relative Motion", AIAA 9th Computational Fluid Dynamics Conference to be held at Buffalo, NY, (1989).
27. Moon, Y. J. and Liou, M.-S., "Conservative Treatment of Boundary Interfaces for Overlain Grids and Multi-level Grid Adaptations", AIAA Paper 89-1980-CP, (1989).
28. Fox, J. and Allee, E., "Experimental/Computational Study of a Transonic Aircraft with Stores". AIAA Paper 89-1832, (1989).
29. Dietz, W. E., Jacocks, J. L., and Fox, J. H., "Application of Domain Decomposition to the Analysis of Complex Aerodynamic Configurations", SIAM Conference on Domain Decomposition Methods, Houston, TX, (1989).
30. Steger, J. L. and Rizk, Y. M., "Generation of Three Dimensional Body-Fitted Coordinates Using Hyperbolic Partial Differential Equations". NASA TM 86753, (1985).
31. Eisenman, P. R. and Erlebacher, G., "Grid Generation for the Solution of Partial Differential Equations", ICASE Report No. 87-57,(1987).
32. Ying, S. X., Steger, J. L., Schiff, L. B., and Baganoff, D., "Numerical Simulation of Unsteady, Viscous, High Angle of Attack Flows Using a Partially Flux-Split Algorithm". AIAA Paper No. 86-2179, (1986).
33. Steger, J. L., Ying, S. X., and Schiff, L.B., "A Partially Flux-Split Algorithm for Numerical Simulation of Compressible Inviscid and Viscous Flow". *Proceedings of the Workshop on Computational Fluid Dynamics*, Institute of Nonlinear Sciences, U. Calif., Davis, (1986).
34. Spangler, R. H., "Results of Tests Using a 0.03 Scale Model (47-OTS) of the Space Shuttle Integrated Vehicle in the AEDC 16 Foot Transonic Propulsion Wind Tunnel (IA105A)", NASA CR 160851, Vol.2, (1981).
35. Rockwell International Internal Letter SAS/AERO/83-094, "STS-5 Postflight Report on Ascent External Aerodynamic Loads", March (1983).
36. Van Dalsem, W. R. and Steger, J. L., "Using the Boundary-Layer Equations in Three-Dimensional Viscous Flow Simulation", AGARD Conference Proceedings No. 412, Aix-en-Provence, France, (1986).

GENERATION AND USE OF UNSTRUCTURED GRIDS FOR TURBOMACHINERY CALCULATIONS

Dana R. Lindquist
Michael B. Giles
Massachusetts Institute of Technology
Cambridge, MA 02139

ABSTRACT

This paper presents a wavefront mesh generator for two dimensional triangular meshes as well as a brief description of the solution method used with these meshes. The interest is in creating meshes for solving the equations of fluid mechanics in complex turbomachinery problems, although the mesh generator and flow solver may be used for a larger variety of applications. The focus is on the flexibility and power of the mesh generation method for triangulating extremely complex geometries and in changing the geometry to create a new mesh. Two turbomachinery applications are presented which take advantage of this method: the analysis of pylon/strut and pylon/OGV interaction in the bypass of a turbofan.

MESH GENERATOR

In recent years the use of unstructured triangular meshes in computational fluid dynamics has grown in popularity. The main reason for going to triangular cells is the ability to compute the flowfield around complex geometries since in these cases it is easier to create a triangular mesh than a quadrilateral mesh, if a quadrilateral mesh can even be created. The first question that one encounters when deciding to work with triangles is how to create the mesh. This paper presents a mesh generator which was originally based on the work of Lo [1] and extended by Peraire et al [2,3]. The method works by advancing a front through the domain to be triangulated, creating points as they are needed. The result is a very powerful and flexible mesh generator.

The computational domain is specified as a number of closed objects inside an outer boundary. Each of these curves are defined as piecewise cubic splines based on a set of points given by the user. These boundaries are divided into segments which represent a node distribution on the boundary and compose the initial front. This front then moves into the domain to be triangulated, creating triangles as it goes. A new triangle is made up of two nodes on the front and either a newly created node or another node on the front. The front moves inward until it totally collapses in on itself. An example of the process is shown in Figure 1 where the wave front is denoted by the darker line.

For the mesh generator to determine the size of the triangles throughout the region, a desired mesh size must be given for each point in the triangulated region. Here this is done by creating a background mesh of large triangles with mesh parameters given at the nodes. A general point in the region will lie inside a background mesh triangle, and the local mesh parameters are found by a linear interpolation of the values at the background nodes.

Some less desirable triangles can be created by the process, for example where the front finally collapses, therefore the final mesh is smoothed. The smoothing of the final grid is done in two steps. First, the triangulation is made to conform to the rules for a Delaunay mesh. This is done by examining all sets of two adjacent triangles. The face between the triangles is rotated if the current face location is on the longer diagonal as shown in Figure 2. Next the nodes are displaced slightly so the mesh is relaxed. The new location of a node is given by

$$x_i^{new} = x_i + \frac{\omega}{n}\sum_{k=1}^{n}(x_k - x_i) \qquad (1)$$

where i is the node to be smoothed and the sum is over the n nodes surrounding node i. A value of $\omega = 0.3$ is used for the relaxation factor. The combination of these two steps in smoothing the grid is quite effective in eliminating any undesirable cells as can be seen in Figure 1.

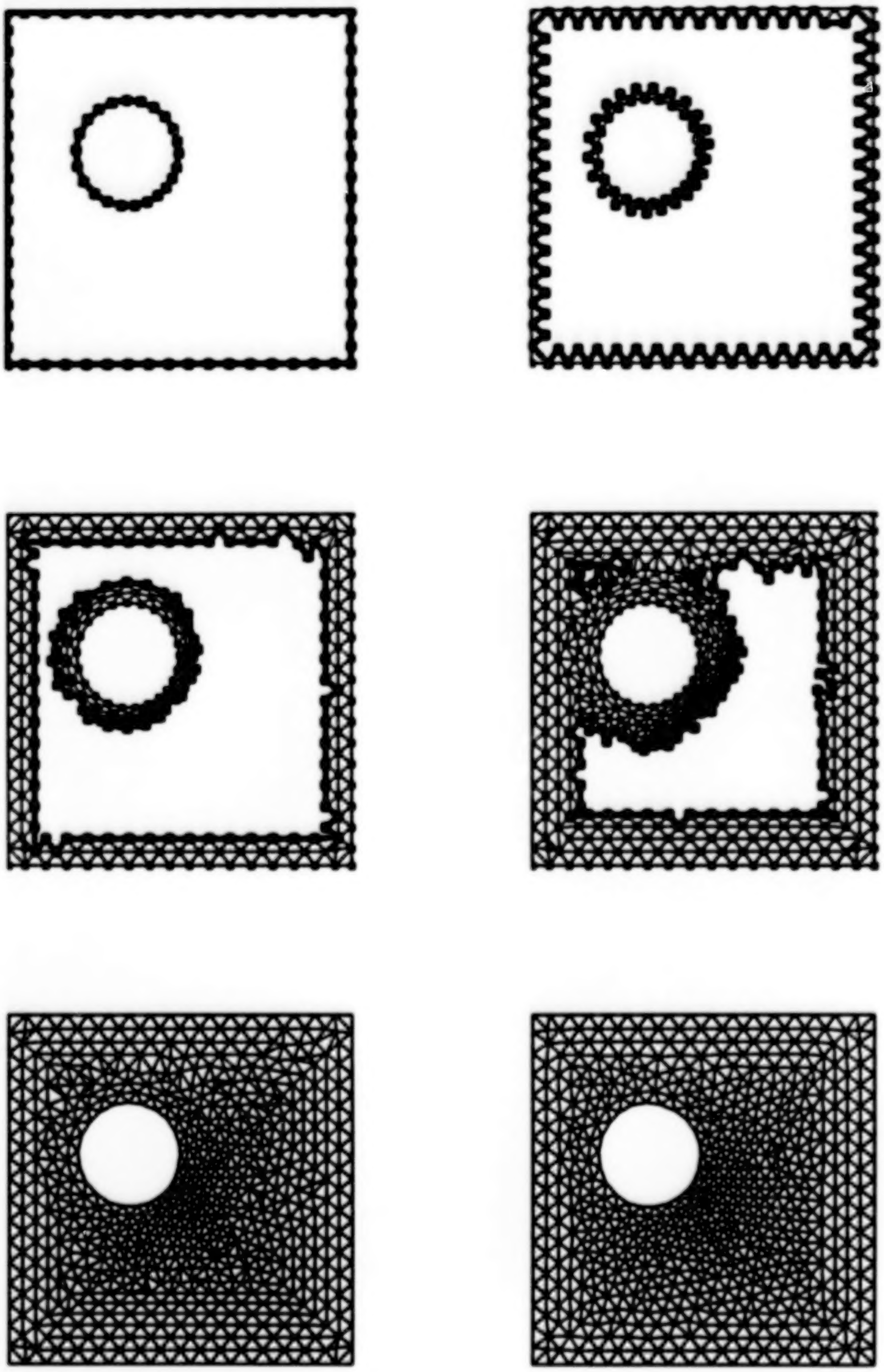

before smoothing

after smoothing

Figure 1: Mesh at various stages in the advancing front method.

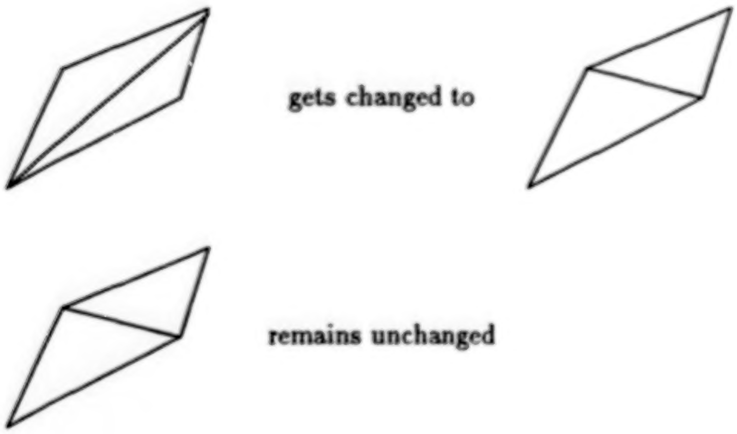

Figure 2: Mesh smoothing to create Delaunay triangulation.

The focus of the discussion here will be on the flexibility and power in generating grids for extremely complex geometries with very little user time required in the definition of the problem. Interested readers are referred to the papers by Peraire et al [2,3] for a discussion on the exact algorithm for front advancement. It would suffice to say that the 2D mesh generator consists of over 3000 lines of code of which most involve conditional statements. The only part of the code which will vectorize is a few lines involving a search. Peraire et al [4] have successfully extended this method to three dimensions. The biggest difficulty from a user interface point of view in three dimensions is setting up a background mesh size distribution. Instead of using a background mesh, some other method which defines the distribution on the boundaries and smooths it through the region could be used.

To illustrate the ease of creating a mesh, the specifics involved in creating the mesh in Figure 1 will be shown as an example. As previously stated, the outer boundary of the domain and the objects inside the domain are specified by the user as a set of point which define a closed curve. Two other files are required, one which describes the orientation of the objects and another which describes the background mesh.

Objects:

Here, two objects are used: a square which is defined from $x = -1, 1$ and $y = -1, 1$, and a circle with center at the origin and radius 1. The points defining these objects are in files OBJECT.SQUARE and OBJECT.CIRCLE respectively.

The object files contain additional information about the type of boundary condition to be applied to segments of the boundary. The boundary condition could correspond to an inlet, outlet, solid wall or a set of periodic surfaces.

Orientation:

The file FGRID.SQUARE is shown below along with the geometry for the problem. This file describes the orientation of the objects in the domain. The several lines of the file are:

Line 1: title for the mesh

Line 2: name of the object file which in this case is OBJECT.SQUARE

Line 3: tells whether the mesh will be created inside or outside the object where a positive number means the mesh is inside

Line 4: four real values which give the factor by which the data is scaled, the angle by which the data is rotated about the origin in the data, and the amount in the x and y directions by which the data is translated

Last 3 lines: the same kind of information given above about the data in file OBJECT.CIRCLE

FGRID.SQUARE

```
circle inside a square
OBJECT.SQUARE
1
1. 0. 0. 0.
OBJECT.CIRCLE
-1
0.3 0. -.3 .2
```

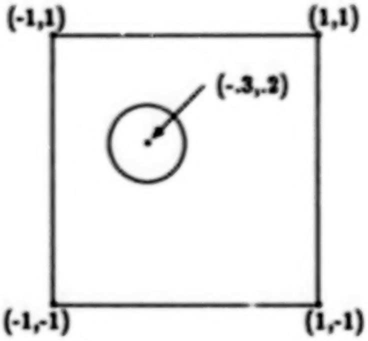

It is clear that objects can be easily rotated, scaled and placed anywhere in the domain. This means it is easy to change the location of an object or drop another object into the domain.

Background:

The information about the background mesh for this case is given in file BACK.SQUARE which is shown below. This file has information giving the node locations and the mesh parameters at the nodes as well as the way the nodes are connected to create a mesh. The several lines of the file are:

Line 1: number of nodes in the background mesh which in this case it 5

Next 5 lines: each node is given a consecutive numbers from the top of the list and has three real values which give the x and y locations of the nodes and the desired standard length of the cell

Line 7: number of cells in the background mesh which in this case is 4

Next 4 lines: each line contains the three node numbers listed counter-clockwise which make up the background cells

BACK.SQUARE

```
 5
-1.  -1.   .1
 1.  -1.   .1
 1.   1.   .1
-1.   1.   .1
 0.   0.   .05
 4
 1    2    5
 2    3    5
 3    4    5
 4    1    5
```

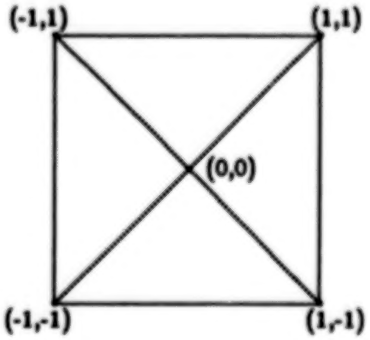

The current version of the code requires the user to set up the background mesh by hand. This turns out to be a little tedious when a complicated mesh size distribution is desired. In the future an interactive method of creating the background mesh will be created where the user can place and move points using a mouse and connect these points again using a mouse.

A few other examples of meshes created using this method are shown in Figures 3 and 4. In Figure 3 a very unusual mesh was created. The point which should be most emphasized in connection with this example is that once the object files were created for the letters C, F and D, it was a simple matter to get the mesh. In Figure 4 a more standard mesh was created about a T7 turbine blade. The background mesh is shown to illustrate how course a background mesh can be to get a realistic cell size distribution. It can be seen that resolution is obtained around the leading edge where it is needed, but the cells are coarser in the rest of the region.

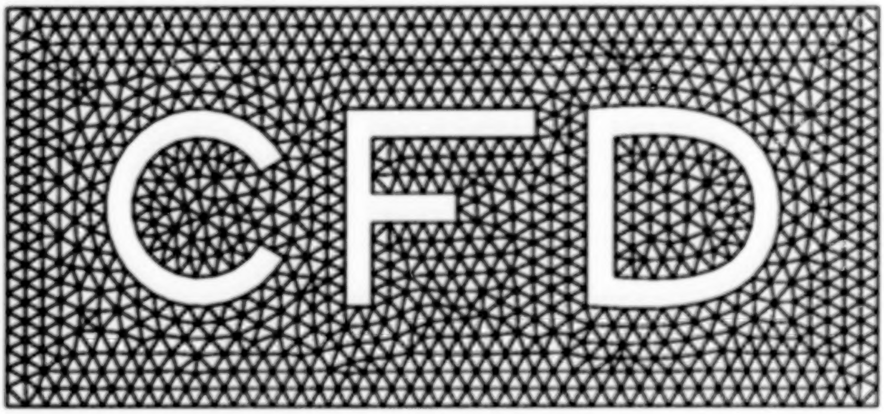

Figure 3: Mesh around an unusual configuration.

FLOW SOLVER

The calculations were performed using UNSFLO [5], a Ni-type, Lax-Wendroff, Euler program which has the capability of computing on an unstructured triangular or quadrilateral mesh, or a mesh consisting of a mix of these cell types. The algorithm is fairly straight forward, but the numerical smoothing used has been found to have a large effect on the accuracy of the solution. The dissipative operator which we call numerical smoothing is composed of two parts, a fourth difference operator throughout the flowfield and another operator which is required to capture shocks and other discontinuities. Due to its importance to the accuracy of the solution, the fourth difference operator will be discussed here.

To compute the fourth difference operator, a second difference of a second difference is found. These operators are not necessarily the same, and in UNSFLO they are not. The first is a relatively simple operator which gives a non-zero second difference for a linear function on an irregular mesh. The second operator is more complex, but results in a zero second difference for a linear function. By examining the effect of the second difference operator on a linear function the accuracy of the operator is tested, since for second order or higher accuracy the contribution must be zero.

A typical cell is shown in Figure 5 with corresponding nodes labeled 1, 2 and 3. The operators will be described in terms of a contribution from the cell to one of the nodes. The total contribution to a node comes from all the cells surrounding the node.

The low-accuracy second difference operator is not dependent on the location of the nodes surrounding the node for which the second difference is computed, but merely on the function values at these nodes. For a triangular mesh the contribution from cell A to the second difference at node 1 is

$$(D^2S)_{1A} = (S_3 + S_2 - 2S_1) \tag{2}$$

where S is the variable for which the second difference is computed. This second difference is conservative since the total contribution of each cell to its nodes is zero.

The high-accuracy second difference operator consists of finding the first derivative for each cell and then combining the derivatives on the cells surrounding a node to form a second difference. Unlike the low-accuracy second difference operator, this operator is dependent on the mesh geometry. Referring to Figure 5 the first derivative with respect to x is found for cell A

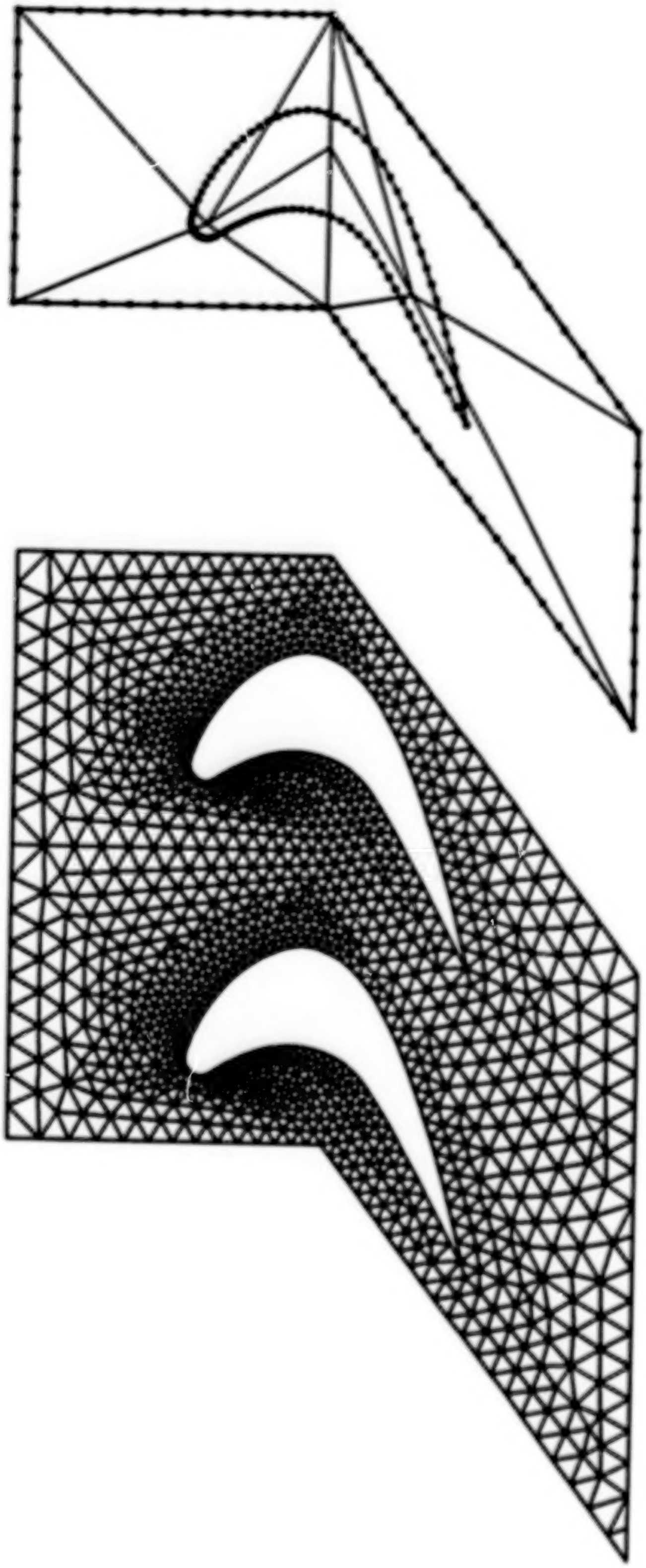

Figure 4: Mesh around T7 turbine blade and background mesh. The mesh contains 1127 cells and 652 nodes.

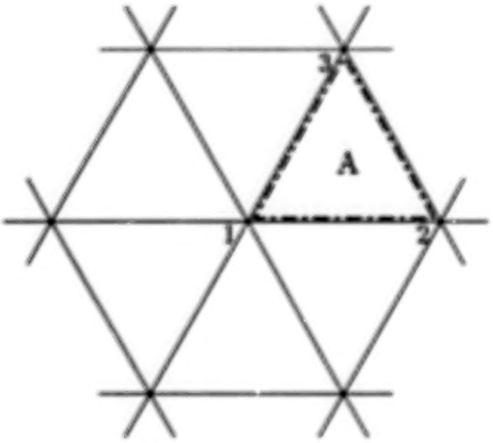

Figure 5: Triangular cell

$$\begin{aligned}(S_x)_A &= \frac{1}{A_A}\iint_{cell\,A}\frac{\partial S}{\partial x}dx\,dy \\ &= \frac{1}{A_A}\int_{1-2-3} S dy \\ &= \frac{1}{2\,A_A}[(S_2+S_1)(y_2-y_1)+(S_3+S_2)(y_3-y_2)+(S_1+S_3)(y_1-y_3)] \qquad (3)\end{aligned}$$

and similarly for the derivative with respect to y. A similar process is performed to create a second difference. The integration is taken around all the triangles which surround the node for which the second difference is computed, using the derivative values calculated at the cells. To get a second difference instead of a second derivative, there is no division by the area of the integrated region. The contribution to the second difference at node 1 from cell A is

$$\begin{aligned}(D^2S)_{1A} &= \int_{2-3}[(S_x)_A dy-(S_y)_A dx] \\ &= (S_x)_A(y_3-y_2)-(S_y)_A(x_3-x_2) \qquad (4)\end{aligned}$$

This second difference operator is conservative since again the total contribution of each cell is zero, but unlike the previous operator it is second order accurate.

On all boundaries, solid wall or farfield, boundary conditions must be implemented for the second difference operators. For the low-accuracy operator the contribution to a node on the boundary is simply the contribution from the cells surrounding that node which are inside the domain as given in Equation (2). The high-accuracy operator involves a line integral in Equation (4) which must be closed when considering a node on the boundary. To do this the integral is continued along the boundary faces on either side of the node in question using the value of (S_x) and (S_y) from the cell directly inside the boundary.

Clearly, to get the fourth difference operator either of these second difference operators could be used. Two methods were examined by Lindquist [6,7]. The first method is to use the low-accuracy second difference twice by operating first on the state vector and then operating on this second difference. This fourth difference is conservative, but is second order accurate only on a uniform mesh since the second difference operator used is only second order accurate on a uniform mesh. The second method is to compute a second difference of the state vector using the high-accuracy method and operate on this second difference with the low-accuracy second difference. This operator is second order accurate since the first operator is second order accurate and conservative since the second operator is conservative.

The second method is more expensive than the first, but the effect per iteration is an increase of only 5-10% which is a small increase for the gain in accuracy. The fourth difference is multiplied by a coefficient, between 0.0001 and 0.01, to control the amount of smoothing which is added to the scheme.

A modification to the high accuracy second difference operator was made by Holmes and Connell [8] which is particularly useful in creating a more accurate operator when the aspect ratio of the cells is high. This modification adds a weighting factor the the operator which is based on the geometry of the mesh.

APPLICATIONS

There are applications in turbomachinery where a standard grid generator is useless. In particular, two problems arise: the grid generator assumes a particular geometry configuration or grid clustering is desired in a specific locality. Two cases will be discussed here which involve both these situations. The problem is the analysis of pylon/strut and pylon/OGV interaction in the bypass of a turbofan. The configuration is clearly complex and high grid resolution is only required around the struts or OGVs, particularly in the leading edge region. In both cases UNSFLO, the solver described in the previous section, was used.

The first application is a pylon/strut interaction. The geometry for this case is similar to that published in Reference [9]. Figure 6 shows the computational domain, which represents the complete bypass annulus unwrapped into a two-dimesnional domain. At the center is the top pylon, and at the top and bottom of the domain are the two surfaces of the bottom pylon plus a section of periodic boundary. The eight struts all have a NACA 0012 profile and are inclined at angles of −10°, 0°, 7°, 20°, −20°, −7°, 0°, 10°, listed from top to bottom. The specification of this geometry required just three files, one describing the outer boundary (the two pylons plus the inflow, outflow and periodic boundaries), one describing a NACA 0012 airfoil of unit chord, and one describing how the full gemoetry is composed from these two files by the appropriate scaling, rotations and translations. To change the inclination of any of the struts requires only a minor change to the last file. Figure 6 also shows the background mesh which is used to control the mesh spacing, as well as the initial grid points on the boundaries. The final mesh shown in Figure 6 has cells which are three times the size used in the computation since the final mesh spacing is quite small, but the blowup if the blade nearest the pylon is of the actual mesh. For obvious reasons, the mesh spacing has been controlled so that the grid is very fine around the struts, particularly their leading edges, and is fairly coarse around the pylons. Overall, this case uses approximately 120,000 cells and 60,000 nodes.

The high stagger angles of the struts was chosen to generate lift such that the lift-related potential field of the struts would approximately cancel the blockage-related potential field of the pylons, and hence reduce the unsteady upstream interaction with the fan. The flow calculation, with the inflow being at zero incidence and $M_\infty = 0.386$ reveals a problem with this approach. Because of the high lift, each of the two struts which are most inclined has a strong normal shock with a peak Mach number of 1.8 just behind the leading edge as shown in Figures 7, 8 and 9. The loss at this shock is so large that the accompanying vorticity leads to an inviscid separation near the trailing edge which is shown in Figure 10. The strong shock loss in this case suggests that it is a better idea to design the struts to be non-lifting, and instead tailor the OGV's, which are just upstream of the struts but are not included in this calculation, to prevent the potential field of the pylons from interacting with the fan.

The second application is a pylon/OGV interaction. The proper geometry in this case has 28 OGV's around the annulus but to reduce the computational cost the calculation was performed with 14 OGV's, maintaining the size and position of the OGV's and the pylon, and therefore doubling the relative blockage effect of the pylon. There are two reasons for presenting this case. The first is that it is another complicated example of unstructured grid generation with good control over grid spacing which varies by over two orders of magnitude. The second reason is that the results of the flow calculation exhibit a self-excited propagating flow instability which greatly ressembles rotating stall. Rotating stall has previously been calculated in two dimensions by a coupled vortex-boundary layer method [10] and by a Navier-Stokes calculation [11]. In the former case a propagating stall cell with large blockage was calculated, whereas in the latter case the blockage was not very severe and could almost be described as an unsteady boundary layer separation rather than a propagating stall. These two computations used five blade passages, which clearly places some restrictions on the stall cell character due to the periodicity constraints. In comparison to these other two calculations, the present calculation is believed to be the first solving the Euler equations which predicts a large stall cell blockage, and uses sufficiently many blade passages that the effect of the periodicity assumption is believed to be minimal.

The flow calculation was begun in a steady-state mode in which the Euler equations are time-marched using local timesteps. This did not converge to a steady-state, but produced results that looked very much like a single rotating stall cell. The computation was then switched into a time-accurate unsteady mode with a constant timestep, and continued until it settled into a periodic solution in which there were two very similar 'stall cells', approximately three blade passages in size. Figure 12 shows contour plots of entropy at four different instants. It clearly shows the high entropy of the 'stalled' fluid and the downward propagation of the 'stall cell'. Figure 13 shows an enlarged view of the 'stall cell' with velocity vectors at each grid point.

Although it must be emphasised that this is an inviscid calculation, the basic unsteady propagation mechanism is very similar to that of a two-dimensional stall cell [12]. As the stall cell approaches a particular vane, the blockage due to the reduced mass flow through the stalled passage causes an increase in the flow incidence on the new vane. This increased incidence leads to a strong normal shock, and the vorticity this produces leads to an inviscid separation. As the incidence increases, the shock strengthens and both the shock and the separation point move forward towards the leading edge until it develops into a leading edge separation with a free shear layer. The transfer of momentum across the shear layer due to numerical smoothing causes the separated fluid to grow into a strong passage. This is the part of the cycle which is probably most incorrectly modelled by the Euler equations; in reality, the retarding viscous force at the blade surface would prevent the growth of such a strong vortex. In the computation the passage vortex grows until it blocks most of the passage. At this time, the passage is near the rear of the rotating stall cell. The blockage due to the other stalled passages now reduces the incidence and supresses the leading edge separation. The flow reattaches at the leading edge and then progressively drives the passge vortex downstream, and the passage returns ultimately to its unstalled state. The ratio of the stall propagation speed to the mean inflow axial velocity is approximately 0.3, a value which is within the range of experimental data for stall propagation.

CONCLUSIONS

The wavefront method of mesh generation has been found to be extremely powerful. It provides a straightforward method of defining the geometry of the computational domain and the ability to easily modify that geometry. The variation of cell size can be specified and changed to fit the current problem. Most of the complexity of the mesh generator is in the code which lets the user concentrate on the current application. Only two dimensional problems are described here, but the method has been successfully extended to three dimensions by Peraire et al [4]. In complicated cases the majority of the user time spent in grid generation is in the specification of the background mesh controlling the grid spacing. It is thought that in three dimensions this may become a problem which deserves attention.

The two applications which are presented demonstrate the ability to analyze complex geometries. The mesh generator and the flow solver for these problems were the same as would be used for a single blade problem. This greatly reduces the need for several flow solvers or grid generation codes. The flowfield solutions provide useful insights into the design of bypass struts and the calculation of rotating stall.

REFERENCES

[1] S. H. Lo, "A New Mesh Generation Scheme for Arbitrary Planar Domains," *International Journal for Numerical Methods in Engineering* Vol. 21, pp. 1403-1426, 1985.

[2] J. Peraire, M. Vahdati, K. Morgan and O. C. Zienkiewicz, "Adaptive Remeshing for Compressible Flow Computations," *Journal of Computational Physics*, Vol. 72, No. 2, October 1987.

[3] J. Peraire, J. Peiro, K. Morgan and O. C. Zienkiewicz, "Finite Element Mesh Generation and Adaptive Procedures for CFD," GAMNI/SMAI Conference on Automated and Adaptive Mesh Generation, October 1-2, 1987.

[4] J. Peraire, J. Peiro, L Formaggia, K. Morgan, O. C. Zienkiewicz, "Finite Element Euler Computations in Three Dimensions," *AIAA 26th Aerospace Sciences Meeting*, AIAA-87-0032, January 1988.

[5] M. B. Giles, "UNSFLO: A Numerical Method For Unsteady Inviscid Flow In Turbomachinery," Technical Report #195, MIT Gas Turbine Laboratory, October 1988.

[6] D.R. Lindquist, "A Comparison of Numerical Schemes on Triangular and Quadrilateral Meshes," SM thesis, Massachusetts Institute of Technology, May 1988.

[7] D. R. Lindquist and M. B. Giles, "A Comparison of Numerical Schemes on Triangular and Quadrilateral Meshes," 11th International Conference on Numerical Methods in Fluid Dynamics, June 1988.

[8] D. G. Holmes and S. D. Connell, "Solution of the 2D Navier-Stokes Equations on Unstructured Adaptive Grids," *Proceedings of the AIAA 9th Computational Fluid Dynamics Conference*, AIAA Paper 89-1932, June 1989.

[9] H. Kodama and S. Nagano, "Potential Pressure Field by Stator/Downstream Strut Interaction," *Journal of Turbomachinery*, Vol 111, pp. 197-203, April 1989.

[10] P. R. Spalart, "Simulation of Rotating Stall by the Vortex Method," *Journal of Propulsion*, Vol. 1, No. 3, pp. 235-241, May-June 1985.

[11] F. Davoudzadeh, N.-S. Liu, S. J. Shamroth and S. J. Thoren, "A Navier-Stokes Study of Rotating Stall in Compressor Cascades," *AIAA/ASME/SAE/ASEE* 24th *Joint Propulsion Conference*, AIAA Paper 88-3265, July 1988.

[12] F. E. Marble, "Propagation of Stall in a Compressor Blade Row," *Journal of the Aeronautical Sciences*, Vol. 22, 1955.

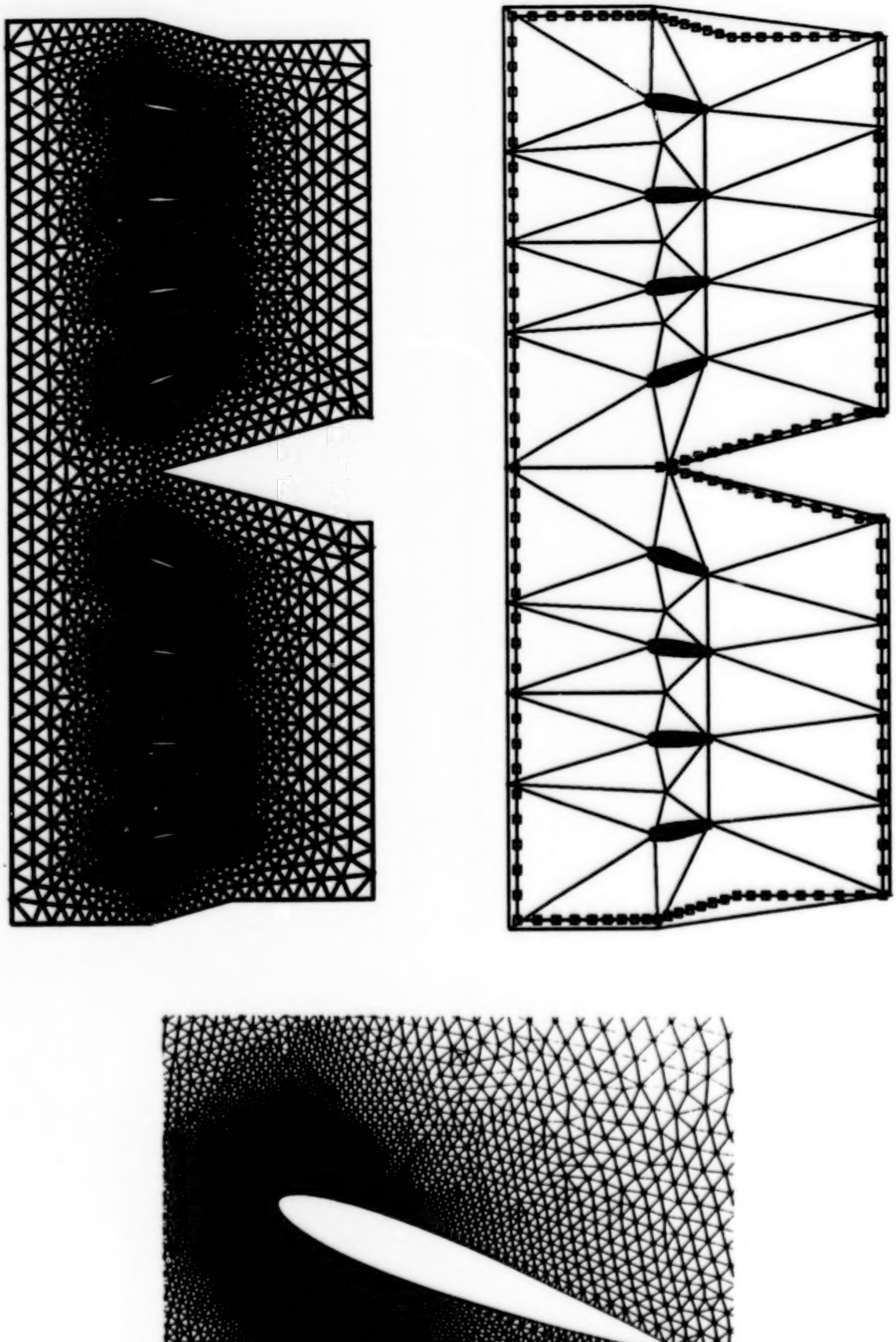

Figure 6: Pylon/strut - Background mesh and the complete mesh with three times the actual mesh cell size and a blowup around one of the blades from the actual mesh.

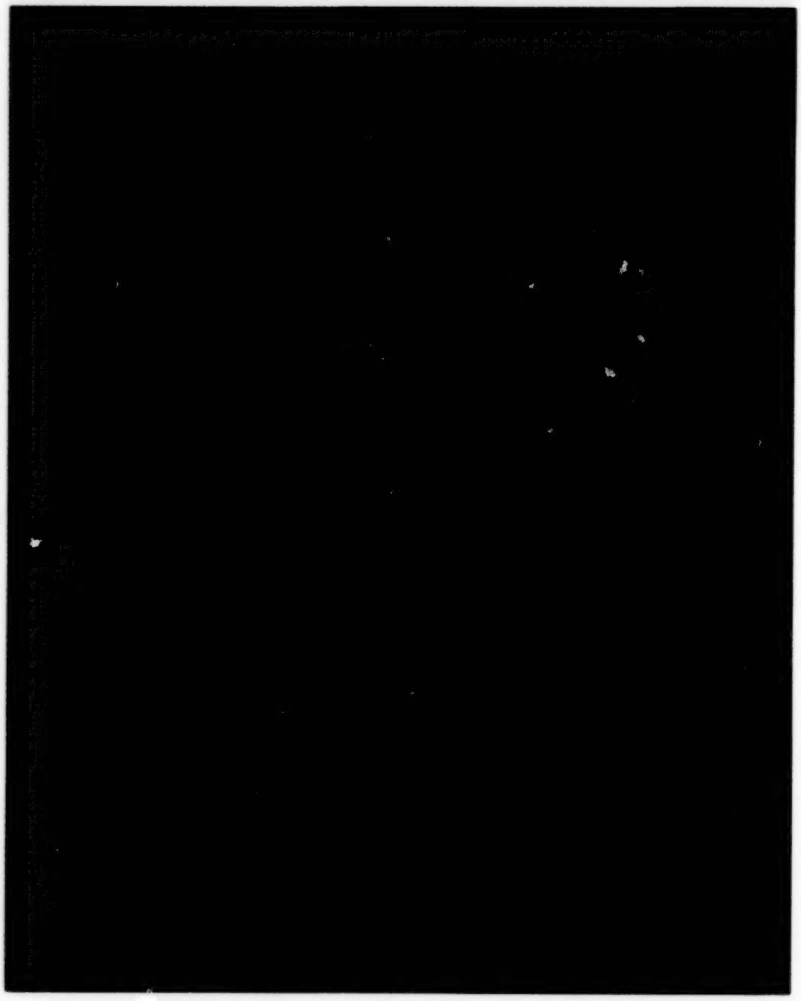

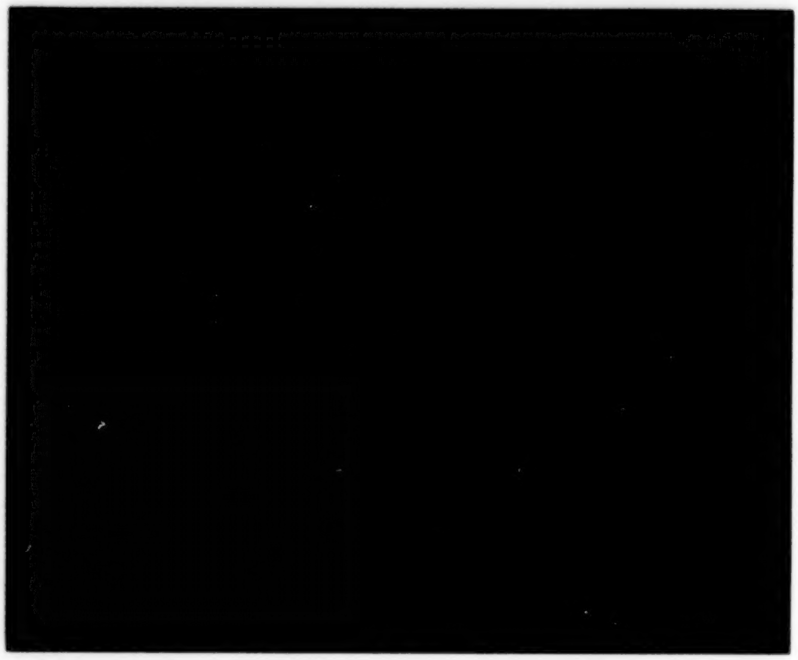

Figure 7: Pylon/strut - Mach number contours with a blowup around the strut nearest the large pylon.

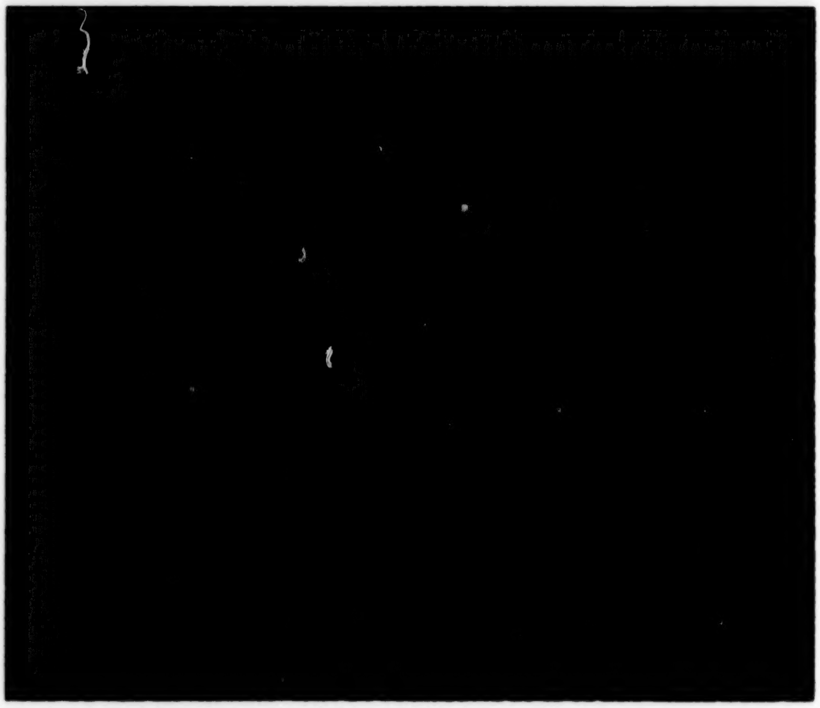

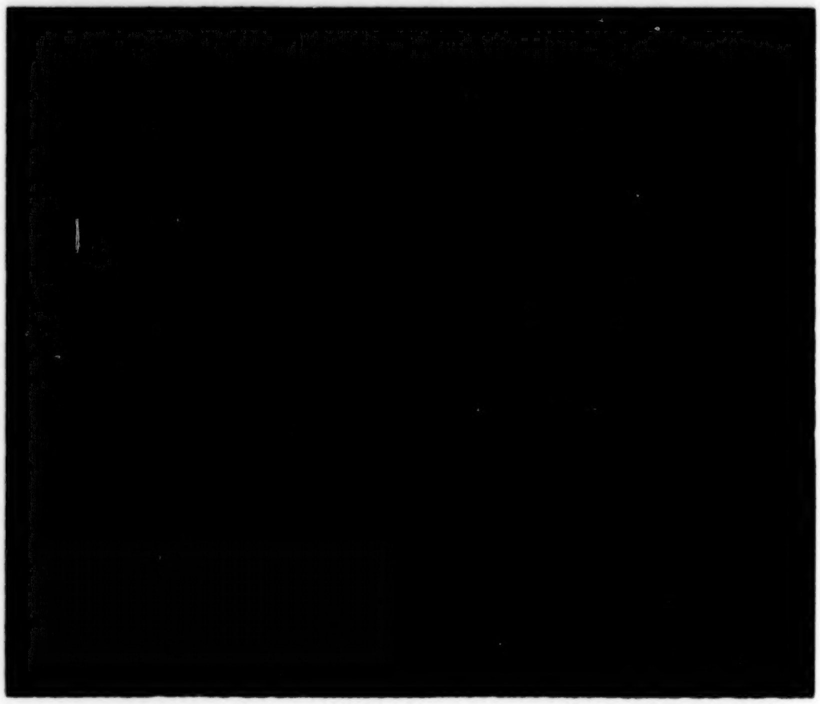

Figure 8: Pylon/strut - Mach number contours and computational grid of blowups around the strut nearest the large pylon.

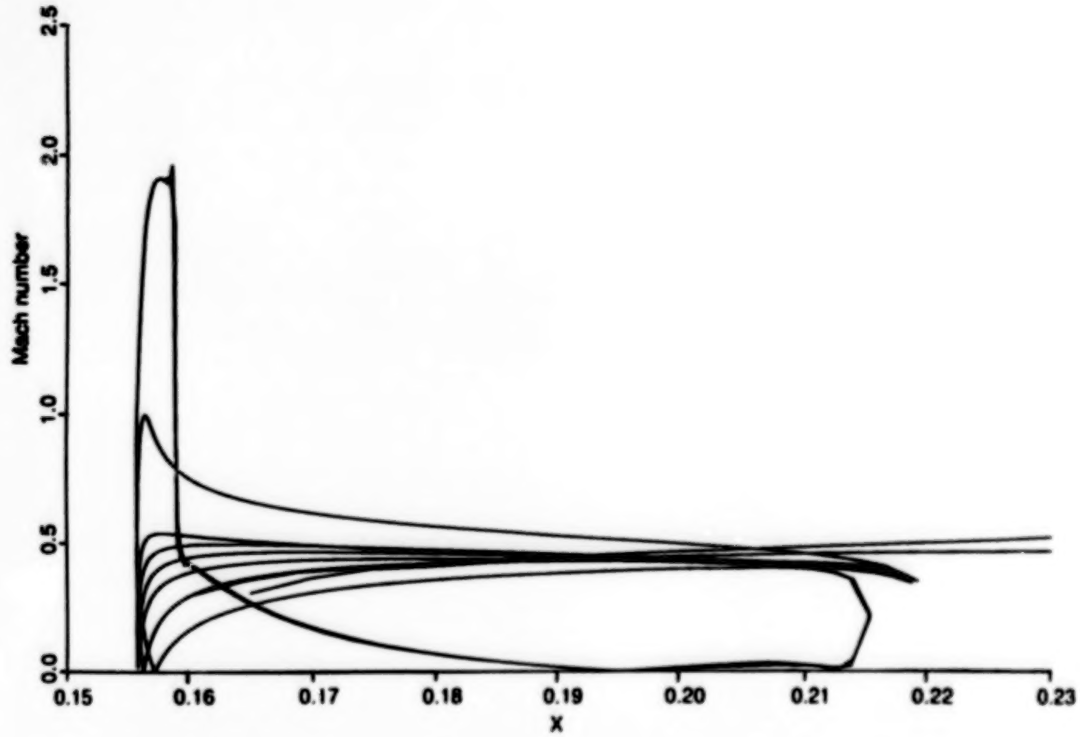

Figure 9: Pylon/strut - Mach number distribution on the pylons and struts.

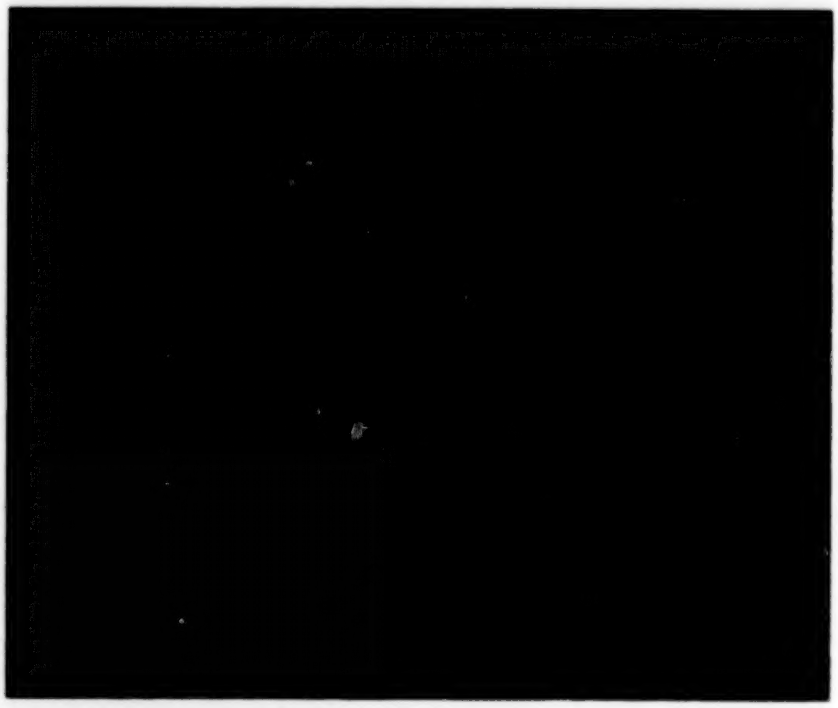

Figure 10: Pylon/strut - Mach number contours and flow vectors showing separation around the trailing edge of the strut nearest the large pylon.

BLANK

PAGE

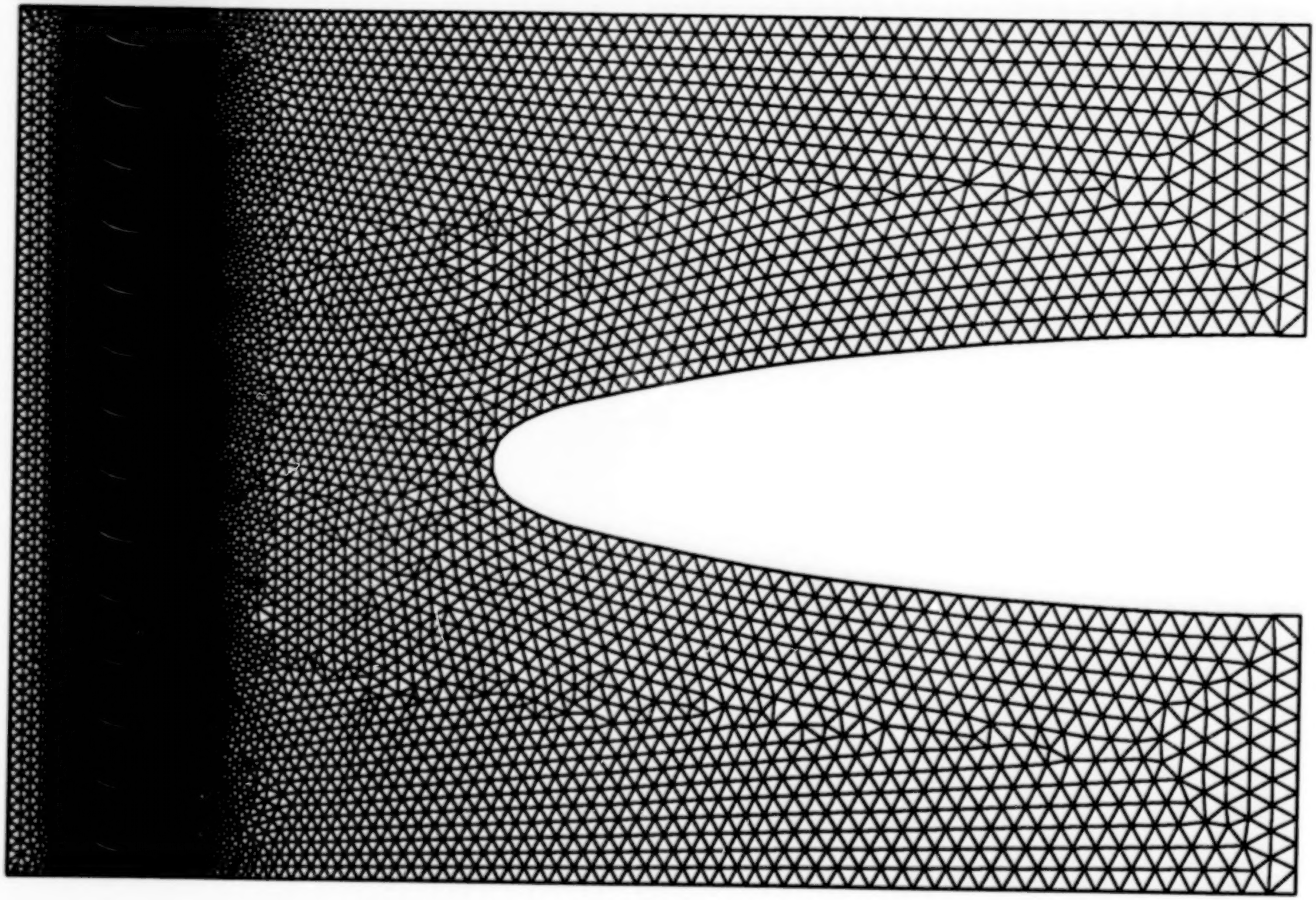

Figure 11: Pylon/OGV - Computational grid of complete domain.

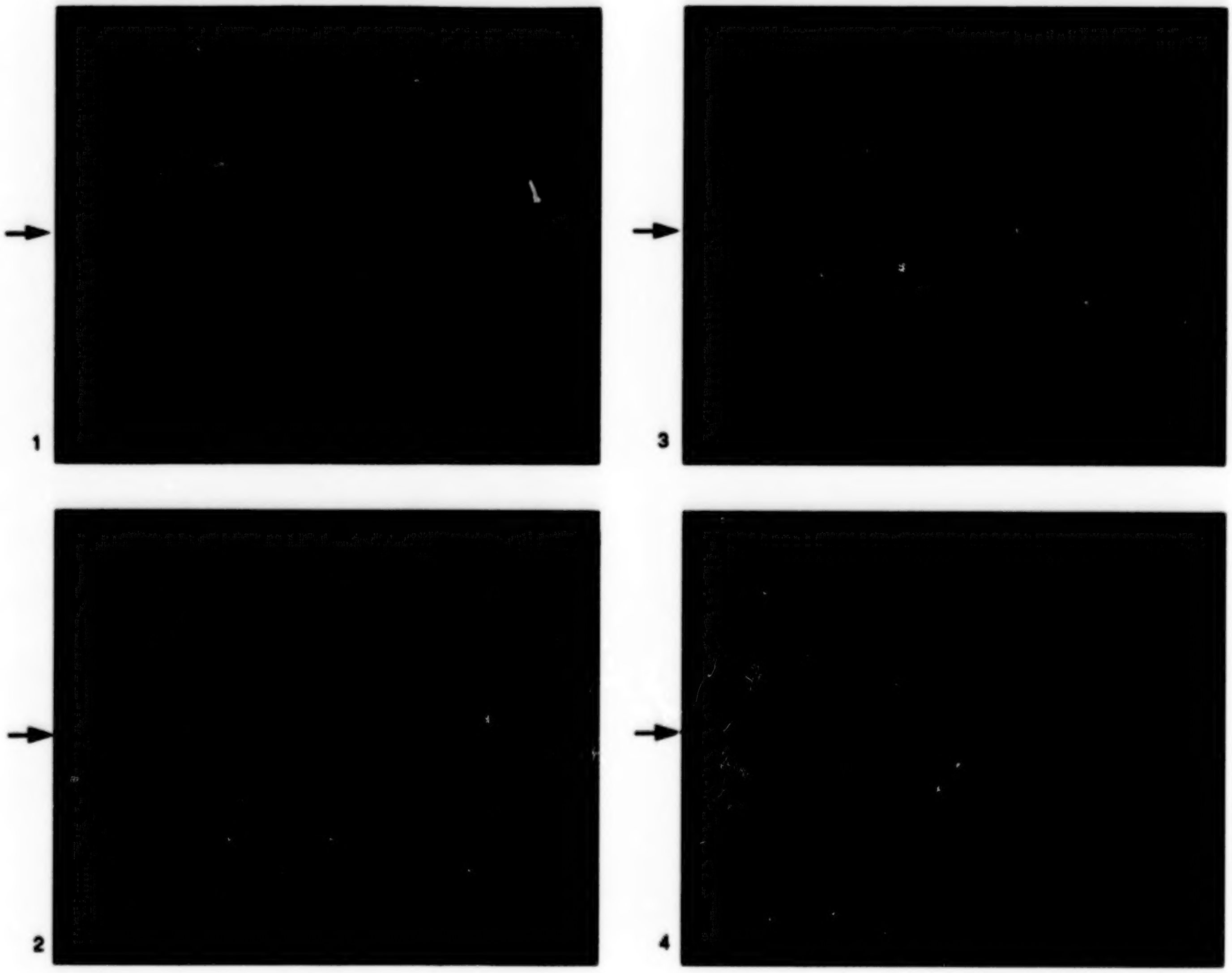

Figure 12: Pylon/OGV - Entropy contours at four different stages in a cycle.

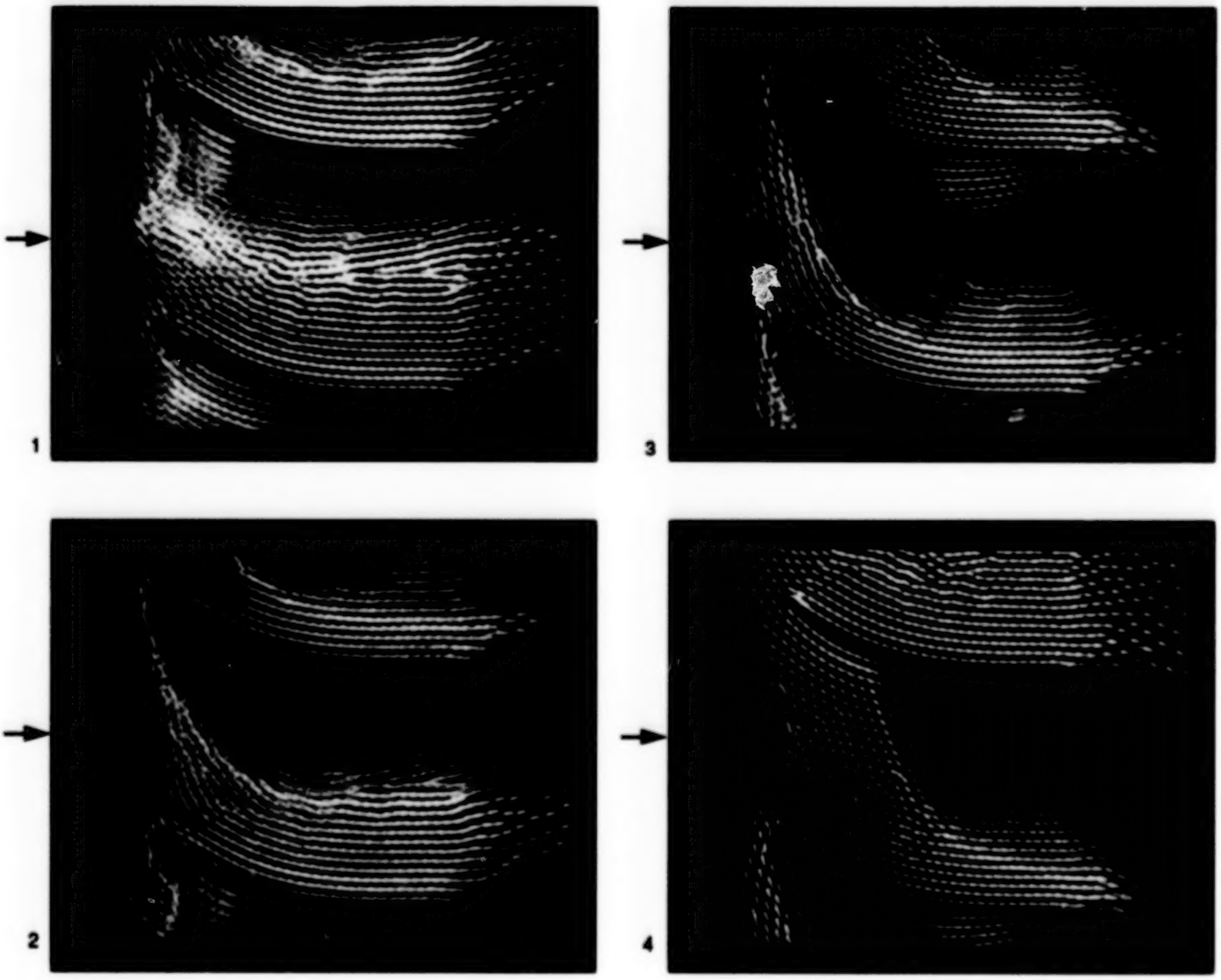

Figure 13: Pylon/OGV - Blowup of entropy contours with flow vectors from Figure 12.

UNSTRUCTURED GRID GENERATION USING THE DISTANCE FUNCTION

Barna L. Bihari and Sukumar R. Chakravarthy
Rockwell International Science Center
Thousand Oaks, California

ABSTRACT

A new class of methods for obtaining level sets to generate unstructured grids is presented. The consecutive grid levels are computed using the distance function, which corresponds to solving the Hamilton-Jacobi equations representing the equations of motion of fronts propagating with curvature-dependent speed. The relationship between the distance function and the governing equations will be discussed as well as its application to generating grids. Multiply connected domains and complex geometries are handled naturally, with a straightforward generalization to several space dimensions. The grid points for the unstructured grid are obtained simultaneously with the grid levels. The search involved in checking for overlapping triangles is minimized by triangulating the entire domain one level at a time.

INTRODUCTION

A paper on fronts propagating with curvature-dependent speed by Osher and Sethian (Ref. 6) has motivated us to research the possibility of applying the theory of propagating fronts to grid generation. While this theory has a potential to be used for generating structured grids, powerful and well-tested methods already exist to tackle that problem. However, generating the appropriate unstructured mesh for use with finite element or finite difference methods is still a difficult step given the fact that the success of the method depends largely on a correct discretization of the domain. Several ideas and practical algorithms have been proposed in the past (Ref. 2-5,7); however, this techniuqe is radically different from all of them in several ways.

The idea underlying the grid generation procedure presented comes from the relationship between grid levels and fronts propagating with curvature-dependent speed. The front at the next time level corresponds to the next grid level and satisfies all the requirements generally imposed on a well-generated grid. The equation of motion for a front propagating with curvature-dependent speed is an initial-value Hamilton-Jacobi equation with a right-hand side that depends on curvature effects. The surface is viewed as a level set of the solution to this equation which, as it evolves in time, yields a different level set and thus, the next grid level.

While this method will work with any consistent initialization of the Hamilton-Jacobi variable, by carefully choosing the initial condition, the equation may not have to be solved. As will be shown later, setting the Hamilton-Jacobi variable to a function of the distance from a point in the computational domain to the initial surface, (i.e., geometry), results in a solution to the equation with no diffusion term. That is, the level set corresponding to a particular value is used as a grid level and, by repeatedly using a contour-plotter-like search algorithm, all the grid levels are readily obtained.

To accurately match prescribed outer boundaries of the domain, they are treated the same way as the geometry: they will be represented by another front that also moves, but inward. The strategy for triangulation is based on a "level-by-level" principle which assumes that all curves obtained from the contour plotter are closed curves (loops).

I. EQUATIONS OF MOTION

Some theoretical results will now be presented in anticipation of our later discussion of the actual grid generation scheme. Given a simple, closed, smooth initial curve $\gamma(0)$ in $\mathbb{R}^2$ (Ref. 6), let $\gamma(t)$, $t \in [0,\infty)$ be a one-parameter family of curves representing the grid levels. The $\gamma(t)$ curves are generated by propagating the initial curve normal to itself with speed $F = F(K)$, where K is the curvature. Let $X(s,t) = (x(s,t), y(s,t))$ be the position vector that parametrizes $\gamma(t)$ by s, $0 \le s \le S$, $X(0,t) = X(S,t)$. By convention, the interior is on the left in the direction of increasing s, resulting in a counter-clockwise orientation of γ. The equations of motion can now be written as:

$$
\begin{aligned}
x_t &= F(K)\,\frac{y_s}{(x_s^2 + y_s^2)^{1/2}} \\
y_t &= -F(K)\,\frac{x_s}{(x_s^2 + y_s^2)^{1/2}}
\end{aligned}
\qquad (1.1)
$$

with the initial condition $X(s,0) = \gamma(0)$, $s \in [0,S]$ given. The formula for the curvature is

$$
K = \frac{y_{ss}x_s - x_{ss}y_s}{(x_s^2 + y_s^2)^{3/2}} \quad . \qquad (1.2)
$$

With $t = f(x,y)$, K becomes

$$
K = \frac{f_{xx}f_y^2 - 2f_{xy}f_xf_y + f_{yy}f_x^2}{(f_x^2 + f_y^2)^{3/2}} \quad .
$$

As shown in Ref. 6, the function f satisfies

$$
F^2(f_x^2 + f_y^2) = 1 \qquad (1.3)
$$

if the curve γ stays smooth and nonintersecting.

Using these facts, the system (1.1) can now be transformed into a second order Hamilton-Jacobi equation. Let $\phi(x,y,t)$ be a Lipschitz continuous function such that $\phi(x,y,0) > 1$ inside the closed curve γ, $\phi(x,y,0) < 1$ outside γ, and $\phi(x,y,0) = 1$ on γ. We may then write

$$
\begin{aligned}
f_x &= -\frac{\phi_x}{\phi_t} \\
f_y &= -\frac{\phi_y}{\phi_t}
\end{aligned}
$$

which, using Eq. (1.3) implies

$$F^2(\phi_x^2 + \phi_y^2) = \phi_t^2 \quad .$$

In general, the curve could propagate inward or outward, but keeping grid generation in mind, choose the direction of propagation to be outward, thus obtaining

$$\phi_t + F(K)H(\nabla\phi) = 0 \tag{1.4}$$

with $H(\nabla\phi) = -(\phi_x^2 + \phi_y^2)^{1/2}$, which is now a Hamilton-Jacobi equation in ϕ where

$$K = -\frac{\phi_{xx}\phi_y^2 - 2\phi_{xy}\phi_x\phi_y + \phi_{yy}\phi_x^2}{(\phi_x^2 + \phi_y^2)^{3/2}} \quad .$$

After solving for ϕ in time, the position of the propagating curve at time t can be obtained by looking for the locations where $\phi(x,y,t) = 1$. By appropriately choosing the speed function F, the smoothness of the successive curves can be controlled as well.

2. INITIAL CONDITIONS

One simple and, as it will turn out, very useful choice for initializing ϕ is

$$\phi(x,y,0) = 1 \pm d((x,y);\ \gamma(0)) \tag{2.1}$$

where $d(X;\ \gamma)$ is the distance from point $X = (x,y)$ to the curve γ, and the "+" sign is chosen for points inside the curve $\gamma(0)$ and the "-" sign is chosen for the points outside the curve. Thus, ϕ will be exactly one for points lying on $\gamma(0)$. We shall term the initialization (2.1) as the ***distance function***.

Proposition: The level curve of the distance function at a level d_o is precisely the level curve of a solution ϕ to Eq. (1.4) with $F(K) = C$ that corresponds to $\phi = 1$.

Proof: $F(K) = C$, a constant speed function, implies that every point on the initial curve is moving normal to itself with the same speed; hence, all of them cover an equal distance δ in time τ. Thus, every point on the new curve $\gamma(\tau)$ will be δ away from the original curve $\gamma(0)$, where

$\phi(x_0,y_0,0) = 1$ for $\gamma(0) = \{(x_0,y_0)\}$,

and

$\phi(x_1,y_1,\tau) = 1$ for $\gamma(\tau) = \{(x_1,y_1)\}$.

$\gamma(\tau)$ would therefore correspond to one level curve of the distance function, i.e.,

$\phi(x_1,y_1,0) = 1 - \delta\,\mathrm{sgn}C$.

This completes the proof.

Applying this result to grid level generation for unstructured mesh where the speed function F is constant, we note that no time integration of Eq. (1.4) is needed. Using the distance function, the grid levels are instantly obtained by simply specifying a set of values and then searching for the locations where the grid function (our Hamilton-Jacobi variable ϕ initialized by Eq. (2.1)) is equal to those values.

3. MESH GENERATION ALGORITHM

Using the above preliminary analysis, we have developed an algorithm that generates the nodes and triangulates between them one level at a time, also providing for arbitrary clustering of the triangles by modifying the distance function described in the previous section.

3.1 Grid Function

Because of the necessity of a grid function, the first step is to set up the computational domain which is a rectangular domain covering the entire region to be triangulated. This region will then be discretized as a cartesian grid, with equal spacing in both the x and y directions. Since this is merely an intermediate step, we keep this overlaid grid as simple and coarse as possible. Typically, the grid spacing will be greater or equal to the minimum side required for the unstructured elements to be generated.

To each point of this computational grid, we assign a grid function initialized as prescribed by Eq. (2.1). The spacing of the computational grid should be fine enough to resolve the sharp corners and the interior openings of the inner and outer boundaries. The boundaries are prescribed by the user in the form of patches, where the program has the built-in capability of point redistribution within each patch. The nodes of the interior boundaries are entered in counter-clockwise order, while the nodes of the exterior boundary are entered in clockwise order. All the curves representing the boundaries are assumed to be closed loops, with the possibility of several inner loops, corresponding to multiply connected domains (Fig. 1). For our example of Fig. 1, a contour plot of the grid function over the region of interest is illustrated in Fig. 2.

3.2 Generation of Interior Nodes

For each grid level, using a contour-plotter-like algorithm, we search for the locations in the computational domain, where the grid function matches a prescribed value. This value will obviously be less than one, and will depend on the nodal density and current grid level. It is important that the contour algorithm follows the contour levels in a continuous fashion, thus yielding closed curves. Simultaneously with following these contour curves, the nodes are generated as well by simply recording the coordinates of equally (or nonequally for varying nodal densities) spaced points along the curves. Once two complete adjacent contour levels are obtained with the corresponding points, no more points are generated, until the triangulation of this set of "ribbons" is complete (Figs. 3 and 4). This inherent topological structure of the nodes is a main advantage of the method, since it greatly reduces the search time necessary to form the best triangles.

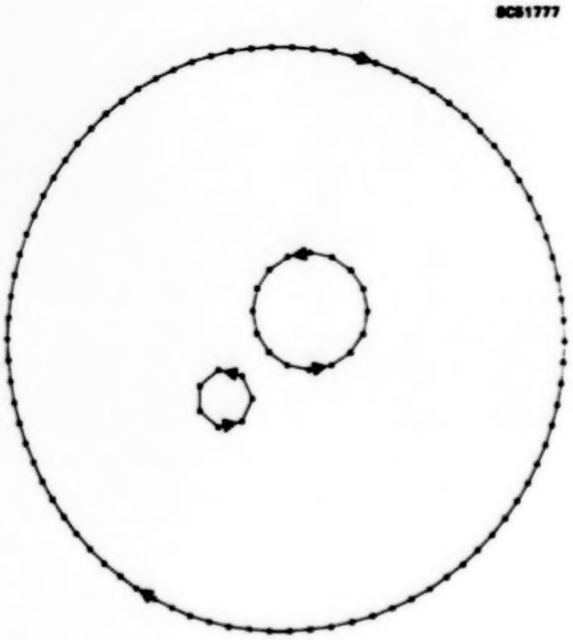

Fig. 1

Boundary of the domain to be triangulated.

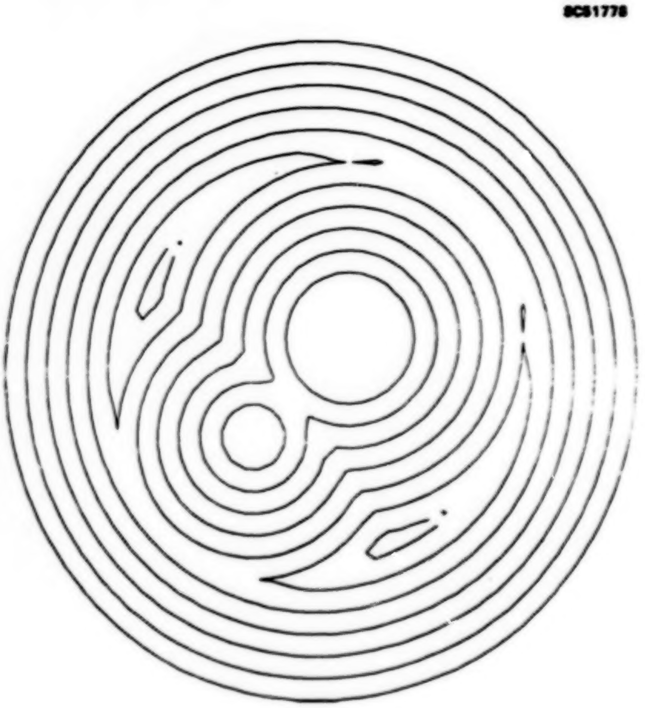

Fig. 2

Contour level curves of the grid function between 0 and 1

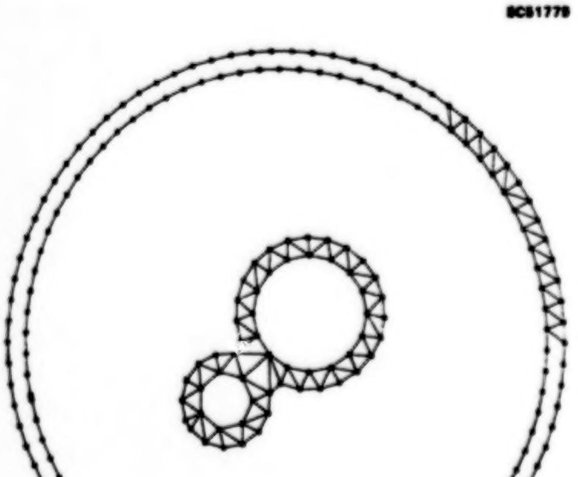

Fig. 3

Triangulation in progress in the first subregion: between the initial curves and the first level set.

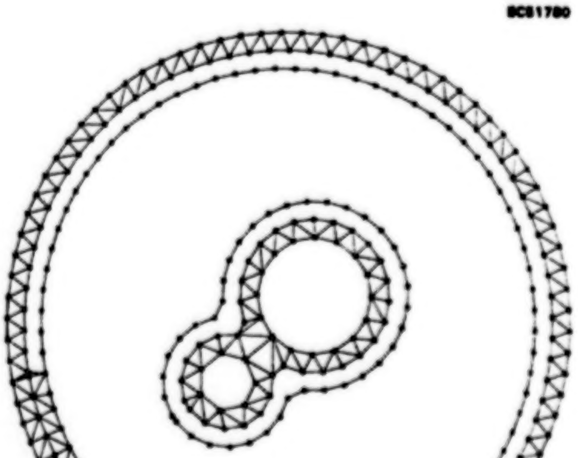

Fig. 4

Triangulation in progress in the second subregion: between the first and second level sets.

3.3 Forming Triangular Elements

Once two adjacent contour levels are known, the triangulation in the region enclosed by them is relatively straightforward. The algorithm that connects the nodes to form triangular elements has the following major steps:

1. Choose an initial "base" AB by connecting two adjacent nodes A and B on one of the contour loops that corresponds to a higher contour level.
2. For each triangle to be formed do:
    - 2a. Using the current base AB as the base of the triangle, choose the third vertex C such that the resulting triangle will, in some sense, be optimal. The criterion used will be elaborated later.
    - 2b. Update the array that contains the sides, with information about the newly created triangle, as well as the array that contains the elements (triangles).
    - 2c. Choose a new base AB from one of the two newly created sides AC or BC of the latest element, and if the other side does not belong to a contour loop, enqueue it for later use. If no more sides are available as eligible bases, stop. Otherwise go back to step 2a.

Criterion for determining vertex C:

The base AB is a directed vector, and the third vertex C will only be chosen from points to its ***right***. All those nodes that belong to the contour loops enclosing our current region of interest are considered. After analyzing the criteria proposed by Cavendish (Ref. 2) and Lo (Ref. 3), we found that those are unnecessarily complicated and time consuming. Given the special setting of our formulation, the following choice of node C guarantees optimal triangulation (Fig. 5):

> choose C so that the norm max(|AC|, |BC|) is minimized over all C that lie to the right of AB.

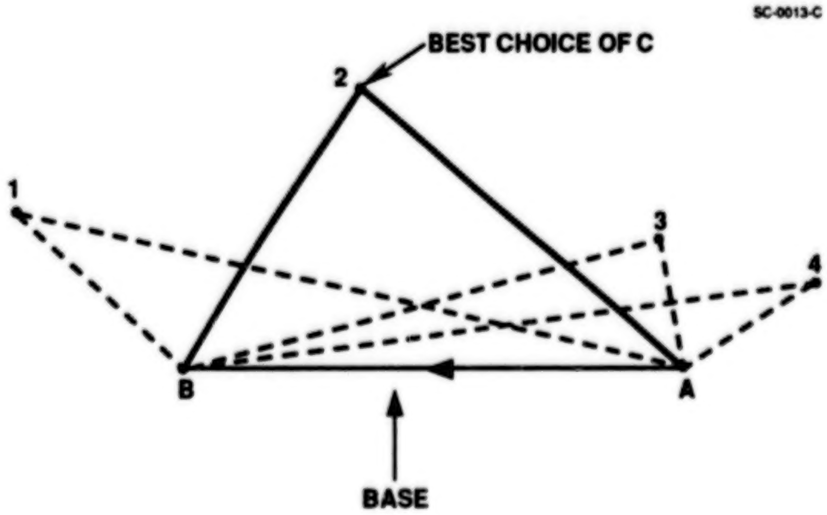

Fig. 5 Criterion for choosing the "best" third vertex C for triangle ABC.

Once the "best" C is selected, we must ensure that it indeed yields a triangle that will not overlap any other existing triangles. In practice, this is done by checking if any of the existing sides would partly or entirely lie within triangle ABC. If this happens, this choice of C is marked and thrown away, and the same criterion is used to select a new C from the remaining available nodes. Once again, the fact that only a relatively small number of nodes are considered in the checking routine greatly reduces the computational time required in the search.

Note that this triangulation scheme is indeed a "greedy algorithm" in that it looks only one step ahead and only tries to create the best ***next*** triangle without weighing the impact of this choice on later choices. However, because connecting the nodes is very much a local process, there are typically only two or three good choices at each step, hence they cannot result in radically different triangulations. In fact, because of the regular spacing of the nodes lying on contour loops, only about 1% of the best C's get eliminated due to overlapping.

Once the current region of interest is triangulated, the program obtains the next set of nodes (step 3.3 above) which, in turn, will define the next region of interest. Steps 3.2 and 3.3 follow each other until the whole domain is covered. During the above triangulation process, information about neighboring elements and connected nodes is being stored as well, which could be useful input to some flow solvers. The entire triangulated domain is shown in Fig. 6.

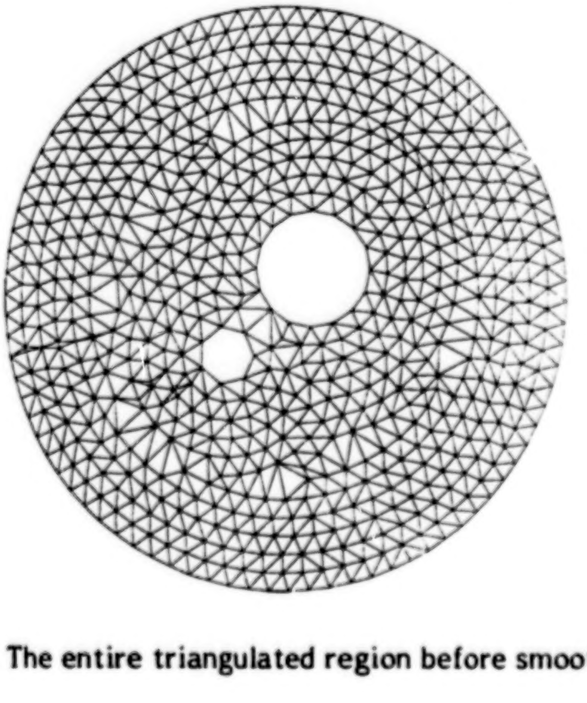

Fig. 6 The entire triangulated region before smoothing.

3.4 Smoothing

Once the whole domain is triangulated, to further regularize the elements, we apply a very simple and effective smoothing algorithm (suggested by Cavendish in Ref. 2). This process consists of replacing the coordinates of each node by the average of the coordinates of those surrounding nodes that it is connected to by a side. That is, each node is replaced by the centroid of the surrounding polygon. Since this algorithm follows the order in which the nodes were generated, at each step, the most updated coordinates are used. To accelerate convergence, we suggest that at each smoothing cycle the order is reversed, hence, propagating the smoothing in the opposite direction. Generally, two smoothing cycles result in triangles sufficiently close to a satisfactory set of nodes. The final, smoothed triangulated domain after two smoothing steps is shown in Fig. 7.

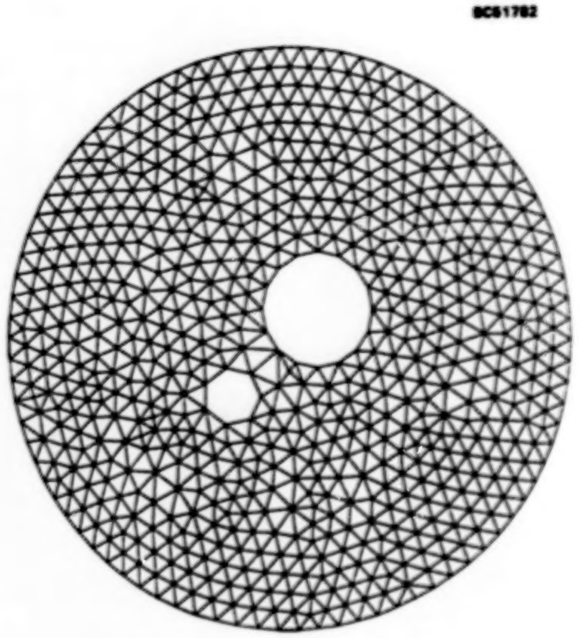

Fig. 7 Triangulated region after two cycles of smoothing.

4. CLUSTERING OF NODES NEAR BOUNDARY CURVES

To achieve varying nodal densities within the computational domain, we use the grid function described earlier. Modifying the formula used in Eq. (2.1), the grid function will not be a function linearly decreasing with the distance from the boundary curves, instead, an average of decreasing exponential functions of distances from each boundary curve. The boundaries are entered as patches, and each patch has a clustering factor c_i associated with it. The grid function at each point will then be divided by a weighted average of all the c_i's. That is:

$$\phi_{jk} = 1 \pm d((x,y);\ \gamma(0))/a_{jk} \tag{4.1}$$

where

$$a_{jk} = \frac{\sum_{i=1}^{n} c_i w_{jk}^i}{\sum_{i=1}^{n} w_{jk}^i} \tag{4.2}$$

and

$$w_{jk}^i = e^{-d((x_{jk},y_{jk});\gamma_i(0))\cdot b} \tag{4.3}$$

Here n is the total number of patches, ϕ_{jk} is the grid function at grid point (j,k), $\gamma_i(0)$ is the notation used for the ith patch representing the geometry or outer boundary, and b is a scaling factor dependent on the dimensions of the whole domain. It is clear from Eqs. (4.2) and (4.3) that the scaling used in Eq. (4.1) is very heavily dependent on geometry patches close to the point (j,k), while the influence of every other patch is relatively small and it diminishes exponentially as the distance to that patch increases. Averages must be taken to ensure a smooth grid function so the contour algorithm will work. Figure 8 illustrates our initial example with the ratio of the largest and smallest cells being 10 (that is, $\max\limits_{1\le i\le n} (c_i)/ \min\limits_{1\le i\le n} (c_i) = 10$) before smoothing, while the effect of smoothing (after two cycles) is shown in Fig. 9.

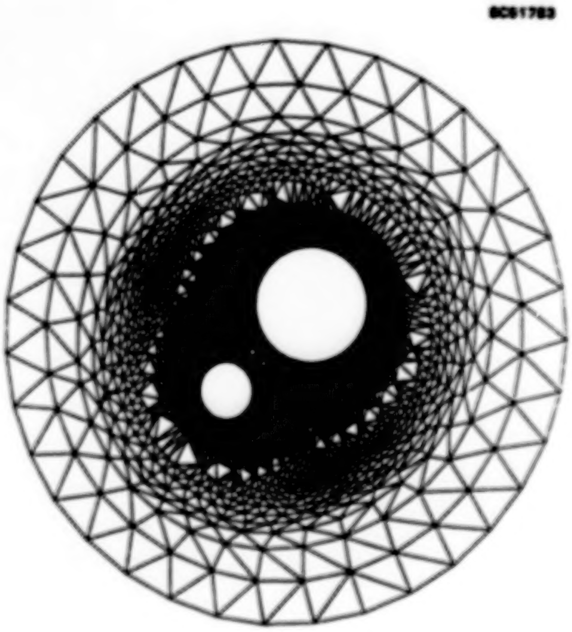

Fig. 8

Clustered triangular mesh around the two inner circles before smoothing.

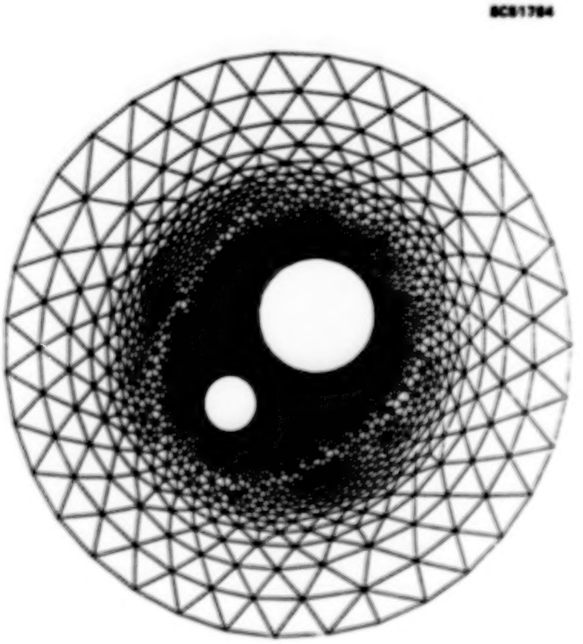

Fig. 9

Clustered mesh of Fig. 8 after two cycles of smoothing.

5. THE GENERAL PROGRAM

A flow chart containing the main building blocks of the program is now presented to illustrate the logic of the algorithm.

1. Input the geometry and outer boundary data, and clustering parameters for the patches.
2. Redistribute points along geometry and outer boundary loops according to required clustering.
3. Initialize grid function over computational domain
4. Until the whole domain is covered, do:
    - 4a. Find contour level for next grid function value; simultaneously generate nodes on the obtained loops.
    - 4b. Connect nodes in subregion enclosed by two sets of contour loops.
5. Do twice:
    - 5a. Smooth the entire region.

6. FURTHER EXAMPLES

The example used thus far is relatively simple; to illustrate how this method tackles very complex, multi-connected geometries, several examples of different characteristics follow.

Figure 10 shows the word "GRID" with equally spaced mesh around it. The same geometry is used in Fig. 11, where we have a clustered mesh instead, with the ratio of the largest and smallest elements being 10. Note the exponentially decaying influence of the clustering factor associated with each geometry segment as the distance to them increases throughout the domain.

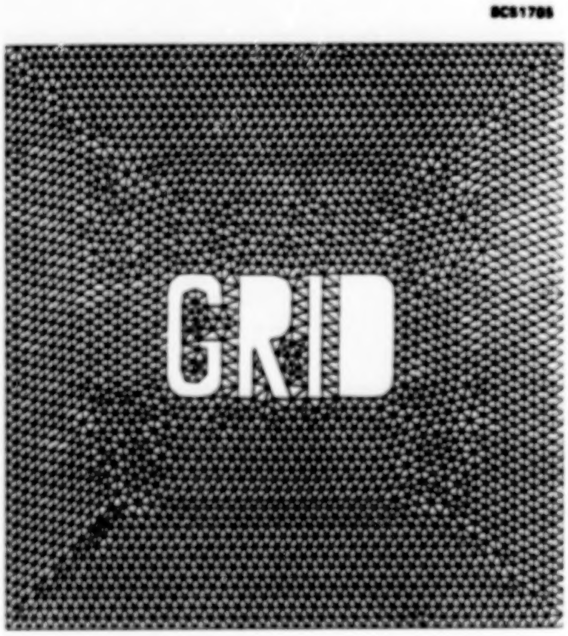

Fig. 10

Smoothed, equally spaced mesh around the word "GRID".

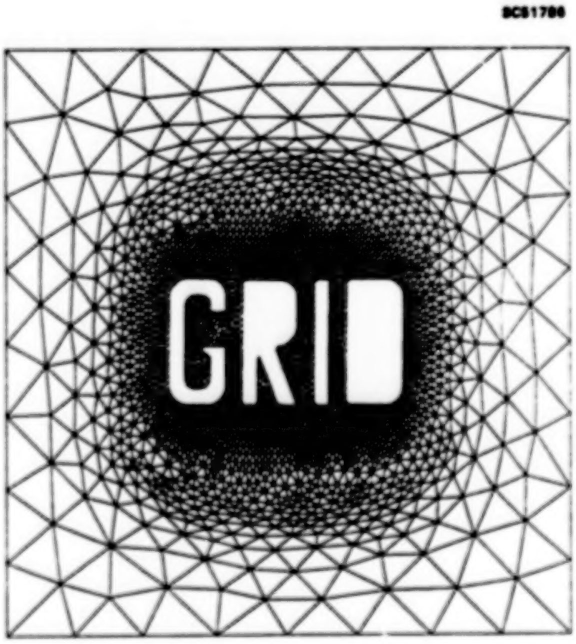

Fig. 11

Smoothed, clustered mesh around the word "GRID".

Figure 12 shows a grid for the "bomb-bay" problem, where heavy clustering is required in the cavity area and near the wall, while a quite course grid is sufficient as the far field is approached. Figure 13 shows a blowup of the cavity area.

7. CONCLUSIONS

A new, two-dimensional unstructured grid generator has been developed using the distance function to obtain the interior nodes for a prescribed, possibly multiconnected domain, where the nodal density can vary throughout the domain. The algorithm eliminates the need to break up the domain into several subdomains and triangulate each of those subdomains separately. Dense clustering of nodes is made possible with the density of the nodes varying smoothly.

The natural question arises as to whether this method could have an extension to three dimensions. The preliminary analysis given at the beginning of this paper convinces us that the theory of curves moving with curvature-dependent speed can be easily generalized to surfaces

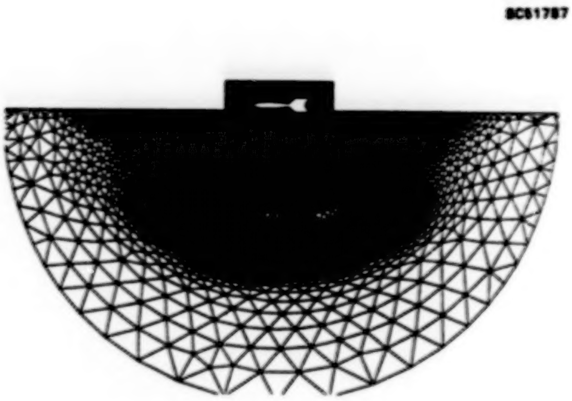

Fig. 12

Clustered mesh in the cavity area of the bomb-bay problem.

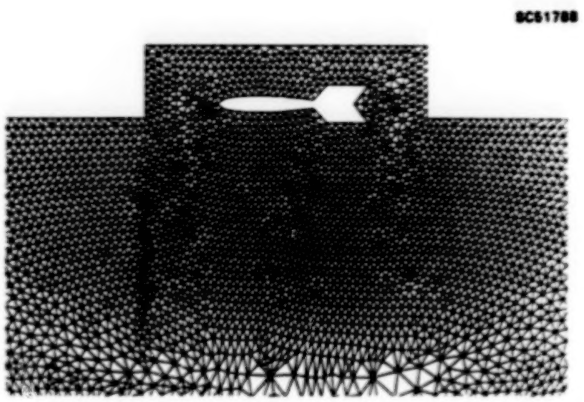

Fig. 13

Close-up of the bomb-bay mesh of Fig. 12.

in an n-dimensional space. Similarly, the proposition proved earlier also holds for any n-dimensional space; hence, the distance function can be used in the same way in three dimensions. Even obtaining the isosurfaces (which correspond to contour curves in two dimensions), representing the different grid levels, is relatively straightforward. However, to pick up the nodes on these isosurfaces according to a prescribed distribution function is the same problem as surface-gridding, which can be a complicated and time-consuming problem by itself. Once the nodes are known, forming the tetrahedral elements would be a process similar to that of triangulation described above, with search done on a level-by-level basis again. The same concepts would apply in three dimensions, with faces replacing sides, and intersection of planar sections replacing intersection of line segments. The criterion for choosing the best tetrahedron could be applied in its present form as well; we simply choose the fourth point of a tetrahedron to minimize the maximum of the three edges to be created. The three dimensional background grid, however, which has to resolve the smallest element, may have to be quite dense, thus creating a new, and perhaps unsurpassable bottleneck. Further results for extending the method to three dimensions will be reported in future work.

ACKNOWLEDGEMENTS

We would like to thank Stanley Osher, Kuo-Yen Szema and Chung-Lung Chen for their constructive comments and help in writing this paper.

REFERENCES

1. Barles, G., "Remarks on a Flame Propagation Model," Institut de Recherche en Informatique et Automatique (INRIA), Sophia Antipolis, France, Report No. 464, 1985.
2. Cavendish, J.C., "Automatic Triangulation of Arbitrary Planar Domains for the Finite Element Method," International Journal for Numerical Methods in Engineering, Vol. 8, 679-696 (1974).
3. Lo S.H., "A New Mesh Generation Scheme for Arbitrary Planar Domains," International Journal for Numerical Methods in Engineering, Vol. 21, 1403-1426 (1985).
4. Löhner, R., "Some Useful Data Structures for the Generation of Unstructured Grids," Communications in Applied Numerical Methods, Vol. 4, No. 1, 123-135 (1988).

5. Löhner, R. and Parikh, P., "Generation of Three-Dimensional Unstructured Grids by the Advancing-Front Method," International Journal for Numerical Methods in Fluids, Vol. 8, No. 10, 1135-1149 (1988).
6. Osher, S. and Sethian, J.A., "Fronts Propagating with Curvature-Dependent Speed: Algorithms Based on Hamilton-Jacobi Formulations," Journal of Computational Physics, Vol. 79, No. 1, November 1988.
7. Yerry, M.A. and Shephard, M.S., "Automatic Three-Dimensional Mesh Generation by the Modified-Octree Technique," International Journal for Numerical Methods in Engineering, Vol. 20, 1965-1990 (1984).

COMPUTATIONAL STUDY OF THREE DIMENSIONAL VISCOUS FLOW THROUGH A TURBINE CASCADE USING MULTI-DOMAIN SPECTRAL TECHNIQUE

Earl W. Renaud
Choon S. Tan
Massachusetts Institute of Technology
Cambridge, MA 02139

ABSTRACT

The three dimensional viscous flow through a planar turbine cascade is numerically simulated by direct solution of the incompressible Navier-Stokes equations. Flow dependence in the spanwise direction is represented by direct expansion in Chebyshev polynomials, while the discretisation on planes parallel to the endwalls is accomplished using the spectral element method. Elemental mapping from the physical to the computational space use an algebraic mapping technique. A fractional time stepping method that consists of an explicit nonlinear convective step, an implicit pressure correction step, and an implicit viscous step is used to advance the Navier-Stokes equations forward in time. Results computed at moderate Reynolds numbers show a three dimensional endwall flow separation, a midspan separation of the blade suction surface boundary layer, and other three-dimensional features such as the presence of a saddle point flow in the endwall region. In addition, the computed skin friction lines are shown to be orthogonal to the surface vorticity lines, demonstrating the accuracy achievable in the present method.

INTRODUCTION

Blade rows in modern axial flow turbines are often designed with rather high loadings and low aspect ratios (ref. [1]) (to increase power density and decrease part counts), this results in strong endwall secondary flows, often extending to midpan. These strong secondary flows have been known to be a source of (total pressure) loss through the blade row (ref. [2]). A large number of experimental investigations (ref. [3]-[4]) have been carried out in plane and annular cascades to obtain data which have been used to develop a physical understanding of the generation of secondary flows. Concurrent with these studies, theoretical efforts have been made (ref. [5]) to develop analytic models for predicting flowfields and the losses associated with the existence of secondary flows. These efforts have led to a global understanding of the secondary flow phenomena. However, the detailed mechanisms responsible for these secondary losses are not understood to the extent that a quantitative model can be formulated in terms of the secondary flow. Such an understanding is essential for developing a reliable model for the prediction of the losses associated with endwall secondary flows (ref. [6]). An approach to address this issue would be to make use of a numerical simulation scheme that can generate an accurate solution of the three-dimensional flow in a planar turbine cascade. The high order accuracy obtainable in a calculation based on the spectral element technique makes it ideally suited to such an investigation.

This paper presents a computation of the three dimensional viscous flow through a planar turbine cascade by a multi-domain spectral element method. The goal of this investigation is to develop a reliable computational tool that can be used to gain an improved understanding of secondary flow and loss generation in turbine cascade endwall regions. The spectral element technique used in this investigation offers the advantages of high order accuracy, minimal dispersion and dissipation errors and geometric flexibility, all of which are essential to a quantitative study of the fundamental phenomena underlying the generation of secondary flow and the associated loss in turbine cascades. In the following, we first present the governing equations and outline an efficient technique for advancing the solution in time. This is followed by a brief concise description of the spatial discretisation and formulation of the spectral element method. The last two sections present an application of the method to the calculation of the three dimensional viscous flow through a planar turbine cascade.

GOVERNING EQUATIONS AND TEMPORAL DISCRETIZATION

The equations governing the flow are the incompressible Navier-Stokes equations written in rotational form,

$$\frac{\partial \vec{V}}{\partial t} = \vec{V} \times \vec{\omega} - \nabla P_t + \frac{1}{Re}\nabla^2 \vec{V} \tag{1}$$

$$\nabla \cdot \vec{V} = 0 \tag{2}$$

Here, $\vec{V}$ is the velocity field normalised by upstream axial velocity at midspan, $\vec{\omega} = \nabla \times \vec{V}$ is the vorticity field, P_t is the total pressure normalized by twice the upstream axial dynamic head, and Re is the Reynolds number based on the upstream axial velocity at midspan and blade axial chord.

The solution to Eqs.(1-2) is advanced forward in time using a fractional time stepping scheme (ref. [7]), consisting of a non-linear convective step, a pressure step imposing continuity, and a viscous correction step imposing the no-slip boundary condition. The non-linear convection step is implemented through an explicit third order Adams-Bashforth scheme that yields

$$\hat{\vec{V}}^{n+1} - \vec{V}^n = \frac{\Delta t}{12}[23(\vec{V} \times \vec{\omega})^n - 16(\vec{V} \times \vec{\omega})^{n-1} + 5(\vec{V} \times \vec{\omega})^{n-2}] \tag{3}$$

Once $\hat{\vec{V}}$ is determined, we are left with an unsteady Stokes problem which can be split in time as follows. First, the pressure correction step is discretized in time by a Backward Euler method, yielding

$$\frac{\hat{\hat{\vec{V}}}^{n+1} - \hat{\vec{V}}^{n+1}}{\Delta t} = -\nabla P_t \tag{4}$$

and

$$\nabla \cdot \hat{\hat{\vec{V}}}^{n+1} = 0 \tag{5}$$

subject to the boundary condition

$$\hat{\hat{\vec{V}}}^{n+1} \cdot \vec{e}_n = 0 \tag{6}$$

on the blade surface and endwalls. Computationally, the above step is reformulated as a solution for P_t by taking the divergence of Eqn.(4) and applying Eqn.(5) to yield

$$\nabla^2 P_t = \nabla \cdot (\frac{\hat{\vec{V}}^{n+1}}{\Delta t}) \tag{7}$$

subject to the boundary condition

$$\frac{\partial P_t}{\partial n} = \frac{\hat{\vec{V}}^{n+1} \cdot \vec{e}_n}{\Delta t} \tag{8}$$

on the solid walls. The velocity field $\hat{\hat{\vec{V}}}^{n+1}$ that satisfies continuity identically is then computed from Eqn.(4).

Following the solution of the pressure step is the viscous correction step imposing the non-slip boundary condition on the solid surfaces. The step is discretised using the implicit Crank-Nicholson scheme, giving

$$(\nabla^2 - \frac{2Re}{\Delta t})(\vec{V}^{n+1} + \vec{V}^n) = -\frac{2Re}{\Delta t}(\hat{\hat{\vec{V}}}^{n+1} + \vec{V}^n) \tag{9}$$

subject to the appropriate non-slip boundary conditions on the solid surfaces. At the inflow, the velocity is assumed known, while at the outflow a homogeneous Neumann boundary condition is imposed.

SPATIAL DISCRETIZATION AND ELEMENTAL MAPPING

Spatial discretization in Z

Since the geometry is invariant in the spanwise dimension (planar cascade), one can choose a direct spectral expansion for the flow variation in the Z direction. The need to account for different boundary conditions on the endwalls (Dirichlet for the velocity and Neumann for the pressure) leads us to define an eigenfunction expansion

$$F_l(Z) = \sum_m f_{lm} T_m(Z) \tag{10}$$

satisfying the following Sturm-Liouville problem,

$$\frac{d^2 F_l(Z)}{dZ^2} = \lambda_l^2 F_l(Z), \tag{11}$$

subject to homogeneous Neumann boundary conditions for the pressure and homogeneous Dirichlet boundary conditions for the velocity. These functions are constructed separately for the viscous velocity step and pressure step in a preprocessing procedure via the tau method (ref. [8]). The Chebyshev polynomials $T_m(Z)$ are given as

$$T_m(Z) = cos(m \, cos^{-1} Z) \tag{12}$$

with the collocation points chosen at

$$Z_k = cos \frac{\pi k}{L}. \tag{13}$$

It should be noted that the choice of collocation points can be arbitrary, yet the distribution given in Eqn.(13) can be shown to give an error that satisfies the minimax criterion (ref. [9]). In addition, such a choice also results in good resolution of the viscous boundary layers near the endwall.

Spatial discretization in the X-Y plane

The complexity of the geometry prohibits a simple global spectral discretization of the flow variables in the (X, Y) plane. The region is instead divided into a number of subdomains, or spectral elements, following the techniqe developed by Patera (ref. [10]). In each i^{th} subdomain or element we can expand the flow variables as

$$\left\{ \begin{array}{c} \vec{V} \\ p \end{array} \right\} = \sum_{j=0}^{N_X} \sum_{k=0}^{N_Y} \sum_{l=0}^{N_Z} \left\{ \begin{array}{c} \vec{V}_{jkl} \\ p_{jkl} \end{array} \right\} h_j^i(\xi^i) h_k^i(\eta^i) F_l(Z) \tag{14}$$

where $F_l(Z)$ are the interpolants from the direct expansion in the spanwise direction given in Eqn.(10) above, and $h_m(S)$ are high order local Lagrangian interpolants in tems of Chebyshev polynomials. These can be writen as

$$h_m(S) = \frac{2}{M} \sum_{n=0}^{M} \frac{1}{\bar{C}_m \bar{C}_n} T_n(S_m) T_n(S) \tag{15}$$

with

$$\bar{C}_m = \left\{ \begin{array}{llll} 1 & for & m \neq 0 & or \quad M \\ 2 & for & m = 0 & or \quad M \end{array} \right. \tag{16}$$

where the S_m are the collocation points in the computational space.

Elemental Mapping

The mapping from the phyical coordinate space (X, Y, Z) to the local natural coordinate space $(\xi, \eta, \varsigma)^i$ is given by an isoparametric tensor-product mapping (ref. [11]),

$$(X, Y)^i = \sum_{j=0}^{J} \sum_{k=0}^{K} (X, Y)_{jk}^i h_j^i(\xi^i) h_k^i(\eta^i), \tag{17}$$

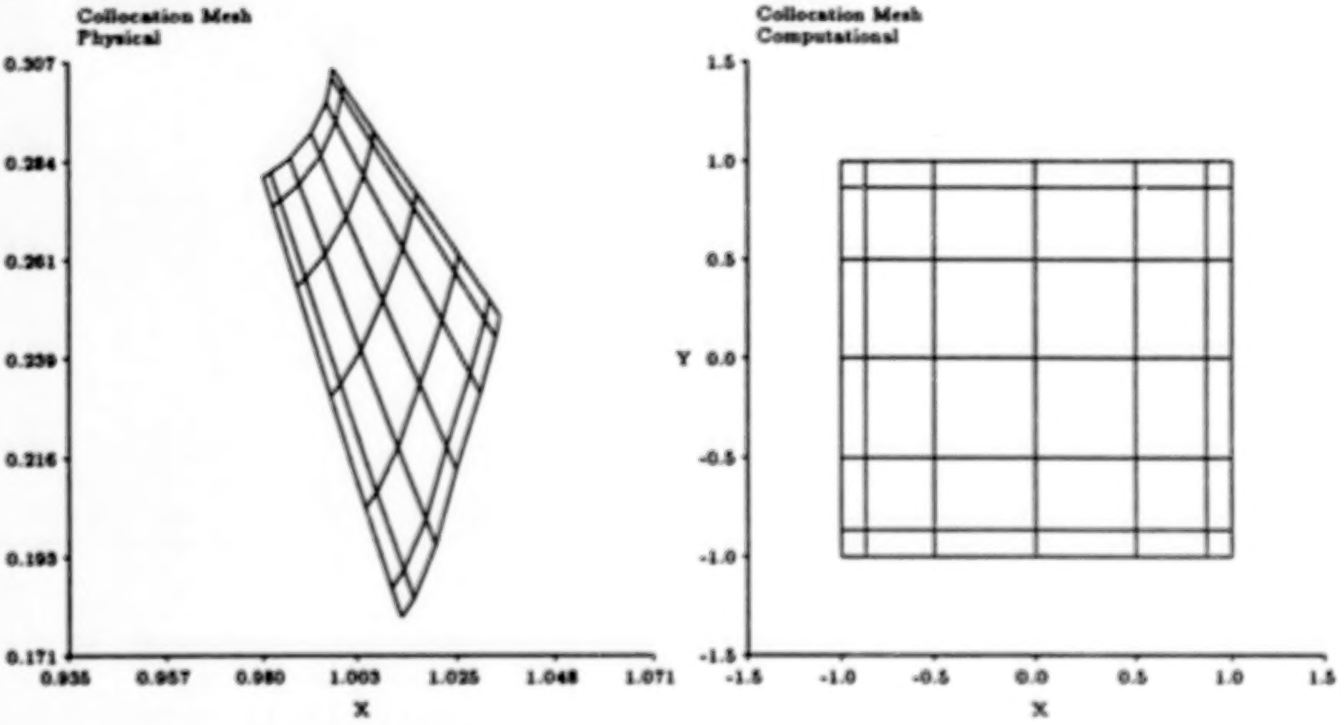

Figure 1: Element collocation grid in physical and computational space.

where we have chosen $\varsigma = Z$, with the collocation points in the elemental computational space defined as

$$(\xi, \eta, z)^i_{jkl} = \left(cos\frac{\pi j}{J} cos\frac{\pi k}{K} cos\frac{\pi l}{L} \right)^i \tag{18}$$

where $j, k, l = 0 \rightarrow J, K, L$.

To complete the definition of the mapping from the physical coordinate space (X, Y, Z) to the elemental computational space $(\xi, \eta, \varsigma)^i$, we need to define the collocation points in the physical space $(X, Y)^i_{jk}$. This can be accomplished by several different methods. The first is through the use of an analytic conformal functional mapping, which can be used whenever the elements are rectangular in some suitable regular curvilinear coordinate system. A second and less restrictive method uses a Laplace equation to generate a linear functional variation in two dimensions over the element in physical space. The functional values are then used to map the points in the computational space to the physical element. The third method is an algebraic method using elements with two linear and two generally curved sides. Due to its relative simplicity, ease of implementation and geometric generality, the algebraic method is used here.

In the algebraic method, we first define a general parametric function $X(S) = f_X(S)$ and $Y(S) = f_Y(S)$ on each side of each element. Collocation points are then distributed along each element side in arc length according to the formula

$$\begin{Bmatrix} X \\ Y \end{Bmatrix}_m = f_{X,Y}(S_m) \tag{19}$$

where the collocation arc lengths S_m are defined as in Eqn.(12). Next, making use of the linearity of two opposing sides, the interior points are defined along straight lines connecting the points on opposing curved sides, distributed according to Eqn.(19) as illustrated in Figure (1).

The final discretized equations are obtained by substituting Eqn.(14) into the relevant temporal discretizations, Eqns.(3-9). For a complete derivation of the final discretized equations, and a detailed description of the computational cyle, see Tan (ref. [12]).

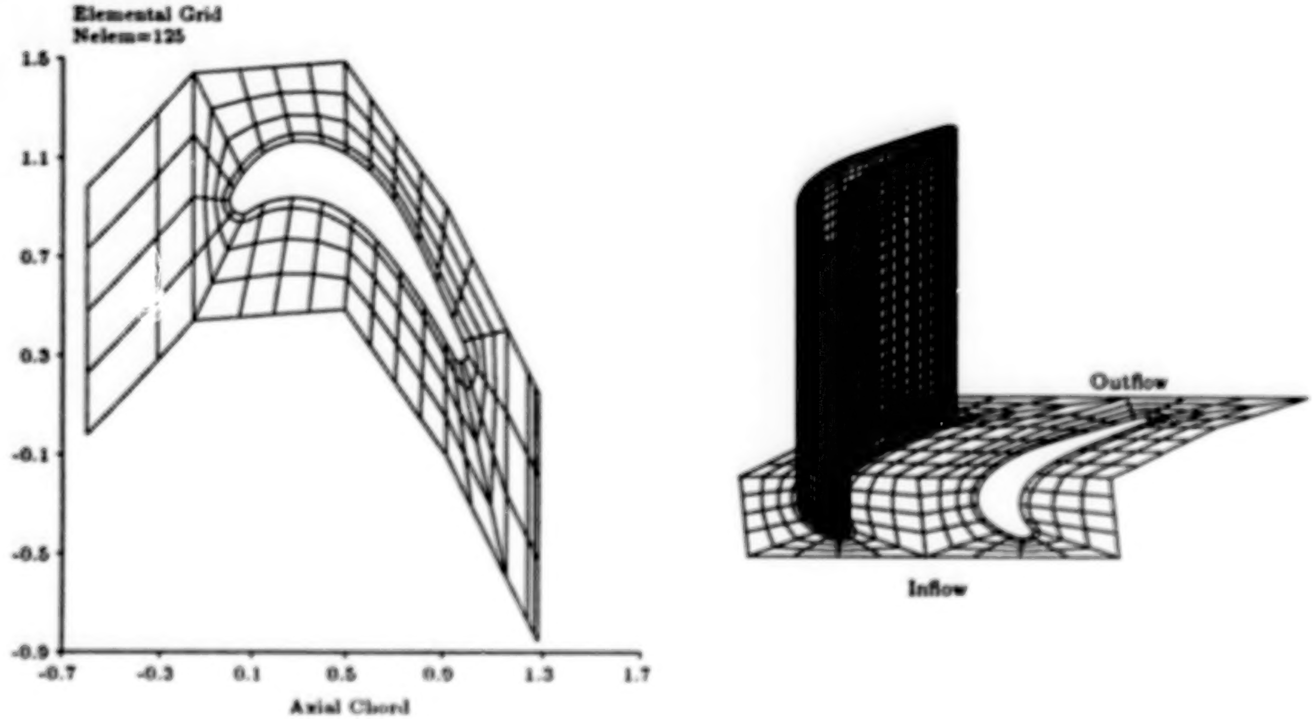

Figure 2: Elemental grid and cascade geometry

APPLICATION

Objective

The computational method above has been used to calculate the three-dimensional viscous flow through a planar cascade at moderate Reynolds number. Although the flow through turbine cascades generally occurs at Reynolds numbers that would be considered "large", a decision has been made to restrict the investigation to a laminar flow regime. This has several implications for the application of the results. The first is that the loss levels that are calculated will not be applicable to realistic machine geometries. The second is that any phenomena that has its origin in small scale turbulent motion will not be reproduced in the simulation. Lastly boundary layer parameters such as momentum and displacement thickness will not reflect those of the cascade operated at large Reynolds numbers. Yet it is felt that these restrictions do not invalidate the results of the simulation. Since the generation of secondary flow is a kinematic process with characteristic length scales of an order much larger than those associated with small scale turbulent motion, a laminar simulation will produce secondary flows with structure and form similar to the higher Reynold number case. In addition, the relationship between these secondary flow structures and the mechanisms by which they are responsible for an increase in loss should not depend on the small scale turbulent structure of the flow. Therefore, conclusions drawn about this relationship, based on the simulation, should be applicable to the general high Reynolds number turbulent flow situation.

Cascade Geometry and Inflow Conditions

The cascade blade cross section is that used by Langston (ref. [13]) in his benchmark experimental investigation, invariant in the spanwise direction, with a solidity of 1.0 and a blade aspect ratio of 2.0, both based on axial chord. The cascade extends over the region $Z = (-1, 1)$ in the spanwise direction. Figure (2) shows the spatial discretization in the X, Y plane, where the $X - Y$ plane is divided into 125 spectral elements, with each element representing a seven by seven by thirty three Chebyshev expansion, as indicated in Eqn.(14). Figure (2) also shows a graphic representation of one blade and one endwall, with each level on the blade surface corresponding to one collocation point of the direct expansion in the spanwise direction.

The inflow condition to the cascade consist of a circumferentially uniform flow at a angle of 45.5 degrees from axial.

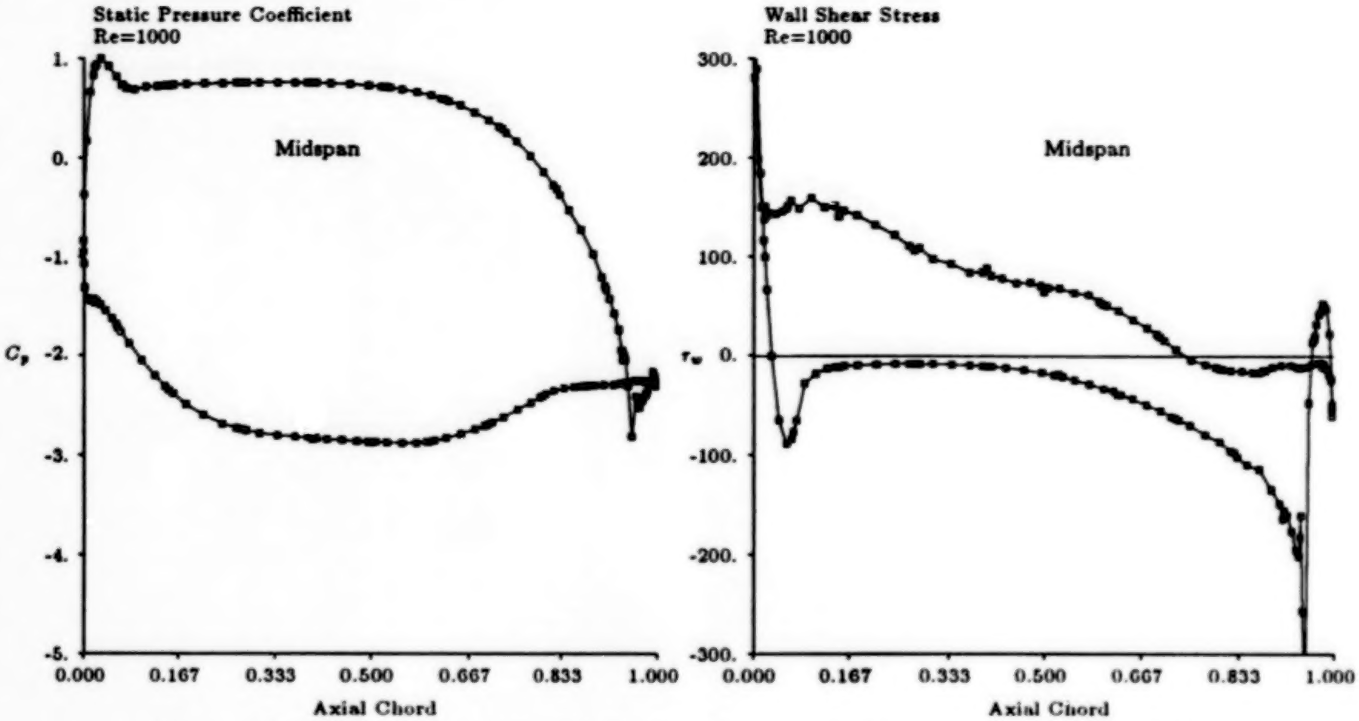

Figure 3: Midspan static pressure distribution (a), and wall shear stress distribution (b).

The spanwise variation consists of an eighth order polynomial profile

$$\begin{aligned} \vec{V}_x &= (1 - Z^8) \\ \vec{V}_y &= \frac{1}{tan45.5^o}(1 - Z^8) \\ \vec{V}_z &= 0 \end{aligned} \tag{20}$$

representing the incoming endwall boundary layer. The boundary layer parameters for this layer are summarized in Table (1), normalized both by axial chord, and by leading edge radius.

Table 1: Boundary layer parameters of inlet velocity profile

Parameter	$(chord)$	$(R_{L.E.})$
δ	.5623	10.46
δ^*	.1110	2.066
θ	.0517	.9612
Re_θ	51.666	

NUMERICAL RESULTS

Presented in this section are numerical results for the flow through a planar turbine cascade, using the inflow conditions given above and a Reynolds number of 1000. The simulation was conducted with a time step size of $\Delta t = 3.0 \times 10^{-4}$, which was limitted by stability restrictions on the explicit convection step. The results presented show the solution after six thousand time steps, or a nodimensional time of $\tau = 1.8$.

Computed results of the flow at midspan are shown in Figures (3-5). Figure (3.a) show the midspan surface static pressure coefficient, defined as

$$C_P = \frac{P - P_\infty}{P_{T_\infty} - P_\infty} \tag{21}$$

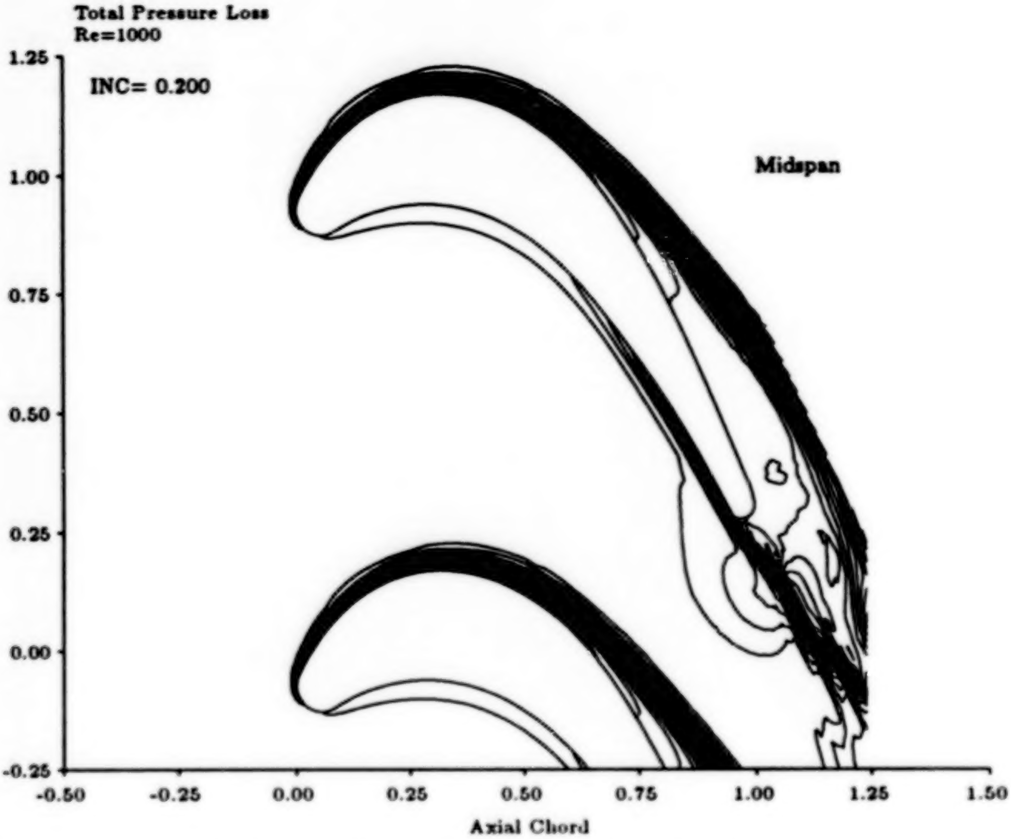

Figure 4: Midspan total pressure loss coefficient contours.

The distribution shown has a smooth chordwise variation, with none of the oscillations that are suggestive of insufficient resolution in a spectral calculation. This computed static pressure distribution agrees with that measured by Langston (ref. [13]), with the exception of a higher minimum suction side pressure. This suggests the presence of a laminar boundary layer separation on the suction surface. Indeed, the plot of shear stress distribution on the blade shown in Figure (3.b), indicates that this laminar separation occurs at a point on the suctions surface where the value of the wall shear stress vanishes, at $X = .741$. Positive shear stress on the suction surface behind the separation is indicative of reverse flow in the separated region. Contours of total pressure loss coefficient in Figure (4), defined as

$$C_{P_T} = \frac{P_{T_\infty} - P_T}{P_{T_\infty} - P_\infty}. \tag{22}$$

show a rapid thickening of the suction side boundary layer which then separates in the reqion of adverse pressure gradient. The comparitively thin boundary layer on the pressure side evolves with negligable total pressure loss up to mid-chord. This may suggest that only a small fraction of the blade profile loss is generated on the pressure surface. Examination of the results in Figure (4) indicate a region of low total pressure near the trailing edge. This region of low total pressure outside the boundary layer can be attributed to the unsteadiness associated with the presence of vortex shedding and the separated flow region. Contours of the static pressure distribution, shown in Figure (5), clearly indicate the occurence of vortex shedding. The closed circular countours immediately downstream of the trailing edge are characteristic of shed vorticies.

Numerical results of the endwall flow region are presented in Figures (6-11). Figure (6) shows a comparison of the velocity and vorticity vectors at a height of $\Delta Z = .005$ above the endwall. At this spanwise location very near the endwall the velocity and vortitity vectors are orthogonal and proportional, demonstrating the accuracy attainable using the described computational method.

Figure (7.a) is a plot of the two dimensional projection of the velocity vectors near the endwall, at a height of $\Delta Z = .019$ above the endwall. The figure clearly shows the separation line that is a result of the formation of the horseshoe vortex at the blade leading edge. The line begins just behind the saddle point, shown in Figure (7.b), and

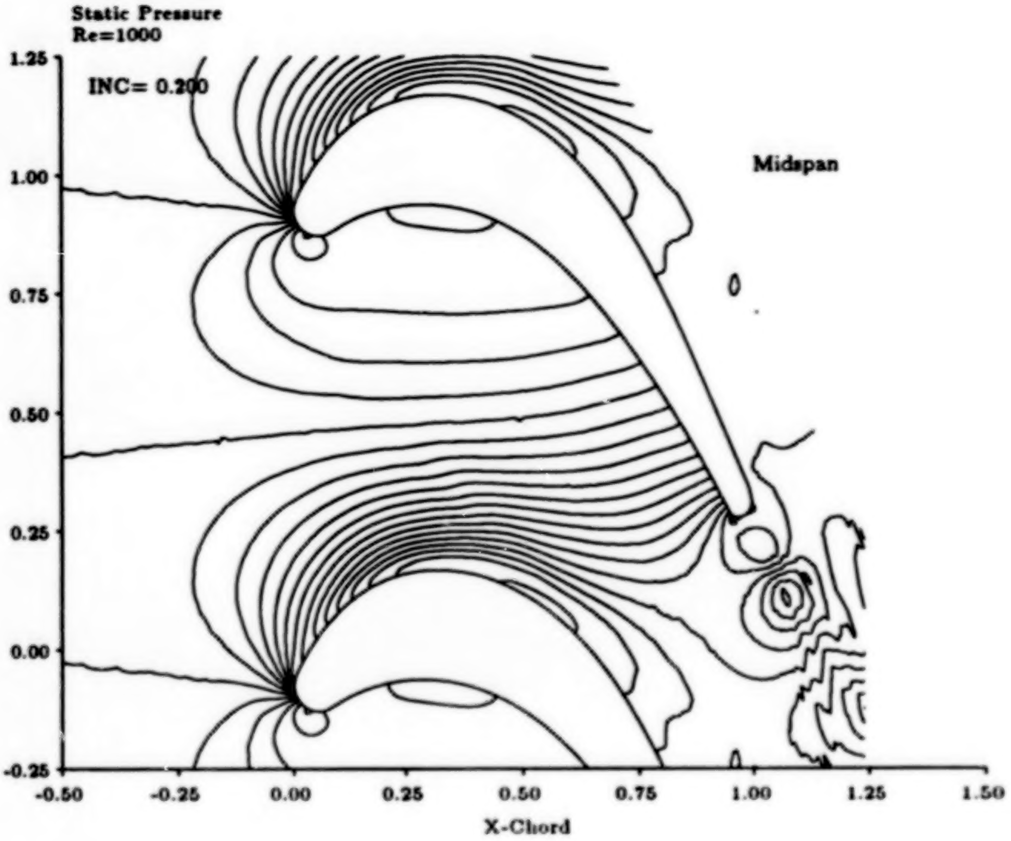

Figure 5: Midspan static pressure coefficient contours.

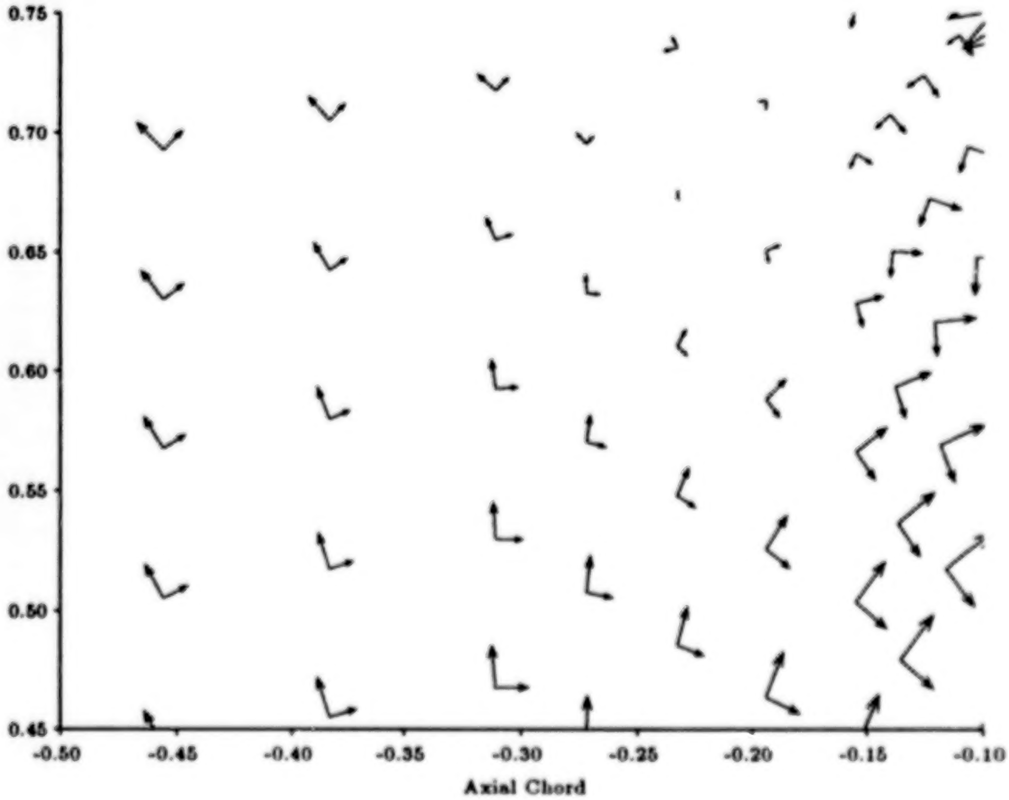

Figure 6: Comparison of velocity and vorticity vectors above cascade endwall in the region of the saddle point.

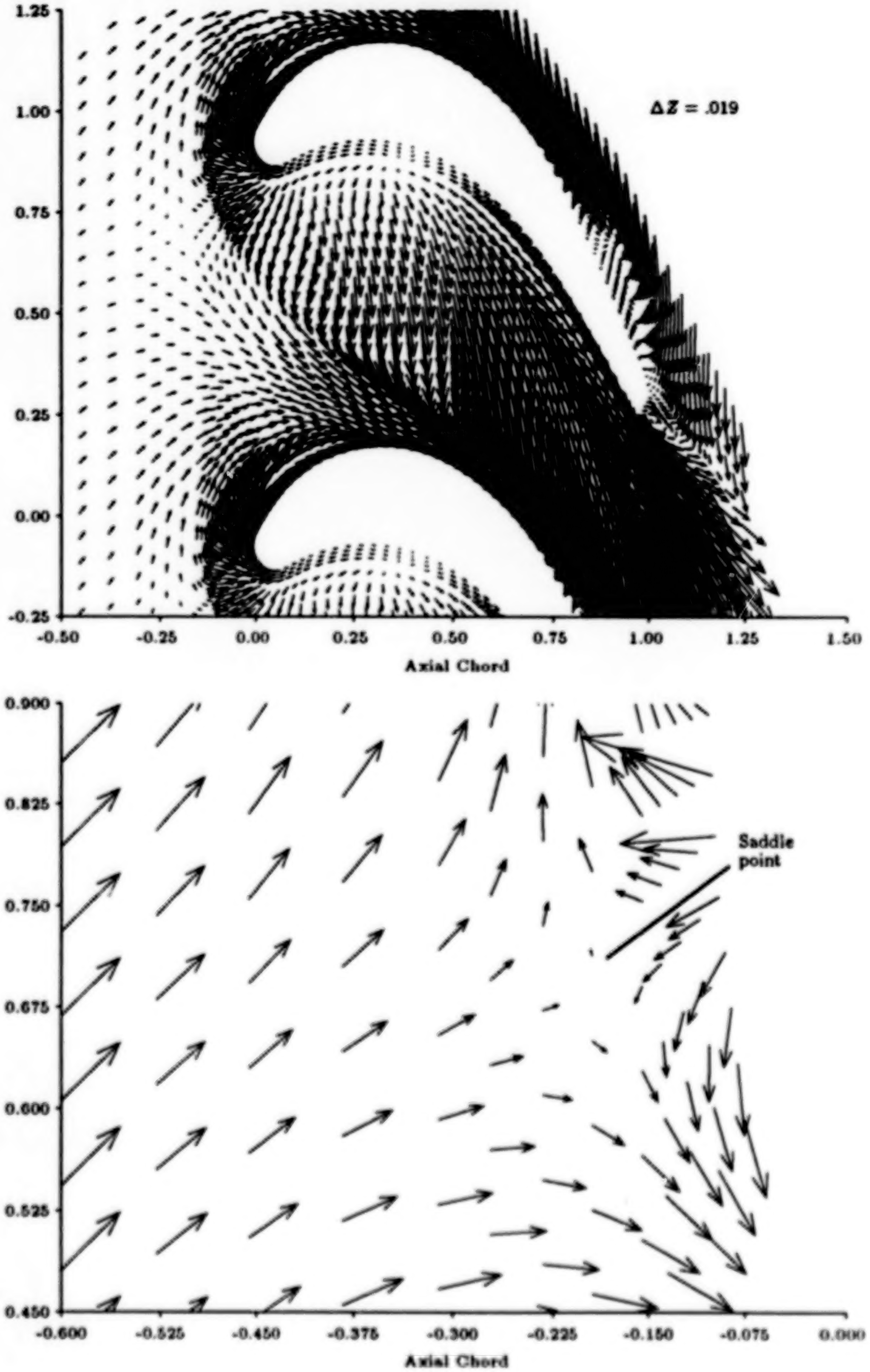

Figure 7: Velocity vectors above cascade endwall (a) and an enlargement of the region near the saddle point (b).

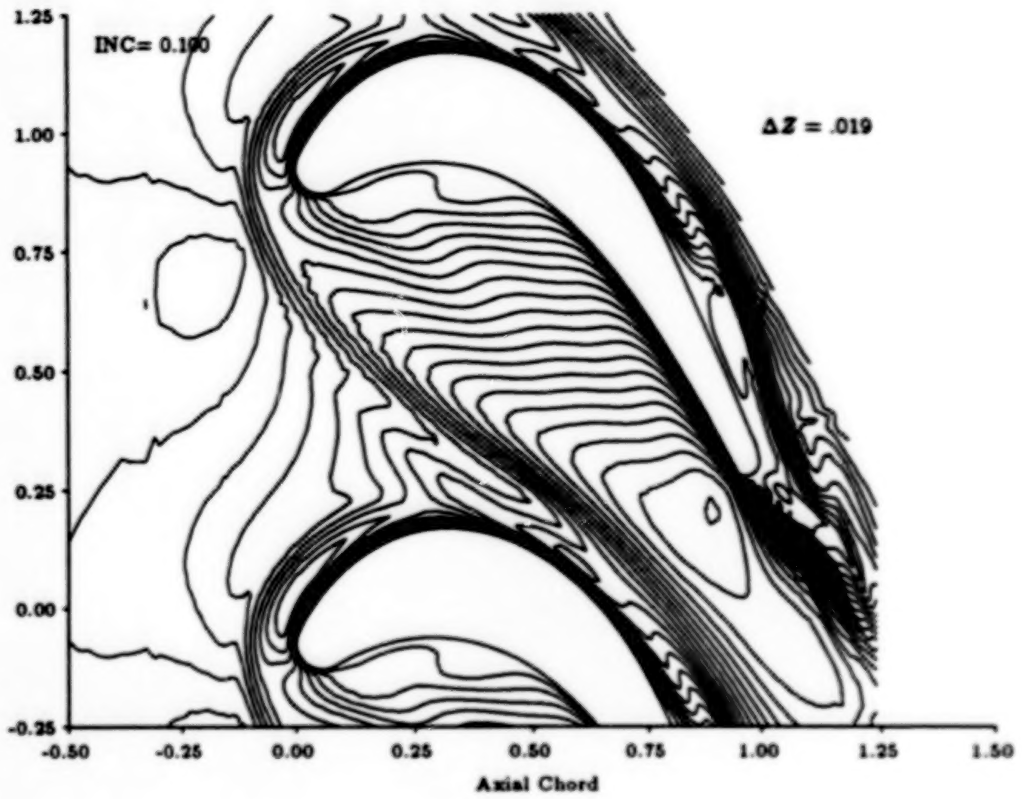

Figure 8: Total velocity contours at $Z = -.98$.

extends across the blade passage toward the suction surface of the adjacent blade. Behind this line the velocity is signifigantly higher, indicating that the incoming endwall boundary layer separates and convects toward the blade suction surface, as can be seen in Figure (10), which shows contours of total pressure loss coefficient (Eqn.(22)) on constant axial planes. Figure (8) shows a contour plot of the total velocity magnitude at the same spanwise location as the vectors in Figure (7.a). The separation line can clearly be seen extending across the passage, with a signifigant increase in total velocity magnitude occuring across the line. This increase in velocity appears to be nearly uniform over the length to the separation line. Thus, the acceleration of the upstream boundary layer on one side of the line and the higher velocity fluid on the other side of the line are of equal magnitude. This means that the pressure gradient in the streamwise direction must be continuous across the line. This can be seen in Figure (9) which is a contour plot of the static pressure on the passage enwall. The plot shows that the strength of the streamwise pressure gradient is continuous accross the separation line, as the total velocity distribution suggested. The Figure also shows the "trough" of static pressure on the endwall that has been observed by Langston (ref. [13]). This trough is characteristic of the formation of a horseshoe vortex structure.

Figure (11) shows contours of streamwise vorticity, defined as

$$\omega_s = \vec{\omega} \cdot \frac{\vec{V}}{|\vec{V}|} \tag{23}$$

plotted at a height $\Delta Z = .019$ above the endwall. The figure shows the saddle point ahead of the horseshoe vortex and the formation of the vortex at the blade leading edge. The highest level of streamwise vorticity is concentrated directly behind the separation line, underneath and in front of the horseshoe votex core. This structure can be identified as a counter vortex, cause by the high shear levels beneath the larger horseshoe vortex.

CONCLUDING REMARKS

A multi-domain spectral method is used to calculate the three-dimensional viscous flow through a planar turbine

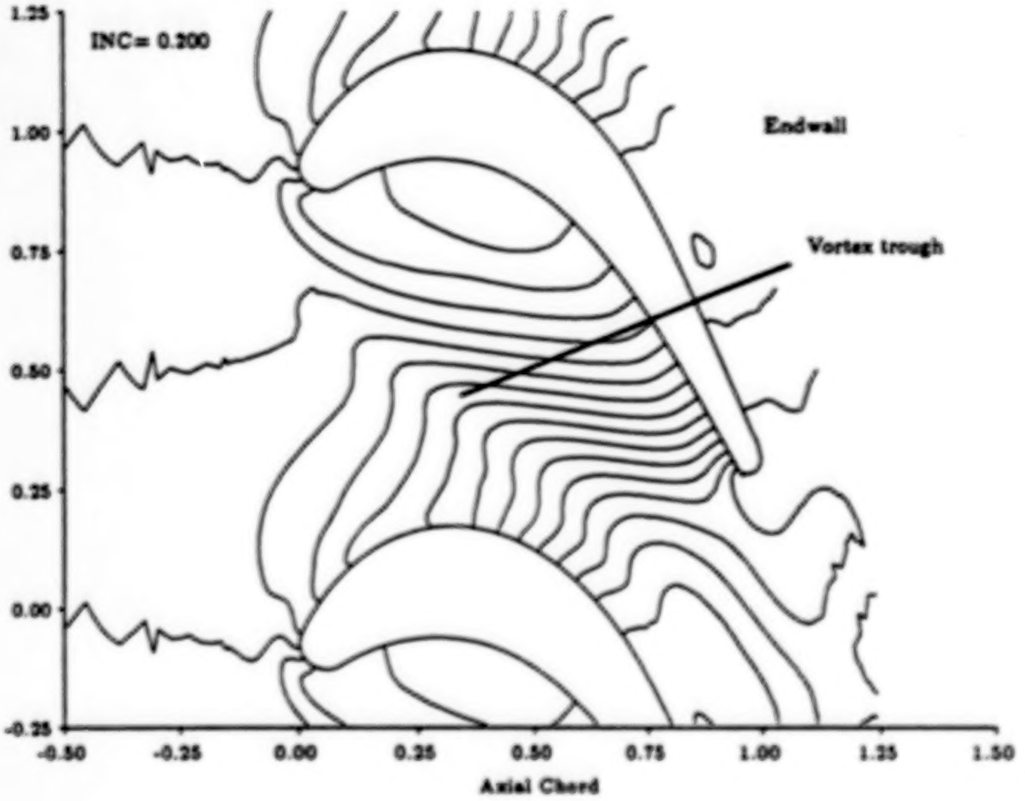

Figure 9: Static pressure contours on cascade endwall.

cascade at moderate Reynolds number. The solution uses a series expansion in Chebyshev polynomials to represent the flow dependence in the spanwise direction, while discretization on planes parallel to the endwalls is accomplished using the spectral element method. The elemental mapping from the physical to computational space is accomplished by using an algebraic mapping procedure developed for the calculation. The computational method is then applied to a planar cascade of turbine blades using Langston's profile.

The midspan static pressure loading is found to be qualitatively similar to that measured by Langston, with the exception of the presence of a boundary layer speration on the suction side.

The chosen spatial discretization is found to give an adequate resolution of the flow features in the endwall region. These features include the formation of a horseshoe vortex about the leading edge, and the resulting separation of the upstream boundary layer. The static pressure distribution on the endwall shows the presence of a static pressure trough that is characteristic of the formation of a horseshoe vortex system. In addition, there is evidence of a small intense counter vortex underneath the horseshoe vortex. The separation of the incoming boundary layer results in the presence of high velocity fluid near the wall behind the separation line. This causes an increase in endwall shear stress in that region, which may result in increased total pressure loss in the cascade.

The presented application of a spectral element technique to the calculation of turbine cascade flows shows that the spectral method can be used as a computational tool to gain an improved understanding of secondary flow in axial flow turbines.

ACKNOWLEDGMENTS

This work was supported through NASA Lewis Grant NAG3-660, Dr. J. Adamczyk Program Manager, and by the Air Force Office of Scientific Research, through the AFRAPT program, grant AFOSR-85-0288.

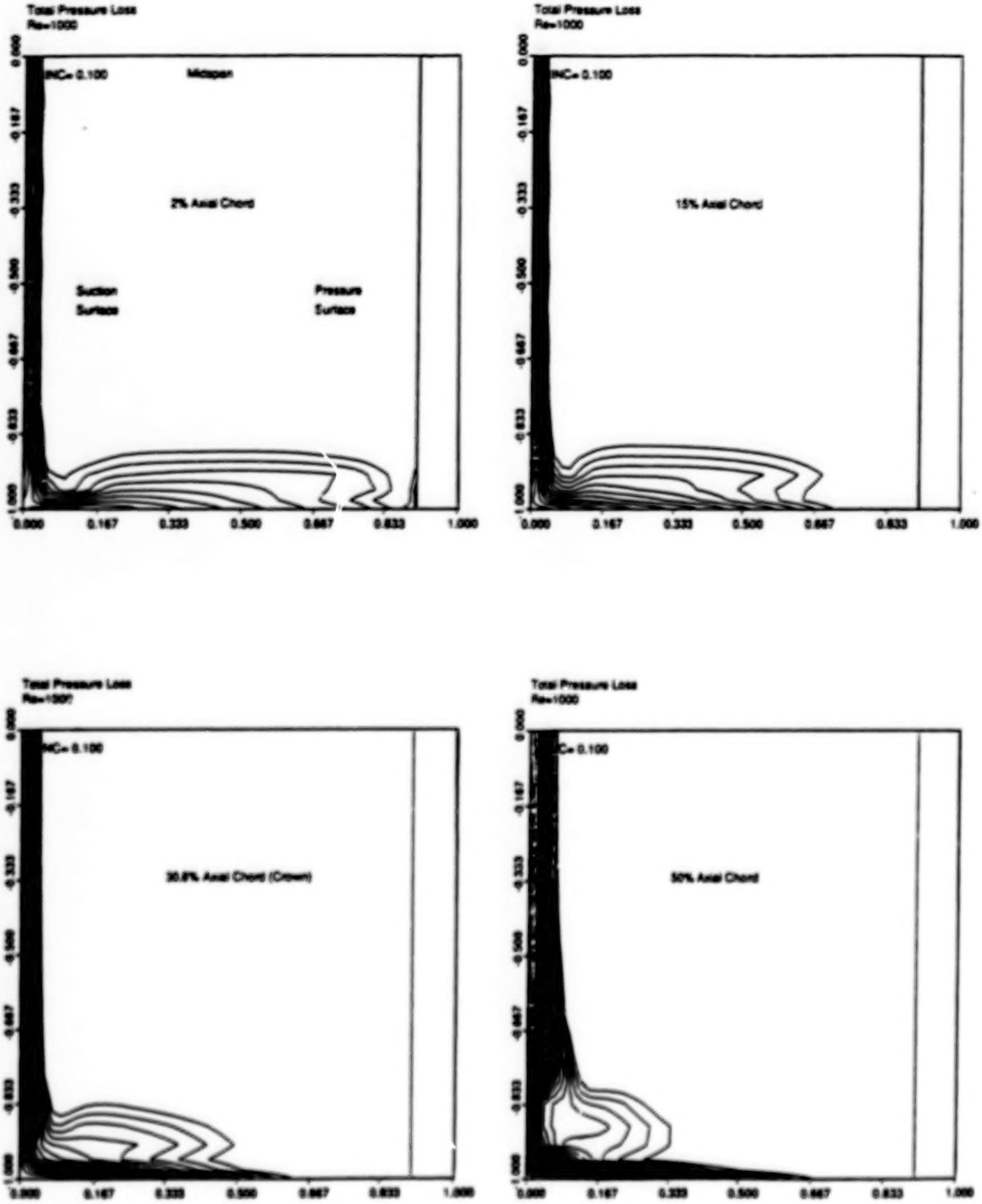

Figure 10: Total pressure loss coefficient contours on various axial planes.

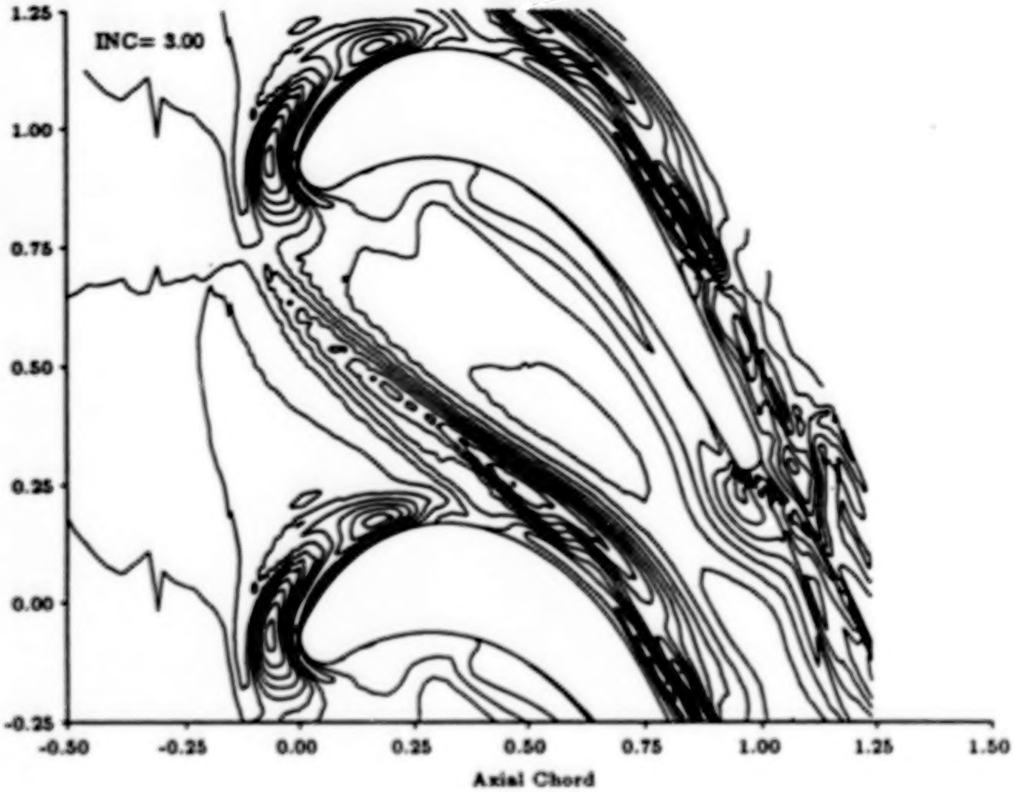

Figure 11: Streamwise component of vorticity above endwall.

REFERENCES

[1] Sharma, O. P., Pratt & Whitney Aircraft Co., Hartford, CT, private communication (1989).

[2] Dunham, J., and Came, P. M., "Improvements to the Ainley-Mathieson Method of Turbine Performance Prediction," *J. Eng. Pow.* **92** 252-256 (1970).

[3] Herbert, G. J., and Tiederman, W. G., " Comparison of Steady and Unsteady Secondary Flows in a Turbine Cascade," ASME Paper 89-GT-79, (1989).

[4] Sharma, O. P., Butler, T. L., Joslyn, H. D., and Dring, R. P., "Three-Dimensional Unsteady Flow in an Axial Flow Turbine" *J. Prop. Pow.* **1** No.1 (1989).

[5] Gregory-Smith, D. G., "Secondary Flows and Losses in Axial Flow Turbines," *J. Eng. Pow.* **104** 819-822 (1989).

[6] Sharma, O. P., Renaud, E. W., Butler, T. L., Millsaps, K. T., Dring, R. P., and Joslyn, H. D., "Rotor Stator Ineraction in Multi-Stage Axial-Flow Turbines," AIAA Paper 88-3013 (1988).

[7] Orszag, S. A., and Kells, L., *J. Fluid Mech.* **96** (1980).

[8] Tan, C. S., *J. Comput. Phys.* **59**, No.1, (1985).

[9] Gottlieb, P., and Orszag, S. A., *Numerical Analysis of Spectral Methods: Theory and Application*, SIAM, Philadelphia (1977).

[10] Patera, A. T., " A Spectral Element Method for Fluid Dynamics: Laminar Flow in a Channel Expansion," *J. Comput. Phys.* **54**, 468-488 (1989).

[11] Korczak, K. Z., and Patera, A. T., *J. Comput. Phys.* **62**, 361 (1986).

[12] Tan, C. S., " A Multi-domain Spectral Computation of Three-Dimensional Laminar Horseshoe Vortex Flow Using Incompressible Navier-Stokes Equations", *J. Comput. Phys.* **85**, No.1, 130-158 (1989).

[13] Langston, L. S., Nice, M. L., and Hooper, R. M., " Three-Dimesnional Flow Within a Turbine Cascade Passage," *J. Eng. Pow.*, **85** 21-28 (1989).

[14] Schlichting, H., *Boundary Layer Theory*, McGraw-Hill, New York (1955).

A FINITE-DIFFERENCE, FREQUENCY-DOMAIN NUMERICAL SCHEME FOR THE SOLUTION OF THE LINEARIZED UNSTEADY EULER EQUATIONS

James R. Scott
NASA Lewis Research Center
Cleveland, Ohio 44135

Hafiz M. Atassi
University of Notre Dame
Notre Dame, Indiana 46556

ABSTRACT

A numerical method is developed for solving periodic, three-dimensional, vortical flows around lifting airfoils in subsonic flow. The first-order method that is presented fully accounts for the distortion effects of the nonuniform mean flow on the convected upstream vortical disturbances. The unsteady velocity is split into a vortical component which is a known function of the upstream flow conditions and the Lagrangian coordinates of the mean flow, and an irrotational field whose potential satisfies a nonconstant-coefficient, inhomogeneous, convective wave equation. Using an elliptic coordinate transformation, the unsteady boundary value problem is solved in the frequency domain on grids which are determined as a function of the Mach number and reduced frequency. Extensive comparisons are made with known solutions to unsteady vortical flow problems, and it is seen that the agreement is in general very good for reduced frequencies ranging from 0 up to 4.

I. INTRODUCTION

Most flows encountered in aerodynamics are high speed flows where the Reynolds number is large and the effects of viscosity are confined to small regions such as boundary layers and wakes. Because major portions of these flow fields are essentially inviscid and irrotational, potential flow theory has been used extensively by aerodynamicists in the analysis of flows about streamlined bodies. Today steady potential flow solvers are widely used in the design of aircraft wings, turbomachinery blades, and helicopter rotors.

In many real flow applications, however, the flow is not steady but unsteady. Frequently the unsteadiness in the flow is due to the occurrence of upstream vortical disturbances that are convected downstream and induce an unsteady flow field as they interact with the body. For an aircraft wing, such upstream flow distortion can be caused by atmospheric turbulence. For propeller and turbomachinery blades, the vortical disturbances may be caused by the viscous wakes of an upstream rotor or stator, installation effects, or upstream turbulence.

When viewed from the blade frame of reference, the upstream vortical disturbances will appear as propagating vorticity waves that are called gusts. There are a number of undesirable effects that can be associated with such vortical gusts. They will, for example, induce unsteady forces on the airfoil surface which can cause forced vibrations and radiate noise into the far field. In some instances, the impinging gusts may cause flow separation and loss of aerodynamic performance. For rotating blades, the fundamental frequency of the upstream disturbances will equal the blade passing frequency. If the frequency of the aerodynamic excitation equals a natural frequency of the rotating blades and the amplitude is sufficient, then catastrophic structural failure may result.

Another possible source of unsteadiness in the flow is the unsteady motion of the airfoils or blades themselves. Such unsteady structural motion can be caused by structure-borne vibrations as well as the flow-induced oscillations described above. There can also be unsteady interactions between the airfoil motion and the incident disturbances which can dampen or increase the magnitude of the airfoil unsteady motion.

Because of the undesirable effects associated with these unsteady flows, there is considerable interest in controlling and understanding the aerodynamic excitations which can cause such unsteady blade motion.

Up until recently, most numerical efforts to solve these kinds of unsteady flows concentrated on potential methods. The early work dealt with solving the unsteady small disturbance potential equation as a way of obtaining the unsteady flow around oscillating airfoils or cascades. Later work was directed toward solving the linearized unsteady potential equation and the unsteady full potential equation. Potential methods have proven to work well for oscillating airfoil problems, but unfortunately they cannot adequately account for the vortical part of the flow. Previous potential formulations which have included the effects of the upstream vorticity have invoked the linear thin airfoil approximation and assumed that the imposed vortical gust is convected without distortion by the nonuniform mean flow. This was the approach used by McCroskey and Goorjian [1] and McCroskey [2]. However, as shown by Goldstein and Atassi [3], Atassi [4], and Scott and Atassi [5], the assumption that the gust is convected without distortion is not justified and is a poor approximation for flows with a spatially varying mean flow. This is especially true for turbomachinery and propeller flow fields where the blades are heavily loaded and there are strong mean flow gradients.

In the past few years, computational efforts in unsteady aerodynamics have concentrated on the so-called primitive variable methods in which the unsteady Euler or Navier-Stokes equations are solved in time along with certain specified boundary conditions. Unlike the potential methods, the primitive variable methods are equally well-suited to both oscillating airfoil problems and flows with convected upstream vorticity. The main difficulty associated with these methods is that they are too expensive to be used for routine engineering calculations such as are encountered in design work. In addition, uncertainties about physically correct far field boundary conditions leaves some question as to the accuracy of the solutions.

In a previous paper [5], the authors presented a linearized unsteady aerodynamic analysis for subsonic vortical flows around lifting airfoils which represents an alternative to the potential and primitive variable methods. The analysis that was presented in [5] offers the computational efficiency of potential methods, but at the same time accounts for the convection and distortion of the upstream vorticity by the nonuniform mean flow. Our analysis is therefore equally well-suited to vortical flow problems as well as to oscillating airfoil problems. In addition, since our linearization is about the nonuniform mean flow, the full nonlinear effects of the mean flow are accounted for. Only the unsteady part of the flow is linearized. These features, coupled with the inherent efficiency of the linearized approach, make our analysis an ideal solution method for unsteady aerodynamic flow fields.

In [5] we presented the mathematical formulation of the general linearized boundary value problem, and demonstrated the capabilities of our approach by presenting numerical solutions for a large variety of unsteady vortical flows. The numerical results presented showed in detail the effects of airfoil thickness, angle of attack, camber, and Mach number on the unsteady lift and moment of isolated airfoils subjected to periodic vortical gusts in subsonic flows.

In the present paper our major purpose is to present the details of the frequency domain numerical scheme that has been developed to implement our linearized unsteady aerodynamic analysis. Since we presented the full formulation of the analysis in [5], we will only summarize the resulting boundary value problem in the present paper. This will be done in the following section. Following that will be the main section of the paper which presents our frequency domain numerical scheme. Finally, in Section IV, we present a large variety of numerical results which demonstrate the validation of our codes.

II. LINEARIZED UNSTEADY AERODYNAMIC FORMULATION

Consider an inviscid, compressible flow past a two-dimensional airfoil placed at nonzero incidence to a stream with uniform upstream velocity U_∞ in the x_1 direction. We assume in the present discussion that the fluid is an ideal, non-heat conducting gas with constant specific heats, and that there are no shocks in the flow. Under the above assumptions there will be a steady potential flow around the airfoil so that we may write

$$\vec{U}_0(\vec{x}) = \vec{\nabla}\Phi_0, \tag{2.1}$$

where 0 subscripts are used to denote steady mean flow quantities.

Let us assume that far upstream an unsteady vortical disturbance is imposed on the flow. The only restriction that we place on the upstream disturbance is that it can be expressed as a generalized Fourier integral so that we may write

$$\vec{u}_\infty(\vec{x} - \vec{i}U_\infty t) = \int_{\vec{k}} \vec{a}(\vec{k}) e^{i\vec{k}\cdot(\vec{x} - \vec{i}U_\infty t)} d\vec{k} \tag{2.2}$$

and in addition, that its length scale l' and characteristic velocity u_∞ are such that the condition

$$\frac{c}{U_\infty} \ll \frac{l'}{u_\infty} \tag{2.3}$$

is satisfied, where c is the airfoil chord length. We thus require that the time scale associated with the mean flow be an order of magnitude less than the time scale associated with the upstream unsteady disturbances. Since our concern is with flows that have large scale upstream disturbances in which l' is the same order of magnitude as the chord length c, condition (2.3) essentially reduces to the requirement that $u_\infty \ll U_\infty$.

Since we present a linearized mathematical formulation, we may without loss of generality consider a single Fourier component of the incident vortical disturbance, and solve for more general disturbances by superposition. We therefore consider incident vortical gusts of the form

$$\vec{u}_\infty = \vec{a} e^{i\vec{k}\cdot(\vec{X} - \vec{i}U_\infty t)}, \tag{2.4}$$

where $\vec{a}$ and $\vec{k}$ must satisfy

$$\vec{a} \cdot \vec{k} = 0 \tag{2.5}$$

to ensure that the continuity equation is satisfied.

In general, the components of $\vec{X}$ in equation (2.4) are not the spatial coordinates, but rather are Lagrangian coordinates of the mean flow. For the case of two-dimensional mean flow the components of $\vec{X}$ are given by

$$X_2 = \frac{\Psi_0}{\rho_\infty U_\infty} \tag{2.6}$$

and

$$X_3 = x_3, \tag{2.7}$$

where Ψ_0 is the stream function of the mean flow and x_3 is the spatial coordinate in the spanwise direction. The component X_1 is defined by

$$X_1 = U_\infty \Delta, \tag{2.8}$$

where Δ is the Lighthill "drift" function [6], which can be expressed in terms of Φ_0 and Ψ_0 as

$$\Delta = \frac{\Phi_0}{U_\infty{}^2} + \int_{-\infty}^{\Phi_0} \left(\frac{1}{U_0{}^2} - \frac{1}{U_\infty{}^2}\right) d\Phi_0, \tag{2.9}$$

where the integration is carried out on $\Psi_0 = \text{constant}$. The difference in Δ between two points on a streamline is the time it takes a mean flow fluid particle to traverse the distance between those two points. Note that for the thin airfoil case in which the mean flow is a uniform parallel flow, the components of $\vec{X}$ reduce precisely to the spatial coordinates.

We assume that the total unsteady flow field can be represented by

$$\vec{U}(\vec{x},t) = \vec{U}_0(\vec{x}) + \vec{u}(\vec{x},t) \tag{2.10}$$

$$p(\vec{x},t) = p_0(\vec{x}) + p'(\vec{x},t) \tag{2.11}$$

$$\rho(\vec{x},t) = \rho_0(\vec{x}) + \rho'(\vec{x},t) \tag{2.12}$$

$$s(\vec{x},t) = s_0 + s'(\vec{x},t) \tag{2.13}$$

where the entropy s_0 is constant, and $\vec{u}$, p', ρ', and s' are the unsteady perturbation velocity, pressure, density and entropy, respectively. Quantities with 0 subscripts are the steady mean flow quantities which are assumed to be known. Note that these quantities obey the steady nonlinear equations of motion, so that the linearization of the unsteady flow is about the fully nonlinear mean flow.

Substituting relations (2.10) - (2.13) into the nonlinear Euler equations and neglecting products of small quantities, one obtains the linearized continuity, momentum, and energy equations

$$\frac{D_0\rho'}{Dt} + \rho'\vec{\nabla}\cdot\vec{U}_0 + \vec{\nabla}\cdot(\rho_0\vec{u}) = 0 \tag{2.14}$$

$$\rho_0\left(\frac{D_0\vec{u}}{Dt} + \vec{u}\cdot\vec{\nabla}\vec{U}_0\right) + \rho'\vec{U}_0\cdot\vec{\nabla}\vec{U}_0 = -\vec{\nabla}p' \tag{2.15}$$

$$\frac{D_0 s'}{Dt} = 0, \tag{2.16}$$

where $\frac{D_0}{Dt} = \frac{\partial}{\partial t} + \vec{U}_0\cdot\vec{\nabla}$ is the convective derivative associated with the mean flow.

It is shown in References 7 and 8 that if the unsteady velocity is decomposed into the sum of a known vortical component and an unknown potential component, then the problem for determining the unsteady flow may be reduced to solving a single, non-constant coefficient, inhomogeneous convective wave equation which may be written

$$\frac{D_0}{Dt}\left(\frac{1}{{c_0}^2}\frac{D_0\phi}{Dt}\right) - \frac{1}{\rho_0}\vec{\nabla}\cdot(\rho_0\vec{\nabla}\phi) = \frac{1}{\rho_0}\vec{\nabla}\cdot(\rho_0\vec{u}^{(R)}), \tag{2.17}$$

where

$$\vec{u}(\vec{x},t) = \vec{u}^{(R)} + \vec{\nabla}\phi. \tag{2.18}$$

The unsteady pressure is related to ϕ through the equation

$$p' = -\rho_0(\vec{x})\frac{D_0\phi}{Dt}. \tag{2.19}$$

The vortical velocity $\vec{u}^{(R)}$ is a known function of the mean flow Lagrangian coordinates and the upstream vortical disturbances and is given by

$$\vec{u}^{(R)} = [\vec{\nabla}(\vec{a}\cdot\vec{X})]e^{i\vec{k}\cdot(\vec{X}-\vec{i}U_\infty t)} + \vec{\nabla}\tilde{\phi}, \tag{2.20}$$

where

$$\tilde{\phi} = \frac{i}{k_1}\left(a_1 + \frac{a_2k_1 - a_1k_2}{1 + ia_0U_\infty k_1}\frac{1 - e^{-ik_2X_2}}{k_2}\right)e^{i\vec{k}\cdot(\vec{X}-\vec{i}U_\infty t)}, \tag{2.21}$$

and

$$\vec{a} = (a_1, a_2, a_3) \qquad \text{and} \quad a_0 = -\left(\frac{\partial U_0}{\partial n}\right)_S^{-1}. \tag{2.22}$$

Here n denotes the direction of the outward unit normal, S denotes the stagnation point near the airfoil leading edge, and $U_0 = |\vec{U_0}|$ is the magnitude of the mean velocity. (See [5] or [8] for more details concerning the purpose and derivation of the function $\tilde{\phi}$.)

Finally, the potential ϕ must satisfy the boundary conditions

$$\vec{\nabla}\phi\cdot\vec{n} = 0 \qquad \text{airfoil surface} \tag{2.23}$$

$$\frac{D_0}{Dt}(\Delta\phi) = 0 \qquad \text{wake} \tag{2.24a}$$

$$\Delta[\vec{\nabla}\phi\cdot\vec{n}] = 0 \qquad \text{wake} \tag{2.24b}$$

$$\vec{\nabla}\phi \rightarrow -\vec{\nabla}\tilde{\phi} \quad \text{as} \quad x_1 \rightarrow -\infty, \tag{2.25}$$

where equation (2.23) is the impermeability condition at the airfoil surface, equations (2.24a) and (2.24b) impose continuity of the pressure and normal velocity across the wake, and equation (2.25) ensures that $\vec{u}(\vec{x},t) \rightarrow \vec{u}_\infty(\vec{x},t)$ as $x_1 \rightarrow -\infty$.

The linearized boundary value problem for the unsteady gust response problem thus consists of the governing equation (2.17) and boundary conditions (2.23) – (2.25), together with the requirement that ϕ is continous at the airfoil trailing edge.

III. NUMERICAL SCHEME

Reformulation and Nondimensionalization of the Boundary Value Problem

For numerical purposes it is necessary to reformulate the boundary value problem presented in the previous section into a form more suitable for numerical computations. Of particular concern is condition (2.25). In order to facilitate the implementation of the far field boundary condition, it is convenient to replace ϕ by a function whose gradient vanishes as $r \to \infty$, where r is the distance from the airfoil center.

To this end, we introduce the potential functions ϕ_1 and ϕ_2, where

$$\phi = \phi_1 - \phi_2 \tag{3.1}$$

and ϕ_2 is a known function which is constructed such that

$$|\phi_2 - \tilde{\phi}| \to 0 \qquad \text{as} \quad r \to \infty. \tag{3.2}$$

Equation (3.1) together with conditions (2.25) and (3.2) then show that the new potential function ϕ_1 will satisfy

$$\vec{\nabla}\phi_1 \to \vec{\nabla}\phi_2 - \vec{\nabla}\tilde{\phi} \to 0 \qquad \text{as} \quad r \to \infty. \tag{3.3}$$

The problem may then be reformulated in terms of the unknown potential ϕ_1.

To satisfy condition (3.2), the function ϕ_2 must take the form

$$\phi_2 = \frac{i}{k_1}(a_1 + \frac{a_2 k_1 - a_1 k_2}{1 + i a_0 U_\infty k_1} \frac{1 - e^{-ik_2 X_2}}{k_2}) e^{i\vec{k}\cdot(\vec{X}_e - \vec{i} U_\infty t)}, \tag{3.4}$$

where the vector $\vec{X}_e$ satisfies

$$|\vec{X}_e - \vec{X}| \to 0 \qquad \text{as} \quad r \to \infty. \tag{3.5}$$

To satisfy this condition for the general problem of vortical flows around lifting airfoils, we define $\vec{X}_e$ as follows:

$$X_{e,1} = \frac{\Phi_0}{U_\infty} - \frac{\Gamma}{\pi U_\infty} \text{sgn}(\Psi_0)[\frac{\pi}{2} + \text{sgn}(\Psi_0)\tan^{-1}(\frac{\rho_\infty \Phi_0}{\beta_\infty \Psi_0})][1 - e^{-(\Phi_0^2 + \frac{\Psi_0^2}{\rho_\infty^2})(\frac{2}{c U_\infty})^2}] \tag{3.6}$$

$$X_{e,2} = X_2 \tag{3.7}$$

$$X_{e,3} = X_3. \tag{3.8}$$

The expression for $X_{e,1}$ is obtained by making a far field expansion of Lighthill's drift function Δ in terms of Φ_0 and Ψ_0. Note that the first term in the expansion is just $\frac{\Phi_0}{U_\infty}$, and that the second term arises due to the circulation around the airfoil. Since the second term vanishes for airfoils with zero circulation, it is clear that the formulation of the source term for nonlifting airfoils is much simpler than for lifting airfoils.

We also point out that the first factor in brackets in equation (3.6) is discontinuous and undefined at the points on the airfoil where $\Phi_0 = 0, \Psi_0 = 0^+$ and $\Phi_0 = 0, \Psi_0 = 0^-$. The second factor in brackets is not part of the expansion itself, but is included to remove the discontinuity in $X_{e,1}$. By including the second factor in brackets and defining $X_{e,1} = 0$ at $\Phi_0 = 0$, $\Psi_0 = 0$, we obtain an expression for $X_{e,1}$ which is everywhere continuous. It is important that $X_{e,1}$ be continuous along the airfoil surface, for if it were not, the potential function ϕ_1 would have to satisfy a discontinuous airfoil boundary condition. (See condition (3.10) below.) By defining $X_{e,1}$ as in (3.6), we obtain an expression for $\vec{X}_e$ which is everywhere continuous and also ensures that conditions (3.5) and (3.2) will be satisfied for both lifting and nonlifting airfoils.

Finally, the parameter $\beta_\infty = \sqrt{1 - {M_\infty}^2}$, where M_∞ is the free stream Mach number, and c is the airfoil chord length. The β_∞ term arises due to a Gothert's rule correction on the mean velocity so that the expression for $X_{e,1}$ is valid for both compressible and incompressible flows.

Before presenting the reformulated boundary value problem in terms of the potential ϕ_1, we present the nondimensionalization of the problem. We normalize as follows:

$x_1, x_2, x_3, X_1, X_2, X_3, X_{e,1}$	by	$\frac{c}{2}$
Φ_0, Γ	by	$\frac{c}{2}U_\infty$
Ψ_0	by	$\frac{c}{2}\rho_\infty U_\infty$
U_0, c_0	by	U_∞
ρ_0	by	ρ_∞
p'	by	$\rho_\infty U_\infty \lvert\vec{a}\rvert$
t, Δ	by	$\frac{c}{2U_\infty}$
ω	by	$\frac{2U_\infty}{c}$
k_1, k_2, k_3	by	$\frac{2}{c}$
$\phi, \tilde{\phi}, \phi_1, \phi_2$	by	$\frac{c}{2}\lvert\vec{a}\rvert$
$\vec{a}$	by	$\lvert\vec{a}\rvert$

The normalized wave number $k_1 = \frac{\omega c}{2U_\infty}$, where ω and U_∞ are the dimensional angular frequency and free stream velocity, respectively, is called the reduced frequency.

We will assume throughout the remainder of the present section, unless stated otherwise, that all quantities are nondimensional.

The governing equation for ϕ_1 is then

$$\frac{D_0}{Dt}\left(\frac{1}{{c_0}^2}\frac{D_0\phi_1}{Dt}\right) - \frac{1}{\rho_0}\vec{\nabla}\cdot(\rho_0\vec{\nabla}\phi_1) = \frac{1}{\rho_0}\vec{\nabla}\cdot(\rho_0\vec{u}^{(R)})$$

$$+ \frac{D_0}{Dt}\left(\frac{1}{{c_0}^2}\frac{D_0\phi_2}{Dt}\right) - \frac{1}{\rho_0}\vec{\nabla}\cdot(\rho_0\vec{\nabla}\phi_2) \tag{3.9}$$

and the boundary conditions are

$$\vec{\nabla}\phi_1 \cdot \vec{n} = \vec{\nabla}\phi_2 \cdot \vec{n} \qquad \text{airfoil surface} \tag{3.10}$$

$$\frac{D_0}{Dt}[\Delta(\phi_1 - \phi_2)] = 0 \qquad \text{wake} \tag{3.11a}$$

$$\Delta[\vec{\nabla}(\phi_1 - \phi_2) \cdot \vec{n}] = 0 \qquad \text{wake} \tag{3.11b}$$

$$\vec{\nabla}\phi_1 \to 0 \quad \text{as} \quad x_1 \to -\infty. \tag{3.12}$$

For completeness we also present the nondimensional expressions for the potential functions $\tilde{\phi}$ and ϕ_2, for the unsteady velocity and pressure, and for the upstream velocity disturbances.

$$\tilde{\phi} = \frac{i}{k_1}(a_1 + \frac{a_2k_1 - a_1k_2}{1 + ia_0k_1}\frac{1 - e^{-ik_2X_2}}{k_2})e^{i\vec{k}\cdot\vec{X} - ik_1t} \tag{3.13}$$

$$\phi_2 = \frac{i}{k_1}(a_1 + \frac{a_2k_1 - a_1k_2}{1 + ia_0k_1}\frac{1 - e^{-ik_2X_2}}{k_2})e^{i\vec{k}\cdot\vec{X}_e - ik_1t}, \tag{3.14}$$

where

$$X_1 = \Delta, \quad X_2 = X_{e,2} = \Psi_0, \quad X_3 = X_{e,3} = x_3 \tag{3.15}$$

$$X_{e,1} = \Phi_0 - \frac{\Gamma}{\pi}\text{sgn}(\Psi_0)[\frac{\pi}{2} + \text{sgn}(\Psi_0)\tan^{-1}(\frac{\Phi_0}{\beta_\infty\Psi_0})][1 - e^{-(\Phi_0^2+\Psi_0^2)}] \tag{3.16}$$

$$\vec{u}(\vec{x}, t) = \vec{u}^{(R)} + \vec{\nabla}(\phi_1 - \phi_2) \tag{3.17}$$

where

$$\vec{u}^{(R)} = [\vec{\nabla}(\vec{a} \cdot \vec{X})]e^{i\vec{k}\cdot\vec{X} - ik_1t} + \vec{\nabla}\tilde{\phi}. \tag{3.18}$$

$$p' = -\rho_0(\vec{x})\frac{D_0(\phi_1 - \phi_2)}{Dt}. \tag{3.19}$$

$$\vec{u}_\infty = \vec{a}e^{i\vec{k}\cdot\vec{X} - ik_1t} \tag{3.20}$$

Determination of Mean Potential Flow

In order to obtain numerical solutions to equation (3.9) and its associated boundary conditions, one must first obtain the steady potential flow about the airfoil for the given flow conditions. This will in general require the use of a standard potential flow solver such as FLO36.[9]

However, an examination of equations (3.13) through (3.18) indicates that the most natural choice of independent variables in which to solve equation (3.9) are Φ_0 and Ψ_0, the mean flow potential and stream functions. Since standard potential flow codes solve the steady problem in terms of the spatial coordinates x_1 and x_2, there is some difficulty in obtaining the steady solution as a function of Φ_0 and Ψ_0.

Another difficulty arises due to the fact that the grids used by steady flow solvers are not suitable for the unsteady calculation. As reported in References 10 and 11, accurate solution of equation (3.9) over a large range of flow conditions requires using grids which are determined as a function of both the reduced frequency k_1 and the free stream Mach number M_∞. This means that in general it will be necessary to interpolate the solution from the steady grid onto the appropriate unsteady grid.

Because of the loss of accuracy that can result from such an interpolation process, and also because of the need to know the mean flow as a function of Φ_0 and Ψ_0, an analytical scheme that can obtain the compressible, subsonic flow about isolated airfoils was developed. The scheme is based on the idea that, except for a small inner region surrounding the airfoil, the flow gradients are not too large. Thus in the large outer region extending to infinity, the mean flow is essentially governed by a set of linear equations. As a result, one can use Gothert's Rule, whereby the compressible flow about a given airfoil can be obtained from the incompressible flow about a similar airfoil.

If we let α_C, θ_C, and γ_C denote the angle of attack, thickness ratio, and camber ratio of the given airfoil in a compressible flow, then the transformed airfoil for the incompressible flow field has angle of attack, thickness ratio, and camber ratio given by

$$\left.\begin{aligned} \alpha_I &= \beta_\infty\, \alpha_C \\ \theta_I &= \beta_\infty\, \theta_C \\ \gamma_I &= \beta_\infty\, \gamma_C \end{aligned}\right\} \tag{3.21}$$

where I subscripts denote quantities from the incompressible flow field. Using dimensional quantities and denoting the compressible velocity by $(U_\infty + u_C, v_C)$ at the point (x, y) and the incompressible velocity by $(U_\infty + u_I, v_I)$ at the point (x_I, y_I), the spatial coordinates and velocity in the compressible and incompressible planes are related by

$$x = x_I \tag{3.22a}$$

$$y = \frac{y_I}{\beta_\infty} \tag{3.22b}$$

and

$$u_C = \frac{u_I}{{\beta_\infty}^2} \tag{3.23a}$$

$$v_C = \frac{v_I}{\beta_\infty}. \tag{3.23b}$$

It is assumed here that the free stream velocity U_∞ is aligned with the x axis, and that the angle of attack, thickness ratio, and camber ratio of the airfoil are such that the perturbation velocities are small compared to U_∞. The potential and stream functions of the compressible flow field are then related to the potential and stream functions of the incompressible flow field by

$$\Phi_0 - U_\infty x = \frac{1}{{\beta_\infty}^2}(\Phi_I - U_\infty x_I) \tag{3.24a}$$

$$\Psi_0 - U_\infty y = \frac{1}{\beta_\infty}(\Psi_I - U_\infty y_I) \tag{3.24b}$$

Using (3.22), and assuming that all quantities have been nondimensionalized as in the previous section, equations (3.24) can be rewritten

$$\Phi_I - M_\infty^2 x_I = \beta_\infty^2 \Phi_0 \tag{3.25a}$$

$$\Psi_I = \beta_\infty \Psi_0 \tag{3.25b}$$

The problem is then, given (Φ_0, Ψ_0), solve equations (3.25) for (Φ_I, Ψ_I) and then use relations (3.22) and (3.23) to determine the spatial coordinates (x, y) and velocity components (u_C, v_C) of the compressible flow field. If this can be done, then we have the compressible flow field determined as a function of (Φ_0, Ψ_0). Note that this assumes that we can determine (x_I, y_I) and (u_I, v_I) as functions of (Φ_I, Ψ_I). Since there is a one to one correspondence between (x_I, y_I) and (Φ_I, Ψ_I), and between (u_I, v_I) and (Φ_I, Ψ_I), this is not a difficulty. At the least, it can always be done numerically. For the special case of Joukowski airfoils, however, it is possible to express the complex potential (Φ_I, Ψ_I) in terms of the polar coordinates (r, θ), and then obtain (x_I, y_I) and (u_I, v_I) through known functional expressions of (r, θ).

For the case of incompressible flow around a Joukowski airfoil the complex potential is given by

$$\Phi_I + i\,\Psi_I = \zeta' e^{-i\alpha_I} + \frac{a^2 e^{i\alpha_I}}{\zeta'} + \frac{\Gamma_I}{2\pi i}\ln\left(\frac{\zeta'}{a}\right) + K \tag{3.26}$$

where K is an arbitrary constant and

$$\zeta' = \zeta - \zeta_{0'} = re^{i\theta}. \tag{3.27}$$

Here $\zeta_{0'} = -\epsilon + i\epsilon'$ is a complex constant, and the parameters a, ϵ, and ϵ' depend on the airfoil geometry. Γ_I is the steady circulation around the airfoil and is given by

$$\Gamma_I = -4\pi a \sin(\alpha_I + \beta) \tag{3.28}$$

where β is defined by

$$\sin\beta = \frac{\epsilon'}{a}. \tag{3.29}$$

The spatial coordinates (x_I, y_I) are determined from r and θ through the Joukowski transformation

$$x_I + i\, y_I = \zeta + \frac{d^2}{\zeta} \tag{3.30}$$

where the parameter d satisfies

$$(\epsilon + d)^2 + \epsilon'^2 = a^2. \tag{3.31}$$

Finally, the velocity components (u_I, v_I) are given by

$$u_I - i\, v_I = \frac{\zeta^2[\zeta' + a e^{i(2\alpha_I+\beta)}]}{((\zeta + d)\zeta'^2} \quad - \quad 1. \tag{3.32}$$

Using relations (3.26) through (3.30), equations (3.25) can be expressed in terms of r and θ as

$$\left.\begin{array}{c} (r + \frac{a^2}{r})\cos(\theta - \alpha_I) - [2a\sin(\alpha_I + \beta)]\theta + K \\ -M_\infty^2[r\cos\theta - \epsilon + \frac{d^2(r\cos\theta-\epsilon)}{(r\cos\theta-\epsilon)^2+(r\sin\theta+\epsilon')^2}] = \beta_\infty^2\Phi_0 \\ \\ (r - \frac{a^2}{r})\sin(\theta - \alpha_I) + 2a\sin(\alpha_I + \beta)\ln(\frac{r}{a}) = \beta_\infty\Psi_0 \end{array}\right\} \tag{3.33}$$

If for given Φ_0 and Ψ_0 we can solve equations (3.33) for r and θ, then equations (3.30) and (3.32) can be used to get (x_I, y_I) and (u_I, v_I), and equations (3.22) and (3.23) can be used to obtain (x, y) and (u_c, v_c). Once we have obtained (u_c, v_c), the other mean flow quantities can then be obtained from Bernoulli's law for polytropic gases.

We note that, while the system of equations (3.33) is highly nonlinear in the unknowns r and θ, it can be routinely solved by two-dimensional Newton iteration. Once a subroutine has been developed to solve equations (3.33), the compressible steady flow around any Joukowski airfoil can be very efficiently obtained. In addition, the mean flow is obtained for arbitrary Φ_0 and Ψ_0, so that there is no restriction whatsoever on the particular grid that may be used for the unsteady calculation.

The only limitation in obtaining the mean potential flow by this particular approach is the underlying assumption that u_C and v_C must be small compared to U_∞. This means that the method will not give a good approximation in the inner region and particularly near the stagnation point where the perturbation velocities are of the same order of magnitude as U_∞. However, extensive testing of this particular approach and comparing with the steady potential flow solver FLO36 has shown that the region of inaccuracy is very small. Figures 1 through 4 show Mach number comparisons between the present approximate analytical scheme and FLO36. The comparison is made at grid points along fixed grid lines used by FLO36. It is seen that the agreement overall is quite good, with the exception of grid points on the airfoil surface that are near the stagnation point. Because of this inaccuracy, we use FLO36 to calculate the mean flow quantities along the airfoil surface itself, and use the approximate analytical scheme off the airfoil except in a small region just upstream of the stagnation point. In this region, for airfoils that have steady loading, the velocities are calculated using a Taylor series expansion. For airfoils without steady loading, the velocities are calculated from a local analytical solution which is patched to the outer solution.

Frequency Domain Formulation

An inspection of equations (3.13), (3.14), (3.18), and (3.20) indicates that the time dependence of the present boundary value problem comes entirely through the harmonic term e^{-ik_1t}. It is therefore possible to make a transformation from the time domain into the frequency domain by a simple change of dependent variable. By transforming the problem into the frequency domain, time is completely eliminated from the problem and it is possible to significantly simplify the mathematical formulation of the boundary value problem.

For the case of two-dimensional mean flow, we transform into the frequency domain by making the following change of dependent variable:

$$\phi_1 = \varphi e^{-ik_1t+ik_3x_3} \tag{3.34}$$

By including the ik_3x_3 term in the transformation, the harmonic dependence on the spanwise component x_3 is also eliminated, since all of the $e^{ik_3x_3}$ terms then factor out from each side of the equation. This is of course possible in view of (3.20) and (3.15).

Before presenting the governing equation in the new dependent variable φ, we introduce the linear operators $\mathcal{L}$ and $\mathcal{L}_0$ to simplify the notation.

$$\mathcal{L} = \frac{D_0}{Dt}\left(\frac{1}{c_0{}^2}\frac{D_0}{Dt}\right) - \frac{1}{\rho_0}\vec{\nabla}\cdot(\rho_0\vec{\nabla}) \tag{3.35}$$

and

$$\mathcal{L}_0 = M_\infty^2\frac{D_0^2}{Dt_0^2} - \left(\frac{\partial^2}{\partial\Phi_0^2} + \frac{\partial^2}{\partial\Psi_0^2} + \frac{\partial^2}{\partial x_3^2}\right) \tag{3.36}$$

where

$$\frac{D_0}{Dt_0} = \frac{\partial}{\partial t} + \frac{\partial}{\partial\Phi_0} \tag{3.37}$$

The governing equation then takes the form

$$\mathcal{L}\phi_1 = \frac{1}{\rho_0}\vec{\nabla}\cdot(\rho_0\vec{u}^{(R)}) + \mathcal{L}\phi_2 \tag{3.38}$$

The operator $\mathcal{L}_0$ is essentially the operator for the linear thin airfoil gust response problem. By writing the governing equation in the following equivalent form, the left hand side of the equation will exhibit the character of the thin airfoil operator in the far field since $\mathcal{L} \to \mathcal{L}_0$ there.

$$\mathcal{L}_0\phi_1 + (\mathcal{L} - \mathcal{L}_0)\phi_1 = \frac{1}{\rho_0}\vec{\nabla} \cdot (\rho_0 \vec{u}^{(R)}) + \mathcal{L}\phi_2 \tag{3.39}$$

We then have in terms of φ

$$\mathcal{L}_0\phi_1 + (\mathcal{L} - \mathcal{L}_0)\phi_1 =$$

$$e^{-ik_1t+ik_3x_3}\Big\{-[\beta_\infty^2 \frac{\partial^2\varphi}{\partial\Phi_0^2} + \frac{\partial^2\varphi}{\partial\Psi_0^2} + 2ik_1M_\infty^2 \frac{\partial\varphi}{\partial\Phi_0} + (k_1^2M_\infty^2 - k_3^2)\varphi]$$

$$+ [k_1^2M_\infty^2 - \frac{k_1^2M^2}{U_0^2} - ik_1U_0^2\frac{\partial}{\partial\Phi_0}(\frac{M^2}{U_0^2})]\varphi \tag{3.40}$$

$$+ [M^2(\frac{\partial U_0^2}{\partial\Phi_0} - 2ik_1) + 2ik_1M_\infty^2 + U_0^4\frac{\partial}{\partial\Phi_0}(\frac{M^2}{U_0^2}) - \frac{U_0^2}{\rho_0}\frac{\partial\rho_0}{\partial\Phi_0}]\frac{\partial\varphi}{\partial\Phi_0}$$

$$+ (\beta_\infty^2 - \beta^2U_0^2)\frac{\partial^2\varphi}{\partial\Phi_0^2} + (1 - U_0^2)\frac{\partial^2\varphi}{\partial\Psi_0^2} - \frac{U_0^2}{\rho_0}\frac{\partial\rho_0}{\partial\Psi_0}\frac{\partial\varphi}{\partial\Psi_0}\Big\},$$

where M is the local Mach number of the mean flow.

Equation (3.40) may be simplified further by making the following change of both dependent and independent variables:

$$\varphi = \psi e^{-iK_0\Phi} \tag{3.41a}$$

where

$$K_0 = \frac{k_1M_\infty^2}{\beta_\infty^2} \tag{3.41b}$$

and

$$\Phi = \Phi_0 \tag{3.42a}$$

$$\Psi = \beta_\infty\Psi_0 \tag{3.42b}$$

Expressing equation (3.40) in terms of ψ and the new independent variables Φ and Ψ, one gets

$$\mathcal{L}_0\phi_1 + (\mathcal{L} - \mathcal{L}_0)\phi_1 =$$

$$e^{-ik_1t+ik_3x_3}e^{-iK_0\Phi}\Big\{-\beta_\infty^2[\frac{\partial^2\psi}{\partial\Phi^2} + \frac{\partial^2\psi}{\partial\Psi^2} + (\frac{k_1^2M_\infty^2}{\beta_\infty^4} - \frac{k_3^2}{\beta_\infty^2})\psi] \tag{3.43}$$

$$+ A_1\psi + A_2\frac{\partial\psi}{\partial\Phi} + A_3\frac{\partial\psi}{\partial\Psi} + A_4\frac{\partial^2\psi}{\partial\Phi^2} + A_5\frac{\partial^2\psi}{\partial\Psi^2}\Big\}$$

where $A_1 ... A_5$ are functions of (Φ, Ψ) defined by

$$A_1(\Phi,\Psi) = \frac{k_1^2 M_\infty^2}{\beta_\infty^2} - \frac{k_1^2 M^2}{U_0^2} - ik_1 U_0^2 \frac{\partial}{\partial \Phi}\left(\frac{M^2}{U_0^2}\right) \tag{3.44a}$$

$$- iK_0\left[M^2\left(\frac{\partial U_0^2}{\partial \Phi} - 2ik_1\right) + U_0^4 \frac{\partial}{\partial \Phi}\left(\frac{M^2}{U_0^2}\right) - \frac{U_0^2}{\rho_0}\frac{\partial \rho_0}{\partial \Phi}\right] + \frac{k_1^2 M_\infty^4}{\beta_\infty^4}\beta^2 U_0^2$$

$$A_2(\Phi,\Psi) = M^2\left(\frac{\partial U_0^2}{\partial \Phi} - 2ik_1\right) + U_0^4 \frac{\partial}{\partial \Phi}\left(\frac{M^2}{U_0^2}\right) - \frac{U_0^2}{\rho_0}\frac{\partial \rho_0}{\partial \Phi} + 2iK_0 \beta^2 U_0^2 \tag{3.44b}$$

$$A_3(\Phi,\Psi) = -\frac{U_0^2}{\rho_0}\frac{\partial \rho_0}{\partial \Psi} \tag{3.44c}$$

$$A_4(\Phi,\Psi) = \beta_\infty^2 - \beta^2 U_0^2 \tag{3.44d}$$

$$A_5(\Phi,\Psi) = 1 - U_0^2 \tag{3.44e}$$

Note that in the far field the functions $A_1 ... A_5$ tend to zero so that the right hand side of (3.43) reduces to that of the linear thin airfoil theory.[12]

To complete the frequency domain formulation, it is necessary to present the right hand side of the governing equation (3.39). We will refer to the right hand side of (3.39) as the source term and denote it by $e^{-ik_1 t + ik_3 x_3} S$. To facilitate the presentation of the source term, we will write the governing equation as

$$\mathcal{L}_0 \phi_1 + (\mathcal{L} - \mathcal{L}_0)\phi_1 = e^{-ik_1 t + ik_3 x_3}\, S \tag{3.45a}$$

or

$$\mathcal{L}_0 \phi_1 + (\mathcal{L} - \mathcal{L}_0)\phi_1 = e^{-ik_1 t + ik_3 x_3}\, (S_1 + S_2 + S_3 - S_4) \tag{3.45b}$$

where

$$e^{-ik_1t+ik_3x_3}\, S_1 = \frac{\vec{\nabla}\rho_0}{\rho_0} \cdot \{[\vec{\nabla}(\vec{a}\cdot\vec{X})]e^{i\vec{k}\cdot\vec{X}-ik_1t} + \vec{\nabla}\tilde{\phi}\} \tag{3.46a}$$

$$e^{-ik_1t+ik_3x_3}\, S_2 = \vec{\nabla} \cdot \{[\vec{\nabla}(\vec{a}\cdot\vec{X})]e^{i\vec{k}\cdot\vec{X}-ik_1t} + \vec{\nabla}\tilde{\phi}\} \tag{3.46b}$$

$$e^{-ik_1t+ik_3x_3}\, S_3 = \frac{D_0}{Dt}(\frac{1}{{c_0}^2}\frac{D_0\phi_2}{Dt}) \tag{3.46c}$$

$$e^{-ik_1t+ik_3x_3}\, S_4 = \frac{1}{\rho_0}\vec{\nabla}\cdot(\rho_0\vec{\nabla}\phi_2) \tag{3.46d}$$

The frequency domain governing equation is then given by

$$\begin{aligned} & -\beta_\infty^2[\frac{\partial^2\psi}{\partial\Phi^2} + \frac{\partial^2\psi}{\partial\Psi^2} + (\frac{k_1^2M_\infty^2}{\beta_\infty^4} - \frac{k_3^2}{\beta_\infty^2})\psi] \\ & + A_1\psi + A_2\frac{\partial\psi}{\partial\Phi} + A_3\frac{\partial\psi}{\partial\Psi} + A_4\frac{\partial^2\psi}{\partial\Phi^2} + A_5\frac{\partial^2\psi}{\partial\Psi^2} \\ & = e^{iK_0\Phi}(S_1 + S_2 + S_3 - S_4) \end{aligned} \tag{3.47}$$

where $A_1 ... A_5$ are defined by equations (3.44) and $S_1 ... S_4$ are defined by equations (3.46). In the far field both the coefficients $A_1 ... A_5$ and the source term $S_1 + S_2 + S_3 - S_4$ tend to zero so that the equation reduces to a Helmholtz equation.

We conclude this section by presenting the frequency domain formulation of the airfoil and wake boundary conditions given by equations (3.10), (3.11a) and (3.11b). In terms of the new coordinates (Φ, Ψ) and the new dependent variable ψ, equation (3.10) for the airfoil boundary condition becomes

$$\frac{\partial\psi}{\partial\Psi} = -\frac{e^{iK_0\Phi}}{\beta_\infty}[\frac{a_1\beta_\infty\Gamma}{\pi}\frac{1-e^{-\Phi^3}}{\Phi} + \frac{a_2 + ia_0a_1k_2}{1 + ia_0k_1}]e^{ik_1X_{e,1}}. \tag{3.48}$$

The wake boundary condition (3.11a) becomes

$$(-ik_1 + U_0^2\frac{\partial}{\partial\Phi})[\Delta(\psi e^{-iK_0\Phi} - \varphi_2)] = 0, \tag{3.49a}$$

where

$$e^{-ik_1t+ik_3x_3}\,\varphi_2 = \phi_2 \tag{3.49b}$$

and where $\Delta(\psi e^{-iK_s\Phi} - \varphi_2)$ denotes the jump in the quantity $(\psi e^{-iK_s\Phi} - \varphi_2)$ across the vortex sheet behind the airfoil. Finally, condition (3.11b) becomes

$$\Delta[\vec{\nabla}(\psi e^{-iK_s\Phi} - \varphi_2)\cdot\vec{n}] = 0. \tag{3.49c}$$

Transformation into Computational Coordinates and Formulation of the Numerical Boundary Value Problem

Our basic numerical approach to solving equation (3.47) is to use the method of finite difference approximations. By discretizing the flow field and employing finite differences at each grid point, a large linear system of equations is obtained which can be solved using a matrix solver.

Previous experience in solving equation (3.47) for the case of flat plate and symmetric airfoils has shown that the independent variables (Φ, Ψ) are not suitable computational coordinates for the gust response problem.[10,11] There are difficulties in obtaining consistently accurate results over a large range of Mach numbers and reduced frequencies, and also problems with the implementation of far field boundary conditions. A transformation of the independent variables is needed which not only provides an adequate distribution of grid points around the airfoil in the near field, but also provides a distribution of grid points in the far field which is suitable for acoustic wave propagation and the implementation of far field, radiation type boundary conditions.

In order to satisfy these requirements, we make a transformation into the elliptic coordinates (η, ξ) with the transformation

$$\Phi = a^* \cos(\pi\eta)\cosh(\pi\xi) \tag{3.50a}$$

$$\Psi = a^* \sin(\pi\eta)\sinh(\pi\xi). \tag{3.50b}$$

where a^* is an arbitrary constant which will be defined later. Note that in the far field the elliptic coordinates reduce essentially to cylindrical coordinates, and that the $\Phi - \Psi$ plane is mapped into a semi-infinite strip in the $\eta - \xi$ plane.

With this change of variables, the governing equation takes the following form:

$$\begin{aligned}
&-\beta_\infty^2\Big[\frac{\partial^2\psi}{\partial\eta^2} + \frac{\partial^2\psi}{\partial\xi^2} + J(\eta,\xi)\Big(\frac{k_1^2 M_\infty^2}{\beta_\infty^4} - \frac{k_3^2}{\beta_\infty^2}\Big)\psi\Big] \\
&+ A_1\, J(\eta,\xi)\,\psi + T_1\frac{\partial\psi}{\partial\xi} + T_2\frac{\partial\psi}{\partial\eta} + T_3\frac{\partial^2\psi}{\partial\xi^2} + T_4\frac{\partial^2\psi}{\partial\eta^2} + T_5\frac{\partial^2\psi}{\partial\eta\partial\xi} \\
&= e^{iK_s\Phi}(S_1 + S_2 + S_3 - S_4)\, J(\eta,\xi).
\end{aligned} \tag{3.51}$$

Here $J(\eta,\xi)$ is the Jacobian of the transformation (3.50) which is given by

$$J(\eta,\xi) = \pi^2 a^{*2}[\sin^2(\pi\eta) + \sinh^2(\pi\xi)]\,, \tag{3.52}$$

and the T_i coefficients are known functions of η and ξ.

The airfoil boundary condition (3.48) has also been transformed through the change of variables (3.50). Expressing condition (3.48) in the variables (η,ξ), one gets

$$\frac{\partial\psi}{\partial\xi} = -a^*\pi\,\sin(\pi\eta)\,\frac{e^{iK_0\Phi}}{\beta_\infty}\,[\,\frac{a_1\beta_\infty\Gamma}{\pi}\,\frac{1-e^{-\Phi^2}}{\Phi} + \frac{a_2 + ia_0a_1k_2}{1+ia_0k_1}\,]e^{ik_1X_{s,1}}. \tag{3.53}$$

We now proceed to discuss the remaining boundary conditions. First, the wake boundary condition (3.49a) may be integrated so that it becomes

$$\Delta(\psi e^{-iK_0\Phi}) = \Delta\varphi_2 + [\Delta(\psi e^{-iK_0\Phi})_{t.e.} - \Delta\varphi_{2_{t.e.}}]e^{ik_1\int_{\Phi_{t.e.}}^{\Phi}\frac{d\Phi}{U_0^2}}\,, \tag{3.54}$$

where the subscript *t.e.* denotes quantities at the airfoil trailing edge. Note that, in general, both ψ and Φ are discontinuous across the wake, so that in evaluating $\Delta(\psi e^{-iK_0\Phi})$, it is necessary to take into account the jump in both ψ and Φ. This condition is imposed for grid points on the lower side of the wake.

On the upper side of the wake, we impose condition (3.49c), which specifies that the normal velocity component of the unsteady velocity is continuous across the wake. This may be written

$$\left[U_0\,\frac{\partial}{\partial\Psi}(\psi e^{-iK_0\Phi} - \varphi_2)\right]^+ = \left[U_0\,\frac{\partial}{\partial\Psi}(\psi e^{-iK_0\Phi} - \varphi_2)\right]^- \tag{3.55}$$

where "+" and "−" superscripts denote above and below the wake, respectively, and the derivatives in (3.55) are taken to be one-sided.

In order to proceed further in the development of the boundary conditions (3.54) and (3.55) in terms of the computational coordinates (η,ξ), it is necessary to first discuss in more detail the transformation (3.50). First, the constant a^* is determined from the condition that the airfoil trailing edge point on the suction side, where $\Phi = a^*, \Psi = 0$, should map into the point $\eta = 0, \xi = 0$, and the stagnation point, where $\Phi = -a^*, \Psi = 0$ should map into the point $\eta = 1, \xi = 0$. Then a^* must be determined from

$$a^* = \frac{1}{2}\int_{t.e.}^{s.p.} U_0\,ds \tag{3.56}$$

where s denotes the arc length along the airfoil surface, *t.e.* denotes the airfoil trailing edge, and *s.p.* denotes the stagnation point. The steady solver FLO36 is used to locate the stagnation point, and the integration in (3.56) is carried out using trapezoidal integration.

The suction surface of the airfoil, then, corresponds to the line segment on the η axis between 0 and 1, and the pressure surface corresponds to the line segment on the η axis between 1 and $\eta_{t.e.-}$, where $\eta_{t.e.-} < 2.0$ (See Figure 5.) The pressure side of the wake then corresponds to the line segments given by $\{\eta_{t.e.-} < \eta \leq 2.0,\ \xi = 0\}$, and $\{\eta = 2.0,\ \xi > 0\}$. The suction side of the wake corresponds to the positive ξ axis. The upper boundary of the $\eta - \xi$ grid, which is given by $\{\xi = \xi_{max},\ 0 \leq \eta \leq 2\}$, corresponds to the far field boundary in the $\Phi - \Psi$ plane.

Because of the discontinuity in Φ across the wake grid line, the grid points on the upper and lower sides of the wake in the physical plane (the $x_1 - x_2$ plane) do not coincide. This presents some difficulty in the implementation of boundary conditions (3.54) and (3.55), inasmuch as these conditions both specify a relation that must be satisfied across the wake. The difficulty can be removed, however, by simply using a linear averaging of ψ at the two adjacent grid points to represent ψ at an arbitrary point in between. Using such a linear averaging, then, boundary condition (3.54), which is imposed for wake grid points on the pressure side, becomes

$$\left[(\psi e^{-iK_0\Phi})\right]^{+}_{avg} - \left[(\psi e^{-iK_0\Phi})\right]^{-}$$

$$= \Delta\varphi_2 + [\Delta(\psi e^{-iK_0\Phi})_{t.e.} - \Delta\varphi_{2t.e.}]e^{ik_1\int_{\Phi_{t.e.}}^{\Phi}\frac{d\Phi}{U_0^2}}. \tag{3.57}$$

The discontinuity in Φ across the wake also leads to a shift in the location of the corresponding grid points in the physical plane on opposite sides of the wake. Because of this shift, the last several grid points on the pressure side in the physical plane extend past the last suction side wake grid point, so that the above averaging technique cannot be employed. (See Figure 5) However, because these last few points are in the far field where the mean flow is nearly uniform, the function ψ behaves essentially as in the case of the thin airfoil problem, and is approximately an odd function of Ψ. By assuming ψ to be an odd function with respect to Ψ in the far field, condition (3.54) becomes

$$\left[(\psi e^{-iK_0\Phi})\right]^{-} = -\frac{1}{2}\Delta\varphi_2 - \frac{1}{2}[\Delta(\psi e^{-iK_0\Phi})_{t.e.} - \Delta\varphi_{2t.e.}]e^{ik_1\int_{\Phi_{t.e.}}^{\Phi}\frac{d\Phi}{U_0^2}} \tag{3.58}$$

for extra far field wake grid points on the pressure side.

For wake grid points on the suction side, the linear averaging technique can be used for all points, and condition (3.55) becomes

$$\left[U_0\frac{\partial}{\partial\Psi}(\psi e^{-iK_0\Phi} - \varphi_2)\right]^{+} = \left[U_0\frac{\partial}{\partial\Psi}(\psi e^{-iK_0\Phi} - \varphi_2)\right]^{-}_{avg}. \tag{3.59}$$

Expressing this in η and ξ, one gets

$$\left[e^{-iK_0\Phi}\frac{U_0}{\sinh(\pi\xi)}\frac{\partial\psi}{\partial\eta}\right]^+ - \left[e^{-iK_0\Phi}\frac{U_0}{\sin(\pi\eta)}\frac{\partial\psi}{\partial\xi}\right]^-_{avg}$$

$$= U_0^+\left(\frac{\partial\varphi_2^+}{\partial\Psi} - \frac{\partial\varphi_2^-}{\partial\Psi}\right) \qquad (3.60)$$

when the averaged values of ψ lie on the η axis. When the averaged values of ψ lie on the right hand boundary of the $\eta-\xi$ grid $\{\eta = 2.0,\ \xi > 0\}$, (3.59) becomes

$$\left[e^{-iK_0\Phi}\frac{U_0}{\sinh(\pi\xi)}\frac{\partial\psi}{\partial\eta}\right]^+ - \left[e^{-iK_0\Phi}\frac{U_0}{\sinh(\pi\xi)}\frac{\partial\psi}{\partial\eta}\right]^-_{avg}$$

$$= U_0^+\left(\frac{\partial\varphi_2^+}{\partial\Psi} - \frac{\partial\varphi_2^-}{\partial\Psi}\right) \qquad (3.61)$$

In order to complete the formulation of the boundary conditions, it is only necessary to specify conditions at the airfoil trailing edge and in the far field. At the trailing edge, there are two grid points that coincide, one corresponding to the suction side of the airfoil and one corresponding to the pressure side. It is therefore necessary to impose two conditions at the trailing edge point. At the point on the suction side, which corresponds to $(\eta, \xi) = (0, 0)$, the Jacobian of the coordinate transformation (3.50) vanishes. Since the Kutta condition requires that the velocity at the trailing edge be finite, we are led to the requirement that

$$\frac{\partial\psi}{\partial\eta} = 0 \quad \text{at} \quad (\eta, \xi) = (0, 0). \qquad (3.62)$$

At the pressure side trailing edge point, we impose the condition that the unsteady pressure is continuous,

$$p'_{t.e.+} = p'_{t.e.-} \quad \text{at} \quad (\eta, \xi) = (\eta_{t.e.-}, 0). \qquad (3.63)$$

We point out that since the Jacobian vanishes at the suction side trailing edge point, it is not possible to directly calculate the pressure in $\eta-\xi$ coordinates at that point. However, it can be calculated using a Taylor series expansion from neighboring points. By using this approach, condition (3.63) can be satisfied.

In presenting the far field boundary condition, we first comment that while condition (3.12) expresses the mathematical requirement that $\vec{\nabla}\phi_1 \to 0$ at upstream infinity, this condition cannot be imposed throughout the far field on a boundary at a finite distance from the airfoil. To implement such a condition would impose a reflecting boundary condition which can lead to large errors in the solution.

To correctly model the physics of the present unsteady boundary value problem requires that the far field boundary condition be such that it allows outgoing acoustic waves to leave the solution domain without being reflected back into the computational grid. This can be accomplished, for example, by using separation of variables along with a series expansion for the far field solution ψ and only accepting those terms in the series which represent outgoing waves. The difficulty with this approach, however, is that it leads to a matrix which requires pivoting and therefore longer solution times. In addition, since ψ is not continuous across the wake, but the series expansion for ψ is continuous everywhere, there is an incompatibility near the wake which can lead to a poor solution in the far field.

An alternative to the series expansion approach is to use a Sommerfield radiation condition on the unsteady pressure. This approach avoids both the difficulties associated with the series expansion method and is also easier to implement. The Sommerfield radiation condition for the pressure is the approach used in the present work, and may be written in operator notation as

$$\left[\frac{\partial}{\partial R} - i\sqrt{(\frac{k_1 M_\infty}{\beta_\infty^2})^2 - (\frac{k_3}{\beta_\infty})^2}\right](\frac{\partial}{\partial \Phi} - i\frac{k_1}{\beta_\infty^2})\,\psi = 0 \tag{3.64}$$

where

$$\Phi = R\cos\Theta \tag{3.65a}$$

$$\Psi = R\sin\Theta. \tag{3.65b}$$

Neglecting $\frac{1}{R}\frac{\partial}{\partial\Theta}$ terms, this reduces to

$$\cos\Theta\frac{\partial^2\psi}{\partial R^2} - i\left[\sqrt{(\frac{k_1 M_\infty}{\beta_\infty^2})^2 - (\frac{k_3}{\beta_\infty})^2}\cos\Theta \;+\; \frac{k_1}{\beta_\infty^2}\right]\frac{\partial\psi}{\partial R}$$

$$-\frac{k_1}{\beta_\infty^2}\left[\sqrt{(\frac{k_1 M_\infty}{\beta_\infty^2})^2 - (\frac{k_3}{\beta_\infty})^2}\right]\psi = 0 \tag{3.66}$$

This condition is applied for all grid points such that $0 < \eta < 2$, $\xi = \xi_{\max}$.

Numerical Method

In the previous section we presented the transformation into computational coordinates and the development of the numerical boundary value problem. The problem to be solved numerically consists of the governing equation (3.51), and the boundary conditions (3.53), (3.57), (3.58), (3.60), (3.61), (3.62), (3.63) and (3.66). As mentioned previously, our basic numerical approach is to use the method of finite difference approximations, and then to solve the resulting linear system of equations using a matrix solver.

The first step in obtaining numerical solutions to equation (3.51) and its associated boundary conditions for a given flow configuration is to calculate the source term S and the coefficient functions $A_1 ... A_5$. This requires the evaluation of Lighthill's drift function and its first and second partial derivatives with respect to Ψ, and the evaluation of the mean flow quantities and their partial derivatives with respect to Φ and Ψ at each interior grid point. The mean flow quantities are obtained through the analytical scheme presented previously in the present paper, and their derivatives are calculated using four point differencing.

It should be emphasized that accurate evaluation of the source term is essential if accurate solutions to equation (3.51) are to be obtained, and this in turn depends largley upon the accurate evaluation of the drift function. If the drift function is not evaluated accurately, then the source term will not tend to zero in the far field and the numerical scheme will become unstable. One of the major advantages of using the analytical scheme outlined previously in this section to obtain the mean flow is that it can determine the mean velocities at arbitrary (Φ, Ψ). This means that for fixed Ψ, i.e. on a given streamline, we can determine the mean velocities for arbitrary Φ. Since evaluation of the drift function requires the integration of the expression $(\frac{1}{U_0^2} - \frac{1}{U_\infty^2})$ with respect to Φ on a fixed streamline, it is very easy to do the numerical integrations necessary to accurately evaluate the drift function Δ. In the actual calculations, we evaluate Δ at a given grid point as the sum of an analytically determined part and a numerically determined part. The analytical part comes from a far field expansion for Δ which is given by

$$\Delta = \Phi_0 - \frac{\Gamma}{\pi}\mathrm{sgn}(\Psi_0)\Big[\frac{\pi}{2} + \mathrm{sgn}(\Psi_0)\tan^{-1}(\frac{\Phi_0}{\beta_\infty \Psi_0})\Big] \qquad (3.67)$$

This expression can be used to accurately calculate Δ at some point far upstream, and then since Δ is additive, the remaining portion of the integration can be done numerically from the upstream location to the given grid point. The numerical integration is done using the trapezoid rule with variable spacing in Φ to ensure accurate resolution near the airfoil. The first and second partial derivatives of Δ are approximated using four point differencing.

Once S and $A_1 ... A_5$ have been calculated, they can be stored separately and passed to the subroutine which sets up the matrix equation to be solved.

We now proceed to discuss the differencing used for the governing equation and boundary conditions. To represent equation (3.51) we use the standard nine-point, central difference computational molecule which is second order accurate in η and ξ. We assume in general that the spacing in each direction is nonuniform. Details of the grid spacing will be discussed momentarily. Each of the boundary conditions (3.53), (3.62), (3.63), and (3.66) are implemented using four-point, one-sided differencing which is third order accurate for (3.53), (3.62), and (3.63), and second order accurate for (3.66). Boundary conditions (3.60) and (3.61) are both implemented using three-point, one-sided differencing which is second order accurate.

Obtaining a numerical solution to the finite difference equations representing the governing equation (3.51) and its associated boundary conditions requires solving a large matrix equation whose size is equal to twice the number of grid points. There are difficulties in solving this linear system of equations because the matrix is not block tridiagonal and does not have a regular block structure which can be exploited. In addition, iterative solvers have convergence problems because the diagonal dominance of the matrix changes as the parameters M_∞, k_1, and k_3 are varied.

Because of these difficulties, a general purpose sparse matrix solver was developed which stores only the nonzero entries of the matrix and can solve an arbitrary sparse matrix equation using Gaussian elimination. The solver basically works by using an ordered list to represent the nonzero entries of each row in the matrix, and then inserts and deletes new entries in the rows of the matrix as multiples of each row are added to other rows to carry out the elimination process. The only requirement for the solver to work is that the matrix must be arranged such that it remains reasonably sparse during the elimination procedure.

The sparse solver has both a pivoting and non-pivoting feature. However, as pivoting during the elimination process proved to be unnecessary, the pivoting feature was not used. By not pivoting during the elimination, it was possible to increase the storage efficiency of the solver and thereby solve larger systems of equations. The increased storage efficiency was gained by using a mapping function to map sub-blocks of the rectangular two-dimensional arrays containing the nonzero entries of the matrix and their associated column numbers into singly dimensioned arrays which contained less unused storage. By using this technique, the storage efficiency of the solver was increased by about 25 percent.

The final issue to be discussed in regard to our numerical scheme is the method of grid determination. As reported previously,[10,11] it is not possible to use a single grid and obtain accurate solutions to the gust response problem for a large range of reduced frequencies. Rather, the unsteady grid must be determined as a function of both the mean flow Mach number and the reduced frequency.

This requirement is dictated by both the accuracy of the far field boundary condition (3.66), and the need to adequately model the airfoil boundary condition (3.56) and the wake boundary conditions (3.57) and (3.58). The accuracy of the far field boundary condition depends on the reduced frequency k_1 and free stream Mach number M_∞ in such a way that the parameter $\frac{k_1 M_\infty}{\beta_\infty^2} R$, where R is the distance to the far field boundary, should remain at least $O(1)$. This shows that the location of the outer boundary of the grid must be determined as a function of k_1 and M_∞. In addition, there should be enough grid points per wavelength to accurately represent the airfoil and wake boundary conditions. Due to the harmonic terms containing the parameters K_0 and k_1, this shows that the η and ξ spacing have to be determined as a function of k_1 and M_∞.

The spacing in the η direction is constant for $0 \leq \eta \leq 1$, and then changes slightly but constant again for $1 \leq \eta \leq \eta_{t.e.-}$, and finally constant again, but slightly different from the two previous intervals, for $\eta_{t.e.-} \leq \eta \leq 2$. The spacing on $0 \leq \eta \leq \eta_{t.e.-}$ determines the spacing on the airfoil surface. Normally the number of grid points in the η direction varies from 40 for the low frequencies up to about 70 for reduced frequencies of 4.

An optimal spacing of the grid points in the wake (the ξ direction) turns out to be more difficult to achieve than the spacing on the airfoil. Numerical studies of the thin airfoil gust response problem showed that the optimal choice of spacing was 12 uniformly spaced grid points per wavelength. For the case of the thin airfoil, the wake boundary condition analogous to condition (3.57) is much simpler, and it is possible to choose the spacing of the ξ grid points such that they are uniformly spaced along the waves. However, for the general problem of nonuniform mean flows, the waves in the wake are distorted due to the $e^{ik_1\int_{\Phi_{t.e.}}^{\Phi}\frac{d\Phi}{U_0^2}}$ term, and it is no longer possible to determine the grid point spacing such that they are uniformly spaced along the waves. This does not prove to be a difficulty, however, because in the far field the general problem of vortical flows past a lifting airfoil reduces essentially to a linear problem as the mean flow tends to become uniform. So we may determine the wake spacing as in the case of the flat plate airfoil, and in the far field the grid points will be nearly uniformly spaced along the waves.

For a flat plate airfoil, the wake boundary condition which imposes the continuity of the pressure is given, corresponding to the transformation (3.50), by

$$\psi_{wake,j} = \psi_{t.e.}e^{i\frac{k_1}{\beta_\infty^2}[a^*\cosh(\pi\xi_j)-a^*]}. \tag{3.68}$$

In order to have uniformly spaced grid points along the waves in the wake, the argument of the exponential function should vary by equal fractional increments of π. To place 12 grid points per wavelength, we are then led to the requirement that the location of the $j\,th$ ξ grid point be determined from the relation

$$\frac{k_1}{\beta_\infty^2}[a^*\cosh(\pi\xi_j) - a^*] \;=\; j\,\frac{2\pi}{12}. \tag{3.69}$$

Solving for ξ_j, we get

$$\xi_j = \frac{1}{\pi}\cosh^{-1}\Big(j\,\frac{\pi\beta_\infty^2}{6a^*k_1} + 1\Big). \tag{3.70}$$

This is the method for determining the ξ spacing in the far field. Near the airfoil the above procedure leads to a spacing which is too coarse to be used. So near the airfoil we use uniform ξ spacing which remains constant at some value $\Delta\xi$, until a point is reached such that the ξ_j determined from (3.70) satisfy $\xi_{j+1} - \xi_j \leq \Delta\xi$. From that point on, the spacing of the ξ grid points is determined from (3.70).

IV. CODE VALIDATION

Extensive efforts were taken to validate the computer codes which were developed to implement the numerical solution procedure which was outlined in the previous section. The validation process consisted of a combination of comparing numerical results with known analytical solutions to the classical thin airfoil gust response problems, comparing with the second order theory of Goldstein and Atassi[3] and Atassi,[4] comparing with the first order numerical results of Atassi and Grzedzinski,[13] and calculating solutions to limiting case problems i.e., as Mach number, thickness, angle of attack, or camber go to zero.

Sample computation times for the results presented varied considerably, depending on the reduced frequency, Mach number, and airfoil loading. For thin, unloaded airfoils, with low reduced frequency gusts, typical solution times were about 20 seconds per frequency on the Cray X-MP at the NASA Lewis Research Center. The higher frequencies for these airfoils required on the order of 60 CPU seconds per frequency, with slightly higher solution times as the Mach number increases. For thick, symmetric, unloaded airfoils, the solution times range from about 40 seconds for the lower frequencies up to about 150 seconds for the highest frequencies. Finally, for loaded airfoils, the solution times ranged from about 250 seconds for the low frequencies up to around 1200 seconds for the highest reduced frequencies. No effort was made to optimize the computational efficiency of the scheme, as our main purpose was to validate its accuracy.

In the results that follow, comparisons are made for one-dimensional (transverse) gusts, two-dimensional (transverse and longitudinal) gusts, and fully three-dimensional gusts. See Figures 6, 7, and 8.

The first step in the validation process was to compare numerical results with known solutions to the classical thin airfoil gust response problems. In Figures 9 and 10 we present comparisons between numerical and analytical results for the normalized unsteady lift for vortical flows past flat plate airfoils with zero thickness. The normalized unsteady lift, commonly called the response function, is defined by

$$R_L(k_1, k_3, M_\infty) = \frac{L'}{\pi \rho_\infty c U_\infty |\vec{a}| e^{i\omega t}} \tag{4.1}$$

where L' is the unsteady lift. Figure 9.a shows a comparison between numerical results and the Sears solution[14] for the case of a one-dimensional (transverse) gust in incompressible flow, and Figures 9.b and 9.c compare numerical results and analytical results obtained from a Possio solver for a one-dimensional gust at Mach numbers of .5 and .8. The reduced frequency values at which the comparisons are made range from 0 to 4.0, and are shown below the plot. The point on the real axis and furthest to the right corresponds to $k_1 = 0$, and the other points along the curve correspond in order to the other reduced frequency values. Figures 10.a through 10.c compare numerical results and analytical results from a Possio solver for three-dimensional gusts for Mach numbers of .1, .5, and .8. The conditions on the gust wave number parameters are shown below the plots. As can be readily seen, there is excellent agreement between the numerical and analytical results. The only loss of accuracy occurs when both the Mach number and reduced frequency become large.

In order to assess the accuracy of the present numerical scheme for vortical flows around thin airfoils in which the mean flow is not uniform, we compare with the second order theory of Goldstein and Atassi [3] and Atassi.[4] The results given by Atassi assume a zero thickness airfoil, but account for the effects of airfoil camber and angle of attack on the airfoil unsteady response. In Figure 11, we compare the numerically computed response function with the second order theory for an incompressible flow with a two-dimensional gust about an airfoil with an angle of attack of two degrees and a camber ratio of .05. The numerically computed response function is for a 6% thick Joukowski airfoil, while the second order theory does not take into account the airfoil thickness. The reduced frequency values used for the comparison are shown below the plot. As can be seen, the numerical results for the 6% thick airfoil show a slightly larger lift at the low frequencies, but a slightly smaller lift at the higher frequencies for k_1 up to about 3.0. As shown in the results presented in [5] and [15], this effect can be attributed entirely to the thickness of the airfoil, so that the agreement is very good for reduced frequencies ranging from 0 up to about 3.0. For the frequencies higher than 3.0, it is not possible to make any firm conclusion on the accuracy of the numerical results.

To validate the numerical scheme for airfoils with thickness, we compare with the results of Atassi and Grzedzinski.[13] In Figure 12, we show comparisons for one-, two-, and three-dimensional gusts for incompressible flows around a 12% thick Joukowski airfoil with zero degrees angle of attack and zero camber ratio. The reduced frequency values for the comparison range from .2 to 2.5 and are shown on the plots. We limit the comparison to this range of k_1, since this is roughly the range of validity of the Green's function approach of Atassi and Grzedzinski. The agreement between the two sets of results is good in general.

The final step in the validation process was to calculate the solutions to various limiting case problems. The limiting case of $M_\infty \to 0$, i.e., the incompressible case, was covered above where the numerical results were compared to the Sears solution. We now present results for the limiting cases of airfoil thickness, angle of attack, and camber.

In Figures 13 through 16, we compare numerical results for the unsteady lift and moment about the airfoil center of a 3% thick, symmetric Joukowski airfoil with that of a flat plate airfoil with zero thickness. Analogous to the response function R_L for the unsteady lift, we define the response function R_M for the unsteady moment by

$$R_M(k_1, k_3, M_\infty) = \frac{M'}{\frac{\pi}{2}\rho_\infty c^2 U_\infty |\vec{a}| e^{i\omega t}} \tag{4.2}$$

where M' is the unsteady moment about the airfoil center. Figures 13 and 14 present results for $M_\infty = .1$, and Figures 15 and 16 present results for $M_\infty = .6$. For both Mach numbers, it is seen that the small airfoil thickness has little effect on the unsteady response, except for high reduced frequencies in the two-dimensional gust case, where the magnitude of the unsteady lift is reduced by 15 - 20 percent. It would appear from these results that thickness effects become more important at the higher frequencies for the case of the two-dimensional gust.

Figures 17 and 18 present comparisons between results for a 12% thick symmetric Joukowski airfoil at zero degrees angle of attack and one degree angle of attack. All plots are for a free stream Mach number of .1. As in the case of airfoil thickness, the strongest effect is seen in the two-dimensional gust case. However, here there is a significant effect both for the low and high reduced frequencies. At the low frequency end, the effect is primarily a reduction in the magnitude of the unsteady lift, while at the high end it is primarily a change in phase of the unsteady lift. We also point out that, in agreement with the theoretical results of Atassi,[4] for the transverse gust case in which the gust has only an upwash component, the steady loading on the airfoil has virtually no effect on the unsteady lift.

Finally, in Figures 19 through 20, we compare results for a 12% thick Joukowski airfoil with no camber with a 12% thick Joukowski airfoil with a camber ratio of .02. The free stream Mach number for all plots is .1, and the angle of attack is zero degrees. The effect here is exactly analogous to the effect of small angle of attack, except that it is stronger in this case due to the increased steady loading on the airfoil. For the one degree angle of attack airfoil the steady lift coefficient was .12, while for the 2% cambered airfoil the steady lift coefficient was .27. In each case, the reduction of the quasi-steady lift ($k_1 = 0 = k_2$) for the two-dimensional gust is directly proportional to the steady loading on the airfoil with a proportionality constant of 0.26. Using the theoretical results of Atassi reported in [4], it can be shown that for zero thickness airfoils in a two-dimensional gust in incompressible flow, the reduction in the quasi-steady lift for airfoils with small camber and angle of attack is proportional to the steady lift coefficient with a proportionality constant of $\frac{1}{\pi}\frac{k_2}{|k|} = .23$. The difference between the numerical and theoretical values of the proportionality constant can be accounted for by the fact that the theoretical result does not account for the thickness of the airfoil, and also assumes a parabolic profile for the airfoil camber line.

In Reference 15 a more general study of how the two-dimensional quasi-steady lift changes in response to mean airfoil loading showed that for airfoils with heavier loading and Mach number effects the value of the proportionality constant was about .25. We thus conclude that the reduction in the two-dimensional quasi-steady lift due to mean airfoil loading is roughly proportional to the steady lift coefficient of the loaded airfoil with a proportionality constant of .25.

Before concluding the discussion of numerical results, the authors would like to emphasize the significance of the method of grid determination which was outlined in the previous section. In Figure 21 we present numerical results which demonstrate the kinds of errors that can occur as a result of using an inappropriate grid. The results shown in these figures were generated without determining the grid as a function of the reduced frequency. For each case shown, the same grid was used for all frequencies in the calculation. The grid used for each Mach number was the one normally used only for the highest reduced frequency. By using the grid for the highest frequency, it was assured that there would be sufficient grid resolution to resolve the waves for the lower frequencies. But as can be seen, the agreement is not nearly as good as when the grid is determined as a function of both the Mach number and reduced frequency. These results show the effect of keeping the outer boundary fixed, and not varying it with the reduced frequency in order to ensure that the representation of the far field boundary condition is sufficiently accurate.

The results in Figure 22 show the kinds of errors that can occur when the grid points are not suitably spaced in the far field. The grids used for the results in Figure 22 used an exponentially decreasing spacing which was varied to ensure that there were enough grid points per wavelength to adequately model the wavelike structure of the solution. In addition, the location of the far field boundary was also varied to ensure that the far field boundary condition would be sufficiently accurate. However, as the results show, there are large errors in the response function curves. This is due to the fact that exponential spacing is not suitable for this kind of wave propagation problem.

V. CONCLUSION

In the present paper the authors have presented a finite-difference, frequency-domain numerical scheme for the solution of unsteady, subsonic vortical flows around lifting airfoils. The present method is an alternative to the potential and primitive variable methods, and due to its inherent efficiency and ability to correctly handle the convection and distortion of the upstream vorticity by the nonuniform mean flow, represents an ideal solution method for unsteady aerodynamic flow fields.

The computer codes that have been developed to implement the present numerical approach have been validated through extensive comparisons with known solutions to unsteady vortical flow problems and through the calculation of various limiting case problems. The numerical results have shown that our numerical scheme can calculate with very good accuracy the solutions to a large variety of unsteady vortical flow problems. We conclude that for symmetric airfoils and loaded airfoils with small mean loading, the present scheme is very accurate for reduced frequencies ranging from 0 up to at least 4.0, for both incompressible and compressible flows. For more heavily loaded airfoils, the scheme has similar accuracy for reduced frequencies ranging from 0 up to around 3.0. For reduced frequencies above 3.0, it is not possible to make any firm conclusion on the accuracy of the present numerical scheme for airfoils with substantial mean loading. This is an area that requires further study.

Among the most important features of our numerical approach are the transformation of the independent variables into elliptic coordinates, the method of determining the unsteady grid as a function of the Mach number and reduced frequency, the far field radiation condition for the unsteady pressure, the general purpose direct sparse matrix solver, and the formulation and method of evaluation of the source term.

Finally, the authors are in the process of extending the present linearized unsteady aerodynamic analysis and numerical solution procedure to include transonic flows. Details will be presented in a future paper.

REFERENCES

1. McCroskey, W.J. and Goorjian, P.M., "Interactions of Airfoils with Gusts and Concentrated Vortices in Unsteady Transonic Flow," AIAA Paper 83-1691, July 1983.
2. McCroskey, W. J., "The Effects of Gusts on the Fluctuating Airloads of Airfoils in Transonic Flow," *Journal of Aircraft*, Vol. 22, No. 3, March 1985, pp. 236-243.
3. Goldstein, M. E. and Atassi, H. M., "A Complete Second-Order Theory for the Unsteady Flow About an Airfoil Due to a Periodic Gust," *J. Fluid Mech.*, Vol. 74, 1976, pp. 741-765.
4. Atassi, H.M., "The Sears Problem for a Lifting Airfoil Revisited - New Results," *J. Fluid Mech.* Vol. 141, 1984, pp. 109-122.
5. Scott, J.R. and Atassi, H.M., "Numerical Solutions of the Linearized Euler Equations for Unsteady Vortical Flows Around Lifting Airfoils," AIAA Paper 90-0694, January 1990.
6. Lighthill, M.J., "Drift" *J. Fluid Mech.*, Vol. 1, 1956, pp. 31-53.
7. Goldstein, M. E., "Unsteady Vortical and Entropic Distortions of Potential Flows Round Arbitrary Obstacles," *J. Fluid Mech.*, Vol. 89, 1978, pp. 433-468.
8. Atassi, H. M. and Grzedzinski, J., "Unsteady Disturbances of Streaming Motions Around Bodies," *J. Fluid Mech.*, Vol. 209, Dec. 1989, pp. 385-403.
9. Jameson, A. and Caughey, D.A., "A Finite Volume Method for Transonic Potential Flow Calculations," *Proceedings of the AIAA 3rd Computational Fluid Dynamics Conference*, Williamsburg, Va., July 1979, pp. 122-146.
10. Atassi, H. M. and Scott, J. R., "Analysis of Nonuniform Subsonic Flows About a Row of Moving Blades," *Proceedings of the Fourth International Symposium on Unsteady Aerodynamics and Aeroelasticity of Turbomachines and Propellers*, H. E. Gallus and S. Servaty, eds., Institute fur Strahlantriebe und Turbomachine, University of Aachen, Federal Republic of Germany, 1988, pp. 39-67.
11. Scott, J. R. and Atassi, H. M., "Numerical Solution of Periodic Vortical Flows About a Thin Airfoil," AIAA Paper 89-1691, June, 1989.
12. Atassi, H.M., "Unsteady Vortical Disturbances Around Bodies," *Proceedings of the Tenth U. S. National Congress of Applied Mechanics*, J.P. Lamb, ed., ASME, 1986, pp. 475-484.
13. Atassi, H.M. and Grzedzinski, J., "Three-Dimensional Periodic Distortions of Flows Around Lifting Airfoils," University of Notre Dame Report, Aerodynamics Group, No. 8, 1986.
14. Sears, W. R., "Some Aspects of Non-stationary Airfoil Theory and Its Practical Applications." *J. Aero. Sci.*, Vol. 8, No. 3, 1941, pp. 104-108.
15. Scott, J.R., "Compressible Flows with Periodic Vortical Disturbances Around Lifting Airfoils," Ph. D. Dissertation, University of Notre Dame, Notre Dame, IN, 1990.

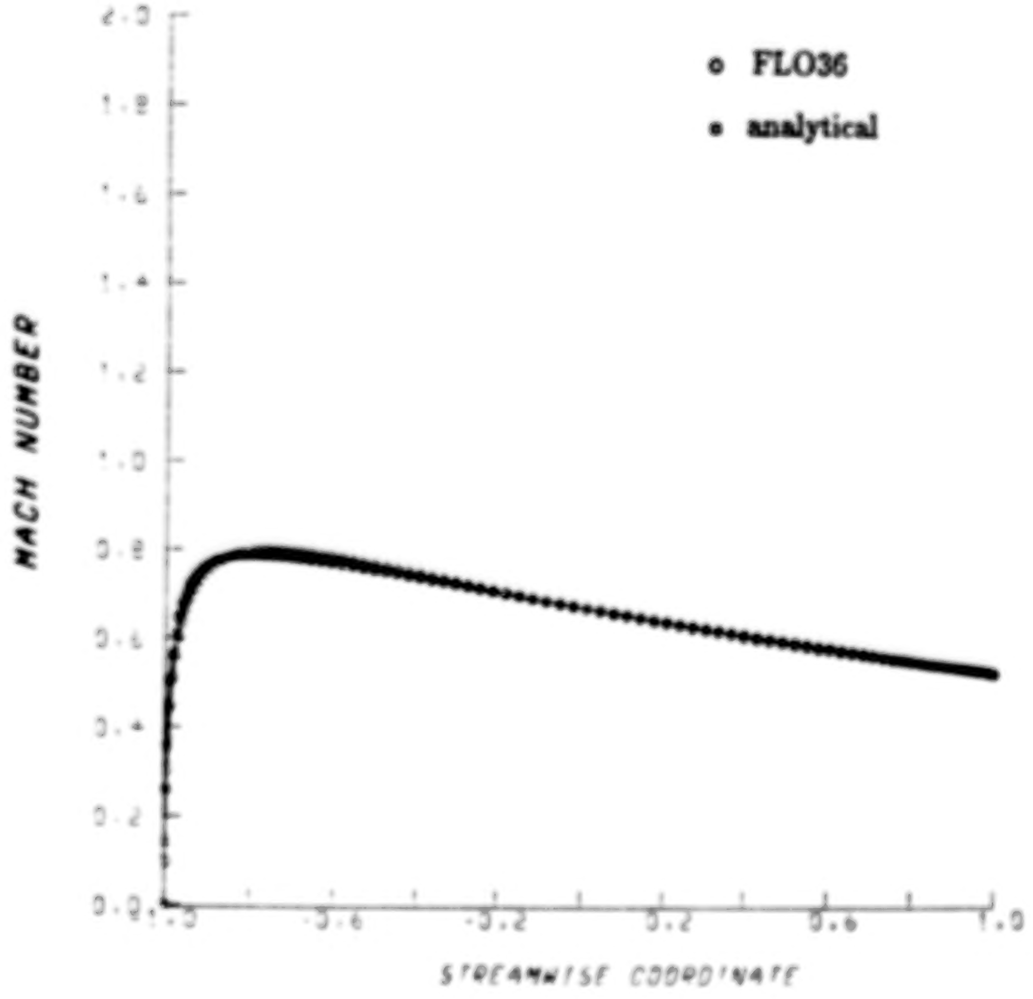

Figure 1. Comparison of Mach number at the airfoil surface between FLO36 and the present analytical scheme. $M_\infty = .6$, $\alpha = 0°$, camber = 0, thickness = .12.

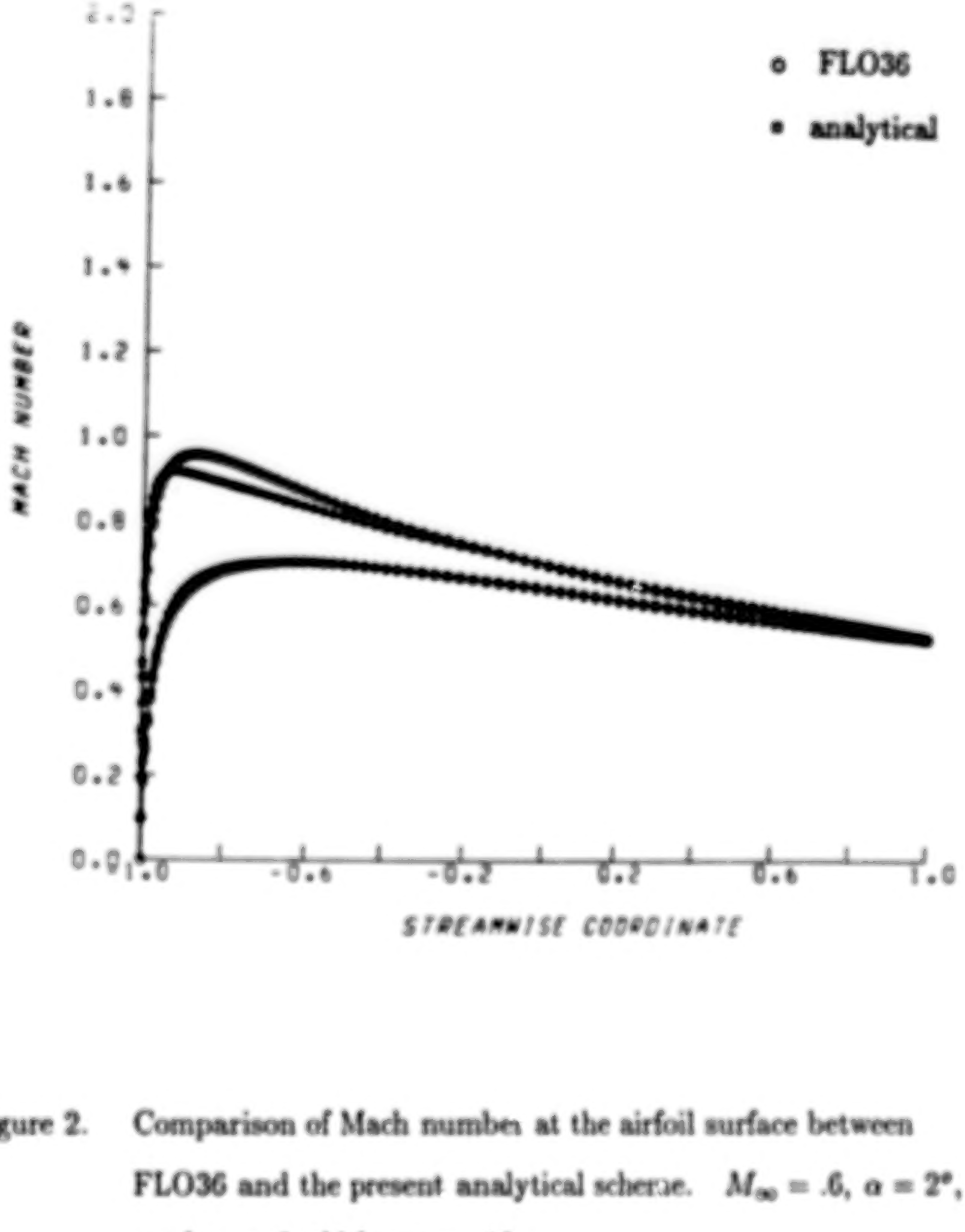

Figure 2. Comparison of Mach number at the airfoil surface between FLO36 and the present analytical scheme. $M_\infty = .6$, $\alpha = 2°$, camber = 0, thickness = .12.

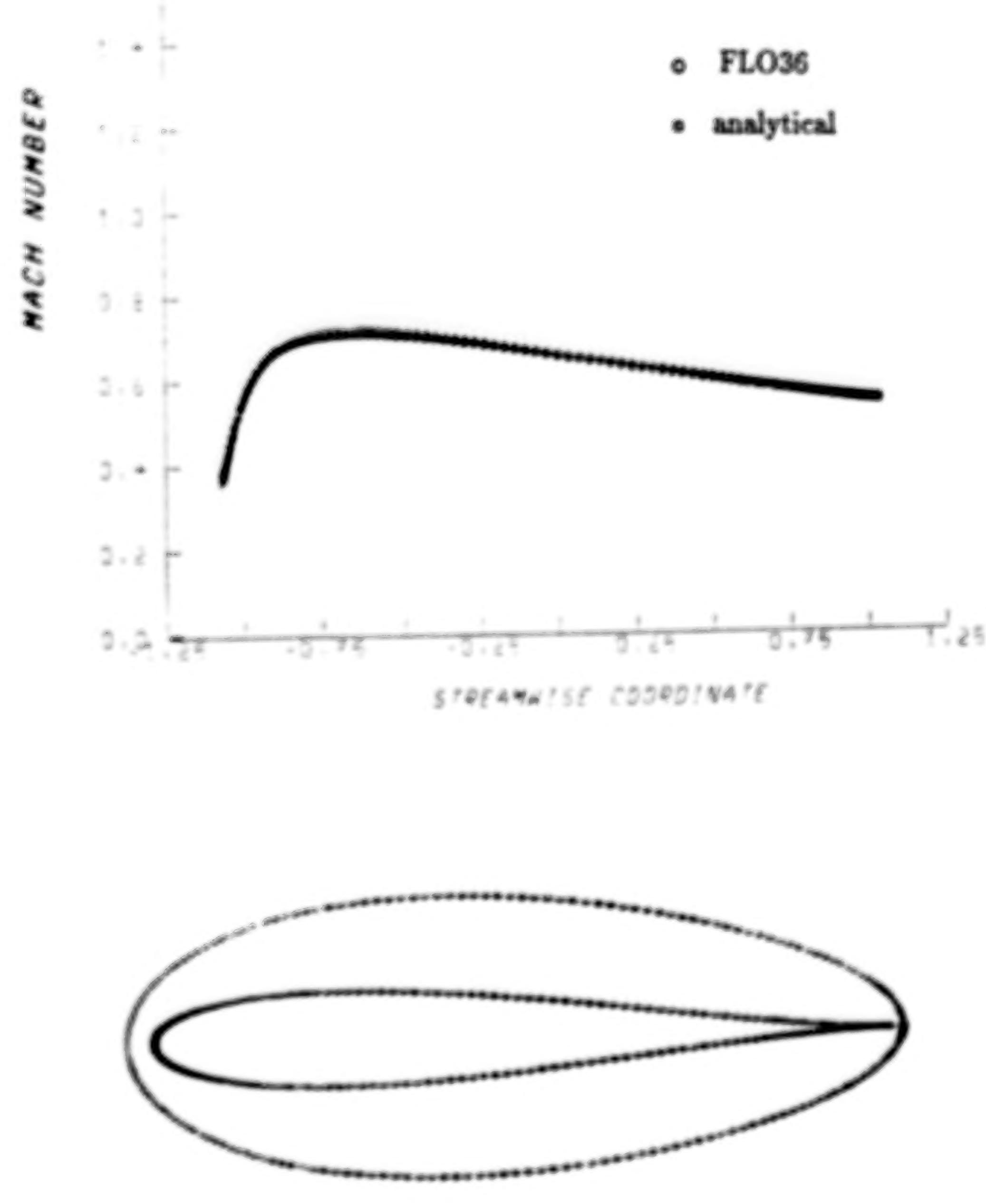

Figure 3. Comparison of Mach number along a FLO36 grid line which wraps around the airfoil. $M_\infty = .6$, $\alpha = 0°$, camber = 0, thickness = .12.

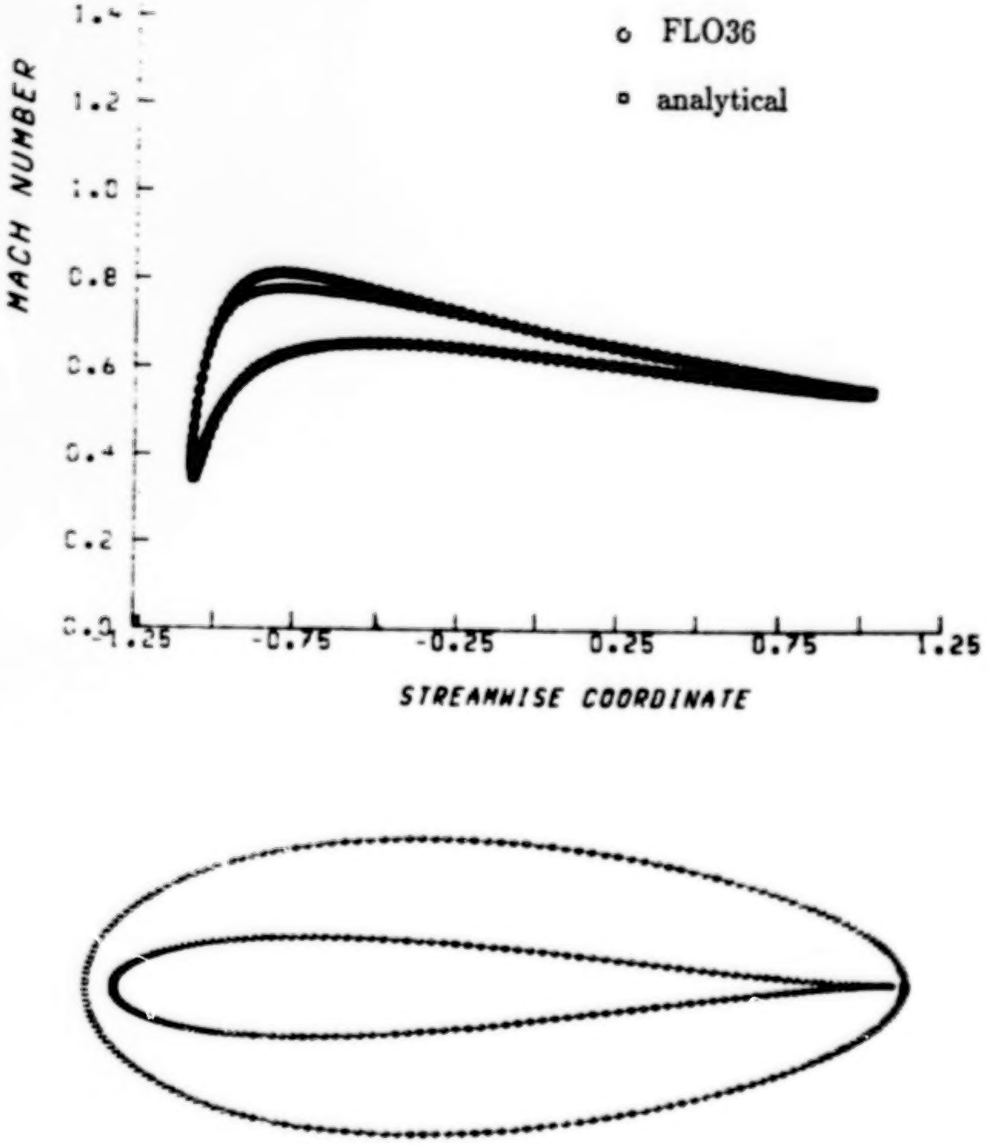

Figure 4. Comparison of Mach number along a FLO36 grid line which wraps around the airfoil. $M_\infty = .6$, $\alpha = 2^o$, camber = 0, thickness = .12.

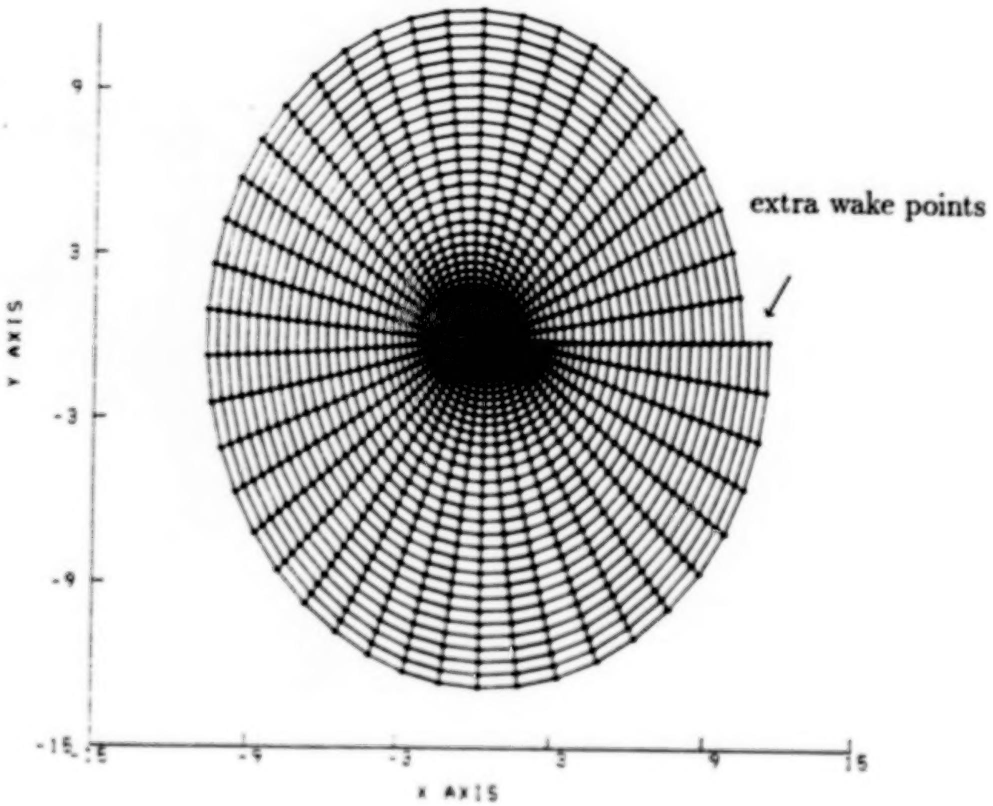

PHYSICAL GRID

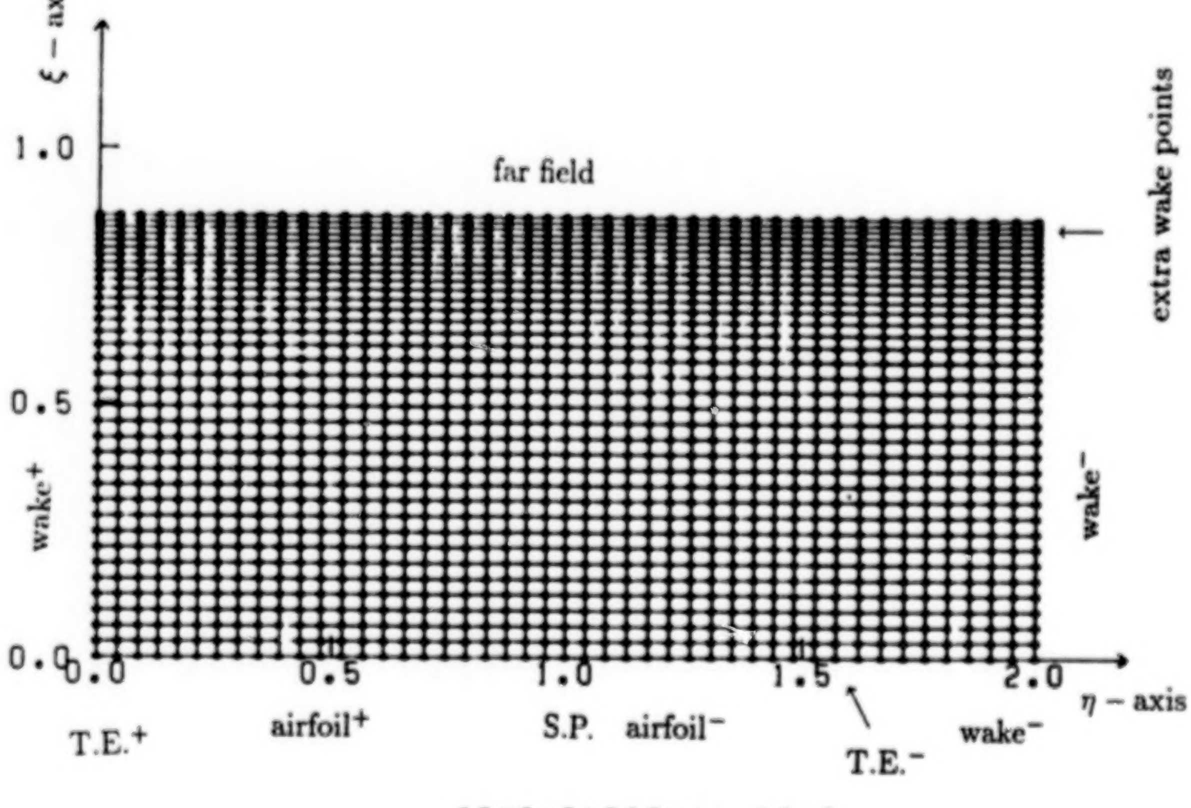

COMPUTATIONAL GRID

Figure 5. Computational and physical grids.

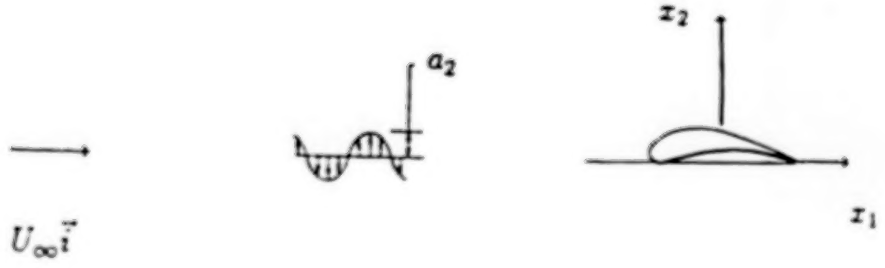

Figure 6. Airfoil in a transverse gust.

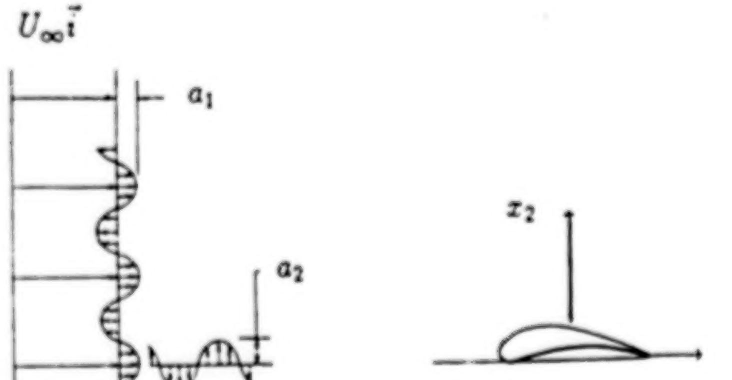

Figure 7. Airfoil in a transverse and longitudinal gust.

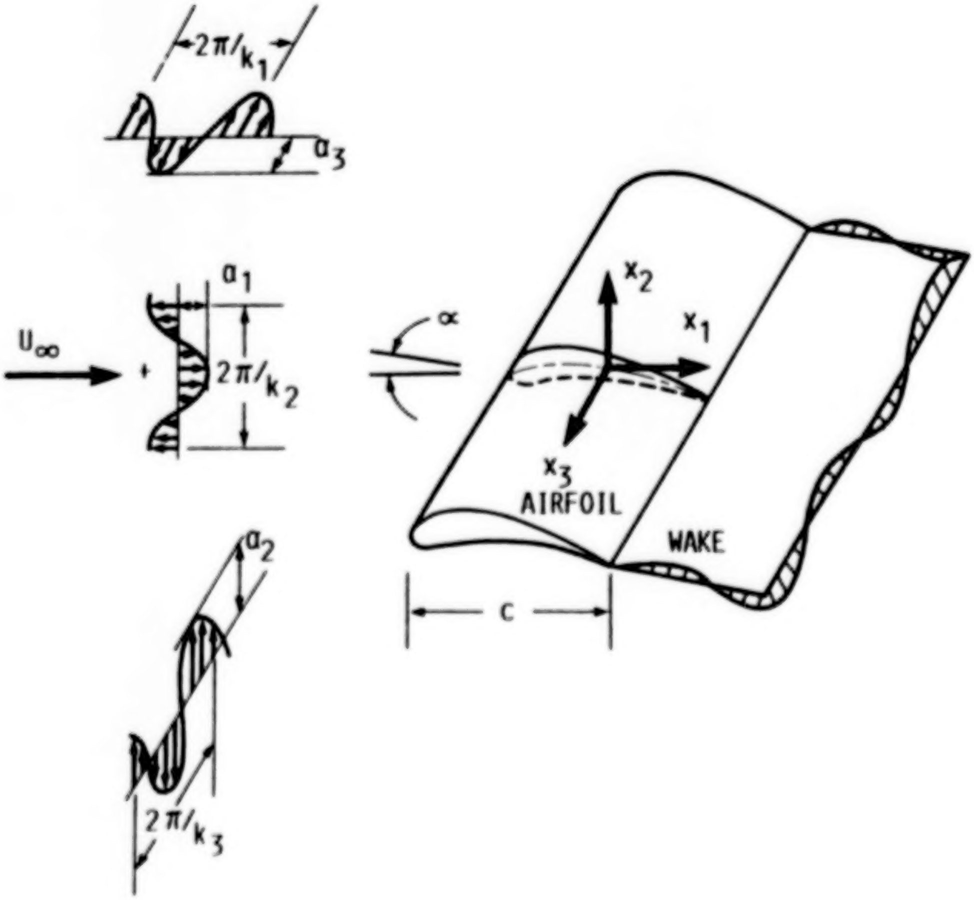

Figure 8. Airfoil in a three-dimensional gust.

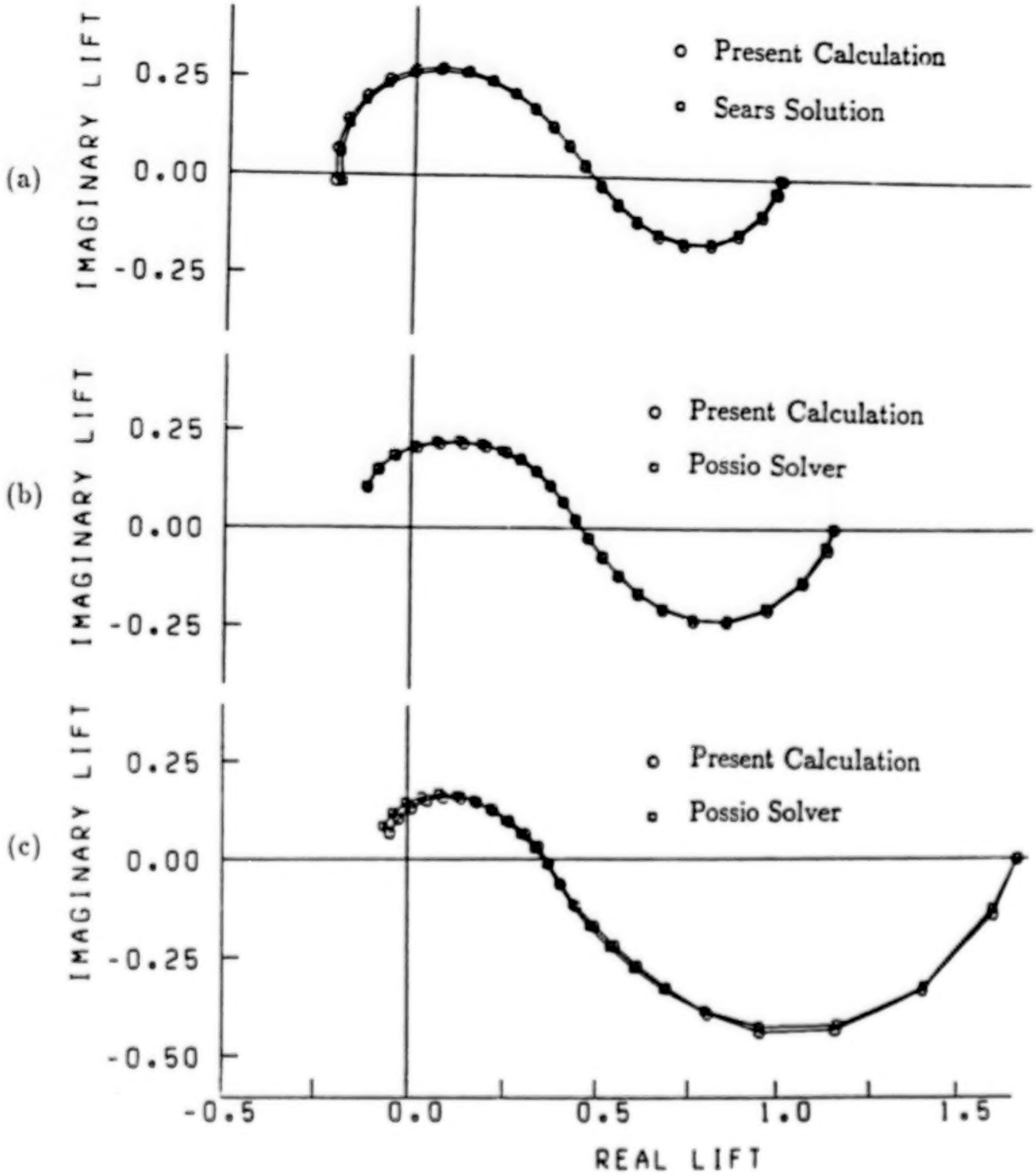

Figure 9. Comparison between the numerically computed unsteady lift and analytical results for a flat plate airfoil in a transverse gust at (a) $M = 0.1$, (b) $M = 0.5$, and (c) $M = 0.8$
$k_1 = 0.0, 0.007, 0.027, 0.062, 0.110, 0.172, 0.248, 0.338, 0.442, 0.561, 0.694, 0.842, 1.01, 1.18, 1.38, 1.59, 1.82, 2.07, 2.33, 2.62, 2.93, 3.26, 3.62, 4.01$

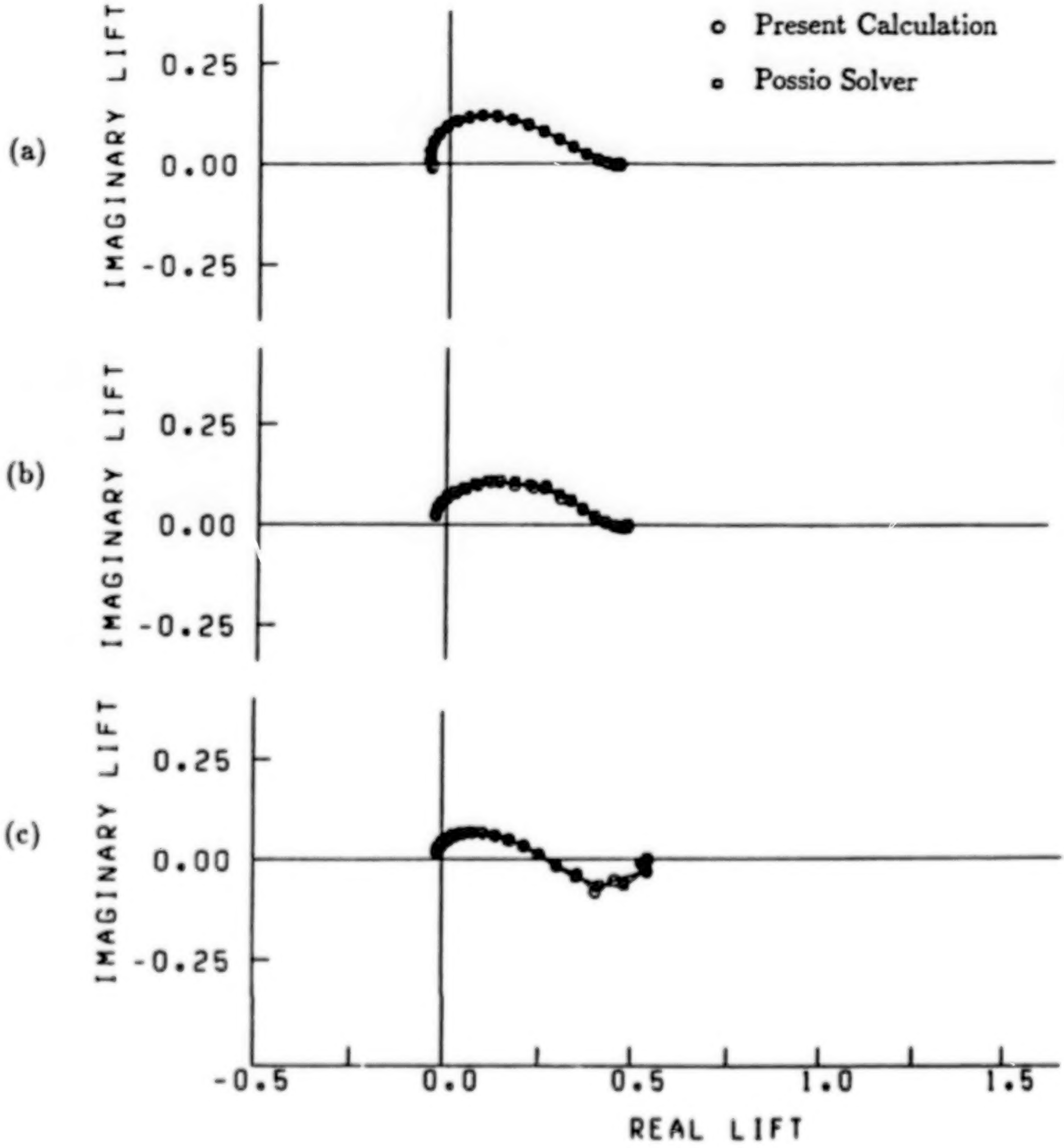

Figure 10. Comparison between the numerically computed unsteady lift and analytical results for a flat plate airfoil in a three-dimensional gust at (a) $M = 0.1$, (b) $M = 0.5$, and (c) $M = 0.8$
$k_3 = 0.442$, $|\vec{a}| = 1$, $\frac{a_2}{a_1} = -\frac{7}{4}$, $k_1 = k_2$, $\vec{a} \cdot \vec{k} = 0$, $a_2 > 0$
$k_1 = 0.0, 0.007, 0.027, 0.062, 0.110, 0.172, 0.248, 0.338, 0.442, 0.561, 0.694, 0.842, 1.01, 1.18, 1.38, 1.59, 1.82, 2.07, 2.33, 2.62, 2.93, 3.26, 3.62, 4.01$

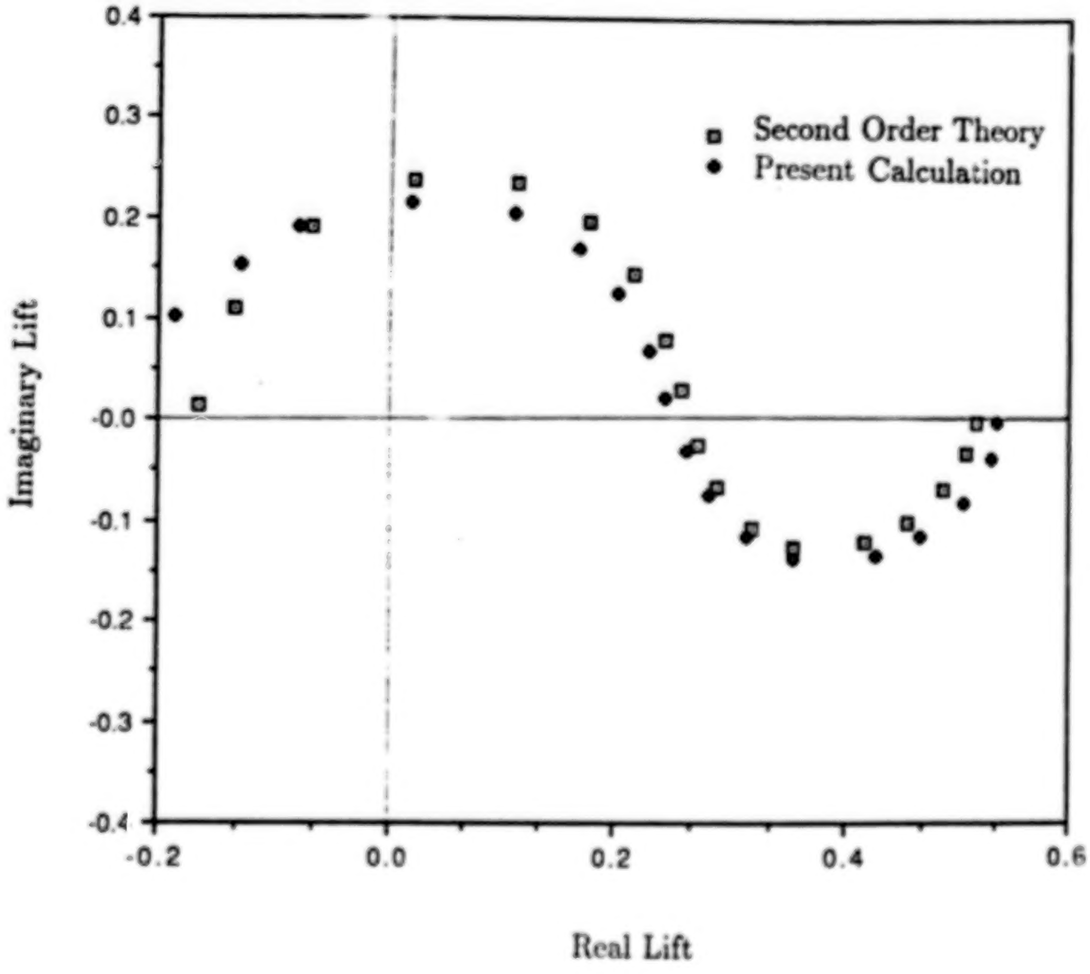

Figure 11. Comparison between the numerically computed unsteady lift and the second order theory for an airfoil in a transverse and longitudinal gust. The second order theory does not account for the thickness of the airfoil. $M_\infty = .1$, $\alpha = 2^o$, camber = .05, thickness ratio = .06. $-a_1 = a_2 = .7071$, $k_1 = k_2, a_3 = k_3 = 0$
k_1 = 0.0, 0.01, 0.03, 0.06, 0.1, 0.2, 0.3, 0.45, 0.6,
0.8, 1.0, 1.3, 1.6, 2.0, 2.5, 3.0, 3.5, 4.0

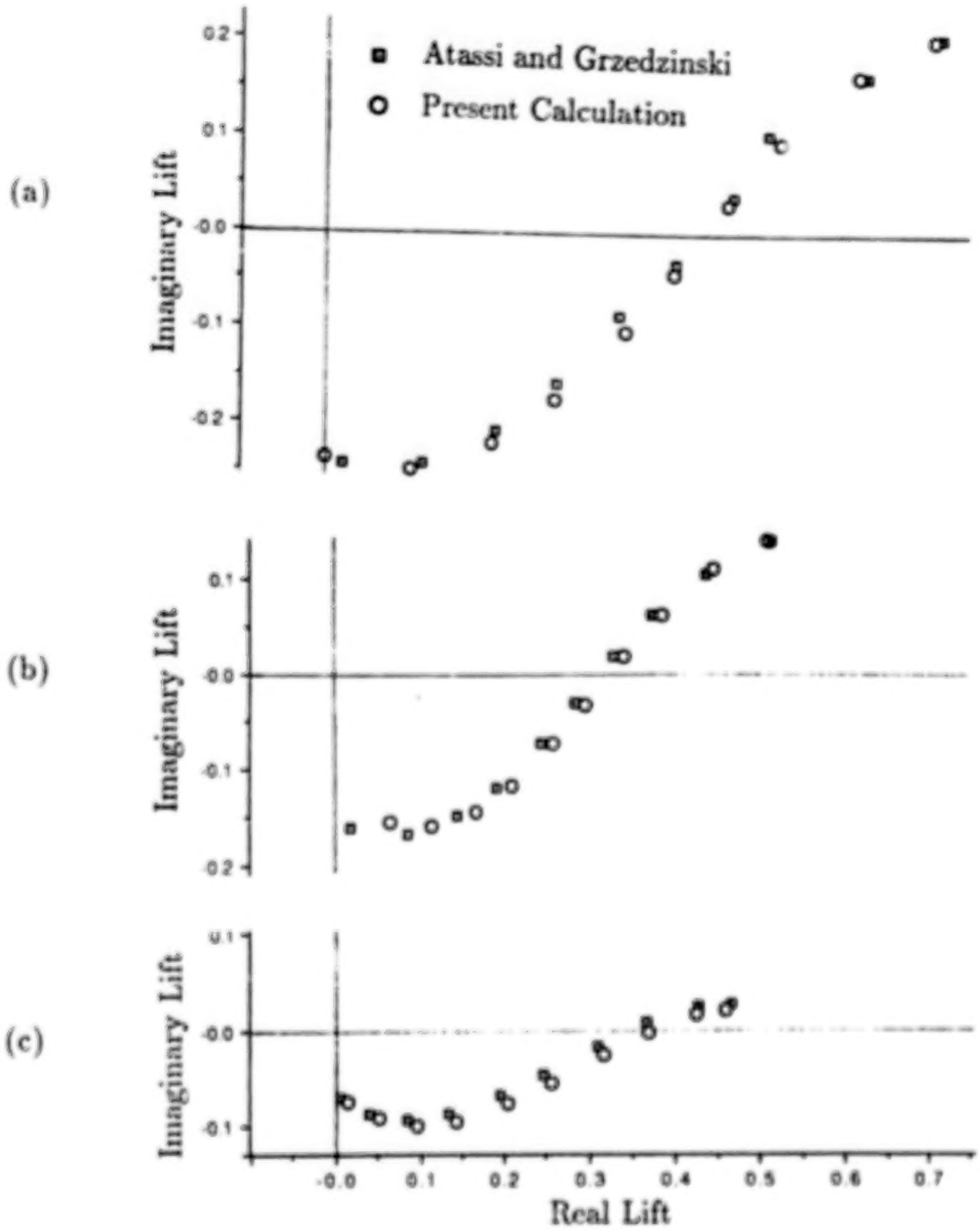

Figure 12. Comparison between the numerically computed unsteady lift and the first order results of Atassi and Grzedzinski for a (a) transverse gust, (b) transverse and longitudinal gust with $-a_1 = a_2 = .7071$, $k_1 = k_2$, $a_3 = k_3 = 0$, and (c) a three-dimensional gust with $k_3 = 0.4$, $|\vec{a}| = 1$, $\frac{a_2}{a_1} = -\frac{7}{4}$, $k_1 = k_2$, $\vec{a} \cdot \vec{k} = 0$, $a_2 > 0$. $M_\infty = .1$, $\alpha = 0$, camber = 0, thickness ratio = .12. Results shown are the complex conjugate values of the unsteady lift.

$k_1 = 0.2, 0.3, 0.45, 0.6, 0.8, 1.0, 1.3, 1.6, 2.0, 2.5$

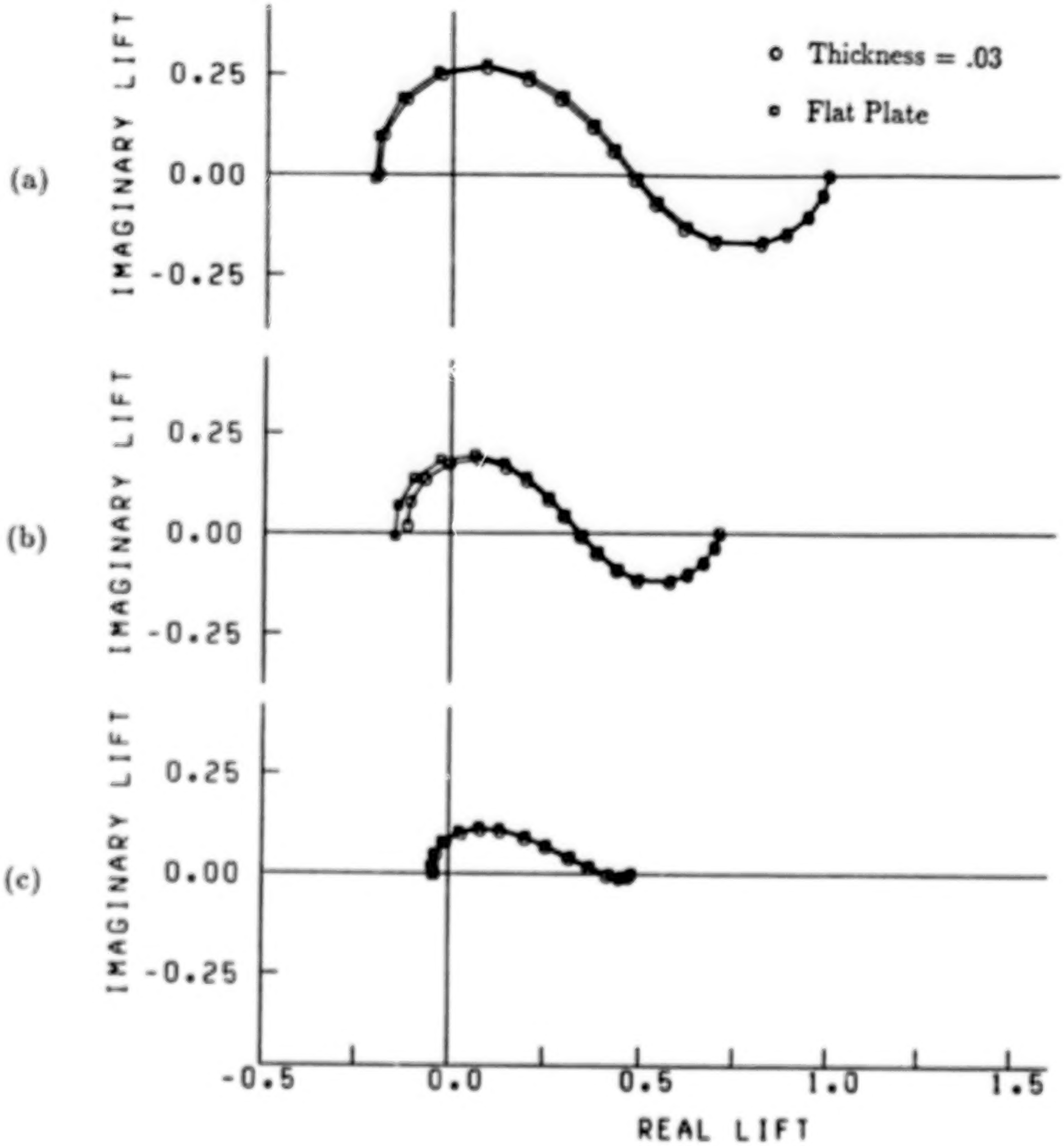

Figure 13. Comparison between the unsteady lift of a flat plate airfoil and a 3 percent thick Joukowski airfoil in a (a) transverse gust, (b) transverse and longitudinal gust with $-a_1 = a_2 = .7071$, $k_1 = k_2$, $a_3 = k_3 = 0$, and (c) a three-dimensional gust with $k_3 = 0.4$, $|\vec{a}| = 1$, $\frac{a_2}{a_1} = -\frac{7}{4}$, $k_1 = k_2$, $\vec{a} \cdot \vec{k} = 0$, $a_2 > 0$. $M_\infty = .1$, $\alpha = 0$, camber = 0. k_1 = 0.0, 0.01, 0.03, 0.06, 0.1, 0.2, 0.3, 0.45, 0.6, 0.8, 1.0, 1.3, 1.6, 2.0, 2.5, 3.0, 3.5, 4.0

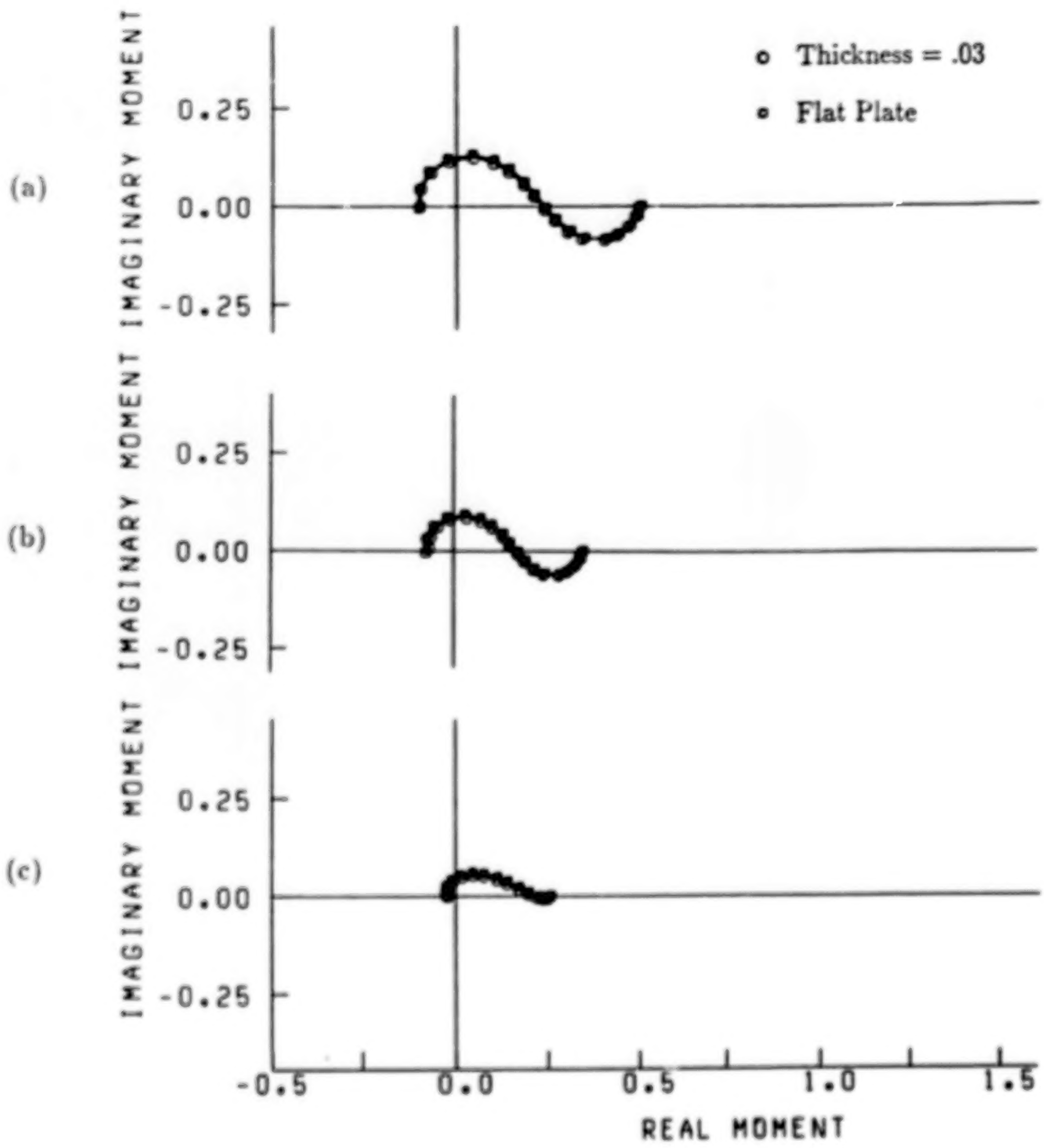

Figure 14. Comparison between the unsteady moment of a flat plate airfoil and a 3 percent thick Joukowski airfoil in a (a) transverse gust, (b) transverse and longitudinal gust with $-a_1 = a_2 = .7071$, $k_1 = k_2$, $a_3 = k_3 = 0$, and (c) a three-dimensional gust with $k_3 = 0.4$, $|\vec{a}| = 1$, $\frac{a_2}{a_1} = -\frac{7}{4}$, $k_1 = k_2$, $\vec{a} \cdot \vec{k} = 0$, $a_2 > 0$. $M_\infty = .1$, $\alpha = 0$, camber $= 0$. $k_1 = 0.0, 0.01, 0.03, 0.06, 0.1, 0.2, 0.3, 0.45, 0.6,$
0.8, 1.0, 1.3, 1.6, 2.0, 2.5, 3.0, 3.5, 4.0

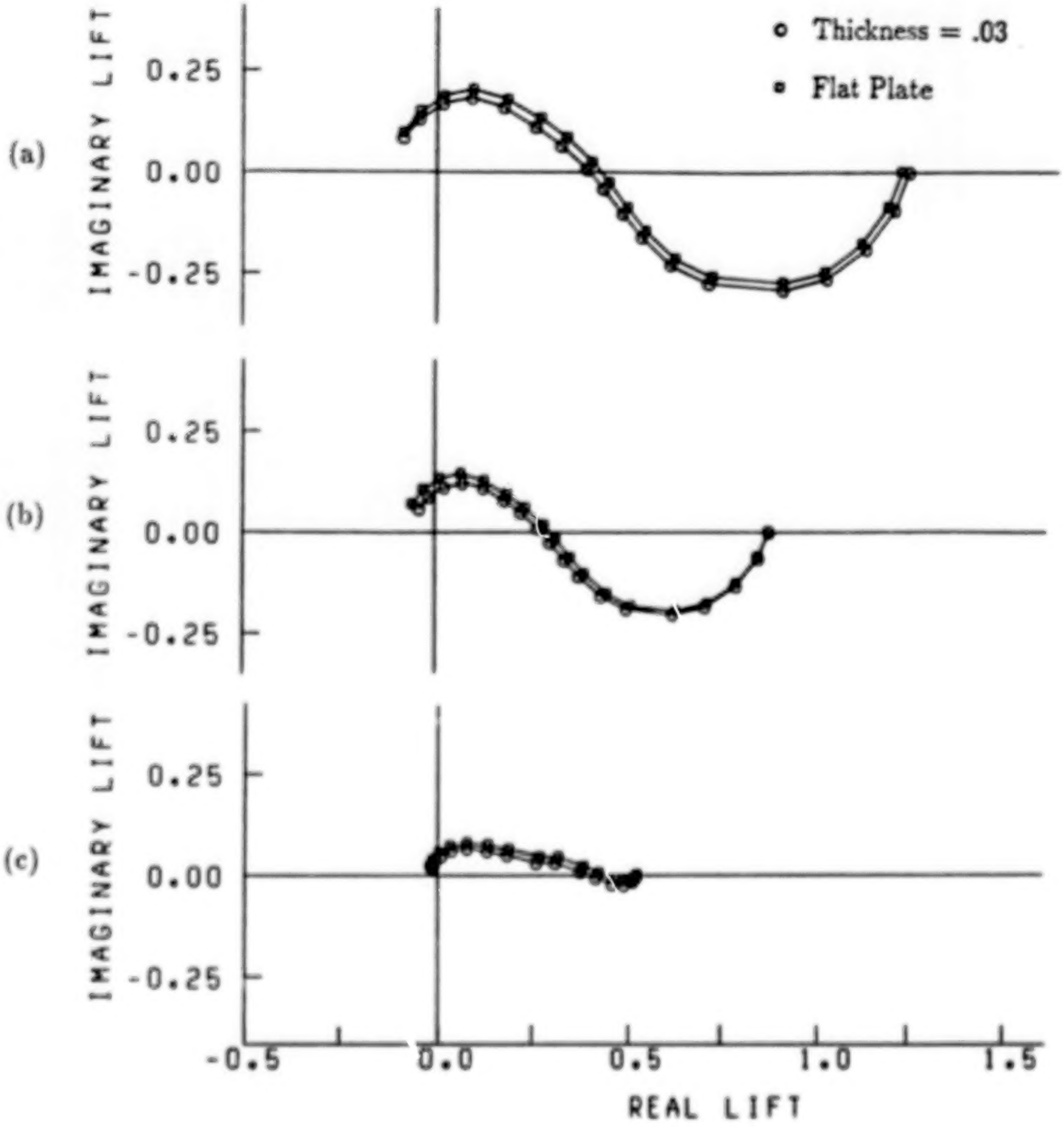

Figure 15. Comparison between the unsteady lift of a flat plate airfoil and a 3 percent thick Joukowski airfoil in a (a) transverse gust, (b) transverse and longitudinal gust with $-a_1 = a_2 = .7071$, $k_1 = k_2$, $a_3 = k_3 = 0$, and (c) a three-dimensional gust with $k_3 = 0.4$, $|\vec{a}| = 1$, $\frac{a_2}{a_1} = -\frac{7}{4}$, $k_1 = k_2$, $\vec{a} \cdot \vec{k} = 0$, $a_2 > 0$. $M_\infty = .6$, $\alpha = 0$, camber $= 0$. $k_1 = 0.0, 0.01, 0.03, 0.06, 0.1, 0.2, 0.3, 0.45, 0.6,$ $0.8, 1.0, 1.3, 1.6, 2.0, 2.5, 3.0, 3.5, 4.0$

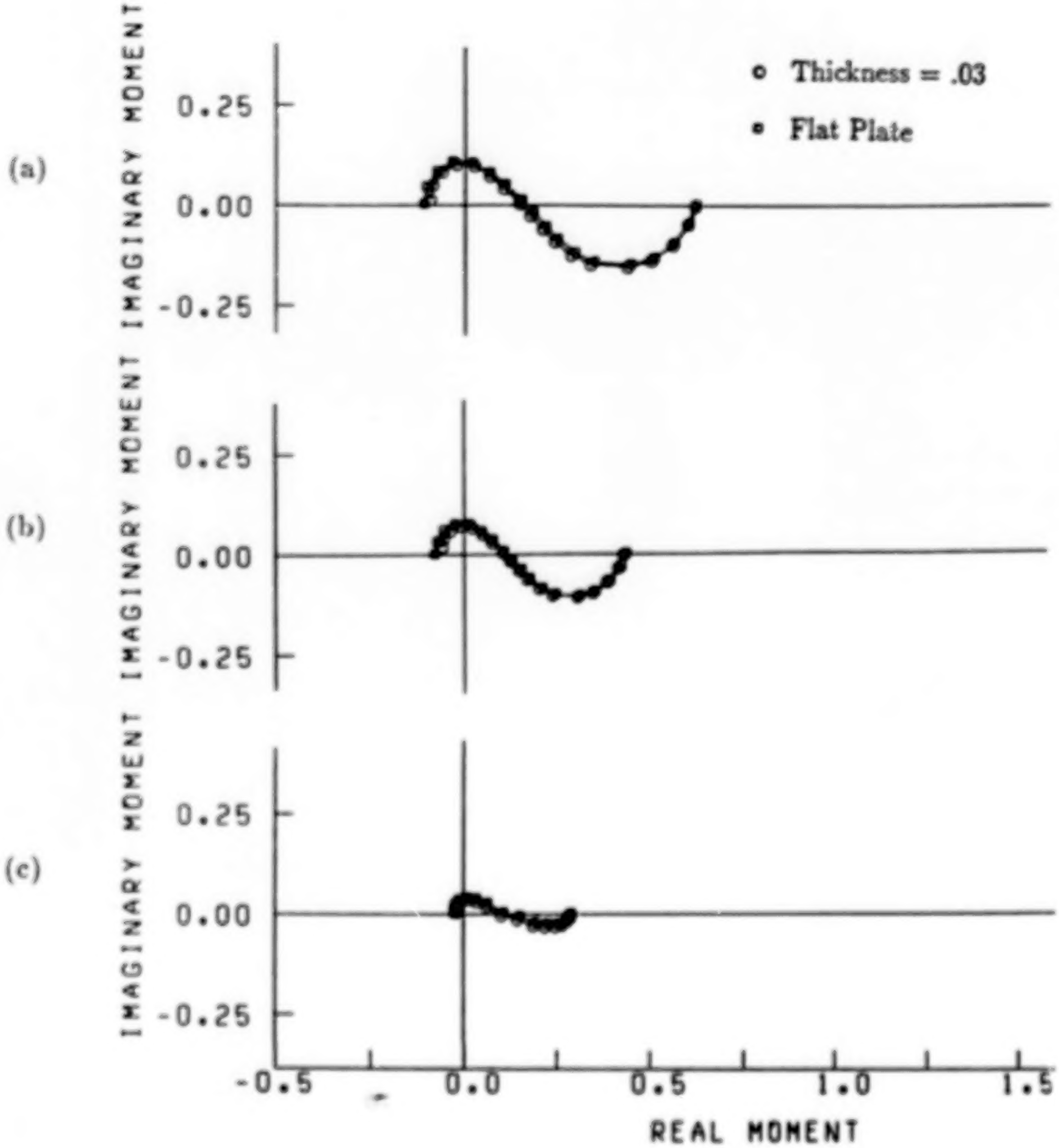

Figure 16. Comparison between the unsteady moment of a flat plate airfoil and a 3 percent thick Joukowski airfoil in a (a) transverse gust, (b) transverse and longitudinal gust with $-a_1 = a_2 = .7071$, $k_1 = k_2$, $a_3 = k_3 = 0$, and (c) a three-dimensional gust with $k_3 = 0.4$, $|\vec{a}| = 1$, $\frac{a_2}{a_1} = -\frac{7}{4}$, $k_1 = k_2$, $\vec{a} \cdot \vec{k} = 0$, $a_2 > 0$. $M_\infty = .6$, $\alpha = 0$, camber = 0. $k_1 = 0.0, 0.01, 0.03, 0.06, 0.1, 0.2, 0.3, 0.45, 0.6,$ $0.8, 1.0, 1.3, 1.6, 2.0, 2.5, 3.0, 3.5, 4.0$

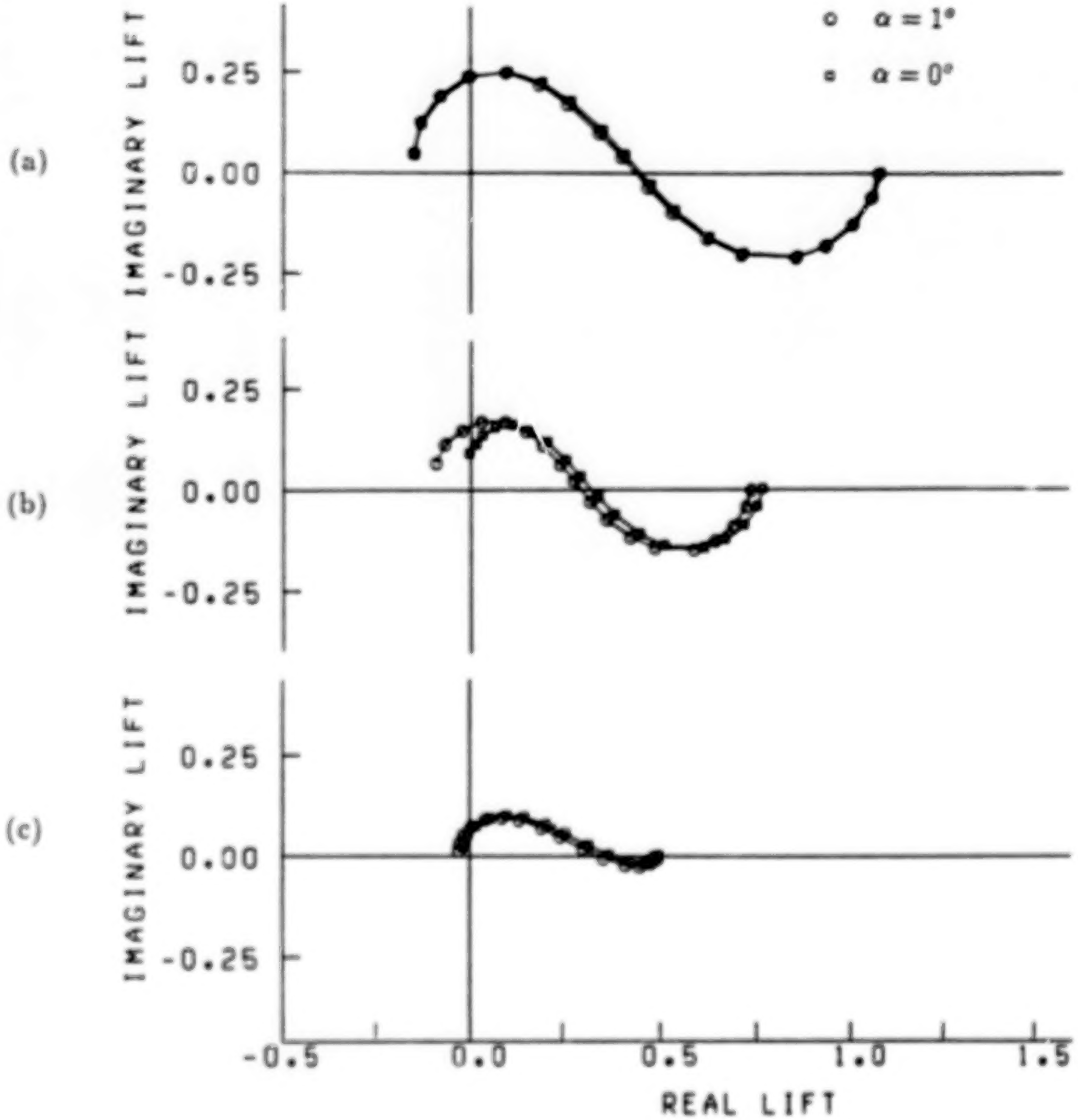

Figure 17. Comparison between the unsteady lift of a 12 percent thick, Joukowski airfoil at 0° angle of attack and 1° angle of attack for a (a) transverse gust, (b) transverse and longitudinal gust with $-a_1 = a_2 = .7071$, $k_1 = k_2$, $a_3 = k_3 = 0$, and (c) a three-dimensional gust with $k_3 = 0.4$, $|\vec{a}| = 1$, $\frac{a_2}{a_1} = -\frac{7}{4}$, $k_1 = k_2$, $\vec{a} \cdot \vec{k} = 0$, $a_2 > 0$. $M_\infty = .1$, camber = 0, thickness ratio = .12.

k_1 = 0.0, 0.01, 0.03, 0.06, 0.1, 0.2, 0.3, 0.45, 0.6, 0.8, 1.0, 1.3, 1.6, 2.0, 2.5, 3.0, 3.5, 4.0

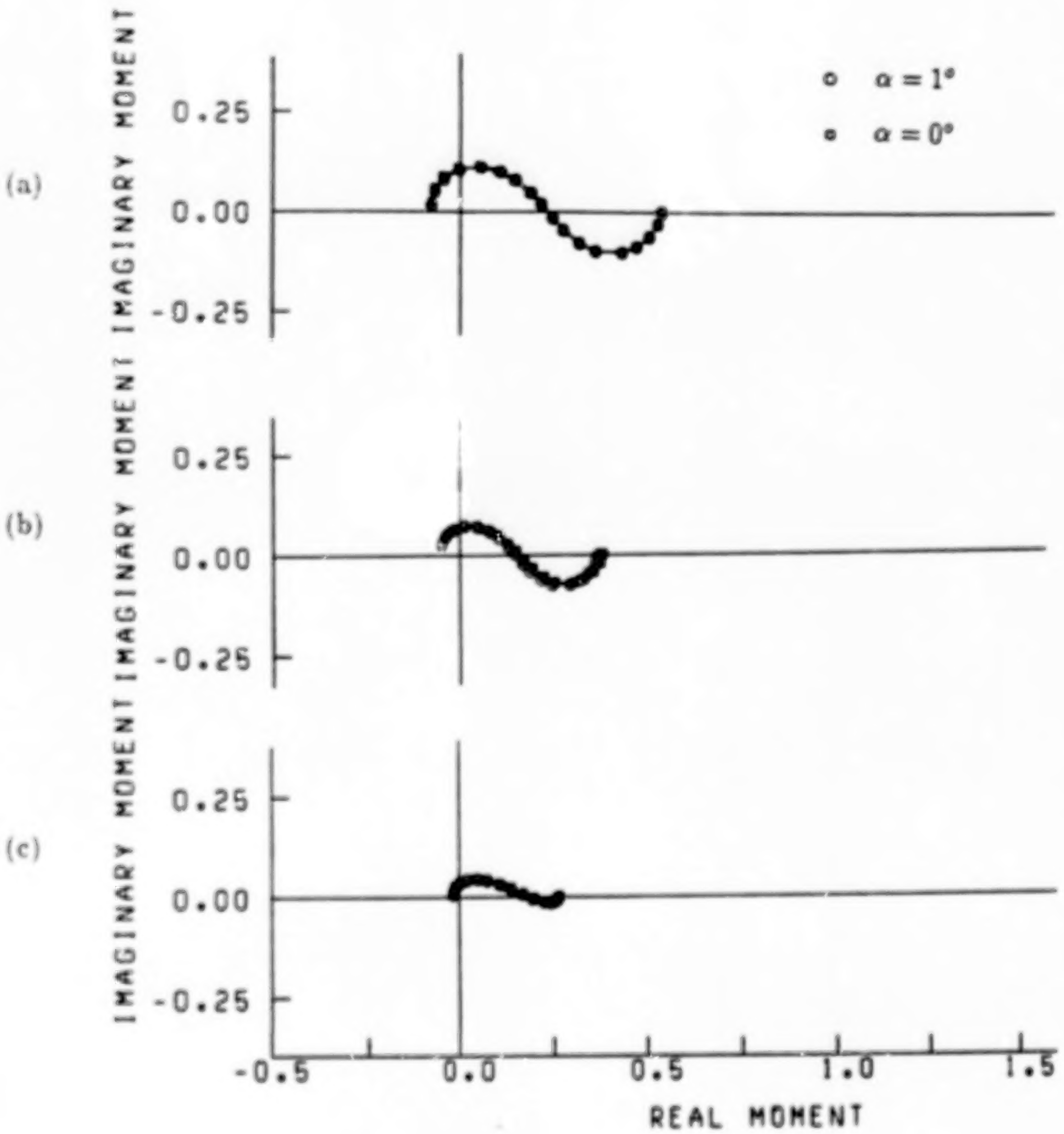

Figure 18. Comparison between the unsteady moment of a 12 percent thick, Joukowski airfoil at 0° angle of attack and 1° angle of attack for a (a) transverse gust, (b) transverse and longitudinal gust with $-a_1 = a_2 = .7071$, $k_1 = k_2$, $a_3 = k_3 = 0$, and (c) a three-dimensional gust with $k_3 = 0.4$, $|\vec{a}| = 1$, $\frac{a_2}{a_1} = -\frac{7}{4}$, $k_1 = k_2$, $\vec{a} \cdot \vec{k} = 0$, $a_2 > 0$. $M_\infty = .1$, camber = 0, thickness ratio = .12.

$k_1 = 0.0, 0.01, 0.03, 0.06, 0.1, 0.2, 0.3, 0.45, 0.6,$
$0.8, 1.0, 1.3, 1.6, 2.0, 2.5, 3.0, 3.5, 4.0$

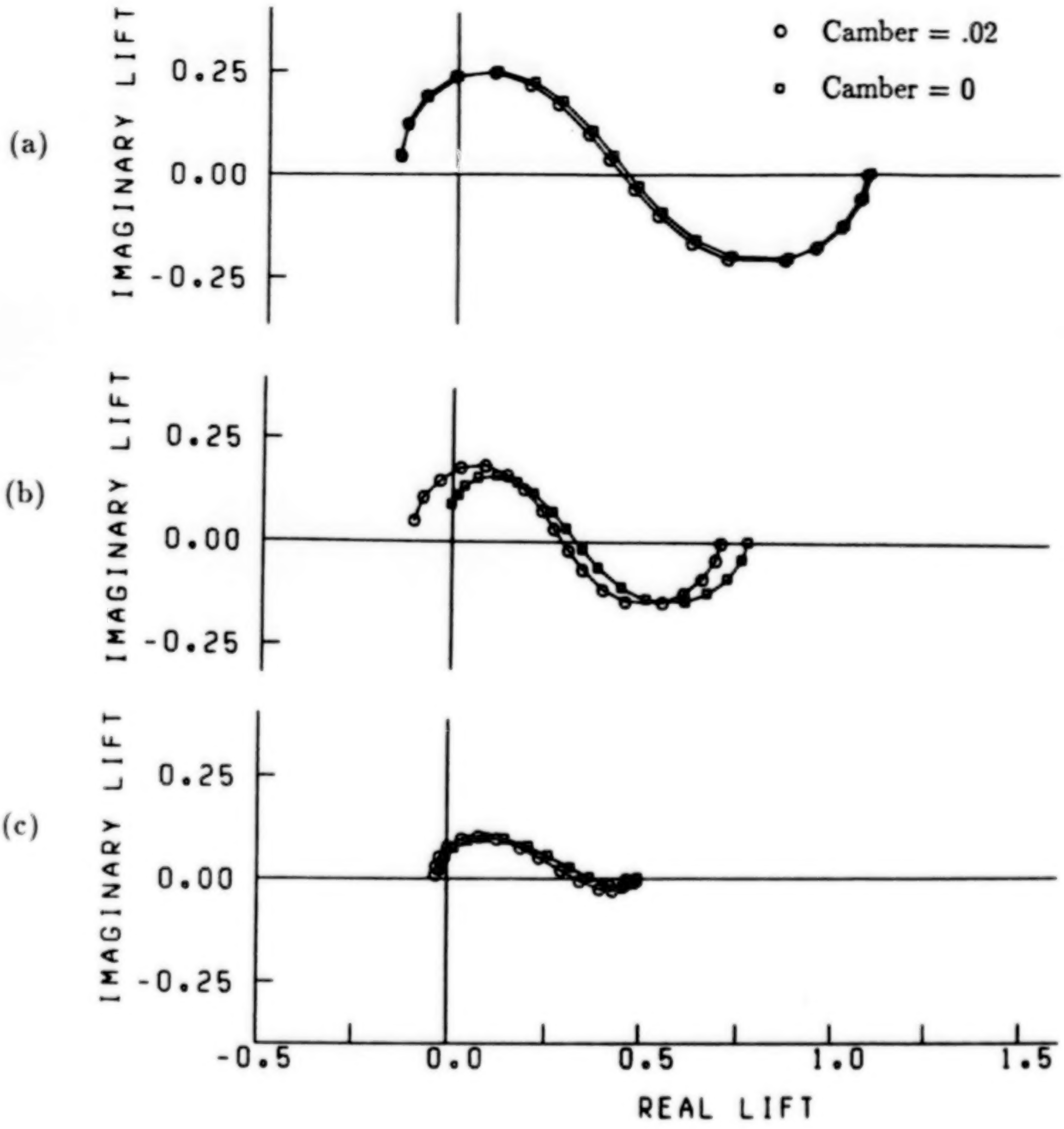

Figure 19. Comparison between the unsteady lift of an uncambered Joukowski airfoil and an airfoil with camber ratio of .02 for a (a) transverse gust, (b) transverse and longitudinal gust with $-a_1 = a_2 = .7071$, $k_1 = k_2$, $a_3 = k_3 = 0$, and (c) a three-dimensional gust with $k_3 = 0.4$, $|\vec{a}| = 1$, $\frac{a_2}{a_1} = -\frac{7}{4}$, $k_1 = k_2$, $\vec{a} \cdot \vec{k} = 0$, $a_2 > 0$. $M_\infty = .1$, $\alpha = 0°$, thickness ratio = .12.

$k_1 = 0.0, 0.01, 0.03, 0.06, 0.1, 0.2, 0.3, 0.45, 0.6,$

$0.8, 1.0, 1.3, 1.6, 2.0, 2.5, 3.0, 3.5, 4.0$

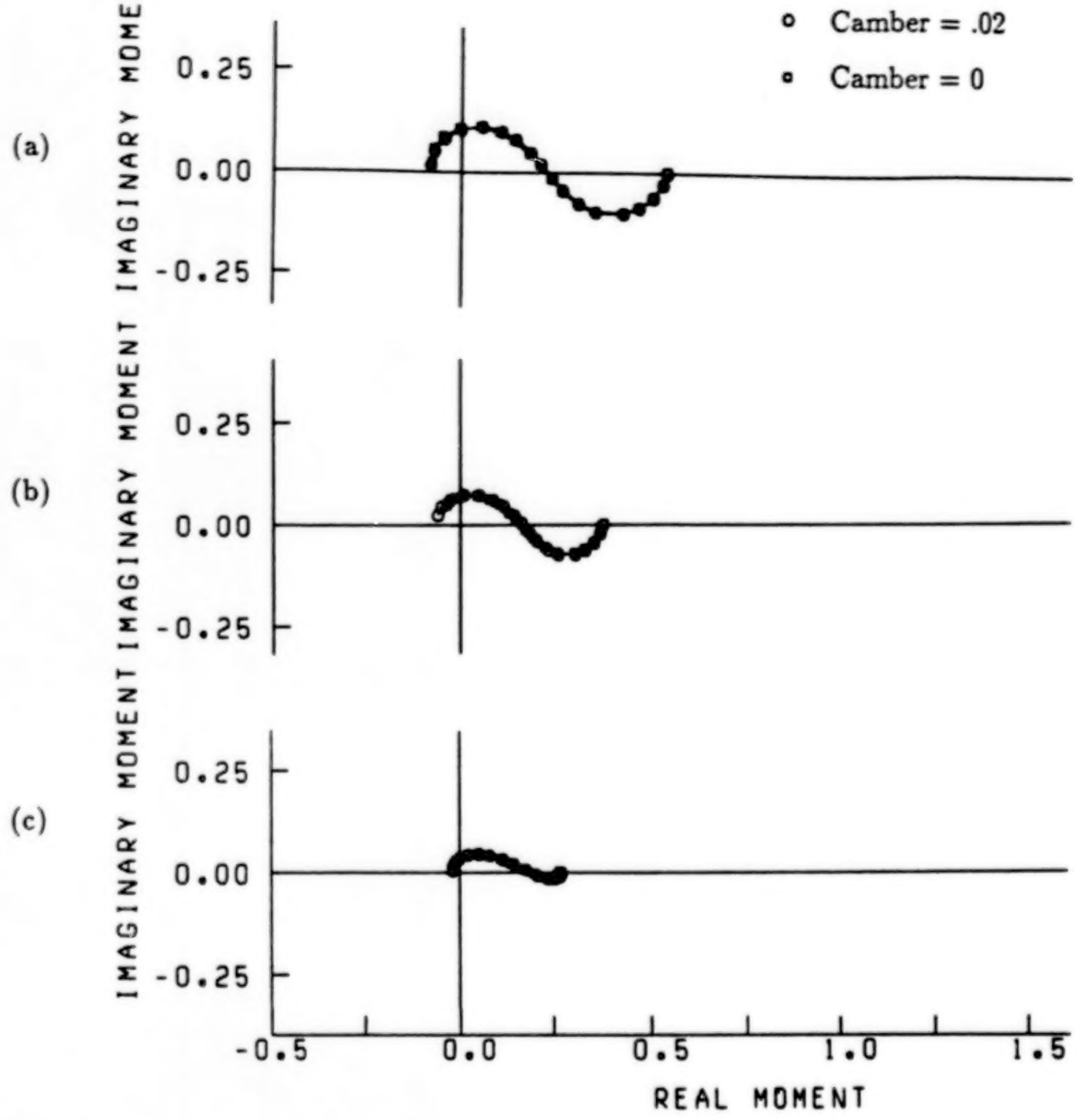

Figure 20. Comparison between the unsteady moment of an uncambered Joukowski airfoil and an airfoil with camber ratio of .02 for a (a) transverse gust, (b) transverse and longitudinal gust with $-a_1 = a_2 = .7071$, $k_1 = k_2$, $a_3 = k_3 = 0$, and (c) a three-dimensional gust with $k_3 = 0.4$, $|\vec{a}| = 1$, $\frac{a_2}{a_1} = -\frac{7}{4}$, $k_1 = k_2$, $\vec{a} \cdot \vec{k} = 0$, $a_2 > 0$. $M_\infty = .1$, $\alpha = 0^\circ$, thickness ratio = .12.

$k_1 = 0.0, 0.01, 0.03, 0.06, 0.1, 0.2, 0.3, 0.45, 0.6,$
$0.8, 1.0, 1.3, 1.6, 2.0, 2.5, 3.0, 3.5, 4.0$

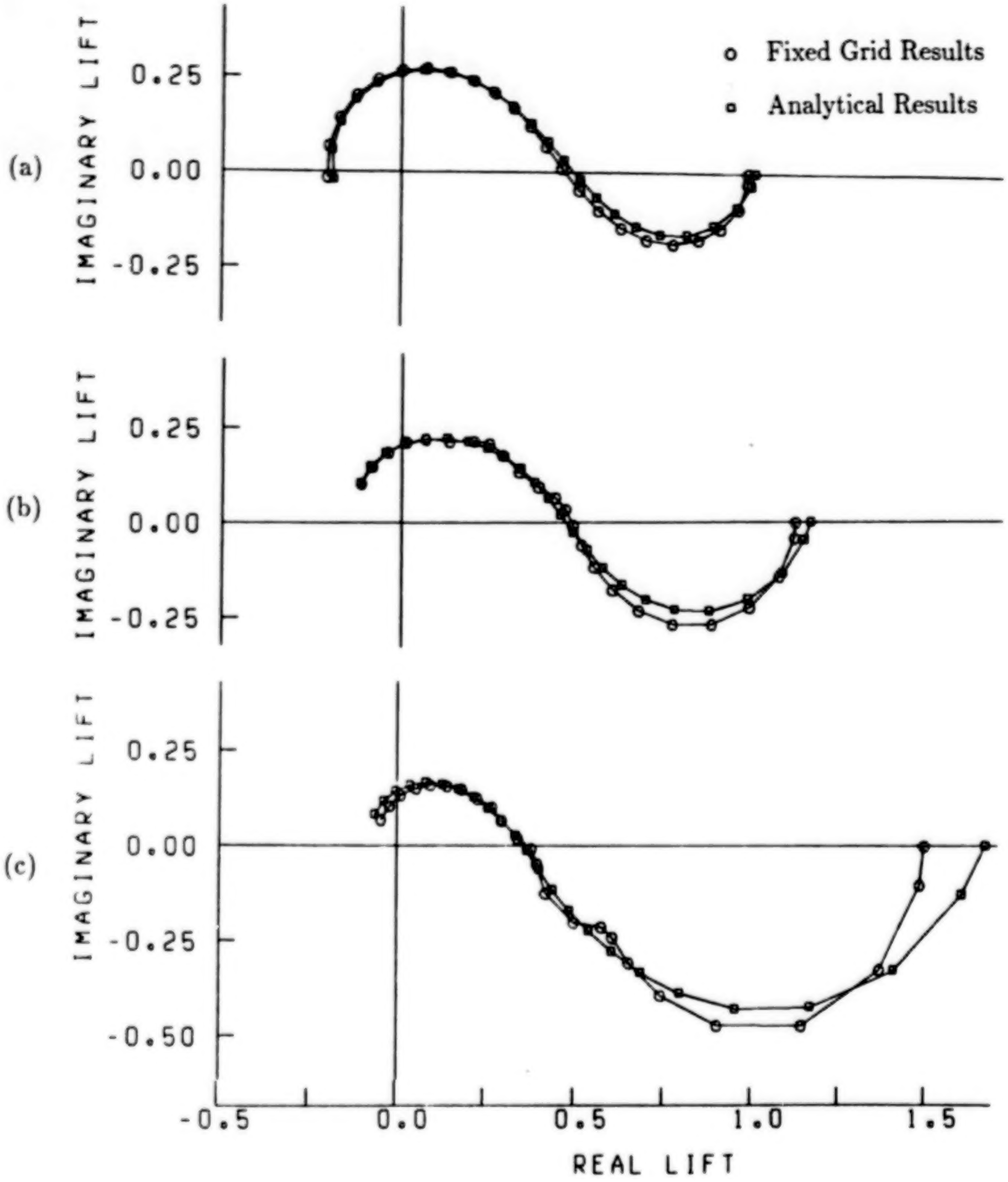

Figure 21. Comparison between numerical results generated on a fixed grid and analytical results for a flat plate airfoil in a transverse gust at (a) $M = 0.1$, (b) $M = 0.5$, and (c) $M = 0.8$.
$k_1 = 0.0, 0.007, 0.027, 0.062, 0.110, 0.172, 0.248, 0.338, 0.442, 0.561, 0.694, 0.842, 1.01, 1.18, 1.38, 1.59, 1.82, 2.07, 2.33, 2.62, 2.93, 3.26, 3.62, 4.01$

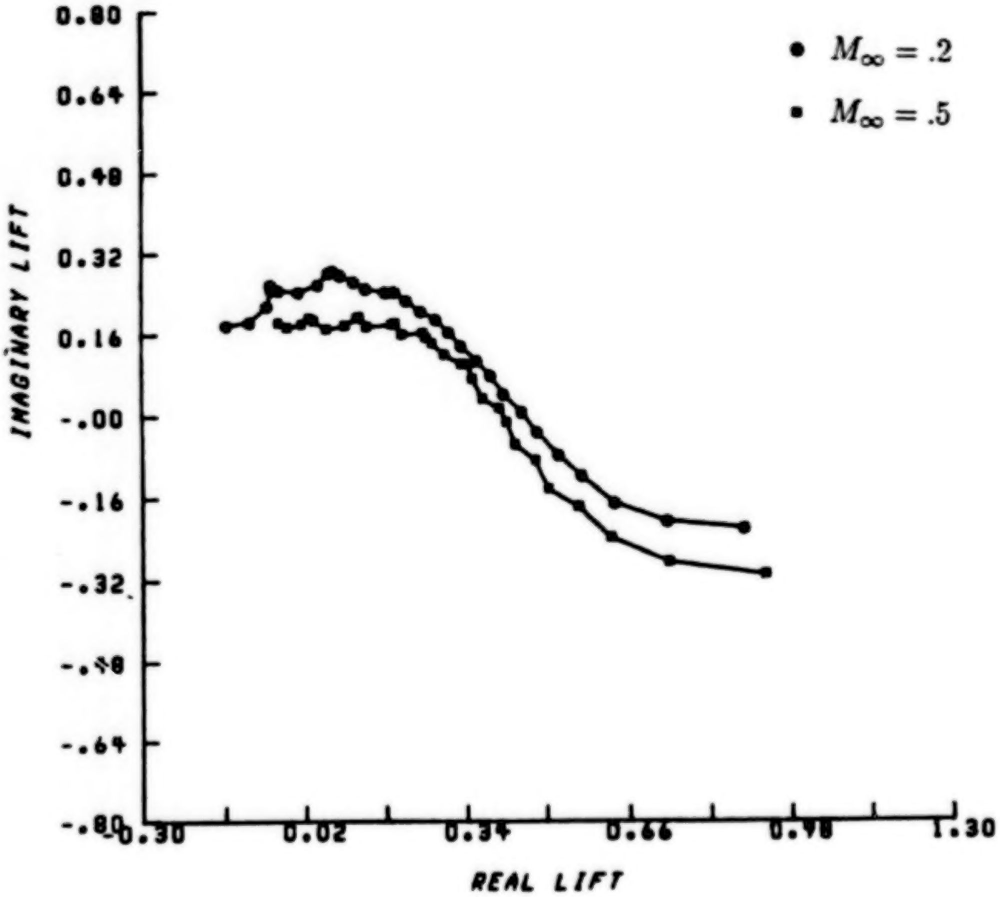

Figure 22. Numerical results for the unsteady lift of a 12 percent thick, symmetric Joukowski airfoil in a transverse gust. Results show grid dependent errors due to exponentially decreasing spacing in the ξ direction which was used in place of condition (3.70).

k_1 = 0.1, 0.2, 0.3, 0.4, 0.5, 0.6, 0.7, 0.8, 0.9, 1.0,
1.1, 1.2, 1.3, 1.4, 1.5, 1.6, 1.7, 1.8, 1.9, 2.0,
2.1, 2.2, 2.3, 2.4, 2.5, 2.6, 2.7, 2.8, 2.9, 3.0

A PRESSURE FLUX-SPLIT TECHNIQUE FOR COMPUTATION OF INLET FLOW BEHAVIOUR

H.S. Pordal, P.K. Khosla and S.G. Rubin
University of Cincinnati
Cincinnati, Ohio 45221-0343

ABSTRACT

A method for calculating the flow field in aircraft engine inlets is presented. The phenomena of inlet unstart and restart inlet are investigated. Solutions of the Reduced Navier Stokes (RNS) equations are obtained with a time consistent direct sparse matrix solver that computes the transient flow field both internal and external to the inlet. Time varying shocks and time varying recirculation regions can be efficiently analyzed. The code is quite general and is suitable for the compution of flow for a wide variety of geometries and over a wide range of Mach and Reynolds numbers.

INTRODUCTION

At supersonic flight mach numbers the flow within an aircraft engine inlet is very complex. Oblique and normal shocks are present and viscous interactions can be quite significant. These effects are amplified by the presence of adverse pressure gradients, and shock-boundary layer interaction plays an important role in determining the flow behaviour. At supersonic flight conditions, the performance of the inlet/diffuser depends critically on the nature of the shock interaction and, in particular, on the location of the terminal shock. At off-design flight conditions, for a given diffuser geometry, a shock can move ahead of the cowling so that inlet unstart occurs. This causes a sharp reduction in mass flow and pressure recovery and an associated large increase in drag. The shock can be swallowed (engine restart) by increasing the throat area or by decreasing the back pressure. The performance of the inlet then returns to the design value. These complex flow phenomena cannot be accurately predicted with analytical techniques. Computational methods can provide a reasonable estimate of the critical flow phenomena. Toward this goal, the present authors have previously investigated inviscid and low Reynolds numbers flow in two dimensional and axisymmetric inlets (1,2,3).

The present study deals with an investigation of the flow characteristics in typical aircraft engine inlets at large Reynolds number. A two dimensional/ axisymmetric flow solver for inlet flow field studies has been developed. The governing equations are written in general non-orthogonal curvilinear coordinates and are discretized using a form of flux vector splitting (4). This procedure was formulated previously by Rubin and Khosla (4,5). The discretization procedure remains the same for viscous and inviscid, incompressible, subsonic, transonic and supersonic flows, see Rubin and Khosla (6-10), and has been extended for three dimensional (11), as well as unsteady flow (1,2,3,12,13) computations. A significant feature of this procedure is that it does not require the addition of explicit artificial viscosity. Numerical dissipation due to the accuracy of the discretization can be minimized on sufficiently fine grids, see Rubin and Himansu (14).

For unsteady flow computations, in order to capture the transient behaviour efficiently, a more robust and time consistent procedure has been developed. A direct sparse matrix solver (15,16) has been appropriately modified for coupled systems of equations and is applied herein. The choice of the direct solver is dictated by considerations of stability, robustness, accuracy and time consistency. For steady computations, the solution technique permits large time increments and has strong convergence properties; whereas, for transient flows, time consistency is maintained in an efficient manner. Implicit, time consistent procedures based on approximate factorization, e.g. ADI techniques, typically do not have strong convergence properties and may require added transient or steady state artificial viscosity (17). The sparse matrix direct solver, considered herein, retains the simplicity and robustness of the time marching procedure and, as in the steady-state global relaxation formulation, explicitly added artificial viscosity is not required. Moreover, for time dependent computations, the time step limitation for the direct solver is much less severe than that for other time marching procedures.

The flow in an inlet at large Reynolds number is inherently turbulent. A simple algebraic two layer eddy viscosity (Baldwin-Lomax) model is used herein for turbulent flow computations. Section 2 presents the governing equations. The boundary conditions and discretization are described in Sections 3 and 4, respectively. Section 5 deals with the solution procedure and the results are discussed in Section 6.

GOVERNING EQUATIONS

The RNS equations are obtained from the full NS equations by neglecting the viscous diffusion terms in an appropriate streamwise direction, as well as all viscous diffusion terms in the normal momentum and energy balances. In this context, the RNS system represents a composite of the Euler plus second-order boundary layer equations. The conservation form of the RNS equations are written in general non-orthogonal curvilinear co-ordinates (ξ,η), so that an arbitrary grid generation technique can be applied.

Continuity Equation:

$$(\rho gr)_\tau + (\rho grU)_\xi + (\rho grV)_\eta = 0. \tag{1a}$$

X Momentum Equation:

$$\begin{gathered}[\rho gr(UX_\xi + VX_\eta)]_\tau + (\rho grU^2X_\xi)_\xi + (\rho grUVX_\eta)_\xi + (\rho grUVX_\xi)_\eta + (\rho grV^2X_\eta)_\eta + \\ r(PY_\eta)_\xi - r(PY_\xi)_\eta - ((\mu rX_\xi[U(X_\xi X_\xi - Y_\xi Y_\xi) + V(X_\eta X_\xi - Y_\xi Y_\eta)]_\eta/g)_\eta \\ -((2\mu rY_\xi[2(UX_\xi Y_\xi + VX_\eta Y_\xi)_\eta + (VrY_\eta X_\xi + UrY_\xi X_\xi)_\eta/r]/(3g))_\eta)/(Re_\infty)=0\end{gathered} \tag{1b}$$

Y Momentum Equation:

$$\begin{gathered}[\rho gr(VY_\eta + UY_\xi)]_\tau + (\rho grU^2Y_\xi)_\xi + (\rho grUVY_\eta)_\xi + (\rho grUVY_\xi)_\eta + (\rho grV^2Y_\eta)_\eta \\ -r(PX_\eta)_\xi + r(PX_\xi)_\eta - ((\mu rY_\xi[U(Y_\xi Y_\xi - X_\xi X_\xi) + V(Y_\eta Y_\xi - X_\xi X_\eta)]_\eta/g)_\eta - r(2\mu X_\xi \\ [3(UY_\xi X_\xi + VY_\eta X_\xi)_\eta - (VrX_\xi Y_\eta + UrX_\xi Y_\xi)_\eta/r + (UY_\xi X_\xi + VX_\eta Y_\xi)_\eta]/(3g))_\eta/(Re_\infty) - \\ (r\mu Y_\xi[U(Y_\xi Y_\xi - X_\xi X_\xi) + V(Y_\xi Y_\eta - X_\eta X_\xi)]_\eta/(g))_\eta/(Re_\infty)=0\end{gathered} \tag{1c}$$

Energy Equation:

$$\begin{gathered}(\rho grH)_\tau + (\rho grHU)_\xi + (\rho grHV)_\eta = (r(\gamma-1)M_\infty^2/[1+.5(\gamma-1)M_\infty^2])(Pg)_\tau - \\ ([\mu rY_\xi(HY_\xi)_\eta/g]_\eta + [\mu rX_\xi(HX_\xi)_\eta/g]_\eta)/(Re_\infty Pr)\end{gathered} \tag{1d}$$

Equation of State:

$$P + (\gamma-1)\rho V^2/(2\gamma) = (\gamma-1)[\ 1/((\gamma-1)M_\infty^2)) + .5\ ]\ (\rho H/\gamma) \tag{1e}$$

U and V are the contravariant velocity components in the ξ and η directions, respectively; ρ is the density; P is the pressure; H is the total enthalpy; μ is the coefficient of viscosity; γ is the ratio of specific heats; Re_∞ is the reynolds number; Pr is prandtl number and M_∞ is the free stream mach number. The quantities X_ξ, X_η, Y_ξ, Y_η are metrics associated with the coordinate transformation; r is the radial location. Two dimensional flow equations are recovered by setting r to one in (1a-e); g is the transformation jacobian and τ is time. For viscous flow computations, the X and Y momentum equations are appropriately combined to obtain the momentum balance in the ξ and η directions. Viscous diffusion terms are retained in the ξ momentum equation; all viscous dissipation terms in the η momentum and energy equations are neglected.

In the equations (1a-e), all distances have been normalized with respect to the inlet throat radius; the velocities, density, temperature, total enthalpy, viscosity are non-dimensionalized with respect to the corresponding freestream values; the pressure is non-dimensionalized with respect to twice the free stream dynamic pressure.

INITIAL AND BOUNDARY CONDITIONS

For viscous flow computations, the inviscid values are prescribed for the initial guess. Boundary conditions are such that, at the inflow U, V, ρ, P and H are all prescribed. At the outflow, for boundaries outside of the inlet and far from regions of reversed flow, the negative eigenvalue fluxes are neglected. For internal flow boundaries, the back pressure is specified. This is consistent with the operational or experimental conditions of the inlet. Far from the surface of the cowling, uniform flow conditions are imposed. At the surface, for inviscid flow calculations, zero normal velocity or injection is specified. For viscous flow computations, additional no slip and adiabatic wall temperature conditions have been prescribed for most computations. However, cold wall temperature conditions have also been considered in some calculations. A wall pressure condition is not required. The surface pressure is computed as part of the solution. For external outer boundaries, the free stream pressure is specified. More details on boundary conditions as applied to internal flows are available in reference (1,2,3,18).

DISCRETIZATION

The RNS equations are discretized based on a pressure flux-split technique. The differencing has been described in previous references (1-4) and is only briefly reviewed here. All convective or ξ derivatives are upwind or flux vector differenced. The η derivatives in the continuity and η momentum equations are mid point trapezoidal or two-point (central) differenced, whereas, the η derivatives in the ξ momentum and energy equations are three point central differenced. The three point η differencing in the ξ momentum and energy equations works quite well for normal shocks, but leads to oscillations ahead of strong oblique shocks. These oscillations are eliminated with mid-point differencing, similar to that used for the continuity and η momentum equations. For compression regions the ξ momentum equation, written at an appropriate half point is employed. For expansion regions, the original central differencing scheme is retained. The details of this analysis are given in reference (1).

The streamwise pressure gradient is flux-split (4). This splitting is consistent with the flow physics and does not involve any discontinuous switching across shocks or contact discontinuities. The pressure gradient is given by

$$P_\xi = (\omega_{i-1/2})(P_i - P_{i-1})/\Delta\xi_i + (1 - \omega_{i+1/2})(P_{i+1} - P_i)/\Delta\xi_{i+1}$$

The parameter ω is computed as follows. For unsteady flows, where a differential form of the energy equation is employed, see reference (4), the cartesian form of ω is

$$\omega = M_\xi^2 \text{ for } M_\xi < 1. \text{ and } \omega = 1. \text{ for } M_\xi > 1.$$

For curvilinear co-ordinates the eigenvalue analysis indicates that the parameter ω should be redefined as follows (for details see reference 3)

$$\omega = M_\xi^2 \cdot g^2/(Y_\eta^2 + X_\eta^2) \text{ for } M_\xi < 1. \text{ and } \omega = 1 \text{ for } M_\xi > 1.$$

Where Y_η, X_η and g are the metric quantities described previously in section 2.

The flux form of the streamwise pressure gradient term, with ω given at the half point is second-order accurate, see reference (4), and captures very sharp normal shocks, e.g. over three grid points. It should be noted that the flux splitting is employed only in the main flow or ξ direction. In the normal, and/or secondary flow direction, as described previously, central two or three-point differencing is applied. This discretization is capable of capturing very strong normal shocks. However, a complete flux-split formulation in both co-ordinate directions is required when considering very strong oblique shock waves, e.g., hypersonic free streams. It must be noted that, though the convective streamwise derivatives are approximated using first-order differencing the accuracy of the overall scheme is somewhere between first and second-order for RNS solutions. This analysis has previously been discussed in references (5,8). In reversed flow regions, the streamwise convection terms in the ξ momentum and energy equation are flux vector or upwind differenced and this requires that the parameter ω be set to zero, see references (2,3,4,11,14). An alternate form of flux-splitting in both ξ and η directions is currently being examined.

In subsonic attached flow regions, upstream influence is transmitted through the negative eigenvalue flux or forward differenced part of P_ξ. At the leading edge, upstream influences originate from both the upper and lower surfaces of the cowling. This is modelled as an averaged form of the ξ momentum equation, written at two half points. The details of this procedure are discussed in reference (3).

Turbulence Model

For turbulent flow computations the Baldwin-Lomax (B-L) model (19) is used. This is an algebraic, two layer eddy viscosity model. The inner model is based on the Prandtl-Van Driest formulation and the outer model is based on a modified clauser formulation. The distribution of vorticity is used to determine the length scales so that the necessity for finding the outer edge of the boundary layer is removed. Details of this model are discussed in references (19,20). It is known that for highly curved geometries or large regions of recirculation of the B-L model is inadequate. For the present study these effects are generally not dominant.

SOLUTION PROCEDURE

The discretized equations are quasilinearized and written in a nine point star in delta form.

$$A_{ij}\delta\phi_{ij-1} + B_{ij}\delta\phi_{ij} + C_{ij}\delta\phi_{ij+1} + D_{ij}\delta\phi_{i-1j} + E_{ij}\delta\phi_{i+1j} + AM_{ij}\delta\phi_{i-1j-1} + CM_{ij}\delta\phi_{i-1j+1} + EM_{ij}\delta\phi_{i+1j-1} + EP_{ij}\delta\phi_{i+1j+1} = G_{ij} \quad (2)$$

where $\delta\phi$ is the solution vector, the coefficients A_{ij} ... EM_{ij} are (5x5) matrices and G_{ij} is a (5x1) vector .

For supersonic regions where there is no upstream influence, E_{ij}, EM_{ij} and EP_{ij} are zero and the method reduces to a standard initial value problem. This system can then be easily solved using a marching technique such as line relaxation. However, for subsonic flow fields and fine meshes the convergence rates of such iterative techniques are generally significantly reduced. Moreover, for unsteady flows the physical time step limitation can also be severe (13). Iterative schemes for strongly interacting flows are also susceptible to false transients that further reduce time step requirements. Most of the difficulties that are associated with iterative or approximate factorization techniques can be overcome by the use of a direct solver. In the present study the choice of direct solver is dictated by considerations of stability, robustness and time consistency.

The Yale Sparse Matrix Package (YSMP), developed by Eisenstadt (14), and modified for coupled systems [15] and for the boundary conditions detailed previously, is applied here. This is an efficient solver as it stores only non-zero elements, and reorders the matrix using a minimum degree algorithm to minimize fill-in during the LU decomposition. However, for fine meshes and large numbers of mesh points, the memory requirement for the direct solver can become significant. Although memory associated with present day computers has constantly been increasing, access is still limited. To overcome this limitation, a domain decomposition strategy is employed. The computational domain is appropriately split into subdomains with suitable overlap between adjacent regions. Since we are dealing with flow fields that involve moving shocks, the overlap has to be sufficiently broad to accomodate the complete shock. Since captured shocks are spread over three to four grid points, an overlap of five points is specified. For further details see reference (2).

RESULTS

In the first part of the present investigation a two dimensional inlet (flat plate diffuser) is considered. The present authors have previously investigated inviscid and viscous laminar flow (Re# 12000) for this geometry, see references (1,2). Rather interesting flow physics is highlighted even by this simple geometry. Flow behaviour within a more complex geometry, axisymmetric inlet with a centerbody and cowling was also investigated. The results of this analysis are discussed in reference (3). Most results are for $M_\infty = 2.5$. Higher Mach numbers were considered and these results are presented in reference [2].

The unstart and restart of a two dimensional inlet are investigated herein.

Supersonic flow between two parallel plates with a sufficiently high back pressure is computed. Computations were performed on a 57 x 154 grid ($\Delta X = 0.024$, $\Delta Y_{min} = 0.00003$). In the normal direction, 97 points are placed inside the diffuser and the remainder are appropriately distributed outside. The internal flow field (between the center-line and cowling) and the external flow field, are computed simultaneously. For this grid, the CPU time per iteration on the Cray Y-MP8 is about 35 seconds per iteration. The memory requirement for the above grid using domain decomposition strategy (5 domains each of approximately 15 x 154) is a little over three megawords.

In the present investigation, unstart and restart are investigated by changing the back pressure. At unstart a bow shock stands ahead of the inlet (fig.1a-b). An inviscid solution, for an unstarted inlet, as described in reference (1), was used as an initial solution to compute the viscous flow. Steady viscous turbulent flow (Re# 1000000) solutions for an unstarted inlet were then obtained. Convergence at each time step requires approximately 3 to 5 iterations or 150 CPU seconds. The steady state viscous results requires 25 time steps. The unstarted inlet (back pressure ratio Pb/Pi=7.2) was restarted by decreasing the back pressure ratio to 6. This is well below the critical value. Figures 2a-b depict the time history of the

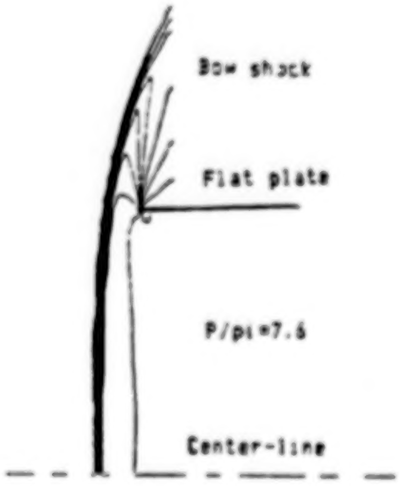

Fig.1a Unstarted Inlet

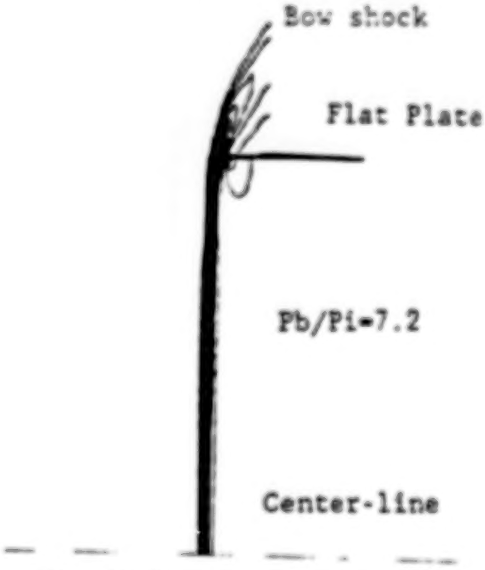

Fig.1b Unstarted Inlet

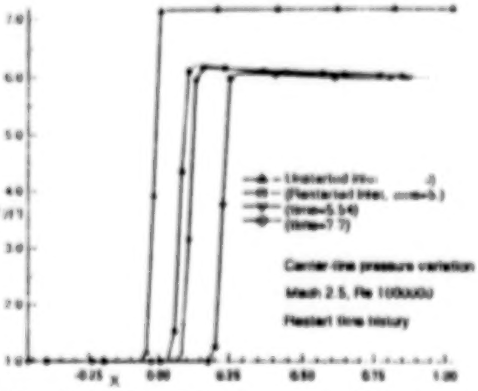

Fig.2a Time History of Unstart
(Centerline Pressure)

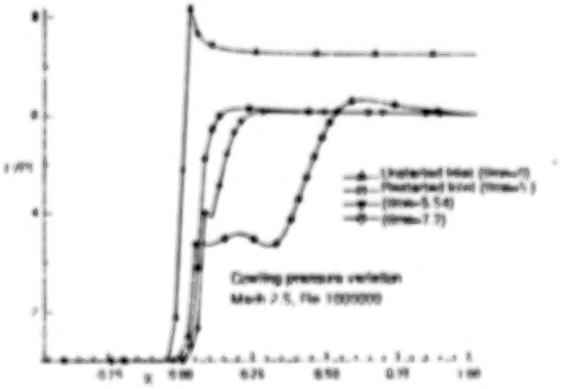

Fig.2b Time History of Unstart
(Cowling Pressure)

restart process. Once the shock is swallowed the adverse pressure gradient associated with the shock generates a reversed flow region at the cowling surface. Since the shock location varies with time, the separation region is also in constant flux. A steady state is never achieved.

At a non-dimensionalized time τ of 5.0 where $\tau = \frac{tU_\infty}{L}$ and L is the throat half-width, the normal shock is swallowed (inlet restart) and lies very close to the inlet tip. At this location the terminal normal shock merges with the inlet leading edge oblique shock. The cowling pressure distribution (fig.2b) indicates a single shock close to the inlet lip. However, at time 5.54 the pressure distribution (fig.2b) indicates a double shock. Due to the separation, the boundary layer thickens considerably and this generates a strong leading edge oblique shock. At time 7.7 the pressure contours (fig.3a) indicate a very complex shock structure close to the surface. An oblique shock originates from the leading edge of the cowling lip and this shock intersects the triple point associated with the normal shock. The velocity vectors (fig.3b) depict the recirculation zone associated with the triple point shock.

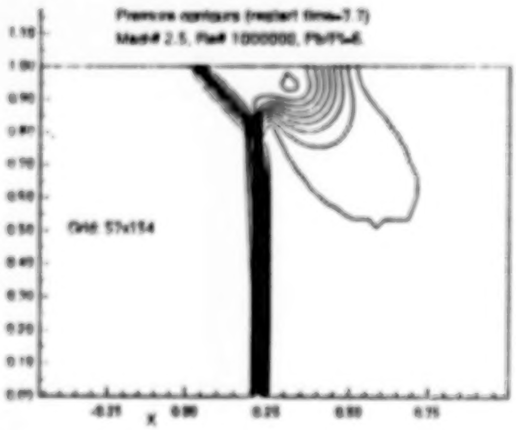

Fig.3a Shock Boundary Layer Interaction (pressure contours)

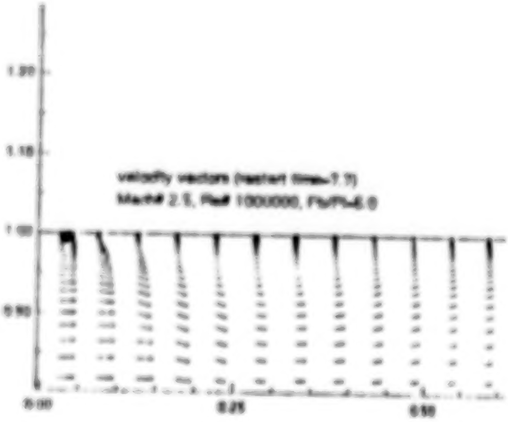

Fig.3b Velocity Vectors

Unstart of the inlet was then obtained by gradually increasing the back pressure from 6. to 7.2. As a first step, a restarted inlet with the swallowed shock very close to the cowling lip was considered. Laminar flow at a Reynolds number of 12000 was first investigated. Figures 4a-b depict the time history leading to unstart.

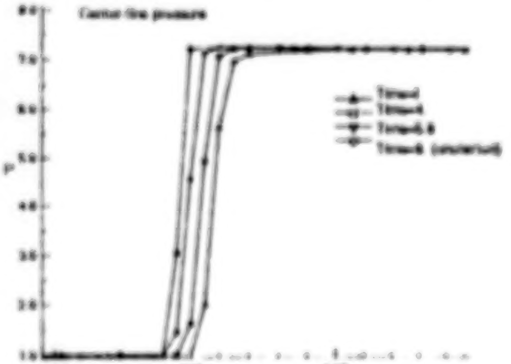

Fig.4a Time History of Unstart (mach# 2.5, Re# 12000)

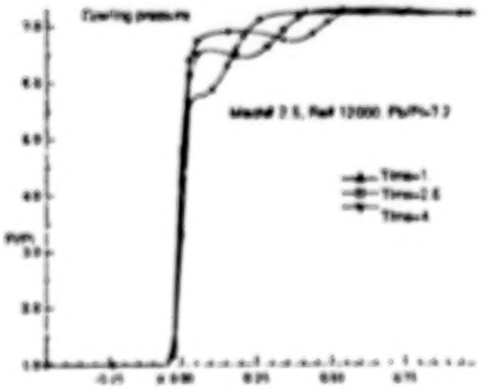

Fig.4b Time History of Unstart

Time history is recorded from the time instant $(t=t_0)$ at which the back pressure is held constant at Pb/Pi=7.2. Figures 4c-d indicate that the pressure along the cowling at the shock gradually rises and a pressure pulse travels within the boundary layer towards the inlet exit. This pressure pulse is associated with a shed vortex. The skin friction, figs. 4c-d, and the velocity vector plots (figs. 5a-b)

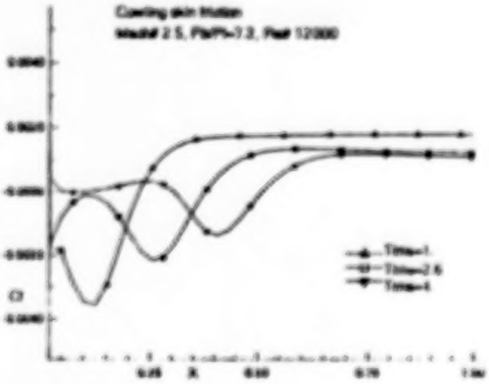

Fig.4c Skin Friction

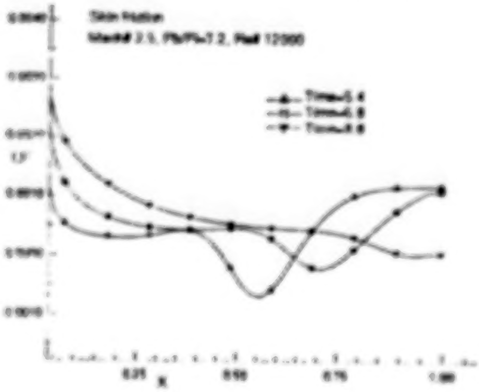

Fig.4d Skin Friction

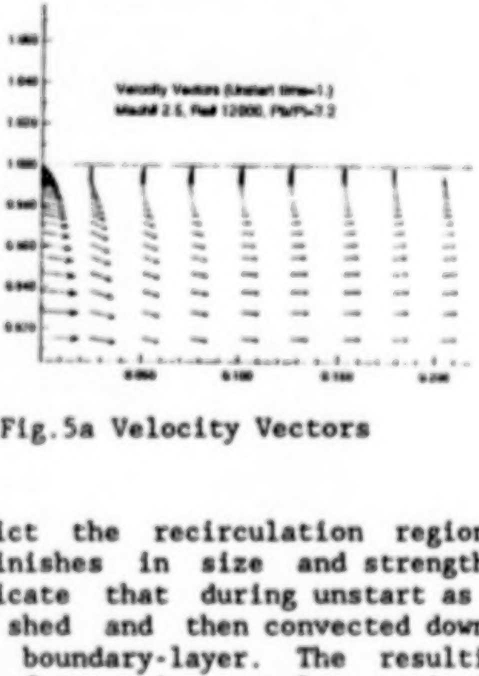

Fig.5a Velocity Vectors

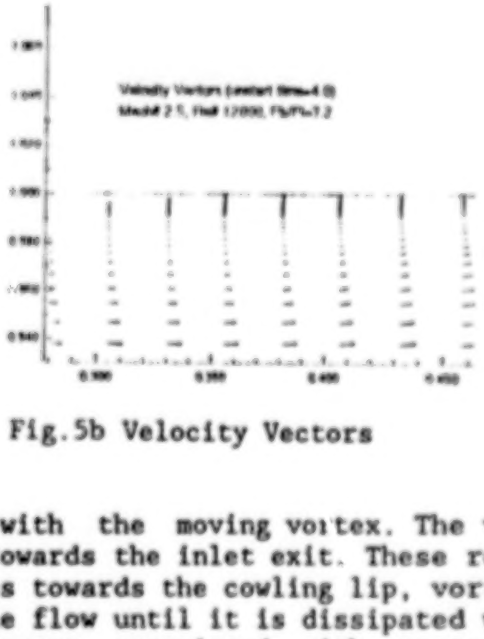

Fig.5b Velocity Vectors

depict the recirculation region associated with the moving vortex. The vortex diminishes in size and strength as it moves towards the inlet exit. These results indicate that during unstart as the shock moves towards the cowling lip, vorticity is shed and then convected downstream with the flow until it is dissipated within the boundary-layer. The resulting flow phenomena associated with unstart is therefore quite complex as it involves moving shocks and recirculation regions as well as vortex shedding and associated viscous-inviscid interactions. Current investigations include the effect of surface bleed to reduce the severity of vortex interaction.

The effects of the turbulence model was then considered. Unstart flow conditions obtained for a Reynolds number of 1000000 were investigated. The time history leading from start to unstart is depicted in Figures 6a-b. A comparison of Figure 2b (restart) and Figure 6a (unstart) indicate that the shock speed for the unstart condition is much smaller than that for the restart condition. The skin friction (fig. 6b) indicates that as the shock moves out of the inlet, the associated

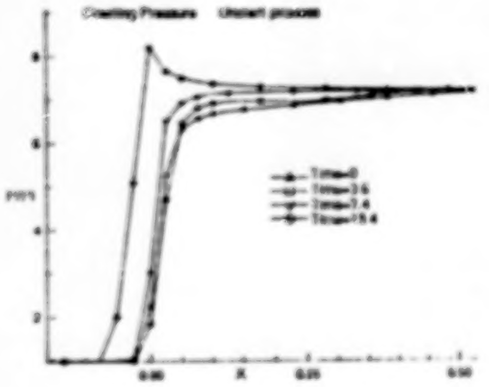

Fig.6a Time History of Unstart
(mach# 2.5, Re-1000,000)

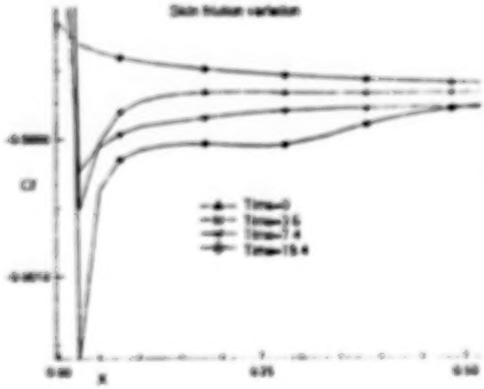

Fig.6b Skin friction

recirculation bubble diminishes in size and eventually vanishes when unstart (time-19.4) conditions are achieved. For the turbulent flow calculations, the vorticity is immediately dissipated and shedding is not observed.

For the flat plate diffuser, which represents a starting point for the simulation of transient inlet behaviour, neither computational or experimental results are available for comparison. However, there is qualitative agreement with flow visualization studies. This has been discussed in reference (2). The only detailed and quantitative assessment of accuracy is through grid refinement studies. These have previously been carried out and are discussed in reference (2). The code has also been validated for other geometries by comparing with other known solutions in reference (1).

In the second part of this study, supersonic flow in an axisymmetric inlet with a centerbody (fig.7) is investigated. In this study, the inviscid flow solution has been obtained. Computations were performed on an 89 x 115 grid. For supersonic inflow, a conical shock is formed at the tip of the centerbody. A second shock originates from the tip of the cowling and lies within the inlet (fig. 8). This

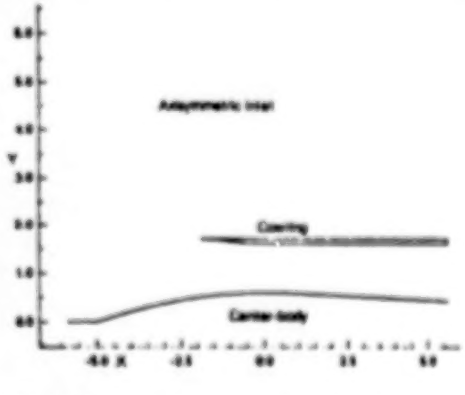

Fig.7 Axisymmetric Inlet

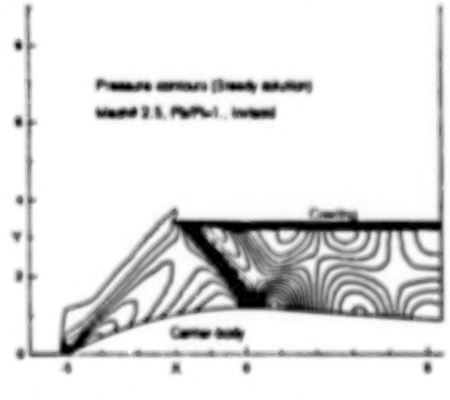

Fig.8 Pressure Contours

represents the design case and there is no mass spillage. If the back pressure at the inlet exit is raised, a terminal normal shock is formed. Figure 9a shows the pressure distribution for a back pressure to free stream pressure ratio (Pb/Pi) of

8. A terminal shock is formed and lies close to the exit (fig. 9b). If the back pressure is sufficiently high, the mass flow behind the normal shock is larger than that allowable for the given throat area. As a result, the shock moves toward the throat of the inlet and is eventually expelled from the inlet. This results in spillage of the excess mass and inlet unstart. This phenomena is further investigated herein.

A sufficiently large back pressure is applied; i.e., (Pb/Pi) - 9. The time history leading to unstart is depicted in figures 9a-b. The pressure contours (figs 10a-d) depict the complex shock pattern that exists at various time intervals during unstart. At a non-dimensional time of 208., the terminal normal shock interacts with the cowling conical shock (fig. 10c). At a time of 259, the shock is expelled (fig. 10d) and the inlet unstarts. The expelled shock interacts with the centerbody conical shock and this results in a bow shock ahead of the inlet (fig.10d). The surface pressure distribution at various times is shown in figures 11a-b (fig.10). Viscous computations for this geometry are under investigation and these results will be reported in a subsequent paper.

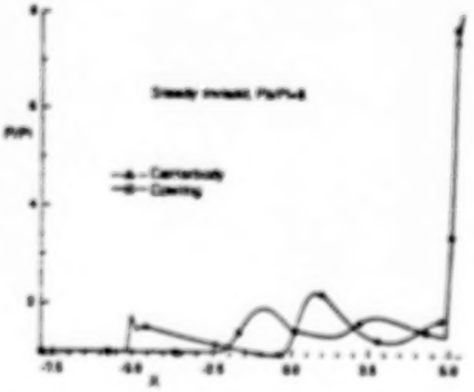

Fig.9a Pressure Distribution

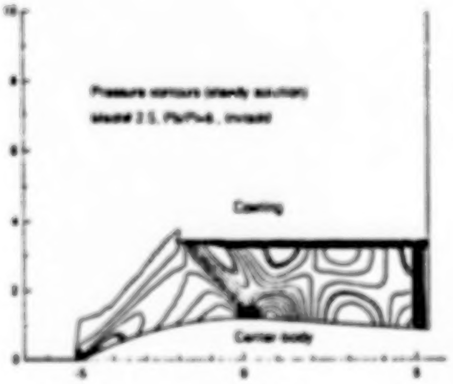

Fig.9b Pressure Contours

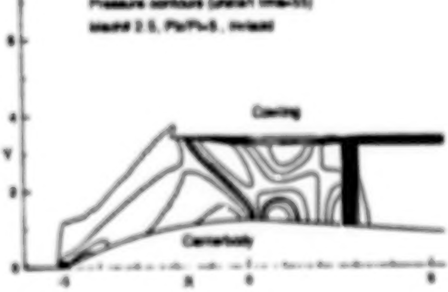

Fig.10a Pressure Contours

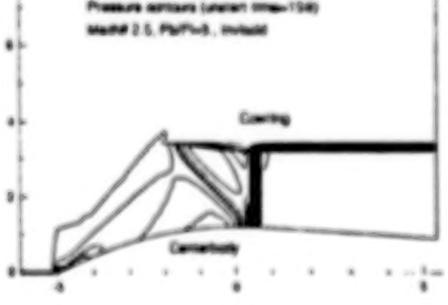

Fig.10b Pressure Contours

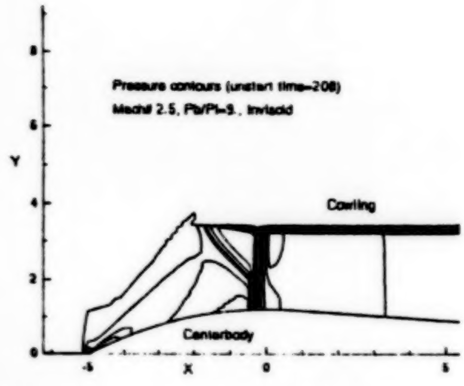

Fig.10c Pressure Contours

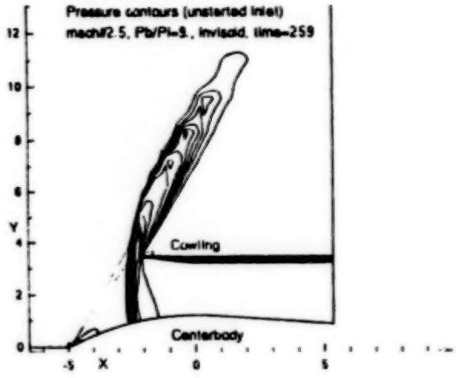

Fig.10d Pressure Contours

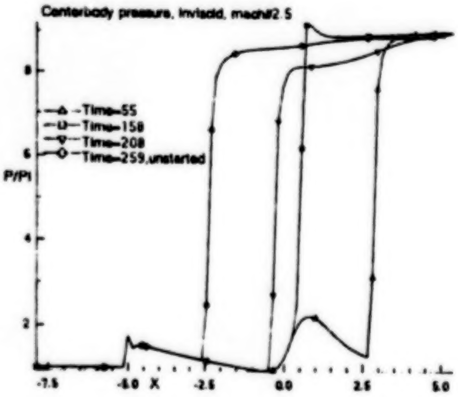

Fig.11a Centerbody Pressure Variation

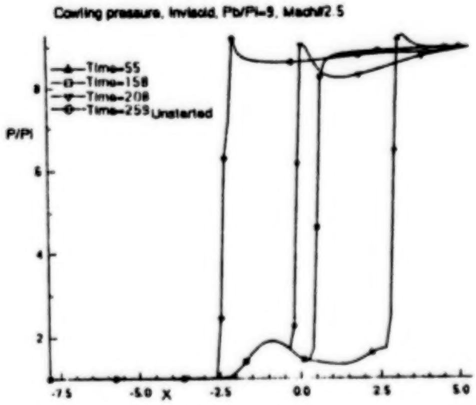

Fig.11b Cowling Pressure Variation

SUMMARY

A RNS flux-split computational procedure has been applied to investigate unstart/restart of aircraft engine inlets. A two-dimensional flat plate diffuser and an axisymmetric inlet with a centerbody has been considered. A sparse matrix direct solver combined with a domain decomposition strategy has been used to efficiently compute the complete transient flow behavior for a variety of back pressure ratios.

Unstart and/or restart of the inlet was initiated by changing the back pressure. The associated transients were efficiently captured. The applicability of the RNS flux-split procedure for unsteady flows involving moving shocks, time varying recirculation regions and shed vorticity has been demonstrated.

ACKNOWLEDGEMENT

The work has been supported in part by the NASA Lewis Research Center (T.Benson, Technical Monitor) under Grant No. NAG 3-716 and in part by the AFOSR (L. Sakell, Technical Monitor) under Contract No. F49620-85-C-0027.

The computations have been performed on the Cray Y-MP at the Ohio Supercomputer Center.

REFERENCES

1. Pordal, H.S., Khosla, P.K. and Rubin, S.G. Flux-Split Solution Procedure for the Euler Equations, International Conference on Compuatational Techniques and Applications, Brisbane, Australia, 1989.
2. Pordal, H.S., Khosla, P.K. and Rubin, S.G. A Flux-Split Solution Procedure for Unsteady Flow Calculations, To be Presented at the International Symposium on Nonsteady Fluid Dynamics, Toronto, Canada, 1990.
3. Pordal, H.S., Khosla, P.K. and Rubin, S.G. A Flux-Split Solution Procedure for Unsteady Inlet Flows, 28th Aerospace Sciences Meeting, AIAA 90-0585, Reno, Nevada, 1990.
4. Rubin, S.G, Reduced Navier Stokes/Euler Pressure Relaxation and Flux Vector Splitting, Computers and Fluids, Vol. 16, No. 4, pp. 285-290, 1988.
5. Rubin, S.G. and Reddy, D.R., Analysis of Global Pressure Relaxation for Flows with Strong Interaction and Separation, Computers and Fluids, Vol.11, No.4, pp. 281-306, 1986.
6. Khosla, P.K., and Lai, H.T., Global PNS Solutions for Subsonic Strong Interaction Flow Over a Cone-Cylinder Boat-Tail Configuration, Computers and Fluids, Vol. 11, No. 4, pp. 325-339, 1983.
7. Rubin, S.G., A Review of Marching Procedures for PNS Equations, Proceedings of a Symposium on Numerical and Physical Aspects of Aerodynamic Flows, Springer-Verlag, CA, pp. 171-186, 1982.
8. Rubin, S.G. and Reddy, D.R., Global PNS Solution for Laminar and Turbulent Flows, 6th Computational Fluid Dynamics Conference, AIAA 83-1911, Denver, MA, 1983.
9. Khosla, P.K. and Lai, H.T., Global Relaxation Procedure for Compressible Solutions of the Steady-State Euler Equations, Computers and Fluids, Vol.15, No. 2, pp. 215-218, 1987.
10. Ramakrishnan, S.V. and Rubin, S.G., Global Pressure Relaxation for Steady, Compressible, Laminar, Two Dimensional Flows with Full Pressure Coupling and Shock Waves., Report AFL 84-100, University of Cincinnati, 1984.
11. Himansu, A., Khosla, P.K. and Rubin, S.G., Three Dimensional Recirculating Flows, 27th Aerospace Sciences Meeting, AIAA 89-0552, Reno, Nevada, 1989.
12. Ramakrishnan, S.V. and Rubin, S.G., Numerical Solution of Unsteady Compressible Reduced Navier Stokes Equations, 24th Aerospace Sciences Meeting, AIAA 86-0205, Reno, Nevada, 1986.
13. Ramakrishnan, S.V. and Rubin, S.G., Time Consistent Pressure Relaxation Procedure for Compressible Reduced Navier Stokes Equations, AIAA Journal, Vol. 25, No. 7, pp. 905-913, 1987.
14. Rubin, S.G. and Himansu, A., Convergence Properties of High Reynolds Number Separated Flow, Accepted for publication, International Journal for Numerical Methods in Fluids, 1989.
15. Bender, E.E., The use of Direct Sparse Matrix Solver and Newton Iteration for the Numerical Solution of Fluid Flow, Ph'd thesis, University of Cincinnati, 1988.
16. Eisenstadt, S.G., Gursky, M.C., Schultz, M.H. and Sherman, A.H., Yale Sparse Matrix Package II. The Non-Symmetric Codes, Report 114, Yale University Department of Computer Science, 1977.
17. Khosla, P.K. and Rubin, S.G., Consistent Strongly Implicit Iterative Procedure for Two Dimensional Unsteady and Three Dimensional Space-Marching Flow Calculations, Computers and Fluids, Vol. 15, No. 4, pp. 361-377, 1987.

18. Reddy, D.R.,and Rubin, S.G., Consistent Boundary Condition for Reduced Navier Stokes Scheme Applied to Three Dimensional Internal Viscous Flows, 26th Aerospace Sciences Meeting, AIAA 88-0714, Reno, Nevada, 1988.
19. Baldwin, B.S. and Lomax, H., Thin Layer Approximation and Algebraic Model for Separated Turbulent Flows, 16th Aerospace Sciences Meeting, AIAA 78-257, Huntsville, Alabama, 1978.
20. Visbal, M. and Knight, D., The Baldwin-Lomax Turbulence Model for Two-Dimensional Shock-Wave Boundary-Layer Interactions, AIAA Journal, Vol. 22, No.7, pp. 921-927, July, 1984.

SIMULATION OF TURBOMACHINERY FLOWS

John J. Adamczyk
National Aeronautics and Space Administration
Lewis Research Center
Cleveland, Ohio 44135

ABSTRACT

With the interest in jet propulsion at the end of World War II, aerodynamicists were challenged to develop mathematical models which could be used to design turbomachinery components for jets. NASA Lewis engineers and scientists played a major role in meeting this challenge. This paper highlights some of their accomplishments as well as those of others. The paper also addresses several problems which must be solved if jet propulsion technology is to advance.

INTRODUCTION

NASA Lewis Research Center has a long history of developing mathematical models of turbomachinery flows and of constructing numerical algorithms to solve the equations associated with these models. That history began in the late forties and fifties with the modeling of axial, centrifugal, and mixed flow machinery. Stantiz, Wu, Ellis, Hamrick, Hansen, Klapproth, Goldstein, Prain, Costello, Cummings, Sinnette, and Yohner are just a few of the names behind this pioneering work. Both "Axial Compressors" (NASA SP-36, ref. 1) and "Aerodynamics of Turbines and Compressors" (ref. 2) give excellent accounts of Lewis' many contributions. Similar projects were pursued concurrently by academic and industrial researchers, of which Marble (ref. 3) and Smith (ref. 4) are exemplary.

Most of these early works can be divided into two categories, blade-to-blade (cascade plane) and throughflow (meridional plane) analyses. Although the blade-to-blade analyses originated from isolated airfoil theory, throughflow analyses had no direct counterpart in external aerodynamics and were unique, at this time, because they accounted for the effects of vorticity on the development of the flow field. In fact, the external aerodynamic community has only very recently found it necessary to include the effects of vorticity outside of boundary layer regions in the analysis of aircraft components.

Although throughflow analyses were the first to find wide use, it was not until the seventies that these blade-to-blade analyses were developed to a point that designers could use them with confidence. Before they could be directly useful to designers, throughflow analyses had to await the development of digital computers and of blade element correlations which corrected for the effects of viscosity and in-passage shocks.

In 1954 NASA Lewis undertook a comprehensive effort (lasting nearly three years) to correlate the available data on axial flow compressors for the purpose of design. These correlations, which were developed according to blade element theory, corrected for the effects of viscosity on blade element efficiency and for the flow angle exiting the element (ref. 1). A similar effort was undertaken by turbine aerodynamicists at Lewis (ref. 5). At the same time, a number of nongovernment efforts with similar goals yielded correlations for the departure of the flow angle from the mean chamber line. These correlations were used to establish the flow turning produced by a blade element and the pressure distribution along the element surface.

In the late fifties the desire for a higher pressure ratio per stage forced designers to consider transonic blading. This new class of blading necessitated the development of models for estimating the losses created by an in-passage shock. Such a model was developed by Miller and Hartmann (ref. 6). Today updated versions of this model, which account for the oblique inclination of the shock wave relative to the flow direction, can be found in many throughflow analyses. A more recent addition to the list of models used with throughflow analyses introduces the effects of spanwise mixing on the radial distribution of total temperature, total pressure, and angular momentum. These models associate the mixing process with either the development of secondary flows, Adkins and Smith (ref. 7), or turbulent diffusion, Gallimore and Cumpsty (ref. 8). Although these models have been shown to give comparable results, the issue of the controlling mixing process is still being debated.

With the development of blade element correlations, all of the parts were in place to attempt a computer execution of a throughflow simulation. One of the first publications which illustrated the capabilities of this new technology for compressor design was authored by Wright and Novak (ref. 9). This publication was followed by a number of others, of which Crouse et al. (ref. 10) and Hearsey (ref. 11) have resulted in computer codes that are available to the compressor design community. All three of these publications relied on the streamline curvature procedure to solve the throughflow equations.

In the mid and late sixties Katsanis pioneered the development of aerodynamic analysis codes for turbomachinery which used matrix iteration procedures to solve the finite difference form of the fluid flow modeling equations. One of these was a throughflow analysis code, co-written with McNally and known as "Meridional" (ref. 12), which is still widely used by turbomachinery designers. Recently Katsanis added to "Meridional" the ability to analyze more than one blade row, and a publication which outlines this enhancement is forthcoming. Katsanis also succeeded in developing a blade-to-blade analysis code. This code and its successor, TSONIC (ref. 13), was one of the first blade-to-blade analysis codes to find wide acceptance by designers. These codes provided a reliable estimate of the blade surface pressure and Mach number distribution. McNally later developed a boundary layer analysis (ref. 14) which could be used with TSONIC to estimate the blade boundary growth and blade element total pressure loss at design conditions. Today the codes developed by Katsanis and McNally, or similar codes, are routinely used to design subsonic and mildly transonic compressors as well as turbine blade sections.

In the mid seventies Garabedian and Korn (ref. 15) developed a hodograph procedure for designing supercritical, shock-free airfoil sections. The relevance of their work to turbomachinery blade element design was immediately recognized. With the assistance of Korn, Stephens (ref. 16) succeeded in using this procedure to redesign a cascade of airfoils which had previously been designed with the Pratt & Whitney cascade design codes. Back-to-back performance tests clearly showed the performance improvements that could be attained by using this hodograph direct design procedure. These gains came from improved control of the diffusion rate of the suction surface flow. For compressors, designers have been able to duplicate the arbitrary shapes associated with this hodograph design concept by using existing blade element geometry generators. Today, one finds these cascade sections routinely used in many advanced compressor designs. An additional illustration of the progress that has been achieved in blade-to-blade analysis is the recent publication of Davis, Hobbs, and Weingold (ref. 17). These authors succeeded in predicting the total pressure loss of a cascade of airfoils over its useful range of operation to within experimental accuracy. Today, cascade tests are used primarily to validate and calibrate computer codes and in experimental studies of fluid dynamic phenomena that establish empirical relationships utilized in cascade flow simulation.

With the introduction of supercomputers in the late seventies, it became feasible to use three-dimensional codes to analyze a blade row in the final stages of design. The first component to benefit from this capability was the fan. This application was brought about, in large part, by the work of Thompkins and Oliver (ref. 18) and Denton and Singh (ref. 19). Nearly all of the fan designs executed today (ref. 20) are evaluated by using three-dimensional Euler codes with corrections added to account for the effects of viscosity. These codes have demonstrated their ability to accurately predict the structure and strength of the in-passage shock, a capability that has resulted in improved fan performance. However, there remains the issue of accurate loss prediction for both design and off-design operating conditions.

The references cited in this introduction are by no means complete. They represent the author's best attempt to condense the many publications written over the years on the subject of turbomachinery flow modeling and simulation.

The progress made in modeling and simulating turbomachinery flows since the late forties is most impressive. There are, however, many unsettled issues and unsolved problems which remain, and computational fluid dynamics can help resolve them. The rest of this paper outlines some of these problems.

WHERE DO WE GO FROM HERE?

What follows is an attempt to identify turbomachinery-related flow problems whose solutions remain to be found or are less than satisfactory. (These problems were identified by a number of sources.) The solution of these problems would greatly advance design. Their solution is not simply bigger and faster computers. Fluid flow modeling as well as experimental fluid mechanics will have to be combined with numerical simulation to develop solutions to these problems which have a timely impact on the design process. All three of these disciplines are needed, for without each of them, the end result will fall short of meeting the needs of designers.

These problems can be divided into four categories: (1) intra-blade-row flows, (2) inter-blade-row flows, (3) component interactions, and (4) interdisciplinary interactions.

One of the most important intra-blade-row flow problems is the prediction of relative total pressure loss at design and off-design operation. In addressing this problem, we must first assess our ability to predict the loss of both subsonic and transonic compressor and turbine blade rows at design conditions. We need to establish the requirements to attain grid-independent solutions. The deficiencies of the simulation codes need to be established and an engineering assessment made of the merit of correcting them. For off-design operation, the prediction of loss is made more complicated by large regions of flow separation and large radial migrations of flow. In addition, vortex shedding may occur and the endwall flow may become unstable, causing the flow field to be unsteady. The impact of these unsteady flows on the intra- and inter-blade-row flow field has just begun to be examined. These intra-blade-row flow structures appear to establish the stability limits for compressors.

Another important problem whose solution is far from optimal is the design of endwall blade sections. It has been known for some time that the maximum loss for compressors occurs in this region. In addition, recent experimental studies have shown this region to be critical in establishing the stall stability limit. For turbines, the endwall region is the origin of large-scale, secondary flow structures which are known to have a significant impact on blade row performance and life. These secondary flows can also influence the performance and life of the neighboring downstream blade row. To date we have simply acknowledged the existence of the endwall flow region in our designs or employed empirically derived flow control concepts to improve the quality of the flow in this region. We need to establish why some of these concepts worked, while others failed. We need to develop design criteria for the endwall region which are more closely related to the controlling flow physics than those we have today.

The second group of problems is associated with the flow process in multistage machinery induced by blade row interactions. Currently two approaches are being examined to analyze these problems. The first involves simulating the unsteady flow field generated by more than one blade row. The second attempts to simulate the time-averaged flow field within a typical passage of a blade row embedded in a single or multistage configuration. This approach introduces the effects of neighboring blade rows by means of semiempirical models of blade forces, energy sources, and both momentum and energy correlations. Significant progress has been made using both approaches. The unsteady simulations have provided new insight into the complex blade row interactions which occur in transonic machinery, whereas the time-averaged flow simulations have been useful in modeling the complex flow fields within multistage configurations. These two approaches to multi-blade-row simulation can complement each other. The unsteady simulations can provide a data base for calibrating the models used to close the time-averaged flow modeling equations, and the time-averaged simulations can provide answers to many problems which would be prohibitive to solve with an unsteady code.

It would be of great benefit to define and execute numerical simulations which go beyond those that have been accomplished to date. Numerical simulations need to be executed which focus on specific issues or questions pertaining to the flow physics controlling the performance and the life of a blade row. Codes used in these studies need to be carefully documented for their ability to accurately capture the space and time scales associated with these flow processes. The costs of obtaining this information will be substantial, and thus every attempt should be made to document the simulation code. In addition, every attempt should be made to make the results available to as many researchers as feasible.

The third area focuses on problems which result from component interactions. Very often these problems are concerned with system transient behavior during stall or surge or the response of the system to a flow distortion. Because of the diverse range of space and time scales associated with these problems, the only practical means of addressing them is to resolve only those flow structures which have a first order effect on the system response. The direct effects of those structures which are of secondary importance are either neglected or approximated. An example of this approach is the model developed by Moore and Greitzer (ref. 21) for predicting the onset and recovery from surge and rotating stall. This model has reproduced many of the observed responses of compression systems during post stall operation. The equations associated with this model are challenging to solve, and because of the insight gained from them, they should be of interest to the CFD community.

Much more needs to be done in the area of component interaction modeling. Because most models are either quasi one dimensional or two dimensional, they cannot effectively treat problems for which the tangential and radial scales are nearly equal.

Solving the last problem requires the application of two or more disciplines. Problems which fit under this category are flutter and forced vibration of blading, hot section life prediction, and finally, engine simulation and control. We have made significant progress in the last 10 years in predicting when flutter will occur in high speed fans and advanced turboprops. This progress is partly due to new, unsteady aerodynamic models which include the effects of aerodynamic loading and blade sweep. We have developed analyses which examine flutter in the frequency domain and more recently have begun to address the problem in the time domain. Additional work, however, is needed in predicting part speed or stall flutter.

Aerodynamically induced, forced vibrations seem to be a problem which refuses to go away. They can occur whenever the natural frequency of a blade crosses the frequency of the aerodynamic excitation. The resulting blade vibration amplitude is dependent on the excitation level, the aerodynamic damping, the structural damping, and the mode of vibration. Because we generally uncover the problem only after the machine has been built, it is costly to solve. We have begun to address forced vibration with unsteady aerodynamic models which include the effect of blade loading and blade thickness. These models are either based on the asymptotic theory or rapid distortion or are numerical solutions of either the Reynolds-averaged form of the Navier-Stokes equations or Euler equations. Asymptotic models provide the rapid solutions which are very important to designers, whereas numerical simulations help establish the limits of these asymptotic models and address those problems which are beyond their capability. Both approaches should be further developed.

The prediction of the life of a component in the hot section of an engine has been, and continues to be, an area of intense activity at NASA Lewis. The impact of material properties, the stress state of the structure, the environment, and both the gas-side and air-side surface heat transfer on engine hot section life were investigated intensively under the NASA Lewis HOST program. The interested researcher should read reference 22 for more details about this program.

The confluence of the solutions to the problems that were discussed is an engine simulator. Developing a numerical propulsion system simulator (NPSS) is truly a grand challenge, requiring a coordinated, multidisciplinary research effort. NASA Lewis (ref. 23) is currently in the midst of planning such a program whose ultimate goal is a detailed, front-to-back computation of an engine, including its aero-thermal-structural response, the combustion process, and its response both to control inputs and external disturbances. To achieve such a capability, an hierarchy of engine systems, component-specific models, and component subsystem models of varying degrees of fidelity will have to be developed and mathematically "coupled." Managing the computation and data flow within the host computing engine will also be challenging. It is estimated that a saving of 25 to 40 percent in engine development costs and manpower would result from NPSS technology - significant numbers given the cost of engine development. Equally important, NPSS technology will permit us to explore and test new concepts without committing large outlays of funds and manpower. NPSS would screen out those concepts of little or no value, and those which promise to have significant impact could be introduced into production at reduced cost and time.

CONCLUSIONS

The last 40 years have produced significant advances in our understanding, modeling, and simulation of turbomachinery flows. With these advancements has come increased component efficiency, reduced weight, and increased durability. The engineers and scientists at NASA Lewis have played a major role in bringing this about. Today, the challenges we face as turbomachinery aerodynamicists are as demanding as those of the past. The researchers at NASA Lewis in partnership with their colleagues in industry and in universities are addressing many of them. The research program they have put in place emphasizes experimentation, modeling, and simulation. All three of these elements are needed, for without one of them, the end product would fall short of meeting its goal. The confluence of this research will be an engine simulator which will permit a detailed front-to-back computation of an engine. Such a simulator would reduce engine development costs 25 to 40 percent and allow the introduction of new concepts in a timely fashion.

ACKNOWLEDGMENT

The author wishes to express his thanks to Kristine Dugas for her assistance in the draft of this manuscript.

REFERENCES

1. Johnson, I.A.; and Bullock, R.O., eds.: Aerodynamic Design of Axial-Flow Compressors. NASA SP-36, 1965.

2. Hawthorne, W.R.: Aerodynamics of Turbines and Compressors. High Speed Aerodynamics and Jet Propulsion, Vol. X, Princeton University Press, 1964.

3. Marble, F.E.: The Flow of a Perfect Fluid Through an Axial Turbomachine with Prescribed Blade Loading. J. Aeronaut. Sci., vol. 15, no. 8, Aug. 1948, pp. 473-485.

4. Smith, L.H., Jr.: Three-Dimensional Flow in Axial-Flow Turbomachinery, Part 1, Theoretical Determination of Secondary Flow. Rep. I-14, Mechanical Engineering Dept., The Johns Hopkins University, Nov. 1953.

5. Glassman, A.J.: Turbine Design and Application: NASA SP-290, Vols. 1,2,3, 1975.

6. Miller, G.R.; and Hartmann, M.J.: Experimental Shock Configurations and Shock Losses in a Transonic-Compressor Rotor at Design Speed," NACA RM-E58A14b, June 1958.

7. Adkins, G.G., Jr.; and Smith, L.H., Jr.: Spanwise Mixing in Axial-Flow Turbomachines. J. Eng. Power, vol. 104, no. 1, Jan. 1982, pp. 97-110.

8. Gallimore, S.J. and Cumpsty, N.A.: Spanwise Mixing in Multistage Axial Flow Compressors. ASME Paper 86-GT-20, June 1986.

9. Wright, L.C. and Novak, R.A.: Aerodynamic Design and Development of the General Electric CJ805-23 Aft-Fan. ASME Paper 60-WA-270, June 1960.

10. Crouse, J.E.; Janetzke, D.C.; and Schwirian, R.E.: A Computer Program for Computing Compressor Blading from Simulated Circular Arc Elements on Conical Surfaces. NASA TN D-5437, 1969.

11. Hearsey, R.M.: A Computer Program for Axial Compressor Design, Vol. 1, Theory Descriptions, and Users Instructions. AFAPL-TR-73-66-VOL-1, Dayton University, July 1973. (Avail. NTIS, AD-764733.)

12. Katsanis, T.; and McNally, W.D.: Revised FORTRAN Program for Calculating Velocities and Streamlines on the Hub-Shroud Midchannel Stream Surface of an Axial-, Radial-, or Mixed-Flow Turbomachine or Annular Duct, Vol. II - Programmer's Manual. NASA TN D-8431, 1977.

13. Katsanis, T.: FORTRAN Program for Calculating Transonic Velocities on a Blade-to-Blade Stream Surface of a Turbomachine. NASA TN D-5427, 1969.

14. McNally, W.D.: FORTRAN Program for Calculating Compressible Laminar and Turbulent Boundary Layers in Arbitrary Pressure Gradients. NASA TN D-5681, 1970.

15. Garabedian, P.R. and Korn, D.G.: Numerical Design of Transonic Airfoils. Numerical Solution of Partial Differential Equations-II, B. Hubbard, ed., Academic Press, 1971, pp. 253-271.

16. Stephens, H.E.: Application of Supercritical Airfoil Technology to Compressor Cascades: Comparison of Theoretical and Experimental Results. AIAA Paper 78-1138, July 1978.

17. Davis, R.L.; Hobbs, D.E.; and Weingold, H.D.: Prediction of Compressor Cascade Performance Using a Navier-Stokes Technique. J. Turbomachinery, vol. 110, no. 4, Oct. 1988, pp. 520-531.

18. Thompkins, W.T., Jr.; and Oliver, D.A.: Three-Dimensional Flow Calculation for a Transonic Compressor Rotor. Through-Flow Calculations in Axial Turbomachinery, AGARD-CP-195, AGARD, Paris, France, 1976.

19. Denton, J.D.; and Singh, U.K.: Time Marching Methods for Turbomachinery Flow Calculation. Applications of Numerical Methods to Flow Calculations in Turbomachines, VKI-LEC-SER-1979-7, Von Karman Institute for Fluid Dynamics, Rhode-Saint-Genese, Belgium, 1979. (Avail. NTIS.)

20. Cedar, R.D.; and Holmes, D.G.: The Calculation of the Three-Dimensional Flow Through a Transonic Fan Including the Effect of Blade Surface Boundary Layers, Part-Span Shroud, Engine Splitter and Adjacent Blade Rows. ASME Paper 89-GT-325, 1989.

21. Moore, F.K. and Greitzer, E.M.: A Theory of Post-Stall Transients in Axial Compression Systems: Part I - Development of Equations. J. Eng. Gas Turbines Power, vol. 108, no. 1, Jan. 1986, pp. 68-76.

22. Sokolowski, D.E.: Toward Improved Durability in Advanced Aircraft Engine Hot Sections. NASA TM-4087, 1989.

23. Miller, B.A., et al.: A Perspective on Future Directions in Aerospace Propulsion System Simulation. NASA TM-102038, 1989.

NUMERICAL SOLUTIONS OF 2-D MULTI-STAGE ROTOR/STATOR UNSTEADY FLOW INTERACTIONS

R.-J. Yang and S. -J. Lin
Rocketdyne Division, Rockwell International
Canoga Park, CA 91303

ABSTRACT

Rai's method [1,2] of single-stage rotor/stator flow interaction is extended to handle multi-stage configurations. In this study, a two-dimensional Navier-Stokes multi-zone approach has been used to investigate unsteady flow interactions within two multi-stage axial turbines. The governing equations are solved by an iterative, factored, implicit finite-difference, upwind algorithm. Numerical accuracy is checked by investigating the effect of time step size, the effect of subiteration in the Newton-Raphson technique and the effect of full viscous vs thin-layer approximation. Computed results are compared well with experimental data. Unsteady flow interactions, wake cutting and the associated evolution of vortical entities are discussed.

INTRODUCTION

In the past, a major portion of the computational analysis of turbomachinery was focused on steady-state solutions of isolated airfoils. In the case of rotor-stator configurations, there are aerodynamic interactions between stationary vanes (stator) and rotating blades (rotor). During the interactions, the flow is inherently unsteady because of potential effects, the cutting of wakes of upstream airfoils by downstream airfoils and vortex shedding by blunt trailing edges of the airfoils. The interaction effects are known to affect many aspects of turbomachinery performance including blade loading, stage efficiency, heat transfer, stall margin and noise generation. To understand the flow physics and thus to improve or aid designs, an accurate transient solution of the entire turbomachine would be very useful.

Rai [1] presented a one-stator/one-rotor interaction study. His calculation was performed on a system of patched and overlaid grids using the unsteady, thin-layer, Navier-Stokes equations in two-dimension. The airfoil geometries and flow conditions are the same as that in Ref.[3]. A good agreement between the calculation and the experimental result of Ref.[3] was obtained in the case of time-averaged surface pressures on the stator and rotor. Unsteady fluctuating pressure amplitudes were also in reasonable agreement. Rai[2] extended his method to do multi-stator/multi-rotor calculation with a closer approximation to the experimental airfoil geometries.

It was found the time-averaged pressures were nearly identical to those of one-stator/one-rotor case. However, a significant improvement in unsteady fluctuating pressure amplitude and phase were obtained. Yang et al. [4] applied the method of Rai[1] to calculate the unsteady aerodynamics of a one-stator/one-rotor configuration in the high pressure oxidizer turbopump of the space shuttle main engine. It described the vortex shedding and wake cutting process and the associated unsteady convection of large scale vortical motion. It also found small time step size was required to resolve unsteady components in the flow field. Lin and Yang [5] applied the method of Rai [2] to simulate multi-stator/multi-rotor configuration in the high pressure fuel turbopump of the space shuttle main engine. It performed spatial and temporal accuracy studies to determine maximum time step and grid sizes within engineering accuracy and with minimum computational costs. The study showed that a factor of ten could be achieved in reducing computer time by judiciously enlarging time step size and reducing total number of grid points for the configurations considered. Griffin and McConnaughey [6] applied Rai's method [1] to compute unsteady heat transfer coefficients for stator/rotor configurations. Their computed results were compared well with experimental data.

The studies reported previously are for single-stage configurations. It is useful to extend Rai's method to have multi-stage capability because most turbomachines have multi-stage rotating components. Especially for the case if one is interested in those parts after first stage. The reason is that wake effects are important to characterize aerothermal behavior in the downstream stages. If one uses a single-stage approach, a time dependent wake condition at inlet has to be specified. Usually the wake condition is not known except provided by experiments. For a general approach, using a multi-stage method, the wake information is obtained from numerical solutions without invoking experimental data. This paper presents the extension of Rai's single-stage method to multi-stage case.

In extending Rai's method to multi-stage case, two technical aspects have to be addressed. First is the grid generation procedure and second is the flow solver. These issues will be described in the technical approach section. To validate our new codings, a calculation using the United Technology Research Center one and half stages large scale rotating rig case is performed. Computed results in the form of time-averaged static pressure and unsteady fluctuating pressure amplitude on airfoil surfaces are presented and compared with experimental data. Numerical accuracy is investigated by a series of tests, namely, the effect of time step size, the effect of iteration in the Newton-Raphson technique and the effect of full viscous vs thin-layer approximation. Finally, an application of the method to a six stages axial turbine in the space shuttle main engine low pressure oxidizer turbopump is demonstrated in the paper.

TECHNICAL APPROACH

Rai's single-stage ROTOR code [2] is adopted as a basis in the present study. The extension of the code to multi-stage case is described as follows:

(a) Grid Generation Procedure

There are two kinds of grid system often used in rotor/stator interaction study. One is single deforming grid system and another is multi-zone grid system. Single deforming grid system suffers the grid skewness problem if the separation distance between vane and blade is small. Multi-zone grid system avoids the problem and has been demonstrated as an efficient system for rotor/stator interaction problems[1,2]. The ROTOR code uses patched and overlaid grids for single-stage case. Its extension to multi-stage case is straight forward. For each airfoil, there are two grid zones, namely, one inner 'O-' grid, and one outer 'H-' grid. The inner 'O-' grid encloses the airfoil surface and accurately resolves the leading and trailing edges. The 'O-' grid is generated using an elliptic grid generator with the condition that the grid be orthogonal to the airfoil surface. The 'H-' grid is generated algebraically with the requirement that the metric coefficients be continuous across the periodic lines where periodic boundary conditions are imposed. A region of overlap exists between the 'O-' and 'H-' grids. The vane and blade grid systems are separated by a common patched boundary to facilitate movements of the rotor grid system without any distortion of the grid lines. Information transfer between the different zones is affected by proper imposition of interface boundary conditions. Note that for a single-stage case, there is only one moving patched boundary. For a n-stage case, there are 2n-1 moving patched boundaries.

(b) Flow Solver

The ROTOR code solves the unsteady, thin-layer Navier-Stokes equations in the 'O-' grid zones, and the unsteady Euler equations in the 'H-' grid zones. The governing equations are cast in the strong conservation form. The numerical procedure used to solve the governing equations is an iterative, factored, implicit scheme. The governing equations are replaced by a fully implicit finite-difference approximation. Numerical fluxes are evaluated by the third-order accurate upwind-biased Osher scheme. The resulting system of nonlinear equations is solved by the Newton-Raphson iteration technique. To solve these difference equations at each iteration level, an approximate factorization method is used. This technique leads to system of coupled linear difference equations having narrow block-banded structures which can be solved efficiently by a LU decomposition method. Some subiterations may be used at each time step to reduce linearization and factorization errors.

The major effort of the present modification to the ROTOR code is to treat multiple moving patched boundary conditions correctly. During the interaction process, rotor airfoils move relative to stator airfoils. Accurate method for information transfer between stationary and moving grids are necessary for multi-stage interaction problems. Rai[1] has developed a highly accurate method used for single-stage problems. Its extension to the multi-stage case is straight forward. In an independent study, Gundy-Burlet et al. [7] also presented a new code, STAGE-2, for a multi-stage compressor calculation.

(c) Boundary Condition

The use of multiple zones in simulating flows over rotor/stator configurations results in several computational boundaries, namely, inlet, exit, solid surface, periodic and zonal (overlap and patch) boundaries. The boundary conditions used at each of these boundaries are addressed briefly below.

For subsonic flow conditions, characteristic analysis requires three in-flow quantities and one out-flow quantity to be specified. Currently, the total pressure, the Riemann invariant corresponding to the right running characteristic, and the in-flow angle are specified at the inlet, and the Riemann invariant corresponding to the left running characteristic, is extrapolated from the interior to the inlet boundary. At the exit, the static pressure is specified, and three other variables are extrapolated from the interior. 'No-slip' and adiabatic wall boundary conditions are applied at the solid surfaces. It should be noted that in the case of the rotor airfoil 'no-slip' does not imply zero absolute velocity at the surface of the airfoil, but rather, zero relative velocity. The implementation of periodic boundary conditions is straight forward.

The present grid system (for instance see figure 2) consists the following two zonal boundaries:

(1) The overlap boundary between the inner and outer zones for the rotor and stator. The grid of outer zone exists concurrently with the grid of the inner zone in the inner zone area. Information transfer from the inner zone to the outer zone takes place within the inner zone.

(2) The patch boundary between the outer stator zone and the outer rotor zone. A one-grid overlap exists at this boundary, ie, the outer stator zone penetrate the outer rotor zone to the extent of one grid point (in the direction of the axis of the hub) and vice versa.

For the zonal boundaries (1) and (2), the boundary points are integrated by using the following relation:

$$(\tilde{Q}^{p+1} - \tilde{Q}^{p})_{z.b.} = 0$$

where $\tilde{Q}$ is the vector of flow variables, the subscript z.b. refers to the points on a zonal boundary, the superscript p is the p-th Newton-Raphson iteration at a given time step. This is followed by an explicit, corrective interpolation procedure at the end of each iteration wherein the value of $\tilde{Q}$ along the zonal boundary are obtained from interpolating the dependent variables of the neighboring grid in which the zonal boundaries lies. The zonal boundary can be treated in a manner such that the fluxes across them satisfy conservation condition. Since the current calculations are entirely subsonic and free of discontinuities, physically meaningful solutions can be obtained even with the use of nonconservative form of the equations. Therefore, the nonconservative overlap and patch boundary conditions used here can be expected to yield accurate solutions. Additional details regarding the implementation of zonal boundaries can be found in Ref.[1,8].

(d) Turbulence Model

Flows associated with rotor/stator configurations are unsteady in nature due to periodic interaction effects. In addition, the flow might have transition from laminar to full turbulence along airfoil surfaces. Near the trailing edges of airfoils, there exist large scale wake structures. Conventional turbulence models are developed to calculate steady mean flows. For unsteady turbulent flows, advanced turbulence models are required. As a starting point for the rotor/stator flow calculations, the Baldwin-Lomax model [10] is used in the current studies. The kinematic viscosity is evaluated using the Sutherland's law.

COMPUTED RESULTS AND DISCUSSION

Two cases with different rotor/stator configurations and flow conditions are calculated by integrating the equations of motion and the boundary conditions described earlier. Case one is the United Technology Research Center (UTRC) 1.5 stages large scale rotating rig (LSRR). Case two is the 6 stages axial turbine in the space shuttle main engine (SSME) low pressure oxidizer turbopump (LPOTP).

Case 1: UTRC 1.5 stages LSRR

Figure 1 shows the configuration. There are 22:28:28 airfoils in each blade row, respectively. In the computation we pick up 21:28:28 airfoils, a common factor of 7, so that only 3:4:4 airfoils are simulated by using periodic boundary condition to accommodate the effects of other airfoils. To keep blockage effects the same, the first stage stator airfoil geometry is enlarged by a factor of 22/21 keeping the pitch-to-chord ratio constant. The first stage rotor and second stage stator airfoil geometries are kept the same as the experiment in [9]. The inner 'O-' grid zone for each airfoil contains 101 * 21 points. For outer 'H-' grid zone, the first stage stator airfoil contains (65 * 31 - 39 * 18) points, the rotor airfoil contains (65 * 31 -40 * 19) points, and the second stage stator airfoil contains (88 * 31 - 39 * 18) points, respectively. The total grid points for the entire 11 airfoils are about 40,000 points. Fig. 2 shows the grid system (for sake of clarity, not every grid line is plotted). The flow conditions are : the inlet Mach number is 0.07, Reynolds number is $4.0 * 10^4$ per inch (this Reynolds number is very close to the experimental value used in [3,9] and is lower than the value used by Rai in [1,2]), the flow coefficient is 0.78 (ratio of inlet flow velocity to rotor velocity). Since the quantities that are prescribed at the inlet boundary are the Riemann invariants and not the dependent variables themselves, the values of u, v, p and ρ obtained at the inlet, when solution becomes periodic in time are generally different from those used to determine the Riemann invariants. To match the inlet flow condition, the ratio of the exit static pressure to the inlet total pressure needs to be adjusted and the calculations need to be continued until the calculated flow coefficient is equal to the specified value. In the present calculation, the final pressure ratio is 0.95.

Figure 3 shows the time-averaged pressure coefficient Cp and unsteady pressure envelope on the airfoil surfaces. The pressure coefficient is defined as

$$C_p = \frac{P_{avg} - (P_t)_{inlet}}{1/2\rho_{inlet}\omega^2}$$

where P_{avg} is the static pressure averaged over one composite cycle, $(P_t)_{inlet}$ is the averaged total pressure at the inlet, ρ_{inlet} is the averaged density at the inlet, and ω is the velocity of the rotor airfoils. The shaded area represents the range of the fluctuating pressure in a composite cycle. A composite cycle corresponds to the motion of the rotor through an angle equal $6\pi/21$ where 21 is the number of first stage stator airfoils. Clearly, there is a good agreement between the prediction and experimental data. The figure indicates that the unsteadiness is appreciable only on the first stage stator airfoil suction side near its trailing edge. On the other hand, the flow is seen to be unsteady over the entire first stage rotor and second stage stator surfaces. The fluctuating pressure on the first stage stator is due to the upstream potential interaction between the downstream airfoils and the first stage stator airfoil, while that on the first stage rotor and the second stage stator is due to the combined influence of potential interaction, wake/airfoil and wake/wake interactions.

It has been shown that the predicted time-averaged pressure coefficients agree quite well with the experimental data. Generally speaking, the first order mean flow quantities are easier to be computed than the second order fluctuating flow quantities. Our experience indicated that small time step size was required to resolve fluctuating quantities associated with small time scale. For numerical accuracy check up, we perform the following investigations: the effect of full viscous vs thin-layer approximation, the effect of time step size, and the effect of subiteration. During these investigations, it showed that mean flow quantities nearly have no change with respect to these factors. Therefore only fluctuating pressure amplitudes are presented in the following.

(a) Full viscous vs thin-layer approximation

For most engineering flow calculations, grid meshes are placed parallel to streamwise direction (say ξ direction). It is generally believed that the streamwise viscous effect can not be resolved unless fine grid mesh is used in the streamwise direction. Therefore, thin-layer approximation, ie, neglect of streamwise viscous term, is used in the flow calculations. For the current geometry, 'O-'grid mesh is used to wrap around airfoil surfaces. Local flow near leading and trailing edges of the airfoils is not parallel to body surfaces. Especially near trailing edges, the ξ direction has dominant viscous effect and should not be neglected. Therefore, the effect of full viscous calculation is investigated.

Figure 4 shows the results of fluctuating pressure amplitude coefficients for both full viscous and thin-layer computations (3000 time steps per composite cycle and 3 subiterations are used in the calculations) and comparisons with the experimental data. The magnitude of temporal pressure fluctuating $\tilde{C}_p$ is defined as

$$\tilde{C}_p = \frac{P_{max} - P_{min}}{1/2\rho_{inlet}\omega^2}$$

where P_{max} and P_{min} are the maximum and minimum pressure occurring over a composite cycle at a given point. Full viscous and thin-layer computations both agree well with the experimental data. It demonstrates that the viscous effect on unsteady pressure fluctuation near trailing edges of the airfoils is small comparing with inviscid mechanism. It is known that the shear layer type of wake is unstable. It is an inviscid instability so that the shear layers would roll up into discrete vortical entities. The pressure fluctuation associated with the evolution of the inviscid vortical entities tend to be larger than that associated with viscous effects.

(b) The effect of time step size

Time resolution to temporal flow structures is one of the major factors in determining numerical accuracy for unsteady flow problems. Time scales associated with the rotor/stator unsteady flow interaction are rotor rotation time scale, vortex shedding time scale, wake convection time scale and acoustic time scale. These scales may range from very large to very small, depending on geometry and flow conditions. At this time, we know of no published analytical model describing how to choose time step size for this kind of unsteady flow calculation. We perform the following calculations using 2000, 3000, 4500 time steps, respectively, in a composite cycle.

Three subiterations are used in each calculation. Figure 5 shows the computed results and compares with the experimental data. The result indicates the following: (1) as time step sizes getting smaller, solutions coincide with each other asymptotically, (2) small time step size is necessary to resolve temporal structure of vortical entities and (3) upstream potential effect on the first stage stator fluctuating pressure is well resolved within the time step sizes considered as evidenced in Fig.5(a).

(c) The effect of subiteration

The nonlinear equations of the Navier-Stokes equations are solved by the Newton-Raphson iteration technique in the present ROTOR code. Linearization and factorization errors can be driven to zero at each time step if a solution can be converged by the Newton-Raphson iteration. It is known that using compressible flow formulation to simulate low Mach number flow may result in large factorization error within the frame work of ADI method. We perform the calculations to investigate the combined effects of linearization and factorization errors on the fluctuating pressure amplitude. We use 4500 time steps in a composite cycle; 1, 2 and 3 subiterations are employed respectively. Since temporal truncation errors are the same in these cases, any differences in the solutions are due to linearization and factorization errors. Figure 6 shows the computed results and compares with the experimental data. Solutions using 2 and 3 subiterations both are nearly identical to each other. Results with 1 subiteration, only small deviations from the experimental data are observed. Comparing figures 5 and 6 (see the case of 4500 steps/cycle with 2 subiterations and 3000 steps/cycle with 3 subiterations, these two cases have the same computing costs), it is felt that the effect of time step size is more effective in reducing the errors. Heuristically, small time step size reduces linearization, factorization, and temporal truncation errors. Then we ask: is subiteration necessary if a smaller time step size is used? We perform the calculations using 6000 steps/cycle with 1 subiteration. The computed results turn out to be nearly identical to that of 4500 steps/cycle with 1 subiteration. Thus subiteration is still necessary to reduce linearization and factorization errors.

Figures 7 and 8 show the pressure and Mach number contours at one instant. At first stage stator passages, flow features are almost unchanged except near its trailing edges. Differences are observed at the first stage rotor and second stage stator passages. The differences are due to wakes effects. Wakes are generated by the trailing edges of the stator and rotor airfoils. The wakes would roll up into vortical entities. These entities are embedded in and convected by the mean flow. Because of the rotor rotation, the wakes generated by the first stage stator are chopped and sheared (rotor suction side has higher velocity than pressure side) and convected along the rotor passages. They interact with the rotor airfoils and other wakes generated by the rotor trailing edges. The combined wakes are convected into second stage passages and more complex interaction takes place. Figure 9, unsteady vectors, and figure 10, entropy contours, illustrate the phenomena described above. Unsteady vectors are obtained by subtracting the mean flow vectors from the instantaneous flow vectors. They clearly reveal large scale structures of vortical entities. Figure 10 also reveals that wakes remain coherent downstream. Along rotor passage, high loss fluid is convected toward suction side and low loss fluid is transported toward pressure side to replace the migrated wake fluid. The high loss fluid mixes with rotor wake and are convected coherently into second stage stator passage. Many complicated interactions, for instance wake/wake, wake/airfoil interactions, occur in the second stage.

Case 2: SSME 6 stages LPOTP

There are 43 and 67 airfoils in the first stage stator and rotor respectively. From the second stage to sixth stage, there have identical configuration with 61 and 67 airfoils in the stator and rotor respectively. As a demonstration, only 12 airfoils are chosen in the computation, ie, the ratio of the stator airfoil to rotor airfoil is 1:1 from the first stage to sixth stage. By doing this and keeping blockage effects the same, the first stage stator airfoil is scaled by a factor of 43/67 and those stator airfoils after the first stage are scaled by a factor of 61/67, keeping the pitch-to-chord ratio constant. The geometries of rotor airfoils in the entire six stages are unchanged. The flow conditions are: the inlet Mach number is 0.05, Reynolds number is $2.5 * 10^6$ per inch, the flow coefficient is 0.396. During the initial calculation, we use 500 steps/cycle with 1 subiteration to eliminate transient disturbances. At the same time, the exit static pressure is adjusted to establish the specified flow coefficient. It takes about 30 cycles (around 8 hours of CPU time on a CRAY-YMP machine) to converge a mean flow solution. Since there is no experimental data available for this case, for a conservative approach, we continue the calculation using 2000 steps/cycle with 3 subiterations. It takes another 5 cycles to achieve a time-periodic solution.

Figure 11 shows the time-averaged pressure coefficient Cp and unsteady pressure envelope on the stator and rotor airfoils for the six stages turbine. Similar to the case 1, the unsteadiness is appreciable only on the first stator suction side near the trailing edge of the airfoil, and the unsteadiness is spread over the entire stator and rotor airfoils after the first stage stator. Near the trailing edge of every airfoil, the shear layer type of wake would roll up into vortical entities. The evolution of the vortical motion along downstream passages produces unsteady flow fluctuations. It is interesting to note that the time-averaged Cp profiles are almost repeatable (except a constant level difference) along the downstream stages. Figures 12 and 13 show instantaneous pressure and entropy contours. They depict different instantaneous flow features from stage to stage. The flow within the downstream stages is more complicated than the upstream stages. The time variation of the static pressure at an identical location in both stator and rotor airfoil surfaces are shown in figure 14. The major shape is similar, but local variations do exist. It is believed that the major contribution to the unsteadiness is from the adjacent wake effects. Futher upstream wakes have minor contribution because of physical and numerical dissipations. Even so, the figure clearly shows time variations of the pressure history, indicating the importance of using multi-stage computation to obtain accurate transient flow informations.

SUMMARY

Rai's method of single-stage rotor/stator flow interaction has been extended to compute multi-stage configurations. Two different axial multi-stage turbines are simulated: the 1.5 stages of the UTRC LSRR and the 6 stages SSME LPOTP. Numerical accuracy for the UTRC case is checked by investigating the effect of full viscous vs thin-layer approximation, the effect of time step size and the effect of subiteration in the Newton-Raphson technique. The shear layer type of wake near the trailing edge of every airfoil would roll up into large scale vortical entities. It is an inviscid mechanism associated with the evolution of the vortical entities. The unsteady pressure fluctuation produced by the inviscid mechanism is larger than that of viscous effect. Small time step size is effective in reducing errors caused by linearization, factorization and truncation, however, subiteration is still necessary to reduce linearization and factorization errors.

Wakes are convected coherently into downstream stages. Interactions between wake/airfoil and wake/wake are common. For the case of 6 stages SSME LPOTP, though there have identical stage geometries along downstream, yet the time variation of the flow field is different from stage to stage. The use of multi-stage computation is necessary to obtain transient flow informations for the multi-stage machine.

ACKNOWLEDGEMENT

This work was sponsored by NASA Marshall Space Flight Center under contract no. NAS8-40000. Computation resources are provided by NAS systems at NASA Ames Research Center. The authors would like to express their appreciation for the support and encouragement given by Dr. M. M. Rai and his colleagues at NASA Ames and Dr. H. V. McConnaughey at NASA MSFC. Color graphics are made by Mr. K. Sheedy at Rocketdyne.

REFERENCES

1. Rai, M. M., 'Navier-Stokes Simulations of Rotor-Stator Interactions Using Patched and Overlaid Grids,' AIAA J. of Propulsion and Power, Vol.3, No.5, (1987).

2. Rai, M. M. and Madavan, N. K., 'Multi-Airfoil Navier-Stokes Simulations of Turbine Rotor-Stator Interaction,' AIAA Paper 88-0361, (1988).

3. Dring, R. P., Joslyn, H. D., Hardin, L. W. and Wagner, J. H., 'Turbine Rotor-Stator Interaction,' ASME J. of Engineering for Power, Vol.104, (1982).

4. Yang, R. -J., Lin, S. -J. and Rai, M. M., 'Unsteady Aerodynamics of Rotor-Stator Interaction in a Turbine Stage,' AIAA Paper 88-0360, (1988).

5. Lin, S.-J. and Yang, R. -J., 'Multi-Blade Navier-Stokes Simulations of Rotor-Stator Interaction in a Turbine Stage,' AIAA Paper 89-0326, (1989).

6. Griffin, L. W. and McConnaughey, H. V., 'Prediction of the Aerodynamic Environment and Heat Transfer for Rotor/Stator Configurations,' ASME Paper No. 89-GT-89, 1989.

7. Gundy-Burlet, K. L., Rai, M. M. and Dring, R. P., 'Two-Dimensional Computations of Multi-Stage Compressor Flows Using a Zonal Approach,' AIAA Paper 89-2452, (1989).

8. Rai, M. M., 'A Conservative Treatment of Zonal Boundaries for Euler Equation Calculations,' J. of Computational Physics, Vol.62, (1986).

9. Dring, R. P., Blair, M. F., Joslyn, H. D., Power, G. D. and Verdon, J. M., ' The Effects of Inlet Turbulence and Rotor/Stator Interactions on the Aerodynamics and Heat Transfer of a Large-Scale Rotating Turbine Model,' Final Report, NASA CR-4079, (1986).

10. Baldwin, B. S. and Lomax, H., 'Thin-Layer Approximation and Algebraic Model for Separated Turbulent Flows,' AIAA Paper 78-257, (1978).

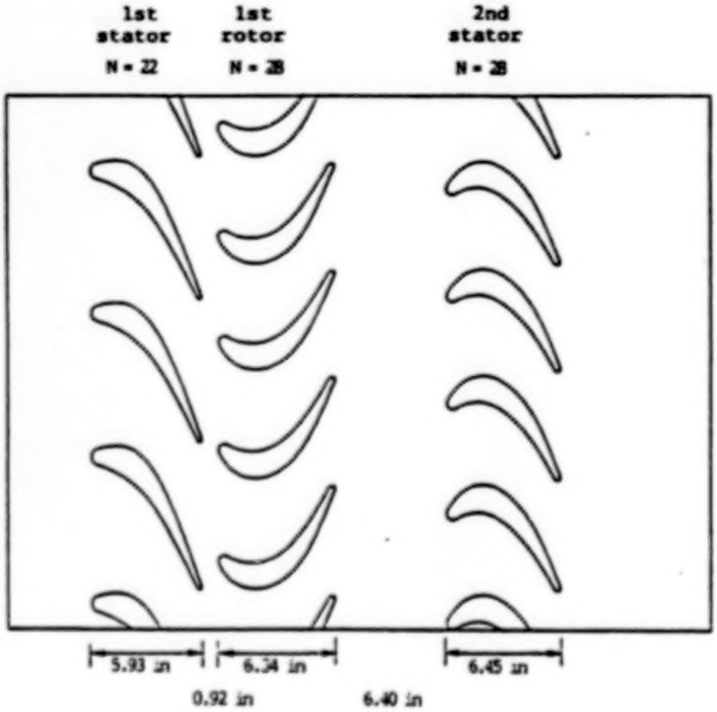

Fig. 1 UTRC 1.5 stages LSRR

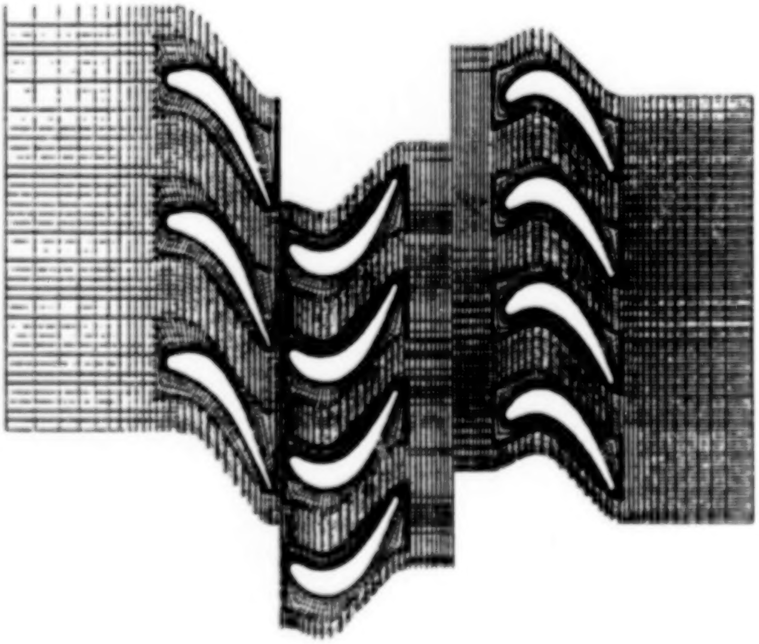

Fig. 2 Multi-zone grid system

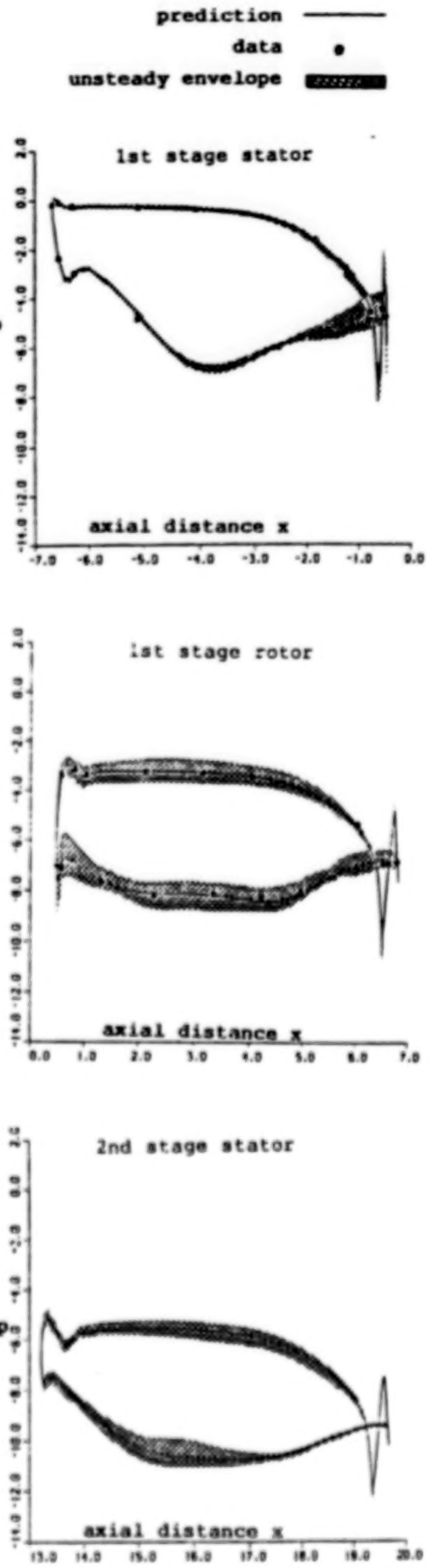

Fig. 3 Time-averaged pressure coefficient and unsteady pressure envelope on airfoil surfaces.

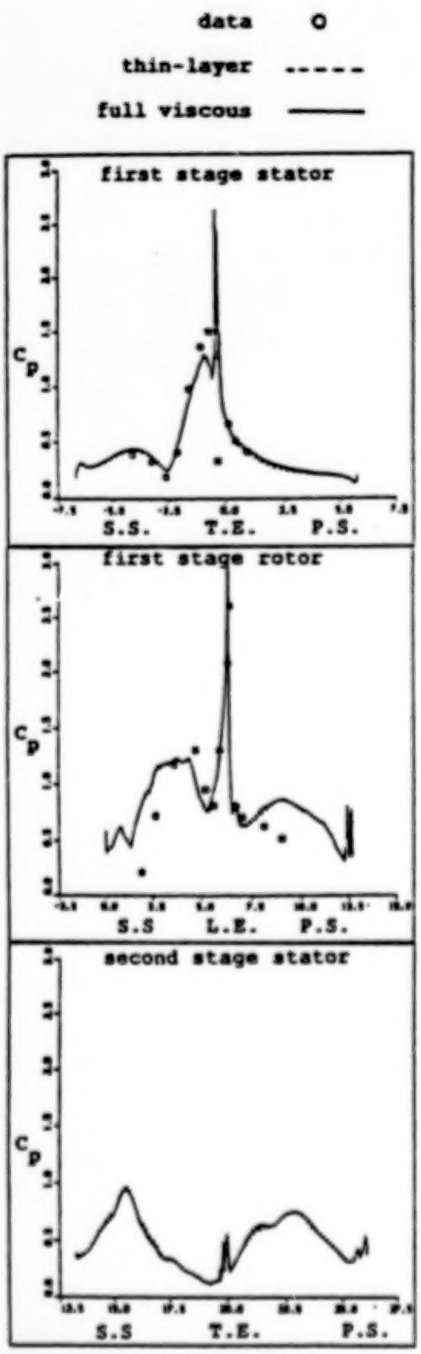

Fig. 4 The effect of full viscous vs thin-layer calculations on the fluctuating pressure amplitude

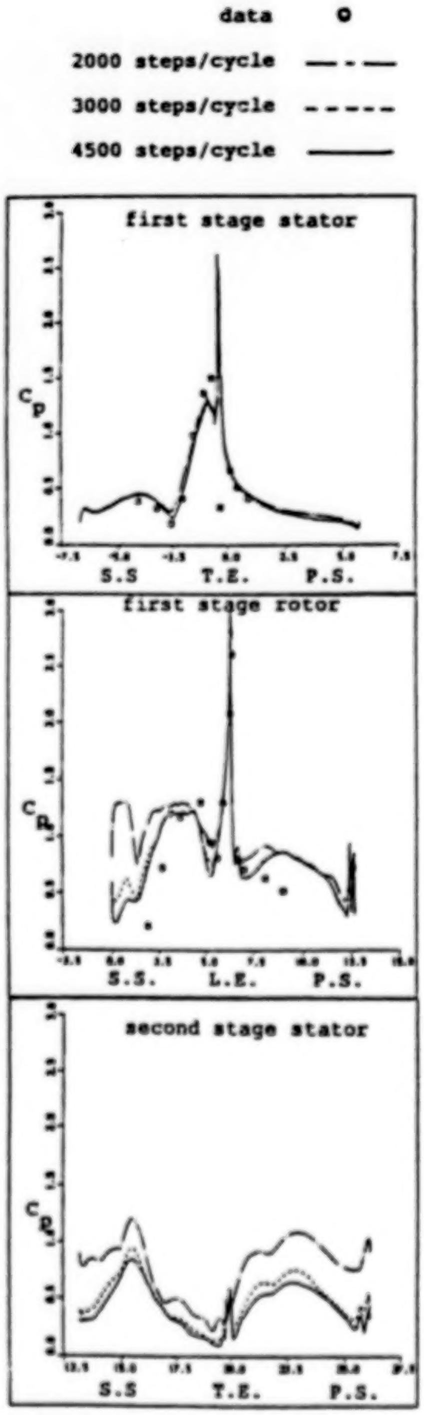

Fig. 5 The effect of time step size on the fluctuating pressure amplitude.

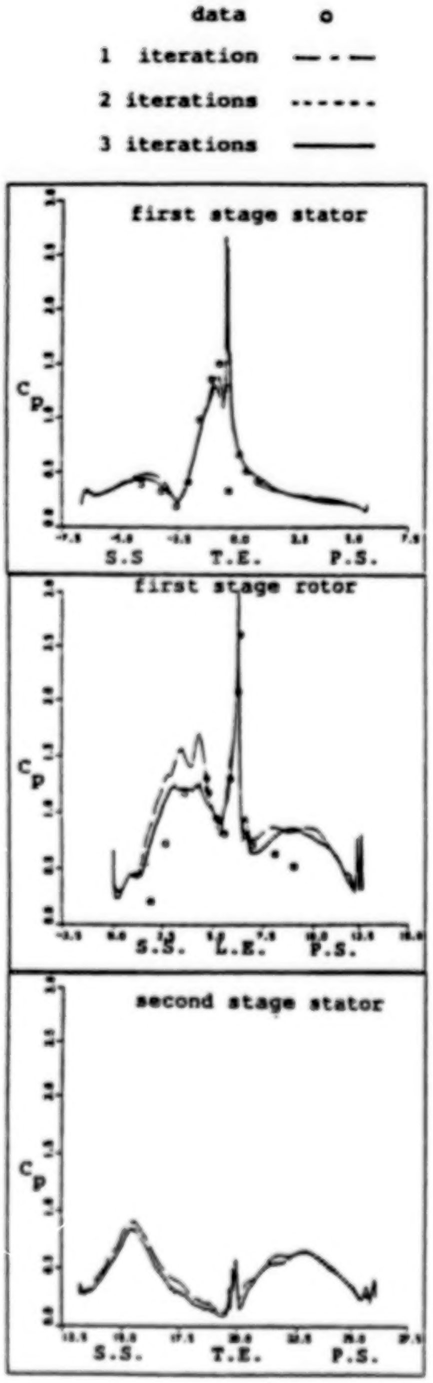

Fig. 6 The effect of subiteration on the fluctuating pressure amplitude.

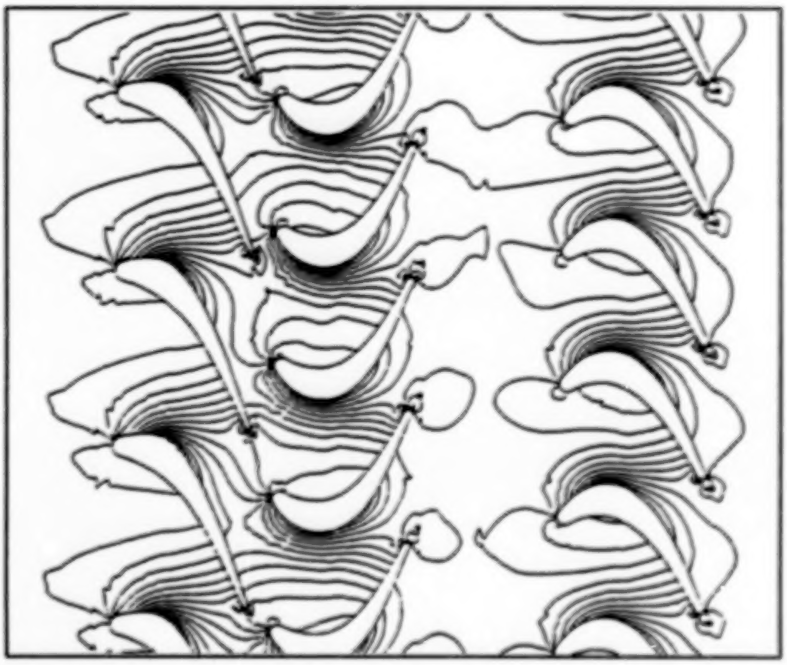

Figure 7: UTRC LSRR instantaneous pressure contours.

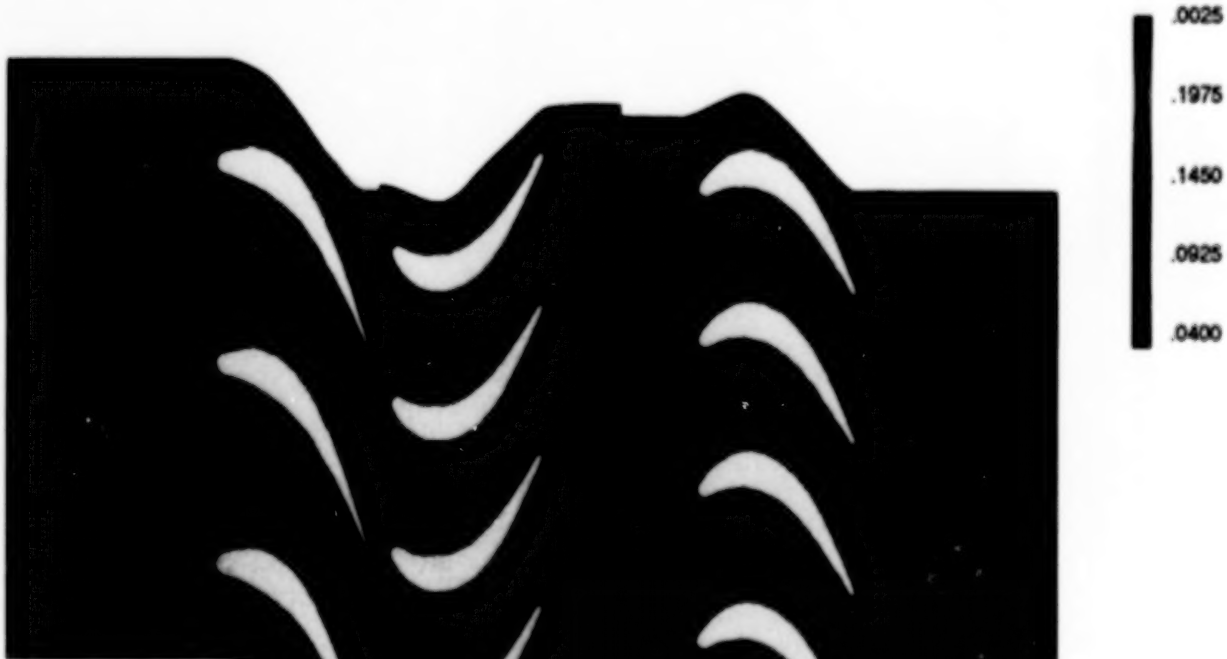

Figure 8: UTRC LSRR instantaneous Mach number contours.

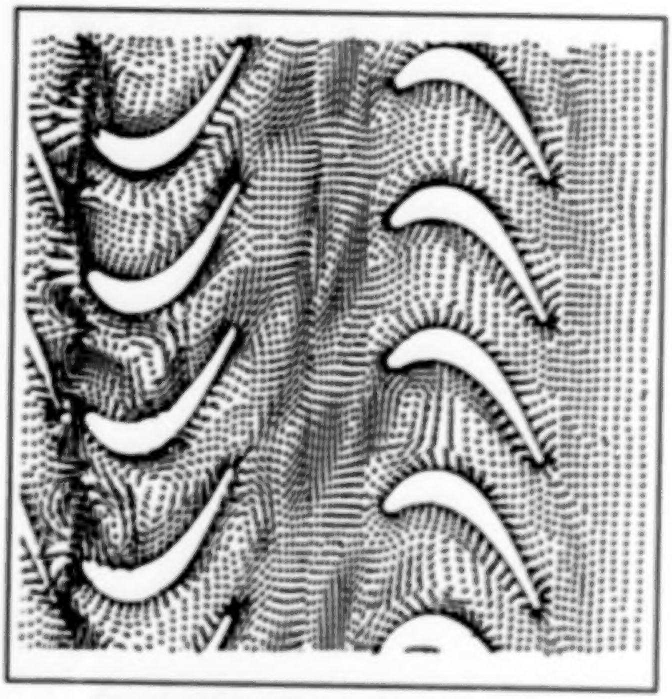

Figure 9: UTRC LSRR unsteady velocity vectors.

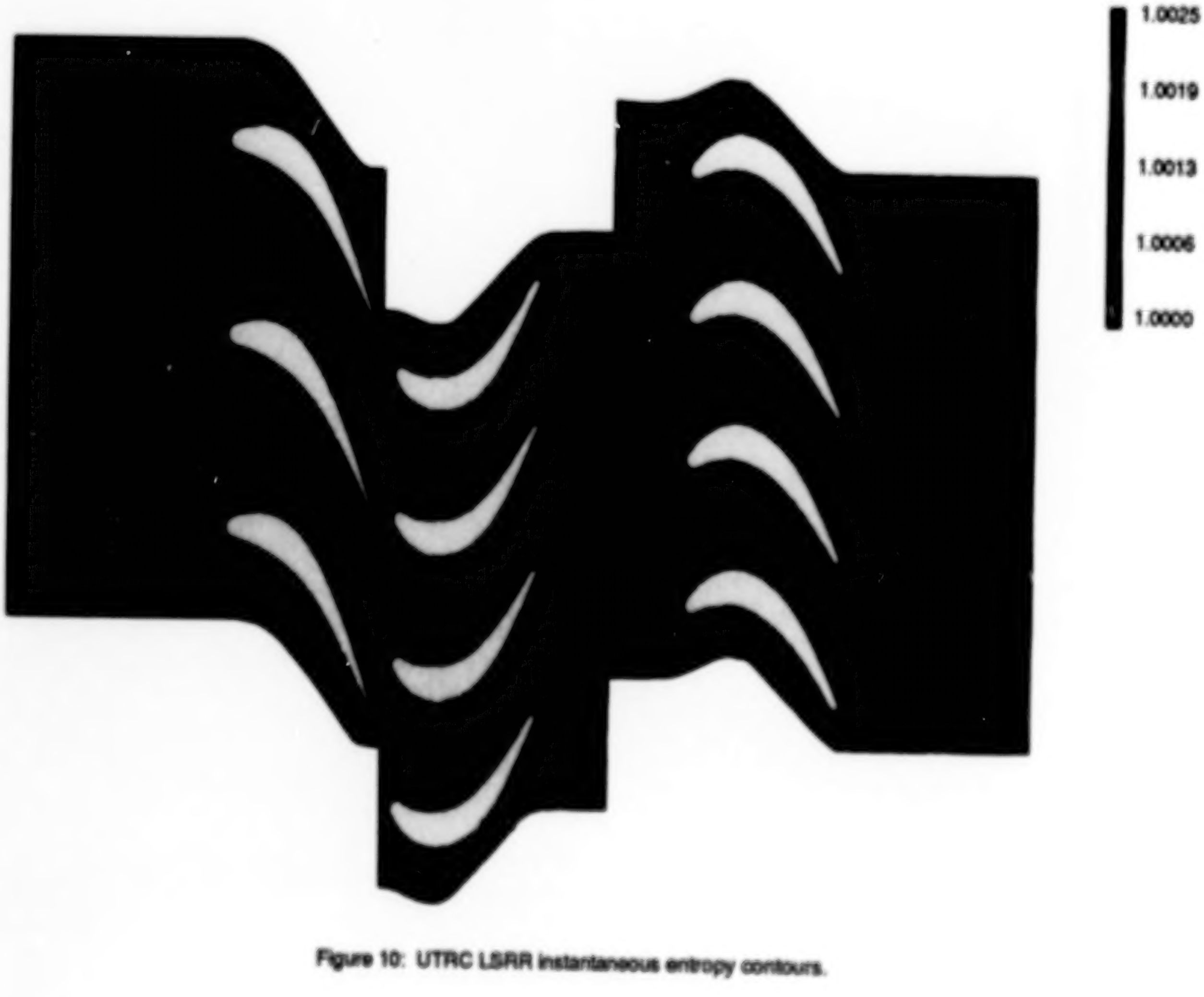

Figure 10: UTRC LSRR instantaneous entropy contours.

PRESSURE COEFFICIENT ON STATOR SURFACE

time-averaged ——— unsteady envelope ▨

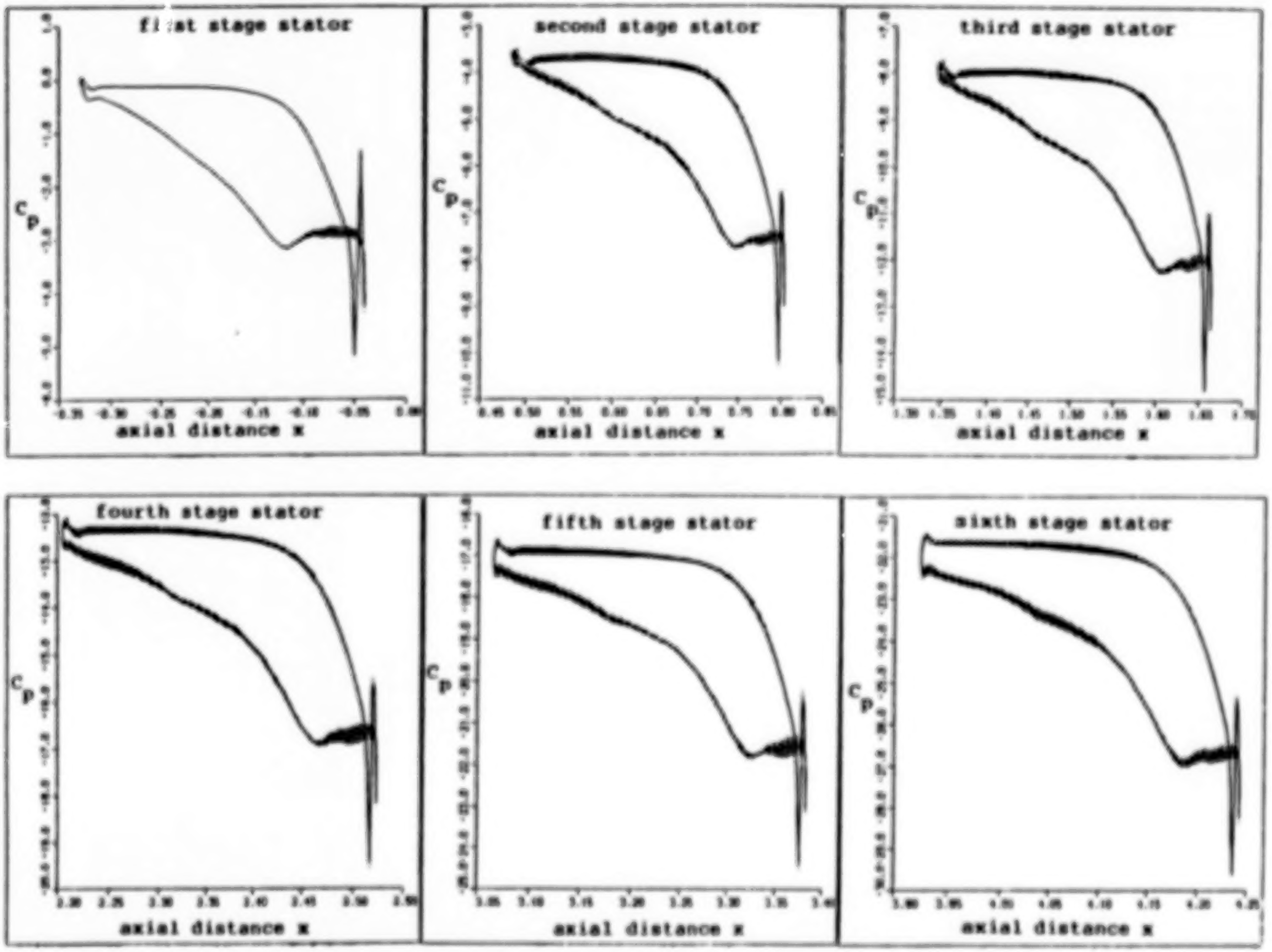

Fig. 11(a) SSME 6 stages LPOTP time-averaged pressure coefficient and unsteady pressure envelope on stator surfaces.

PRESSURE COEFFICIENT ON ROTOR SURFACE

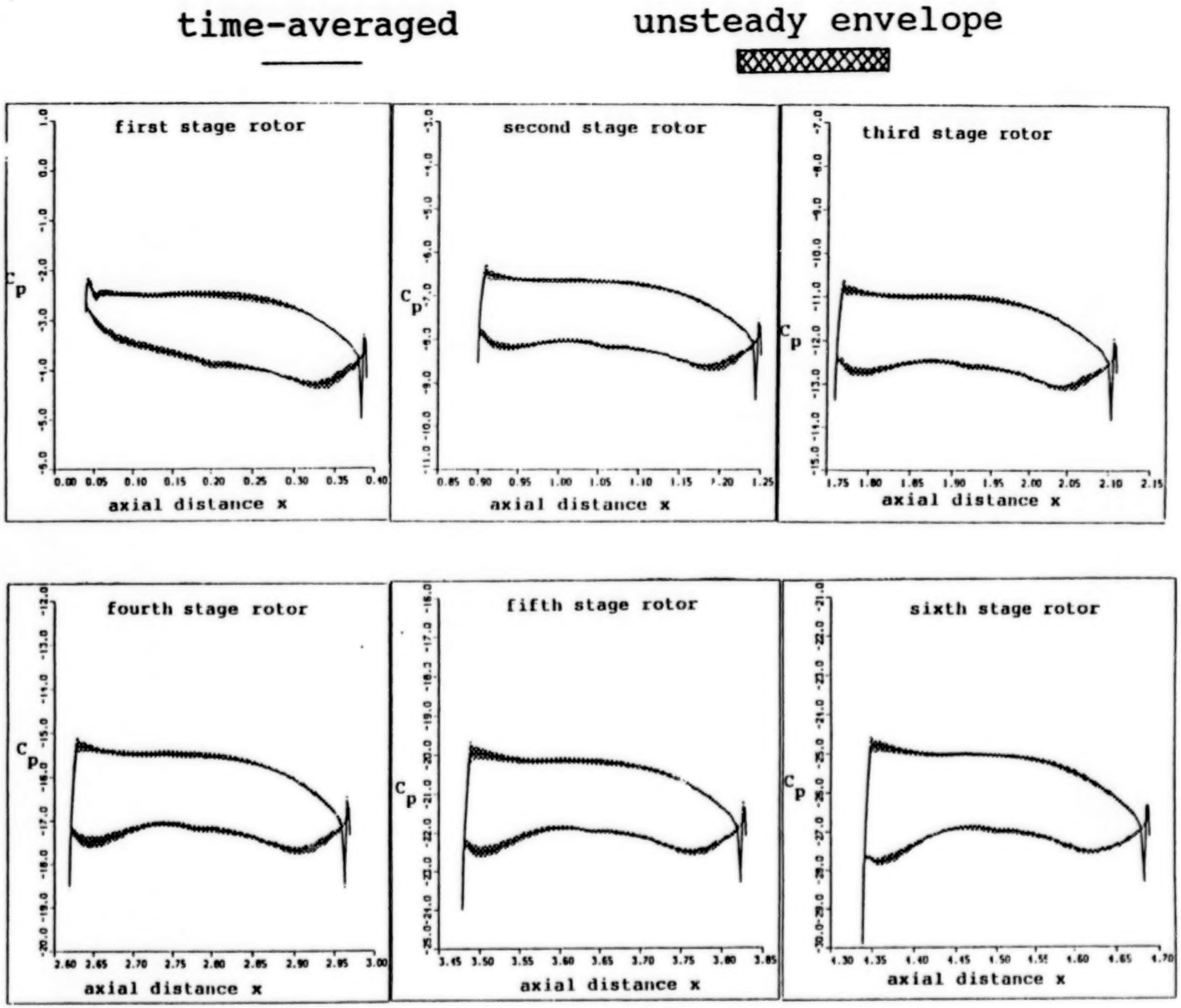

Fig. 11(b) SSME 6 stages LPOTP time-averaged pressure coefficient and unsteady pressure envelope on rotor surfaces.

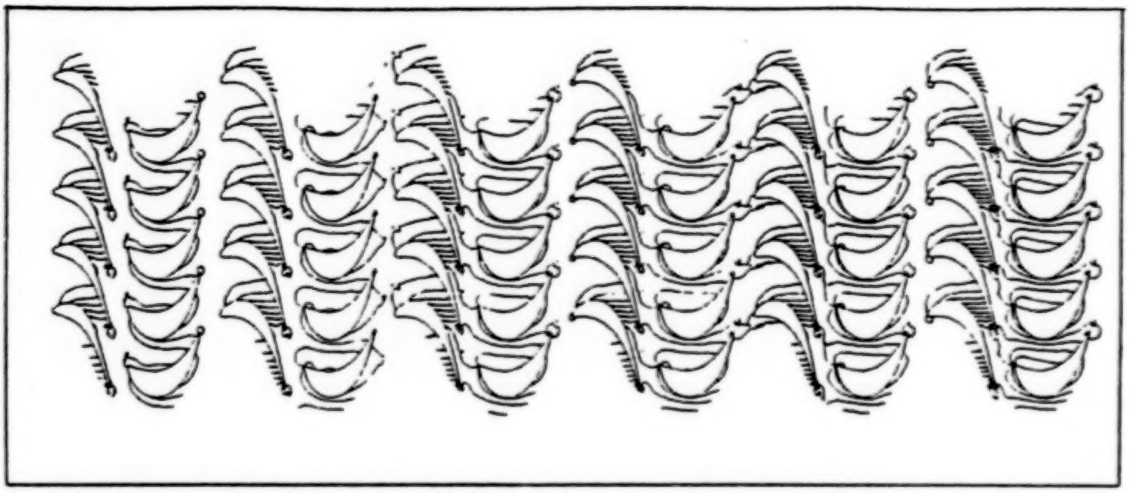

Fig. 12 SSME 6 stages LPOTP instantaneous pressure contours.

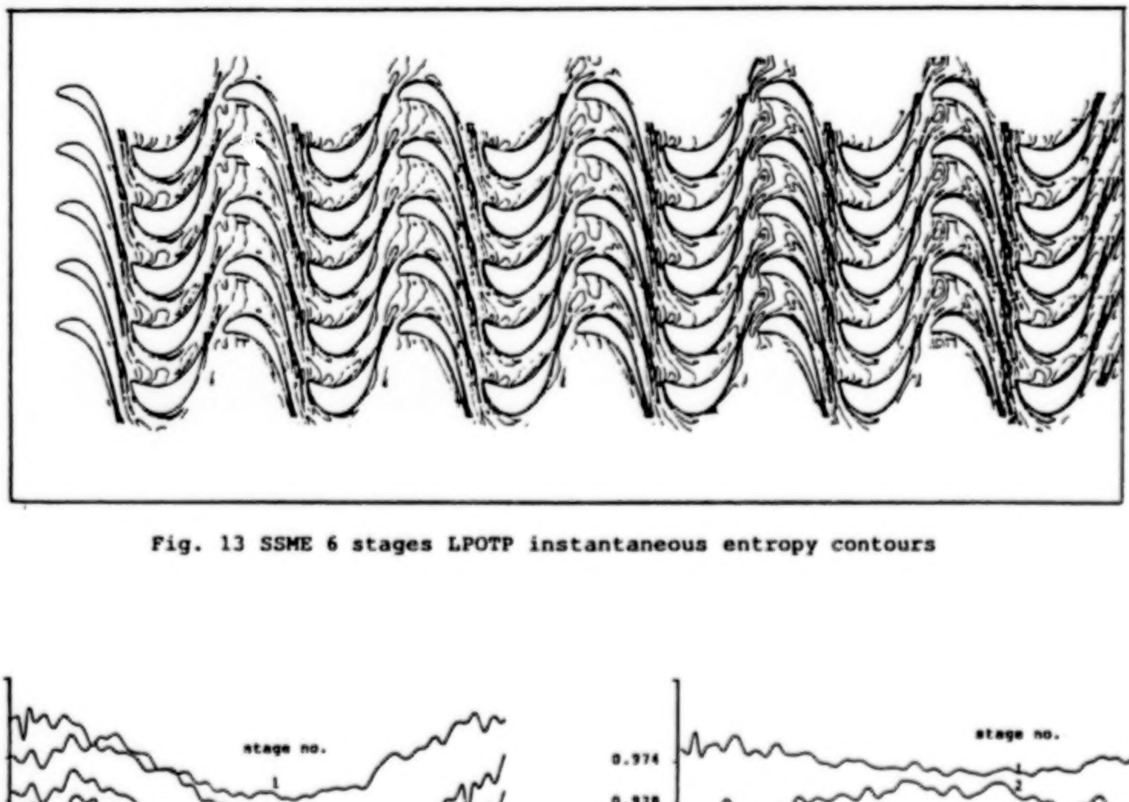

Fig. 13 SSME 6 stages LPOTP instantaneous entropy contours

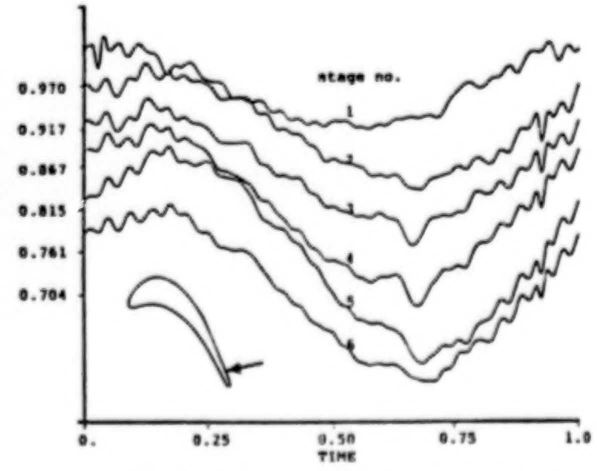

Fig. 14(a) Pressure history on stator surface

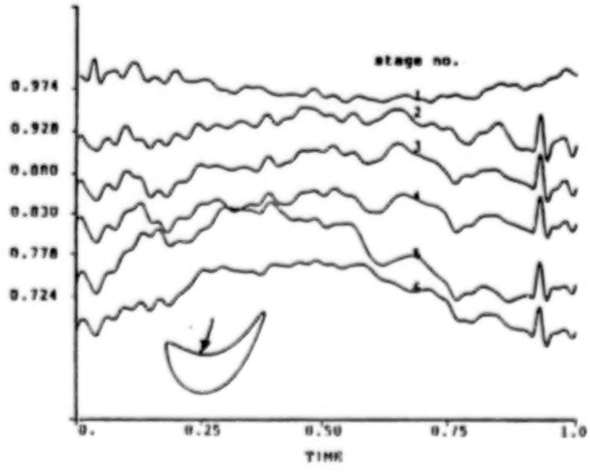

Fig. 14(b) Pressure history on rotor surface

TRANSONIC CASCADE FLOW CALCULATIONS USING NON-PERIODIC C-TYPE GRIDS

Andrea Arnone*
Institute for Computational Mechanics in Propulsion
Lewis Research Center
Cleveland, Ohio 44135
and
Meng-Sing Liou and Louis A. Povinelli
National Aeronautics and Space Administration
Lewis Research Center
Cleveland, Ohio 44135

ABSTRACT

A new kind of C-type grid is proposed for turbomachinery flow calculations. This grid is non-periodic on the wake and results in minimum skewness for cascades with high turning and large camber. Euler and Reynolds averaged Navier-Stokes equations are discretized on this type of grid using a finite volume approach. The Baldwin-Lomax eddy-viscosity model is used for turbulence closure. Jameson's explicit Runge-Kutta scheme is adopted for the integration in time, and computational efficiency is achieved through accelerating strategies such as multigriding and residual smoothing. A detailed numerical study has been carried out for a turbine rotor and for a vane. A grid dependence analysis is presented and the effect of artificial dissipation is also investigated. Comparison of calculations with experiments clearly demonstrates the advantage of the proposed grid.

INTRODUCTION

The history of turbomachinery design has seen important evolution in recent years. While the need for efficiency and weight reduction has driven a designer to investigate the details of the complex flowfields in which each component is expected to operate, Computational Fluid Dynamics (CFD), however, has progressed rapidly and increased its reliability as an effective designing tool. Thus, it is reasonable to see CFD taking an indispensable role in the future design and optimization of turbomachinery. In the past few years several two and three-dimensional codes for solving inviscid flows have reached a high level of maturity and are commonly used in turbomachinery applications(see e.g. references 1 and 2). However, the inviscid predictions do not provide any information about heat transfer and boundary-layer thickening, which are important quantities in the analysis of internal flows, specifically in turbomachines, and generally require solutions of Navier-Stokes equations. Although important progress has been made in

---

*Currently at University of Florence, Florence, Italy.

Work funded by Space Act Agreement C99066G.

solving the Navier-Stokes equations (e.g. references 3-6), more work still needs to be done in terms of robustness and accuracy, and especially in terms of turbulence modelling. In addition, in the case of cascade flow solutions, the grid generation process seems to be an item that still needs to be improved.

Rotor and stator cascades of modern turbomachinery are often characterized by a high turning geometry and/or by strong flow deviations from the axial so that the generation of meshes capable of picking up the flow details is not straightfoward. Procedures that use periodicity generally give rise to highly distorted meshes. In the present work, this problem is solved by the introduction of non-periodic elliptic C-type grids. The removal of periodicity allows the grid to be only slightly distorted even for cascades having a large camber and a high stagger angle. On these new kinds of grids the Euler and Navier-Stokes equations are efficiently solved using a Runge-Kutta scheme in conjunction with accelerating techniques like multigridding and variable coefficient implicit residual smoothing. The two-layer eddy-viscosity model of Baldwin and Lomax is used for the turbulence closure.

Due to the complexity of transonic cascade flows, it was believed worthwhile to investigate the convergence in space of the computed solutions. A grid independence study is carried out in both grid directions, and also the effect of the fourth order dissipation on the boundary layer is discussed by comparing the wall skin friction coefficient.

The capability of the procedure is shown by comparing computed results to experiments for a typical highly loaded gas turbine rotor and for a high turning nozzle. With the accelerating strategies, a solution for viscous flow can be obtained in a few minutes on a modern supercomputer.

COMPUTATIONAL GRID

It is known that the grid structure must be selected carefully in order to achieve an accurate resolution of a complex flow field. When dealing with the construction of grids for turbomachinery blade passages the following aspects are of importance: (a) accurate leading and trailing edge flow description, (b) description of the wake, and (c) imposition of periodicity.

Sheared H-type grids are fairly common in turbomachinery applications. They are easy to generate and to extend to three-dimensional applications. Unfortunately those grids provide poor leading and trailing edge flow reproduction. On the leading edge truncation errors due to the grid distortion introduce extra entropy which is transported downstream on the blade surface.

Those kind of problems do not exist on O-type grids. However, in this case the difficulty lies in the wake where clustering grid and avoiding distortion is desired. In addition, when the flow is transonic, O-type meshes are not suitable for a fine reproduction of the outlet shock system.

Therefore, with respect to the first two points, we can conclude that, if a single grid structure is chosen, the C-type seems to have the best overall capability.

For item (c) it is evident that a simple point-to-point correlation is the easiest way of imposing periodicity between the various blades. Unfortunately it is common in turbine blading to have high turning geometry with an outlet flow that is strongly deviated from the axial. In such a case, the imposition of the circumferential grid correspondence results in highly distorted grids and this distortion is reflected in a low resolution of the flow gradients. Our experience in computing transonic cascade flows has suggested that when the outlet flow angle (from the axial) exceeds 70 degrees, it is difficult to reproduce the shock system correctly, and the sheared H-type grids often work better than the C-type.

We therefore believed it was necessary to break the point-to-point grid correspondence to allow a better grid orientation. The grid periodicity can be removed on the external part of the mesh or on the wake. In practice, only one of the two options is sufficient. We selected the second one for two reasons. Firstly, the wake can be roughly followed as a straight line and interpolations between the coarse and fine part of the domain are straightfoward. Secondly, this solution allows the trailing-edge shock to intersect the coarse part of the mesh as far as possible. This point will become evident later as we discuss the calculated results.

The non-periodic C-type grids used for the present calculations are generated with an elliptic procedure that solves the discretized Poisson equations using a relaxation procedure by Sorenson(ref. 7). Forcing functions as proposed by Steger and Sorenson(ref. 8) are used to control the grid spacing and orientation at the wall, while on the external part of the mesh periodicity conditions are imposed. Grids for viscous flow are obtained from the inviscid grids by adding lines with the desired spacing distribution.

COMPUTATIONAL METHOD

Governing Equation and Spatial Discretization

The unsteady Euler and Reynolds averaged Navier-Stokes equations are discretized in space using a finite-volume approach and a cell-centered scheme by Jameson(refs. 9 and 6). The effect of turbulence is taken into account by using the eddy-viscosity hypothesis and the two-layer mixing length algebraic model of Baldwin and Lomax(ref. 10). Also, the simple transition model suggested in reference 10 is adopted. On the wake, where the grid is not periodic, linear interpolations are used to compute the necessary flow quantities.

Artificial Dissipation and Boundary Conditions

In order to ensure stability and to prevent odd-even point decoupling, artificial dissipation terms are added to both the Euler and Navier-Stokes equations. This paper uses the Jameson artificial dissipation model which is a blending of the second and fourth differences. Smoothing fluxes are computed on the boundary so that no errors in the conservation property are introduced globally from the artificial dissipation (e.g., references 2, 11, and 12). Boundary conditions are treated via the theory of characteristics. Total enthalpy, total pressure, and the flow angle are specified at the subsonic-axial inlet while the outgoing Reimann invariant is taken from the interior. At the subsonic-axial outlet, the static pressure is prescribed and the outgoing Reimann invariant, the total enthalpy, and the component of velocity parallel to the boundary are extrapolated. On the solid wall the momentum equation and the tangency or no-slip conditions are used to compute the pressure, which is the only variable needed from the cell-centered discretization.

Time-Stepping Scheme

The solution is advanced in time towards a steady-state solution using an explicit four-stage Runge-Kutta scheme. Good, high-frequency damping properties that are important for the multigrid process are obtained from this scheme by performing two evaluations of the dissipative terms at the first and second stages. For economy the contribution of the viscous terms is computed only at the first stage and then frozen for the remaining stages.

Convergence Acceleration

Four techniques are employed to improve the computational efficiency: (1) local time-stepping, (2) residual smoothing, (3) multigrid, and (4) grid refinement. When only the steady-state solution is of interest, local time-stepping and implicit residual smoothing can be used to improve the robustness and the convergence of the basic scheme. In the present work the variable coefficient formulation of the implicit smoothing(references 13 and 6) is used and the time step is computed locally on the basis of a fixed Courant number (typically 5). However most of the reduction in the computational effort is obtained through a multigrid method. Jameson's Full Approximation Storage (FAS) scheme(reference 14) and a V-type cycle with subiterations are used as multigrid strategies. In addition, a grid refinement procedure is used to provide an efficient initialization of the flow field. This strategy is implemented in conjunction with multigrid to obtain a Full-Multigrid process (FMG)(also reference 11).

INVISCID TRAILING EDGE FLOW REPRESENTATION

The flow near rounded trailing edges is generally separated both on the pressure and suction side of the blade. These separations lead to the formation of two vortices characterized by low flow speed and high vorticity. Obviously this kind of flow pattern can not be reproduced with an inviscid approach. In fact inviscid solutions tend to give strong and unrealistic over-expansions near those regions. These over-expansions produce extra entropy which is transported downstream as a spurious wake that should not exist by the inviscid assumption. In addition, according to theory, if the grid is made very fine a Kutta condition must be imposed to ensure a steady state solution. A practical way of overcoming this problem is by adding a wedge to the trailing edge of the blade to simulate the recirculation zone. The first author's experience(reference 12) suggests that a wedge of a length of about three times the trailing edge thickness gives satisfactory results when it is oriented so that no net pressure load is carried from the added part of the blade. To show the usefulness of this procedure, inviscid computations with and without the trailing edge wedge will be presented in the next section.

RESULTS AND DISCUSSION

Some applications of the computational procedure that has been briefly described are presented in this section. Numerical results are given for a rotor gas turbine blade (fig. 1) and for a nozzle (fig. 2). Both of these geometries result in high turning flows with strong outlet deviations from the axial. Flows at transonic speed are considered. Figures 1 and 2 display periodic and non-periodic inviscid grids together with enlargements of viscous grids. The good grid shapes of the non-periodic C-type are evident, which in the end lead to improvement of solutions over that on the periodic grids.

Inviscid transonic cases are solved using a 449×17 non-periodic C-type mesh. For those grids 129 points are located on the suction side of the blade and 65 on the pressure one, while on the fine and coarse part of the wake there are respectively 160 and 95 points. Such a fine outlet grid has been introduced for a fine reproduction of the shock system downstream of the blade passage. Moreover, as shown by the authors, an excessive smearing of the trailing-edge shock can noticeably influence the blade load. For viscous calculations two different mesh sizes are used because of the different Reynolds numbers at which the proposed blade has been tested (references 15-17). The rotor blade has an outlet Reynolds number of about 800,000 and the 449×33 grid is used with spacing at the wall in the normal direction equal to 5×10^{-5} chords for the first cell. For the nozzle, the outlet Reynolds number is 2.2 million. The mesh number is increased to 449×49 and the spacing at the wall reduced to 2.5×10^{-5} chords to resolve the near-wall profile.

In order to check the convergence of the solutions, a grid-independence analysis is presented for the case of the gas turbine rotor. The influence of the transition and of the artificial dissipation are also investigated in terms of pressure and skin friction coefficient.

The full-multigrid process includes three grid levels with, respectively, two, three, and four grids. Twenty-five cycles are performed on the first two levels and 350 on the final one. To give a complete description of the code performance for most of the test case we report convergence history, a comparison of the computed surface isentropic Mach number with experimental data, and flow contours. In addition, inviscid predictions with and without the additional wedge at the trailing edge are discussed.

Turbine Rotor Blade

The Von Karman Institute gas turbine rotor blade (VKI LS-59) is a high loaded blade with a thick, rounded, trailing edge (see fig.1). This blade was extensively tested experimentally by Sieverding(ref. 16) and Kiock(ref. 15) and numerically by several authors (e.g. refs. 1,6,16). For this blade, computations are carried out for flow regimes that vary from subsonic to typically transonic.

A subsonic calculation obtained for an isentropic outlet Mach number (M_{2is}) of 0.81 is summarized in figs.3 and 4. Due to the absence of shocks the grid size has been now reduced to 199×17 for the Euler equations and 257×33 for the viscous one. In the viscous calculation a fine mesh is used near the leading and trailing edges in order to pick up details of the stagnation point and of the recirculation region. The efficiency of the FMG procedure is given through the convergence histories of fig.3(a) where most of the slowdown in the viscous calculation is caused by the fine trailing edge mesh and from the flow complexity in this region. The over-expansions at the rounded trailing edge of the inviscid solution are visible in fig.3(b) where experimental and computed surface isentropic Mach number are compared. For this case no important difference in terms of pressure distribution is noticed between the fully turbulent and transitional solution.

The VKI LS-59 case has been selected for the accuracy-convergence analysis. Figures 3 (c) and (d) report the skin friction coefficient distribution for the condition of fully turbulent and transitional flow. Hereafter, the skin friction coefficient C_f will be presented for both surfaces of the suction and pressure sides with coordinate x/c running from 0 to 1.0 and 1.0 to 2.0 respectively, and with stagnation point at 1.0. The transition, whose criterion follows the Baldwin and Lomax model(ref. 10), occurs near the leading edge on the pressure side and near the midcord on the suction one. Computed results are presented for various values of the averaged y^+, from 0.2 to 4, using 49 points in the blade-to-blade direction. The solid line ($y^+ = 2$) is considered as a reference solution and corresponds to the grid spacing previously described. For the fully turbulent case the convergence is achieved with a $y^+ = 1$, while for the transitional case some difference is noticed because of a shift in the location of transition. Also, the geometrical stretching at the wall has been varied from 1.05 to 1.3 and no significant difference has been found.

The influence of the artificial dissipation is displayed in fig. 4(a), where the coefficient for the fourth order has been reduced by factors of two and four with respect to the default value. In the case of using one quarter of the default value, convergence "levels off" after residual has dropped four orders.

One of the usefull properties of the multigrid is that the solution approaches the final value in quite a uniform way. This is shown in fig. 4(b) where the solution after 100 cycles on the finest grid level is compared with a solution after 400 cycles. Except that the transition location on the suction side is not in the final position, the solution remains unchanged on the pressure side after 100 cycles.

Mach number contours for the present test are given in fig. 4(c). Figures 4(d) and (e) show an enlargement of the grid and of Mach number contours near the leading edge. The flow is well-behaved and the stagnation point sharply captured. Details of the trailing edge are shown in figs. 4(f)-(h). The flow pattern as well as the two vortices downstream of the separation on the suction and pressure side of the blade are clearly reproduced. We note that even though the solutions have been obtained by solving the full Navier-Stokes equations, the grid spacing in the streamwise direction is still not fine enough to resolve full Navier-Stokes terms. In fact the thin-layer solution looks identical in the recirculating zones.

The flow predictions corresponding to a sonic isentropic exit condition are shown in figs.5 and 6. Figures 5 (a) and (b) show the convergence histories and the surface Mach number distributions for the two inviscid calculations and for the transitional viscous one. The unrealistic over-expansions of the inviscid rounded trailing edge solution are now much evident. These over-expansions produce about the same amount of total pressure loss as the viscous prediction so that the strength of the suction-side shock is roughly the same for the two calculations but the location is different. In fact, the over-expansion near the pressure side of the trailing edge and the absence of boundary-layer effects cause the inviscid rounded trailing-edge shock to be predicted ahead of the viscous one. On the contrary, the Euler solution obtained with the additional wedge exhibits a stronger shock with respect to the experiments. This is not surprising and is consistent with the inviscid assumption. Moreover the low entropy production of the wedge solution causes the real exit Mach number to be about 2% higher than the experimental value.

The skin frictions distribution for the fully turbulent and transitional flows are plotted in fig. 5(c). In both cases a separation bubble is predicted at the foot of the shock on the suction side. The pressure side is basically all turbulent while on the suction side the transition is caused by the shock. Differences are visible also in the distribution of surface isentropic Mach number in fig. 5(d). The shock is sharper in the transitional prediction.

Due to the presence of shocks we select this flow condition to perform a grid independence study in the streamwise direction. Three grids with respectively 64, 96 and 128 points on the suction side have been introduced. Results are summarized in fig. 6(a) where it is evident that the space-convergence is basically achieved.

Density contours for the above calculations are given in fig. 6 along with an available Schlieren picture, courtesy of Prof. Claus Sieverding of VKI. The spurious wake of the inviscid, rounded, trailing-edge solution is evident. The intensity is similar to that of the viscous results. All the solutions predict correctly the trailing edge shock on the suction side. Such a shock crosses the non-periodic wake without being excessively smeared from the coarse part of the grid. On the contrary, the throat shock system is quite different among various calculations. Since it is also different from channel to channel in the Schlieren picture, it is difficult to draw a final conclusion as to the validity of calculations except for the fact that the viscous wake seems not sufficiently diffuse. We will discuss this problem later.

Computations relative to an isentropic exit Mach number of 1.2 are illustrated in figs. 7 through 8. In terms of surface Mach number (fig. 7(b)) the situation is qualitatively similar to the previous case but now the transitional prediction agrees better with experiments. The suction side transition is still located near the shock but now no separation is predicted by the Baldwin-Lomax model.

The structure of the vortices is depicted in fig. 7(d). The exit flow angle causes the pressure-side vortex to be compressed and the suction-side one to be expanded. Due to the presence of fish-tailing shocks the recirculation region is longer with respect to the subsonic case. The orientation of the wedge obtained with the no net pressure load criteria agrees very well with the shape of the viscous prediction.

Density contours are given in fig.8. The wedge solution exhibits a higher reflection of the throat shock but all the solutions sharply capture the fish-tailing shocks and the expansion region downstream of the throat shock. The interaction between the wake and the suction-side, trailing-edge shock causes some reflection. This phenomenon is not due to the interpolations on the wake as it is nonexistent in the wedge solution.

For the three viscous calculations we have discussed, the computed exit flow angle and the loss coefficient are compared to experiments in figs. 9 and 10. The agreement is excellent especially in terms of loss coefficient which is generally difficult to match, but unfortunately is one of the final goals in turbomachinery calculations.

Turbine Nozzle

As a second application we selected a typical high turning turbine nozzle like the VKI LS-82 (see fig.2). This vane has been designed and tested at the Von Karman Institute(ref. 17). The inlet flow is axial and turned from the blade by about 80 degrees so that the resulting outlet flow is strongly deviated from axial and this is typical of modern high work vanes. The flow about this geometry is very complex especially in the transonic regime. The proper grids are needed in order to pick up details of the shock system. Standard periodic grids give rise to strong distortions as evident from fig.2, in contrast to which the grid we are proposing gives low distortion.

The sonic outlet condition has an exit Reynolds number of 1.5×10^6 . Convergence histories and comparison with experiments are given in fig.11. In terms of surface Mach number the situation is not much different from the previous blade. Good agreement is obtained through the viscous solution, while some overestimation in the shock strength is noticed in the inviscid calculations. The transition is now predicted very close to the leading edge on both the blade sides so that the viscous solution is basically fully turbulent. Comparison between Schlieren picture and computed density contours is reported in fig. 12. The shock system is reasonably captured on the whole; the suction-side shock, downstream of the throat, is smeared from the thick boundary layer and does not cross the strong wake sharply. As evident from the Schlieren picture the trailing-edge flow is very complex and is only roughly reproduced by the present viscous calculation.

For a high speed case we compute the condition corresponding to an exit isentropic Mach number of 1.43. The agreement with experiments is good (see fig. 13(b)) and the suction-side shock is captured in all the calculations. The density contours of fig. 14 clearly indicate the good reproduction of the whole shock system. Now the computed trailing-edge flow agrees better with the Schlieren picture. However the suction-side, trailing-edge, shock is strongly smeared from the coarse part of the grid on the non-periodic wake. Such a circumstance can be easily avoided by allowing the outlet part of the grid to turn towards the axial direction as depicted in fig 15. With this grid the fish-tailing shocks can be computed on the finer part of the grid. The wake smeared by the numerical procedure is now compensated for the fact that the Baldwin-Lomax turbulence model generally predicts lower diffusion in the wake region than what experiments suggest.

Density and pressure contours for the previously discussed grid are given in fig. 15. Obviously for such a computation the exit static pressure can not be imposed to be constant without producing undesired reflection. In the present calculation the shape of the circumferential pressure distribution is taken from the interior while the averaged exit value is imposed to match the experimental one. The level of the shock reproduction is remarkable, being sharply captured on the whole computational domain as well as the expansion regions. As anticipated the wake is smeared and basically disappears after being crossed by the strong trailing-edge shock. This seems more realistic from the physical point of view but much effort is needed to understand and correctly predict this kind of interaction in turbomachinery blading.

Code Performance

The code in its present form is only partially vectorized due to the fact that it was originally developed for scalar machines. A speed-up factor of about 3.5 has been obtained by unrolling the short do-loops on the four equations of motion (continuity, x- and y-momentum, and energy) and allowing the residual smoothing to be vectorized on parallel lines. The viscous calculation on the 449×33 grid presented previously were obtained in about 300 sec on Cray X-MP at NASA Lewis Research Center. But with the full-multigrid acceleration, all the solutions converge after

200 cycles, which take 110 sec on NAS Cray Y-MP. For design applications a subsonic solution on a 257×33 grid converges after about 50 multigrid cycles on the finest grid level (four decade drops in the residual) and this can be obtained in 30 sec on the Cray X-MP.

CONCLUSIONS

A new kind of C-type grid has been introduced, this grid is non-periodic on the wake and allows very good flow predictions for cascades with high turning and large camber. The central difference finite volume scheme with artificial dissipation originally developed for external flows has proven to be accurate and to converge well for cascade viscous flows. With the described accelerating strategies, accurate transonic viscous solutions can be obtained in less than two minutes on a modern supercomputer. Good overall prediction can be obtained with the Baldwin-Lomax turbulence model. However in transonic turbine blading the trailing-edge flow is very complex and strongly influences the whole flowfield so that additional effort is needed, especially in turbulence modelling in order to obtain detailed and realistic flow simulations. An appropriate prediction of the wake and of the transition are other important topics that require further development.

ACKNOWLEDGMENT

All the schlieren pictures reported in this paper are provided by Prof. Claus Sieverding who is gratefully acknowledged.

REFERENCES

1. Ni, R. H.,"Multiple-Grid Scheme for Solving the Euler Equations," *AIAA Journal*, **20**, 1565-1571(1981).
2. Holmes, D. G., and Tong, S. S.,"A Three-Dimensional Euler Solver for Turbomachinery Blade Rows," *Transaction of the ASME*, **107**, 258-264(1985).
3. Chima, R. V.,"Inviscid and Viscous Flows in Cascades with an Explicit Multiple-grid Algorithm," *AIAA Journal*, **23**, 1556-1563(1985).
4. Hah, C., and Selva, R. J.,"Navier-Stokes Analysis of Flow and Heat Transfer Inside High-Pressure-Ratio Turbine Blade Rows," AIAA Paper 90-0343 (1990).
5. Nakahashi, K., Nozaki, O., Kikuchi, K., and Tamura, A., "Navier-Stokes Computations of Two- and Three-Dimensional Cascade Flowfields," *Journal of Propulsion and Power*, **5**, 320-326(1989).
6. Arnone, A., and Swanson, R. C.,"A Navier-Stokes Solver for Cascade Flows,", NASA CR 181682(1988).
7. Sorenson, R. L.,"A Computer Program to Generate Two-Dimensional Grids About Airfoils and Other Shapes by the Use of Poisson's Equation," NASA TM 81198, 1980.
8. Steger, J. L., and Sorrenson, R. L.,"Automatic Mesh-Point Clustering Near a Boundary in Grid Generation with Elliptic Partial Differential Equations," *Journal of Computational Physics*, **33**, 405-410(1979).

9. Jameson, A., Schmidt, W., and Turkel, E.,"Numerical Solutions of the Euler Equations by Finite Volume Methods Using Runge-Kutta Time-Stepping Schemes," AIAA Paper 81-1259(1981).
10. Baldwin, B. S., and Lomax, H.,"Thin Layer Approximation and Algebraic Model for Separated Turbulent Flows," AIAA Paper 78-0257(1978).
11. Swanson, R. C., and Turkel, E.,"Artificial Dissipation and Central Difference Schemes for the Euler and Navier-Stokes Equations," AIAA Paper 87-1107(1987).
12. Arnone, A., and Stecco, S. S.,"Inviscid Cascade Flow Calculations Using a Multigrid Method," ASME Turbo Expo, Toronto,1989.
13. Martinelli, L., "Calculations of Viscous Flows with a Multigrid Method," Ph.D. dissertation, MAE Department, Princeton University(1983).
14. Jameson, A.,"Transonic Flows Calculations," MAE Report 1651, Princeton University (1983).
15. Kiock, R., Lehthaus, F., Baines, N. C., and Sieverding, C. H., "The Transonic Flow Through a Plane Turbine Cascade as Measured in Four European Wind Tunnels," *Journal of Engineering for Gas Turbines and Power*, **108**, 277-285(1986).
16. Sieverding, C. H.,"Experimental Data on Two Transonic Turbine Blade Sections and Comparison with Various Theoretical Methods," VKI Report, LS59(1973).
17. "Workshop on 2D and 3D Flow Calculations in Turbine Bladings,", VKI Report, LS82-05(1982).

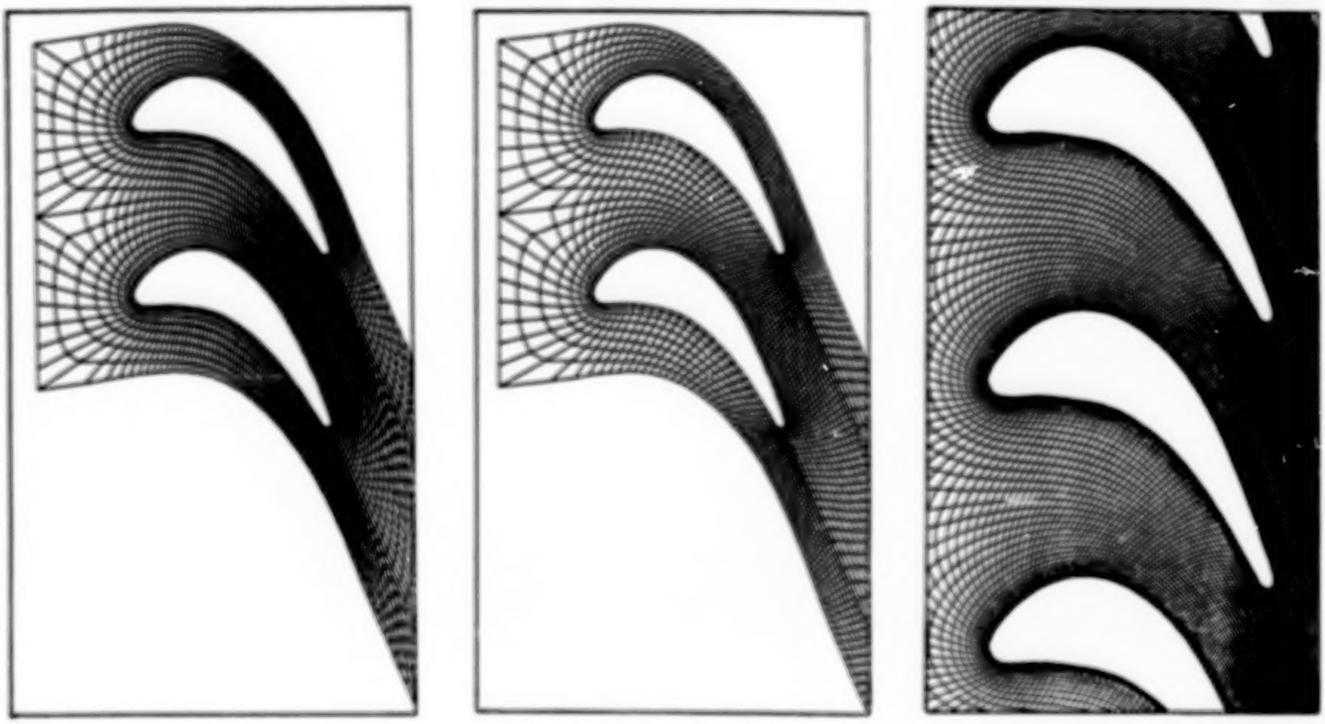

a) 145 × 9 periodic C grid b) 145 × 9 non-periodic C grid c) 449 × 33 non-periodic viscous C grid

FIG. 1 Computational grids for the VKI LS-59 rotor blade

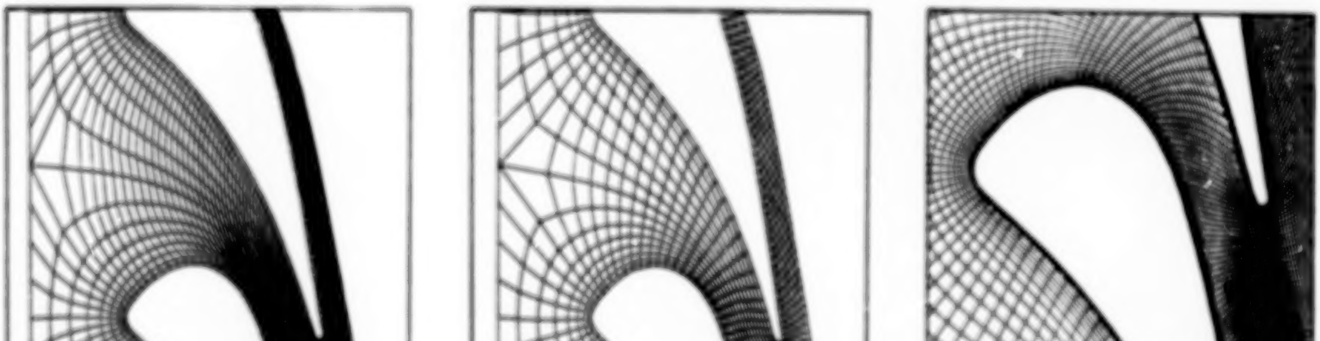

a) 145 × 9 periodic C grid b) 145 × 9 non-periodic C grid c) **449 × 49** non-periodic viscous C grid

FIG. 2 Computational grids for the VKI LS-82 nozzle

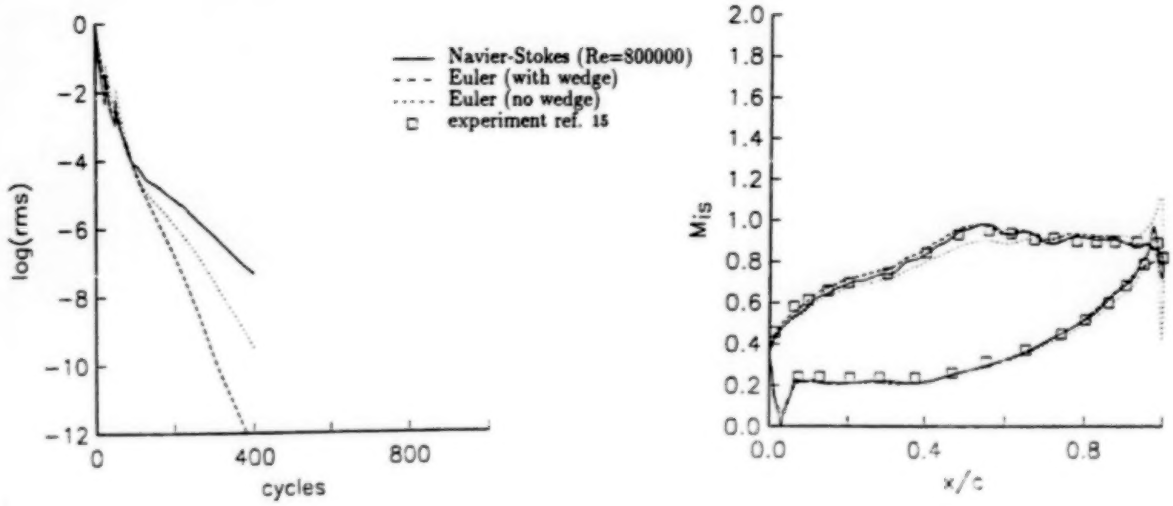

a) Convergence histories

b) Surface isentropic Mach number distribution

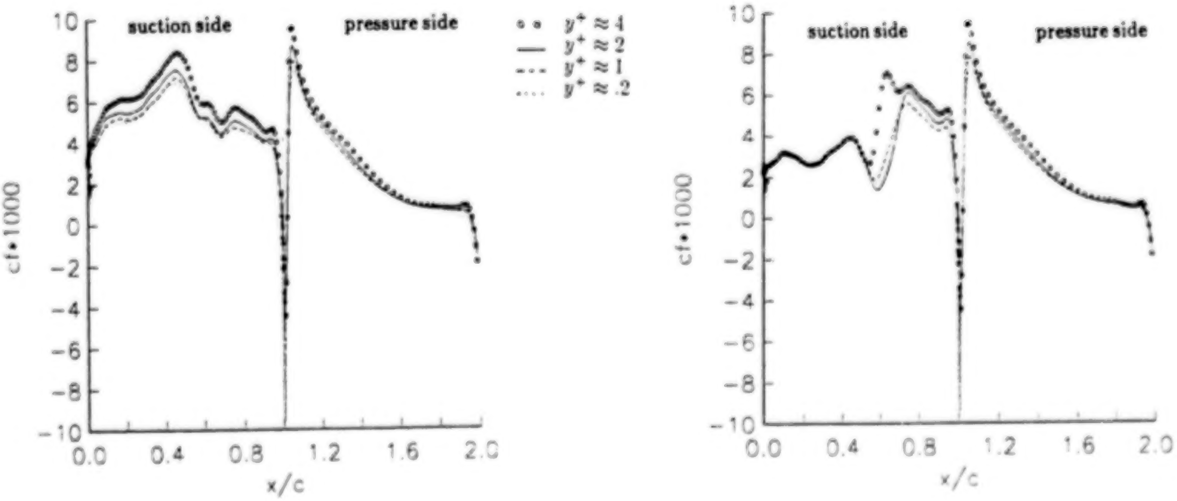

c) Fully-turbulent skin friction distribution

d) Transitional skin friction distribution

FIG. 3 VKI LS-59 gas turbine rotor blade (M_{2is} =.81)

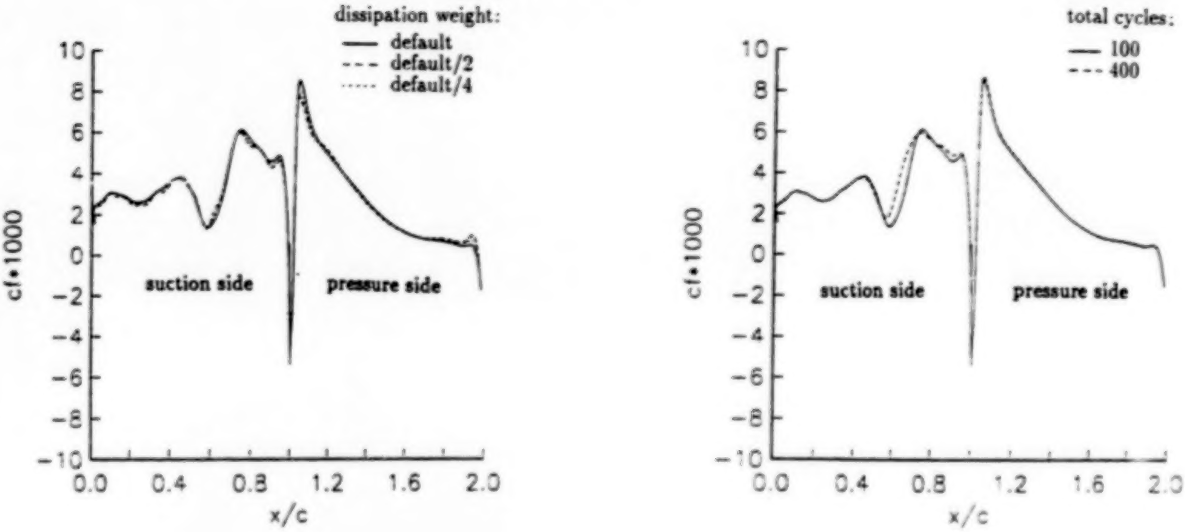

a) Transitional skin friction distribution

b) Transitional skin friction distribution

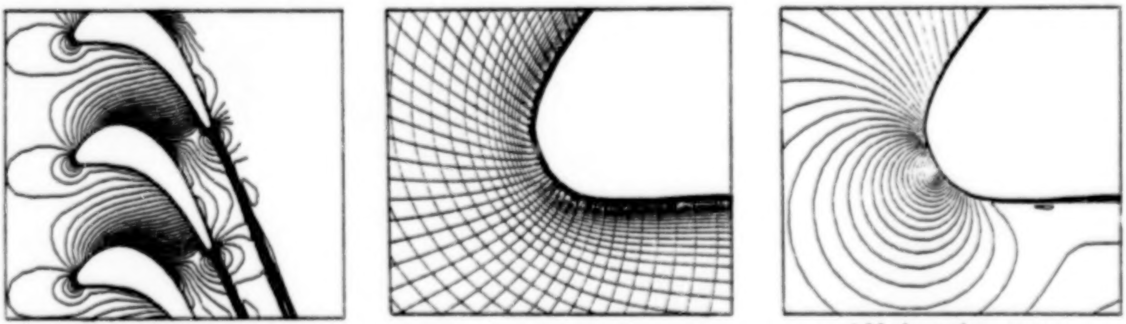

c) Mach number contours

d) Leading edge grid

e) Mach number contours near the leading edge

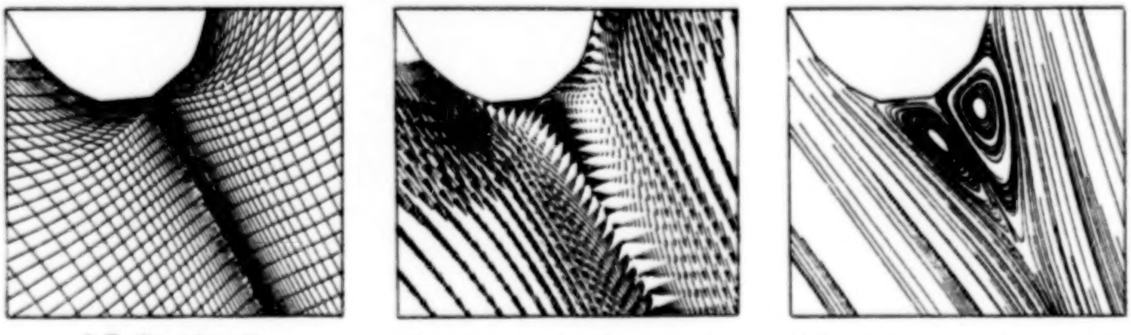

f) Trailing edge grid

g) Velocity vectors near the trailing adge

h) Particle traces near the trailing adge

FIG. 4 VKI LS-59 gas turbine rotor blade (M_{2is} =.81)

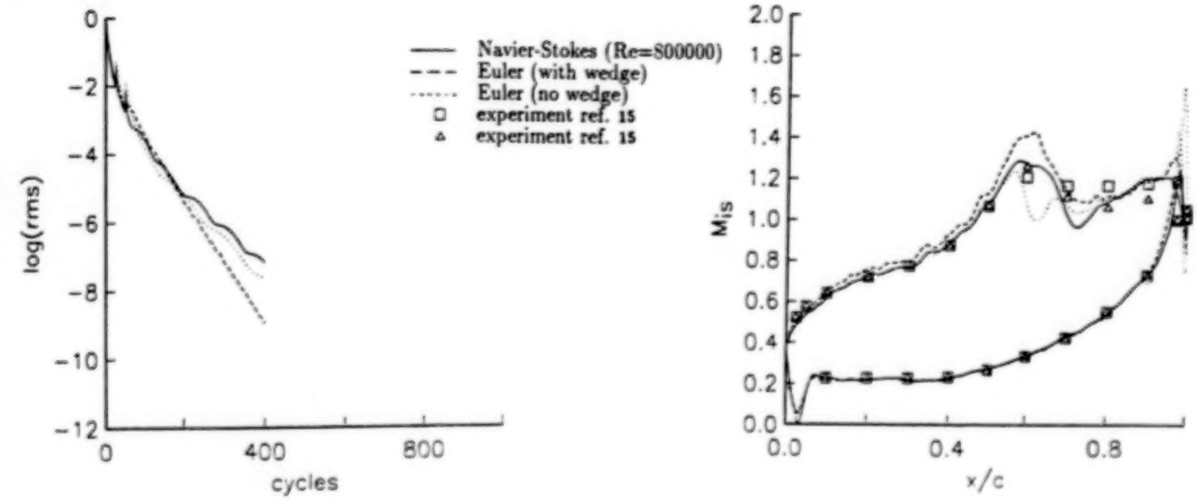

a) Convergence histories

b) Surface isentropic Mach number distribution

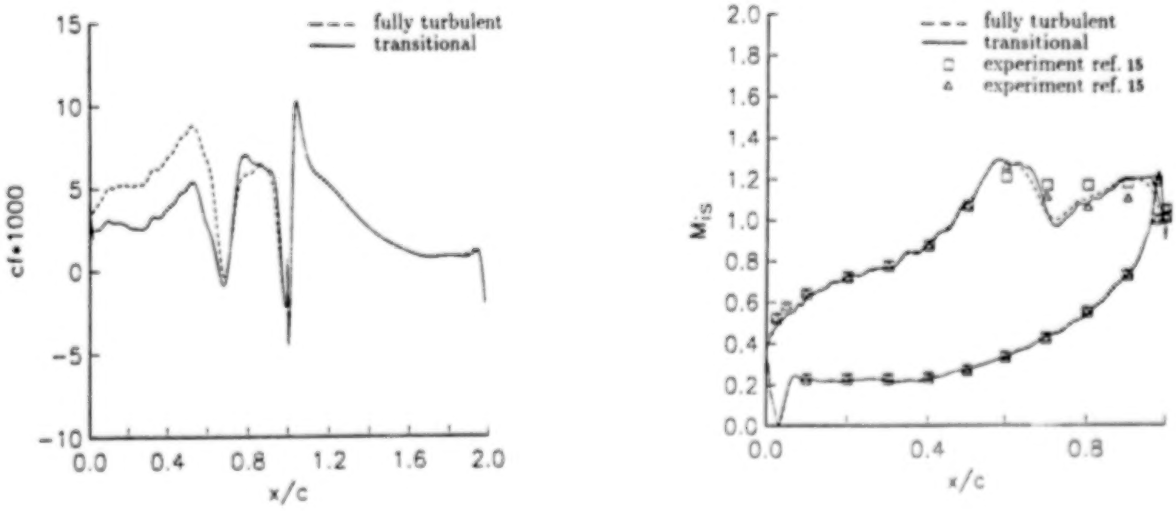

c) Skin friction distribution

d) Surface isentropic Mach number distribution

FIG. 5 VKI LS-59 gas turbine rotor blade (M_{2is} =1.0)

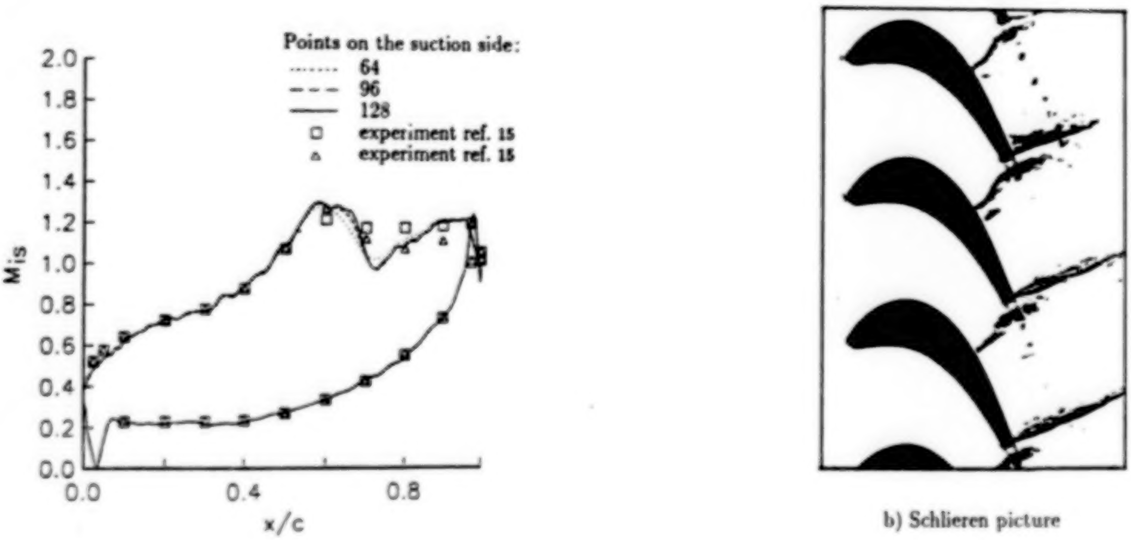

b) Schlieren picture

a) Surface isentropic Mach number distribution

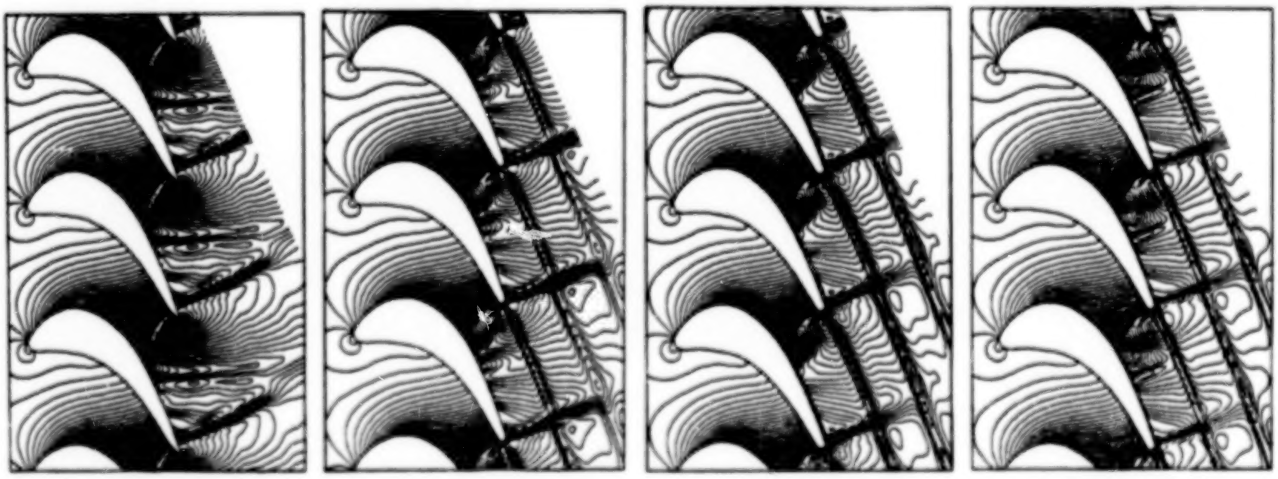

c) Density contours
Euler(with wedge)

d) Density contours
Euler(no wedge)

e) Density contours
(fully turbulent)

f) Density contours
(transitional)

FIG. 6 VKI LS-59 gas turbine rotor blade (M_{2is} =1.0)

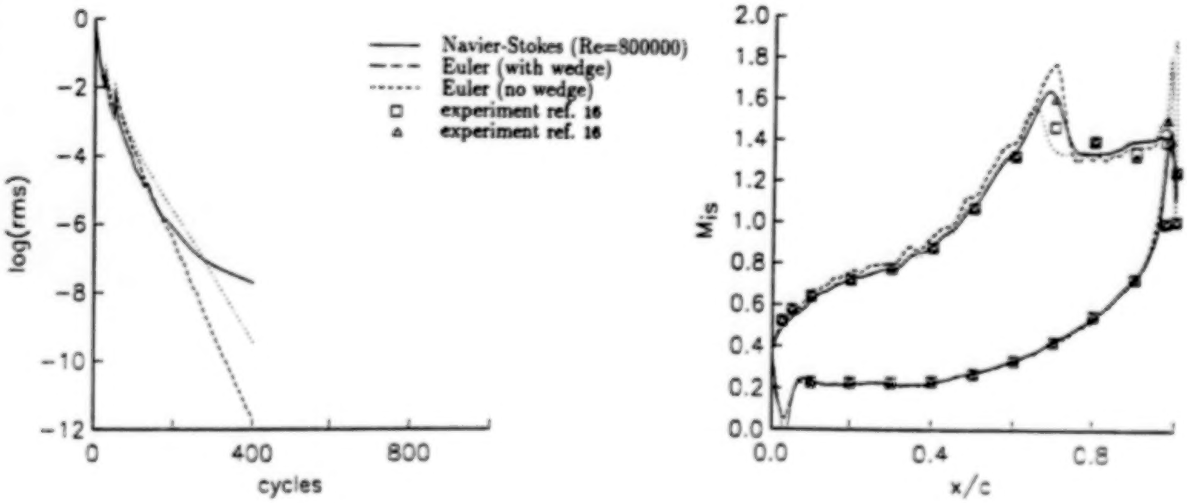

a) Convergence histories

b) Surface isentropic Mach number distribution

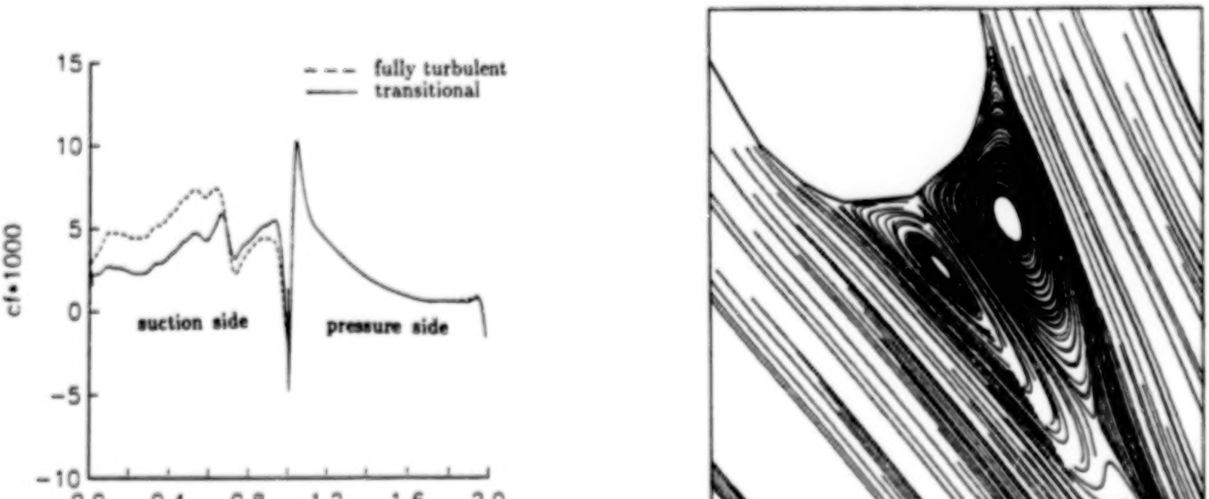

c) Skin friction distribution

d) Particle traces near the trailing edge

FIG. 7 VKI LS-59 gas turbine rotor blade (M_{2is} =1.2)

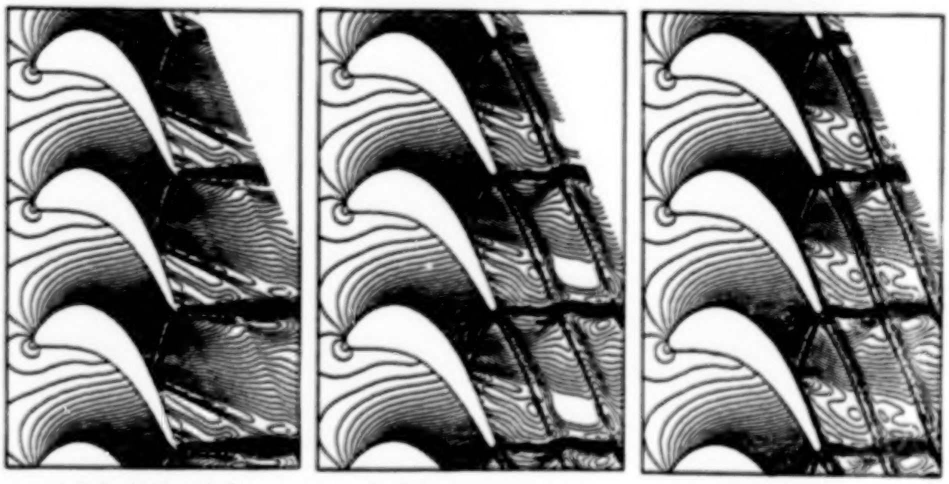

a) Euler (with wedge) b) Euler (no wedge) c) Transitional

FIG. 8 Density contours for the VKI LS-59 blade (M_{2is} =1.2)

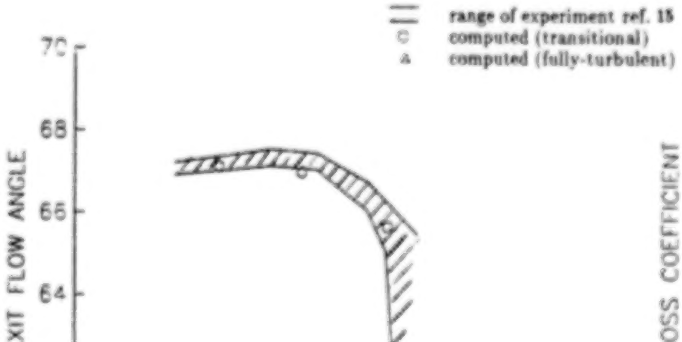

FIG. 9 Computed and experimental exit flow angle

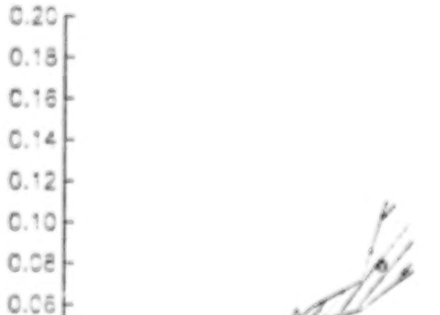

FIG. 10 Computed and experimental loss coefficient

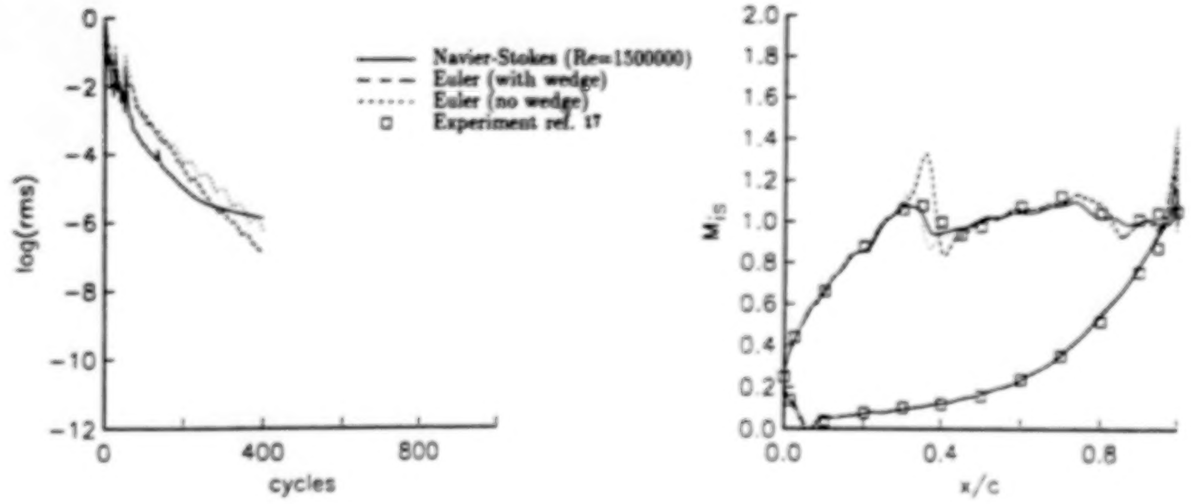

a) Convergence histories

b) Surface isentropic Mach number distribution

FIG. 11 VKI LS-82 nozzle (M_{2is} =1.0)

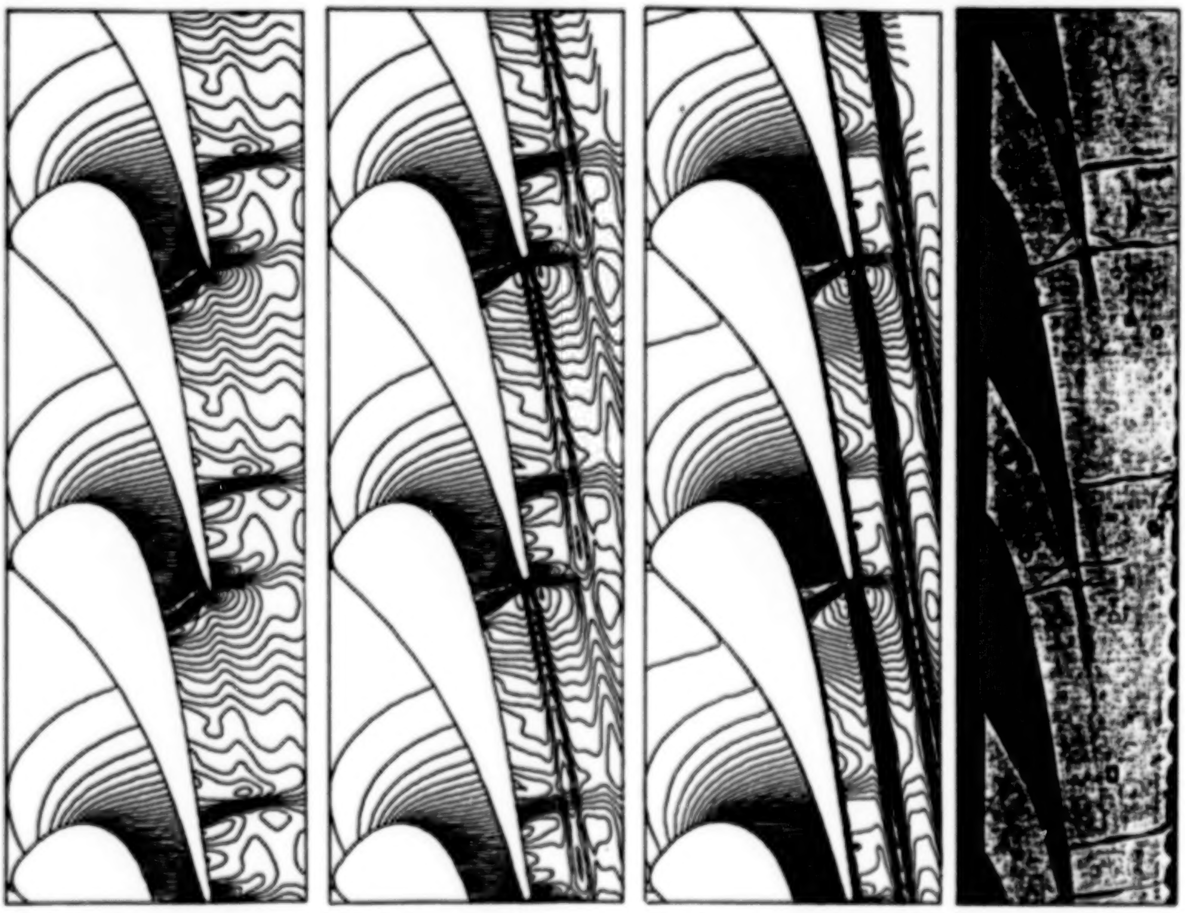

a) Euler (with wedge)

b) Euler (no wedge)

c) Navier-Stokes

d) Schlieren picture

FIG. 12 Density contours and Schlieren picture for the VKI LS-82 nozzle (M_{2is} =1.0)

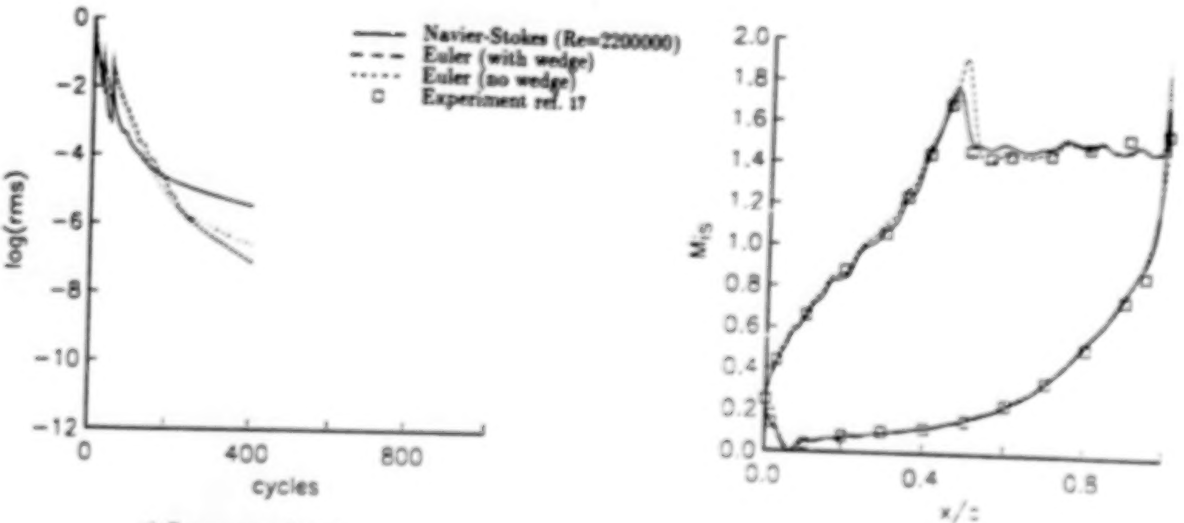

a) Convergence histories

b) Surface isentropic Mach number distribution

FIG. 13 VKI LS-82 nozzle (M_{2is} =1.43)

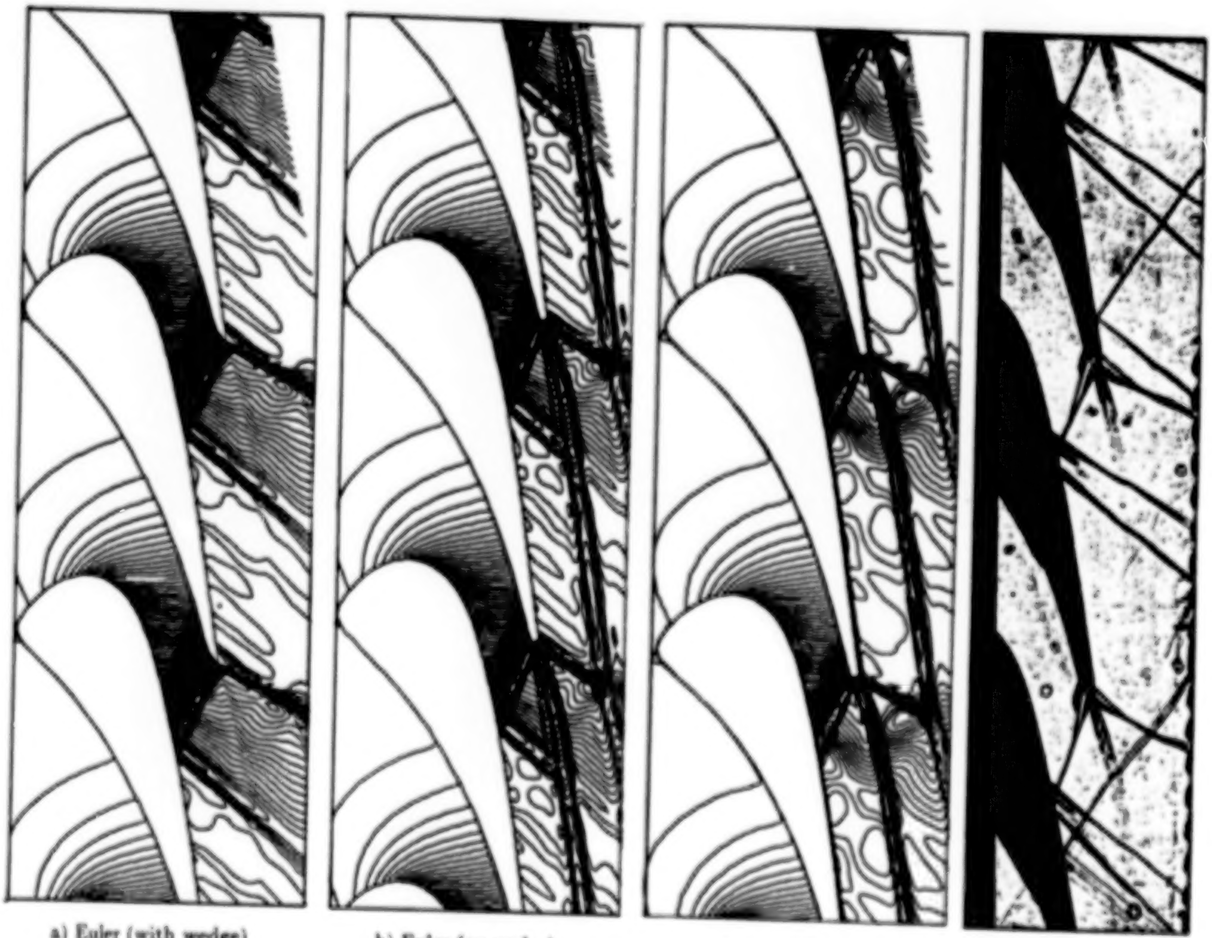

a) Euler (with wedge)

b) Euler (no wedge)

c) Navier-Stokes

d) Schlieren picture

FIG. 14 Density contours and Schlieren picture for the VKI LS-82 nozzle (M_{2is} =1.43)

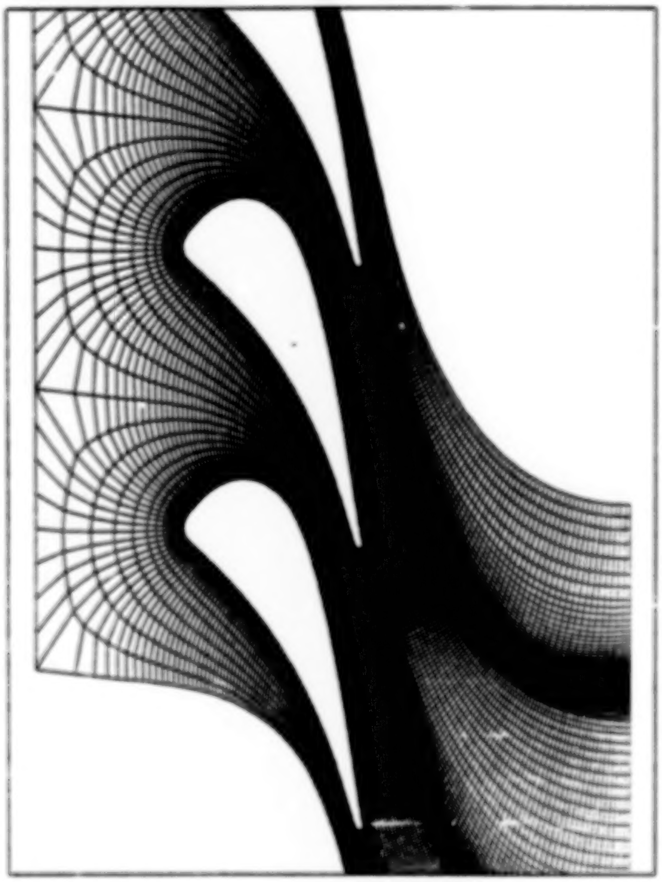

a) 449 x 49 non-periodic C-type grid

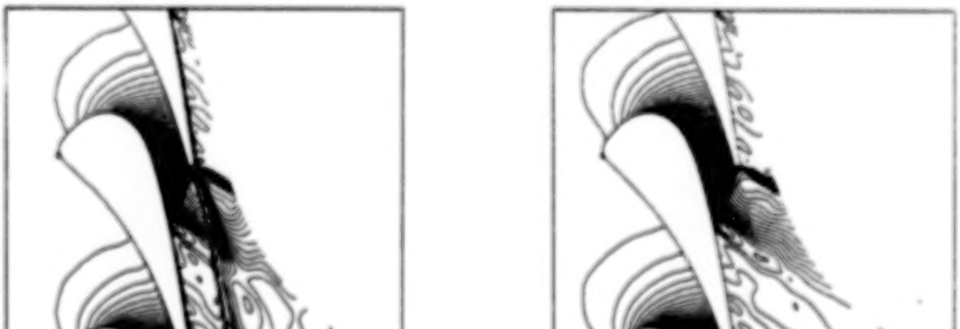

b) Density contours

c) Pressure contours

FIG. 15 VKI LS-82 nozzle (M_{2is} =1.43)

COMPUTATION OF SUPERSONIC AND LOW SUBSONIC CASCADE FLOWS USING AN EXPLICIT NAVIER-STOKES TECHNIQUE AND THE k-ε TURBULENCE MODEL

R. F. Kunz, B. Lakshminarayana
Department of Aerospace Engineering
Pennsylvania State University
University Park, PA, 16802

ABSTRACT

A fully explicit two-dimensional flow solver, based on a four-stage Runge-Kutta scheme, has been developed and utilized to predict two-dimensional viscous flow through turbomachinery cascades for which experimental data is available. The formulation is applied to the density averaged Navier-Stokes equations. Several features of the technique improve the ability of the code to predict high Reynolds number flows on highly stretched grids. These include a low Reynolds number compressible form of the k-ε turbulence model, anisotropic scaling of artificial dissipation terms and locally varying timestep evaluation based on hyperbolic and parabolic stability considerations. Comparisons between computation and experiment are presented for both a supersonic and a low-subsonic compressor cascade. These results indicate that the code is capable of predicting steady two-dimensional viscous cascade flows over a wide range of Mach numbers in reasonable computation times.

NOMENCLATURE

Symbols Used

a	speed of sound
c	chord length
c_p	specific heat at constant pressure
C_f	skin friction coefficient
C_p	pressure coefficient
e	internal energy per unit mass

e_o	total energy per unit mass ($= e + V^2/2$)
E, F	flux vectors
U,V	contravariant velocity components
J	Jacobian of curvilinear transformation
k	turbulent kinetic energy
L	turbulence length scale
n, s	blade normal and tangential coordinates
p	static pressure
Pr	Prandtl number
q_i	cartesian components of heat transfer rate vector
Q	primary transport variable vector
R	residual vector
S	source term vector
t	pitch length
T	static temperature
T_u	turbulence intensity
u, v	cartesian velocity components
V	magnitude of total velocity
x, y	cartesian coordinates
α	exponent in artificial dissipation scaling function
β_1, β_2	incidence and deviation angles
δ_{ij}	Kronecker delta
$\delta_{\xi\xi}, \delta_{\eta\eta}, \delta_{\xi\xi\xi\xi}, \delta_{\eta\eta\eta\eta}$	central differencing operators
δ_1, δ_2	displacement and momentum thickness
γ	specific heat ratio
Δt	local timestep
ε	isotropic turbulent kinetic energy dissipation rate
κ_2, κ_4	artificial dissipation constants
μ_l, μ_t	molecular and turbulent viscosities
ν_{ij}	pressure monitoring parameter for artificial dissipation
ξ, η	curvilinear coordinates
ρ	density
σ_2, σ_4	artificial dissipation weighting functions
τ_{ij}	cartesian components of stress tensor
ω	total pressure loss coefficient

Superscripts and Subscripts Used

c	convective
i, j	grid indices in streamwise and pitchwise directions respectively
l	laminar
m	cascade mean value (average of inlet and outlet quantities)
o	stagnation
t	turbulent
v	viscous
w	wall
θ	cascade pitchwise direction
∞	inlet freestream
$*$	quantity scaled by metric Jacobian
$'$	fluctuating quantity in time averaging
$''$	fluctuating quantity in density averaging
$\sim$	density averaged quantity
$-$	time averaged quantity

INTRODUCTION

Computation of viscous flows by numerically solving the Navier-Stokes equations has become increasingly feasible due in most part to the ever increasing speed and memory of digital computers. State of the art CFD codes available today are capable of calculating steady 3-D viscous flows about entire vehicles, and even unsteady viscous flows in 3-D turbomachinery stages. However, despite the rapid advance towards exploiting the power of computers now available, some serious limitations of these codes have yet to be adequately resolved. Surely the most profound of these limitations is the lack of accurate, general turbulence models. Secondary to this, but of much concern, is the role of artificial dissipation in Navier-Stokes calculations.

Explicit schemes, such as the Runge-Kutta methods first applied to the solution of the Euler equations by Jameson, Schmidt and Turkel[1] offer several appealing characteristics in application to fluid flow computations. Such schemes are easily vectorizable, amenable to convergence acceleration techniques, and can be extended to unsteady flow computations in a straightforward manner. However, because of the stiffness associated with the explicit treatment of transport equations which contain large source terms, incorporation of higher order turbulence models, which contain such source terms, has not been popular in explicit flow solvers.

Often, algebraic eddy viscosity models are used to approximate the apparent stresses in explicit codes. These models have little computational overhead and do not adversely affect the stability of the scheme. Though very useful in computing attached or slightly separated boundary layer flows, such models have well recognized drawbacks in the computation of complex flows where multiple length scales exist and where the transport of turbulent length scales is important. Though the k-ε turbulence model also has major deficiencies [see Speziale[2], Lakshminarayana[3] for example], it does provide the transport of length scale which is computed based on local fluid and turbulence properties. The model has been shown to provide better predictions than algebraic models for 2-D flow with adverse pressure gradient [Kirtley and Lakshminarayana[4]] and for 2-D shock-boundary layer flow on curved surfaces [Degrez and VanDromme[5]]. It therefore seemed worthwhile to try to use it to provide an improved engineering approximation to the complex cascade flowfields investigated herein.

Implicit flow solvers have been used for well over a decade to compute compressible turbulent flows using various forms of the k-ε turbulence model. However, there have been only a few attempts to incorporate the model into an explicit solution procedure. In these cases, the stiffness problems associated with explicit treatment of the k-ε model have been circumvented by incorporating semi-implicit treatment of the source terms [Liu[6]], implementation of an algebraic inner layer model coupled to a high Reynolds number form of the k-ε model in the outer layer [Liu[6]], or by using wall functions to model, rather than to resolve, the near wall region where source terms and grid aspect ratio can be large [Grasso and Speziale[7], Eliasson[8], Holmes and Connell[9]].

The use of higher order turbulence models, and the precise control of levels of artificial dissipation, can improve the accuracy of high Reynolds number flow computations about complex configurations. The main thrust of this investigation is the incorporation of a low Reynolds number compressible form of the k-ε turbulence model into a purely explicit scheme, and the application of the technique to flows across a wide range of Mach numbers. In addition to this, some recently published improvements in controlling artificial dissipation levels in the computation of viscous flows on highly stretched grids are tested and incorporated. Two complex cascade flows are computed, for supersonic and low subsonic freestream conditions. For the supersonic cascade, isentropic blade Mach number, shock-boundary layer structure and wake loss profiles are compared with experimentally measured values. Pressure distribution and boundary layer profiles of velocity and turbulent kinetic energy are compared with data for the subsonic cascade. The results are shown to be quite good within the accuracy of the turbulence model and experimental data used.

GOVERNING EQUATIONS AND TURBULENCE MODEL

In the present development, the density weighted averaging attributed to Favre[10] is used. This decomposition has advantages in flow computations with variable density [see Jones[11]]. Specifically, the averaged governing equations are of simpler form and the physical interpretation of terms in the equations is clearer than when conventional time averaging is used. Reynolds (time) averaging, defined for a scalar, ϕ, as

$$\phi = \bar{\phi} + \phi' \ , \text{where } \bar{\phi} = \lim_{T\to\infty} \frac{1}{T}\int_{t_0}^{t_0+T} \phi \, dt \quad , \qquad (1)$$

is used for pressure, density, molecular stress tensor and molecular heat flux vector. Favre (density) averaging, defined for scalar, ϕ, as

$$\phi = \tilde{\phi} + \phi'' \ , \text{where } \tilde{\phi} = \frac{\overline{\rho\phi}}{\bar{\rho}} \quad , \qquad (2)$$

is used for velocity components, internal energy, turbulent kinetic energy and turbulent energy dissipation rate.

The resulting density averaged two-dimensional Navier-Stokes equations can be written in conservative form in generalized body fitted coordinates as :

$$\frac{\partial \hat{Q}}{\partial t} + \left(\frac{\partial \hat{E}_c}{\partial \xi} + \frac{\partial \hat{F}_c}{\partial \eta}\right) = \left(\frac{\partial \hat{E}_v}{\partial \xi} + \frac{\partial \hat{F}_v}{\partial \eta}\right) + \hat{S} \quad , \qquad (3)$$

where

$$\widehat{Q}=\frac{1}{J}\begin{pmatrix}\overline{\rho}\\ \overline{\rho}\widetilde{u}\\ \overline{\rho}\widetilde{v}\\ \overline{\rho}\widetilde{e}_o\end{pmatrix},\quad \widehat{E}_c=\frac{1}{J}\begin{pmatrix}\overline{\rho}\widetilde{U}\\ \overline{\rho}\widetilde{u}\widetilde{U}+\xi_x\overline{p}\\ \overline{\rho}\widetilde{v}\widetilde{U}+\xi_y\overline{p}\\ \left(\overline{\rho}\widetilde{e}_o+\overline{p}\right)\widetilde{U}\end{pmatrix},\quad \widehat{F}_c=\frac{1}{J}\begin{pmatrix}\overline{\rho}\widetilde{V}\\ \overline{\rho}\widetilde{u}\widetilde{V}+\eta_x\overline{p}\\ \overline{\rho}\widetilde{v}\widetilde{V}+\eta_y\overline{p}\\ \left(\overline{\rho}\widetilde{e}_o+\overline{p}\right)\widetilde{V}\end{pmatrix},$$

$$\widehat{E}_v=\frac{1}{J}\begin{pmatrix}0\\ \xi_x\tau_{xx}+\xi_y\tau_{yx}\\ \xi_x\tau_{xy}+\xi_y\tau_{yy}\\ \xi_x\left(\widetilde{u}\tau_{xx}+\widetilde{v}\tau_{xy}-q_x\right)+\xi_y\left(\widetilde{u}\tau_{yx}+\widetilde{v}\tau_{yy}-q_y\right)\end{pmatrix}, \tag{4}$$

$$\widehat{F}_v=\frac{1}{J}\begin{pmatrix}0\\ \eta_x\tau_{xx}+\eta_y\tau_{yx}\\ \eta_x\tau_{xy}+\eta_y\tau_{yy}\\ \eta_x\left(\widetilde{u}\tau_{xx}+\widetilde{v}\tau_{xy}-q_x\right)+\eta_y\left(\widetilde{u}\tau_{yx}+\widetilde{v}\tau_{yy}-q_y\right)\end{pmatrix},$$

$$\widehat{S}=\begin{pmatrix}0\\0\\0\\0\end{pmatrix}.$$

The metric terms based on a standard coordinate transformation $(x,y) \dashrightarrow (\xi,\eta)$ are given by

$$\xi_x=\frac{\partial\xi}{\partial x},\quad \xi_y=\frac{\partial\xi}{\partial y},\quad \eta_x=\frac{\partial\eta}{\partial x},\quad \eta_y=\frac{\partial\eta}{\partial y},$$

$$J=\xi_x\eta_y-\eta_x\xi_y\ . \tag{5}$$

The Jacobian, J, at each gridpoint is equal to 1/(average area of adjacent cells). The contravariant velocity components are given by

$$\widetilde{U}=\xi_x\widetilde{u}+\xi_y\widetilde{v}\ ,\quad \widetilde{V}=\eta_x\widetilde{u}+\eta_y\widetilde{v}\ . \tag{6}$$

Incorporating an eddy viscosity formulation, the effective stress tensor and the effective heat flux vector are given in cartesian coordinates by :

$$\tau_{ij}=\tau_{lij}-\overline{\rho u_i'' u_j''}=\left(\mu_l+\mu_t\right)\left[\left(\frac{\partial\widetilde{u}_i}{\partial x_j}+\frac{\partial\widetilde{u}_j}{\partial x_i}\right)-\frac{2}{3}\delta_{ij}\frac{\partial\widetilde{u}_k}{\partial x_k}\right]-\frac{2}{3}\delta_{ij}\overline{\rho}\widetilde{k}\ ,$$

$$q_i = -k\frac{\partial \bar{T}}{\partial x_i} + \overline{\rho u_i'' e''} = -c_p\left(\frac{\mu_l}{Pr_l} + \frac{\mu_t}{Pr_t}\right)\frac{\partial \tilde{T}}{\partial x_i} \quad . \tag{7}$$

In the derivation of Equations 4 and 7, it has been assumed that the time averaged molecular stress tensor and the molecular heat flux vector are equivalent to their density averaged values. This approximation should be a good one since, compared to turbulent diffusion, molecular diffusion is only significant near solid boundaries, where local Mach number and hence density fluctuations are small. The apparent heat flux vector has been modelled by incorporating the gradient diffusion hypothesis. The laminar Prandtl number, Pr_l, is set to 0.72 for air. The turbulent Prandtl number, Pr_t, is set to the standard value of 0.90.

In the present work, the density averaged k-ε equations are numerically decoupled from the density averaged mean flow equations. Specifically, at each iteration, the four mean flow equations are updated using "frozen" values of eddy viscosity and turbulent kinetic energy from the previous iteration. Likewise, the coupled k-ε equations are then updated using the "frozen" mean flow quantities just computed.

Low Reynolds number forms of the compressible k-ε equations can be written in the same form as Equation 3 where the scaled variable vectors become :

$$\hat{Q} = \frac{1}{J}\begin{pmatrix}\bar{\rho}\tilde{k}\\ \bar{\rho}\tilde{\varepsilon}\end{pmatrix} , \quad \hat{E}_c = \frac{1}{J}\begin{pmatrix}\bar{\rho}\tilde{k}\tilde{U}\\ \bar{\rho}\tilde{\varepsilon}\tilde{U}\end{pmatrix} , \quad \hat{F}_c = \frac{1}{J}\begin{pmatrix}\bar{\rho}\tilde{k}\tilde{V}\\ \bar{\rho}\tilde{\varepsilon}\tilde{V}\end{pmatrix} ,$$

$$\hat{E}_v = \frac{1}{J}\begin{pmatrix}\left[\mu_l + \frac{\mu_t}{Pr_k}\right]\left[(\nabla\xi\cdot\nabla\xi)\frac{\partial\tilde{k}}{\partial\xi} + (\nabla\xi\cdot\nabla\eta)\frac{\partial\tilde{k}}{\partial\eta}\right]\\ \left[\mu_l + \frac{\mu_t}{Pr_\varepsilon}\right]\left[(\nabla\xi\cdot\nabla\xi)\frac{\partial\tilde{\varepsilon}}{\partial\xi} + (\nabla\xi\cdot\nabla\eta)\frac{\partial\tilde{\varepsilon}}{\partial\eta}\right]\end{pmatrix} , \tag{8}$$

$$\hat{F}_v = \frac{1}{J}\begin{pmatrix}\left[\mu_l + \frac{\mu_t}{Pr_k}\right]\left[(\nabla\eta\cdot\nabla\xi)\frac{\partial\tilde{k}}{\partial\xi} + (\nabla\eta\cdot\nabla\eta)\frac{\partial\tilde{k}}{\partial\eta}\right]\\ \left[\mu_l + \frac{\mu_t}{Pr_\varepsilon}\right]\left[(\nabla\eta\cdot\nabla\xi)\frac{\partial\tilde{\varepsilon}}{\partial\xi} + (\nabla\eta\cdot\nabla\eta)\frac{\partial\tilde{\varepsilon}}{\partial\eta}\right]\end{pmatrix} ,$$

$$\hat{S} = \frac{1}{J}\begin{pmatrix} P - \overline{\rho\varepsilon} + \mathcal{D} \\ \left(C_1 f_1 P - C_2 f_2 \overline{\rho\varepsilon}\right)\frac{\tilde{\varepsilon}}{\tilde{k}} + \mathcal{E} \end{pmatrix} ,$$

where the production term P is given in cartesian coordinates as

$$\begin{aligned} P = &\left\{2\mu_t\frac{\partial\tilde{u}}{\partial x} - \left[\frac{2}{3}\bar{\rho}\,\tilde{k} + \mu_t\left(\frac{\partial\tilde{u}}{\partial x} + \frac{\partial\tilde{v}}{\partial y}\right)\right]\right\}\frac{\partial\tilde{u}}{\partial x} \\ &+ \left\{2\mu_t\frac{\partial\tilde{v}}{\partial y} - \left[\frac{2}{3}\bar{\rho}\,\tilde{k} + \mu_t\left(\frac{\partial\tilde{u}}{\partial x} + \frac{\partial\tilde{v}}{\partial y}\right)\right]\right\}\frac{\partial\tilde{v}}{\partial y} \\ &+ \mu_t\left(\frac{\partial\tilde{u}}{\partial y} + \frac{\partial\tilde{v}}{\partial x}\right)^2 . \end{aligned} \tag{9}$$

The mass averaged turbulent kinetic energy and isotropic component of turbulent kinetic energy dissipation rate are defined as

$$\tilde{k} = \frac{\frac{1}{2}\overline{\rho u_i'' u_i''}}{\bar{\rho}} , \quad \tilde{\varepsilon} = \frac{\overline{\nu\rho\frac{\partial u_i''}{\partial x_j}\frac{\partial u_i''}{\partial x_j}}}{\bar{\rho}} . \tag{10}$$

The eddy viscosity is obtained from

$$\mu_t = \frac{C_\mu f_\mu \bar{\rho}\,\tilde{k}^2}{\tilde{\varepsilon}} . \tag{11}$$

The particular form of low Reynolds number model used in the code was originally devised by Chien for incompressible flow[12]. Compressible forms have been given by Coakley[13] and more recently by Nichols[14]. For this model, the constants and functions in Equations 8 through 11 are given by

$$f_\mu = 1 - \exp(-.0115y^+) , f_1 = 1 , f_2 = 1 - \frac{2}{9}\exp(-R_T^2/36) ,$$

$$R_T = \frac{\bar{\rho}\,\tilde{k}^2}{\mu_l\tilde{\varepsilon}} , y^+ = \frac{\bar{\rho} n u^*}{\mu_l} , u^* = \sqrt{\frac{\tau_w}{\bar{\rho}}} , \tag{12}$$

$$\mathfrak{D} = -\frac{2\mu_l\tilde{k}}{n^2} , \mathfrak{E} = -\frac{2\mu_l\tilde{\varepsilon}}{n^2} \exp(-.5y^+) ,$$

$$C_\mu = 0.09 , C_1 = 1.35 , C_2 = 1.80 , Pr_k = 1.0 , Pr_\varepsilon = 1.3 .$$

Following Hobson[15], the blade normal coordinate, n, in Equations 12, is replaced by absolute distance from leading and trailing edge, upstream and downstream of the passage respectively.

The transport variable, ε, used in this model is the isotropic component of the dissipation rate, though the ε equation is derived for the total dissipation rate. As discussed by Jones[16], at high local Reynolds numbers, the anisotropic component of dissipation is negligible, so the model remains valid in these regions. Near a solid wall, however, the anisotropic dissipation component is not negligible, and the isotropic component, ε, goes to zero. The term, $\mathfrak{D}$, accounts for the non-zero value of total dissipation near the wall, so that the model also remains valid near solid walls and retains the convenience of specifying the $\varepsilon = 0$ boundary condition there.

It should be noted, that although the k-ε equations have been cast in compressible form, the modelling assumptions invoked here are essentially those for incompressible flow. Specifically, terms in the unmodelled k and ε equations which contain density fluctuation terms, ρ', are neglected. Also, pressure diffusion terms are neglected.

No thin layer approximations are made in either the mean flow or turbulence transport equations.

NUMERICAL SOLUTION

Discretization

The H-grid flow solver used in the present studies incorporates a standard 4-stage Runge-Kutta scheme as first applied to Euler calculations by Jameson, Schmidt and Turkel[1],

$$\begin{aligned}
\hat{Q}^1 &= \hat{Q}^n + \frac{1}{4}\Delta t\,\hat{R}(\hat{Q}^n)\\
\hat{Q}^2 &= \hat{Q}^n + \frac{1}{3}\Delta t\,\hat{R}(\hat{Q}^1)\\
\hat{Q}^3 &= \hat{Q}^n + \frac{1}{2}\Delta t\,\hat{R}(\hat{Q}^2)\\
\hat{Q}^{n+1} &= \hat{Q}^n + \Delta t\,\hat{R}(\hat{Q}^3) .
\end{aligned} \tag{13}$$

Here, the residual, $\hat{R}$, is defined according to

$$\hat{R} = -\left(\frac{\partial \hat{E}_c}{\partial \xi} + \frac{\partial \hat{F}_c}{\partial \eta}\right) + \left(\frac{\partial \hat{E}_v}{\partial \xi} + \frac{\partial \hat{F}_v}{\partial \eta}\right) + \hat{S} \quad . \tag{14}$$

The scheme is fourth order accurate in time. Second order accurate central differences are used to discretize the derivatives in Equation 14. Viscous and source terms are evaluated prior to the first stage, convective terms are computed at every stage. The stability region for the scheme is shown in Figure 1.

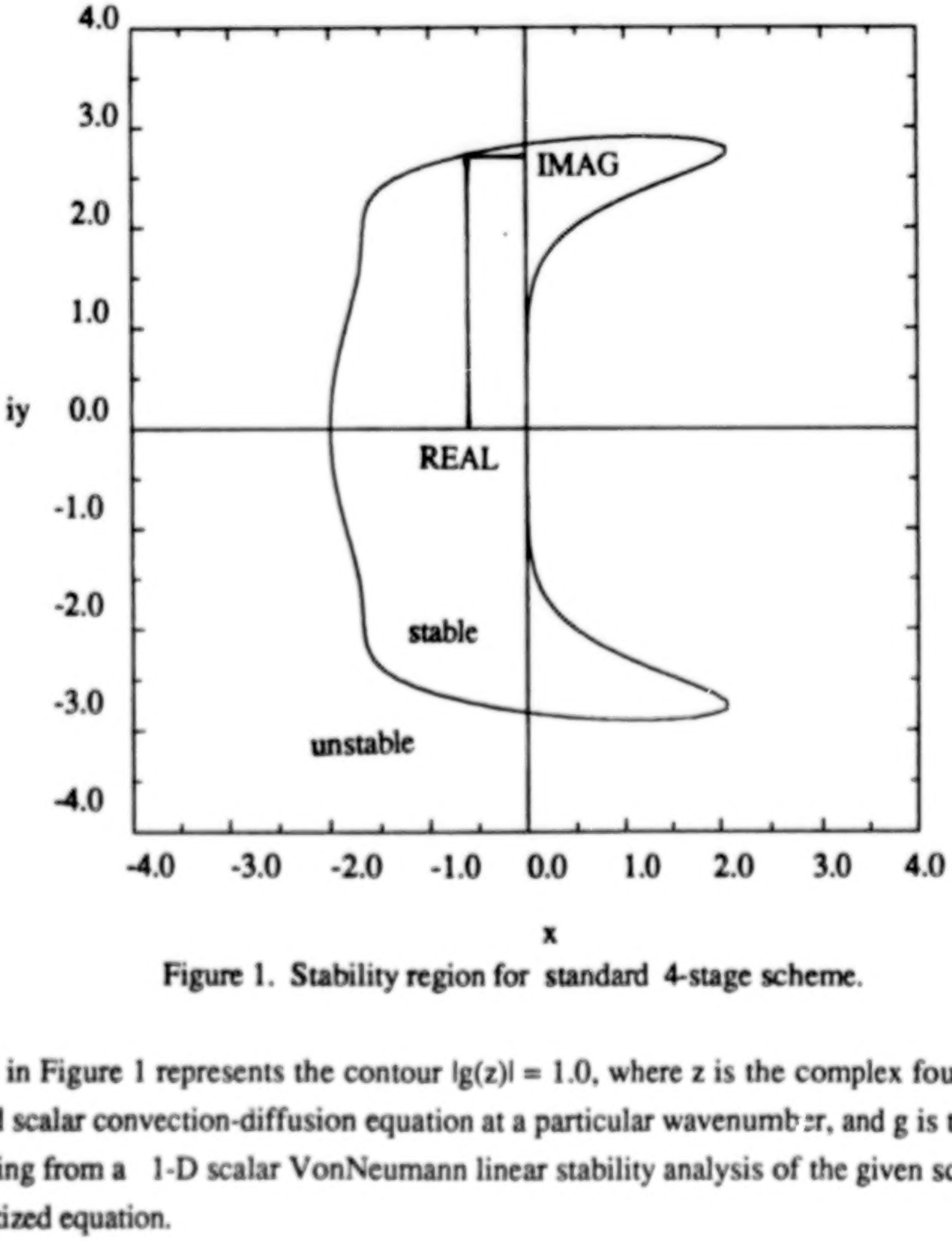

Figure 1. Stability region for standard 4-stage scheme.

The curve in Figure 1 represents the contour $|g(z)| = 1.0$, where z is the complex fourier symbol of a discretized scalar convection-diffusion equation at a particular wavenumber, and g is the amplification factor arising from a 1-D scalar VonNeumann linear stability analysis of the given scheme applied to this discretized equation.

The differencing molecule used to discretize the flux vectors in computational space is shown in Figure 2. Flux vectors, $\hat{E}$ and $\hat{F}$, are computed at mid-points between nodes. For viscous fluxes, this scheme incorporates information from all nine points in the differencing molecule. This approach requires three times the storage for metric terms than if viscous fluxes were computed on the grid vertices themselves (13 point molecule). However, the truncation error associated with discretizing the viscous fluxes on a uniform cartesian mesh using a thirteen point scheme is $O(4\Delta x^{2)} + O(4\Delta y^{2)}$ as compared to $O(\Delta x^{2)} + O(\Delta y^{2)}$ for the nine point molecule, consistent with the truncation error of the convective fluxes. It is also easier to apply periodic and wall-function boundary conditions with the more compact differencing molecule.

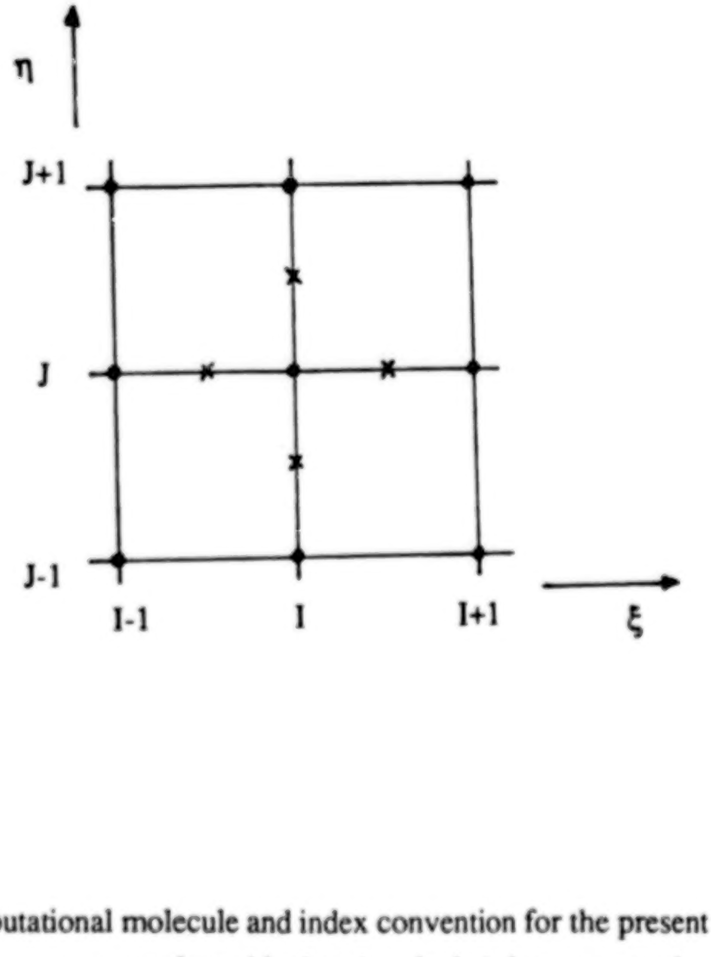

Figure 2. Computational molecule and index convention for the present scheme. Flux vectors computed at midpoints (marked x) between vertices.

To accelerate the solution to steady state, locally varying timesteps are computed based on a linear stability analysis of the discretized Navier-Stokes equations. The resulting timestep specification is given as :

$$\Delta t = \mathrm{MIN}\ \left[\ \Delta t_c\ ,\ \Delta t_v\ \right] = \mathrm{MIN}\ \left[\ \frac{\mathrm{IMAG}}{|\tilde{U}| + |\tilde{V}| + a\sqrt{(\nabla\xi\cdot\nabla\xi) + (\nabla\eta\cdot\nabla\eta) + |2(\nabla\xi\cdot\nabla\eta)|}}\ ,\right.$$

$$\left.\frac{\mathrm{REAL}}{\frac{4\gamma}{\tilde{\rho}}\left(\frac{\mu_l}{Pr_l} + \frac{\mu_t}{Pr_t}\right)\left[(\nabla\xi\cdot\nabla\xi) + (\nabla\eta\cdot\nabla\eta)\right] + \frac{4}{3\tilde{\rho}}(\mu_l + \mu_t)\left[7|\nabla\xi\cdot\nabla\eta| + \sqrt{(\nabla\xi\cdot\nabla\xi)(\nabla\eta\cdot\nabla\eta)}\right]}\ \right] \quad . \qquad (15)$$

Here, IMAG and REAL are input parameters corresponding to operational CFL and VonNeumann numbers chosen to ensure stability (see Figure 1). A similar expression is given by Martinelli [17]. The first term in the brackets in Equation 15 arises from the convection operators, the latter term corresponds to physical viscous terms. Note that for the present uncoupled approach, the turbulent kinetic energy does not appear in the stablility expressions.

For large Reynolds number flows, the H-grids used must be highly stretched in the pitchwise direction, in order to adequately resolve near-wall gradients. Consequently, the metric terms, η_x, η_y in Equation 15 can become very large near the J = 1 and J = NJ boundaries. Also, when using a two equation turbulence model, as in the present study, the eddy viscosity, μ_t, can be very large near the J = 1 and J = NJ boundaries, upstream and downstream of the blades, where wall damping effects are negligible This combination of large eddy viscosity and grid metrics causes the viscous stability term to dominate in these regions, and it has been found that it is crucial to include the influence of these terms in determining a stable local timestep. For the supersonic and subsonic cascade test cases computed herein, $\Delta t_v < \Delta t_c$ for 40.0% and 7.5 % of the grid points at convergence, respectively.

Even for the computation of steady, one-dimensional, inviscid flows, the use of highly stretched grids gives rise to significantly reduced convergence rates in explicit schemes. This affect arises due to characteristic propagation speed in the streamwise direction. In two dimensions an analagous situation arises when the computational mesh is clustered in one curvilinear coordinate direction to resolve regions where flowfield gradients are large. Specifically, the maximum local stable timestep in regions where the mesh is highly clustered in the η direction, is inversely proportional to the metric term, $\sqrt{(\nabla\eta\cdot\nabla\eta)}$, which can be very large. It is the nature of this inviscid effect which often allows one to use a local timestep based solely on inviscid considerations, for viscous flow computations.

The k and ε equations each contain non-linear production and destruction source terms which can be very large near solid boundaries. According to linear stability theory, such terms can also severely reduce convergence rates if a purely explicit scheme is used to discretize the equations. It was found that by incorporating a composite viscous-inviscid timestep specification, the stability restrictions on the k-ε solution are not much more severe than the restrictions on the mean flow equations discussed above. In fact, it was possible to compute high Reynolds number flows with this turbulence model using a purely explicit treatment in reasonable computation times. A local timestep for the k-ε equations of approximately 1/4 of the stable mean flow timestep was satisfactory for the cascade flows computed herein. Converged solutions were thereby obtained in computation times approximately twice those of solutions using an algebraic eddy viscosity model. This is illustrated for turbulent flat plate flow computations presented in the Results section.

Artificial Dissipation

Central difference schemes applied to hyperbolic equations that do not contain any inherent dissipation require the addition of artificial dissipation, to damp high wave number disturbances. These disturbances can be introduced into linear problems through inconsistent boundary condition treatment or machine roundoff error. In non-linear problems, such disturbances can be introduced through aliasing of sub-grid scale non-linear disturbances, to lower, resolvable wave numbers. Even for viscous flow calculations, artificial dissipation must be introduced into the scheme because the physical viscous terms are only effective in damping frequencies at higher wave numbers than can be resolved on practical grids.

In the present work, artificial dissipation is added to the discretized mean flow equations as

$$\hat{R} = -\left(\frac{\partial \hat{E}_c}{\partial \xi} + \frac{\partial \hat{F}_c}{\partial \eta}\right) + \left(\frac{\partial \hat{E}_v}{\partial \xi} + \frac{\partial \hat{F}_v}{\partial \eta}\right) + D(Q) + \hat{S} \tag{16}$$

Here, D(Q) represents a mixed 2nd and 4th order nonconservative artificial dissipation operator similar to that devised by Jameson, Schmidt and Turkel[1].

$$\begin{aligned} D(Q) &= D_\xi(Q) + D_\eta(Q)\,, \\ D_\xi(Q) &= S_{2\xi}\delta_{\xi\xi}Q + S_{4\xi}\delta_{\xi\xi\xi\xi}Q\,, \\ D_\eta(Q) &= S_{2\eta}\delta_{\eta\eta}Q + S_{4\eta}\delta_{\eta\eta\eta\eta}Q\,. \end{aligned} \tag{17}$$

The fourth order operators are included to damp high wave number errors and the second order operators are included to improve shock capturing.

As pointed out by Pulliam[18], artificial dissipation terms should operate on physical values of the flowfield variables and as such must be appropriately scaled by the metric Jacobian. Artificial dissipation terms must also be scaled by the local timestep to ensure that the steady state solution is independent of the timestep. In addition to the above consistency requirements on the dissipation scaling, levels of dissipation should always be reduced to levels adequate to stabilize a scheme without altering the accuracy of the solution. For the computation of viscous flows on highly stretched grids, this latter requirement is a sensitive matter.

For high Reynolds number flows, very highly stretched grids must be used to resolve body normal gradients in near wall regions. If the artificial dissipation terms in both the ξ and η directions are scaled by the local timestep, on grids which are highly stretched in the η direction, excessive dissipation is introduced in the ξ direction. This effect is discussed by Caughey and Turkel[19] and Swanson and Turkel[20]. This excessive dissipation may reduce accuracy and convergence rates in viscous flow computations. A recently devised eigenvalue scaling of the artificial dissipation terms, due to Martinelli[17] alleviates this problem. Since the present technique is primarily used to compute viscous flows on highly stretched grids, anisotropic dissipation scaling factors similar to those used by Martinelli are incorporated. $S_{2\xi}$, $S_{2\eta}$, $S_{4\xi}$, $S_{4\eta}$ in Equation 17 are defined

$$\begin{aligned} S_{2\xi} &= \frac{\sigma_{2\xi}}{J}\left[\frac{1}{\Delta t_{c\xi}}\left(1+\frac{\Delta t_{c\xi}}{\Delta t_{c\eta}}\right)^{\alpha}\right], \quad S_{2\eta} = \frac{\sigma_{2\eta}}{J}\left[\frac{1}{\Delta t_{c\eta}}\left(1+\frac{\Delta t_{c\eta}}{\Delta t_{c\xi}}\right)^{\alpha}\right], \\ S_{4\xi} &= \frac{\sigma_{4\xi}}{J}\left[\frac{1}{\Delta t_{c\xi}}\left(1+\frac{\Delta t_{c\xi}}{\Delta t_{c\eta}}\right)^{\alpha}\right], \quad S_{4\eta} = \frac{\sigma_{4\eta}}{J}\left[\frac{1}{\Delta t_{c\eta}}\left(1+\frac{\Delta t_{c\eta}}{\Delta t_{c\xi}}\right)^{\alpha}\right]. \end{aligned} \tag{18}$$

Here, $\Delta t_{c\xi}$, $\Delta t_{c\eta}$, are timesteps corresponding to unit CFL limit for the inviscid one-dimensional problem in each direction,

$$\Delta t_{c\xi} = \frac{1}{|U| + a\sqrt{(\nabla\xi\cdot\nabla\xi)}}, \quad \Delta t_{c\eta} = \frac{1}{|V| + a\sqrt{(\nabla\eta\cdot\nabla\eta)}}. \tag{19}$$

The choice of unit CFL scaling in the numerator of Equation 19 ensures that the steady state solution will be independent of the operational CFL limit used to compute local timesteps. If $\alpha = 1$, Equation 18 reduces to standard isotropic scaling. As mentioned above, this introduces excessive dissipation in the ξ direction in regions where the grid is stretched in the η direction. If $\alpha = 0$, the scaling becomes purely anisotropic. If the grid is very highly stretched in the η direction, such scaling may not provide enough dissipation in the ξ direction, resulting in reduced convergence rates. For intermediate values of α

between 1/2 and 2/3, Martinelli[17], Swanson and Turkel[20] and Radespiel and Swanson[21] have shown good convergence rates for Euler and Navier-Stokes calculations on highly clustered grids.

Another scaling issue is important in the computation of viscous flows. All of the mean flow equations with the exception of the continuity equation contain physical dissipation terms. Also, near solid boundaries, physical dissipation terms in the energy equation are quite small, in the absence of heat transfer effects. However, near solid boundaries, the viscous fluxes in the momentum are quite large and are themselves adequate to provide smoothing. In these same regions, second and fourth derivatives of the transport variables can be quite large leading to large values of artificial dissipation there. This well recognized phenomenon [see Davis, Ni and Carter[22] and Swanson and Turkel [20] for instance] gives rise to very large nonphysical values of total dissipation in the near wall region. Often some sort of geometric decay function is used to control the levels of artificial dissipation in these regions to reduce the magnitude of numerical to physical smoothing to acceptable levels. In the present work, the scaling functions in Equation 18 are multiplied by a normalized square of the local velocity, $V^2/V^2_{-\infty}$, for the momentum equations.

Following Jameson, Schmidt and Turkel[1], the non-linear weighting functions in Equation 18 are determined from

$$\begin{aligned} \sigma_{2\xi} &= \kappa_2 \, \mathrm{MAX}\left(v_{\xi i+1,j}, v_{\xi i,j}, v_{\xi i-1,j}\right) , \\ \sigma_{4\xi} &= - \ \mathrm{MAX}\left(0, \kappa_4 - \sigma_{2\xi}\right) , \end{aligned} \tag{20}$$

where the monitoring parameters v, are normalized second derivatives of pressure,

$$v_{\xi i,j} = \frac{\left|p_{i+1,j} - 2\, p_{i,j} + p_{i-1,j}\right|}{\left|p_{i+1,j} + 2\, p_{i,j} + p_{i-1,j}\right|} , \tag{21}$$

and $\kappa_2 \equiv 1/4$, $\kappa_4 \equiv 1/64$. Expressions similar to Equations 20 and 21 are used in the η direction. When shocks are not anticipated in the flowfield, κ_2 is set equal to zero so that the artificial dissipation added to the mean flow is fourth order only.

To examine the effects of the scalings given, two numerical experiments were conducted. The subsonic cascade described below was used as a numerical test bed. The reader is referred to the next section for specifics on this flow configuration.

The first experiment attempted to isolate the influence of eigenvalue scaling on accuracy and convergence. The test case was run for five thousand iterations using the following values of α in Equation 18 : $\alpha = 1$ (standard isotropic scaling), $\alpha = 0$ (purely anisotropic scaling) and $\alpha = 2/3$ (intermediate scaling). In Figure 3, the convergence histories for the three cases are plotted.

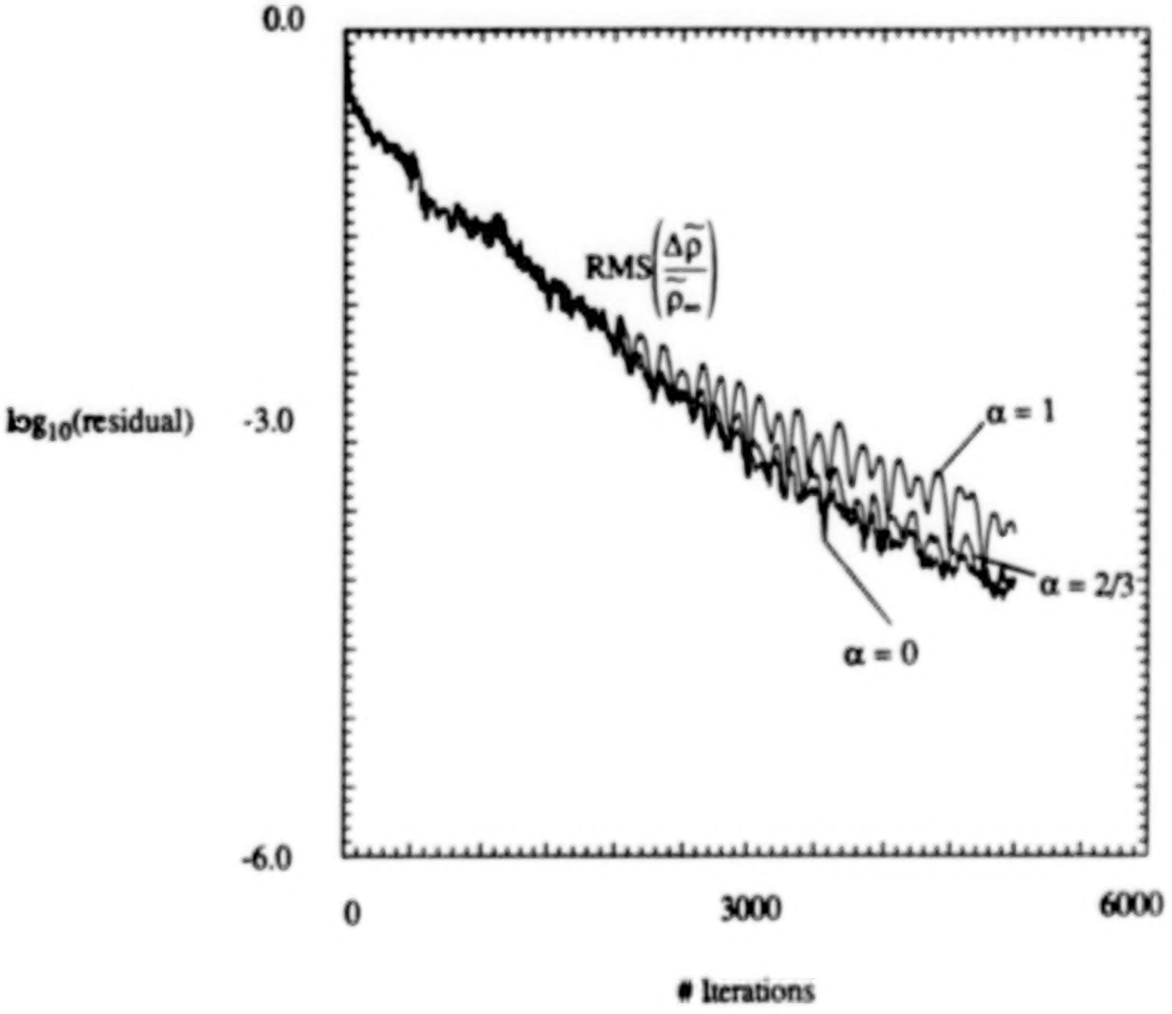

Figure 3. Convergence histories for various eigenvalue scalings.

Scaling the dissipation anisotropically does provide an improved convergence rate for this case as expected. In addition, purely anisotropic scaling provides somewhat superior convergence rate than the weighted scaling ($\alpha = 2/3$). This suggests that, for this case, such scaling does not reduce dissipation in the ξ direction to the point of destabilizing the solution. The influence of these scalings on accuracy was found to be negligible.

The second experiment sought to detect the influence of spurious dissipation levels in near wall boundaries, and to see how the proposed velocity scaling affects solution convergence and accuracy. When the ratio of artificial to physical dissipation terms in Equation 16 were compared, it was found that for this test case, at convergence, artificial dissipation levels were as high as ten times the physical dissipation terms at the first several grid points adjacent to the wall! By incorporating the velocity scaling exactly as proposed above, it was possible to reduce the artificial to physical dissipation ratio to less than .01 in the near wall region, except in the immediate vicinity of the leading and trailing edges. The convergence rates compared very closely, but as shown in Figure 4, the converged solutions showed some discrepancy.

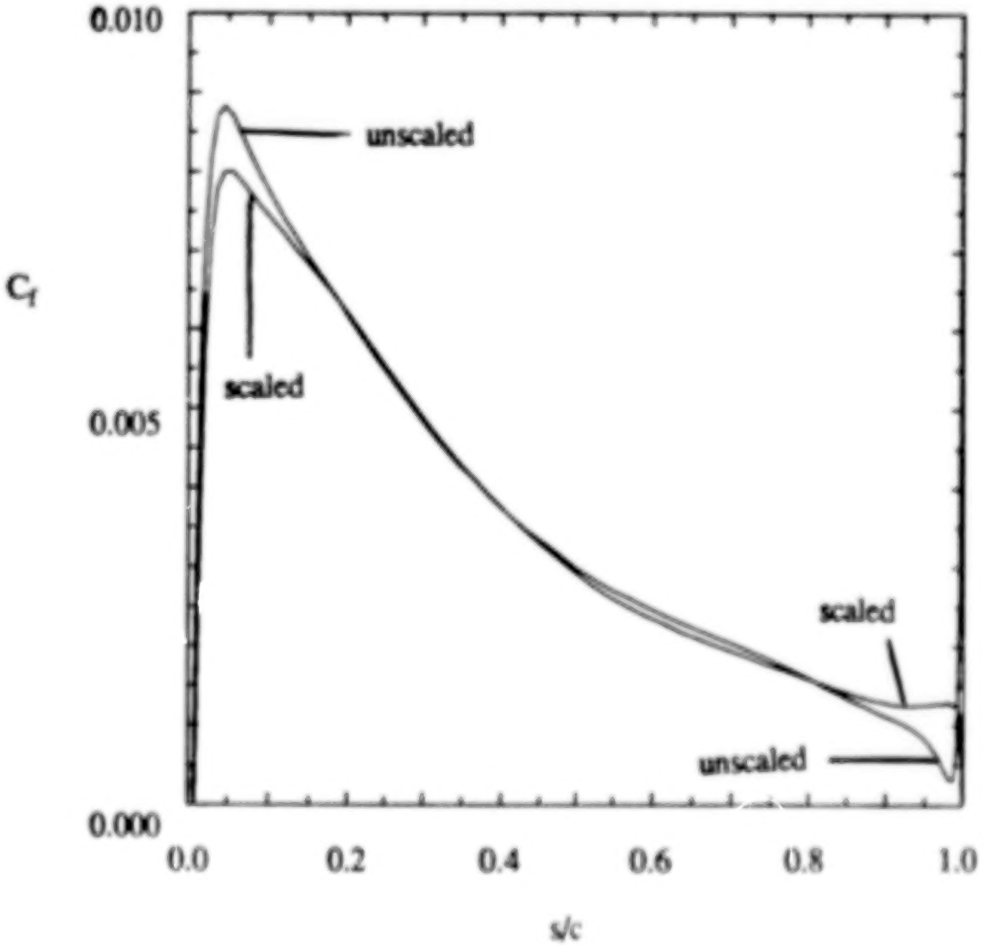

Figure 4. Comparison of predicted skin friction coefficient, along the suction surface of the test cascade, with and without velocity scaling of the artificial dissipation.

It is clear from this figure that unnecessary levels of artificial dissipation in boundary layers can affect solution accuracy in practical application.

Both eigenvalue scaling (with $\alpha = 2/3$) and local velocity scaling were used in all computations that follow.

It is worth noting, that the dissipation scaling considerations addressed here are especially important when a multigrid acceleration scheme is used. Careful tuning of artificial dissipation levels is crucial when performing explicit multigrid calculations on highly stretched grids. This is because inadequate or excessive dissipation can diminish the high wave number damping properties of the driving scheme thereby rendering multigrid acceleration less effective[23].

Lack of adequate grid resolution in the ξ direction just upstream and downstream of the blade edges, causes the wall damping function, f_μ, in Equation 12 to be effective only over two to four grid points in this direction. This gives rise to very large streamwise gradients in k and ε at the leading and trailing edges, which in turn leads to slowly growing oscillations in these variables. It was found necessary to smooth these oscillations by incorporating small amounts of second order artificial dissipation in the k and ε equations in a manner consistent with Equations 16 and 17, with $S_{2\xi} = S_{2\eta} \cong 0.002$, $S_{4\xi} = S_{4\xi} = 0.0$.

Boundary and Initial Conditions

Along blade surfaces the no-slip condition is imposed upon the velocities, pressure is extrapolated from adjacent grid points, and density is computed based on specified wall temperature or heat transfer rate. At the inlet, total pressure and total temperature are specified. For subsonic inflow, either inlet flow angle or pitchwise velocity are specified, and the R^- characteristic is extrapolated along η = constant grid lines from the interior of the computational domain. At subsonic outflow boundaries, static pressure is specified and velocity components and entropy are extrapolated along η = constant grid lines. Along periodic boundaries, cyclic information is used when discretizing derivatives in the η direction.

Constant values of k and ε are imposed at the inflow boundary based on specified freestream turbulence intensity and length scale,

$$T_{u\infty} = \frac{\sqrt{\frac{2}{3}\tilde{k}_\infty}}{\tilde{V}_\infty} , \tag{19}$$

$$L_\infty = \frac{C_\mu \tilde{k}^{3/2}}{\tilde{\varepsilon}} .$$

Typically , the freestream length scale is set between .001 and .01 times the pitch of the blade passage. At the outflow boundary, values of k and ε are extrapolated along η = constant grid lines from the interior of the computational domain. Turbulent kinetic energy and isotropic dissipation rate are set to zero along solid boundaries, as discussed in the turbulence model section.

The flowfield is initialized using standard quasi-1D analysis to provide uniform initial velocity profiles along each ξ = constant grid line. This gives rise to huge production terms in the k-ε equations, and can cause solutions to become rapidly unstable. This problem is alleviated by running the code in laminar mode for a couple hundred iterations to develop a slight boundary layer, thereby reducing the size of these terms.

RESULTS AND DISCUSSION

Computational Considerations

The code has been validated for laminar and turbulent flat plate boundary layer flows, where nearly exact agreement with theory and experiment were obtained. In addition, it has been applied to laminar flow about a circular arc bump in a channel, as well as to turbulent flow about a similar configuration with a heated wall using an algebraic eddy viscosity model. These two model problems had been computed by Chima and Johnson[24] and Davis, Ni and Carter[22] respectively. The present method yielded nearly exact agreement with these two sets of results. Implicit residual smoothing is available to accelerate the convergence to steady state of the mean flow. However, successful implementation of implicit smoothing for the turbululence transport equations has not been realized. For consistency, then, residual smoothing was not used in obtaining any of the proceeding results.

For turbulent flow calculations, the highly vectorized code executes at 2.8×10^{-5} CPU seconds / (gridpoint * iteration) on the Cray Y-MP 8/32 at the Pittsburgh Supercomputer Center. When an algebraic eddy viscosity model is used, the execution rate is 1.7×10^{-5} CPU seconds / (gridpoint * iteration). Since the same near wall resolution is needed for these two models, similar grids must be used. Experience with the code has shown that mean density residual converges slightly more slowly when using the k-ε model, so the total overhead associated with using the higher order model is less than a factor of 2.0.

To illustrate the above considerations, convergence histories are presented here for the prediction of developing turbulent flow over a flat plate. Both the algebraic eddy viscosity model due to Baldwin and Lomax[25] and the present two-equation model were used.

Both cases converged very slowly due to the extremely high aspect ratio of the grid (1.2 x 10^4 at the trailing edge of the plate). The convergence history for the computations is shown in Figure 5. It took approximately 10000 iterations for both calculations to converge to within engineering accuracy (taken to be a 4.5 order of magnitude drop in the RMS density residual). Note that the convergence rates are similar. This illustrates that it is primarily "inviscid" stablity constraints, and not the stiffness associated with large source terms in the turbulence transport equations, which give rise to the slower convergence rates which occur when explicit schemes are used to compute turbulent flows on highly stretched meshes.

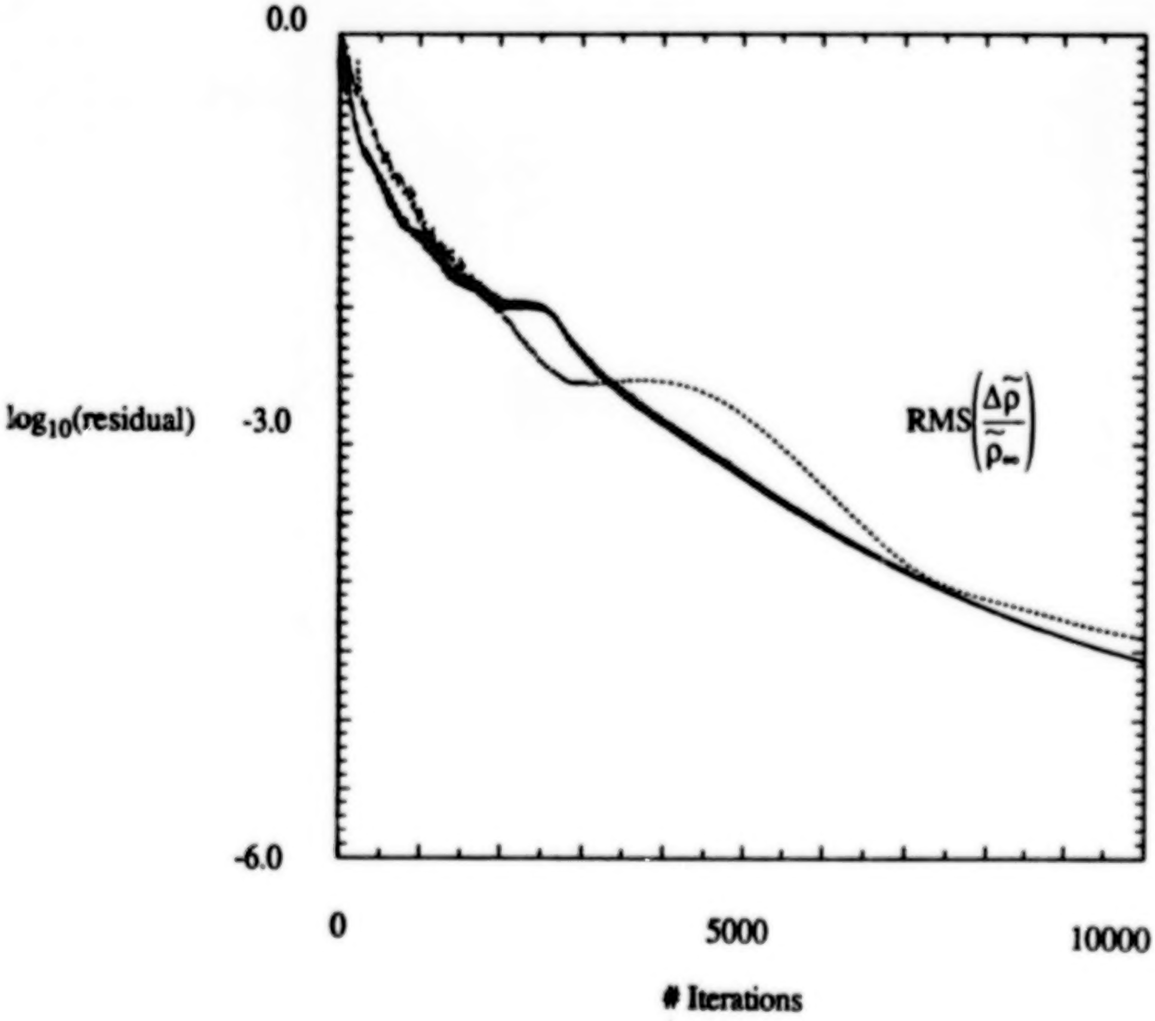

Figure 5. Convergence history for turbulent flat plate boundary layer calculations (solid line = Baldwin and Lomax, dashed line = k-ε).

DFVLR PAV-1.5 Supersonic Compressor Cascade

The first cascade to be investigated is the PAV-1.5 supersonic compressor cascade tested at DFVLR by Schreiber[26]. This pre-compression blade was designed especially to investigate shock-boundary layer interaction with separation. At the test freestream Mach number, a standoff leading edge shock forms, which gives rise to a separated shock-boundary layer interaction aft of mid chord on the suction surface of the adjacent passage. Though the measured absolute inlet Mach number was supersonic, the blade row stagger angle was high so the axial component of the inlet velocity was subsonic. This gives rise to the "unique incidence" condition wherein there exists a fixed relationship between inlet Mach number and inlet flow angle. Beyond a critical Mach number this condition exists and inlet conditions become independent of back pressure. This phenomena as well as the complex wave interaction field within the passage and shock-boundary-layer interaction provide a challenging test case for both numerical scheme and turbulence model.

The computed case was experimentally tested in air at an inlet Mach number of 1.53 and a maximum attainable static pressure ratio of 2.13. The measured axial velocity density ratio of 1.02 indicates that the flow was close to two-dimensional. The Reynolds number based on chord was 2.7 x 10^6. The inlet turbulence intensity was measured using a Laser-two-focus (L2F) velocimeter to be no more than 1 %, which is the value used in the computations. As mentioned above, the inlet Mach number is supersonic, but axial velocity at the inlet to the computational domain is subsonic allowing left running characteristics to propagate out of the inlet plane. For this reason, subsonic inlet boundary conditions were specified : p_o = 101325 N/m^2, T_o = 300 K, $V_{\theta\infty}$= 379.5 m/s^2. At the subsonic exit plane the backpressure, p_e = 56500 N/m^2, was specified corresponding to the experimentally measured pressure ratio of the cascade, $p_2/p_1 = 2.13$.

The 129 x 100 computational mesh used was generated using Sorenson's[27] GRAPE code, modified by Gorski[28] to generate H-grids, and is shown in Figure 6. The blade normal grid spacing at the wall was prescribed as .000011 chord. This yielded values of $y^+ \leq 1$ at grid points adjacent to the walls. Except in the immediate vicinity of the leading and trailing edges, the suction and pressure surface boundary layers had at least 9 grid points with values of $y^+ \leq 20$.

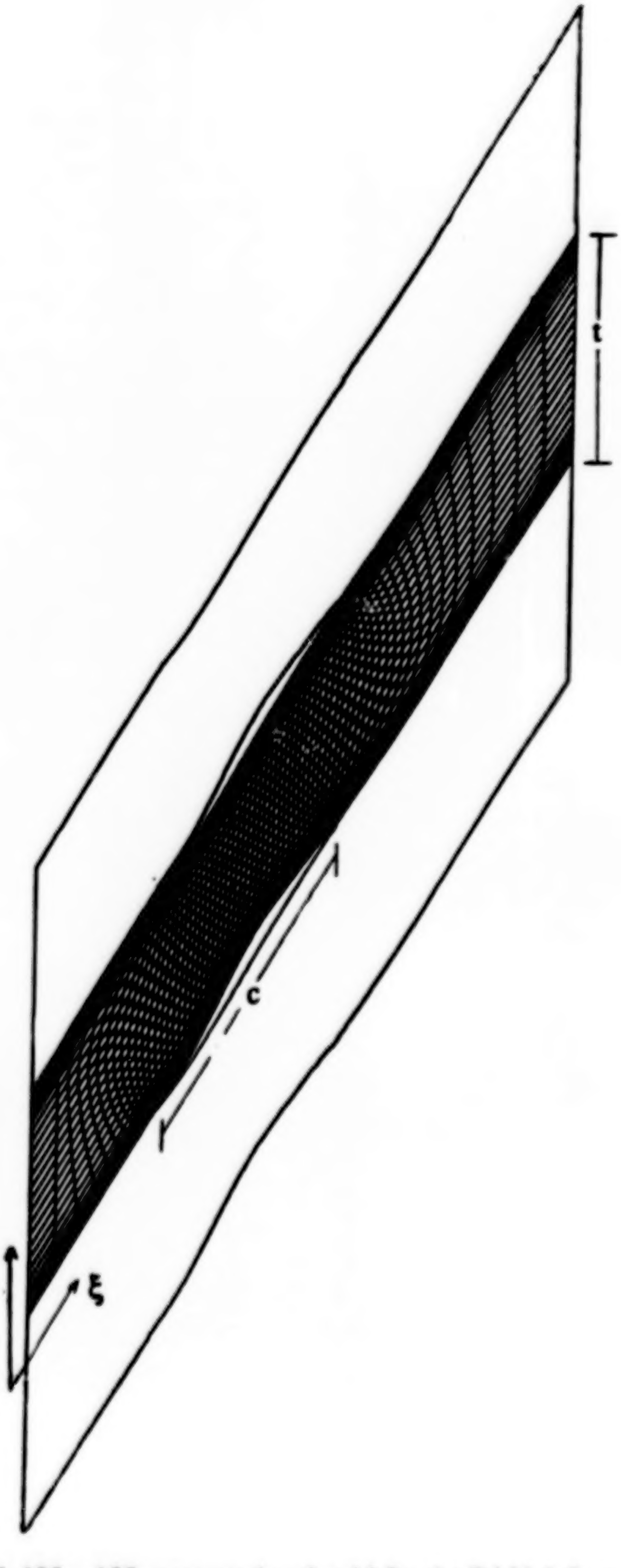

Figure 6. 129 x 100 computational grid for the PAV-1.5 cascade.
For clarity, only every other grid line is shown in both ξ and η directions.

The convergence history for this computation is shown in Figure 7. It took approximately 6500 iterations for this calculation to converge within engineering accuracy as measured by the invariance of total number of supersonic gridpoints in the field. This corresponded to approximately 39 minutes of CPU time on the Pittsburgh Cray. It was not possible to "cold start" the initialized flowfield at the specified pressure ratio, as the code became rapidly unstable when this was attempted. Rather, the back pressure had to be increased in a stepwise fashion with iteration (notice "jumps" in convergence at iteration 500, 1000, 2000), until the experimentally imposed pressure ratio could be specified at iteration 2000. It is felt that the "unhealthy" convergence history is due in part to the highly clustered grid and also to the nearly choked operating condition.

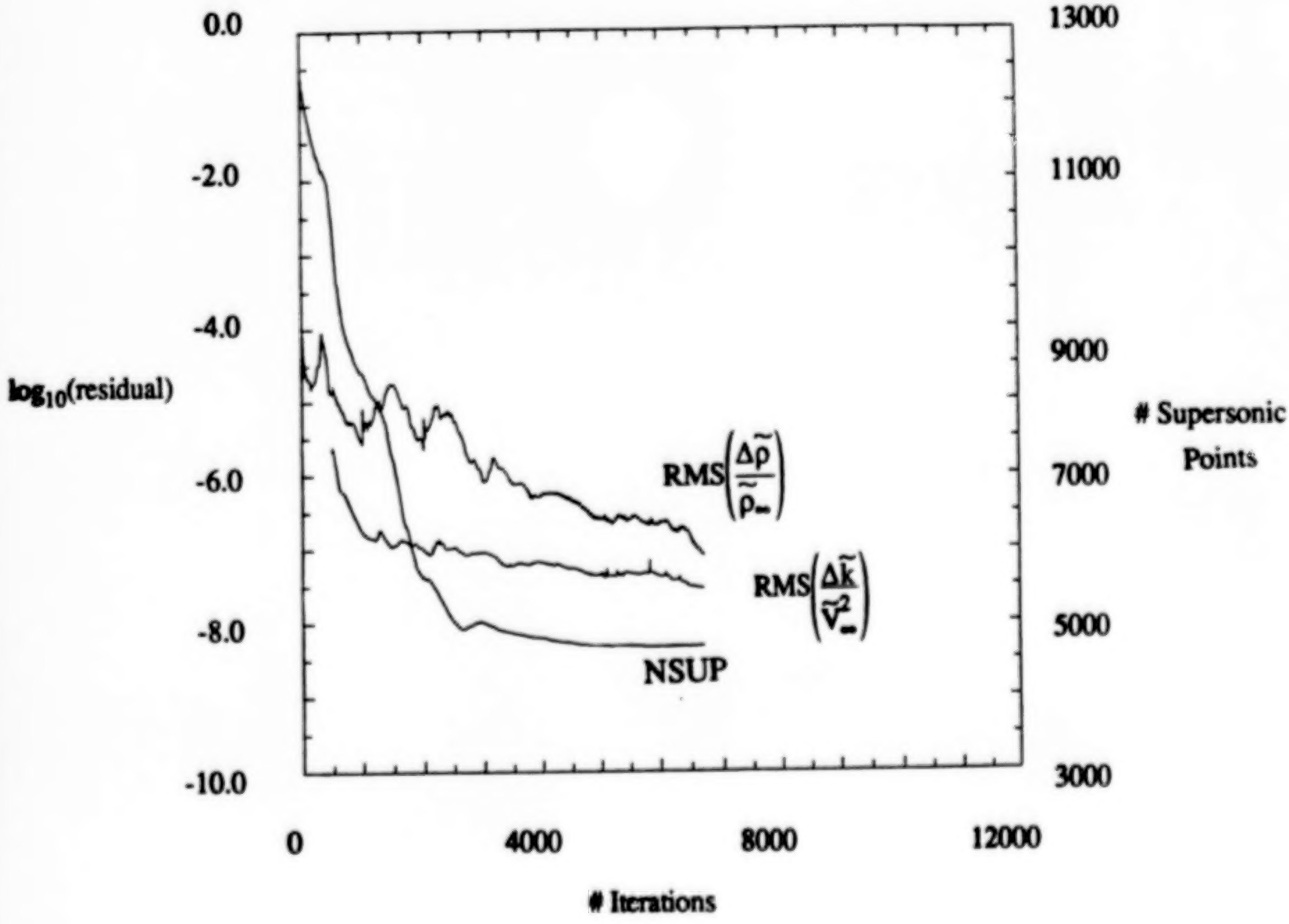

Figure 7. Convergence history for PAV-1.5 cascade computation.

In Figure 8, a hand rendering of the shock wave pattern deduced from L2F measurements has been reproduced from Reference 28, alongside the computed shock wave pattern presented as divergence of velocity contours, and Mach number contours.

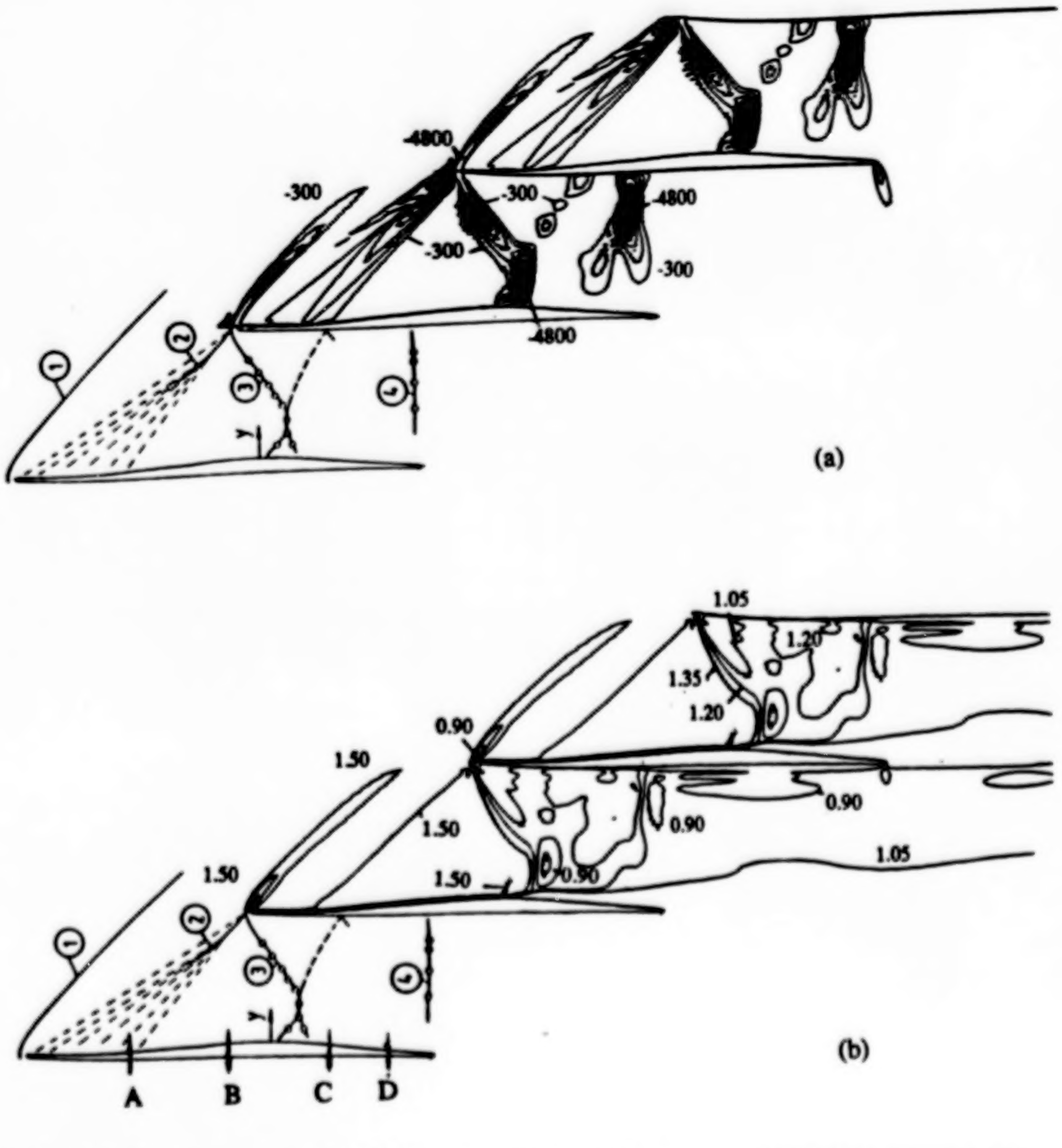

Figure 8. Shock wave pattern for PAV - 1.5 cascade. a) Divergence of velocity contours (-300 to -4800 by -500 $[s^{-1}]$). b) Mach number contours (0.9 to 1.5 by .15). In each diagram, the top two passages show computed contours. The bottom passage is the shock wave pattern deduced from flow visualization and L2F measurements, reproduced from Schreiber[26]. Stations labelled A-D correspond to .25, .50, .75 and .90 chord.

The key features of the flowfield are evident in this diagram, including the bow, lamda and passage shocks. In both experiment and computation, the bow shock is seen to impinge on the suction surface boundary layer of the adjacent passage. This gives rise to a lambda shock structure, a rapid thickening and separation of the boundary layer, and a Mach reflection which impinges on the pressure surface of the same passage. The high pressure ratio operating condition of this test case gives rise to a normal passage shock which impinges upstream of midchord on the pressure surface. This feature is also evident in both experiment and computation. The computation also shows some evidence of an oblique trailing edge shock, typical of supersonic compressor cascades at high operating pressure ratios.

In Figure 9, the predicted isentropic blade surface Mach number is plotted against the experimental values.

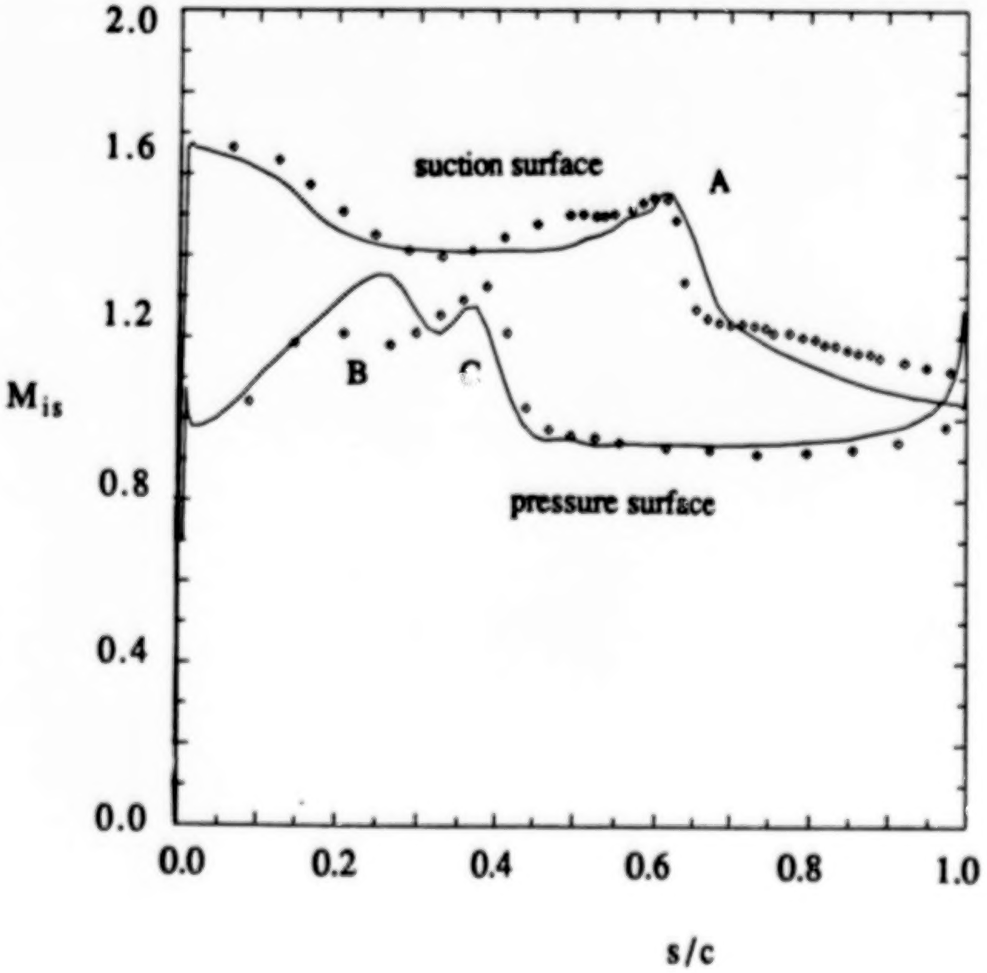

Figure 9. Isentropic blade surface Mach numbers for PAV-1.5 cascade computation. Calculated (solid line) and experimental values (symbols).

The calculation and experiment show fairly good agreement. The features labelled A, B and C in Figure 9 correspond to local compression regions where the bow shock impinges on the suction surface, the Mach reflection impinges on the pressure surface and the passage shock impinges on the pressure surface.

In Figure 10, the computed total pressure ratio is compared with traverse probe measurements at an axial location 0.09 chord downstream of the cascade exit plane.

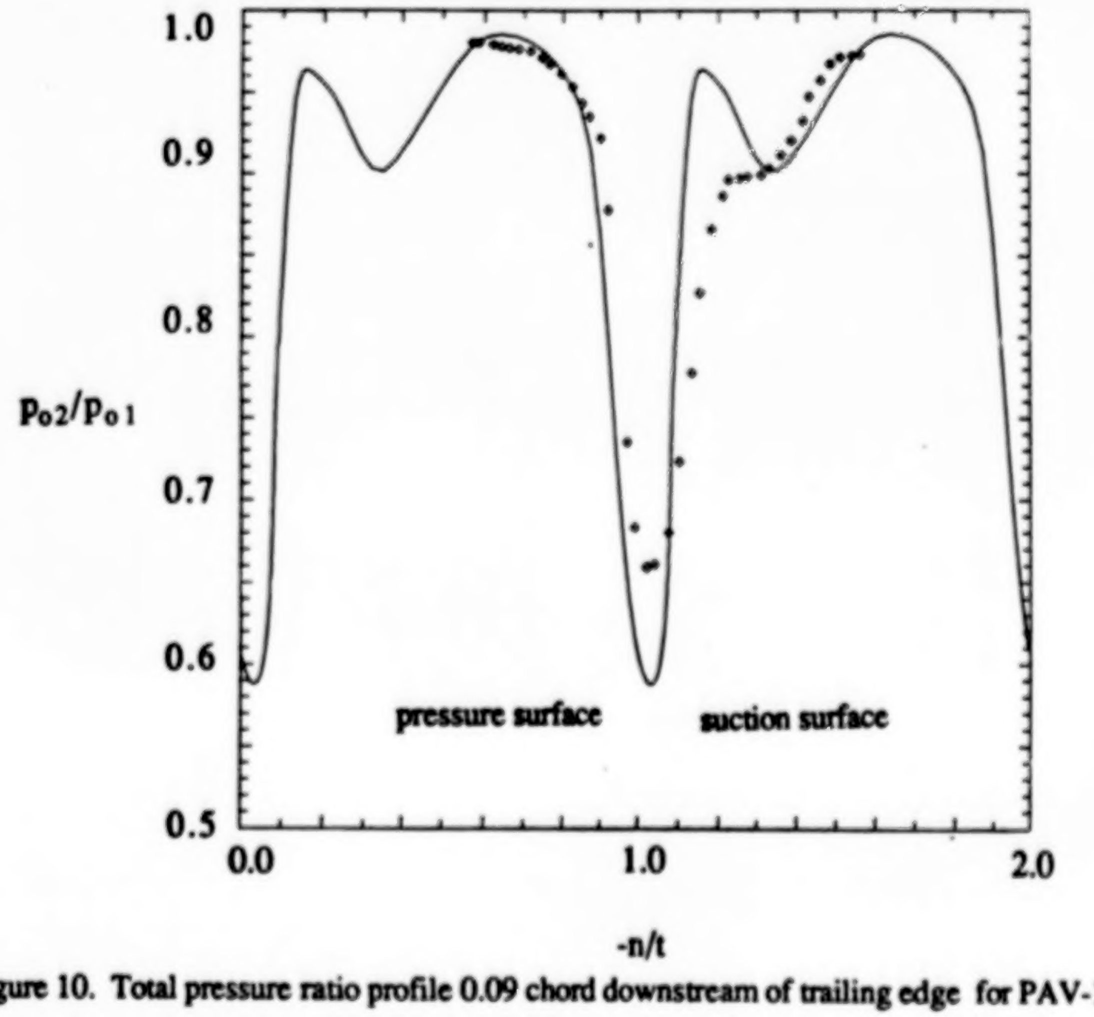

Figure 10. Total pressure ratio profile 0.09 chord downstream of trailing edge for PAV-1.5 cascade computation. Calculated (solid line) and experimental values (symbols).

The wake profile and loss distribution is reasonably well predicted, with the losses associated with the lambda shock system underpredicted. The wake centerline total pressure ratio is predicted reasonably well considering the difficulty in measurement at this location. It is noted that the results presented are not fully grid independent. Modifications in the pitchwise grid clustering near midpassage gave rise to as much as a 2% chord difference in the impingement location of the bow shock on the suction surface and a 5% chord difference in the location of the passage shock. The loss distribution aft of the blade was hardly affected, but the blade surface Mach number distributions varied noticably.

In Figure 11, computed velocity and turbulence intensity profiles at four locations on the suction and pressure surfaces are presented.

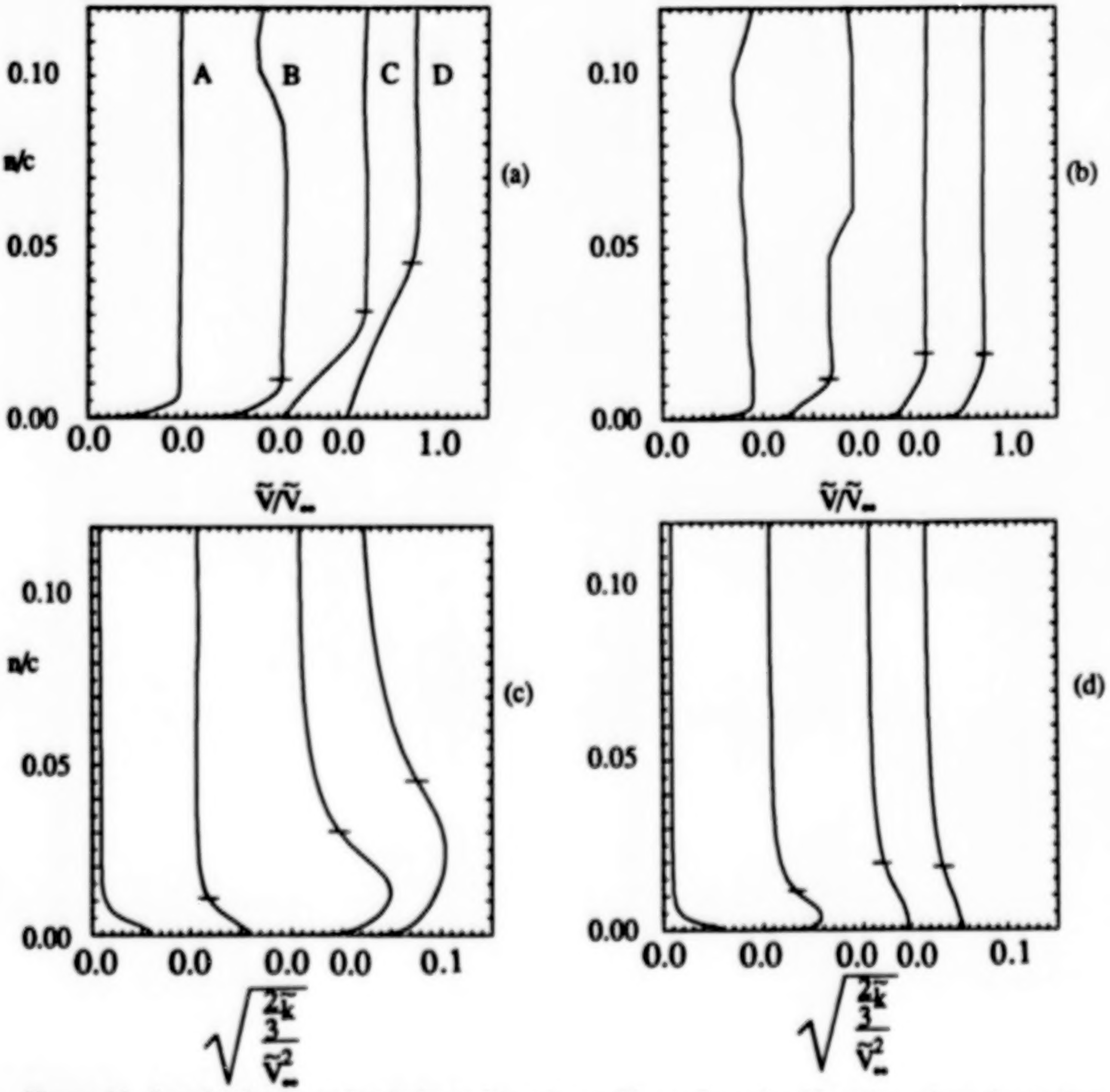

Figure 11. Local velocity and turbulence intensity profiles at four chord locations along the suction (a and c) and pressure (b and d) surfaces for the PAV-1.5 cascade computation. The hash marks correspond to the estimated boundary layer thicknesses reported by Schreiber[26]. Refer to Figure 7 for the chord locations corresponding to A-D.

Along the suction surface, the predicted boundary layer is seen to remain quite thin for this high Reynolds number flow, thickening to about .01 chord at midchord. At .75 chord the boundary layer has separated due to the bow shock impinging at .67 chord, and the boundary layer thickness is seen to have rapidly increased to approximately .03 chord. At .90 chord, the separated boundary layer has grown to .05 chord. The turbulence intensity profile behaves in a manner consistent with a boundary layer separation. Namely, aft of the onset of separation the turbulent kinetic energy boundary layer thickens rapidly and the peak in intensity appears well away from the blade surface. Careful examination of Figure 11 (c) also shows that the turbulence intensity has been amplified well outside of the boundary layer. This amplification is presumably due to the influence of the shock on the normal stress components of the production term in the turbulent kinetic energy equation.

The predicted boundary layers along the pressure surface are seen to remain quite thin along the entire blade. The influence of the passage shock at .40 chord is seen to thicken the boundary layer at .50 chord, but the flow reattaches and the boundary layer thickness remains approximately .02 chord from .75 to .90 chord. Similar trends are noticed in the local turbulence intensity profiles, with the typical peak away from the blade just aft of separation, returning very close to the wall some distance after reattachment.

The blade normal coordinate in Figure 11 is measured along grid lines which veer from perpendicular to the blade sufficiently far from the surface. The "kinks" in the velocity profiles at station B on the pressure and suction surfaces are caused by these curved grid lines intersecting the passage and bow shocks respectively.

Predicted and measured performance parameters for this cascade, operating at the given conditions are presented in Table 1.

Schreiber[26], provided measured loss coefficients at maximum attainable cascade pressure ratio for a number of operating inlet Mach numbers. For comparison, the code was run at two additional operating points within the envelope of the experimental tests. Figure 12 shows computed total pressure loss coefficients at all three operating points computed, along with the envelope of experimental loss coefficients. Computed values lie within the envelope of experimental values. It is noted, that Schreiber attributes the scatter in measured loss coefficient to variations in experimental axial velocity density ratio.

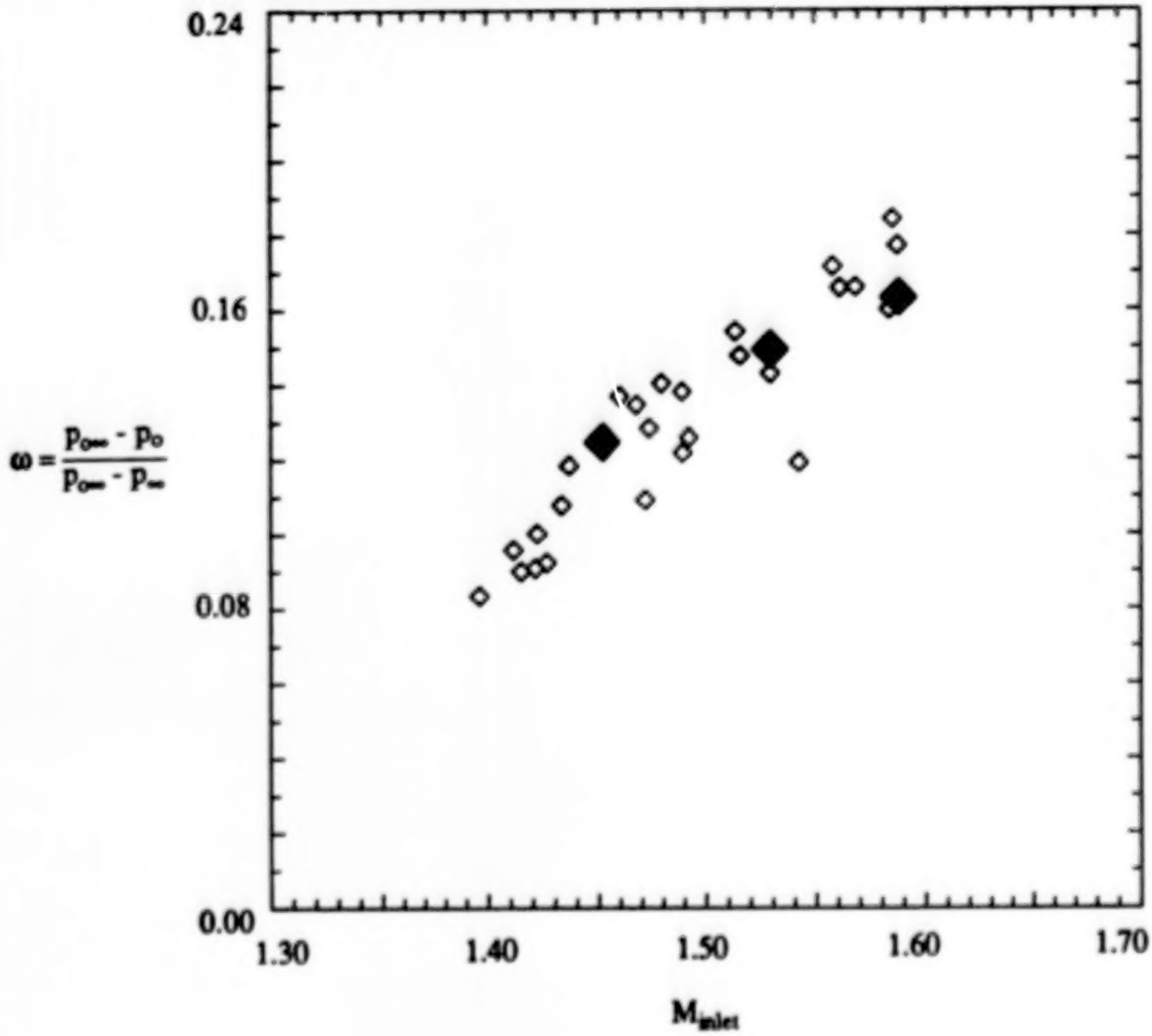

Figure 12. Total pressure loss coefficients at several cascade operating points, experiment[26] and computation (solid symbols).

ARL-Double Circular Arc Subsonic Compressor Cascade

The second cascade flow to be computed is the Applied Research Laboratory (ARL) double circular arc cascade tested at Penn State by Zierke and Deutch[29]. The computed case was tested at a negative incidence of 1.5 degrees. The working fluid was air at standard atmosphere with an inlet velocity of 32.9 m/s (inlet Mach number = 0.1). The Reynolds number based on chord was 5.0×10^5. Inlet turbulence intensity was measured at 1.8 %. The measured axial velocity ratio was measured to be between 0.97 and 1.03, indicating that the flow was close to two-dimensional.

It is noted that the present solution method, which incorporates a compressible formulation of the Navier-Stokes equations is not well suited to this low Mach number flow.

The 129 x 85 computational mesh used was generated using the GRAPE code, and is shown in Figure 13.

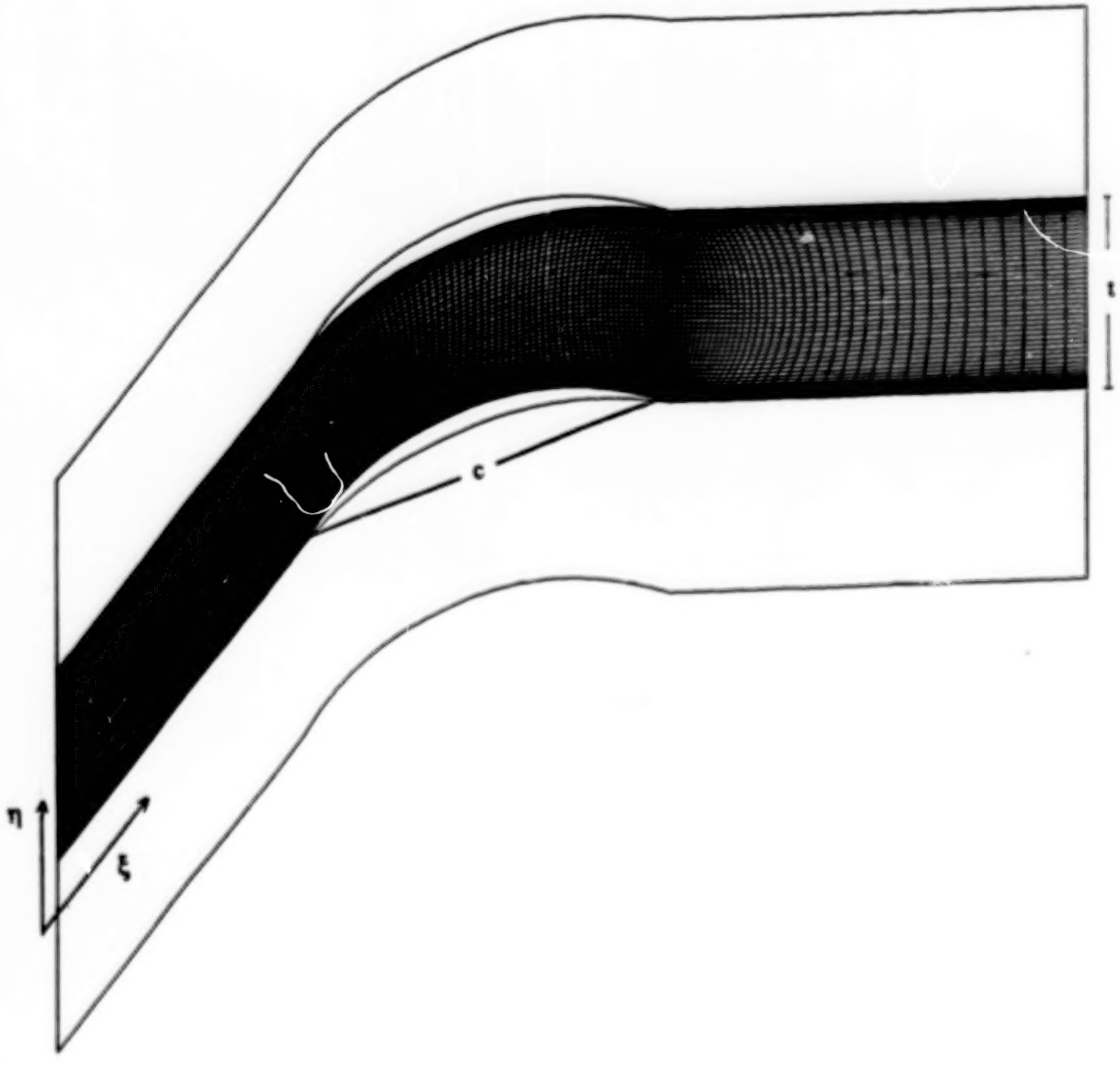

Figure 13. 129 x 85 Computational grid for the ARL DCA cascade.

Grid spacing in the blade normal direction was set to .000023 chord on the blade surfaces. This yielded values of $y^+ \leq 1$ at grid points adjacent to the walls. Except in the immediate vicinity of the leading and trailing edges, the suction and pressure surface boundary layers had at least 11 grid points with values of $y^+ \leq 20$.

It was only possible to obtain a steady solution when a coarse "preliminary" grid was used for this case. These coarse grid calculations overpredicted skin friction along the entire length of the suction surface, so the flow remain attached and a steady state solution was achieved. The more refined grid adequately resolved both inner layer and core flow regions yielding more accurate skin friction and boundary layer profiles. However, because both calculation and experiment show regions of mean flow reversal near the trailing edge, it was not possible to obtain a steady solution. The convergence history for this computation is shown in Figure 14. It took approximately 7000 iterations for this calculation to acquire a 4.5 order of magnitude drop in the RMS density residual. This corresponds to approximately 36 minutes of CPU time on the Cray Y-MP. However as shown in Figure 14, the residual changes begin to increase and then level off. This is attributed to periodic shedding of vorticity from the aft portion of the suction surface.

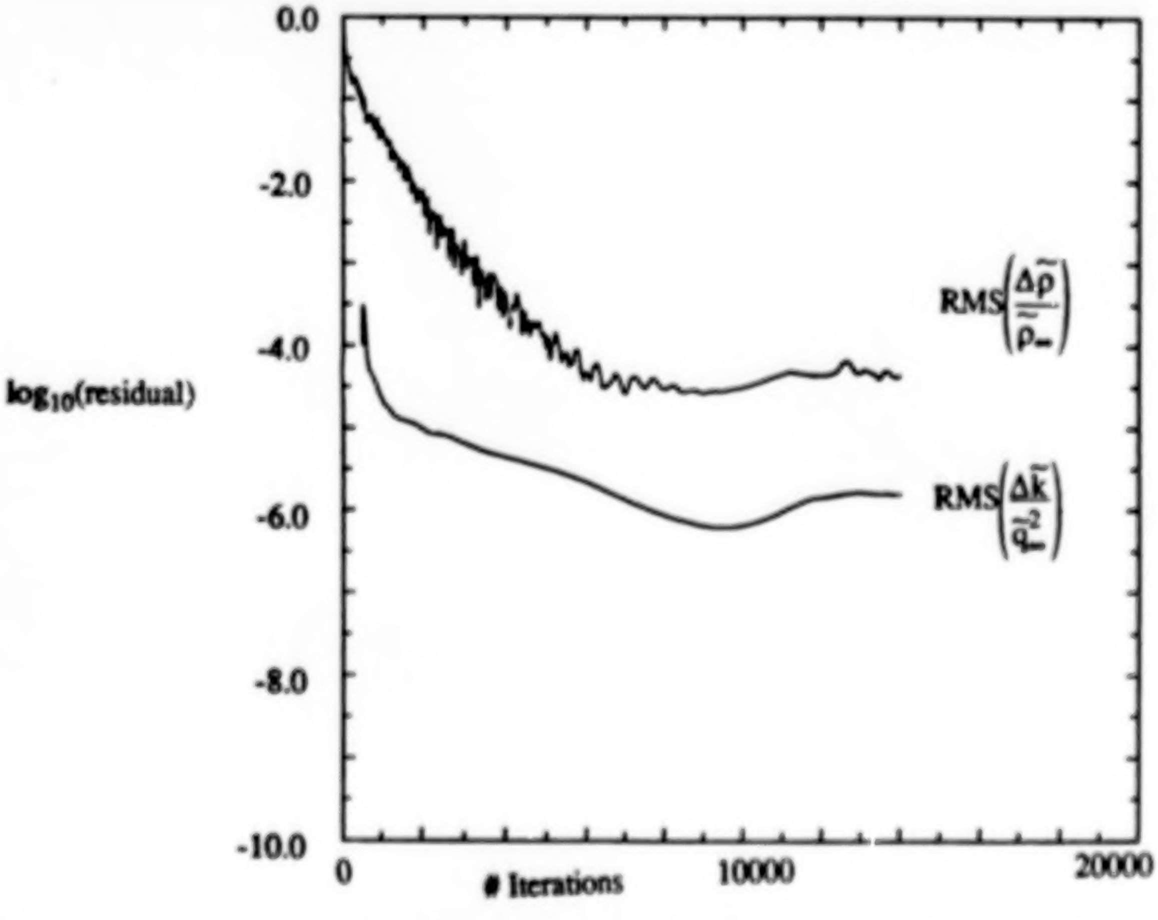

Figure 14. Convergence history for ARL DCA cascade computation.

Despite the lack of a steady state solution, the flow along the blade remained relatively unchanged after 7000 iterations except for quasi-periodic shifts in the boundary layer velocity and turbulence intensity profiles. The measured flow also showed a small region of mean backflow near the trailing edge of the blade[29], and for that reason was also probably somewhat unsteady. In Figure 15, comparison is made between computed blade surface pressure coefficient and measured values. Agreement is good along both blade surfaces.

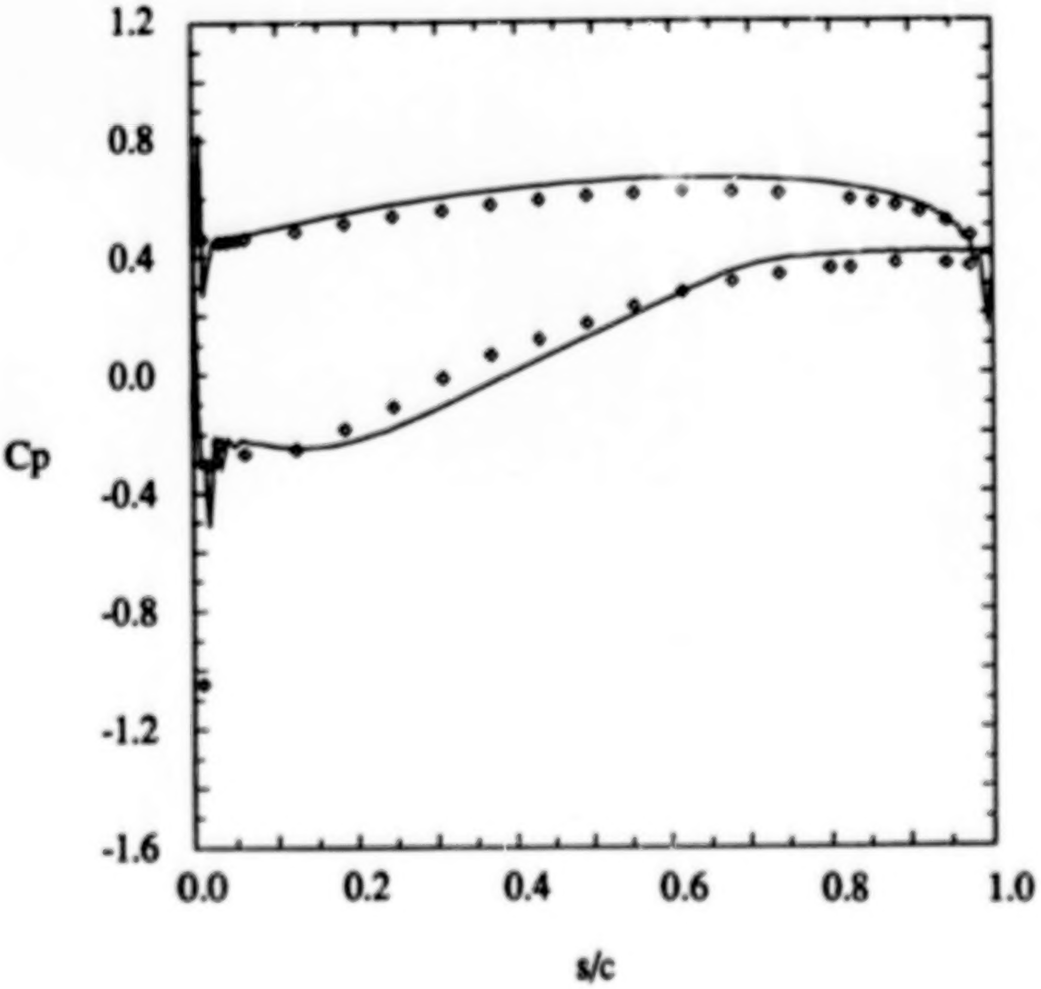

Figure 15. Pressure coefficient for ARL DCA cascade computation. Calculated (solid line) and experimental values (symbols).

The oscillations in the pressure distributions near the leading and trailing edges in Figure 15 are caused by the velocity scaling of the artificial dissipation. The H-grid used gives rise to highly skewed regions near the relatively blunt leading and trailing edges of this configuration, causing the velocity scaling presented "as is" to give rise to these oscillations. Though the cascade flow is not significantly affected by this effect, it may be worth investigating improved scaling.

In Figure 16 the predicted boundary layer profiles at three chordwise locations on the suction surface are plotted with those measured by laser doppler velocimeter. Agreement is excellent at 20 % chord and 50% chord and reasonable at 90 % chord.

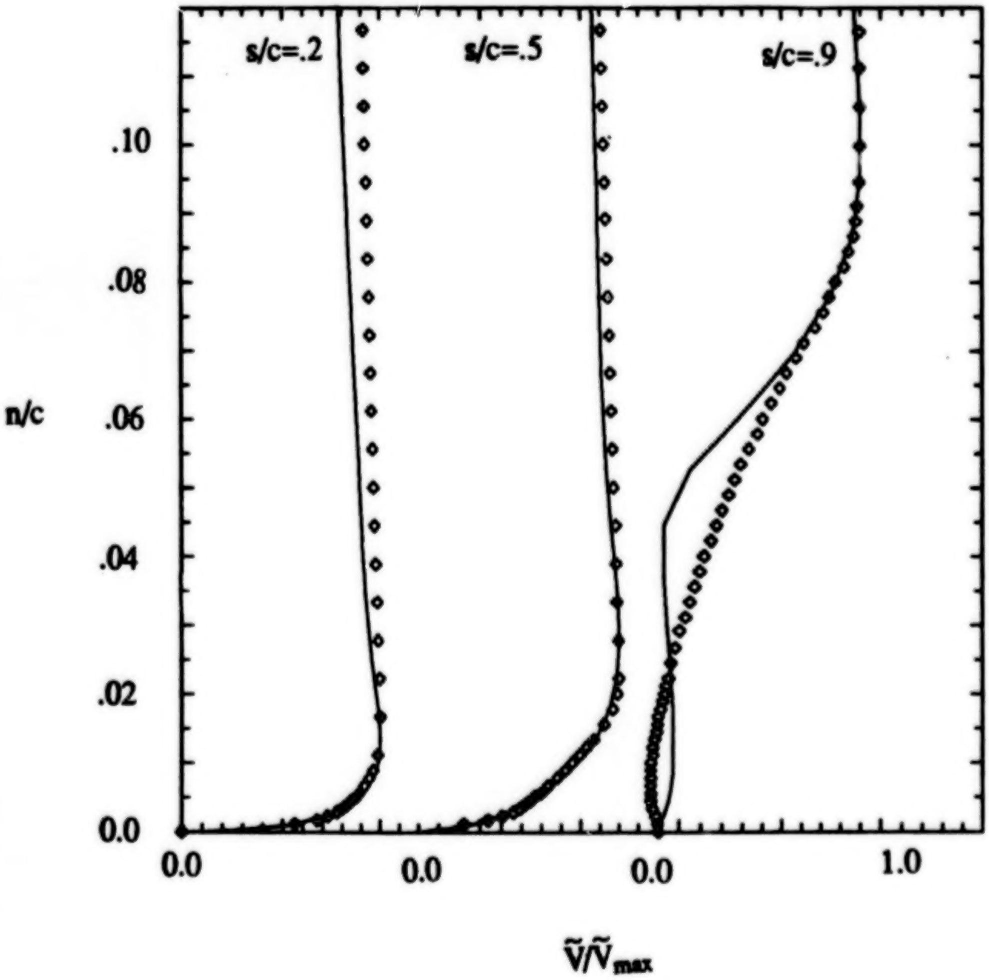

Figure 16. Boundary layer profiles at three chord locations along the suction surface for the ARL DCA cascade computation. Calculated (solid line) and experimental values (symbols).

Local turbulence intensity profiles are presented for three chordwise locations on the suction surface in Figure 17. As above, agreement between calculation and experiment is good at the first two stations, and reasonable in the aft portion of the blade.

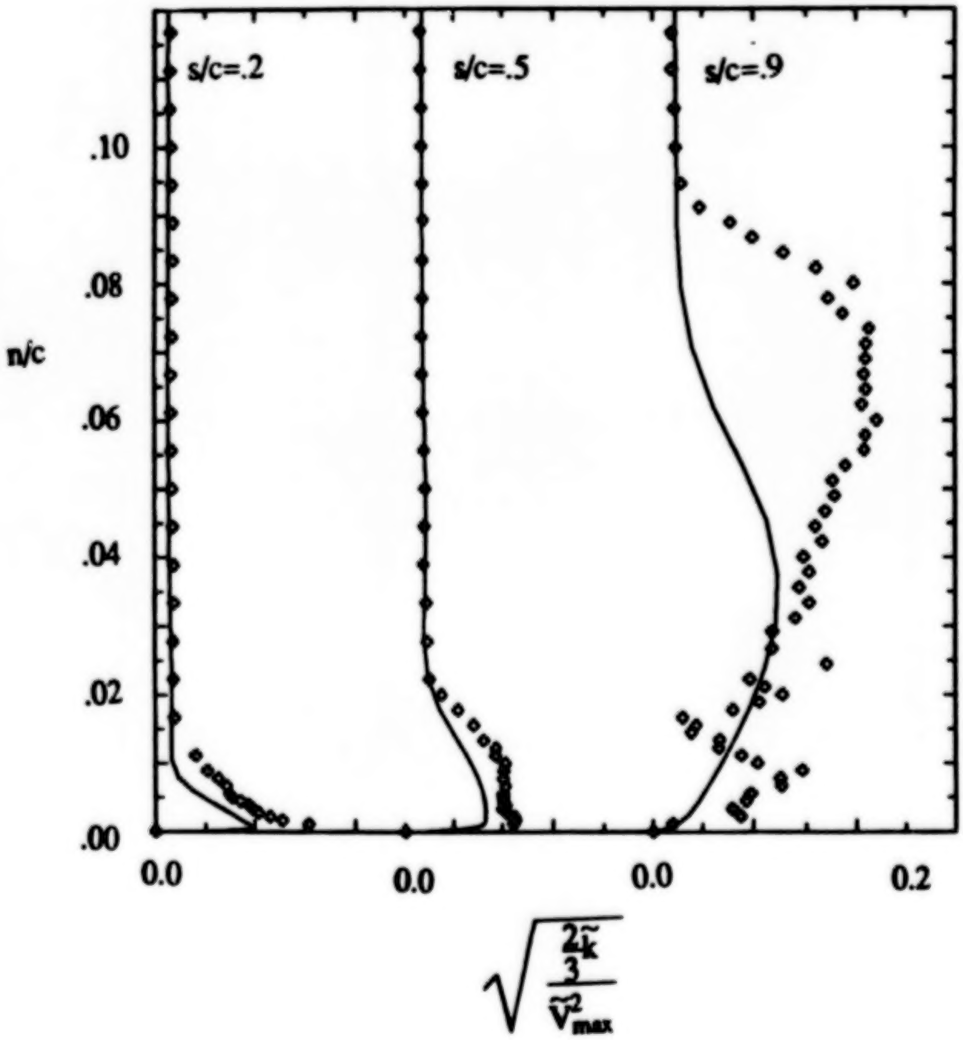

Figure 17. Local turbulence intensity profiles at three chord locations along the suction surface for the ARL DCA cascade computation. Calculated (solid line) and experimental values (symbols).

Predicted and measured performance parameters for this cascade are also presented in Table 1.

Table 1. Comparison of Cascade Flow Parameters for Computed Cases

Flowfield Parameter		PAV-1.5			ARL DCA	
	Measured	Computed	Difference	Measured	Computed	Difference
C_L^{a}	≅ 0.43	0.38	≅ 12 %	0.82	0.88	7 %
ω^{b}	0.144	.149	3.4 %	0.094	0.111	18 %
β_1	-1.8°	-1.3°	0.5°	-1.5°	prescribed	NA
β_2	2.7°	3.1°	0.4°	14.1°	13.0°	1.1°
$s/c_{sep_{ss}}$	.63	.67	6.3 %	.45	none	NA
$s/c_{sep_{ps}}$	≅ 0.40	.40	≅ 0.0	none	none	NA
AVDR	1.02	1	NA	0.97-1.03	1	NA

[a] lift coefficient computed from $C_L = \dfrac{(\text{Lift per unit span})_{\perp V_m}}{.5\rho_m V_m^2}$

[b] pressure loss coefficients computed from $\omega = \dfrac{p_{o\infty} - p_o}{.5\rho_\infty V_\infty^2}$ for ARL and $\omega = \dfrac{p_{o\infty} - p_o}{p_{o\infty} - p_\infty}$ for PAV.

CONCLUSIONS

A Navier-Stokes procedure has been developed and applied to a supersonic and a low subsonic compressor cascade. A compressible low Reynolds number form of the k-ε turbulence model was used. It was found in this study that :

1) A fully explicit treatment of the turbulence transport equations is possible. The computational overhead associated with this treatment is reasonable.

2) It is crucial to incorporate local timestep constraints based on stability analysis of the full viscous mean flow equations if the k-ε model is used for an H-grid cascade configuration.

3) The highly stretched grids needed to resolve near-wall physics warrant eigenvalue and local velocity scaling of artificial dissipation terms to improve accuracy and convergence rates.

4) Flowfield predictions were found to be good for a supersonic cascade and fair for a low subsonic cascade.

5) Overall cascade performance parameters were well predicted for the supersonic cascade but not well predicted for the low subsonic cascade, due to flowfield unsteadiness and turbulence model shortcomings.

Currently, several improvements and extensions to the technique are under way, including incorporation of multigridding, turbulence model corrections to account for streamline curvature and pressure strain, point implicit treatment of source terms in the turbulence transport equations, improved vectorization of the code and extension to three dimensions.

ACKNOWLEDGEMENTS

The first author was supported by a United States Army Research Office fellowship, through the grant DAAL03-86-G-0044, monitored by Dr. T. L. Doligalski. In addition, the following individuals were very helpful in providing assistance and suggestions in the course of carrying out this work : R. Chima, S. Connell, G. Dulikravich, H. Schreiber.

REFERENCES

1) Jameson, A., Schmidt, W., Turkel, E., "Numerical Solutions of the Euler equations by Finite Volume Methods Using Runge-Kutta Time-Stepping Schemes," AIAA Paper 81-1259 (1981).

2) Speziale, C. G., "Discussion of Turbulence Modelling: Past and Future," ICASE Report 89-58 (1989).

3) Lakshminarayana, B., "Turbulence Modelling for Complex Flows," AIAA Paper 85-1652 (1985).

4) Kirtley, K., Lakshminarayana, B., "Computation of Internal Incompressible Separated Flows Using a Space Marching Technique," AIAA Paper 85-1624 (1985).

5) Degrez, G., VanDromme, D., "Implicit Navier-Stokes Calculations of Transonic Shock/Turbulent Boundary-Layer Interactions," from Turbulent Shear-Layer/Shock-Wave Interactions, edited by J. Delery, IUTAM Symposium, Palaiseau, France, Springer-Verlag,1985).

6) Liu, J. S., "Navier-Stokes Cascade Analysis With the k-ε Turbulence Model," Ph.D. Thesis, MAE, Case Western Reserve University (1987).

7) Grasso, F., Speziale, C. G., "Supersonic Flow Computations by Two-Equation Turbulence Modelling," AIAA Paper 89-1951 (1989).

8) Eliasson, P., "Solutions to the Navier-Stokes Equations Using a k-ε Turbulence Model," Flygtekniska Forsoksanstalten TN 1988-19, Stockholm (1988).

9) Holmes, D. G., Connell, S. D., "Solution of the 2D Navier-Stokes Equations on Unstructured Adaptive Grids," AIAA Paper 89-1932 (1989).

10) Favre, A., "Equations des Gaz Turbulents Compressibles: 1. Formes Generales," Journal de Mechanique, Vol. 4 (1965).

11) Jones, W. P., "Models for Turbulent Flows with Variable Density and Combustion," from Prediction Methods for Turbulent Flows, edited by W. Kollmann, Hemisphere (1980).

12) Chien, K., "Predictions of Channel and Boundary-Layer Flows with a Low-Reynolds-Number Turbulence Model," AIAA Journal, Vol. 20, No.1, January (1982).

13) Coakley, T. J., "Turbulence Modelling Methods for the Compressible Navier-Stokes Equations," AIAA Paper 83-1693 (1983).

14) Nichols, R. H., "A Two-Equation Model for Compressible Flows," AIAA Paper 90-0494 (1990).

15) Hobson, G. V., Private Communication (1989).

16) Jones, W. P., Launder, B. E., "The Prediction of Laminarization With a Two-Equation Model of Turbulence," International Journal of Heat and Mass Transfer, Vol. 15 (1972).

17) Martinelli, L., "Calculation of Viscous Flows with Multigrid Methods," Ph.D. Thesis, MAE Department, Princeton University (1987).

18) Pulliam, T. H., "Artificial Dissipation Models for the Euler Equations," AIAA Journal, Vol. 24, No. 12, December (1986).

19) Caughey, D. A., Turkel, E., "Effects of Numerical Dissipation on Finite Volume Solutions of Compressible Flow Problems," AIAA Paper 88-0621 (1988).

20) Swanson, R., Turkel, E., "Artificial Dissipation and Central Difference Schemes for the Euler and Navier-Stokes Equations," NASA CR-178296 (1987).

21) Radespiel, R., Swanson, R., "An Investigation of Cell Centered and Cell Vertex Schemes for the Navier Stokes Equations," AIAA Paper 89-0548 (1989).

22) Davis, R. L., Ni, R., Carter, J. E., "Cascade Viscous Flow Analysis Using the Navier-Stokes Equations," AIAA Paper 86-0033 (1986).

23) Swanson, R., Private Communication (1990).

24) Chima, R. V., Johnson, G. M., "Efficient Solutions of the Euler and Navier-Stokes Equations With a Vectorized Multiple-Grid Algorithm," AIAA Journal, Vol. 23, No. 1, January (1985).

25) Baldwin, B. S., Lomax, H., "Thin Layer Approximation and Algebraic Model for Separated Turbulent Flows," AIAA Paper 78-257 (1978).

26) Schreiber, H. A., "Experimental Investigations on Shock Losses of Transonic and Supersonic Compressor Cascades," AGARD CP-401, Paper No. 11 (1988).

27) Sorenson, R. L., "A Computer Program to Generate Two-Dimensional Grids About Airfoils and Other Shapes by the Use of Poisson's Equation," NASA TM-81198 (1980).

28) Gorski, J., "Generation of H-Type Grids Using the GRAPE Code," Internal Memo, Department of Aerospace Engineering, Penn State University (1983).

29) Zierke, W. C., Deutsch, S., "The Measurement of Boundary Layers on a Compressor Blade in Cascade: Part 4 -- Flow Fields for Incidence Angles of -1.5 and -8.5 Degrees," ASME Paper 89-GT-72 (1989).

Flux-Vector Splitting for the 1990s

Bram van Leer

The University of Michigan
Department of Aerospace Engineering
Ann Arbor, MI 48109-2140

Abstract

The development of flux-vector splitting through the 1970s and 1980s is reviewed. Attention is given to the diffusive nature of flux-vector splitting, which makes it an undesirable technique for approximating the inviscid fluxes in a Navier-Stokes solver. Several proposed improvements, including a brand-new one, are discussed and illustrated by a simple, yet revealing, numerical test case. Finally, an outlook for flux-vector splitting in the 1990s is presented.

1 Introduction

Flux-vector splitting is a technique for achieving upwind bias in numerical flux functions for the Euler equations. It has been very popular during the Euler era (the 1980s), but has lost much of its appeal with the rise of Navier-Stokes solvers, since it causes undesirably high errors in boundary layers. Ironically, it shares this deficiency with other flux functions that are widely used in Navier-Stokes codes [1].

Flux-vector splitting is a natural consequence of regarding a fluid as an ensemble of particles. Measured along any coordinate, some particles will move forward, other ones backward; this automatially splits the fluxes of mass, momentum and energy into forward and backward fluxes, i.e.

$$\mathbf{F} = \mathbf{F}^{+} + \mathbf{F}^{-}. \tag{1}$$

On a computational grid these split fluxes immediately allow upwind differencing:

$$\left(\frac{\partial \mathbf{F}}{\partial x}\right)_j := \frac{\mathbf{F}_j^{+} - \mathbf{F}_{j-1}^{+}}{\Delta x} + \frac{\mathbf{F}_{j+1}^{-} - \mathbf{F}_j^{-}}{\Delta x}. \tag{2}$$

A full update step with the first-order upwind flux-split scheme for the Euler equations can be regarded as an approximate way to integrate the collisionless Boltzmann equation

$$\frac{\partial \phi(q)}{\partial t} + q\frac{\partial \phi(q)}{\delta x} = 0 \tag{3}$$

for the distribution function $\phi(q)$ of the particle velocity q. For the sake of numerical simplicity the velocity distribution in practice usually is not chosen to be Maxwellian (see, however, [2]). Because of this, and the finite length of the time-step, the velocity distribution in any cell at the end of a time-step is not of the same functional form as at the start of the time-step, when it was assumed to be an "equilibrium" distribution. Replacing the final, non-equilibrium distribution by an equilibrium distribution with the same integrated mass, momentum and energy in each cell instantaneously simulates the effect of the particle collisions. Euler schemes based on flux-vector splitting may therefore be termed Boltzmann-type schemes [3].

2 A gallery of flux-vector splittings

2.1 The Beam Scheme, alias Steger-Warming splitting

The first Boltzmann-type scheme in use for integrating the Euler equations was developed for astrophysical calculations around 1970 by Kevin Prendergast [4]; it is based on a velocity distribution consisting of delta-functions, whence the name "Beam Scheme":

$$\phi(q) = \rho_s \delta[q - (u - \sigma)] + (\rho - 2\rho_s)\delta(q - u) + \rho_s \delta[q - (u + \sigma)]. \tag{4}$$

Here ρ is the density, ρ_s is the density of the particles in each side beam, u is the mass-averaged flow velocity, and σ is a dispersion velocity not less than the speed of sound. In the special case that σ equals the speed of sound, and the specific internal energy that is *not* in the form of x-translations (in the Beam Scheme a passively convected quantity) is equidistributed over the side beams, the flux splitting becomes identical to the well-known splitting of Steger and Warming [5], developed in the late 1970s without regard to a velocity distribution. This equivalence was discovered by Van Albada [6].

The Beam-Scheme interpretation is advantageous, for instance, when formulating the flux splitting for gases with an equation of state more complicated that the ideal-gas law [7].

2.2 Van Leer's splitting

The most popular splitting subsequently developed, Van Leer's [8], again is not derived from or associated with any *a priori* chosen velocity distribution, but from certain mathematical constraints. The main design features of Van Leer's splitting are:

- the split fluxes are continuously differentiable (Beam/Steger-Warming fluxes are non-differentiable in sonic and stagnation points, which is inappropriate when approximating a first-order system of conservation laws);
- for subsonic flow the Jacobians of the split fluxes have a zero eigenvalue, which accounts for crisp numerical profiles of stationary shocks.

If the second constraint is relaxed, a one-parameter family of continuously differentiable split fluxes can be generated [9]; these are the simplest possible in the sense that they are at most quartic in the Mach number, just as the Van Leer fluxes. The differences among members of this family arise only in the energy-flux splitting.

Extensions of these fluxes to real gases are also included in [9], but have been given by several other authors [7] [10].

2.3 Hänel's energy-flux splitting

The above family of energy-flux splittings includes the one originally proposed by Hänel [11]:

$$F^{\pm}_{\mathrm{energy}} = F^{\pm}_{\mathrm{mass}} H, \tag{5}$$

where H is the specific total enthalpy. Advantages of this formula are:

- it is as simple as can be;
- it admits steady Euler solutions with constant total enthalpy throughout the flow.

Hänel claims that this flux splitting, when used in Navier-Stokes calculations, gives more accurate total-enthalpy values in the boundary layer. This may have been observed for the lower flow speeds; in the hypersonic flow regime the improvement is insignificant (see further in Section 5).

3 Flux-vector splitting as an approximate Riemann solver

Flux-vector splitting can be used beyond the first-order upwind scheme; in a higher-order MUSCL-type code [12] it simply takes the same place as any "approximate Riemann solver," such as Roe's [13] or Osher's [14]. It is one more way to merge the two state vectors on the left and right side of a cell interface into one flux vector, namely, by

$$\mathbf{F}(\mathbf{U}_L, \mathbf{U}_R) = \mathbf{F}^{+}(\mathbf{U}_L) + \mathbf{F}^{-}(\mathbf{U}_R). \tag{6}$$

4 Dissatisfaction with flux-vector splitting

Dissatisfaction with flux-vector splitting in Navier-Stokes codes stems from the dissipative properties of flux-vector splitting: contact discontinuities and slip surfaces are diffused, even when these are stationary and aligned with the grid [8] [3]. This is in contrast to flux-difference splittings such as Roe's and Osher's. A serious consequence is that the attached boundary layers to be resolved by Navier-Stokes codes get artificially broadened, and adiabatic-wall temperatures become inaccurate; numerical solutions obtained with flux-difference splitting are vastly superior [1].

This can be easily understood from, for instance, the net transverse-momentum flux across the boundary layer, as computed with flux-vector splitting (B denotes bottom cell, T top cell):

$$\begin{aligned} \rho v u :&= F^{+}_{\mathrm{mass}B} u_B + F^{-}_{\mathrm{mass}T} u_T & (7) \\ &= (F^{+}_{\mathrm{mass}B} + F^{-}_{\mathrm{mass}T})\frac{u_B + u_T}{2} - (F^{+}_{\mathrm{mass}B} - F^{-}_{\mathrm{mass}T})\frac{u_T - u_B}{2}. & (8) \end{aligned}$$

When the net mass flux

$$F^{\mathrm{net}}_{\mathrm{mass}} = F^{+}_{\mathrm{mass}B} + F^{-}_{\mathrm{mass}T} \tag{9}$$

vanishes, the second term in the momentum flux still causes numerical diffusion.

5 Improvements to flux formulas

Hänel [15] has suggested to replace the above formula for the transverse-momentum flux by one borrowed from *flux-difference* splitting:

$$\rho v u := F^{\mathrm{net}}_{\mathrm{mass}} u_{\mathrm{upwind}}, \tag{10}$$

with

$$\begin{aligned} u_{\mathrm{upwind}} &= u_B \quad \text{if } F^{\mathrm{net}}_{\mathrm{mass}} \geq 0, & (11) \\ u_{\mathrm{upwind}} &= u_T \quad \text{if } F^{\mathrm{net}}_{\mathrm{mass}} < 0. & (12) \end{aligned}$$

This mixture of flux-vector splitting and flux-difference splitting prevents the numerical broadening of the boundary layer, but does not improve the accuracy of the wall temperature. It further introduces pressure irregularities across the boundary layer.

Nevertheless, the partial success of Hänel's modified transverse-momentum flux suggests that a further improvement can be obtained by introducing a similar formula for the energy flux, i.e.:

$$\rho v H := F^{\mathrm{net}}_{\mathrm{mass}} H_{\mathrm{upwind}}, \tag{13}$$

with

$$H_{\mathrm{upwind}} = H_B \quad \text{if } F^{\mathrm{vert}}_{\mathrm{mass}} \geq 0, \tag{14}$$

$$H_{\mathrm{upwind}} = H_T \quad \text{if } F^{\mathrm{vert}}_{\mathrm{mass}} < 0. \tag{15}$$

A numerical test confirms the improvement, as shown in Figures 1 and 2. Plotted are the temperature and pressure distributions from the solution to the conical-flow problem of [1], as computed with the Roe fluxes, the Van Leer fluxes, the two Hänel modifications of Equations 5 and 10, and the extra modification 13 suggested in this section. The wall temperature computed with Equation 13 is significantly closer to the correct value of 11.7 than for the other Van Leer-type splittings; unfortunately, the pressure irregularity remains. Convergence histories for the four calculations are shown in Figure 3 and indicate that the modified schemes are as robust as the original Van Leer scheme.

It is clear that we have hardly begun to investigate mixtures of flux-vector and flux-difference splitting; the success of the formula introduced in this paper suggests that there is something to gain here. The advantage of a simple blended formula over full flux-difference splitting is that it will allow a complete linearization for use in implicit schemes; for Roe's flux formula, for instance, only an incomplete linearization is acceptable in practice (see the horrendous complete formula in [16]).

6 Can pure flux-vector splitting be saved?

However promising the above improvement may be, an intriguing question still remains:

- Is it possible at all to construct a flux-vector splitting that does not diffuse a grid-aligned boundary layer?

This question can be rephrased as:

- Is it possible to split the Euler fluxes such that both F^{+}_{mass} and F^{-}_{mass} vanish with the flow speed?

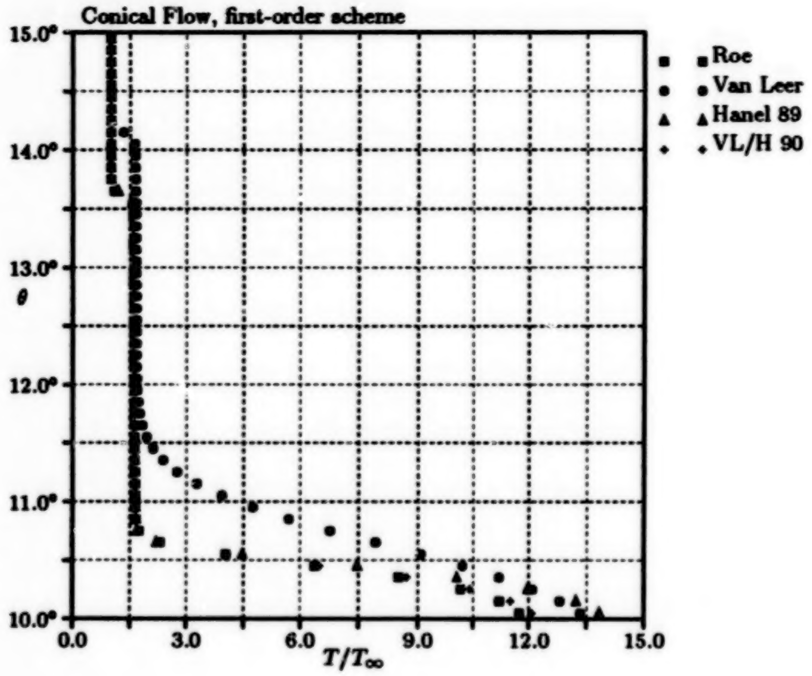

Figure 1: Numerical solution of the Navier-Stokes equations for self-similar hypersonic flow ($M_\infty = 7.95$) over a 10° cone; shown are the non-dimensional temperature distributions computed with four different flux functions.

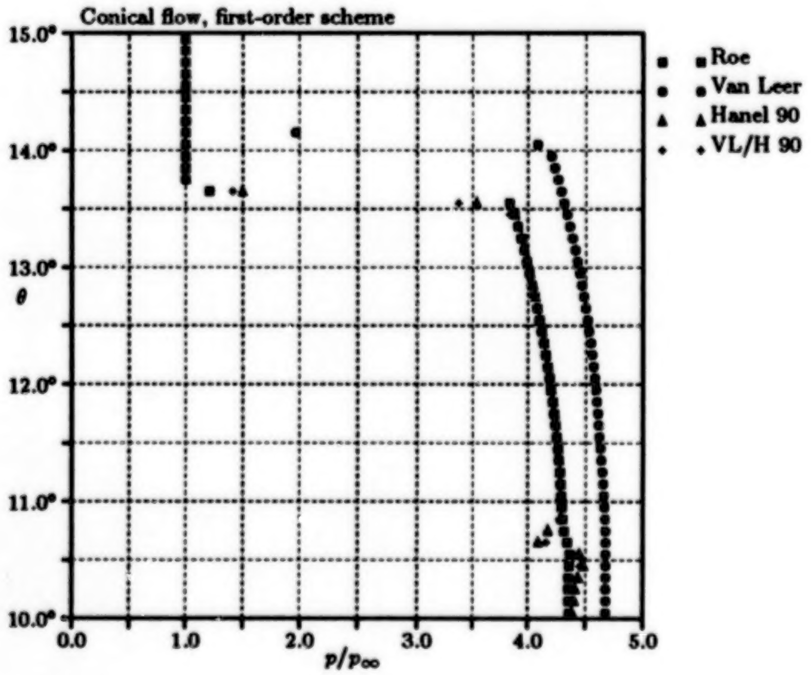

Figure 2: Same solutions as in Figure 1; pressure distributions.

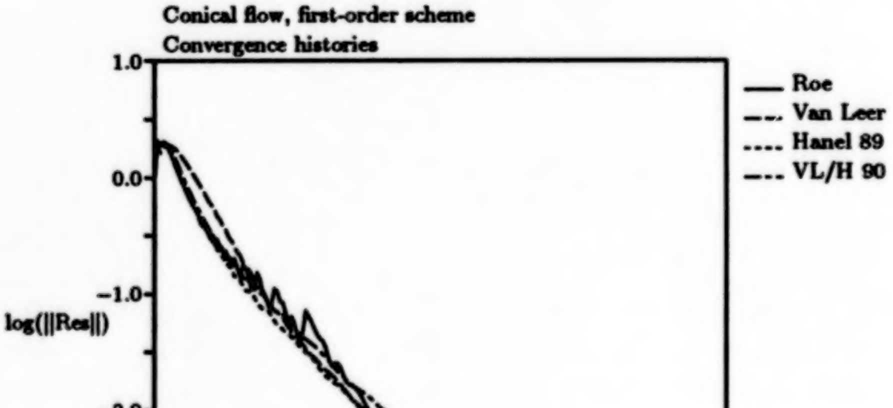

Figure 3: Residual histories of the solutions in Figures 1 and 2.

If indeed this were possible, the form of the flux splitting for small v would follow immediately from symmetry considerations:

$$\begin{aligned} F^{\pm}_{\text{mass}} &= \frac{1}{2}\rho v + O(v^2), && (16) \\ F^{\pm}_{\text{mom}\|} &= \frac{1}{2}p \pm \alpha\rho c v + O(v^2), && (17) \\ F^{\pm}_{\text{mom}\perp} &= \frac{1}{2}\rho u v + O(v^2), && (18) \\ F^{\pm}_{\text{energy}} &= \frac{1}{2}\rho H v + O(v^2), && (19) \end{aligned}$$

where c is the sound speed and α is a positive-valued free parameter. For vanishing α this splitting leads to central differencing, which will be neutrally stable for $v = 0$ and unstable for $v \neq 0$, if forward time-differencing is used. Positive values of α will introduce some dissipation, but it is clear that at least a multi-stage time-stepping algorithm must be used to render stability.

A greater problem is that the above flux values for small v must smoothly join the branches for larger v, that is, the standard Van Leer-Hänel fluxes. So far, the numerical experience is that the overall flux splitting can not be stabilized. This result, however, is not conclusive; the possibility of constructing a continuously differentiable flux splitting that reduces to the above formulas for slow flow, and is stable for all flow speeds when used in a suitable time-marching scheme, still remains open.

7 Multi-dimensional flux-vector splitting

The interpretation of flux-vector splitting as a consequence of positive and negative particle speeds included in a distribution function makes it possible to extend the concept to the multi-dimensional Euler equations in a grid-independent way. For instance, when extending the Beam Scheme into two dimensions, we may consider introducing just one "beam" moving with the average flow velocity, and a circular "front" moving, relative to the average flow, with the dispersion velocity:

$$\phi(q_x, q_y) = \rho_{\text{beam}}\delta\left(\sqrt{(q_x - u)^2 + (q_y - v)^2}\right) + \rho_{\text{front}}\delta\left(\sqrt{(q_x - u)^2 + (q_y - v)^2} - \sigma\right). \quad (20)$$

The standard two-dimensional extension of the distribution function calls for five beams; the two added beams represent the velocity dispersion in the y-direction. This introduces a directional bias in numerical solutions; in particular, shock waves oblique to the grid may be excessively smeared. The above distribution function should eliminate this effect; the penalty for its use is that the expressions for the fluxes out of a cell are more complicated.

Extension of the Van Leer fluxes in a grid-independent way is more problematic, as these do not derive from a given distribution function. It is possible, *a posteriori*, to find some velocity distribution that explains the one-dimensional Van Leer fluxes; this could then be extended in an omnidirectional way. The resulting fluxes, however, would be somewhat arbitrary, and very complicated. It would be preferable to derive the multi-dimensional version from purely algebraic considerations; this approach remains to be investigated.

8 An outlook for flux-vector splitting

Flux-vector splitting is still alive, even for Navier-Stokes applications. It may be mixed with flux-difference splitting, for the sake of preventing numerical diffusion of boundary layers, and there may still be a way to avoid this diffusion in a pure flux-vector splitting. More work needs to be done; the reward could be a simple and robust, easily linearized inviscid-flux formula, with an accuracy rivalling that of Roe's flux formula.

Acknowledgement

The numerical experiments of Section 5 were carried out by Wen-Tzong Lee, doctoral candidate in the Department of Aerospace Engineering at the University of Michigan.

References

[1] B. van Leer, J. L. Thomas, P. L. Roe, and R. W. Newsome, "A comparison of numerical flux formulas for the Euler and Navier-Stokes equations," in *AIAA 8th Computational Fluid Dynamics Conference*, 1987.

[2] S. M. Deshpande, "Kinetic theory based new upwind methods for inviscid compressible flows," AIAA Paper 86-0275, 1986.

[3] A. Harten, P. D. Lax, and B. van Leer, "Upstream differencing and Godunov-type schemes for hyperbolic conservation laws," *SIAM Review*, vol. 25, 1983.

[4] R. H. Sanders and K. H. Prendergast, "The possible relation of the three-kiloparsec arm to explosions in the galactic nucleus," *Astrophysical Journal*, vol. 188, 1974.

[5] J. L. Steger and R. F. Warming, "Flux-vector splitting of the invisicid gas dynamics equations with application to finite-difference methods," *Journal of Computational Physics*, vol. 40, pp. 263–293, 1981.

[6] G. D. van Albada, B. van Leer, and J. W. W. Roberts, "A comparative study of computational methods in cosmic gas dynamics," *Astronomy and Astrophysics*, vol. 108, 1982.

[7] M. Vinokur and Y. Liu, "Equilibrium gas flow computations II: An analysis of numerical formulations of conservation laws," AIAA Paper 88-0127, 1988.

[8] B. van Leer, "Flux-vector splitting for the Euler equations." ICASE Report 82-30, 1982.

[9] M. S. Liou, B. van Leer, and J.-S. Shuen, "Splitting of inviscid fluxs for real gases," *Journal of Computational Physics*, 1990. To appear.

[10] B. Grossman and R. W. Walters, "Analysis of flux-split algorithms for Euler's equations with real gases," AIAA Paper 87-1117-CP, 1987.

[11] D. Hänel, R. Schwane, and G. Seider, "On the accuracy of upwind schemes for the solution of the Navier-Stokes equations," AIAA Paper 87-1105-CP, 1987.

[12] W. K. Anderson, J. L. Thomas, and B. van Leer, "A comparison of finite-volume flux-vector splittings for the Euler equations," AIAA Paper 85-0122, 1985.

[13] P. L. Roe, "The use of the Riemann problem in finite-difference schemes," *Lecture Notes in Physics*, vol. 141, 1980.

[14] S. Osher and F. Solomon, "Upwind schemes for hyperbolic systems of conservation laws," *Mathematics and Computation*, vol. 38, 1982.

[15] D. Hänel and R. Schwane, "An implicit flux-vector splitting scheme for the computation of viscous hypersonic flow," AIAA Paper 89-0274, 1989.

[16] T. J. Barth, "Analysis of implicit local linearization techniques for upwind and TVD algorithms," AIAA Paper 87-0595, 1987.

ON THE APPLICATION OF ENO SCHEME WITH SUBCELL RESOLUTION TO CONSERVATION LAWS WITH STIFF SOURCE TERMS

Shih-Hung Chang*
Department of Mathematics, Cleveland State University
Cleveland, Ohio 44115

ABSTRACT

Two approaches are used to extend ENO schemes to treat conservation laws with stiff source terms. One approach is the application of Strang's time-splitting method. Here the basic ENO scheme and Harten's modification using subcell resolution, ENO/SR scheme, are extended this way. The other approach is a direct method and a modification of ENO/SR. Here the technique of ENO reconstruction with subcell resolution is used to locate the discontinuity within a cell and the time evolution is then accomplished by solving the differential equation along characteristics locally and advancing in the characteristic direction. This scheme is denoted ENO/SRCD. All the schemes are tested on the equation of LeVeque and Yee (NASA TM 100075, 1988) modeling reacting flow problems. Numerical results show that these schemes handle this intriguing model problem very well, especially with ENO/SRCD which produces perfect resolution at the discontinuity.

1. INTRODUCTION

Recently, in studying numerical methods for reacting flow problems, LeVeque and Yee (ref.5) considered certain fundamental questions concerning the extension of current finite difference techniques developed for non-reacting flows to reacting flows. Namely, can one: (i) develop stable methods, (ii) obtain "high resolution" results with sharp discontinuities and second order accuracy in smooth regions, and (iii) obtain the correct jumps at the correct locations? They introduced and studied the following one-dimensional scalar conservation law with parameter-dependent source term

$$u_t + u_x = \psi(u), \tag{1}$$

$$\psi(u) = -\mu\, u\,(u - \frac{1}{2})\,(u - 1), \tag{2}$$

where μ is a parameter. This equation becomes stiff when the parameter μ is large. Although this linear advection equation with a source term represents only a simple model of reacting flow problems, by studying its numerical solutions one would encounter some of the difficulties sure to occur in solving more realistic models.

---

*Research was partially supported under Cleveland State University RCAC Grant, Ohio OBOR Grant in the Research Challenge Program, and NASA Space Act Agreement C99066G while the author was in residence at the Institute for Computational Mechanics in Propulsion (ICOMP), NASA Lewis Research Center, Cleveland, Ohio 44135

In their study, two different approaches were used to construct second order accurate numerical methods. One approach was to use a modification of MacCormack's predictor-corrector method for conservation laws (ref.6), together with two TVD-like versions with appropriate limiters (ref.8,9). The other approach was based on the second order accurate Strang's time-splitting method (ref.7). Their numerical tests revealed that stable and second order schemes can be devised by using either of these approaches. However, in studying the ability of these methods in dealing with propagating discontinuities, it was reported that for a certain reasonably fixed mesh and for the very stiff case, all the methods produced solutions that look reasonable and yet are completely wrong, because the discontinuities are in the wrong locations. Their investigation pointed out that the main difficulty is the smearing of the discontinuity in the spatial direction, which in turn introduced a nonequilibrium state into the calculation. To avoid this difficulty, it will be necessary to increase the resolution near the discontinuity, at least for the purpose of evaluating $\psi(u)$.

The purpose of this paper is to show that numerical methods can be devised to overcome the above mentioned difficulties. We will demonstrate this by extending ENO schemes to treat conservation laws with source terms. We will construct numerical schemes which, when applied to Eq.(1), will produce stable solutions with excellent resolutions at the correct locations of discontinuities. We choose to describe the extensions for the following equation

$$u_t + a\,u_x = \psi(u), \qquad a > 0, \tag{3}$$

where the source term $\psi(u)$ arises from the chemistry of the reacting species. It can be handled similarly for $a < 0$.

The basic ENO scheme (ref.4) depends on an essentially non-oscillatory reconstruction procedure. Harten (ref.3) recently modified this procedure using subcell resolution. The notion of subcell resolution is based on the observation that unlike point values, cell averages of a discontinuous piecewise-smooth function contain information about the exact location of the discontinuity within the cell. Using this observation in his study of conservation laws, Harten (ref.3) obtained a modification of the basic ENO scheme, which he denoted ENO/SR, achieving significant improvement in the resolution of contact discontinuities. Basically, when good approximations to the locations of discontinuities inside the cells are obtained, it is then possible to have good reconstruction of the solution at each time step. Here we will also demonstrate that when the information on the location of the discontinuity is used in treating the source term, significant improvement in numerical results can be obtained.

One approach that we use to extend ENO and ENO/SR is the application of Strang's time-splitting method(ref.7), in which one alternates between solving the conservation law without the source term and the ordinary differential equation modeling the chemistry. The other approach is a direct method and a modification of ENO/SR. Here we use the technique of ENO reconstruction with subcell resolution to locate the discontinuity within a cell and then accomplish the time evolution by solving the differential equation along characteristics locally and advancing in the characteristic direction. Since the subcell resolution and the characteristic direction are essential in the design of this scheme, it is denoted ENO/SRCD. In ref.1, ENO/SRCD was originally implemented using the time-splitting method.

In section 2, we will first describe the construction of ENO/SRCD and then the extensions of ENO and ENO/SR schemes for Eq.(3). In section 3, we present the numerical results obtained from using these schemes on the model problem of LeVeque and Yee (ref.5). A conclusion will be given in section 4.

2. CONSTRUCTION OF THE SCHEMES

We observe that along the characteristic $x = x_0 + at$, the solution to (3) evolves according to the ODE

$$\frac{d}{dt}u(x_0 + at, t) = \psi(u(x_0 + at, t)), \tag{4}$$

with initial data $u(x_0, 0)$. In the scheme ENO/SRCD, this equation will be solved approximately from the time step t_n to t_{n+1}. At t_n, suppose that we have obtained the numerical solution $v^n = \{v_j^n\}$, where v_j^n represents an approximation to $\overline{u}_j^n$, the cell average of u over $[x_{j-\frac{1}{2}}, x_{j+\frac{1}{2}}]$ at t_n. Then, to obtain v^{n+1}, we use the following steps:

1. Obtain a reconstruction, $R(x; v^n)$, of the solution from the given values v^n.
2. Locate the discontinuity, if any, within each cell using the subcell resolution technique and modify the reconstruction $R(x; v^n)$ to obtain $\hat{R}(x; v^n)$.
3. Advance $\hat{R}(x; v^n)$ via the ODE (4) along the characteristics to the t_{n+1} level and then take cell averages to complete v^{n+1}.

In ENO/SRCD, steps 1 and 2 will follow the ENO reconstruction procedure with subcell resolution of Harten (ref.3). The reconstructed solution function $R(x; v^n)$ here is a piecewise quadratic polynomial obtained by using the primitive function approach. For the sake of completeness, we will describe in straightforward terms the procedures used. For more details and general discussions on reconstruction with subcell resolution, see ref.3.

Step 1. ENO Reconstruction

Over each cell $[x_{j-\frac{1}{2}}, x_{j+\frac{1}{3}}]$, choose i such that $j - 2 \leq i \leq j$ and minimizes the following:

$$|v_{i+2}^n - 2v_{i+1}^n + v_i^n| = min\,\{|v_{k+2}^n - 2v_{k+1}^n + v_k^n| : k = j-2, j-1, j\}.$$

Let $R_j(x; v^n)$ denote the reconstructed quadratic polynomial over this cell. Then

$$R_j(x; v^n) = a_j + s_j\,(x - x_j) + \frac{1}{2}\,c_j\,(x - x_j)^2, \tag{5}$$

where

$$\begin{aligned} c_j &= (v_{i+2}^n - 2\,v_{i+1}^n + v_i^n)/(\Delta x)^2, \\ s_j &= (v_{i+1}^n - v_i^n)/\Delta x + (j - i - \frac{1}{2})\,c_j\,\Delta x, \\ a_j &= v_j^n - c_j\,(\Delta x)^2/24. \end{aligned} \tag{6}$$

Step 2. Modification by Subcell Resolution

To detect a discontinuity in a cell $[x_{j-\frac{1}{2}}, x_{j+\frac{1}{2}}]$, we define

$$F_j(z) = \frac{1}{\Delta x}\left[\int_{x_{j-\frac{1}{2}}}^{z} R_{j-1}(x;v^n)\,dx + \int_{z}^{x_{j+\frac{1}{2}}} R_{j+1}(x;v^n)\,dx\right] - v_j^n. \tag{7}$$

In our numerical experiment, the following criterion is used. If

$$|s_j| > |s_{j-1}|,\ |s_j| > |s_{j+1}|, \quad \text{and} \quad F_j(x_{j-\frac{1}{2}})\,F_j(x_{j+\frac{1}{2}}) \le 0, \tag{8}$$

we consider that there is a discontinuity at θ_j in this cell satisfying

$$F_j(\theta_j) = 0. \tag{9}$$

The location θ_j can then be approximated by using any standard root-finding method. We simply use the bisection method in our experiment.

Now, if there is a discontinuity inside the cell at θ_j, a modified reconstruction $\hat{R}_j(x;v^n)$ is used , where

$$\hat{R}_j(x;v^n) = \begin{cases} R_{j-1}(x;v^n), & x_{j-\frac{1}{2}} \le x < \theta_j, \\ R_{j+1}(x;v^n), & \theta_j < x \le x_{j+\frac{1}{2}}. \end{cases}$$

Otherwise, we use

$$\hat{R}_j(x;v^n) = R_j(x;v^n).$$

Step 3. Time Evolution and Cell Averaging

Consider the case $a\,\Delta t < \Delta x$ and that there exists a discontinuity at θ_j inside the cell $[x_{j-\frac{1}{2}}, x_{j+\frac{1}{2}}]$ with

$$\theta_j \le x_{j+\frac{1}{2}} - a\,\Delta t,$$

as shown in Figure 1. At the t_n level, $R_{j-1}(x;v^n)$ is used as the solution to the left of θ_j and $R_{j+1}(x;v^n)$ to the right of θ_j. Since the solution to Eq.(3) evolves according to the ODE (4) along characteristics, we can obtain approximate solution values at the t_{n+1} level by solving Eq.(4) and advancing in the characteristic direction. If $w(x,t_{n+1})$ denotes the solution of Eq.(4) at t_{n+1} over $[x_{j-\frac{1}{2}}, x_{j+\frac{1}{2}}]$, obtained by using the initial values $R_{j-1}(x;v^n)$ on $[x_{j-\frac{1}{2}} - a\,\Delta t, \theta_j)$ and $R_{j+1}(x;v^n)$ on $(\theta_j, x_{j+\frac{1}{2}} - a\,\Delta t]$, the numerical solution v_j^{n+1} is then an approximation to

$$\frac{1}{\Delta x}\int_{x_{j-\frac{1}{2}}}^{x_{j+\frac{1}{2}}} w(x,t_{n+1})\,dx.$$

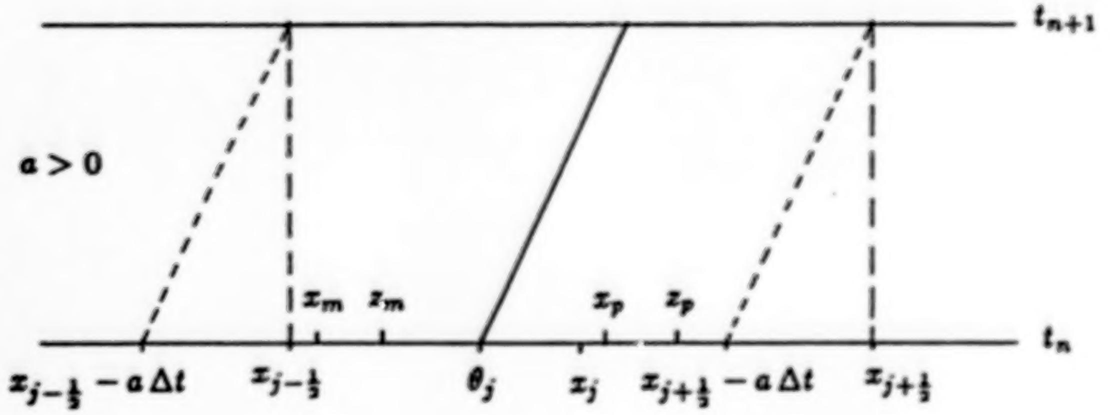

Fig. 1. The case $\theta_j \le x_{j+\frac{1}{2}} - a\,\Delta t$

In our present implementation we use the following simple computation. Let x_m and x_p denote the midpoints in the intervals $(x_{j-\frac{1}{2}} - a\,\Delta t, \theta_j)$ and $(\theta_j, x_{j+\frac{1}{2}} - a\,\Delta t)$ respectively (see Fig. 1). Then we compute

$$\begin{aligned} w_m &= R_{j-1}(x_m; v^n) + \Delta t\, \psi(R_{j-1}(x_m; v^n)), \\ w_p &= R_{j+1}(x_p; v^n) + \Delta t\, \psi(R_{j+1}(x_p; v^n)), \\ v_j^{n+1} &= \left[w_m\,(\theta_j - x_{j-\frac{1}{2}} + a\,\Delta t) + w_p\,(x_{j+\frac{1}{2}} - \theta_j - a\,\Delta t) \right] / \Delta x. \end{aligned} \tag{10}$$

In the above computation, w_m and w_p are obtained from the Euler's method. If the modified Euler method is desired, for example, one simply computes

$$\begin{aligned} w_m^* &= R_{j-1}(x_m; v^n) + \Delta t\, \psi(R_{j-1}(x_m; v^n)), \\ w_m &= R_{j-1}(x_m; v^n) + \frac{\Delta t}{2} \left[\psi(R_{j-1}(x_m; v^n)) + \psi(w_m^*) \right], \end{aligned}$$

similarly for w_p^* and w_p, and then v_j^{n+1} by (10). Other locations of θ_j and the cases with regions without discontinuities can be treated similarly and easily. It is quite simple to modify the above scheme to obtain higher order versions.

The extension of ENO and ENO/SR schemes to treat conservation laws with source terms will be done by using Strang's time-splitting method (ref.7). With respect to Eq.(3), the numerical solution v^{n+1} is computed from v^n by

$$v^{n+1} = S_\psi(\frac{\Delta t}{2})\, S_f(\Delta t)\, S_\psi(\frac{\Delta t}{2})\, v^n, \tag{11}$$

where $S_f(\Delta t)$ represents the numerical solution operator for the conservation law without the source term

$$u_t + a\,u_x = 0, \qquad a > 0, \tag{12}$$

over a time step Δt, and $S_\psi(\frac{\Delta t}{2})$ represents the numerical solution operator for the ordinary differential equation

$$u_t = \psi(u) \tag{13}$$

over $\Delta t/2$. Thus the basic ENO and ENO/SR are used here as the operator $S_f(\Delta t)$. The extended schemes will still be denoted ENO and ENO/SR respectively.

The following second order version of the ENO scheme has been used in ref.2. In our computational experiment, it produces slightly better results than other second order versions.

ENO Scheme:

For the operator $S_f(\Delta t)$, we use

$$S_f(\Delta t)\,v_j^n = v_j^n - \frac{\Delta t}{\Delta x}\left(\bar{f}_{j+\frac{1}{2}} - \bar{f}_{j-\frac{1}{2}}\right), \tag{14}$$

where

$$\begin{aligned}\bar{f}_{j+\frac{1}{2}} = \bar{f}^{ENO}_{j+\frac{1}{2}} = \frac{1}{2}\Big[&f^R\big(\tilde{v}_j(x_{j+\frac{1}{2}},t_n),\tilde{v}_{j+1}(x_{j+\frac{1}{2}},t_n)\big)\\ &+f^R\big(\tilde{v}_j(x_{j+\frac{1}{2}},t_{n+1}),\tilde{v}_{j+1}(x_{j+\frac{1}{2}},t_{n+1})\big)\Big],\end{aligned} \tag{15}$$

with

$$\begin{aligned}\tilde{v}_j(x_{j+\frac{1}{2}},t_n) &= v_j^n + \frac{\Delta x}{2}\,s_j,\\ \tilde{v}_{j+1}(x_{j+\frac{1}{2}},t_n) &= v_{j+1}^n - \frac{\Delta x}{2}\,s_{j+1},\\ \tilde{v}_j(x_{j+\frac{1}{2}},t_{n+1}) &= v_j^n + \frac{\Delta x}{2}\,s_j - \Delta t\,a\,s_j,\\ \tilde{v}_{j+1}(x_{j+\frac{1}{2}},t_{n+1}) &= v_{j+1}^n - \frac{\Delta x}{2}\,s_{j+1} - \Delta t\,a\,s_{j+1},\end{aligned}$$

where the s_j's used in the above computation come from (6) in step 1 and $f^R(v_L,v_R)$ denotes the flux at the origin in a Riemann problem with v_L to the left and v_R to the right.

Now, let us describe the operator $S_\psi(\Delta t)$. Here we will follow steps 1 and 2 to find the discontinuity θ_j, if any. Let us use the same notations introduced before and refer to Fig.1. Also, let z_m and z_p denote the midpoints in the intervals $(x_{j-\frac{1}{2}},\theta_j)$ and $(\theta_j,x_{j+\frac{1}{2}})$ respectively. Then, for approximating cell averages and for the case $\theta_j \le x_{j+\frac{1}{2}} - a\,\Delta t$, we use

$$\begin{aligned}S_\psi(\Delta t)\,v_j^n = v_j^n + \frac{\Delta t}{2\,\Delta x}\Big[&\psi(R_{j-1}(z_m;v^n))\,(\theta_j - x_{j-\frac{1}{2}}) + \psi(w_m)\,(\theta_j - x_{j-\frac{1}{2}} + a\,\Delta t)\\ &+\psi(R_{j+1}(z_p;v^n))\,(x_{j+\frac{1}{2}} - \theta_j) + \psi(w_p)\,(x_{j+\frac{1}{2}} - \theta_j - a\,\Delta t)\Big],\end{aligned} \tag{16}$$

where w_m and w_p are the same as in (10). Again, other situations are handled similarly.

The resulting algorithm then takes the following form:

$$v_j^{n+1} = S_\psi(\frac{\Delta t}{2})\, S_f(\Delta t)\, S_\psi(\frac{\Delta t}{2})\, v_j^n. \tag{17}$$

ENO/SR Scheme:

The operator $S_f(\Delta t)$ is now replaced by Harten's second order ENO scheme with subcell resolution (ref.3). It is given in the form of Eq.(14) with

$$\bar{f}_{j+\frac{1}{2}} = \bar{f}_{j+\frac{1}{2}}^{ENO} + \hat{g}_{j+\frac{1}{2}},$$

where $\bar{f}_{j+\frac{1}{2}}^{ENO}$ will be the same as in (15) and the correction term $\hat{g}_{j+\frac{1}{2}}$ is computed as follows. If the discontinuity condition (8) is not satisfied, then

$$\hat{g}_{j+\frac{1}{2}} = \frac{a}{12}(\nu - 1)(2\nu - 1)\, c_j\, (\Delta x)^2, \qquad \nu = a\,\Delta t/\Delta x;$$

else

$$\hat{g}_{j+\frac{1}{2}} = \begin{cases} \left[(\Delta x - a\,\Delta t)\,(v_j^n - a\,\Delta t\, s_j/2) - b_{j-1}(x_{j-\frac{1}{2}}, x_{j+\frac{1}{2}} - a\,\Delta t)\right]/\Delta t, \\ \qquad\qquad \text{when} \quad F_j(x_{j+\frac{1}{2}} - a\,\Delta t)\, F_j(x_{j-\frac{1}{2}}) > 0, \\ \left[b_{j+1}(x_{j+\frac{1}{2}} - a\,\Delta t, x_{j+\frac{1}{2}}) - a\,\Delta t\,(v_j^n + (\Delta x - a\,\Delta t)\, s_j/2)\right]/\Delta t, \\ \qquad\qquad \text{otherwise}, \end{cases}$$

and the expression $b_j(y_1, y_2)$ is used to mean

$$b_j(y_1, y_2) = \int_{y_1}^{y_2} R_j(x; v^n)\, dx.$$

In the above computation, all the c_j's, s_j's, and a_j's come from (6) in step 1. The operator $S_\psi(\Delta t)$ will be the same as in (16) and the final algorithm also takes the same form as in (17).

3. COMPUTATIONAL RESULTS

We use the same fixed mesh and initial data as in the model problem of LeVeque and Yee (ref.5) to test the ability of the above schemes in dealing with propagating discontinuities. Thus, we apply all the schemes to Eq.(1) together with the initial condition

$$u(x,0) = \begin{cases} 1, & \text{if} \quad x \le 0.3, \\ 0, & \text{if} \quad x > 0.3. \end{cases}$$

We take $\Delta x = 0.02$, $\Delta t = 0.015$, and the domain in x to be from 0 to 1. For comprison with ref.5, we also show the results at $t = 0.3$ and for the cases $\mu = 1$, 10, 100, and 1000. For all cases, ENO/SRCD produces a perfect resolution as shown in Figure 2. Figure 3 shows the computed results using ENO and ENO/SR schemes for $\mu = 1$, 10, and 100. Here one can see that the results from ENO/SR are also almost perfect. For the very stiff case, $\mu = 1000$, both ENO and ENO/SR fail to produce stable solutions for the above mesh in our computational experiment. However, when we reduce the size of Δt to one half of the original, i.e., $\Delta t = 0.0075$, and march 40 time steps, very good result is again obtained from ENO and perfect resolution is obtained from ENO/SR as shown in Figures 4a and 4b respectively. We understand that reducing Δt means the reduction of stiffness of the problem. The difficulty arises from the fact that in both ENO and ENO/SR schemes, the computation of the numerical flux $\overline{f}^{ENO}_{j+\frac{1}{2}}$ still produces "large" error in the spatial direction.

The computational results obtained here compare favorably to those in LeVeque and Yee (ref.5).

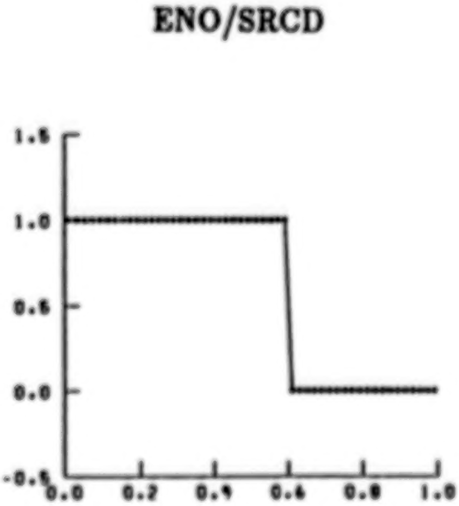

Fig. 2. Numerical results at $t = 0.3$ using ENO/SRCD scheme with discontinuous initial data and $\mu = 1, 10, 100, 1000$. $\Delta x = 0.02$, $\Delta t = 0.015$, ——: true solution, ···: computed solution

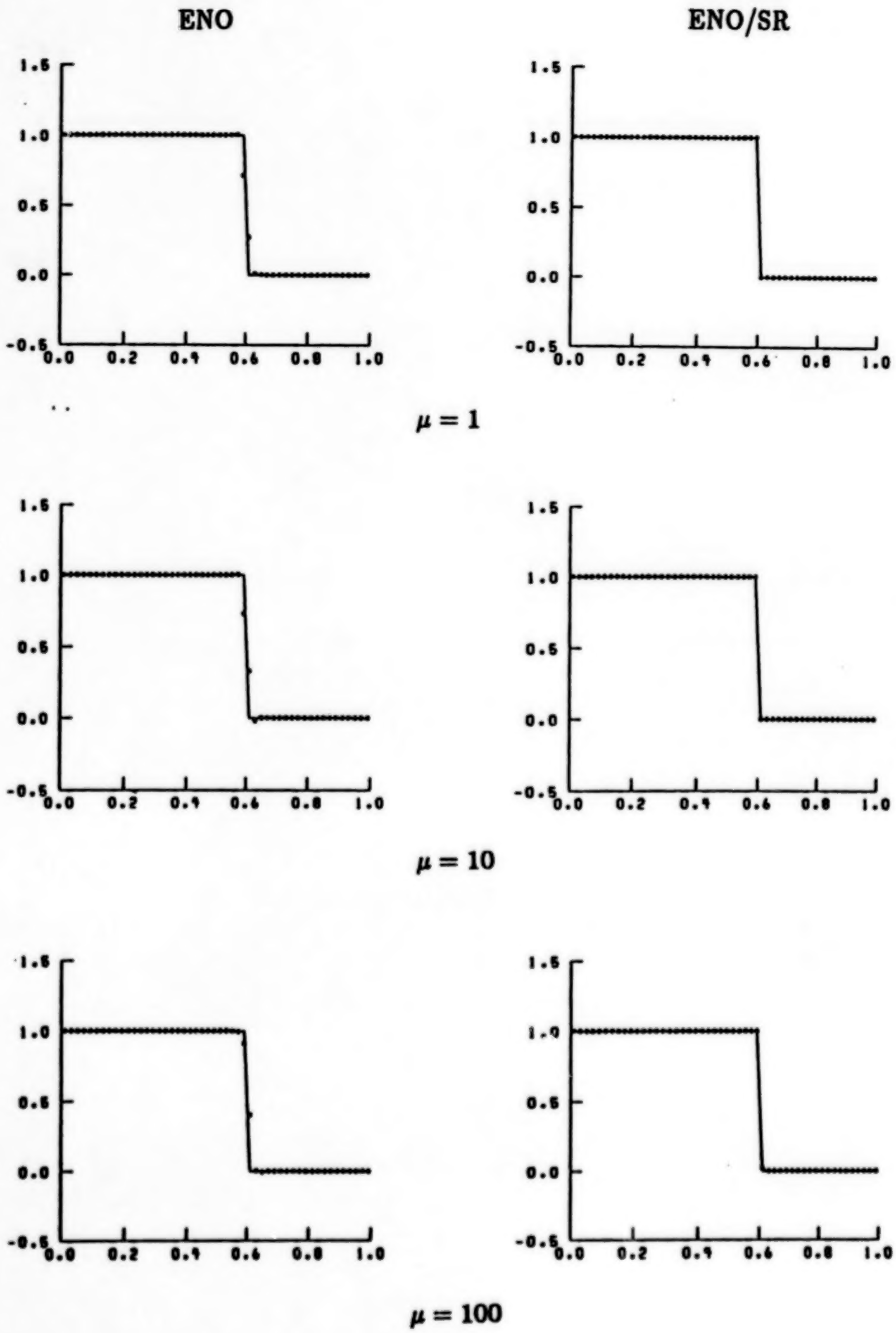

Fig. 3. Numerical results at $t = 0.3$ using ENO (first column) and ENO/SR (second column) schemes with discontinuous initial data for $\mu = 1$ (first row), $\mu = 10$ (second row), and $\mu = 100$ (third row). $\Delta x = 0.02$, $\Delta t = 0.015$, ——: true solution, ···: computed solution

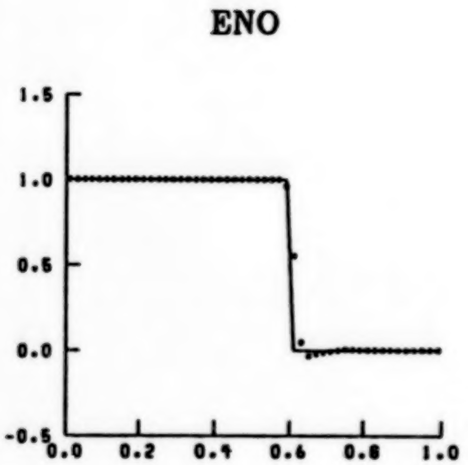

Fig. 4a. Numerical results at $t = 0.3$ using ENO scheme with discontinuous initial data and $\mu = 1000$.
$\Delta x = 0.02$, $\Delta t = 0.0075$, ——: true solution, $\cdots$: computed solution

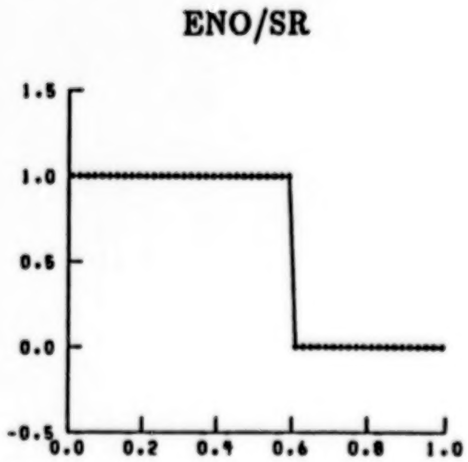

Fig. 4b. Numerical results at $t = 0.3$ using ENO/SR scheme with discontinuous initial data and $\mu = 1000$.
$\Delta x = 0.02$, $\Delta t = 0.0075$, ——: true solution, $\cdots$: computed solution

4. CONCLUSIONS

We have extended the basic ENO and Harten's ENO/SR schemes to treat conservation laws with source terms. Two approaches are used. One is to apply Strang's time-splitting method, in which one alternates between solving the conservation law without the source term and the ordinary differential equation modeling the chemistry. The other is a modification of ENO/SR and a direct method, which uses the technique of ENO reconstruction with subcell resolution to locate the discontinuity within a cell and then accomplishes the time evolution by solving the differential equation along characteristics locally and advancing in the characteristic direction. We call this scheme ENO/SRCD. All the schemes are tested on the equation of LeVeque and Yee (ref.5) modeling reacting flow problems. The ENO/SRCD scheme produces perfect resolution at the propagating discontinuity. The extensions of basic ENO and ENO/SR via time-splitting also perform very well, especially with ENO/SR showing almost perfect results, except for the very stiff case where some adjustment in the time step-size is needed.

REFERENCES

1. Chang, S.H., "On the Application of Subcell Resolution to Conservation Laws with Stiff Source Terms," NASA Technical Memorandum 102384, November 1989.
2. Chang, S.H. and Liou, M.S., "A Numerical Study of ENO and TVD Schemes for Shock Capturing," NASA Technical Memorandum 101355, September 1988.
3. Harten, A., "ENO Schemes with Subcell Resolution," J. Comp. Phys., 83(1989), pp. 148-184.
4. Harten, A., Engquist, B., Osher, S., and Chakravarthy, S., "Uniformly High Order Accurate Essentially Non-Oscillatory Schemes III," J. Comp. Phys., 71(1987), pp. 231-303.
5. LeVeque, R.J. and Yee, H.C., "A Study of Numerical Methods for Hyperbolic Conservation Laws with Stiff Source Terms," NASA Technical Memorandum 100075, March 1988.
6. MacCormack, R.W., "The Effect of Viscosity in Hypervelocity Impact Cratering," AIAA Paper 69-354, 1969.
7. Strang, G., "On the Construction and Comparison of Difference Schemes," SIAM J. Numer. Anal., 5(1968), pp. 506-517.
8. Yee, H.C., "Upwind and Symmetric Shock-Capturing Schemes," NASA Ames Technical Memorandum 89464, 1987.
9. Yee, H.C. and Shinn, J.L., "Semi-Implicit and Fully Implicit Shock-Capturing Methods for Hyperbolic Conservation Laws with Stiff Source Terms," AIAA Paper 87-1116, June 1987.

COST-EFFECTIVE ACCURATE COARSE-GRID METHOD FOR HIGHLY CONVECTIVE MULTIDIMENSIONAL UNSTEADY FLOWS

B. P. Leonard and H. S. Niknafs
The University of Akron
Akron, OH 44325

ABSTRACT

A fundamentally multidimensional convection scheme is described based on vector transient interpolation modelling rewritten in conservative control-volume form. Vector third-order upwinding is used as the basis of the algorithm; this automatically introduces important cross-difference terms that are absent from schemes using component-wise one-dimensional formulas. Third-order phase accuracy is good; this is important for coarse-grid large-eddy or full simulation. Potential overshoots or undershoots are avoided by using a recently developed universal limiter. Higher order accuracy is obtained locally, where needed, by the cost-effective strategy of adaptive stencil expansion in a direction normal to each control-volume face; this is controlled by monitoring the absolute normal gradient and curvature across the face. Higher (than third) order cross-terms do not appear to be needed. Since the wider stencil is used only in isolated narrow regions (near discontinuities), extremely high (in this case, seventh) order accuracy can be achieved for little more than the cost of a globally third-order scheme.

INTRODUCTION

The authors have recently developed (reference 1) a cost-effective strategy for obtaining very high accuracy results for one-dimensional convective simulation on practical (i.e., coarse) grids. The method automatically produces tight nonoscillatory resolution of discontinuities without distorting smooth profiles or clipping very narrow extrema. All these desirable features are obtained for little more cost than that of the basic third-order upwind scheme on which the algorithm is based (reference 2). Figure 1 shows what can be achieved in one dimension. The figure shows computed points together with the exact solution for four profiles: a unit step, an isolated sine-squared wave $20\Delta x$ wide, a semi-ellipse $20\Delta x$ wide, and a narrow Gaussian ($\sigma = 1.94\Delta x$); at the time shown, the profiles have been translated by pure convection 45 mesh-widths to the right (100 time-steps at a Courant number of 0.45). This particular example is based on third-order upwinding in smooth regions with automatic adaptive stencil expansion to seventh- or ninth-order upwinding locally, as needed, determined by monitoring the local absolute gradient across face $(i + \frac{1}{2})$, say,

$$\text{GRAD} = |\phi_{i+1} - \phi_i| \tag{1}$$

and the corresponding local absolute average curvature

$$\text{CURVAV} = 0.5\,|(\phi_{i+2} - \phi_{i+1}) - (\phi_i - \phi_{i-1})| \tag{2}$$

The algorithm also includes an automatic discriminator which decides when to apply the universal limiter (described in reference 3) and when to relax the limiter constraints. Ideally, the discriminator should activate the limiter in order to suppress unphysical numerical oscillations which would otherwise occur near sudden changes in gradient – each side of the step and at the "feet" of the semi-ellipse – without concomitant loss of resolution of the physical extrema (especially the narrow peak of the Gaussian profile). Clearly from Figure 1, this has been achieved; simulation of the sine-squared and Gaussian profiles is essentially exact, whereas resolution of the large-gradient regions of the other profiles is very tight.

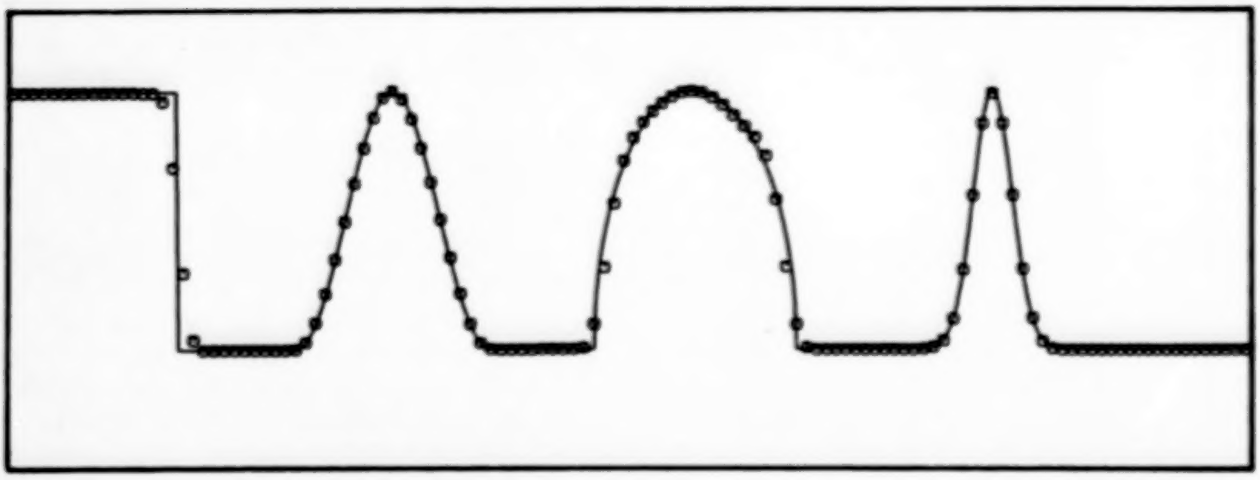

Figure 1. One-dimensional pure convection of four profiles using the cost-effective 3/7/9th-order scheme described in reference 1.

The main purpose of the present paper is to show how to extend these desirable features to multidimensional flow problems. As is well known, one-dimensional algorithms do not automatically generalize to two and three dimensions simply by using the one-dimensional scheme component-wise in each direction. However, by using the concept of vector transient interpolation modelling

$$\phi(\mathbf{x}, t + \Delta t) = \phi(\mathbf{x} - \mathbf{v}\Delta t, t) \tag{3}$$

fundamentally multidimensional convection schemes can be generated with the same properties as their one-dimensional counterparts. Very high accuracy (in both space and time) can be obtained in a simple single-time-step explicit update formulation by converting time evolution into a spatial interpolation problem at the earlier time-level, as represented by Equation (3). The multidimensional algorithms will be demonstrated in two dimensions. Once this is done, it becomes clear how to extend to three dimensions. To paraphrase a well-known aerospace quotation: algorithmically, there is a giant leap between one-dimension and two, but only a small step between two and three.

In order to demonstrate the process of converting Equation (3) into conservative control-volume form, two-dimensional transient interpolation modelling will be considered for first-order upwinding, and three second-order schemes: Lax-Wendroff (reference 4), second-order upwinding and Fromm's method (reference 5). The two-dimensional extension of the QUICKEST scheme (reference 2) represents a uniformly third-order polynomial interpolation algorithm (UTOPIA). As with QUICKEST in one dimension, UTOPIA is susceptible to unphysical overshoots and undershoots if sudden changes in gradient are involved. Essentially nonoscillatory results can be obtained by applying the universal limiter of reference 3 to the individual control-volume fluxes. Although UTOPIA has excellent phase accuracy, short-wavelength resolution is, of course, limited to third order. In principle, arbitrarily higher order resolution can be obtained locally – as in the one-dimensional scheme demonstrated in Figure 1 – by local adaptive stencil expansion. It appears that stencil expansion in a direction normal to a particular control-volume face is much more effective than expansion in the transverse direction. Thus, although transverse terms are included to third order, higher order stencil expansion is taken only in the normal direction. Results for a third/seventh-order scheme are given for the well-known rotating-velocity-field benchmark test problem using three test profiles: a cylinder, a cone, and a narrow Gaussian. In the results given here, an *ad hoc* discriminator is used in order to relax the limiter constraints near physical extrema. An automatic multidimensional discriminator is currently under development.

CONTROL-VOLUME FORMULATION

For simplicity, consider a two-dimensional square mesh (of unit grid size) with a control-volume using standard compass-point labelling. Equation (3) can be rewritten as

$$\phi_P^{n+1} = \phi(0,0,t+\Delta t) = \phi(-u\Delta t, -v\Delta t, t) = \phi^n(-u\Delta t, -v\Delta t) \tag{4}$$

where $\phi^n(x,y)$ represents the behaviour of the convected field variable in the (upstream-biassed) vicinity of the control volume. The following algorithms depend on the functional form asumed for $\phi^n(x,y)$. Assume that u and v are both positive and (for the moment) constant.

First-Order Upwinding

For example, consider the bilinear expression

$$\phi^n(x,y) = a + bx + cy + dxy \tag{5}$$

The four constants, a, b, c, and d, need to be evaluated; it is appropriate to use collocation at four nodal points with an upstream bias – in this case (u and v positive), these would be

$$\phi_P^n, \ \phi_W^n, \ \phi_S^n, \text{ and } \phi_{SW}^n \tag{6}$$

as shown in Figure 2, giving

$$\phi^n = \phi_P^n + (\phi_P^n - \phi_W^n)x + (\phi_P^n - \phi_S^n)y + [(\phi_P^n - \phi_W^n) - (\phi_S^n - \phi_{SW}^n)]xy \tag{7}$$

as can be easily checked by putting x and y equal to 0 or -1, independently. Using Equation (4), the explicit update algorithm becomes (for $u>0$ and $v>0$)

$$\phi_P^{n+1} = \phi_P^n - c_x(\phi_P^n - \phi_W^n) - c_y(\phi_P^n - \phi_S^n) + c_x c_y[(\phi_P^n - \phi_W^n) - (\phi_S^n - \phi_{SW}^n)] \tag{8}$$

where c_x and c_y are the respective component Courant numbers. Equation (8) can be written in the general conservative control-volume form

$$\phi_P^{n+1} = \phi_P^n + c_x\phi_w - c_x\phi_e + c_y\phi_s - c_y\phi_n \tag{9}$$

where the lower-case subscripts refer to face values, and

$$\phi_e(i,j) = \phi_w(i+1,j) \tag{10}$$

and

$$\phi_n(i,j) = \phi_s(i,j+1) \tag{11}$$

guaranteeing convective conservation. This is achieved by identifying the face values as

$$\phi_w = \phi_W^n - \frac{c_y}{2}(\phi_W^n - \phi_{SW}^n) \tag{12}$$

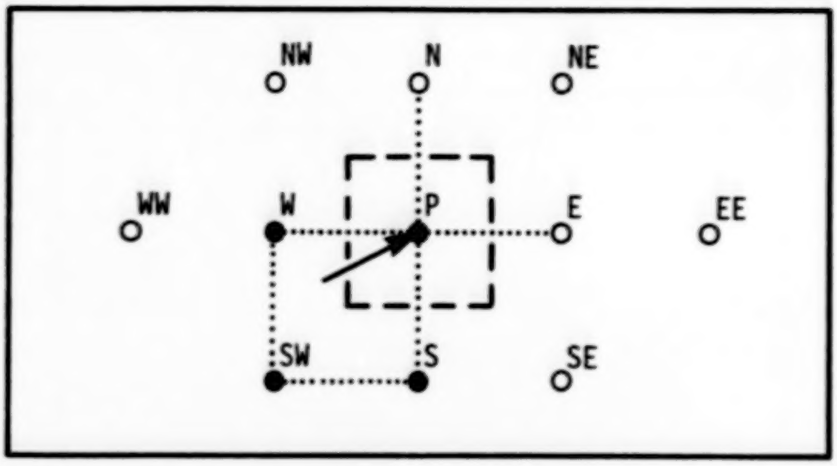

Figure 2. Compass-point notation, showing nodes involved in the first-order upwind scheme (solid dots) for $u,v>0$.

and

$$\phi_s = \phi_S^n - \frac{c_x}{2}(\phi_S^n - \phi_{SW}^n) \tag{13}$$

again for u, $v>0$, of course. Equation (12), for example, can be rewritten in a form valid for positive and negative velocities as

$$\phi_w = \phi_w^L - \frac{\mathrm{SGN}(c_x)}{2}\,\mathrm{GRADN} - \frac{c_y}{2}\,\mathrm{GRADT} \tag{14}$$

introducing the linearly interpolated face-value

$$\phi_w^L = \frac{1}{2}(\phi_P^n + \phi_W^n) \tag{15}$$

the normal gradient across the west face

$$\mathrm{GRADN} = \phi_P^n - \phi_W^n \tag{16}$$

with upwind bias determined by the sign of c_x

$$\mathrm{SGN}(c_x) = \pm 1 \quad \text{for } c_x \gtrless 0 \tag{17}$$

and the upwind-biassed transverse gradient

$$\mathrm{GRADT} = \phi_W - \phi_{SW} \quad \text{for } c_x>0 \text{ and } c_y>0 \tag{18}$$

$$= \phi_{NW} - \phi_W \quad \text{for } c_x>0 \text{ and } c_y<0 \tag{19}$$

$$= \phi_P - \phi_S \quad \text{for } c_x<0 \text{ and } c_y>0 \tag{20}$$

$$= \phi_N - \phi_P \quad \text{for } c_x<0 \text{ and } c_y<0 \tag{21}$$

A similar expression can be written for ϕ_s. Then the east and north face values are obtained from Equations (10) and (11). Finally, if c_x and c_y appearing in Equation (14) (and the analogous expression for ϕ_s) are interpreted as local face values of the respective component Courant numbers, the formulas can be considered to be valid for a spatially varying convecting velocity field.

Second-Order Central

Consider the second-order expression

$$\phi^n = a + bx + cx^2 + dy + ey^2 + fxy \tag{22}$$

The six constants are determined by collocation at six nodal points: ϕ_P and the four surrounding points (ϕ_N, ϕ_S, ϕ_E, and ϕ_W) together with one additional point. As with first order, the latter point is chosen on the basis of upwind bias: ϕ_{SW} for $u>0$, $v>0$; ϕ_{NW} for $u>0$, $v<0$; ϕ_{SE} for $u<0$, $v>0$; and ϕ_{NE} for $u<0$, $v<0$. The stencil is sketched in Figure 3(a) for $u, v>0$. After evaluating the constants, using Equation (4), and rewriting in conservative control-volume form, the following formula results for the west face

$$\phi_w = \phi_w^L - \frac{c_x}{2}\,\mathrm{GRADN} - \frac{c_y}{2}\,\mathrm{GRADT} \tag{23}$$

with a similar expression for ϕ_s. As in the one-dimensional case, the difference between this and first-order upwinding, Equation (14), is the appearance of c_x itself rather than $\mathrm{SGN}(c_x)$ in the coefficient of the normal gradient term. Note that the transverse gradient term retains the same form.

Equation (23) is the basis of the single-time-step explicit form of the Lax-Wendroff (reference 4) or Leith (reference 6) scheme extended to two dimensions in conservative control-volume form. The first two terms on the right of Equation (23) represent the one-dimensional formula; the transverse gradient term is the significant addition for two dimensions. It should be clear that in three dimensions there would be an additional upwind-biassed transverse gradient term in the z-direction (multiplied by $-c_z/2$). The same would apply in the case of first-order upwinding.

Other Second-Order Schemes

If the stencil shown in Figure 3(b) is used to evaluate the constants in Equation (22), the two-dimensional form of second-order upwinding results. The one-dimensional form was originally discussed (in passing) by Fromm (reference 5) and was made popular in the aerospace industry by Warming and Beam (reference 7). The resulting formula (for the west face, for example) can be written

$$\phi_w = \phi_w^L - \frac{c_x}{2}\,\mathrm{GRADN} - \frac{(1-c_x)}{2}\,\mathrm{CURVN} - \frac{c_y}{2}\,\mathrm{GRADT} \tag{24}$$

where CURVN is the upwind-biassed normal curvature given by

$$\mathrm{CURVN} = \phi_P^n - 2\phi_W^n + \phi_{WW}^n \quad \text{for } c_x > 0 \tag{25}$$

or

$$\mathrm{CURVN} = \phi_E^n - 2\phi_P^n + \phi_W^n \quad \text{for } c_x < 0 \tag{26}$$

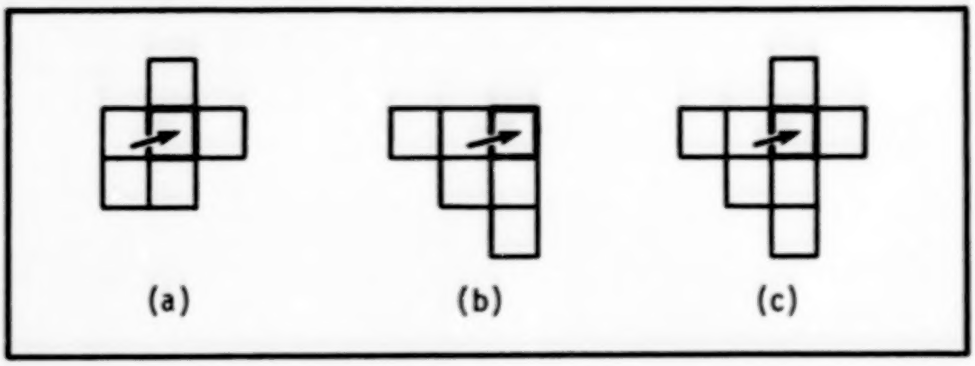

Figure 3. Second-order two-dimensional stencils ($u,v>0$). (a) Lax-Wendroff. (b) Second-order upwinding. (c) Fromm's method.

at the west face. Clearly, the appearance of the normal curvature term represents the significant difference between second-order upwinding and the second-order central formula. The same is true in one dimension. Fromm's so-called "zero-average-phase-error" method (reference 5) represents a simple average between the second-order central and second-order upwind schemes. By comparing Equations (23) and (24), it is seen that this merely reduces the CURVN coefficient by an additional factor of 2. The stencil is shown in Figure 3(c).

Third-Order Upwinding – UTOPIA

In one dimension, Fromm's method was an attempt to offset the lagging dispersion (phase error) of the Lax-Wendroff scheme by averaging it with second-order upwinding (containing inherent leading phase error). This was only partially successful; however, using the same one-dimensional stencil, it is possible to eliminate entirely the troublesome (third-derivative) dispersion term in the truncation error of the second-order schemes. The resulting explicit third-order upwind (QUICKEST) scheme has excellent phase behaviour; leading phase error stems from a small fifth-derivative term – and this is inherently damped by a fourth-derivative dissipation term (without introducing an artificial second-derivative diffusion term). The corresponding two-dimensional scheme is based on the third-order polynomial expression

$$\phi^n = a + bx + cx^2 + dx^3 + ey + fy^2 + gy^3 + hxy + ix^2y + jxy^2 \tag{27}$$

requiring 10 (upwind-biassed) collocation points. The appropriate stencil (for $u,v>0$) is sketched in Figure 4(a). The resulting formula for the west face value can then be written

$$\phi_w = \phi_w^L - \frac{c_x}{2}\,\mathrm{GRADN} - \frac{(1-c_x^2)}{6}\,\mathrm{CURVN} - \frac{c_y}{2}\,\mathrm{GRADT} + \left(\frac{c_y^2}{6} - \frac{c_y}{4}\right)\mathrm{CURVT} + \left(\frac{c_x c_y}{3} - \frac{c_y}{4}\right)\mathrm{TWIST} \tag{28}$$

where two new terms are evident. The upwind-biassed transverse curvature is given (for the west face) by

$$\mathrm{CURVT} = \phi_{NW}^n - 2\phi_W^n + \phi_{SW}^n \quad \text{for } c_x > 0 \tag{29}$$

or

$$\mathrm{CURVT} = \phi_N^n - 2\phi_P^n + \phi_S^n \quad \text{for } c_x < 0 \tag{30}$$

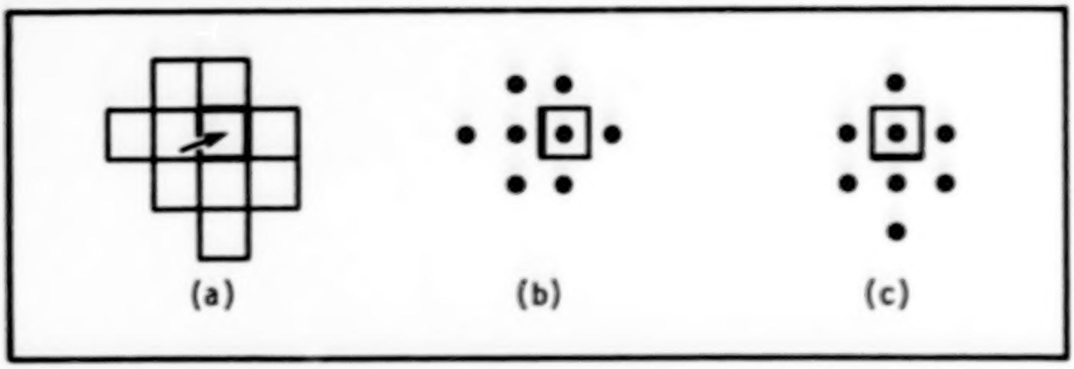

Figure 4. UTOPIA stencils. (a) Complete stencil for $u,v>0$. (b) West face stencil for arbitrary u,v. (c) South face stencil for arbitrary u,v.

The upwind-biassed "twist" term is given by

$$\text{TWIST} = (\phi_P^n - \phi_S^n) - (\phi_W^n - \phi_{SW}^n) \quad \text{for } c_y > 0 \tag{31}$$

or

$$\text{TWIST} = (\phi_N^n - \phi_P^n) - (\phi_{NW}^n - \phi_W^n) \quad \text{for } c_y < 0 \tag{32}$$

Figure 4(b) shows the stencil involved in computing the west face value when both positive and negative convecting velocity components are allowed for; Figure 4(c) shows the corresponding south face stencil. Extension to three dimensions requires additional GRADT, CURVT, and TWIST terms in an obvious manner.

UNIVERSAL LIMITER

As in the one-dimensional case, use of the two-dimensional second- and third-order schemes may result in unphysical oscillatory solutions if sharp changes in gradient are involved. In the case of the third-order scheme, this usually involves only relatively small (up to about 5%) overshoots or undershoots, at worst (reference 2). Even so, it seems desirable to eliminate this type of error (because of the possibility of nonlinear feedback instabilities in coupled equations). A universal limiting procedure, described in reference 3 for the one-dimensional case can be directly applied at each control-volume face. One first computes the multidimensional-stencil convected face value, given by Equation (28), for example. Then the "normalized" value is computed; for $c_x > 0$ at the west face, this would be

$$\tilde{\phi}_w = \frac{(\phi_w - \phi_{WW}^n)}{(\phi_P^n - \phi_{WW}^n)} \tag{33}$$

At the same time, the normalized adjacent upstream node value is computed

$$\tilde{\phi}_W = \frac{(\phi_W^n - \phi_{WW}^n)}{(\phi_P^n - \phi_{WW}^n)} \tag{34}$$

Then, if $0 \le \tilde{\phi}_W \le 1$, the normalized face value is constrained by

$$\tilde{\phi}_w \ge \tilde{\phi}_W \tag{35}$$

and

$$\tilde{\phi}_w \leq \min(\tilde{\phi}_W/|c_x|, 1) \tag{36}$$

Outside of the monotonic range (i.e., if $\tilde{\phi}_W < 0$ or > 1) one could use any simple nonoscillatory scheme such as

$$\tilde{\phi}_w = \tilde{\phi}_W \tag{37}$$

Then the (unnormalized) face value is reconstructed using

$$\phi_w = \phi^n_{WW} + \tilde{\phi}_w(\phi^n_P - \phi^n_{WW}) \tag{38}$$

If $c_x < 0$, the normalized west face value is given by

$$\tilde{\phi}_w = \frac{(\phi_w - \phi^n_E)}{(\phi^n_W - \phi^n_E)} \tag{39}$$

and the normalized adjacent upstream value is then

$$\tilde{\phi}_P = \frac{(\phi^n_P - \phi^n_E)}{(\phi^n_W - \phi^n_E)} \tag{40}$$

A similar procedure is used for the south face (based on the sign of c_y at that face). The east and north (limited) values are then given by conservation, as usual.

ADAPTIVE STENCIL EXPANSION

The uniformly third order polynomial interpolation algorithm (UTOPIA) described above is clearly limited in terms of short-wavelength resolution. In order to gain higher resolution, the same cost-effective strategy of adaptive stencil expansion – as used with such success in the one-dimensional case (reference 1) – can be used in two and three dimensions, as well. Stencil expansion in a direction normal to a particular control-volume face is fundamental for higher order resolution. Higher order transverse, twist, and other cross-terms, beyond the third-order terms of Equation (28), appear to have very little effect. Accordingly, suggested stencils for two-dimensional fifth- and seventh-order upwinding are shown in Figures 5(a) and 5(b), respectively (for $u, v > 0$). In other words, these are higher order one-dimensional schemes (reference 3) applied component-wise, together with the complete third-order cross-terms; omission of the latter terms causes severe anisotropic distortion and significant loss of accuracy in velocity fields oblique (or skew) to the grid.

Because of the (component-wise) one-dimensional nature of the proposed stencil expansion, the process can be automated by exactly the same procedure as used in the one-dimensional case. This is described in detail in reference 1. In the multidimensional code the one-dimensional adaptive stencil expansion criteria are applied independently at each of the west, south (and, in 3D, bottom) faces. In "smooth" regions, the respective values of GRAD and CURVAV are well below (pre-assigned) thresholds so that the (unlimited) UTOPIA scheme is being used. For most flows of practical interest, this will account for the overwhelming bulk of grid points, especially in three dimensions. Near isolated regions involving large values of GRAD or CURVAV at particular control-volume faces, thresholds will be exceeded, automatically switching the algorithm to fifth or seventh (or, in principle, arbitrarily higher) order at those particular points.

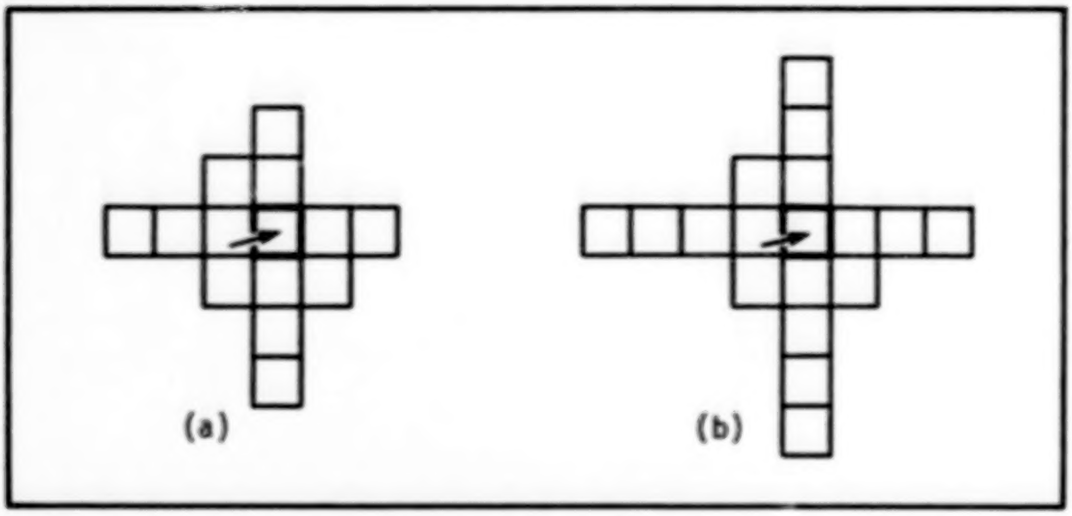

Figure 5. Stencil expansion (for $u,v > 0$) from fully third-order upwind to (a) quasi-fifth-order upwind; (b) quasi-seventh-order upwind.

Two things should be noted. First, the higher order stencils will be needed only in very narrow regions (by definition of sharp change in value or gradient), thus requiring the more expensive computation at a relatively small number of grid points. This is an extremely cost-effective way to achieve very high accuracy on practical (i.e., coarse) grids – obviously an important consideration for three-dimensional simulation. Secondly, it should be clear that the location of the higher order stencils automatically changes as the flow evolves. As in the one-dimensional simulations described in reference 1, phase-accuracy is therey extremely tight. This is a critical attribute for any code designed to be used in large-eddy or full Navier-Stokes simulations.

G-EXPANSION TECHNIQUE

It is an instructive exercise to make a Fourier-von Neumann analysis (reference 8) of the multidimensional formulas discussed above and to compare Taylor expansions of their complex amplitude ratio (sometimes called "amplification factor"), G, with that of the exact solution (for constant v). This also gives some indication of how to incorporate higher order diffusion terms. For example, consider the exact complex amplitude ratio (reference 9) for the two-dimensional constant-coefficient convection-diffusion equation

$$G = \exp[-\alpha(\theta_x^2 + \theta_y^2)]\exp[-i(c_x\theta_x + c_y\theta_y)] \tag{41}$$

where α is the nondimensional diffusion parameter and the θ's are nondimensional wave-number components. A Taylor expansion of Equation (41) gives

$$G = 1 - \alpha(\theta_x^2 + \theta_y^2) - \frac{(c_x\theta_x + c_y\theta_y)^2}{2} + \frac{(c_x\theta_x + c_y\theta_y)^4}{24}$$

$$+ \frac{(c_x\theta_x + c_y\theta_y)^2\alpha(\theta_x^2 + \theta_y^2)}{2} + \frac{\alpha^2(\theta_x^2 + \theta_y^2)^2}{2} + \dots \qquad \text{(continued)...}$$

$$- i(c_x\theta_x + c_y\theta_y)\left\{\begin{array}{l} 1 - \alpha(\theta_x^2 + \theta_y^2) - \dfrac{(c_x\theta_x + c_y\theta_y)^2}{6} + \dfrac{(c_x\theta_x + c_y\theta_y)^4}{120} \\ \quad + \dfrac{(c_x\theta_x + c_y\theta_y)^2\alpha(\theta_x^2 + \theta_y^2)}{6} + \dfrac{\alpha^2(\theta_x^2 + \theta_y^2)^2}{2} + \cdots \end{array}\right\} \tag{42}$$

At second order, note the appearance of the cross-term, $c_x\theta_x c_y\theta_y$. This is accounted for by the GRADT term in the two-dimensional second-order formulas. Component-wise application of one-dimensional second-order algorithms would miss this important term. Similarly, the cross-terms in the UTOPIA scheme are responsible for matching *all* convection terms in Equation (42) through third order in θ_x and θ_y. It is a relatively simple matter to match diffusion terms to this order, as well, building on experience with the one-dimensional QUICKEST scheme developed in reference 2 and more fully explored in reference 10. In this case, the west face value, for example becomes

$$\begin{aligned} \phi_w = \phi_w^L - \frac{c_x}{2}\,\text{GRADN} - \left|\frac{(1-c_x^2)}{6} - \frac{\alpha_x}{2}\right|\text{CURVN} - \frac{c_y}{2}\,\text{GRADT} \\ + \left(\frac{c_y^2}{6} - \frac{c_y}{4} + \frac{\alpha_y}{2}\right)\text{CURVT} + \left(\frac{c_x c_y}{3} - \frac{c_y}{4}\right)\text{TWIST} \end{aligned} \tag{43}$$

which should be compared with the pure-convection formula, Equation (28). The corresponding west face gradient is given by

$$\Delta x\left(\frac{\partial\phi}{\partial x}\right)_w = \text{GRADN} - \frac{c_x}{2}\,\text{CURVN} - \frac{c_y}{2}\,\text{TWIST} \tag{44}$$

The three-dimensional extensions of Equations (43) and (44) should, by now, be clear.

BENCHMARK TEST PROBLEMS

The well-known "rotating-velocity-field" convection problem is used as a benchmark test. The velocity field is that of solid-body rotation so that a given initial profile should be swept around as if it were imbedded in a rotating solid. For pure convection, the exact solution is thus known. The following three initial profiles are considered: a cylinder with a base diameter of 16 mesh-widths; a cone with the same base diameter; and a relatively narrow Gaussian distribution ($\sigma = 2$ mesh-widths). The computation is carried out on a 55 × 55 grid with a maximum Courant number near 0.8. Figure 6 shows results of the Lax-Wendroff simulation after one-half rotation in the counter-clockwise direction; the exact solutions have been juxtaposed, for reference. Note the typical trailing (phase-lag) oscillations, especially in the case of the cylinder. Figure 7 shows the corresponding two-dimensional second-order upwind simulation. In this case, phase-lead dispersion (partially obscured) occurs ahead of the simulated profile. Two nonoscillatory (TVD) schemes designed by Roe (reference 11) are shown in Figures 8 and 9. As seen, the Minmod results are quite diffusive for all profiles. Superbee does a reasonably good job on the cylinder, but tends to steepen and clip the other profiles. This is a well-known shortcoming of second-order-based TVD schemes, especially those of supercompressive type that rely on negative artificial diffusion to enhance discontinuity resolution; this is explained in detail in reference 3. Finally, figure 10 shows results that can be obtained using methods described in this paper. The results shown are for a seventh-order upwind scheme including all third-order (but no higher) cross-terms. An *ad hoc* discriminator is used to relax limiter constraints in the vicinity of physical maxima; as mentioned before, an automatic multidimensional discriminator (similar to that described in reference 1 for one dimensional flow) is under development. This, of course, will be necessary before the code is applicable to general flow problems. Note from Figure 10 that resolution of the cylinder is better than that of Superbee, but without gross distortion of the other profiles.

CONCLUSION

The high-convection code described in this paper includes a number of features that are important for cost-effective accurate simulation of multidimensional unsteady flows on practical grids. Being based on third-order upwinding, the code is totally free of artificial numerical diffusion (or viscosity); this is important because schemes based on artificial-viscosity methods are often solving the wrong problem – i.e., an artificially *low*-convection problem rather than the physical *high*-convection problem. UTOPIA contains all necessary cross-terms to third order, thus matching all terms in the Taylor expansion of the complex amplitude ratio through to third order in the wave-number components. This guarantees excellent phase behaviour and isotropy regardless of the stream-to-grid angle. Codes based on second-order (or even fourth-order) *central* schemes inherently contain serious dispersion errors. Inclusion of the GRADT term should improve isotropy (in theory) – but this is usually masked by gross dispersion.

Although far more accurate than first- and second-order methods, third-order upwinding may give rise to slight overshoots or undershoots. This tendency can be eliminated by using the universal limiter, developed in reference 3, on each control-volume face, independently. If higher order resolution is required, the strategy of adaptive stencil expansion – increasing accuracy (above third order) only where needed – is extremely cost-effective. This is controlled by monitoring the absolute normal gradient and curvature across control-volume faces; as certain (pre-assigned) thresholds are exceeded, the code automatically switches to (in principle, arbitrarily) higher order accuracy at the face in question. Finally, in order to give full resolution to local extrema, the limiter constraints need to be automatically relaxed in such regions (in addition to using a higher order stencil). A fully automatic pattern-recognition discriminator of this type has been designed for one dimension (reference 1); the same principles appear to be applicable to multidimensional flows, as well, but a completely automatic multidimensional discriminator of this type is still under development.

REFERENCES

1. Leonard, B.P. and Niknafs, H.S., "Sharp Monotonic Resolution of Discontinuities Without Clipping of Narrow Extrema," *Computers and Fluids*, in press (1990).
2. Leonard, B.P., "A Stable and Accurate Convective Modelling Procedure Based on Quadratic Upstream Interpolation," *Computer Methods in Applied Mechanics and Engineering*, **19**, 59-98 (1979).
3. Leonard, B.P., "Universal Limiter for Transient Interpolation Modeling of the Advective Transport Equations: The ULTIMATE Conservative Difference Scheme," NASA TM 100916 (ICOMP-88-11), NASA-Lewis Research Center.
4. Lax, P.D. and Wendroff, B., "Systems of Conservation Laws," *Communications on Pure and Applied Mathematics*, **13**, 217-237 (1960).
5. Fromm, J.E., "A Method for Reducing Dispersion in Convective Difference Schemes," *Journal of Computational Physics*, **3**, 176-189 (1968).
6. Leith, C.E., "Numerical Simulation of the Earth's Atmosphere," *Methods in Computational Physics*, **4**, 1-28 (1965).

7. Warming, R.F. and Beam, R.M., "Upwind Second-Order Difference Schemes and Applications in Aerodynamic Flows," *AIAA Journal*, 14, 1241-1247 (1976).
8. Fletcher, C.A.J., *Computational Techniques for Fluid Dynamics*, Vols. I and II, Springer-Verlag, Berlin (1988).
9. Leonard, B.P., "Note on the von Neumann Stability of the Explicit FTCS Convective Diffusion Equation," *Applied Mathematical Modelling*, 4, 401-402 (1980).
10. Leonard, B.P., "Elliptic Systems: Finite Difference Method IV," in *Handbook of Numerical Heat Transfer*, (eds. W.J. Minkowicz, *et al.*), 347-378, Wiley, New York (1988).
11. Roe, P.L., "Characteristic-Based Schemes for the Euler Equations," *Annual Reviews of Fluid Mechanics*, 18 (eds. M. Van Dyke, *et al.*), Annual Reviews Inc. (1986).

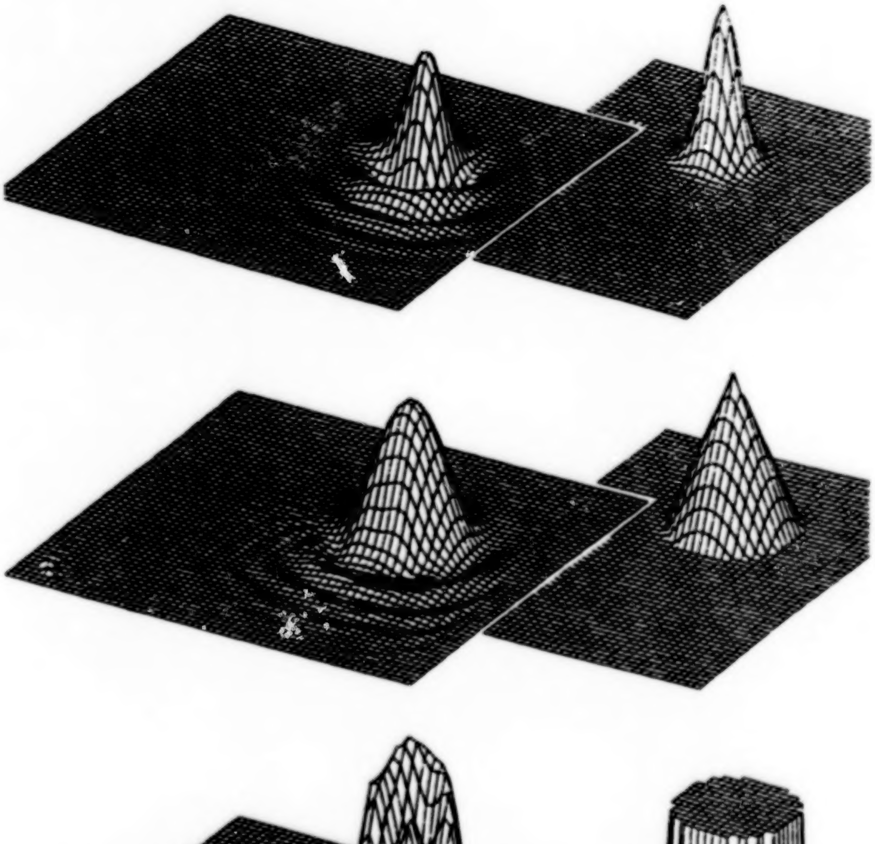

Figure 6. Lax-Wendroff simulation after one-half rotation counterclockwise compared with exact result.

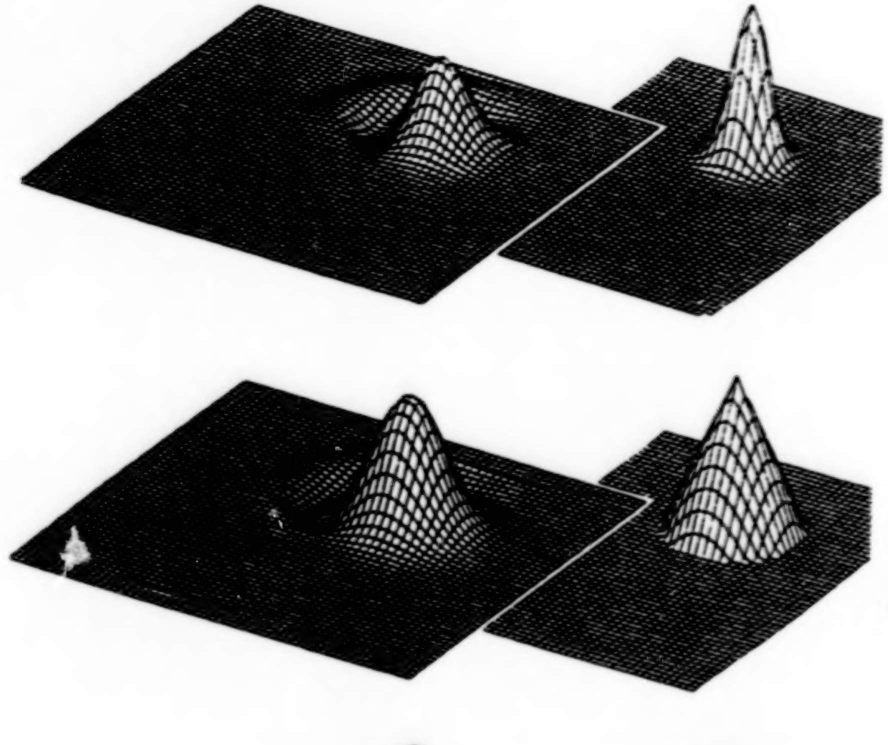

Figure 7. Second-order upwinding results after half rotation.

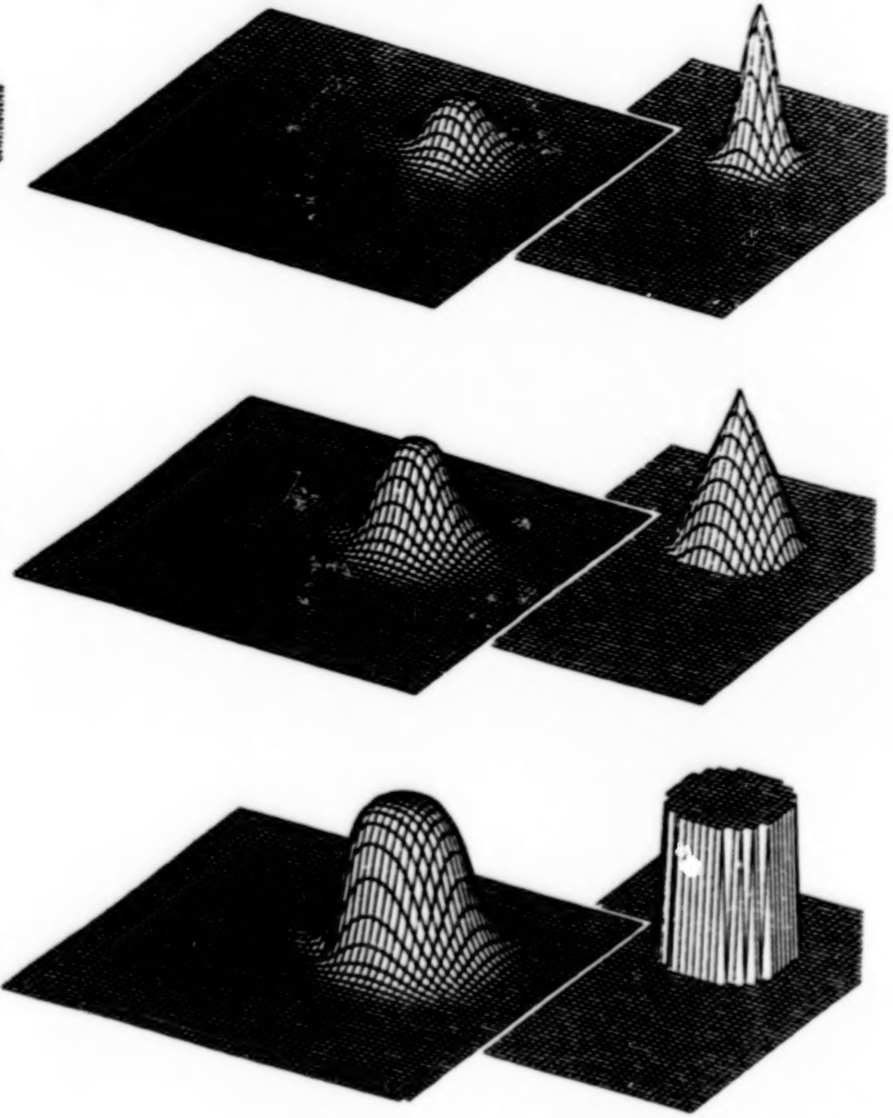

Figure 8. TVD-Minmod results.

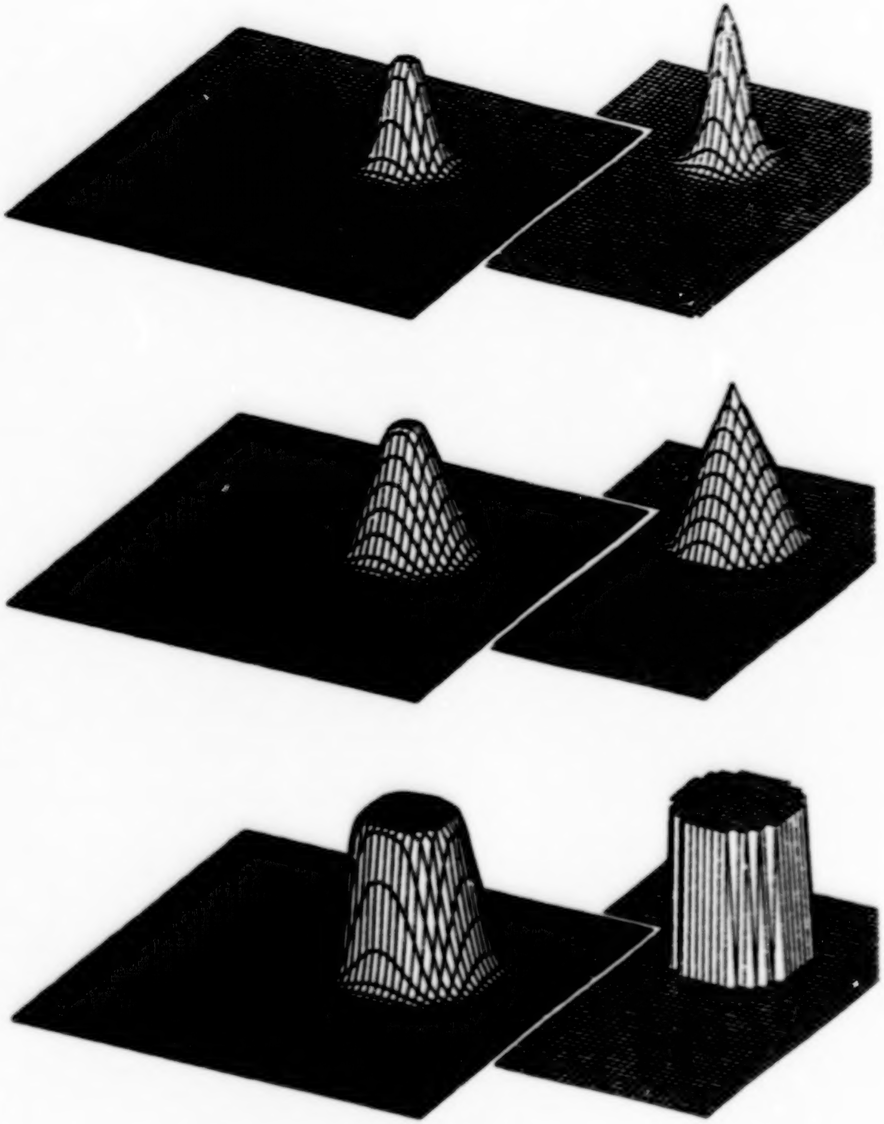

Figure 9. TVD-Superbee results.

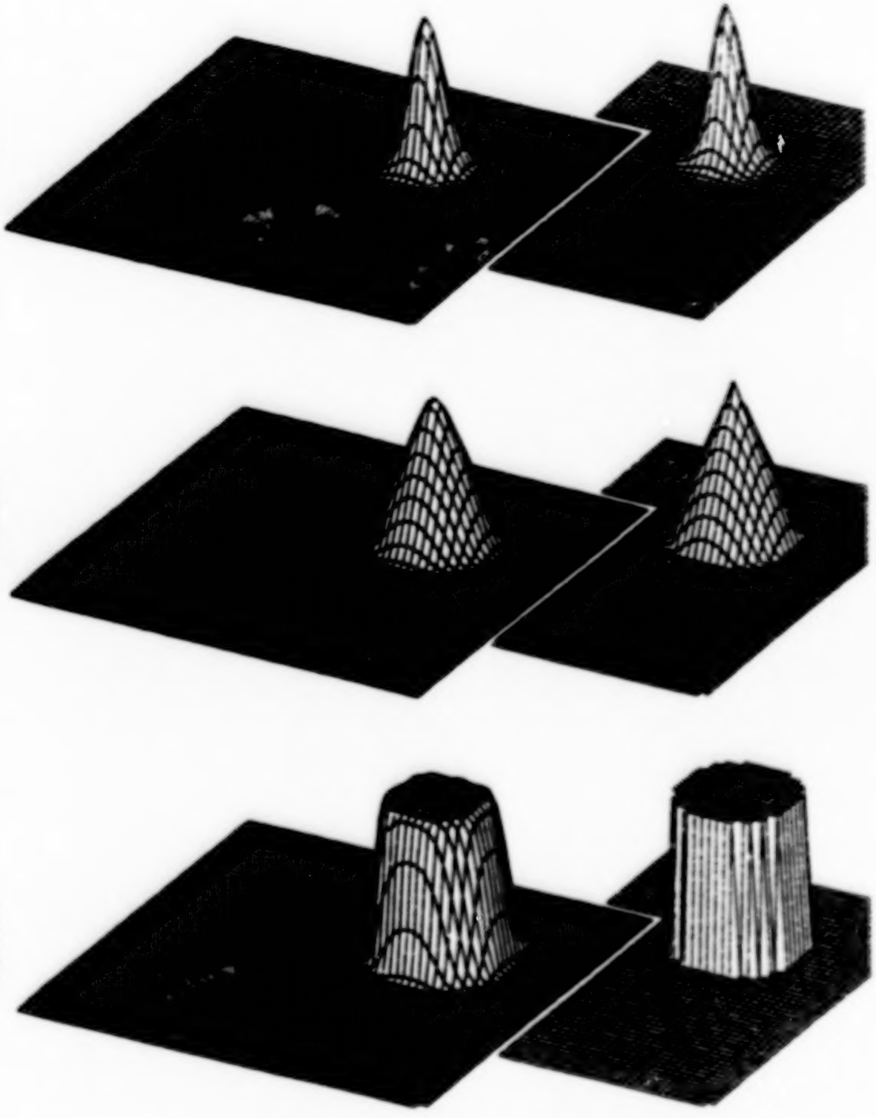

Figure 10. Results using the 3rd/7th-order method.

CHOICE OF VELOCITY VARIABLES
FOR COMPLEX FLOW COMPUTATION

W. Shyy
Department of Aerospace Engineering, Mechanics
and Engineering Science
University of Florida, Gainesville, Florida 32611-2031

G. C. Chang
Chung Shan Institute of Science and Technology, Taiwan, ROC

ABSTRACT

The issue of adopting the velocity components as dependent velocity variables for the Navier-Stokes flow computations is investigated. The viewpoint advocated here is that a numerical algorithm should preferably honor both the physical conservation law in differential form and the geometric conservation law in discrete form. With the use of Cartesian velocity vector, the momentum equations in curvilinear coordinates can retain the full conservation-law form and satisfy the physical conservation laws. With the curvilinear velocity components, source terms appear in differential equations and hence the full conservation law form can not be retained. In discrete expressions, algorithms based on the Cartesian components can satisfy the geometric conservation-law form for convection terms but not for viscous terms; those based on the curvilinear components, on the other hand, cannot satisfy the geometric conservation-law form for either convection or viscous terms. Several flow solutions for domain with ninety-degree and three-hundred-sixty-degree turnings are presented to illustrate the issues of using the Cartesian velocity components and the staggered grid arrangement.

INTRODUCTION

Numerical methods for solving the Navier-Stokes flow have been under intensive development for sometime. As is well known, the fundamental issues encountered in the numerical computation arise from many sources, including the construction of appropriate discrete operators for various mechanisms, especially convection terms, the manner of grid distribution, the method of solution procedure of large number of linearized equations, the treatment of the numerical boundary conditions, and the handling of coupling among the dependent variables [1,2]. The present work attempts to investigate a related fundamental question relevant to computing complex fluid flows arising from propulsion components, namely the "suitability" of choosing a specific type of velocity variables as the primary dependent variables of the governing equations [3].

With regard to the choice of the velocity variables, in gross terms, one has the options of using the Cartesian, contravariant, or covariant components as the primary variables. Although comments have been made regarding the suitability of each of these choices [4-6], they are mostly speculations. A more detailed and systematic study is desirable, as is attempted here.

First the relationship between the Cartesian (u, v) and contravariant (U, V) velocity components are defined as follows:

$$U = y_\eta u - x_\eta v \tag{1}$$

$$V = -y_\xi u + x_\xi v \tag{2}$$

Then the continuity equation in ξ- and η-coordinates can be written in the similar form with the contravariant velocity components to that in x- and y-coordinates with the Cartesian velocity components, i.e.,

$$(\rho u)_x + (\rho v)_y = 0 \tag{3}$$

$$(\rho U)_\xi + (\rho V)_\eta = 0 \tag{4}$$

where the subscripts ξ and η denote the partial derivatives along the curvilinear coordinate lines. With regard to the covariant velocity components, defined as $\bar{U}$ and $\bar{V}$ here, i.e.,

$$\bar{U} = x_\xi u + y_\xi v \tag{5}$$

$$\bar{V} = x_\eta u + y_\eta v \tag{6}$$

the continuity equation written in the covariant velocity components is

$$(\rho\alpha_1\bar{U} + \rho\beta_1\bar{V})_\xi + (\rho\alpha_2\bar{U} + \rho\beta_2\bar{V})_\eta = 0 \tag{7}$$

where

$$\alpha_1 = \frac{q_{11}\, q_{22}^2}{J} \tag{8a}$$

$$\beta_1 = \alpha_1\, (\vec{e}_\xi \cdot \vec{e}_\eta) \tag{8b}$$

$$\alpha_2 = \frac{q_{11}^2\, q_{22}}{J} \tag{8c}$$

$$\beta_2 = \alpha_2\, (\vec{e}_\xi \cdot \vec{e}_\eta) \tag{8d}$$

$$q_{11} = (x_\xi{}^2 + y_\xi{}^2)^{1/2} \tag{8e}$$

$$q_{22} = (x_\eta{}^2 + y_\eta{}^2)^{1/2} \tag{8f}$$

$$J = x_\xi y_\eta - x_\eta y_\xi \tag{8g}$$

$\vec{e}_\xi$ and $\vec{e}_\eta$ are unit vectors along ξ- and η-directions, respectively, i.e.,

$$\vec{e}_\xi = \frac{x_\xi \vec{e}_x + y_\xi \vec{e}_y}{q_{11}} \tag{9}$$

$$\vec{e}_\eta = \frac{x_\eta \vec{e}_x + y_\eta \vec{e}_y}{q_{22}} \tag{10}$$

PHYSICAL AND GEOMETRIC CONSERVATION LAWS

When considering the various possible choices of velocity variables, one of the primary criteria is that in the framework of finite-volume formulation, a fully conservation-law form of governing equations is usually more desirable since it can satisfy the physical laws more easily and accurately. This consideration has a particularly important implication on the convection terms of the momentum equations since they are nonlinear and are usually a major source of numerical difficulty. With the Cartesian coordinates, the convection terms in momentum equations are of the form of $(\rho uu)_x + (\rho vu)_y$, which is fully conservative. In a curvilinear coordinate system, these terms can be transformed in a straight forward manner with the use of the Cartesian velocity components as the primary dependent variables to the form of $(\rho Uu)_\xi + (\rho Vu)_\eta$ which is also fully conservative.

However, when either the contravariant or the covariant velocity components are used as the primary dependent variables, the fully conservative form can no longer be guaranteed since the linear momentum is conserved along a straight line, not a curved line. Thus the differential equations for both the contravariant and the covariant velocity components involve the source terms arising from the curvature of the coordinate lines. Furthermore, in the numerical implementation, the contravariant components ρU and ρV on each boundary of the mesh are defined as the mass flux between the two end points of the mesh boundary [7] and their values can artificially change with different grid systems. Hence, for the same flowfield the values of those contravariant and covariant velocity components can be greatly affected by the ways that the grid systems are generated. These aspects can cause difficulties in preserving high degrees of numerical accuracy in satisfying the conservation laws.

To demonstrate this point, consider the purely convective equation

$$(\rho uu)_x + (\rho vu)_y = 0 \tag{11}$$

One of the most basic tests of the numerical accuracy of any computational algorithm for Eq. (11) can be made by generating a grid system with arbitrary skewness and nonuniformity and then to use this grid system to check the numerical accuracy of it by solving a uniform flow field of, say, $\rho=1$, $u=1$, and $v=1$. With this condition, Eq. (11) is trivially satisfied in the differential sense. Hence it serves as a good case to test whether an algorithm can honor the geometric aspect of the conservation laws in a discrete form. Here we call this requirement the geometric conservation law [8] since the governing equations retain the conservation-law form but contain only the geometric quantities. The transformed equation of Eq. (11) with the Cartesian velocity components as dependent variables in curvilinear coordinates then becomes

$$(\rho Uu)_\xi + (\rho Vu)_\eta = 0 \tag{12}$$

which with the uniform flowfield is reduced to

$$(y_\eta - x_\eta)_\xi + (-y_\xi + x_\xi)_\eta = 0 \tag{13}$$

Referring to Fig. 1, Eq. (13) is discretized as follows:

$$\begin{aligned} &(y_\eta - x_\eta)_e - (y_\eta - x_\eta)_w \\ &+ (-y_\xi + x_\xi)_n - (-y_\xi + x_\xi)_s = 0 \end{aligned} \tag{14}$$

where e, w, n and s denote the east-, west-, north-, and south-face of the mesh, respectively. If a consistent finite-volume formulation is adopted, as shown in [7], by approximating the derivative of the metric terms in Eq. (14) with the difference between two end points of the mesh line, then Eq. (14) becomes

$$\begin{aligned} &[(y_{i+1,j+1} - y_{i+1,j}) - (x_{i+1,j+1} - x_{i+1,j})] \\ &- [(y_{i,j+1} - y_{i,j}) - (x_{i,j+1} - x_{i,j})] \\ &+ [-(y_{i+1,j+1} - y_{i,j+1}) + (x_{i+1,j+1} - x_{i,j+1})] \\ &- [-(y_{i+1,j} - y_{i,j}) + (x_{i+1,j} - x_{i,j})] = 0 \end{aligned} \tag{15}$$

which is satisfied exactly, regardless of how skew or nonuniform the meshes are. It is also noted that one of the merits of this test problem is that since the flowfield is uniform, the whole focal point is directed toward the satisfaction of geometric requirements; other issues such as the appropriate approximation of the convection effects do not arise here.

Since our primary interest is for Navier-Stokes flow computation, it is useful to point out that the above geometric conservation law is applicable to the pressure gradient terms as well. However, the same requirements cannot be rigorously satisfied by the viscous terms (for flowfields of constant velocity gradients) due to the appearance of the nonlinear metric products associated with the coordinate transformation of the second-order derivative terms. Overall, one can summarize the situation by stating that with the use of Cartesian velocity components, the Navier-Stokes equations can be written in the strong conservation-law form in the curvilinear coordinate system. In terms of numerically satisfying the geometric conservation law, the first order derivatives, including the convection and pressure terms, can always achieve it. The degree of satisfaction of the viscous terms, on the other hand, is dependent upon the actual grid distribution.

For the use of curvilinear components, say, the contravariant vector, the equation corresponding to Eq. (11) can be obtained by performing a chain-rule type of coordinate transformation,

$$\left[\rho U^2/q_{11} \right]_\xi + \left\{ \begin{matrix} 1 \\ 1\ 1 \end{matrix} \right\} \rho U^2/q_{11} + \left\{ \begin{matrix} 1 \\ 1\ 2 \end{matrix} \right\} \rho UV/q_{11}$$

$$+ (q_{11}/q_{22}) \left[\rho UV/q_{11} \right]_\eta + \left\{ \begin{matrix} 1 \\ 1\ 2 \end{matrix} \right\} \rho UV/q_{22} + \left\{ \begin{matrix} 1 \\ 2\ 2 \end{matrix} \right\} \rho V^2 q_{11}/(q_{22})^2$$

$$- (\rho U/q_{11}) U_\xi - (\rho U/q_{22}) V_\eta = 0 \qquad (16)$$

where the Christoffel symbols of the second kind are defined as

$$\left\{ \begin{matrix} 1 \\ 1\ 1 \end{matrix} \right\} = \frac{y_\eta x_{\xi\xi} - x_\eta y_{\xi\xi}}{J} \qquad (17a)$$

$$\left\{ \begin{matrix} 1 \\ 1\ 2 \end{matrix} \right\} = \frac{y_\eta x_{\xi\eta} - x_\eta y_{\xi\eta}}{J} \qquad (17b)$$

$$\left\{ \begin{matrix} 1 \\ 2\ 2 \end{matrix} \right\} = \frac{y_\eta x_{\eta\eta} - x_\eta y_{\eta\eta}}{J} \qquad (17c)$$

It is now obvious that Eq. (16) not only possesses more terms than Eq. (11), but more critically it contains source terms resulting from the curvature of the coordinate line. Hence, it is no longer of the fully conservative form which can cause difficulties with the finite-volume formulation, especially if the grid system contains substantial nonuniformity and skewness. The fact that q_{11} and q_{22} are nonlinear with respect to the metric terms resulting from the coordinate transformation further compounds the difficulty of exactly satisfying the conservation law in a discrete manner. Similar case can be made to the equation cast in terms of the covariant velocity components.

The other observation related to satisfaction of the geometric conservation law can be made by studying the continuity equation written in terms of the covariant velocity components. Equation (7) demonstrates that the conservation law can be preserved in differential form for the covariant velocity components. However, because the terms α and β involve nonlinear combinations of metric terms, the geometric conservation law cannot be always honored in a skewed mesh system. It is clear that since the physical conservation laws are the ones that we ultimately strive to satisfy, the numerical algorithms not only preferably should be written to satisfy the strong conservation law in differential form, but also should satisfy the geometric conservation law in discrete manners. The latter requirement cannot be satisfied as long as the equations contain nonlinear metric terms regardless of whether the fully conservation law form is adopted in the differential equations or not.

In summary, it has been demonstrated here that with either the contravariant and covariant velocity vectors, the momentum equations in curvilinear velocity vectors are no longer of full conservation-law forms. The curvatures of the grid lines introduce extra source terms into the governing equations which cause the degrees of satisfaction of physical conservation laws sensitive to the uniformity and skewness of the mesh distribution. For the continuity equation, on the other hand, the contravariant velocity can maintain both the fully conservative form and compactness of the equation. Table I summarizes the points discussed above. It appears that a combined use of the contravariant velocity components, for the continuity equation, and the Cartesian velocity components, for momentum equations, is a good balance [7,9]. This practice has particular merits in a pressure-correction type of algorithm where the velocity corrections are derived based on the information of pressure correction. As discussed in [9], the contravariant components should be used in the velocity-correction procedure to ensure the satisfaction of the conservation laws.

Table I. Choice of Primary velocity variables versus satisfying physical and geometric conservation-law forms for momentum and continuity equations

	Momentum Equations			
	Convection	Pressure	Viscous	Continuity Equation
Cartesian	satisfies both physical and geometric laws	satisfies both physical and geometric laws	satisfies physical but not geometric laws	satisfies both pysical and geometric laws
Contravariant	does not satisfy either law	satisfies both laws	does not satisfy either law	satisfies both laws
Covariant	does not satisfy either law	satisfies both laws	does not satisfy either law	satisfies physical but not geometric law

GRID SYSTEM

In [7,9], a staggered grid system has also been, adopted. As shown in Fig. 1, the Cartesian and contravariant velocity components are defined at the middle of east-west and north-south faces, respectively. That is, in 2-D curvilinear coordinates designated as ξ-lines and η-lines, u and U components are defined at the middle of η-lines of the mesh, and v and V components are defined at the middle of ξ-lines of the mesh. All the scalar variables including pressure, temperature, and density are located at the geometric center of the four vertices defining the mesh. References [4-6] suggest that with the combined use of the Cartesian velocity components and the staggered grid arrangement, difficulties arise when the grid lines turn ninety degrees from the original orientations, and the benefits of the grid staggering are lost.

A detailed discussion has been given in this regard in Ref. [3]. It was demonstrated that, if the metric terms between (x,y) and (ξ,η) coordinates are nonconstant, then the spurious pressure oscillations do not appear in both the staggered and nonstaggered grid. For the staggered grids, moreover, the problem of spurious pressure oscillations can be prevented even with the constant metric terms. One can simply define the curvilinear coordinates to be non-parallel to the Cartesian coordinates. Afterall, there is no reason to always insist on defining the ξ-lines in the inlet region to be parallel to x-lines.

Besides the algorithms utilizing the staggered grid arrangement, methods based on the nonstaggered grid arrangement have also been proposed for both the pressure and density-based algorithms, e.g., [10,11]. These methods require special procedures to prevent the decoupling of the velocity and pressure fields from exhibiting the chequerboard oscillations. For example, in [10] an explicit fourth-order pressure dissipation term is added to the pressure correction equation to suppress the spurious oscillations. However, with the use of finite mesh sizes, in reality the artificially added fourth-order gradient term may not be smaller than the original lower order derivative terms especially when there are large gradients present in the flowfield, as demonstrated by a Fourier type of analysis [12]. Hence the actual degrees of numerical accuracy may be affected by the numerical smoothing procedure. Furthermore, it is also well known [1] that artificially generated boundary conditions are needed for the pressure in a nonstaggered grid system. With the use of the staggered grid system, there is no need to devise artificial boundary conditions for the pressure correction equation [7] regardless of the orientation of the coordinate system. In terms of the momentum equations, since in general both P_ξ and P_η terms appear in both u- and v- momentum equations, some extrapolation procedures will still be needed for both types of grid arrangement. Table II summarizes the need of prescribing pressure boundary conditions in staggered and nonstaggered grid systems.

Table II. Grid systems versus need of pressure boundary conditions

	u-momentum equation	v-momentum equation	Continuity (or pressure) equation
Staggered Grid	needs artificial condition for p_η only	needs artificial condition for p_ξ only	needs no artificial condition
Non-staggered Grid	needs artificial conditions for both p_ξ and p_η	needs artificial conditions for both p_ξ and p_η	needs artificial condition

PRACTICAL FLOW EXAMPLES

Several examples of direct relevance to the aforementioned issues are presented. Results of flows in domains with ninety-degree and three-hundred-sixty-degree turnings are shown here. The first example shown is a diffuser with 90-degree turning (called a draft tube) which, as shown schematically in Fig. 3, has a fivefold increase of cross-sectional area from the inlet to the outlet. The shape of cross-section also varies from circular at inlet to rectangular at outlet. For this flow device, the static pressure recovery factor depends greatly on the inlet flow conditions imposed by the turbine runner exit velocity profiles. A series of theory/data comparisons has been conducted under different operating conditions [14,15]. Selected results of turbulent flow cases with $Re=10^6$ will be presented here. The numerical solutions were obtained by using the standard $k-\epsilon$ two-equation turbulence closure. Four grid sizes, with 7x11x13, 11x15x45, 18x21x61 and 21x29x81 nodes, have been adopted to assess numerical accuracy with respect to spatial resolution. The convection terms in the momentum equations were approximated by the second-order upward scheme. Both viscous and pressure terms were approximated by the standard central difference schemes.

Figures 2a and 2b show direct photographic information of two different operating conditions, full load and partial load. Figure 3a illustrates a 3-D view of the draft tube flow characteristics at full load condition. The velocity vectors are shown at the inlet and outlet sections. All the solid lines starting at the center region of the inlet section and finishing at the outlet section represent the streaklines of the mean velocity flow field. The twisted streaklines starting at the draft tube inlet center simulate correctly the straight rope observed at full load condition as shown in Figure 2a. The typical contra-rotating (opposite to the runner direction) free vortex flow at the draft tube inlet is shown in Figure 3b. The display of the velocity vectors in the main stream direction at the mid-section is represented in Figure 3c. The very weak velocity core, observed at the middle of the conical section, also indicates the presence of a rope at the center.

Figures 4a to 4c illustrate the draft tube behavior at partial load condition with a very high co-rotating inlet swirl. The display of the velocity vectors in the main stream direction at the mid-section indicates that a large flow recirculation zone is taking place in the conical section. The twisted spiral streaklines starting from the draft tube inlet center are very similar to the spiral rope observed in the laboratory flow visualization as shown in Figure 2b.

In order to study the evolution of the static and dynamic pressures along the main flow direction, massflow-weighted average values of these properties at each cross section are calculated. The numerical results are then compared with the experimental data in Figure 5. At the ordinate, the pressures are normalized by the inlet dynamic pressure. At the abscissa the center line length is normalized by the draft tube inlet diameter. Results from the two finer grid systems predict very well the variation of all the pressures, specially in the accelerating region located at the end of the elbow section. The agreements between prediction and measurement worsen as grid resolutions degrade.

The flow behavior in the elbow draft tube, with an optimal inlet swirling flow, was investigated in detail with pitot traverses taken from several cross sections. The experimental data are compared with numerical results. The display of the velocity vectors in the main flow direction is shown in Figure 6. The numerical result obtained with the 18x21x61 grid system is presented. Observation of the velocity vector distribution at different elevation and plan views indicates clearly that a large recirculation zone occurs at the middle of the elbow section. Further downstream, flow separation appears at the center and near the top of the draft tube. Also toward the outlet of the draft tube, the flow is somewhat shifted to one side wall. This tendency is more accentuated with a stronger inlet swirling flow. The comparison of the predicted head losses with experimental data is shown in Figure 7. The head loss is about 2% for optimal load, but it increases rapidly for off-design conditions. The numerical result agrees very well with laboratory measurement for the whole range of the runner operating conditions, except for very high swirl intensity at partial load where flow instability was observed during the test.

The next example is also a 90-degree turning duct but with neither area changes nor cross-sectional shape variations. Figure 8 shows some schematic illustration of the geometry, grid distribution, and velocity as well as static pressure solution. Figure 9 shows the static pressure distribution along the center line of the outer and inner walls. Same as the previous examples, no oscillation of pressure field are observed.

As a further demonstration, a flow domain of 360-degree turning, the so-called casing, is used. The schematic representations of the casing, including the overall geometry, the evolution of the size of cross-section, and representative grid distributions are summarized in Fig. 10. The fluid enters from the upstream inlet and exits through the inner circumferencial surface. The grid system is of the size of 95x21x13 nodes. Figure 11 shows a top-view of a casing with smooth and continuous turning. Figure 12 shows the computed particle trajectories in short time durations and static pressure distributions in the middle top-view plane for a laminar flow. The Reynolds number based on the fluid kinematic viscosity, the incoming uniform velocity and the inlet diameter of the present case is 100. It can be seen that throughout the whole flow domain, no spurious oscillations are present in numerical solution. With the given Reynolds number, the flow in the casing shows combined characteristics of that through a pipe (in the outer portion of the casing) and that into a sink (in the inner portion of the casing). Figure 13 shows a turbulent flow calculation with $Re=10^6$ and with the standard $k-\epsilon$ model. For the high Reynolds number flow, there is less influence of the mean pressure gradient along the circumferential direction than along the radial direction. Again, no spurious oscillations are present in Fig. 13.

CONCLUSIONS

The present work aims at investigating the fundamental issues of adopting the velocity variables and grid systems for computing the complex fluid flow in irregular geometries with the employment of a non-orthogonal curvilinear coordinate system. It is clear that the strong conservation-law in differential forms can be completely retained by the use of Cartesian velocity components. However, the use of the covariant or contravariant velocity components generally introduces source terms into the differential governing equations due to the curvature effects. In the framework of the finite-volume approach, the momentum equations based on the Cartesian velocity components can satisfy the geometric conservation law for both convection and pressure terms. The second derivative (viscous) terms involve nonlinear metric terms and hence do not guarantee the satisfaction of the geometric conservation law. For the equations based on the curvilinear velocity components, the nonlinear metric terms appear in both the first and second derivative terms. Coupled with the curvature source terms, the utilization of the curvilinear velocity components as the primary variables makes the degree of satisfaction in terms of honoring the geometric conservation law more influenced by the grid skewness. A unique issue facing the use of the Cartesian velocity components along with a staggered grid arrangement is that of a 90-degree turning. It is demonstrated here that satisfactory solutions can be obtained with this approach even with the 90-degree and 360-degree turnings.

REFERENCES

1. Peyret, R. and Taylor, T. D., Computational Methods for Fluid Flow, Springer-Verlag, New York (1983).

2. Correa, S. M. and Shyy, W., "Computational Models and Methods for Continuous Gaseous Turbulent Combustion," Prog. Energy Combust. Sci., 13, 249-292 (1987).

3. Shyy, W. and Vu, T. C., "On the Adoption of Velocity Variable and Grid System for Fluid Flow Computation in Curvilinear Coordinates," accepted for publication in J. Comput. Phys..

4. Yang, H. Q. and Yang, K. T., "Buoyant Flow Calculations with Non-Orthogonal Curvilinear Coordinates for Vertical and Horizontal Parallelpiped Enclosures," Inter. J. Numer. Meths. Engrg., 25, 331-345 (1988).

5. Karki, K. C. and Patankar, S. V., "Calculation Procedure for Viscous Incompressible Flows in Complex Geometries," Numer. Heat Transf., 14, 295-307 (1988).

6. Wittig, S., Bayer, H. J. and Noll, B., "On the Application of Finite-Difference Techniques for the Computation of the Flow Field in Gas Turbine Combustors with Complex Geometries," in Combustion and Fuels in Gas Turbine Engines, AGARD CP No. 422, Paper No. 28 (1988).

7. Shyy, W., Tong, S.-S. and Correa, S. M., "Numerical Recirculating Flow Calculation Using a Body-fitted Coordinate System," Numer. Heat Transf., 8, 99-131 (1985).

8. Thomas, P. D. and Lombard, C. K., "Geometric Conservation Law and Its Application to Flow Computations on Moving Grids," AIAA J., 17, 1030-1037 (1979).

9. Braaten, M. E. and Shyy, W., "A Study of Recirculating Flow Computation Using Body-fitted Coordinates: Consistency Aspects and Mesh Skewness," Numer. Heat Transf., 9, 559-574 (1986).

10. Rhie, C. M., "A Pressure Based Navier-Stokes Solver Using the Multigrid Method," AIAA Paper No. 86-0207 (1986).

11. Kwak, D. K., Chang, J. L. C., Shanks, S. P. and Chakravarthy, S. R., "An Incompressible Navier-Stokes Flow Solves in Three-Dimensional Curvilinear Coordinate System Using Primitive Variables," AIAA Paper NO. 84-0253 (1984).

12. Shyy, W., "A Study of Finite Difference Approximations to Steady-State Convection-Dominated Flow Problems," J. Comput. Phys., 57, 415-438 (1985).

13. Vu, T. C. and Shyy, W., "Viscous Flow Analysis as a Design Tool for Hydraulic Turbine Components," ASME J. Fluids Engrg., (to appear).

14. Vu, T. C. and Shyy, W., "Viscous Flow Analysis for Hydraulic Turbine Draft Tubes," ASME J. Fluids Engrg., (to appear).

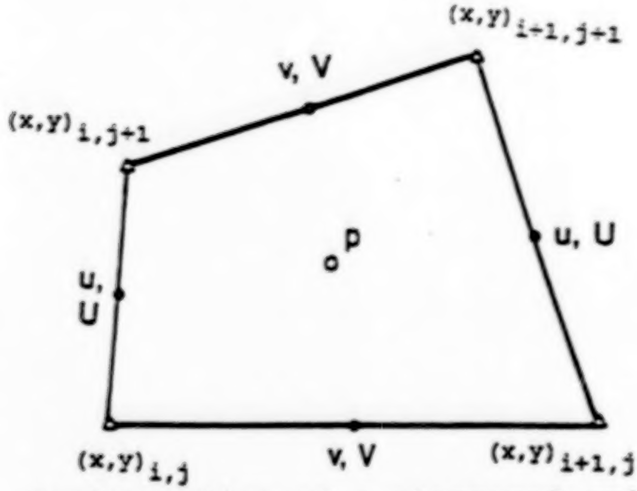

Fig. 1 Configuration of a staggered grid system.

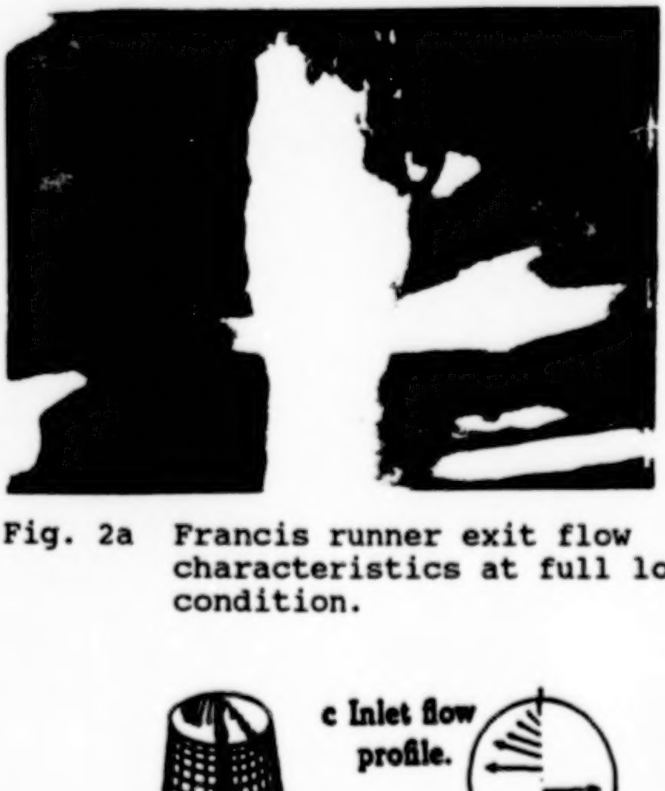

Fig. 2a Francis runner exit flow characteristics at full load condition.

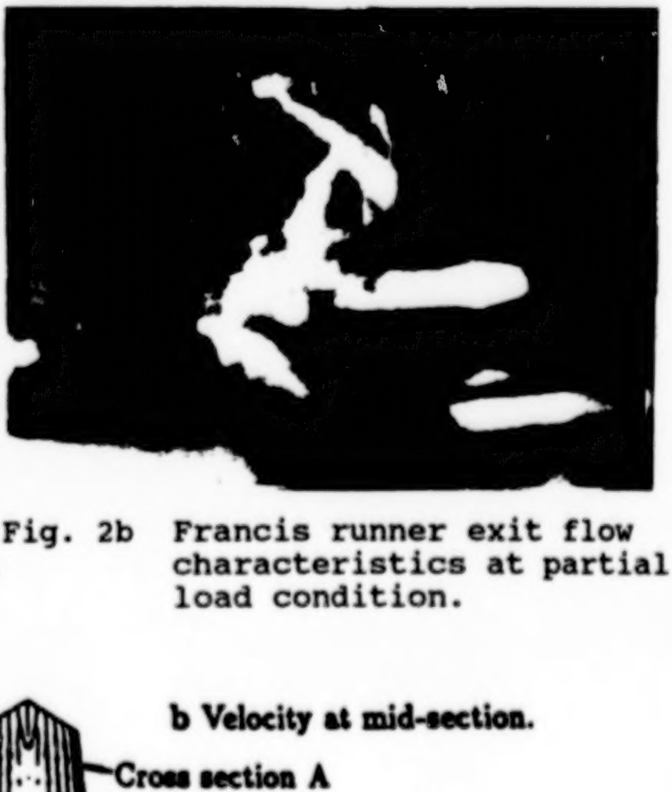

Fig. 2b Francis runner exit flow characteristics at partial load condition.

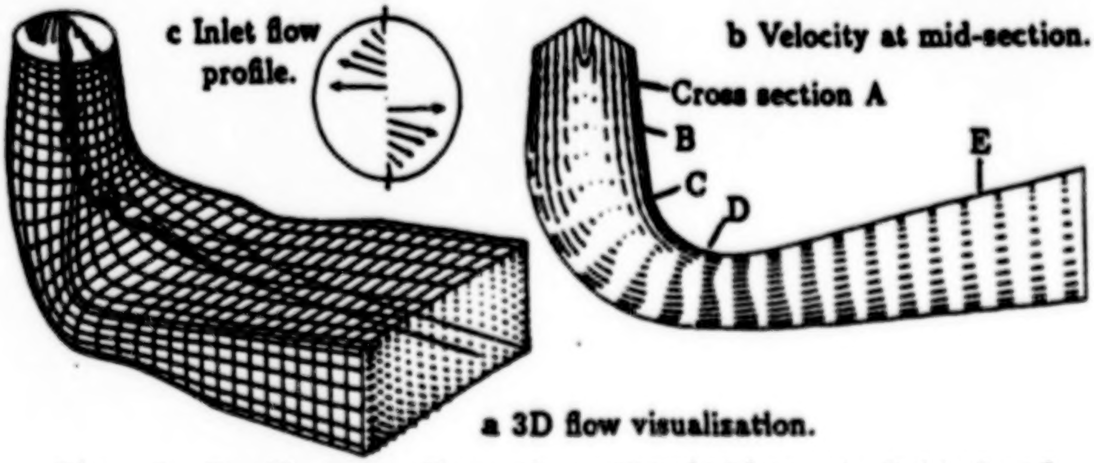

Fig. 3 Draft tube flow characteristics at full load condition.

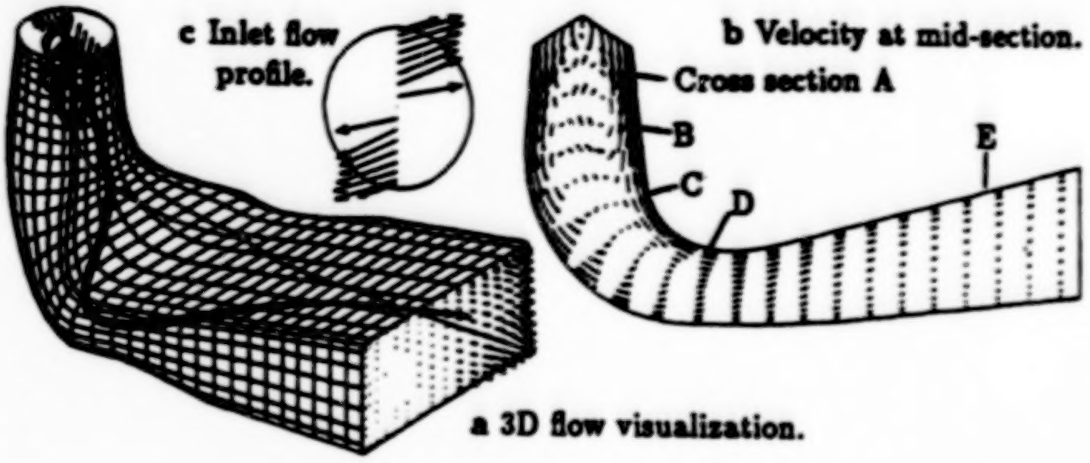

Fig. 4 Draft tube flow characteristics at partial load condition.

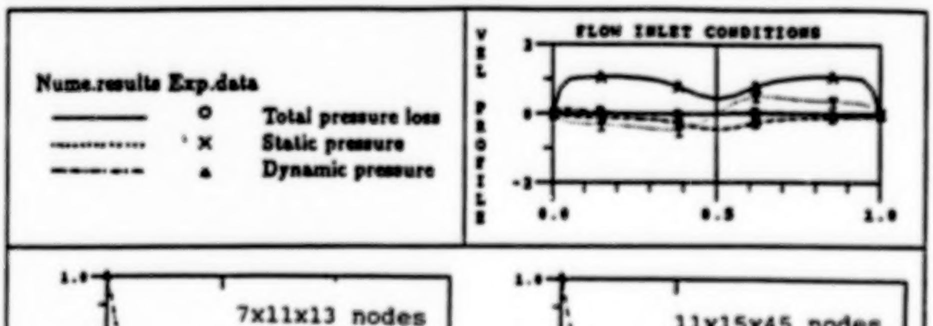

Fig. 5 Flow behavior with inlet swirling flow. Evolution of dynamic and static pressure and of total pressure loss.

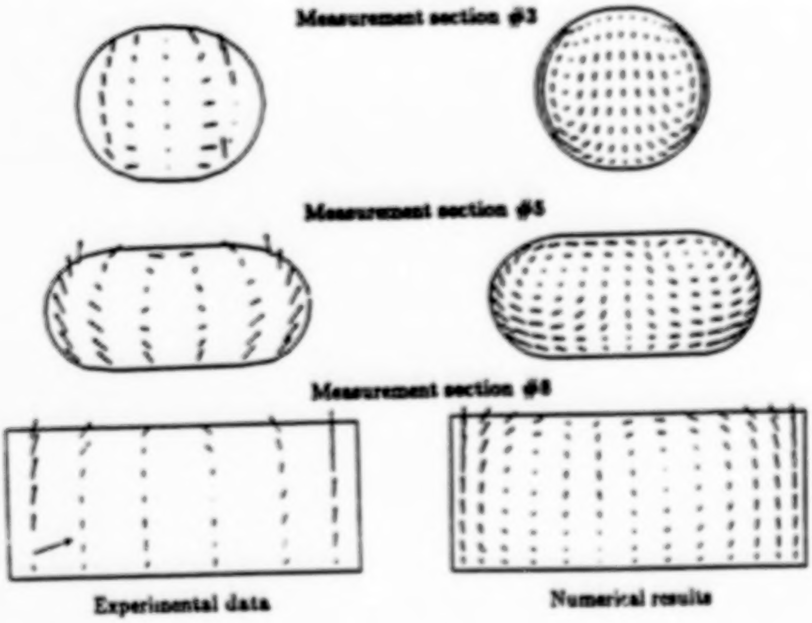

Fig. 6 Flow behavior with inlet uniform flow - Secondary flow (Flow coming toward the reader).

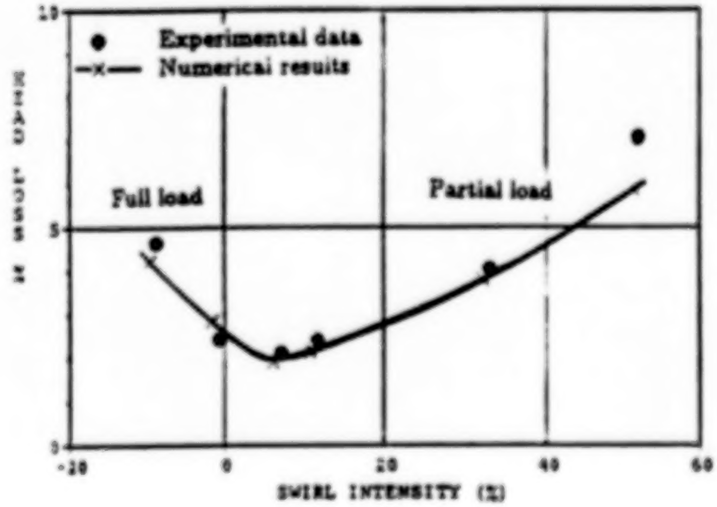

Fig. 7 Head losses in an elbow draft tube for different turbine operating conditions. Comparison between numerical results and experimental data.

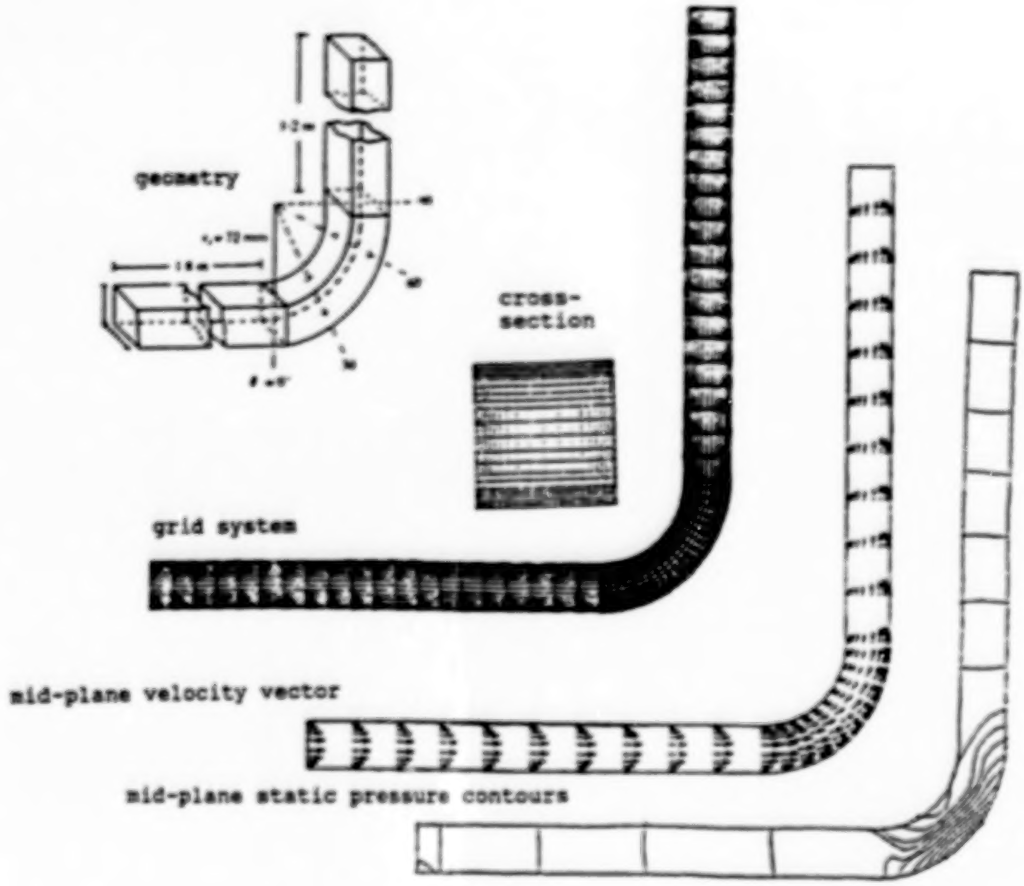

Fig. 8 Geometry, grid, velocity, and pressure of a 90-degree turning duct of constant cross-section.

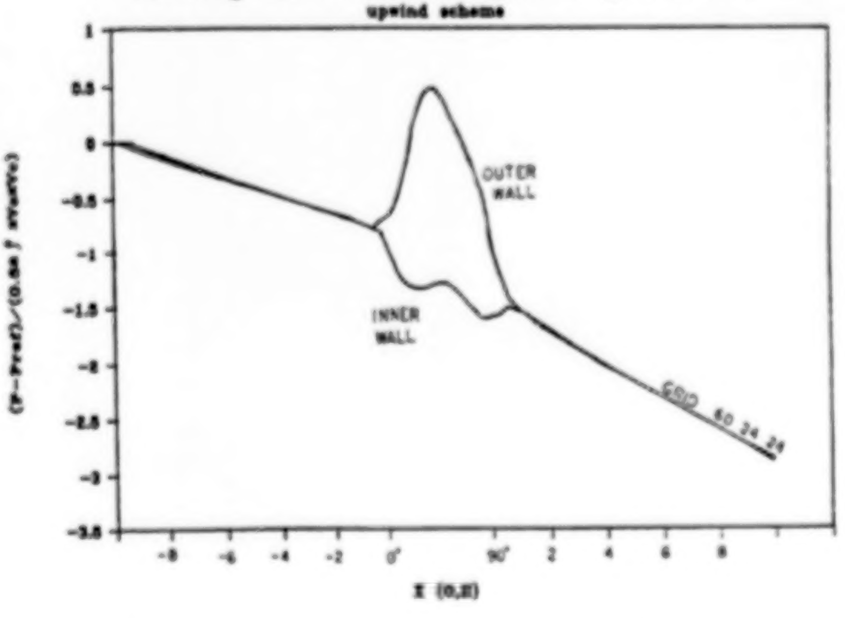

Fig. 9 Static pressure along center line of 90-degree turning duct with constant cross-section.

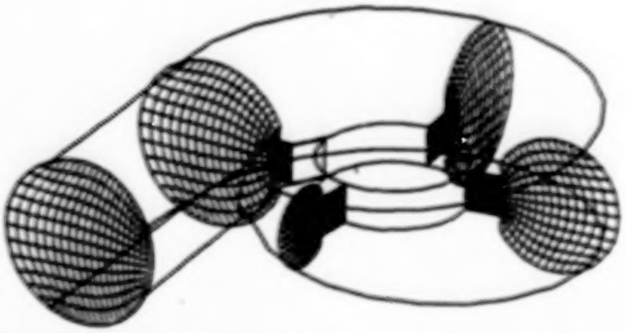

Selection grid distribution in cross-sectional planes

Fig. 10 Geometry and grid system of casing with 360-degree turning.

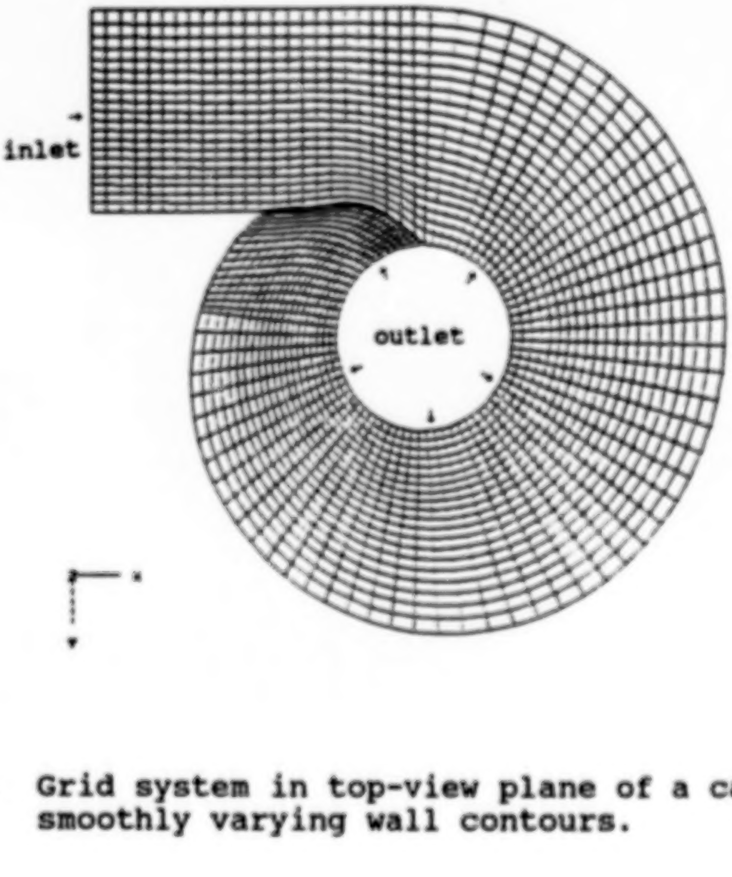

Fig. 11 Grid system in top-view plane of a casing with smoothly varying wall contours.

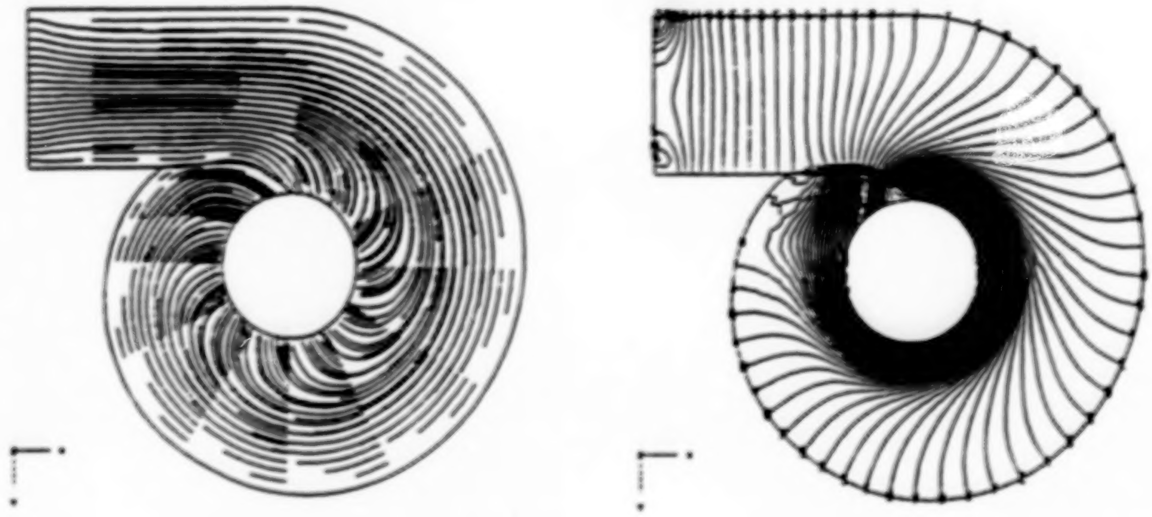

particle trajectories static pressure contours

Fig. 12 Solution of laminar flow (Re=100) in a casing with smoothly varying wall contours.

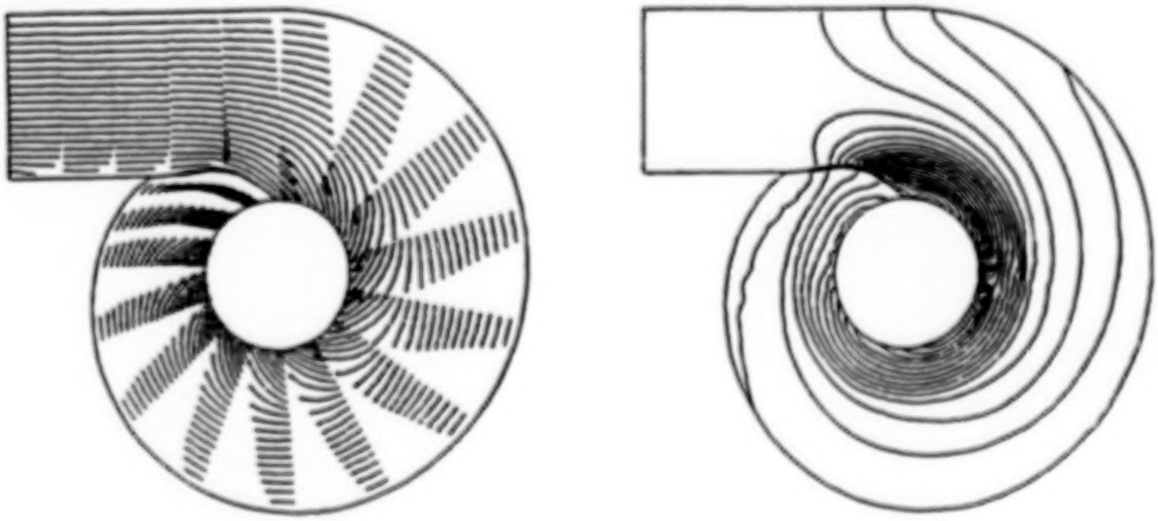

particle trajectories static pressure contours

Fig. 13 Solution of turbulent flow (Re=10^6) in a casing with smoothly varying wall contours.

DISTRIBUTED MINIMAL RESIDUAL (DMR) METHOD FOR ACCELERATION OF ITERATIVE ALGORITHMS

Seungsoo Lee and George S. Dulikravich
Pennsylvania State University
University Park, Pennsylvania, U.S.A.

ABSTRACT

A new method for enhancing convergence rate of iterative algorithms for the numerical integration of systems of partial differential equations has been developed. It is termed the Distributed Minimal Residual (DMR) method and it is based on general Krylov subspace methods. The DMR method differs from the Krylov subspace methods by the fact that the iterative acceleration factors are different from equation to equation in the system. At the same time, the DMR method can be viewed as an incomplete Newton iteration method. The DMR method has been applied to Euler equations of gasdynamics and incompressible Navier-Stokes equations. All numerical test cases were obtained using either explicit four stage Runge-Kutta or Euler implicit time integration. The formulation for the DMR method is general in nature and can be applied to explicit and implicit iterative algorithms for arbitrary systems of partial differential equations.

INTRODUCTION

After linearization caused by the discretization, the systems of governing equations associated with , say, fluid flows are recast into the following linear system of algebraic equations

$$\mathbf{AX} = \mathbf{b} \qquad (1)$$

where **X** is the vector of unknowns and **A** is an N×N matrix which depends on the discretized scheme, and is assumed to be non-singluar. The matrix **A** is usually sparse and as N becomes larger, it is not economical to solve the system of equations directly. Instead, iterative methods are usually utilized.

The Conjugate Gradient (CG) method and the Conjugate Residual (CR) method, are widely used for approximating the solution of the system (Huynh, ref. 1; Faddeev and Faddeeva, ref. 2). Both methods give the exact solution in at most N steps in the absence of round-off errors. However, the

CG method and the CR method require the matrix **A** to be symmetric, positive definite. A large number of generalizations of these methods applicable to systems with a non-symmetric matrix have been made. The success of the generalization of the CG and CR methods is reflected in the introduction of a series of algorithms capable of treating non-symmetric problems (OTHMIN by Vinsome, ref. 3; ORTHDIR and ORTHRES by Young and Jea, ref. 4; GMRES by Saad and Schultz, ref. 5; Wigton et al., ref. 6). The Minimal Residual method (Hafez, ref. 7) and the Generalized Nonlinear Minimal Residual method (Huang and Dulikravich, ref. 8) can be thought of as generalizations of the conjugate residual method.

In this paper, a new method of enhancing convergence rate of iterative algorithms for systems of partial differential equations is developed. The method is entitled Distributed Minimal Residual (DMR) method (Lee et al., ref. 9-14) and it is related to a general Krylov subspace method from which it differs in two aspects. First, the DMR method attempts to improve on a straight application of a Krylov subspace method by using a separate sequence of acceleration factors for each equation in the system. In application of the DMR method to Euler equations of inviscid gasdynamics, for example, the acceleration factors for continuity equation differ from those for two momentum equations and for energy equation. This approach requires fewer consecutive solutions to be stored. Effectively, the DMR method periodically preconditions the system. Second, the DMR method does not involve the orthogonalization procedure which most of Krylov subspace methods utilize to reduce the number of numerical operations. The DMR method uses corrections from only two or three consecutive solutions for a successful application.

The prime objective of this paper is to develop the theory of the DMR method and to examine the effectiveness of the DMR method by applying it to different systems of partial differential equations: Euler equations of inviscid gasdynamics and incompressible flow Navier-Stokes equations. Runge-Kutta time stepping method and Euler implicit method were used as two basic iterative algorithms.

DISTRIBUTED MINIMAL RESIDUAL (DMR) METHOD

Let us consider a system of partial differential equations that are integrated iteratively so that their residual vector at iteration level t is given by

$$\mathbf{R}^t = \frac{\partial \mathbf{E}^t}{\partial x} + \frac{\partial \mathbf{F}^t}{\partial y} + \frac{\partial \mathbf{G}^t}{\partial z} \tag{2}$$

where $\mathbf{E}^t$, $\mathbf{F}^t$, $\mathbf{G}^t$ are the generalized flux vectors (at iteration level t) that act in the directions x, y, z, respectively. The future residual at iteration level t+1 is given by

$$\mathbf{R}^{t+1} = \frac{\partial \mathbf{E}}{\partial x}^{t+1} + \frac{\partial \mathbf{F}}{\partial y}^{t+1} + \frac{\partial \mathbf{G}}{\partial z}^{t+1} \tag{3}$$

Assume that each component of the solution vector at iteration level t+1 is extrapolated from the corresponding previous M consecutive iteration levels. Then, we can say that

$$q_1^{t+1} = q_1^t + \omega_1^1 \Delta q_1^1 + \omega_1^2 \Delta q_1^2 + \cdots + \omega_1^M \Delta q_1^M$$

$$q_2^{t+1} = q_2^t + \omega_2^1 \Delta q_2^1 + \omega_2^2 \Delta q_2^2 + \cdots + \omega_2^M \Delta q_2^M$$

$$\cdots\cdots\cdots\cdots\cdots\cdots\cdots\cdots\cdots\cdots$$

$$q_L^{t+1} = q_L^t + \omega_L^1 \Delta q_L^1 + \omega_L^2 \Delta q_L^2 + \cdots + \omega_L^M \Delta q_L^M \tag{4}$$

Here, the subscripts 1, 2, 3, ..., L designate the particular component of the solution vector **Q**, that is, the particular equation in the system. The superscripts 1, 2, 3, ..., M designate the particular iteration level counting backward from the present iteration level, t. Thus, the superscript 1 means the first previous iteration level. The superscript 2 means the second previous iteration level, etc. This can be expressed in a more compact form as

$$\mathbf{Q}^{t+1} = \mathbf{Q}^t + \sum_{m=1}^{M} \Theta^m \tag{5}$$

where

$$\Theta^n = \begin{bmatrix} \omega_1^n \Delta_1^n \\ \omega_2^n \Delta_2^n \\ \cdot \\ \cdot \\ \cdot \\ \omega_L^n \Delta_L^n \end{bmatrix} = \omega_1^n \begin{bmatrix} \Delta_1^n \\ 0 \\ \cdot \\ \cdot \\ \cdot \\ 0 \end{bmatrix} + \omega_2^n \begin{bmatrix} 0 \\ \Delta_2^n \\ \cdot \\ \cdot \\ \cdot \\ 0 \end{bmatrix} + \cdots + \omega_L^n \begin{bmatrix} 0 \\ 0 \\ \cdot \\ \cdot \\ \cdot \\ \Delta_L^n \end{bmatrix} \tag{6}$$

Here, ω's are the acceleration (weighting) factors to be calculated, Δ's are the iterative corrections computed with the original non-accelerated scheme, M denotes the total number of consecutive time steps from which the corrections are combined.

Using Taylor series expansion in time for $\mathbf{R}^{t+1}$ and truncating the terms that are higher than second order in Δt, Eq. 3 becomes approximately

$$\mathbf{R}^{t+1} = \mathbf{R}^{t} + \sum_{m=1}^{M} \left[\frac{\partial}{\partial x}\mathbf{A}^{t}\cdot + \frac{\partial}{\partial y}\mathbf{B}^{t}\cdot + \frac{\partial}{\partial z}\mathbf{C}^{t}\cdot\right]\mathbf{\Theta}^{m} \tag{7}$$

The global domain residual can be defined as

$$R^{t} = \sum_{D} \mathbf{R}^{tT}\,\mathbf{R}^{t} \tag{8}$$

where $\sum_{D}$ denotes summation over the computational domain D, and the superscript T represents transpose of a vector. In order to minimize the future global residual, R^{t+1}, the ω's are determined from the following conditions

$$\frac{\partial R^{t+1}}{\partial \omega_{r}^{m}} = 0 \tag{9}$$

From Eq. 8 this leads to

$$\begin{aligned} -\sum_{D} \mathbf{R}^{tT} \left[\frac{\partial}{\partial x}\mathbf{A}^{t}\cdot + \frac{\partial}{\partial y}\mathbf{B}^{t}\cdot + \frac{\partial}{\partial z}\mathbf{C}^{t}\cdot\right]\frac{\partial \mathbf{\Theta}^{m}}{\partial \omega_{r}^{m}} \\ = \sum_{D}\sum_{n}^{M} \left\{\left[\frac{\partial}{\partial x}\mathbf{A}^{t}\cdot + \frac{\partial}{\partial y}\mathbf{B}^{t}\cdot + \frac{\partial}{\partial z}\mathbf{C}^{t}\cdot\right]\mathbf{\Theta}^{n}\right\}^{T}\cdot \\ \left\{\left[\frac{\partial}{\partial x}\mathbf{A}^{t}\cdot + \frac{\partial}{\partial y}\mathbf{B}^{t}\cdot + \frac{\partial}{\partial z}\mathbf{C}^{t}\cdot\right]\frac{\partial \mathbf{\Theta}^{m}}{\partial \omega_{r}^{m}}\right\} \end{aligned} \tag{10}$$

where

$$\frac{\partial \mathbf{\Theta}^{m}}{\partial \omega_{r}^{m}} = \left[\Delta_{p}^{m}\delta_{pr}\right] \tag{11}$$

and δ_{pr} is the Kronecker delta. However, from Eq. 6 we have that

$$\Theta^n = \sum_q^L \omega_q^n \frac{\partial \Theta^n}{\partial \omega_q^n} \tag{12}$$

Noticing that $\frac{\partial \Theta^n}{\partial \omega_q^n}$ is not a function of ω, it follows that

$$- \sum_D \mathbf{R}^{tT} \left[\frac{\partial}{\partial x}\mathbf{A}^{t}\cdot + \frac{\partial}{\partial y}\mathbf{B}^{t}\cdot + \frac{\partial}{\partial z}\mathbf{C}^{t}\cdot \right] \frac{\partial \Theta^m}{\partial \omega_r^m}$$

$$= \sum_D \sum_n^M \sum_q^L \omega_q^n \left\{ \left[\frac{\partial}{\partial x}\mathbf{A}^{t}\cdot + \frac{\partial}{\partial y}\mathbf{B}^{t}\cdot + \frac{\partial}{\partial z}\mathbf{C}^{t}\cdot \right] \frac{\partial \Theta^n}{\partial \omega_q^n} \right\}^T \cdot$$

$$\left\{ \left[\frac{\partial}{\partial x}\mathbf{A}^{t}\cdot + \frac{\partial}{\partial y}\mathbf{B}^{t}\cdot + \frac{\partial}{\partial z}\mathbf{C}^{t}\cdot \right] \frac{\partial \Theta^m}{\partial \omega_r^m} \right\} \tag{13}$$

Let

$$\mathbf{a}_q^n = \left[\frac{\partial}{\partial x}\mathbf{A}^{t}\cdot + \frac{\partial}{\partial y}\mathbf{B}^{t}\cdot + \frac{\partial}{\partial z}\mathbf{C}^{t}\cdot \right] \frac{\partial \Theta^n}{\partial \omega_q^n} \tag{14}$$

Then Eq. 13 becomes

$$- \sum_D \mathbf{R}^{tT} \mathbf{a}_r^m = \sum_n^M \sum_q^L \sum_D \omega_q^n \mathbf{a}_q^{nT} \mathbf{a}_r^m \tag{15}$$

For simplicity, let

$$c_{q\,r}^{nm} = \sum_D \mathbf{a}_q^{nT} \mathbf{a}_r^m \tag{16}$$

and

$$b_r^m = - \sum_D \mathbf{R}^{tT} \mathbf{a}_r^m \tag{17}$$

Then, the system of algebraic equations (Eq. 15) can be written as

$$\sum_n^M \sum_q^L \omega_q^n \, c_{q\,r}^{nm} = b_r^m \tag{18}$$

or

$$\begin{bmatrix} c^{11}_{11} & c^{11}_{21} & \dots & c^{11}_{L1} & c^{21}_{11} & \dots & c^{M1}_{L1} \\ c^{11}_{12} & c^{11}_{22} & \dots & c^{11}_{L2} & c^{21}_{12} & \dots & c^{M1}_{L2} \\ \vdots & \vdots & \vdots & \vdots & \vdots & \vdots & \vdots \\ c^{11}_{1L} & c^{11}_{2L} & \dots & c^{11}_{LL} & c^{21}_{1L} & \dots & c^{M1}_{LL} \\ c^{12}_{11} & c^{12}_{21} & \dots & c^{12}_{L1} & c^{22}_{11} & \dots & c^{11}_{L1} \\ \vdots & \vdots & \vdots & \vdots & \vdots & \vdots & \vdots \\ c^{1M}_{1L} & c^{1M}_{2L} & \dots & c^{1M}_{LL} & c^{11}_{1L} & \dots & c^{MM}_{LL} \end{bmatrix} \begin{bmatrix} \omega^1_1 \\ \omega^1_2 \\ \vdots \\ \omega^1_L \\ \omega^2_1 \\ \vdots \\ \omega^M_L \end{bmatrix} = \begin{bmatrix} b^1_1 \\ b^1_2 \\ \vdots \\ b^1_L \\ b^2_1 \\ \vdots \\ b^M_L \end{bmatrix} \tag{19}$$

representing the system of L×M linear algebraic equations for the L×M optimum acceleration factors ω. For example, if we are periodically to combine corrections from $M = 2$ consecutive time steps to extrapolate the solution and to solve a system of $L = 4$ partial differential equations, we need to solve simultaneously $L \times M = 8$ algebraic equations for 8 values of ω.

Notice that when the convergence is achieved, the b's become zero (Eq. 17), thus making the ω's zero. In other words, the accuracy of the fully converged solution will not be affected by using the DMR method. Furthermore, if the matrix $c^{nm}_{q\,r}$ is positive definite, it can be shown easily that the ω's minimize the global residual, R^{t+1}, at iteration level t+1. Using a different sequence of acceleration factors for each partial differential equation in the original system is equivalent to using a different time step for each equation or selectively preconditioning the system. The DMR method, therefore, can be understood as the combination of a preconditioning method and a Krylov subspace method. Also, we can think of the DMR method as an incomplete Newton iteration. This point can be illustrated by the following fact. When the acceleration factors vary not only from equation to equation, but also from grid point to grid point, and when we use just one solution in the DMR formulation, it can be shown that the DMR method is equivalent to the Newton iterations.

APPLICATION OF THE DMR METHOD TO EULER EQUATIONS OF GASDYNAMICS

The introduction of the successful numerical algorithms such as the Euler implicit method and the explicit Runge-Kutta time stepping method made it relatively inexpensive to perform the numerical integration of the systems of partial differential equations governing compressible flows. Most of such algorithms, however, suffer from slow convergence at low Mach numbers. The reasons for this are the rapidly increased stiffness and the singular behavior of the original system of compressible flow equations at low Mach numbers. The singular behavior of the system near Mach number zero can be removed by eliminating the singularity of the system by a perturbation technique (Briley, ref. 15; Choi, ref. 16). The stiffness of the system at low Mach numbers can be reduced by preconditioning the system (Turkel, ref. 17; Choi, ref. 16). The DMR method is used to alleviate the difficulty associated with the increased stiffness of the Euler equations for low Mach number compressible flows.

Euler Equations for Compressible flows

The Euler equations for a two-dimensional unsteady inviscid flow expressed in a generalized non-orthogonal curvilinear coordinates (ξ, η) without body forces or heat transfer, can be written in a vector form as

$$\frac{\partial \tilde{\mathbf{Q}}}{\partial t} + \frac{\partial \tilde{\mathbf{E}}}{\partial \xi} + \frac{\partial \tilde{\mathbf{F}}}{\partial \eta} = 0 \qquad (20)$$

where

$$\tilde{\mathbf{Q}} = \frac{1}{J}\begin{bmatrix} \rho \\ \rho u \\ \rho v \\ e \end{bmatrix} \qquad \tilde{\mathbf{E}} = \frac{1}{J}\begin{bmatrix} \rho U \\ \rho U u + p\xi_x \\ \rho U v + p\xi_y \\ (e+p)U \end{bmatrix} \qquad \tilde{\mathbf{F}} = \frac{1}{J}\begin{bmatrix} \rho V \\ \rho V u + p\eta_x \\ \rho V v + p\eta_y \\ (e+p)V \end{bmatrix} \qquad (21)$$

The subscripts x and y represent first (partial) derivatives with respect to x and y, respectively. Here, ρ is the density, p is the thermodynamic pressure, e is the total energy per unit volume, while u, and v are the Cartesian velocity components along x and y axis, respectively. J is the Jacobian determinant, $\frac{\partial(\xi,\eta)}{\partial(x,y)}$, while U and V are the contravariant velocity vector components defined as

$$\begin{bmatrix} U \\ V \end{bmatrix} = \begin{bmatrix} \xi_x & \xi_y \\ \eta_x & \eta_y \end{bmatrix}\begin{bmatrix} u \\ v \end{bmatrix} \qquad (22)$$

Numerical Algorithm

The artificial dissipation suggested by Steger and Kutler (ref. 18) was used in the form

$$D(J\tilde{Q}) = \frac{\varepsilon}{8J\Delta t}\nabla^4\left[J\tilde{Q}\right] \qquad (23)$$

where ∇^4 is the biharmonic differential operator in ξ, η coordinates and ε is a parameter. The residual vector $\hat{\mathbf{R}}$ of Euler equations for compressible flow including the artificial dissipation is

$$\hat{\mathbf{R}} = \frac{\partial\tilde{\mathbf{E}}}{\partial\xi} + \frac{\partial\tilde{\mathbf{F}}}{\partial\eta} + \frac{\varepsilon}{8J\Delta t}\nabla^4\left[J\tilde{Q}\right] \qquad (24)$$

After discretization, the governing equations become a set of ordinary differential equations, which can be integrated by the Runge-Kutta time stepping method (Jameson et al., ref. 18).

$$\begin{aligned} \tilde{Q}^0 &= \tilde{Q}^t \\ \Delta\tilde{Q}^k &= -\alpha_k\Delta t\hat{\mathbf{R}}^{k-1} \qquad k = 1,2,\ldots,K \\ \tilde{Q}^{t+1} &= \tilde{Q}^t + \Delta\tilde{Q}^K \end{aligned} \qquad (25)$$

where α_k are the coefficients for each of the K stages of the Runge-Kutta scheme required to advance the solution from the time level t to the time level t+1. For example, α_k = 1/4, 1/3, 1/2 and 1 for the four stage Runge-Kutta scheme.

The time steps for each direction are estimated (MacCormack and Baldwin, ref. 19) from

$$\Delta t_\xi = \frac{CFL}{|U| + c(\xi_x^2 + \xi_y^2)^{1/2}} \qquad \Delta t_\eta = \frac{CFL}{|V| + c(\eta_x^2 + \eta_y^2)^{1/2}} \qquad (26)$$

where c is the local speed of sound and CFL is the Courant-Friedrichs-Lewy number. The maximum time step is given as

$$\Delta t = \frac{\Delta t_\xi \Delta t_\eta}{\Delta t_\xi + \Delta t_\eta} \qquad (27)$$

The implicit characteristic boundary procedure of Chakravarthy (ref. 20) was used, though the scheme itself is explicit. Entropy per unit mass ($s = p/\rho^{\gamma}$), total enthalpy per unit mass, $h = (e+p)/\rho$, and flow angle ($\tan(\alpha) = v/u$) are specified at the inflow boundary. For a subsonic downstream outflow boundary (ξ = constant), the equation corresponding to the negative eigenvalue, $U - c(\xi_x^2 + \xi_y^2)^{1/2}$, is substituted with a constant back pressure, p_b. For a solid wall boundary (η = constant), the equation corresponding to the positive eigenvalue, $V + c(\eta_x^2 + \eta_y^2)^{1/2}$, is substituted with a tangency boundary condition, $V = 0$.

Upon applying the DMR method to the system of Euler equation of gasdynamics, Eq. 14, becomes

$$\mathbf{a}_q^m = \left[\frac{\partial}{\partial \xi}\tilde{\mathbf{A}}^{t}\cdot \; + \frac{\partial}{\partial \eta}\tilde{\mathbf{B}}^{t}\cdot \; + \mathbf{D}\mathbf{J}\cdot\right]\frac{\partial \Theta^m}{\partial \omega_q^m} \tag{28}$$

where $\tilde{\mathbf{A}}$ and $\tilde{\mathbf{B}}$ are the Jacobian matrices in the transformed coordinates

$$\tilde{\mathbf{A}} = \frac{\partial \tilde{\mathbf{E}}}{\partial \tilde{\mathbf{Q}}} \qquad\qquad \tilde{\mathbf{B}} = \frac{\partial \tilde{\mathbf{F}}}{\partial \tilde{\mathbf{Q}}} \tag{29}$$

Results for Compressible Euler Equations

A two-dimensional flow analysis code has been developed in FORTRAN according to the previous theory for Euler equations of gasdynamics using finite differencing. All computational results were obtained on CRAY-YMP at NAS facility using automatic vectorization.

The test case for the code was flow around a circular cylinder. The outer boundary of the computational domain was located at 20 times the radius of the cylinder. A 66×32 cell computational grid was used in this test case. The computations were performed with and without the DMR method in conjunction with the four stage Runge-Kutta (RK) scheme. The convergence histories are plotted in terms of the number of iterations and in terms of the CPU time (Fig. 1). The maximum allowable CFL number (CFL = 2.8) was used in both accelerated and non-accelerated computations. The free stream Mach number was chosen to be 0.05 which is practically an incompressible flow. The DMR method saves over 60 % of total CPU time in this critical flow test case. The surface pressure coefficient (Fig. 2) matches well with the incompressible potential flow solution.

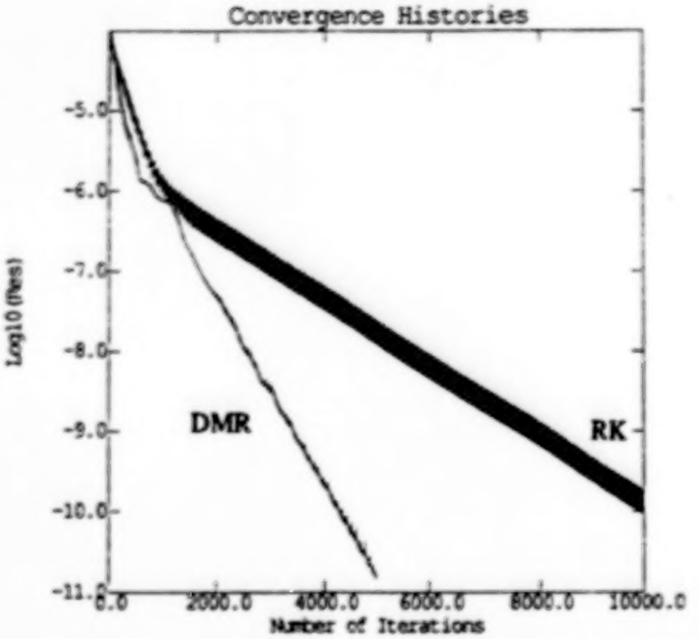

Figure 1 Convergence histories for the inviscid flow around a circular cylinder with $M_\infty = 0.05$

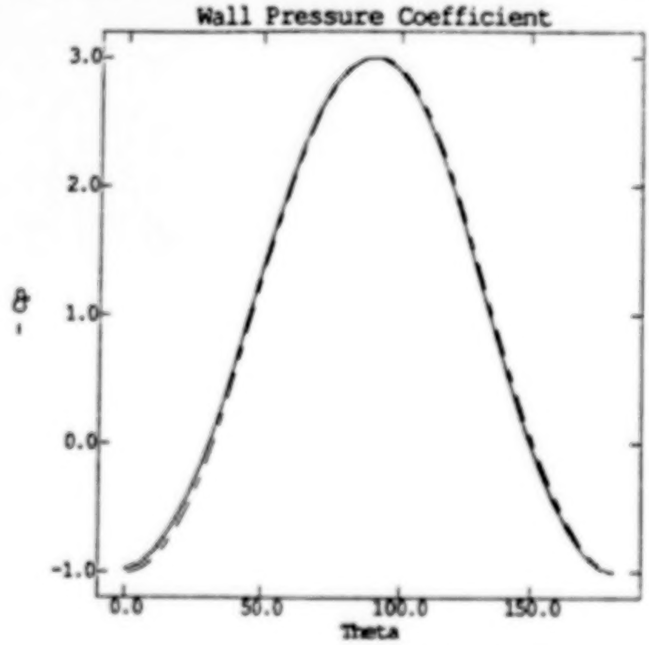

Figure 2 Wall pressure coefficient distribution for the inviscid flow around a circular cylinder: numerical with $M_\infty = 0.05$ (solid line); analytical with $M_\infty = 0$ (dotted line)

APPLICATION OF THE DMR METHOD TO INCOMPRESSIBLE NAVIER-STOKES EQUATIONS

The main difficulty associated with the incompressible flow computations is caused by the absence of a time derivative term in the continuity equation. One of the methods for solving the incompressible

Navier-Stokes equations was originated by Chorin (ref. 21). In this concept, an artificially time dependent derivative term $\frac{\partial(p/\beta)}{\partial t}$ is added to the continuity equation with a user specified control parameter β. The artificial time derivative diminishes as the solution converges to its steady state. The added term forces the system to be of a mixed parabolic-hyperbolic type, which allows the use of time marching techniques. Later, Choi and Merkle (ref. 22), and Kwak et al. (ref. 23) used an Alternating Direction Implicit (ADI) method in conjunction with the artificial compressibility method.

Incompressible Flow Navier-Stokes Equations

The two-dimensional Navier-Stokes equations in a general non-orthogonal curvilinear coordinates ξ, η are given as

$$\frac{\partial \tilde{\mathbf{Q}}}{\partial t} + \frac{\partial \tilde{\mathbf{E}}}{\partial \xi} + \frac{\partial \tilde{\mathbf{F}}}{\partial \eta} = D^2(J\tilde{\mathbf{Q}}) \tag{30}$$

The solution vector and the flux vectors in the transformed coordinates are given as

$$\tilde{\mathbf{Q}} = \frac{1}{J}\begin{bmatrix} p/\beta \\ u \\ v \end{bmatrix} \qquad \tilde{\mathbf{E}} = \frac{1}{J}\begin{bmatrix} U \\ Uu+\xi_x p \\ Uv+\xi_y p \end{bmatrix} \qquad \tilde{\mathbf{F}} = \frac{1}{J}\begin{bmatrix} V \\ Vu+\eta_x p \\ Vv+\eta_y p \end{bmatrix} \tag{31}$$

where p is the pressure. Notice that the artificial compressibility has been added in the continuity equation. The physical viscous terms in the general coordinates are given by

$$D^2(J\tilde{\mathbf{Q}}) = [\frac{\mathbf{S}}{J} g_{ij}\left(J\tilde{\mathbf{Q}}\right)_{,j}]_{,i} \tag{32}$$

where g_{ij} is the contravariant matrix tensor

$$g_{ij} = \nabla x'_i \nabla x'_j \tag{33}$$

Here, x'_i means ξ or η depending on the index i

$$\mathbf{S} = \frac{1}{Re}\mathrm{diag}(0,1,1) \tag{34}$$

where Re is the Reynolds number.

The Navier-Stokes equations are mixed parabolic/hyperbolic partial differential equations. According to the eigenvalue analysis of the hyperbolic part of the equations, the Jacobian matrices in the transformed coordinates have real eigenvalues

$$\tilde{\mathbf{A}} = \frac{\partial \tilde{\mathbf{E}}}{\partial \tilde{\mathbf{Q}}} = \mathbf{K}(U,\xi_x,\xi_y) \tag{35}$$

$$\tilde{\mathbf{B}} = \frac{\partial \tilde{\mathbf{F}}}{\partial \tilde{\mathbf{Q}}} = \mathbf{K}(V,\eta_x,\eta_y)) \tag{36}$$

where the matrix **K** is defined as

$$\mathbf{K}(k,k_1,k_2) = \begin{bmatrix} 0 & k_1 & k_2 \\ \beta k_1 & k+k_1 u & k_2 u \\ \beta k_2 & k_1 v & k+k_2 v \end{bmatrix} \tag{37}$$

Here, k_1 and k_2 are either ξ_x and ξ_y or η_x and η_y depending on the direction to be considered, and $k = k_1 u + k_2 v$. The eigenvalues of the matrix **K** are given by

$$\Lambda = \mathrm{diag}(k - c,\ k + c,\ k) \tag{38}$$

where the equivalent speed of sound, c, is given as

$$c = \sqrt{k^2 + \beta(k_1^2 + k_2^2)} \tag{39}$$

Notice that one of the eigenvalues is negative. This means that the incompressible flow is equivalently "subsonic" in the sense of different signs of the eigenvalues and that c will influence stiffness of the system. Thus, the direction of characteristics should be considered when applying boundary conditions.

Numerical Methods

The residual vector including the fourth order artificial dissipation (Eq. 23) is defined as

$$\hat{\mathbf{R}} = \frac{\partial \tilde{\mathbf{E}}}{\partial \xi} + \frac{\partial \tilde{\mathbf{F}}}{\partial \eta} - D^2(\mathrm{J}\tilde{\mathbf{Q}}) + \mathrm{D}(\mathrm{J}\tilde{\mathbf{Q}}) \tag{40}$$

After spatial derivative terms were discretized, the governing equations were integrated either by the explicit Runge-Kutta time-stepping algorithm (Eq. 25) or by an Euler implicit method with approximate factorization (Beam and Warming, ref. 24). To reduce the computational effort, the artificial dissipation and the viscous part of the residual are calculated only once every global time level and kept unchanged during the four stages of the Runge-Kutta scheme. This does not deteriorate the stability of the time stepping algorithm.

The Euler implicit scheme with factorization for the incompressible Navier-Stokes equations results in

$$\begin{aligned} &\left[\mathbf{I} + \Delta t\left\{\frac{\partial}{\partial \xi}\tilde{\mathbf{A}}\cdot - \frac{\partial}{\partial \xi}\left(\frac{\mathbf{S}g_{11}}{\mathrm{J}}\frac{\partial}{\partial \xi}\mathrm{J}\cdot\right)\right\}\right] \\ &\cdot\left[\mathbf{I} + \Delta t\left\{\frac{\partial}{\partial \eta}\tilde{\mathbf{B}}\cdot - \frac{\partial}{\partial \eta}\left(\frac{\mathbf{S}g_{22}}{\mathrm{J}}\frac{\partial}{\partial \eta}\mathrm{J}\cdot\right)\right\}\right]\Delta\tilde{\mathbf{Q}} = -\Delta t\hat{\mathbf{R}} \end{aligned} \tag{41}$$

Time Step Limitations and Boundary Conditions

The allowable time increments of the explicit scheme are severely restricted by the stability limit, while for an implicit scheme the time step restrictions are caused by the factorization errors. The time step is determined by considering the hyperbolic part of the system and the parabolic part of the system separately and by combining these time steps as suggested by MacCormack and Baldwin (ref. 19). The system becomes hyperbolic when viscosity is neglected. Then, the stability bound of the resulting system is determined by the CFL (Courant-Friedrichs-Lewy) number. The maximum allowable time steps for each of the coordinate directions are defined as

$$\Delta t_{h\xi} = \frac{\mathrm{CFL}}{|\mathrm{U}| + c_\xi} \qquad \Delta t_{h\eta} = \frac{\mathrm{CFL}}{|\mathrm{V}| + c_\eta} \tag{42}$$

so that the combined maximum time step for the hyperbolic part of the system is defined by

$$\Delta t_h = \frac{\Delta t_{h\xi} \Delta t_{h\eta}}{\Delta t_{h\xi} + \Delta t_{h\eta}} \tag{43}$$

When the convective part of the acceleration is neglected, the system becomes of parabolic type. The stability of the parabolic type system is dictated by the non-dimensional number σ (von Neumann number). For each generalized coordinate direction, the maximum time steps are defined by

$$\Delta t_{p\xi} = \frac{\sigma Re}{g_{11}} \qquad \Delta t_{p\eta} = \frac{\sigma Re}{g_{22}} \tag{44}$$

and the combined maximum time step for the parabolic part is given by

$$\Delta t_p = \frac{\Delta t_{p\xi} \Delta t_{p\eta}}{\Delta t_{p\xi} + \Delta t_{p\eta}} \tag{45}$$

The total maximum time step is estimated conservatively as

$$\Delta t = \frac{\Delta t_h \Delta t_p}{\Delta t_h + \Delta t_p} \tag{46}$$

For the explicit Runge-Kutta method, Eq. 46 was used to estimate the maximum time step. However, for the Euler implicit method, only CFL limitation was used to compute the time step, that is

$$\Delta t = \frac{\Delta t_{h\xi} \Delta t_{hn}}{\Delta t_{h\xi} + \Delta t_{h\eta}} - \tag{47}$$

It was assumed that the flow is inviscid at the inlet and exit planes causing the system of equations to become hyperbolic in time near the inlet and exit. As stated earlier, the incompressible Navier-Stokes equations have one negative eigenvalue, and the rest of the eigenvalues are positive. Thus, one equation should be considered with two boundary conditions at the inlet. At the exit, two equations with one boundary condition must be applied. At the inlet, u and v velocity vector components were specified, while the back pressure p was specified at the exit. The flow was assumed to be locally one-dimensional at the inlet and exit boundaries in order to transform locally the equation into the characteristic form. At the solid wall, the velocity vector components, u and v, were set to zero, and the surface pressure was extrapolated from the grid points next to the wall from the condition that $\frac{\partial p}{\partial n} = 0$.

Residual Smoothing

One of the successful attempts to accelerate the convergence of the Runge-Kutta scheme is Implicit Residual Smoothing (IRS) introduced by Jameson and Baker (ref. 25). With this method, it is possible to use much higher values of CFL. The residual is smoothed through the following equation

$$\left[1 - \theta\delta_{\xi}^{2}\right]\left[1 - \theta\delta_{\eta}^{2}\right]\hat{\mathbf{R}}^{*} = \hat{\mathbf{R}} \tag{48}$$

where δ^2 designates the central difference operator for a respective second derivative, and θ is the smoothing coefficient. Thus, when using the IRS we have to solve two scalar tri-diagonal matrices. Since their coefficients are constants, the tri-diagonal matrices are decomposed into upper and lower bi-diagonal matrices so that at every application of the IRS only forward and backward substitutions are needed to get the smoothed residual.

The application of the DMR method to incompressible Navier-Stokes equations differs from the formulation for its application to the Euler equations of gasdynamics only by the following term

$$\mathbf{a}_{q}^{m} = \left[\frac{\partial}{\partial\xi}\bar{\mathbf{A}}^{1}\cdot + \frac{\partial}{\partial\eta}\bar{\mathbf{B}}^{1}\cdot - D^{2}\mathrm{J}\cdot + \mathrm{DJ}\cdot\right]\frac{\partial\Theta^{m}}{\partial\omega_{q}^{m}} \tag{49}$$

Computational Results for Navier-Stokes Equations

A steady, laminar, viscous flow normal to a solid wall (Hiemenz flow) was the first test case. Reason for this choice of the test case is that the analytic solution for the Hiemenz flow is known (Panton, ref. 26). The accuracy of the codes (the explicit Runge-Kutta method and the Euler implicit method) can be verified by comparing the computed solution with the analytic solution.

The flow corresponding to the Reynolds number 400 based on the free stream velocity and a body dimension, R_o, of the wall was computed with and without the DMR method in conjunction with explicit and implicit codes. The computational grid consisted of 60×29 cells, and the dimensions of the computational domain were $H = R_o$ and $L = 2R_o$. In the case of an explicit Runge-Kutta (RK) method, the maximum allowable CFL number of 2.8 was used and the von Neumann number was $\sigma = 0.4$. A small amount of the fourth order artificial dissipation was added to get a smooth solution ($\varepsilon = 0.05$). Using numerical experimentation it was found that the fastest convergence is obtained with the artificial compressibility coefficient $\beta = 2$, and that the DMR method should be applied every 10 iterations by combining 3 consecutive solutions.

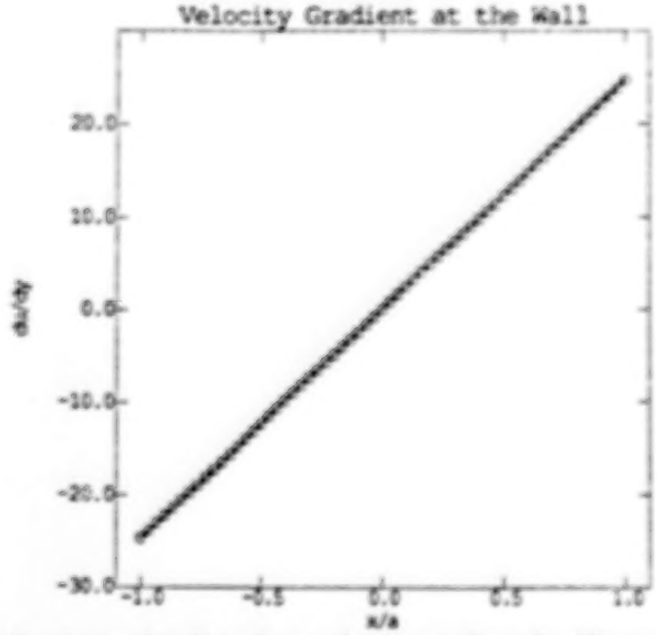

Figure 3 Distributions of wall surface velocity gradient for Hiemenz flow (RK: solid line; analytic solution: circles)

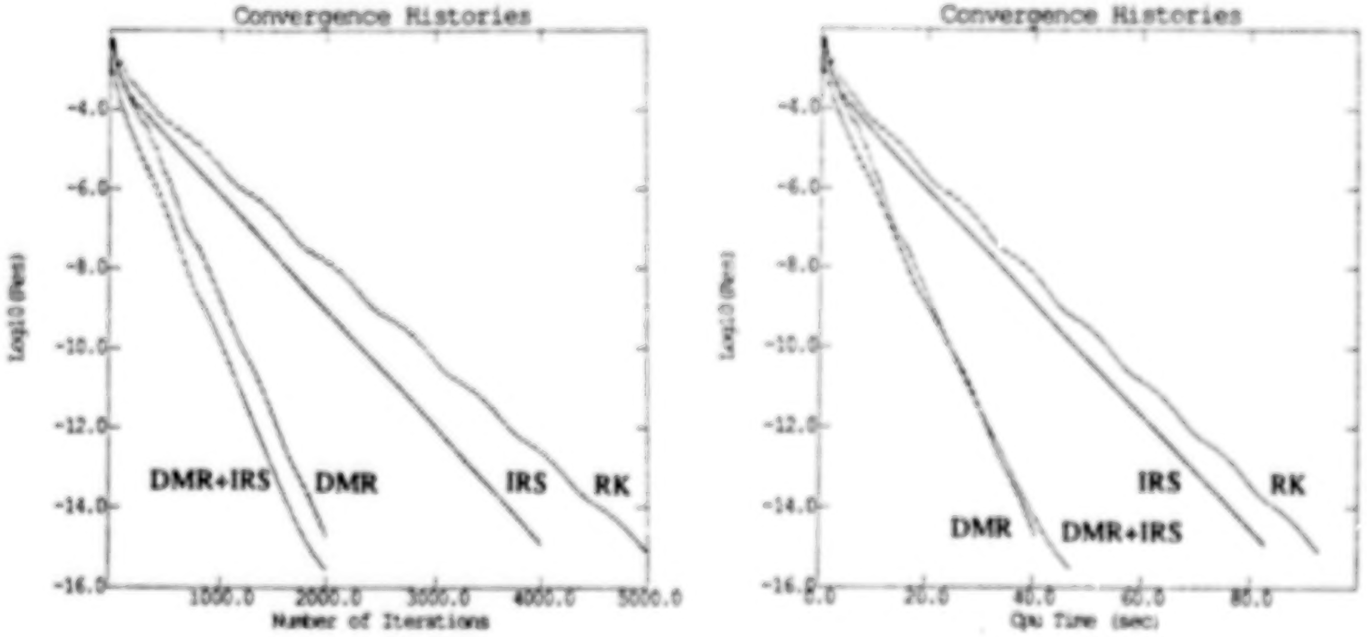

Figure 4 Convergence histories of the RK method for Hiemenz flow with Re = 400

The computed distribution of the wall surface velocity gradient, $\frac{\partial u}{\partial y}$, was compared with that of the analytic solution (Fig. 3), showing an excellent agreement. Figure 4 shows that the residual was reduced 12 orders of magnitude in 5000 iterations without the DMR method, while the same reduction in residual could be achieved in 2000 iterations with the DMR method indicating 60 % reduction in CPU time. The implicit residual smoothing was also implemented with and without the DMR method. The basic RK method gives the slowest convergence, the IRS gives faster convergence than the basic RK method, while the DMR method gave the second best convergence. The most rapid convergence in terms of the number of iterations was achieved by combining the implicit residual smoothing and the DMR method. However, the DMR method alone offered maximum time savings (over 55%).

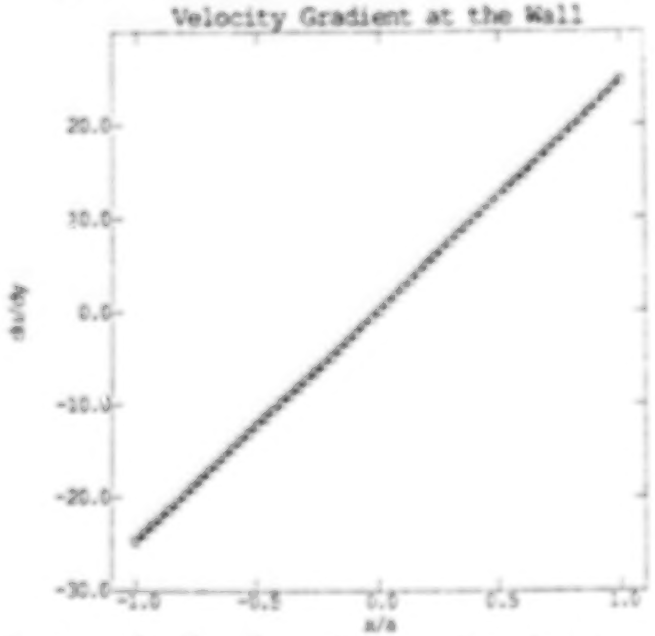

Figure 5 Distributions of wall surface velocity gradient for Hiemenz flow (Euler implicit: solid line; analytic solution: circles)

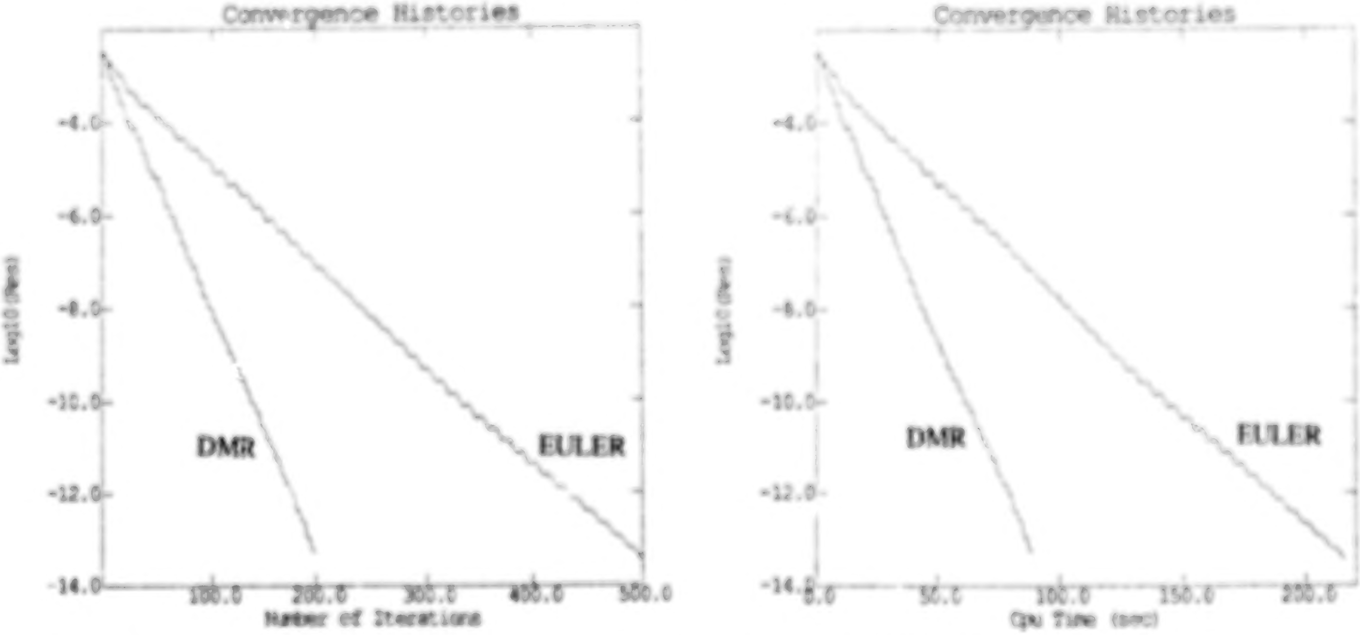

Figure 6 Convergence histories of the Euler implicit method for Hiemenz flow with Re = 400

The implicit code was also exercised for the test of the Hiemenz flow with the same conditions as in the test case for the explicit code (Re = 400). The computed surface velocity gradient distribution was compared with the analytic solution (Fig. 5). Good agreement can be observed. CFL number of 10 was used in this computation. Also, the fourth order artificial dissipation with $\varepsilon = 0.25$ was added. The optimal value of the artificial compressibility coefficient β was found by numerical experiments to be $\beta = 5$. The DMR method was found to give the fastest convergence when applied to the implicit Euler scheme every 5 iterations by combining 5 consecutive solutions. Figure 6 shows that the DMR method offers approximately 60% reduction in CPU time indicating that the DMR method can be successfully applied to implicit methods.

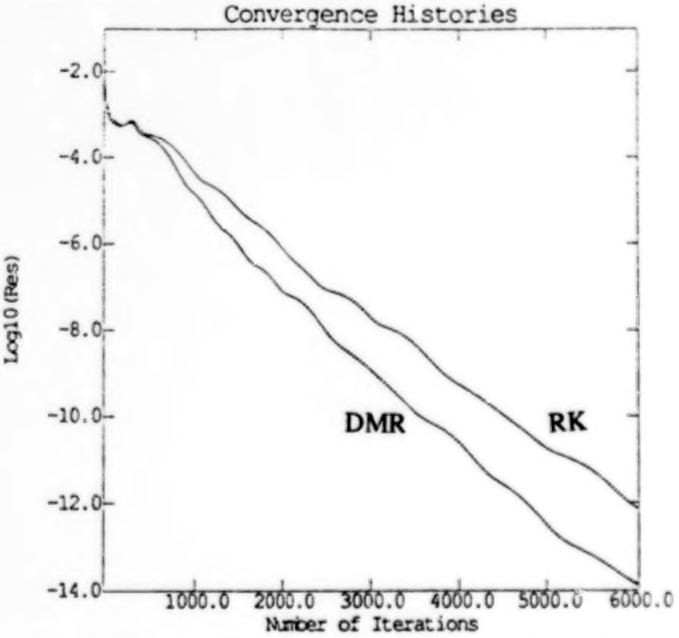

Figure 7 Convergence histories for viscous flow around a circular cylinder with Re = 20 (RK)

The last test case was a laminar flow around a circular cylinder. The highly clustered grid of 66×44 cells was used. Flow with Reynolds numbers of 20 was computed with the RK method and the Euler implicit method. The CFL and von Neumann numbers were CFL = 2.8 and $\sigma = 0.4$, respectively, for the RK method, and CFL = 10 was used for the Euler implicit method. The DMR method was applied every 30 iterations for the RK method, while every 10 iterations for the Euler implicit method. For both methods, two consecutive solutions were used with the DMR method, though these combinations of the number of solutions and the frequency of the DMR application are not optimal. The artificial compressibility coefficient was $\beta = 1$ for both methods. The convergence histories of the RK method and the Euler implicit method with and without the DMR method are presented in Figures 7 and 8. The DMR method offers more savings with the Euler implicit method (30%) than with the RK method (10%). The wall pressure distributions and the wall vorticity distributions were compared with the computational results of Choi (1989) in Figures 9 and 10 showing reasonable agreement.

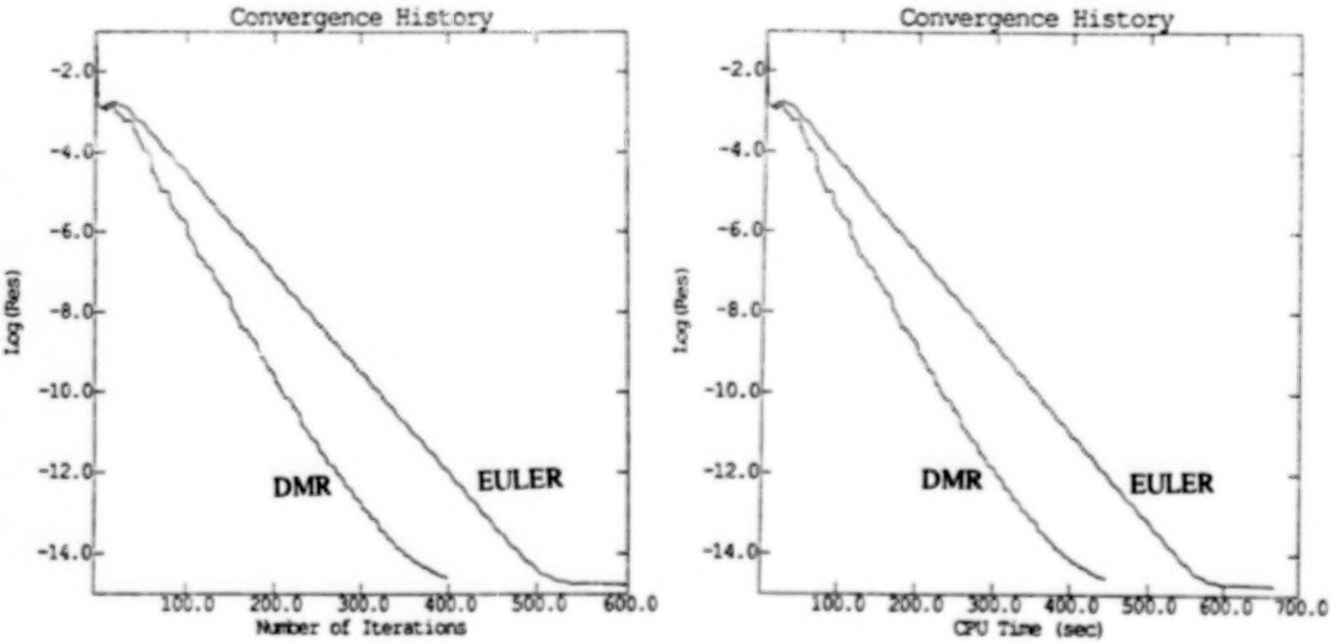

Figure 8 Convergence histories for viscous flow around a circular cylinder with Re = 20 (Euler implicit)

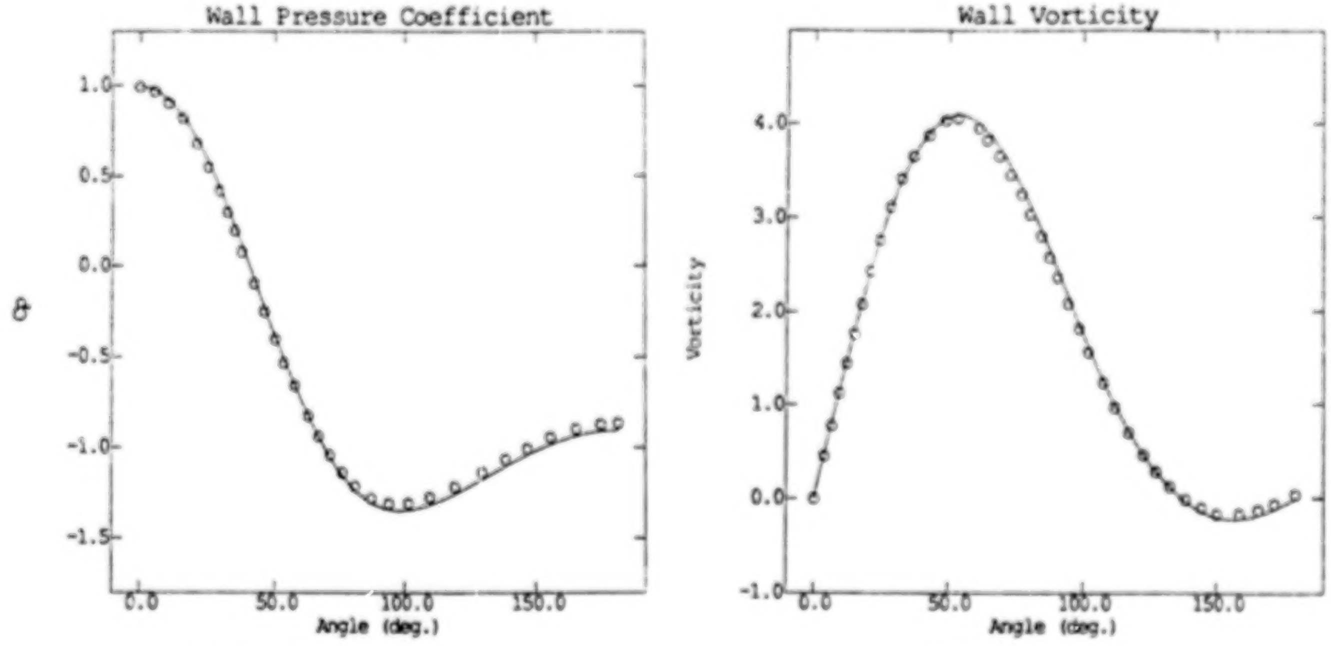

(a) Pressure coefficient

(b) Vorticity

Figure 9 Wall pressure coefficient distributions and vorticity distributions for flow around a circular cylinder at Re = 20 (RK)

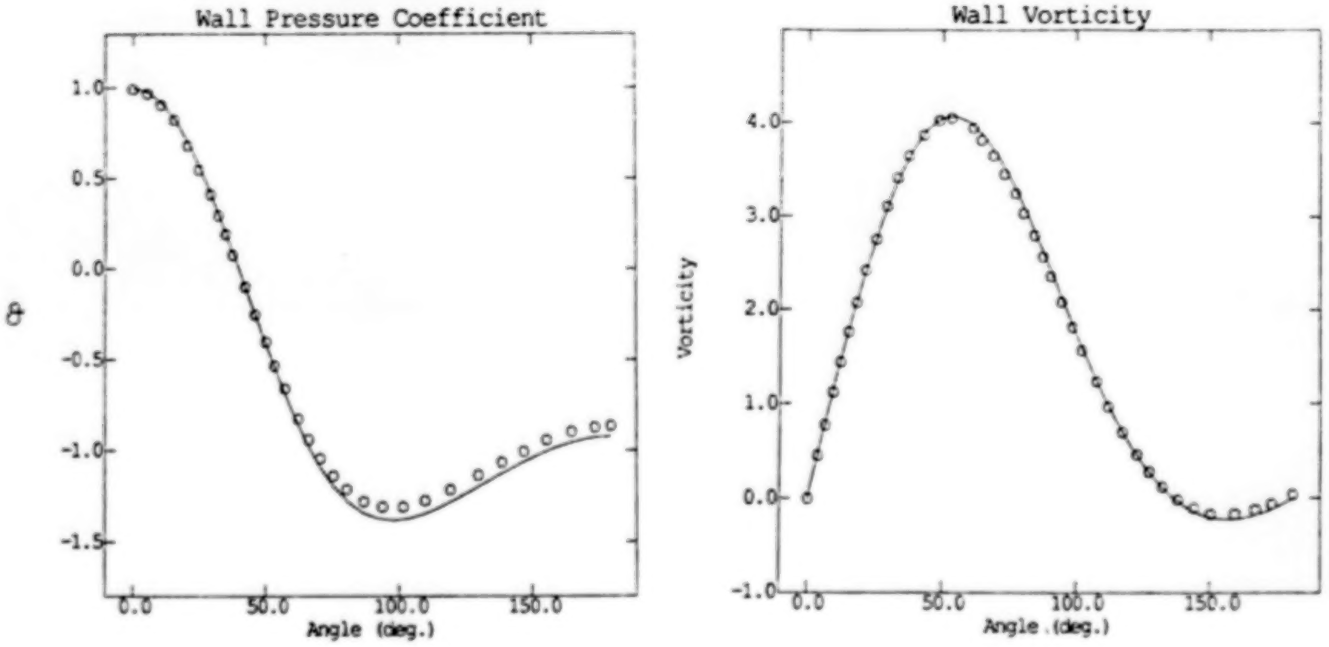

(a) Pressure coefficient (b) Vorticity

Figure 10 Wall pressure coefficient distributions and vorticity distributions for flow around a circular cylinder at Re = 40 (Euler implicit)

CONCLUSIONS

The DMR method was found capable of reducing the computation time by 20-80% depending on the test case. When directly compared with an implicit residual smoothing, the DMR method performed consistently better and more reliably.

REFERENCES

1 Huynh, Q. Q, "Iterative Preconditioned Gradient-Newton Type methods for Modern Shock Computations," Dept. of Computer Sciences, Uppsala University, Report No. 107, 1987.

2 Faddeev, D. K. and Faddeeva, V. N, Computational Methods of Linear Algebra, Trans. by Williams, R. C., 1963, W. H. Freeman and Company. San Francisco, California.

3 Vinsome, P. K. W., "ORTHMIN, and Iterative Method for Solving Sparse Sets of Simultaneous Linear Equations," Proc. Fourth Symposium on Reservoir Simulation, Society of Petroleum Engineers of AIME, 1976.

4 Young, D. M. and Jea, K. C., "Generalized Conjugate-Gradient Acceleration of Non-symmetrizable Iterative Methods," Linear Algebra Appl., Vol. 34, 1980.

5 Saad, Y, and Schultz, M, "Conjugate Gradient-Like Algorithms for Solving Non-symmetric Linear Systems," Mathematics of Computation, Vol. 44, No. 170, 1985.

6 Wigton, L. B., Yu, N. J. and Young, D. P., "GMRES Acceleration of Computational Fluid Dynamics Codes," AIAA Paper 85-1494, 1985.

7 Hafez, M., Parlette, E., and Salas, M. D., "Convergence Acceleration of Iterative Solutions of Euler Equations for Transonic Flow Computations," AIAA Paper 85-1641, July 1985.

8 Huang, C. Y. and Dulikravich, G. S., "Fast Iterative Algorithms Based on Optimized Explicit Time-Stepping," Computer Methods in Applied Mechanics and Engineering, 63, Aug. 1987, pp. 15-36.

9 Lee, S., Dulikravich, G. S. and Dorney, D., "Distributed Minimal Residual (DMR) Method for Explicit Algorithms Applied to Nonlinear Systems," presented at the Conference on Iterative Methods for Large Linear Systems, Austin, Texas, Oct. 19-21, 1988.

10 Dulikravich, G. S., Dorney, D. J. and Lee, S., "Iterative Acceleration and Physically Based Dissipation for Euler Equations of Gasdynamics," Proceedings of ASME WAM'88, Symposia on Advances and Applications in Computational Fluid Dynamics, edited by O. Baysal, FED - Vol. 66, Chicago, IL, Nov. 28 - Dec. 2, 1988, pp. 81-92.

11 Lee, S., Dulikravich, G. S. and Dorney, D. J., "Acceleration of Iterative Algorithms for Euler Equations of Gasdynamics," AIAA Paper 89-0097, Reno, NV, Jan. 1989; Also, accepted for publication in AIAA Journal, 1990.

12 Lee, S. and Dulikravich, G. S., "Accelerated Computation of Viscous, Steady Incompressible Flows," ASME paper 89-GT-45, Gas Turbine and Aeroengine Congress and Exposition, Toronto, Canada, June 4-8, 1989.

13 Lee, S. and Dulikravich, G. S., "A Fast Iterative Algorithm for Incompressible Navier-Stokes Equations," Proceedings the 10th Brazilian Congress of Mechanical Engineering, Rio de Janeiro, Brazil, Dec. 7-10, 1989.

14 Lee, S., Acceleration of Iterative Algorithms for Euler and Navier-Stokes Equations, Ph. D. Thesis, Department of Aerospace Engineering, Pennsylvania State University, May 1990.

15 Briley, W. R, McDonald, H. and Shamroth, S. J., "A Low Mach Number Euler Formulation and Application to Time-Iterative LBI Schemes," AIAA Journal, Vol. 21, No. 10, Oct. 1983.

16 Choi, Y., Computation of Low Mach Number Compressible Flow, Ph. D. Thesis, Department of Mechanical Engineering, Pennsylvania State University, 1989.

17 Turkel, E, "Preconditioned Methods for Solving the Incompressible and Low Speed Compressible Equations," Journal of Computational Physics, Vol. 72, No. 2, Oct. 1987, pp. 277-298.

18 Jameson, A., Schmidt, W., and Turkel, E., "Numerical Solutions of the Euler Equations by Finite Volume Methods Using Runge-Kutta Time-Stepping Scheme," AIAA paper 81-1259, Palo Alto, CA, June, 1981.

18 Steger, J. L. and Kutler, P., "Implicit Finite-Difference Procedure for the Computation of Vortex Wakes," AIAA Journal, Vol. 15, No. 7, July 1977, pp. 581-590.

19 MacCormack, R. W. and Baldwin, B. S., "A Numerical Method for Solving the Navier-Stokes Equations With Application to Shock-Boundary Layer Interaction," AIAA Paper 75-1, Jan. 1975.

20 Chakravarthy, S. R., "Euler Equations - Implicit Schemes and Implicit Boundary Conditions," AIAA paper 82-0228, AIAA 20th Aerospace Sciences Meeting, Orlando, Florida, Jan. 11-14, 1982.

21 Chorin, A. J., "A Numerical Method for Solving Incompressible Viscous Flow Problems," Journal of Computational Physics, Vol. 2, 1967, pp. 12-26.

22 Choi, D. and Merkle, C. L., "Application of Time-Iterative Schemes to Incompressible Flows," AIAA Journal, Vol. 23, No.10, Oct. 1985, pp. 1518-1524.

23 Kwak, D., Chang, J. L. C., Shanks, S. P. and Chakravarthy, S. R., "An Incompressible Navier-Stokes Flow Solver in Three Dimensional Curvilinear Coordinate System Using Primitive Variables," AIAA Journal, Vol. 24, No. 3, March 1986, pp. 390-396.

24 Beam, R. M. and Warming, R. F., "Implicit Numerical Methods for the Compressible Navier-Stokes and Euler Equations," Lecture Notes Series 1982-04, von Karman Institute for Fluid Dynamics, Belgium, 1982.

25 Jameson, A., and Baker, T. J., "Solution of the Euler Equations for Complex Configurations," Proceedings of AIAA 6th Computational Fluid Dynamics Conference, AIAA, New York, 1983, pp. 293-302.

26 Panton, R. L., Incompressible Flow, John Wiley and Sons, Inc., New York, New York, 1984.

A PRESSURE BASED METHOD FOR THE SOLUTION OF VISCOUS INCOMPRESSIBLE TURBOMACHINERY FLOWS

G. V. Hobson*
and
B. Lakshminarayana

Department of Aerospace Engineering
Pennsylvania State University
University Park, PA 16803

ABSTRACT

A new technique has been developed for the solution of the incompressible Navier-Stokes equations. The numerical technique, derived from a pressure substitution method (PSM), overcomes many of the deficiencies of the pressure correction method. This technique allows for the direct solution of the actual pressure in the form of a Poisson equation which is derived from the pressure weighted substitution of the full momentum equations into the continuity equation. Two-dimensional internal flows are computed with this method and the prediction of cascade performance is presented. The extension of the pressure correction method for the solution of three-dimensional flows is also presented.

NOMENCLATURE

$C_{\epsilon 1}, C_{\epsilon 2}, C_{\mu}$	coefficients in turbulence model
C_p	specific heat at constant pressure
E	turbulent constant dependent on wall roughness
f_1, f_2, f_{μ}	low-Reynolds number turbulence model coefficients
G_1, G_2, G_3	contravariant velocities
h	static enthalpy
H_1, H_2, H_3	transformation metrics
$J_{\xi}, J_{\eta}, J_{\zeta}$	flux vectors
J	Jacobian of the transformation
k	turbulent kinetic energy
L	turbulent length scale
p	static pressure
Pr_t	turbulent Prandtl number
Re	Reynolds number
Re_t	turbulent Reynolds number, $\rho k^2/\mu\epsilon$

---

* Presently; Turbopropulsion Laboratory
Naval Postgraduate School
Monterey, CA 93943

Re_y	turbulent Reynolds number, $\rho y\sqrt{k}/\mu$
S^ϕ	source term (for variable ϕ)
T	static temperature
T'	fluctuating temperature
Tu	turbulence intensity, $\sqrt{(\overline{u'^2})}\,/U_i$
u_i	mean velocity in direction x_i, $(u_1,u_2,u_3) \equiv (u,v,w)$
u'_i	fluctuating velocity in direction x_i
U_i	inlet total velocity
x_i	Cartesian coordinate, $(x_1,x_2,x_3) \equiv (x,y,z)$
y^+	non-dimensionalized normal distance, $y\sqrt{(\tau_w/\rho)}/\nu$
α,β,γ	transformation metrics
δ_{ij}	Kronecker delta
ϵ	dissipation rate of turbulent kinetic energy
κ	von Karman constant, 0.42
μ	molecular viscosity
μ_{eff}	effective viscosity, $\mu + \mu_t$
μ_t	turbulent viscosity
ν	kinematic viscosity
Φ	dissipation function
ϕ	scalar variable
ϕ'	fluctuating dissipation
ρ	density of fluid
Γ^ϕ	effective diffusion coefficient (for variable ϕ)
σ_k,σ_ϵ	coefficients in turbulence model
τ_w	shear stress on the wall
ξ,η,ς	transformed coordinates
$\Delta\xi,\Delta\eta,\Delta\varsigma$	computational domain grid spacing
ω_p	relaxation parameter for pressure equation
$\omega_u,\omega_v,\omega_w$	relaxation parameter for momentum equations

Subscripts

0	central grid point in finite difference molecule
d	downstream face of control volune
D	downstream grid point
e	east face of control volume
E	east grid point
i,j,k	tensor indices
i	inlet flow conditions

n	north face of control volume
N	north grid point
o	outlet flow conditions
P	first grid point away from the wall
s	south face of control volume
S	south grid point
u	upstream face of control volume
U	upstream grid point

INTRODUCTION

Turbomachinery flows are amongst the most complex encountered in engineering. These flows are three dimensional and highly turbulent and may include heat transfer. Unsteadiness and compressibility in turbomachinery flows are also relevant but will not be considered in this paper. Higher order turbulence models are also needed to resolve the transitional and near wall flow phenomena, which are important for loss and heat transfer predictions. Flow separation should also be accurately predicted with such models as these regions are inevitably present in modern highly loaded turbine and compressor blade rows.

This paper is mainly concerned with the development of a more efficient pressure based method and its application to turbomachinery incompressible flows.

A brief review of the relevant works follows. Hah (ref. 1) solved the uncoupled equations on a staggered grid. Higher order discretization was used for the convection terms to reduce numerical diffusion. The quadratic upsteam (QUICK) differencing by Leonard (ref. 2) and skew upwinding scheme by Raithby (ref. 3) were extended and modified. An algebraic Reynolds stress model modified for the effect of streamline curvature and rotation was used for the closure of the governing equations. Comparison with experimental data for an end-wall turbine cascade flow, showed that various complex three-dimensional viscous flow phenomena were well predicted.

An excellent review paper by Patankar (ref. 4) puts the treatment of convection and diffusion into perpective. He refers to a study done by Patel and Markatos (ref. 5) who evaluated eight different discretization schemes to solve the two-dimensional convection-diffusion equations. "They found that QUICK and its variants gave accurate and cost effective solutions when they converged. However they failed to converge for high flow rates and coarse grids." The situation becomes more acute for supersonic flows for which Patel et al. (ref. 6) concluded that the upwind scheme is the best choice.

Patankar (ref. 4) observes, "Thus, we have gone around full circle. Lower-order schemes such as upwind are stable and monotonic but lead to false diffusion. Higher-order schemes such as QUICK eliminate false diffusion but produce wiggles and often fail to converge. The search for the perfect method is still not over."

Rhie and Chow (ref. 7) presented a solution of the Navier-Stokes equations in general curvilinear coordinates on a non-staggered grid. A specific algorithm based on pressure weighting (PWM) was developed to suppress the pressure oscillations. This development was a major breakthrough for the solution of the fluid flow equations in generalised coordinates. They used the pressure correction method (PCM) to couple the momentum and continuity equations. The standard form of the k-ϵ model was used to describe the turbulence for flows over airfoils with and without trailing edge separation.

Recently, Rhie (ref. 8), extended his scheme to employ the pressure implicit split operator (PISO) concept with a multigrid procedure to enhance convergence. Within the several levels of pressure correction, the density was treated implicitly for the correction of the mass flow imbalance. This treatment was applicable for compressible flows. The method was tested for a wide range of flows, including three-dimensional driven cavity and a turbine end-wall cascade.

Three different formulations for non-staggered grids have been suggested by Shih and Ren (ref. 9). Some employ the Poisson equation for pressure, in place of the continuity equation. All of the algorithms, proposed by them, solve for the pressure directly and not the pressure correction as in the SIMPLE algorithm. When the continuity equation is used, a Pressure Substitution Method (PSM) is employed. However the equations were solved in non-conservative form, thus resulting in a purely finite difference method.

Hobson and Lakshminarayana (ref. 10) presented a control volume formulation of the pressure substitution method for the solution of the Navier-Stokes equations describing incompressible flows. The application of this method to two-dimensional cascade flows is presented. The Low-Reynolds number k-ϵ turbulence model according to Lam and Bremhorst (ref. 11) is used to resolve the turbulence within the flow.

Three-dimensional flows are calculated with the pressure correction method similar to that used by Rhie (ref. 12) and the standard High-Reynolds number k-ϵ turbulence model including wall functions is used. The computation of turbulent flow in a turbine end-wall cascade is presented.

THEORETICAL FORMULATION

The Incompressible Viscous Flow Equations

For steady-mean incompressible flow, the time-averaged continuity equation and the Reynolds averaged Navier-Stokes equation can be written in Cartesian tensor form:

$$\frac{\partial(\rho u_i)}{\partial x_i} = 0 \qquad [1]$$

$$\frac{\partial(\rho u_i u_j)}{\partial x_j} = -\frac{\partial p}{\partial x_j} + \frac{\partial}{\partial x_j}\left\{\mu\left[\frac{\partial u_j}{\partial x_i} + \frac{\partial u_i}{\partial x_j}\right] - \rho\overline{u_i' u_j'}\right\} \qquad [2]$$

where ρ is the mean density, u_j the mean velocity, p the mean pressure and μ the molecular viscosity. The instantaneous velocity, u_i', with an overbar "—" implies a time averaged quantity.

For the prediction of heat transfer in non-isothermal flows through turbines, the incompressible energy equation is also solved. The form used is given as follows,

$$\frac{\partial(\rho u_i h)}{\partial x_j} = \frac{\partial}{\partial x_j}\left\{\Gamma^T \frac{\partial T}{\partial x_i} - \rho\overline{u_i' h'}\right\} + \mu(\overline{\Phi} + \overline{\phi'}) \quad [3]$$

where h is the static enthalpy, Γ^T the thermal conductivity of the gas, T the static temperature. Once again, the averaged fluctuating correlations are present, which will be described in the next section. The dissipation function, $\overline{\Phi}$, is

$$\overline{\Phi} = \left[\frac{\partial u_j}{\partial x_i} + \frac{\partial u_i}{\partial x_j}\right]\frac{\partial u_j}{\partial x_i} \quad [4]$$

Assuming that the specific heat, C_p, is constant and the gas is ideal, the static enthalpy is replaced by the static temperature, according to the following relationship.

$$h = C_p T \quad [5]$$

Two-Equation Low-Reynolds Number Turbulence Model

To solve equations [2] and [3], one must specify the Reynolds shear stress, $\rho\overline{u_i'u_j'}$, and heat flux, $\rho\overline{u_i'T'}$. A turbulent or "eddy" viscosity, μ_t, and a turbulent Prandtl number, Pr_t, are defined according to the Boussinesq approximation (ref. 13) such that,

$$-\rho\overline{u_i'u_j'} = \mu_t\left[\frac{\partial u_j}{\partial x_i} + \frac{\partial u_i}{\partial x_j}\right] - \frac{2}{3}k\delta_{ij} \quad [6]$$

$$-\rho\overline{u_i'T'} = \frac{\mu_t}{Pr_t}\left[\frac{\partial T}{\partial x_i}\right] \quad [7]$$

where δ_{ij} is the Kronecker delta and k is the turbulent kinetic energy.

The isotropic eddy viscosity model was used to obtain an effective viscosity, μ_{eff}, which is the sum of the turbulent viscosity and molecular viscosity.

For the purpose of this paper, the turbulent Prandtl number will be assumed constant and equal to 0.9. Although this is not generally true, it has been found to be a reasonably good approximation for most boundary layer flows with mild temperature gradients. The role of the turbulence model now becomes that of determining the correct value of μ_t.

From the k-ϵ turbulence model, as proposed by Launder and Spalding (ref. 14), the turbulent eddy viscosity μ_t is given by,

$$\mu_t = f_\mu C_\mu \rho \frac{k^2}{\epsilon} \qquad [8]$$

where k is the turbulent kinetic energy and ϵ is the turbulent energy dissipation and each are defined as follows,

$$k = \frac{1}{2}\overline{u_i' u_i'} \qquad [9]$$

$$\epsilon = \frac{\mu}{\rho}\overline{\frac{\partial u_i'}{\partial x_j}\frac{\partial u_i'}{\partial x_j}} \qquad [10]$$

The modelled equations for the transport of k and ϵ are given as follows,

$$\frac{\partial(\rho u_i k)}{\partial x_j} = \frac{\partial}{\partial x_j}\left[\frac{\mu_t}{\sigma_k}\frac{\partial k}{\partial x_j}\right] + \mu_t\left[\frac{\partial u_j}{\partial x_i} + \frac{\partial u_i}{\partial x_j}\right]\frac{\partial u_j}{\partial x_i} - \epsilon \qquad [11]$$

$$\frac{\partial(\rho u_i \epsilon)}{\partial x_j} = \frac{\partial}{\partial x_j}\left[\frac{\mu_t}{\sigma_\epsilon}\frac{\partial \epsilon}{\partial x_j}\right] + f_1 C_{\epsilon 1}\mu_t \frac{\epsilon}{k}\left[\frac{\partial u_j}{\partial x_i} + \frac{\partial u_i}{\partial x_j}\right]\frac{\partial u_j}{\partial x_i} - f_2 C_{\epsilon 2}\frac{\epsilon^2}{k} \qquad [12]$$

Upon consideration of equations [8], [11] and [12], one can see that there are five empirical constants; C_μ, $C_{\epsilon 1}$, $C_{\epsilon 2}$, σ_k, σ_ϵ, and three empirical functions; f_μ, f_1, and f_2. The values, of the five constants, used in this paper are those suggested as "standard" by Launder and Spalding (ref. 14). These assume the following values,

$$C_\mu=0.09,\ C_{\epsilon 1}=1.44,\ C_{\epsilon 2}=1.92,\ \sigma_k=1.0,\ \sigma_\epsilon=1.3 \qquad [13]$$

Turbulent motions immediately adjacent to the wall are significantly influenced by the presence of the wall. Here the magnitude of the effective turbulent viscosity becomes small, and the effects of the molecular viscosity become important. Experimental work has shown that in some turbulent flow situations, there exists a common structure or behavior near the wall. Under these conditions both the mean velocities and the measurable turbulence quantities exhibit nearly universal behavior. The knowledge of this structure has allowed the formulation and use of the so-called wall-functions. These functions algebraically bridge the near wall region and eliminate the need for more expensive and time consuming calculations with a fine grid near the wall.

Unfortunately, there are many flow situations of interest where this near-wall similarity breaks down. Large pressure gradients are found in the leading edge and trailing edge regions of turbomachinery blade profiles due to the high streamline curvature in these areas. This, and mass transfer at the wall, for example, both alter the near-wall flow, thus wall functions cannot be used. To incorporate these effects into the turbulence models, a variety of suggestions have been made. The purpose of the functions f_μ, f_1 and f_2 is to provide a similar modification to the k-ϵ model, thus extending the validity of the equations through the viscous sub-layer to the wall. Use is made of two "turbulent Reynolds numbers." These are defined as follows,

$$Re_t = \frac{\rho k^2}{\mu \epsilon} \qquad [14]$$

$$Re_y = \frac{\rho y \sqrt{k}}{\mu} \qquad [15]$$

Patel et al. (ref. 15) give a good description of these functions.

The three functions given by Lam and Bremhorst (ref. 11) are as follows:

$$f_\mu = \left[1.0 - \exp^{(-0.0165 Re_y)}\right]^2 \left[1.0 + \frac{20.5}{Re_t}\right] \qquad [16]$$

$$f_1 = 1.0 + \left[\frac{0.05}{f_\mu}\right]^3 \qquad [17]$$

$$f_2 = 1.0 - \exp(-Re_t^2) \qquad [18]$$

This turbulence model has been chosen for use in this paper for a number of reasons. First, it has been used, by Rodi and Scheuerer (ref. 16), to predict transitional flow over a turbine blade with a boundary layer code. Second, when compared to other LRN k-ϵ models it has been shown by Patel et al. (ref. 15) to be amongst the best in predicting the characteristics of fully turbulent flow. Third it has very simple boundary conditions and in general the model is clean and straightforward to code.

Transformation of the Basic Equations

The continuity equation [1] can be expanded to give,

$$\frac{\partial(\rho u)}{\partial x} + \frac{\partial(\rho v)}{\partial y} + \frac{\partial(\rho w)}{\partial z} = 0 \qquad [19]$$

The set of conservation equations describing the transport of momentum [2] can be written in Cartesian coordinates for a scalar variable as,

$$\frac{\partial(\rho u\phi)}{\partial x} + \frac{\partial(\rho v\phi)}{\partial y} + \frac{\partial(\rho w\phi)}{\partial z} = \frac{\partial}{\partial x}\left[\Gamma^{\phi}\frac{\partial\phi}{\partial x}\right] + \frac{\partial}{\partial y}\left[\Gamma^{\phi}\frac{\partial\phi}{\partial y}\right] + \frac{\partial}{\partial z}\left[\Gamma^{\phi}\frac{\partial\phi}{\partial z}\right] + S^{\phi} \qquad [20]$$

where Γ^{ϕ} is an effective diffusion coefficient and S^{ϕ} denotes the source term. For the momentum equations the source term is a function of the pressure gradient. When new independent variables ξ, η and ς are introduced, Eq. [19] and [20] changes according to the following transformation $\xi=\xi(x,y,z)$, $\eta=\eta(x,y,z)$ and $\varsigma=\varsigma(x,y,z)$ as represented in Fig. 1.

The transformation of partial derivatives is presented in the Appendix. Upon substitution and after some manipulation the basic equations [19] and [20] are transformed into the following form.

$$\frac{\partial(\rho G_1)}{\partial\xi} + \frac{\partial(\rho G_2)}{\partial\eta} + \frac{\partial(\rho G_3)}{\partial\varsigma} = 0 \qquad [21]$$

$$\frac{\partial(\rho G_1\phi)}{\partial\xi} + \frac{\partial(\rho G_2\phi)}{\partial\eta} + \frac{\partial(\rho G_3\phi)}{\partial\varsigma} = \frac{\partial}{\partial\xi}\left\{\Gamma^{\phi}\left[\alpha\frac{\partial\phi}{\partial\xi} + H_1\frac{\partial\phi}{\partial\eta} + H_2\frac{\partial\phi}{\partial\varsigma}\right]\right\} +$$
$$\frac{\partial}{\partial\eta}\left\{\Gamma^{\phi}\left[H_1\frac{\partial\phi}{\partial\xi} + \beta\frac{\partial\phi}{\partial\eta} + H_3\frac{\partial\phi}{\partial\varsigma}\right]\right\} + \frac{\partial}{\partial\varsigma}\left\{\Gamma^{\phi}\left[H_2\frac{\partial\phi}{\partial\xi} + H_3\frac{\partial\phi}{\partial\eta} + \gamma\frac{\partial\phi}{\partial\varsigma}\right]\right\} + S^{\phi} \qquad [22]$$

Vector Form of the Basic Equations

Only the source term S^{ϕ} takes on a different form for the three different directions. These are,

$$(1)\ \phi = u; \quad S^{\phi} = -\frac{\partial p}{\partial x} = -\xi_x\frac{\partial p}{\partial\xi} - \eta_x\frac{\partial p}{\partial\eta} - \varsigma_x\frac{\partial p}{\partial\varsigma}$$

$$(2)\ \phi = v; \quad S^{\phi} = -\frac{\partial p}{\partial y} = -\xi_y\frac{\partial p}{\partial\xi} - \eta_y\frac{\partial p}{\partial\eta} - \varsigma_y\frac{\partial p}{\partial\varsigma} \qquad [23]$$

$$(3)\ \phi = w; \quad S^{\phi} = -\frac{\partial p}{\partial z} = -\xi_z\frac{\partial p}{\partial\xi} - \eta_z\frac{\partial p}{\partial\eta} - \varsigma_z\frac{\partial p}{\partial\varsigma}$$

The source terms for the scalar equations considered such as the energy, turbulent kinetic energy and dissipation equations are mainly of scalar form.

Discretization of the Transport Equations

The conservative form of the equation is derived for numerical computation, the integral form of the continuity equations [21] over the control volume, as shown in Fig. 2, is obtained as follows,

$$\int_u^d\int_s^n (\rho G_1)_w^e \, d\eta d\varsigma + \int_u^d\int_w^e (\rho G_2)_s^n \, d\xi d\varsigma + \int_s^n\int_w^e (\rho G_3)_u^d \, d\xi d\eta = 0 \qquad [24]$$

and the transport equation [22] is,

$$\begin{aligned}
&\int_u^d\int_s^n (\rho G_1\phi)_w^e \, d\eta d\varsigma + \int_u^d\int_w^e (\rho G_2\phi)_s^n \, d\xi d\varsigma + \int_s^n\int_w^e (\rho G_3\phi)_u^d \, d\xi d\eta = \\
&\int_u^d\int_s^n \left\{\Gamma^\phi\left(\alpha\frac{\partial\phi}{\partial\xi} + H_1\frac{\partial\phi}{\partial\eta} + H_2\frac{\partial\phi}{\partial\varsigma}\right)\right\}_w^e d\eta d\varsigma \quad + \\
&\int_u^d\int_w^e \left\{\Gamma^\phi\left(H_1\frac{\partial\phi}{\partial\xi} + \beta\frac{\partial\phi}{\partial\eta} + H_3\frac{\partial\phi}{\partial\varsigma}\right)\right\}_s^n d\xi d\varsigma \quad + \\
&\int_s^n\int_w^e \left\{\Gamma^\phi\left(H_2\frac{\partial\phi}{\partial\xi} + H_3\frac{\partial\phi}{\partial\eta} + \gamma\frac{\partial\phi}{\partial\varsigma}\right)\right\}_u^d d\xi d\eta \quad + \\
&\int_u^d\int_s^n\int_w^e S^\phi \, d\xi d\eta d\varsigma \qquad [25]
\end{aligned}$$

where n, s, e, w, u and d are the locations of the intersection between the control volume faces and the grid lines.

Equations [24] and [25] can be rearranged as follows:

$$(\rho G_1 \Delta\eta\Delta\varsigma)_w^e + (\rho G_2 \Delta\xi\Delta\varsigma)_s^n + (\rho G_3 \Delta\xi\Delta\eta)_u^d = 0 \qquad [26]$$

and,

$$\begin{aligned}
&(J_\xi \Delta\eta\Delta\varsigma)_w^e + (J_\eta \Delta\xi\Delta\varsigma)_s^n + (J_\varsigma \Delta\xi\Delta\eta)_u^d = \\
&\left\{\Gamma^\phi\left(H_1\frac{\partial\phi}{\partial\eta} + H_2\frac{\partial\phi}{\partial\varsigma}\right)\Delta\eta\Delta\varsigma\right\}_w^e \quad + \\
&\left\{\Gamma^\phi\left(H_1\frac{\partial\phi}{\partial\xi} + H_3\frac{\partial\phi}{\partial\varsigma}\right)\Delta\xi\Delta\varsigma\right\}_s^n \quad + \\
&\left\{\Gamma^\phi\left(H_1\frac{\partial\phi}{\partial\xi} + H_3\frac{\partial\phi}{\partial\eta}\right)\Delta\xi\Delta\eta\right\}_u^d \quad + \quad S^\phi\Delta\xi\Delta\eta\Delta\varsigma \qquad [27]
\end{aligned}$$

where,

$$J_{\xi} = \rho G_1 \phi - \Gamma^{\phi} \alpha \frac{\partial \phi}{\partial \xi}$$

$$J_{\eta} = \rho G_2 \phi - \Gamma^{\phi} \beta \frac{\partial \phi}{\partial \eta} \qquad [28]$$

$$J_{\varsigma} = \rho G_3 \phi - \Gamma^{\phi} \gamma \frac{\partial \phi}{\partial \varsigma}$$

which are the flux vectors through the faces of the control volume in Fig. 2.

The source term is assumed to be acting at the centre, and constant within the control volume.

The discretized form of the continuity equation [26] has been described in detail by Hobson and Lakshminarayana (ref. 10) for two-dimensional flows. Equation [27] is discretized by using central differencing and linear interpolation in the computational domain. The coefficients of the resulting difference equation are modified according to the hybrid scheme of Spalding (ref. 17). For a cell Reynolds number less than or equal to two the hybrid scheme uses central differencing including both the convection and diffusion terms. As the cell Reynolds number exceeds two the hybrid scheme switches to upwind differencing with only the convective contribution; the diffusion terms are neglected.

Boundary Conditions

No-slip boundary conditions are used for the velocities at a solid wall, where they are all set equal to zero. For cascade flows, periodic boundary conditions are implemented upstream and downstream of the blades on the periodically generated meshes. When solving along a periodic line in the blade-to-blade plane, two consequences result, which alter the tri-diagonal implicit matrix system of size N, which is usually used to solve between solid boundaries. First, an additional grid point is incorporated into the system, resulting in an N+1 system of simultaneous equations. Second, a cyclic tri-diagonal matrix system results, which is solved with the algorithm presented by Napolitano (ref. 18).

The inlet flow velocities are specified and fully developed flow is assumed to exist at the exit plane. The exit plane has to be situated far enough downstream of the blade row, where the assumption that the streamwise gradients are small is valid.

For the pressure substitution method the boundary condition required to solve the pressure equation is that the normal derivative of the pressure vanishes at solid boundaries, which is a reasonable assumption for high Reynolds number.

The boundary condition required to solve the pressure correction equation is that the normal derivative of the pressure correction, p', vanishes at the boundary in the computational domain. The actual pressure value at the boundary is determined by extrapolation from the interior nodes to the wall with the condition of zero normal derivative of the pressure.

Since Neumann boundary conditions are used for either the pressure correction method or the pressure substitution method, the pressure must be kept constant at one grid point. This control point is usually taken to be one of the inlet grid points, where the pressure gradients are small.

For the solution of the energy equation to predict the variation of heat transfer coefficients over turbine blades, the blade wall temperature is specified from experimental results.

The inlet turbulent kinetic energy and dissipation rate is determined by specifying an inlet turbulence intensity, Tu, and length scale, L_i, associated with the inlet flow. Most sets of experimental data have the turbulence intensity quoted, however the length scale has to be determined from the physical dimensions of the turbulence generator. In most cascade tests, grids are used upstream of the cascade, to generate the required turbulence levels. The length scale is of the order of the characteristic dimension of the rods that make up the grid. The inlet turbulent kinetic energy is thus determined from the following,

$$k_i = \frac{3}{2} (Tu\ U_i)^2 \qquad [29]$$

where U_i is the inlet total velocity. The inlet dissipation rate is then determined from the following,

$$\epsilon_i = \frac{k^{\frac{3}{2}}}{L_i} \qquad [30]$$

The boundary condition at the wall for the turbulent kinetic energy, k, takes on two definitions. For the "standard" form of the equations, with wall functions, the following condition is applied.

$$\left.\frac{\partial k}{\partial y}\right|_{wall} = 0 \qquad [31]$$

The value of k is set equal to zero at the wall in the LRN model.

The idea behind the wall function method is that the turbulent length scale increases linearly, with distance from the wall beyond the viscous sublayer. The fluxes of momentum to the wall are then supposed, if the first grid point is in the fully turbulent region, to obey the relation,

$$\frac{u_p}{(\tau/\rho)_w} C_\mu^{1/4} k^{1/2} = \frac{1}{\kappa} \ln\left[\rho E y_p \frac{(C_\mu^{1/2} k_p)^{1/2}}{\mu}\right] \qquad [32]$$

Here u_p, τ_w, and y_p are, respectively, the time-averaged velocity of the fluid at the first grid point P away from the wall, the shear stress on the wall in the direction of the velocity u_p and the distance of the point P from the wall. E is a constant and is a function of the wall roughness, approximately equal to 9.0 for a smooth wall, and κ (=0.42) is the von Karman constant.

When calculating k_p, it is necessary to assign a value for the average energy-dissipation rate over the control volume, this is to be deduced from the assumption that,

$$\int_0^{y_p} \epsilon \, dy = C_\mu \frac{k_p^{3/2}}{\kappa} \ln\left[\frac{\rho E y_p (C_\mu^{1/2} k_p)^{1/2}}{\mu}\right] \qquad [33]$$

The appearance of this logarithmic function results from the necessity to presume that,

$$\epsilon_p = \frac{(C_\mu^{1/2} k_p)^{3/2}}{\kappa y_p} \qquad [34]$$

which is the boundary condition used for the dissipation rate of turbulent kinetic energy.

For the LRN model the boundary condition for the dissipation equation is,

$$\frac{\partial \epsilon}{\partial y} = 0 \qquad [35]$$

It is clear that the boundary conditions for the low-Reynolds number model are simpler than wall functions, particularly in their implementation into a computer code. Because of the requirement that the viscous sublayer be adequately resolved, the LRN was used only for two-dimensional flows. Wall functions were used for the three-dimensional flow test cases as a result of limited computer memory.

Solution Algorithm and Relaxation Technique

The pressure substitution method (PSM) is used for the solution of two-dimensional flows and is fully described in reference 10. Upstream and downstream of the cascade the periodic solver according to Napolitano (ref. 20) is used and between the blade surfaces a tri-diagonal matrix solver is used for the successive line under-relaxation (SLUR) of the computational domain. Implicit solution is in the cross-stream direction and the line sweeps are performed in the streamwise direction.

The three-dimensional calculations were carried out with the pressure correction method. This algorithm is fully described by Rhie (ref. 12) and is a logical extension of the two-dimensional form as described in reference 7. The alternating direction implicit (ADI) method with the implicit periodic solver is used to calculate the three-dimensional flow through an end wall cascade.

The alternating direction implicit (ADI) method will be described by refering to Fig. 3. SLUR proceeds by taking all lines in the same direction in a repetitive manner. The convergence rate can be improved by following the sequence by rows, say, by a second sequence in the column direction. Such sequencing was used in the cross-stream plane for the cascade flows and this planar solution was advanced in the streamwise direction.

If there are I=1,NI grid points in the blade-to-blade direction and J=1,NJ grid points in the spanwise direction, as shown in Fig. 3, then on a cross-stream plane between the blades the ADI solution is performed from grid points 2 to NI-1 and 2 to NJ-1. However upstream (from grid points K=2 to KSTART) and downstream (from K=KFINIT to NK-1) of the cascade, as mentioned earlier, an additional periodic grid point is included in the blade-to-blade surface. Thus for the ADI line sweep in the blade-to-blade direction the periodic solver is used between grid points 1 and NI-1 (the values at NI then being set equal to those at 1). During the second ADI sweep in the spanwise direction, an additional line relaxation is performed on the periodic line, at I=1, from J=2 to NJ. Once again, to ensure periodicity the values at I=NI along the line J=2,NJ-1 are set equal to those at I=1. This completes an ADI sweep in the cross plane of the computational domain representing a cascade geometry. The solution is now advanced in the streamwise, or K, direction.

As the periodic solver is an extension of the Thomas algorithm (ref. 19), this solution procedure is believed to be consistent. The experience gained with the periodic solver in the solution of two-dimensional flows, showed that periodic solutions are efficiently achieved in an implicit manner, and thus was readily extended to three-dimensional flows.

RESULTS AND DISCUSSION

Laminar Flow in a Cascade

The test case is that of flow through a cascade of symmetrical NACA 0012 airfoils, which Rosenfeld and Wolfshtein (ref. 20) also computed. A comparison between the convergence histories of the pressure correction method (PCM) and the new pressure substitution method (PSM) was conducted for this configuration.

The cascade had a solidity, or pitch-to-chord ratio, of 1.0, and the airfoils had a stagger angle of 30 degrees. The Reynolds number, based on chord length, of the inlet total velocity was 1000. The incidence angle was varied between -10 and 15 degrees. They used 81x37 grid points with a computational "O" type grid. Their formulation was based on the vorticity and stream function equations.

The present computations were performed on a "H" type grid with 57x51 grid points. Almost the same number of grid points were used for the two studies, however the "O" grid used by Rosenfeld and Wolfshtein (ref. 20) gives more grid points on the airfoil surface that the present "H" grid. The comparison between the PSM and PCM algorithms were performed at various relaxation parameters for the momentum equations.

Fig. 4 shows the comparison of the convergence rate for the highest relaxation parameters ($\omega_u = \omega_v = 0.8$, and $\omega_p = 1.0$). The PSM shows a significant improvement over the PCM which seems to indicate that at least the initial stages of convergence of the PSM is more favorably affected by the relaxation parameter than the PCM. The above test case was compared with zero degrees inlet incidence angle. A comparison of the predicted static pressure coefficient over the airfoil with that computed by Rosenfeld and Wolfshtein (ref. 20) is presented in Fig. 5. The absolute levels of pressure coefficient do not compare well. However, the predicted negative lift coefficient ($C_L = -0.0310$) is within 4% of that predicted by Rosenfeld and Wolfshtein (ref. 20) who predicted $C_L = 0.0322$. The negative lift force created at this incidence angle causes a negative turning angle of -0.7 degrees through the cascade. The predictions using the PSM and PCM resulted in plots on the same curve.

An additional test case was computed with the PSM to predict the flow at the -10 degrees incidence case. The comparison with the predicted pressure coefficient as computed by Rosenfeld and Wolfshtein (ref. 20) is shown in Fig. 6. This comparison is better than the zero degree incidence test case, and the predicted $C_L = -0.389$ compares within 3% of their prediction of $C_L = -0.39711$. The present method does not suffer from pressure field oscillations around the trailing edge.

Turbulent Flow Through a Cascade of Double Circular Arc Profiles with Flow Detachment

For the test case of turbulent flow through a cascade, the predictions made by the present method were compared with the experimental data obtained by Zierke and Deutsch (ref. 21). The blade section was a double circular arc, The computed test case was for the near design case of -1.5 degrees incidence.

The modified version of the GRAPE code was used to generate the H-grid which extended half a chord upstream and one and a half chords downstream of the blade. The inlet angle of the grid was aligned with the incoming flow at 51.5 degrees and the outlet grid angle was set equal to the measured outlet flow angle of 2.1 degrees. The Navier-Stokes calculations were on a 130 streamwise by 100 tangential computational grid as shown in Fig. 7. The residuals were reduced by four orders of magnitude in roughly 2000 iterations. This corresponded to 20 minutes on the ETA-10 supercomputer, only using the optimization capabilities of the compiler which vectorizes inner DO-loops. The slope of the convergence plots were not monotonic and flattened out after 300 iterations.

Fig. 8 shows a comparison of the calculated and measured static pressure distribution. The experimental measurements indicated a possible separation region near the trailing edge. Surface flow visualisation tests using the chemical sublimation method showed, with a 95% confidence level, a region of low shear stress at 45.1% ±2.3% chord.

The comparison of the blade surface skin friction distribution is presented in Fig. 9. Transition of the pressure surface boundary layer from laminar to turbulent flow is predicted by the technique. The onset of transition is predicted to be at 10% chord, which is early compared to the experimentally determined transition process. Transition seems to be complete by 30% chord, thus the length of the transitional region is in agreement with that determined experimentally. The experimental points were determined by fitting a spline through the measured boundary layer profiles. The level of skin friction coefficient in the fully turbulent region is accurately predicted, as well as the final increase at the trailing edge. Good agreement is achieved between the predicted and experimental skin friction coefficient on the suction surface of the blade. Shown on this figure is the separation point as determined by the flow visualisation technique and the separation point as predicted by the code with good agreement. The levels of skin friction are very close to zero over most of the rear part of the blade.

Turbulent Flow Through a Cascade of Turbine Nozzles Including Heat Transfer

The computer program was used to compute turbine cascade flows for which Turner (ref. 22) conducted heat transfer measurments. A review of the literature showed that few incompressible flow experiments, including heat transfer measurements, have been documented. Turner (ref. 22) tested a nozzle blade section, as shown in Fig. 10, that was the same as the one used by Bayley and Turner (ref. 23) and Bayley and Wood (ref. 24). The blade chord was 70 mm and the aspect ratio and pitch-to-chord ratio were 1.34 and 0.65, respectively. The stagger angle was 40.6 degrees, and the inlet and outlet flow angles were 0.0 and 61.0 degrees, respectively. Three exit Mach numbers (0.75, 0.65, 0.55) were considered. At each Mach number tests were done at three turbulence intensities, namely 5.9%, 2.2% and 0.45%.

The cascade tunnel delivered 1.5 atmospheres of air, at 90 degrees C, to the test section. The blades were internally cooled with air at 20 degrees C, which produced a sufficient temperature gradient for heat transfer experiments. At the highest turbulence level the average gas-to-wall temperature difference was 28 degrees C and 40 degrees C at the lowest turbulence level. The exit Reynolds number based on the nozzle chord was $1.05\mathrm{x}10^6$.

Since the present predictions are valid for incompressible flow, only the low Mach number test case was considered. For this test case, the aerodynamic experimental test data were obtained from Bayley and Wood (ref. 24). Although porous blade sections were tested, they did present blade surface velocity distributions for the solid blades.

The turbulence of the flow at entry to the cascade was varied by placing various grids and drilled plates one chord distance upstream of the blade. Unfortunately, neither the diameter of the grids nor their character dimensions were quoted by Turner (ref. 22). The turbulence length scale, L_i, was thus set equal to the leading edge radius (0.26cm) of the nozzle blades for all the test cases considered. This value was used in equation [30] to determine the inlet levels of the dissipation rate ϵ.

As shown in Fig. 10, a 100x132 computational H-grid was used with the normal grid spacing at the blade surface such that the first grid point was at a y^+ of 1.0. The inlet angle of the grid to the cascade was set equal to zero degrees, and the exit grid angle was set equal to 60 degrees.

The predicted velocity distribution over the blade surface is compared to the distribution calculated from the static pressure measurements in Fig. 11. The local velocity was derived by assuming isentropic expansion from the inlet total pressure to the static pressure, either measured or predicted, recorded on the blade surface. The sudden acceleration of the flow around the leading edge on the suction surface is captured, and the subsequent acceleration on the front section of the blade. The maximum velocity level is accurately predicted, and the diffusion process that results on the suction surface after the turbine throat is adequately resolved. The level of local velocity is slightly high on the rear section of the suction surface. The rapid diffusion process on the rear part of the suction surface results in flow separation which is predicted at the trailing edge. The continual flow acceleration process on the pressure surface is well predicted over its entire length.

Turner (ref. 22) showed that the mean heat transfer results for a turbine blade operating at one Reynolds number, but at different turbulence levels, vary substantially. At a Reynolds number of $1.0\text{x}10^6$ the mean heat transfer coefficient varied from $8.5\text{x}10^2$ to $1.05\text{x}10^3$ for varying inlet turbulence intensity levels from 0.45 to 5.9% respectively. For different turbulence levels the slope of the Nusselt number versus Reynolds number also varied, the actual slopes are presented by Turner. A distinct increase in the blade surface temperature was measured. No data were presented on the cooling system heat transfer, thus a complete energy balance could not be determined for the cascade. The measured distribution of surface temperature at 0.45 and 5.9%, as shown in Fig. 12, was used as temperature boundary conditions. Linear interpolation was used between these two levels to determine the temperature boundary conditions at 2.2% turbulence intensity.

An example of the prediction of the variation of local heat transfer coefficient over the surface of the blade is presented in Fig. 13 for varying inlet turbulence intensities. As mentioned earlier the stagnation point is situated on the pressure surface, this is illustrated by the maximum heat transfer rates in this region which is offset toward the concave surface. The levels of heat transfer are in good agreement with the experimental data in the stagnation point region. No sudden transition from a purely laminar to a purely turbulent flow is observed, and this trend is well predicted by the program. At an inlet turbulence intensity level of 5.9% the predictions show some form of transition of the boundary. Although this is not in complete agreement with the experimental data, this could be due to the mixing augmentation on the concave surface dominating the favorable pressure gradient. It is well established that in a two-dimensional boundary layer, flow over a convex surface damps mixing, while a concave surface leads to augmentation as described by Bradshaw (ref. 25). On the pressure surface the prediction of the increase in the average heat transfer coefficients for increasing turbulence levels is very good. This is surprising, considering that a constant turbulent Prandtl number (=0.9) was used for these calcuations. The average gas-to-wall temperature difference was 30°C; however, the gas-to-wall temperature ratio $(T_{gas}/T_{wall} \approx 1.09)$ was representative of those found in the uncooled turbine stages of a gas turbine engine.

For the suction surface, a sharp increase in heat transfer between 80% and 90% chord is apparent for the low turbulence levels, and the increase is between 50% and 90% for the high turbulence level case. Fig. 11 indicates that on this surface a favorable pressure gradient, decreasing in magnitude, extends 60% of the chord downstream of the leading edge. The boundary layer then experiences an adverse pressure gradient and the high heat transfer rates in this region are indicative of transition from laminar to turbulent flow. For the 0.45% and 2.2% test cases the transition process was experimentally determined to be abrupt, which the LRN turbulence model is not able to accurately simulate. Once again the model, although only for low turbulence levels, has tended to smear the transition process over a longer distance and the onset of transition is predicted to occur too close to the leading edge. The experimental data showed little or no effect for increasing turbulence levels from 0.45% to 2.2% over the front 70% chord of the suction surface. A further increase in turbulence to 5.9% produced a significant increase in heat transfer. The length of transition of the boundary layer for this case is longer than the low freestream turbulence intensity test cases. The transition process is adequately predicted for this high turbulence level case, which is the one of the strong points of the LRN k-ϵ turbulence model. The prediction showed an increase in heat transfer from 0.45% to 2.2% which is not in agreement with the experimental data. This could be due to the interpolated blade surface temperature that was used as the boundary conditions for the 2.2% turbulence case. The actual blade surface temperature, which was not documented, could be different from that used. This could explain the discrepancy between these results.

Flow in a Turbine End Wall Cascade

The final three-dimensional flow test case considered is secondary flow and losses in a turbine cascade. Gregory-Smith and Graves (ref. 26) investigated the flow in a cascade of large scale rotor blades of some 110 degrees of turning. The flow was traversed with 3-hole and 5-hole cobra type pressure probes. Hot-wire anemometry measurements were also carried out in the linear cascade consisting of blades scaled from the midspan section of a high-pressure turbine rotor design. The main geometric parameters for the cascade are given in Table 1. The blade profile coordinates were obtained from Gregory-Smith (ref. 27).

Table 1 Cascade Geometric Parameters

Inlet flow angle	42.75 deg.
Inlet blade angle	52.25 deg.
Exit flow angle	-66.60 deg.
Exit blade angle	-67.50 deg.
Blade chord	216 mm
Blade axial chord	175 mm
Span	457 mm
Pitch	191 mm
Reynolds number (based on chord and exit velocity)	5×10^5

The estimated inlet (99%) boundary layer thickness was 102.0 mm, the displacement thickness was 12.1 mm and the momentum thickness was 9.9 mm. These data were obtained at the first slot which was 14% of an axial chord upstream of the cascade. The measured inlet free-stream turbulence intensity was 1.4% which was due to the honeycomb flow straightener placed upstream of the cascade. The inlet boundary layer profile agrees well with a 0.12 power law profile. This profile was used for the input velocity distribution during the computational analysis.

The three-dimensional "H" grid was generated from a two-dimensional blade-to-blade grid which was projected in the spanwise direction. Grid clustering was used at the endwalls, at the blade sufaces and around the leading edge and trailing edge of profile. In the cross-plane, 31 x 31 grid points were used with 81 in the streamwise direction. A three-dimensional view of the grid is presented in Figure 14. Although the problem is symmetrical about the mid-span plane, the computation was performed for the complete cascade to check the code's ability to compute a symmetric solution.

The three-dimensional flowfield was initialised with the solution of the two-dimensional flow through the cascade. The two-dimensional version of the code was run to 500 iterations, giving two orders of magnitude convergence. The velocity field showed most of the correct features of two-dimensional flow through a cascade. As the LRN turbulence model was used (on this coarse grid) the boundary layer growth is most probably too rapid; however, this was considered to be a good initial guess for the three-dimensional flow.

The velocity field was scaled in the spanwise direction according to the inlet boundary layer profile at the endwalls. The pressure distribution was assumed constant in the spanwise direction. Less than one order of magnitude convergence was obtained for this case, which took 4000 CPU seconds on the ETA-10 at the John von Neumann Computer Center. Because of limited computation time the solution was not continued further.

The main objective of this test case is to attempt to qualitatively predict the three-dimensional viscous phenomena inside a turbine blade passage.

Fig. 15 shows the velocity vector plot for the end wall region. Flow reversal occurs at the leading edge which is associated with the roll-up of the inlet boundary layer at the leading into the so-called horse-shoe vortex. The subsequent movement of this vortex is not captured as the secondary flow convects the pressure side vortex over to the suction surface of the adjacent blade too rapidly.

The horse-shoe vortex and passage vortex begin in the leading region close to the endwall. An "H" grid does not allow the adequate resolution of the severe flow gradients in this region. This region should be resolved with a "C" grid which is continuous around the leading edge. A higher order turbulence model needs to be considered if the finer details of this complex flow is to be adequately resolved.

CONCLUSIONS

Various test cases have been presented. These show that in two dimensions the pressure substitution method is superior to the pressure correction method. This method is ideally suited for the computation of incompressible flows.

For complex flow situations such as turbulent flow through a compressor or turbine cascade, the code exhibits satisfactory convergence behavior. The global parameters such as pressure distribution, lift coefficient and heat transfer are well predicted within engineering accuracy. The agreement between the computed and measured blade surface skin friction coefficients and heat transfer coefficients is very good. Details of the leading edge flow and particularly the trailing edge separation have been resolved, which shed more light on these complex flow regions.

For flow over curved surfaces with large pressure gradients the minimum turbulence model that must be used is the low-Reynolds number k-ϵ model. Its ability to predict transition dependent on freestream turbulence intensity is well known, and it was used in the present study to predict separated flow and flow through a turbine nozzle including heat transfer.

Experimental investigations of turbulent flow through cascades should include detailed measurements of the inlet freestream turbulence intensity and turbulence length scales. These two parameters are of vital importance for the correct specification of the inlet boundary conditions.

The three-dimensional turbulent flow through a turbine end wall cascade has been qualitatively resolved. To increase the accuracy of the predictions it is recommended that a higher order turbulence model be used which can simulate the laminar flow leading edge region.

ACKNOWLEDGEMENTS

The authors wish to acknowledge the John von Neumann Supercomputer Center for providing computational time under grant NAC 817, and for partial support from the National Aeronautics and Space Administration through grant NSG 3266 with P. Sockol as the grant monitor.

REFERENCES

1. Hah, C., "A Navier-Stokes Analysis of Three-Dimensional Turbulent Flows Inside Turbine Blade Rows at Design and Off-Design Conditions," *ASME J. Eng. for Power*, Vol. 106, pp. 421-429, (1984).
2. Leonard, B. P., "A Stable and Accurate Convective Modelling Procedure Based on Quadratic Upstream Interpolation," *Computer Methods in Applied Mechanics and Engineering*, Vol. 19, pp. 59-98, (1979).
3. Raithby, G. D., "Skew Upstream Differencing Schemes for Problems Invloving Fluid Flow," *Computer Methods in Applied Mechanics and Engineering*, Vol. 9, pp. 153-164, (1976).
4. Patankar, S. V., "Recent Developments in Computational Heat Transfer," *Journal of Heat Transfer*, Vol. 110, pp. 1037-1045, (1988).
5. Patel, M. K. and Markatos, N. C., "An Evaluation of Eight Discretization Schemes for Two-Dimensional Convection-Diffusion Equations," *International Journal for Numerical Methods in Fluids*, Vol. 6, pp. 129-154, (1986).
6. Patel, M. K., Cross, M., Markatos, N. C. and Mace, A. C. H., "An Evaluation of Eleven Discretization Schemes for Predicting Elliptic Flow and Heat Transfer in Supersonic Jets," *International Journal of Heat and Mass Transfer*, Vol. 30, pp. 1907-1925, (1986).
7. Rhie, C. M. and Chow, W. L., "Numerical Study of the Turbulent Flow Past an Airfoil with Trailing Edge Separation," *AIAA Journal*, Vol. 21, pp. 1525-1532, (1983).
8. Rhie, C., "A Pressure Based Navier-Stokes Solver Using the Multigrid Method," AIAA Paper 86-0207, AIAA 24th Aerospace Sciences Meeting, Reno, NV, (1986).
9. Shih, T. M. and Ren, A. L., "Primitive-Variable Formulations Using Nonstaggered Grids," *Numerical Heat Transfer*, Vol. 7, pp. 413-428, (1984).
10. Hobson, G. V. and Lakshminarayana, B., "Fully Elliptic Incompressible Flow Calculations on Regular Grid by a New Pressure Substitution Method," AIAA paper 90-0239, AIAA 28th Aerospace Sciences Meeting, Reno, NV, (1990).
11. Lam, C. K. G. and Bremhorst, K., "A Modified Form of the k-ϵ Model for Predicting Wall Turbulence," *Journal of Fluids Eng.*, Vol. 103, pp. 456-460, (1981).
12. Rhie, C., "A Three-Dimensional Passage Flow Analysis Method Aimed at Centrifugal Impellers," *Computers and Fluids*, Vol. 13, No. 4, pp. 443-460, (1985).
13. Boussinesq, J., "Theorie de l'ecoulement tourbillant," Memoires Presentes par Divers Savants Sciences Mathematique at Physiques, Academie des Sciences, Paris, France, Vol. 23, p. 46, (1877).
14. Launder, B. E. and Spalding, D. B., "The Numerical Computation of Turbulent Flows," *Computer Methods in Applied Mechanics and Engineering*, pp. 269-289, (1974).
15. Patel, V.C., Rodi, W. and Scheuerer, G., "A Review and Evaluation of Turbulence Models for Near Wall and Low Reynolds Number Flows," *AIAA Journal*, Vol. 23, pp. 1308-1319, (1985).
16. Rodi, W. and Scheuerer, G., "Calculation of Heat Transfer to

Convection-Cooled Gas Turbine Blades," *Journal of Eng. for Power*, Vol. 107, pp. 620-627, (1985).

17. Spalding, D. B., "A Novel Finite Difference Formulation for Differential Expressions Involving Both First and Second Derivatives," *Int. Journal for Numerical Methods in Engineering*, Vol. 4, pp. 551-559, (1972).
18. Napolitano, M., "A Fortran Subroutine for the Solution of Periodic Block-Tridiagonal Systems," Communications in Applied Numerical Methods, Vol. 1, pp. 11-15, (1985).
19. Thomas, L. H., "Elliptic Problems in Linear Difference Equations over a Network," Watson Sci. Comput. Lab. Rept., Columbia University, New York, (1949).
20. Rosenfeld, M. and Wolfshtein, M., "Numerical Calculations of a Laminar Two Dimensional Straight Cascade Flow," *Computer and Fluids*, Vol. 12, pp. 293-310, (1984).
21. Zierke, W. C. and Deutsch, S., "The Measurement of Boundary Layers on a Compressor Blade in Cascade: Part 4-Flow Fields for Incidence Angles of -1.5 and -8.5 Degrees," ASME 89-GT-72 (To be published in the *J. Turbomachinery*)
22. Turner, A. B., "Local Heat Transfer Measurements on a Gas Turbine Blade," *J. Mechanical Engineering Science*, Vol. 13, No. 1, (1971).
23. Bayley, F. J. and Turner, A. B., "The Heat Transfer Performance of Porous Gas Turbine Blades," *The Aeronaut. J. R. Aeronautical Soc.* 72, (1968).
24. Bayley, F. J. and Wood, G. R., "Aerodynamic Performance of Porous Gas Turbine Blades," *The Aeronautical Journal of the Royal Aeronautical Society*, Vol. 73, pp. 789-796, (1969).
25. Bradshaw, P., "Effects of Streamline Curvature on Turbulent Flow," Agardograph No. 169, (1973).
26. Gregory-Smith, D. G. and Graves, C. P., "Secondary Flows and Losses in a Turbine Cascade," AGARD Conference Proceedings No. 351, Viscous Effects in Turbomachines, (1983).
27. Gregory-Smith, D. G., Private Communications, (1989).

APPENDIX A

Partial derivatives of any function are transformed according to,

$$
\begin{aligned}
\frac{\partial}{\partial x} &= \xi_x \frac{\partial}{\partial \xi} + \eta_x \frac{\partial}{\partial \eta} + \zeta_x \frac{\partial}{\partial \zeta} \\
\frac{\partial}{\partial y} &= \xi_y \frac{\partial}{\partial \xi} + \eta_y \frac{\partial}{\partial \eta} + \zeta_y \frac{\partial}{\partial \zeta} \qquad [A1] \\
\frac{\partial}{\partial z} &= \xi_z \frac{\partial}{\partial \xi} + \eta_z \frac{\partial}{\partial \eta} + \zeta_z \frac{\partial}{\partial \zeta}
\end{aligned}
$$

where,

$$\begin{aligned}
\xi_x &= (y_\eta z_\zeta - y_\zeta z_\eta)/J \\
\xi_y &= -(x_\eta z_\zeta - x_\zeta z_\eta)/J \\
\xi_z &= (x_\eta y_\zeta - x_\zeta y_\eta)/J \\
\eta_x &= -(y_\xi z_\zeta - y_\zeta z_\xi)/J \\
\eta_y &= (x_\xi z_\zeta - x_\zeta z_\xi)/J \\
\eta_z &= -(x_\xi y_\zeta - x_\zeta y_\xi)/J \\
\zeta_x &= (y_\xi z_\eta - y_\eta z_\xi)/J \\
\zeta_y &= -(x_\xi z_\eta - x_\eta z_\xi)/J \\
\zeta_z &= (x_\xi y_\eta - x_\eta y_\xi)/J
\end{aligned} \tag*{[A2]}$$

and,

$$J = \begin{vmatrix} x_\xi & x_\eta & x_\zeta \\ y_\xi & y_\eta & y_\zeta \\ z_\xi & z_\eta & z_\zeta \end{vmatrix} \tag*{[A3]}$$

which is the Jacobian of the transformation.

The contravariant velocities are defined as,

$$\begin{aligned}
G_1 &= \xi_x u + \xi_y v + \xi_z w \\
G_2 &= \eta_x u + \eta_y v + \eta_z w \\
G_3 &= \zeta_x u + \zeta_y v + \zeta_z w
\end{aligned} \tag*{[A4]}$$

and the additional transformation metrics as,

$$\begin{aligned}
\alpha &= \xi_x^2 + \xi_y^2 + \xi_z^2 \\
\beta &= \eta_x^2 + \eta_y^2 + \eta_z^2 \\
\gamma &= \zeta_x^2 + \zeta_y^2 + \zeta_z^2
\end{aligned} \tag*{[A5]}$$

and,

$$\begin{aligned}
H_1 &= \xi_x\eta_x + \xi_y\eta_y + \xi_z\eta_z \\
H_2 &= \xi_x\zeta_x + \xi_y\zeta_y + \xi_z\zeta_z \\
H_3 &= \eta_x\zeta_x + \eta_y\zeta_y + \eta_z\zeta_z
\end{aligned} \tag*{[A6]}$$

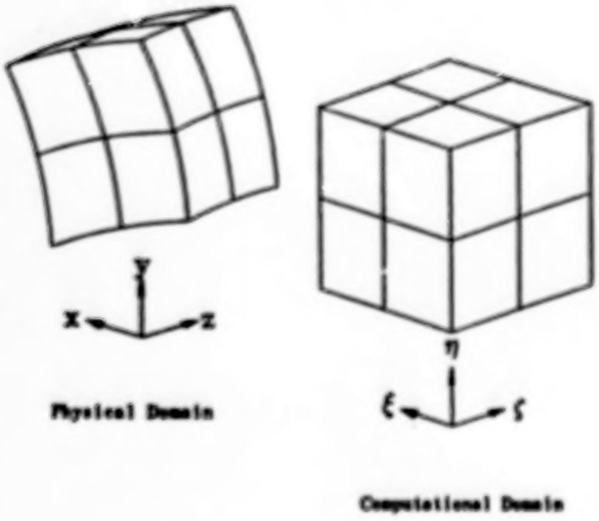

Fig. 1 Transformation Representation

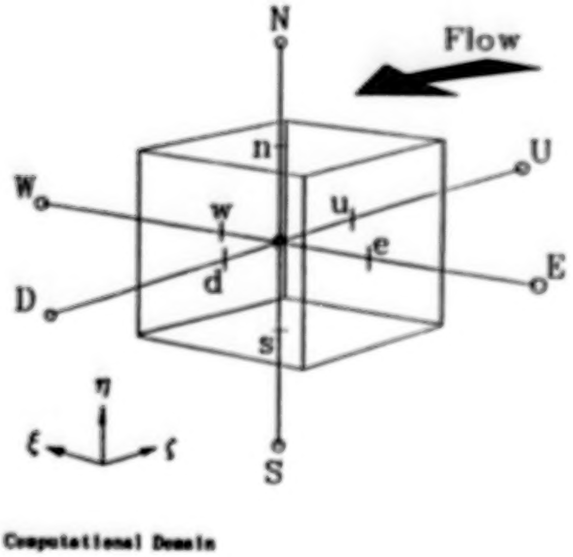

Fig. 2 Control Volume

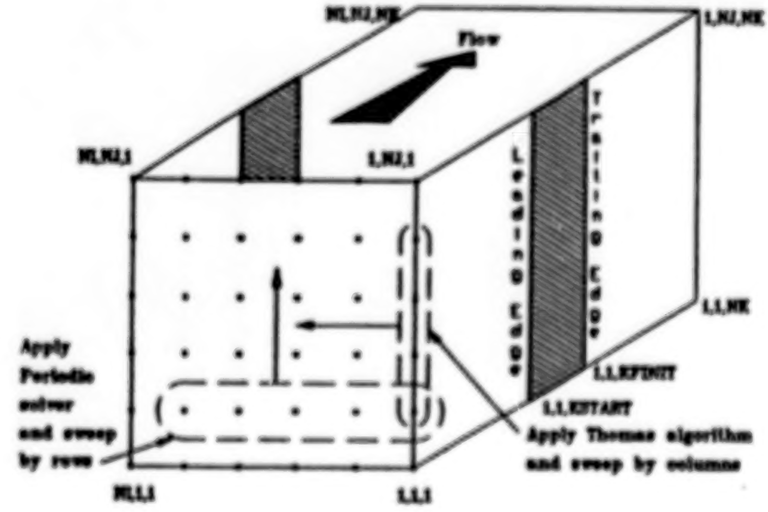

Fig. 3 Alternating Direction Implicit Relaxation of a Three-Dimensional Cascade Geometry

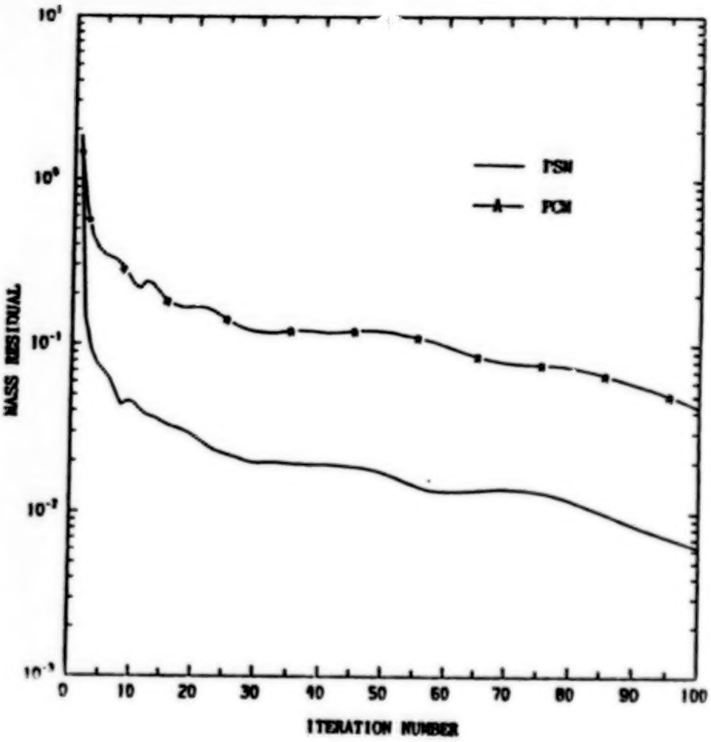

Fig. 4 Comparison of Convergence Rates for PSM and PCM; Laminar Flow in a Cascade, $\omega_u = \omega_v = 0.8$, $\omega_p = 1.0$

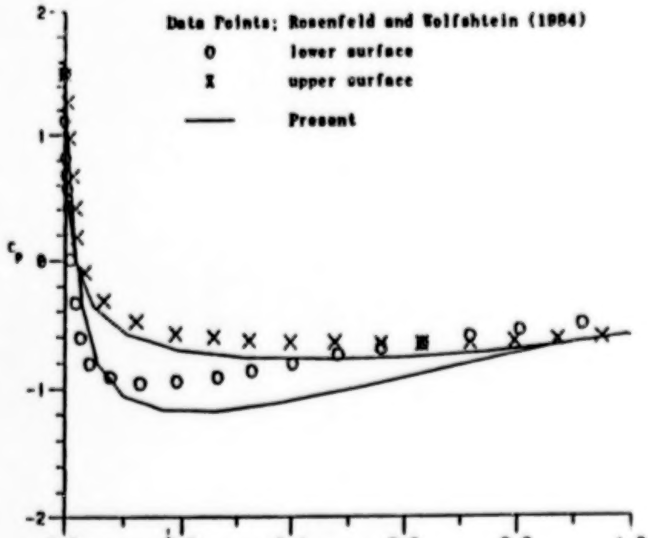

Fig. 5 Comparison of Predicted Pressure Coefficient for a Straight Cascade of NACA 0012 Blade Profiles at 30 Deg. Stagger and 0.0 Deg. Incidence

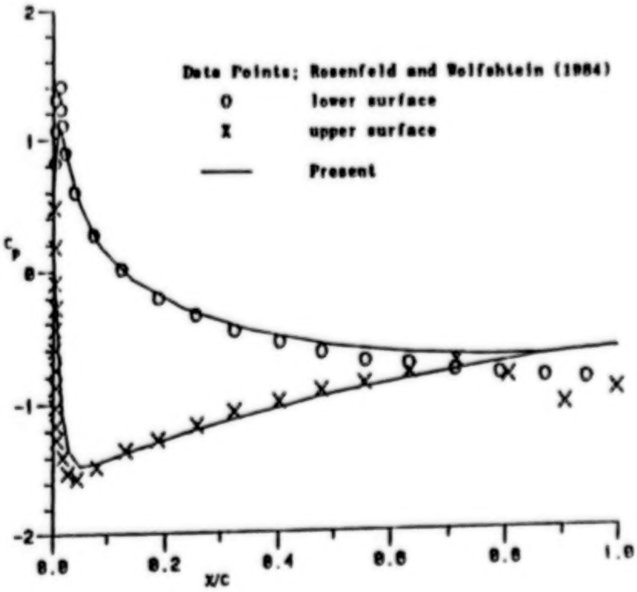

Fig. 6 Comparison of Predicted Pressure Coefficient for a Straight Cascade of NACA 0012 Blade Pr at 30 Deg. Stagger and -10.0 Deg. Incidence

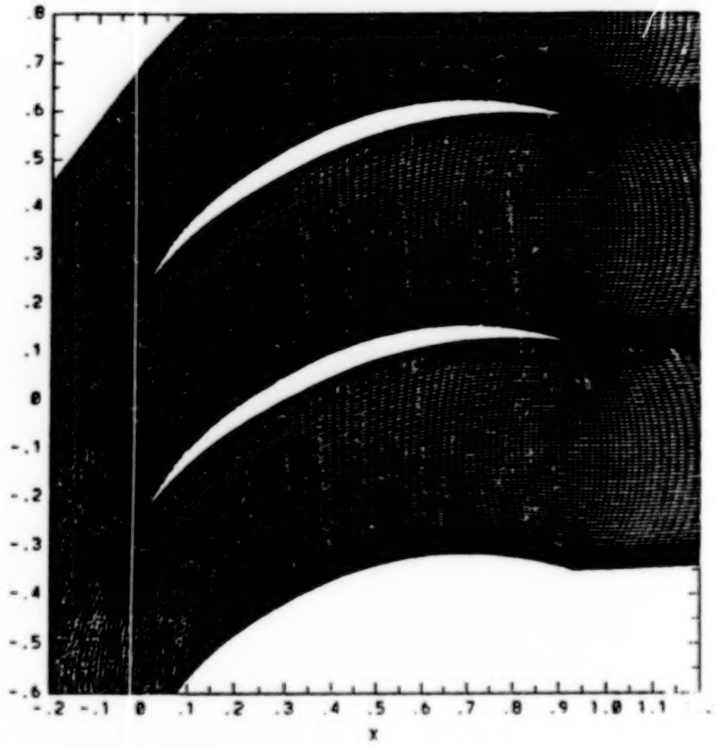

Fig. 7 Computational Grid for the Double Circular Arc Cascade

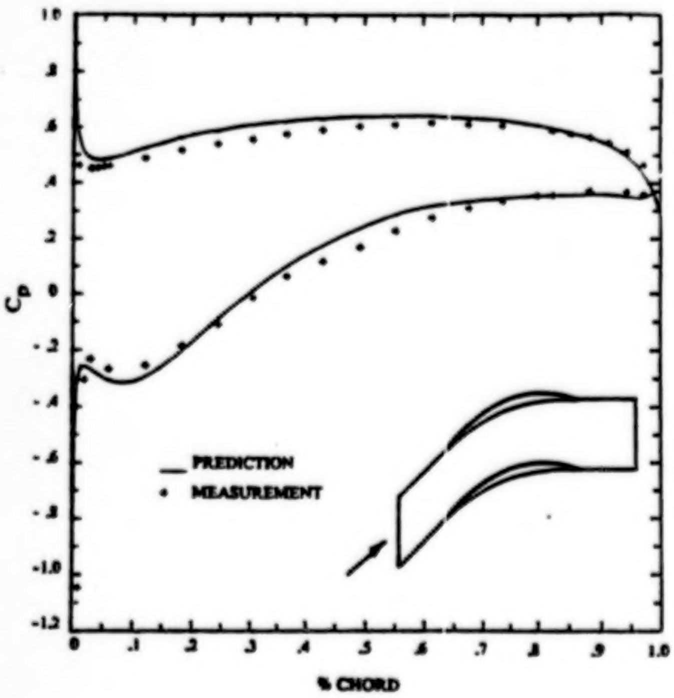

Fig. 8 Comparison between Experimental and Computed Static Pressure Coefficient for DCA Cascade

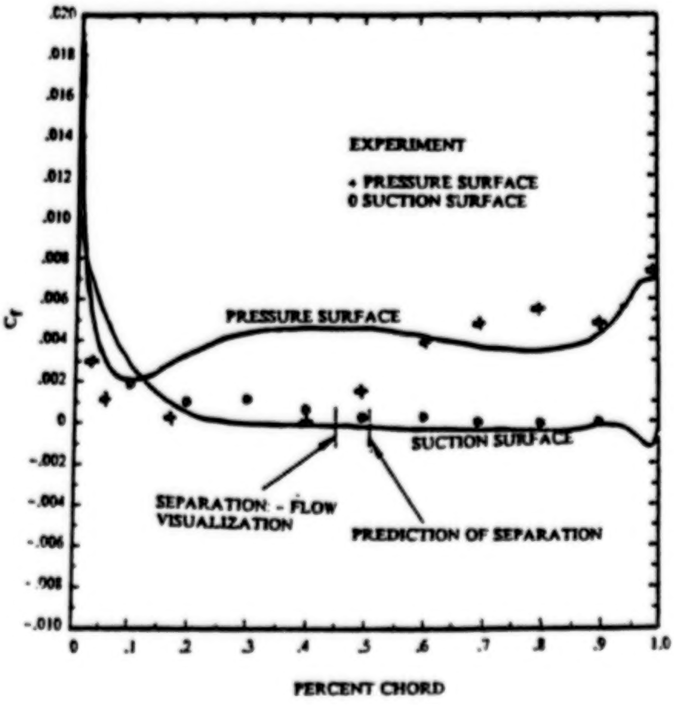

Fig. 9 Comparison of the Computed and Measured Skin Friction Coefficient on the Blade Surface

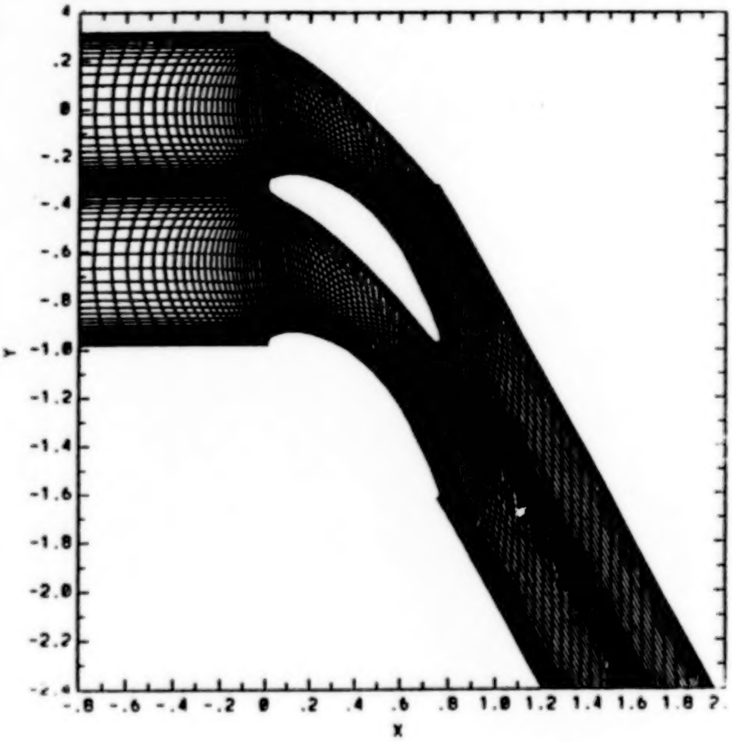

Fig. 10 Computational Grid for the Turbine Nozzle Cascade

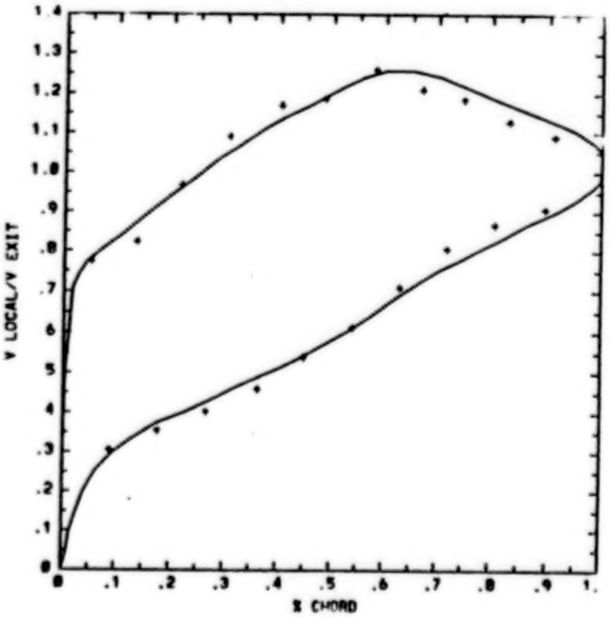

Fig. 11 Comparison of the Predicted and Measured Local Velocity Distribution for the Turbine Nozzle

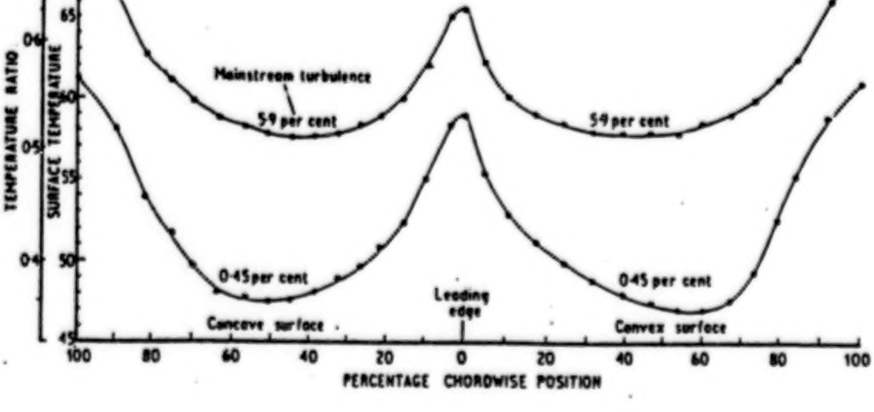

Fig. 12 Measured Blade Surface Temperature Distribution: Turner (ref. 22)

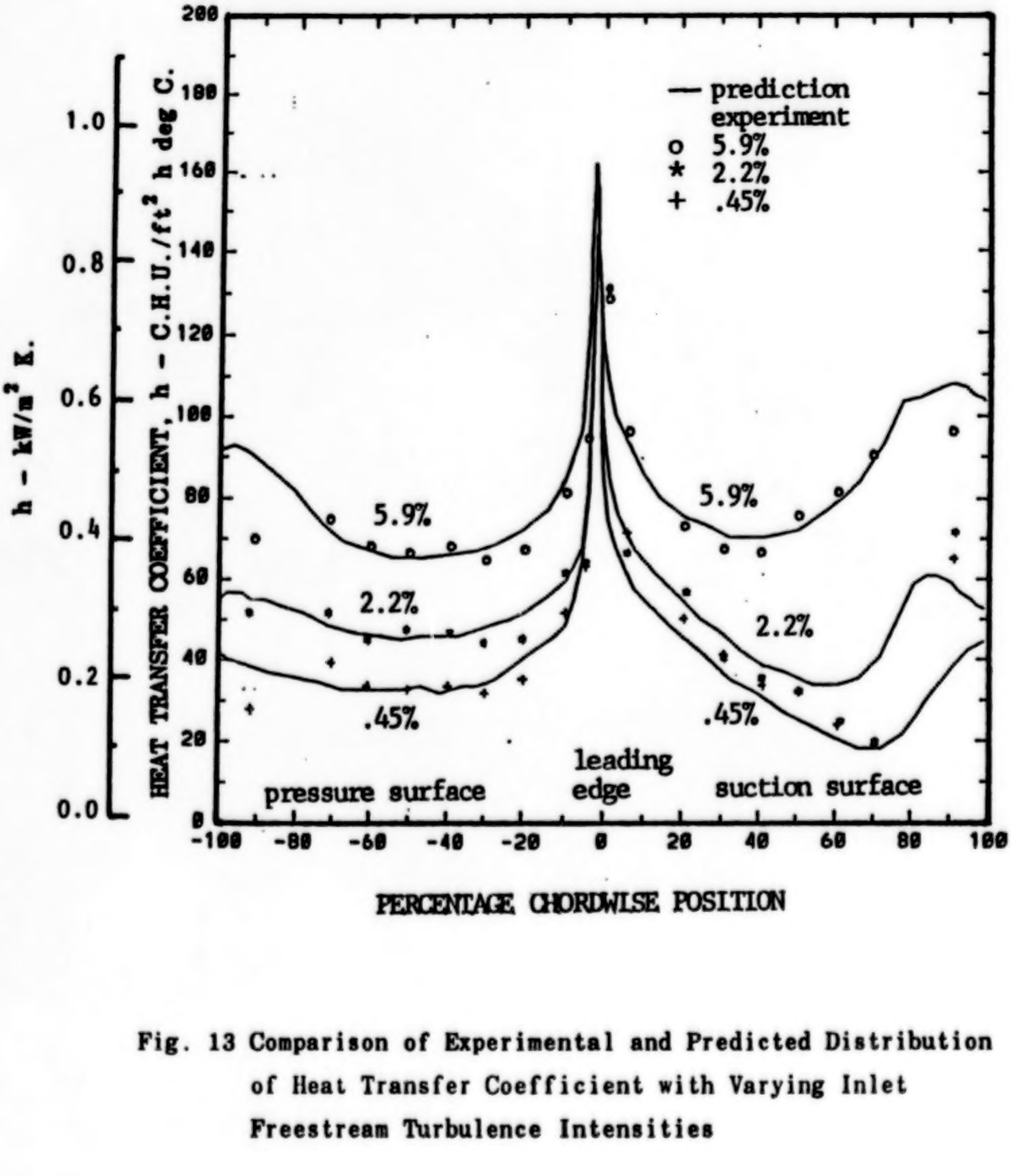

Fig. 13 Comparison of Experimental and Predicted Distribution of Heat Transfer Coefficient with Varying Inlet Freestream Turbulence Intensities

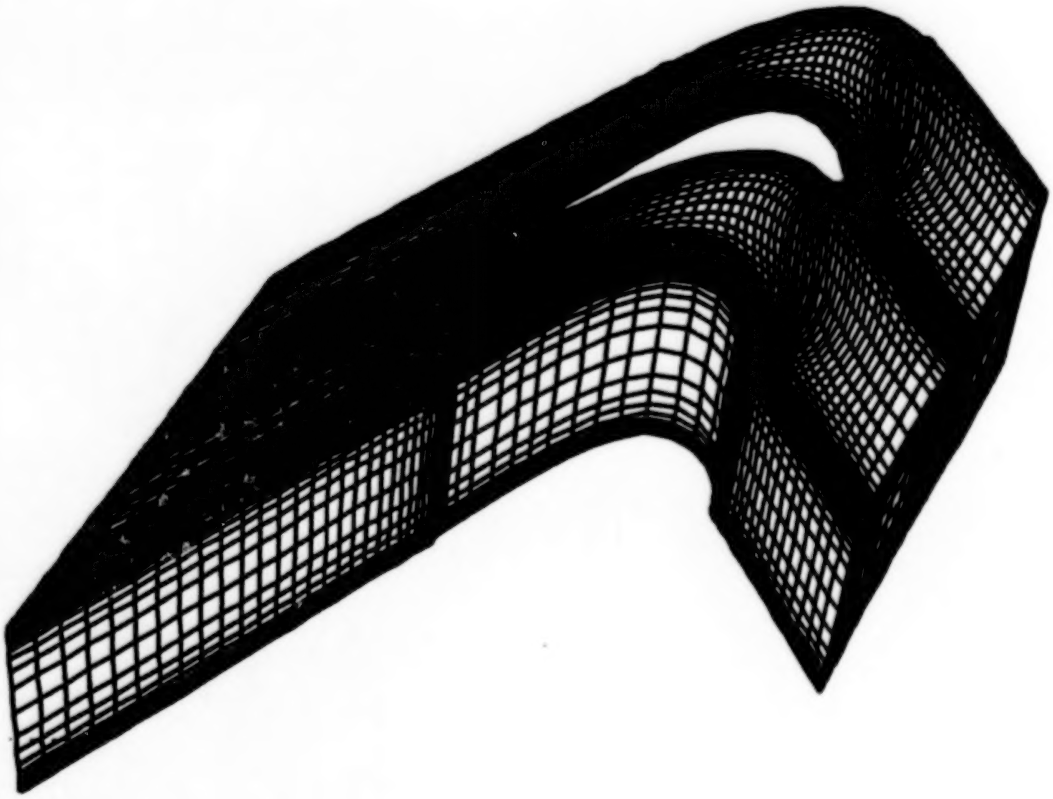

Fig. 14 Computational Grid for the Turbine End Wall Cascade

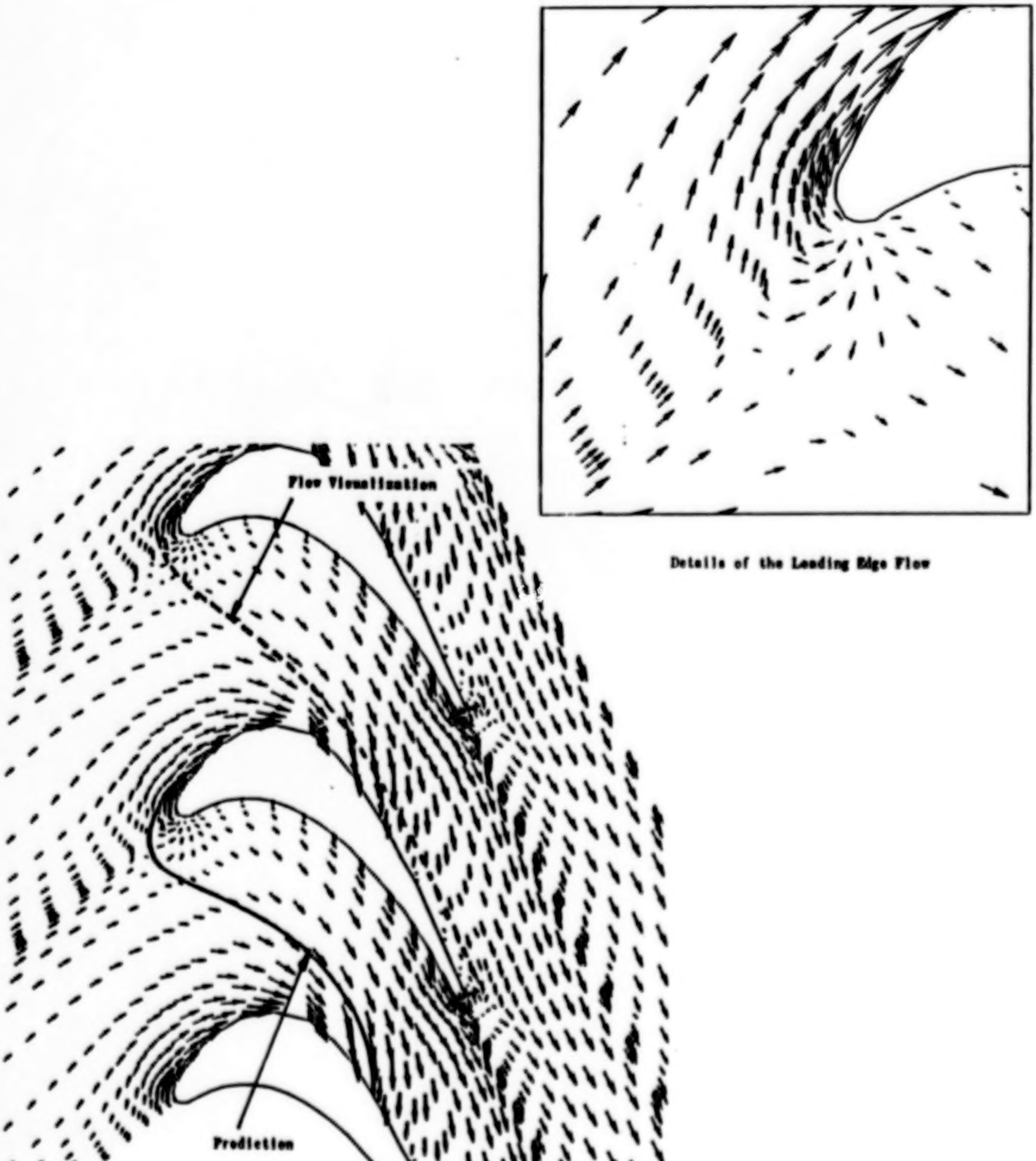

Details of the Leading Edge Flow

Fig. 15 End-Wall Velocity Vector Plot Showing the Development of the Horse Vortex System

A MULTIDIMENSIONAL FINITE ELEMENT METHOD FOR CFD

Darrell W. Pepper and Joseph W. Humphrey
Advanced Projects Research, Inc.
5301 N. Commerce Ave.
Moorpark, CA 93021

ABSTRACT

A finite element method is used to solve the equations of motion for 2- and 3-D fluid flow. The time-dependent equations are solved explicitly using quadrilateral (2-D) and hexahedral (3-D) elements, mass lumping, and reduced integration (when appropriate). A Petrov-Galerkin technique is applied to the advection terms. The method requires a minimum of computational storage, executes quickly, and is scalable for execution on computer systems ranging from PCs to supercomputers.

NOMENCLATURE

A	global advection matrix
$a_{i,j}$	local advection matrix
C	gradient matrix
C^T	divergence matrix
E_T	total energy
F_u	body force term for x momentum
F_v	body force term for y momentum
F_w	body force term for z momentum
F_E	load vector for energy equation
$k_{i,j}$	local diffusion matrix
K	global diffusion matrix
$m_{i,j}$	local mass matrix
M	global mass matrix
M_∞	Mach number
N	basis function
p	pressure
P_r	Prandtl number
R_a	Rayleigh number
R_e	Reynolds number
S	boundary segment
T	temperature
t	time
$\underline{u}$	horizontal velocity
$\bar{u}$	velocity vector
U_∞	reference velocity
v	lateral velocity
w	vertical velocity
x	horizontal coordinate
y	lateral coordinate
z	vertical coordinate

W	weighting function
α	Petrov-Galerkin parameter
β	Petrov weighting factor
γ	ratio of specific heats
Δt	time step
κ	thermal diffusivity
ρ	density
σ_{xx}	x-coordinate viscous stress
σ_{xy}	x-y viscous shear
σ_{xz}	x-z viscous shear
σ_{yy}	y-coordinate viscous stress
σ_{yz}	y-z viscous shear
σ_{zz}	z-coordinate viscous stress
Ω	area (2-D); volume (3-D)

Subscripts

i,j,k	local node index
x	x direction
y	y direction
z	z direction
∞	free stream
_	column vector

Superscripts

T	transpose
-1	inverse
n	previous time value
n+1	new time value
x	x direction
y	y direction
z	z direction
$\hat{u}$	trial value
$\bar{u}$	average value

INTRODUCTION

Numerical modeling of multidimensional fluid flow is a difficult, computationally intensive effort. When the physical domain is simple, finite difference methods (FDM) are typically used as a matter of convenience and historical preference. If the domain is irregular, boundary fitted coordinates are usually employed [1]; however, such techniques are not easy to use, particularly when generating 3-D grids, and require the transformation of the governing equations. Finite element methods (FEM), while mathematically more robust and convenient to use in complex geometries, can tax the limits of the largest computers. In an effort to alleviate these constraints, a modified FEM, which is competitive with the FDM in storage and speed, is used to solve a set of example problems in 2- and 3-D for both incompressible and compressible flows. The FEM is based on the method discussed in Pepper and Singer [2] and Pepper and Humphrey [3].

The modified FEM employs simple, well known alterations to the conventional FEM: mass lumping, reduced integration, and application of Petrov-Galerkin weighting. Lumping the time derivative term into one diagonal allows simple explicit time integration to be used and the mass matrix to be easily inverted. One point quadrature, as opposed to 2x2 (bilinear quadrilateral) or 2x2x2 (hexahedral) Gauss points, yields integral values obtained at the element centroid. This procedure permits explicit evaluation of the integral terms on a local level, i.e., per element without regard for bandwidth. The application of reduced quadrature has been found to be very effective when the element is not too distorted [4]; however, care must be exercised in generating the initial mesh to insure aspect ratios and distortions are minimal.

Velocities within the advection terms are averaged over an element and a Petrov-Galerkin formulation applied [5]. Application of the Petrov-Galerkin technique helps maintain stability but does not overly dampen the solution, compared to the more commonly utilized upwinding techniques and anti-dispersive schemes applied in FDMs [6].

Performance of the algorithm on current scalar/vector machines is good [2]; many multidimensional problems can be run on low-end computers. The performance of the FEM is significantly improved on a parallel computer. Since the method is explicit in time, vectorization and parallelization are relatively easy. A version of the method has been written and optimized for execution on an Alliant VFX/40 mini-supercomputer with 4 processors.

GOVERNING EQUATIONS

The mathematical relations which describe the transport of fluid motion and energy are the equations for conservation of mass, momentum, and energy. The governing equations for three-dimensional flow can be written in non-dimensional form as [6]

Conservation of Mass

$$\frac{\partial \rho}{\partial t}+\frac{\partial \rho u}{\partial x}+\frac{\partial \rho v}{\partial y}+\frac{\partial \rho w}{\partial z}=0 \qquad (1)$$

Conservation of Momentum

x-direction

$$\rho\frac{\partial u}{\partial t}+\rho u\frac{\partial u}{\partial x}+\rho v\frac{\partial u}{\partial y}+\rho w\frac{\partial u}{\partial z}=-\frac{\partial p}{\partial x}+\frac{\partial \sigma_{xx}}{\partial x}+\frac{\partial \sigma_{xy}}{\partial y}+\frac{\partial \sigma_{xz}}{\partial z} \qquad (2)$$

y-direction

$$\rho\frac{\partial v}{\partial t}+\rho u\frac{\partial v}{\partial x}+\rho v\frac{\partial v}{\partial y}+\rho w\frac{\partial v}{\partial z}=-\frac{\partial p}{\partial y}+\frac{\partial \sigma_{xy}}{\partial x}+\frac{\partial \sigma_{yy}}{\partial y}+\frac{\partial \sigma_{yz}}{\partial z} \qquad (3)$$

z-direction

$$\rho\frac{\partial w}{\partial t}+\rho u\frac{\partial w}{\partial x}+\rho v\frac{\partial w}{\partial y}+\rho w\frac{\partial w}{\partial z}=-\frac{\partial p}{\partial z}+\frac{\partial \sigma_{xz}}{\partial x}+\frac{\partial \sigma_{yz}}{\partial y}+\frac{\partial \sigma_{zz}}{\partial z} \qquad (4)$$

Conservation of Energy

$$\frac{\partial E_t}{\partial t}+\frac{\partial(E_t+p)u}{\partial x}+\frac{\partial(E_t+p)v}{\partial y}+\frac{\partial(E_t+p)w}{\partial z}=\frac{\partial}{\partial x}(u\sigma_{xx}+v\sigma_{xy}+w\sigma_{xz}-q_x)$$

$$+\frac{\partial}{\partial y}(u\sigma_{xy}+v\sigma_{yy}+w\sigma_{yz}-q_y)+\frac{\partial}{\partial z}(u\sigma_{zx}+v\sigma_{zy}+w\sigma_{zz}-q_z) \qquad (5)$$

where ρ is density, u is horizontal velocity, v is lateral velocity, w is vertical velocity, p is pressure, E_t is total energy, q_x, q_y, and q_z are the gradient flux terms for heat conduction, and $\sigma_{xx}, \sigma_{xy}, \sigma_{xz}$, etc., are the normal and tangential viscous stress terms,

$$\sigma_{xx}=\frac{2}{3R_e}\left(2\frac{\partial u}{\partial x}-\frac{\partial v}{\partial y}-\frac{\partial w}{\partial z}\right), \sigma_{yy}=\frac{2}{3R_e}\left(2\frac{\partial v}{\partial y}-\frac{\partial u}{\partial x}-\frac{\partial w}{\partial z}\right), \sigma_{zz}=\frac{2}{3R_e}\left(2\frac{\partial w}{\partial z}-\frac{\partial u}{\partial x}-\frac{\partial v}{\partial y}\right) \qquad (6)$$

$$\sigma_{xy}=\frac{1}{R_e}\left(\frac{\partial v}{\partial x}+\frac{\partial u}{\partial y}\right), \quad \sigma_{xz}=\frac{1}{R_e}\left(\frac{\partial u}{\partial z}+\frac{\partial w}{\partial x}\right), \quad \sigma_{yz}=\frac{1}{R_e}\left(\frac{\partial v}{\partial z}+\frac{\partial w}{\partial y}\right) \qquad (7)$$

where $R_e=\rho_\infty U_\infty L/\mu_\infty$. For compressible flow, pressure and temperature are obtained from the equation of state

$$p=(\gamma-1)\rho e \qquad (9)$$

$$T=\frac{\gamma M_\infty^2 p}{\rho} \qquad (10)$$

where e is internal energy, $M_{inf}=V_\infty/\sqrt{\gamma R T_\infty}$ is the free stream Mach number, and γ is the specific heat ratio.

The Euler form of the governing equations is easily obtained by dropping the second order viscous terms [3]. In this instance, the tangential and normal velocity components at solid boundaries must be calculated; this is conveniently handled using simple cosine relations [7].

For incompressible flow, the energy equation reduces to the equation for the scalar transport of temperature. The pressure is obtained from solution of the "discrete" momentum equations and a simple Poisson equation based on the SIMPLE algorithm developed by Patankar [8]. A potential function, which is solved from the Poisson equation, is used to correct the velocity components calculated in the previous time step.

THE FINITE ELEMENT METHOD

Bilinear isoparametric quadrilateral elements are used to discretize two-dimensional problem domains and trilinear hexahedral elements for three-dimensions. The standard weak formulation of the Galerkin weighted residual technique is employed to cast Eqs. (1-5) into their integral form:

Conservation of Mass

$$\int_\Omega\left(\frac{\partial\rho}{\partial t}+\frac{\partial\rho u}{\partial x}+\frac{\partial\rho v}{\partial y}+\frac{\partial\rho w}{\partial z}\right)W_i\,d\Omega=0 \qquad (11)$$

Conservation of Momentum

x-direction

$$\int_{\Omega}\left(\rho\frac{\partial u}{\partial t}+\rho u\frac{\partial u}{\partial x}+\rho v\frac{\partial u}{\partial y}+\rho w\frac{\partial u}{\partial z}+\frac{\partial p}{\partial x}-\frac{\partial\sigma_{xx}}{\partial x}-\frac{\partial\sigma_{xy}}{\partial y}-\frac{\partial\sigma_{xz}}{\partial z}\right)W_i\,d\Omega=0 \tag{12}$$

y-direction

$$\int_{\Omega}\left(\rho\frac{\partial v}{\partial t}+\rho u\frac{\partial v}{\partial x}+\rho v\frac{\partial v}{\partial y}+\rho w\frac{\partial v}{\partial z}+\frac{\partial p}{\partial y}-\frac{\partial\sigma_{xy}}{\partial x}-\frac{\partial\sigma_{yy}}{\partial y}-\frac{\partial\sigma_{yz}}{\partial z}\right)W_i\,d\Omega=0 \tag{13}$$

z-direction

$$\int_{\Omega}\left(\rho\frac{\partial w}{\partial t}+\rho u\frac{\partial w}{\partial x}+\rho v\frac{\partial w}{\partial y}+\rho w\frac{\partial w}{\partial z}+\frac{\partial p}{\partial z}-\frac{\partial\sigma_{xz}}{\partial x}-\frac{\partial\sigma_{yz}}{\partial y}-\frac{\partial\sigma_{zz}}{\partial z}\right)W_i\,d\Omega=0 \tag{14}$$

Conservation of Energy

$$\int_{\Omega}\Big(\frac{\partial E_t}{\partial t}+\frac{\partial(E_t+p)u}{\partial x}+\frac{\partial(E_t+p)v}{\partial y}+\frac{\partial(E_t+p)w}{\partial z}-\frac{\partial}{\partial x}(u\sigma_{xx}+v\sigma_{xy}+w\sigma_{xz}-q_x)$$

$$-\frac{\partial}{\partial y}(u\sigma_{yx}+v\sigma_{yy}+w\sigma_{yz}-q_y)-\frac{\partial}{\partial z}(u\sigma_{zx}+v\sigma_{zy}+w\sigma_{zz}-q_z)\Big)W_i\,d\Omega=0 \tag{15}$$

where Ω denotes the computational domain and W_i is the weighting function. The ρ, u, v, and E_t variables are represented by the trial approximations

$$\left.\begin{aligned}
\rho(x,y,z,t)&=\sum N_i(x,y,z)\hat{\rho}_i(t)\\
u(x,y,z,t)&=\sum N_i(x,y,z)\hat{u}_i(t)\\
v(x,y,z,t)&=\sum N_i(x,y,z)\hat{v}_i(t)\\
w(x,y,z,t)&=\sum N_i(x,y,z)\hat{w}_i(t)\\
E_t(x,y,z,t)&=\sum N_i(x,y,z)\hat{E}_{t_i}(t)\\
T(x,y,z,t)&=\sum N_i(x,y,z)\hat{T}_i(t)\\
p(x,y,z,t)&=\sum N_i(x,y,z)\hat{p}_i(t)
\end{aligned}\right\} \tag{16}$$

where N_i is the linear basis function; in this instance, $W_i = N_i$. The matrix equivalent formulations of Eqs. (11-15) can be expressed as

$$M\dot{\underline{\rho}}+\bar{u}C^T\underline{\rho}+\underline{\rho}C^T\bar{u}=0 \tag{17}$$

$$M\dot{\underline{u}}+K\underline{u}+A(\bar{u})\underline{u}+C^x p=F_x \tag{18}$$

$$M\dot{\underline{v}}+K\underline{v}+A(\bar{u})\underline{v}+C^y p=F_y \tag{19}$$

$$M\dot{\underline{w}}+K\underline{w}+A(\bar{u})\underline{w}+C^z p=F_z \tag{20}$$

$$M\dot{\underline{E}}_t + K\underline{E}_t + A(\bar{u})\underline{E}_t = F_E \tag{21}$$

where the $\cdot$ refers to time differentiation, _ denotes column vector, and $\bar{u}$ is the velocity vector. The matrix coefficients are defined (using integration by parts for the second order viscous terms) as

$$M = m_{i,j} = \int_\Omega N_i N_j \, d\Omega \tag{22}$$

$$K = k_{i,j} = \int_\Omega \left(\frac{\partial N_i}{\partial x}\frac{\partial N_j}{\partial x} + \frac{\partial N_i}{\partial y}\frac{\partial N_j}{\partial y} + \frac{\partial N_i}{\partial z}\frac{\partial N_j}{\partial z} \right) d\Omega \tag{23}$$

$$A(\bar{u}) = a_{i,j} = \int_\Omega \left(u_k N_k N_i \frac{\partial N_j}{\partial x} + v_k N_k N_i \frac{\partial N_j}{\partial y} + w_k N_k N_i \frac{\partial N_j}{\partial z} \right) d\Omega \tag{24}$$

$$C^x = c^x_{i,j} = \int_\Omega N_i \frac{\partial N_j}{\partial x} \, d\Omega \tag{25}$$

$$C^y = c^y_{i,j} = \int_\Omega N_i \frac{\partial N_j}{\partial y} \, d\Omega \tag{26}$$

$$C^z = c^z_{i,j} = \int_\Omega N_i \frac{\partial N_j}{\partial z} \, d\Omega \tag{27}$$

$$C^T = \begin{pmatrix} C^x \\ C^y \\ C^z \end{pmatrix} \tag{28}$$

$$F_u = \int_{\partial\Omega} N_i \left(n_x \frac{\partial u}{\partial x} + n_y \frac{\partial u}{\partial y} + n_z \frac{\partial u}{\partial z} \right) dS_u \tag{29}$$

$$F_v = \int_{\partial\Omega} N_i \left(n_x \frac{\partial v}{\partial x} + n_y \frac{\partial v}{\partial y} + n_z \frac{\partial v}{\partial z} \right) dS_v \tag{30}$$

$$F_w = \int_{\partial\Omega} N_i \left(n_x \frac{\partial w}{\partial x} + n_y \frac{\partial w}{\partial y} + n_z \frac{\partial w}{\partial z} \right) dS_w \tag{31}$$

$$F_T = \int_{\partial\Omega} N_i \left(n_x \frac{\partial T}{\partial x} + n_y \frac{\partial T}{\partial y} + n_z \frac{\partial T}{\partial z} \right) dS_E \tag{32}$$

where the i, j, and k subscripts denote summation over the local nodes within an element and dS_u, dS_v, dS_w. dS_E represent the boundary segments over which u, v, w, and E_t are specified.

Based on the procedure discussed in Pepper and Humphrey [3], the following modifications are employed:

Mass Lumping

Equation (22) is modified to the form

$$M = \delta_{i,j}\int_{\Omega} N_i \, d\Omega \tag{33}$$

where $\delta_{i,j}$ is the Kronecker delta. This operation produces a diagonal matrix in lieu of the sparse global matrix consisting of n x n nodes, thus eliminating the need for implicit matrix solution - hence $[M]^{-1} = 1/M_i$.

Reduced Integration

The value of an integral over an element is obtained at the element centroid using one Gauss point. The shape function becomes

$$N_i = \frac{1}{4} \quad (2-D) \tag{34a}$$

$$N_i = \frac{1}{8} \quad (3-D) \tag{34b}$$

The advection velocities are evaluated at the centroid of an element and multiplied by the average gradient over the element, i.e.,

$$a^x_{i,j} = \bar{u}\int_{\Omega} N_i \frac{\partial N_j}{\partial x} d\Omega = \bar{u} c^x_{i,j} \tag{35}$$

$$a^y_{i,j} = \bar{v}\int_{\Omega} N_i \frac{\partial N_j}{\partial y} d\Omega = \bar{v} c^y_{i,j} \tag{36}$$

$$a^z_{i,j} = \bar{w}\int_{\Omega} N_i \frac{\partial N_j}{\partial z} d\Omega = \bar{w} c^z_{i,j} \tag{37}$$

where

$$A = a^x_{i,j} + a^y_{i,j} + a^z_{i,j}$$

The average velocities are obtained as

$$\bar{u} = \frac{1}{4}\sum_{i=1}^{4} u_i, \quad \bar{v} = \frac{1}{4}\sum_{i=1}^{4} v_i \quad (2-D) \tag{38a}$$

$$\bar{u} = \frac{1}{8}\sum_{i=1}^{8} u_i, \quad \bar{v} = \frac{1}{8}\sum_{i=1}^{8} v_i, \quad \bar{w} = \frac{1}{8}\sum_{i=1}^{8} w_i \quad (3-D) \tag{38b}$$

The gradient terms are simple 4x4 matrices in 2-D and 8x8 matrices in 3-D. For example, $c^x_{i,j}$ is defined for the 2-D quadrilateral as

$$c^x_{i,j} = \frac{1}{8}\begin{pmatrix} a & b & -a & -b \\ a & b & -a & -b \\ a & b & -a & -b \\ a & b & -a & -b \end{pmatrix} \tag{39}$$

where $a = y_2 - y_4$ and $b = y_3 - y_1$.

The diffusion terms are evaluated in 2-D as

$$k^x_{i,j} = \int_\Omega \frac{\partial N_i}{\partial x}\frac{\partial N_j}{\partial x} d\Omega = \frac{16}{\Omega_e} c^x_{i,j} c^x_{j,i} \tag{40a}$$

$$k^y_{i,j} = \int_\Omega \frac{\partial N_i}{\partial y}\frac{\partial N_j}{\partial y} d\Omega = \frac{16}{\Omega_e} c^y_{i,j} c^y_{j,i} \tag{40b}$$

and in 3-D

$$k^x_{i,j} = \int_\Omega \frac{\partial N_i}{\partial x}\frac{\partial N_j}{\partial x} d\Omega = \frac{64}{\Omega_e} c^x_{i,j} c^x_{j,i} \tag{41a}$$

$$k^y_{i,j} = \int_\Omega \frac{\partial N_i}{\partial y}\frac{\partial N_j}{\partial y} d\Omega = \frac{64}{\Omega_e} c^y_{i,j} c^y_{j,i} \tag{41b}$$

$$k^z_{i,j} = \int_\Omega \frac{\partial N_i}{\partial z}\frac{\partial N_j}{\partial z} d\Omega = \frac{64}{\Omega_e} c^z_{i,j} c^z_{j,i} \tag{41c}$$

where

$$K = k^x_{i,j} + k^y_{i,j} + k^z_{i,j}$$

The gradient terms have been incorporated to take advantage of the $c^x_{i,j}$, $c^y_{i,j}$, and $c^z_{i,j}$ formulations.

Petrov-Galerkin

The weighting functions associated with the Petrov-Galerkin formulation are obtained by perturbing the shape functions such that

$$W_i = N_i + \frac{\alpha \rho h_e}{2\bar{u}}\left(u\frac{\partial N_i}{\partial x} + v\frac{\partial N_i}{\partial y} + w\frac{\partial N_i}{\partial z} \right) \tag{42}$$

where h_e is the element size [3] and α is defined as

$$\alpha = \coth \beta_i - \frac{1}{\beta_i} \qquad i = 1,2 \tag{43}$$

with $\beta_1 = |\bar{u}| h_e R_e / 2$, which is the cell Reynolds number; for the energy equation, $\beta_2 = P_r \beta_1$. For the Euler equations, R_e nor P_r appear in the expressions for β. This form of anisotropic balancing diffusion acts in the direction of the propagation of the perturbation (velocity field). The precise amount of artificial diffusion (for eliminating the shortest waves) and direction in which it must be added for optimizing accuracy are calculated for each element.

Time Integration

An explicit forward-in-time Euler scheme is used to advance the discretized equations in time. For example, u is solved from the relation

$$\underline{u}^{n+1} = \underline{u}^n + \Delta t M^{-1}(F_u - K\underline{u}^n - A(\bar{u})\underline{u}^n - C^x p) \tag{44}$$

Application of this scheme to the continuity, v- and w-momentum and energy equations follows similarly. Since the discretized equations are solved explicitly, a stability constraint on the time step must be imposed. The Courant and diffusive limits associated with a forward Euler scheme are calculated over each element, and the time step adjusted to the minimum value within the computational domain.

EXAMPLES

A set of six example problems are solved by the FEM to demonstrate the versatility of the method. Most of the examples were initially run on an IBM PC AT (enhanced with a 33MHz accelerator board [9]) and an Everex 25MHz 386 machine; the first four problems required nodal meshes using less than 2000 nodes. Although problems requiring upwards of 5000 nodes have been successfully run on PCs [2], such jobs may require many hours of calculational effort.

The example problems were also run on an Alliant VFX/40 mini-supercomputer. A Silicon Graphics Personal IRIS workstation served as a graphical front end to the Alliant. This combination of hardware allowed near real time graphical displays of the transient solutions as they converged to steady state. Convergence was assumed to be reached when differences between old and new values (all variables) equalled 10^{-4}.

Example 1:

The first problem deals with fluid recirculation within a square cavity ($0 \leq x \leq 1; 0 \leq y \leq 1$), as shown in Fig. 1(a,b). The top surface represents a fluid moving horizontally left to right at u=1, v=0 with R_e = 5000; the remaining three walls are no-slip surfaces.

A non-uniform rectangular mesh of 51x51 nodes is used to model the fluid motion. Ghia, et al [10] and Gresho, et al [4] also analyzed flow in a cavity for a large range of Reynolds numbers. Figure 1(b) shows the streamline distributions, and agrees with their published results. A primary vortex develops within the center region of the cavity; secondary vorticies occur at the two bottom corners and near the upper left corner.

Example 2:

In the second problem, natural convection within a rectangular enclosure is simulated for $R_a=10^5$ and $P_r=1$. A 20x20 nodal mesh is used with zero initial conditions for u, v, and T (Fig. 2(a)).

At $R_a=10^5$, two distinct cells develop from one large single cell shortly after the calculation is begun. This recirculation pattern is consistent with multicellular development as the Rayleigh number increases. Fig. 2(b,c) shows the streamlines and isotherms for steady state conditions, and agree with results in the literature [11]. At higher Rayleigh numbers, a finer grid is required near the walls to properly account for the boundary layer growth.

Example 3:

The ability of the FEM to model convective cooling of a heated block is demonstrated in the third example problem. Prediction of the recirculation zone behind the block and the thermal plume eminating from the block are examined for $R_e=P_e=2000$. The problem geometry and mesh are shown in Fig. 3(a,b); the mesh consists of 732 nodes (665 2-D elements).

Since the mesh is coarse, spurious results are expected for $R_e=P_e=2000$; at lower values, the mesh is adequate. In this case, the ability of the Petrov-Galerkin scheme to control dispersion errors (oscillations in the solution) is assessed. Figure 4(a,b,c,d) shows velocity vectors and isotherms (with and without Petrov-Galerkin weighting). At high Reynolds numbers, the FEM yields poor velocity distributions without Petrov-Galerkin weighting; the temperature distribution shows appreciable dispersion - such solutions generally indicate inadequate mesh refinement. Use of Petrov-Galerkin reduces the oscillations and provides a good solution with a less than optimal mesh.

Example 4:

In the fourth problem, a planar 15° ramp sits on the lower wall of a two-dimensional duct. The inlet Mach number is 2.28. Based on 1-D ideal analysis (weak solution for attached shock waves), an oblique shock develops at an angle of 40° relative to the freestream. Figure 5(a,b,c) shows the flow schematic and problem geometry. The shock reflects off the top wall at an angle of 40.5°. In region 2, $M_2 = 1.69$ and p_2/p_1 (static) = 2.34. In region 3, $M_3 = 1.15$ and $p_3/p_1 = 4.91$.

Figure 6(a,b) shows density contours and velocity vectors for the viscous solution. A time step of $\Delta t = 10^{-4}$ is initially required. The boundary layer development is apparent; at the upper wall, the reflected shock interacts with the boundary layer and creates a small recirculation zone. For this viscous solution, $R_e = 10^4$; turbulence has not been included in the model as yet. Although the shock is smeared, the shock angle and downstream Mach numbers agree with the 1-D analysis. A more optimized grid refinement (more uniformity and nodes) is required to reduce spreading of the shock. Using 2x2 Gauss points versus one Gauss point increases accuracy, but also increases the compute time.

Example 5:

The fifth problem is concerned with supersonic flow over a projectile within a two-dimensional chamber. This problem is similar to the Scramaccelerator work conducted by Pratt, et al [12] and Humphrey [13]; the projectile is designed so that the reflected shock off the tube wall initiates combustion (oblique detonation wave), thereby producing an increase in pressure behind the shocks and a net thrust forward. In this example, the upper wall moves at u=1 (non-dimensional). Approach flows for Mach 2.68 (nose angle 20°) and Mach 5 (nose angle 25°) are simulated with the initial flow field assumed to be uniform (i.e., equal to the inlet conditions) throughout the domain. The problem geometry and mesh are shown in Fig. 7.

Figure 8(a,b,c,d) shows pressure and Mach contours for Mach 2.68 and Mach 5 inlet conditions, respectively. An oblique bow shock forms over the nose and reflects off the top wall. High pressure gradients develop in the region between the wall and the projectile. Figure 9(a,b) shows an expanded view of the velocity vectors in front of the projectile. In Fig. 9(a), boundary layer separation occurs on the upper part of the nose as a result of the interaction with the reflected shock; in this case, the inlet flow speed is not high enough and the shock inhibits forward motion. At Mach 5 and a 25° leading edge (Fig. 9b), the oblique shock reflects off the upper wall and strikes the projectile just behind the shoulder (near optimal performance). A weak shock train is created in the thin region between the upper wall and projectile body; boundary layer separation occurs along the top of the projectile body. The predicted oblique shock angles and downstream flow conditions near the front shoulder of the projectile agree quantitatively with 2-D results obtained by Pratt, et al [12] using a modified SALE algorithm [14].

Example 6:

For the last problem, 3-D flow is calculated around a set of heated obstacles which are convectively cooled by cold air. The physical domain and mesh are shown in Fig. 10(a,b). The mesh consists of 2868 hexahedral elements (which easily permits execution on a Personal IRIS workstation); the Reynolds number is $R_e=10^3$ and $P_r=1.0$. This type of problem is commonly encountered in the computer industry where cooling of computer chips is critical.

Figure 11(a,b) gives normal and perspective views of the 3-D velocity vectors within the channel. Recirculation of the flow occurs behind the blocks, and small secondary cells develop in the corners. The pressure and isotherm distributions are shown in Fig. 12(a,b) for the x-y plane near the top of the channel. Distinct thermal plumes eminate from the heated blocks; plume impingement from the left forward block occurs on the small mid-stream block. It is well known that when flow separates at the corners of blocks, horseshoe-like vortices are generated [15]. Further work is underway to examine this phenomena using a 28,000 hexahedral element mesh on the Alliant.

CONCLUSIONS

A finite element method using simple modifications is used to solve 2- and 3-D problems for compressible and incompressible flows with heat transfer. The modified FEM employs equal order basis functions for all unknown variables, mass lumping, reduced quadrature, and Petrov-Galerkin weighting; transient solutions are solved using an explicit Euler scheme. Formulation of the local (and global) matrices are simple, and solution speeds are quick. The technique yields accurate results for a wide variety of flows providing the elements are not too distorted. The method appears attractive for workstation class machines.

ACKNOWLEDGEMENTS

We wish to thank Mr. Andy Singer, Advanced Projects Research, Inc., for his help in generating many of the graphical displays, and Dr. Juan Heinrich and Mr. Frank Brueckner, University of Arizona, Tucson, Arizona, for their assistance in generating the Scramaccelerator results.

REFERENCES

1. Thompson, J. F., "Numerical Solution of Flow Problems using Body Fitted Coordinate Systems," *Computational Fluid Dynamics*, 1, (W. Kollman, ed.), Hemisphere Pub. Co., Washington, D.C. (1980).

2. Pepper, D. W. and Singer, A. P., "Calculation of Convective Flow on the Personal Computer using a Modified Finite Element Method," to appear in Num. Heat Transfer (1990).

3. Pepper, D. W. and Humphrey, J. W., "A Hybrid Finite Element Method for Compressible Flow," AIAA Paper 90-0399 (1990).

4. Gresho, P. M., Chan, S. T., Lee, R. L., and Upson, C. D., "Modified Finite Element Method for Solving the Time-Dependent Incompressible Navier-Stokes Equations, Part 1: Theory," Int. J. Num. Methods in Fluids, 4, 557-598 (1984).

5. Yu, C. C. and Heinrich, J. C., "Petrov-Galerkin Methods for the Time-Dependent Convective Transport Equation," Int. J. Num. Methods in Eng., 23, 883-901 (1986).

6. Anderson, D. A., Tannehill, J. C., and Pletcher, R. H., *Computational Fluid Mechanics and Heat Transfer*, Hemisphere Pub. Co., Washington, D. C. (1984).

7. Shapiro, R. A., "An Adaptive Finite Element Solution Algorithm for the Euler Equations," MIT Report CFDL-TR-88-7 (1988).

8. Patankar, S. V., *Numerical Heat Transfer and Fluid Flow*, Hemisphere Pub. Co., Washington, D.C. (1980).

9. Definicon Systems, Inc., "PM Series Product Manual," Definicon Systems, Inc., 1100 Business Center Circle #5, Newbury Park, CA 91320 (1989).

10. Ghia, U., Ghia, K., and Shin, C., "High-Re Solutions for Incompressible Flow Using the Navier-Stokes Equations and a Multi-grid Method," J. Comp. Phys., 48, 387-401 (1982).

11. Jones, I. P. and Thompson, C. P. (ed.), "Numerical Solutions for a Comparison Problem on Natural Convection in an Enclosed Cavity," AERE-R 9955, Harwell, England (1980).

12. Pratt, D. T., Humphrey, J. W., and Glenn, D. E., "Morphology of a Standing Oblique Detonation Wave," AIAA Paper 87-1785 (1987).

13. Humphrey, J. W., "Study of an Oblique Detonation Wave Ramaccelerator Driven Hypersonic Test Facility," APRI Final Report, NASA Langley Contract NAS1-18802 (1989).

14. Amsden, A. A., Ruppel, H. M., and Hirt, C. W., "SALE: A Simplified Arbitrary Lagrangian-Eulerian Computer Program for Fluid Flow at All Speeds," Los Alamos Nat. Lab. Report LA-8095, UC-32 (1980).

15. Hunt, J. C., Abell, C. J., Peterka, J. A., and Woo, H., "Kinematical Studies of the Flows around Free or Surface Mounted Obstacles; Applying Topology to Flow Visualization," J. Fluid Mech., 86, 1, 179-200 (1978).

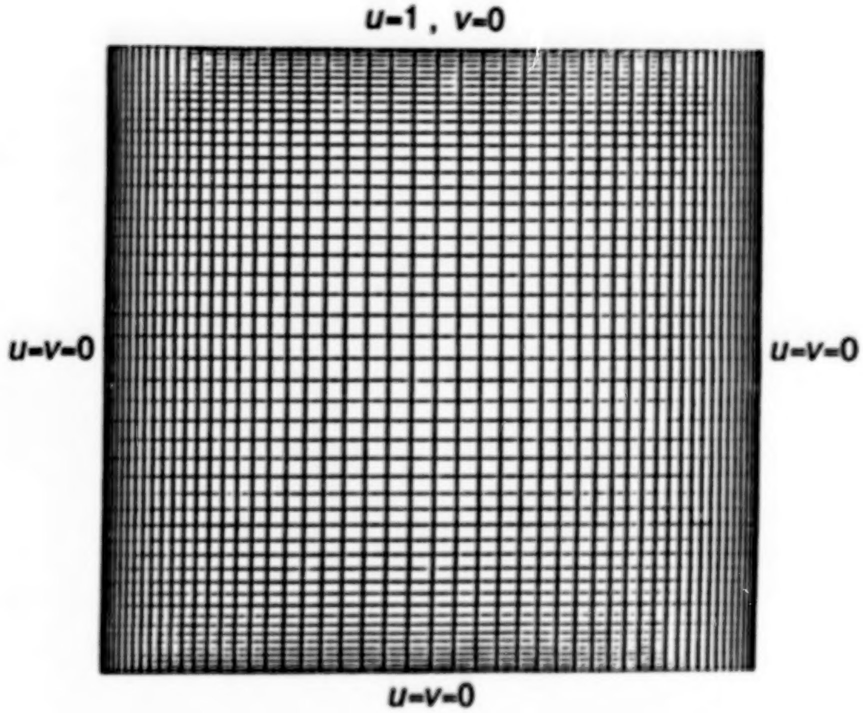

a.) Mesh

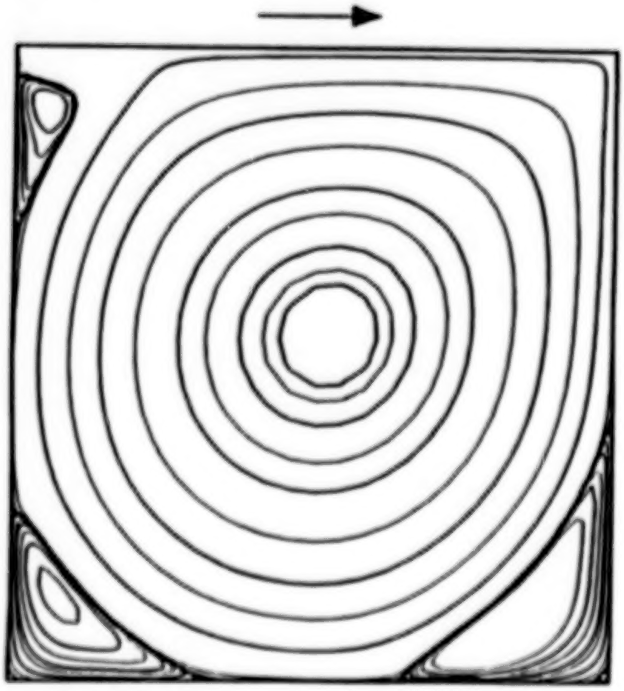

b.) Streamlines

Figure 1. Flow in a Cavity - Re=5000

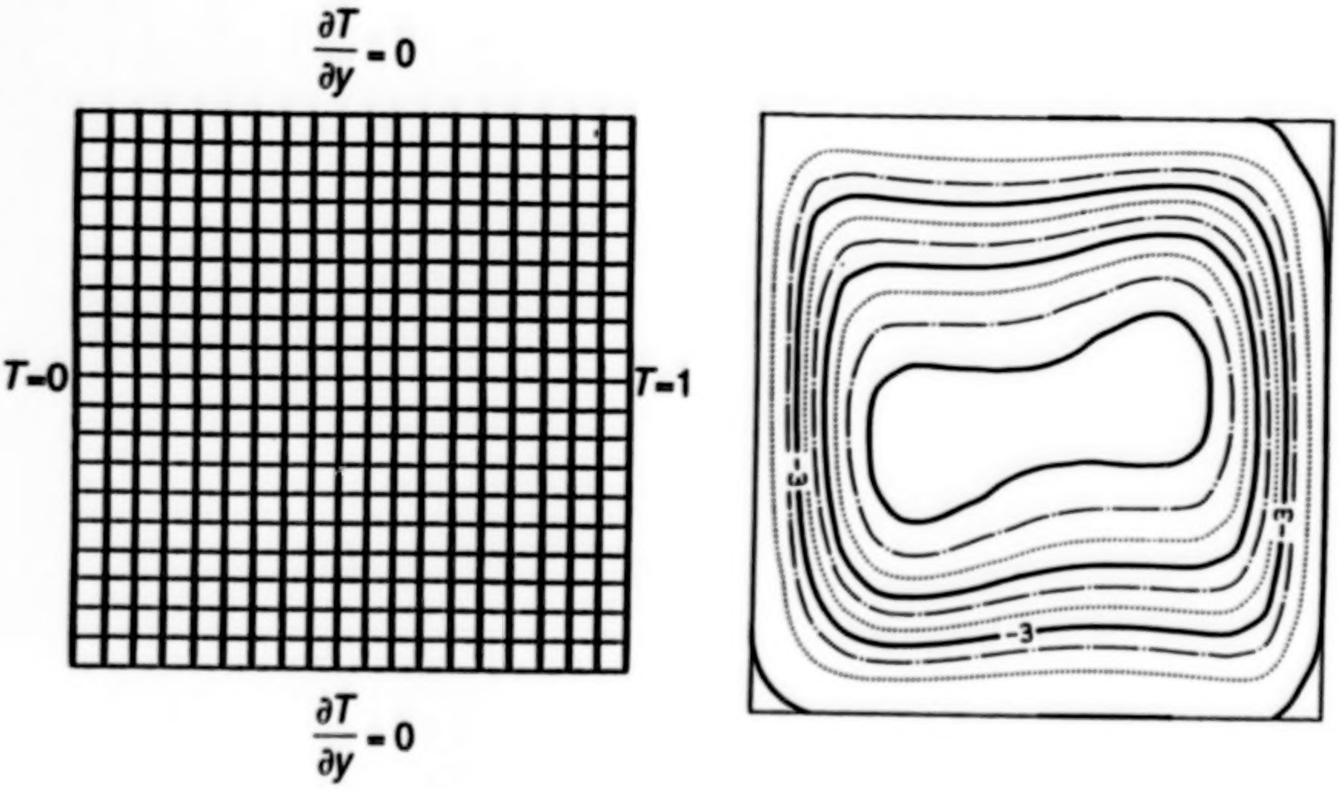

a.) Mesh

b.) Streamlines

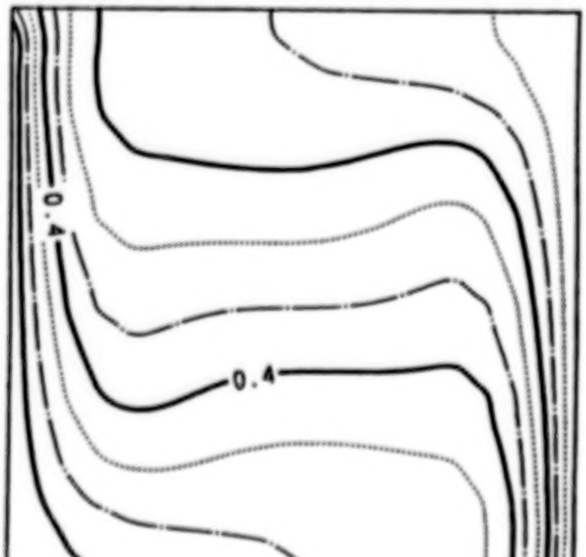

c.) Isotherms

Figure 2. Natural Convection - Ra = 10^5

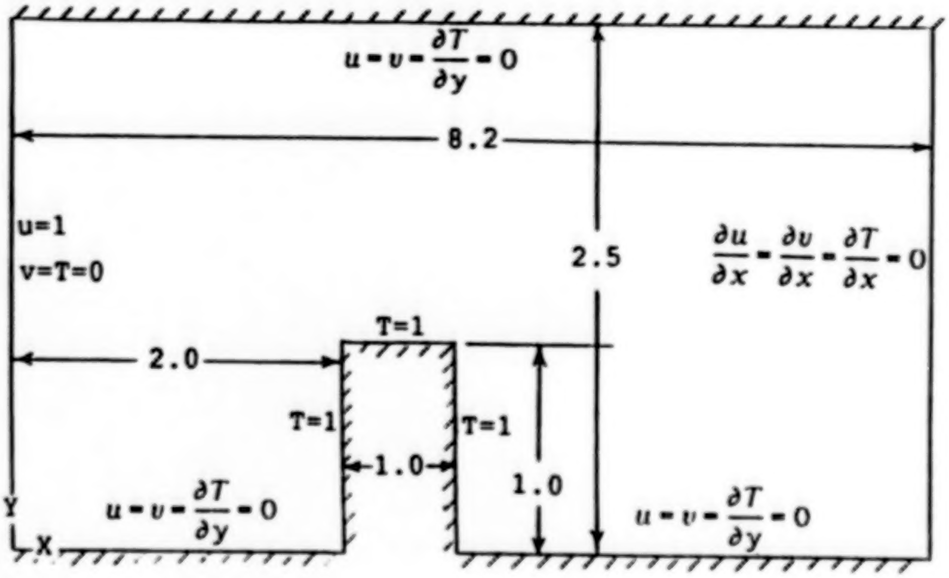
$u = v = \frac{\partial T}{\partial y} = 0$
8.2
u=1
v=T=0
2.5
$\frac{\partial u}{\partial x} = \frac{\partial v}{\partial x} = \frac{\partial T}{\partial x} = 0$
T=1
2.0
T=1
T=1
1.0
1.0
$u = v = \frac{\partial T}{\partial y} = 0$
$u = v = \frac{\partial T}{\partial y} = 0$
Y
X

a.) Boundary Conditions

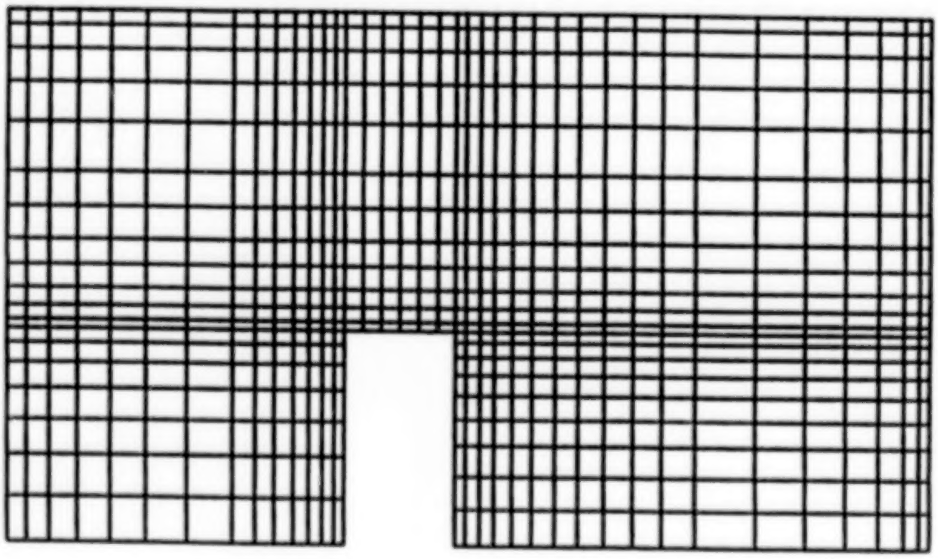

b.) Mesh

Figure 3. Forced Convective Cooling - Re=Pe=2000

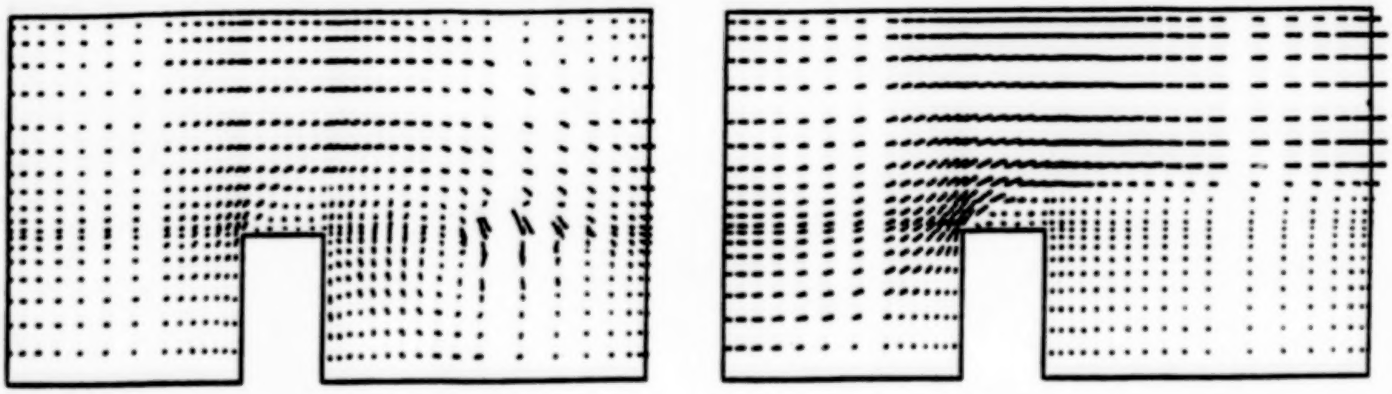

a.) w/o Petrov-Galerkin Weighting

c.) Velocity Vectors
(w/ Petrov-Galerkin Weighting)

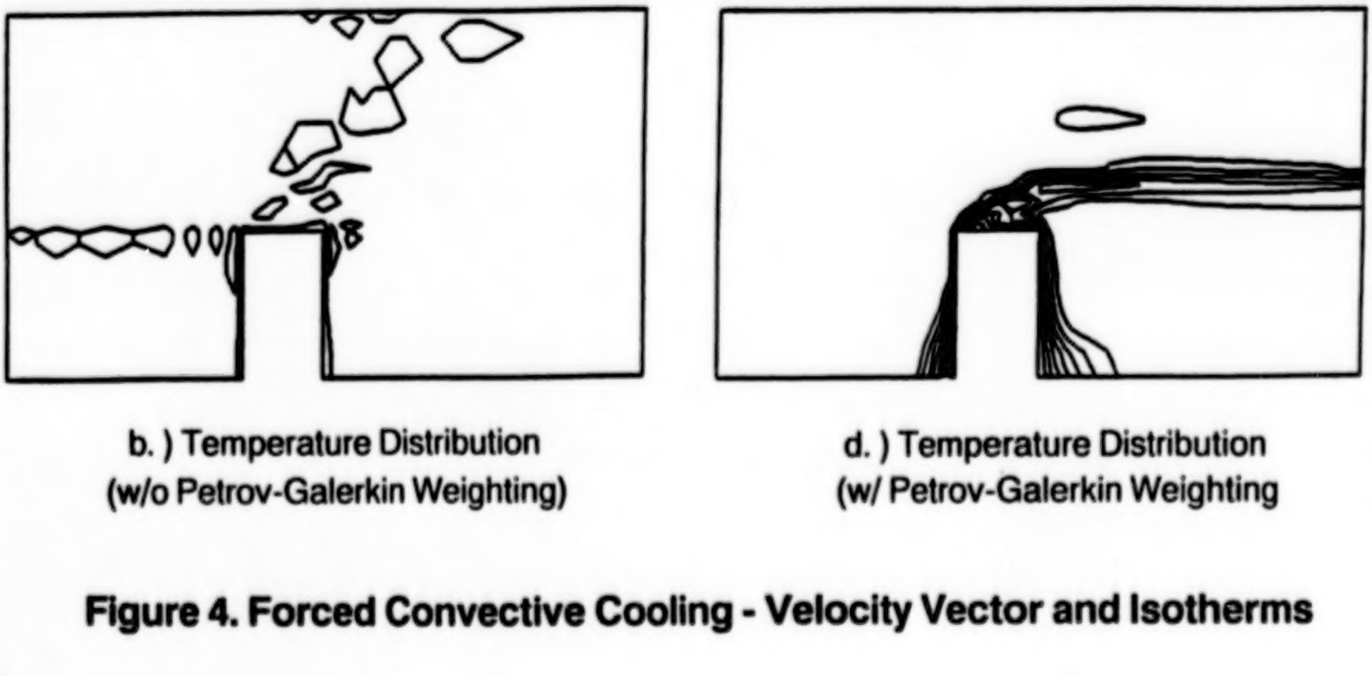

b.) Temperature Distribution
(w/o Petrov-Galerkin Weighting)

d.) Temperature Distribution
(w/ Petrov-Galerkin Weighting

Figure 4. Forced Convective Cooling - Velocity Vector and Isotherms

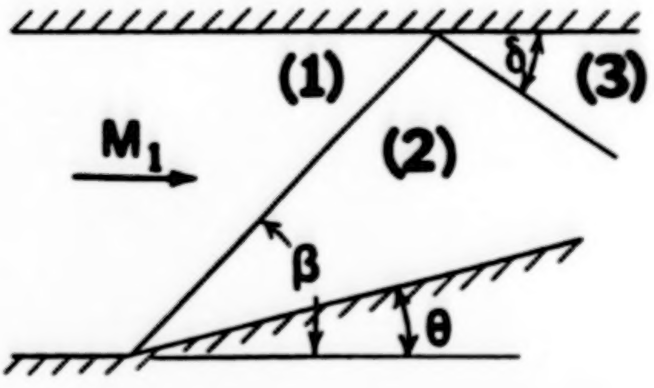

a.) Flow schematic for 15° Ramp
(0 = 15°; δ = 40.5°;β = 40°)

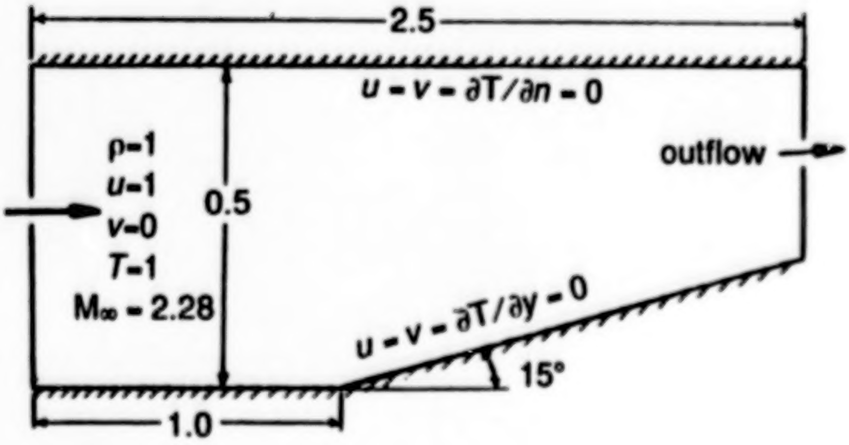

b.) Problem domain

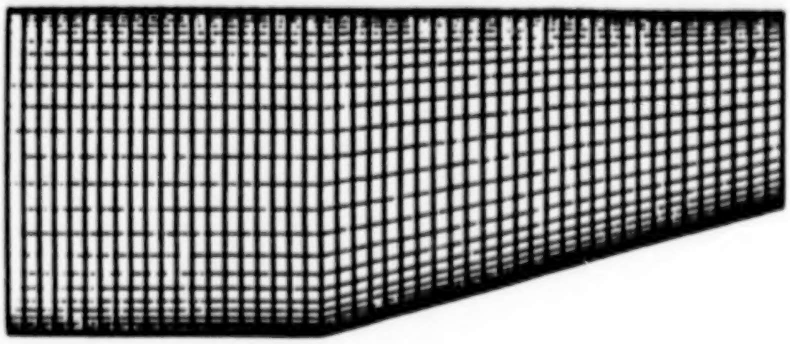

c.) Mesh for viscous solution

Figure 5. Supersonic flow over a 15° Ramp

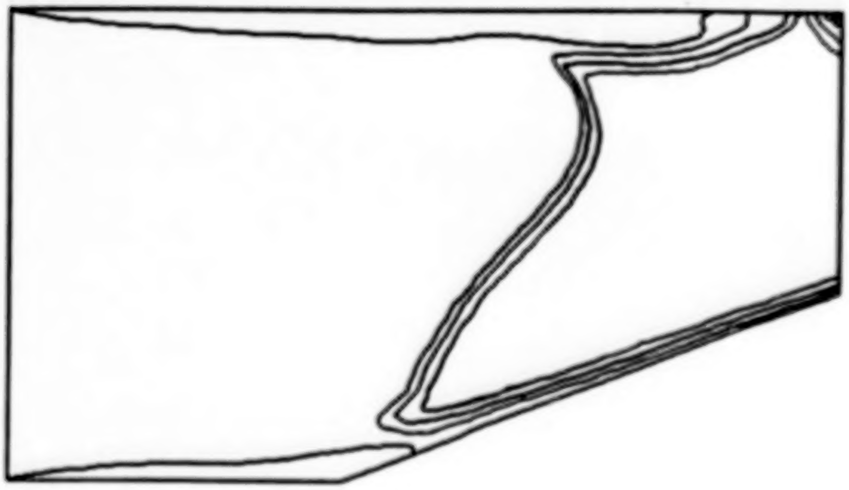

a.) Density contours

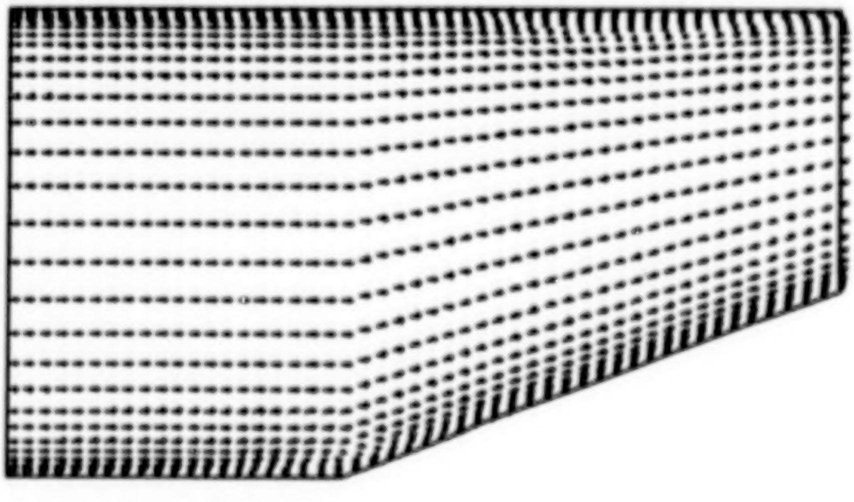

b.) Velocity vectors

Figure 6. Supersonic Flow over a 15° Ramp - Viscous Solution

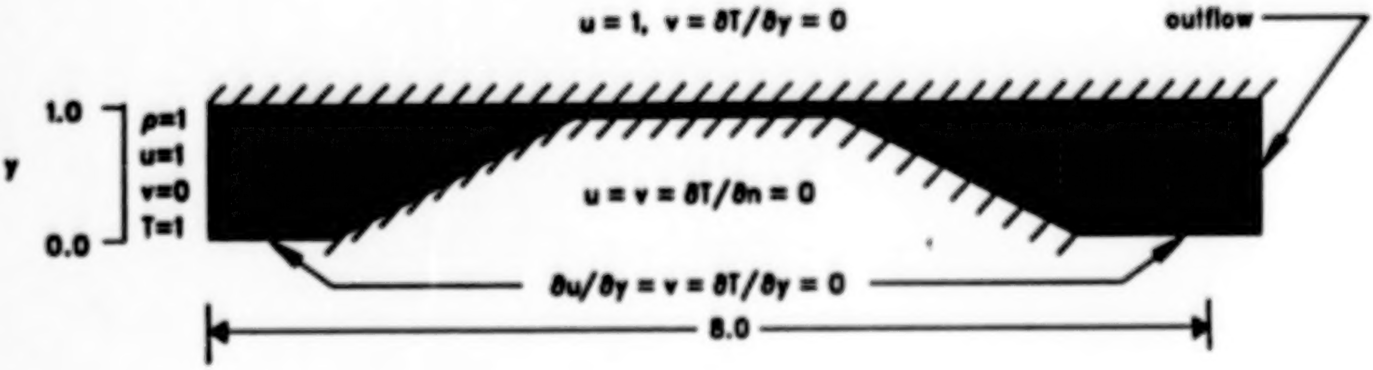
$u = 1,\ v = \partial T/\partial y = 0$
outflow
1.0
y
0.0
$\rho=1$
$u=1$
$v=0$
$T=1$
$u = v = \partial T/\partial n = 0$
$\partial u/\partial y = v = \partial T/\partial y = 0$
8.0

Figure 7. Scramaccelerator Configuration

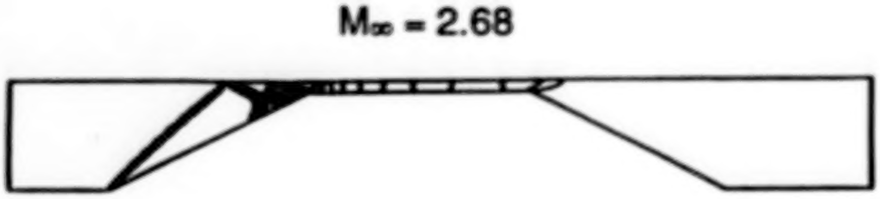

a.) Pressure Contours

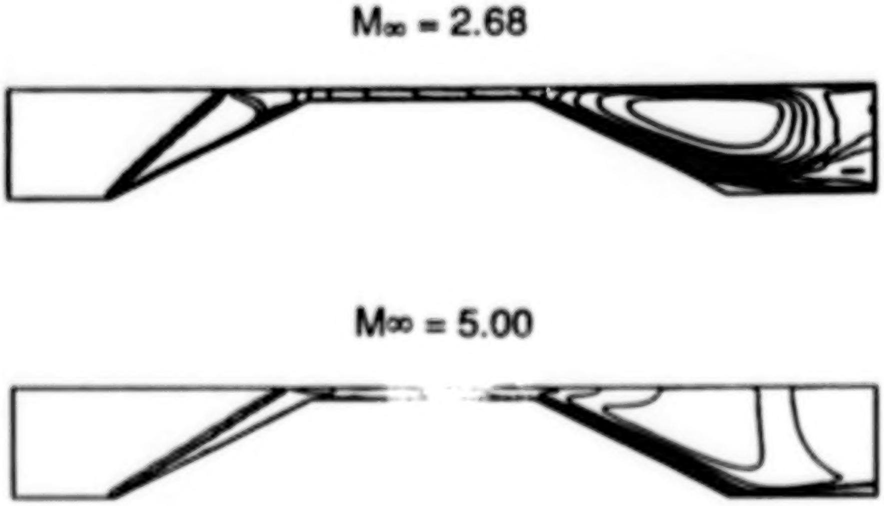

b.) Mach Contours

Figure 8. Scramaccelerator

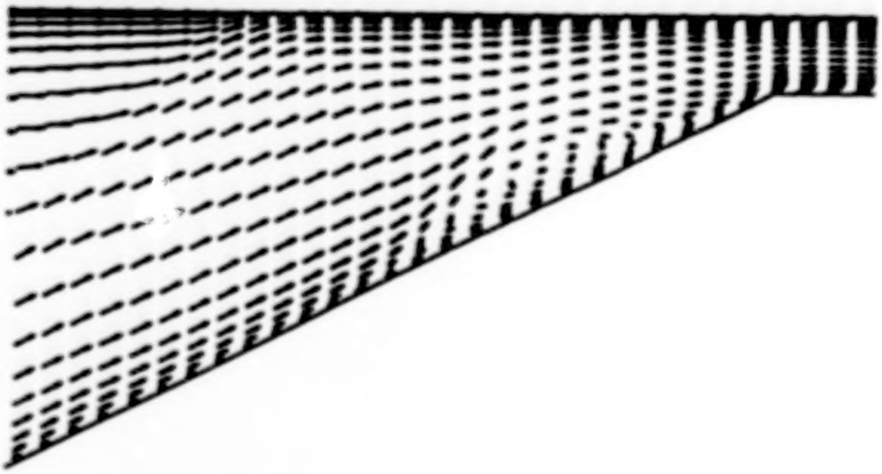

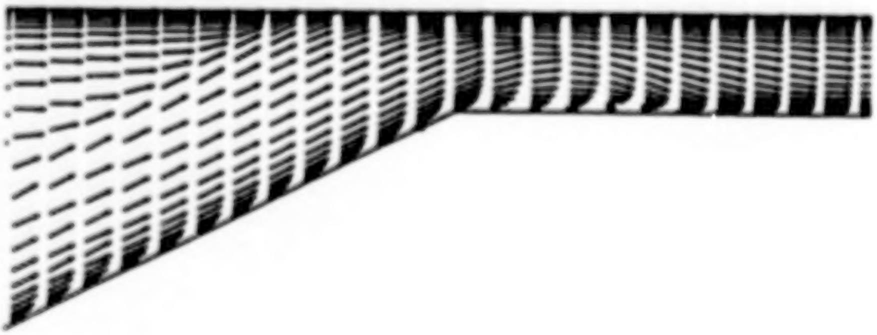

Figure 9. Inlet Velocity Distribution - Scramaccelerator

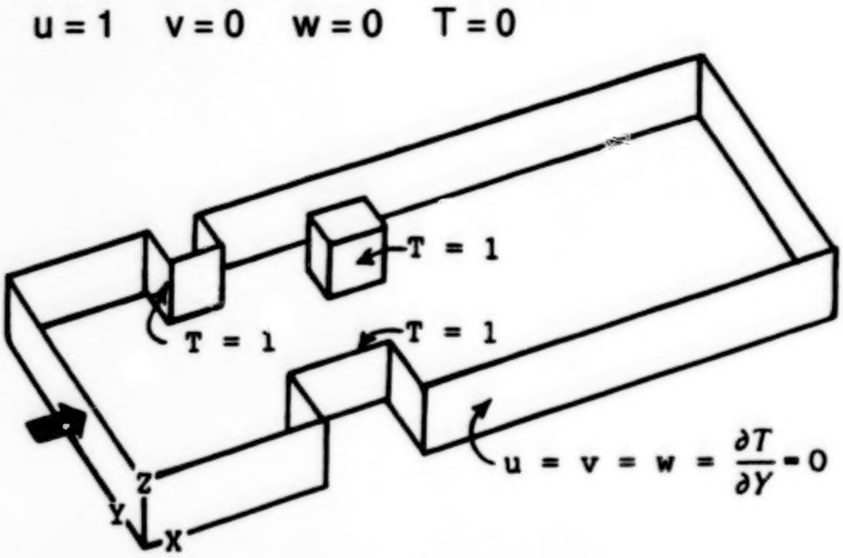

a.) Boundary Conditions

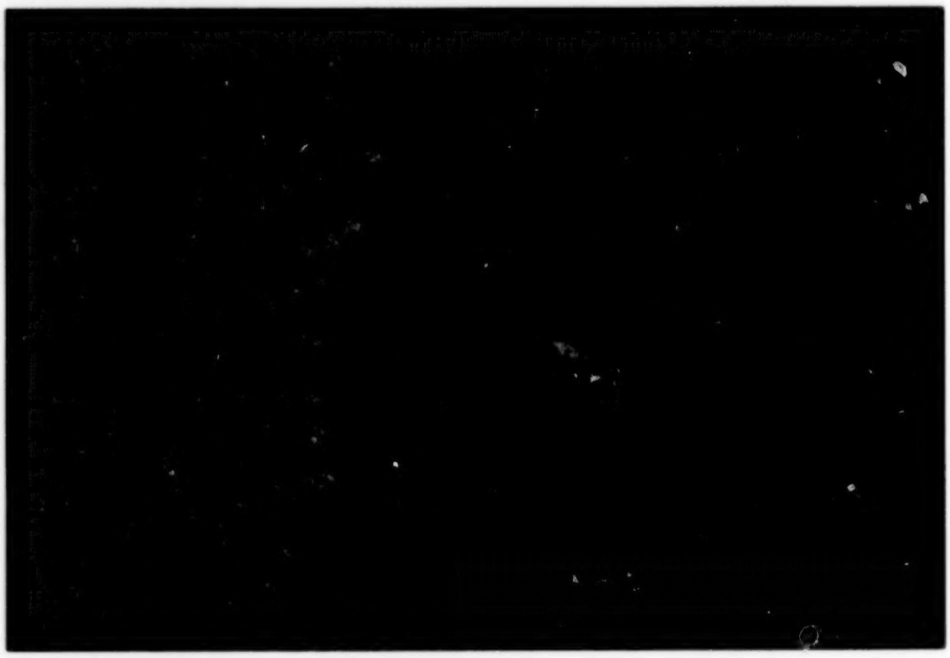

b.) Mesh

Figure 10. Channel with Obstacles - Forced convective Flow

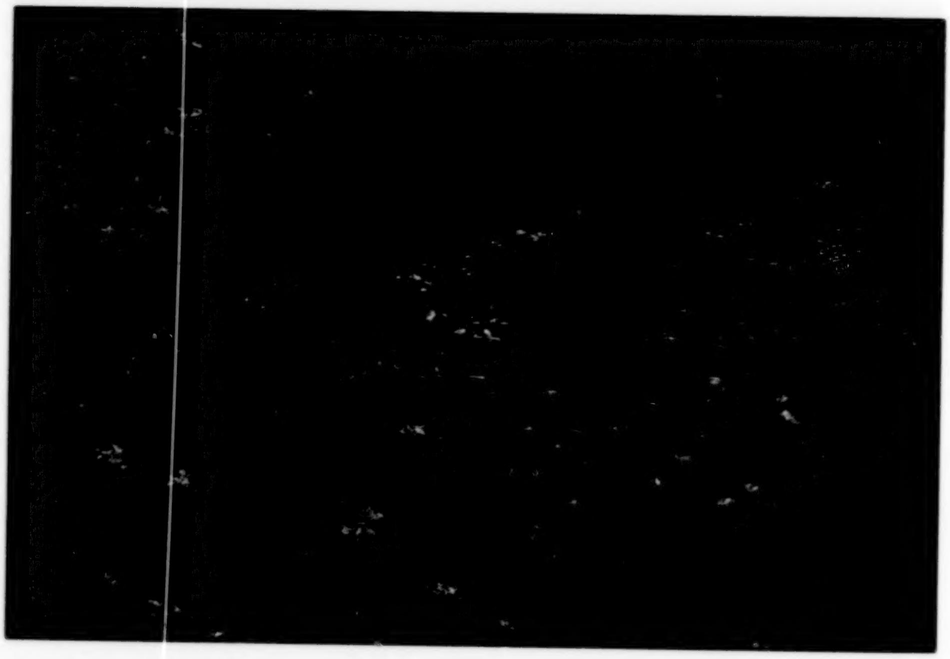

a.) View from Above

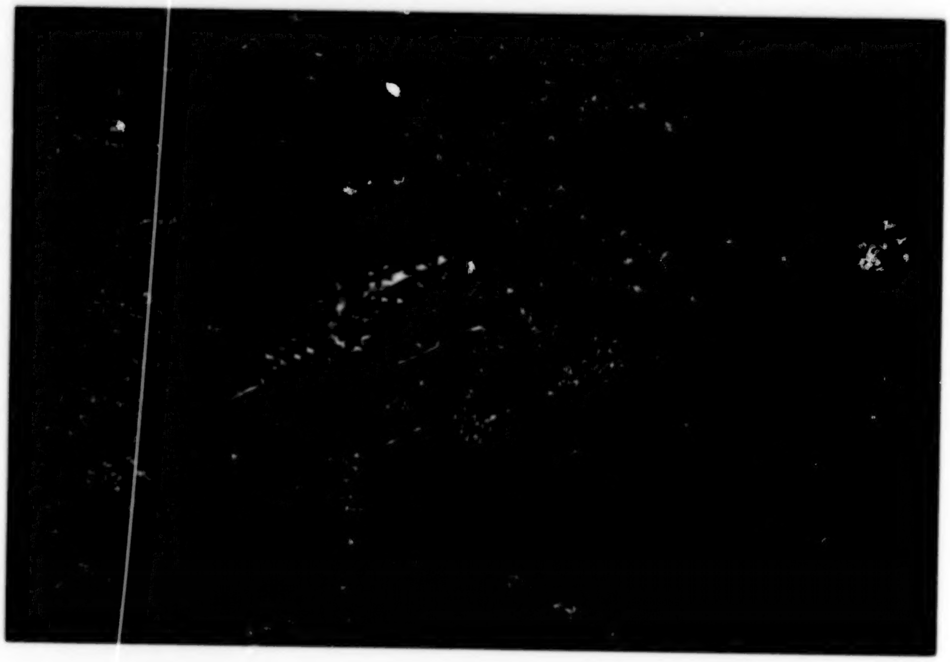

b.) Perspective View

Figure 11. Velocity Distribution

a.) Pressure

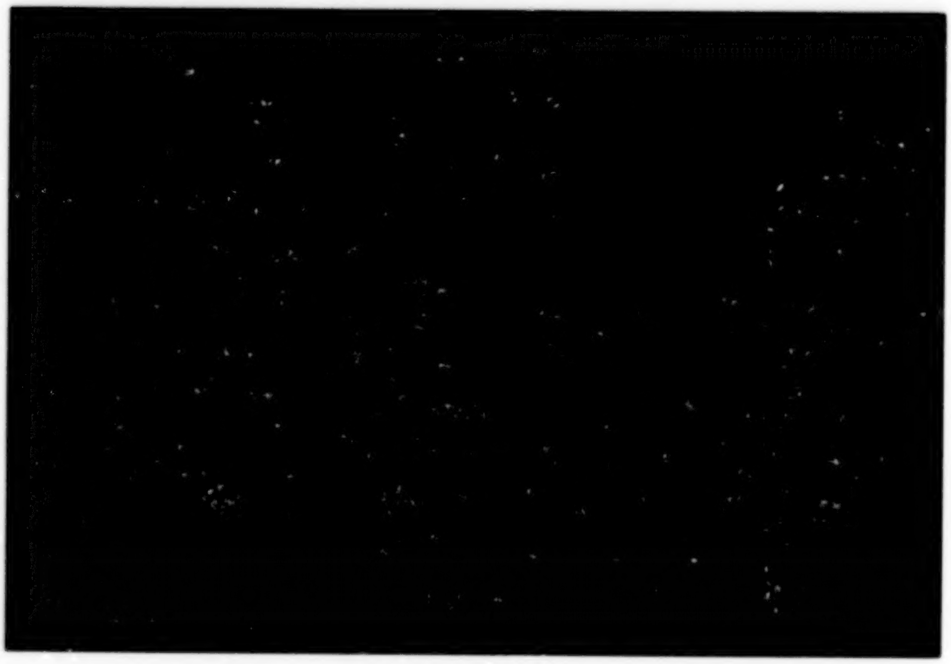

b.) Isotherms

Figure 12. distribution in X-Y Plane

THE PDF METHOD FOR TURBULENT COMBUSTION

S.B. Pope
Cornell University
Ithaca, NY 14853

ABSTRACT

PDF methods provide a means of calculating the properties of turbulent reacting flows. They have been successfully applied to many turbulent flames, including some with finite-rate kinetic effects. Here the methods are reviewed with an emphasis on computational issues and on their application to turbulent combustion.

1. INTRODUCTION

PDF methods have been applied to a variety of turbulent flows both with, and without, combustion. Generally, single-phase, low-Mach-number flows have been considered, in which radiation is not a major factor. For such flows, the fundamental dependent variables are the velocities $\underline{U}(\underline{x},t)$ and the compositions $\underline{\phi}(\underline{x},t)$ (e.g., the species mass fractions and enthalpy). Different probabilistic approaches to modelling turbulent flows can be categorized according to the statistics of $\underline{U}(\underline{x},t)$ and $\underline{\phi}(\underline{x},t)$ that are considered. For example, in a mean-flow closure $\langle\underline{U}(\underline{x},t)\rangle$ and $\langle\underline{\phi}(\underline{x},t)\rangle$ are the primary dependent variables: in second-order closures the variances $\langle u_i u_j\rangle$, $\langle\phi'_\alpha \phi'_\beta\rangle$ and covariances $\langle u_i \phi'_\alpha\rangle$ are also included. Angled brackets denote means (i.e., mathematical expectations) and $u_i(\underline{x},t) = U_i(\underline{x},t) - \langle U_i(\underline{x},t)\rangle$ and $\phi'_\alpha(\underline{x},t) = \phi_\alpha(\underline{x},t) - \langle\phi_\alpha(\underline{x},t)\rangle$ are the fluctuating components of U_i and ϕ_α, respectively.

In pdf methods, the dependent variable is a probability density function (pdf) or joint pdf of $\underline{U}(\underline{x},t)$, $\underline{\phi}(\underline{x},t)$. The pdf contains information equivalent to all the moments; and hence pdf methods are, in this sense, more comprehensive than moment closures (e.g. second-order closures). The methods that have proved most successful are based on one-point, one-time pdf's, which contain information at each point in the flow separately, but no joint information at two or more distinct points.

In the last 15 years, pdf methods have advanced from being only of theoretical interest to a small group of specialists, to being a practical approach for calculating the properties of turbulent reactive flows. As the review below indicates, in additional to having been applied to idealized flames and simple laboratory flames, the methods have been applied to flames requiring multistep chemical kinetics (e.g. Pope 1981a, Chen & Kollmann 1988a), as well as to computationally difficult flows (e.g. that in the cylinder of a spark-ignition engine, Haworth & El Tahry 1989a,b).

The purpose of this paper is to review the work on pdf methods, with some emphasis on the numerical issues, and on the applications to turbulent combustion.

In the next section the different pdf methods are described, along with the associated modelling. Monte Carlo methods have proved to be the most successful means of solving pdf transport equations. The essence of these solution techniques is described in Section 3. The theoretical foundations of pdf methods (including the modelling and Monte Carlo solution algorithms) are comprehensively described by Pope (1985). The purpose of Sections 2 and 3 is to describe briefly the principal features, with no attempt at rigor. Section 4 reviews the applications of pdf methods to turbulent diffusion flames and premixed flames. (Recent applications to constant-density inert flows have been reviewed by Pope 1989a.) In the Discussion and Conclusions some of the outstanding problems and future directions are assessed.

2. PDF METHODS

2.1 Definitions and Properties

Let ϕ denote the value of a composition variable (the mass fraction of oxygen, for example) at a particular location $\underline{x}_0$ and time t_0 in a turbulent reactive flow. It is supposed that the flow can be realized any number of times, and the time t is measured from the initiation of the flow. Thus from each realization we obtain a value of ϕ; and, given the nature of turbulence, these values are, in all probability, different. In other words ϕ is a random variable. On a given realization, it is not possible to determine beforehand the value of ϕ that will obtain. But it is possible to ascribe probabilities to its value being in a given interval: this can be done through the pdf.

For every random variable we introduce an independent (sample-space) variable: in particular, ψ is the sample-space variable corresponding to ϕ. The cumulative distribution function (cdf), $F_\phi(\psi)$, is then defined as the probability that ϕ is less than ψ:

$$F_\phi(\psi) \equiv \text{Prob}\{\phi<\psi\} \, . \tag{1}$$

And the pdf of ϕ, $f_\phi(\psi)$, is defined by

$$f_\phi(\psi) \equiv \frac{d}{d\psi} F_\phi(\psi) \, . \tag{2}$$

While $F_\phi(\psi)$ is a probability function, $f_\phi(\psi)$ is a probability *density* function. That is, $f_\phi(\psi)$ is the probability *per unit* ψ of the event $\phi=\psi$: or, equivalently, $f_\phi(\psi)d\psi$ is the probability of the event $\psi\le\phi<\psi+d\psi$.

The three fundamental properties of the pdf (in addition to Eq. 2) are:

$$f_\phi(\psi) \ge 0 \, , \tag{3}$$

since probabilities are non-negative;

$$\int_{-\infty}^{\infty} f_\phi(\psi)\, d\psi = 1 \quad , \tag{4}$$

since $\text{Prob}\{\phi<\infty\} = 1$ and $\text{Prob}\{\phi<-\infty\} = 0$; and, for any (non-pathological) function $Q(\phi)$:

$$\langle Q\rangle = \int_{-\infty}^{\infty} f_\phi(\psi)\, Q(\psi) d\psi \, . \tag{5}$$

This last equation shows that if the pdf is known, then the expectation of any function of the random variable can be calculated. In particular the mean $\langle\phi\rangle$ and the m-th central moment $\langle\phi'^m\rangle$ $(m>1)$ can be determined (if it exists).

For a general turbulent reactive flow we need to consider a set of $\sigma \geq 1$ composition variables $\underline{\phi} = \{\phi_1,\phi_2, ...,\phi_\sigma\}$. Accordingly the σ sample-space variables $\underline{\psi} \equiv \{\psi_1,\psi_2, ...,\psi_\sigma\}$ are introduced, and the joint pdf of $\underline{\phi}$, $f_{\underline{\phi}}(\underline{\psi})$, is defined to be the probability density of the compound event $\underline{\phi} = \underline{\psi}$ (i.e. $\phi_1 = \psi_1$, $\phi_2 = \psi_2$, ..., $\phi_\sigma = \psi_\sigma$).

Clearly the joint pdf defined at the particular location $\underline{x}_0$ and time t_0, can be defined at any $(\underline{x},t)$: we denote by $f_{\underline{\phi}}(\underline{\psi};\underline{x},t)$ the joint pdf of $\underline{\phi}(\underline{x},t)$. It is important to realize that this is a one-point, one-time joint pdf: it contains no joint information between $\underline{\phi}$ at two or more positions or times. The pdf method described in the next sub-section is based on $f_{\underline{\phi}}(\underline{\psi};\underline{x},t)$, which is called the *composition joint pdf*.

The second pdf method described (in Section 2.3) is based on the *velocity-composition joint pdf*, $f(\underline{V},\underline{\psi};\underline{x},t)$. Here, $\underline{V} = \{V_1,V_2,V_3\}$ are the three independent velocity variables; and f is the probability density of the compound event $\{\underline{U}(\underline{x},t) = \underline{V}, \underline{\phi}(\underline{x},t) = \underline{\psi}\}$.

In the treatment of variable-density flows, two further probability functions prove useful, and are now defined. By assumption (see Pope 1985), the composition variables are sufficient to determine the fluid density. If the composition is $\underline{\phi}$, the density is given by the function $\rho_\sigma(\underline{\phi})$, which can be determined from a thermodynamic calculation. Consequently at $(\underline{x},t)$ the fluid density is

$$\rho(\underline{x},t) = \rho_\sigma(\underline{\phi}[\underline{x},t]) \,. \tag{6}$$

Having made the distinction between the different functions $\rho(\underline{x},t)$ and $\rho_\sigma(\underline{\phi})$, we now follow conventional (if imprecise) notation and denote both by ρ.

Favre, or density-weighted, pdf's are defined by, for example:

$$\tilde{f}_\phi(\psi) = \rho(\psi)f_\phi(\psi)/\langle\rho\rangle \,. \tag{7}$$

It then follows that density-weighted means are given by

$$\tilde{Q} \equiv \langle\rho Q\rangle/\langle\rho\rangle = \int_{-\infty}^{\infty} Q(\psi)\tilde{f}(\psi)d\psi \,, \tag{8}$$

(cf. Eq. 5). The mass density function F is defined by

$$F(\underline{V},\underline{\psi},\underline{x};t) = \rho(\underline{\psi})f(\underline{V},\underline{\psi};\underline{x},t) \,. \tag{9}$$

The use of these functions is made apparent in the next two subsections.

2.2 Composition Joint PDF Equation

Dopazo and O'Brien (1974) were the first to consider the transport equation for $\tilde{f}_{\underline{\phi}}(\underline{\psi};\underline{x},t)$. Since then a number of different derivations have been given (e.g. Pope 1976, Janicka et al. 1978a,b, O'Brien 1980, Pope 1985). Here we state the result, and refer the reader to Pope (1985) for a detailed derivation.

The compositions evolve according to the conservation equation

$$\frac{D\phi_\alpha}{Dt} = -\frac{1}{\rho}\frac{\partial J_i^\alpha}{\partial x_i} + S_\alpha \, , \tag{10}$$

where $\underline{J}^\alpha$ is the (molecular) diffusive flux of ϕ_α, and S_α — a known function of $\underline{\phi}$ — is the rate of creation of ϕ_α due to chemical reaction. The pdf transport equation corresponding to Eq. (10) is

$$\frac{\partial \tilde{f}_{\underline{\phi}}}{\partial t} + \tilde{U}_i \frac{\partial \tilde{f}_{\underline{\phi}}}{\partial x_i} + \frac{\partial}{\partial \psi_\alpha}[S_\alpha(\underline{\psi})\tilde{f}_{\underline{\phi}}] =$$

$$-\frac{1}{\langle\rho\rangle}\frac{\partial}{\partial x_i}[\langle u_i''|\underline{\psi}\rangle \tilde{f}_{\underline{\phi}}] + \frac{\partial}{\partial \psi_\alpha}[\langle \frac{1}{\rho}\frac{\partial J_i^\alpha}{\partial x_i}|\underline{\psi}\rangle \tilde{f}_{\underline{\phi}}] \, . \tag{11}$$

On the left-hand side, the first two terms represent the rate of change following the mean flow. The third term is — in composition space — the divergence of the flux of probability due to reaction. It is the form of this term that gives this pdf method the advantage over other statistical approaches: since $\underline{S}(\underline{\psi})$ is known, $\tilde{f}_{\underline{\phi}}$ is the subject of the equation, and ψ_α is an independent variable, the term contains no unknowns. Thus however complicated and non-linear the reaction scheme, in the composition joint pdf equation the effect of reaction is in closed form, requiring no modelling.

In contrast the terms on the right-hand side require modelling. The quantity $\langle\underline{u}''|\underline{\psi}\rangle$ is the mean of the Favre velocity fluctuation ($\underline{u}'' \equiv \underline{U}-\tilde{\underline{U}}$) conditional upon the event $\underline{\phi} = \underline{\psi}$. It represents the transport of $\tilde{f}_{\underline{\phi}}$ in physical space by the fluctuating velocity. Although there have been other suggestions, this term is generally modelled by gradient diffusion:

$$\langle\rho\rangle\langle u_i'' \,|\, \underline{\psi}\rangle \tilde{f}_{\underline{\phi}} = -\Gamma_T \frac{\partial}{\partial x_i}\tilde{f}_{\underline{\phi}} , \tag{12}$$

where Γ_T is a turbulent diffusivity. Such gradient transport models are, of course, subject to many objections, especially when applied to variable-density reactive flows.

The final term in Eq. (11) represents the effect of molecular mixing. It is generally treated by a stochastic mixing model (see e.g. Flagan & Appleton 1974, Pope 1982, 1985). While some aspects of this modelling are discussed below, the cited references should be consulted for a full account.

The composition joint pdf equation is not a self-contained model: mean momentum equations must be solved for $\tilde{\underline{U}}$; and a turbulence model (k-ε, say) is needed to determine both Γ_T ($\sim k^2/\varepsilon$) and the mixing rate ($\sim \varepsilon/k$) used in the stochastic mixing model.

2.3 Velocity-Composition Joint PDF Equation

Two shortcomings of the composition pdf approach are that turbulent transport ($\langle u_i''|\underline{\psi}\rangle$) has to be modelled, and that the velocity and turbulence fields have to be treated separately. Both these shortcomings are overcome in the velocity-composition joint pdf approach.

The instantaneous momentum equation is

$$\rho \frac{DU_j}{Dt} = \frac{\partial \tau_{ij}}{\partial x_i} - \frac{\partial p}{\partial x_j} + \rho\, g_j\,, \tag{13}$$

where τ_{ij} is the stress tensor, p the pressure, and $\underline{g}$ the gravitational acceleration.

From this equation (and that for $\underline{\phi}$, Eq. 10) the following equation can be derived (Pope 1985) for the mass density function $F(\underline{V},\underline{\psi},\underline{x};t)$ (Eq. 9):

$$\frac{\partial F}{\partial t} + V_j \frac{\partial F}{\partial x_j} + \left[g_j - \frac{1}{\rho(\underline{\psi})} \frac{\partial \langle p\rangle}{\partial x_j}\right] \frac{\partial F}{\partial V_j} + \frac{\partial}{\partial \psi_\alpha} \left[F\, S_\alpha(\underline{\psi})\right] =$$

$$\frac{\partial}{\partial V_j}\left[\left\langle -\frac{\partial \tau_{ij}}{\partial x_i} + \frac{\partial p'}{\partial x_j} \,\middle|\, \underline{V},\underline{\psi}\right\rangle F/\rho(\underline{\psi})\right] + \frac{\partial}{\partial \psi_\alpha}\left[\left\langle \frac{\partial J_j^\alpha}{\partial x_j} \,\middle|\, \underline{V},\underline{\psi}\right\rangle F/\rho(\underline{\psi})\right]. \tag{14}$$

None of the terms on the left-hand side requires modelling. In order, the terms represent: rate of change with time; transport in position space (by both mean and fluctuating components of velocity); transport in velocity space (by gravity and the mean pressure gradient); and, as before, transport in composition space due to reaction.

The terms requiring modelling (on the right-hand side of Eq. 1) are means conditional on the compound event $\{\underline{U}(\underline{x},t) = \underline{V},\ \underline{\phi}(\underline{x},t) = \underline{\psi}\}$. The final term — as in the composition pdf equation — represents molecular mixing. The remaining term represents transport in velocity space due to molecular stresses and the fluctuating pressure gradient. A discussion of its modelling is deferred to the next subsection.

It may be seen, then, that the velocity-composition joint pdf method retains the advantage of treating reaction without approximation, and, in addition, treats transport in physical space (turbulent convection) exactly, thus avoiding gradient-diffusion assumptions. It also provides a more complete closure: The mean velocity $\underline{\tilde{U}}(\underline{x},t)$, the Reynolds stresses, and indeed all one-point velocity-composition statistics can be calculated from F. The model equation for F is not quite self-contained because the modelled terms require a knowledge of the turbulent time scale (k/ε) which cannot be deduced from F.

2.4 Lagrangian Viewpoint

Thus far the Eulerian view has been adopted: we have considered functions (e.g. $F(\underline{V},\underline{\psi},\underline{x};t)$) at a fixed position $\underline{x}$. It proves extremely helpful, both to the modelling and to the numerical solution technique, to take the alternative Lagrangian viewpoint also.

Let $\underline{x}^+(t)$, $\underline{U}^+(t)$ and $\underline{\phi}^+(t)$ denote the position, velocity and composition of the fluid particle that was at a reference point $\underline{x}_0$ at a reference time t_0. These particle properties evolve according to:

$$\frac{d\underline{x}^+(t)}{dt} = \underline{U}^+(t) = \underline{U}(\underline{x}^+[t],t), \tag{15}$$

since, by definition, a fluid particle moves with the local fluid velocity;

$$\frac{dU_j^+}{dt} = A_j \equiv g_j - \frac{1}{\rho(\underline{\phi}^+)}\left[\frac{\partial\langle p\rangle}{\partial x_j}\right]_{\underline{x}^+} + \left\{\frac{\partial\tau_{ij}}{\partial x_i} - \frac{1}{\rho(\underline{\phi}^+)}\,\frac{\partial p'}{\partial x_j}\right\}_{\underline{x}^+} \tag{16}$$

(from Eq. 13); and,

$$\frac{d\phi_\alpha^+}{dt} = \Theta_\alpha \equiv S_\alpha(\underline{\phi}^+) - \frac{1}{\rho(\underline{\phi}^+)}\left\{\frac{\partial J_i^\alpha}{\partial x_i}\right\}_{\underline{x}^+} . \tag{17}$$

(from Eq. 10).

The connection between these equations for the properties of a fluid particle, and the equation for the mass density function *F* (Eq. 14) is immediately apparent. Equation (14) can be written

$$\frac{\partial F}{\partial t} + \frac{\partial}{\partial x_j}\left[F\langle U_j^+|\rangle\right] + \frac{\partial}{\partial V_j}\left[F\langle A_j|\rangle\right] + \frac{\partial}{\partial \psi_\alpha}\left[F\langle\Theta_\alpha|\rangle\right] = 0, \tag{18}$$

where the expectations are conditional on the compound event $\{\underline{x}^+(t) = \underline{x}, \underline{U}^+(t) = \underline{V}, \underline{\phi}^+(t) = \underline{\psi}\}$. Further, it may be noticed that the terms in braces in Eqs. (16)-(17) appear on the right-hand side of Eq. (14) — that is, they need to be modelled — whereas all other terms appear on the left-hand side and are treated exactly.

2.5 Stochastic Models

The standard approach to turbulence modelling is to construct constitutive relations for the unknown correlations (see, e.g. Lumley 1978). In the context of the mass density function, this approach is to model the unknown conditional expectations on the right-hand side of Eq. (14) in terms of known quantities, i.e. functions or functionals of $F(\underline{V},\underline{\psi},\underline{x};t)$. But the Lagrangian viewpoint offers a different approach to modelling: namely to use stochastic processes to simulate unknown contributions to $\underline{U}^+(t)$ and $\underline{\phi}^+(t)$ (i.e. the terms in braces in Eqs. 16 and 17).

To illustrate this approach we consider $\underline{U}^*(t)$ — a stochastic model for $\underline{U}^+(t)$. If the model is accurate then $\underline{U}^*(t)$ is (statistically) an accurate approximation to $\underline{U}^+(t)$. In general the time series $\underline{U}^*$ is not differentiable. Consequently we express the models in terms of the infinitesimal increment

$$d\underline{U}^*(t) \equiv \underline{U}^*(t+dt) - \underline{U}^*(t)\,, \tag{19}$$

rather than in terms of the derivative $d\underline{U}^*/dt$. Note that for a deterministic, differentiable process, (e.g. $\underline{U}^+(t)$), the infinitesimal increment is non-random (i.e. zero variance) and is of order dt.

In view of the equation for $\underline{U}^+(t)$ (Eq. 16), the increment $d\underline{U}^*$ can be written

$$dU_j^* = \left(g_j - \frac{1}{\rho(\underline{\phi}^*)}\left[\frac{\partial\langle p\rangle}{\partial x_j}\right]_{\underline{x}^*}\right)dt + dU_j^s\,, \tag{20}$$

where (similar to $\underline{U}^*$) $\underline{x}^*$ and $\underline{\phi}^*$ are models of $\underline{x}^+$ and $\underline{\phi}^+$. The stochastic increment $d\underline{U}^s$ models the effects of the fluctuating pressure gradient and viscous stresses, while the term in dt is an exact expression for the effect of gravity and the mean pressure gradient.

Two types of models have been used. The first type — of which the stochastic mixing model is an example — are called *particle interaction* models. In the terminology of stochastic processes, these are *point processes*. According to these models, the infinitesimal increment $d\underline{U}^s$ is nearly always zero. But with probability of order dt, the increment is of order unity. Thus the time series is a piecewise constant, with of order unity jumps per unit time.

The second type of model use *diffusion processes* in which $d\underline{U}^s$ is a random variable with (conditional) mean and variance both of order dt. Note that this implies that the rms is of order $dt^{1/2}$, and hence the process — though continuous — is not differentiable. The different variants of the Langevin model are diffusion processes (see e.g. Pope 1983, 1985, Haworth & Pope 1986, 1987a).

For more information on this general modelling approach the reader is referred to Pope (1985), while the current status of the Langevin model is described by Haworth & Pope (1987a).

3. NUMERICAL SOLUTION ALGORITHMS

The velocity-composition joint pdf $f(\underline{V},\underline{\psi};\underline{x},t)$ is a single function defined in a multi-dimensional space. In general f depends on the three velocity variables, σ composition variables, three spatial variables, and time — $(7+\sigma)$ independent variables in all. In many cases the dimensionality may be less, but still large. For example, in a statistically stationary and two-dimensional flow with a single composition variable, $f(\underline{V},\psi_1;x_1,x_2)$ depends on 6 independent variables. The composition joint pdf $f_{\phi}(\underline{\psi};\underline{x},t)$ in general depends on $(4+\sigma)$ variables; but, for the simpler flow cited above, $f_{\phi}(\psi_1;x_1,x_2)$ is a function of just 3 variables.

Given the large dimensionality of joint pdf's it is clear that conventional grid-based numerical methods (e.g. finite differences) are impractical for all but the simplest of cases. Just to provide an accurate representation of a function of 6 independent variables is a major task. Consequently, although one or two finite-difference solutions have been obtained for $f_{\phi}(\psi_1;x_1,x_2)$ (e.g. Janicka & Kollmann 1978a,b), currently all investigators are using Monte Carlo methods instead.

In the next subsection the general Monte Carlo method devised by Pope (1985) to solve for the velocity-composition joint pdf is outlined. Then, in section 3.2, Monte Carlo solution algorithms for the composition joint pdf are reviewed.

3.1 Monte Carlo Method for the Velocity-Composition Joint PDF

The Monte Carlo method to solve the modelled equation for the velocity-composition joint pdf is conceptually simple and natural. Rather than discretizing the space, we discretize the mass of fluid into a large number N of representative or *stochastic particles*. At a given time t, let M be the total mass of fluid within the solution domain. Then each stochastic particle represents a mass $\Delta m \equiv M/N$ of fluid. The n-th particle has position $\underline{x}^{(n)}(t)$, velocity $\underline{U}^{(n)}(t)$, and composition $\underline{\phi}^{(n)}(t)$.

Starting from appropriate initial conditions, the particle properties are advanced in time by the increments

$$d\underline{x}^{(n)}(t) = \underline{U}^{(n)}(t)\, dt\,, \tag{21}$$

$$d\underline{U}^{(n)}(t) = [\underline{g} - \rho(\underline{\phi}^{(n)})^{-1}\nabla\langle p\rangle]dt + d\underline{U}^s\,, \tag{22}$$

$$d\underline{\phi}^{(n)}(t) = \underline{S}(\underline{\phi}^{(n)})dt + d\underline{\phi}^s \, , \tag{23}$$

where $d\underline{U}^s$ and $d\underline{\phi}^s$ are the stochastic increments that simulate molecular processes and the fluctuating pressure gradient. At symmetry boundaries particles are reflected; at inflow boundaries particles are added with appropriate properties; and, at outflow boundaries particles are discarded. While wall boundaries have been treated (Anand et al. 1989a) a comprehensive account of this treatment is not available in the literature.

The correspondence between the ensemble of stochastic particles and the joint pdf has been established by Pope (1985). The main results are:

i) The expected density of the stochastic particles in physical space ($\Delta m \sum_{n=1}^{N} \langle \delta(\underline{x}-\underline{x}^{(n)}(t)) \rangle$) is equal to the fluid density $\langle \rho(\underline{x},t) \rangle$.

ii) The joint pdf of the stochastic particle properties $\underline{U}^{(n)}(t)$, $\underline{\phi}^{(n)}(t)$ is the density-weighted joint pdf $\tilde{f}(\underline{V},\underline{\psi};\underline{x}^{(n)}[t],t)$.

iii) From particle properties, expectations (e.g. $\tilde{\underline{U}}(\underline{x},t)$) can be approximated as ensemble averages, with a statistical error of order $N^{-1/2}$.

Several implementations of this algorithm, and variants of it, have been reported. For example, the turbulent jet diffusion flame calculations reported in Section 4 are performed using a "boundary-layer" variant (see Pope 1985). Haworth & Pope (1987b) report a variant of the algorithm designed specifically for self-similar shear flows. From a numerical standpoint this work is of particular interest, because the convergence of the method (as $N^{-1/2}$) is demonstrated. The basic algorithm has been implemented and demonstrated for statistically two-dimensional recirculating flows by Anand et al. (1989b). Haworth & El Tahry (1989a,b) reports calculations of the three-dimensional time-dependent flow in the cylinder of a spark-ignition engine. In this case the pdf algorithm is coupled to a conventional finite-volume algorithm that is used to calculate the mean pressure and turbulent time scale fields.

3.2 Monte Carlo Algorithms for the Composition Joint PDF

Two different algorithms have been proposed to solve the modelled transport equation for the composition joint pdf.

The second of these (chronologically) was proposed by Pope (1985), and is similar to that described above for the velocity-composition joint pdf. Again, it is a grid-free algorithm in which the mass of fluid is discretized into N stochastic particles, the n-th of these having position $\underline{x}^{(n)}(t)$ and composition $\underline{\phi}^{(n)}(t)$. In each time step the composition is incremented according to Eq. (23), while the position is incremented by

$$d\underline{x}^{(n)}(t) = \tilde{\underline{U}}(\underline{x}^{(n)}[t],t)dt + d\underline{x}^s \, , \tag{24}$$

where the stochastic component $d\underline{x}^s$ causes a random walk to simulate gradient diffusion. No implementations of this algorithm have been reported in the literature.

The first Monte Carlo algorithm for the composition joint pdf was devised by Pope (1981b). In this method there is a finite-difference grid in physical space. At each grid node, the composition joint pdf is represented by N particles, the n-th having composition $\underline{\phi}^{(n)}(t)$. Reaction and mixing are performed according to Eq. (23), while particles are moved from node to node to simulate convection and turbulent diffusion.

This algorithm is used in the premixed flame calculation of Pope (1981a) and McNutt (1981), and in the diffusion flame calculations of Nguyen & Pope (1984), Jones & Kollmann (1987) and Chen & Kollmann (1988a).

4. TURBULENT FLAME CALCULATIONS

4.1 Turbulent Diffusion Flames

Some of the first pdf calculations are of turbulent diffusion flames (Frost 1975, Janicka, Kolbe and Kollmann 1978a,b, Bywater 1982, Nguyen & Pope 1984). The calculations reported by Nguyen & Pope (1984) are the first use of the Monte Carlo method for jet flames. The results include demonstrations of convergence of the solutions as $N^{-1/2}$ tends to zero.

In the calculations cited above, the thermochemistry is handled in a simple manner — by assuming chemical equilibrium, for example. This reduces the number of compositions to just one; namely, the mixture fraction. Finite-rate, multi-step kinetics have been used by Pope & Correa (1986) (see also Correa, Gulati & Pope 1988), Jones & Kollmann (1987) and Chen & Kollmann (1988a,b). A computational challenge is to implement the integration of the rate equation, i.e.

$$\frac{d\underline{\phi}}{dt} = \underline{S}(\underline{\phi}) . \tag{25}$$

in an efficient manner. All investigators have used table-look-up algorithms.

Considerable attention has been paid to the CO/H_2-air turbulent diffusion flame studied experimentally by Drake et al. (1984). Using the velocity-composition joint pdf approach Pope & Correa (1986) and Correa, Gulati and Pope (1988) report calculations based on a partial equilibrium assumption. This reduces the number of compositions to two: the mixture fraction and a reaction progress variable (for the radical recombination reactions). Again using the velocity-composition joint pdf approach, Haworth, Drake & Blint (1988) and Haworth, Drake, Pope & Blint (1988) have made calculations of this flame using a flamelet model.

4.2 Turbulent Premixed Flames

The composition joint pdf approach (using the Monte Carlo method) has been applied to premixed flames by Pope (1981a) and McNutt (1981). The purpose of the former calculation was to demonstrate the ability of the pdf method to handle nonlinear reaction kinetics. A three-variable kinetic scheme was used to calculate the oxidation of CO and formation of NO in a propane-air flame stabilized behind a perforated plate.

The works of McNutt (1981), Pope & Anand (1984) and Anand & Pope (1987) are concerned with the idealized case of a statistically steady and one-dimensional turbulent premixed flame. In the last of these, the velocity-composition joint pdf method is used, and the effects of variable density are studied. It is shown that, like the Bray-Moss-Libby model (Bray, Libby & Moss 1985), the pdf method is capable of accounting for counter-gradient transport and large turbulence energy production due to heat release. The application of the method to a spark-ignited turbulent flame ball is described by Pope & Cheng (1986).

Turbulent premixed combustion usually occurs in the flamelet regime (Pope 1987). This fact presents a challenge to any statistical approach, since the small scales of the composition fields are no longer governed by the turbulent straining motions, but are determined by reaction and diffusion occurring in thin flame sheets. Pope & Anand (1984) present and demonstrate a model applicable to the flamelet regime. But, as discussed by Pope (1985, 1987), this model is not entirely satisfactory.

An alternative approach to treating flamelet combustion is the stochastic flamelet model of Pope & Cheng (1988). This can be viewed as a pdf approach, in which a modelled pdf equation is solved by a Monte Carlo method. In this case, however, the pdf is not that of fluid properties (i.e. velocity and composition) but is rather the pdf of flamelet properties (i.e. position, area and orientation of flamelets).

5. DISCUSSION AND CONCLUSION

The works reviewed in the previous section demonstrate that pdf methods provide a practicable means of calculating the properties of turbulent reactive flows. Calculations have been made with thermochemical schemes involving up to three composition variables with finite-rate kinetics (e.g. Pope 1981a, Chen & Kollmann 1988a). And the Monte Carlo method used to solve the pdf equations has been implemented for a variety of flows including two-dimensional recirculating flows (Anand et al. 1989a) and the three-dimensional transient flow in a spark-ignition engine (Haworth & El Tahry 1989a,b).

The most advanced method considered here is the velocity-composition joint pdf approach. Compared to moment closures, this approach has the advantage that reaction can be treated exactly without approximation. Compared to the composition joint pdf approach it has the advantages that turbulent transport is treated exactly, and that a separate turbulence model is not needed to determine the Reynolds stresses.

A short-coming of the velocity-composition joint pdf approach is that it does not provide a completely self-contained model, in that the turbulence frequency $\langle\omega\rangle \equiv \langle\varepsilon\rangle/k$ must be determined by separate means. For example, in some calculations of simple free shear layers, it has been assumed that $\langle\omega\rangle$ is constant across the flow, and scales with the mean-flow velocity and length scales (e.g. Haworth & Pope 1987a, Pope & Correa 1986). In more complex flows, another approach is to solve the standard model equation for $\langle\varepsilon\rangle$ (e.g. Haworth & El Tahry 1989a) or, similarly, to solve a modelled equation for $\langle\omega\rangle$ deduced from those for k and $\langle\varepsilon\rangle$ (Anand et al. 1989b).

A natural extension is to consider $f(\underline{V},\underline{\psi},\zeta;\underline{x},t)$ — the joint pdf of velocity, composition and dissipation. This is the probability density function of the compound event $\{\underline{U}(\underline{x},t) = \underline{V}, \underline{\phi}(\underline{x},t) = \underline{\psi}, \varepsilon(\underline{x},t) = \zeta\}$, where $\varepsilon(\underline{x},t)$ is the instantaneous mechanical dissipation. Following some preliminary investigations (Pope & Haworth 1986, Pope & Chen 1987) a satisfactory model equation for $f(\underline{V},\underline{\psi},\zeta;\underline{x},t)$ has been developed (Pope 1989b). The incorporation of dissipation within the pdf allows more realistic and accurate modelling. But more important, the single equation for $f(\underline{V},\underline{\psi},\zeta;\underline{x},t)$ provides a completely self-contained model for turbulent reactive flows.

We now discuss three areas in which progress can be expected in the next five years.

The first area is in the turbulent mixing models. As discussed in Section 2, the stochastic mixing models used lead to the composition time series being discontinuous — clearly contrary to the physics of the problem. Nevertheless, in spite of their lack of physical appeal, the stochastic models have many advantages over alternative suggestions, and, for inert mixing their performance is generally acceptable. But for reactive flows, especially in the flamelet regime, their performance is highly suspect. We expect that stochastic models will be improved and refined to account better for the microstructure of the composition fields, and also to allow mixing and reaction to proceed simultaneously at finite rates.

The second area of expected progress is in the computational implementation of complex kinetics. When the Monte Carlo method is used to solve the joint pdf equation for an inert flow involving σ compositions, the computer time and storage increases at most linearly with σ. But with reaction, in a naive implementation, for each particle, on each time step, it is necessary to solve the coupled set of σ ordinary differential equations

$$\frac{d\phi_\alpha}{dt} = S_\alpha(\phi_1,\phi_2,\ldots,\phi_\sigma)\,,\quad \alpha = 1,2,\ldots,\sigma\,. \qquad (26)$$

The right-hand side (which is a combination of reaction rates) is computationally expensive to evaluate, and, as is well known, the set of equations is likely to be stiff. Hence such a naive implementation is impracticable for all but the lowest values of σ.

As mentioned in Section 4.1, the alternative approach followed by all investigators is to implement Eq. (26) more efficiently through a different table look-up scheme (e.g. Pope & Correa 1986, Jones & Kollmann 1987). To date this has been done on an ad hoc basis. It is expected that progress will be made in the development of a general methodology.

The third area of expected progress is in the determination of the mean pressure field $\langle p(\underline{x},t)\rangle$ within the Monte Carlo algorithm. For thin shear flows, the mean pressure is readily determined by invoking the boundary-layer approximations. For statistically-stationary, constant-density, two-dimensional recirculating flow, an algorithm to determine $\langle p\rangle$ has been developed and demonstrated (Anand et al. 1989a). But for the general case a computationally efficient and robust algorithm needs to be developed. (In the three-dimensional transient calculations of Haworth & El Tahry 1989a,b, the Monte Carlo method is coupled to a finite-volume code that determines $\langle p\rangle$.)

ACKNOWLEDGEMENTS

This work is supported in part by the National Science Foundation (Grant CBT-8814655) and in part by the U.S. Air Force Wright Aeronautical Laboratory, Wright-Patterson AFB, under contract No. F33615-87-C-2821.

REFERENCES

Anand, M.S. and Pope, S.B. (1987) Combust. Flame, 67, 127.
Anand, M.S., Pope, S.B. and Mongia, H.C. (1989a) in Turbulent Reactive Flows, Lecture Notes in Engineering, 40, Springer-Verlag, 672.
Anand, M.S., Pope, S.B. and Mongia, H.C. (1989b) Seventh Symposium on Turbulent Shear Flows, Stanford University, 3.3.1.
Bray, K.N.C., Libby, P.A. and Moss, J.B. (1985) Combust. Flame 61, 87.
Bywater, R.J. (1982) AIAAJ 20, 824.
Chen, J-Y. and Kollmann, W. (1988a) Twenty-Second Symp. (Int'l) on Combust., p. 645, The Combustion Institute.
Chen, J-Y. and Kollmann, W. (1988b) Sandia Report SAND88-8837.
Correa, S.M., Gulati, A. and Pope, S.B. (1988) Combust. Flame 72, 159.
Dopazo, C. and O'Brien, E.E. (1974) Acta Astronaut. 1, 1239.
Drake, M.C., Pitz, R.W., Correa, S.M. and Lapp, M. (1984) Twentieth Symp. (Int'l) on Combust., p. 327, The Combustion Institute.
Flagan, R.C. and Appleton, J.P. (1974) Combust. Flame, 23, 249.
Frost, V.A. (1975) Fluid Mech. Sov. Res. 4, 124.
Haworth, D.C. and El Tahry, S.H. (1989a) Bull. Am. Phys. Soc. 33, 2281.
Haworth, D.C. and El Tahry, S.H. (1989b) Seventh Symposium on Turbulent Shear Flows Stanford University.
Haworth, D.C. and Pope, S.B. (1986) Phys. Fluids, 29, 387.
Haworth, D.C. and Pope, S.B. (1987a) Phys. Fluids, 30, 1026.
Haworth, D.C. and Pope, S.B. (1987b) J. Comp. Phys., 72, 311.
Haworth, D.C., Drake, M.C. and Blint, R.J. (1988) Combust. Sci. Technol., 60, 287.
Haworth, D.C., Drake, M.C., Pope, S.B. and Blint, R.J. (1988) Twenty-Second Symp. (Int'l) on Combust., p. 589, The Combustion Institute.
Janicka, J., Kolbe, W. and Kollmann, W. (1978a) J. Non-Equilib. Thermodyn. 4, 47.

Janicka, J., Kolbe, W. and Kollmann, W. (1978b) Proc. Heat Transf. Fluid Mech. Inst., 296, Stanford University Press.

Jones, W.P. and Kollmann, W. (1987) in Turbulent Shear Flows 5 (F. Durst et al., eds.) Springer-Verlag, p. 296.

Lumley, J.L. (1978) Adv. Appl. Mech. 18, 123.

McNutt, D.G. (1981) M.S. Thesis, Mass. Inst. Technol.

Nguyen, T.V. and Pope, S.B. (1984) Combust. Sci. Technol., 42, 13.

O'Brien, E.E. (1980) in Turbulent Reactive Flows (eds. P.A. Libby and F.A. Williams) p. 185, Springer-Verlag.

Pope, S.B. (1976) Combust. Flame, 27, 299.

Pope, S.B. (1981a) Eighteenth Symp. (Int'l) on Combust., p. 1001, The Combustion Institute.

Pope, S.B. (1981b) Combust. Sci. Technol. 25, 159.

Pope, S.B. (1982) Combust. Sci. Technol. 28, 131.

Pope, S.B. (1983) Phys. Fluids, 26, 3448.

Pope, S.B. (1985) Prog. Energy Combust. Sci. 11, 119.

Pope, S.B. (1987) Ann. Rev. Fluid Mech. 19, 237.

Pope, S.B. (1989a) in Recent Advances in Computational Fluid Dynamics Lecture Notes in Engineering, Springer-Verlag, 43.

Pope, S.B. (1989b) Cornell University, Report FDA-89-06.

Pope, S.B. and Anand, M.S. (1984) Twentieth Symp. (Int'l) on Combust., p. 403, The Combustion Institute.

Pope, S.B. and Cheng, W.K. (1986) Twenty-First Symp. (Int'l) on Combust., p. 1473, The Combustion Institute.

Pope, S.B. and Cheng, W.K. (1988) Twenty-Second Symp. (Int'l) on Combust., p. 781, The Combustion Institute.

Pope, S.B. and Correa, S.M. (1986) Twenty-First Symp. (Int'l) on Combust., p. 1341, The Combustion Institute.

Pope, S.B. and Haworth, D.C. (1986) in Turbulent Shear Flows 5, p. 44 (F. Durst et al. eds.) Springer-Verlag.

PRESSURE ALGORITHM FOR ELLIPTIC FLOW CALCULATIONS WITH THE PDF METHOD

M.S. Anand
Allison Gas Turbine
Indianapolis, Indiana 46206

S.B. Pope
Cornell University
Ithaca, New York 14853

H.C. Mongia
Allison Gas Turbine
Indianapolis, Indiana 46206

ABSTRACT

An algorithm to determine the mean pressure field for elliptic flow calculations with the probability density function (pdf) method is developed and applied. The pdf method is a most promising approach for the computations of turbulent reacting flows. Previous computations of elliptic flows with the method have been performed in conjunction with conventional finite-volume based calculations that provided the mean pressure field. The algorithm developed and described here permits the mean pressure field to be determined within the pdf calculations. The pdf method incorporating the pressure algorithm is applied to the flow past a backward-facing step. The results are in good agreement with data for the reattachment length, mean velocities, and turbulence quantities including triple correlations.

INTRODUCTION

The understanding and modeling of turbulent reacting flows is of great importance due to the occurrence of such flows in most practical combustion devices. The probability density function (pdf) method offers several advantages over conventional turbulence models for the computations of turbulent reacting flows (ref. 1). In this method a modeled transport equation for the joint pdf of velocities and scalars is solved using the Monte Carlo technique. The primary advantages of the pdf method are that, in the pdf transport equation, terms representing convection and reaction appear in closed form and need not be modeled. Hence, conventional turbulence models such as the k-ε or second-moment closure models which are based on gradient-diffusion assumptions are entirely avoided. Also, any arbitrarily complex finite-rate reactions that are beyond the reach of conventional turbulent reaction models can be treated without approximation or restrictive assumptions.

Until recently, most of the flows studied using the pdf method have been two-dimensional (2-D parabolic or 1-D time-dependent) in nature. These studies (refs. 2-7 to name a few) have demonstrated the potential advantages of the pdf method especially for reacting flows. There are no theoretical limitations for applying the pdf method for complex (2-D or 3-D) elliptic flows. However, a suitable algorithm for extracting the mean pressure field within the pdf solution algorithm is needed.

A pdf method for elliptic flows was first demonstrated by Anand, et al. (ref. 8) for a 2-D flow. The method was applied to 3-D in-cylinder flows by Haworth and El Tahry (Refs. 9, 10). In this method, the Monte Carlo (MC) calculations for the pdf are combined with conventional finite-volume (FV) calculations (ref. 11) for mean fields. The mean pressure field and the turbulent time scale are supplied to the MC calculations by the FV calculations. In turn, the MC calculations supply to the FV calculations the Reynolds stresses extracted from the pdf solution, thereby avoiding the use of conventional turbulence models. This combined algorithm exploits the advantages of both methods to yield an economical algorithm for pdf calculations of elliptic flows. This method was intended to demonstrate the feasibility of pdf calculations for such flows.

However, for more complex flows, especially variable density and reacting flows with fast or finite-rate multistep chemistry, the coupling between the two methods becomes quite complex and it becomes more difficult to fully exploit the advantages of the pdf method. Therefore, it is desirable to perform pdf calculations independently, without recourse to FV calculations. This paper describes an algorithm by which pdf calculations are performed independently and economically (in terms of computer resources required) for complex elliptic flows. While the present work focusses on the determination of the mean pressure field within the pdf calculations, parallel work is in progress (ref. 12) that deals with the determination of the turbulent time scale. For the present work, the turbulent time scale is supplied to the calculations as described later in this paper. The relevant equations for determining the mean pressure are presented, the solution strategy and the numerical scheme are developed and suitably implemented in the pdf calculations. The method is applied to a sample elliptic flow, namely the recirculating flow behind a backward-facing step, and compared against data of reference 13.

THE PDF METHOD

A very brief description of the pdf method is presented here. The reader is referred to reference 1 and other studies listed in the introduction for more details.

The joint pdf, $f(\underline{V}, \underline{\psi}; \underline{x}, t)$, is the probability density of the simultaneous event $\underline{U}(\underline{x}, t) = \underline{V}$ and $\underline{\phi}(\underline{x}\ t) = \underline{\psi}$, where $\underline{U}$ is the velocity vector, $\underline{\phi}$ is a set of scalars, and $\underline{V}$ and $\underline{\psi}$ are independent variables in the velocity-scalar space. Starting from the usual conservation equations for mass (continuity), momentum and the scalar quantities, the transport equation for the joint pdf can be derived as described in reference 1. In this equation, the terms involving convection, reaction, body forces and the mean pressure gradient (including the variable density effects in those terms) appear in closed form and need not be modeled. Hence, the use of conventional turbulence and reaction models is avoided. However, the terms in the pdf equation representing the effects of viscous dissipation, fluctuating pressure gradient and molecular diffusion need to be modeled. A Lagrangian viewpoint is adopted in modeling and solving the joint pdf equation. The modeled pdf transport equation is solved by the Monte Carlo technique.

In the Monte Carlo solution technique, notional particles representing fluid particles are distributed throughout the solution domain. Each particle is attributed with values for the velocity components, spatial coordinates, and scalar quantities. Each of these values evolves according to its corresponding Lagrangian evolution equation which incorporates modeled terms where needed. The solution of these evolution equations constitutes the solution of the pdf transport equation (ref. 1). Means of any functions of the independent variables are determined by appropriately summing over the values of all the particles in small spatial subvolumes and fitting splines over the whole domain to these sums.

In the context of the scope of the present study, the scalar quantities are ignored in the presentation except to note that the density ρ is a function of the scalar variables. During an interval of time dt, the change in particle position $\underline{x}^*$ is given by

$$dx_i^* = U_i^* dt, \tag{1}$$

where $\underline{U}^*$ is the particle velocity. With the use of the simplified Langevin model (refs. 2, 3) the increment in $\underline{U}^*$ in the interval dt is given by:

$$dU_i^* = -\frac{1}{\rho^*}\frac{\partial\langle P\rangle}{\partial x_i}\,dt - \left(\frac{1}{2}+\frac{3}{4}C_o\right)(U_i^* - \tilde{U}_i\rangle)\,\omega\,dt + (C_o k\omega)^{1/2}\,dW_i(t) \tag{2}$$

where angled brackets indicate mean quantities, tilde denotes density-weighted (Favre) means, $\langle P\rangle(\underline{x}^*)$ is the mean pressure, ρ^* is the density of the particle, $\tilde{\underline{U}}(\underline{x}^*)$ is the Eulerian mean velocity, k is the turbulent kinetic energy, $\omega(\underline{x}^*)$ is the turbulent frequency, C_0 is a universal constant and $\underline{W}(t)$ is an isotropic Wiener process. The last two terms in Eq 2 jointly represent the effects of viscous dissipation and fluctuating pressure gradient. The value $C_0 = 2.1$ was determined by Anand and Pope (ref. 2) and has been used in the present study. The quantities $\tilde{\underline{U}}$ and k are easily extracted from the pdf solution at time t. In previous studies, the mean pressure gradient has been determined through boundary-layer assumptions or has been supplied by the accompanying finite-volume calculations. Its determination within the pdf calculations for elliptic flows is the topic of this paper. The determination of ω is also discussed.

PRESSURE ALGORITHM

Overview

The pressure algorithm is constructed for steady-state, constant- or variable-density, high-Reynolds-number flows. The equation for mean pressure is the Poisson equation (Eq. 4) derived from the mean momentum equation (Eq. 3):

$$\frac{\partial}{\partial x_i}\langle\rho U_i U_j\rangle = \frac{-\partial\langle P\rangle}{\partial x_j}, \tag{3}$$

$$\frac{\partial^2\langle P\rangle}{\partial x_j \partial x_j} = -\frac{\partial^2}{\partial x_i \partial x_j}\langle\rho U_i U_j\rangle. \tag{4}$$

Since the right-hand side of the equation can be evaluated from the pdf solution, Eq. 4 can be solved for the mean pressure $\langle P\rangle$ with appropriate boundary conditions. Starting from arbitrary initial conditions, if an iterative or psuedo-time marching algorithm is used to reach the steady-state for variable-density flows, then, because the transient terms are absent from Eq. 4, the mean pressure given by Eq. 4 is not correct until the steady-state is achieved. This is true even for constant-density cases unless the initial velocity field satisfies the continuity equation and Eq. 4 is solved in a coupled manner with the mean momentum equation which is not solved directly in the pdf method. A consequence is that the mean continuity equation

$$\frac{\partial}{\partial x_i}\langle\rho U_i\rangle = 0, \tag{5}$$

will not be satisfied. Given a field that does not satisfy Eq. 5, a velocity correction $\Delta\underline{U}$ can be obtained by

$$\Delta U_i = \frac{1}{\langle\rho\rangle}\frac{\partial\Phi}{\partial x_i}. \tag{6}$$

By requiring that $\{\langle\rho U_i\rangle + \langle\rho\rangle\Delta U_i\}$ be divergence free, we obtain a Poisson equation for Φ:

$$\frac{\partial^2\Phi}{\partial x_i \partial x_i} = -\frac{\partial}{\partial x_i}\langle\rho U_i\rangle. \tag{7}$$

These observations suggest the following basic algorithm: every so-many steps

1. solve Eq. 7 for Φ
2. add the velocity correction obtained from Eq. 6
3. solve Eq. 4 for $\langle P\rangle$

The spirit of the algorithm is similar to that of the SIMPLER algorithm used in conventional FV calculations (ref. 11). However, the solution strategy and the implementation in the pdf calculations are markedly different.

Boundary Conditions for $\langle P\rangle$

The mean pressure $\langle P\rangle$ is uniquely determined (to within an arbitrary constant) by Eqs. 3 and 4. That is, given $R_{ij} \equiv -\langle\rho U_i U_j\rangle$, $\langle P\rangle$ can be determined from the Poisson equation (Eq. 4) with the Neumann boundary conditions provided by Eq. 3:

$$\frac{\partial\langle P\rangle}{\partial n} = n_j \frac{\partial}{\partial x_i} R_{ij}, \tag{8}$$

where $\underline{n}$ is the outward pointing normal and n is a coordinate in that direction.

The numerical solution of a Poisson equation with Neumann conditions everywhere is somewhat perilous. Unless suitably treated, the coefficient matrix is singular; and a solution exists only if the boundary conditions are precisely consistent with the source. To avoid these difficulties, and to make the same boundary conditions applicable to Φ (see below), a Dirichlet condition is used at the outflow boundary. There the flow is approximately parallel (to the x-axis) and fully developed, and so the lateral momentum equation becomes (approximately)

$$\frac{\partial}{\partial y}(\langle\rho\rangle\widetilde{v''^2}) = -\frac{\partial\langle P\rangle}{\partial y}, \tag{9}$$

where v" denotes the lateral velocity fluctuation. Hence the Dirichlet condition used at the outflow boundary is

$$\langle P\rangle = -\langle\rho\rangle\,\widetilde{v''^2} + P_o \tag{10}$$

The arbitrary constant P_o in the pressure solution is chosen each time so as to match a known pressure at any given point in the solution domain.

Boundary Conditions for Φ

At walls, planes of symmetry, and inflow boundaries, the normal component of the velocity correction should be zero. Hence the Neumann condition

$$\frac{\partial \Phi}{\partial n} = 0, \tag{11}$$

is appropriate. At the outflow boundary, specifying the Dirichlet condition, $\Phi = 0$, results in there being no tangential velocity correction, but allows a correction to the normal velocity. This is necessary if the mass flow rate in differs from the mass flow rate out.

NUMERICAL SOLUTION

In the context that the Monte Carlo calculations are grid-free and the mean fields are represented by spline-fits, it is advantageous to solve the Poisson equations (Eqs. 4 and 7) in a way that is completely consistent with the spline representation of the mean fields. The following discussion is in the context of 2-D flows, but its extension to 3-D flows is straightforward.

Let $g(x,y)$ be any function within the solution domain. Then its spline representation is

$$g(x,y) = \sum_{\alpha=1}^{M} \sum_{\beta=1}^{N} G^{\alpha\beta} \, a_\alpha(x) b_\beta(y), \tag{12}$$

where $a_\alpha(x)(\alpha = 1, M)$ are the basis functions in x, $b_\beta(y)(\beta = 1, N)$ are those in y, and $G^{\alpha\beta}$ are the spline coefficients. Let $Q_i^{\alpha\beta}$ be the spline coefficients of $-\langle \rho U_i \rangle$, and let $R_{ij}^{\alpha\beta}$ be those of $-\langle \rho U_i U_j \rangle$. With the substitution of the appropriate spline representations, the Poisson equations (Eq. 7 and Eq. 4) become

$$\sum_\alpha \sum_\beta \Phi^{\alpha\beta} (a_\alpha'' b_\beta + a_\alpha b_\beta'') = \sum_\alpha \sum_\beta (Q_1^{\alpha\beta} a_\alpha' b_\beta + Q_2^{\alpha\beta} a_\alpha b_\beta'), \tag{13}$$

and

$$\sum_\alpha \sum_\beta P^{\alpha\beta} (a_\alpha'' b_\beta + a_\alpha b_\beta'') =$$

$$\sum_\alpha \sum_\beta (R_{11}^{\alpha\beta} a_\alpha'' b_\beta + 2R_{12}^{\alpha\beta} a_\alpha' b_\beta' + R_{22}^{\alpha\beta} a_\alpha b_\beta''), \tag{14}$$

where $\Phi^{\alpha\beta}$ and $P^{\alpha\beta}$ are the spline coefficients of Φ and $\langle P \rangle$, and primes denote differentiation.

Equations 13 and 14, along with the appropriate boundary conditions can each be represented by

$$\underline{\underline{A}} \cdot \underline{a} = \underline{b}, \tag{15}$$

where $\underline{a}$ is the solution (spline coefficients of $\langle P \rangle$ or Φ) and $\underline{\underline{A}}$ is the coefficient matrix. Since both $\langle P \rangle$ and Φ satisfy the same types of equations and boundary conditions, their coefficient matrices are identical. Further, since $\underline{\underline{A}}$ is a constant matrix (independent of R_{ij} and Q_i), its $\underline{\underline{LU}}$ decomposition need be performed once only, and then Eq. (15) can be solved many times by back substitution. The source vector $\underline{b}$ is different for $\langle P \rangle$ and Φ and changes from iteration to iteration as the steady-state is approached.

The structure of matrix $\underline{A}$ is shown in Figure 1, with x's indicating the only entries in $\underline{A}$ when cubic B-splines (refs. 1, 14) are used. A special band solver, which exploits the structure of the matrix $\underline{A}$ was developed to minimize the storage and computational requirements. The solver uses LU decomposition and Gaussian elimination with partial pivoting. As pointed out earlier, the LU decomposition is performed only once and the Poisson equation is solved repeatedly by back substitution. The work to perform back substitution is of order $MN(4M + 5)$ operations: just 34,000 for $N = M = 20$ used typically ($M = N = 21$ in the present study).

The majority of the work is done in calculating $\underline{b}$. This involves forming splines for $\langle \rho U_i \rangle$ and $\langle \rho U_i U_j \rangle$ with appropriate boundary conditions. These splines need to be very accurate especially since their derivatives and second derivatives are to be evaluated (see Eqs. 4 and 7). Also, the boundary conditions used in forming these splines have a significant influence on the solution of the Poisson equations. Both the issues need careful consideration.

In general, the splines in the pdf calculations are formed using the cross-validation procedure (refs. 1, 14), by which splines are fit to two independent sets of sums (or samples) from each of the spatial bins such that the resulting spline is the best fit for both sets of samples. This procedure considerably reduces the error in the spline fit with respect to the actual function, compared to the error with a simple least-square spline fit with a single set of samples. For spline-fits

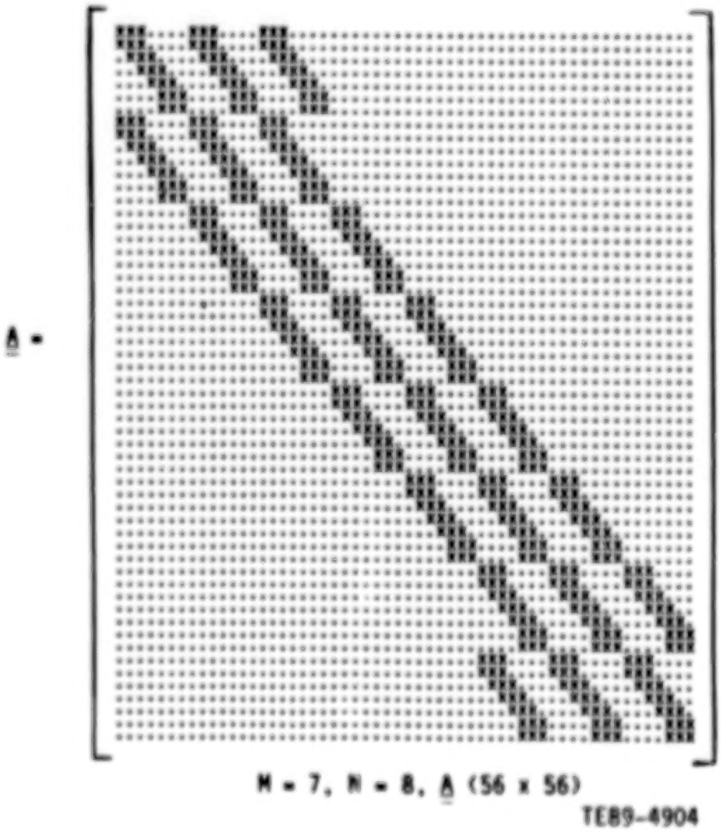

Figure 1. Structure of the coefficient matrix $\underline{A}$ ($MN \times MN$) for sample values of M and N. There are 5 bands, each with a width of 5 and separated by a width of $M - 5$. The total bandwidth is $4M + 5$.

Table 1: Boundary conditions for splines needed to evaluate $\underline{b}$

Quantity q	Inflow boundary normal to x	Outflow boundary normal to x	Wall normal to x	Wall normal to y
$\langle U \rangle$	$q_x = 0^*$	$q_x = 0$	$q = 0$	—**
$\langle V \rangle$	$q = 0$	$q = 0$	—	$q = 0$
$\langle U^2 \rangle$	$q_x = 0$	$q_x = 0$	$q_x = 0$	$q_y = 0$
$\langle U^2 \rangle_x$	$q = 0$	$q = 0$	$q = 0$	$q_y = 0$
$\langle V^2 \rangle$	$q_x = 0$	$q_x = 0$	$q_x = 0$	$q_y = 0$
$\langle V^2 \rangle_y$	$q_x = 0$	$q_x = 0$	$q_x = 0$	$q = 0$
$\langle UV \rangle$	$q_x = 0$	$q_x = 0$	$q_x = 0$	$q_y = 0$
$\langle UV \rangle_x$	$q = 0$	$q = 0$	$q = 0$	$q_y = 0$

* subscripts x and y denote differentiation with respect to x and y, respectively

**— indicates that no boundary condition is specified

in two-dimensions, four independent samples are needed. However, even with cross-validation, although the first derivatives are acceptable, the second derivatives evaluated from the cubic spline fits can have errors significant enough to adversely affect the solution of Eq. 4 and hence the convergence of the whole pressure algorithm. Hence for Eq. 4, splines are fit for Rij as well as to its appropriate first derivative from which the required second derivative is evaluated by a single differentiation. From the same raw sums for Rij four different cross-validated splines are formed for Rij using four different sets of values for M and N (the number of basis functions). The first derivatives evaluated from each of the four splines form the samples, although not entirely independent, for the spline-fit for the first derivative. This procedure significantly reduces the errors in the second derivatives evaluated and results in a stable solution of Eq. 4. The four splines were formed in the present study with values of M (=N) equal to 17, 19, 21 and 25. It is also necessary to specify a consistent set of boundary conditions for the spline fits. The quantities splined for solving Eqs. 4 and 7 and the boundary conditions used are listed in Table 1. Note that the density has been assumed constant. The table should be applicable to variable-density flows also, with the conventional means replaced by Favre means. Additionally, boundary conditions for $\langle \rho \rangle$ will be needed—a zero normal-gradient condition at all boundaries is suggested.

IMPLEMENTATION

The development and the implementation of the algorithm to solve for the pressure field within the Monte Carlo solution algorithm were evolutionary processes. Primary concerns were to obtain an accurate pressure solution and also keep the computational times low. The algorithm can be summarized as follows:

1. form the matrix $\underline{A}$ and perform its $\underline{LU}$ decomposition
2. initially set $\langle P\rangle = 0$ everywhere
3. march the pdf calculations by a step in psuedo-time
4. perform velocity correction; i.e.
   - o form splines of $\langle\rho\rangle$ and $\langle\rho U_i\rangle$
   - o solve Eq. 7 by back substitution for Φ
   - o correct particle velocities by Eq. 6
5. on the first step and subsequently, every S steps update pressure; i.e. solve for the pressure correction $\Delta\langle P\rangle$ from Eq. 4

$$\nabla^2 \Delta\langle P\rangle = \frac{\partial^2 R_{ij}}{\partial x_i \partial x_j} - \nabla^2 \langle P\rangle^{old}, \tag{16}$$

   and reset the mean pressure by

$$\langle P\rangle^{new} = \langle P\rangle^{old} + r\Delta\langle P\rangle, \tag{17}$$

   where r is a relaxation parameter.

6. if steady-state has not been reached, go to step 3
7. stop

Two parameters S and r related to pressure updates, are introduced. For the case studied, neither parameter influenced the results significantly. The pressure updates are considerably more expensive than velocity corrections. The pressure updates need not be performed frequently since the velocity corrections, which cause a similar effect as the pressure corrections, are made every step. Also, the velocity corrections are quite small from step to step (especially if continuity is satisfied initially) so that the pressure updates are not necessary every step. It is better to update the pressure after the velocity field has evolved appreciably, say every 10 to 20 steps. For the present study, values between 0.5 to 0.8 were used for the relaxation factor without any apparent effect on the results or the number of steps needed for convergence.

Although convergence is not difficult to achieve, it is difficult to monitor. Several parameters were considered as indicators of convergence. But, due to the stochastic nature of the calculations and due to the fact that the solution evolves slowly from step to step, a robust and reliable parameter has not been found. In the present study; the convergence was inferred by comparing the results at the 200th step with those at the 220th and the 250th step and concluding that the results were unchanged within statistical errors.

TEST CASE AND INITIAL CONDITIONS

The pressure algorithm and the pdf calculations were tested for the flow past a backward facing step with data from reference 13. The schematic of the flow is shown in Figure 2. The step height is H and the centerline mean axial velocity in the channel is U_{ref}. The fluid used in the experiments was water, and the Reynolds number based on H and U_{ref} was approximately 12,000.

The inlet velocity pdf was prescribed to be Gaussian for each of the velocity components with the means and variances being those of fully developed turbulent

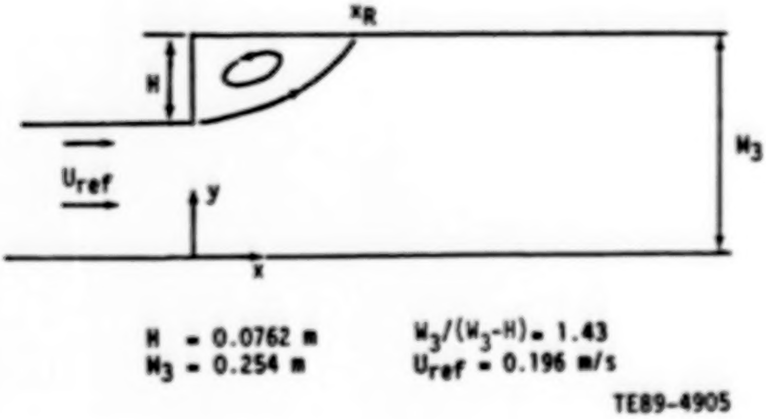

Figure 2. Schematic of the flow considered. Backward-facing step studied experimentally by Pronchick and Kline (1983).

flow in the inlet channel as calculated by the k-ε model. The inlet turbulent kinetic energy is distributed into the three components according to $k = \langle u'^2 \rangle = 2\langle v'^2 \rangle = 2\langle w'^2 \rangle$. The turbulence levels at the inlet have little effect on the final results since most of the shear and turbulence production occur in the recirculation zone within the solution domain. The initial pdf in the solution domain was set equal to the inlet pdf and the initial mean pressure was zero everywhere. The solution domain extended from the step (x/H = 0) to x/H = 15 and between the two walls in the y-direction.

The turbulent frequency ($\omega = \varepsilon/k$, where ε is the dissipation rate of k) is calculated at each step from the current value of k by

$$\omega = k^{0.5}/\ell, \tag{18}$$

where the turbulent length scale ℓ is supplied from the k-ε solution of ref. 8 (see Eq. 19) and is held constant throughout the calculations:

$$\ell = k^{1.5}/\varepsilon. \tag{19}$$

The choice of supplying ℓ was preferred over the choices of supplying ω or ε from the k-ε solution since the profiles of ℓ were nearly uniform across the flow (approximately 0.2 W_3) except near the walls where the values decrease. This way, the ω used in the calculations (Eq. 18) would be more consistent with the current values of k. As mentioned earlier, work is in progress (ref. 12) that deals with the determination of ω within the pdf calculations.

RESULTS AND DISCUSSION

The number of particles used in the simulation was 60,000. The number of spatial bins used was 1500 (50 in x X 30 in y). The computations were performed for 250 steps with pressure updates every 20 steps and the pressure relaxation factor of 0.8. The time interval for each step was 0.3 H/U_{ref}. This time interval was less than one-tenth of the turbulent time scale (inverse of ω) over most of the flow domain except for small regions near the wall where it was between one-fifth and one-tenth of the turbulent time scale. The calculations reached a steady-state around the 200th step. As noted earlier, a more precise way of determining convergence needs to be identified.

The final results shown here (except for the mean pressure) are calculated from spline-fits to sums formed over 50 steps after steady-state has been reached. This contributes significantly to reducing the statistical error in the splined results especially for the triple and higher correlations which are more prone to such error. This procedure, as an alternative to increasing the number of particles in the simulation, allows the computer storage requirement to be kept at a modest level.

The computed reattachment length of 6.65H is in good agreement with the experimentally observed reattachment length (x_{RE}) of 6.75H. The results for mean velocities and various turbulent quantities are shown in Figures 3 - 11. The results are shown for different axial stations normalized with respect to the experimental reattachment length:

$$x^* = (x - x_{RE}) / x_{RE} \tag{20}$$

Overall, the results are in excellent agreement with data both in magnitude and in qualitative trends. It is noteworthy that the turbulence quantities, especially the third moments (which cannot be calculated with the k-ε model, and are modeled in second-moment closures) are in good agreement with data. The slight disagreement between some of the computed turbulent quantities and the data in the vicinity of y/H=2.0 could be due to the inadequacy of the prescription of the turbulent frequency in the present study. It is expected that the use of the stochastic dissipation model (ref. 12) will remedy this deficiency.

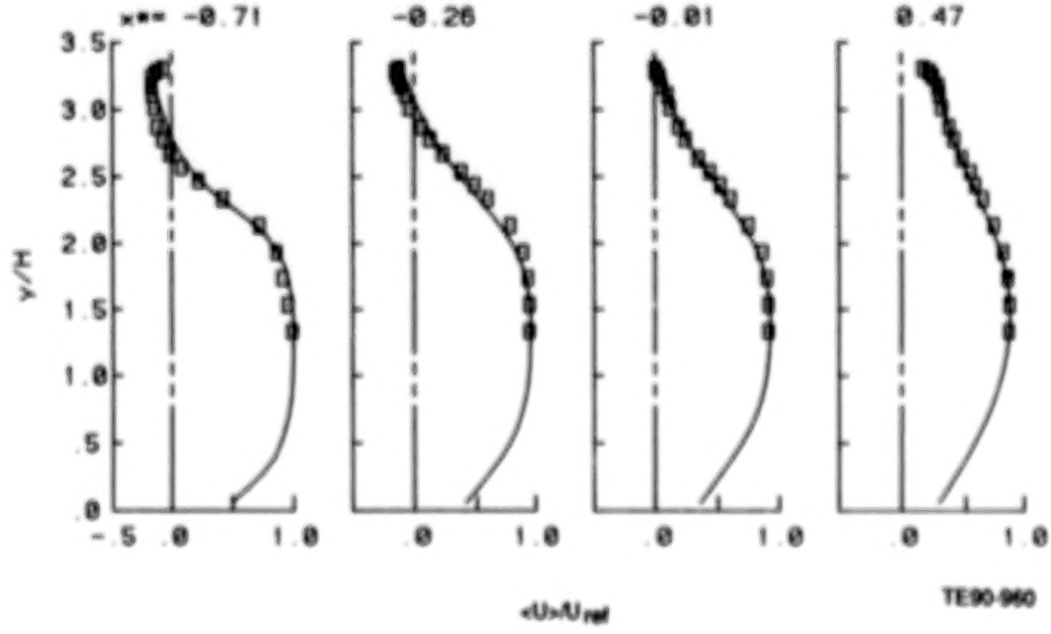

Figure 3. Computed mean streamwise velocity profiles (lines) compared against data (symbols).

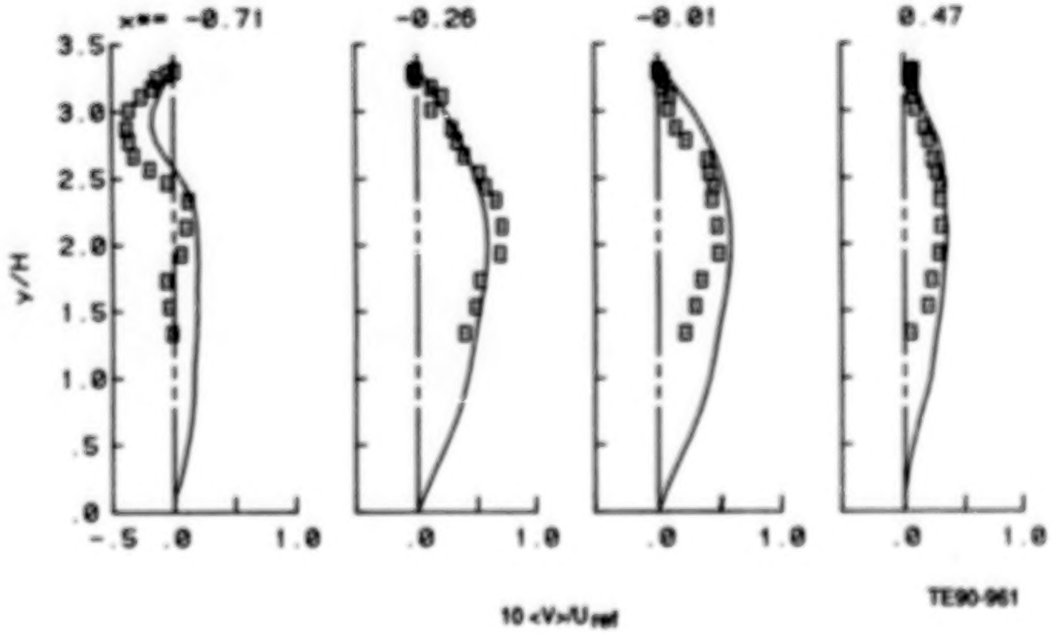

Figure 4. Computed mean transverse velocity profiles (lines) compared against data (symbols).

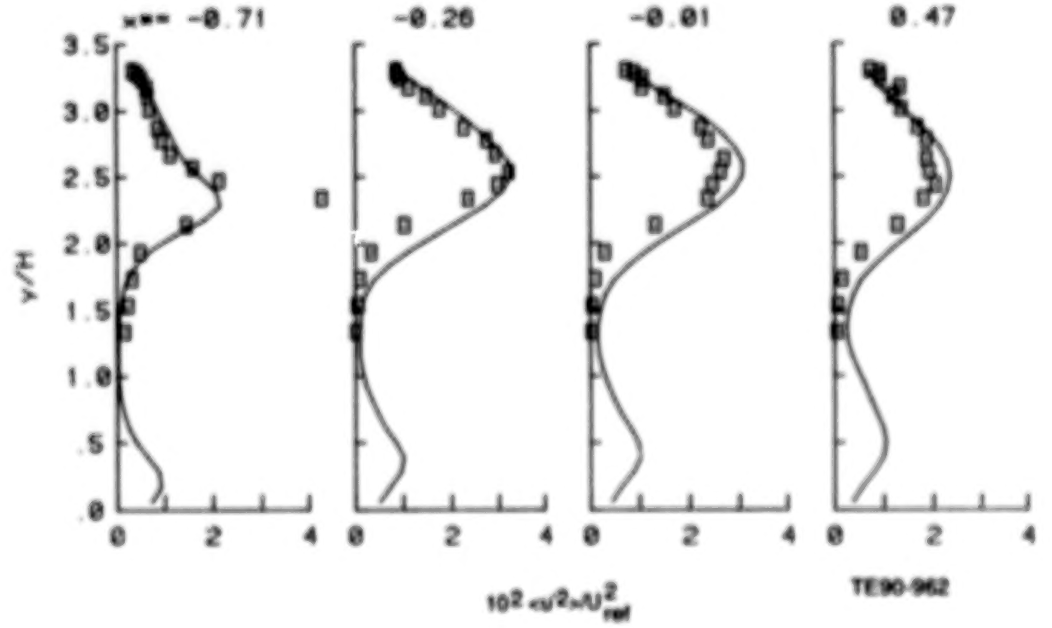

Figure 5. Computed streamwise velocity variance profiles (lines) compared against data (symbols).

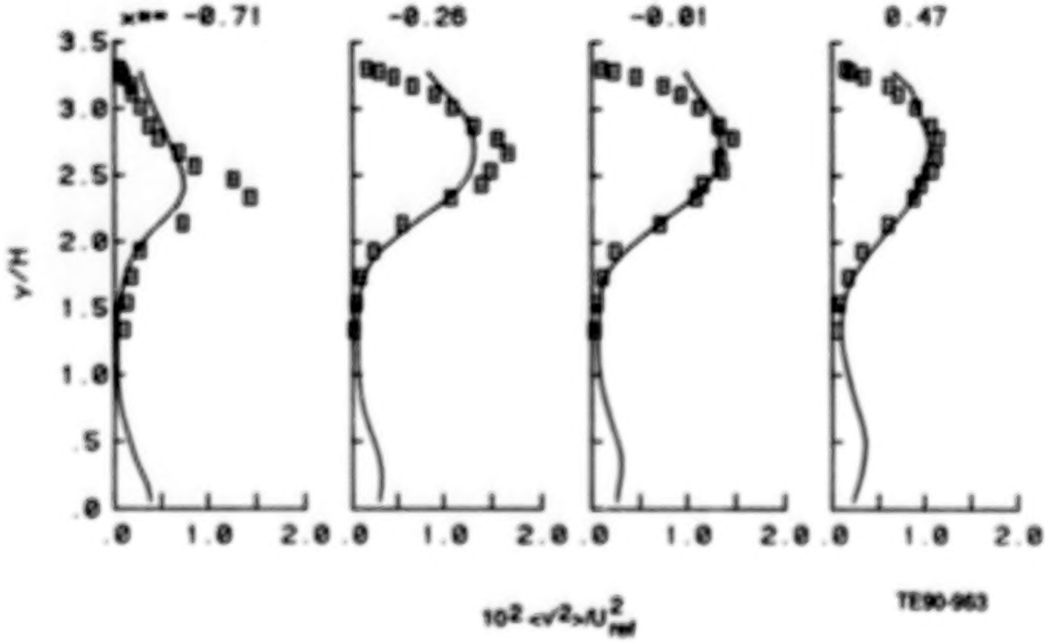

Figure 6. Computed transverse velocity variance profiles (lines) compared against data (symbols).

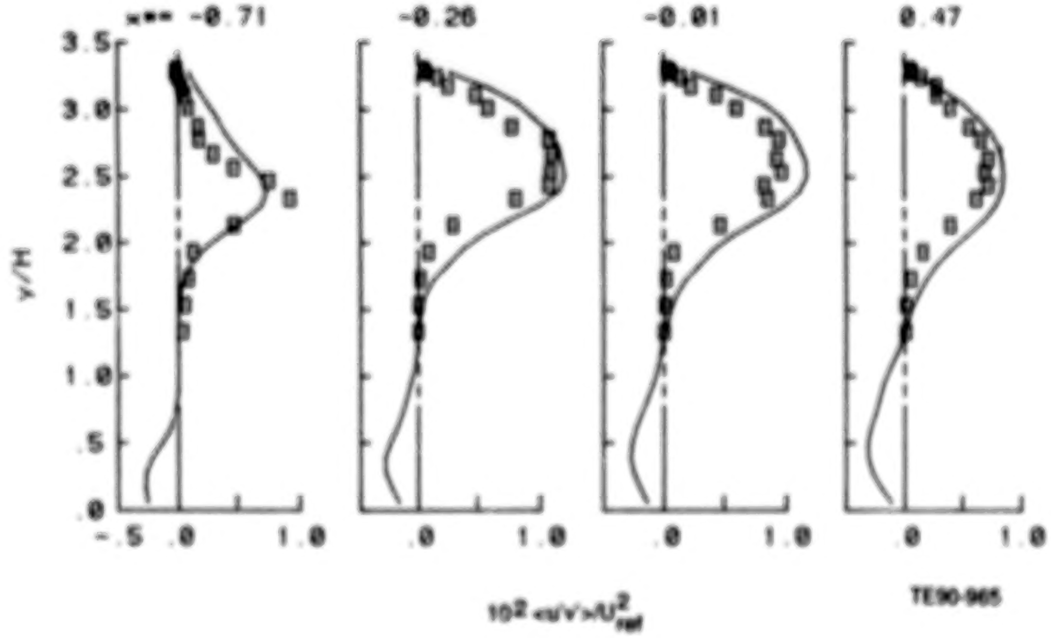

Figure 7. Computed shear stress profiles (lines) compared against data (symbols).

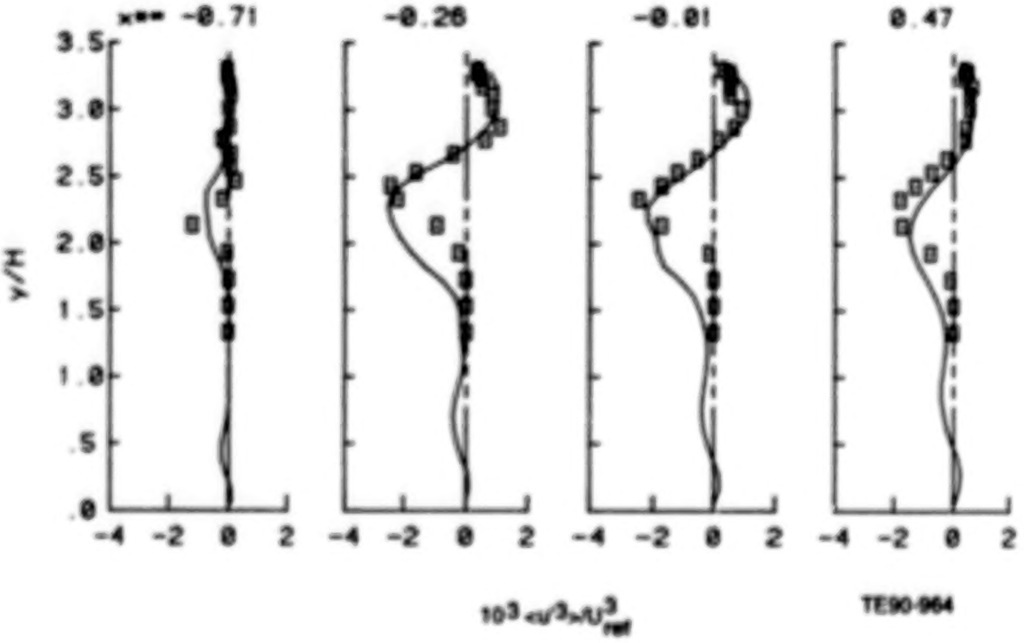

Figure 8. Computed $\langle u'^3 \rangle$ profiles (lines) compared against data (symbols).

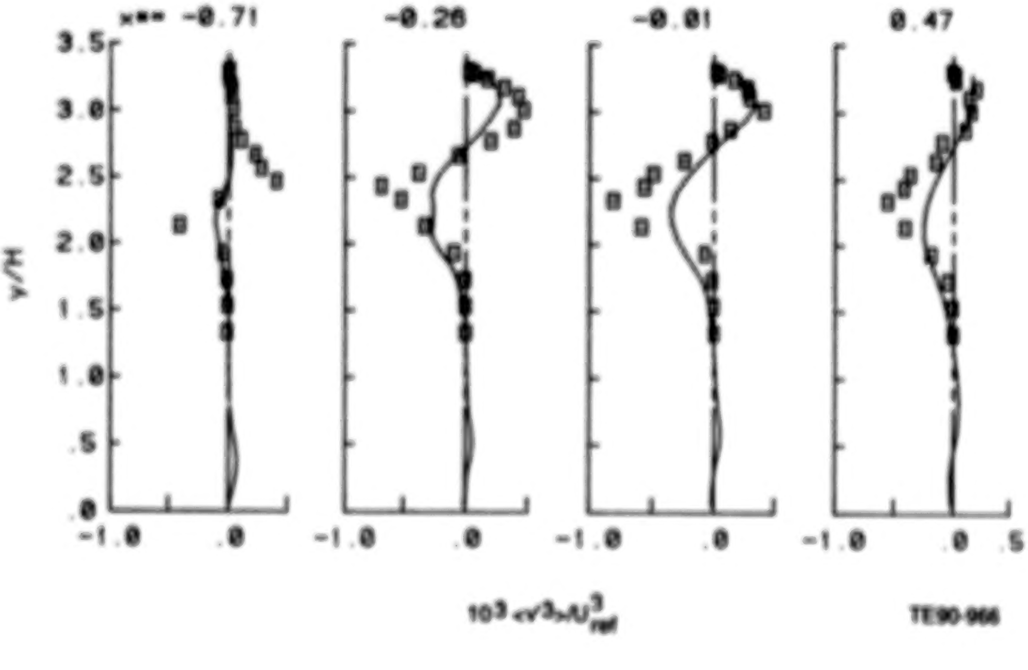

Figure 9. Computed $\langle v'^3 \rangle$ profiles (lines) compared against data (symbols).

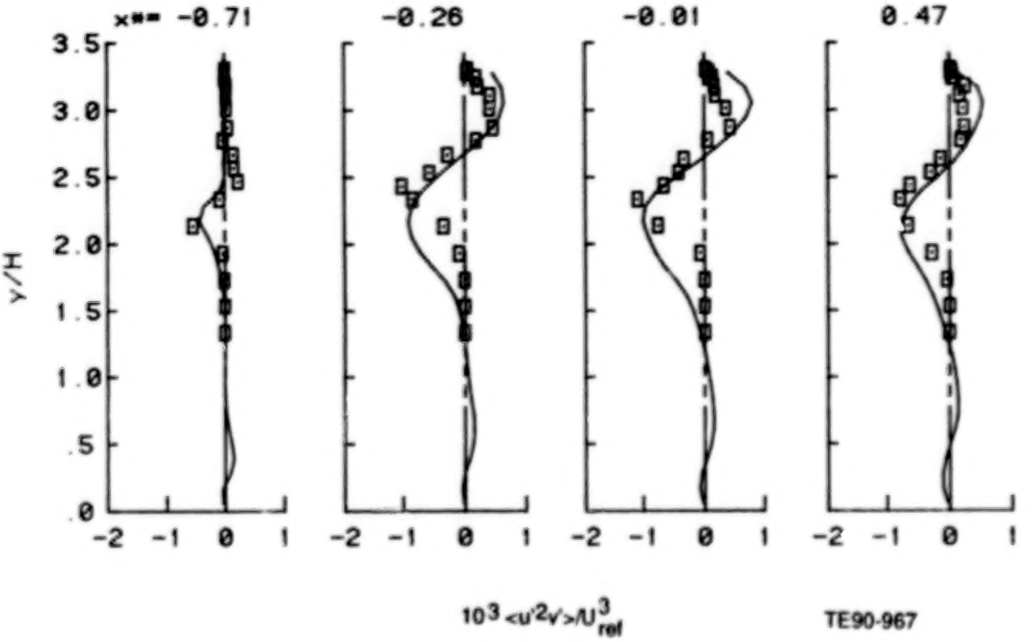

Figure 10. Computed $\langle u'^2 v'\rangle$ profiles (lines) compared against data (symbols).

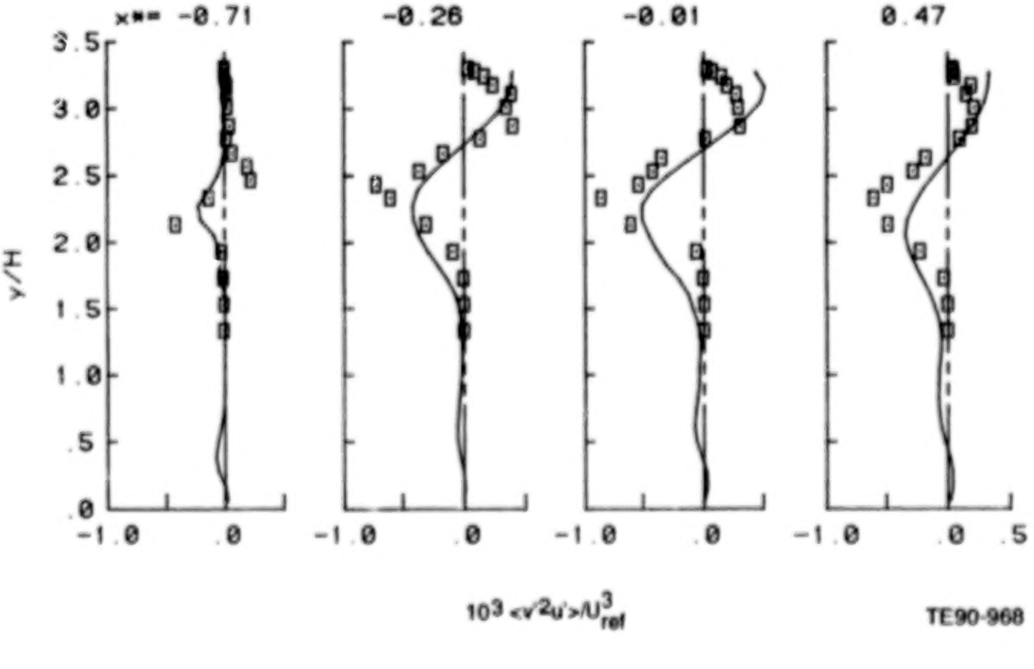

Figure 11. Computed $\langle v'^2 u'\rangle$ profiles (lines) compared against data (symbols)

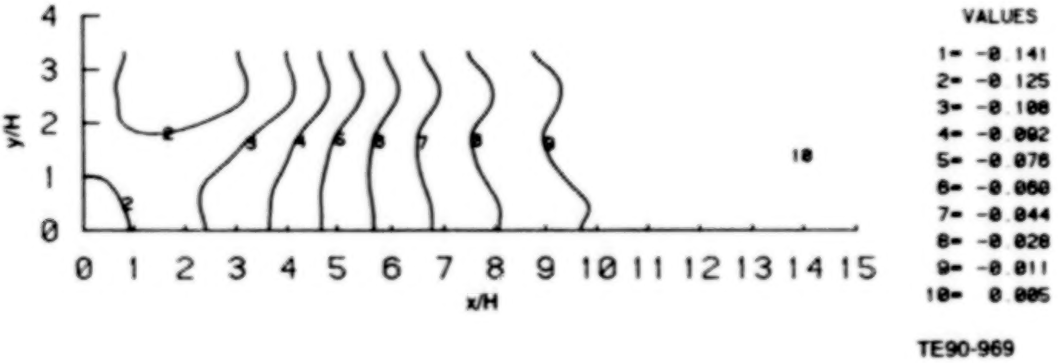

Figure 12. Computed contours of mean pressure (normalized by ρU_{ref}^2).

The contours of the calculated mean pressures are shown in Figure 12. The value at the right bottom corner of the solution domain is held fixed at zero in the calculations. The magnitudes and shapes of the contours are comparable to those obtained from previous calculations with the k-ε model and the combined FV/MC pdf method (ref. 8). This fact, in conjunction with the accurate prediction of the mean velocity field, shows that the pressure algorithm is functioning satisfactorily.

Approximately 1.3 megawords of storage was required for the computations. The total CPU time required for the computations (250 steps) on a CRAY XMP-22 was approximately 11 minutes. This reflects an order of magnitude reduction over the estimated time it would have taken with a simple straightforward implementation of the algorithm. Nearly 55 percent of the computational time is spent in computations related to the pressure algorithm, namely forming sums and splines for pressure updates and velocity corrections, in spite of limiting the frequency of pressure updates and improving the efficiency of the spline-fitting routines. However, the total computational time of approximately 11 minutes and the storage required are still very modest for pdf calculations of an elliptic flow.

CONCLUSIONS

An algorithm to determine the mean pressure in steady-state constant or variable-density elliptic flow calculations with the pdf method has been developed and implemented economically. The algorithm and the pdf calculations have been tested for a sample recirculating flow; namely the flow behind a backward-facing step.

The computed results are in excellent agreement with data for the mean velocity field and various turbulence quantities including triple corrections. The computed reattachment length is in good agreement with the experimental value. These comparisons have served to validate the pressure algorithm and its implementation.

The pressure algorithm will be validated for variable-density elliptic flows as well. Further, with the inclusion of the stochastic dissipation model (ref. 12), fully independent pdf calculations of complex elliptic flows will be possible.

ACKNOWLEDGMENT

This work is supported in part by the U.S. Air Force Wright Aeronautical Laboratory under contract No. F33615-87-C-2821 titled "Combustor Design Model Evaluation". Dr. W. M. Roquemore and Mr. D. Shouse are the Air Force project scientists.

REFERENCES

1. Pope, S. B. "PDF Methods for Turbulent Reactive Flows," Progress in Energy and Combustion Science., Vol 11, pp 119-192, 1985.
2. Anand, M. S. and Pope, S. B., "Diffusion Behind a Line in Grid Turbulence," Turbulent Shear Flows 4, eds. L. J. S. Bradbury, et al., Springer-Verlag, pp 46-61, 1985.
3. Haworth, D. C. and Pope, S.B., "A PDF Modeling Study of Self-Similar Turbulent Free Shear Flows," Physics of Fluids, Vol 30, pp 1026-1044, 1987.
4. Anand, M.S., Pope, S.B., "Calculations of Premixed Turbulent Flames by PDF Methods," Combustion and Flame, Vol 67, No. 2, pp 127-142, 1987.
5. Pope, S.B., and Correa S. M., "Joint PDF Calculations of a Non-equilibrium Turbulent Diffusion Flame," Twenty-First Symposium (International) on Combustion, The Combustion Institute, Pittsburgh, pp 1341-1348, 1986.
6. Pope, S. B., and Cheng, W. K., "Statistical Calculations of Spherical Turbulent Flames," Twenty-First Symposium (International) on Combustion, The Combustion Institute, Pittsburgh, pp 1473-1481, 1986.
7. Masri, A. R., and Pope, S. B., "PDF Calculations of Piloted Turbulent Nonpremixed Flames of Methane," Combustion and Flame, to be published, 1990.
8. Anand M. S., Pope, S. B., and Mongia, H. C., "A PDF Method for Turbulent Recirculating Flows," U. S.-France Joint Workshop on Turbulent Reactive Flows, Rouen, France, 6-10 July 1987. Also in Turbulent Reactive Flow, Lecture Notes in Engineering, 40, Springer-Verlag, pp 672-693, 1989.
9. Haworth, D. C., and El Tahry, S. H., "Application of PDF Method to In-Cylinder Flows in Reciprocating Engines," in Seventh Symposium on Turbulent Shear Flows, pp 13.1.1, Stanford University, 1989.
10. Haworth, D. C., and El Tahry, S. H., General Motors Research Laboratories, Report GMR-6844, 1989.
11. Patankar, S. V., Numerical Heat Transfer and Fluid Flow, Hemisphere, 1980.
12. Pope, S. B., and Chen, Y. L., "The Velocity-Dissipation PDF Model for Turbulent Flows," submitted to Physics of Fluids A, December 1989.
13. Pronchick, S. W., and Kline, S. J., "An Experimental Investigation of the Structure of Turbulent Reattaching flow Behind a Backward-Facing Step," Report MD-42, Stanford University, Stanford, California, 1983.
14. de Boor, C., A Practical Guide to Splines, Springer-Verlag, New York, 1978.

Implicit Solution of Three-Dimensional Internal Turbulent Flows

V. Michelassi*
Institute for Computational Mechanics in Propulsion
NASA Lewis Research Center
Cleveland, Ohio

M.-S. Liou and L.A. Povinelli
National Aeronautics and Space Administration
Lewis Research Center
Cleveland, Ohio

and

F. Martelli
University of Florence
Florence, Italy

ABSTRACT

The scalar form of the approximate factorization method was used to develop a new code for the solution of three-dimensional internal laminar and turbulent compressible flows. The Navier-Stokes equations in their Reynolds-averaged form were iterated in time until a steady solution was reached. Evidence was given to the implicit and explicit artificial damping schemes that proved to be particularly efficient in speeding up convergence and enhancing the algorithm robustness. A conservative treatment of these terms at the domain boundaries was proposed in order to avoid undesired mass and/or momentum artificial fluxes. Turbulence effects were accounted for by the zero-equation Baldwin-Lomax turbulence model and the q-ω two-equation model. For the first, an investigation on the model behavior in case of multiple boundaries was performed. The flow in a developing S-duct was then solved in laminar regime at a Reynolds number (Re) of 790 and in a turbulent regime at Re=40,000 by using the Baldwin-Lomax model. The Stanitz elbow was then solved by using an inviscid version of the same code at $M_{inlet}=0.4$. Grid dependence and convergence rate were investigated showing that for this solver the implicit damping scheme may play a critical role for convergence characteristics. The same flow at $Re=2.5 \cdot 10^6$ was solved with the Baldwin-Lomax and the q-ω models. Both approaches showed satisfactory agreement with experiments, although the q-ω model was slightly more accurate.

INTRODUCTION

With the advent of more and more powerful supercomputers, the numerical solution of three-dimensional turbulent flows became possible (ref. 1). Although it is well known that lower order turbulence closures fail to reproduce secondary motions of Prandtl's second kind (turbulence driven), they normally succeed in predicting secondary flows of the first kind (pressure driven). Therefore, for many complex configurations it has been possible to obtain fairly accurate results with zero- and two-equation turbulence models (ref. 2) with a reasonable prediction of pressure driven secondary flows.

For three-dimensional blade-passage flows, a correct prediction of the wake behavior was obtained by Yokota (ref. 3) by means of the standard high-Reynolds-number form of the k-ϵ two-equation model with the wall function approach. However, the zero-equation model implemented in reference 3 did not give a satisfactory depiction of the flow in the wake region. For the prediction of blade pressure distribution, the

---

*On leave from the University of Florence, Italy.

Work funded by Space Act Agreement C99066G.

Baldwin-Lomax (ref. 4) zero-equation turbulence model was found to give accurate results in several flow configurations (ref. 5) despite the low convergence rate. For incompressible internal flows with no separation, good results were obtained by Towne (ref. 6) with a zero-equation turbulence model and a parabolized Navier-Stokes solver. Still, for practical flow configurations, quite long computing times are necessary mainly because of the large number of points usually required for a detailed description of the flow field. Moreover, the nonlinearities associated with nearly all turbulence models can play a significant role in slowing down the convergence rate to the steady state solution. This behavior occurs in both the implicit and explicit flow solvers and is intrinsic to the turbulence models, zero or two-equation.

In two dimensions, a wide variety of flow conditions have been accurately solved by means of low-Reynolds-number forms of the k-ϵ model in which the effect of laminar viscosity is explicitly accounted for (refs. 7 to 9). In nearly all of the flow conditions investigated, these forms proved to be more accurate than the standard high-Re formulation, provided that a sufficient number of grid points were located inside the viscous and buffer layers; in fact, secondary motions and losses are mainly driven by what happens close to walls so that a correct description of this flow region is crucial for an accurate simulation of the flow pattern. Rodi (ref. 9) found that the low Reynolds number forms of the k-ϵ model could predict secondary flows that are normally lost with the high Reynolds number form. Unfortunately, the first author (ref. 7) found that some of these forms were extremely stiff from a numerical point of view. The stiffness was mainly caused by the low-Reynolds-number effect terms in which exponential functions are introduced to model the wall effects.

From this standpoint, it appeared worthwhile to investigate some features of turbulence models for internal turbulent flows by using an implicit algorithm. Since complex flow patterns, such as separation and dominant viscous effects, are expected in internal flows, the implicit approach was selected to increase the robustness and convergence rate of the numerical procedure when zero and two-equation turbulence models are used.

DESCRIPTION OF THE ALGORITHM

Navier-Stokes Equations

The Boussinesq hypothesis allows the turbulent shear stresses to be related to the mean strains via the so-called eddy viscosity so that, under this assumption, the three-dimensional Reynolds-averaged compressible Navier-Stokes (N-S) equations can be written in divergence form and, subsequently, be transformed from the Cartesian coordinate system (x,y,z) to the generalized curvilinear coordinate system (ξ,η,ζ). The resulting set of equations can be written in vector form as follows:

$$\frac{\partial \bar{Q}}{\partial t} + \frac{\partial \bar{E}}{\partial \xi} + \frac{\partial \bar{F}}{\partial \eta} + \frac{\partial \bar{G}}{\partial \zeta} = \frac{\partial \bar{E}_v}{\partial \xi} + \frac{\partial \bar{F}_v}{\partial \eta} + \frac{\partial \bar{G}_v}{\partial \zeta}$$

where $\bar{Q}$ is the vector of unknowns; $\bar{E}$, $\bar{F}$, and $\bar{G}$ are the flux vectors of the convective terms; $\bar{E}_v$, $\bar{F}_v$, and $\bar{G}_v$ are the flux vectors of the diffusive terms, the complete definition of which can be found in reference 19.

In the set of equations, ρ is the fluid density, p is the static pressure, e is the total energy per unit volume, a is the sound speed, and (U,V,W) are the Cartesian components of the velocity vector. According to the Boussinesq assumption, the diffusion coefficients for momentum and energy are defined as follows:

$$\mu_{eff} = \mu_l + \mu_t \quad \text{and} \quad \mu_h = \frac{\mu_l}{Pr_l} + \frac{\mu_t}{Pr_t}$$

in which μ_l is the laminar viscosity, which was considered to be independent of the static temperature, and μ_t is the turbulent viscosity obtained from the turbulence model. In this set of calculations the turbulent

Prandtl number Pr_t was set equal to 0.90 and the laminar Prandtl number Pr_l was 0.72.

Discretization

The flux vectors are discretized by using centered finite differences. The metrics are usually obtained from a chain rule expansion of x_ξ, x_η, x_ζ, y_ξ, y_η, y_ζ, z_ξ, z_η, and z_ζ. When the centered discretization is used for the metrics, it can be shown that in three dimensions the metric invariants are not satisfied (ref. 10). This may result in a large discretization error. However, it is possible to satisfy the invariants by a simple averaging technique that gives metrics that are similar to those computed by a finite volume method. For example, ξ_x is computed as follows

$$\xi_x = J\left(\chi_\zeta\left(\frac{\partial y}{\partial \eta}\right) \chi_\eta\left(\frac{\partial z}{\partial \zeta}\right) - \chi_\eta\left(\frac{\partial y}{\partial \zeta}\right) \chi_\zeta\left(\frac{\partial z}{\partial \eta}\right)\right)$$

in which J is the Jacobian of the coordinate transformation and χ is a central average operator. This averaging process was found to ensure better mass conservation properties in the present calculations expecially for highly stretched grids.

Approximate Factorization; Scalar Form

The approximate factorization method first proposed by Beam and Warming (ref. 11) splits an n-dimensional operator into the product of n one-dimensional operators. This technique provides a strong link between the equations insofar as they are solved fully coupled. The main drawback of this method lies in the necessity of a time-consuming block tridiagonal or pentadiagonal matrix inversion. This problem becomes more evident in three dimensions where the coupled solution yields a 5x5 block tridiagonal matrix. In order to make this algorithm more efficient and still maintain its strong implicit nature Pulliam (refs. 10 and 12) proposed a scalar form of the approximate factorization. The form of the standard algorithm in three dimensions can be written as follows:

$$[\, I+\Theta\Delta t\left(\delta_\xi A - \delta_\xi^2 A_v\right)] \bullet [\, I+\Theta\Delta t\left(\delta_\eta B - \delta_\eta^2 B_v\right)] \bullet [\, I+\Theta\Delta t\left(\delta_\zeta C - \delta_\zeta^2 C_v\right)] \bullet \Delta Q = RHS \tag{1}$$

in which I is the identity matrix; θ is a parameter that allows the explicit-implicit nature of the space operator to be weighted (in the present calculations, since the steady state solution was sought, $\theta=1$ was used which gave first-order accuracy in time); δ is a centered difference operator; Δt is the time step; $\Delta Q=Q^{n+1}-Q^n$; $Q=J\,\bar{Q}$; A, B, and C are the convective Jacobians; A_v, B_v, and C_v are the diffusive Jacobians in the three directions ξ, η, and ζ; and RHS represents the convective and diffusive fluxes and is defined as

$$RHS=\Delta t\left(-\frac{\partial \bar{E}}{\partial \xi} - \frac{\partial \bar{F}}{\partial \eta} - \frac{\partial \bar{G}}{\partial \zeta} + \frac{\partial \bar{E}_v}{\partial \xi} + \frac{\partial \bar{F}_v}{\partial \eta} + \frac{\partial \bar{G}_v}{\partial \zeta}\right)$$

The Jacobian matrices A, B, C, A_v, B_v, and C_v, which can be found in Pulliam (ref. 10), are full and require a general inversion process. Pulliam and Chaussee (ref. 12) proposed a more efficient procedure by making some simplifications. First, the hyperbolic property of the convective Jacobians allows the diagonalization as

$$A = T_\xi \Lambda_\xi T_\xi^{-1} \; ; \quad B = T_\eta \Lambda_\eta T_\eta^{-1} \; ; \quad C = T_\zeta \Lambda_\zeta T_\zeta^{-1} \tag{2}$$

in which T are the eigenvector matrices, defined in reference 12. The eigenvalues of the Jacobians in three dimensions, Λ, are given by

$$\begin{aligned} \Lambda_\xi &= D\left[U,\ U,\ U,\ U+a\sqrt{\xi_x{}^2+\xi_y{}^2+\xi_z{}^2},U-a\sqrt{\xi_x{}^2+\xi_y{}^2+\xi_z{}^2}\right] \\ \Lambda_\eta &= D\left[V,\ V,\ V,\ V+a\sqrt{\eta_x{}^2+\eta_y{}^2+\eta_z{}^2},V-a\sqrt{\eta_x{}^2+\eta_y{}^2+\eta_z{}^2}\right] \\ \Lambda_\zeta &= D\left[W,\ W,\ W,\ W+a\sqrt{\zeta_x{}^2+\zeta_y{}^2+\zeta_z{}^2},W-a\sqrt{\zeta_x{}^2+\zeta_y{}^2+\zeta_z{}^2}\right] \end{aligned} \tag{3}$$

where U, V, and W are the unscaled contravariant velocities and D stands for main diagonal only. It is now possible to introduce equations (2) into equation (1) with eigenvalues defined in equation (3). Doing so, it is impossible to diagonalize both the convective and diffusive Jacobians since they have a totally different set of eigenvectors. Neglecting the diffusive Jacobians and assuming the eigenmatrix to be locally constant, equation (1) can be rewritten as

$$T_\xi \bullet [I+\Theta\Delta t(\delta_\xi\Lambda_\xi)] \bullet N \bullet [I+\Theta\Delta t(\delta_\eta\Lambda_\eta)] \bullet P \bullet [I+\Theta\Delta t(\delta_\zeta\Lambda_\zeta)] \bullet T_\zeta^{-1} \bullet \Delta Q = RHS \tag{4}$$

in which the two matrices, $N=T_\xi^{-1}\,T_\eta$ and $P=T_\eta^{-1}\,T_\zeta$ have the nice property of being solution independent so that they can be computed only once (ref. 12). Obviously, equation (4) is only an approximation of the full form but it requires only a scalar tridiagonal or pentadiagonal matrix inversion since the Λ matrices are diagonal; this implies a reduction of nearly 50% of the operations required by the standard algorithm. We note that, even though the interior domain is solved implicitly, the boundary conditions are imposed in a fully explicit manner. This was done by setting $\Delta Q=0$ at the domain boundaries during the implicit sweeps.

Since the steady state solution is sought, the following local time-stepping formula, based on the approximate constant CFL condition is introduced, in which the contribution of the diffusive terms is accounted for

$$\begin{aligned} \Delta t_\xi &= |U| + a\sqrt{\xi_x^2+\xi_y^2+\xi_z^2} + \mu_{eff}\,Re^{-1}\,(\xi_x^2+\xi_y^2+\xi_z^2) \\ \Delta t_\eta &= |V| + a\sqrt{\eta_x^2+\eta_y^2+\eta_z^2} + \mu_{eff}\,Re^{-1}\,(\eta_x^2+\eta_y^2+\eta_z^2) \\ \Delta t_\zeta &= |W| + a\sqrt{\zeta_x^2+\zeta_y^2+\zeta_z^2} + \mu_{eff}\,Re^{-1}\,(\zeta_x^2+\zeta_y^2+\zeta_z^2) \end{aligned}$$

$$\Delta t = \frac{CFL}{\Delta t_\xi + \Delta t_\eta + \Delta t_\zeta}$$

Implicit Treatment of Diffusive Terms

For inviscid solutions, the only assumption done to derive the algorithm is that the differentiation of the eigenmatrices is neglected in equation (4). In addition, when solving the N-S equations, the Jacobians of the diffusive terms are normally assumed to be negligible. This does not cause any stability or convergence problems for external flows where the diffusion dominated region is small and restricted to a limited part of the computational domain. But this simplification may cause troubles for internal flows where the diffusion dominated region can be large. According to this, for internal flows it is convenient to introduce an approximation of the eigenvalues of the diffusive terms jacobian and put it into equation (4). Two forms of this approximation have been considered.

- Pulliam's approximation.

Pulliam (ref. 10) proposes an approximate form of the diffusive Jacobian eigenvalues that was obtained by intense numerical testing. This form is

$$
\begin{aligned}
\Lambda^{\mathrm{v}}_{\xi} &= (\rho\ \mu_{\mathrm{eff}}\ \mathrm{Re}^{-1}\ ({\xi_x}^2+{\xi_y}^2+{\xi_z}^2)\ \mathrm{J}^{-1}) \cdot D\,[1,1,1,1,1] \\
\Lambda^{\mathrm{v}}_{\eta} &= (\rho\ \mu_{\mathrm{eff}}\ \mathrm{Re}^{-1}\ ({\eta_x}^2+{\eta_y}^2+{\eta_z}^2)\ \mathrm{J}^{-1}) \cdot D\,[1,1,1,1,1] \qquad (5) \\
\Lambda^{\mathrm{v}}_{\zeta} &= (\rho\ \mu_{\mathrm{eff}}\ \mathrm{Re}^{-1}\ ({\zeta_x}^2+{\zeta_y}^2+{\zeta_z}^2)\ \mathrm{J}^{-1}) \cdot D\,[1,1,1,1,1]
\end{aligned}
$$

In the present set of calculations it was found convenient not to weight the eigenvalues with the Jacobian of the coordinate transformation J^{-1}. These expressions are included on the implicit side of equation (4): for instance, the ξ direction implicit operator reads

$$[\ \mathrm{I} + \Theta\ \Delta t\ (\delta_{\xi}\ \Lambda_{\xi} - \delta^2_{\xi}\Lambda^{\mathrm{v}}_{\xi})\ ]$$

- Present approximation.

The exact form of the diffusive terms Jacobian can be computed from the related flux vectors. For the three sweeps the main diagonal of such matrix may be conveniently approximated as

$$
\begin{aligned}
{\Lambda_{\xi}}^{\mathrm{v}} &= D\,[0,\alpha_{\xi},\alpha_{\xi},\alpha_{\xi},\gamma\ \mathrm{Pr}^{-1}\alpha_{\xi}] \\
{\Lambda_{\eta}}^{\mathrm{v}} &= D\,[0,\alpha_{\eta},\alpha_{\eta},\alpha_{\eta},\gamma\ \mathrm{Pr}^{-1}\alpha_{\eta}] \qquad (6) \\
{\Lambda_{\zeta}}^{\mathrm{v}} &= D\,[0,\alpha_{\zeta},\alpha_{\zeta},\alpha_{\zeta},\gamma\ \mathrm{Pr}^{-1}\alpha_{\zeta}]
\end{aligned}
$$

in which

$$
\begin{aligned}
\alpha_{\xi} &= \mu_{\mathrm{eff}}\ \mathrm{Re}^{-1}\ \mathrm{J}^{-1}\ ({\xi_x}^2+{\xi_y}^2+{\xi_z}^2)\ \frac{\partial(\rho^{-1}\mathrm{J})}{\partial\xi} \\
\alpha_{\eta} &= \mu_{\mathrm{eff}}\ \mathrm{Re}^{-1}\ \mathrm{J}^{-1}\ ({\eta_x}^2+{\eta_y}^2+{\eta_z}^2)\ \frac{\partial(\rho^{-1}\mathrm{J})}{\partial\eta} \\
\alpha_{\zeta} &= \mu_{\mathrm{eff}}\ \mathrm{Re}^{-1}\ \mathrm{J}^{-1}\ ({\zeta_x}^2+{\zeta_y}^2+{\zeta_z}^2)\ \frac{\partial(\rho^{-1}\mathrm{J})}{\partial\zeta}
\end{aligned}
$$

Regarding the extra-diagonal terms as negligible, the previous diagonal matrices are a good approximation of the diffusive terms Jacobians and can be put into the implicit side of equation (4): for instance, the ξ direction implicit operator reads

$$[\ \mathrm{I} + \Theta\ \Delta t\ (\delta_{\xi}\ \Lambda_{\xi} - \delta_{\xi}\Lambda^{\mathrm{v}}_{\xi})\ ]$$

in which the diffusive terms contribution is approximated as a first order derivative. It is possible to prove that the first approximation increases the main diagonal dominance by summing to it an extra term, whereas in the second approximation an artificial term is subtracted from the off-diagonal components while leaving the main diagonal unchanged. A comparison of the two approaches, equations (5) and (6), was performed on a simple straight channel geometry at $\mathrm{Re}\simeq 1000$ and $\mathrm{M}_{\mathrm{inlet}}=0.3$ in a laminar flow regime. For this very simple flow configuration there were no differences in convergence rate between the two approaches, and it was also possible to drop the diffusive terms on the implicit side of equation (4) without altering convergence. Differences started to appear at Re=50 because of the highly diffusive nature of the flow. Figure 1(a) shows the best convergence history of the algorithm without any implicit treatment of the diffusive terms that were obtained at CFL=5. (The lower curve refers to the averaged residuals, and the upper curve refers to the maximum.) Figures 1(b) and 1(c) refer to equations (5) and (6). There are no appreciable differences between the two convergence rates obtained at CFL=10 since both curves show nearly the same slope. The same result could be obtained if the Baldwin-Lomax turbulence model was used. At least for this class of flows the approximate implicit treatment of diffusive terms given by equation (6) did not prove to be more efficient than equation (5). Further testing is necessary in order to verify this result at higher Mach numbers when differences in the convergence between equations (5) and (6) may appear since the density derivatives do not tend to vanish for compressible flows rather than for incompressible flows.

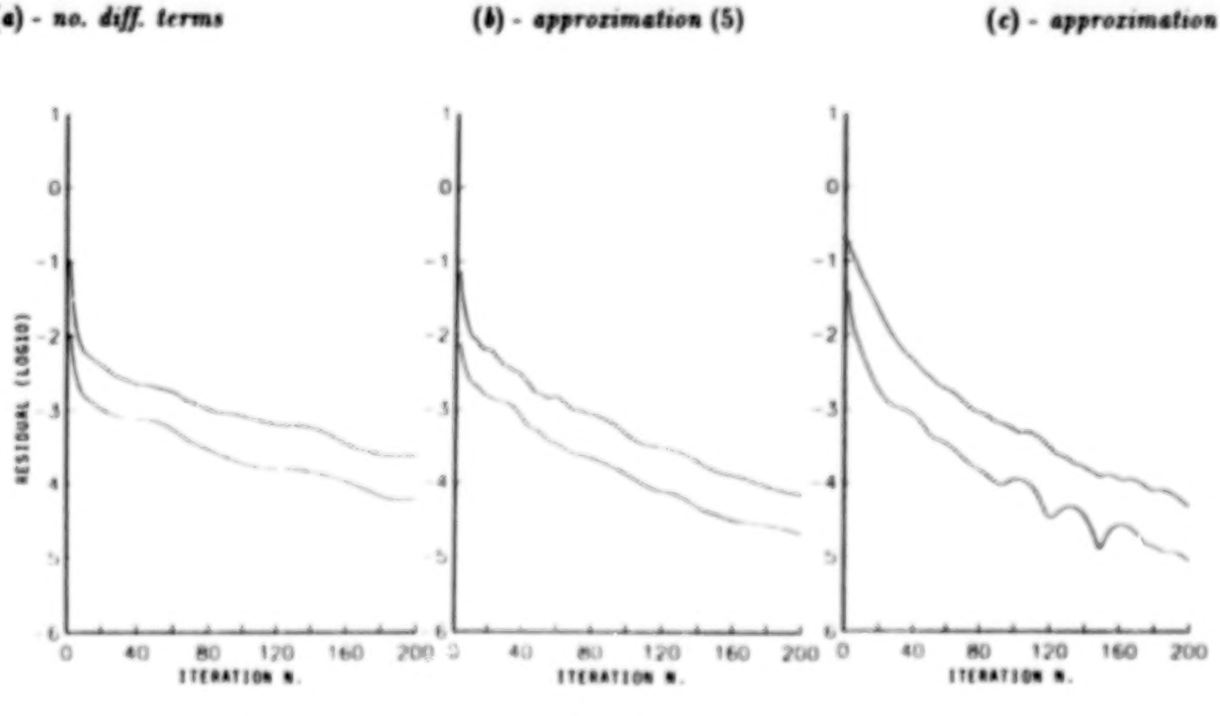

(*a*) - *no. diff. terms* (*b*) - *approximation* (5) (*c*) - *approximation* (6)

Figure 1. Convergence tests for implicit treatment of diffusive terms.

Added Explicit and Implicit Damping

When using centered finite differences, it is necessary to introduce an artificial damping scheme in order to prevent odd-even velocity-pressure decoupling that occurs whenever the local Peclet number exceeds 2 in large-gradient regions. Moreover, the three-dimensional approximate factorization method can be proved to be unconditionally unstable since, when performing a linear stability analysis, one of the amplification factors is found to be slightly larger than one. This weak instability can be easily overcome by using an artificial damping scheme. From the two-dimensional version of the approximate factorization, it is also known that fourth order artificial damping is necessary to damp the numerical modes associated with the highest frequencies. Following the basic guideline given by Jameson et al. (ref. 13) and Pulliam (ref. 14), a blended implicit-explicit second plus fourth order nonlinear damping scheme was introduced in the present solver.

- Explicit 2^{nd} and 4^{th} order damping.

In the original formulation, the artificial damping is simply equally scaled according to the local Δt in the three space directions. This could be done mainly because the damping scheme has been first applied to inviscid flows. For viscous flow calculations, Pulliam (ref. 10) found it convenient to scale the damping terms according to the directional spectral radius σ. The scheme for the ξ direction sweep yields

$$D_{\xi}^{(2)}+D_{\xi}^{(4)} = \delta_{\xi}\Big(\big((\sigma J^{-1})_{i+1,j,k}+(\sigma J^{-1})_{i,j,k}\big)\big(\omega_{i,j,k}^{(2)}\delta_{\xi}\,(Q_{i,j,k}) - \omega_{i,j,k}^{(4)}\delta_{\xi}(Q_{i,j,k})\big)\Big) \tag{7}$$

The complete definitions of $\omega^{(2)}$ and $\omega^{(4)}$ are given following Pulliam

$$T_{i,j,k} = \frac{\left|p_{i+1,j,k} - 2p_{i,j,k} + p_{i-1,j,k}\right|}{\left|p_{i+1,j,k} + 2p_{i,j,k} + p_{i-1,j,k}\right|}$$

$$\omega_{i,j,k}^{(2)} = \Omega^{(2)}\,\Delta t\,\max(T_{i-1,j,k}, T_{i,j,k}, T_{i+1,j,k})$$

$$\omega_{i,j,k}^{(4)} = \max(0., \Omega^{(4)}\,\Delta t - \omega_{i,j,k}^{(2)}) \tag{8}$$

and the unscaled spectral radius is defined as

$$\sigma_{i,j,k} = |U| + a\sqrt{\xi_x^2 + \xi_y^2 + \xi_z^2}$$

Since the present set of calculations has been performed for shock-free flow fields, the shock sensor term defined in equation (8) was switched off by always taking $T_{i,j,k}$. Nevertheless, this modification does not really affect the damping scheme since the second order term is active only in presence of shocks. Actually, this scheme gives only fourth order damping in smooth shock-free flow fields so that in most of the calculations $\Omega^{(2)}$ was set equal to zero whereas the fourth order weight, $\Omega^{(4)}$, ranges from 1/16 to 1/12.8.

Equation (7) is then added to the RHS of equation (4),

$$RHS = RHS + \Delta t\,(D_{\xi}^{(2)} + D_{\xi}^{(4)} + D_{\eta}^{(2)} + D_{\eta}^{(4)} + D_{\zeta}^{(2)} + D_{\zeta}^{(4)})$$

- Implicit 2nd or 4th order damping.

To enhance the algorithm stability and convergence rate, it is helpful to include the artificial damping terms on the implicit side. For both the 2nd and the 4th order damping, the implicit treatment augments the diagonal dominance of the scalar system with a beneficial effect on the convergence rate. As it was pointed out by Pulliam (ref. 10), there is a stability limit for the weights that can be used for the artificial damping terms. This limit is actually connected to the magnitude of the amplification factor of the scheme modified with the artificial terms. To obtain the best convergence rates the implicit damping had to be the exact Jacobian of the explicit counterpart added to the right-hand-side. In case the second order damping is treated implicitly, equation (4) must be modified to include the added implicit terms: for instance, the ξ sweep implicit side will be

$$\Big\{I+\Theta\Delta t\Big(\delta_{\xi}\Lambda_{\xi} - \delta_{\xi}\Big(((\sigma J^{-1})_{i+1,j,k}+(\sigma J^{-1})_{i,j,k})(\omega_{i,j,k}^{(2)}\delta_{\xi}J_{i,j,k})\Big)\Big)\Big\} \tag{9}$$

This form maintains the tridiagonal nature of the Jacobian matrix.

When treating the fourth order damping implicitly, the differentiation of the Jacobian matrix brings about a scalar pentadiagonal system that can be written for the ξ sweep as

$$\Big\{I+\Theta\Delta t\Big(\delta_{\xi}\Lambda_{\xi} - \delta_{\xi}\Big(((\sigma J^{-1})_{i+1,j,k}+(\sigma J^{-1})_{i,j,k})(\omega_{i,j,k}^{(4)}\delta_{\xi}^{3}J_{i,j,k})\Big)\Big)\Big\} \tag{10}$$

A brief set of tests on a straight channel geometry proved that the 4th order implicit damping (eq. (10)) could bring a large gain in convergence rate with respect to the 2nd order (eq. (9)). For a straight three-dimensional channel with approximately 10^4 points with an inlet-section-width to channel-length ratio of 15 (typical of internal flows geometries), the tridiagonal solver associated with equation (9) could be run at CFL=2 which gave the convergence history shown in figure 2(a), whereas the pentadiagonal solver associated with equation (10) proved to be much more robust and gave the much higher convergence rate shown in figure 2(b) with CFL=10. Despite an increase of around 25% in computational time to invert the pentadiagonal matrix with respect to the tridiagonal one, the implicit 4th order option proved to be much faster and more robust, and was retained in all of the calculations.

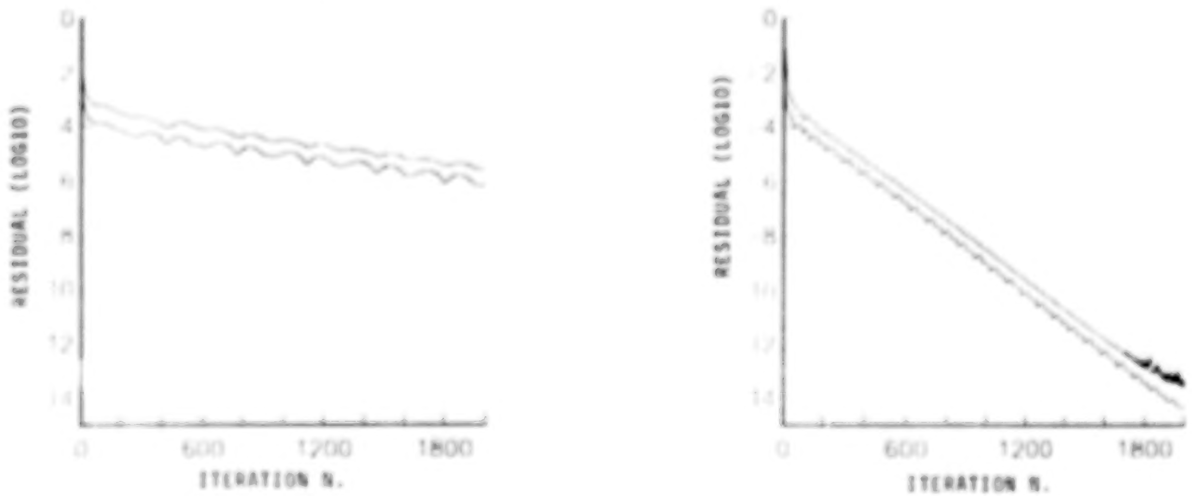
(*a*) *tridiagonal*

(*b*) *pentadiagonal*

Figure 2. Convergence tests for tridiagonal or pentadiagonal solvers.

- Wall treatment of artificial damping.

It is well known that any kind of artificial damping term introduces an error that has to be minimized in order not to affect the solution heavily. Among the various approaches that can be found in the literature, the nonlinear damping formulation proposed by Jameson et al. (ref. 13) ensures that the second order terms are introduced only at shocks while keeping the fourth order in the smooth region of the computational domain. However, it is possible to prove that, if the presence of the boundaries is not properly accounted for when introducing the artificial terms, nonzero momentum and mass fluxes can be produced at the boundaries. This fact can be easily seen by considering figure 3. Figure 3(a) shows the fourth order damping weights applied at every single point i for the ξ direction. The fourth order difference stencil used here is

$$\delta_\xi^4(Q_{i,j,k}) = Q_{i-2,j,k} - 4\,Q_{i-1,j,k} + 6\,Q_{i,j,k} - 4\,Q_{i+1,j,k} + \;Q_{i+2,j,k}$$

The fourth order damping is normally switched off at $i=1$ and $i=2$ so that no special treatment at the wall is required. Figure 3(a) shows that, doing so, the sum of the fourth order damping weights for every locaton i is zero only in the internal flow field for $i \geq 5$. This ensures that no net fluxes are added only in the internal domain, while the sum of the artificial damping weights yields nonzero values for $1 \leq i \leq 4$. These weights actually correspond to a nonzero third order derivative centered at $i=(2+1/2)$. The same procedure may be followed for the second order damping that is switched off at $i=1$ (figure 3(b)). The sum of the weights for every location i is zero only for $i \geq 3$. This yields a first order derivative centered at $i=1/2$, that corresponds to a first order flux at the wall. These flux errors can be easily controlled in two dimensions by a grid refinement in the wall proximity where high gradients are expected. In three-dimensional internal flows we are forced to use coarser grids and the wall boundary condition is applied on very large surfaces with the result of possible large mass errors. To control the mentioned flux errors, a third order derivative, with the differencing stencil given by

$$\delta_\xi^3(Q_{i,j,k}) = -Q_{i-1,j,k} + 3\,Q_{i,j,k} - 3\,Q_{i+1,j,k} + Q_{i+2,j,k}$$

was added at $i=2$ to balance the fourth order damping weight. The same procedure was followed to balance the second order damping at the wall where a first order derivative, with the differencing stencil given by

$$\delta_\xi(Q_{i,j,k}) = -Q_{i-1,j,k} + Q_{i,j,k}$$

was added at $i=2$.

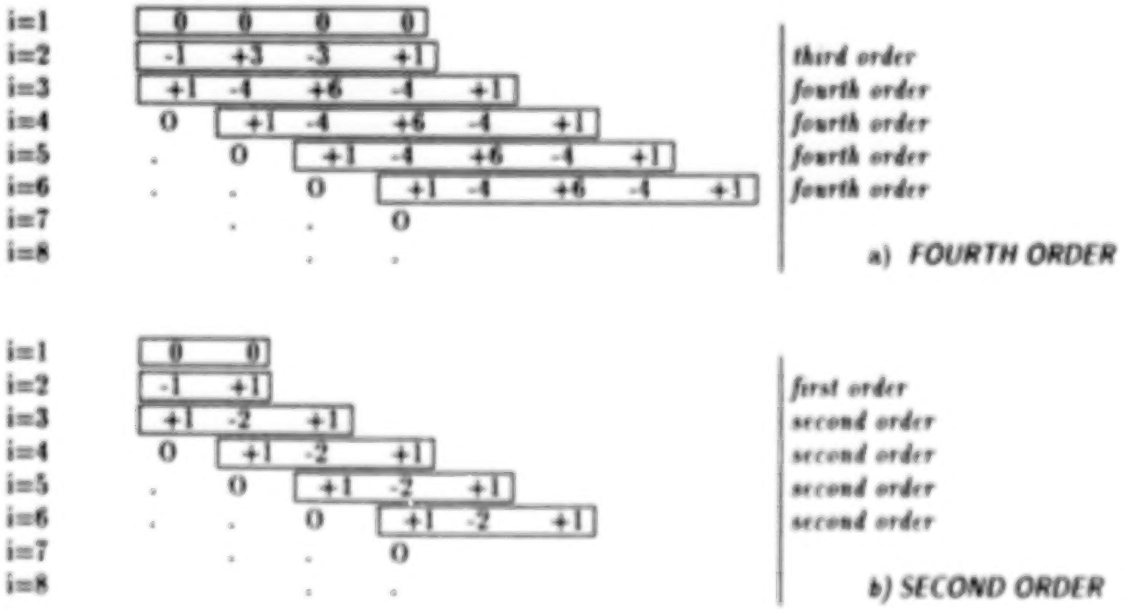

Figure 3. Artificial dissipation treatment at boundaries.

TURBULENCE MODELS

Baldwin-Lomax for Multiple Boundaries

The standard version of the Baldwin-Lomax (ref. 4) zero-equation turbulence model was implemented here. This two-layer model divides the flow field into an inner layer close to the wall, in which viscous effects are dominant, and an outer layer. The influence of the solid wall is damped according to the Van Driest exponential function.

This algebraic turbulence model was originally developed for a single boundary layer, but in three-dimensional internal flows the presence of multiple boundaries causes the interaction of more than one boundary layer. Whereas the inner, or viscous layer, is driven by what happens on the closest wall only, for the outer layer an averaging procedure is necessary to account for the various wall effects. In the present set of calculations three approaches have been examined to account for the presence of more than one boundary layer.

- **Wall Treatment 1**

Only the geometrically closest wall is considered to compute the outer viscosity without any averaging.

- **Wall Treatment 2**

The inner layers are driven by the closest wall only, whereas the viscosity in the outer layer is computed with a simple weighted average according to the inverse of each wall distance as follows

$$\mu_{t,outer} = \frac{1}{\sum_{w}^{N} \frac{1}{W_w}} \sum_{w}^{N} \left(\frac{\mu_{t,outer}^{w}}{W_w}\right)$$

where W_w is the wall distance, w is the wall number, and N is number of walls present in a cross section.

- **Wall Treatment 3**

In case only one boundary layer is present, the Van Driest damping succeeds in modeling the wall effect. Starting from this standpoint, the inner layer viscosities are computed using only the closest wall contribution, while the viscosity in the outer layer is computed as a simple weighted average according to the inverse of the value of the Van Driest damping expression for each wall.

q-ω two-equation Model

In a previous investigation, Michelassi (ref. 7) found that the low-Reynolds number forms of the two-equations models, like k-ε, could give accurate prediction of two-dimensional incompressible separated flows. Unfortunately, these forms were found to be numerically stiff, mainly on account of the correction terms introduced to model the low-Re effects that necessitate a strong mesh refinement in the sublayer. Furthermore, an initial profile for the turbulent quantities has to be specified consistently to start the calculations. A first attempt to implement the Chien's and the Rodi's two-layer low-Reynolds number forms of the k-ε model did not bring any converged result mainly because of difficulties in specifying both a sufficient mesh refinement and proper initial profiles for complex three-dimensional flows. Coakley (ref. 15), reassembling the Jones and Launder low-Reynolds-number form of k-ε model, proposed the q-ω two-equation model, in which the effect of molecular viscosity is directly modelled: This formulation ensured better numerical behavior as compared with other low-Re formulations. This vector form of the model transport equations rewritten in our notation is (ref. 19)

$$\frac{\partial \bar{Q}}{\partial t} + \frac{\partial \bar{E}}{\partial \xi} + \frac{\partial \bar{F}}{\partial \eta} + \frac{\partial \bar{G}}{\partial \zeta} = \frac{\partial \bar{E}_v}{\partial \xi} + \frac{\partial \bar{F}_v}{\partial \eta} + \frac{\partial \bar{G}_v}{\partial \zeta} + \bar{H} \qquad (11)$$

in which $\bar{H}$ stands for the sink and source terms vector. The full definition of the flux vectors can be found in reference 19. The two transported quantities, q and ω, are related to the more familiar k and ε via the following relations:

$$q = k^{1/2} \ ; \ \omega = \epsilon / k \qquad (12)$$

It is important to observe that ε appearing in equation (12) is the isotropic part of the dissipation rate; this quantity does not account for any nonisotropic effect (for example, the presence of a wall) and tends to zero on solid boundaries. (Conversely, the total dissipation rate tends to a finite value related to the wall shear stress.) This choice allows ω to be used as an unknown since, assuming that both k and ϵ are going to zero at the wall with the same slope, ω tends to a finite value.

q-ω Solution

The two transport equations for q and ω are implicitly solved by using the same algorithm given in equation (1). The two equations are solved in a sequential manner and decoupled from the flow variables mainly because the coupling is provided only by the coefficients of the diffusive terms and the sink and source terms. Because of this choice, the scalar three-diagonal algorithm was implemented for the turbulence model solution. The only difference with respect to the solution of the N-S equations is the presence of the sink-source vector $\overline{H}$ in equation (11). This term can be included in the three sweeps:

$$\begin{aligned}
&[\, I+\Theta\Delta t\left(-H_j\, c_\xi + \delta_\xi A - \delta_\xi^2 A_v\right)]*\\
&[\, I+\Theta\Delta t\left(-H_j\, c_\eta + \delta_\eta B - \delta_\eta^2 B_v\right)]*\\
&[\, I+\Theta\Delta t\left(-H_j\, c_\zeta + \delta_\zeta C - \delta_\zeta^2 C_v\right)]*\Delta Q = RHS
\end{aligned} \tag{13}$$

where the same definitions given for equation (1) hold with the only addition to the Jacobian being the sink and source terms, H_j, that are weighted in the three sweeps according to c_ξ, c_η, c_ζ, and $c_\xi+c_\eta+c_\zeta=1$. This Jacobian is computed neglecting the contribution of the damping function D. Its form for the two q and ω equations is

$$H_j^q = \frac{\partial H^q}{\partial(\rho J^{-1} q)} = \frac{1}{2}\frac{C_\mu DS}{\omega} - \frac{1}{3} P_d - \frac{\omega}{2}$$

$$H_j^\omega = \frac{\partial H^\omega}{\partial(\rho J^{-1}\omega)} = -\frac{2}{3} C_1 D P_d - C_2\, 2\omega$$

in which S and P_d are production terms (ref. 19). In place of their exact form, Coakley (ref. 15) proposes an approximation of the Jacobians based on the turbulent viscosities that should ensure the dominance of the main diagonal. Figure 4 shows the comparison of the convergence rates of every single variable obtained without any sink or source terms Jacobian, with the exact Jacobian, and with Coakley's approximation in a typical internal flow geometry. Surprisingly, there is no big gain in introducing the Jacobian in the implicit side of the operator since with the three formulations it was always possible to obtain the same residual reduction in 300 iterations. The choice of the sweeps in which the two Jacobians H_j^q and H_j^ω are introduced is not important. The error introduced in the approximate factorization of the implicit side of equation (13) increases roughly a factor proportional to H_j when introducing the Jacobian in the three sweeps, thereby choosing $c_\xi=c_\eta=c_\zeta=1/3$: this has only a weak influence on the convergence rate. Nevertheless, in the present calculations typically the best convergence rates have been obtained by using $c_\xi=0$, $c_\eta=0.5$, and $c_\zeta=0.5$, where ξ is the main flow direction and η and ζ are the fine grid directions.

Although physical evidence shows that the turbulent kinetic energy k is zero at solid walls, the boundary condition for ϵ, and consequently ω, is less evident. For the q-ω model, Coakley (ref. 15) found it convenient to impose a zero-normal derivative at the wall; this condition was retained in the present calculations.

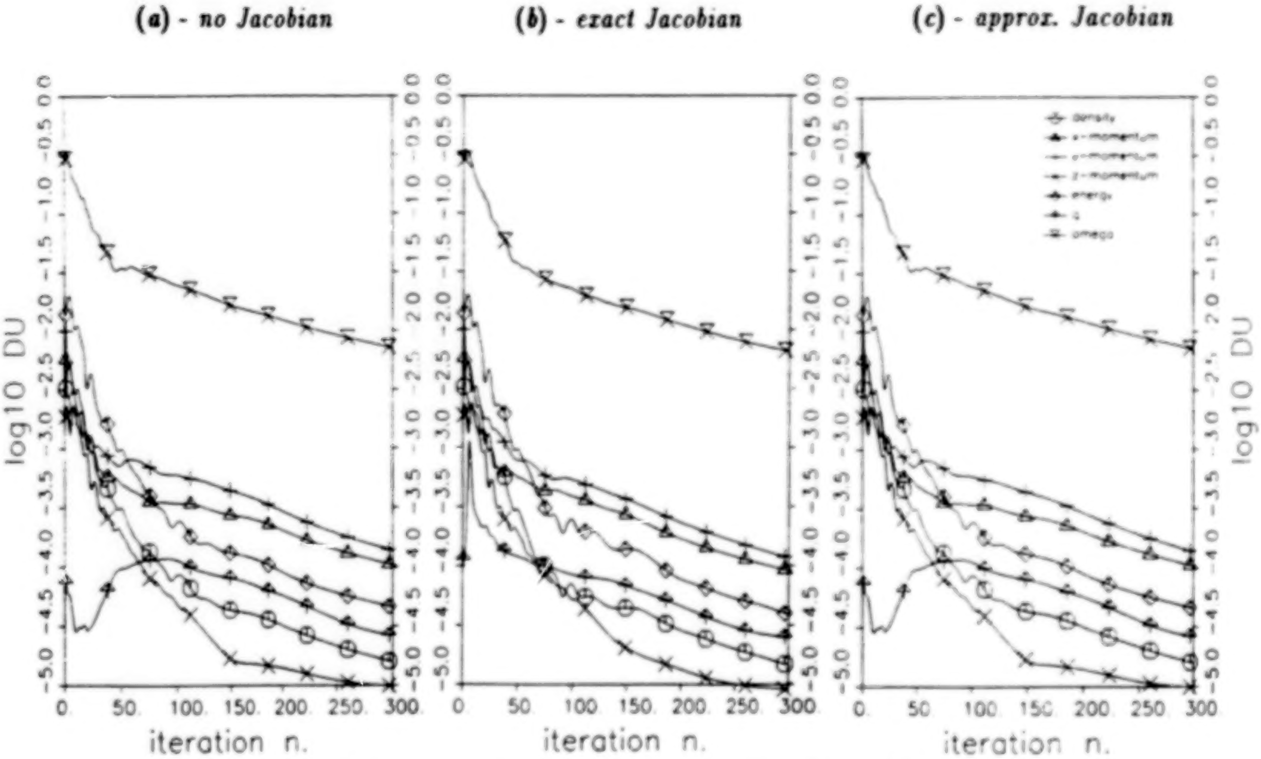

Figure 4. Convergence tests for implicit treatment of q-ω sink-source terms.

RESULTS

Incompressible S-duct

A first validation of the code was performed by computing the flow in an S-duct with a constant area cross section. The measurements (ref. 16) were taken for an incompressible fluid (water). The S-duct is given by two 22.5° bends with 4-cm hydraulic diameter and 28-cm mean radius of curvature. This geometry was regarded as an interesting test since flow passages with similar shapes are often used to redirect the flow for air intakes in aeronautical engines. The efficiency of such ducts may be heavily affected by the presence of secondary flows so that the ability of a code to detect secondary velocities is essential for a proper depiction of the flow pattern.

The sketch of the flow domain is shown in figure 5. Since the geometry and the flow were symmetric with respect to the x-r plane, it was possible to study only one-half of the duct by imposing a symmetric boundary condition on the same plane. For the laminar flow regime, the Reynolds number, Re, based on the inlet bulk velocity, Ub, and hydraulic radius was 790. The grids employed for this calculation are shown in figure 6. The coarser grid (figure 6(a)) has $70\times29\times15$ points with a ratio between two consecutive grid cells in the cross flow directions of 1.1, and the refined one (figure 6(b)) has $80\times59\times30$ points with the same stretching ratio in the cross flow plane. The fluid adopted in the experiments is water so that, in order to have negligible compressibility effects, the isentropic Mach number was set equal to 0.1 (which gives the inlet total pressure, outlet static pressure ratio) to ensure minor density changes.

The flow pattern and the growth of the secondary motions is mainly pressure driven because of the very smoothly bending walls that cause no flow separation. Still, this kind of flow necessitates a very accurate prediction of the boundary layer, even in laminar regime, otherwise the secondary flows may be incorrectly predicted or completely lost. Figure 7(a) shows the measured (circles) and computed velocity profiles with the two grids mentioned above (dashed line is the coarser grid; solid line is the refined grid) for the 5 sections (indicated in fig. 5) on the symmetry plane reported in the experiments. The slight discrepancies in the computed velocities with the two grids at section 1, where the double-S starts, may be attributed to the thinner boundary layer predicted with the refined grid that produced a flatter velocity profile. Nevertheless, the agreement with experiments is fairly good. The agreement does not deteriorate for sections 2, 3, and 4 in both the coarse and refined grids. Section 5 clearly shows that the secondary motions could not be predicted by the coarse grid, whereas they are fairly well reproduced by the refined one. This behavior is thought to be independent of the grid points in the main flow direction, (as it will be demonstrated in a further test) in which only 10 points are added in the refined grid, and it is closely related to the poor resolution of the boundary layer provided by the coarse grid in which the cross-flow momentum diffusion is clearly overestimated.

Figure 7(b) shows the velocity profiles for the midspan section (r=1/2) at the same five sections. Basically the same comments given for the symmetry plane could be repeated here for the first three sections, whereas on section 4 and 5 agreement deteriorates in proximity of the symmetry plane. This may be attributed to the poor grid quality close to the symmetry plane, but also to the fact that in the calculations a zero gradient condition was imposed in the direction normal to that plane, whereas experiments show that the velocity gradient is far from being zero on the same plane for section 4. The typical computed secondary motion pattern at the exit of the second bend is shown in figure 7(c): The complex flow pattern exhibits two counter-rotating vortices in proximity of the two curved walls.

Nearly 1500 iterations were necessary to reach an averaged residual of the order of 10^{-5} on the refined grid, but typically less than half of these iterations were necessary to obtain the same residual with the coarser grid. These calculations were performed with an early version of the code where only the second order implicit damping was implemented so that the slow convergence rate may be attributed to both the small Mach number and to the small CFL number that could not exceed 2 without encountering stability problems.

The turbulent flow regime was run at the experimental condition of Re=40.000. For this calculation, it was necessary to provide a more stretched grid at the wall, so that the 80×59×30 grid was reassembled with a point expansion ratio in the cross flow directions equal to 1.3. This provided the necessary point clustering at the boundaries to describe the thin boundary layer and allowed the first point at the wall to be placed at $y^+ \approx 2$. For this test case, the Baldwin-Lomax model was implemented with wall treatment 1 (see section on Baldwin-Lomax for multiple boundaries).

Figure 8(a) shows the set of measured and computed velocity profiles on the symmetry plane for the same five cross sections given in figure 5. For this flow configuration the agreement is reasonably good, especially at cross sections 4 and 5 where the pressure gradients induce a strong secondary motion that seems to be correctly predicted by the present solver insofar as the agreement with measurements does not deteriorate as the second bend exit is approached and the secondary velocities reach their maximum. The momentum transfer to the external part of the second bend, particularly evident in sections 4 and 5, is reproduced well since the computed velocity profile asymmetry seems to be in close agreement with experiments.

Figure 8(b) shows the computed and measured velocities on the midspan plane along the duct. The agreement is again good for the five sections and better than that found for the laminar flow regime mainly because the measured velocity profiles exhibit a zero gradient on the symmetry plane that is correctly modelled by the symmetry condition imposed on the x-r plane. Still, at sections 3 and 4 the kink in the velocity profile close to the wall is not correctly predicted.

The static pressure coefficient in the main flow direction, defined as

$$C_p = \frac{p - p_{\text{inlet}}}{\frac{1}{2}\rho U_b^2}$$

is shown figure in 8(c) at three different locations (z=0,r=0), (z=0,r=1), and (r=1/2,z=1/2). The agreement is generally good. The pressure trend is correctly predicted together with the head loss.

Figure 8(d) shows the convergence history obtained with CFL=2: For this calculation the same early version of the code mentioned previously was used. The solid upper line refers to the maximum residual, and the dashed one refers to the averaged residual; the spikes present in the first curve correspond to the updating of the turbulent viscosity performed every five iterations. It is remarkable that the pressure distribution did not change after the first 500 iterations, whereas to get the correct velocity profiles, it was found necessary to reach a residual of the order of 10^{-5} to 10^{-6}.

Stanitz Elbow

The flow in the accelerating rectangular elbow with 90° turning and variable cross section described by Stanitz (ref. 17) has been computed with an inviscid version of the code and with both the Baldwin-Lomax and q-ω turbulence models. This test case was selected since it provides a good set of measurements including wall pressure distribution and visualization of secondary flows at the elbow exit section. The shape of the elbow was analytically computed by Stanitz to give no separation with a strong area reduction and a specified pressure distribution on the side wall under incompressible flow conditions. A sketch of the experimental setup is shown in figure 9. The flow and the elbow geometry are symmetric with respect to the x-y midspan plane thereby allowing a zero normal gradient condition. Among the various flow conditions investigated in reference 17, we selected the one with $M_{exit}=0.4$ and with no spoiler at the duct inlet with a thin initial boundary layer.

- Inviscid Calculations

A first set of tests was performed with an inviscid version of the code. The convergence characteristics of the scalar form of the approximate factorization could be tested for inviscid calculations where the necessity of accounting for the diffusive terms on the implicit side of equation (4) drops. Only the pressure distribution on the walls of the elbow was compared with measurements in this set of calculations: no attempt was made to specify an experimental inlet profile of total pressure that was kept flat. The inlet boundary condition was specified extrapolating the Riemann invariant from the first section inside the duct (ref. 18). Two grids were used: a 25×15×11 grid and a 50×15×11 grid with constant grid spacing in the cross-flow directions. The grid point locations in the streamwise direction were made to coincide with the points supplied by Stanitz (ref. 17) for the description of the elbow geometry with the addition of three cross sections at the outlet to allow the use of a zero gradient condition.

Figure 10 shows the qualitative static pressure and Mach number isolines on the symmetry plane of the elbow. The small wiggles visible at the domain exit are due to the very small 4th order damping weight that was set equal to $\Omega^{(4)}=1/256$, together with $\Omega^{(2)}=0$. The small value of the fourth order damping weight is allowed by the very coarse grid in the cross flow direction that automatically introduced a numerical diffusion. Despite the very coarse grids implemented here, the static pressure distribution p_s, defined as

$$P_s = \frac{p - p_{exit}}{p_{total} - p_{exit}}$$

shown in figure 11, reveals a fairly good agreement with experiments. Although the pressure drop position is located correctly for the two grids on both the side and symmetry planes, the kink in the static pressure distribution on the suction surface at the side wall could not be reproduced since it is caused by the presence of secondary flows. The pressure distribution appears to be independent of secondary flows induced by viscous effects until the first part of the bend is reached. The local pressure rise located at $S=2$ (where S is the streamwise coordinate along the centerline) is introduced by the growth of secondary velocities and is totally lost by the inviscid solver. The solution proved also to be fairly grid independent, at least to the grid refinement in the main flow direction: No additional tests were performed to verify the influence of the point distribution in the cross-stream direction.

The implicit treatment of 2^{nd} and 4^{th} order artificial damping was compared using the 50x15x11 grid. Figure 12 shows the comparison between the two implicit damping schemes; the solid line refers to the 2^{nd} order implicit damping with $\Omega^{(2)}=1/4$, and the dashed line refers to the 4^{th} order implicit option with $\Omega^{(4)}=1/256$. The gain in convergence rate is remarkable; in fact, the fourth order solver could be run at CFL=10, whereas the second order one could not be run at CFL≥5. Any further increase of the artificial damping weights gave slower convergence histories. Unfortunately the same convergence rate is not obtainable for viscous calculations because of the strong point clustering and viscous effects not exactly accounted for on the implicit side of the operator.

- Viscous Calculations

The viscous calculations in turbulent flow regime were performed on the five grids summarized in table I. The use of various point clustering and distribution allowed a comprehensive investigation on the mesh dependence of the calculations. With this set of grids it was possible to verify the influence of the grid points number in the main flow direction, with 51 or 99 points, and the cross flow direction with 31x21 and 41x31 points with expansion ratios of 1.2 and 1.3. The refined grid (number 5) shown in figure 13 adopts the same distribution of points in the main flow direction that was used for the refined grid in the inviscid calculations and which allowed placing the first grid point at the wall at $y^+\approx 1$. The Reynolds number, Re, based on the total conditions at the inlet section is approximately $2.5\cdot 10^{+6}$.

grid number	points	expansion ratio
1	50x31x21	1.2
2	50x41x31	1.2
3	99x31x21	1.2
4	50x31x21	1.3
5	51x41x31	1.3

Table I. Grids for viscous calculations on Stanitz elbow.

These calculations were mainly aimed at the proper prediction of the wall pressure distribution that is heavily affected by the growth of secondary velocities and a qualitative comparison of the secondary flows predicted by the Baldwin-Lomax zero-equation model and the q-ω two equation model. The choice of the experimental spoilerless configuration allowed the turbulence models to be compared for a very thin boundary layer that required a heavy point stretching at the wall. Regarding the inlet boundary condition, in the Baldwin-Lomax model the inlet turbulent viscosity was extrapolated from inside the domain, and in the q-ω model a flat turbulent kinetic energy profile with various turbulence levels was specified at the inlet section while ω was extrapolated from inside the domain.

The first set of tests concerns the Baldwin-Lomax model with the different wall treatments mentioned. With the experimental total pressure profile specified at the inlet section, the computed static pressure profiles are compared with the measurements in figure 14. The plots refer to the static pressure distribution in the section corners on the side wall and the symmetry plane. It is evident that the way the outer viscosity is computed may play a significant role in the correct prediction of the pressure distribution. Wall treatment 1, in which only the closest wall is considered, and 2, in which the outer turbulent viscosity is weighted according to the inverse of the wall distance, do not show large changes even if the two approaches are considerably different. For both techniques, the agreement with experimental results is fairly good on the pressure side of both the side wall and the symmetry plane. The suction side on both planes shows that the static pressure is overestimated. This is probably due to the presence of computed secondary flows much stronger than the experimental ones. The computed pressure drop induced by the presence of the bend and the strong flow acceleration is smoother than the measured one: This phenomena is caused by high turbulent viscosities that induce a heavy momentum diffusion in the cross-flow direction followed by a static pressure redistribution and growth of the boundary layer thickness. The agreement with measurements improves with the turbulent viscosities averaging given by wall treatment 3. No big changes between the multiple wall treatments are found for the pressure side of both the side wall and the symmetry plane where it was always possible to have accurate results. Differences start to appear on the suction side where multiple wall treatment 3 shows the closest agreement with experiments. Still the pressure minimum located at S=2, where velocities on the cross section start to develop, is not captured. This test suggests that the averaging technique based on the Van Driest damping expression for the mixing length can give reasonable predictions. All of the computations with the Baldwin-Lomax model were performed with multiple wall treatment 3.

The results of the mesh dependence tests for the Baldwin-Lomax model are summarized in figure 15, where the computed static pressure distribution in the four corners of the cross sections using different grids are compared with measurements. The pressure distribution profiles show that there are practically no differences between the predictions obtained with grids 1 and 3. This proves that an increment of the grid points number in the main flow direction does not produce any gain in terms of accuracy: This is strictly connected to the boundary layer resolution that is not improved by using grid 3. The growth of secondary flows is influenced by the low momentum regions located close to the wall, the correct simulation of which is not ensured by the two grids. Conversely, the implementation of grid 2 clearly improves the accuracy of the results. The static pressure profile on the suction side of the side wall is in better agreement with experiments than the pressure distributions given by grids 1 and 3. It is worthwhile observing that the use of a more refined grid in the cross flow direction shows that the computed pressure minimum on the suction side is correctly located, even if its value is still overestimated, whereas this local minimum, located approximately at S=2, is completely lost with the other two grids. Nevertheless, the static pressure distribution on the symmetry plane appears to be weakly affected by grid refinement. No further investigation was performed by varying the cross-flow points expansion ratio.

The flow simulation with the q-ω model required more tests since it was necessary to investigate both the dependence on the mesh refinement and on the inlet turbulence level. The use of grids with expansion ratios equal to 1.2 did not ensure significant improvements in results since not enough points were located close to the wall. In order to have a reasonable definition of the turbulent kinetic energy peak at the wall, the grid expansion ratio was fixed at 1.3. The results of the first set of tests are summarized in figure 16 in which, adopting the coarse grid 4, the inlet turbulence level was changed to verify its influence on the static pressure distribution. Even when the inlet turbulence level is decreasing from 5.0% to 0.1%, the computed profiles progressively approach the measurements, the predictions are still far from experiments for the suction side of both the symmetry plane and the side wall. This indicates the presence of a large momentum diffusion that is possibly caused by insufficient mesh refinement or too high turbulence level, or both. Figure 17 shows the results obtained with grid 5 and lower turbulence levels. Figures 16 and 17 show that the refined grid with the same turbulence level brings some improvement of the agreement with experiments, proving that the coarser grid was largely inadequate for this flow configuration (see, for instance, the 0.1% level). The growth of the secondary flows is evident in figure 17 where the static pressure distribution computed with the inviscid approach is compared with the results of the two-equation model obtained with different turbulence levels.

The direct comparison of the turbulent calculations with the inviscid computation, in which the same pressure distribution is found on both the side wall and the symmetry plane because of the absence of secondary motions, shows large differences on the suction side only starting from S=2 where experiments deviate from the inviscid solution. The 1% turbulence level, not reported in figure 17, appeared to bring still a too high momentum diffusion so that this level was progressively decreased from 0.5% to 0.1%. The static pressure distribution on the pressure wall is mainly driven by convective phenomena, whereas the distribution on the suction wall is largely influenced by diffusion processes: this is the reason why the pressure side distribution is always reproduced well and is nearly independent of the inlet turbulence level. The final result obtained with grid 5 and a 0.1% turbulence level shows a fairly good agreement with experiments on both the suction and pressure sides and seems to reproduce quite correctly the location and the influence of secondary flows.

The predicted pressure distributions obtained by the Baldwin-Lomax model with wall treatment 3 and the q-ω model are very similar, but the two-equation model proved to be marginally more accurate especially on account of the static pressure distribution on the suction side. Figure 18 shows that the two models predict approximately the same static pressure pattern on the symmetry plane with nearly the same pressure drop due to the acceleration of the flow. Still, from figure 19, where the Mach number isolines are shown on the same symmetry plane, it is possible to observe that the zero equation model predicts a slightly thicker boundary layer than the one predicted with the q-ω. These differences start immediately after the inlet section and become more evident as the exit section is approached. This indicates a different turbulent viscosity distribution in the wall region. The Baldwin-Lomax model was in fact found to predict a sharper growth of the turbulent viscosity in the wall region: still the two models gave comparable values of the turbulent viscosity in the flow core. The differences in the boundary layer thickness are evident in figure 20 where the velocities in the exit section of the channel are plotted. Although both the turbulence models show the same flow pattern, the two-equation model predicts the center of the secondary recirculation closer to the wall than that predicted by the zero-equation model in which the location of the center appeared to be in better agreement with experiments. This confirms a weaker cross-flow momentum diffusion given by the two-equation model as compared with the zero-equation model. This is caused by the aforementioned differences in the turbulent viscosities. It is remarkable that both formulations predict a small secondary vortex in the wall corner of the suction and pressure walls.

An interesting qualitative comparison of the predicted and measured secondary flows is given by figure 21. Figure 21(a) shows the experimental flow visualization by injecting a smoke filament inside the boundary layer close to the side wall at the inlet section of a reduced model of the channel. The low-momentum particles located well within the boundary layer are bent towards the suction wall by the pressure gradients, but the high-momentum particles exhibit a weaker turning. Figure 21(b) shows the secondary flow predicted by the zero equation model, and figure 21(c) refers to the results obtained with the q-ω model. From this comparison it is evident that the zero-equation model predicts a smoother turning of the velocities which is in slightly better agreement with the experimental picture than the q-ω model.

A typical total pressure loss distribution on the channel exit section is given in figure 22. The results computed with the Baldwin-Lomax model and grids 1 and 2 show the much thicker boundary layer obtained with the coarser grid. The refined grid ensures a correct description of secondary flows together with the location and magnitude of the total pressure losses.

Concerning computational details, with the present research version of the code, 6000 sec were necessary to perform 2500 iterations with the q-ω turbulence model with a 63.550-point grid on a Cray Y-MP supercomputer, which ensured an overall residual of the order of 10^{-6}, whereas a reduction of approximately 30% in CPU time could be obtained by using the zero-equation model. As mentioned by Coakley (ref. 15), the q-ω model was found to be remarkably insensitive to the initial field specified to start the calculations for q and ω. In the present tests it has always been possible to start the model with a flat distribution of the turbulence quantities. For the viscous calculations it was found to be good practice to keep CFL$<$10 together with 1/32 as the weight for the fourth order artificial damping. The total absence of shocks allowed the second order artificial damping to be eliminated in all calculations. Moreover, the aforementioned wall treatment of the fourth order damping ensured inlet-outlet mass errors of the order of 0.5%.

CONCLUDING REMARKS

The scalar form of the approximate factorization coupled with a turbulence model proved to be suitable for solving turbulent internal flows where diffusive terms play a dominant role. The introduction of an approximate treatment of the diffusive terms proved to increase convergence of the algorithm for internal flow configurations. Nevertheless, the implicit treatment of these terms must be tested for a wider range of geometries and Reynolds numbers. The influence of Mach number on convergence rate needs to be investigated especially for the proposed approximate implicit treatment of diffusive terms based on a space derivative of the fluid density: New tests are currently being performed.

For the Stanitz elbow geometry the Baldwin-Lomax turbulence model proved to give results in acceptable agreement with experiments provided that the presence of multiple boundaries is properly accounted for. The low-Re q-ω two-equation model version investigated here proved to be suitable for three-dimensional computations and gave a satisfactory description of the flow field with a manageable number of grid points and only a small increase of computational time with respect to the algebraic model.

ACKNOWLEDGMENTS

The first author would like to express his gratitude to ICOMP and the Internal Fluid Mechanics Division of NASA Lewis Research Center for providing facilities and computer time for this work.

REFERENCES

1. T.H. Pulliam, L. Steger. "Implicit Finite Difference Simulations of Three-Dimensional Compressible Flows," *AIAA Journal, Volume* 18, *N.2, February* 1980.

2. A. Ballantyne, C. J. Knight, J. C. Kreatsoulas, D. Lee. "Experimental/Computational Study of Viscous Flow in a Contracting Rectangular Elbow," *AIAA Journal, Volume* 26, *N.* 12, *December*, 1988.

3. J. W. Yokota. "A Diagonally Inverted LU Implicit Multigrid Scheme for the 3-D Navier-Stokes Equations and a Two Equation Model of Turbulence." NASA CR-182209, 1988.

4. B. S. Baldwin, H. Lomax. "Thin Layer Approximation and Algebraic Model for Separated Turbulent Flows." *Proceedings AIAA* 16th *Aerospace Sciences Meeting*, 1978.

5. R. V. Chima, J. W. Yokota. "Numerical Analysis of Three-Dimensional Viscous Internal Flows." NASA TM-100878, 1988.

6. C. E. Towne. "Computation of Viscous Flow in Curved Ducts and Comparison with Experimental Data." NASA TM-83548, 1984.

7. V. Michelassi. "Testing of Turbulence Models with an Artificial Compressibility Solution Method." Report SFB (Sonderforschungsbereich, University of Karlsruhe) 210 T49, University of Karlsruhe, Karlsruhe, West Germany, January, 1989.

8. F. Martelli, V. Michelassi. "An Implicit Factored Solver for Inner Turbulent Flows," *Proceedings AIAA/ASME/SAE/ASEE* 24th *Joint Propulsion Conference, July* 1988.

9. W. Rodi. "Recent Development in Turbulence Modelling," *Proceedings* 3rd *Symposium on Refined Flow Modelling and Turbulence Measurements, July*, 1988.

10. T. H. Pulliam. "Efficient Solution Methods for The Navier-Stokes Equations," Von Karman Institute For Fluid Dynamics, Lecture Notes on Numerical Techniques for Viscous Flows Calculations in Turbomachinery Bladings, Bruxelles, January 1986.

11. R. M. Beam, R. F. Warming, "Implicit Numerical Methods for the Compressible Navier-Stokes and Euler equations," Von Karman Institute For Fluid Dynamics, Lecture Notes on Computational Fluid Dynamics, Bruxelles, February 1982.

12. T. H. Pulliam, D. S. Chaussee, "A Diagonal Form of an Implicit Approximate-Factorization Algorithm." *Journal of Computational Physics, N.* 39, 1981.

13. A. Jameson, W. Schmidt, E. Turkel. "Numerical Solutions of the Euler Equations by Finite Volume Methods Using Runge-Kutta Time-Stepping Schemes." *AIAA* 14th *Fluid and Plasma Dynamics Conference, July* 1981.

14. T. H. Pulliam. "Artificial Dissipation Model for the Euler Equations." *AIAA Journal, Volume* 24, *N.*12, 1986.

15. T. J. Coakley. "Turbulence Modeling Methods for the Compressible Navier-Stokes Equations." *Proceedings AIAA* 16th *Fluid and Plasma Dynamics Conference, July* 1983.

16. A. M. K. P. Taylor, J. H. Whitelaw, M. Yianneskis. "Developing Flow in S-Shaped Ducts, I- Square Cross-Section Duct." NASA CR-3550, 1982.

17. J. D. Stanitz, W. M. Osborn, J. Mizisin. "An Experimental Investigation of Secondary Flow in an Accelerating Rectangular Elbow." NACA TN-3015, 1953.

18. R. V. Chima. "Development of an Explicit Multigrid Algorithm for Quasi-Three Dimensional Viscous Flows in Turbomachinery." NASA TM-87128, 1986.

19. V. Michelassi, M.-S. Liou, L. A. Povinelli. "Implicit Solution of Three-Dimensional Internal Turbulent Flows." NASA TM-103099, 1990.

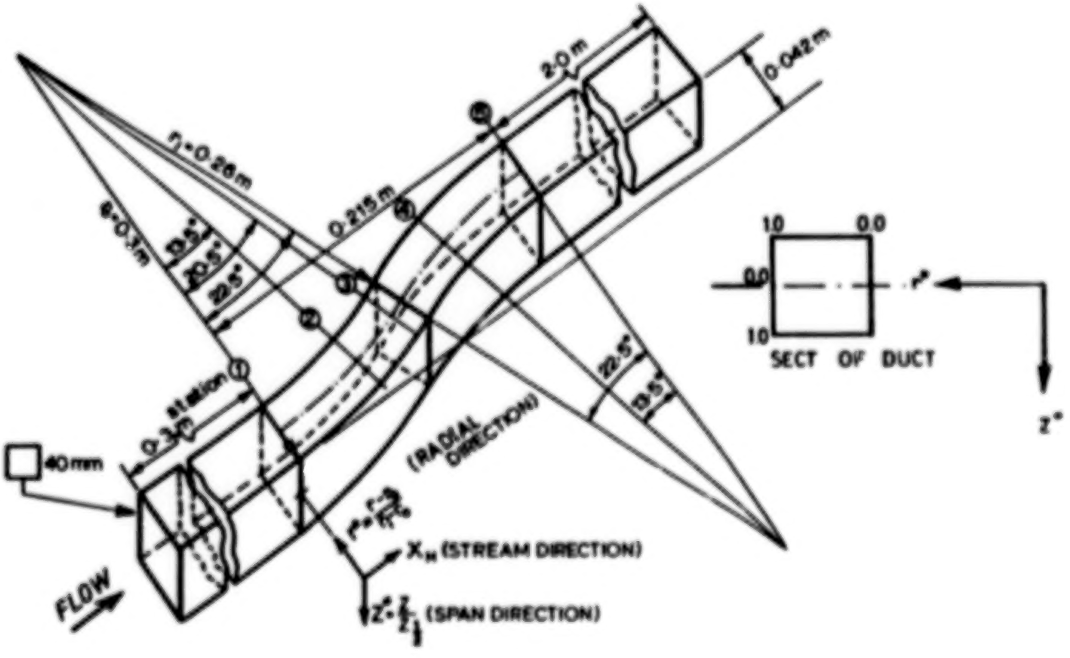

Figure 5. S-duct: Sketch of experimental setup.

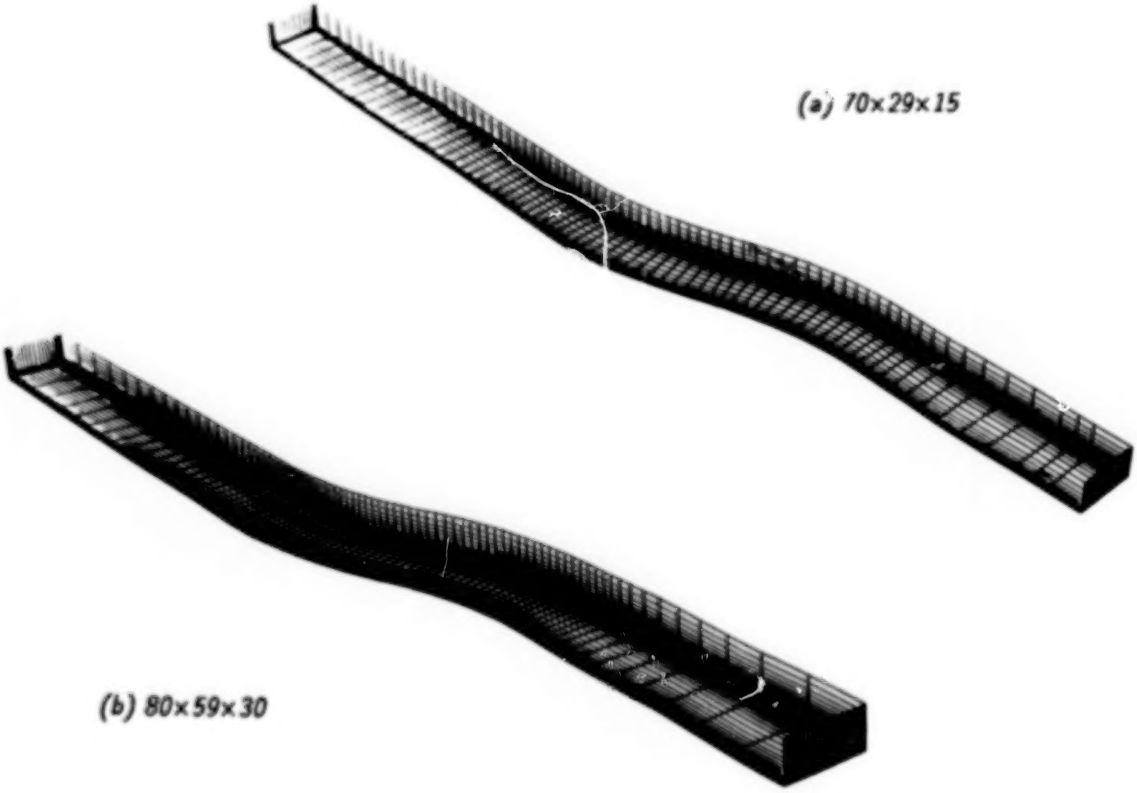

Figure 6. S-duct: Computational grids.

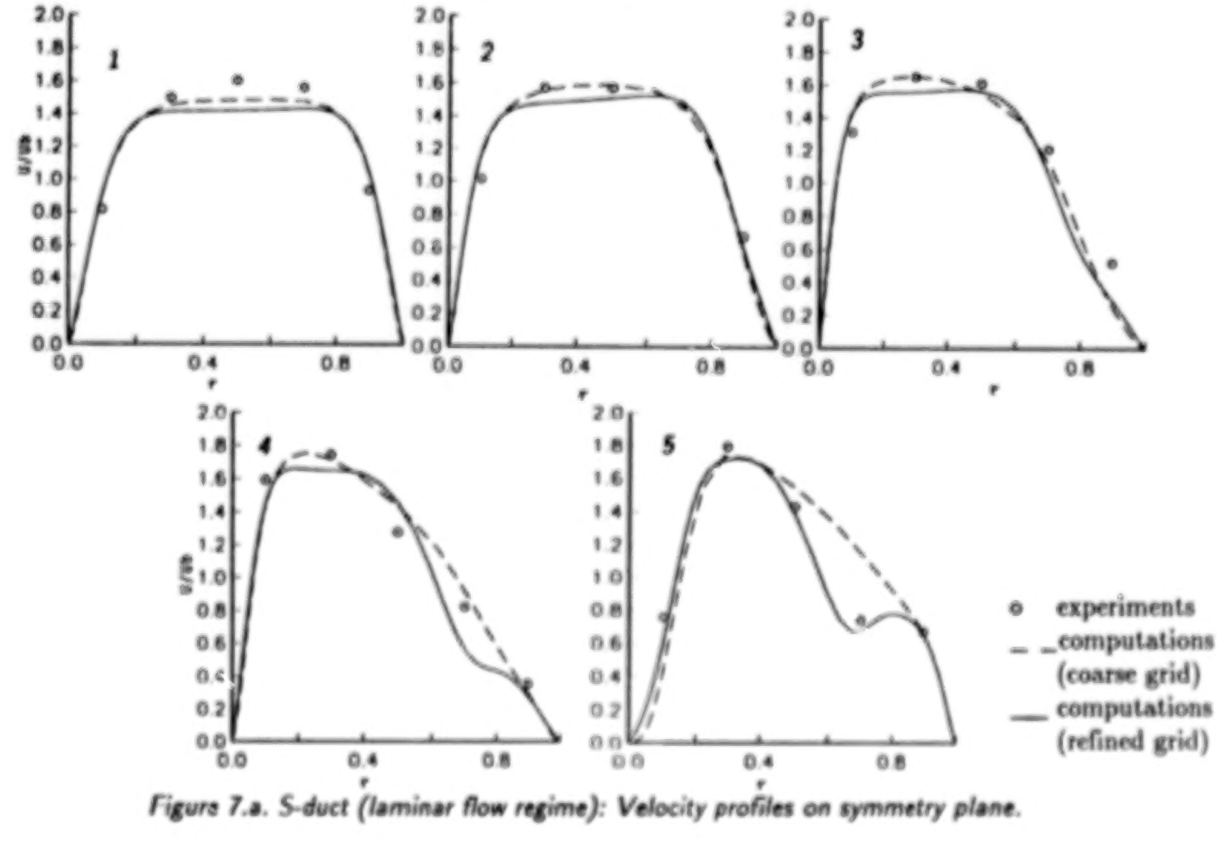

Figure 7.a. S-duct (laminar flow regime): Velocity profiles on symmetry plane.

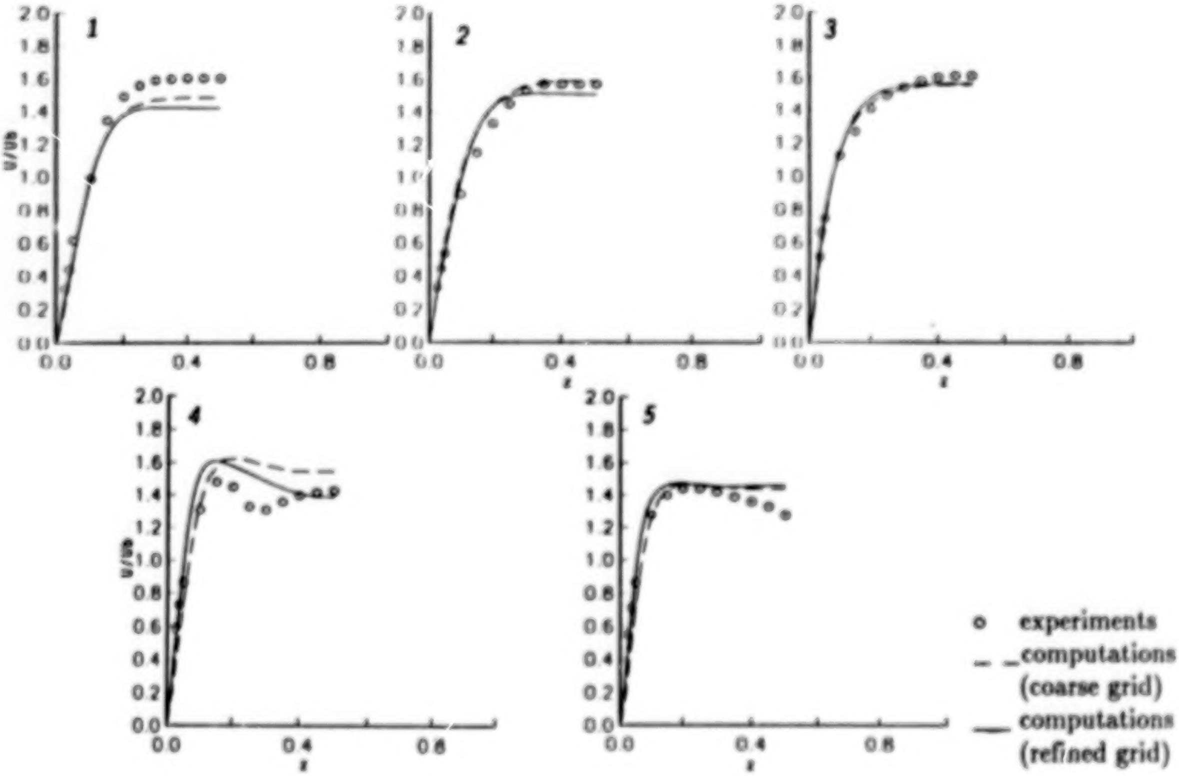

Figure 7.b. S-duct (laminar flow regime): Velocity profiles on midspan.

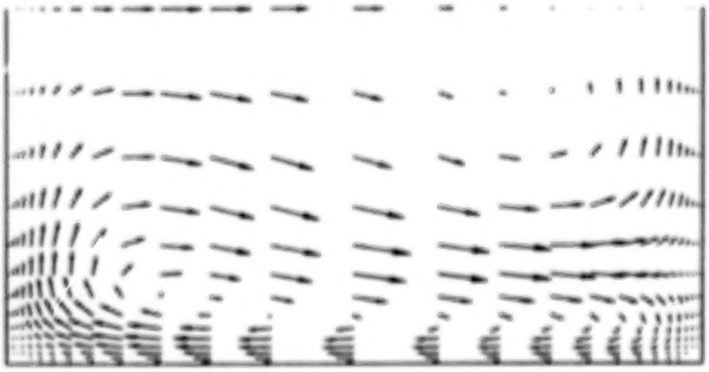

Figure 7.c. S-duct (laminar flow regime): Secondary velocity at bend exit.

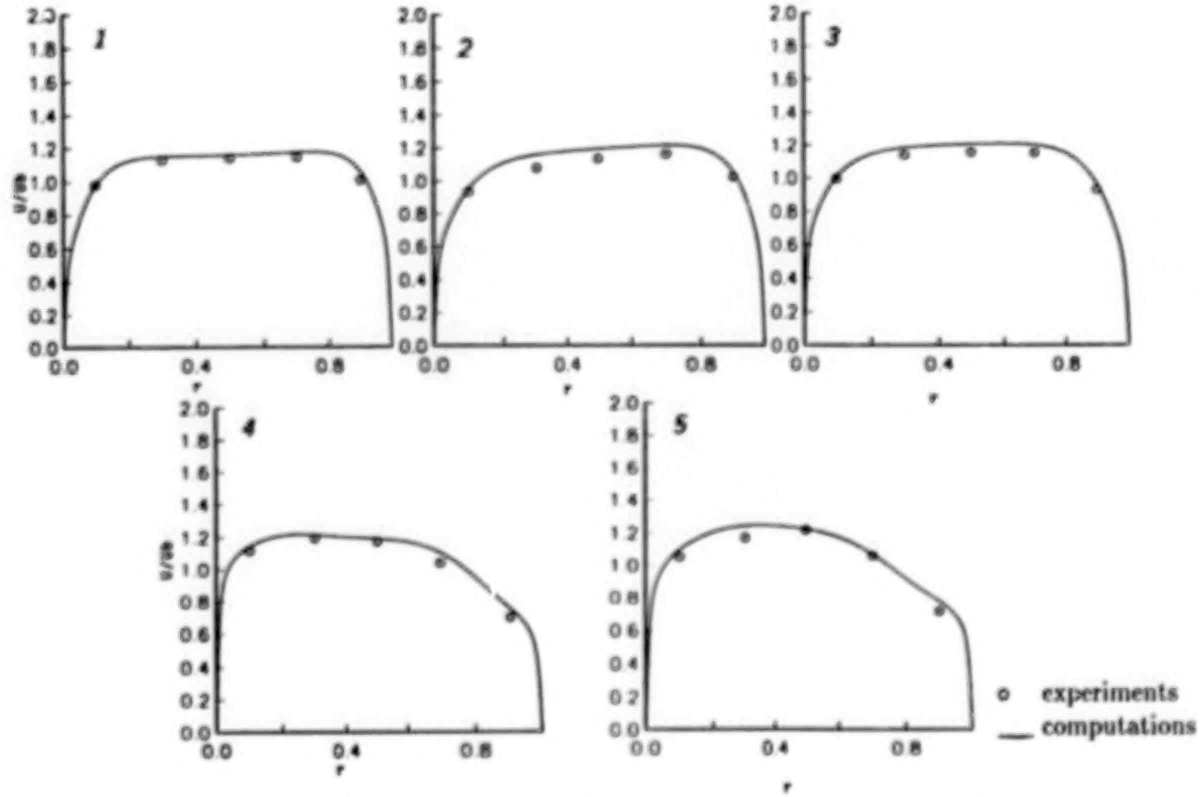

Figure 8.a. S-duct (turbulent flow regime): Velocity profiles on symmetry plane.

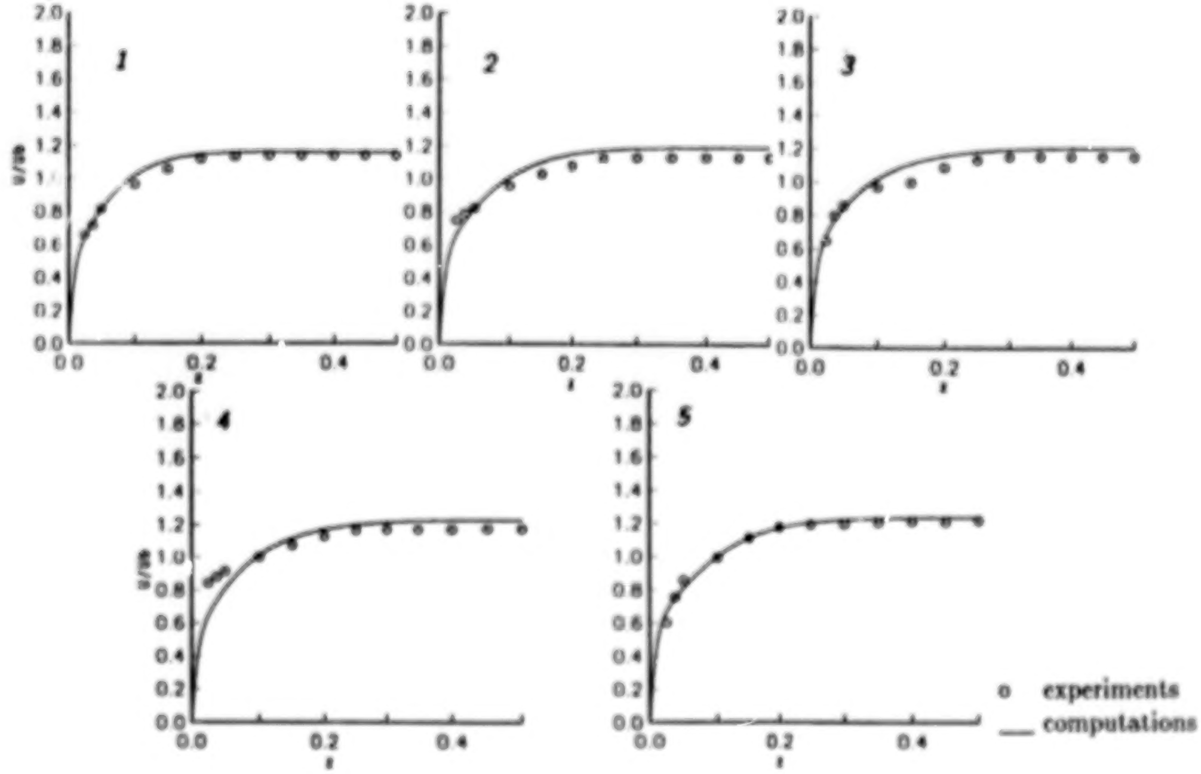

Figure 8.b. S-duct (turbulent flow regime): Velocity profiles on midspan.

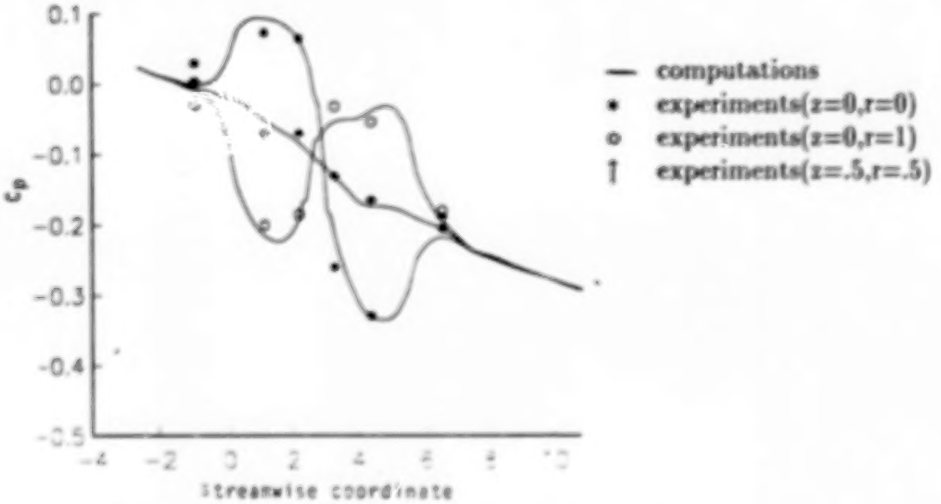

Figure 8.c. S-duct (turbulent flow regime): Wall C_p distribution.

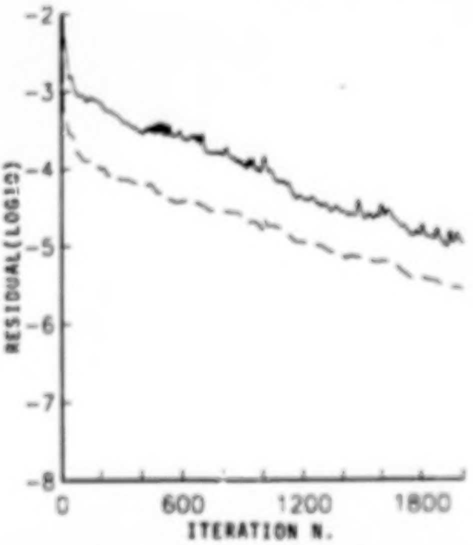

Figure 8.d. S-duct (turbulent flow regime): Convergence history.

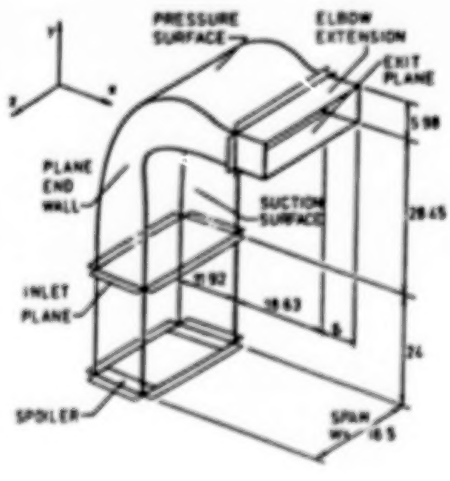

Figure 9. Stanitz elbow: Sketch of experimental set-up.

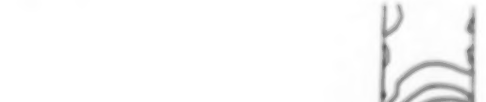

Figure 10.a. Stanitz elbow: Inviscid pressure isolines.

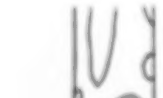

Figure 10.b. Stanitz elbow: Inviscid Mach number isolines.

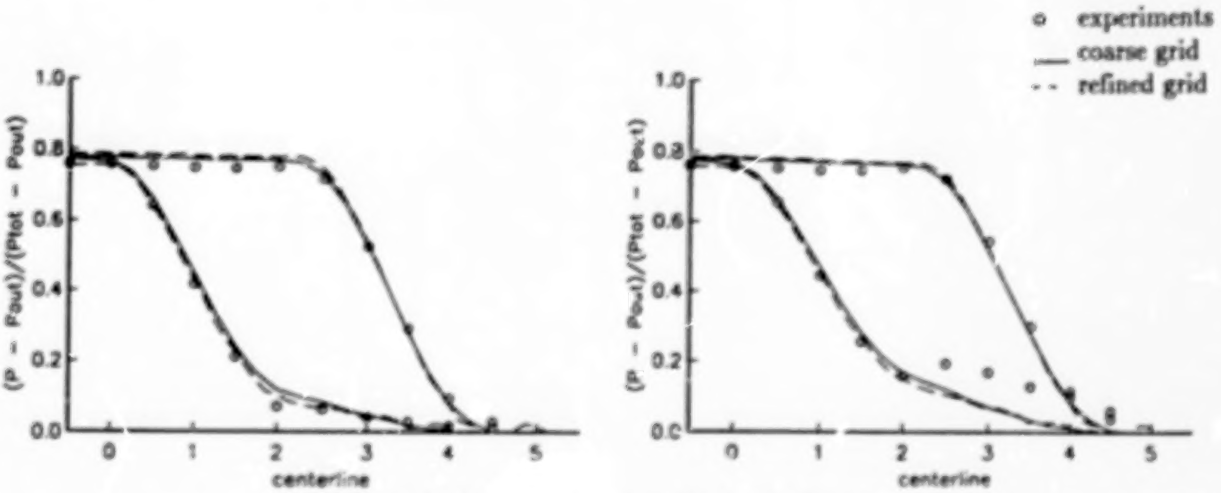

Figure 11. Stanitz elbow: Inviscid C_p distribution.

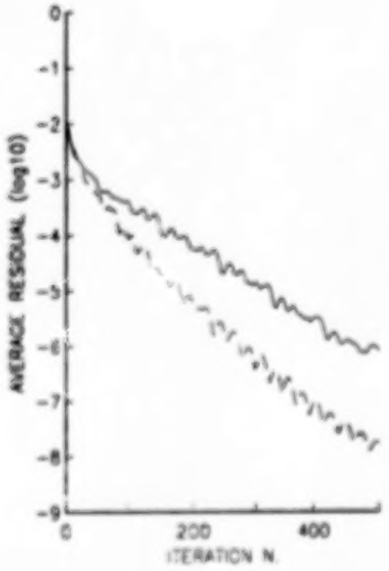

Figure 12. Stanitz elbow: Convergence history.

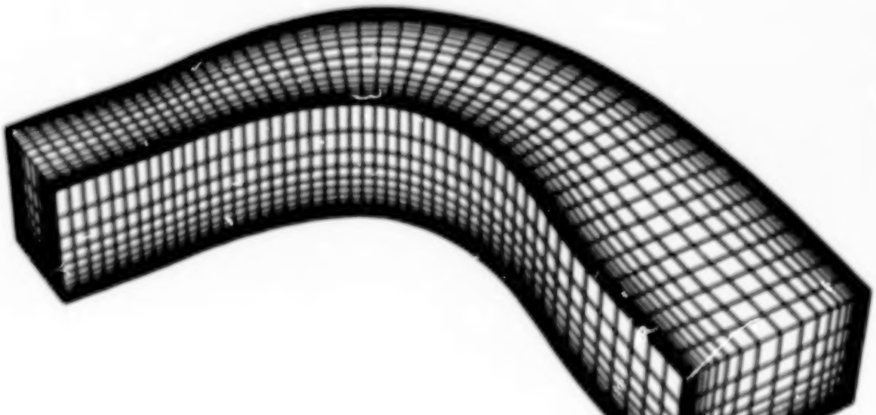

Figure 13. Stanitz elbow: Refined 50×41×31 grid.

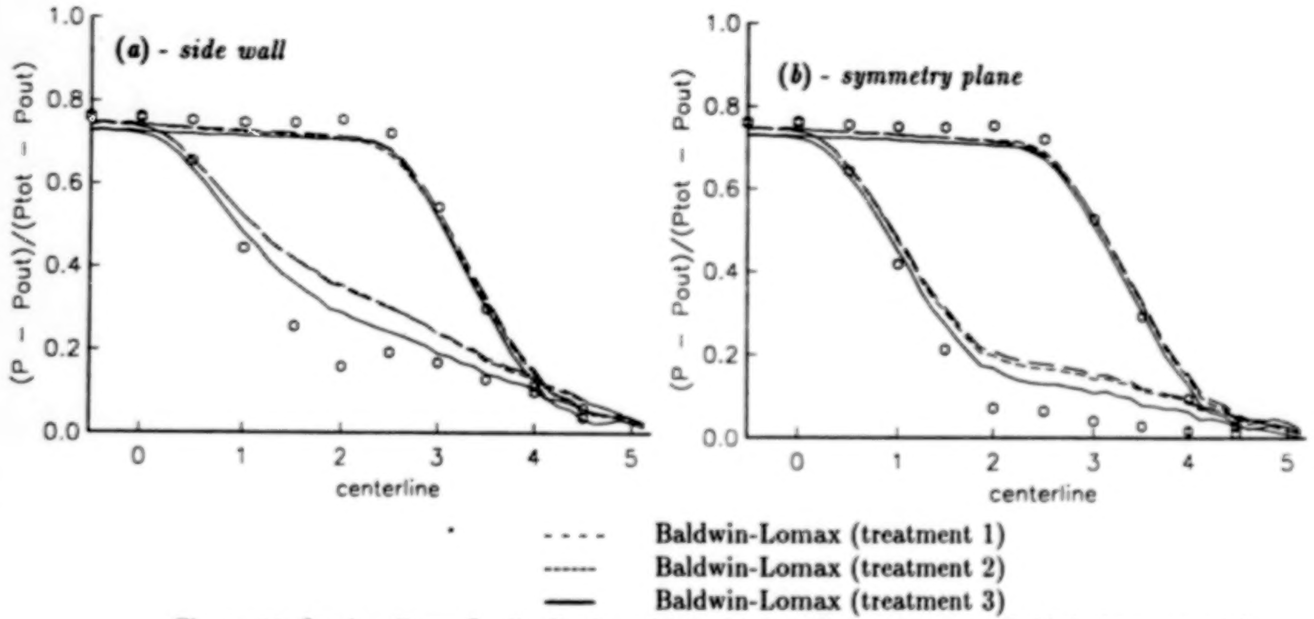

Figure 14. Stanitz elbow: C_p distribution with multiple wall treatments by Baldwin-Lomax model.

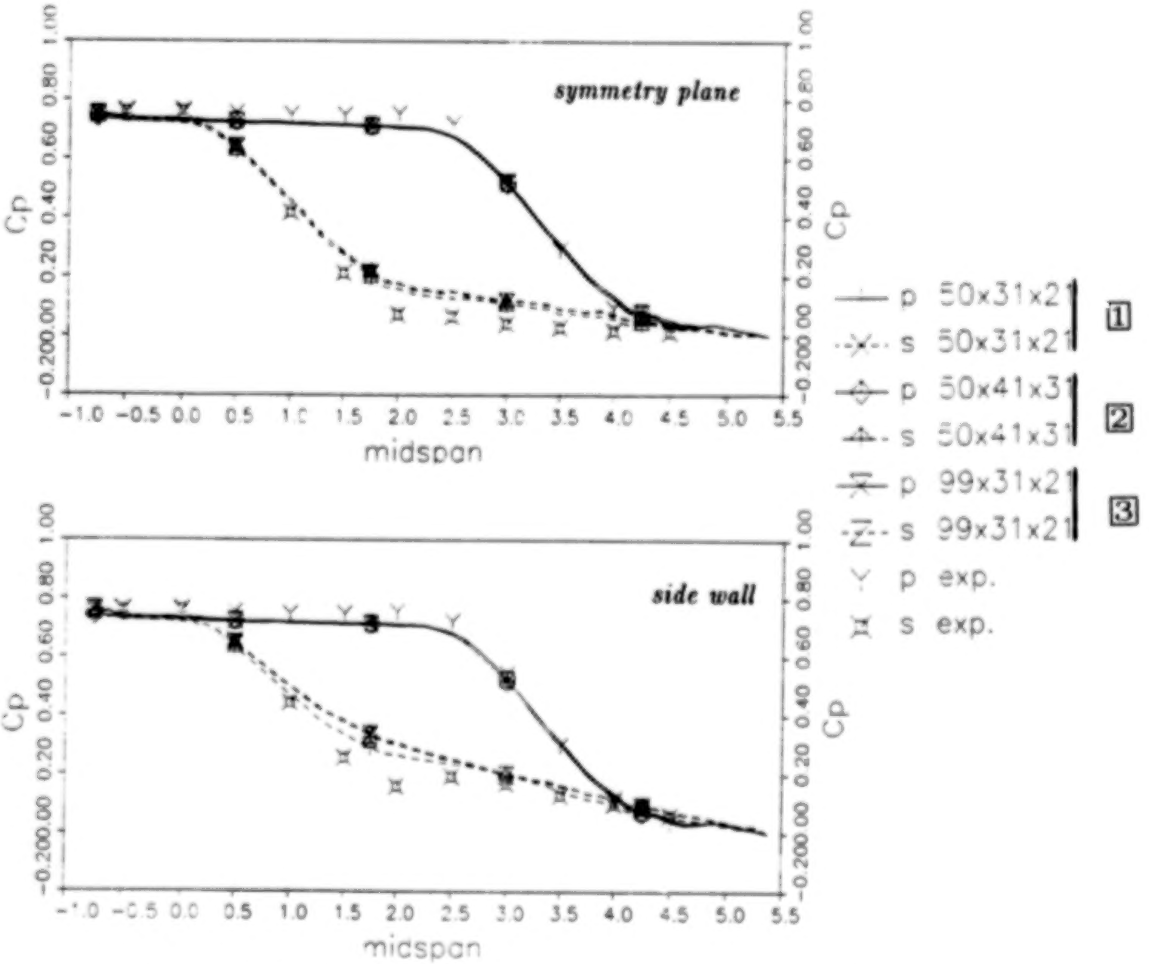

Figure 15. Stanitz elbow: C_p dependence on grid points by Baldwin-Lomax model.

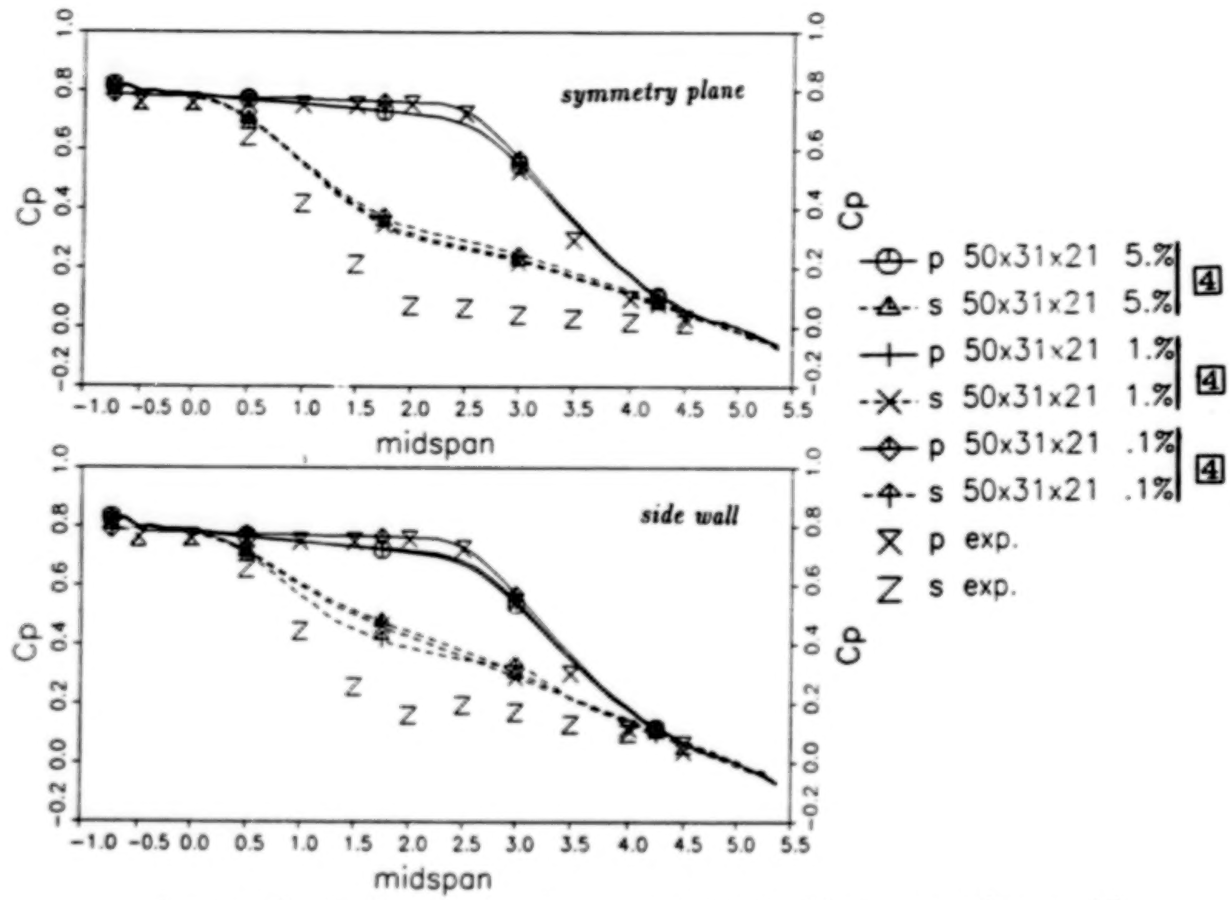

Figure 16. Stanitz elbow: C_p dependence on turbulence level by q-ω model (coarse grid).

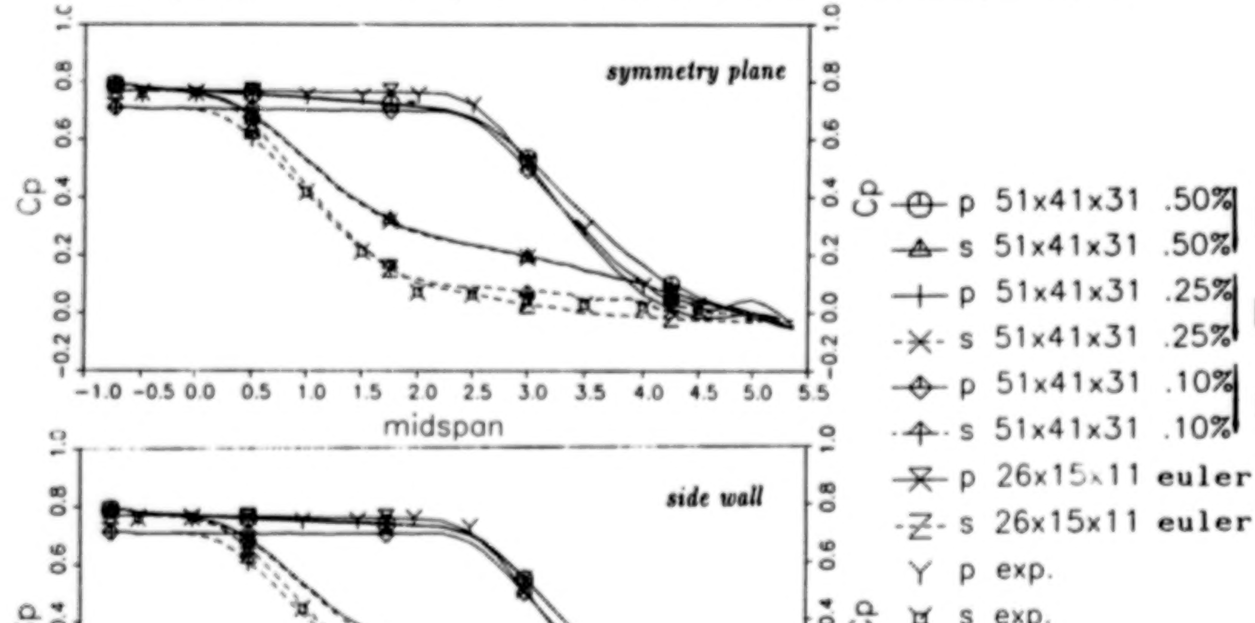

Figure 17. Stanitz elbow: C_p dependence on turbulence level by q-ω model (refined grid).

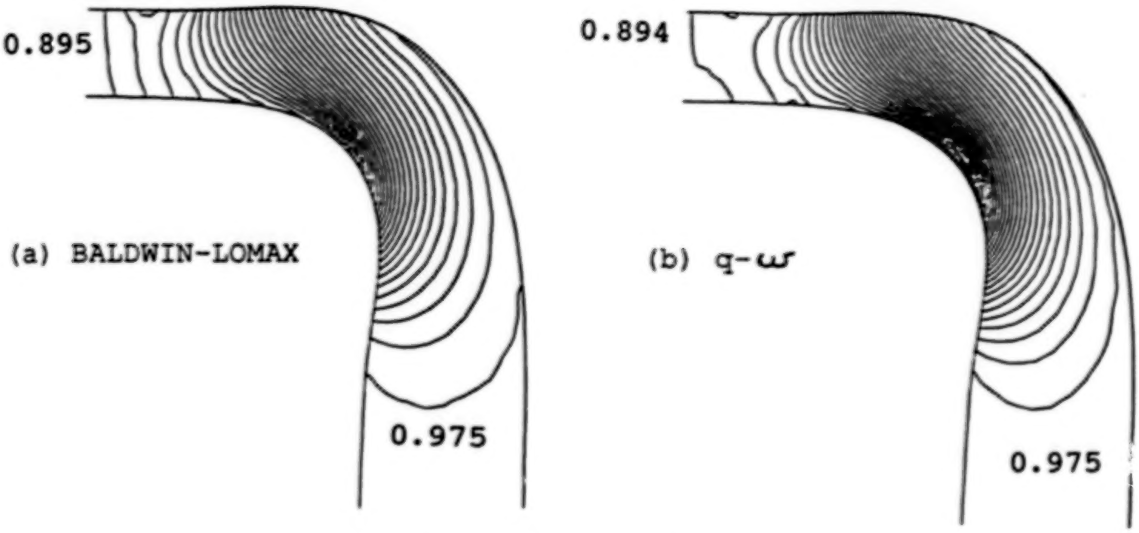

Figure 18. Stanitz elbow: Static pressure isolines on symmetry plane.

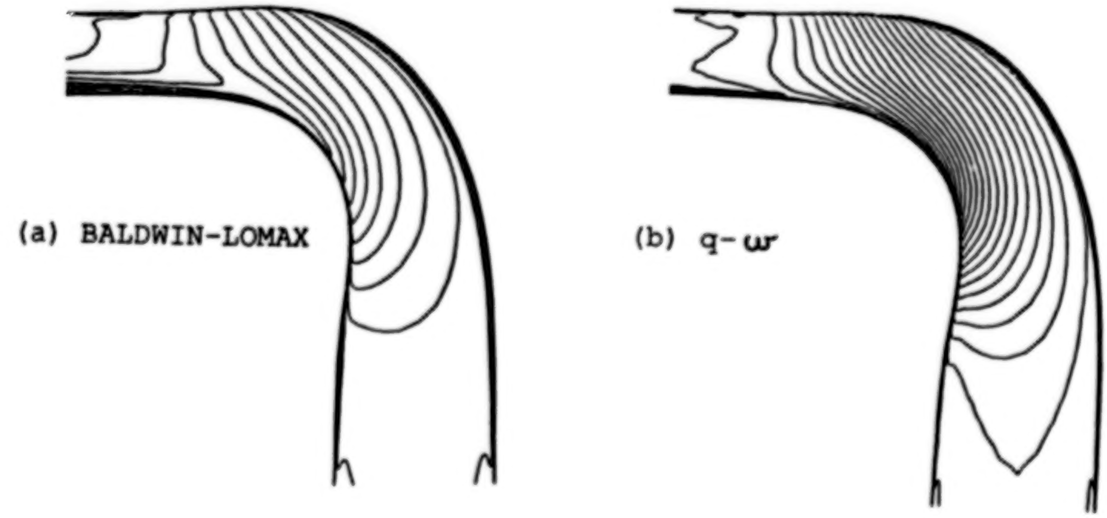

Figure 19. Stanitz elbow: Mach number isolines on symmetry plane.

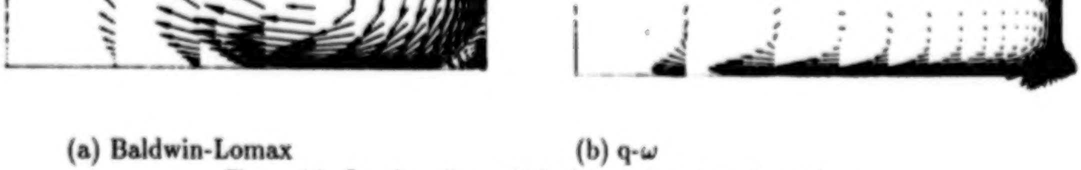

(a) Baldwin-Lomax (b) q-ω

Figure 20. Stanitz elbow: Velocity vectors at exit section.

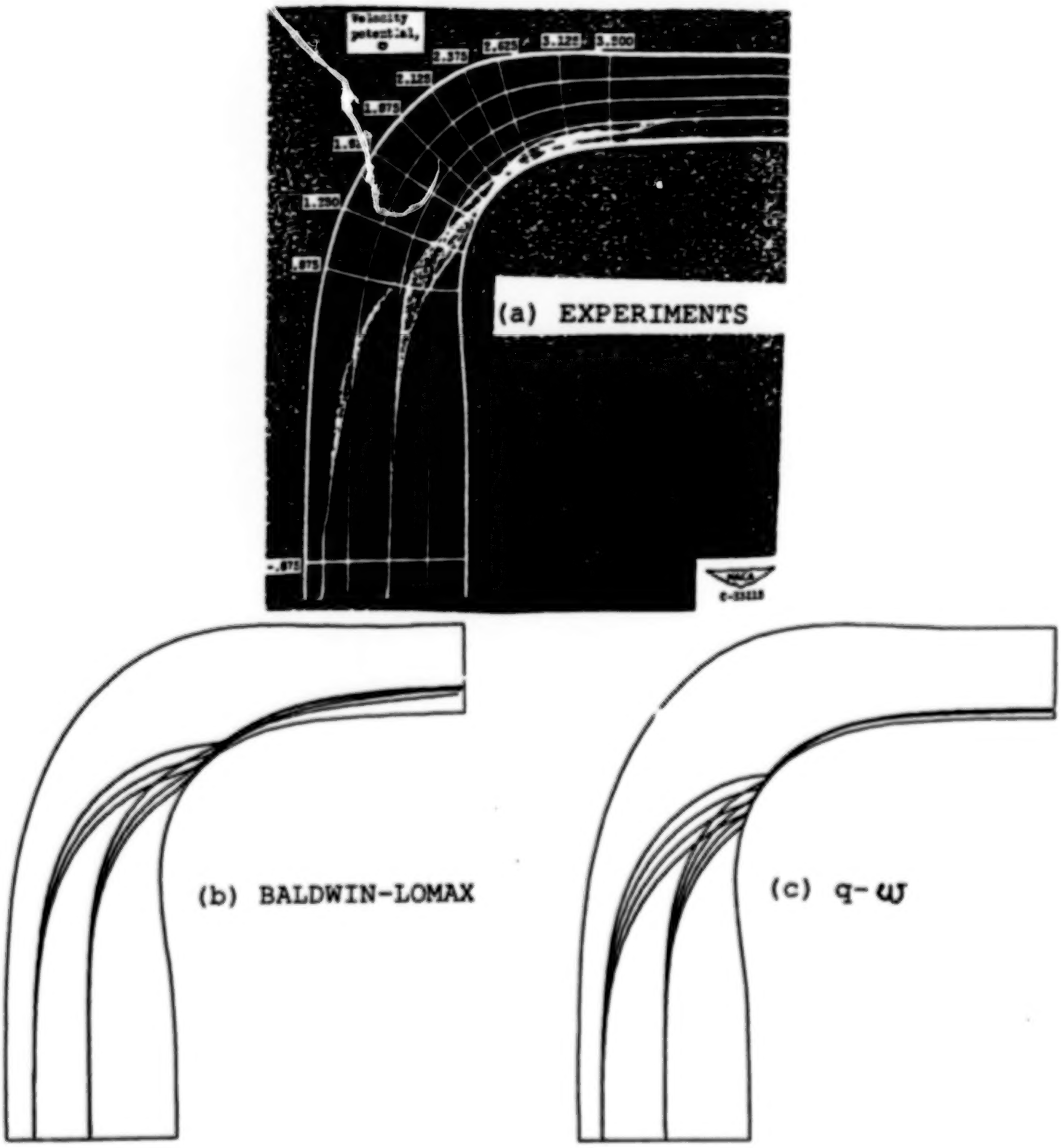

Figure 21. Stanitz elbow: Secondary flows visualization.

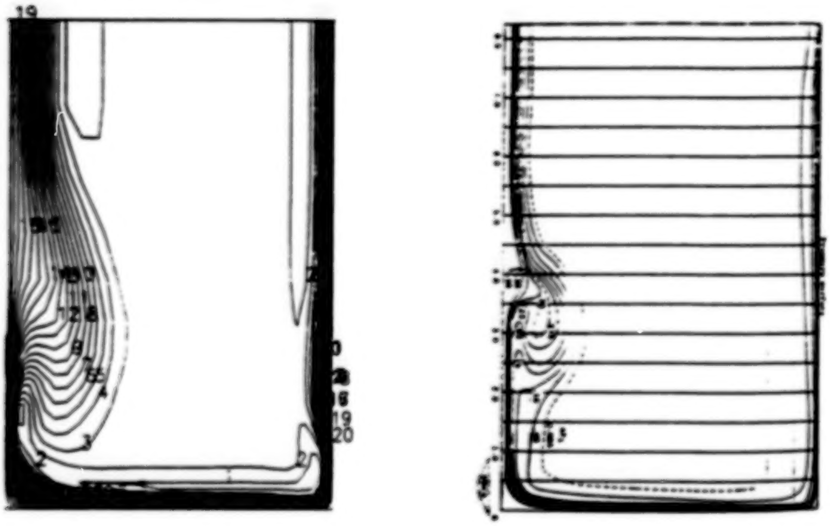

computations (51×31×21)   experiments

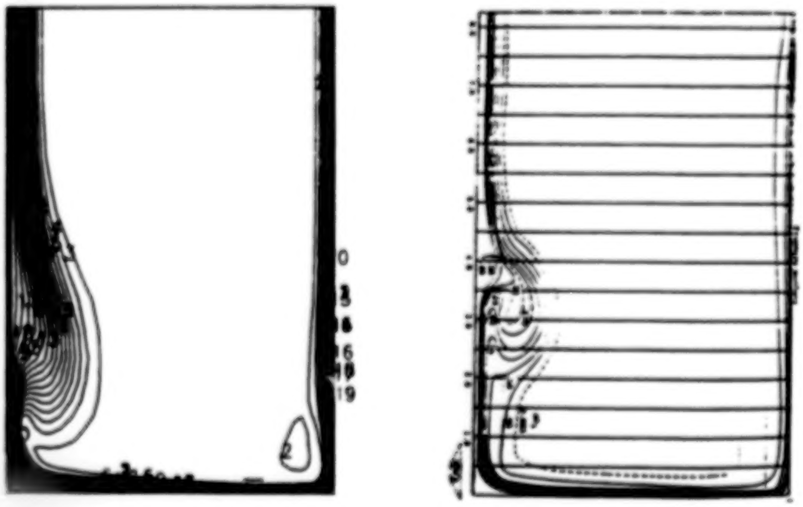

computations (51×41×31)   experiments

Figure 22. Stanitz elbow: Total pressure losses.

BLANK PAGE

NUMERICAL INVESTIGATION OF AN INTERNAL LAYER IN TURBULENT FLOW OVER A CURVED HILL

S.-W. Kim*
Institute for Computational Mechanics in Propulsion
NASA Lewis Research Center
Cleveland, Ohio

ABSTRACT

Numerical investigation of incompressible and compressible turbulent flows over strongly curved surfaces is presented. The turbulent flow equations are solved by a pressure based Navier-Stokes equations solver. In the method, the conservation of mass equation is replaced by a pressure correction equation applicable for both incompressible and compressible flows. The turbulence is described by a multiple-time-scale turbulence model supplemented with a near-wall turbulence model. The numerical results show that the internal layer is a strong turbulence field which is developed beneath the external boundary layer and is located very close to the wall. The development of the internal layer is attributed to the enormous mean flow strain rate caused by the streamline curvature. The external boundary layer flow responds rather slowly to the streamline curvature, thus the turbulence field in the forward corner of the curved hill is characterized by two turbulence fields (one belongs to the external boundary layer flow and the other belongs to the internal) interacting with each other. The turbulence intensity of the internal layer is much stronger than that of the external boundary layer so that the development of a new boundary layer in the downstream region of the curved hill depends mostly on the internal layer. These numerical results are in good agreement with the measured data, and show that the turbulence model can resolve the turbulence field subjected to the strong streamline curvature.

NOMENCLATURE

A_u	coefficient for u-velocity correction equation
A_v	coefficient for v-velocity correction equation
c	chord length of axisymmetric bump
c_f	friction coefficient
c_p	pressure coefficient
$c_{p\ell}$	turbulence model constants for ϵ_p equation (ℓ-1,3)
$c_{t\ell}$	turbulence model constants for ϵ_t equation (ℓ-1,3)
$c_{\mu f}$	constant coefficient (-0.09)
f_μ	wall damping function for eddy viscosity equation
f_ϵ	wall damping function for ϵ_w equation
k	turbulent kinetic energy ($k-k_p + k_t$)
k_p	turbulent kinetic energy of eddies in production range
k_t	turbulent kinetic energy of eddies in dissipation range
k_e	effective thermal conductivity ($-k_m + C_p\mu_t/\sigma_T$)
k_m	molecular thermal conductivity
M_∞	free stream Mach number
U_∞	free stream velocity
p	static pressure
P_r	production rate of turbulent kinetic energy

---

*Work funded by Space Act Agreement C99066G.

R	gas constant
R_e	Reynolds number
R_t	turbulent Reynolds number $(=k^2/(\nu\epsilon_1))$
s'	distance measured along the curved hill
T	temperature
(u,v)	time averaged velocities in (x,y) coordinates
$\overline{u'v'}$	Reynolds stress
V	velocity vector $(=(u,v))$
(x,y)	tangential and transverse coordinates
ϵ_p	energy transfer rate of turbulent kinetic energy
ϵ_t	dissipation rate of turbulent kinetic energy
ϵ_1	dissipation rate of turbulent kinetic energy
κ	von Karman constant (=0.41)
μ	molecular viscosity
μ_e	effective viscosity $(=\mu+\mu_t)$
μ_t	turbulent viscosity
ν	kinematic viscosity of fluid
ν_t	turbulent eddy viscosity
ρ	density
σ_{kp}	turbulent Prandtl number for k_p equation
σ_{kt}	turbulent Prandtl number for k_t equations
σ_T	turbulent Prandtl number for energy equation (=0.75)
$\sigma_{\epsilon p}$	turbulent Prandtl number for ϵ_p equation
$\sigma_{\epsilon t}$	turbulent Prandtl number for ϵ_t equation
τ_w	wall shearing stress
Φ	dissipation function for energy equation

Superscripts

$*$	current value
$'$	incremental (or corrective) value

INTRODUCTION

Turbulent flows subjected to various strain rates (in addition to the simple shearing strain rates) caused by streamline curvature, strong pressure gradient, separation and reattachment, swirl velocity and interaction of a multiple number of shear layers are usually called "complex turbulent flows." Calculations of complex turbulent flows using various turbulence models such as the k-ϵ turbulence models, algebraic Reynolds stress turbulence models (ARSM), and Reynolds stress turbulence models (RSM) yield rather unsatisfactory computational results (ref. 1). Many turbulence models, improved by modifying the standard form turbulence equations (usually, the dissipation rate equation for k-ϵ and ARSM and the pressure-strain correlation term for ARSM and RSM) to yield better computational results for a few flow cases, have produced worse agreement with the measured data than the standard turbulence models for other classes of turbulent flows (ref. 2). Unlike many other turbulence models, the present multiple-time-scale turbulence model (hereafter, abbreviated as the M-S model) yields accurate computational results for a number of complex turbulent flows (ref. 3-4). These complex turbulent flows include: a wall-jet, a wake-boundary layer interaction flow, a turbulent flow over a backward-facing step, a confined coaxial swirling jet, and reattaching shear layers in a divergent channel. The numerical results for each of these complex turbulent flows obtained using the M-S model compared as favorably with the measured data as the results obtained using an optimized turbulence model for each flow. More recently, it was shown that the M-S model can resolve the turbulence field subjected to a strong streamline curvature in an incompressible turbulent flow over a curved hill (ref. 5) and in compressible turbulent flows over a curved hill (ref. 6). A few numerical results obtained in the previous studies are presented in this paper. A few differences between the present M-S model and that of Hanjelic et al. (ref. 7) are also reproduced here from reference 3. The historical background of experimental and theoretical researches in turbulent flows subjected to streamline curvature (ref. 5, 8-9) is briefly described below.

Turbulent shear layers over curved surfaces are highly sensitive even to a small amount of streamline curvature (ref. 8). Bradshaw (ref. 8) proposed a curvature correction method based on an assumption that such turbulent flows can be characterized by a "curvature parameter", that is, the ratio of boundary layer thickness to radius of curvature. In the curvature correction method, the mixing length is altered to include the curvature parameter. Many turbulence models incorporating a curvature correction method yield improved computational results for turbulent flows over mildly curved surfaces, and the computational results help to better understand the turbulence structure of such flows; however, these turbulence models still fail to predict the turbulence field for turbulent flows with large streamline curvature. To better understand the turbulence structure over strongly curved surfaces, Baskaran, Smits & Joubert measured various turbulence quantities in a turbulent boundary layer over a curved hill (ref. 9). The measured data showed that an internal layer is formed beneath the external boundary layer and that the internal layer is insensitive to the external boundary layer and the curvature parameter. A numerical investigation of the same turbulent flow using the M-S turbulence model showed that the internal layer is developed beneath the external boundary layer and in the region very close to the wall. It was also found that the internal layer is significantly different from boundary layer flows in the sense that the internal layer is characterized by a strong turbulence field.

The compressible turbulent flows over an axisymmetric curved hill (ref. 10) and the incompressible turbulent flow over a two-dimensional curved hill (ref. 9) share the same physical phenomenon that the turbulence fields are subjected to strong streamline curvatures. However, the compressible flow case involves extra strains caused by the shock wave - turbulent boundary layer interaction in addition to that caused by the streamline curvature. In the compressible flow case, a supersonic pocket is formed in the top region of the curved hill as the free stream Mach number is increased. As the strength of the shock wave is increased with increasing free stream Mach number, the size of the reversed flow region grows extensively due to the shock wave - boundary layer interaction. A number of turbulence models, ranging from algebraic turbulence models to two-equation turbulence models incorporating a streamline curvature correction method, have been tested in references 11-13. It can be found in these references that various turbulence models, except the King-Johnson algebraic turbulence model (ref. 11), fail to predict the reversed flow region at low free stream Mach numbers, which indicates that these turbulence models can not resolve the turbulence field subjected to the streamline curvature. On the other hand, the numerical results obtained using the M-S turbulence model showed that there exists a reversed flow region at low free stream Mach numbers and that the size of the reversed flow region grows extensively due to the shock wave - boundary layer interaction as the free stream Mach number is increased. These numerical results indicate that the M-S turbulence model can resolve the turbulence field subjected to extra strains caused by the streamline curvature and the shock wave - boundary layer interaction (ref. 6).

REYNOLDS AVERAGED NAVIER-STOKES EQUATIONS AND NUMERICAL METHOD

The compressible turbulent flow equations are given as

$$\frac{\partial}{\partial x}(\rho u) + \frac{1}{y^j}\frac{\partial}{\partial y}(y^j \rho v) = 0. \tag{1}$$

$$\frac{\partial}{\partial x}(\rho uu) + \frac{1}{y^j}\frac{\partial}{\partial y}(y^j \rho vu) = \frac{\partial}{\partial x}(\tau_{xx}) + \frac{1}{y^j}\frac{\partial}{\partial y}(y^j \tau_{xy}) - \frac{\partial p}{\partial x} \tag{2}$$

$$\frac{\partial}{\partial x}(\rho uv) + \frac{1}{y^j}\frac{\partial}{\partial y}(y^j \rho vv) = \frac{\partial}{\partial x}(\tau_{yx}) + \frac{1}{y^j}\frac{\partial}{\partial y}(y^j \tau_{yy}) - \frac{\partial p}{\partial y} - j\frac{\tau_{\theta\theta}}{y} \tag{3}$$

$$\frac{\partial}{\partial x}(\rho C_p uT) + \frac{1}{y^j}\frac{\partial}{\partial y}(y^j \rho C_p vT) = \frac{\partial}{\partial x}\left(k_e\frac{\partial T}{\partial x}\right) + \frac{1}{y^j}\frac{\partial}{\partial y}\left(y^j k_e\frac{\partial T}{\partial y}\right) + u\frac{\partial p}{\partial x}$$

$$+ v\frac{\partial p}{\partial y} + \mu_e \Phi \tag{4}$$

where

$$\tau_{xx} = 2\mu_e\frac{\partial u}{\partial x} - \frac{2\mu_e}{3}(\nabla\cdot\mathbf{V}),$$

$$\tau_{xy} = \tau_{yx} = \mu_e\left(\frac{\partial u}{\partial y} + \frac{\partial v}{\partial x}\right),$$

$$\tau_{yy} = 2\mu_e\frac{\partial v}{\partial y} - \frac{2\mu_e}{3}(\nabla\cdot\mathbf{V}),$$

$$\tau_{\phi\phi} = 2\mu_e\frac{v}{y} - \frac{2\mu_e}{3}(\nabla\cdot\mathbf{V}),$$

$$\Phi = \left\{ 2\left(\frac{\partial u}{\partial x}\right)^2 + 2\left(\frac{\partial v}{\partial y}\right)^2 + 2j\left(\frac{v}{y}\right)^2 + \left(\frac{\partial u}{\partial y} + \frac{\partial v}{\partial x}\right)^2 \right\} - \frac{2}{3}(\nabla\cdot\mathbf{V})^2,$$

$$\nabla\cdot\mathbf{V} = \frac{\partial u}{\partial x} + \frac{1}{y^j}\frac{\partial(y^j v)}{\partial y},$$

the density is obtained from the perfect gas law given as $p=\rho RT$, $j=0$ for two-dimensional flows, and $j=1$ for axisymmetric flows. The molecular viscosity and the thermal conductivity were obtained from Sutherland's laws (ref. 14). The specific heat was obtained from a curve-fitted 4-th order polynomial (ref. 15). In the present numerical method, the conservation of mass equation is replaced by a pressure correction equation valid for both incompressible and compressible flows, which is given as

$$\frac{\partial}{\partial x}\left(\frac{u^*}{RT}p'\right) + \frac{1}{y^j}\frac{\partial}{\partial y}\left(y^j\frac{v^*}{RT}p'\right) - \frac{\partial}{\partial x}\left(\rho^* A_u\frac{\partial p'}{\partial x}\right) - \frac{1}{y^j}\frac{\partial}{\partial y}\left(y^j\rho^* A_v\frac{\partial p'}{\partial y}\right) = -\nabla\cdot(\rho^*\mathbf{V}^*) \quad (5)$$

where the first two convective incremental pressure terms in the left hand side of eq. (5) take into account the hyperbolic nature of supersonic flows and enable the capture of shock waves. Details on the present numerical method can be found in references 6 and 16 and are not included in this paper. It would be sufficient to state here that the present numerical method yields accurate computational results even when highly skewed, unequally spaced, curved grids are used. A few differences between the present numerical method and the more general compressible flow solvers are discussed below.

Recall that the compressible flow equations are mostly solved by approximate factorization methods and flux splitting methods. The Beam-Warming method (ref. 17) and the MacCormack method (ref. 18) are representatives of the approximate factorization methods, and the Steiger-Warming method (ref. 19) is a representative of the flux-splitting methods. In this class of methods, the density is solved for as a primary variable and the pressure is obtained from the equation state. For incompressible flows, the pressure no longer depends on the density and hence this class of methods fails for incompressible flows. These methods can also be extended to solve incompressible flows by including an artificial compressibility into the governing flow equations (ref. 20). On the other hand, in the pressure correction methods, the incremental pressure is solved for as a primary variable, hence the method is valid for both incompressible and compressible flows. Another difference between the two classes of methods can be found in the way the second order diffusion term is treated. In the pressure correction methods, the diffusion term is incorporated into the stiffness matrix while, in the other class of methods, the diffusion term is incorporated into the system of equations as the load vector term. For turbulent flows with extensive recirculation zones, the pressure correction methods may be numerically more stable than the other class of methods, conceptually; however, the pressure correction methods have mostly been used for incompressible flows, and the approximate factorization methods and the flux splitting methods have mostly been used for compressible flows. Therefore, definitive advantages and disadvantages of these two classes of methods can not be discussed with confidence as yet.

TURBULENCE EQUATIONS

The M-S turbulence model supplemented with the near-wall turbulence model is described below. The turbulent kinetic energy and the energy transfer rate equations for the energy-containing large eddies are given as

$$\frac{\partial}{\partial x}(\rho u k_p) + \frac{1}{y^j}\frac{\partial}{\partial y}(y^j \rho v k_p) - \frac{\partial}{\partial x}\left(\left(\mu+\frac{\mu_t}{\sigma_{kp}}\right)\frac{\partial k_p}{\partial x}\right) - \frac{1}{y^j}\frac{\partial}{\partial y}\left(y^j\left(\mu+\frac{\mu_t}{\sigma_{kp}}\right)\frac{\partial k_p}{\partial y}\right) = \rho \mathrm{Pr} - \rho\epsilon_p \qquad (6)$$

$$\frac{\partial}{\partial x}(\rho u \epsilon_p) + \frac{1}{y^j}\frac{\partial}{\partial y}(y^j \rho v \epsilon_p) - \frac{\partial}{\partial x}\left(\left(\mu+\frac{\mu_t}{\sigma_{\epsilon p}}\right)\frac{\partial \epsilon_p}{\partial x}\right) - \frac{1}{y^j}\frac{\partial}{\partial y}\left(y^j\left(\mu+\frac{\mu_t}{\sigma_{\epsilon p}}\right)\frac{\partial \epsilon_p}{\partial y}\right)$$

$$= \rho c_{p1}\frac{\mathrm{Pr}^2}{k_p} + \rho c_{p2}\frac{\mathrm{Pr}\,\epsilon_p}{k_p} - \rho c_{p3}\frac{\epsilon_p^2}{k_p} \qquad (7)$$

where $\mathrm{Pr}=\nu_t\Phi$ is the production rate. The turbulent kinetic energy equation and the dissipation rate equations for the fine scale eddies are given as

$$\frac{\partial}{\partial x}(\rho u k_t) + \frac{1}{y^j}\frac{\partial}{\partial y}(y^j \rho v k_t) - \frac{\partial}{\partial x}\left(\left(\mu+\frac{\mu_t}{\sigma_{kt}}\right)\frac{\partial k_t}{\partial x}\right) - \frac{1}{y^j}\frac{\partial}{\partial y}\left(y^j\left(\mu+\frac{\mu_t}{\sigma_{kt}}\right)\frac{\partial k_t}{\partial y}\right) = \rho\epsilon_p - \rho\epsilon_t \qquad (8)$$

$$\frac{\partial}{\partial x}(\rho u \epsilon_t) + \frac{1}{y^j}\frac{\partial}{\partial y}(y^j \rho v \epsilon_t) - \frac{\partial}{\partial x}\left(\left(\mu+\frac{\mu_t}{\sigma_{\epsilon t}}\right)\frac{\partial \epsilon_t}{\partial x}\right) - \frac{1}{y^j}\frac{\partial}{\partial y}\left(y^j\left(\mu+\frac{\mu_t}{\sigma_{\epsilon t}}\right)\frac{\partial \epsilon_t}{\partial y}\right)$$

$$= \rho c_{t1}\frac{\epsilon_p^2}{k_t} + \rho c_{t2}\frac{\epsilon_p\epsilon_t}{k_t} - \rho c_{t3}\frac{\epsilon_t^2}{k_t} \qquad (9)$$

The eddy viscosity is given as

$$\mu_t = \rho c_{\mu f}\frac{k^2}{\epsilon_p} \qquad (10)$$

Eqs. (6) and (8) imply that the turbulent kinetic energy is generated by the instability of the mean fluid motion, is transferred to the high wave number region, and is dissipated by the molecular viscosity of the fluid. This mathematical model is consistent with the physically observed evolution of the turbulent kinetic energy (ref. 21) except that the cascade process of the turbulent kinetic energy is over-simplified and is represented by the single energy transfer rate. This over-simplification is still better justified than the single-time-scale turbulence models if one considers that only the generation and dissipation of turbulent kinetic energy are considered in the latter classes of turbulence models. In eq. (10), the turbulence length scale is related to the energy transfer rate of the energy-containing large eddies rather than the dissipation rate of the fine-scale eddies. The turbulence model constants are given as $\sigma_{kp}=0.75$, $\sigma_{kt}=0.75$, $\sigma_{\epsilon p}=1.15$, $\sigma_{\epsilon t}=1.15$, $c_{p1}=0.21$, $c_{p2}=1.24$, $c_{p3}=1.84$, $c_{t1}=0.29$, $c_{t2}=1.28$, and $c_{t3}=1.66$. The turbulent kinetic energy equations, eqs. (6) and (8), are defined for the entire flow domain while the energy transfer rate equation, the dissipation rate equation, and the eddy viscosity equation are valid for the flow domain away from the near-wall region.

The near-wall turbulence is described by a "partially low Reynolds number" near-wall turbulence model (ref.22). In this near-wall turbulence model, only the turbulent kinetic energy equations are extended to include the near-wall low turbulence region and the energy transfer rate and the dissipation rate inside the near-wall layer are obtained from algebraic equations. The energy transfer rate and the dissipation rate inside the near-wall layer are given as

$$\epsilon_p = \epsilon_t = \frac{\epsilon_1}{f_\epsilon} \tag{11}$$

where $\epsilon_1 = c_{\mu f}^{3/4} k^{3/2}/\kappa y$, $f_\epsilon = 1 - \exp(-A_\epsilon R_t)$, $R_t = k^2/\nu\epsilon_1$, and $A_\epsilon = c_{\mu f}^{3/2}/2\kappa^2$. The eddy viscosity for the near-wall layer is given as

$$\mu_t = \rho\, c_{\mu f}\, f_\mu\, k^2/\epsilon_1 \tag{12}$$

where $f_\mu = 1 - 1./\exp(A_1\sqrt{R_t} + A_2 R_t^2)$, $A_1=0.025$, and $A_2=0.00001$. The eddy viscosity given as eq. (12) grows in proportion to the cubic power of the distance from the wall. It can be found in reference 22 that the near-wall analysis yields the same growth rate of the eddy viscosity in the region very close to the wall. For wall bounded turbulent flows, the equilibrium region extends from $y^+ \approx 30$ to $y^+ \approx 300$. Thus the partition between the near-wall region and the fully turbulent outer region can be located between y^+ greater than 30 and less than 300 approximately. The present near-wall turbulence model is valid for the entire flow domain of equilibrium boundary layer flows. Thus the computational results do not depend appreciably on the location of the partition. However, if the partition is located too far away from the wall (i.e., $y^+>1000$), then the numerical results in the near-wall region may become similar to those obtained using a k-equation turbulence model.

The capability of the present turbulence model to resolve various complex turbulence fields is discussed in this paragraph by comparing the M-S turbulence models with the single-time-scale turbulence models and by comparing the present turbulence model with that of Hanjelic et al. (ref. 7). Recall that the turbulent transport of mass and momentum is governed by the time scale of the energy-containing large eddies and the dissipation of the turbulent kinetic energy is governed by the time scale of the fine scale eddies (ref. 21). In M-S turbulence models, the turbulent transport of mass and momentum is described using the time scale of the large eddies and the dissipation rate is described using the time scale of the fine-scale eddies. On the other hand, in the single-time-scale turbulence models such as the k-ϵ, ARSM, and RSM turbulence models, a single time scale is used to describe both the turbulence transport mechanism and the dissipation rate of turbulent kinetic energy. The single-time-scale turbulence models yield reasonably accurate computational results for simple turbulent flows; however, the predictive capability degenerates rapidly as turbulent flows to be solved become more complex. This nature may due to the use of the time scale of fine-scale eddies to describe the turbulent transport of mass and momentum. Due to the physically consistent nature of the M-S turbulence models, these turbulence models are expected to yield significantly improved computational results compared with the single-time-scale turbulence models. However, the first M-S turbulence model (ref. 7) did not quite come up to the expectations due to a few shortcomings in the closure model. These shortcomings and a few differences between the two M-S turbulence models are reproduced here from reference 3. Firstly, the eddy viscosity equation in reference 7 is given as

$$\mu_t = \rho \, c_{\mu f} \frac{k k_p}{\epsilon_p} \tag{13}$$

Eq. (13) implies that the small scale eddies contained in the dissipation range may not contribute significantly to the turbulent transport of mass and momentum. However, numerical calculations of complex turbulent flows show that the ratio of k_t/k_p can vary significantly in regions where the turbulence is in a strongly inequilibrium state. This anomaly can be cured if k_t is always negligibly small. However, in this case, the multiple-time-scale turbulence model can become a single-time-scale k-ϵ turbulence model. The eddy viscosity, given as eq. (13), is also inconsistent with the near wall mixing length theory or the standard wall functions unless k_t vanishes in the near-wall equilibrium region (ref. 3). Secondly, in the present M-S turbulence model, the variable energy transfer functions were obtained from a physical dimensional analysis. On the other hand, the other M-S turbulence model contains such a variable energy transfer function only in the energy transfer rate equation. Thirdly, in the present M-S turbulence model, the model constants were obtained by solving a five by five system of equations and by numerically optimizing one model constant (c_{p1}) to yield the best solutions for a fully developed channel flow and a plane jet exhausting into a moving stream (ref. 3). One equation for the model constants is obtained from the equilibrium condition. Two equations are obtained by transforming the multiple-time-scale turbulence equations into asymptotic turbulence growth rate equations which are equivalent to that of Harris, Graham & Corrsin (ref. 23). The other two equations are obtained by transforming the present turbulence equations into asymptotic turbulence decay rate equations which are equivalent to that of Harlow and Nakayama (ref. 24). Lastly, of practical importance, arbitrary ratios of k_t/k_p were used as a near wall boundary condition together with the standard wall functions in application to complex turbulent flows (ref. 7 and 25). This boundary condition is inconsistent with the near-wall analysis. A wall function for the M-S turbulence model obtained from a near-wall analysis is given in reference 3 if a wall function needs to be used. Also an arbitrary ratio of k_t/k_p was used as an inlet boundary condition in a number of boundary layer calculations (ref. 25). In this case, the calculated shear layer expands rapidly so that the turbulence field can adjust itself to the ill-posed inlet boundary condition, (ref. 3).

COMPUTATIONAL RESULTS

Incompressible Turbulent Flow over a Curved Hill

The turbulent flow over a curved hill considered in this paper can be found in references 5 and 9. The unit Reynolds number based on the free stream velocity (U_∞=20 m/sec) is 1.33×10^6/meter. A series of numerical tests on the dependence of the computational results on the grid size, the location of the far field boundary, and the boundary conditions prescribed at the far field boundaries can be found in reference 5. The numerical results presented in this paper are almost independent of these numerical uncertainties.

The calculated pressure distribution on the wall of the curved hill is compared with the measured data in Figure 1, where the pressure coefficient was obtained by normalizing the wall pressure by the free stream dynamic pressure ($0.5\rho U_\infty^2$). It can be seen from this figure that the numerical method does not yield an unphysical oscillatory solution for the mesh with the grid aspect ratio as large as a few tens of thousand and that the calculated pressure distribution compares favorably with the measured data.

The calculated displacement thickness is compared with the measured data in Figure 2. It can be seen in the figure that the calculated result and the measured data compare favorably with each other. The calculated displacement thickness near the inlet boundary is slightly larger than the measured data. This slight discrepancy is attributed to the inlet boundary condition used. In the experiment, the flow was made turbulent using a trip wire located 0.65C upstream of the forward corner of the curved hill. In the numerical calculation, the inlet boundary condition was obtained from experimental data for a fully developed boundary layer flow over a flat plate (ref. 5). This inlet boundary condition is somewhat different from that of the tripped turbulent flow; however, it is considered to be a reasonable approximation to the tripped turbulent flow since development of the internal layer is less dependent on the external boundary layer flow (ref. 5) Inclusion of the trip wire in numerical calculation of the entire flow field is prohibitive at present due to the limitation imposed by the computational resources. At a slightly downstream location, the calculated results are in excellent agreement with the measured data. This excellent agreement is due to the fact that the development of the internal layer on the curved hill is only slightly influenced by the approaching external boundary layer flow (ref. 5). It is shown in the figure that the flow approaching the curved hill is highly retarded due to the strong adverse pressure gradient existing near the leading edge of the curved hill and thus the displacement thickness is increased significantly in this region. The same flow slightly beyond the leading edge is subjected to far stronger favorable pressure gradient and is accelerated enormously. Thus the displacement thickness decreases abruptly. Farther downstream, the internal layer is formed gradually and thus the displacement thickness grows gradually until the flow is subjected to separation at the rear end of the curved hill. Near the separation point, these integral parameters increase abruptly again. The present numerical results show that the wavy nature of the displacement thickness is inherent to the flow over the curved hill. It is also interesting to note that any turbulence model incorporating a wall function method may not be able to describe the turbulence field over the curved hill adequately because of the wavy nature of the boundary layer thickness. For example, the optimal distance from the wall where a wall function method can be applied is obscured because of the rapidly varying boundary layer thickness.

The calculated wall shearing stress is shown in Figure 3, where the friction coefficient was obtained by normalizing the wall shearing stress by the free stream dynamic pressure. The measured data and the computational result obtained using a curvature correction method (ref. 9) are also shown in this figure for comparison. It can be seen in the figure that the calculated wall shearing stress for the curved hill is slightly smaller than the measured data near the inlet boundary. This discrepancy indicates that the inlet boundary condition obtained from a fully developed turbulent boundary layer flow is not quite a good approximation of the flow made turbulent with a trip wire. In the figure, "S" represents the separation location and "R" represents the reattachment location. The M-S turbulence model successfully predicts the small reversed flow region near the rear end of the curved hill. The wall shearing stress obtained using a curvature correction method is in close agreement with the measured data. This accurate result may be due to the use of a boundary layer flow solver which incorporates the measured pressure distribution on the wall. However, the curvature correction method still fails to predict the reversed flow region at the rear end of the curved hill.

The calculated Reynolds stress profiles at a few downstream locations are shown in Figure 4. It can be seen in the figure that the calculated Reynolds stress profile at s=0.710 meters is slightly more spread out than the measured data. This discrepancy is again attributed to the inlet boundary condition obtained from a fully developed boundary layer flow. At farther downstream locations, the calculated and the measured Reynolds stresses are in fair agreement with the measured data. The shape of the Reynolds stress profile at s=0.710 meters is similar to that of wall-bounded simple shear layer flows and it belongs to the external boundary layer flow. It is can be seen in the figure that the strength of the Reynolds stress of the external boundary layer flow decays gradually and that of the internal layer grows rapidly as the fluid travels in the downstream direction. At farther downstream locations, these two Reynolds stress profiles merge together and form a new profile which is similar to that of a wall-bounded simple shear layer flow.

Compressible Turbulent Flows over a Curved Hill

The measured data for the transonic flow over an axisymmetric curved hill at various free stream Mach numbers can be found in references 1, 10, and 11. The unit Reynolds number based on the free stream condition is 13.2×10^6/m for M_∞=0.875 and 10×10^6/m for all other free stream Mach numbers. Details on the grid independence study, boundary conditions, and initial guess can be found in reference 6.

The calculated iso-Mach lines, reproduced from reference 6, are shown in Figure 5 where the incremental Mach number between the contour lines is constant for each free stream Mach number. It can be seen from this figure that the present numerical method can cleanly resolve the transonic flows from low to high transonic free stream Mach numbers. The size of the supersonic pocket for M_∞=0.925 also compares favorably with that obtained using the MacCormack scheme (ref. 11).

The calculated separation and reattachment locations are compared with the measured data and the other numerical results in Figure 6. It is shown in the figure that the Jones-Launder k-ϵ turbulence model (ref. 11) and a k-ϵ turbulence model supplemented with a streamline curvature correction method (ref. 12) fail to predict the reversed flow region at low free stream Mach numbers. At low free stream Mach numbers, the present results compare more favorably with the measured data than do those obtained by the MacCormack scheme using the King-Johnson (K-J) turbulence model (ref. 11). As the free stream Mach number is increased, the present method slightly under-predicts the size of the reversed flow region compared with the measured data and the numerical results obtained using the K-J turbulence model. This under-prediction of the reversed flow region is a result of the calculated shocks being located slightly downstream of the measured data.

The Reynolds stress profiles for M_∞=0.875 at a few axial locations are shown in Figure 7. At low free stream Mach numbers for which the shock wave - boundary layer interaction does not exist, the flow separation is caused by the turbulent shear stress developing over the forward part of the curved hill. A successful prediction of such a flow depends on the capability of a turbulence model to correctly describe the turbulence field subjected to the streamline curvature (ref. 5 and 6). As shown in this figure, the present numerical results compare more favorably with the measured Reynolds stress than do the other numerical results at x/c=0.69 and 0.75. It is also shown in the figure that the k-ϵ turbulence model with an improved wall function (ref. 26) significantly over-estimates the Reynolds stress at x/c=0.75. Inside the reversed flow region, x/c=1.0, the present numerical result compares less favorably with the measured data than does the one obtained using the K-J turbulence model. This under-prediction in the magnitude of the Reynolds stress is attributed to the calculated shock and the separation point which are located slightly downstream of the measured data.

CONCLUSIONS AND DISCUSSION

Numerical investigations of incompressible and compressible turbulent flows over curved hills are presented. The turbulence is described by a multiple-time-scale turbulence model supplemented with a "partially low Reynolds number" near-wall turbulence model.

For turbulent flows over a curved hill, the mean flow is subjected to extra strains caused by the streamline curvature. The development of the turbulence field over such a curved surface mostly depends on the extra strains. The capability to predict the reversed flow region in turbulent flows over a curved hill rests on the capability of a turbulence model to properly resolve the turbulence field subjected to the strong streamline curvature. It was shown that the present turbulence model can predict the reversed flow region caused by the streamline curvature for both the incompressible and compressible flows while many other turbulence models incorporating a streamline curvature correction method fail to predict such a reversed flow region. The present numerical results also show that the reversed flow region grows extensively due to the shock wave - turbulent boundary layer interaction at high free stream Mach numbers. These numerical results compare favorably with the measured data and the other numerical results obtained using the King-Johnson turbulence model (ref. 11). These computational results also showed that the multiple-time-scale turbulence model yields significantly more accurate solutions than many other turbulence models for the incompressible flow and the more complex compressible flow which includes the supersonic pocket and the nearly incompressible reversed flow region.

The density-weighted average of the Navier-Stokes equations yields the same turbulent flow equations for incompressible and compressible flows. This suggests that the same turbulence equations can be used for incompressible and compressible flows. However, the use of turbulence models developed for incompressible turbulent flows in numerical calculations of compressible turbulent flows yields poor numerical results, and vice versa. Thus a number of compressibility correction methods were proposed and are in use for compressible flows. On the other hand, it was shown in this paper that the multiple-time-scale turbulence model yields equally accurate numerical results for both incompressible and compressible flows without the use of a compressibility correction. In this regard, the closure level of the multiple-time-scale turbulence model is more consistent with the underlying mathematical assumption of the density-weighted average than that of other turbulence models which include one or another compressibility correction.

REFERENCES

1. S. J. Kline, B. J. Cantwell & G. M. Lilley (ed) Proc 1980-1981 AFOSR-HTTM Stanford Conference on Complex Turbulent Flows, vol. 1-3, Thermoscience Div., Stanford University, 1982.
2. Persen, L. N. "Concepts of Turbulence and CFD Applications", Progress in Aerospace Sciences, **23**, 167-???, 1986.
3. S.-W. Kim and C.-P. Chen, "A Multiple-Time-Scale Turbulence model Based on Variable Partitioning of the Turbulent Kinetic Energy Spectrum", Numer. Heat Transfer, Part B, vol. 16, pp. 193-211, 1989. Also available as NASA CR-179222, 1988.
4. S.-W. Kim, "Calculation of Reattaching Shear Layers in Divergent Channel with a Multiple-Time-Scale Turbulence Model," AIAA Paper 90-0047, 1990.
5. S.-W. Kim, "Numerical Investigation of an Internal Layer in Turbulent Flow over a Curved Hill," NASA TM-102230, 1989.
6. S.-W. Kim, "Numerical Investigation of Separated Transonic Turbulent Flows with a Multiple-Time-Scale Turbulence Model," To appear in Numerical Heat Transfer, 1990, Also available as NASA TM-102499, 1990.
7. K. Hanjelic, B. E. Launder, and R. Schiestel, "Multiple-Time-Scale Concepts in Turbulent Shear Flows" in L. J. S. Bradbury, F. Durst, B. E. Launder, F. W. Schmidt, and J. H. Whitelaw, (eds.), Turbulent Shear Flows, vol. 2, pp. 36-49, Springer-Verlag, New York, 1980.
8. Bradshaw, P. "Effects of Streamline Curvature on Turbulent Flow," AGARDograph 169, 1973.
9. V. Baskaran, A. J. Smits and P. N. Joubert, "A Turbulent Flow over a Curved Hill: Part I. Growth of an Internal Boundary Layer, J. Fluid Mechanics, vol. 182, pp. 47-83, 1987.
10. W. D. Bachalo and D. A. Johnson, "An Investigation of Transonic Turbulent Boundary Layer Separation Generated on an Axisymmetric Flow Model," AIAA Paper 79-1479, 1979.
11. D. A. Johnson, "Transonic Separated Flow Prediction with an Eddy-Viscosity/Reynolds-Stress Closure Model," J. AIAA, vol. 25, pp. 252-259, 1987.
12. C. C. Horstman and D. A. Johnson, "Prediction of Transonic Separated Flows," J. AIAA, vol. 22, No. 7, pp. 1001-1003, 1984.
13. D. A. Johnson, C. C. Horstman and W. D. Bachalo, "Comparison Between Experiment and Prediction for a Transonic Turbulent Separated Flow," J. AIAA, vol. 20, pp. 737-744, 1982.
14. F. M. White, Viscous Fluid Flow, McGraw-Hill, New York, 1974.
15. M. J. Zucrow and J. D. Hoffman, Gas Dynamics, vol. 1, John Wiley & Sons, New York, 1976.
16. S.-W. Kim, "A Control-Volume Based Reynolds Averaged Navier-Stokes Equation Solver Valid at All Flow Velocities," NASA TM-101488, 1989.
17. R. M. Beam and R. F. Warming, "An Implicit Factored Scheme for the Compressible Navier-Stokes Equations," J. AIAA, vol. 16, pp. 393-402, 1978.
18. R. W. MacCormack, "A Numerical Method for Solving the Equations of Compressible Viscous Flow," J. AIAA, vol. 20, pp. 1275-1281, 1982.

19. J. L. Steiger and R. F. Warming, "Flux-Splitting of the Invicid Gasdynamic Equations with Application to Finite Difference Method," J. Comput. Physics, vol. 40, pp. 263-293, 1981.
20. S. E. Rogers, D. Kwak, and J. L. C. Chang, "INS3D - An Incompressible Navier-Stokes Code in Generalized Three-Dimensional Coordinates," NASA TM-100012, 1987.
21. Tennekes, H. & Lumley, J. L. A First Course in Turbulence, MIT Press, London, 1972.
22. S.-W. Kim, "A Near-Wall Turbulence Model and Its Application to Fully Developed Turbulent Channel and Pipe Flows," Numer. Heat Transfer, Part B, vol. 17, pp. 101-122, 1990. Also available as NASA TM-101399, 1988.
23. V. G. Harris, J. A. H. Graham, and S. Corrsin, "Further Experiments in Nearly Homogeneous Turbulent Shear Flow," J. Fluid Mech., vol. 81, pp. 657-687, 1977.
24. F. H. Harlow and P. I. Nakayama, "Transport of Turbulence Energy Decay Rate," Los Alamos Sci. Lab., LA-3854, 1968.
25. G. Fabris, P. T. Harsha, and R. B. Edelman, "Multiple-Scale Turbulence Modelling of Boundary Layer Flows for Scramjet Applications," NASA CR-3433, 1981.
26. M. W. Rubesin and J. R. Viegas, "Turbulence Modelling in Transonic Flow," Transonic Symposium - Theory, Application and Experiment, NASA Langley Research Center, Hampton, Virginia, April, 1988.

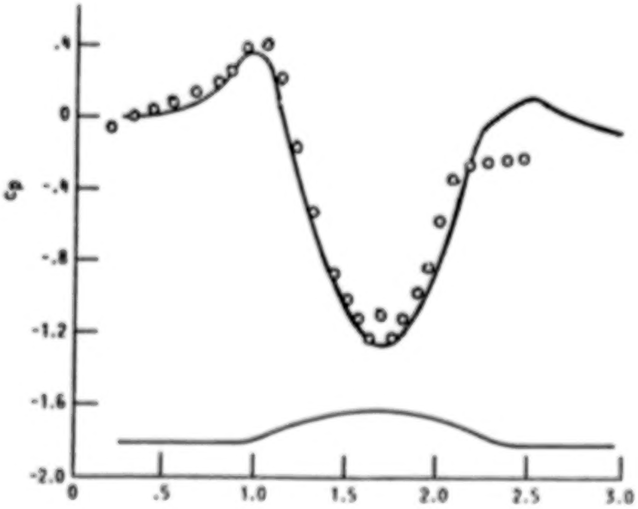

1. Pressure distribution, O: measured data, ——: numerical result.

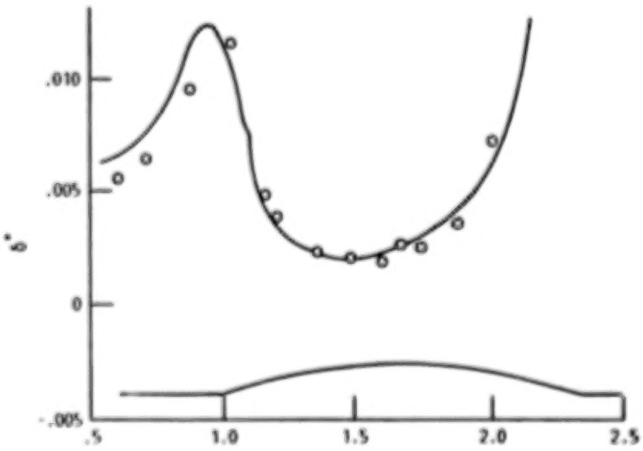

2. Displacement thickness, O: measured data, ——: numerical result.

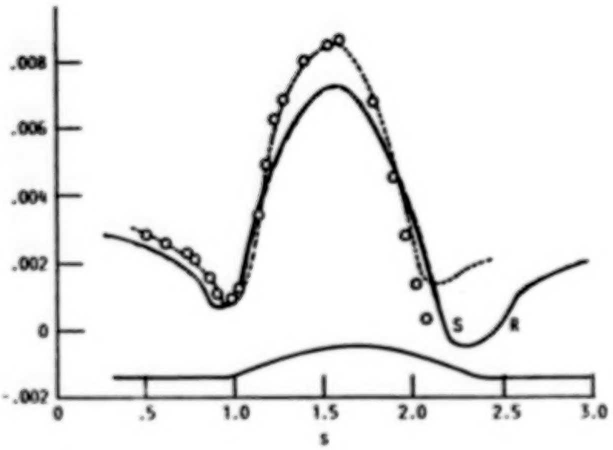

3. Wall shearing stress, O: measured data, ——: present numerical result, -----: numerical result (ref. 9).

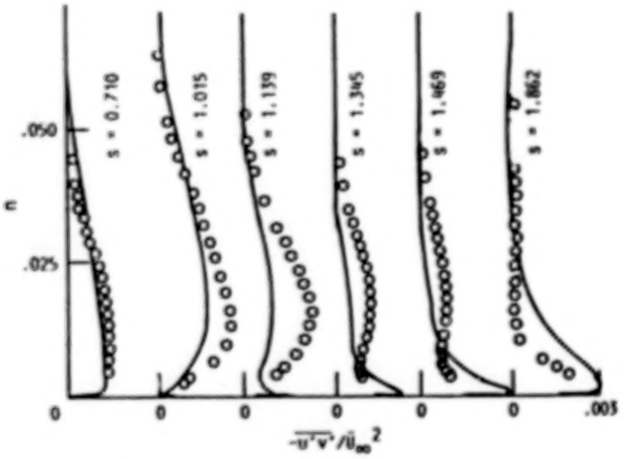

4. Reynolds stress profiles, O: measured data, ——: numerical result.

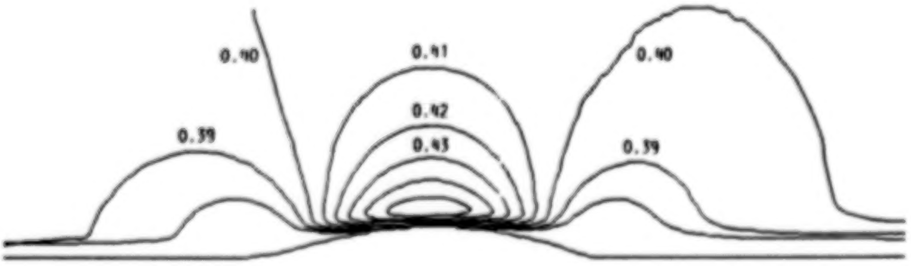

(a) M_∞=0.40,

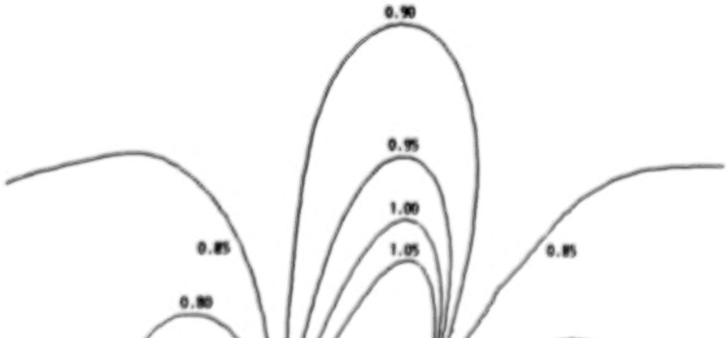

(b) M_∞=0.875,

5. Iso-Mach lines.

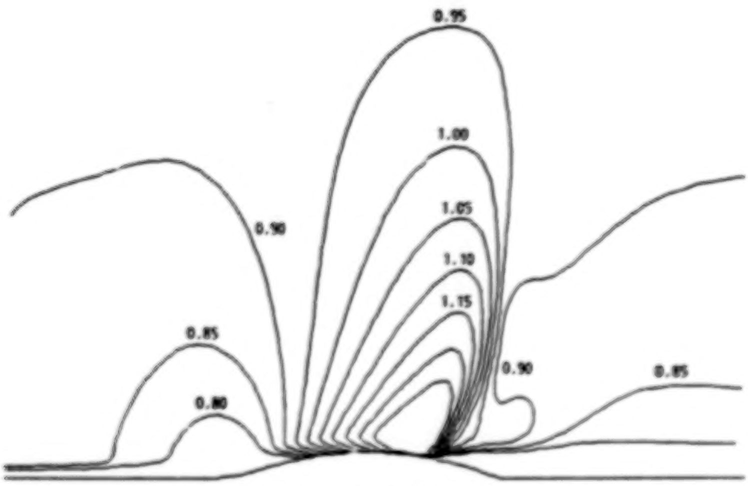

(c) M_∞=0.925.

5. Concluded.

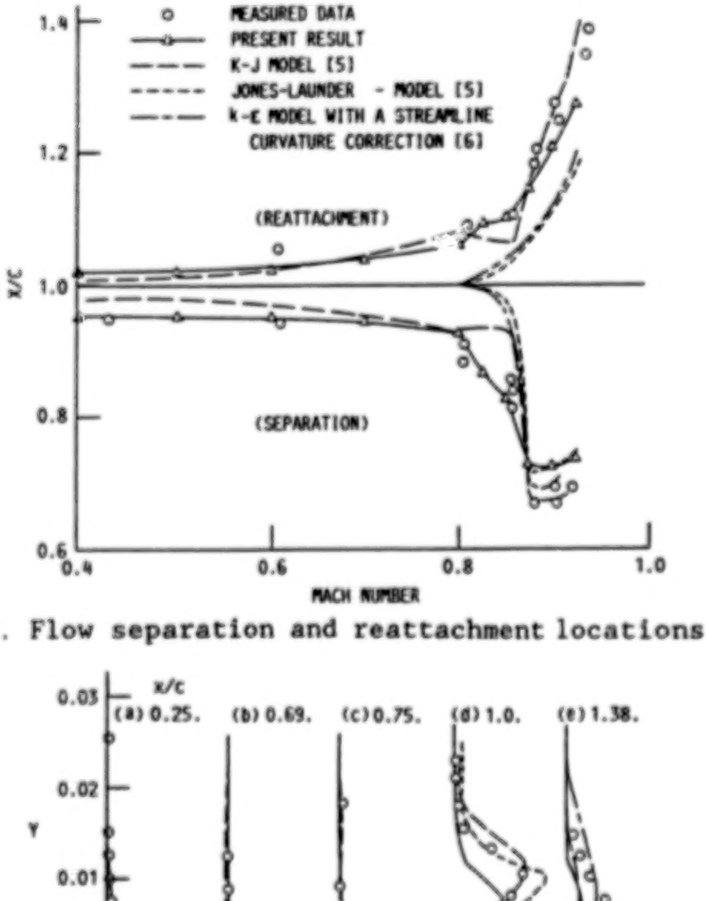

6. Flow separation and reattachment locations

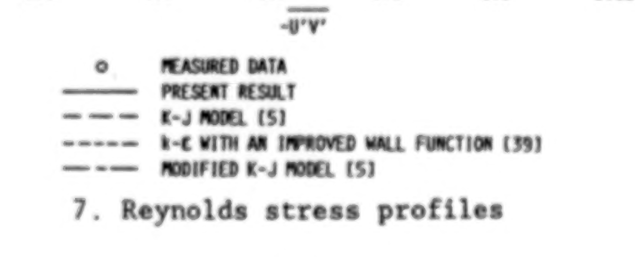

7. Reynolds stress profiles

BLANK PAGE

COMPUTATION OF TURBULENT HIGH SPEED MIXING LAYERS USING A TWO-EQUATION TURBULENCE MODEL

J.R. Narayan
Research Scientist
Analytical Services and Materials, Inc., Hampton, Virginia.
and
B. Sekar
Research Scientist
Vigyan Research Associates, Inc., Hampton, Virginia.

ABSTRACT

A two-equation turbulence model has been extended to be applicable for compressible flows. A compressibility correction based on modelling the dilatational terms in the Reynolds stress equations has been included in the model. The model is used in conjunction with the SPARK code for the computation of high-speed mixing layers. The observed trend of decreasing growth rate with increasing convective Mach number in compressible mixing layers is well predicted by the model. The predictions agree well with experimental data and the results from a compressible Reynolds stress model. The present model appears to be well suited for the study of compressible free shear flows. Preliminary results obtained for reacting mixing layers have also been included.

NOMENCLATURE

b_i	body force of species i
C_1,C_2,C_μ	turbulence model constants
c_p	specific heat at constant pressure
c_{p_i}	c_p for i^{th} species
D_{ij}	binary diffusion coefficient
D_T	thermal diffusion coefficient
E	total internal energy
f_i	mass fraction of species i
$\mathbf{H}$	source vector
H	total enthalpy
h	static enthalpy
h_i	enthalpy of species i
h_i^o	reference enthalpy of species i
k	turbulent kinetic energy
M_i	molecular weight of species i
M_t	Turbulent Mach number
ns	number of chemical species
Pr,Pr_t	laminar and turbulent Prandtl numbers
p	pressure
$\vec{q}$	heat flux vector
R^o	universal gas constant

Sc, Sc_t	laminar and turbulent Schmidt numbers
T	temperature
t	time
Δt	time step
$\mathbf{U}$	dependent variable vector
$\vec{U}$	velocity vector
$\vec{V}_i$	diffusion velocity vector of species i
$\dot{w}_i$	species production rate of species i
X_i	mole fraction of species i
x	streamwise coordinate
x_j	j^{th} coordinate
y	transverse coordinate
α	compressibility correction coefficient
γ	ratio of specific heats
δ_{ij}	Kronecker delta
ϵ	dissipation rate
ϵ_c	compressible dissipation rate
κ	thermal conductivity
λ	second viscosity coefficient
μ	laminar viscosity
μ_t	turbulent viscosity
ν	kinematic viscosity
ρ	density
$\sigma_k, \sigma_\epsilon$	turbulence model constants
τ_{ij}	stress tensor
$\mathbf{\Phi}_j$	flux vector in j^{th} direction

Subscripts

a	high speed stream
b	low speed stream
t	turbulent quantity

INTRODUCTION

In recent years, the development of an airbreathing hypersonic vehicle has received considerable attention. This is a complex task and requires innovative research in many technical areas such as aerodynamics, propulsion, structures and materials. Development of viable propulsion systems for such a vehicle is being pursued at numerous research institutions around the country. One such program is being carried out at the NASA Langley Research Center in which a highly integrated, hydrogen-fueled supersonic combustion ramjet (scramjet) engine is envisioned to be a viable propulsion system for hypervelocity vehicles [1,2]. Due to the complex nature of such a task, numerous research programs have been initiated. One of these research efforts is concerned with understanding the details of the complex flow field inside the engine and evaluating its main features for a range of flow conditions. The work reported here is concerned with this effort in which computational analysis of the scramjet flow field is carried out.

The flow field in the scramjet combustor is highly complex. It is governed by the Navier-Stokes equations coupled with a system of equations describing the chemical reactions that occur. The flow is expected to be turbulent in most part of the combustor. This requires that the analysis be capable of addressing compressible turbulent reacting flows. The interaction between turbulence and chemical reactions is an important issue in the analysis. The presence of turbulence in any flow complicates accurate analysis of the flow due to the wide range of length and time scales. Exact solution of complex flows, such as that in a scramjet combustor, is impossible at present because of these turbulence scales. Hence some form of simplified treatment of the turbulence is mandatory in such problems and turbulence models are used in this regard. Establishing turbulence models that are suitable for flows such as that of the scramjet is very difficult since the effects of turbulence on the flow as a whole and on the chemical reactions in particular are not well understood. The model should be accurate enough in predicting the physics of the problem without increasing the complexity of the solution procedure any more than is necessary.

A variety of turbulence models, which have been used for many different flow configurations, exist today. These models range from the simplest mixing-length or zero-equation models to the most general Reynolds stress closures. Also, other means of analyzing turbulent flows, such as large eddy simulation, are being developed. A useful review of the field was conducted by Nallasamy [3]. One class of models that is widely used in turbulence computations today is the two-equation model. In this model, a differential equation for the mean turbulent kinetic energy and another for some form of the length scale of turbulence are solved along with the averaged forms of the Navier-Stokes equations. These two-equation models have been used with some degree of success for many engineering problems. They are relatively easy to implement in a given solution procedure and are computationally economic in comparison with the more general Reynolds stress models. These models do have their limitations and their applicability to any flow problem must be validated before using them. One of the major restrictions of most of the turbulence models in use today is that they have been developed for incompressible flows. Adhoc modifications to account for compressibility have been made to some of these models. A discussion on this subject is given by Yang et al. [4]. A fully compressible turbulence model of the two-equation and higher order does not exist because the averaged equations for compressible flows are not easily amenable to modelling using any of the known techniques. However, good progress has been made in this area by many researchers and it is hoped that turbulence models applicable to compressible flows should soon be available. In the present analysis, a two-equation model of turbulence has been used with a compressibility correction derived from the Reynolds stress closure model of Sarkar et al. [5]. The two turbulence variables are the turbulent kinetic energy and its dissipation rate. The governing equations are Favre averaged [6] thus including the effects of mean density variations. At present, the model does not include the turbulence-chemical reactions interactions and all the model constants of the incompressible model [7] are retained.

The two-equation model is tested on a spatially developing, primarily supersonic, chemically reacting plane mixing layer. A major portion of the chemical reactions in the scarmjet combustor occur in mixing layers and all the complexities introduced by fluid mechanics, combustion chemistry and the interaction between them are retained by the reacting mixing layer. A detailed discussion on this topic is given by Drummond et al. [1]. Mixing layers have been studied extensively over the years. Some of the earlier work in this area is found in reference [8], which resulted after the conference on free shear flows held at NASA Langley Research Center in 1972, and in reference [9], in which the density effects on subsonic mixing layers have been discussed. Reference [10] gives a good picture of recent developments in the area of turbulent shear flows of which the mixing layer is a subset. However, as with many other compressible flows, reliable experimental data in the area of reacting mixing layers is limited. Availability of reliable experimental data for the purpose of validation is crucial in the development of turbulence models and the lack of this data is one of the reasons why models applicable to reacting flows are not common today.

In the present work, the two-equation model is applied to the high-speed plane mixing layer problem over a wide range of flow conditions without and with chemical reaction. The nonreacting cases are computed for air-air systems. Hydrogen-air combustion models are used for the reacting flows. Single-step and multiple-step reaction systems are used here. The two gas streams that form the mixing layer are supersonic whereas the convective Mach number [11] of the layer varies from subsonic to supersonic values. The computer code SPARK, developed at the NASA Langley Research Center [12], has been used. It solves the governing equations using a fourth order compact scheme. The mean flow variables such as velocity, internal energy, the two turbulence variables and the concentrations of various species such as hydrogen, oxygen, nitrogen etc., are computed. Representative results are presented and pertinent flow features are discussed. The predictions have been compared with those of a Reynolds stress closure [13,14] and also with available experimental data [11,15,16,17]. Major flow characteristics such as the growth rate of the mixing layer, mean velocities, turbulent kinetic energy etc., are used for comparisons.

GOVERNING EQUATIONS

The Navier-Stokes equations along with equations for energy and species continuity which govern flows with multiple species undergoing chemical reaction have been used [18]. These governing equations are

Continuity

$$\frac{\partial \rho}{\partial t} + \nabla \cdot (\rho \vec{U}) = 0 \tag{1}$$

Momentum

$$\frac{\partial (\rho \vec{U})}{\partial t} + \nabla \cdot (\rho \vec{U} \vec{U}) = \nabla \cdot \tau + \rho \sum_{i=1}^{ns} f_i \vec{b}_i \tag{2}$$

where

$$\tau \equiv \tau_{ij} = -p\,\delta_{ij} + \mu\left(\frac{\partial u_i}{\partial x_j} + \frac{\partial u_j}{\partial x_i}\right) + \lambda \frac{\partial u_k}{\partial x_k}\,\delta_{ij} \tag{3}$$

with repeated indices indicating summation.

Energy

The total energy(kinetic + internal) is chosen as the dependent variable in the energy equation, given as

$$\frac{\partial (\rho E)}{\partial t} + \nabla \cdot (\rho \vec{U} E) = \nabla \cdot (\tau \cdot \vec{U}) - \nabla \cdot \vec{q} + \rho \sum_{i=1}^{ns} f_i \vec{b}_i (\vec{U} + \vec{V}_i) \tag{4}$$

where, neglecting radiation heat transfer,

$$\vec{q} = -\kappa \nabla T + \rho \sum_{i=1}^{ns} h_i f_i \vec{V}_i + R^{o} T \sum_{i=1}^{ns} \sum_{j=1}^{ns} \left(\frac{X_j D_{T_i}}{M_i D_{ij}}\right)(\vec{V}_i - \vec{V}_j) \tag{5}$$

Species Continuity

$$\frac{\partial (\rho f_i)}{\partial t} + \nabla \cdot (\rho \vec{U} f_i) = \dot{w}_i - \nabla \cdot (\rho f_i \vec{V}_i) \tag{6}$$

Also,

$$E = \sum_{i=1}^{ns} h_i f_i - \frac{p}{\rho} + \frac{u_k u_k}{2} \tag{7}$$

with repeated indices indicating summation in the kinetic energy term.

$$h_i = h_i^{o} + \int_{T_r}^{T} c_{p_i}\, dT \qquad i = 1, 2, \ldots, ns \tag{8}$$

$$p = \rho R^{o} T \sum_{i=1}^{ns} \frac{f_i}{M_i} \tag{9}$$

The diffusion velocities are found by solving

$$\nabla X_i = \sum_{j=1}^{ns} \frac{X_i X_j}{D_{ij}} (\vec{V}_j - \vec{V}_i) + (f_i - X_i) \frac{\nabla p}{p} + \frac{\rho}{p} \sum_{j=1}^{ns} f_i f_j (\vec{b}_i - \vec{b}_j) +$$

$$\sum_{j=1}^{ns} \frac{X_i X_j}{\rho D_{ij}} \left(\frac{D_{Tj}}{f_j} - \frac{D_{Ti}}{f_i}\right) \frac{\nabla T}{T} \tag{10}$$

Note that if there are ns chemical species, then $i = 1, 2, ..., (ns-1)$ and $(ns-1)$ equations must be solved for the species f_i. The final species mass fraction f_{ns} can then be found by conservation of mass since $\sum_{i=1}^{ns} f_i = 1$.

The procedures for evaluating quantities such as the specific heats, equilibrium constant for the chemical reactions, etc., are described in reference [1]. Also, details regarding the chemistry models, thermodynamic models and the diffusion models are found in reference [1].

Averaged Governing Equations

Density-weighted averaging (also known as Favre-averaging [6]) is used to derive the equations which describe the fully turbulent flow from the above set of equations. The dependent variables, except density and pressure, are written in the form,

$$\phi = \tilde{\phi} + \phi'' \tag{11}$$

where the Favre-mean $\tilde{\phi}$ is defined as

$$\tilde{\phi} \equiv \frac{\overline{\rho\phi}}{\bar{\rho}} \tag{12}$$

In this equation, the overbar indicates conventional time-averaging. Density and pressure are split in the conventional sense as,

$$\rho = \bar{\rho} + \rho' \text{ and } p = \bar{p} + p' \tag{13}$$

The following relations exist in this form of time-averaging:

$$\begin{aligned} \overline{\phi''} &= -\frac{\overline{\rho'\phi'}}{\bar{\rho}} \\ \overline{\rho\phi''} &= 0 \\ \overline{\phi'} &= 0 \end{aligned} \tag{14}$$

The averaged continuity and momentum equations are

$$\frac{\partial\bar{\rho}}{\partial t} + \frac{\partial\bar{\rho}\widetilde{U_i}}{\partial x_i} = 0 \tag{15}$$

$$\frac{\partial\bar{\rho}\widetilde{U_i}}{\partial t} + \frac{\partial\bar{\rho}\widetilde{U_i}\widetilde{U_j}}{\partial x_j} = -\frac{\partial\bar{p}}{\partial x_i} - \frac{\partial\overline{\rho u_i'' u_j''}}{\partial x_j} + \frac{\overline{\partial\tau_{ij}}}{\partial x_j} \tag{16}$$

The total energy E can be written in terms of the total enthalpy(H) as

$$E = H - \frac{p}{\rho} \tag{17}$$

Rewriting the energy equation (4) using the above and time-averaging,

$$\frac{\partial(\bar{\rho}\tilde{H} - \bar{p})}{\partial t} + \frac{\partial(\bar{\rho}\tilde{H} - \bar{p})\widetilde{U_j}}{\partial x_j} = -\frac{\partial}{\partial x_j}(\bar{p}\widetilde{U_j} + \overline{\rho u_j'' H''}) - \frac{\overline{\partial Q_j}}{\partial x_j} + \frac{\overline{\partial u_i \tau_{ij}}}{\partial x_j} \tag{18}$$

In the above equations the body forces contribution has been omitted. Also, $\overline{Q_j}$ represents the averaged heat flux term (equation (5)). The species continuity equation (6) is averaged similarly to get,

$$\frac{\partial\bar{\rho}\tilde{f}_i}{\partial t} + \frac{\partial\bar{\rho}\tilde{f}_i\widetilde{U_j}}{\partial x_j} = \overline{\dot{w}_i} - \frac{\partial}{\partial x_j}(\overline{\rho u_j'' f_i''} + \overline{\rho f_i (V_i)_j}) \tag{19}$$

In this equation, the term $\dot{w}_i$ contains correlations which have not been included in the present model.

The equations for the two turbulence variables, turbulent kinetic energy (k) and the energy dissipation rate (ϵ), are derived by suitably manipulating the momentum and continuity equations (equations (2) and (1)) and utilising equations (11) – (14). Defining k and ϵ as

$$k \equiv \frac{\overline{\rho u_i'' u_i''}}{2\bar{\rho}} \tag{20}$$

$$\epsilon \equiv \frac{\overline{\rho\nu \frac{\partial u_i''}{\partial x_j} \frac{\partial u_i''}{\partial x_j}}}{\bar{\rho}} \tag{21}$$

the equation for the turbulent kinetic energy can be written as

$$\begin{aligned} \frac{\partial \bar{\rho} k}{\partial t} + \frac{\partial \bar{\rho} k \widetilde{U_j}}{\partial x_j} \;=\; & -\overline{\rho u_i'' u_j''}\,\frac{\partial \widetilde{U_i}}{\partial x_j} - \overline{\tau_{ij}\frac{\partial u_i''}{\partial x_j}} - \overline{u_i''}\frac{\partial \bar{p}}{\partial x_i} + \overline{p'\frac{\partial u_i''}{\partial x_i}} \\ & - \frac{\partial}{\partial x_j}\left(\overline{\rho u_i'' u_i'' u_j''} + \overline{p' u_i''}\,\delta_{ij} - \overline{u_i'' \tau_{ij}} \right) \end{aligned} \tag{22}$$

Substituting for τ_{ij} and rearranging terms,

$$\begin{aligned} \frac{\partial \bar{\rho} k}{\partial t} + \frac{\partial \bar{\rho} k \widetilde{U_j}}{\partial x_j} \;=\; & -\overline{\rho u_i'' u_j''}\,\frac{\partial \widetilde{U_i}}{\partial x_j} - \mu\overline{\frac{\partial u_i''}{\partial x_j}\frac{\partial u_i''}{\partial x_j}} - \frac{\partial}{\partial x_j}\left(\overline{\rho u_i'' u_i'' u_j''} + \overline{p' u_i''}\,\delta_{ij}\right) \\ & + \frac{\partial}{\partial x_j}\left(\mu\frac{\partial k}{\partial x_j}\right) - \overline{u_i''}\frac{\partial \bar{p}}{\partial x_i} + \overline{p'\frac{\partial u_i''}{\partial x_i}} + \Theta \end{aligned} \tag{23}$$

where Θ is a set of molecular diffusion-like terms which can be neglected in high Reynolds number flows [4]. The first term on the right hand side of equation (23) is the energy production term, the second one is the dissipation term (21), the third and fourth terms represent diffusion of the turbulent energy and the next two terms represent the effect of compressibility.

The equation for the dissipation rate (ϵ) can be derived in a similar manner. It is not included here because it is quite long and the current model uses a simplified form of this equation. However, the modelled form of this equation, which has been used in the computations, will be included later in this report.

Modelled Equations

The k-ϵ model achieves closure of the equations governing the turbulent flows by invoking the Boussinesq approximation which relates the turbulent stresses (Reynolds stresses) to the mean strain rate. Thus, the Reynolds stress tensor is written as,

$$-\overline{\rho u_i'' u_j''} = \mu_t \left(\frac{\partial \widetilde{U_i}}{\partial x_j} + \frac{\partial \widetilde{U_j}}{\partial x_i}\right) - \frac{2}{3}\,\bar{\rho} k\, \delta_{ij} \tag{24}$$

where μ_t is the turbulent/eddy viscosity defined in terms of some characteristic length and velocity scales. Here the length is taken to the turbulent length scale, $k^{\frac{3}{2}}/\epsilon$, and the velocity scale is assumed to be $k^{\frac{1}{2}}$ leading to the following expression for μ_t.

$$\mu_t = C_\mu\, \rho \frac{k^2}{\epsilon} \tag{25}$$

The correlations between the fluctuating velocity and the scalar fluctuations are modelled in a similar manner using a mean gradient hypothesis and a typical model is,

$$-\overline{\rho u_i'' \phi''} = \frac{\mu_t}{\sigma_\phi}\left(\frac{\partial \tilde{\phi}}{\partial x_i}\right) \tag{26}$$

where σ_ϕ is a coefficient which, normally, is a constant. For $\phi = f_i$, $\sigma_\phi = Sc_t$, and for the static enthalpy, $(\phi = h)$, $\sigma_\phi = Pr_t$.

Using the above, the averaged governing equations can be modified using models for the unknown correlations thus deriving a closed set of equations which can be solved. In this section, these modelled equations will be given. The mean continuity equation (15) does not require any further modelling. The momentum equation (16) has two terms (last two on the right hand side) that require modeling. The modelled momentum equation is,

$$\frac{\partial \bar{\rho}\widetilde{U}_i}{\partial t} + \frac{\partial \bar{\rho}\widetilde{U}_i\widetilde{U}_j}{\partial x_j} = -\frac{\partial \bar{p}}{\partial x_i} - \frac{\partial}{\partial x_j}\left[\,(\mu+\mu_t)\left(\frac{\partial \widetilde{U}_i}{\partial x_j} + \frac{\partial \widetilde{U}_j}{\partial x_i}\right) - \frac{2}{3}\left(\mu\frac{\partial \widetilde{U}_k}{\partial x_k} + \bar{\rho}k\right)\delta_{ij}\right] \tag{27}$$

The correlation $\overline{\rho u_j'' H''}$ in the thermodynamic energy equation (18) is split into its components here as

$$\overline{\rho u_j'' H''} = \overline{\rho u_j'' h''} + \frac{\overline{\rho u_i'' u_i'' u_j''}}{2} + \overline{\rho u_i'' u_j''}\,\widetilde{U}_i \tag{28}$$

The modelled energy equation then is,

$$\begin{aligned}\frac{\partial(\bar{\rho}\tilde{H}-\bar{p})}{\partial t} + \frac{\partial(\bar{\rho}\tilde{H}-\bar{p})\widetilde{U}_j}{\partial x_j} &= \frac{\partial}{\partial x_j}\left[\left(\frac{\mu}{Pr}+\frac{\mu_t}{Pr_t}\right)\frac{\partial \tilde{h}}{\partial x_j} + \left(\mu+\frac{\mu_t}{\sigma_k}\right)\frac{\partial \tilde{k}}{\partial x_j}\,\right] \\ &\quad + \frac{\partial}{\partial x_j}\left(\overline{\tau_{ij}} - \bar{p}\,\delta_{ij} - \overline{\rho u_i'' u_j''}\right)\widetilde{U}_i\end{aligned} \tag{29}$$

where σ_k is a coefficient that appears in the turbulent kinetic energy equation. The intermediate steps that lead to equation (29) are straight forward and hence are not included here. The modelled species continuity equation is

$$\frac{\partial \bar{\rho}\tilde{f}_i}{\partial t} + \frac{\partial \bar{\rho}\tilde{f}_i\widetilde{U}_j}{\partial x_j} = \overline{\dot{w}_i} - \frac{\partial}{\partial x_j}\left[\left(\frac{\mu}{Sc}+\frac{\mu_t}{Sc_t}\right)\frac{\partial \tilde{f}}{\partial x_j}\right] \tag{30}$$

Modelling of the turbulence terms in the equations is a major area of research by itself. Details of the modelling of the various terms are beyond the scope of this paper. Here the models used, along with the relevant references, will be given. The production term is exact in its form and does not need modelling. Modelling of the diffusion terms in the turbulent kinetic energy equation has been a well studied area and the model employed here is one of the most widely used [19]. The terms identified in the previous section as the compressibility terms are included in the present analysis since the flows considered are compressible. Recently, there has been a considerable amount of activity in the area of modelling these compressibility effects for various turbulence models. A short account of some of these modelling efforts can be found in reference [4]. Strahle [20] proposed a global compressibility correction for the turbulent kinetic energy equation. Recently, Sarkar et al. [5] proposed a model for the compressible dissipation in terms of the dissipation rate of turbulent kinetic energy and the local turbulent Mach number. This has been used in the present analysis as the model for the two compressibility terms in the turbulent kinetic energy equation. The compressible dissipation model is

$$\epsilon_c = \alpha M_t^2 \epsilon \tag{31}$$

Here M_t is the local turbulent Mach number defined as $M_t^2 = 2k/a^2$ where a is the local speed of sound and the model constant $\alpha = 1.0$. The modelled turbulent kinetic energy equation is [7]

$$\frac{\partial \bar{\rho}k}{\partial t} + \frac{\partial \bar{\rho}k\widetilde{U}_j}{\partial x_j} = -\overline{\rho u_i'' u_j''}\,\frac{\partial \widetilde{U}_i}{\partial x_j} - \bar{\rho}\epsilon(1+\alpha M_t^2) + \frac{\partial}{\partial x_j}\left[\left(\mu+\frac{\mu_t}{\sigma_k}\right)\frac{\partial k}{\partial x_j}\right] \tag{32}$$

Modelling of the exact equation for the dissipation rate is extremely difficult, even for incompressible flows, due to the lack of understanding of the various complex correlation terms that are present. There have been attempts at including some form of compressibility effects in the ϵ-equation [4] but no viable model has emerged so far. Hence, the incompressible form of the ϵ-equation is used in the present analysis [7]. The modelled form of this equation is

$$\frac{\partial \bar{\rho}\epsilon}{\partial t} + \frac{\partial \bar{\rho}\epsilon \widetilde{U}_j}{\partial x_j} = (C_1 P_k - C_2 \bar{\rho}\epsilon)\,\frac{\epsilon}{k} + \frac{\partial}{\partial x_j}[(\bar{\mu} + \frac{\mu_t}{\sigma_\epsilon})\frac{\partial \epsilon}{\partial x_j}] \tag{33}$$

where P_k is the production term in the turbulent kinetic energy equation (first term on the right hand side of (32). This term can be written as

$$\begin{aligned} P_k &= -\overline{\rho u_i'' u_j''}\,\frac{\partial \widetilde{U}_i}{\partial x_j} \\ &= \mu_t[\,\frac{1}{2}(\frac{\partial \widetilde{U}_i}{\partial x_j} + \frac{\partial \widetilde{U}_j}{\partial x_i})^2 - \frac{2}{3}(\frac{\partial \widetilde{U}_k}{\partial x_k})^2\,] - \frac{2}{3}\bar{\rho}k\frac{\partial \widetilde{U}_k}{\partial x_k} \end{aligned} \tag{34}$$

The model constants used in the analysis are C_μ=0.09, C_1=1.44, C_2=1.92, σ_k=1.0, σ_ϵ=1.3, Pr=0.72, Pr_t=1.0, Sc=0.22 and Sc_t=1.0.

Solution of the Governing Equations

Once the governing equations and required modeling are in hand, the equations are discretised and integrated in space and time towards steady state solutions. The governing equations are written in vector form as follows.

$$\frac{\partial \mathbf{U}}{\partial t} + \frac{\partial \mathbf{\Phi}_j}{\partial x_j} = \mathbf{H} \tag{35}$$

where $\mathbf{U}$ is the vector of dependent variables, $\mathbf{\Phi}_j$ are flux vectors containing convective and diffusive terms (repeated indices indicate summation), and $\mathbf{H}$ are source terms containing production/dissipation terms in the equations. The temporally discrete form of equation (35) can then be written as

$$\mathbf{U}^{n+1} = \mathbf{U}^n - \Delta t\,[\frac{\partial \mathbf{\Phi}_j^n}{\partial x_j} - \mathbf{H}^{n+1}] \tag{36}$$

where n is the old time level and $n+1$ is the new time level. The flux terms are written at the old time level because the equations are advanced in real time at the smallest fluid time scale. The source terms in the k- and ϵ-equations are decoupled by suitable manipulation of the ratio ϵ/k in the present analysis. For example, in the k-equation, the dissipation term is written as,

$$\bar{\rho}\epsilon = \bar{\rho}k\,(\frac{\epsilon}{k}) \tag{37}$$

The term ϵ/k is treated as a known quantity taking its value from the previous time step in the solutions. A similar treatment of the source term is done for the ϵ-equation also. These nonlinear turbulence source terms are treated in a pointwise-implicit manner while solving the turbulence equations. The k- and ϵ-equations are written in the form,

$$(1 - \frac{\partial \mathbf{H}}{\partial \mathbf{U}})\,(\mathbf{U}^{n+1} - \mathbf{U}^n) = -\,\Delta t\,[\frac{\partial \mathbf{\Phi}_j^n}{\partial x_j} - \mathbf{H}^n] \tag{38}$$

The jacobian $\frac{\partial \mathbf{H}}{\partial \mathbf{U}}$ can take different forms depending upon how the source terms are written. In the present computations, this jacobian has the following terms:

$$\frac{\partial H_k}{\partial \bar{\rho}k} = -[\frac{2}{3}D + \frac{\epsilon}{k}\,(1 + \alpha M_t^2)]$$

$$
\begin{aligned}
\frac{\partial H_k}{\partial \bar{\rho}\epsilon} &= 0 \\
\frac{\partial H_\epsilon}{\partial \bar{\rho}k} &= 0 \\
\frac{\partial H_\epsilon}{\partial \bar{\rho}\epsilon} &= -[\frac{2}{3}C_1 D + C_2 \frac{\epsilon}{k}] \qquad (39)
\end{aligned}
$$

where

$$D \equiv \frac{\partial U_j}{\partial x_j} \qquad (40)$$

As an option, the chemical source term is also written implicitly [21] to alleviate the problem of stiffness in the governing equations when chemistry time scales become small as compared to fluid time scales early in a calculation or when the system approaches chemical equilibrium. The governing equations are written in two-dimensional cartesian form for the solutions. It must be pointed out here that even though turbulence is three-dimensional in nature, the contribution of the fluctuating velocity in the third dimension has not been incorporated in the calculations. The discretised equations are solved by means of the elliptic solver SPARK [12]. A fourth-order compact scheme is used in the solution procedure. Details of the code and the solution procedure can be found in [12].

RESULTS AND DISCUSSION

A two-dimensional, high-speed mixing layer is considered in this study. A schematic of this flow problem is given in figure 1. The two streams coming off the splitter plate are supersonic. However, the convective Mach number [11] of the mixing layer ranges from subsonic to supersonic values. The two streams are air for the nonreacting cases whereas the higher-speed stream is comprised of a hydrogen-nitrogen mixture (10% H_2 and 90% N_2) for the reacting mixing layer cases. The inlet mean velocity is assumed to have a hyperbolic tangent profile, thus imitating the flow that exists downstream of the splitter plate edge. Ease of computations prompted this choice of initial profile for the mean velocity. The initial distributions of the turbulent kinetic energy and its dissipation rate are chosen to be compatible with what is observed in such a flow problem. A constant turbulence intensity level is used in the free stream for arriving at the initial distribution of turbulent kinetic energy and the dissipation rate distribution is deduced from the k-field using a length scale parameter. These initial distributions are shown in figure 2. The temperature and pressure are assumed to be initially uniform for both the streams. The free stream turbulence intensity proved to be a sensitive parameter, especially for the supersonic convective Mach number cases. A constant value of the free stream turbulence intensity (with respect to the mean velocity) has been maintained in all the calculations. Hydrogen-oxygen reaction systems are considered in the reacting flow calculations since this solution procedure is to be applied to scramjet combustor flow studies. One-step (one reaction, four species) and multiple-step (eighteen reactions and nine species) reactions have been considered. Different sets of computations were done based on the convective Mach number of the mixing layer. Here, for a given free stream temperature and pressure, the slower speed stream had the same velocity in all the calculations changing only the speed of the faster stream in order to arrive at the required convective Mach number.

In this section, representative results of the calculations are presented. Comparison with available experimental data is done in a limited sense. Also, the solutions are compared with the Reynolds stress closure predictions carried out at NASA Langley [13,14]. Typical predictions of the mean velocity, temperature and turbulent kinetic energy for a convective Mach number of 1.5 are given in figure 3. The free stream Mach numbers of the two streams are 3.2 and 6.2. These figures show the development of the mixing layer in the axial direction and the corresponding changes in the flow variables. A slight shifting of the layer towards the lower speed stream is seen here. The mean temperature increases, from its free stream value, inside the mixing layer. A similar variation is observed in the turbulent kinetic energy distribution. Figure 4 shows the width of the mixing layer (vorticicity thickness) as a function of the streamwise distance. Two values of the convective Mach number have been considered. The growth of the layer is linear after the inital development of the flow and in this linear region, similarity in the mean flow characteristics can be expected. This is seen in figure 5 where the mean velocity and turbulent kinetic energy profiles are plotted in similarity variable coordinates. Here y_c represents the location where the two streams have a common boundary initially.

The major aim of the present work is to extend the widely used incompressible two-equation turbulence model for compressible flows. As mentioned earlier, a compressible correction has been incorporated in the turbulence model used here. The predicted growth rates of the mixing layer with and without the compressibility correction model are plotted in figure 6. For comparison, the results using a global correction model [20] are also included. Here C_δ is defined as,

$$C_\delta = \frac{d\delta}{dx}\frac{U_a + U_b}{U_a - U_b}$$

and C_{δ_0} is its value for incompressible flow (assumed to be at a convective Mach number of 0.1 here). The effect of compressibility on mixing layer is to reduce the growth rate of the layer with increasing convective Mach number. This trend is seen in the figure. For the cases without the compressibility correction and those with the global correction the growth rate seems to reach a constant value after a convective Mach number of about 0.5. However, the effects of compressibility are expected to be more pronounced beyond this point leading one to believe that the calculations without the above correction do not address the important problem of compressibility well. As seen in the figure, the effect of compressibility is well predicted by including the compressibility correction. This has been verified by comparing the predicted growth rate with available experimental data, as shown in figure 7. The growth rates predicted by means of the Reynolds stress closure[13] are also shown in this figure. As with any turbulent flow case, the experimental data here show a wide scatter [11,15,16,17]. This raises the question of whether the convective Mach number is the sole basis for comparison between the wide range of mixing layer data available in the literature. Setting aside this question for the moment, the figure shows that the trend of reduced growth rate with increasing convective Mach number is predicted very well by the k-ϵ model. The comparison between these predictions and the Langley experimental data is excellent in the supersonic range of the convective Mach number.

One of the important aspects of a two-equation model is that it is well suited for application in engineering flow problems from the point of view of ease of adaptability, computational economy etc. However, the model has been found to be lacking in certain flow cases where the Reynolds stress closure may be appropriate. So, one of the main steps in the present analysis has been to compare the k-ϵ predictions with the Reynolds stress closure predictions in order to evaluate its applicability to the flow problem considered. This is done in figure 8. Figure 8a compares the predicted mean axial velocity profiles at representative locations and figures 8b and 8c compare the turbulent kinetic energy and dissipation rate profiles, respectively. The comparisons show that the k-ϵ predictions agree very well with those of the Reynolds stress model [14] and hence for high-speed mixing layer flows applications the two-equation model seems to be suitable. However, it must be reiterated that this conclusion does not necessarily carry over to all compressible flow problems.

Coming back to the question of whether the convective Mach number should be the sole basis for comparing similar mixing layers, calculations were done with different free stream temperatures and velocities. Some of the results are shown in figure 9. In this figure, the free stream pressure is the same (1 atm) for cases 1 to 4 and it is increased by a factor of 2.1 for case 5. The results indicate some dependency of the growth rate on the free stream temperature. The figure also shows the equivalence between two sets of data (cases 1&5 and cases 2&4) thus provoking the above question. The quantity R_δ, given by

$$R_\delta = \frac{\rho U_b}{\mu}\frac{d\delta}{dx}\frac{U_a + U_b}{U_a - U_b}$$

is found to be nearly identical between cases 1 and 5 and between cases 2 and 4 for a given convective Mach number. The streams that form the mixing layer are both air in these cases. This leads to the speculation that in order to have equivalence between two mixing layers, the parameter R_δ must also be considered which is a Reynolds number like parameter for mixing layer.

As mentioned earlier, the computations were sensitive to the initial distributions of the turbulence field. However, the free stream turbulence level does not affect the predicted characteristics of the mixing layer significantly. The compressibility correction term is dependent upon the local turbulent Mach number as defined in equation(31). The magnitude of this term reaches a maximum value approximately equal to one-third the dissipation rate (ϵ) inside the mixing layer. This indicates that the two-equation model without any correction for the effects of compressibility will be grossly in error in predicting compressible flows.

Figures 10 - 12 show the results obtained for a reacting turbulent mixing layer using the model described in this paper. Hydrogen-oxygen reaction is modelled by means of a 18-reaction steps, 9-species system in these calculations. The free stream velocities, pressure and temperature are identical between the two cases. The free stream temperature is 2000 K and the pressure is 1 atm. Comparison between reacting and nonreacting cases are shown in figures 10 and 11. Figure 10 shows the width of the mixing layer for a supersonic convective Mach number. Figures 11 are the mean temperature, axial velocity and turbulent kinetic energy distributions. Examination of these figures indicates that the temperature distribution is altered, as expected, due to the heat release during the chemical reactions. The temperature reaches a peak value of about 2510 K inside the mixing layer. However, the mean dynamic and turbulence fields do not change. The width of the shear layer remains almost constant. Figure 12 shows the distributions of the primary species in the flow. Mass concentrations of hydrogen, oxygen and water vapor are shown. The extent of the reaction zone can be seen clearly here.

CONCLUDING REMARKS

A two-equation turbulence model ($k - \epsilon$) has been modified to be suitable for addressing compressible flows. A compressibility correction model based on modelling the dilatational terms in the Reynolds stress equations has been used. A two-dimensional high-speed mixing layer is studied using the model. Comparisons of the predictions with available experimental data and the predictions of a compressible Reynolds stress closure indicate that the model is well suited for the study of such flows. The decrease in the growth rate of the mixing layer with increasing convective Mach number is well predicted by the model. A parameter which may be useful to establish the equivalence of mixing layers has been identified. Representative solutions of reacting high-speed mixing layers also have been given. This two-equation model is being developed for application to reacting, compressible flows.

ACKNOWLEDGMENTS

This work was supported by Theoretical Flow Physics Branch, Fluid Mechanics Division, NASA Langley Research Center under contract numbers NAS1-18599 (first author) and NAS1-18585 (second author). The authors would also like to acknowledge Dr.M.H.Carpenter for the valuable assistance with the SPARK code and Dr.L.Balakrishnan for providing the Reynolds stress closure data.

References

[1] Drummond, J. P.; Carpenter, M. H.; and Riggins, D. W., "Mixing and Mixing Enhancement in Supersonic Reacting Flows", *High Speed Propulsion Systems: Contributions to Thermodynamic Analysis*, ed. E. T. Curran and S. N. B. Murthy, American Institute of Astronautics and Aeronautics, Washington, D. C., 1990.

[2] Drummond, J. P.; and Weidner, E. H., "Numerical Study of a Scramjet Engine Flowfield", *AIAA J.*, vol. 20, no. 9, Sept. 1982, pp. 1182–1187.

[3] Nallasamy, M., "Turbulence Models and Their Applications To The Prediction of Internal Flows, A Review", *Computers & Fluids*, vol. 15, no. 2, 1987, pp. 151–194.

[4] Yang, Z.Y.; Chin, S.B. and Swithenbank, J., "On The Modelling of The k-Equation For Compressible Flow", Dept. of Mechanical and Process Engg., University of Sheffield, U.K. To be published.

[5] Sarkar, S.; Erlebacher, G.; Hussaini, M. Y.; and Kreiss, H. O., "The Analysis and Modeling of Dilatational Terms in Compressible Turbulence", *NASA CR* 181959, 1989.

[6] Favre, A., "Statistical Equations of Turbulent Gases", *Institut de Mechanique Statistique de la Turbulence, Marseille.*

[7] Jones, W.P. and Launder, B.E., "The Prediction of Laminarisation with a Two-Equation Model of Turbulence", *Int. J. Heat Mass Transfer*, Vol.15, 1972, pp 301-314.

[8] "Free Turbulent Shear Flows", *NASA SP-321,* Vol.1, 1972.

[9] Brown, G. L.; and Roshko, A., "On Density Effects and Large Structure in Turbulent Mixing Layers", *J. Fluid Mech.,* vol. 64, pt. 4, 1974, pp. 775–816.

[10] "Seventh Symposium on Turbulent Shear Flows", Vol.1 and 2 Stanford University, Stanford, California, 1989.

[11] Papamoschou, D. and Roshko, A., "The Compressible Turbulent Shear Layer : An Experimental Study", *J.Fluid Mechanics*, v.197, 1988, pp 453-477.

[12] Carpenter, M. H., "Three-Dimensional Computations of Cross-Flow Injection and Combustion in a Supersonic Flow", AIAA-89-1870, June 1989.

[13] Sarkar, S. and Balakrishnan, L., "Application of a Reynolds Stress Turbulence Model to the Compressible Shear Layer", *ICASE Report* 90-18, 1990.

[14] Balakrishnan, L., Old Dominion University, Private communication.

[15] Birch, S.F. and Eggers, J.M., "A Critical Review of the Experimental Data for Developed Free Turbulent Shear Layers", *NASA SP*-321, 1973, pp 11-40.

[16] Ikawa, H. and Kubota, T., "Investigation of Supersonic Turbulent Mixing Layer with Zero Pressure Gradient", *AIAA Journal*, Vol.13, 1975, pp 566-572.

[17] Wagner, R.D., "Measured and Calculated Mean-Flow Properties of a Two-Dimensional, Hypersonic, Turbulent Wake", *NASA TN* D-6927, 1972.

[18] Williams, F. A.; *Combustion Theory*. Addison-Wesley Publishing Company, Inc., Reading, MA, pp. 358-429, 1965.

[19] Launder, B.E.; Reece, G.J. and Rodi, W., "Progress in the Development of a Reynolds Stress Turbulence Closure", *J. Fluid Mech.*, Vol.68, 1975, pp 537-566.

[20] Strahle, W.C., "Velocity-Pressure Gradient Correlation in Reactive Turbulent Flows", *Combustion Science and Technology*, Vol.32, 1983, pp 289-305.

[21] Drummond, J. P.,"A Two-Dimensional Numerical Simulation of a Supersonic, Chemically Reacting Mixing Layer", *NASA TM* 4055, 1988.

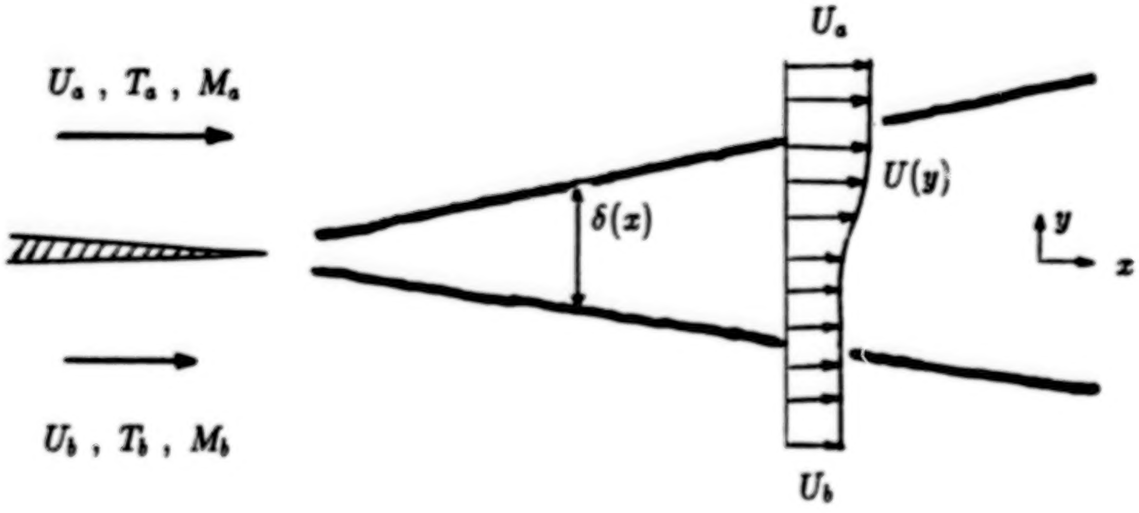

Fig.1 Mixing Layer (schematic)

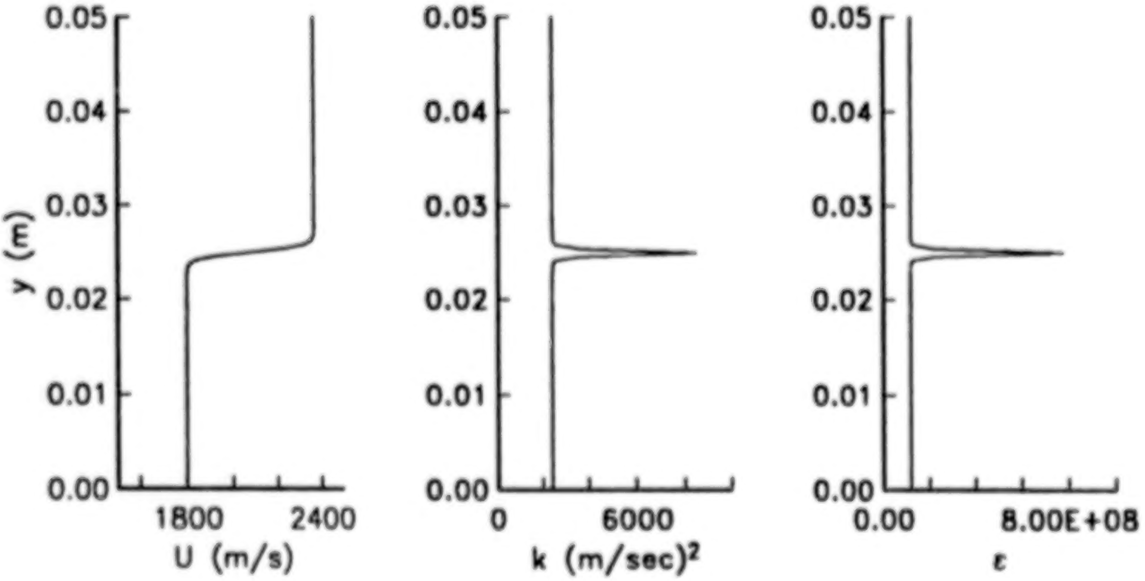

Fig.2 Initial Profiles

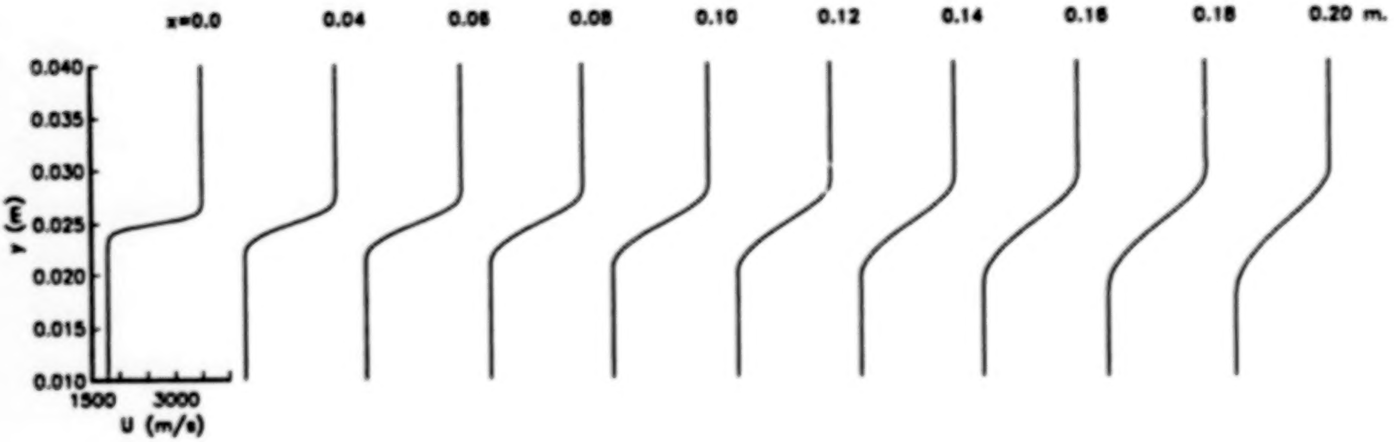

a) Mean Axial Velocity

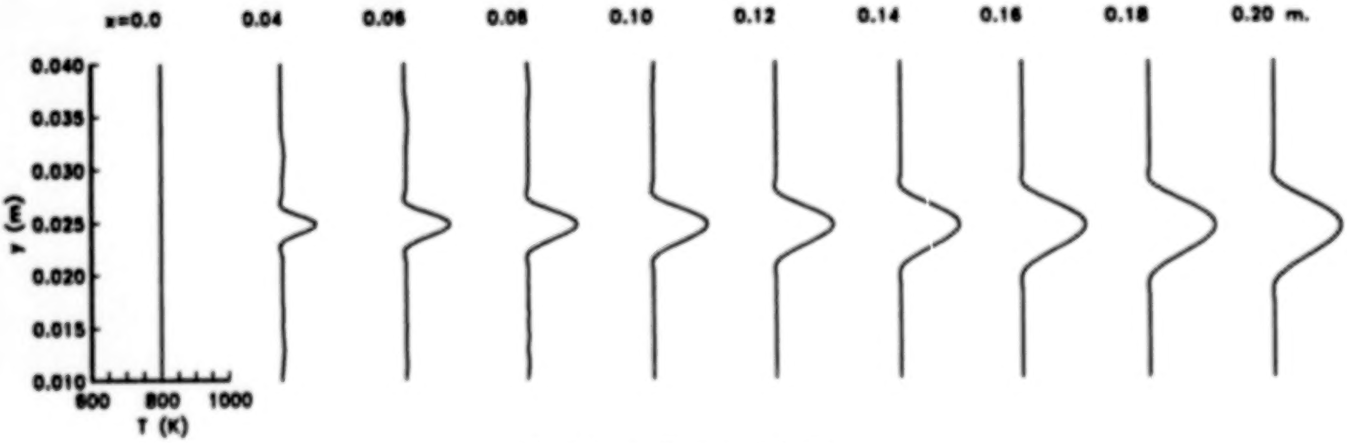

b) Mean Temperature

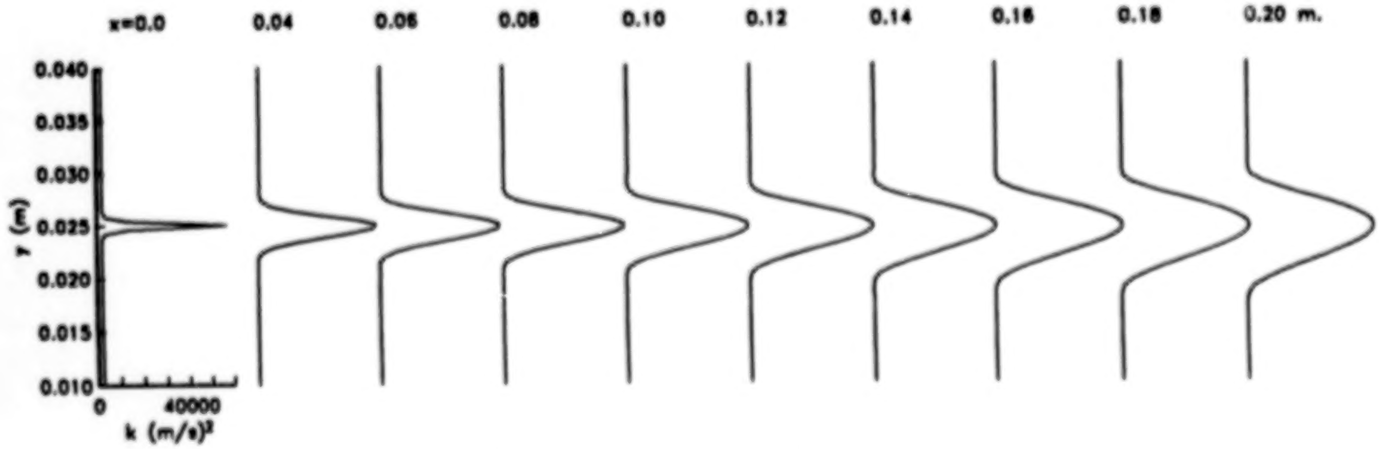

c) Turbulent Kinetic Energy

$M_c=1.5$, $\alpha=1.0$, $T_\infty=800$ K

Fig.3 Predicted Flow Field of Mixing Layer

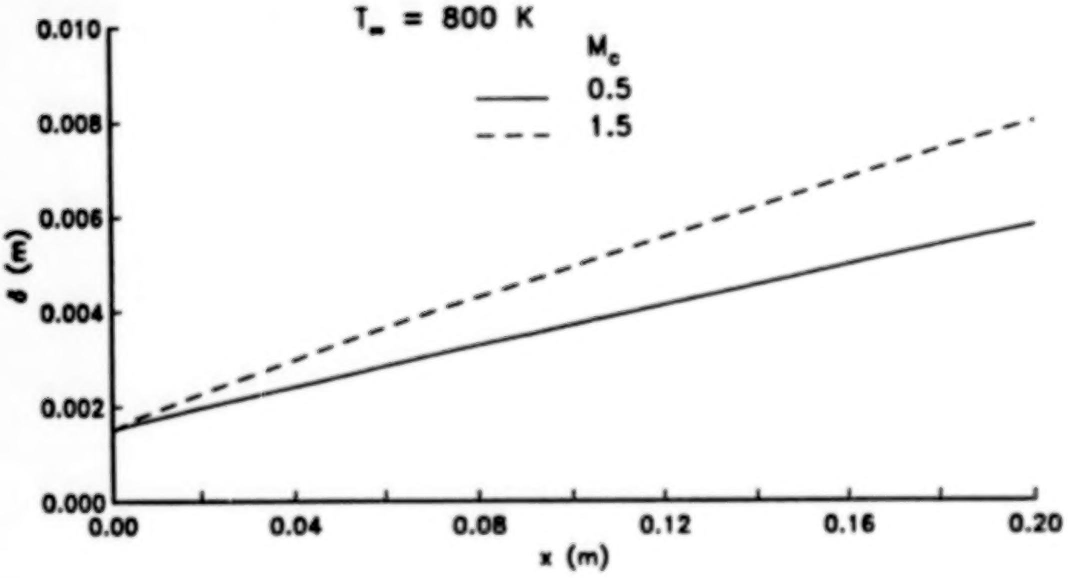

$\delta=(U_a-U_b)/(\partial u/\partial y)_{max}$

Fig.4 Mixing Layer Thickness

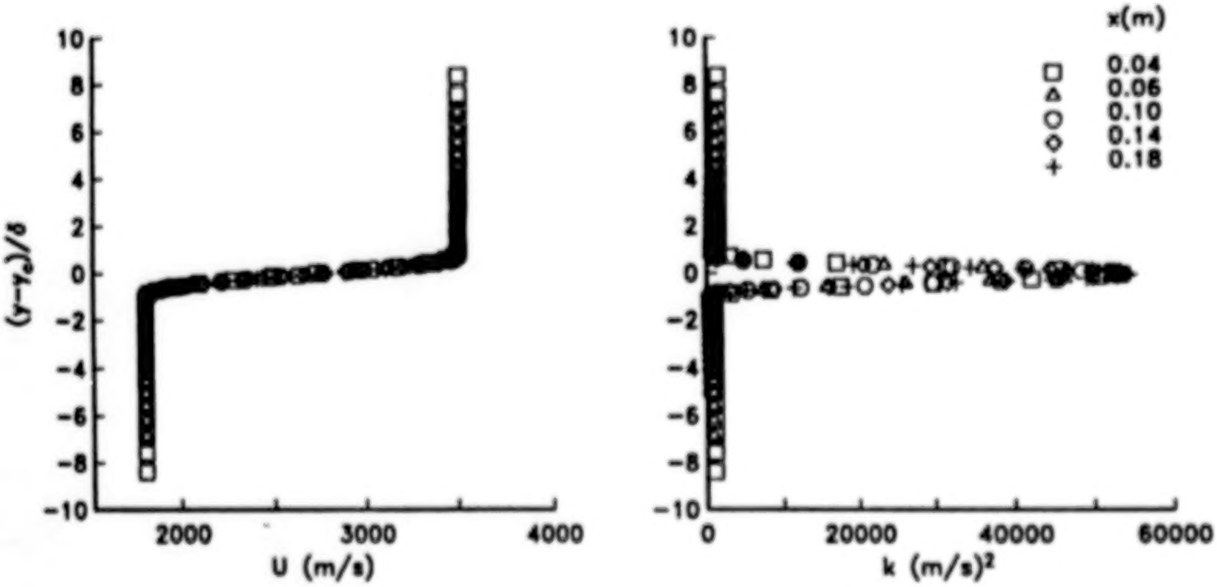

a) Mean axial velocity

b) Turbulent kinetic energy

M_c=1.5, α=1.0, T_∞=800 K

Fig.5 Mixing Layer Similarity Profiles

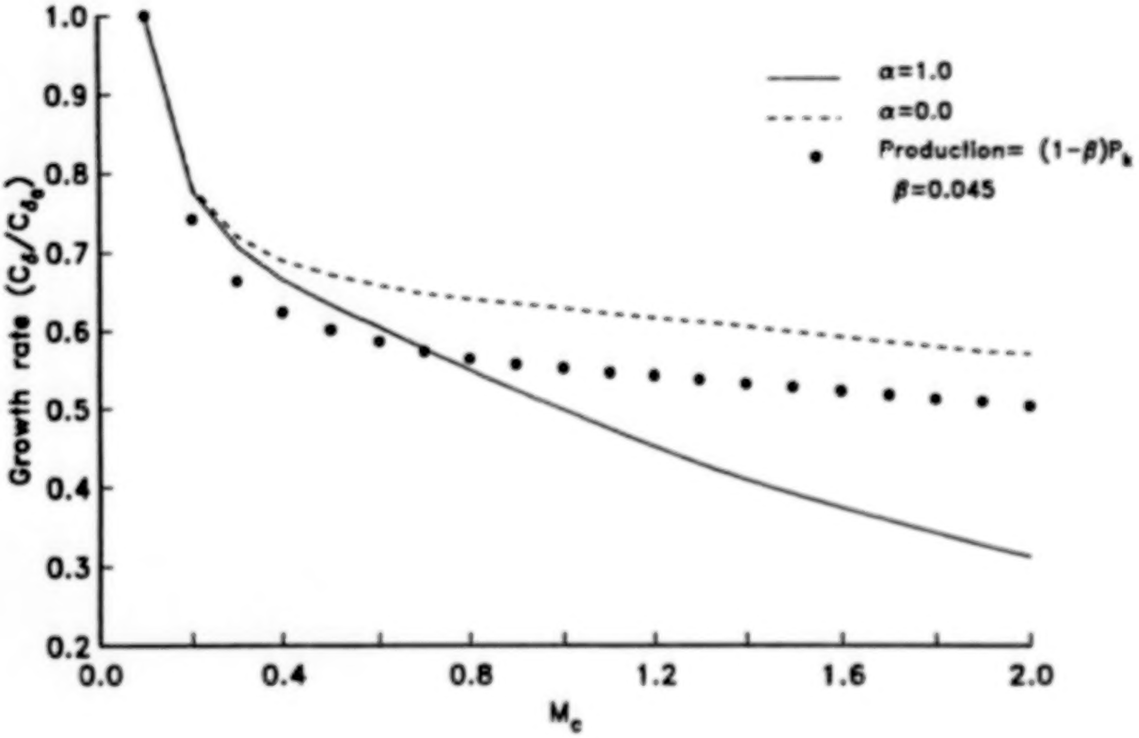

Fig.6 Effect of compressibility correction

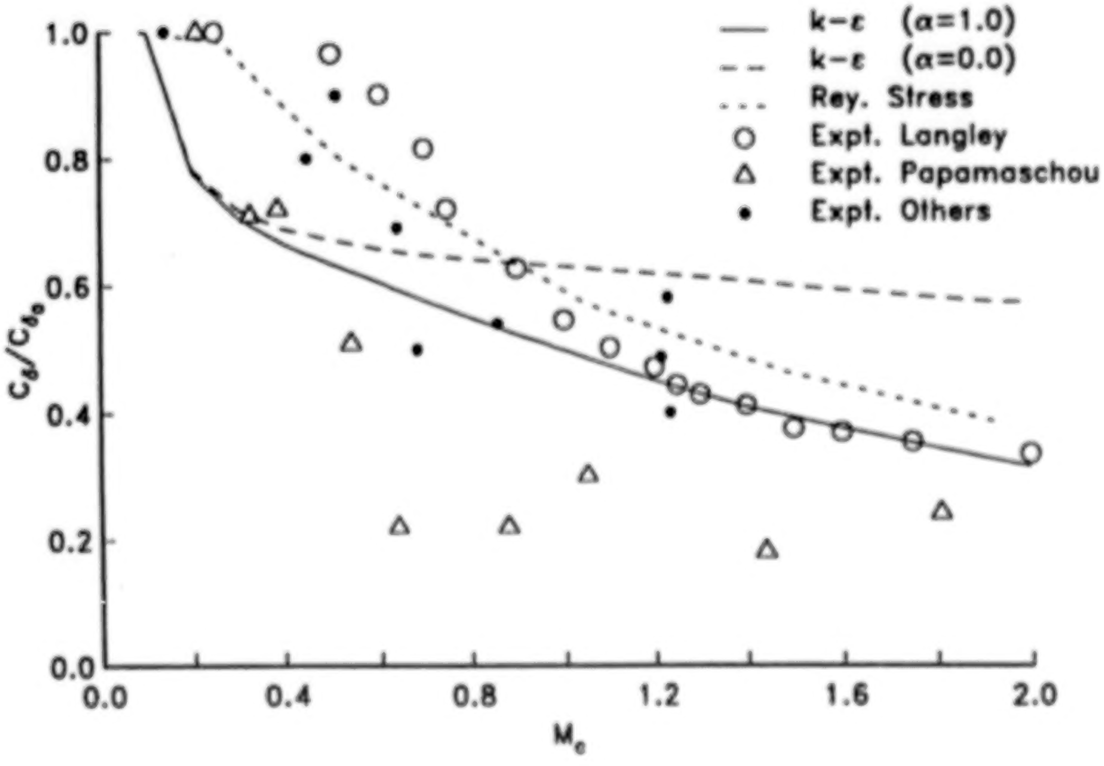

Fig.7 Comparison of growth rate data

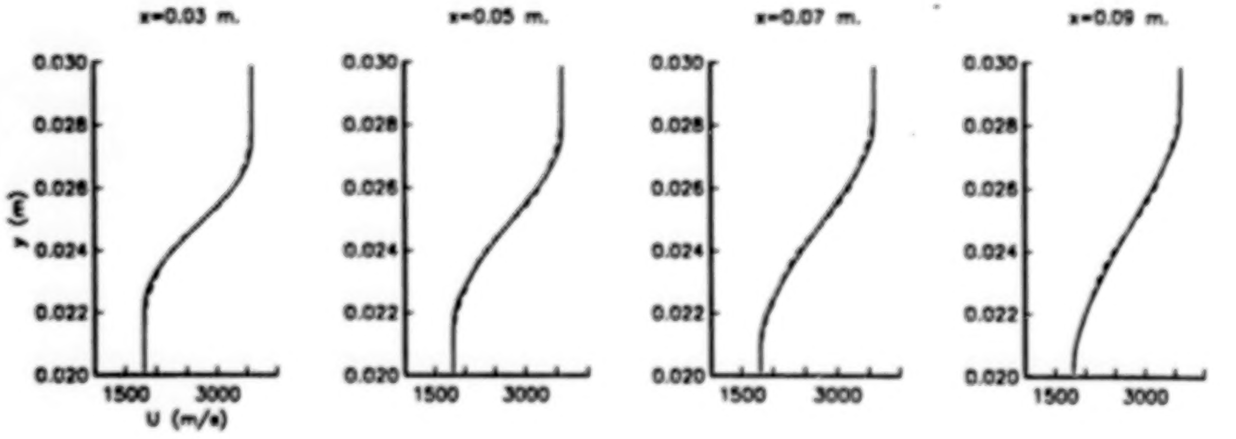

a) Mean Axial Velocity

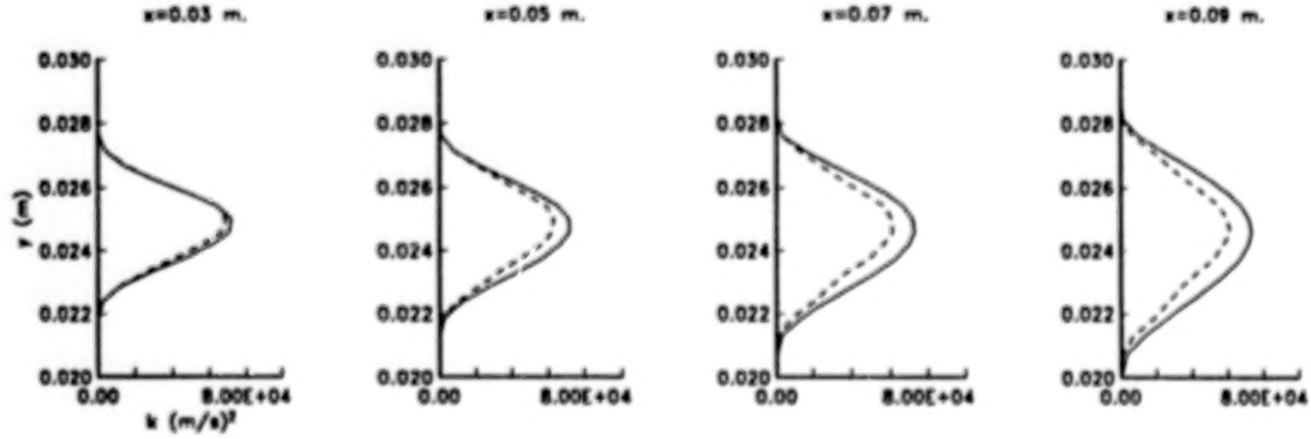

b) Turbulent Kinetic Energy

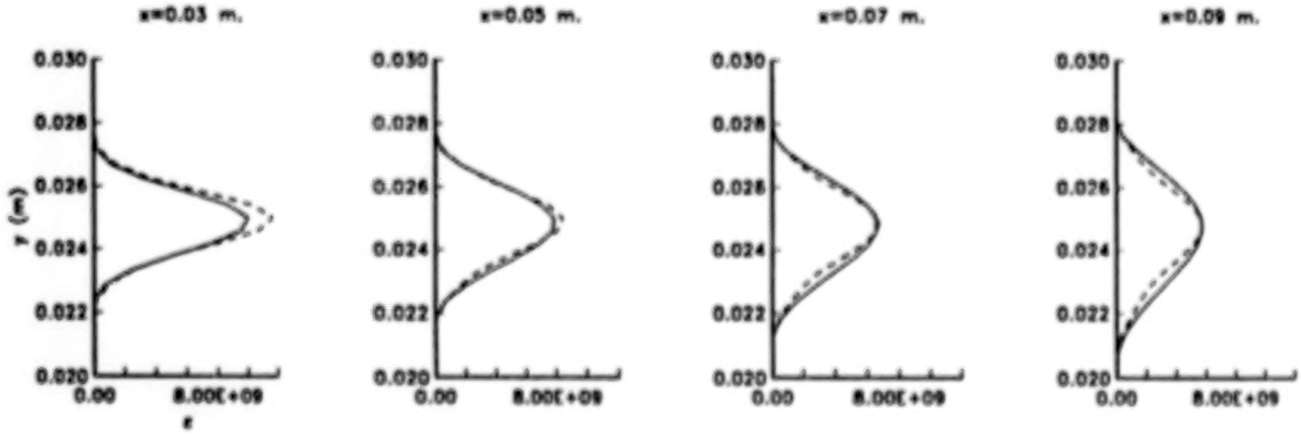

c) Dissipation Rate

T_∞=2000 K, M_c=1.0 α=1.0

Fig.8 Comparison Between k–ε and Reynolds Stress Closures

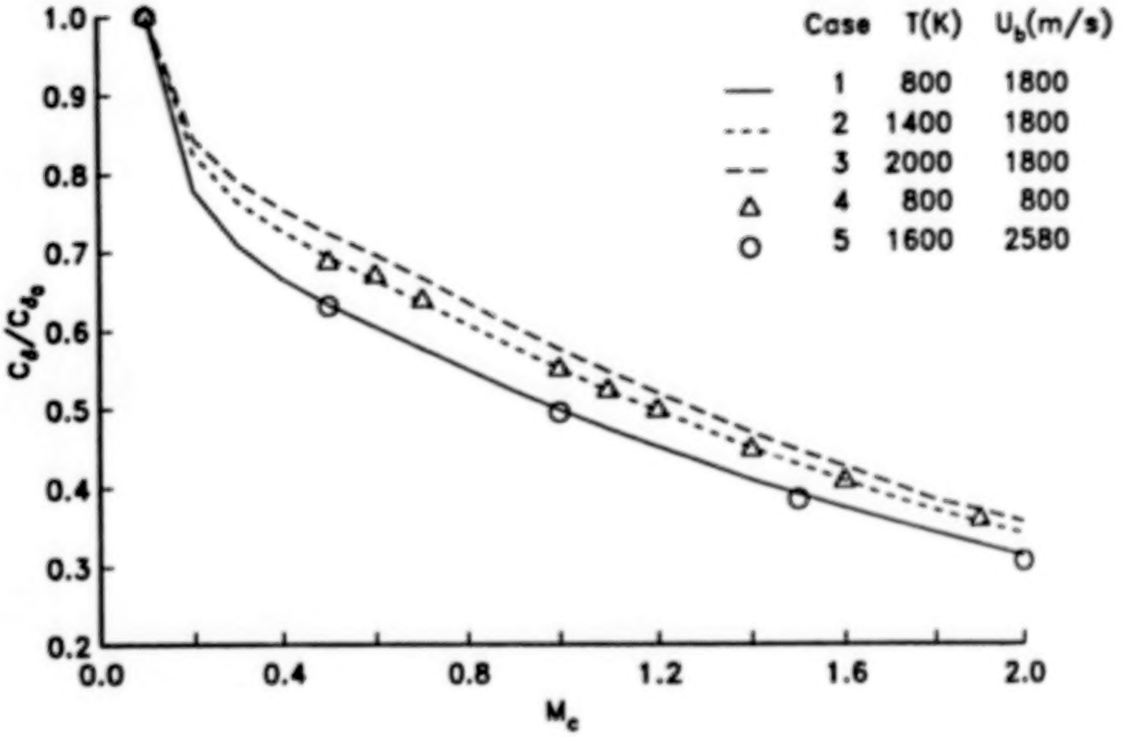

Fig.9 Effect of Temperature on Growth Rate

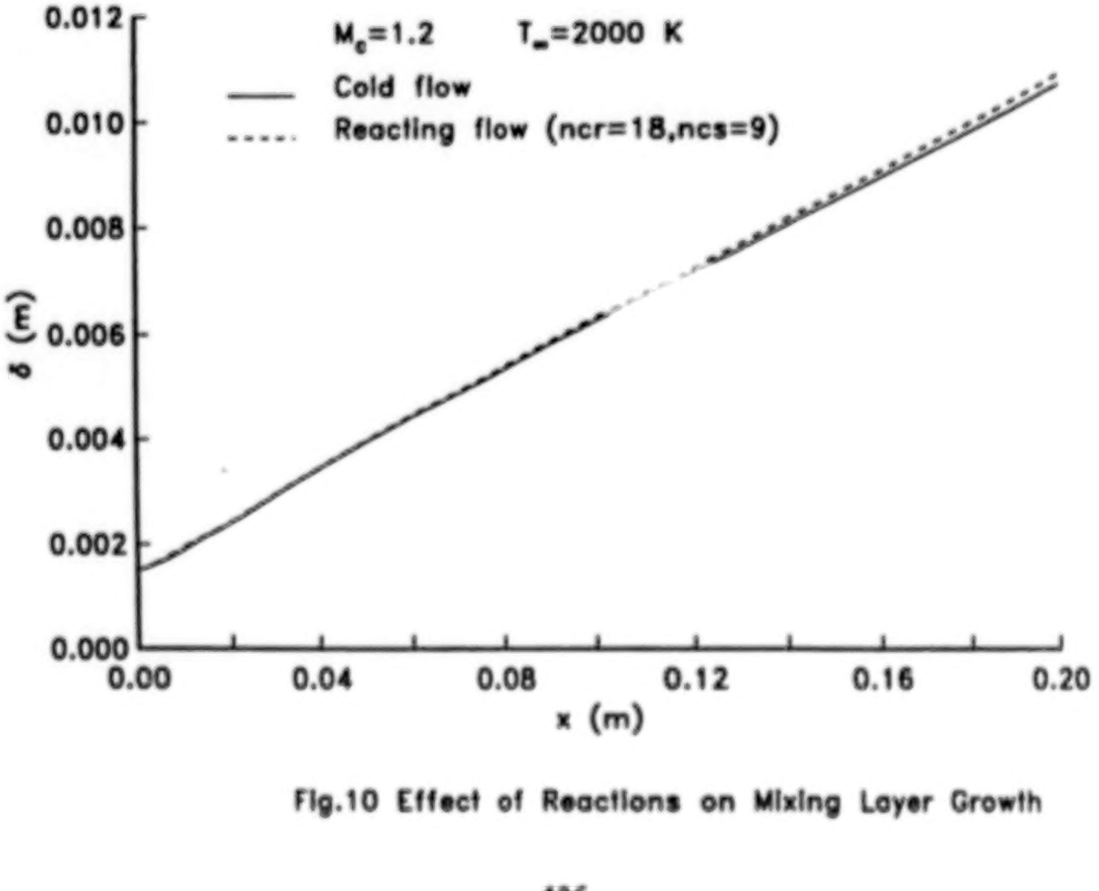

Fig.10 Effect of Reactions on Mixing Layer Growth

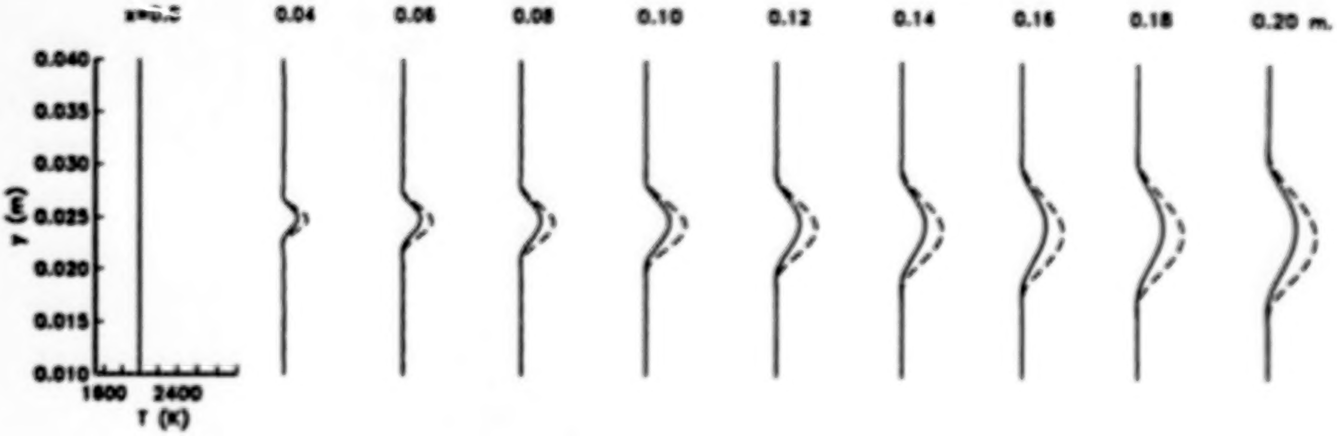

a) Mean Temperature

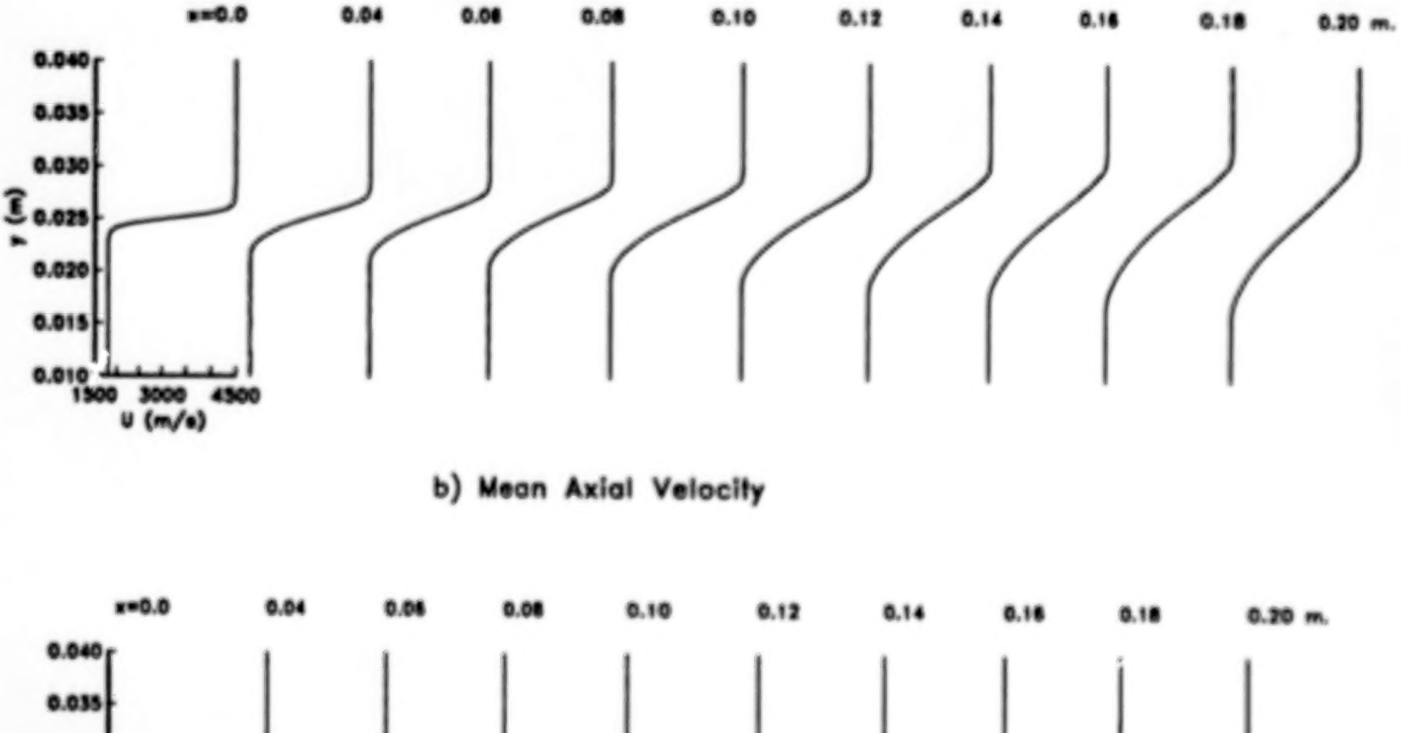

b) Mean Axial Velocity

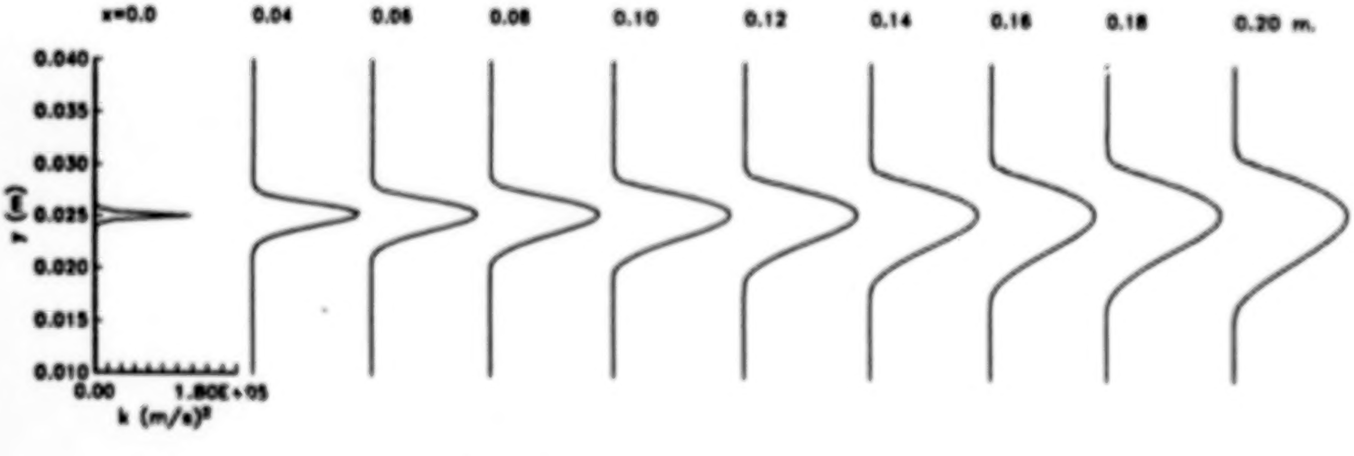

c) Turbulent Kinetic Energy

—— Cold flow

---- Reacting flow

M_c=1.2 , α=1.0 , T_∞=2000 K

Fig.11 Effect of Chemical Reactions on Mixing Layer

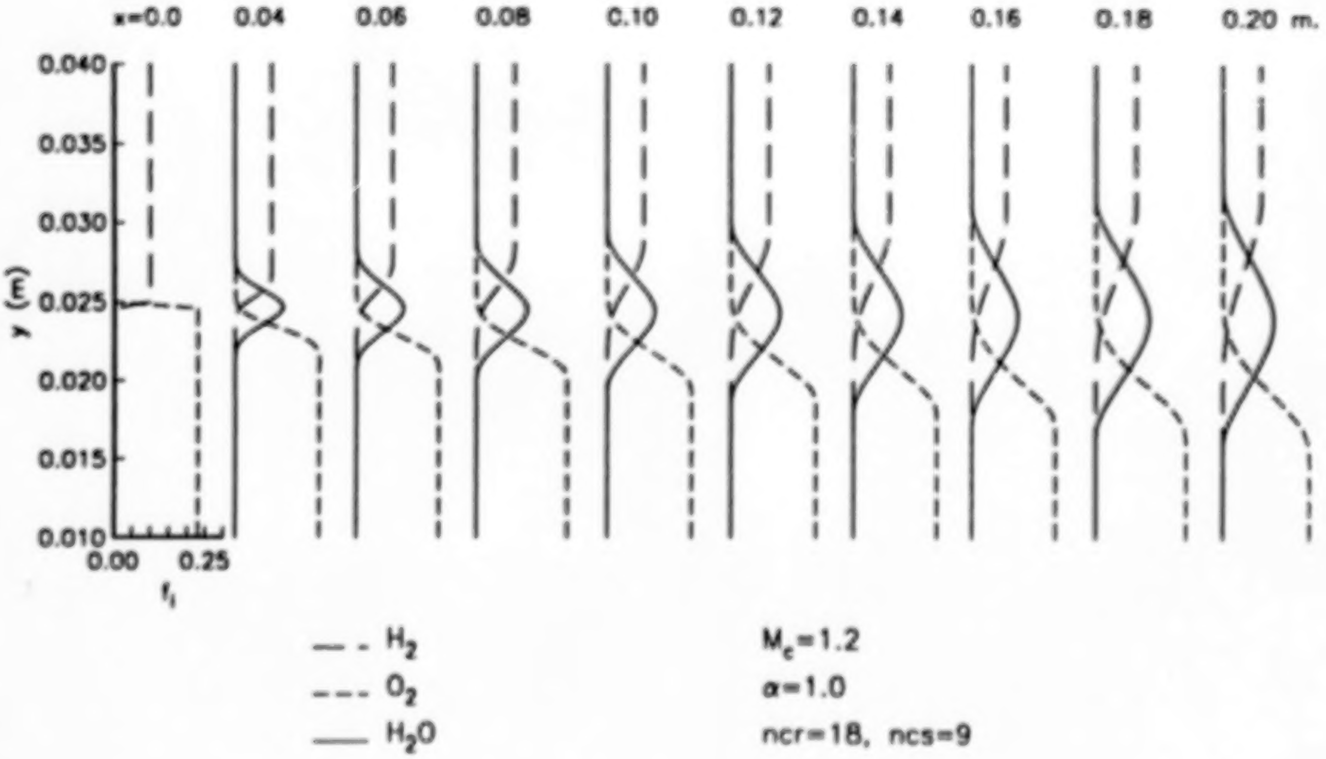

Fig.12 Species Mass Fractions

HEAT TRANSFER, VELOCITY-TEMPERATURE CORRELATION, AND TURBULENT SHEAR STRESS FROM NAVIER-STOKES COMPUTATIONS OF SHOCK WAVE/TURBULENT BOUNDARY LAYER INTERACTION FLOWS

C.R. Wang, W.R. Hingst, and A.R. Porro
National Aeronautics and Space Administration
Lewis Research Center
Cleveland, Ohio 44135

ABSTRACT

The properties of two-dimensional shock wave/turbulent boundary layer interaction flows were calculated by using a compressible turbulent Navier-Stokes numerical computational code. Interaction flows caused by oblique shock wave impingement on the turbulent boundary layer flow were considered. The oblique shock waves were induced with shock generators at angles of attack less than 10° in supersonic flows (Mach 2.5 and 6.0). The surface temperatures were kept at near-adiabatic (ratio of wall static temperature to free-stream total temperature, 0.99) and cold-wall (ratio of wall static temperature to free-stream total temperature, 0.66) conditions. The computational results were studied for the surface heat transfer, velocity-temperature correlation, and turbulent shear stress in the interaction flow fields. Comparisons of the computational results with existing measurements indicated that (1) the surface heat transfer rates and surface pressures could be correlated with Holden's relationship, (2) the mean flow streamwise velocity components and static temperatures could be correlated with Crocco's relationship if flow separation did not occur, and (3) the Baldwin-Lomax turbulence model should be modified for turbulent shear stress computations in the interaction flows.

NOMENCLATURE

C_{cp}	empirical constant for turbulence modeling
C_f	skin friction factor
C_v	specific heat at constant volume
C_{wk}	empirical constant for turbulence modeling
E,F	vectors
F_{kleb}	Klebanoff intermittency factor
F_{wake}	turbulence modeling factor
H	grid dimension (fig. 1(a))
IM	grid dimension (fig. 1(b))

J	Jacobian matrix
JM	grid dimension (fig. 1(b))
k	empirical constant for turbulence modeling
L	grid dimension (fig. 1(a))
ℓ	length scale for turbulence modeling
M	Mach number
Pr	laminar Prandtl number
Pr_t	turbulent Prandtl number
p	static pressure
p_{o2}	pitot pressure
$p_{o\infty}$	free-stream total pressure
Q	heat transfer rate
$Re_{\delta o}$	free-stream Reynolds number, $\rho_e U_e \delta_o / \mu_e$
T	static temperature
$T_{o\infty}$	free-stream total temperature
t	time
U	mean flow velocity component
U_τ	friction velocity
u'	turbulent fluctuation in U
V	mean flow velocity component
v'	turbulent fluctuation in V
X	distance along streamwise direction
X_c	location where minimum grid occurs
Y	normal distance from wall
Y_c	value of Y at which ε values from inner and outer formulas are equal
α	stretching factor
β	stretching factor

γ	recovery factor
δ_0	initial boundary layer thickness
ϵ	eddy viscosity
η	transformed coordinate in Y-direction
θ	angle of attack
λ	stretching factor
μ	absolute viscosity
ξ	transformed coordinate in X-direction
ρ	density
$\tau_{XX}, \tau_{XY}, \tau_{YY}$	normal or shear stress
ω	magnitude of vorticity

Subscripts:

dif	difference between maximum and minimum values
e	far-field condition
max	maximum
min	minimum
o	condition at $X = 0$
r	reference condition
w	surface condition
∞	free-stream condition

INTRODUCTION

Because of recent development efforts for supersonic and hypersonic flight vehicles, generic research in the flow fields of advanced propulsion systems has become an interesting topic of compressible flow studies. Shock wave/turbulent boundary layer interaction flow is an important, basic flow phenomenon within the flow fields of supersonic or hypersonic propulsion systems. The variations of velocity components, surface pressures, and skin friction factors within the interaction flow fields have been studied, and a review of the existing literature is reported by Delery, Marvin, and Reshotko (ref. 1). Under severe operational conditions, surface heat transfer becomes an important element in the design of an advanced propulsion system. From an effort to study the surface heat transfer beneath shock wave/turbulent boundary layer interaction flows, the present authors describe in this paper some preliminary results of their computational analyses of the flow properties in several two-dimensional shock wave/turbulent boundary layer interaction flows. The flow properties were computed by using the Navier-Stokes numerical code developed by Shang, Hankey, and Law (ref. 2), and the computational results were compared with the experimental measurements of Hingst and Porro (W.R. Hingst and A.R. Porro, NASA Lewis Research Center, Cleveland, Ohio, 1989, personal communication), Alzner and Zakkay (ref. 3), and Zakkay and Wang (ref. 4).

First, the shock wave/turbulent boundary layer interaction flows in a Mach 2.5 free stream were studied. Hingst and Porro performed experiments with this type of interaction flow field. They used a shock generator plate at an angle of attack with a Mach 2.5 free stream to produce oblique shock. The interaction of the oblique shock with the naturally occurring boundary layer on the tunnel wall defined the experimental configurations. Tests were conducted to measure the surface static pressure, surface dynamic pressure, and surface heat transfer with near-adiabatic and heated surfaces. The experimental results with the shock generator at 4° and 8° angles of attack were used to verify the present computations.

Second, the shock wave/turbulent boundary layer interactions induced by inserting axisymmetric wedges (wedge angles 4° and 10°) in a Mach 6 free stream were studied. Alzner and Zakkay (ref. 3) and Zakkay and Wang (ref. 4) performed experiments in these flow fields. They measured the surface heat transfer rates, static pressures, and pitot pressures. The turbulent boundary layer developed along a cylindrical center body surface. The ratio between the surface temperature and the total temperature was 0.66. This represented a cold wall condition. These experimental results were used to verify the present computations. This study of Mach 6 interaction flow is important since, in the existing literature, Navier-Stokes computations are limited mostly to Mach 3 cases with adiabatic wall conditions.

Since Shang's Navier-Stokes equation computational code used the Baldwin-Lomax turbulence model (ref. 5), we investigated the capability of this turbulence model in the Navier-Stokes computational code to predict the turbulent shear stresses in an interaction flow. The Reynolds shear stress in a Mach 2.9 interaction flow was also computed. Rose and Johnson (ref. 6) measured the turbulence shear stresses in Mach 2.9 interaction flow. Their turbulence measurements were compared with our computations of Reynolds stress.

The present computational results of the streamwise mean flow velocity components and static temperatures were correlated and compared with Crocco's relationship (ref. 7). The surface pressures and heat transfer rates from the computations were also correlated and compared with Holden's relationship (ref. 8). With these comparisons, the applications of Crocco's and Holden's relationships to estimate the surface heat transfer rates and temperature variations in shock wave/turbulent boundary layer interaction flow are discussed. The preliminary Reynolds stress computations were studied to determine the applicability of Baldwin-Lomax turbulence modeling in interaction flows.

COMPUTATIONAL METHODS

A time-dependent explicit numerical computational code was used to solve the compressible turbulent Navier-Stokes equations and the energy equation for steady-state interaction flow properties. This code was developed (ref. 2) by using MacCormack's finite difference computational scheme (ref. 9). In this code, the physical domain (X,Y) was transformed into a computational domain (ξ,η) with a uniform computational grid along both ξ and η axes. Details of the mathematical manipulations in the coordinate transformations related to the Navier-Stokes equations are given in the text book by Anderson, Tannehill, and Pletcher (ref. 10). However, the conservation equations, coordinate transformations, turbulence modeling, initial and boundary conditions, and numerical scheme used in this study are described briefly in the following paragraphs.

Conservation Equations

The following two-dimensional compressible turbulent Navier-Stokes equations and total energy equation

$$\frac{\partial U}{\partial t} + \frac{\partial E}{\partial X} + \frac{\partial F}{\partial Y} = 0 \qquad (1)$$

with

$$U = \begin{bmatrix} \rho \\ \rho U \\ \rho V \\ E_t \end{bmatrix}$$

$$E = \begin{bmatrix} \rho U \\ \rho U^2 + p - \tau_{XX} \\ \rho UV - \tau_{XY} \\ (E_t + p)U - U\tau_{XX} - V\tau_{XY} + Q_X \end{bmatrix}$$

$$F = \begin{bmatrix} \rho V \\ \rho UV - \tau_{XY} \\ \rho V^2 + p - \tau_{YY} \\ (E_t + p)V - U\tau_{XY} - V\tau_{YY} + Q_Y \end{bmatrix}$$

where

$$E_t = \rho\left(C_v T + \frac{U^2 + V^2}{2}\right)$$

$$\tau_{XX} = \frac{4}{3}(\mu + \epsilon)\,\frac{\partial U}{\partial X} - \frac{2}{3}(\mu + \epsilon)\,\frac{\partial V}{\partial Y}$$

$$\tau_{YY} = \frac{4}{3}(\mu + \epsilon)\,\frac{\partial V}{\partial Y} - \frac{2}{3}(\mu + \epsilon)\,\frac{\partial U}{\partial X}$$

$$\tau_{XY} = (\mu + \epsilon)\left(\frac{\partial V}{\partial X} + \frac{\partial U}{\partial Y}\right)$$

$$Q_X = \frac{C_v\mu}{Pr}\,\frac{\partial T}{\partial X} + \frac{C_v\epsilon}{Pr_t}\,\frac{\partial T}{\partial X}$$

$$Q_Y = \frac{C_v\mu}{Pr}\,\frac{\partial T}{\partial Y} + \frac{C_v\epsilon}{Pr_t}\,\frac{\partial T}{\partial Y}$$

were used to describe the variations of flow properties within two-dimensional interaction flow. In these equations, the turbulence contributions to the momentum and energy transports were related to the gradients of the mean velocity components and the mean static temperature by using the concepts of turbulent eddy viscosity and the Reynolds analogy. A laminar Prandtl number $Pr = 0.73$ and a turbulent Prandtl number $Pr_t = 0.90$ were chosen. These Navier-Stokes equations were written in a two-dimensional orthogonal X-Y coordinate system. Thus, the effect of the center body radius on the axisymmetric interaction flows (refs. 3 and 4) was not considered.

Coordinate Transformations

Figure 1 presents the general concept of the transformations between the physical and the computational domains. The transformations were required to concentrate the computational mesh points within the region where large gradients in the flow properties would occur in the physical domain. Similar coordinate transformations are described in reference 10, and the following transformations were used in this study:

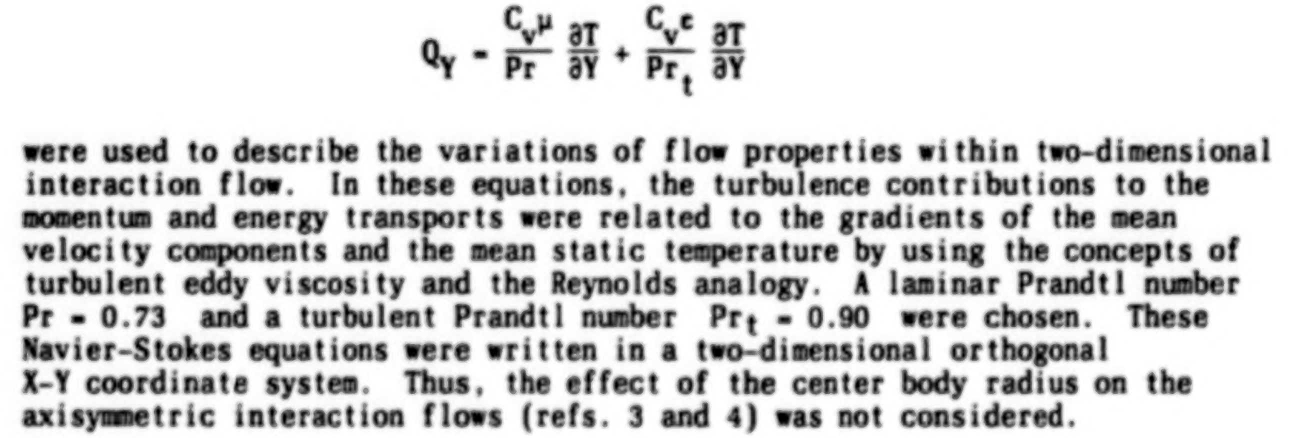

DISTANCE FROM SURFACE, Y
H
δ_0
SHOCK
X_c
L
DISTANCE IN STREAMWISE DIRECTION, X
Y-TRANSFORMED COORDINATE, η
1.0
(I = IM, J = JM)
SHOCK
0
1.0
X-TRANSFORMED COORDINATE, ξ

(a) PHYSICAL DOMAIN.

(b) COMPUTATIONAL DOMAIN.

FIGURE 1. - COMPUTATIONAL GRIDS IN PHYSICAL AND COMPUTATIONAL DOMAINS.

$$\xi = \alpha + \frac{\sinh^{-1}\left[(X/X_c - 1)\sinh(\lambda\alpha)\right]}{\lambda} \tag{2}$$

and

$$\eta = 1 - \frac{\ln\{[\beta + 1 - (Y/H)]/[\beta - 1 + (Y/H)]\}}{\ln[(\beta + 1)/(\beta - 1)]} \tag{3}$$

where

$$\alpha = \frac{L}{2\lambda} \ln\left[\frac{1 + (e^{\lambda} - 1)(X_c/L)}{1 + (e^{-\lambda} - 1)(X_c/L)}\right]$$

with

$$0 \leq \lambda \leq \infty \quad \text{and} \quad 1 \leq \beta \leq \infty$$

Different sizes of the physical domain, the computational grid dimensions IM and JM, and the numerical values for λ and β were chosen for different flow configurations. Together with the computational results, these parameters are presented for each flow field in the latter part of this paper.

Turbulence Modeling

The algebraic turbulence model proposed by Baldwin and Lomax (ref. 5) was used here. It is a two-layer algebraic eddy viscosity model in which the eddy viscosity ε is given by

$$\varepsilon = \begin{cases} \varepsilon_{inner} & Y < Y_c \\ \varepsilon_{outer} & Y \geq Y_c \end{cases}$$

where Y is the normal distance from the wall and Y_C is the value of Y at which ε values from the inner and outer formulas are equal. For a two-dimensional mean flow, the eddy viscosity model can be written as follows:

In the inner layer,

$$\varepsilon = \rho \ell^2 |\omega|$$

where

$$\ell = kY\left[1 - \exp\left(-\frac{Y^+}{A^+}\right)\right]$$

$|\omega|$ is the magnitude of the vorticity

$$|\omega| = \sqrt{\left(\frac{\partial U}{\partial Y} - \frac{\partial V}{\partial X}\right)^2}$$

and

$$Y^+ = \frac{\rho_w U_\tau Y}{\mu_w}$$

In the outer layer,

$$\varepsilon_{outer} = kC_{cp}\rho F_{wake} F_{kleb}$$

where

$$F_{wake} = \text{the smaller of} \begin{cases} Y_{max}F_{max} \\ \text{or} \\ \dfrac{C_{wk}Y_{max}U_{dif}^2}{F_{max}} \end{cases}$$

and

$$F(Y) = Y|\omega|\left[1 - \exp\left(-\frac{Y^+}{A^+}\right)\right]$$

The quantity F_{max} is the maximum value of F that occurs in a profile and Y_{max} is the value of Y at which it occurs. The function $F_{kleb}(Y)$ is the Klebanoff intermittency factor given by

$$F_{kleb} = \left[1 + 5.5\left(\frac{C_{kleb}Y}{Y_{max}}\right)^6\right]^{-1}$$

The quantity U_{dif} is the difference between the maximum and minimum total velocities in the profile:

$$U_{dif} = \left(\sqrt{U^2 + V^2}\right)_{max} - \left(\sqrt{U^2 + V^2}\right)_{min}$$

The second term in U_{dif} is set to be zero.

Baldwin and Lomax determined a set of values for the empirical constants appearing in the above relationships. These values are $A^+ = 26$, $C_{cp} = 1.6$, $C_{kleb} = 0.3$, $C_{wk} = 0.24$, $k = 0.4$, and $\kappa = 0.0168$. However, a different value for $C_{cp} = 2.0$ was used in the present computations.

Numerical Computational Scheme

The governing equations were transformed from the physical domain to the computational domain. The chain rule of partial differentiation was used to rewrite equation (1) as

$$\frac{\partial U_1}{\partial t} + \frac{\partial E_1}{\partial \xi} + \frac{\partial F_1}{\partial \eta} = 0 \tag{4}$$

where

$$U_1 = \frac{U}{J}$$

$$E_1 = \frac{E\xi_X + F\xi_Y}{J}$$

$$F_1 = \frac{E\eta_X + F\eta_Y}{J}$$

and J is the Jacobian matrix of the transformation.

The vectors E_1 and F_1 contain partial derivatives in the viscous and heat transfer terms. These partial derivative terms were also transformed by using equations (2) and (3).

An explicit MacCormack predictor and corrector time iteration with a fourth-order smoothing numerical scheme was used to solve the Navier-Stokes equations for the flow properties within the interaction flow region. Forward finite differencing and backward finite differencing were chosen respectively for the differentiations in the predictor and the corrector steps. The stability factors for CFL and the smoothing terms in the X and Y directions were 0.9, 0.4, and 0.4, respectively, in all of the computations.

The existing Navier-Stokes equation solver (ref. 2) used a time-dependent explicit computational scheme. The initial flow properties and their conditions around the boundary of the physical domain were required to start the computations. With one exception, which will be described later, the following general principles specified the initial and boundary conditions.

Initial Conditions

The properties of a fully developed flat plate turbulent boundary layer flow were used in the initial conditions. These properties were calculated by using the Navier-Stokes equation solver. For this purpose, the initial mean velocity profiles

$$\frac{U}{U_e} = \left(\frac{Y}{\delta_o}\right)^{1/7} \quad \text{and} \quad V = 0$$

were assumed. The local temperature was related to the mean velocity component U by Crocco's relationship,

$$\frac{T}{T_e} = \frac{T_w}{T_e} + \left(1 + 0.2\gamma\, M_e^2 - \frac{T_w}{T_e}\right)\left(\frac{U}{U_e}\right) - 0.2\gamma\, M_e^2\left(\frac{U}{U_e}\right)^2 \tag{5}$$

with the recovery factor $\gamma = 0.9$.

Boundary Conditions

For the initial boundary layer flow computation, the far-field boundary conditions were described by the free-stream conditions. They are $\rho = \rho_e$, $U = U_e$, $V = 0$, and $T = T_e$.

The following conditions,

$$U = 0 \qquad V = 0 \qquad T = T_w \quad \text{and} \quad \frac{\partial p}{\partial Y} = 0 \tag{6}$$

were specified as the boundary conditions at the surface, $Y = 0$. The flow properties at the downstream boundary, $X = L$, were also assumed to be constant along the X-direction. Therefore,

$$\frac{\partial f}{\partial X} = 0 \tag{7}$$

at $X = L$ where $f = \rho$, U, V, and T.

The following procedures defined the far-field boundary conditions for a two-dimensional shock wave/turbulent boundary layer interaction flow field. The computational domain was chosen such that only the impinging oblique shock wave passed the far-field boundary ($Y = H$) and the reflected shock wave crossed the outflow boundary ($X = L$). The two-dimensional inviscid and adiabatic oblique shock wave theories were used to relate the flow properties upstream and downstream of the incoming shock wave. Conditions given in equations (6) and (7) were also imposed at the $Y = 0$ and $X = L$ boundaries, respectively.

RESULTS AND DISCUSSIONS

The previously described computational methods were used to obtain steady-state solutions of the density components, velocity components, and static temperature distributions within the two-dimensional shock wave/turbulent boundary layer interaction flows in references 3 and 4, and in Hingst and Porro's work (W.R. Hingst and A.R. Porro, NASA Lewis Research Center, Cleveland, Ohio, 1989, personal communication). On the basis of these flow properties, the static pressures, skin friction factors, and surface heat transfer rates were also determined. The computational results are described and compared with existing measurements in the following sections. Parameters such as the size of the physical domain L and H, the grid dimensions IM and JM, and the stretching factors λ and β which were chosen in the computations are also listed accordingly.

Interaction Flow Fields at Mach 2.5

The flow properties were computed to predict some of the measurements in Hingst and Porro's work. This reference used a shock generator plate at 4° and 8° angles of attack to produce oblique shock waves in a Mach 2.5 free stream. The oblique shock wave impinged on the turbulent boundary layer along the wind tunnel wall. The experiments measured the surface pressure distributions for a near-adiabatic wall condition ($T_w/T_{o\infty} = 0.99$) and measured the wall temperature distributions for a heated wall condition.

Initial Turbulent Boundary Layer. - Some of the computed properties of the turbulent boundary layer flow in Hingst and Porro's work are presented in figure 2. With the aid of the density profile and Crocco's relationship, Baronti and Libby (ref. 11) developed a compressible turbulent boundary layer flow analysis and found that the velocity in the boundary layer could be correlated in terms of two similarity laws - the law of the wall and the velocity defect law. Baronti and Libby's analysis and the measurements in

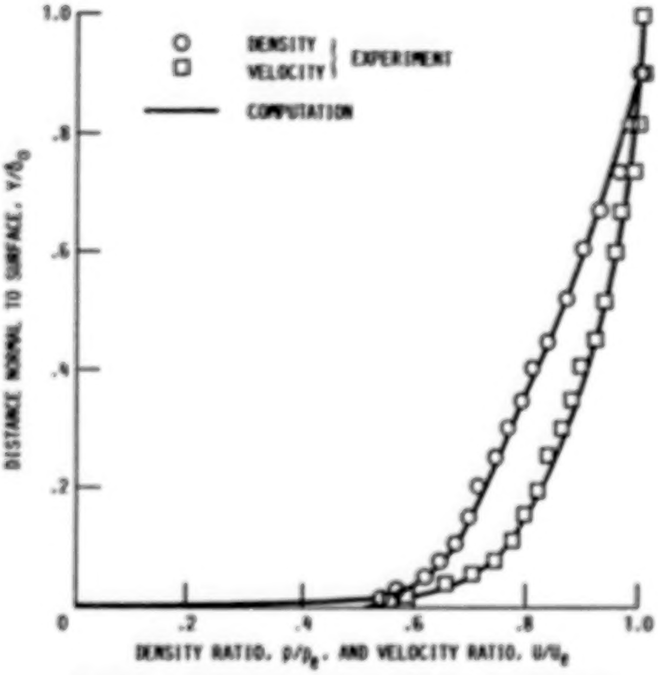

FIGURE 2. - DENSITY AND VELOCITY PROFILES IN COMPRESSIBLE TURBULENT BOUNDARY LAYER FLOW. SURFACE MACH NUMBER, M_e, 2.5; FREE-STREAM REYNOLDS NUMBER, Re_{δ_0}, 0.53×10^6.

Hingst and Porro's work were used to investigate the accuracy of the present computed boundary layer flow properties. For this purpose, the density and the velocity profiles from Hingst and Porro's experiments and the present Navier-Stokes computations were used alternately in Baronti and Libby's analysis (ref. 11). By using the skin friction factor as a parameter, we could represent the velocity profiles in terms of the two similarity laws (fig. 3). A value of $C_{f_0} = 0.0014$ was required to relate the experimental velocity profile to the similarity laws. The present Navier-Stokes computation predicted $C_{f_0} = 0.0015$, which could also correlate the computational velocity profile in terms of the similarity laws. In addition, Navier-Stokes computation predicted a small surface heat transfer rate $Q_{wo} = 1.82 \times 10^3$ W/m² for the near-adiabatic wall condition.

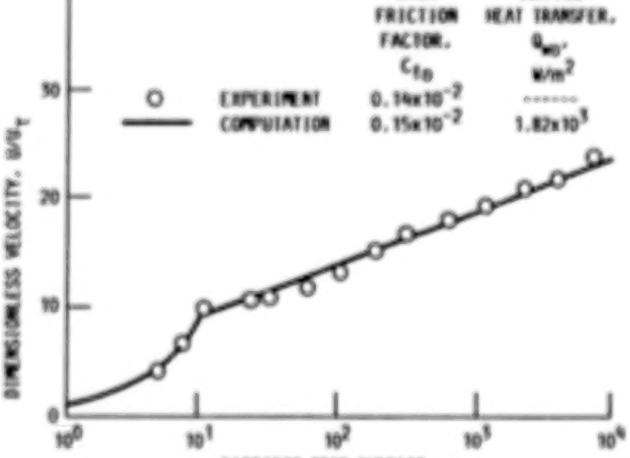

FIGURE 3. - TURBULENT BOUNDARY LAYER VELOCITY PROFILES IN TERMS OF SIMILARITY PARAMETERS U/U_τ AND η (REF. 11). FREE-STREAM MACH NUMBER, M_∞, 2.5.

Hingst and Porro also performed tests of the turbulent boundary layer for a heated wall condition. A section of the wall beneath the boundary layer was heated electrically at constant Q_w, and the surface temperatures along the heated surface were measured. For computational ease, the measured temperatures were used as the wall conditions. The Navier-Stokes computations of the turbulent boundary layer flow were repeated to calculate the surface heat transfer rates along the heated surface (fig. 4). The surface heat transfer rate increased gradually from the initial value Q_{wo} to a constant value $Q_w = 7.15\times10^3$ W/m^2. This constant heat transfer rate is close to the heating rate 7.94×10^3 W/m^2 applied in the experiment. According to the previous observations, the present Navier-Stokes computations of the turbulent boundary layer flow could provide realistic initial flow conditions for the study of the shock wave/turbulent boundary layer interaction flows.

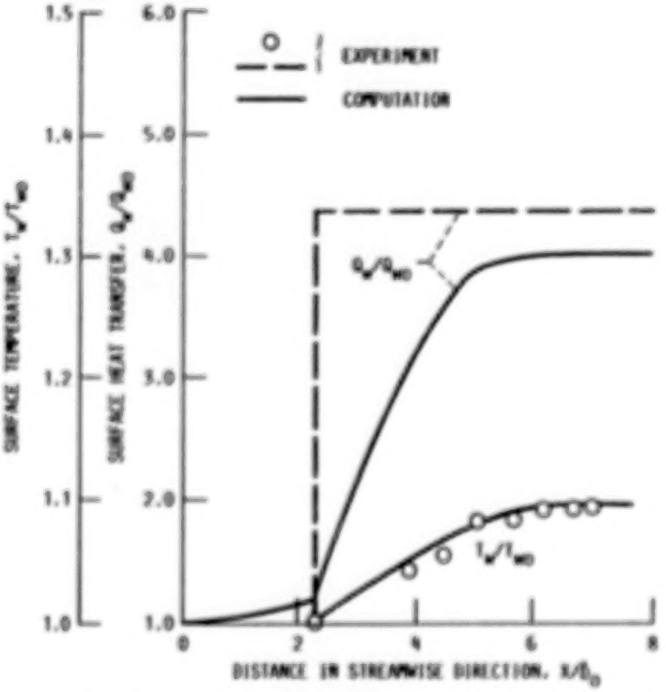

FIGURE 4. - SURFACE TEMPERATURE AND HEAT TRANSFER RATE OF A HEATED TURBULENT BOUNDARY LAYER FLOW. FREE-STREAM MACH NUMBER, M_∞, 2.5; FREE-STREAM SURFACE HEAT TRANSFER RATE AT INITIAL CONDITIONS, Q_{wo}, 1.82×10^3 W/m^2; FREE-STREAM TEMPERATURE AT INITIAL CONDITIONS, T_{wo}, 290 K.

Shock Wave/Turbulent Boundary Layer Interaction. - By using the turbulent boundary layer flow properties as the initial conditions, we computed the flow properties within the oblique shock wave/turbulent boundary layer interaction flow fields in a Mach 2.5 free stream (W.R. Hingst and A.R. Porro, NASA Lewis Research Center, Cleveland, Ohio, 1989, personal communication). Figures 5, 6, 7, and 8 illustrate some results from these computations. Parameters related to the computations are also listed in figures 5 and 6 for reference.

The variations of the static pressure p_w/p_∞ along the Y-direction at several X/δ_0 locations are plotted in figures 5 and 6. The shock wave configurations were determined from these pressure data and were compared with the inviscid flow shock wave locations. The velocity boundary layer edge and the sonic line are also indicated in these figures. These figures show the

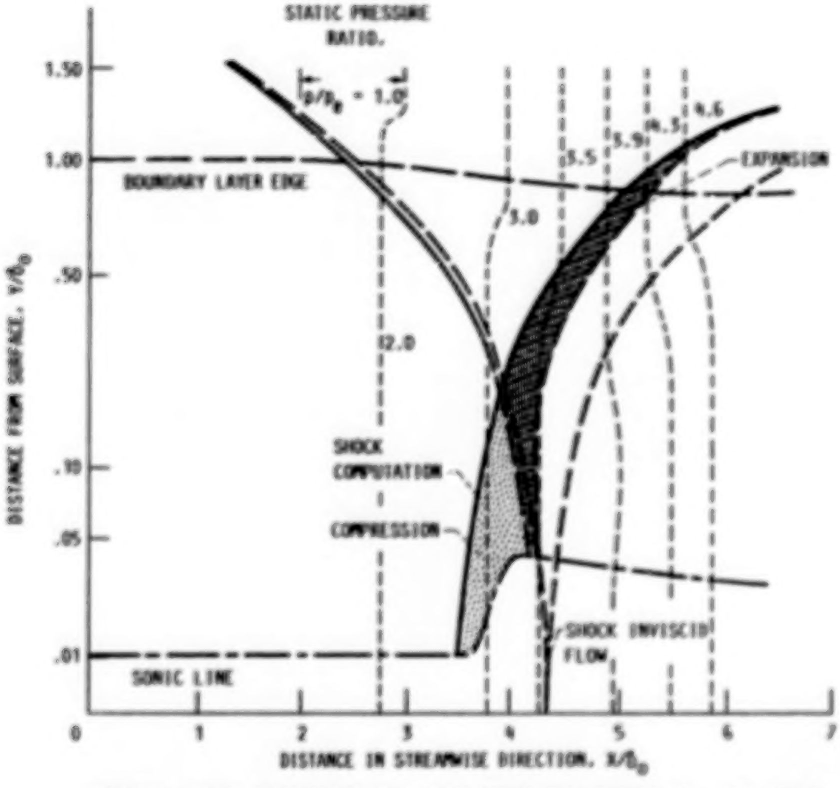

FIGURE 5. - WEAK INTERACTION FLOW. FREE-STREAM MACH NUMBER, M_∞, 2.5; ANGLE OF ATTACK, θ, 4°; GRID DIMENSIONS, IM, 221, AND JM, 119; STRETCHING FACTORS, λ, 5.0, AND β, 1.0012. NUMBERS REFER TO DIMENSIONLESS STREAMWISE DISTANCE, x/δ_0, UNLESS INDICATED OTHERWISE.

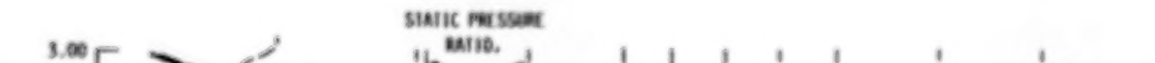

FIGURE 6. - STRONG INTERACTION FLOW. FREE-STREAM MACH NUMBER, M_∞, 2.5; ANGLE OF ATTACK, θ, 8°; GRID DIMENSIONS, IM, 221, AND JM, 119; STRETCHING FACTORS, λ, 5.0, AND β, 1.005. NUMBERS REFER TO DIMENSIONLESS STREAMWISE DISTANCE, x/δ_0, UNLESS INDICATED OTHERWISE.

general characteristics of shock wave/boundary layer interaction flow fields. The subsonic layer was thickened and created compression waves which formed the shock wave in the upstream section of the interaction flow region. This shock wave interacted with the incoming oblique shock wave and the expansion waves due to the reduction of the subsonic layer thickness. The interaction formed the reflected shock wave which passed through the downstream boundary of the computational domain. These shock wave configurations indicated that the shock wave/turbulent boundary layer interaction had an upstream influence distance that was approximately equal to the initial boundary layer thickness.

The variations of surface pressure, skin friction factor, and surface heat transfer rate beneath the interaction flow are plotted in figures 7 and 8. The surface pressures are also compared with the measurements in Hingst and

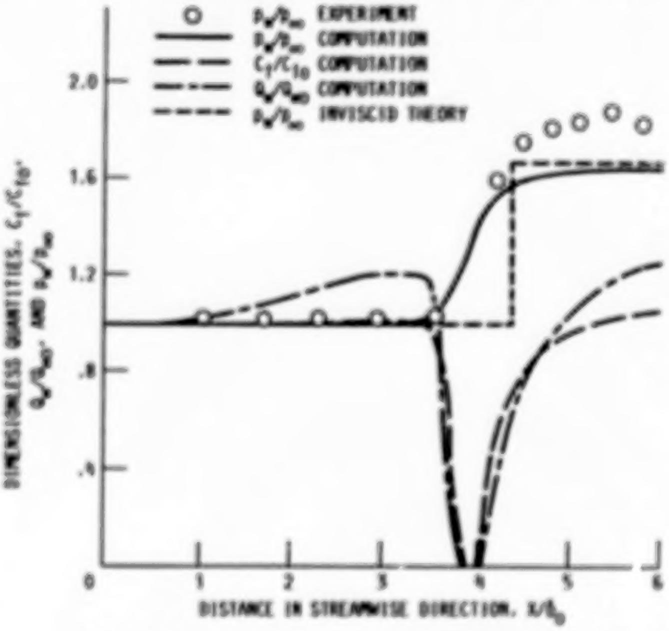

FIGURE 7. - SURFACE PRESSURE, p_w/p_∞; SKIN FRICTION FACTOR, C_f/C_{f0}; AND SURFACE HEAT TRANSFER RATE, Q_w/Q_{w0}, IN WEAK INTERACTION FLOW. FREE-STREAM MACH NUMBER, M_∞, 2.5; ANGLE OF ATTACK, θ, 4°.

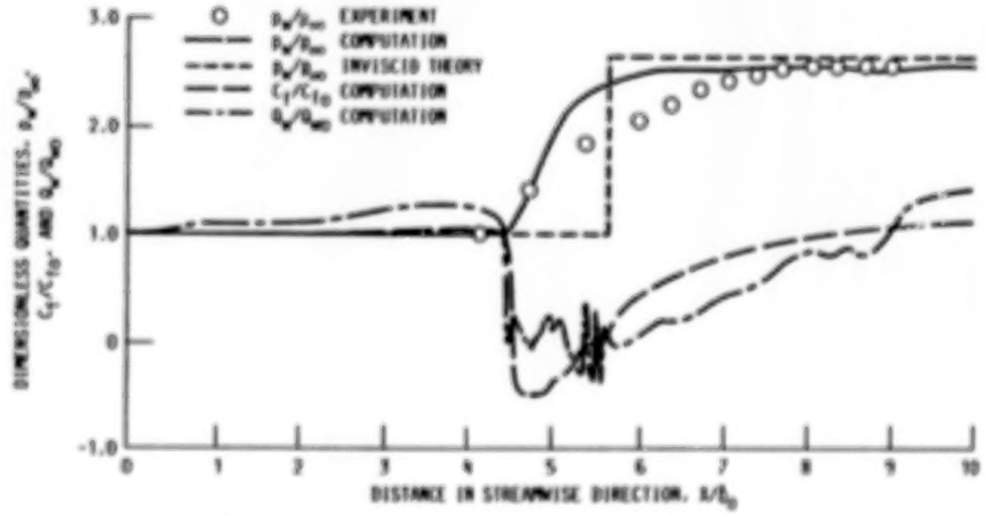

FIGURE 8. - SURFACE PRESSURE, p_w/p_∞; SKIN FRICTION FACTOR, C_f/C_{f0}; AND SURFACE HEAT TRANSFER RATE, Q_w/Q_{w0}, IN STRONG INTERACTION FLOW. FREE-STREAM MACH NUMBER, M_∞, 2.5; ANGLE OF ATTACK, θ, 8°.

Porro's work. The present computations predicted a lower surface pressure level with a wedge angle of 4° and a higher surface pressure level with a wedge angle of 8°. The skin friction factor remained approximately at the initial value before the local surface pressure increased. When the surface pressure increased, the skin friction factor decreased and then increased to a value approximately the same as its initial value. With the free-stream conditions, the oblique shock wave with $\theta = 4°$ induced a weak interaction which did not separate the boundary layer in the interaction flow region. However, the shock wave with $\theta = 8°$ induced a strong interaction which caused a small separation bubble within the interaction flow field. The surface heat transfer rate changed in a pattern similar to that of the skin friction. However, the oblique shock wave induced an increase in the surface heat transfer rates at the upstream locations where the skin friction factors and surface pressures remained the same as the initial conditions. With the strong shock wave interaction, the surface heat transfer rate at the downstream locations did not recover its initial value as quickly as it did in the weak shock wave interaction flow field.

Interaction Flow Fields at Mach 6

Alzner and Zakkay (ref. 3) and Zakkay and Wang (ref. 4) performed experiments to probe the flow fields of oblique shock wave/turbulent boundary layer interaction with Mach 6 free-stream conditions. The experiments were performed with a cold wall ($T_w/T_{0\infty} = 0.66$) condition. The static pressure, pitot pressure, total temperature, and surface heat transfer rate within the interaction flow field were measured. These measurements could verify the Navier-Stokes calculations of the properties of a shock wave/turbulent boundary layer interaction flow with a high free-stream Mach number condition. The present authors also used the computational methods to predict some of the measurements in references 3 and 4. The results are described in the following section.

Initial Turbulent Boundary Layer. - Similar to the study in the Initial Turbulent Boundary Layer portion of the section **Interaction Flow Fields at Mach 2.5**, the Navier-Stokes computational code and Baronti and Libby's analysis were used to predict the initial turbulent boundary layer properties. The measurements in references 3 and 4 were used in the boundary layer flow analysis. Some of the results are shown in figures 9 and 10. The skin friction factors and surface heat transfer rates obtained from the analyses and experiments are also listed and compared in these figures. Excellent agreement between the results from the analyses and experiments was found.

Shock Wave/Turbulent Boundary Layer Interactions. - In the experiments by Alzner and Zakkay (ref. 3), the boundary layer developed along an axisymmetric centerbody in a Mach 6 free stream. An axisymmetric wedge (10° wedge angle) was inserted in the free stream to induce an oblique shock wave. The shock wave impinged on the turbulent boundary layer and a shock wave/turbulent boundary layer interaction flow occurred. The present computational procedures were performed to predict the properties within this interaction flow field. Some of the computational results are shown in figures 11 and 12. Parameters used in the computational scheme are also listed in figure 11.

The static pressure p_w/p_∞ variations along the Y-direction at several X/δ_0 locations are plotted in figure 11. From the pressure variations, the

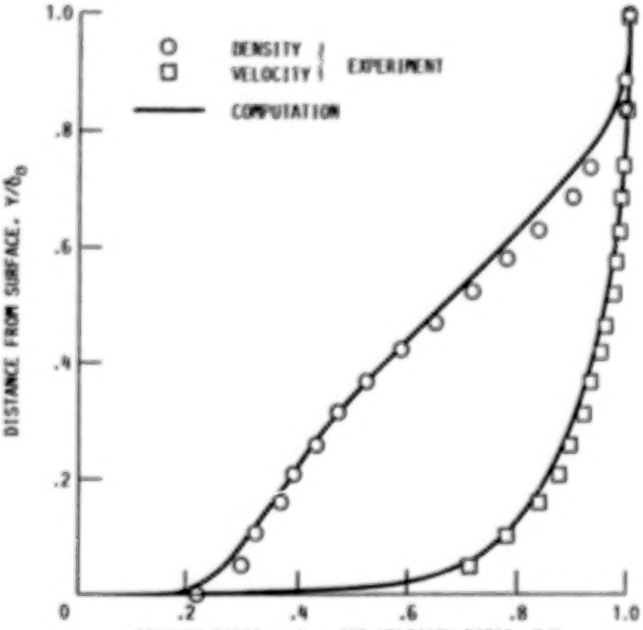

FIGURE 9. - DENSITY AND VELOCITY PROFILES IN TURBULENT BOUNDARY LAYER FLOW. FREE-STREAM MACH NUMBER, M_∞, 6.0; FREE-STREAM REYNOLDS NUMBER, Re_{δ_0}, 3.75×10^6.

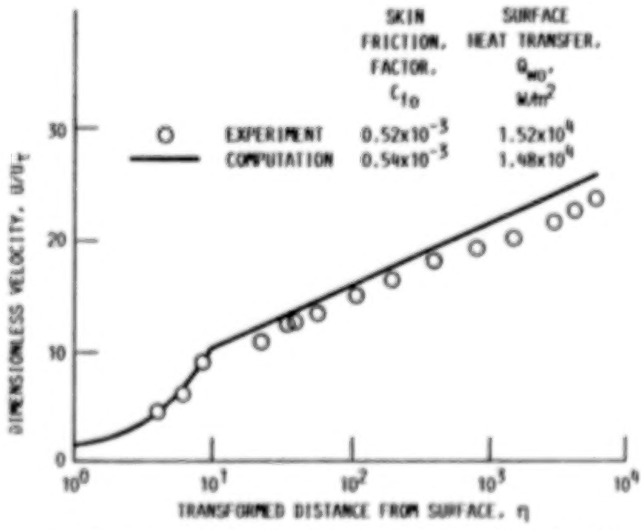

FIGURE 10. - TURBULENT BOUNDARY LAYER VELOCITY PROFILES IN TERMS OF SIMILARITY PARAMETERS U/U_τ AND η (REF. 11). FREE-STREAM MACH NUMBER, M_∞, 6.0

shock wave configurations, compression wave regions, and expansion wave regions were determined. These are shown in figure 11 together with the boundary layer edge and the sonic line locations. The variations of the surface pressure p_w/p_∞, skin friction factor C_f/C_{f0}, and surface heat transfer rate Q_w/Q_{w0} are shown in figure 12. The skin friction factor plot indicates that the flow separated at $X/\delta_0 = 4.90$ and then reattached to the surface at $X/\delta_0 = 5.50$. The surface heat transfer rate increased at upstream locations where the surface pressure and skin friction factor remained the same as the initial conditions. With the cold wall condition $T_w/T_{0\infty} = 0.66$, the surface heat transfer rate increased within the separated flow region and continued to increase after the flow reattached to the surface.

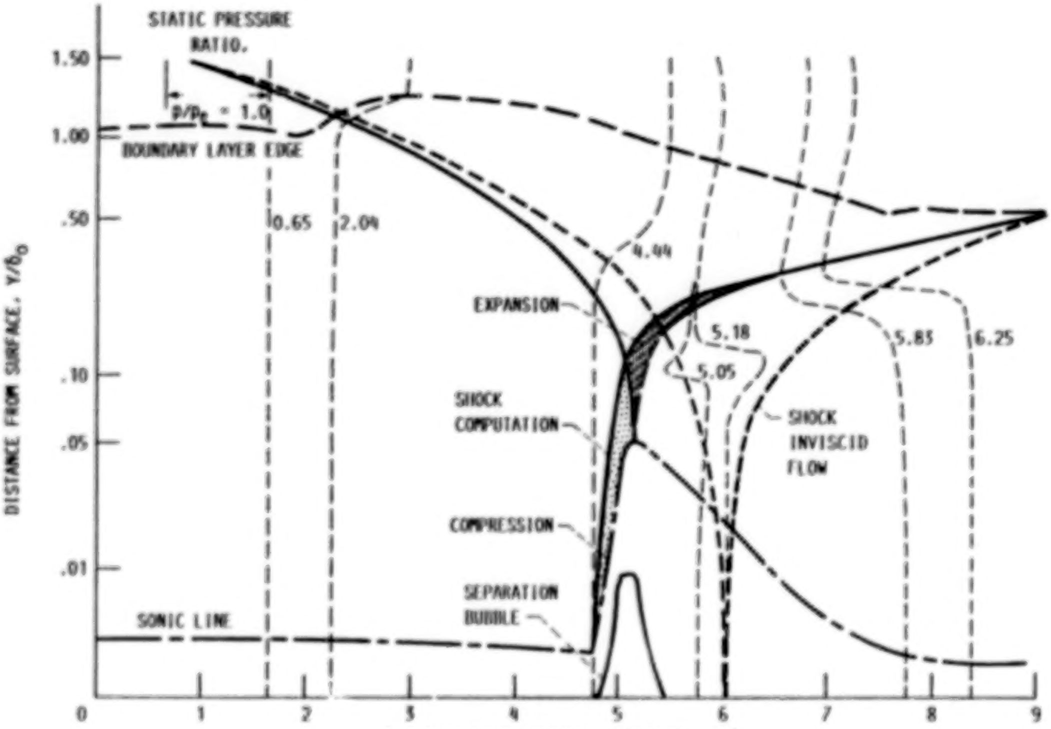

FIGURE 11. - STRONG INTERACTION FLOW. FREE-STREAM MACH NUMBER, M_∞, 6.0; ANGLE OF ATTACK, θ, 10^0; GRID DIMENSIONS, IM, 221, AND JM, 119; STRETCHING FACTORS, λ, 5.0, AND β, 1.0026. NUMBERS REFER TO DIMENSIONLESS STREAMWISE DISTANCE, x/δ_0, UNLESS INDICATED OTHERWISE.

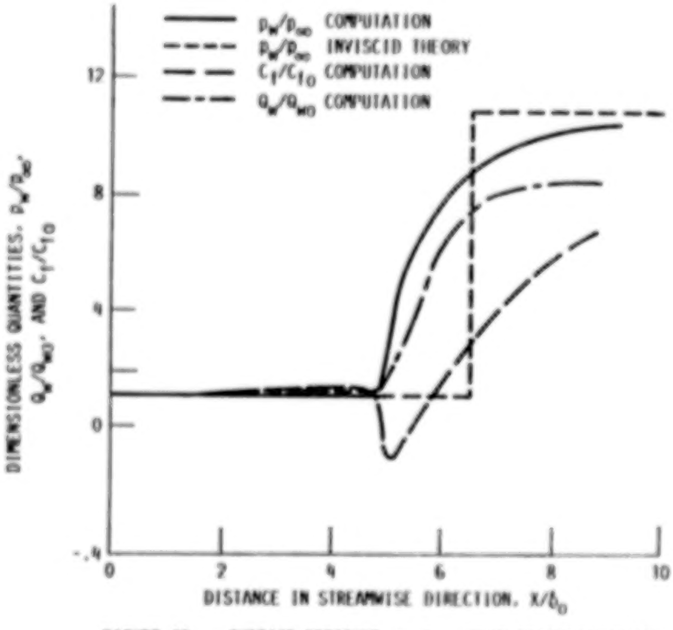

FIGURE 12. - SURFACE PRESSURE, p_w/p_∞; SKIN FRICTION FACTOR, C_f/C_{f0}, AND SURFACE HEAT TRANSFER RATE, Q_w/Q_{w0}, IN STRONG INTERACTION FLOW. FREE-STREAM MACH NUMBER, M_∞, 6.0; ANGLE OF ATTACK, θ, 10^0; FREE-STREAM REYNOLDS NUMBER, Re_{δ_0}, 2.68×10^6.

Zakkay and Wang (ref. 4) also performed a shock wave/turbulent boundary layer interaction flow experiment in a Mach 6 free stream. An axisymmetric cowl (approximately 4° wedge angle) with a gradual turning angle was inserted in the test section of a Mach 6 blow-down wind tunnel facility to produce a longitudinal adverse pressure gradient in the free stream. The turbulent boundary layer developed along the surface of a streamlined axisymmetric centerbody passing through the entire length of the wind tunnel nozzle. Thereby, the boundary layer was subjected to an adverse pressure gradient induced by the compression cowl. The adverse pressure gradient extended downstream for a distance of approximately 10 times the initial boundary layer thickness. The experiment measured the static pressure, pitot pressure, and total temperature profiles within the interaction flow region. The surface heat transfer rates were also measured with the cold wall condition. This experimental data could be used to verify the Navier-Stokes computations of the realistic shock wave/turbulent boundary layer interaction flow properties. Therefore, the present numerical computations were also performed to study the experimental results. Figure 13 shows the schematics of the flow field in the physical domain and the limited region for the computations. Parameters chosen for the computational scheme were also listed for reference.

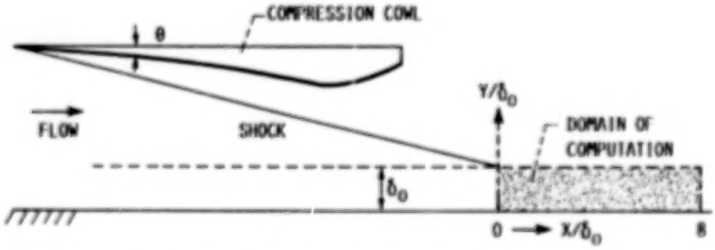

FIGURE 13. - WEAK INTERACTION FLOW WITH COMPRESSION COWL. FREE-STREAM MACH NUMBER, M_∞, 6.0; ANGLE OF ATTACK, θ, 4°; GRID DIMENSIONS, IM, 251, AND JM, 58; STRETCHING FACTORS, λ, 5.0, AND β, 1.0017.

Because of the complex flow field, the initial and boundary conditions for the computations were specified differently from those described in the computation method section of this paper. The initial conditions at $X = 0$ were calculated by using the Navier-Stokes code. The experimental profiles (ref. 4) of the static pressure, pitot pressure, and total temperature were first used to determine preliminary profiles of ρ, U, V, and T at the initial station. These preliminary profiles were chosen as the initial profiles in the Navier-Stokes code, and the code was executed with a coarse grid in the X-direction. The computation was repeated by iterating the initial profiles until it gave static pressures and pitot pressures at $X = 0$ which were compatible to the measurements in reference 4. A surface heat transfer rate $Q_{wo} = 2.61 \times 10^3$ W/m^2 and a skin friction factor $C_{fo} = 0.00052$ were computed, and they agreed well with their values reported in reference 4.

The far-field boundary conditions were also required in the iteration process. These far-field boundary conditions were obtained by matching the static pressures and pitot pressures at $Y = H$. From the previously described coarse grid iteration process, an approximately constant static pressure was found along the Y-direction at the initial station ($X = 0$). By using this static pressure as the downstream static pressure of an oblique shock wave induced by a 3.5° wedge in a Mach 6 free stream, the inviscid flow relations gave a pitot pressure close to that which was measured in reference 4. Thus, the present computational domain was within the downstream side of the oblique shock wave induced by the compression cowl lip. To determine the far-field boundary conditions, we assumed the total pressure to be constant at $Y = H$. On the basis of the ratio of the pitot pressures (ref. 4) and total pressure, the Mach number and the static pressure at any location (X,H) were determined from the inviscid flow theory. The velocity components U and V were then obtained from the inviscid Prandtl-Meyer simple wave relation. The adiabatic flow condition was also assumed at Y = H to define the far-field static temperatures. Some of these far-field boundary conditions are shown in figure 14.

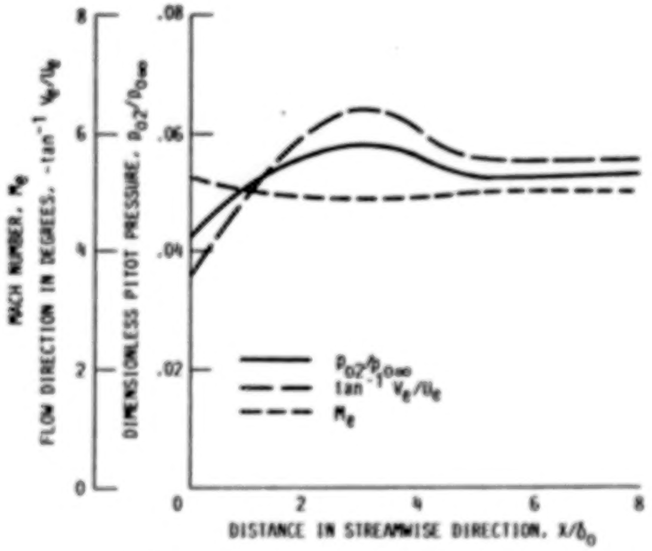

FIGURE 14. - FAR-FIELD BOUNDARY CONDITIONS OF WEAK INTERACTION FLOW. FREE-STREAM MACH NUMBER, M_∞, 6.0; FREE-STREAM REYNOLDS NUMBER, Re_{δ_0}, 3.75×10^6.

With the initial conditions and the far-field boundary conditions given previously, the Navier-Stokes computations of the interaction flow were executed again by using a fine grid in the X-direction. The computational results of the static pressures and the pitot pressures along the Y-direction at three X/δ_0 locations were shown in figures 15 and 16, and they were also compared with the measurements in reference 4. These computations predicted the general patterns of the experimental static and pitot pressure variations. The computations did not indicate flow separation within the interaction flow region. The surface pressure and the surface heat transfer rate variations are shown in figure 17. These computations also approximated the experimental surface pressure and heat transfer rate.

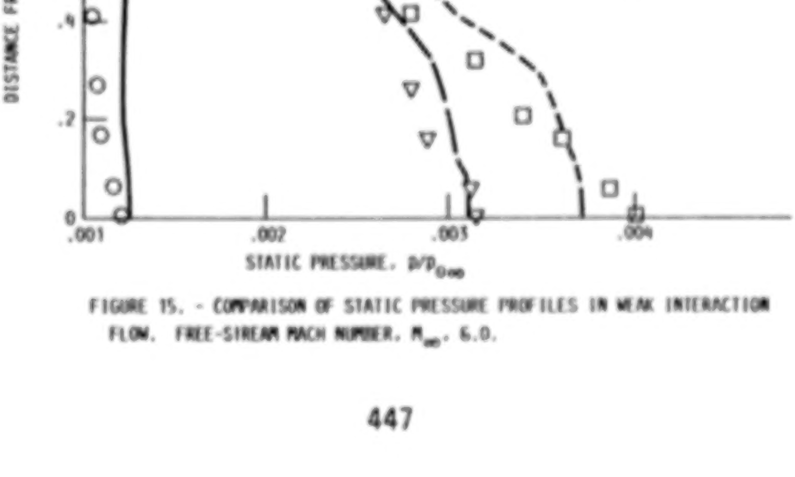

FIGURE 15. - COMPARISON OF STATIC PRESSURE PROFILES IN WEAK INTERACTION FLOW. FREE-STREAM MACH NUMBER, M_∞, 6.0.

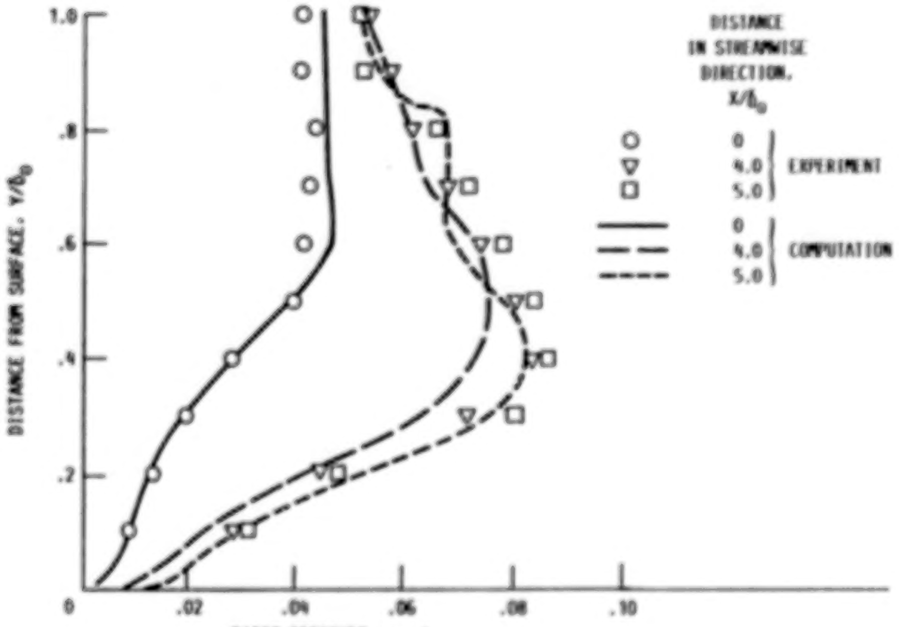

FIGURE 16. - COMPARISON OF PITOT PRESSURES IN WEAK INTERACTION FLOW. FREE-STREAM MACH NUMBER, M_∞, 6.0.

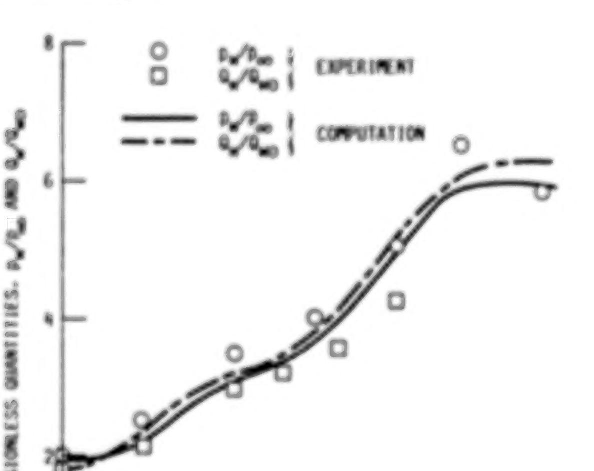

FIGURE 17. - SURFACE PRESSURE, p_w/p_{w0}, AND HEAT TRANSFER, Q_w/Q_{w0}, BENEATH WEAK INTERACTION FLOW. FREE-STREAM MACH NUMBER, M_∞, 6.0.

Surface Heat Transfer and Pressure Correlation

Holden (ref. 8) suggested that, within a supersonic or hypersonic shock wave/turbulent boundary layer interaction flow field, local surface pressure and heat transfer rate could be correlated by

$$\frac{Q_w}{Q_r} = \left(\frac{p_w}{p_r}\right)^{0.85} \tag{8}$$

where P_r and Q_r are the reference pressure and reference heat transfer rate, respectively. This relationship was studied here by using the present computational results of the Mach 6 interaction flow fields.

The surface pressures and heat transfer rates calculated in the two cases of Mach 6 interaction flow fields were normalized respectively with the free-stream static pressure and the turbulent boundary layer heat transfer rate. These two dimensionless quantities, Q_w/Q_{wo} and p_w/p_∞, are correlated in figure 18. The measurements of the surface pressures and heat transfer rates are also normalized and correlated in figure 18 for comparison. The comparison indicates that equation (8) correlated reasonably with the surface heat transfer rates and pressures when the flow did not separate in the interaction flow field. When flow separation occurred, equation (8) predicted a higher surface heat transfer rate than that obtained from the present computations. After the reattachment point, the computation showed that the surface pressure and heat transfer rate recovered the relationship given by equation (8).

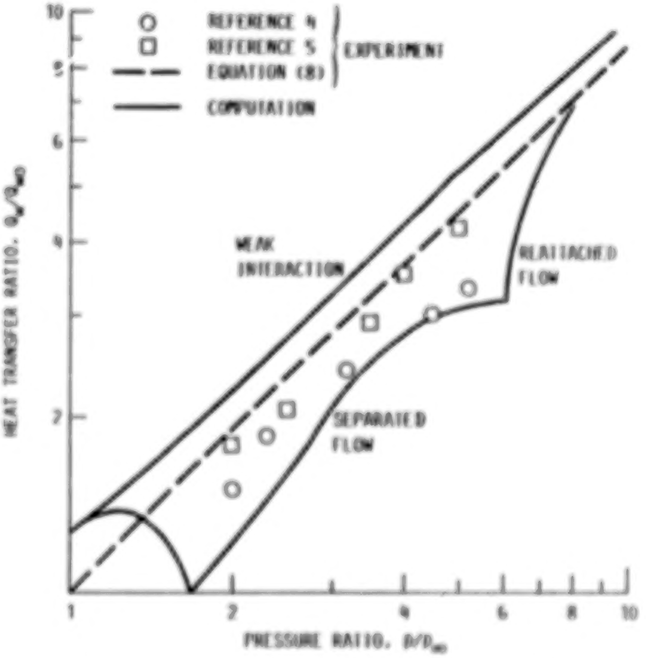

FIGURE 18. - SURFACE PRESSURE AND HEAT TRANSFER CORRELATIONS IN INTERACTION FLOW. FREE-STREAM MACH NUMBER, M_∞, 6.0.

The shock wave impingement increased the surface heat transfer rate at locations upstream of the interaction flow field (figs. 7 and 8). By using this upstream surface heat transfer rate as the reference value, we could reduce the normalized heat transfer rate and correlate it closely with equation (8). It is also interesting to see in figure 18 that the present Navier-Stokes computations predicted surface pressure/heat transfer correlations which enclosed the experimental data in references 3 and 4.

Velocity-Temperature Correlations

Crocco's velocity-temperature relationship equation (5) has been an important part of the compressible turbulent boundary layer flow study. There are certain conditions (such as the requirements of adiabatic wall condition with a streamwise pressure gradient or the requirement that the pressure and wall temperatures be constant with surface heat transfer) which restricted the use of Crocco's relationship. The present computations provided U and T data to study the validity of using equation (5) in a shock wave/turbulent boundary layer interaction flow field.

From the present computations of the interaction flow fields, the dimensionless quantities U/U_e and T/T_e were calculated at locations along the Y-direction at different X/δ_0 stations. Equation (5) was also used to determine T/T_e as functions of the far-field conditions and U/U_e. A recovery factor $\gamma = 0.9$ was used in equation (5). The resulting T/T_e from these two approaches are plotted as functions of U/U_e in figures 19 to 22. For near-adiabatic wall conditions (figs. 19 and 20), equation (5) correlated well the computational results of T/T_e and U/U_e within the unseparated flow region. For the cold wall condition at Mach 6, equation (5) correlated approximately with the computational results (figs. 21 and 22) when there was no flow separation. When flow separation occurred, equation (5) could

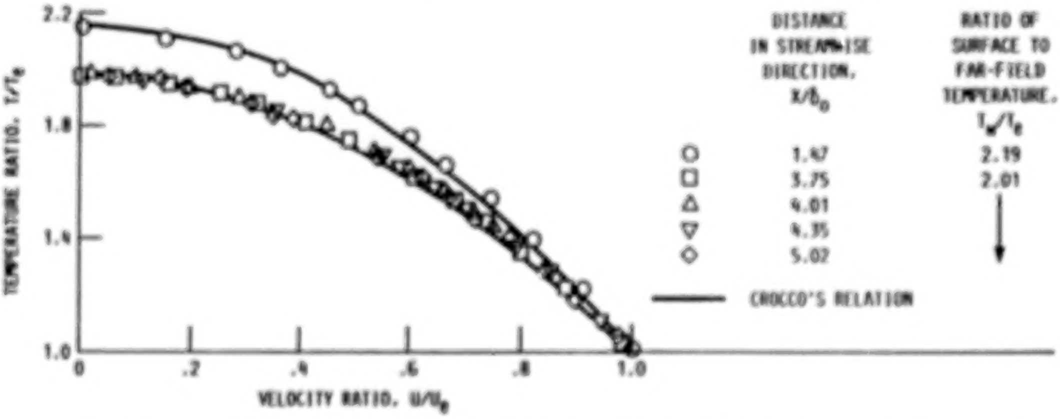

FIGURE 19. - VELOCITY-TEMPERATURE CORRELATIONS IN WEAK INTERACTION FLOW WITH NEAR-ADIABATIC SURFACE TEMPERATURES. FREE-STREAM MACH NUMBER, M_∞, 2.5; ANGLE OF ATTACK, θ, 4°.

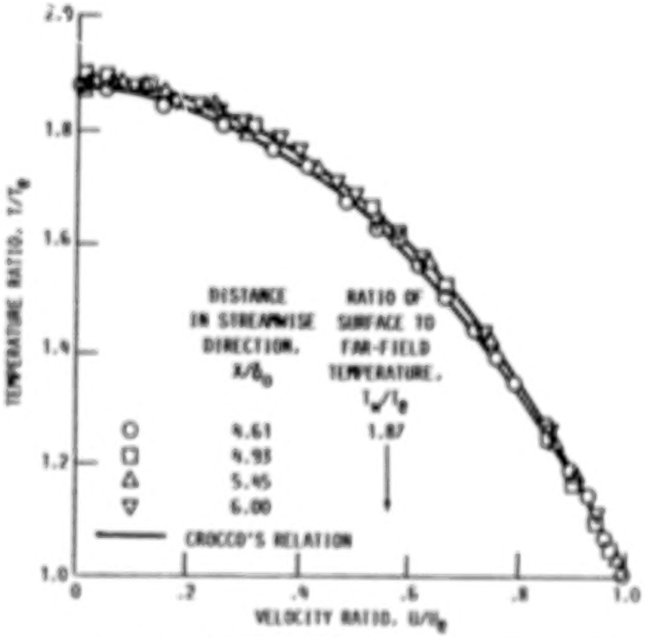

FIGURE 20. - VELOCITY-TEMPERATURE CORRELATIONS IN STRONG INTERACTION FLOW WITH NEAR-ADIABATIC SURFACE TEMPERATURE. FREE-STREAM MACH NUMBER, M_∞, 2.5; ANGLE OF ATTACK, θ, 8°.

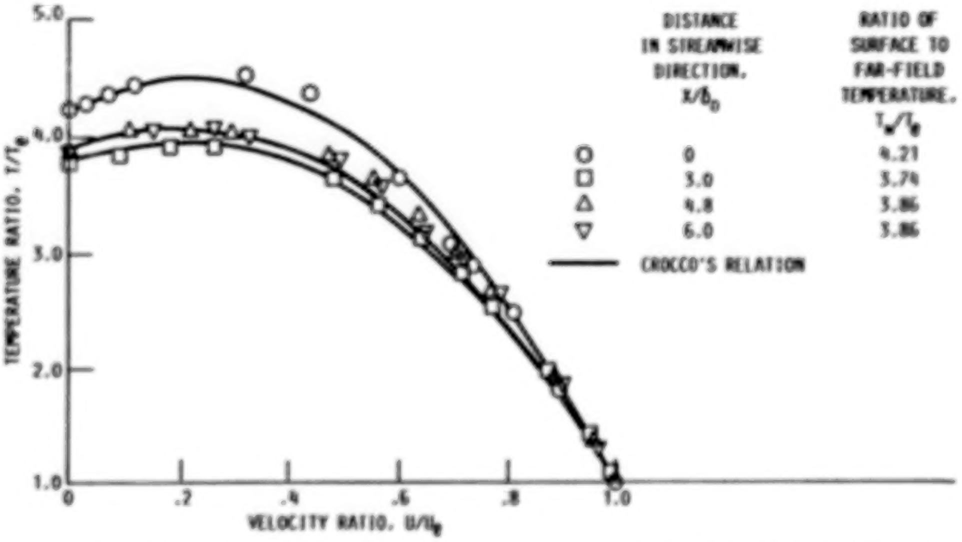

FIGURE 21. - VELOCITY-TEMPERATURE CORRELATIONS IN WEAK INTERACTION FLOW WITH COOLED-WALL CONDITION. FREE-STREAM MACH NUMBER, M_∞, 2.5.

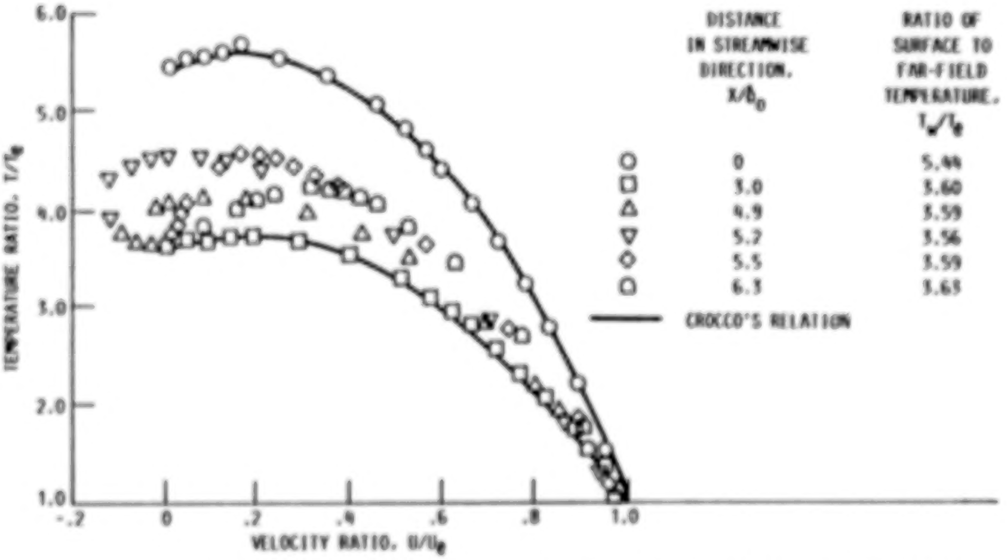

FIGURE 22. - VELOCITY-TEMPERATURE CORRELATIONS IN STRONG INTERACTION FLOW WITH COOLED-WALL CONDITION. FREE-STREAM MACH NUMBER, M_∞, 6.

correlate only the U/U_e and T/T_e within the upstream section of the flow field, and it failed to correlate the U/U_e and T/T_e within the flow region after the location of flow separation. However, the results of U/U_e and T/T_e from the Navier-Stokes computations showed a tendency to regain Crocco's relationship within the reattachment flow region.

Turbulent Shear Stress

The Baldwin-Lomax turbulence model was used to represent the turbulence transport in the present interaction flow computation. It is an algebraic turbulence model which assumes different growth rates of eddy viscosity for inner and outer layers. This model did not require the determination of the boundary layer edge and was convenient for Navier-Stokes computations. Since the empirical constants were chosen by its agreement with the turbulence level for a constant pressure boundary layer at transonic speed, the use of this model outside of the domain of its empirical base should be examined further. Rose and Johnson (ref. 6) measured the Reynolds shear stresses in a shock wave/turbulent boundary layer interaction flow in a Mach 2.9 free stream. Their data could be used to verify the use of the Baldwin-Lomax turbulence model in an interaction flow field. As a first step in this direction, the ability of the Baldwin-Lomax turbulence model to calculate the Reynolds shear stresses within a supersonic turbulent boundary layer flow was also investigated in this study.

In this study, the mean flow properties of the Mach 2.9 turbulent boundary layer flow in reference 6 were calculated by following the methods in the section Initial Conditions (of the Computational Methods section). These mean flow properties and the turbulence model were used to determine the Reynolds shear stresses $-\rho\overline{u'v'}$. A similar computational process was used to define the Reynolds shear stresses within the Mach 6 turbulent boundary layer. The Reynolds stress computations were repeated with different values of C_{cp}. Maise and McDonald (ref. 12) also showed that within the Mach number range of 0 to 5 the effect of compressibility on the normalized shear stress was quite small and was in keeping with Morkovin's hypothesis (ref. 13). The present Reynolds shear stress computations were also studied for the Mach number effect on Baldwin-Lomax turbulence modeling. The computational results of $-\rho\overline{u'v'}$ were normalized with $-\rho U_e^2/2$ to obtain the dimensionless quantity $-2\overline{u'v'}/U_e^2$. Both $-\rho\overline{u'v'}$ and $-2\overline{u'v'}/U_e^2$ are plotted and compared with Klebanoff's results (ref. 14) of $-2\overline{u'v'}/U_e^2$ in an incompressible turbulent boundary layer flow in figures 23 and 24. The corresponding Reynolds stress measurements are also shown in figure 23.

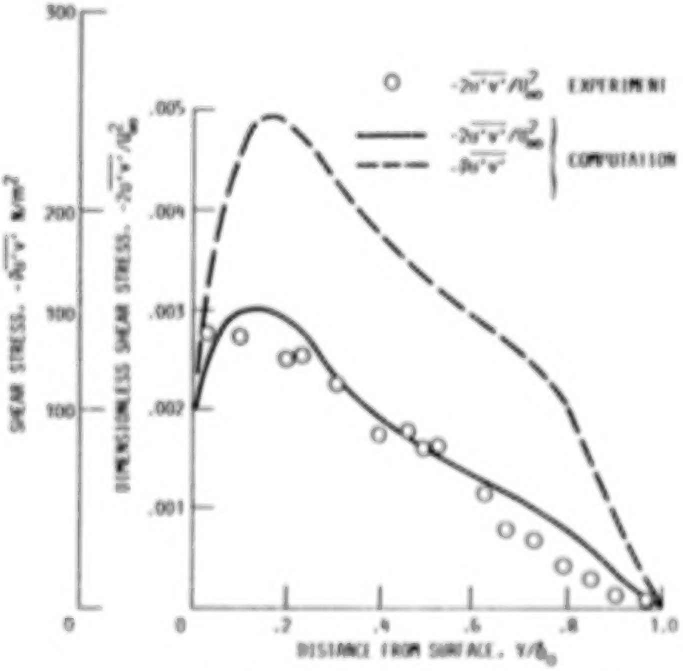

FIGURE 23. - REYNOLDS SHEAR STRESS IN TURBULENT BOUNDARY LAYER. FREE-STREAM MACH NUMBER, M_∞, 2.9; FREE-STREAM REYNOLDS NUMBER, Re_{δ_0}, 1.4×10^6; TURBULENCE CONSTANT, C_{cp}, 2.0. SKIN FRICTION FACTOR, C_{f0}; FOR EXPERIMENT, 0.10×10^{-2}; FOR COMPUTATION, 0.93×10^{-3}; SURFACE HEAT TRANSFER FOR COMPUTATION, Q_{w0}, 0.45×10^3 W/m^2.

Assuming that the Mach number effect on $-2\overline{u'v'}/U^2$ is negligible and that $-2\overline{u'v'}/U_e^2$ in a compressible turbulent boundary layer should agree with the

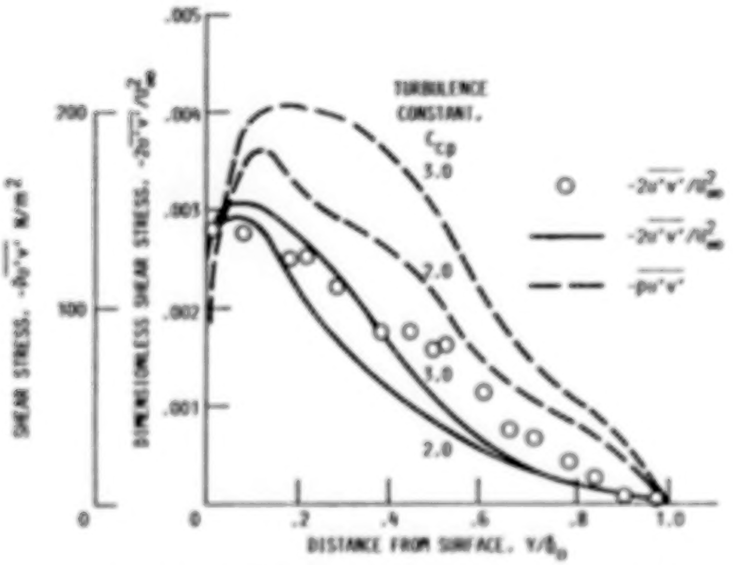

FIGURE 24. - REYNOLDS SHEAR STRESS IN TURBULENT BOUNDARY LAYER. FREE-STREAM MACH NUMBER, M_∞, 6.0; FREE-STREAM REYNOLDS NUMBER, Re_{δ_0}, 2.7×10^5. SKIN FRICTION FRACTOR, C_{f_0}; FOR EXPERIMENT, 0.52×10^{-3}; FOR COMPUTATION, 0.56×10^{-3}; SURFACE HEAT TRANSFER, Q_{w0}; FOR EXPERIMENT, 1.48×10^4 W/m^2; FOR COMPUTATION, 1.54×10^4 W/m^2.

same parameter in an incompressible boundary layer, the results in figures 23 and 24 indicate that different C_{cp} values are required in Baldwin-Lomax turbulence modeling. Figure 23 indicates that $C_{cp} = 2.0$ was required for the Mach 2.9 turbulent boundary layer flow, and this C_{cp} value was used in the present computations. Figure 24 shows that $C_{cp} = 3.0$ was required for a Mach 6 turbulent boundary layer. Without additional modification of the inner layer assumption of the Baldwin-Lomax turbulence modeling, the present Navier-Stokes computations could predict the skin friction factor and surface heat transfer rate beneath a compressible turbulent boundary layer flow.

The present computational methods were also used to determine the turbulent shear stress properties of the shock wave/turbulent boundary layer interaction flow in reference 6. The Baldwin-Lomax turbulence model with $C_{cp} = 2.0$ was used to represent the turbulence transport, and the turbulent shear stresses $-\rho\overline{u'v'}$ within the interaction flow were calculated. The computational results of the turbulent shear stress profiles at three different X/δ_0 locations are plotted in figure 25. They are also compared with the measurements in reference 6. Both the computational and experimental results show that $-\rho\overline{u'v'}$ decreased in the upstream section ($X/\delta_0 < 1.8$) and then increased greatly in the downstream region ($X/\delta_0 \geq 5.0$) of the interaction flow field. However, the computational results of $-\rho\overline{u'v'}$ were larger than the measurements in reference 6. This discrepancy is being investigated.

Experimental analyses of the Reynolds stresses within a shock wave/turbulent boundary layer interaction flow have been reported in some recent studies (refs. 15 and 16). Debieve and Lachame (ref. 15) found that turbulence amplified along a streamline after it crossed a shock wave. Ha Minh and Vandromme (ref. 17) argued that a mixing length turbulence model might not represent the features of turbulence in a shock wave/turbulent boundary layer interaction flow field, and they suggested using the mass-averaged forms of the Reynolds stress equations for the turbulence modeling in Navier-Stokes equations. An analysis was developed by Debieve, Gouin, and Gaviglio (ref. 16)

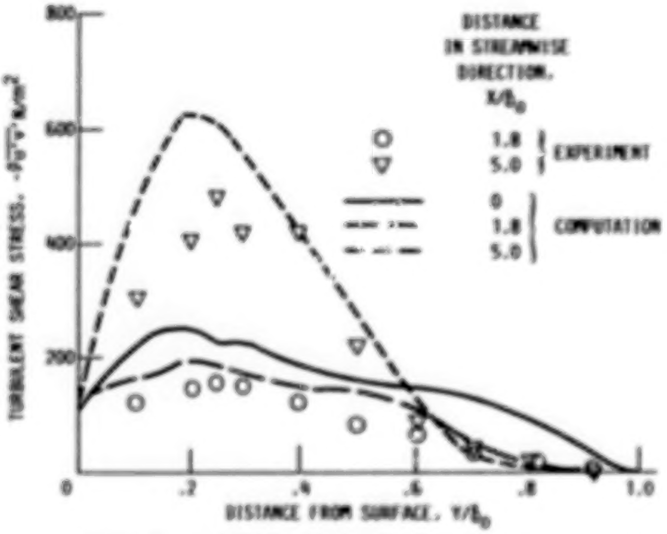

FIGURE 25. - TURBULENT SHEAR STRESSES WITHIN A SHOCK WAVE/ TURBULENT BOUNDARY LAYER INTERACTION REGION.

to relate the mean flow and Reynolds stress tensor evolution in a shock wave/ turbulent boundary layer interaction flow. The applications of this Reynolds stress analysis in the Navier-Stokes computations of the shock wave/turbulent boundary layer interaction flows will be pursued in the near future.

CONCLUSIONS

Numerical computations of Navier-Stokes equations were performed to predict the flow properties within two-dimensional shock wave/turbulent boundary layer interaction flows in Mach 2.5 and 6.0 free streams. The interaction flow fields due to oblique shock wave impingement on a turbulent boundary layer over a flat surface with near-adiabatic ($T_w/T_{O\infty}$ - 0.99) and cold wall ($T_w/T_{O\infty}$ - 0.66) conditions were considered. To minimize the effect of initial conditions on the computations, we calculated the initial turbulent boundary layer properties to ensure that the initial boundary layer velocity and temperature profiles gave the correct skin friction factor and surface heat transfer rate. The computational results were analyzed to study the surface heat transfer rate, velocity-temperature correlation, and turbulent shear stress within the interaction flow fields. These computational results were also compared with existing measurements.

This present study indicates that

1. With the prescribed surface temperature conditions, the shock wave impingement increased the surface heat transfer rate in the upstream section of the interaction flow field, whereas the surface pressure and skin friction remained the same as those of the incoming turbulent boundary layer.

2. With a near-adiabatic surface, the surface heat transfer rate changed in a pattern similar to that of the skin friction within both the weak and strong interaction flow fields.

3. With a weak shock wave interaction over a cold wall, the surface heat transfer rate increased continuously in the downstream direction, and the local surface heat transfer rate and pressure could be correlated with Holden's relationship. With a strong shock wave interaction over a cold wall,

the local surface heat transfer rate also increased but was lower than that predicted by Holden's relationship.

4. With a near-adiabatic surface, Crocco's relationship could correlate the mean flow streamwise velocity components and static temperatures in a weak interaction flow field and in the unseparated region of a strong interaction flow field. For a cold wall condition, Crocco's relationship could only correlate the mean flow streamwise velocity components and static temperature in a weak interaction flow field.

5. When the Baldwin-Lomax turbulence model was used, the Navier-Stokes computations predicted qualitatively the turbulent shear stress $-\overline{\rho u'v'}$ in shock wave/turbulent boundary layer interaction flows. The Baldwin-Lomax turbulence model might require modification in order to represent the turbulence transport in the Navier-Stokes computations of the interaction flows with different free-stream Mach numbers.

This study used simple two-dimensional forms of the Navier-Stokes equations to simulate the complicated shock wave/turbulent boundary layer interaction flow. The radius of curvature in the axisymmetric cases and the three-dimensionality due to flow separation were not considered. However, the present computational results might have indicated that, with proper inflow conditions, an improved Navier-Stokes numerical computational code could calculate the surface heat transfer rates within a shock wave/turbulent boundary layer interaction flow.

REFERENCES

1. Delery, J.; Marvin, J.C.; and Reshotko, E.: Shock-Wave Boundary Layer Interactions. AGARD AG-280, 1986.

2. Shang, J.S.; Hankey, W.L.; and Law, C.H.: Numerical Simulation of Shock Wave-Turbulent Boundary Layer Interaction. AIAA J., vol. 14, no. 10, Oct. 1976, pp. 1451-1457.

3. Alzner, E.; and Zakkay, V.: Turbulent Boundary-Layer Shock Interaction With and Without Injection. AIAA J., vol. 9, no. 9, Sept. 1971, pp. 1769-1771.

4. Zakkay, V.; and Wang, C.R.: Turbulent Boundary Layer in an Adverse Pressure Gradient Without Effect of Wall Curvature. NASA CR-112247, 1972.

5. Baldwin, B.; and Lomax, H.: Thin-Layer Approximation and Algebraic Model for Separated Turbulent Flows. AIAA Paper 78-257, Jan. 1978.

6. Rose, W.C.; and Johnson, D.A.; Turbulence in a Shock-Wave Boundary Layer Interaction. AIAA J., vol. 13, no. 7, July 1975, pp. 884-889.

7. Fernholz, H.H.: A Critical Commentary on Mean Flow Data for Two-Dimensional Compressible Turbulent Boundary Layers. AGARD AG-253, 1980.

8. Holden, M.S.: Shock Wave-Turbulent Boundary Layer Interaction in Hypersonic Flow. AIAA Paper 77-45, Jan. 1977.

9. MacCormack, R.W.: The Effect of Viscosity in Hypervelocity Impact Cratering. AIAA Paper 69-354, Apr. 1969.

10. Anderson, D.A.; Tannehill, J.C.; and Pletcher, R.H.: Computational Fluid Mechanics and Heat Transfer. McGraw-Hill, 1984.

11. Baronti, P.O.; and Libby, P.A.; Velocity Profiles in Turbulent Compressible Boundary Layers. AIAA J., vol. 4, no. 2, Feb. 1966, pp. 193-194.

12. Maise, G.; and McDonald, H.: Mixing Length and Kinematic Eddy Viscosity in a Compressible Boundary Layer. AIAA J., vol. 6, no. 1, Jan. 1968, pp. 73-74.

13. Morkovin, M.U.: Effects of Compressibility on Turbulent Flows. Mechanics of Turbulence. Gordon and Breach Science Publishers, 1964, pp. 367-380.

14. Klebanoff, P.S.: Characteristics of Turbulence in a Boundary Layer With Zero Pressure Gradient. NACA TN-3178, 1955.

15. Debieve, J.E.; and Lachame, J.P.: A Shock Wave/Free Turbulence Interaction. IUTAM Symposium Palaiseau/France 1985, Turbulent Shear-Layer/Shock-Wave Interactions, J. Delery, ed., Springer-Verlag, 1985, pp. 394-402.

16. Debieve, J.E.; Gouin, H.; and Gaviglio, J.: Momentum and Temperature Fluxes in a Shock-Wave Turbulence Interaction. Proceedings of ICHMT/IUTAM Symposium on the Structure of Turbulence and Heat and Mass Transfer, Hemisphere Publishing Co., Washington, DC, 1980, pp. 133-136.

17. Ha Minh, H.; and Vandromme, D.D.: Modeling of Compressible Turbulent Flows: Present Possibilities and Perspectives. IUTAM Symposium Palaiseau/France, Turbulent Shear-Layer/Shock-Wave Interactions, J. Delery, ed., Springer-Verlag, 1985, pp. 13-26.

WAVE MODELS FOR TURBULENT FREE SHEAR FLOWS

W. W. Liou and P. J. Morris
The Pennsylvania State University
University Park, PA 16802

ABSTRACT

New predictive closure models for turbulent free shear flows are presented in this paper. They are based on an instability wave description of the dominant large-scale structures in these flows using a quasi-linear theory. Three models have been developed to study the structural dynamics of turbulent motions of different scales in free shear flows. The local characteristics of the large-scale motions are described using linear theo [illegible] their amplitude is determined from an energy integral analysis. The models have been applied to the study of an incompressible free mixing layer. In all cases, predictions are made for the development of the mean flow field. In the last model , predictions of the time-dependent motion of the large-scale structure of the mixing region are made. The predictions show good agreement with experimental observations.

INTRODUCTION

Though the presence and importance of large-scale coherent structures to the mixing process in free shear flows has been recognized for many years, turbulence models that incorporate these observations have been very limited. The use of direct numerical or large eddy simulations provide a detailed prediction of the large-scale motions in low and high Reynolds number turbulent flows respectively. But these predictions are computationally expensive and are still limited in general to simple boundary conditions. The present model makes use of experimental observations in excited turbulent flows or conditional sampling measurements to provide a simple model of the large scale motions which is computationally inexpensive.

Most current turbulent flow calculations for practical applications use the long time-averaged Navier-Stokes equations. Turbulence models are needed to evaluate the unknown correlation terms, the Reynolds stresses, that appear when the statistical averaging process is applied to the nonlinear convective terms in the equations. This is the closure problem. There are closure models of various orders that have been proposed. These models are usually based on the notion that the high-order moments of fluctuations can be represented reasonably well as functionals of moments of lower order. Work in this regard is voluminous and will not be elaborated on here. Some models are quite successful and have become very popular in engineering flow calculations. However, they usually involve a large number of model constants determined by comparison with experimental data. Thus, these models are not entirely predictive but, in some ways, represent a sophisticated correlation of experimental data.

The present models are based on observations of large-scale coherent structures in free mixing layers. Brown and Roshko (ref.1), among others, observed that these orderly motions dominate the dynamics and the structure of free shear flows like wakes, jets and mixing layers. The structures appear in both low- and high-speed flows. They have also been observed in many flow geometries.

This paper is concerned with new, predictive turbulence models for free shear flows. The models simulate the propagating large-scale structures as spatially travelling instability waves. In this paper, we focus on the validation of the wave models as well as a determination of their limitations. Predictions are made for a two-dimensional incompressible free mixing layer. This will provide guidelines for applications of the models to more complex configurations.

THE WAVE MODELS

The wave models presented here are used to make a direct calculation of the large-scale, characteristic structures. The fundamental idea is that the large-scale structures may be modeled using a quasi-linear theory. The local characteristics of these structures may be described by linear instability theory. This has been demonstrated by the experiments of Gaster, Kit and Wygnanski (ref.2) and Petersen and Samet (ref.3), among others. In their experiments they compared predictions of the amplitude and phase of the axial velocity fluctuations, based on linear stability theory, with phase-averaged measurements in an excited shear layer and a jet. The agreement between predictions and experiment was very good though only normalized distributions of amplitude and phase, not the absolute amplitude, were predicted. This close agreement between the predictions of linear stability theory and the properties of the large-scale coherent sturctures has formed the basis for theories of turbulent mixing and supersonic jet noise generation and radiation. For example, Tam and Morris (ref.4) and Tam and Burton (ref.5, ref.6) predicted the noise radiation from instability waves in supersonic shear layers and jets and obtained very good agreement with experiment. Their analyses showed that the behavior of the large-scale disturbances could be modeled satisfactorily using a quasi-linear theory, even though the waves were not infinitesimal in magnitude. However, an important element of these calculations, the velocity profiles of the mean flow, that are needed for the linear stability calculations, are obtained from experiments. Their approaches provide a closure, but are not predictive. The models proposed here establish a complete closure model using a simple quasi-linear theory for the large-scale motion. In the present model both the mean flow and the time-dependent turbulent motions at the large-scale are obtained simultaneously as a solution.

Analysis

In the present analysis, the turbulent motion is decomposed into three parts,

$$\tilde{f}_i = F_i + f_i + f'_i. \tag{1}$$

The fluctuation with respect to the mean flow, F_i, is separated into a component representing the dominant large-scale motion, f_i, and one representing small-scale fluctuations, f'_i. The mean flow component is obtained by long time-averaging its instantaneous value

$$\overline{\tilde{f}}_i = F_i = \frac{1}{T_1} \int_0^{T_1} \tilde{f}_i \mathrm{dt}. \tag{2}$$

A short time-average is defined by

$$< \tilde{f}_i > = F_i + f_i = \frac{1}{T_2} \int_0^{T_2} \tilde{f}_i \mathrm{dt}. \tag{3}$$

where T_2 is much smaller than T_1, but much larger than the characteristic time scale of the background small-scale fluctuation.

The governing equations for the mean flow can be obtained by substituting flow properties of the form of equation (1) into the Navier-Stokes equations and long time-averaging the equations. The governing equations for the mean flow are

$$\frac{\partial U_i}{\partial x_i} = 0. \tag{4}$$

$$U_j \frac{\partial U_i}{\partial x_j} + \frac{\partial}{\partial x_j}(\overline{u_i u_j} + \overline{u'_i u'_j}) = -\frac{1}{\varrho}\frac{\partial P}{\partial x_i} + \nu \frac{\partial^2 U_i}{\partial x_j \partial x_j}. \tag{5}$$

where the interactions between motions of disparate scales are assumed to be negligible. The boundary-layer approximation is used to simplify further the governing equations in the present case. The resulting equations are

$$\frac{\partial U}{\partial x} + \frac{\partial V}{\partial y} = 0. \tag{6}$$

$$U\frac{\partial U}{\partial x} + V\frac{\partial U}{\partial y} + \frac{\partial}{\partial x}(\overline{u^2} - \overline{v^2}) + \frac{\partial}{\partial y}(\overline{uv}) + \frac{\partial}{\partial y}(\overline{u'v'}) = \nu\frac{\partial^2 U}{\partial y^2}. \tag{7}$$

where the small-scale normal stress terms have been neglected. On the basis of the experimental observations the local characteristics of the large-scale structures are described by the equation of inviscid hydrodynamic stability. The equations of motion for the large-scale fluctuations are linearized. Solutions are sought in the form:

$$\{u, v, p\} = A(x)\ \Re\{[\phi(y), \psi(y), \varphi(y)]\ exp\ [i(\alpha x - \omega t)]\}. \tag{8}$$

where the amplitude appears as a parameter in the local problem and is determined separately. This weakly non-linear approach is usually referred to as a "wave envelope" method. The resulting equation for the fluctuating velocity in the cross-stream direction, y, is the Rayleigh equation.

$$(\alpha U - \omega)(\psi'' - \alpha^2 \psi) - \alpha U'' \psi = 0. \tag{9}$$

where the main stream is in the x-direction of a Cartesian co-ordinate system and $(\ )''$ denotes $\mathrm{d}^2/(\mathrm{d}y)^2$. In deriving this equation, it is assumed that the mean flow is locally parallel in the direction of the main stream.

The amplitude function, $A(x)$, can be determined from the kinetic energy equation for the large-scale motions,

$$U_j \frac{\partial k}{\partial x_j} = -\overline{u_i u_j} \frac{\partial U_i}{\partial x_j} - \frac{\partial}{\partial x_j}(\overline{u_j k} + \frac{\overline{p u_j}}{\varrho}) - \overline{(- < u_i' u_j' >) \frac{\partial u_i}{\partial x_j}}$$

$$- \frac{\partial}{\partial x_j} \overline{(u_i < u_i' u_j' >)} + \textit{viscous terms}. \tag{10}$$

where $k = 1/2\ \overline{u_i u_i}$. At the large scale, the viscous terms are negligible. The production terms on the right hand side are responsible for transferring energy from the mean flow to the coherent turbulent fluctuations. Energy is subsequently extracted from the large-scale motion and dissipated at the high frequency end of the wave number spectrum. The terms containing the residual stress tensor, $- < u_i' u_j' >$, describe the draining of energy from the waves. These terms are of crucial importance in determining the wave amplitude. Little experimental information, however, is available regarding these stresses. In the present paper several approaches have been taken to model this energy transfer mechanism. Initially we assume that the rate of energy dissipation is proportional to

$$\frac{u^3}{l} \tag{11}$$

where l and u are the characteristic length and velocity scales of the large-scale motions. This model assumes that the turbulence is in an equilibrium state for the small-scale fluctuations, in which the rate at which energy is transferred from the large scales is equal to the rate at which energy is dissipated. The net effect of these terms may thus be modeled by

$$C_1 \frac{k^{3/2}}{l}. \tag{12}$$

where C_1 is a model constant. An equation for the amplitude function may be obtained by substituting the wave form expressions, equation (8), into the wave kinetic energy equation, equation (10), and integrating it with respect to y. The resulting equation is

$$\frac{\mathrm{d} G_1 A^2}{\mathrm{dx}} = G_2\, A^2 + G_3\, A^3. \tag{13}$$

where

$$G_1 = \frac{1}{4} \int_{-\infty}^{+\infty} \left[U(\phi\phi^* + \psi\psi^*) + 2.0\, \Re(\phi\varphi^*) \right] \mathrm{d}y\ , \tag{14}$$

$$G_2 = -\frac{1}{2} \int_{-\infty}^{+\infty} \left[\frac{\partial U}{\partial y} \Re(\phi\psi^*) \right] \mathrm{d}y \tag{15}$$

and

$$G_3 = -\frac{C_1}{8\, l} \int_{-\infty}^{+\infty} \left[(\phi\phi^* + \psi\psi^*)^{3/2} \right] \mathrm{d}y. \tag{16}$$

where an asterisk denotes the complex conjugate.

A complete simulation of the large-scale turbulence spectrum would require the inclusion of a broad range of frequency and spanwise wave number components. This was accomplished in the local solution of Tam and Chen (ref.7) and the the integral model of Morris and Giridharan (ref.8). However, it can be shown that for a wide range of frequencies around the least stable mode the Reynolds stress distribution does not vary appreciably. Since sensible and manageable models of maximum efficiency are sought, instead of including all the unstable waves, it is assumed here that the waves of the least stable modes are most effective in extracting energy from the mean flow and are used to describe the overall properties of the coherent structures.

The contribution of the small-scale Reynolds stress gradients in equation (7) has yet to be determined. In the first model described below this contribution is given by a simple eddy viscosity model. Thus, this model, referred to as Model I, requiries the specification of two model constants: one to determine the rate of energy transfer from large to small scales, equation (12), and one for the eddy viscosity model. However, the turbulence models of Tam and Chen (ref.7) and of Morris and Giridharan (ref.8) suggest that the small scales need not play a direct role in the development of the mean flow. Thus in Model II we neglect the contributions of the small-scale Reynolds stresses. Both of these models predict the average behavior of the shear layer.

A third model, Model III, will also be examined. This model simulates the time-dependent motion, at the large scale, associated with the passage of a train of large-scale structures. Experimental observations suggested that, even if initially there exists a continuous spectrum of infinitesimal disturbances upstream of the splitter plate, a disturbance emerges dominating over other neighboring perturbations in the early stages of the flow development. As the flow evolves, however, there are continuous shifts of the dominant component toward lower and lower frequencies. In fact, the growth of an initially small periodic disturbance is often followed by the development of subharmonics. In numerical simulations, however, the initial conditions can be conceived in a much simplier way. Instead of monitoring the disturbances in the complete initial continuous spectrum, a hierarchy of disturbances made up of the initially most unstable mode, according to linear theory, and its subharmonics may be considered. This reflects the "subharmonic evolution model" proposed by Ho and Huang(ref.9). The unsteady turbulent fluctuations of large scale are thus described by the superposition of the instability waves in this hierarchy. This enables the time-dependent flow field at the large scale to be simulated.

The mean flow and the local shapes of the large-scale structures or instability waves are governed by, as stated earlier, the thin-shear-layer and Rayleigh equations, respectively. The solution methods for these equations are the same as in Models I and II. The equation for the amplitude function, however, has to be modified. Firstly, it is assumed that interactions between harmonics are negligible, as there is sufficient phase jitter in the unexcited shear layer. In addition, the details of the process of energy transfer from large to small scales is not modeled explicitly. At the axial location where a given instability wave saturates, or begins to decay, the energy is immediately removed from the system. Thus there is no need to specify either a constant associated with the energy transfer process or the effects of the interaction between the small-scales motion and the mean flow. There are no empirical constants. The amplitude of each instability wave during the unstable or growing region is determined from equation (13) with the energy transfer terms neglected.

A visualization of the unsteady flow field predicted by Model III is made by means of instantaneous flow velocity vector plots and streaklines. The streaklines are produced by injecting passive marker particles at the initial location, $x = x_0$ at various points across the shear layer. The positions of these particles at subsequent times can be calculated using the equations:

$$\frac{d}{dt}x(t) \;=\; U\,[\,x(t)\,,\,y(t)\,]\;+\;u\,[\,x(t)\,,\,y(t)\,,\,t\,] \tag{17}$$

and

$$\frac{d}{dt}y(t) \;=\; V\,[\,x(t)\,,\,y(t)\,)\,]+\;v\,[\,x(t)\,,\,y(t)\,,\,t\,], \tag{18}$$

with

$$x(0) = x_0,\; y_k(0) = y_0\;,\quad k = 1,....m$$

Particles thus move at each time step according to the local instantaneous velocity field.

Numerical Procedure

The boundary-layer approximation renders the system of equations governing the mean flow parabolic. A fourth order Keller–Box scheme is applied to solve the resulting equations. The equation for the instability wave, which is the Rayleigh equation in the present formulation, has been solved using various methods, including a traditional shooting, two spectral and a finite difference methods. For spatial instability, the system of equations generated by the global approximations of the Rayleigh equation forms an eigenvalue problem which is nonlinear in its parameter, the wave number. It may be solved using the Linear Companion Matrix method or a method based on matrix factorization, Bridges and Morris (ref.10). Details of the various solution schemes can be found in Liou and Morris (ref.11). The Rayleigh equation and the equations for the mean flow are solved iteratively at each streamwise location. The convergence criterion for the iterations is

$$\frac{1}{M}\sum_{j}\left|U_{i,j}^{(k+1)} \;-\; U_{i,j}^{(k)}\right| \;\le\; \epsilon_1, \tag{19}$$

where ϵ_1 is a small number and M is the total number of grid points at each streamwise location. The amplitudes of the waves are calculated explicitly using a fourth order Runge–Kutta method applied to the wave energy equation (13).

RESULTS AND DISCUSSIONS

The models have been tested in an incompressible free mixing layer. The flow is sketched in figure (1). A hyperbolic tangent distribution is taken as the shape of the initial streamwise mean velocity, $U(x_0, y)$, i.e.,

$$U\;(\;x_0\;,\;y\;)\;=\;\frac{1}{2}\;(\;1\;+\;\tanh\;(\;30\;y\;)). \tag{20}$$

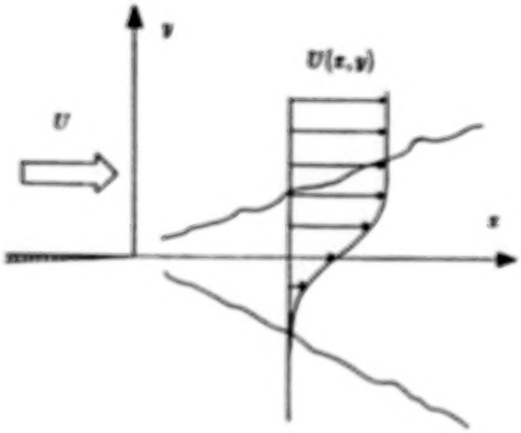

Figure 1. Sketch of a free mixing layer.

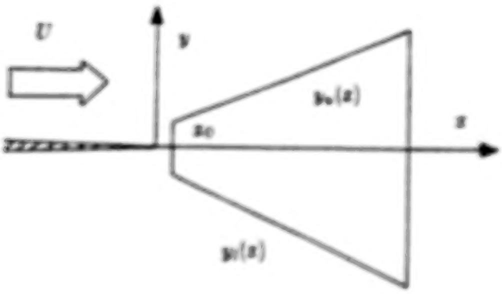

Figure 2. Physical domain.

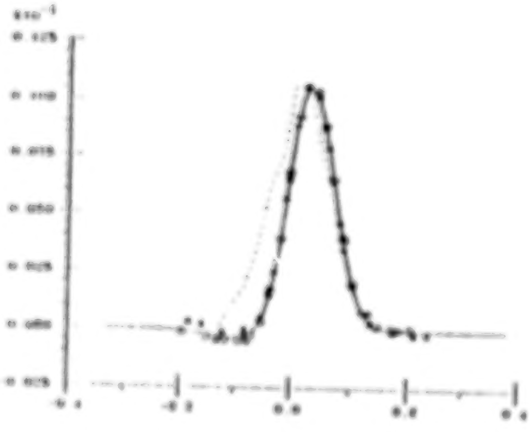

Figure 3. $-\overline{uv}$ in the self-similar region. ⬟ , Chebyshev Collocation (N=11); ▲ , Chebyshev Collocation (N=19); ■ , finite difference (N=11); ● , finite difference (N=25); —— , shooting; - - — , Patel.

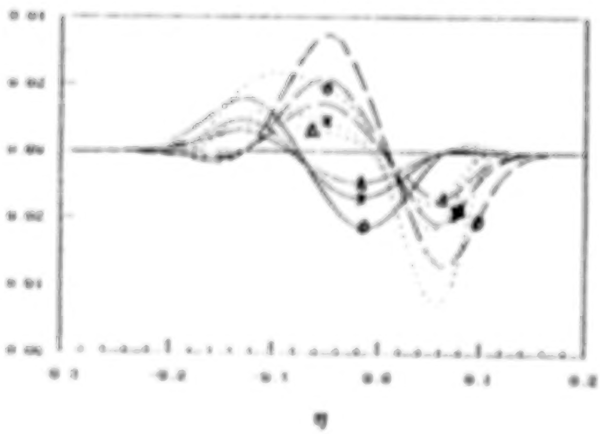

Figure 4. Driving forces across the mixing layer using Model I at ● , x=2.37; ■ , 4.35; ▲ , 6.19. —— , $-(\overline{u^2}-\overline{v^2})_x$; — — , $-(\overline{uv})_y$; - - - - - -, $-(\overline{u'v'})_y$.

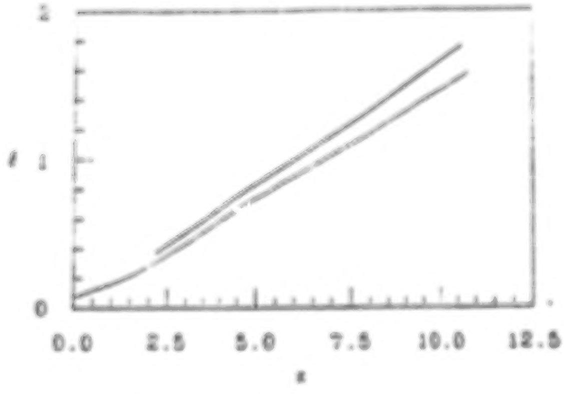

Figure 5. Growth of the mixing layer using Model I.

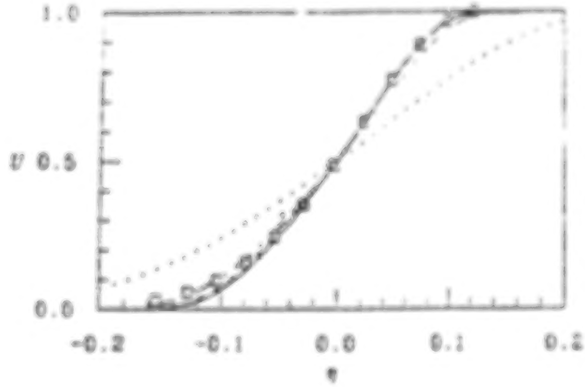

Figure 6. Mean velocity profiles using Model I at - - - - - -, x=0.72; —·— , 1.45; - - - , 2.37; — — , 3.25; — — , 4.35; —— , 6.19. □ , Patel.

The initial cross-stream mean velocity, $V(x_0, y)$, can be set to a small number or zero. The boundary conditions for the mean flow are

$$U\,(\,x\,,\,y_u(x)\,)\;=\;1.0,\quad U\,(\,x\,,\,y_l(x)\,)\;=\;0.0,\;\; V\,(\,x\,,\,y_u(x)\,)\;=\;0.0. \tag{21}$$

where $y_u(x)$ and $y_l(x)$ are the upper and the lower boundaries of the physical domain shown in figure (2). As a test of the ability of the instability wave model to describe large-scale structures and the associated Reynolds stresses, the model was first applied in the self-similar region of the flow with a mean velocity profile from Patel (ref.12). Figure (3) shows the calculated and experimental Reynolds shear stress distributions. Calculated results using a traditional shooting method compare favorably with that using global approximations of various order. Note that all the calculated results have been normalized by the peak experimental value. The discrepancy at the low-speed side of the layer suggested that the momentum exchanges due to the small-scale turbulent motions might not be negligible in this region. It should be noted that this negative value of Reynolds shear stress disappears for small values of velocity in the lower stream. The structures obviously contribute negative shear stress at the low-speed edge of the flow. This counter-gradient transport of momentum gives negative energy production in this region. A similar phenomenon was observed experimentally by Komori and Ueda (ref.13) in the self-similar region of a jet. In fact, regions of negative shear stress can be easily observed if the large-scale structures are excited artificially, for example, see Wygnanski, Oster and Fiedler (ref.14). This counter-gradient momentum transfer decelerates and subsequently reverses the flow on the low-speed side of the mixing layer as the shear layer develops. As noted above, Model I proposes that a contribution from the small-scale Reynolds stresses is required to describe the total turbulent forces that determine the development of the mean flow. Thus, in Model I, a simple eddy-viscosity model is used to model the small-scale Reynolds shear stress,

$$-\overline{u'v'}\;=\;C_2\, l^2\, \left|\frac{\partial U}{\partial y}\right|\left(\frac{\partial U}{\partial y}\right). \tag{22}$$

The model introduces a new parameter, C_2. Latigo (ref.15) argued that the turbulent shear stress contributed by the small-scale motions is about a half of the total shear stress. An estimate of C_2 based on the value that is used in the classical eddy-viscosity models is then obtained. In addition, the force terms associated with the large-scale normal stresses in the mean momentum equations are also retained, since they are found to be of the same order as the other Reynolds stress gradient terms on the low-speed edge of the shear layer. The normal stresses associated with the large-scale structures can be calculated directly by the wave models and involve no further empiricism.

In the numerical calculations, the local solution of the Rayleigh equation is found to be time-consuming. To accelerate the axial marching an adaptive grid has been devised. The grid size in the cross-stream direction in the transformed domain are fixed. The axial step sizes are chosen such that the convergence indices of the first iteration at a downstream station are greater than a fixed number ϵ_2.

$$\frac{1}{M}\sum_j \left| U^1_{i+1,j}\;-\;U_{i,j}\right|\;\geq\;\epsilon_2, \tag{23}$$

The grids are found to cluster in a region where there are large changes of flow properties, for example, when the flow is developing initially.

The initial wave amplitude represents the initial strength of the instability waves or large-scale motions for which there are no quantitative experimental measurements. From a sequence of numerical experiments, however, it is found that flows with relatively strong initial amplitude saturate early. Subsequently the flow develops in a similar manner; only the virtual origin of mixing is changed. The initial amplitudes for the cases presented in this paper are fixed at 10^{-4}. The model constant C_1 of the energy transfer term in the wave kinetic energy equation is taken from a conventional Prandtl energy model, Launder, et. al.(ref.16). It is found that its value has no significant influence on the results of the mixing layer calculations.

First we consider Model I in which turbulent forces associated with the wave shear and normal stresses as well as the small-scale motions are considered. Figure (4) shows the axial forces acting on fluid elements across the layer at various axial stations. The calculated rate of growth of the layer agrees well with the value that is an average taken over various experiments. The averaged experimental value is denoted by the straight line in figure (5). δ is the distance between the points where the local mean velocity is 0.9 and 0.1 of the main stream mean velocity, U. Figure (6) shows the predicted mean velocities at a sequence of downstream stations. The agreement between the predictions and experimental data is good except near the low-speed side of the shear layer. Note that for a free mixing layer, the accuracy of the measured mean flow data in this region is poor due to the rapid variations in the instantaneous flow direction. As can be seen from figure (7), which shows the shear stress distributions across the mixing layer at various stations, the sum of the shear stresses from the large-scale and the small-scale motions agrees well with experimental data. The experimental measurements are the long time-averaged correlations of the turbulent fluctuations. The amplitude of the large-scale fluctuations is plotted in figure (8). The large-scale structures extract energy from the mean flow and strengthen as the flow develops. However, energy is also being transferred to the small scales. The final equilibrium of the large-scale motions amplitude is reached when the energy gained from the mean flow balances the energy lost to the small scales.

In Model I, the small-scale motions play a direct role in the momentum transport process. However, it could be argued that the large-scale structures dominate dynamically the development of free shear flows. Therefore, in Model II only the fluctuations at the large scale are included. This eliminates the need to specify a model constant in the eddy-viscosity model, equation (22). It can be seen from figure (9) that the forces associated with the large-scale normal stresses are apparently able to counter-balance the decelerating effects of the wave shear stress gradients. The predicted mean velocity profiles are presented in figure (10). It shows that the mean flow can be satisfactorily predicted by modeling only the dominant large-scale structures. However, as shown in figure (11), the predicted shear stress distributions do not match the total shear stress distributions measured by Patel (ref.12). This difference does not mean necessarily that the smll-scale stresses should be included. It must be remembered that the present model simulates the entire large-scale spectrum with a single frequency wave that is locally most unstable. Tam and Chen (ref.7), in their local model, included a broad range of instability waves and found

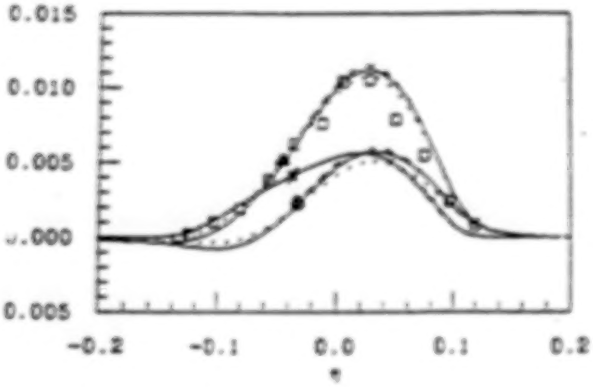

Figure 7. Distributions of the Reynolds shear stresses using Model I at – – – , x=2.37; — — , 4.35; ——— , 6.19. ◻ , Patel; ● , $-\overline{uv}$; ✕ , $-\overline{u'v'}$; ▲ , $-\overline{uv} - \overline{u'v'}$.

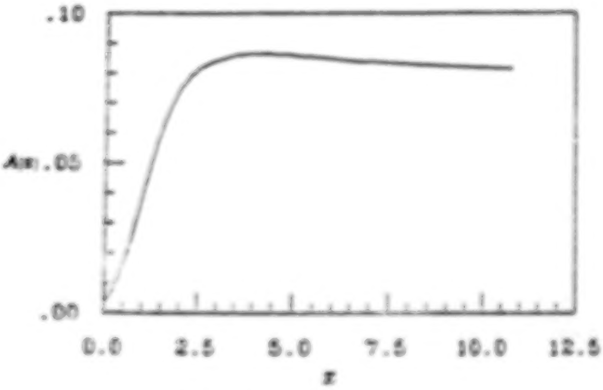

Figure 8. Evolution of the large-scale structure amplitude using Model I.

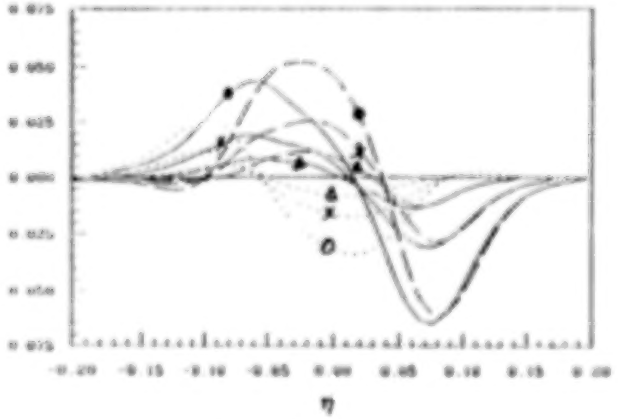

Figure 9. Driving forces across the mixing layer using Model II at ● , x=2.95; ✕ , 5.36; ▲ , 11.36. - - - - - -, $-(\overline{u^2} - \overline{v^2})_x$; — — , $-(\overline{uv})_y$; ——, $-(\overline{uv})_y - (\overline{u^2} - \overline{v^2})_x$.

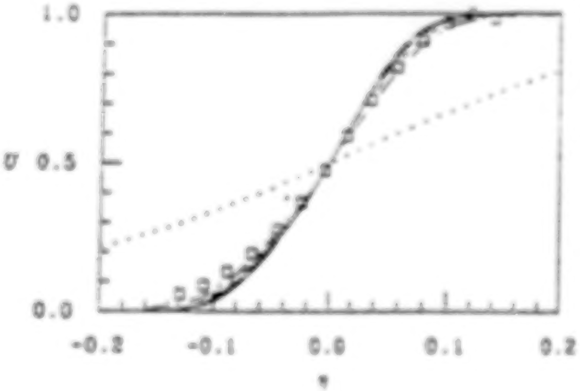

Figure 10. Mean velocity profiles using Model II at ······ , x=0.63; —·—, 2.96; – – –, 7.36; ·-·—, 9.36; —— , 11.36. ◻ , Patel.

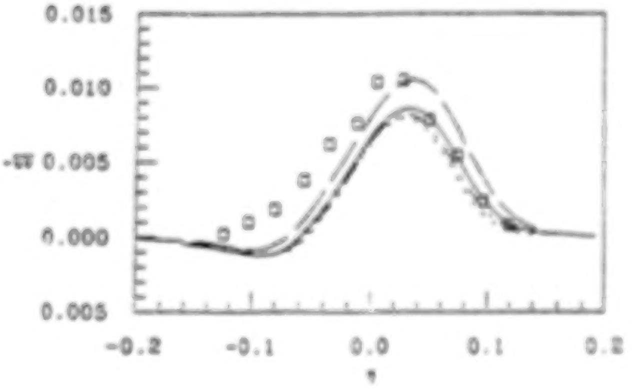

Figure 11. Distributions of wave shear stress using Model II at — —, x=2.96; ——, 7.36; —·—, 9.36; - - - -, 11.36. ◻ , Patel.

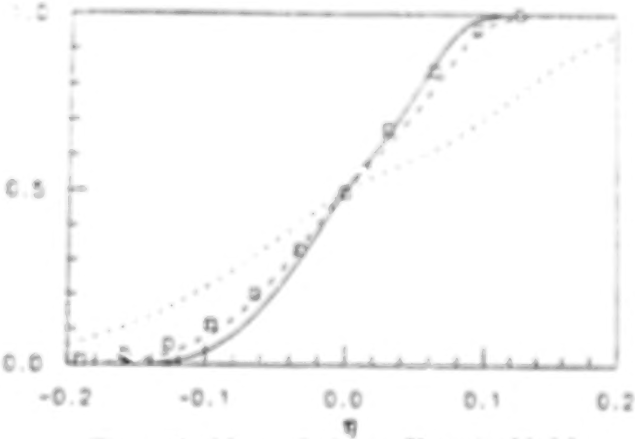

Figure 12. Mean velocity profiles using Model III at ······, x=1.0; – – – , 2.96; ——, 5.96. ◻ , Patel.

good agreement with experiment, without the inclusion of contributions from the small scales. This point requires further investigation. The evolution of the large-scale amplitude using Model II follows a similar behavior to that shown in figure (8). Once again an equilibrium condition is reached where the rate of energy transfer from the mean flow to the large-scale structures balances the rate at which energy is lost by the structures to small scales for eventual dissipation.

Model III simulates the time-dependent motion, at the large scale, associated with the passage of a train of large-scale structures. As the flow develops axially, these hydrodynamic waves become damped because of the growth of the shear layer. Since it is assumed that energy associated with a given wave is removed immediately it becomes neutral, there is no need to obtain damped inviscid solutions by analytic continuation in the complex plane, Tam and Morris (ref.17).

In the preliminary calculations, it was found that an abnormality in the mean velocity distributions appeared near the critical points of saturating waves. Also, most of the shear layer growth occurred on the low speed side of the layer. This gives a non-monotonic velocity distribution near the critical layers of saturating waves and another inflection point appears. Saturating waves thus have to be removed before they become neutral during the axial marching. Wygnanski and Petersen (ref.18) suggested that this abnormality is due to nonlinearities. Composite expansion techniques have been applied to investigate the effect of critical-layer nonlinearity, for example, see Goldstein and Leib (ref.19) and Goldstein and Hultgren (ref.20). Another approach to resolve this issue is to include viscous effects; that is to solve the Orr-Sommerfeld equation. Since the present investigation is directed toward developing simple turbulence models, instead of including other computationally expensive approaches, the effects of the critical point is accounted for by incorporating a small amount of eddy-viscosity in the analysis of the mean flow. With this modification the mean velocity distributions predicted at several downstream stations are shown in figure (12). They are compared with Patel's data using a similarity scale. The additional mixing at the fine scale is diffusive and able to smooth out humps in the flow. In the present calculation, the extra mixedness provided accounts for about 10% of the amount of turbulent momentum exchange that is suggested by conventional models. There are six waves in the hierarchy in this calculation. Since waves are removed successively during the axial marching, the number of waves included depends on the distance the calculation is to be carried downstream. There are some differences between the calculated results and Patel's measurements in figure (12). However, similar characteristics of mean velocity distributions have been reported by Wygnanski et. at. (ref.14), among others, in which free mixing layers are excited externally. Figure (13) shows the development of the wave amplitudes. The additional small-scale mixing increases the initial growth of the layer so that the fundamental mode is removed at a lower amplitude than its subharmonics before its amplitude reaches equilibrium level. The axial width of the layer is shown in figure (14) and is compared with the prediction using Model I. The presence of this stepwise evolution is characteristic of excited flows and would be smoothed out if many waves with slightly different amplitudes and frequencies were included.

Figure (15) shows the transient solutions of the velocity field of the turbulent free mixing layer depicted by Model III in a reference of frame moving at the phase speed of the fundamental wave. Dominant large vorticies can be clearly seen. The downstream development of the neighboring

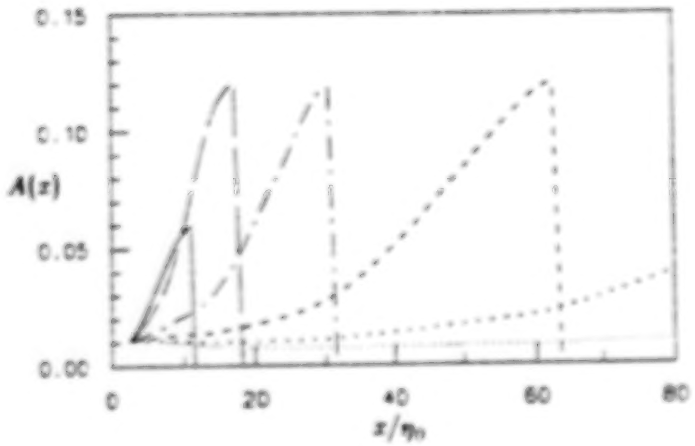

Figure 13. Evolutions of amplitude functions using Model III. ——— , fundamental; — —, 1st subharmonic; —·—, 2nd; — — — , 3rd; ----, 4th; ·········, 5th.

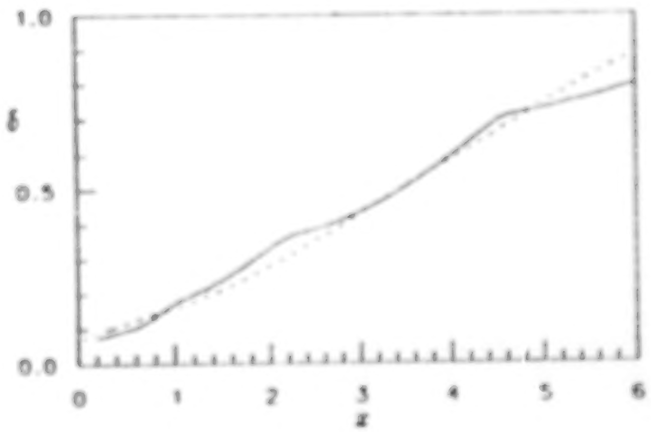

Figure 14. Growth of the mixing layer. ----, model I; ———, model III.

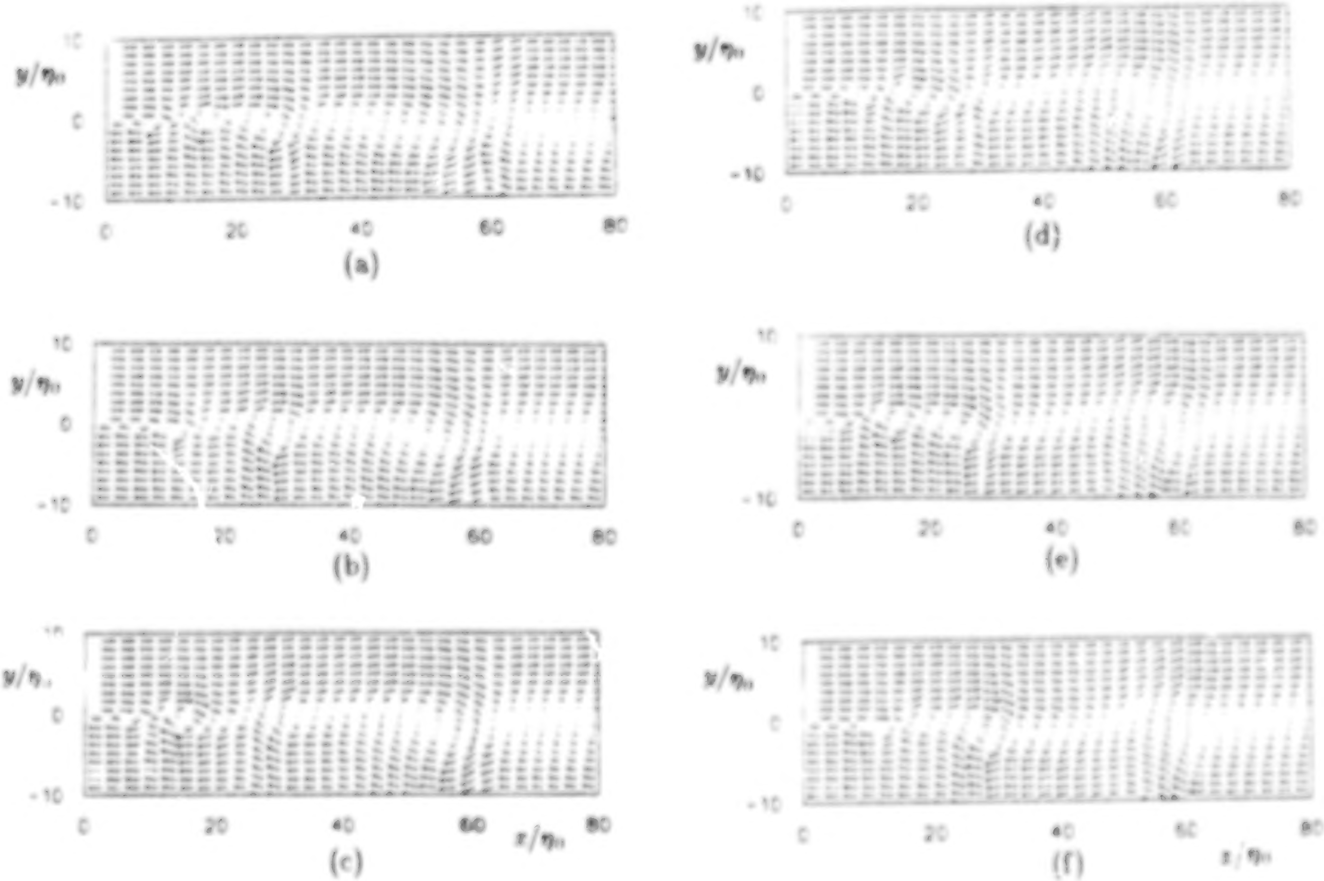

Figure 15. Velocity vector plots at (a) $t=1.5$, (b) 2.5, (c) 3.5 (d) 4.5, (e) 5.5, (f) 6.5.

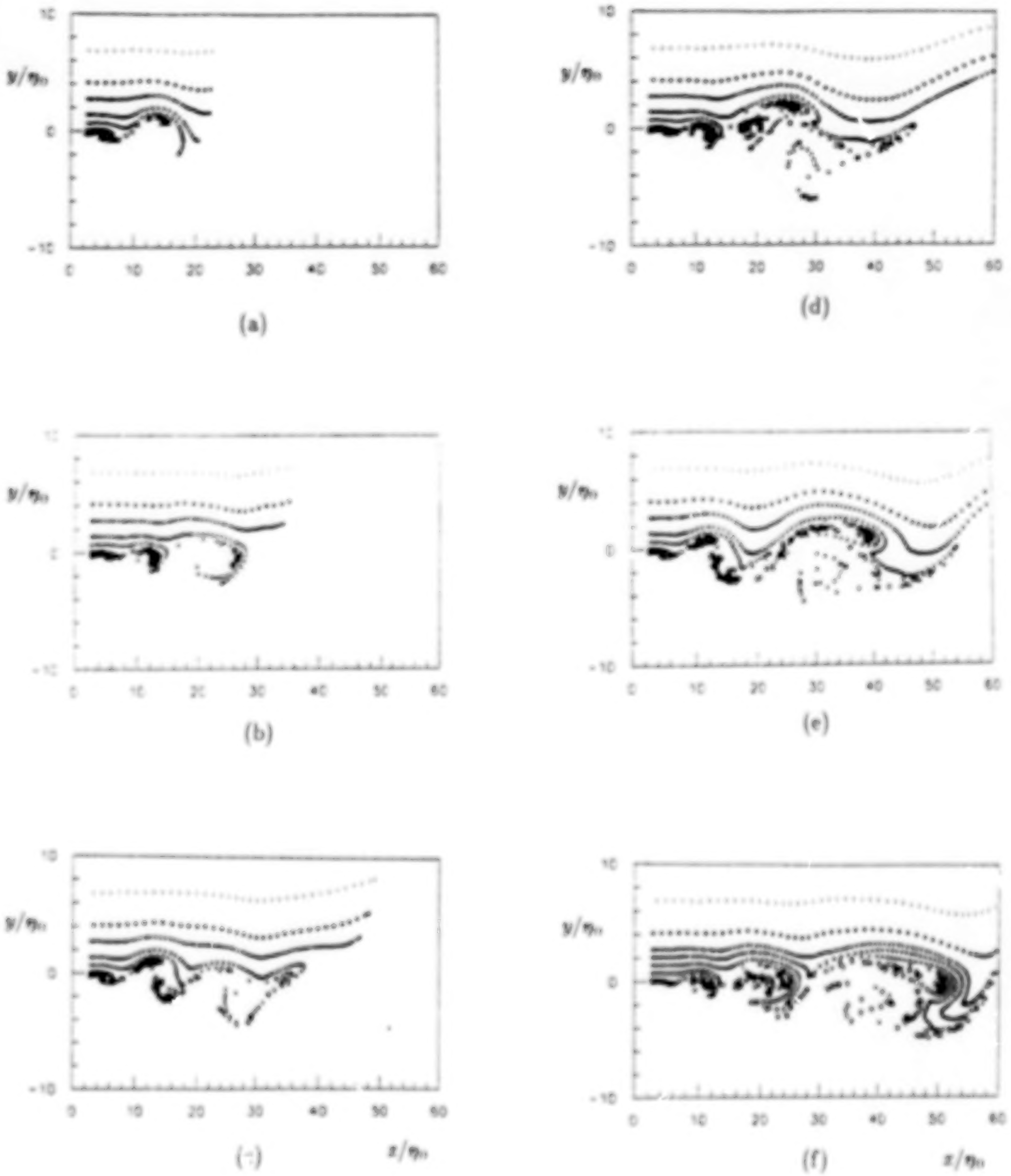

Figure 16. Streakline plots at (a) $t=1.5$, (b) 2.5, (c) 3.5 (d) 4.5, (e) 5.5, (f) 6.5.

vortical structures can also be observed. This can be assisted by streakline plots shown in figure (16). The roll-up of vorticies into larger vortex-like structures can be observed clearly. The initial roll-up is dominated by the fundamental mode. As time progresses, the initial structures convect downstream and roll around each other. These regions of concentrated vorticity then form a single large structure. As the passive particles travel downstream, their motion becomes dominated by lower subharmonics. Vortex-like structures of increasing scale are formed. Subsequently, the rolling process between two adjacent structures repeats as the flow develops further downstream. Careful examination of the figures shows also how the structures are convecting downstream as they form and roll. Large tongues of unmixed fluid are swept across the layer and reach the opposite side of the layer as observed by Brown and Roshko (ref.1). The engulfed fluid elements from the two sides of the layer mix and are drawn into the leading and trailing vortices when passing through the high-strain braid region between the vortices. This provides the environment for further fine-scale mixing.

SUMMARY

Three models based on a quasi-linear theory, that describes the dynamics of the dominant large-scale structures in a free mixing layer have been presented. The closure schemes incorporating the models are able predict the development of the turbulent free mixing layer accurately, even though they contain some assumptions and simplifications. The transient turbulent motions at the large scale in the layer mapped out using Model III possess many features that are apparent in flow visualization experiments, such as the convective nature of the large-scale structures, the large-scale transport of unmixed fluid elements and the roll-up of vortices. The models involve less empiricism than most conventional models. Since large-scale coherent structures appear also in shear flows of other geometries, the closure schemes presented here should be applicable to those cases as well. It is hoped that these models, which originate from observed physical phenomena, will provide efficient tools to model other free shear flows.

REFERENCES

1. Brown, G. L. and Roshko, A., "On Density Effects and Large Structure in Turbulent Mixing Layers," *J. Fluid Mech.*, **64**, 775-816 (1974).
2. Gaster, M., Kit, E. and Wygnanski, I., "Large-scale Structures in a Forced Turbulent Mixing Layer," *J. Fluid Mech.*, **150**, 23-39 (1985).
3. Petersen, R. A. and Samet, M. M., "On the Preferred Mode of Jet Instability," *J. Fluid Mech.*, **194**, 153-173 (1988).
4. Tam, C. K. W. and Morris, P. J., "The Radiation of Sound by the Instability Waves of a Compressible Plane Shear Layer," *J. Fluid Mech.*, **98**, 349-381 (1980).
5. Tam, C. K. W. and Burton, D. E., "Sound Generated by Instability Waves of Supersonic Flows. Part 1. Two-dimensional Mixing Layers," *J. Fluid Mech.*, **138**, 249-271 (1984).
6. Tam, C. K. W. and Burton, D. E., "Sound Generated by Instability Waves of Supersonic Flows. Part 2. Axisymmetric Jets," *J. Fluid Mech.*, **138**, 273-295 (1984).

7. Tam, C. K. W. and Chen, K. C., "A Statistical Model of Turbulence in Two-dimensional Mixing Layers," *J. Fluid Mech.*, **92**, 303-326 (1979)

8. Morris, P. J. and Giridharan, G., "Models for Turbulent Mixing in Compressible Shear Layers," to be published.

9. Ho, C.-M. and Huang, L.-S., "Subharmonics and Vortex Merging in Mixing Layers," *J. Fluid Mech.*, **119**, 443-473 (1982).

10. Bridges, T. J. and Morris, P. J., "Differential Eigenvalue Problems in which the Parameter Appears Nonlinearly," *J. Comp. Phys.*, **55**(3), 437-460 (1984).

11. Liou, W. W. and Morris, P. J., "A Comparison of Finite Difference and Spectral Solutions of the Rayleigh Equation of Hydrodynamic Stability," in preparation.

12. Patel, R. P., "An Experimental Study of a Plane Mixing Layer," *AIAA J.* **11**, 67-71 (1973).

13. Komori, S. and Ueda, H., "The Large-scale Coherent Structure in the Intermittent Region of the Self-preserving Round Free Jet," *J. Fluid Mech.*, **152**, 337-359 (1985).

14. Wygnanski, I., Oster, D. and Fiedler, H., "A Forced, Plane, Turbulent Mixing-layer; A Challenge for the Predictor," in *Turbulent Shear Flows 2*, (ed. by J. L. S. Bradbury et. al.), 314-326, Springer, Berlin (1979).

15. Latigo, B., "Large-scale Sturcture Interactions in a Two-dimensional Trubulent Mixing Layer," *Ph. D. Thesis*, University of Southern California, 1979.

16. Launder, B. E., Morse, A., Rodi, W. and Spalding, D. B., "Prediction of Free Shear Flows; A Comparison of the Performance of Six Turbulence Models," *NASA SP-321*, 1972.

17. Tam, C. K. W. and Morris, P. J., "The Radiation of Sound by the Instability Waves of a Compressible Plane Turbulent Shear Layer," *J. Fluid Mech.*, **98**, 349-381 (1980).

18. Wygnanski, I. J. and Petersen, R. A., "Coherent Motion in Excited Free Shear Flows," *AIAA J.*, **25**, 201-213 (1987).

19. Goldstein, M. E. and Leib, S. J., "Nonlinear Roll-up of Externally Excited Free Shear Layers," *J. Fluid Mech.*, **191**, 481-515 (1988).

20. Goldstein, M. E. and Hultgren, L. S., "Nonlinear Spatial Evolution of an Externally Excited Instability Wave in a Free Shear Layer," *J. Fluid Mech.*, **197**, 295-330 (1988).

COMPUTATION OF LAMINAR VISCOUS-INVISCID INTERACTIONS IN HIGH-SPEED INTERNAL FLOWS

David H. Rudy
James L. Thomas
Ajay Kumar
NASA Langley Research Center
Hampton, VA 23665

ABSTRACT

A review is given of computations for a series of nominally two-dimensional laminar viscous-inviscid interactions. Comparisons were made with detailed experimental shock-tunnel results. The shock wave-boundary layer interactions considered were induced by a compression ramp in one case and by an externally-generated incident shock in the second case. In general, good agreement was reached between the grid-refined calculations and experiment for the incipient- and small-separation conditions. For the highly separated flow, three-dimensional calculations which included the finite-span effects of the experiment were required in order to obtain agreement with the data.

NOMENCLATURE

C_f	skin-friction coefficient, $2\tau_w/\rho_\infty u_\infty^2$
C_h	heat-transfer coefficient, $\dot{q}/\rho_\infty u_\infty(H_\infty - H_w)$
C_p	pressure coefficient, $2p/\rho_\infty u_\infty^2$
H	total enthalpy
L	reference length
M	Mach number
p	pressure
$\dot{q}$	heat-transfer rate
Re	unit Reynolds number, $\rho_\infty u_\infty/\mu_\infty$
T	temperature
u	streamwise velocity
x	streamwise coordinate
β	shock angle
γ	ratio of specific heats
θ	compression-ramp or wedge angle
μ	molecular viscosity
ρ	density
τ	shear stress

subscripts

att	reattachment point
sep	separation point
w	wall
∞	free stream

INTRODUCTION

The propulsion system of advanced hypersonic vehicles will likely use the external vehicle contours as compression and expansion surfaces for the inlet and nozzle, respectively. Thus, the integration of the engine and airframe is an important design consideration. This design process relies heavily upon the development of computer codes with appropriate geometric flexibility and physical models since many of the high Mach-number, high enthalpy flow conditions the vehicle may encounter in flight cannot presently be simulated in ground-based facilities. Part of the process of validating such a code is to assess the code's ability to simulate the complex physics of the vehicle flow field by making comparisons of computed results with available benchmark experimental data. The present paper summarizes the results of such comparisons for two types of shock-boundary layer interactions that can occur in the forebody and inlet portions of the vehicle.

DESCRIPTION OF CODES

The main code used in these studies was CFL3D (Computational Fluids Laboratory 3-D code), which was developed by J. L. Thomas for the thin-layer Navier-Stokes equations and is described in reference 1. This code uses a finite-volume method in which the convective and pressure terms are discretised with the upwind-biased flux-difference splitting technique of Roe. The reconstruction of the cell-centered variables to the cell-interface locations is done using a monotone interpolation of the primitive variables such that third-order accuracy in one-dimensional inviscid flow is obtained. The differencing for the diffusion terms representing shear stress and heat transfer effects corresponds to second-order-accurate central differencing so that the global spatial accuracy of the method is second order. The time-differencing algorithm is a spatially-split approximate-factorisation scheme.

Three other codes were used for comparison with the CFL3D results. Two of these codes use similar recently-developed upwind technology. One was USA-PG2 (Unified Solution Algorithm-Perfect Gas, 2-D), which was developed by S. R. Chakravarthy and is described in reference 2. The other was LAURA (Langley Aerothermodynamic Upwind Relaxation Algorithm), which was developed by P. A. Gnoffo and is described in reference 3. The fourth code, NASCRIN (Numerical Analysis of SCRamjet INlets), was developed by Kumar (refs. 4 and 5) and uses the original unsplit explicit finite-difference technique of MacCormack (ref. 6) to solve the full Navier-Stokes equations. This technique is a two-step, predictor-corrector scheme which is second-order accurate in both space and time. Fourth-order artificial viscosity based on the gradients of pressure and temperature is used near shock waves to suppress numerical oscillations. This code has been previously used to compute a variety of inlet flow fields.

TEST CASES

The two test cases considered in the present study are shown schematically in Fig. 1. Both of these cases are hypersonic flows with viscous/inviscid interactions typical of those found in the flow field within the propulsion system of a hypersonic vehicle. The first of these test cases was the two-dimensional flow over a compression corner formed by the intersection of a flat plate and a wedge tested by Holden and Moselle (ref. 7) in the Calspan 48-inch Shock Tunnel. The flow field shown in Fig. 1(a) shows the separated flow which forms in the corner region for a sufficiently large wedge angle. Downstream of the reattachment point, the boundary layer thins rapidly due to the compression, resulting in large increases in skin friction and heat transfer on the wedge surface. Furthermore, the compression waves produced by the corner coalesce into a shock wave which intersects with the leading-edge shock, producing an expansion fan and a shear layer, both of which affect the flow on the ramp. Three wedge angles tested by Holden and Moselle are considered here. The flow remained attached on the 15-degree wedge, a small separated-flow region occurred with the 18-degree wedge, and a large separated-flow region was produced by the 24-degree wedge.

The nominal flow conditions for this case were $M_\infty = 14.1$, $T_\infty = 160^\circ R$, and $Re = 7.2\text{x}10^4$ per foot. The wall temperature, T_w, was $535^\circ R$. The Reynolds number was low enough that the flow remained completely laminar, thereby eliminating the issue of turbulence modeling from the present study. Furthermore, even though the free-stream Mach number was high, the free-stream temperature was low enough that there were no significant real-gas effects. In the experiment, values of surface pressure, skin friction, and heat transfer were measured in the centerplane of the model which had a spanwise length that was thought to be sufficient to produce two-dimensional flow in the measurement region.

The second test case, shown in Fig. 1(b), was the interaction of an incident shock produced by a shock-generator wedge with a flat-plate boundary layer in hypersonic flow. The features of this flow field are very similar to those produced by the compression corner. In this case, the incident shock produces a separated-flow region. Downstream of this region, the boundary layer thins rapidly due to the compression. As in the first case, measurements were made in the centerplane of the model which had a spanwise length judged sufficient to produce two-dimensional flow in the measurement region. The experimental data were obtained by Holden (ref. 8) in the Calspan 48-inch Shock Tunnel. The nominal flow conditions for this case were $M_\infty = 15.6$, $T_\infty = 77^\circ R$, and $Re = 1.36\text{x}10^5$ per foot. The wall temperature, T_w, was $535^\circ R$. Solutions were computed for two different shock-generator wedge angles, 4.017° and 6.45°. As in the compression-corner experiments, the flow was completely laminar and real gas effects were not significant.

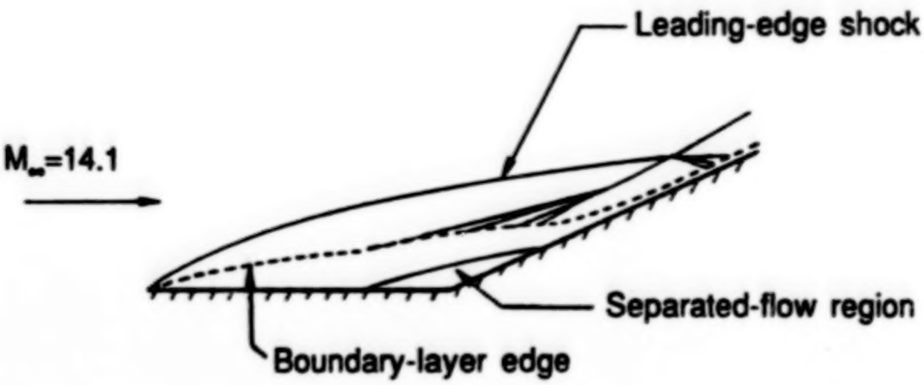

(a.) Compression corner.

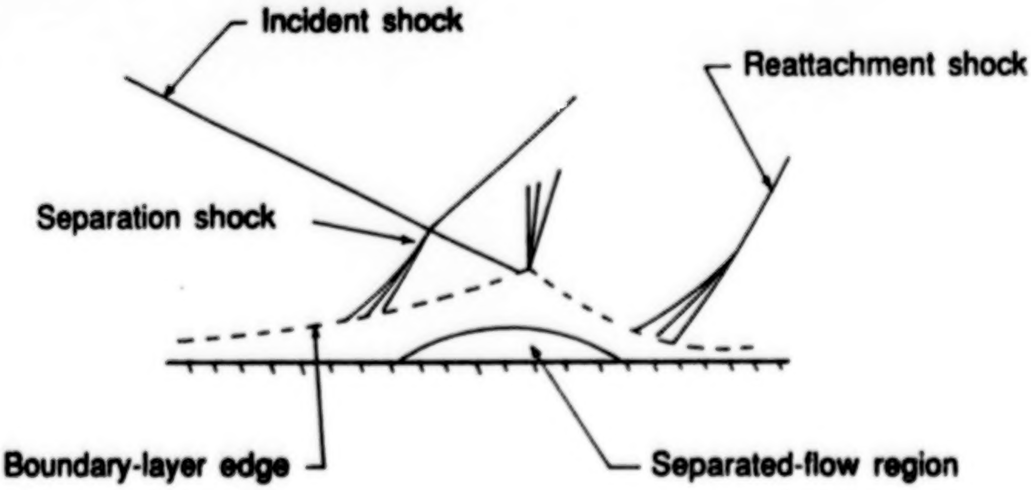

(b.) Shock-boundary layer interaction.

Fig. 1 Test cases.

RESULTS AND DISCUSSION

Compression-corner case

Comparisons were made between the computed solutions from all four codes and experimental data for the 15- and 24-degree wedges using two different grids. (The flow over the 18-degree wedge was computed only with CFL3D, and this result will be shown in the summary plots.) The first grid had 51 points in the streamwise direction and 51 points in the vertical direction. The upper boundary of the grid was parallel to the lower boundary. In the streamwise direction, the grid was clustered near the leading edge of the flat plate and in the corner region. In the normal direction, the grid was clustered near the model surface. Above the wedge, a simple sheared grid was used, producing a non-orthogonal grid in this region. A second grid with twice the resolution was constructed from the first grid using 101 points in each direction while maintaining the same grid stretching. The 101 x 101 grid for the 24-degree wedge is shown in Fig. 2. Calculations were made for other grids using only CFL3D. Additional details for the compression-corner study beyond those summarized below are given in reference 9.

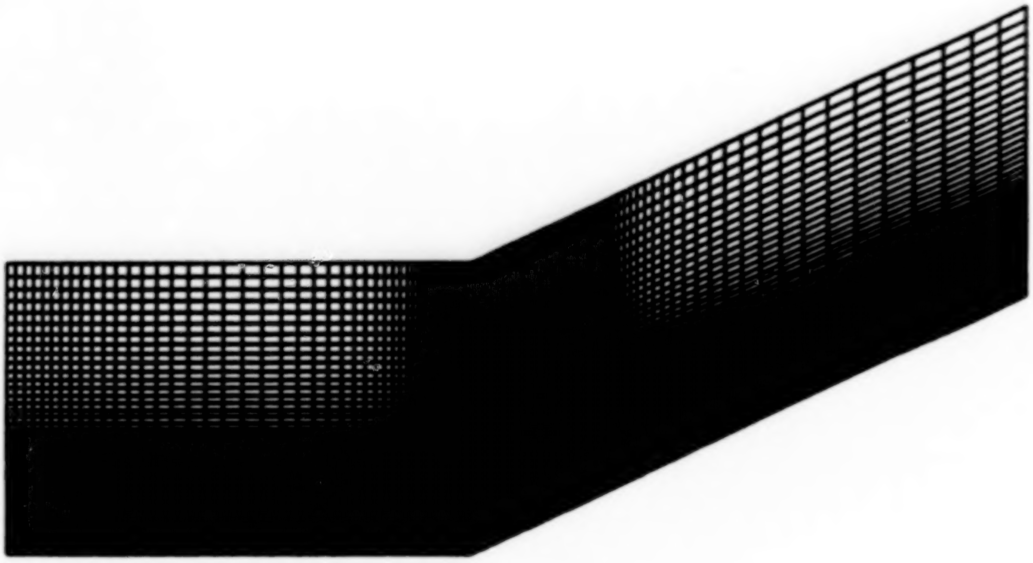

Fig. 2 Grid for 24-degree wedge. 101 x 101.

15° wedge. Fig. 3(a) shows a comparison of the computed surface-pressure coefficient with experimental values for all four codes on two different grids. The pressure coefficient is plotted as a function of x/L, where x is measured from the leading edge of the flat plate and L is the length of the flat-plate portion of the model. It should be noted that all of the plots shown in the present paper for the compression-corner case differ from those given in reference 9 in two ways. First of all, the experimental data have been revised by Holden, who recomputed the free-stream conditions using the tunnel calibration rather than using pitot-tube measurements from the experiment. The resulting change in the surface coefficient data eliminated the need for the one-degree angle-of-attack correction which was necessary in reference 9 to match the experimental values of pressure on the flat-plate portion of the model. Secondly, the data were originally given in reference 7 as a function of the distance along the surface of the model but were interpreted as being a function of the streamwise distance x in the plots in reference 9. Thus, the data on the ramp in reference 9 were shifted slightly downstream from their correct location. As shown in Fig. 3(a), there are only very slight differences in the predictions from the codes for the 51 x 51 grid; however, the solutions are virtually identical for the 101 x 101 grid. The computed pressures are generally higher than the experimental values even on the flat-plate portion of the model. However, the computed pressures were in excellent agreement with those given by hypersonic strong-interaction theory (not shown). The corresponding comparison of the computed surface heat-transfer coefficient with experimental values for all four codes on the two grids is shown in Fig. 3(b). As with the pressure coefficient, the calculations on the 101 x 101 grid produce the best agreement among the codes. The largest differences occur along the ramp.

24° wedge. Fig. 4 shows the comparison of the computed surface-pressure coefficient with experimental values for this case. The codes predict different extents of separation even with the 101 x 101 grid. A solution using a 201 x 201 grid was also made with CFL3D. The predictions for surface pressure, skin friction, and surface heat transfer for this grid were almost identical to those found with the 101 x 101 grid with only a slight increase in the predicted extent of separation. All of the codes demonstrated a trend with grid convergence towards a similar longitudinal extent of separation which is much larger than that found in the experiment. As a result of the larger separation extent, the shock interaction is altered, moving the peak value of pressure on the ramp downstream in comparison to the experiment.

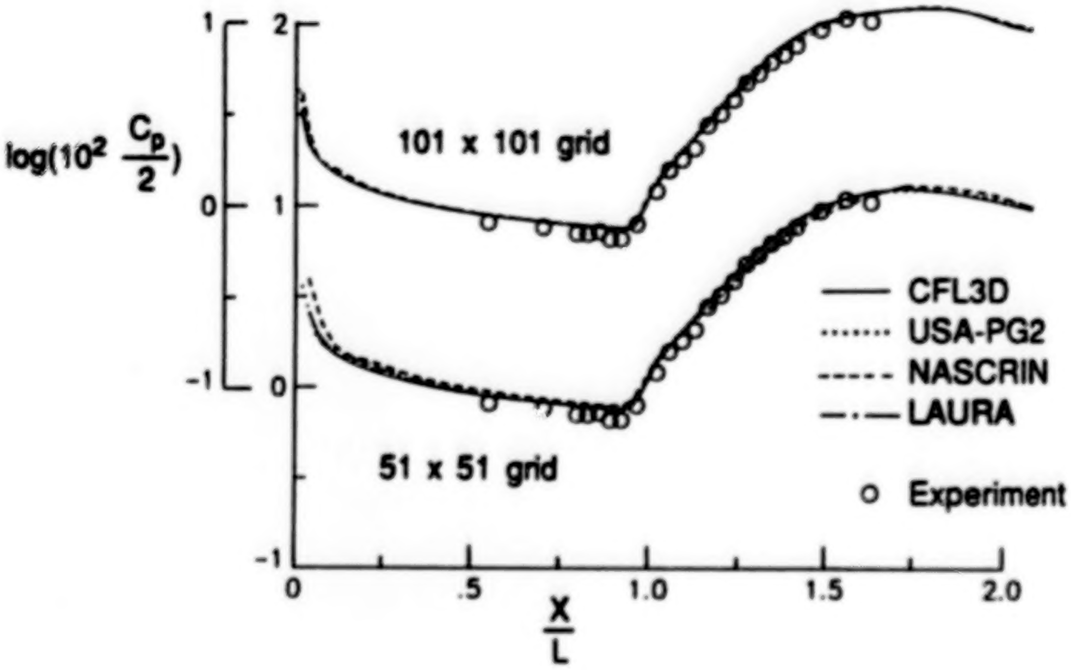

(a.) Surface pressure

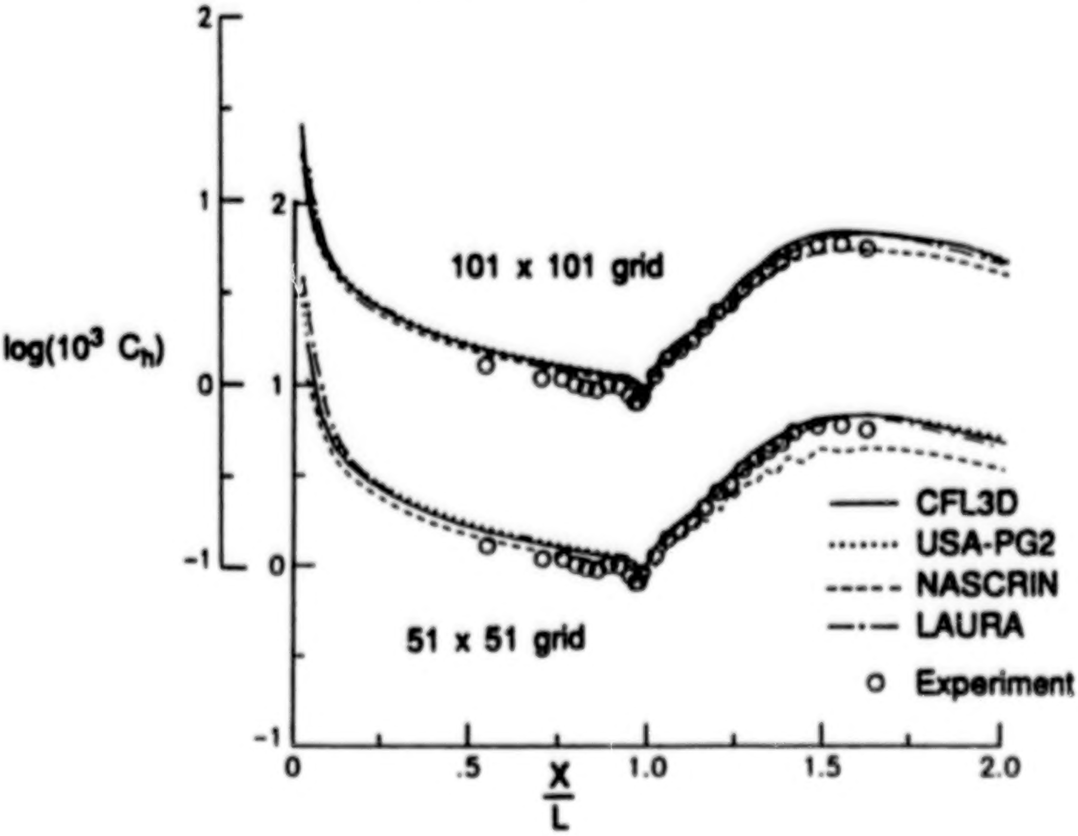

(b.) Surface heat transfer

Fig. 3 Comparison of computation and experiment for 15° wedge.

Since the results from the two-dimensional computations did not match the experimental data, 3-D calculations were made with CFL3D to investigate the possibility of flow in the spanwise direction affecting the flow in the center of the plate. For the experimental data for which comparisons are shown, no side plates were used. The spanwise length of the plate was 2 ft. Calculations were made with two different grids, 51 x 51 x 25 and 101 x 101 x 25. Because the flow is symmetric about the centerplane, the computational domain included only half of the plate. The spanwise grid contained 19 points on the plate and 6 points in the free stream. Approximate supersonic outflow boundary conditions were used at the sides of the computational domain outside of the ramp surface. Fig. 5 shows results from the calculation with a 101 x 101 grid in each streamwise plane. The streamlines in the flow very near the model surface are visualized using particle traces. The separation and reattachment lines show that the size of the separated-flow region decreases across the plate from the centerplane to the edge. The pressure contours in the downstream plane on the ramp at the end of the computational domain show an expansion of the flow in the spanwise direction near the edge of the plate to reduce the pressure to the free-stream value. A comparison of the computed 2-D and 3-D centerplane surface-pressure distributions with experimental data are shown in Fig. 6 using solutions from CFL3D. As shown, the three-dimensional effects produce a smaller separated-flow region in the centerplane than that predicted in the 2-D calculations. The size of the separated-flow region and the pressure level in that region are in excellent agreement with the data for the finest mesh in the 3-D calculation. Furthermore, in the 3-D computation, the time to establish steady-state conditions was approximately 4 ms, which is in agreement with the experiment. However, it took more than 12 ms to establish steady flow in the 2-D computations (ref. 9). The importance of the flow in the spanwise direction on the size of the separation region was shown experimentally by Putnam (ref. 10) for laminar flow over a series of compression ramps with varying span lengths at Mach 10.03. He found that decreasing the span of the ramp produced an almost linear decrease in the size of the separation region for any given ramp deflection angle.

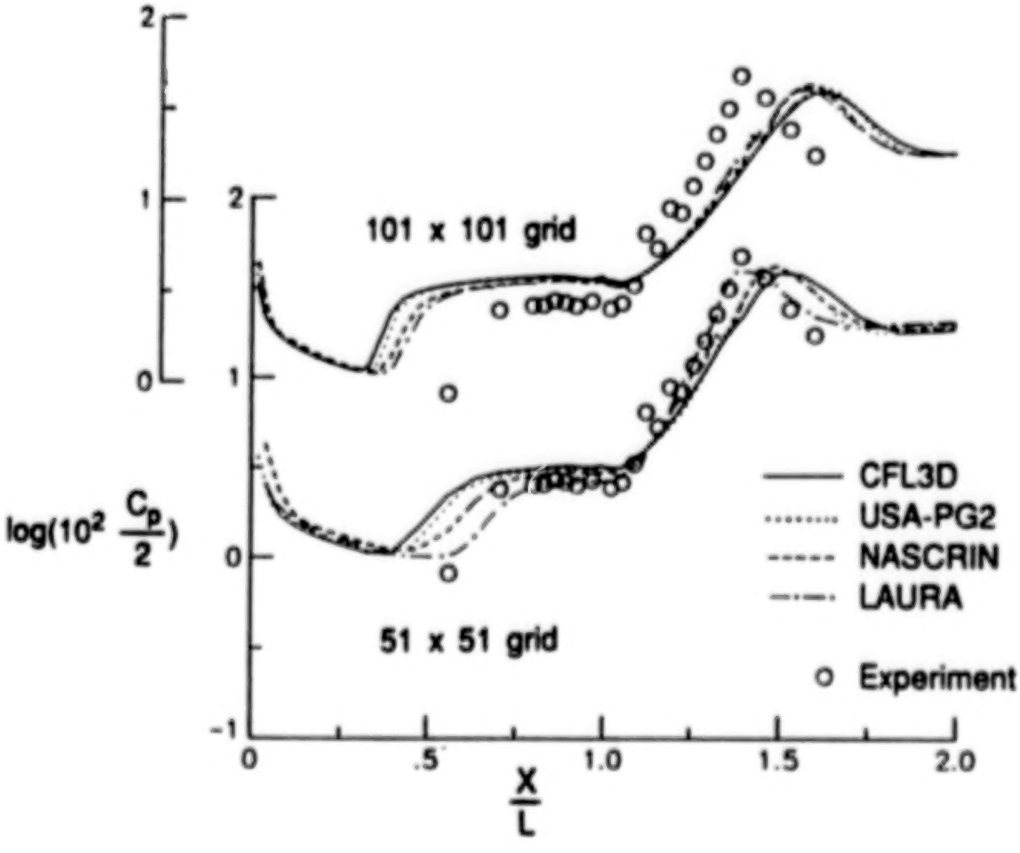

Fig. 4 Comparison of computed and experimental surface pressure for 24° wedge.

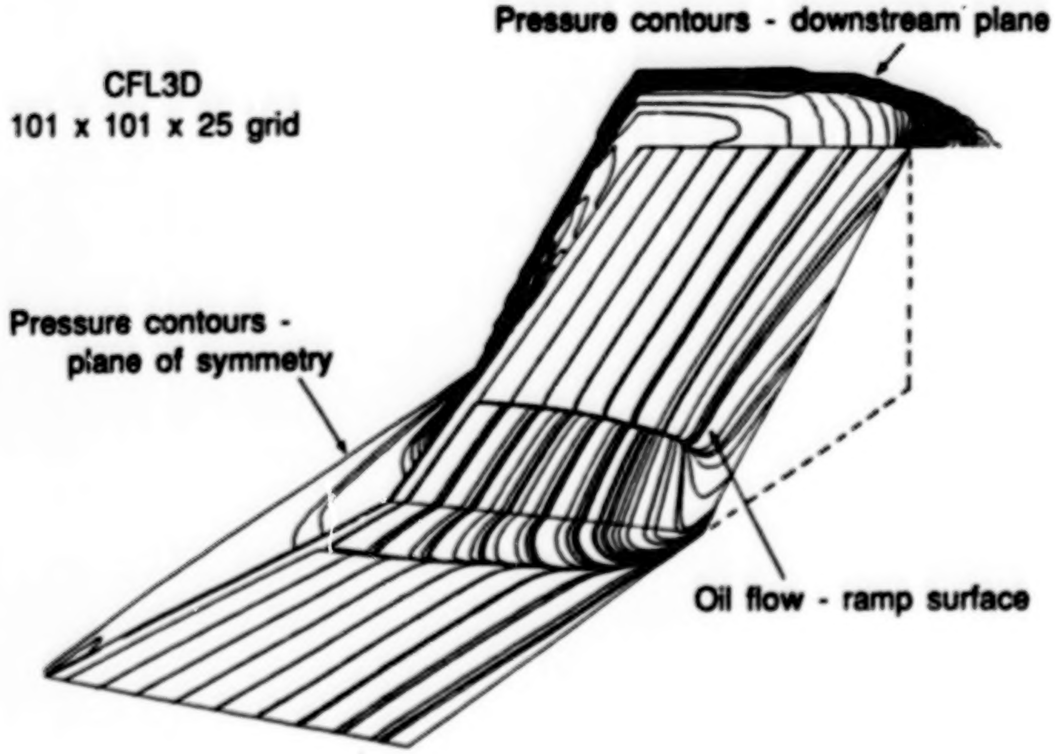
CFL3D
101 x 101 x 25 grid
Pressure contours - downstream plane
Pressure contours - plane of symmetry
Oil flow - ramp surface

Fig. 5 3-D solution using CFL3D for 24° wedge.

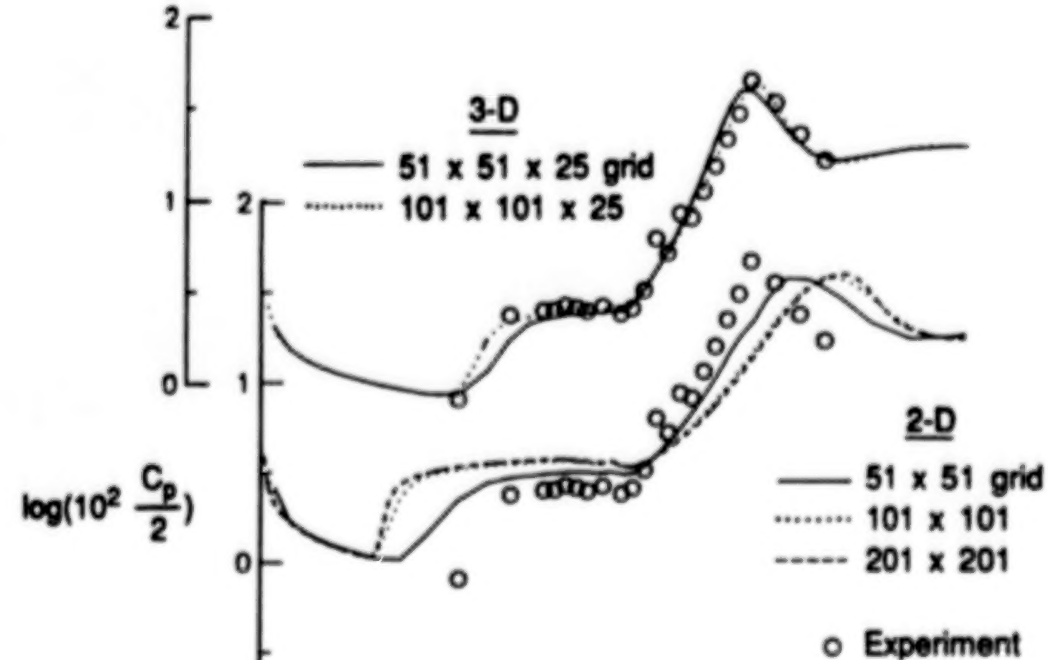

Fig. 6 Comparison of CFL3D computations and experiment for surface pressure for 24° wedge.

Two-dimensional calculations were also made for the 24-degree wedge with CFL3D using the grid topology shown in Fig. 7 which was used by Thareja et al. (ref. 11) in their study of this same test case. In this grid, the spacing in the streamwise direction remained the same as in the previous grid; however, the upper boundary in the normal direction was moved closer to the model surface and the boundary above the flat-plate portion was approximately parallel to the leading edge shock. The cell heights were reduced by a factor of approximately 17 at the leading edge and by a factor of 2.5 at the outflow boundary from those heights in the original grid. Thareja et al. (ref. 11) found that using this grid topology with 101 points in each direction, CFL3D predicted a separated-flow region closer in size to that found experimentally than with the original 101 x 101 grid. Those calculations were repeated in the present study for this 101 x 101 grid as well as for the corresponding 51 x 51 and 201 x 201 grids. The separation extent predicted in these cases is compared in Fig. 8 to the corresponding predictions for the original grids. For each grid topology, a grid density can be found which will produce a separation region that matches the experiment. Surprisingly, the results also indicate that the computations with the wedge outer boundary are less accurate for a given number of points than the computations with the rectangular outer boundary, even though the former has uniformly smaller spacing in the normal direction. Since the axial spacing is the same for both meshes, the resulting cell aspect ratio is substantially higher on the grid with the wedge outer boundary, which may be adversely affecting the spatial convergence. However, for both grid topologies, uniform refinement of the grid spacing increases the size of the separated-flow region. As the number of points is increased, the solutions produced by the two grid topologies appear to be approaching the same limit.

Thareja et al. (ref. 11) also made 2-D computations for the 24-degree wedge with their own upwind scheme using an unstructured adapted mesh developed from the second grid topology. The mesh had quadrilateral elements near the model surface and triangular elements elsewhere. The error indicator for the adaptive remeshing used a combination of second derivatives of density, velocity, and Mach number. Their two-dimensional calculations gave results in excellent agreement with the experimental data, leading Thareja et al. to question the conclusions of reference 9 that the flow was actually three-dimensional in this case. Studies are continuing to better understand why the structured and adaptive unstructured grids give different solutions.

Fig. 7 Grid with wedge outer boundary. 101 x 101.

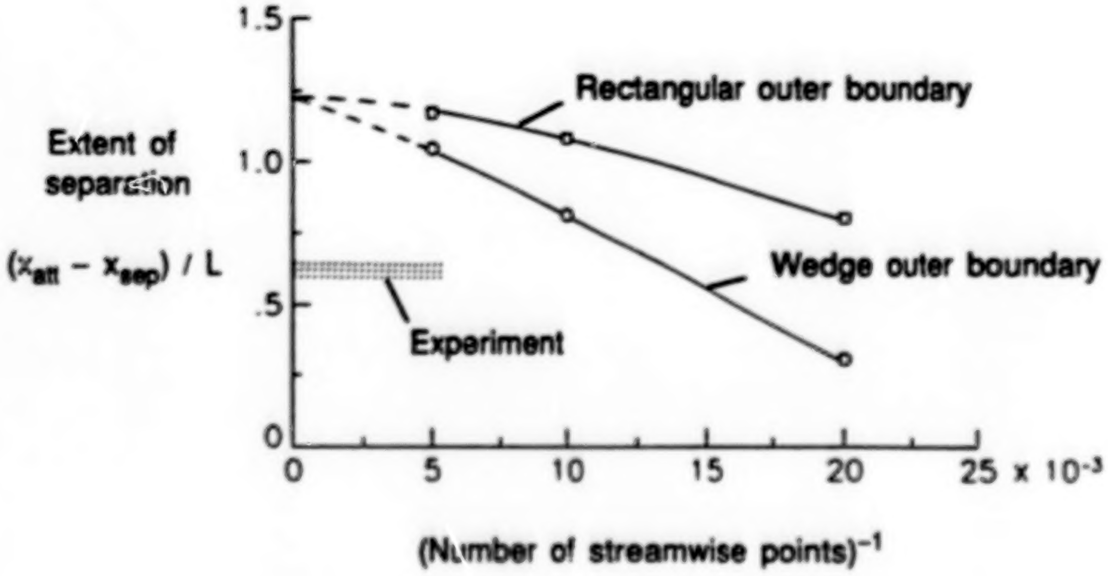

Fig. 8 Effect of grid topology and spacing on extent of separation predicted by CFL3D for 24° wedge.

Summary comparisons. Fig. 9 shows a summary comparison of the CFL3D solutions with experimental data for all three wedges. The 3-D solution in the centerplane is shown for the 24-degree wedge, and 2-D solutions are shown for both the 15- and 18-degree cases. Use of the revised experimental data in these plots eliminated the need for the angle-of-attack correction which was applied in reference 9. Excellent agreement of the calculations with experimental data was found for pressure, heat transfer, and skin friction for all three wedge angles.

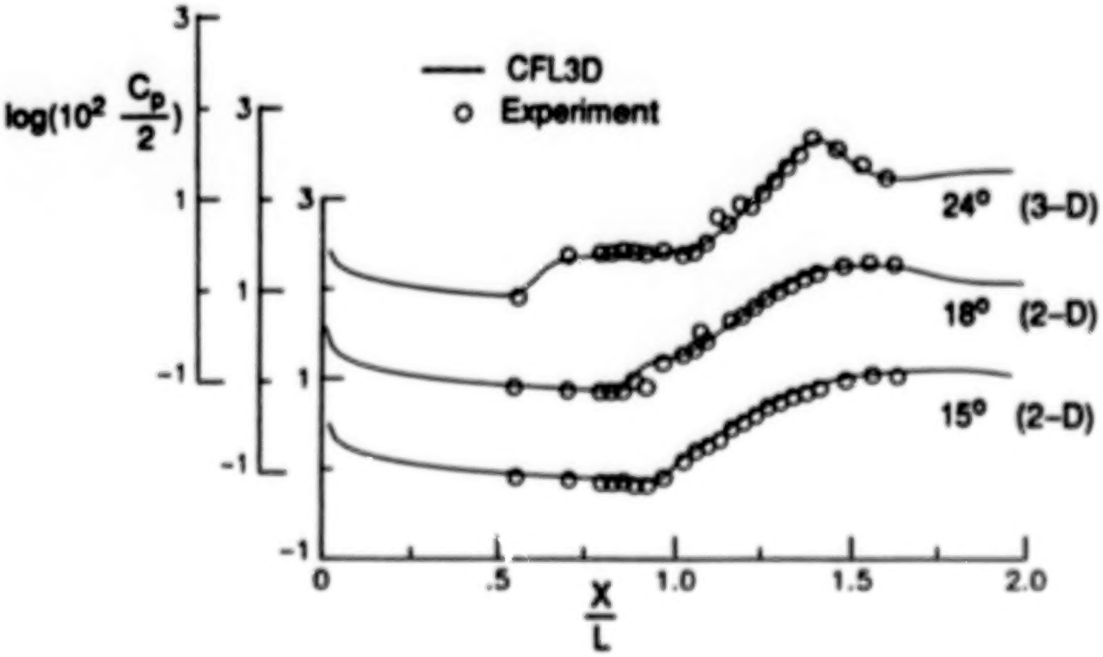

(a.) Surface pressure

Fig. 9 Summary comparison of CFL3D computations with experimental data.

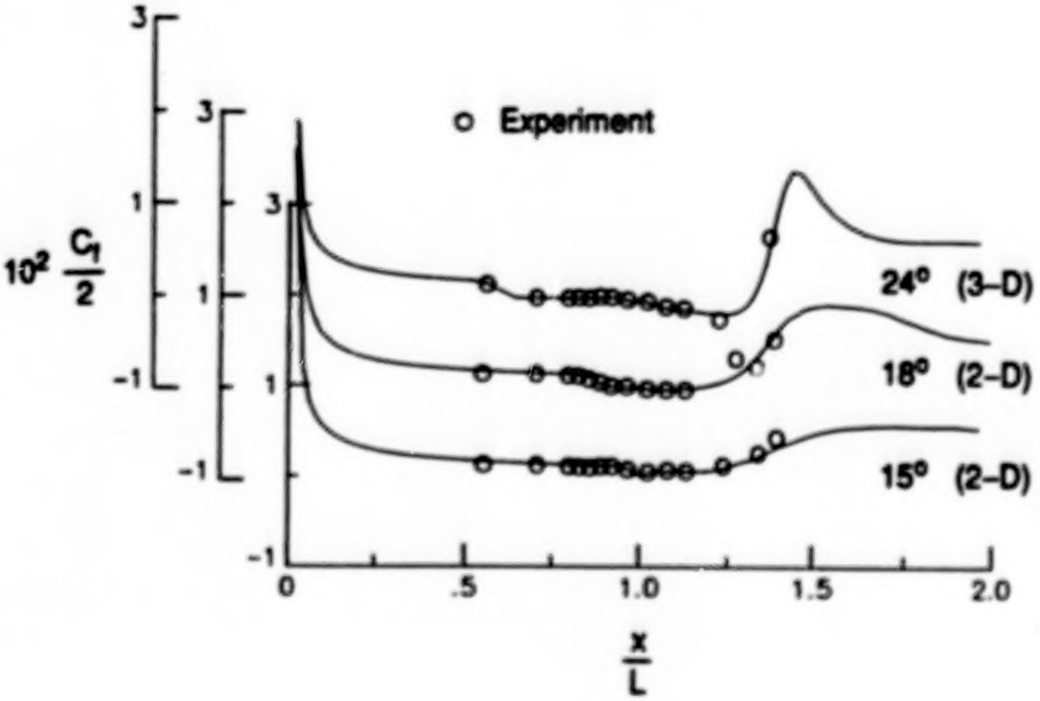

(b.) Skin friction

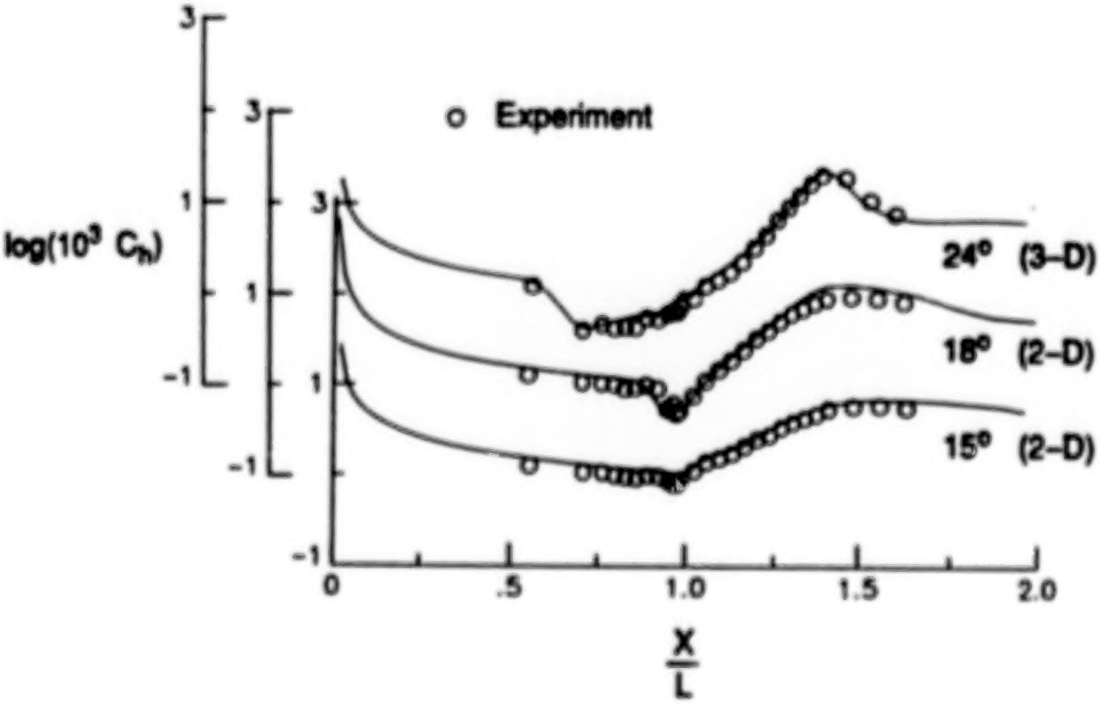

(c.) Surface heat transfer

Fig. 9 Concluded.

Shock-boundary layer interaction case

Computations were made for two of the five shock-generator-wedge angles tested by Holden at $M_\infty = 15.6$. These angles were 4.017° and 6.45°, which represent the smallest and the next-to-the-largest angles tested. The first set of calculations was made in two parts. The flow over the shock-generator wedge was computed separately using CFL3D. The shock angle obtained from this calculation was then used to specify the flow at the upper boundary of the computational domain used to compute flow over the flat plate. For $\theta = 4.017°$, computations were made using three of the codes. For $\theta = 6.45°$, computations were made using only CFL3D and USA-PG2. The grid for the flat plate had 151 points in the streamwise direction which were clustered near the leading edge of the plate and in the shock-boundary layer interaction region. The grid in the normal direction extended 3 inches above the surface of the plate and had 81 points which were clustered near the wall. For $\theta = 4.017°$, the shock angle, β, was 8°, and the shock crossed the upper boundary at the grid point at x=0.912 inches. In this case, the shock position required to properly match the experimentally-observed shock-impingement location was actually upstream of that estimated from the analysis of the computed shock-generator-wedge flow field. For $\theta = 6.45°$, the shock angle was 10.5° and the shock crossed the upper boundary at the grid point at x=6.429 inches.

A comparison of the computed surface-pressure coefficient with experimental data for both wedge angles is shown in Fig. 10. The results for the two upwind codes are virtually identical. The pressure rise in the interaction region computed by NASCRIN occurs slightly downstream of the upwind predictions. This difference is a consequence of the shock wave being introduced along the upper boundary one-half grid cell further downstream in the finite-difference method than in the upwind methods. The expansion downstream of the interaction region is not predicted for either wedge angle by any of the methods.

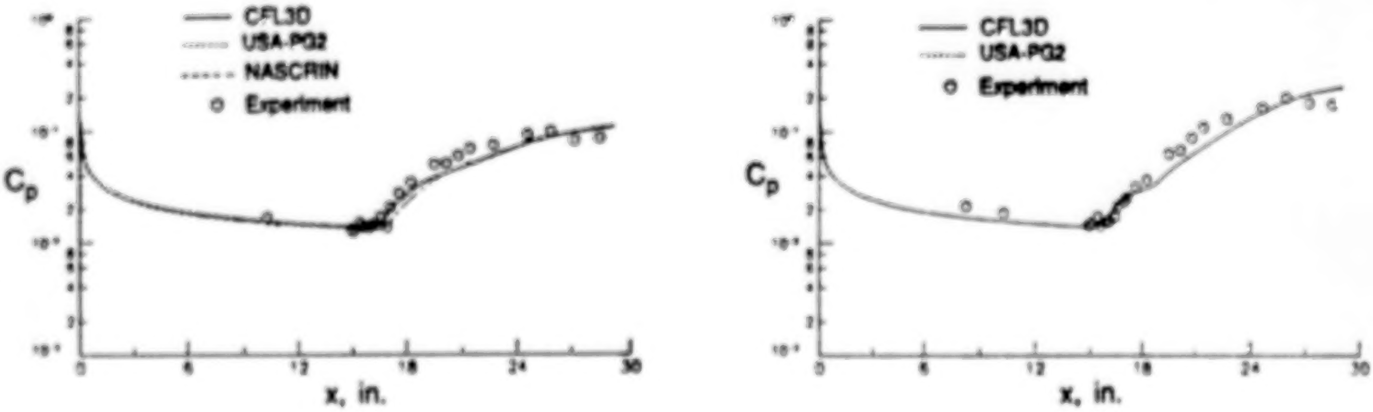

(a.) $\theta = 4.017°$

(b.) $\theta = 6.45°$

Fig. 10 Comparison of computed and experimental surface pressure for shock-boundary layer interaction.

Computations were also made using CFL3D which included the flow over the shock generator wedge as well as the flow over the plate as part of a single simulation. The grid for this case is shown in Fig. 11(a). The grid over the flat plate remained the same as in the previous calculations, and the grid near the wedge contained the same amount of clustering in the normal direction as the grid near the plate. The grid contained 191 points in the streamwise direction and 151 points in the normal direction. The upper boundary downstream of the trailing edge of the shock generator wedge was simulated as a flat plate parallel to the free-stream flow. Contours of pressure and Mach number for the $\theta = 6.45^\circ$ simulation are shown in Figs. 11(b) and (c), respectively. The pressure contours illustrate the intersection of the wedge and flat-plate leading-edge shocks as well as the interaction of the wedge shock with the flat-plate boundary layer. The Mach-number contours highlight the boundary-layer development and the shock waves and also indicate a separation zone in the interaction region on the lower flat plate. The corresponding calculation for the case with $\theta = 4.017^\circ$ produced a wedge shock which impinged on the flat-plate boundary layer downstream of the measured impingement, consistent with the observation noted above for the specified-shock calculations. To match the experimentally-observed impingement location, the height of the trailing edge of the shock-generator wedge above the flat plate was changed from the value of 3.625 inches reported for the experimental configuration to 3.242 inches.

Fig. 12 shows a comparison of the surface-pressure coefficient for the specified-shock calculation and the complete flow-field simulation using CFL3D for $\theta = 6.45^\circ$. The only difference between the two results occurs downstream of the interaction where the complete simulation captures the expansion produced by the flow from the trailing edge of the generator wedge.

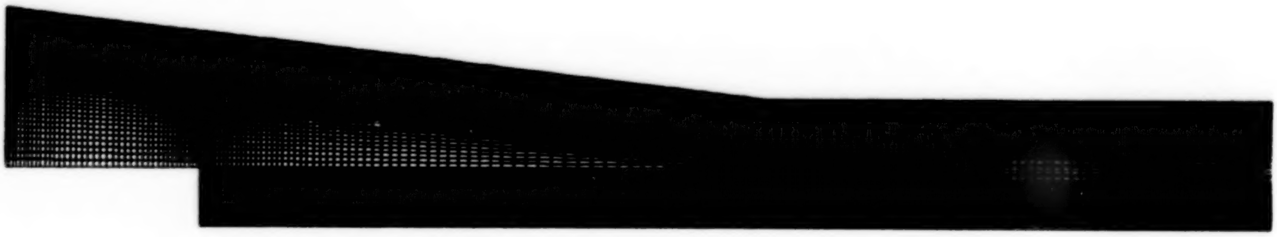

(a.) Grid

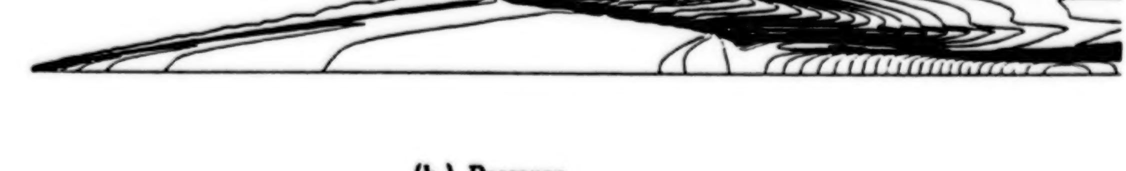

(b.) Pressure

Fig. 11 Grid and computed flow field for CFL3D simulation of complete configuration. $\theta = 6.45^\circ$.

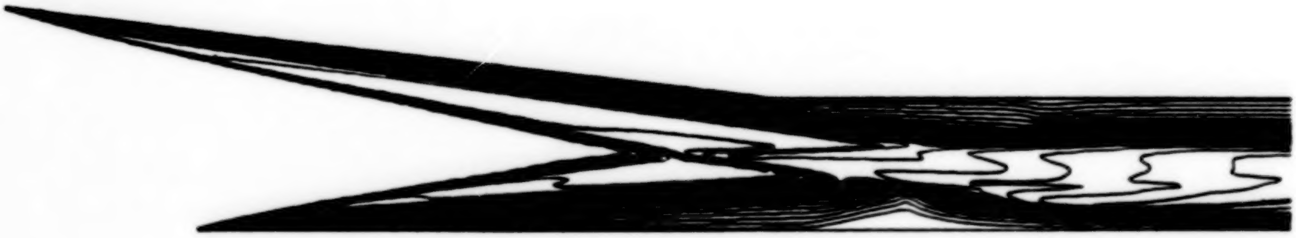

(c.) Mach number

Fig. 11 Concluded

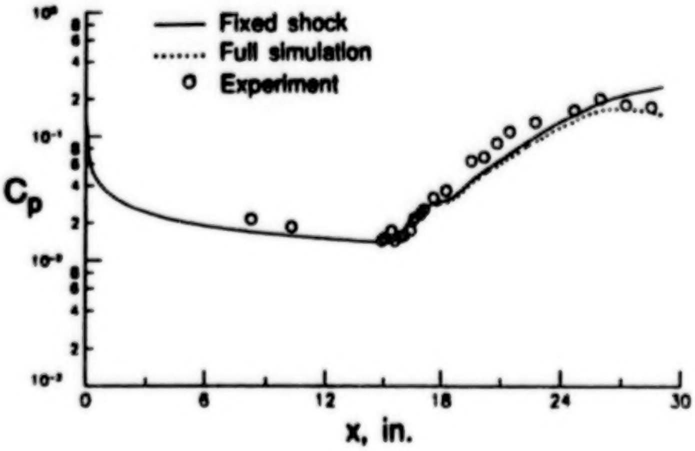

Fig. 12 Comparison of fixed-shock and complete flow-field CFL3D computations. $\theta = 6.45°$.

CONCLUDING REMARKS

Computations for a series of nominally two-dimensional high-speed laminar separated flows were compared with detailed experimental shock-tunnel results. The shock wave-boundary layer interactions considered were induced by a compression ramp in one case and by an externally-generated incident shock in the second case. In general, good agreement was reached between the grid-refined calculations and experiment for the incipient- and small-separation conditions. For the most highly separated flow, three-dimensional calculations which included the finite-span effects of the experiment were required in order to obtain agreement with the data. The finite-span effects were important in determining the extent of separation as well as the time required to establish the steady-flow interaction.

REFERENCES

1. Vatsa, V. N., Thomas, J. L. and Wedan, B. W., "Navier-Stokes Computations of Prolate Spheroids at Angle of Attack," AIAA Paper 87-2627CP (1987).

2. Chakrarthy, S. R., Ssema, K.-Y., Goldberg, U., Gorski, J. J. and Osher, S., "Application of a New Class of High Accuracy TVD Schemes to the Navier-Stokes Equations," AIAA Paper 85-0165 (1985).

3. Gnoffo, Peter. A., "Upwind-Biased, Point-Implicit Relaxation Strategies for Viscous Hypersonic Flow," AIAA Paper 89-1972CP (1989).

4. Kumar, A., "Numerical Simulation of Scramjet Inlet Flow Fields," NASA TP-2517 (1986).

5. Kumar, A., "User's Guide for NASCRIN - A Vectorised Code for Calculating Two-Dimensional Supersonic Internal Flow Fields," NASA TM-85708 (1984).

6. MacCormack, R. W., "The Effect of Viscosity in Hypervelocity Impact Cratering," AIAA Paper 69-354 (1969).

7. Holden, M. S. and Moselle, J. R., "Theoretical and Experimental Studies of the Shock Wave-Boundary Layer Interaction on Compression Surfaces in Hypersonic Flow," ARL 70-0002 (1970).

8. Holden, M. S., "A Study of Flow Separation in Regions of Shock Wave-Boundary Layer Interaction in Hypersonic Flow," AIAA Paper 78-1169 (1978).

9. Rudy, D. H., Thomas, J. L., Kumar, A., Gnoffo, P. A. and Chakravarthy, S. R., "A Validation Study of Four Navier-Stokes Codes for High-Speed Flows," AIAA Paper 89-1838 (1989).

10. Putnam, L. E., "Investigation of Effects of Ramp Span and Deflection Angle on Laminar Boundary-Layer Separation at Mach 10.03," NASA TN D-2833 (1965).

11. Thareja, R. R., Prabhu, R. K., Morgan, K., Peraire, J., Peiro, J. and Soltani, S., "Applications of an Adaptive Unstructured Solution Algorithm to the Analysis of High Speed Flows," AIAA Paper 90-0395 (1990).

TWO AND THREE-DIMENSIONAL SHOCK-SHOCK INTERACTIONS ON THE BLUNT LEADING EDGES OF THE HYPERSONIC INLETS

D. J. Singh*
Old Dominion University
Norfolk, VA

A. Kumar†
NASA Langley Research Center
Hampton, VA

S. N. Tiwari‡
Old Dominion University
Norfolk, VA

ABSTRACT

The effect of shock impingement on the blunt leading edges of the top and the sidewall compression type inlet of a scramjet engine is investigated numerically. The impinging shock is caused by the vehicle forebody. The interaction of this forebody shock with the inlet leading edge shock results in a very complex flowfield containing local regions of high pressure and intense heating. In the present investigation, this complex flowfield is calculated by solving the Navier-Stokes equations using a finite-volume flux splitting technique due to van Leer. To resolve the finer details of the flow structure as well as to predict the surface heat transfer accurately, adaptive grid technique is used in the analysis. Results of the present numerical investigation are compared with available experimental results.

NOMENCLATURE

a = speed of sound
e = total energy per unit volume
E, F, G = inviscid fluxes
E_v, F_v, G_v = viscous flux
J = transformation Jacobian
k = coefficient of thermal conductivity
M = Mach number
Pr = Prandtl number
P = pressure
Q = Conserved Variables
q = heat transfer

---

*Graduate Research Assistant, Department of Mechanical Engineering and Mechanics. Present Affiliation: Analytical Systems and Material Inc., Hampton, VA.

†Head, Theoretical Flow Physics Branch, Fluid Mechanics Division.

‡Eminent Professor, Department of Mechanical Engineering and Mechanics.

Re = Reynolds number
Rn = nose radius
t = time
T = temperature
γ = ratio of specific heats
δ = shock angle
θ = angular position on the body
Λ = sweep angle
ξ, η, ζ = curvilinear coordinates
ρ = density
τ = viscous shear stress

Subscripts

aw = adiabatic wall
D = diameter
s = stagnation line conditions
w = wall conditions
∞ = freestream conditions

INTRODUCTION

In order to properly design the high speed inlets, it is necessary to perform a detailed flowfield analysis under all plausible circumstances. One of the concerns in the inlet design is the possibility of forebody shock interaction with the shocks generated by the blunt leading edges of the inlet compression surfaces (Fig. 1). These interactions cause a very complex flowfield and can result in large increase in pressure and heat transfer over a local region. The large temperature gradients cause thermal stresses which could result in structural failure. In order to relieve the influence of thermal stresses, some form of active cooling is needed. To determine the cooling requirements, pressure and heating rates on the body need to be predicted accurately.

In the present investigation, the interaction of forebody shock with the top wall and the swept sidewall compression inlets is studied. The effect of shock impingement on the cowl of a topwall compression inlet is investigated first. This kind of interaction can be studied using a two-dimensional analysis. The use of full Navier Stokes equations with the solution adaptive grid is made to calculate the flow field. The sidewall compression inlets are investigated next. These inlets have swept back sidewalls to allow for flow spillage. The interaction of forebody shock with the inlet sidewalls produces a fully three-dimensional flowfield due to orientation of the impinging shock as well as sweep of the inlet sidewalls. The three-dimensional thin-layer Navier-Stokes equations are used to calculate this interaction. The cowl and the inlet sidewalls are modeled by two-and three-dimensional blunt wedges respectively. The forebody shock is modeled by a planar shock generated by a sharp wedge. The physical models used to study the shock - shock interactions on the topwall and the sidewall compression inlets are shown in Figs. 2 and 3, respectively.

Edney [1] was the first to study the interaction effects experimentally. He described six types of interaction patterns depending upon the location and strength of the impinging shock. Keyes and Hains [2] continued the work of Edney for higher Mach numbers and a wide range of Reynolds number. Several investigators [3] - [15] have studied the two-dimensional shock-shock interaction on the cowl leading edge. Wieting [3]conducted an experimental study on the shock wave interference over a cylindrical leading edge at Mach 6.3, 6.5 and 8.0. Several semi-empirical approaches have been proposed to theoretically predict the peak heating and pressure (Refs. [4] - [8]) but they rely on several empirical inputs such as the length of transmitted shock which must be known apriori. There are very few numerical studies available due to the complexity of the problem. Tannehill et al. [9,10] presented the first successful numerical simulation of the interaction problem based on the explicit MacCormack method. White [11] solved this problem using the Reynolds-averaged Navier-Stokes equations (based on an implicit finite-volume method) and obtained results for Mach 6.0. Klopfer [12] conducted an extensive study for various Mach numbers using the second-order implicit TVD algorithm. Perry et al. [13] used the Roe scheme to solve the Type IV interactions but did not give any heat transfer results. Moon [14] provided the results for the Type III interference pattern. The study indicated that the flow for this type of interaction in the impingement region is turbulent rather than laminar. Singh et al. [15] solved the flow around complete cowl lip including the downstream effects of shock-shock interactions into the inlet. van Leer's flux vector splitting technique was used to solve the Navier-Stokes equations on the cowl forebody and the parabolized Navier-Stokes equations on the cowl afterbody. In order to properly resolve the gradients, the adaptive grids were used.

The first systematic study of shock interaction heating in supersonic flows up to Mach 5.5 on swept and unswept fins was conducted by Newlander [16] and Carter and Carr [17]. These studies showed the heating enhancements up to 10 times the stagnation line heating for unimpinged case. Beckwith [18] and Bushnell [19] measured the heating rates on a swept cylinder close to its junction with a wedge. Glass et al. [20] investigated the effects of cowl sweep by creating a quasi-two-dimensional flow by sweeping the interaction zone. The axis of impinging shock was aligned parallel to the axis of the cylinder similar to the two-dimensional case [3]. Due to sweep, the component of flow normal to the body decreases and hence the peak values of pressure and heat transfer decrease. Holst et al. [21] conducted the first numerical simulation of full three-dimensional shock-shock interaction problem on an infinite cylinder using the explicit MacCormack scheme. The viscosity was assumed to be an order of magnitude higher than normal to physically thicken the boundary layer. A very coarse grid of 21x21x41 was employed. It gave the first insight of the difficulties associated with numerical simulation of such a complex flow. Due to coarseness of the grid and the assumption of higher viscosity, the resulting solution was at best qualitative in nature. The end effects of the inlet/body junction are neglected and the inlet sidewall is modeled by a wedge with 5^0 compression angle. The sweep angle is 25^0 for Type V interaction and the impinging shock is generated by a sharp wedge. Results of the present investigation are compared with the available experimental results.

GOVERNING EQUATIONS AND COMPUTATIONAL PROCEDURES

The three-dimensional Navier-Stokes equations in fully conservative form can be written in the generalized coordinates as

$$\frac{\partial \hat{Q}}{\partial t} + \frac{\partial(\hat{E} - \hat{E}_v)}{\partial \xi} + \frac{\partial(\hat{F} - \hat{F}_v)}{\partial \eta} + \frac{\partial(\hat{G} - \hat{G}_v)}{\partial \varsigma} = 0 \qquad (1)$$

The inviscid and viscous flux vectors in generalized coordinate system are defined as

$$\hat{Q} = \frac{1}{J}\begin{bmatrix} \rho \\ \rho u \\ \rho v \\ \rho w \\ e \end{bmatrix}, \quad \hat{E} = \frac{1}{J}\begin{bmatrix} \rho U \\ \rho U u + \xi_x p \\ \rho U v + \xi_y p \\ \rho U w + \xi_z p \\ (e+p)U \end{bmatrix}, \quad E_v = \frac{1}{J}\begin{bmatrix} 0 \\ \xi_x\tau_{xx} + \xi_y\tau_{xy} + \xi_z\tau_{xz} \\ \xi_x\tau_{yx} + \xi_y\tau_{yy} + \xi_z\tau_{yz} \\ \xi_x\tau_{zx} + \xi_y\tau_{zy} + \xi_z\tau_{zz} \\ \xi_x b_x + \xi_y b_y + \xi_z b_z \end{bmatrix}$$

$$\hat{F} = \frac{1}{J}\begin{bmatrix} \rho V \\ \rho V u + \eta_x p \\ \rho V v + \eta_y p \\ \rho V w + \eta_z p \\ (e+p)V \end{bmatrix}, \quad F_v = \frac{1}{J}\begin{bmatrix} 0 \\ \eta_x \tau_{xx} + \eta_y \tau_{xy} + \eta_z \tau_{xz} \\ \eta_x \tau_{yx} + \eta_y \tau_{yy} + \eta_z \tau_{yz} \\ \eta_x \tau_{zx} + \eta_y \tau_{zy} + \eta_z \tau_{zz} \\ \eta_x b_x + \eta_y b_y + \eta_z b_z \end{bmatrix}$$

$$\hat{G} = \frac{1}{J}\begin{bmatrix} \rho W \\ \rho W u + \varsigma_x p \\ \rho W v + \varsigma_y p \\ \rho W w + \varsigma_z p \\ (e+p)W \end{bmatrix}, \quad G_v = \frac{1}{J}\begin{bmatrix} 0 \\ \varsigma_x \tau_{xx} + \varsigma_y \tau_{xy} + \varsigma_z \tau_{xz} \\ \varsigma_x \tau_{yx} + \varsigma_y \tau_{yy} + \varsigma_z \tau_{yz} \\ \varsigma_x \tau_{zx} + \varsigma_y \tau_{zy} + \varsigma_z \tau_{zz} \\ \varsigma_x b_x + \varsigma_y b_y + \varsigma_z b_z \end{bmatrix}$$

where U, V, and W are contravarient velocities and are given as,

$$U = \xi_x u + \xi_y v + \xi_z w$$
$$V = \eta_x u + \eta_y v + \eta_z w$$
$$W = \varsigma_x u + \varsigma_y v + \varsigma_z w$$

and

$$b_{x_i} = u_j \tau_{x_i x_j} - \dot{q}_{x_i} \tag{2}$$

The cartesian velocity components are u, v, and w in the x, y, and z directions, respectively. The pressure p is related to the conserved variables through the ideal gas law

$$p = (\gamma - 1)[e - \rho(u^2 + v^2 + w^2)/2] \tag{3}$$

The equations are nondimensionalized in terms of freestream density and speed of sound. The chain rule is used to evaluate the derivatives with respect to (x,y) in terms of (η, ς). The cell volume is 1/J and the surface area of the cell in the η direction is $|\Delta\eta|/J$. The Stokes hypothesis, $\lambda = -\frac{2}{3}\mu$, is used for the bulk viscosity, and the viscosity is evaluated by using the Sutherland's law. The equations were suitably modified for two-dimensional analysis and are given in Ref. [15]. Also, for the three-dimensional analysis the viscous terms in streamwise and crossflow directions (E_v and F_v) were dropped to obtain the thin-layer Navier-Stokes equations.

An implicit, second-order accurate, upwind biased finite-volume scheme developed by Thomas et al. [22] is used to solve the Navier-Stokes equations. The flux vector splitting of van Leer is used for the inviscid part and the viscous terms are centrally differenced. The method is second order accurate in space and first order accurate in time. Beam and Warming [23] type approximate factorization is used to solve the system of equations in two sweeps. The algorithm is described in Refs. [22] and [24].

The wall pressure and heat transfer are nondimensionalized with respect to the unimpinged stagnation point(line) values. For two-dimensional calculations, the unimpinged stagnation values were calculated numerically while for the three-dimensional case they were obtained by approximate correlations in order to be consistent with Ref. [2]. The unimpinged stagnation line pressure is obtained by the Rayleigh-pitot formula as

$$\frac{p_s}{p_\infty} = (\frac{6M_1^2}{5})^{\frac{7}{2}}(\frac{6}{7M_1^2 - 1})^{\frac{5}{2}} \tag{4}$$

where M_1 is the normal Mach number. The stagnation line heat transfer is obtained by the following expression developed by Beckwith and Gallagher [18]

$$q_s = k_\infty \frac{T_{aw} - T_w}{2D}(\frac{2Re_{D,\infty}\mu_s}{M_\infty \mu_\infty})^{\frac{1}{2}}\left[\frac{2T_\infty p_s}{\gamma T_s p_\infty}(\frac{p_s}{p_\infty} - 1)\right]^{\frac{1}{4}} \tag{5}$$

where

$$T_{aw} = T_e(1 + r\frac{\gamma - 1}{2}M_e^2)$$

here r is the recovery factor and is taken as 0.85 and subscript e denotes the boundary layer edge conditions.

The inflow boundary is divided into two parts: freestream conditions are maintained at all grid points above the impingement point (line). For all points below the impingement point (line), the conditions are calculated by Rankine-Hugoniot relations for the given freestream Mach number and the impinging shock angle. The outflow conditions are obtained by first order extrapolation. Along the wall, zero slip, isothermal wall, and zero pressure gradient conditions are imposed.

GRID

The first step in any numerical solution is the discretization of the governing equations from continuous domain to a set of discrete points. The choice of grid points is not an arbitrary one but is governed by the physics of the problem. Since the computer memory and speed limits the number of grid points, it is very crucial to make best use of the available resources. The grid points should conform to the boundaries and be concentrated in the regions of high gradients, such as shocks, boundary layer etc., in order to properly resolve the flow field. They must also be oriented in such a way that the grid is as nearly orthogonal as possible. Since the shock capturing algorithm was employed, the outer boundary was chosen in such a way that there were sufficient number of points between the shock and the outer boundary. The grid points were clustered normal to the body using the exponential stretching. Since heat transfer and skin friction coefficients are very strong function of grid spacing, it is very important to properly resolve the gradients. For impingement case, the distorted bow shock moves closer to the body on one side and away on the other side; thus a large number of grid points is wasted. Near the impingement point, the grid is too coarse to capture finer details of the flow. To alleviate this problem, an adaptive grid system was employed which adapts the grids during the course of the solution in order to follow the developing gradients in the physical solution. The grid points move as the solution develops, concentrating the points where they are needed the most. The total number of points were kept constant. For this, the method developed by Abolhassani et al. [25] was used. It is a very general method with capability to adapt the grids with various variables such as pressure, Mach number, shear stress etc. and is based on variational approach. It is an algebraic method and is formulated in such a way that there is no need for matrix inversion, which makes it computationally very efficient. Since the solution varies predominantly in normal direction, the grid is adapted in only one direction.

RESULTS AND DISCUSSION

The numerical scheme discussed previously has been used to compute the two-and three-dimensional shock-shock interactions on the inlet leading edge of a scramjet engine. As mentioned earlier, only Type IV interaction is considered for the topwall compression inlet since it is the most severe case in terms of pressure and heating rates on the surface. The freestream conditions used are given in Table 1; these were selected due to the availability of the experimental data. The results for the two-dimensional case are discussed first, followed by the three-dimensional results. For all cases, the undisturbed blunt body flow was calculated first and this solution was then used as initial condition for shock impingement calculations.

A schematic of the Type IV interaction is shown in Fig. 4. This type of interaction occurs when the impinging shock strikes the leading edge shock (bow shock) near the stagnation zone, where the shock is nearly normal. This produces a supersonic jet bounded by two shear layers and submerged in subsonic flow. Near the body, it produces jet bow shock and stagnation zone when it strikes the body. This produces a very complex flow field with presence of shocks, shear layers and the jet. Type IV interaction is the most severe case and produces the largest amplification of heating and pressure.

Figure 5 shows the grid used to compute the cowl forebody flowfield. The outer boundary of the computational domain has been adapted to the distorted bow shock, which was obtained by coarse mesh calculations. Since the shock capturing algorithm has been used, the outer boundary was moved far enough to avoid shock interaction with the outer boundary. Due to poor comparison of heating rates and smearing of important flow features, [15], it was decided to use adaptive grids thereby placing the grid points where they are needed the most. Body curvature, pressure and density were chosen as weight functions to adapt the grid to the solution. The body curvature clusters the grid points very close to the body while pressure and density attract the grid points near shocks and shear layers. Thirty percent of the points were allocated for adaption by body curvature, forty percent by pressure and density and the rest were used for creating uniformity of the grid so that the grid is not too coarse in any section.

Temperature and Mach number contours are shown in Figs. 6 and 7, respectively. The distorted bow shock is clearly evident in the figures. The bow shock has moved toward the body on the windward side and away from it on the leeward side. Here windward side is defined as the upper side where the flow passes through the impinging shock before encountering the body. The interaction of the bow shock and the impinging shock produces a supersonic jet surrounded by subsonic flow. The jet terminates with jet shocks and impinges on the body producing a local zone of very high pressure and heating rates. The stagnation point moves towards the windward side. The location of the stagnation point depends upon the strength and orientation of the impinging shock. Since the grid is fine near the shocks and shear layer, the flow features are captured very well. The location of the stagnation point, jet and shear layer orignating from the shock intersection can be seen clearly. The shear layer orignating from the stagnation zone is much thicker on the leeward side as compared to the windward side.

Figure 8 shows the velocity vectors for the cowl forebody flow. Even though the flow is at zero angle of attack, its direction is changed as it passes through the impinging shock. The shear layer on the leeward side is seen clearly orignating from the stagnation point which has moved (as compared to unimpinged case) toward the windward side.

The variation of wall pressure along the cowl forebody surface is shown in Fig. 9. The pressure is nondimensionalized by the stagnation point pressure for unimpinged blunt body flow. In order to properly visualize the effect of shock - shock interaction, the surface pressure for unimpinged blunt body flow for the same free stream conditions is also shown in the figure. The pressure on the windward side increases considerably with a localized zone of high pressure and falls below the surface pressure for unimpinged case on the leeward side. The peak value of pressure is about 9 times the stagnation point value. The results compare very well with the experimental data of Wieting [3] and numerical calculations of Klopfer [12]. It should be noted that for this case the location of the impinging shock was made to coincide with the experimental location by matching the peak pressure location.

Figure 10 shows the heat transfer along the wall on the cowl forebody. The heating rates are nondimensionalized with respect to the stagnation point heating for unimpinged case. It shows a similar behavior as the surface pressure, i.e., an increased heating on the windward side and decreased heating on the leeward side. A localized zone of intense heating is observed on the windward side. The heating rates show a remarkable improvement over the previous calculations. The results compare favorably with the experiment. The discrepancy in the peak is probably due to the unsteadiness in the flow and/or the turbulent nature of the jet as is indicated recently by Moon et al. [14]. For this case, the solution was found to be marginally unsteady as the residual did not go down more than three orders of magnitude. Also the jet oscillated slightly, thereby changing the location of the peak pressure and heating. A similar behaviour was noted for the Type IV interaction in Refs. [12] and [13].

Similar calculations were carried out for Mach 5.94 freestream conditions and the results are shown in Figs. 11 and 12. Qualitatively these results are very similar to the Mach 8.03 conditions. The grid for this case is generated in the same way as for the previous case. The variations of surface pressure and heat transfer are shown in Figs 11 and 12 respectively. The numerical results are compared with the experimental data reported by Tannehill et al. [10] from an unpublished experiment by J. W. Keyes of NASA Langley. The computed values of surface pressure agree very well with the experimental data although the peak pressure is slightly lower than the experimental peak. Although not shown here, the peak value of the pressure matches with the numerical calculations of Tannehill et al. [10]. The variation of heat transfer on the cowl forebody is shown in Fig. 12. For heating rates, the experimental data was reported only at one point. The peak value of the heating is 6.4 times the stagnation point value, which is within the uncertainty range of the experiment.

Now, the results for sidewall compression type inlets will be discussed. As mentioned earlier, the shock-shock interaction on this type of inlet results in a fully three-dimensional flowfield. The results are presented for Type V interaction only. Calculations have been performed for Type IV interaction also [26] but the flowfield didn't converge to a steady state solution. Further investigation of this case is currently underway. The freestream conditions used for the present calculations are given in Table 1.

The schematic diagram of the Type V interference on the swept inlet sidewall is shown in Fig. 13. The interaction of the two shocks of unequal strength produces a lambda shock which divides the flow into two portions separated by a contact discontinuity that begins at the nodal point of the lambda shock. The two sides have the same pressure and the flow direction but different magnitude of velocities, temperature and density across this discontinuity. Due to sweep of the body, the component of flow normal to the body reduces and hence the strength of the intersecting shocks decreases. The peak heating and the pressure impingement occurs at the point where the shear layer impinges at the surface. The peak value depends on various factors such as the Mach number, impinging shock angle, and sweep of the body.

A grid of 29x49x61 has been used which is clustered near the wall and the impingment location to resolve the boundary layer and the shear layer as shown in Fig. 14. Since the flow is symmetric about the stagnation plane, only one half of the flow is considered. As in the previous case, the outer boundary was moved far enough so as to avoid any interference between the shock and the outer boundary. No attempt was made to adapt the grids to the solution.

Figure 15 shows the temperature, Mach number and pressure contours in the stagnation plane with shock impingement. The temperature contours are shown in Fig. 15(a). Due to stretching, the grid away from the surface is coarse; consequently, the shock and the other flow features are smeared over several grid points. The impinging shock is clearly visible in the figure. The bow shock moves away from its unimpinged position and a shear layer is produced. The shear layer interacts with the boundary layer. Also, a transmitted shock is produced which strikes the body causing a jump in pressure and heating rates. These are typical features of the Type V interaction. There are temperature and density gradients across the shear layer. The Mach number contours are shown in Fig. 15(b); the flow is supersonic behind the bow shock and the shear layer can also be seen. Figure 15(c) shows the pressure contours in the stagnation plane. Since the pressure is constant across the shear layer, it is not visible in this figure. Some expansion waves can be seen emanating from the intersection point which reduce the surface pressure as the flow expands.

Figure 16 (taken from Ref. [1]) shows a cylindrical fin coated with temperature sensitive paint and the corresponding schlieren photograph locating regions of high pressure and heat transfer for Type V interference. It should be noted that the freestream conditions for this case are slightly different but it shows a typical Type V interaction. The corresponding numerical solutions are shown in Figs. 17 and 18. The surface pressure contours are shown in Fig. 17 and the stagnation plane pressure contours in Fig. 18. The numerical solution captured the first two (A and B) peaks in pressure and heat transfer. The third peak (C), caused by the flow separation near the end, is absent in the numerical solution due to the assumption of infinite length of the body. The behavior of bow shock near the impingement point is very well captured by the numerical scheme.

The comparison of Figs. 16(b) and 18 shows how well the physical phenomenon is captured by the numerical scheme.

Figures 19 and 20 show the variation of pressure and heat transfer along the surface. They are nondimensionalized with respect to the unimpinged stagnation line values. Figure 19 shows the comparison of stagnation line pressure with the experimental data of Keyes and Hains [2] and numerical calculations of Holst et al. [21]. In the experimental set up, the interaction point was only 3 cm downstream from the end of the cylinder ($z = 0$) and, therefore, there was some relieving effect (Fig. 16). But in the present calculations, the body is assumed as infinite in length and hence no relieving effect is allowed. Due to this discrepancy, the results do not match near the end. However, the results compare fairly well away from the end point. The peak value of the pressure is caused by the interaction of the transmitted shock with the boundary layer and it is very well captured. The flow overexpands and then recompresses back to the unimpinged value. The peak value of the pressure is about 2.2 times the unimpinged stagnation line pressure. The variation of the stagnation line heat transfer is shown in Fig. 20. In this case also, the comparison is poor near the end for the same reasons as explained earlier. But away from the end, results compare fairly well. As expected, the heat transfer follows the same general trend as the pressure. The peak value of heat transfer is about three times the unimpinged stagnation line heat transfer. The experimental data is available only for the stagnation plane.

The results from the present calculations show a remarkable improvement over Holst's calculations due to various factors. The flow field is much better resolved due to a finer grid and no artificial thickening of the boundary layer has been imposed. Also, in Holst's calculations, the flow variables at the $z=0$ boundary were held fixed for all time equal to the unimpinged flow solution, which is incorrect for the impinging shock case.

CONCLUSIONS

The numerical scheme mentioned previously has been used to compute the two-and three-dimensional shock-shock interaction on the inlet walls of the scramjet engine. For the topwall compression inlet(two-dimensional model) the Type IV shock-shock interaction is investigated since it is the most severe one, producing maximum increase in pressure and heating rates. To resolve the finer details of the flow, adaptive grid technique has been used. All flow features were captured by the numerical calculations and the results compare very well with the experimental data. In the case of sidewall compression type inlet (three-dimensional model), the Type V interaction is studied. In this case also the results agree very well with the experimental data.

References

[1] Edney, B. E., " Anomalous Heat Transfer and Pressure Distribution on Blunt Bodies at Hypersonic speeds in the Presence of an Impinging Shock, " Aeronautical Research Institute of Sweden, FAA Report 115, February 1968.

[2] Keyes, J. W. and Hains, F. D., " Analytical and Experimental Studies of Shock Interference Heating in Supersonic Flows, " NASA TN D-7139, May 1973.

[3] Wieting, A. R. and Holden, M. S., " Experimental Study of Shock Wave Interference Heating in Supersonic Flows, " AIAA Paper 87-1511, June 1987.

[4] Morris, D. J. and Keyes, J. W., " Computer Programs for Predicting Supersonic and Hypersonic Interference Flowfield and Heating, " NASA TM X-2725, May 1973.

[5] Keyes, J. W.and Morris, D, J., " Correlations of Peak Heating in Shock Interference Regions at Hypersonic Speeds," Journal of Spacecraft and Rockets, Vol. 9, August 1972, pp. 621-623.

[6] Bramlette, T. T., " Simple Technique for Predicting Type III and IV Shock Interference, " AIAA Journal , Vol. 2, August 1974, pp. 1151-1152.

[7] Markarian, C. F., " Heat Transfer in Shock Wave Boundary layer Interactions, " Naval Weapons Center, China Lake, California, NWC TP 4485, November 1968.

[8] Bertin, J. J., Graumann, B. W., and Goodrich, W. D., " Analysis of High Velocity and Real Gas Effects on the Shock-Interference Pattern for Delta - Wing Orbiters, " AIAA Paper 74-522, June 1974.

[9] Tannehill, J. C., Holst, T. L., and Rakich, J. V., " Numerical Computation of a Two - Dimensional Viscous Blunt Body Flows with an Impinging Shock, " AIAA Journal, Vol. 14, No. 2, February 1976, pp. 204-211.

[10] Tannehill, J. C., Holst, T. L., Rakich, J. V., and Keyes, J. W., " Comparison of a Two - Dimensional Shock Impingement Computation With Experiment, " AIAA Journal, Vol. 14, April 1976, pp. 539-541.

[11] White, J. A. and Rhie, C. M., " Numerical Analysis of Peak Heat Transfer Rates for Hypersonic Flow Over a Cowl Leading Edge, " AIAA Paper 87-1895, June 1987.

[12] Klopfer, G. H. and Yee, H. C., " Viscous Hypersonic Shock-On-Shock Interaction on Blunt Cowl Lips, " AIAA Paper 88-0233, January 1988.

[13] Perry, K. M. and Imley, S. T., " Blunt Body Flow Simulations, " AIAA Paper 88-2904, July 1988.

[14] Moon, Y. J. and Holt, M.," Interaction of an Oblique Shock with Turbulent Hypersonic Blunt Body Flows, " AIAA Paper 89-0272, January 1989.

[15] Singh, D. J., Kumar, A., and, Tiwari, S. N.,"Influence of Shock - Shock Interaction on the Flow Field at Hypersonic Flight Speeds," AIAA 89-2184, July 1989.

[16] Newlander, R. D.," Effects of Shock Impingement on the Distribution of Heat Transfer Coefficient on a Right Circular Cylinder at Mach Number of 2.65, 3.51 and 4.44, " NASA TN D-642, 1961.

[17] Carter, H. S. and Carr, R. E., " Free Flight Investigation of Heat Transfer to an Unswept Cylinder Subjected to an Incident Shock and Flow Interference From an Upstream Body at Mach number up to 5.50," NASA TN D-9909.

[18] Beckwith, I. E., "Experimental Investigation of Heat Transfer and Pressure on a Swept Cylinder in the Vicinity of its Interaction with a Wedge and Flat Plate at Mach Number 4.15 and High Reynolds Numbers, " NASA TN D-2020, 1964.

[19] Bushnell, D. M., " Interference Heating on a Swept Cylinder in Region of Intersection with a Wedge at Mach Number 8, " NASA TN D-3094, 1965.

[20] Glass, C. E., Wieting, A. R., and Holden, M. S., " Effect of leading Edge Sweep on shock-shock interference at Mach 8, " AIAA Paper 89-0271, January 1989.

[21] Holst, T. L., Tannehill, J. C., and Rakich, J. V., " Numerical Computation of Viscous Blunt Body Flows with Planer Impinging Shock," Presented at the NASA Conference on Aerodynamic Analysis Requiring Advanced Computers, March 4-6, 1975, Langley Research Center, Hampton, Virginia.

[22] Thomas, J. L. and Walters, R. W., " Upwind Relaxation Algorithms for the Navier-Stokes Equations, " AIAA Paper 85-1501, July 1985.

[23] Beam, R. M. and Warming, R. F.."An Implicit Factored Scheme for the Compressible Navier Stokes Equation,"AIAA Journal, Vol. 16, 1978, pp.393-401.

[24] Rumsey, C. L., Taylor, S. L., Thomas, J. L., and Anderson, W. K., " Application of an Upwind Navier-Stokes Code to a Two - Dimensional Transonic Airfoil Flow, " AIAA Paper 87-0413, January 1987.

[25] Abolhassani, J. S., Smith, R. E., and Tiwari, S. N., " Grid Adaption for Hypersonic Flow, " AIAA Paper 87-1169, June 1987.

[26] Singh, D. J., Kumar, A., and, Tiwari, S. N.,"Three-Dimensional Shock-Shock Interaction on the Scramjet Inlet," AIAA 90-0529, January 1990.

Table 1: Freestream conditions.

M_∞	Re_D	T_w/T_∞	Rn	δ	Type of Interaction
8.03	387500	2.382	0.076	12.5	IV (2D)
5.94	186000	6.857	0.025	15.0	IV (2D)
5.94	180000	6.611	0.025	10.0	V (3D)

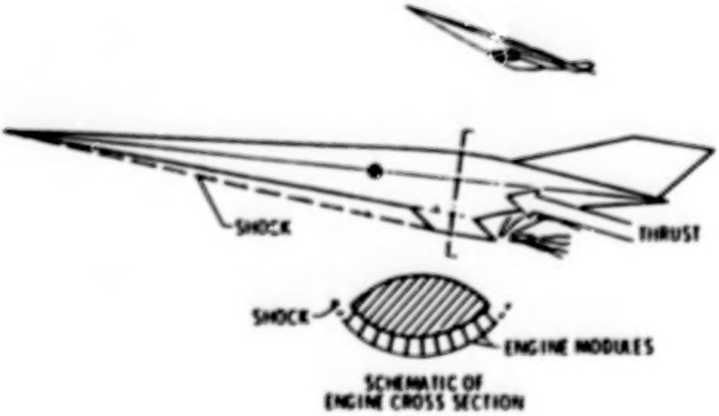

Figure 1: Airframe-integrated scramjet-engine concept.

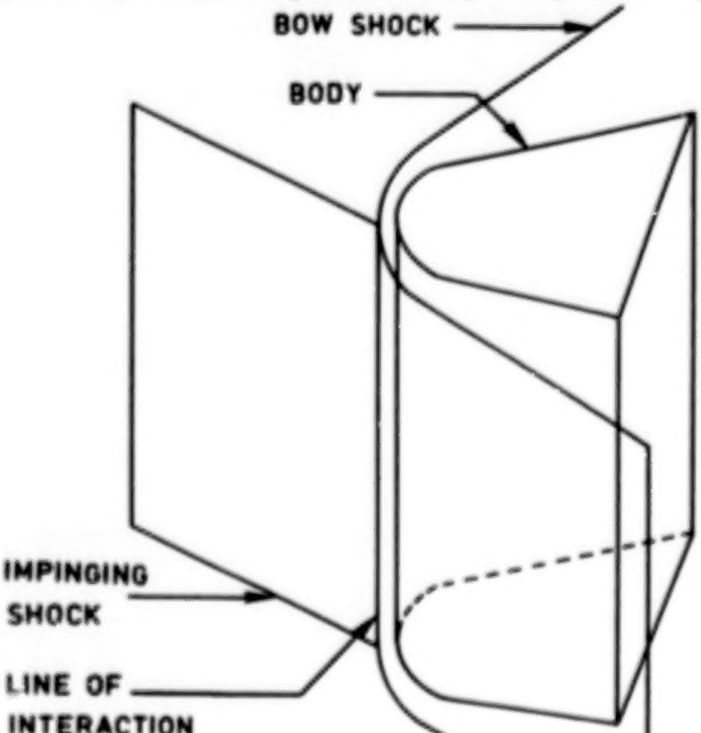

Figure 2: Physical model for shock-shock interaction on the topwall compression inlet (2D).

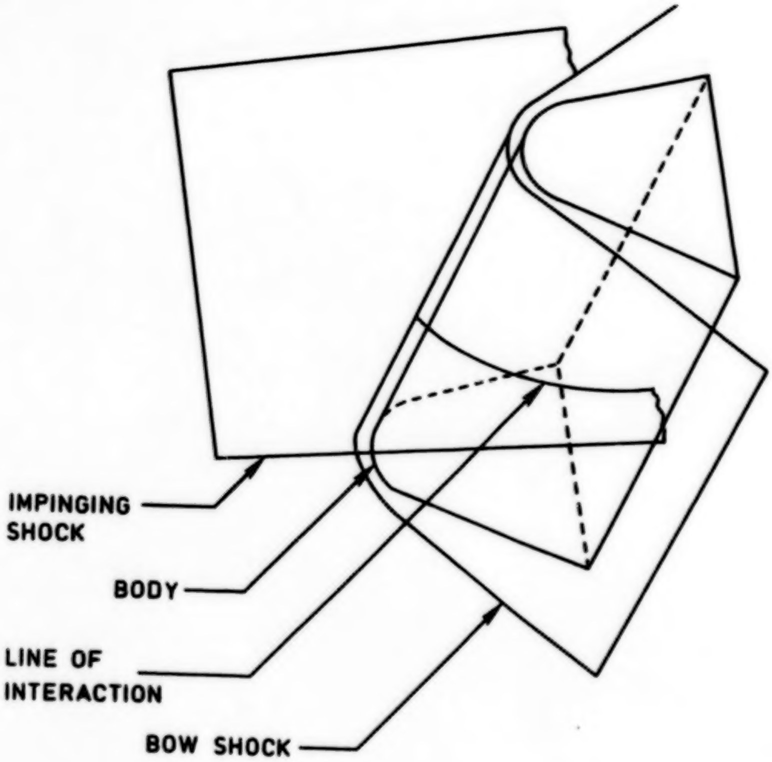

Figure 3: Physical model for shock-shock interaction on the sidewall compression inlet (3D).

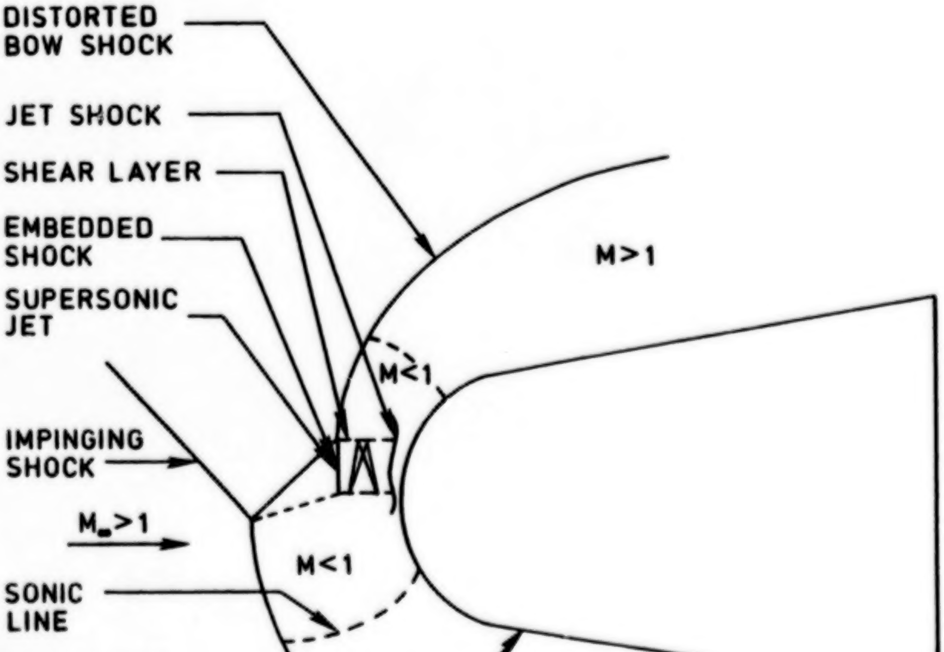

Figure 4: Schematic diagram for the Type IV interaction on the cowl.

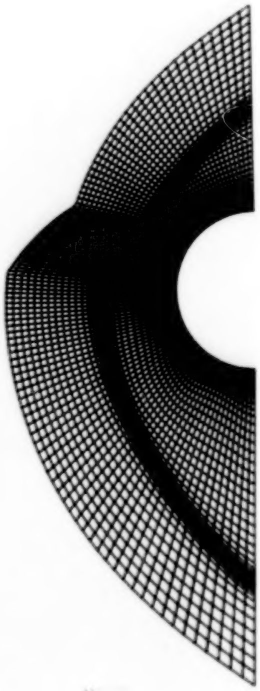

Figure 5: Cowl forebody grid for Mach 8.03 computations (adapted).

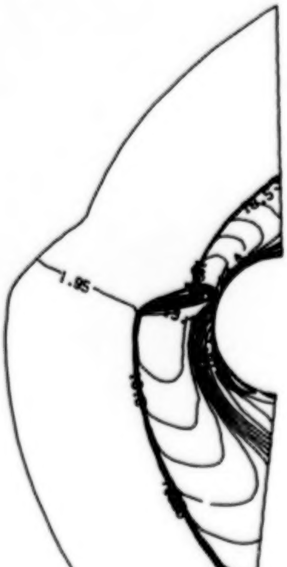

Figure 6: Temperature contours for the cowl forebody, $M_\infty = 8.03$.

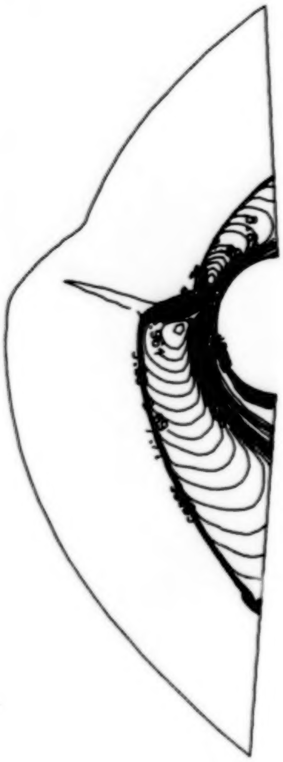

Figure 7: Mach number contours for the cowl forebody , $M_\infty = 8.03$.

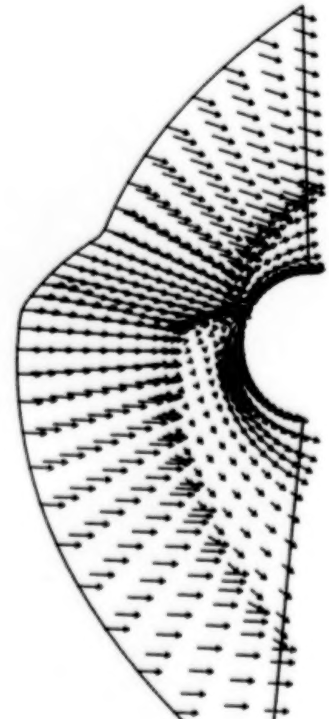

Figure 8: Velocity vectors for the cowl forebody, $M_\infty = 8.03$ with adapted grid.

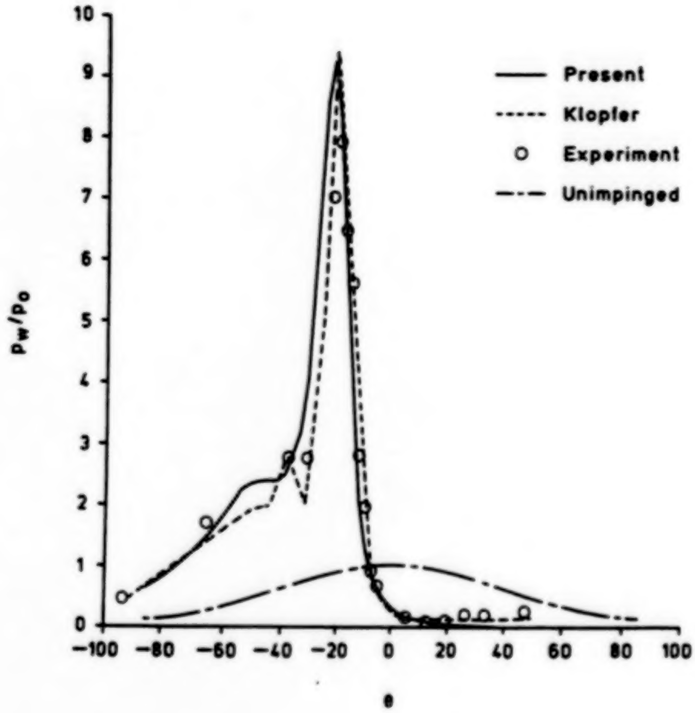

Figure 9: Variation of surface pressure for the cowl forebody, $M_\infty = 8.03$.

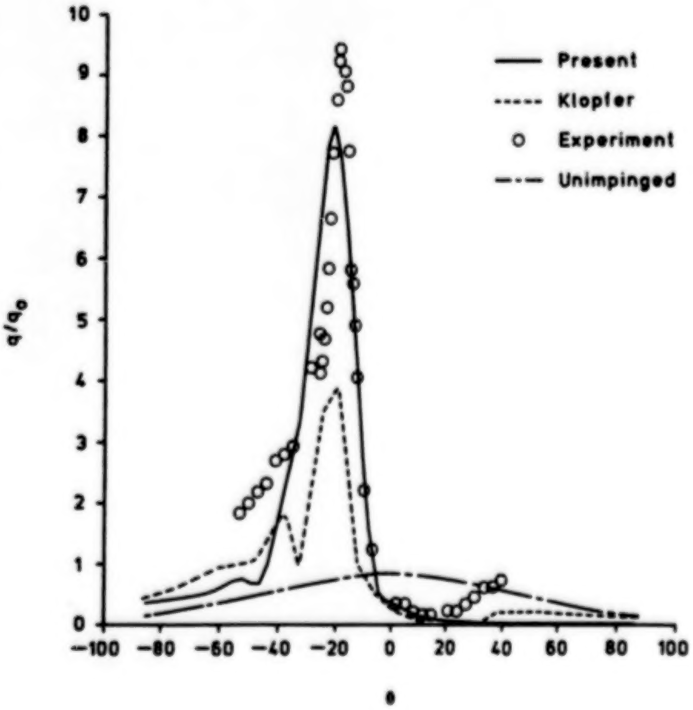

Figure 10: Variation of surface heat transfer for the cowl forebody, $M_\infty = 8.03$.

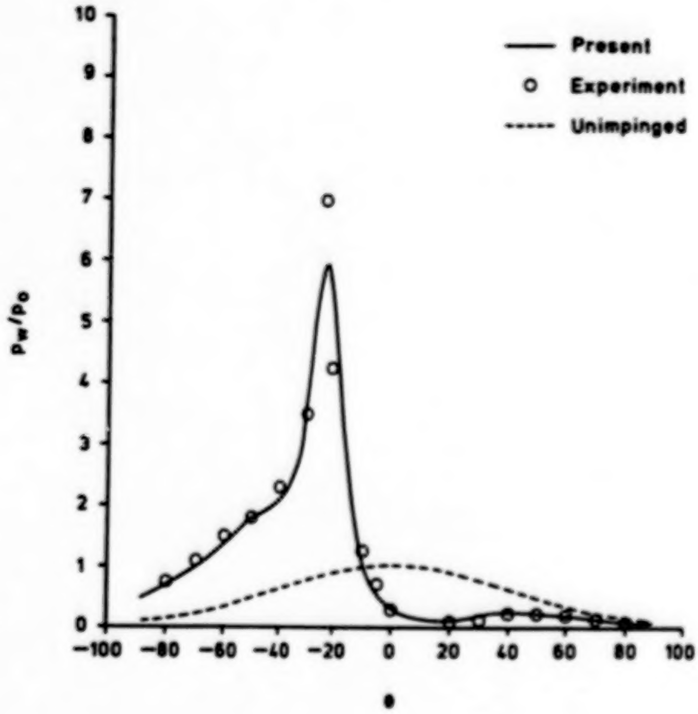

Figure 11: Variation of surface pressure for the cowl forebody, $M_\infty = 5.94$

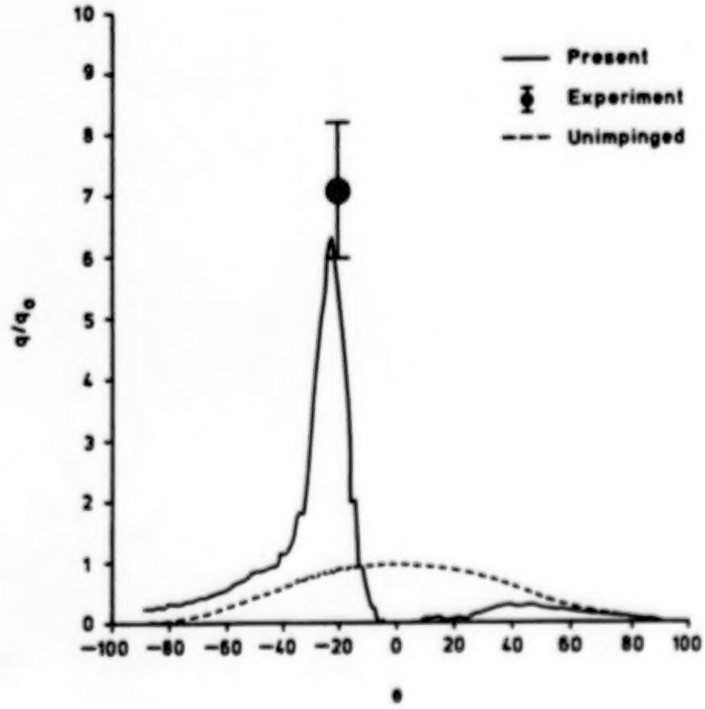

Figure 12: Variation of surface heat transfer for the cowl forebody, $M_\infty = 5.94$.

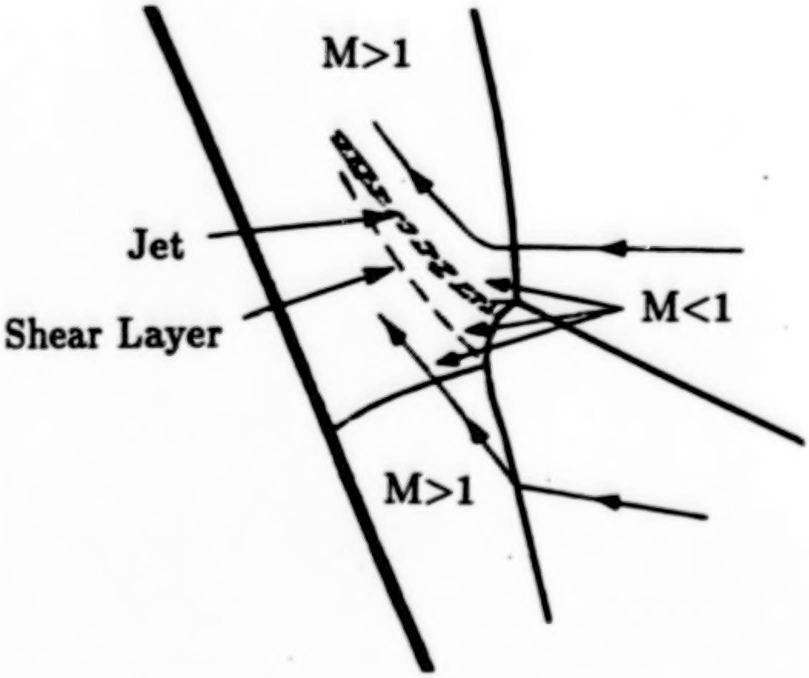

Figure 13: Schematic diagram for Type V interaction on the swept sidewall.

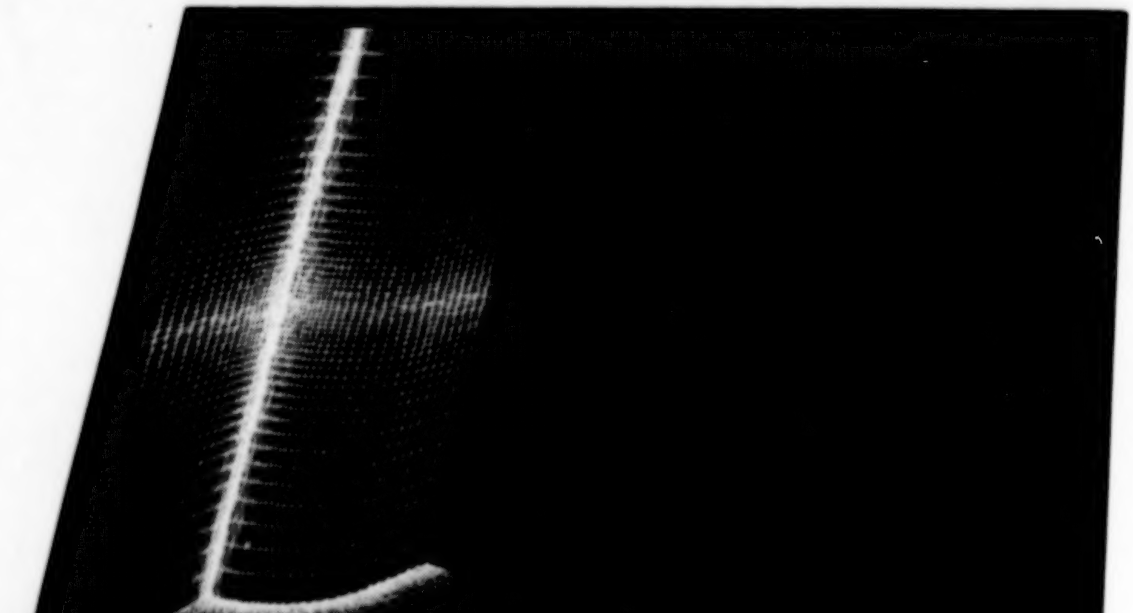

Figure 14: Grid distribution on the inlet sidewall.

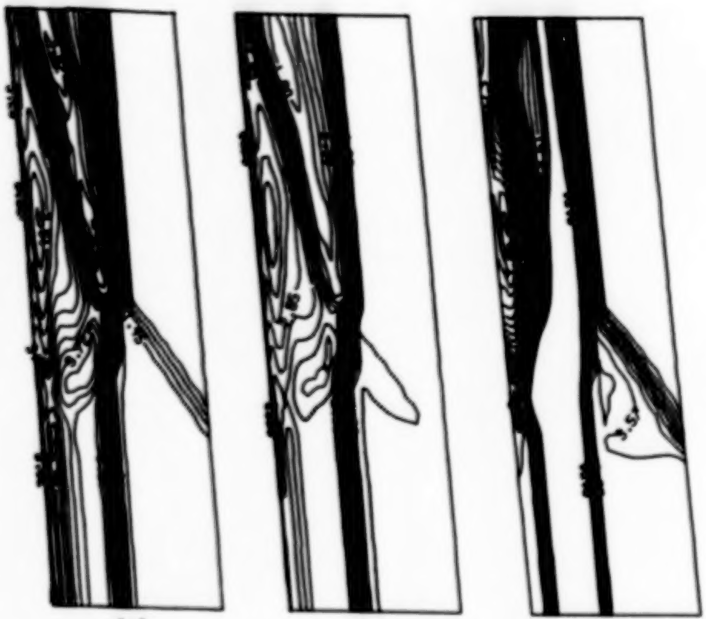

(a) Temperature

(b) Mach Number

(c) Pressure

Figure 15: Temperature, Mach number and Pressure contours in the stagnation plane.

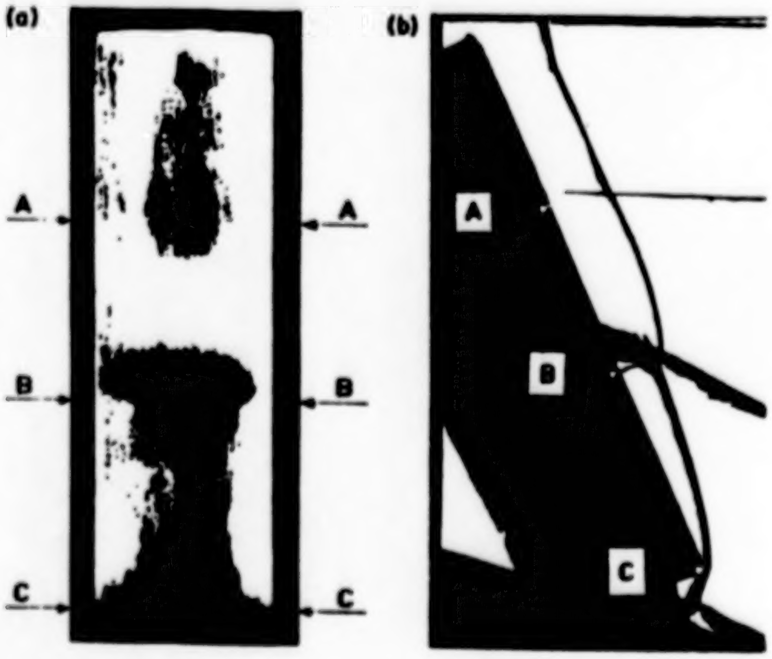

Figure 16: Local regions of high heating rates and corresponding schliern photograph (Ref. 1).

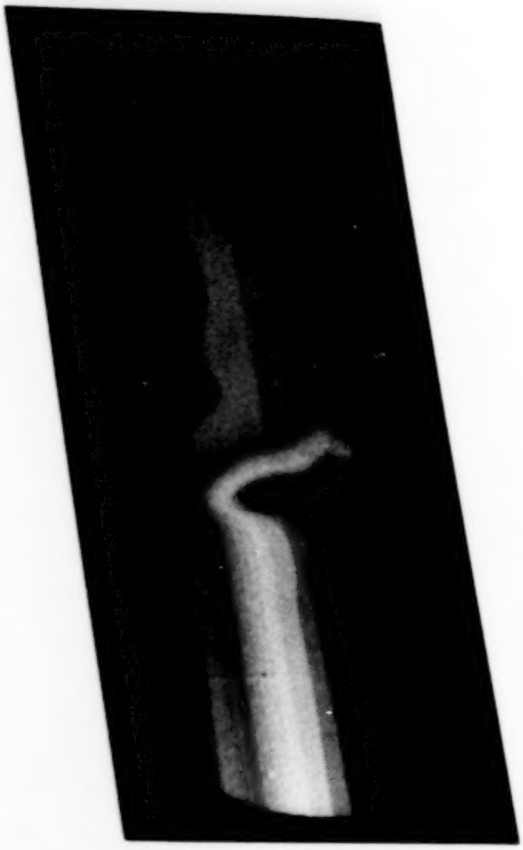

Figure 17: Surface pressure contours on the inlet sidewall.

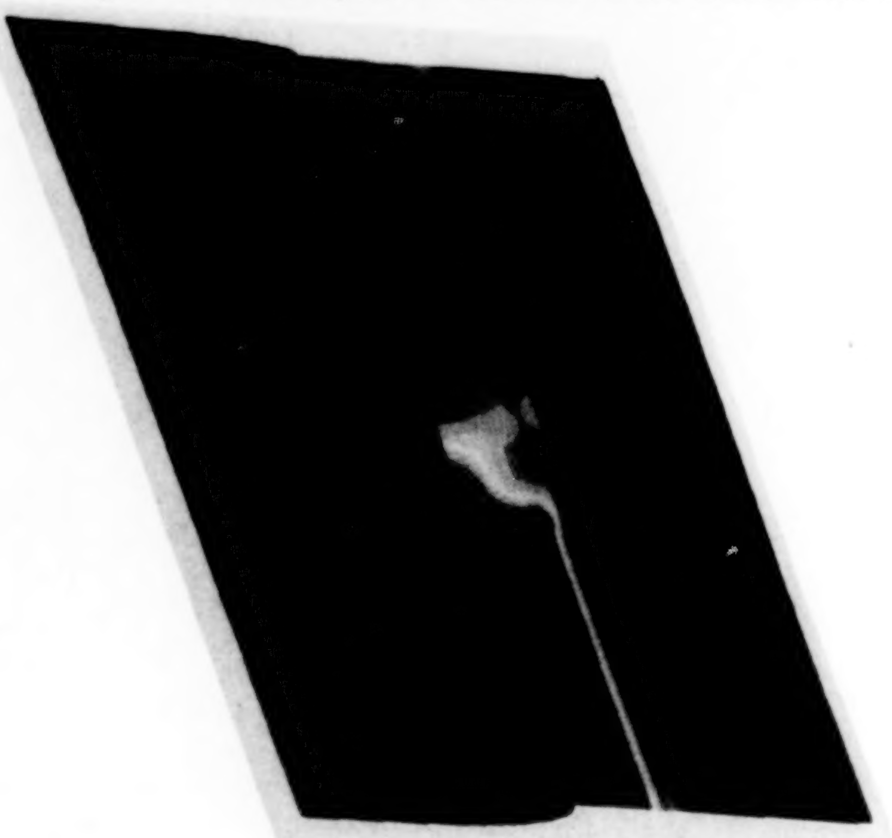

Figure 18: Pressure contours in the stagnation plane.

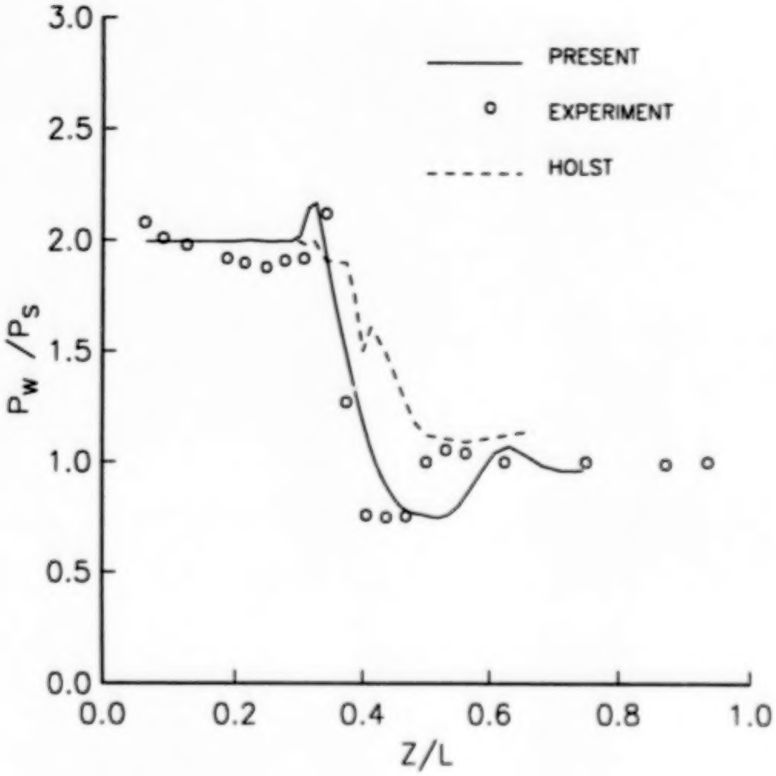

Figure 19: Comparison of surface pressure with the experimental data.

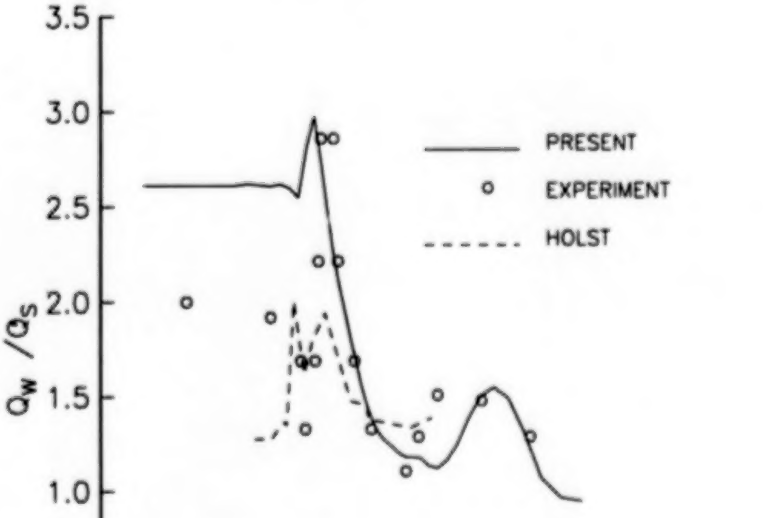

Figure 20: Comparison of surface heat transfer with the experimental data.

ZONAL ANALYSIS OF TWO HIGH-SPEED INLETS

A. D. Dilley, G. F. Switzer, and W. M. Eppard *
Analytical Services and Materials, Inc.
Hampton, VA 23666

ABSTRACT

Using a zonal technique, thin-layer Navier-Stokes solutions for two high-speed inlet geometries are presented and compared with experimental data. The first configuration consists of a three-dimensional inlet preceded by a sharp flat plate. Results with two different grids demonstrate the importance of adequate grid refinement in high-speed internal flow computations. The fine grid solution has reasonably good agreement with experimental heat transfer and pressure values inside the inlet. The other configuration consists of a three-dimensional inlet mounted on a research hypersonic forebody. Numerical results for this configuration have good agreement with experimental pressure data along the forebody, but not inside the inlet. A more refined grid calculation is currently being done to better predict the flowfield in the inlet.

INTRODUCTION

The design and analysis of hypersonic air-breathing vehicles, such as the National Aerospace Plane (NASP), requires accurate prediction of propulsion system performance. Computational Fluid Dynamics (CFD) is being challenged to play a major role in the analysis of hypersonic air-breathing vehicles, because of a lack of ground test facilities to simulate the entire hypersonic flight regime and design time constraints. Existing computational tools are therefore being refined and calibrated using existing wind tunnel data, and wind tunnel tests are planned to enlarge the available hypersonic database. Comparisons of this wind tunnel data with CFD predictions will build confidence in the ability of CFD to provide accurate performance predictions for hypersonic air-breathing vehicles.

The CFD analysis of a hypersonic air-breathing propulsion system requires analysis of the entire vehicle, because the forebody externally compresses the flow ahead of the inlet and the afterbody externally expands the flow from the nozzle. Therefore a nose-to-tail CFD capability is necessary for realistic CFD analyses of hypersonic air-breathing vehicles. In an effort to develop a nose-to-tail capability, a zonal technique has been implemented in an upwind, finite volume thin-layer Navier-Stokes solver, CFL3D (reference 1). Results from the CFL3D code have previously been compared with experimental data for hypersonic laminar and turbulent forebody flows (reference 2), turbulent flow in a two-dimensional hypersonic inlet (references 3 and 4) and hypersonic laminar flows with inviscid/viscous interaction (reference 5). The zonal or patched grid approach was used by Thomas *et al* (reference 4) in the analysis of turbulent flow in several two-dimensional hypersonic inlets. The zonal approach allows regions of a complex flowfield to have different grid topologies while computing the entire flowfield with the same CFD code. Zonal grids may also lead to more efficient solution procedures by tailoring the grids to the local geometry and flow physics, and this can eliminate wasted points and inefficient grid topologies.

A recent joint government/industry code validation effort (Generic Option #2) included an extensive ground test program. The data from these ground tests are now available in a final report (reference 6).

---

*This work was supported by the Computational Methods Branch, Fluid Mechanics Division of NASA Langley Research Center under contract NAS1-18599.

Several inlet models were tested as part of this program, and data from the inlet tests have been used in a code validation effort using the zonal version of CFL3D. The previous code validation of CFL3D (references 3 and 4) involved two-dimensional inlet geometries. The inlets tested as part of the Generic Option #2 program have three-dimensional geometries and are mounted on representative forebodies. Numerical solutions for two of these inlets are compared below with experimental data to calibrate the forebody/inlet zonal approach implemented in CFL3D.

MODEL GEOMETRY AND COMPUTATIONAL GRIDS

Several inlet models were tested in the Calspan 96 Inch Shock Tunnel as part of the Generic Option #2 program. The objective of these tests was to obtain detailed forebody and internal flowfield measurements on NASP-like geometries at NASP-like freestream conditions. The data from the tests was intended to provide a database for validating CFD codes at hypersonic flow conditions. Numerical solutions for two of these inlets, the 2-D Internal Flow Model and the 3-D Forebody/Inlet Integration Model, are compared with data from the final report (reference 6) for the purpose of validating the zonal forebody/inlet version of CFL3D. The geometry definitions of these two configurations were based upon data from the model designers and the final report. All computational grids were generated using a modified transfinite interpolation (algebraic) grid generation method (reference 7).

The 2-D Internal Flow Model is shown in figure 1. This model consists of an inlet preceded by a flat plate. The geometry used in the present study has a sharp leading edge, however a blunt leading edge model was also tested at Calspan. The inlet was designed to have the bow-shock impinge on the cowl-lip at a freestream Mach number of 12. The inlet sidewalls have a sweep of 45 degrees, but no sidewall compression. In this analysis, the cowl leading edge is also sharp. The inlet was designed to be tested at several contraction ratios; the configuration used in this study has a contraction ratio of five.

The grid topology for the 2-D Internal Flow Model is shown in figure 2. The grid for this model consists of five blocks/zones with half the inlet gridded because of symmetry considerations. A two-dimensional boundary layer solution is stored in the first block to initialize the inlet calculation. A one-to-one patch interface boundary condition between blocks one and two communicates the boundary layer solution to the inlet. Block two starts ahead of the 8 degree ramp to capture any ramp-induced separation bubbles. Block three has grid stretching from the sidewall and is patched into block two. The sidewall sweep is modelled in block three by a "jagged" wall/no wall boundary condition allowing the cross-sectional grid to remain in a vertical plane, thus simplifying the grid generation. The internal portion of the inlet consists of the last two blocks. In CFL3D, turbulent flow from two opposing surfaces, such as a cowl and a ramp, cannot be calculated with one computational block, but requires upper and lower computational blocks as shown in figure 2.

The 3-D Forebody/Inlet Integration Model is shown in figure 3. This model has a blunt nosetip with a nose radius of 0.27 inches, followed by a 3 degree forebody. A system of lower surface compression ramps (7 degrees and 11 degrees) precedes the inlet. The inlet module was designed to have the bow-shock impinge on the cowl-lip at a freestream Mach number of 16.5. Also, the inlet module has no sidewall sweep and no sidewall compression. The inlet was designed to test several contraction ratios; the configuration used in this study has a contraction ratio of two.

The grid topology for the 3-D Forebody/Inlet Integration Model is shown in figure 4. The grid consists of three computational zones: the blunt nose, the forebody and the inlet. As before, half the configuration is gridded because of symmetry considerations. The blunt nose zone, the forebody zone and the location of the inlet at the outflow plane of the forebody are indicated in figure 4. The inlet zone (not shown) consists of two internal blocks similar to the 2-D Internal Flow Model. Patch interface boundary conditions connect the zones, allowing information to pass from one zone to the adjacent zone.

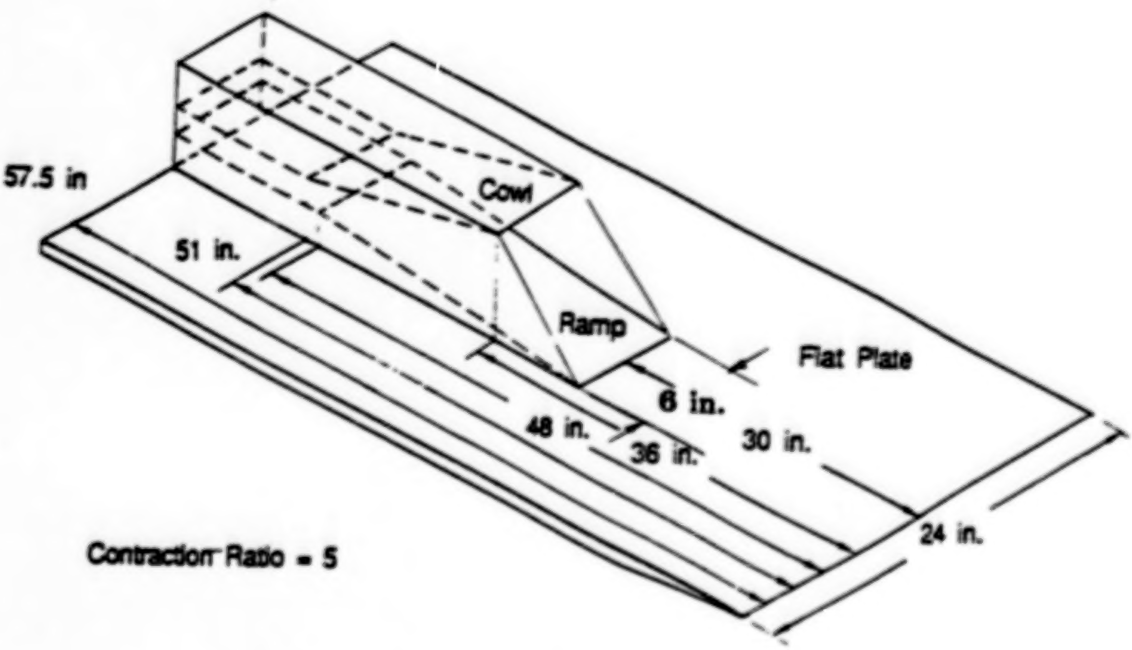

Figure 1. Schematic of 2-D Internal Flow Model.

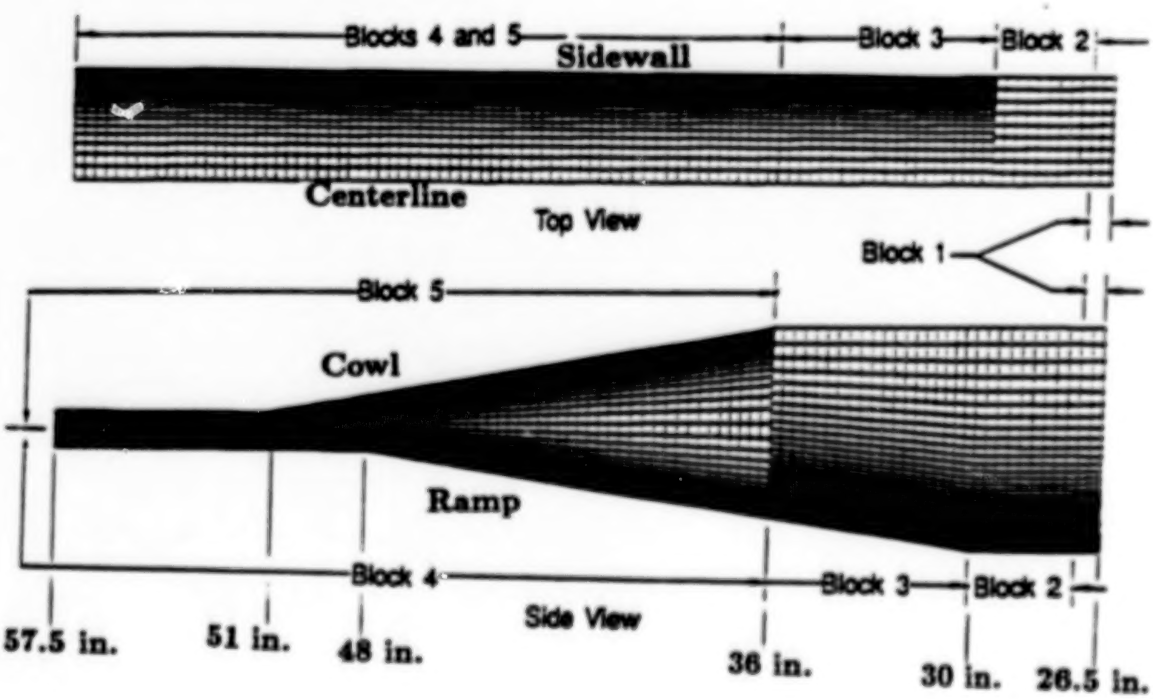

Figure 2. 2-D Internal Flow Model grid topology.

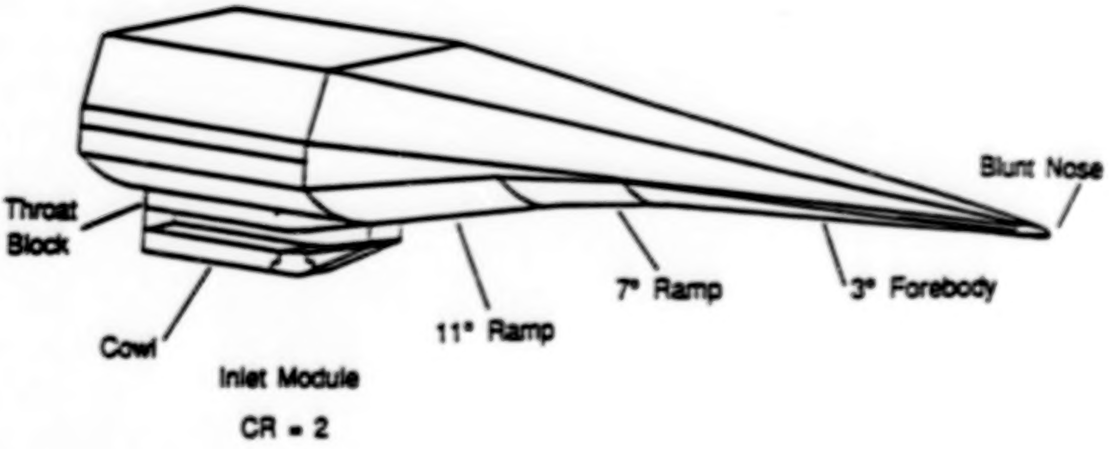

Figure 3. Schematic of 3-D Forebody/Inlet Integration Model.

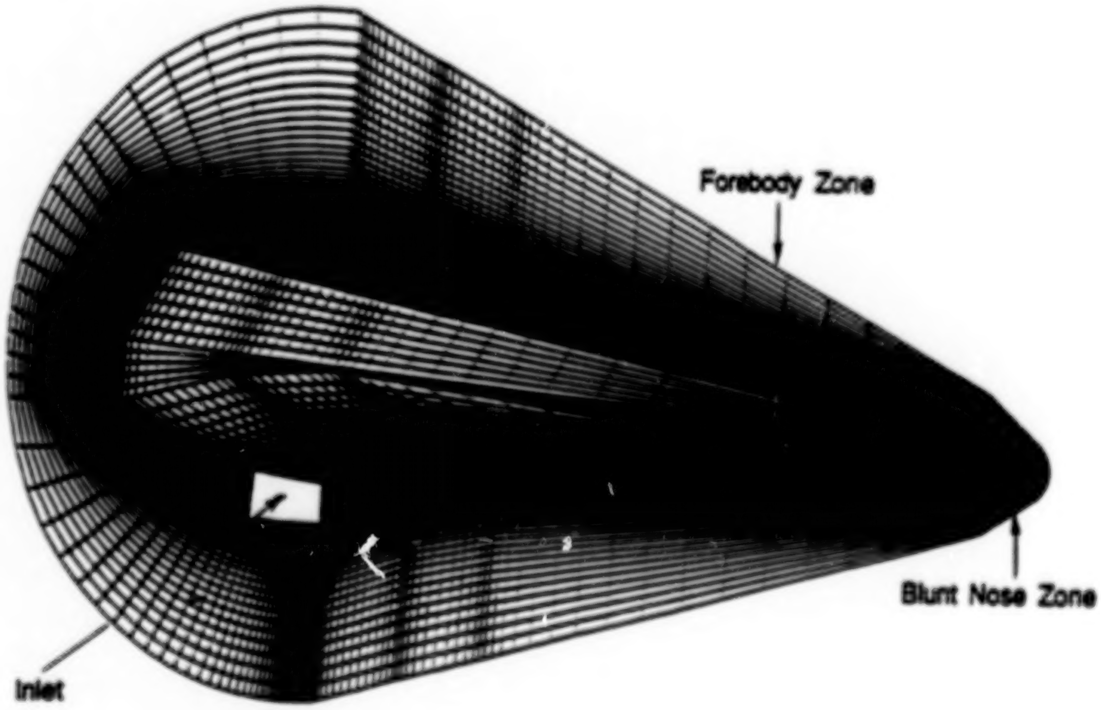

Figure 4. 3-D Forebody/Inlet Integration Model grid topology.

DISCUSSION OF RESULTS

The Generic Option #2 program has provided a large amount of test data on NASP-like geometries at NASP-like freestream conditions. This data is currently being used in validating CFD codes at hypersonic flow conditions. Numerical solutions for two inlet geometries tested at Calspan are compared with test data as part of a code validation effort at the NASA Langley Research Center. In analyzing these comparisons, the term, y^+, will be used. Here, y^+ is defined as:

$$y^+ = \Delta y \frac{(\frac{\tau_w}{\rho})^{\frac{1}{2}}}{\nu} \tag{1}$$

where Δy is the normal distance of the first cell center off the body, ρ is the density, τ_w is the wall shear stress and ν is the kinematic viscosity. Generally, smaller values of y^+ indicate a finer grid near the body. The numerical solutions presented below are not considered to be grid converged, but are of use in assessing the forebody/inlet capabilities of the zonal version of CFL3D. In one case, a grid refinement calculation is underway and results may be available for the oral presentation. Both inlet calculations used a Baldwin-Lomax turbulence model (reference 8) to model turbulent flow regions.

The 2-D Internal Flow Model consists of an inlet module preceded by a flat plate. The model was designed to have high contraction ratio, internal flow passages which admitted instrumentation to make off-body flow field measurements. The model instrumentation was concentrated in the inlet module and included heat transfer and pressure gauges, along with several pitot pressure rake measurement stations. The heat transfer and pressure gauges were located along the centerline of the inlet and 0.35 inches from the sidewalls.

Results for the 2-D Internal Flow Model are shown in figures 5 through 10. The freestream conditions for this case were: a zero degree angle of attack, a Mach number of 12.26 and a Reynolds number of 1.049 million per foot. A two-dimensional laminar boundary layer solution provided the inflow boundary condition. A symmetry-plane boundary condition was imposed at one spanwise boundary and a "jagged" wall/no wall boundary condition at the other spanwise boundary. A fixed wall temperature was imposed on all surfaces. Based on the CFD analysis in the final report (reference 6), linear transition to turbulence on the ramp was initiated at the start of the ramp, and the flow was fully turbulent halfway up the ramp. On the cowl, following a two inch transition region, the flow was fully turbulent after the ramp shock had impinged on the cowl surface. The sidewall was treated as laminar throughout the inlet module. There was no special modelling of the corner interaction between the laminar sidewall and the turbulent cowl/ramp.

Numerical solutions were obtained on two different grids. The coarse grid consisted of five blocks (see figure 2) with 10x75x3 in block one, 10x75x10 in block two, 30x75x20 in block three, 30x38x72 in block four and 30x38x72 in block five. The grid specification gives the number of spanwise points, the number of normal points and the number of axial points. The fine grid was intended to improve the results in the internal portion of the inlet. Therefore, only blocks four and five were refined with 29x49x73 points each. The fine grid reduced the maximum y^+ by a factor of 10.

Qualitative features of the flow are shown in figures 5 and 6. In figure 5, total Mach number contours are plotted at several cross-sections. The effect of the "jagged" wall/no wall boundary condition can be seen in the boundary layer development on the sidewall. In figure 6, total Mach number contours are plotted along the symmetry plane. Separation occurs at the following locations: (1) ahead of the ramp, (2) on the cowl where the ramp shock impinges on the cowl surface and (3) on the ramp where the flow expands over the ramp shoulder. Although not shown, the fine grid solution has larger separation regions than the coarse grid solution. These results contrast with the laminar results of Reddy *et al* (reference 9). That laminar calculation predicted attached flow throughout the inlet. The Mach wave from the strong interaction at the sharp leading edge of the flat plate is evident and impinges on the cowl at approximately 42 inches from the

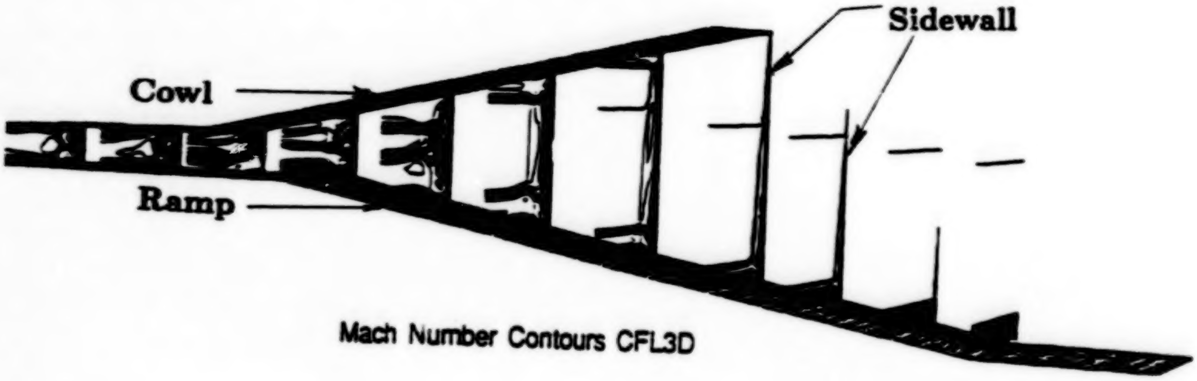

Figure 5. Cross-sectional Mach numbers inside inlet - 2-D Model.

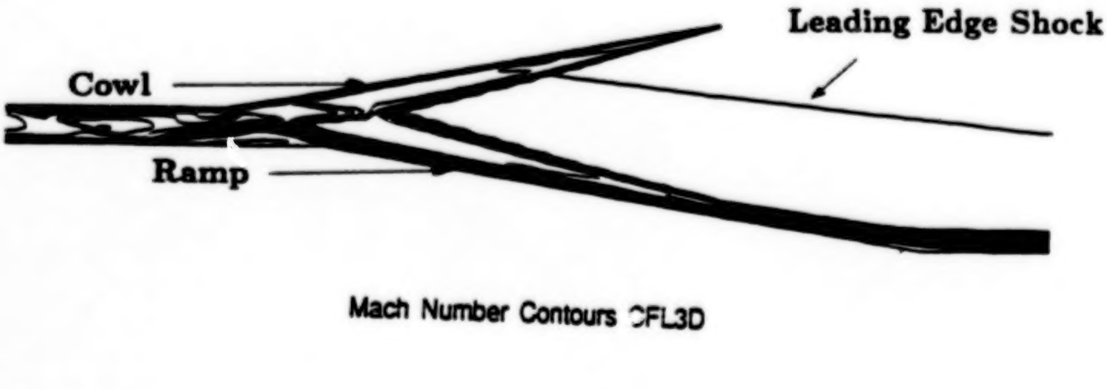

Figure 6. Symmetry plane Mach numbers inside inlet - 2-D Model.

flat-plate leading edge. The coalesced ramp and cowl shock reflect on the ramp surface and the cowl surface before exiting the inlet.

Comparisons of computed surface pressure and experimental pressure data are shown in figures 7 and 8. The heat transfer comparisons are shown in figures 9 and 10. The computed centerline values match the experimental data reasonably well. The fine grid solution has better agreement with the experimental peak heat transfer and pressure, especially on the ramp centerline. The side plane comparisons exhibit similar trends. The fine grid solution has a sharper resolution of internal shocks and their impingement on the ramp and cowl surfaces. The sharper resolution of internal shocks results in more accurate predictions of the peak values of heat transfer and pressure as shown in these figures. The coarse grid solution has a maximum y^+ of approximately 8; whereas the fine grid solution has a maximum y^+ of approximately 0.75 . The improvement in y^+ also results in better heat transfer predictions. Overall, the computed flow features generally match the experiment well.

The 3-D Forebody/Inlet Integration Model consists of a blunt nose forebody with a system of lower surface compression ramps preceding the inlet. The model was designed to study the surface and off-body flowfield characteristics associated with the external/internal contraction regions of an integrated inlet geometry. The model instrumentation included heat transfer and pressure gauges distributed on the lower forebody surface and inside the inlet module, along with several pitot pressure rake measurement stations. Heat transfer and pressure gauges were located on the forebody centerline and on several off-centerline forebody rays. On the inlet cowl and throat block, heat transfer and pressure gauges were located on the centerline and 0.35 inches from the inlet sidewall. The throat block is the extension of the lower forebody surface into the inlet module.

Results for the 3-D Forebody/Inlet Integration Model are shown in figures 11 through 15. The freestream conditions were: a zero degree angle of attack, a Mach number of 11.31 and a Reynolds number of 9.893 million per foot. These conditions correspond to the "undersped condition" given in the final report (reference 6). The blunt nose region was laminar, and transition to turbulence occurred several inches downstream of the blunt nose. Based on the final report (reference 6), the flow was fully turbulent by fuselage station 6, the first heat transfer gauge on the forebody. The flow in the inlet module was treated as fully turbulent from all surfaces, including the sidewall. This was done by using the two wall/one corner turbulence model in CFL3D and two internal computational blocks. The corner modelling allows turbulent flow from a sidewall to interact with turbulent flow from a cowl or a ramp. Symmetry-plane boundary conditions were imposed at the top and bottom centerlines of the forebody and the centerline of the inlet module. The inlet module had no sidewall sweep, therefore a "jagged" wall/no wall boundary condition was not required. A fixed wall temperature was imposed on all forebody and inlet surfaces.

The grid consisted of three computational zones with 41x65x25 on the blunt nose, 65x65x55 on the forebody and 45x65x100 in the inlet. The grid specification gives the number of circumferential points, the number of normal points and the number of axial points. The solution on this grid has a maximum y^+ of approximately 5. To reduce the maximum y^+, a finer grid is being used in a new calculation for this configuration. However, results from that calculation were not available for inclusion in this paper.

Pressure contours in the symmetry plane, in the outflow plane and on the bottom surface of the forebody are shown in figure 11. The bow shock and both ramp shocks are clearly visible in these contours. In figure 12, computed forebody pressures are compared with experimental data along the centerline and along a ray off the centerline. The agreement in this case is good. The forebody heat transfer comparisons (not shown) are poor. Contours of total Mach number at various cross-sections inside the inlet are shown in figure 13. The flow is from left to right. A large buildup of the boundary layer develops on the lower symmetry plane of the forebody and is evident partially into the inlet. Figures 14 and 15 show comparisons of computed pressures with experimental data on the cowl and the throat block of the inlet. The agreement here is not as good as on the forebody. A more refined grid calculation is currently underway. The more refined grid solution is expected to give better resolution of internal shocks, and therefore improve the pressure comparisons in the inlet and provide reasonable heat transfer comparisons. Results from the refined grid calculation may be available for the oral presentation.

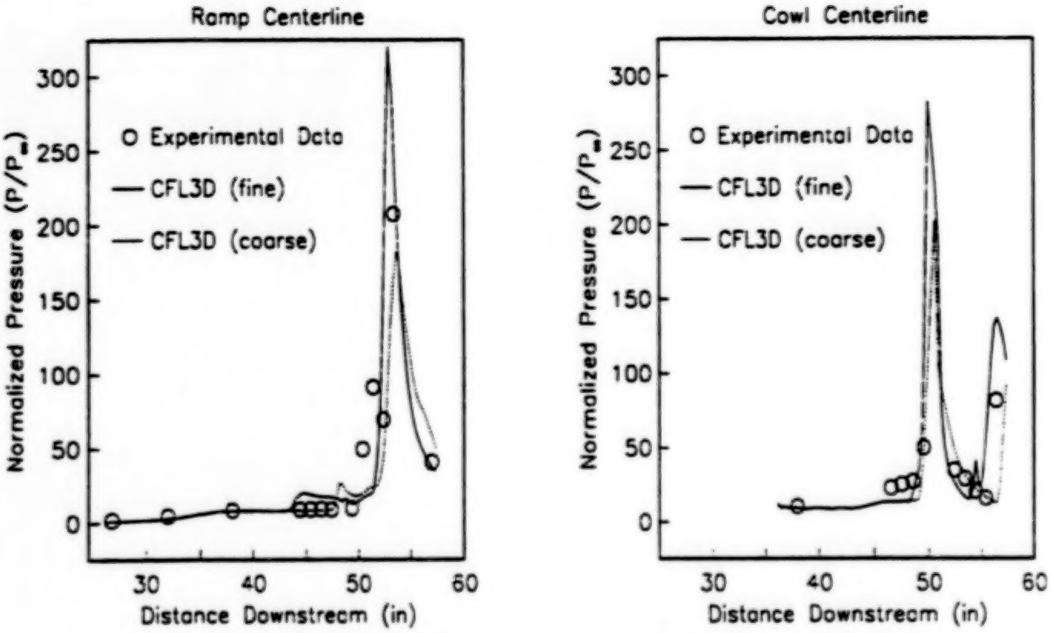

Figure 7. Pressure comparisons between CFL3D and experiment - 2-D Model, ramp centerline and cowl centerline.

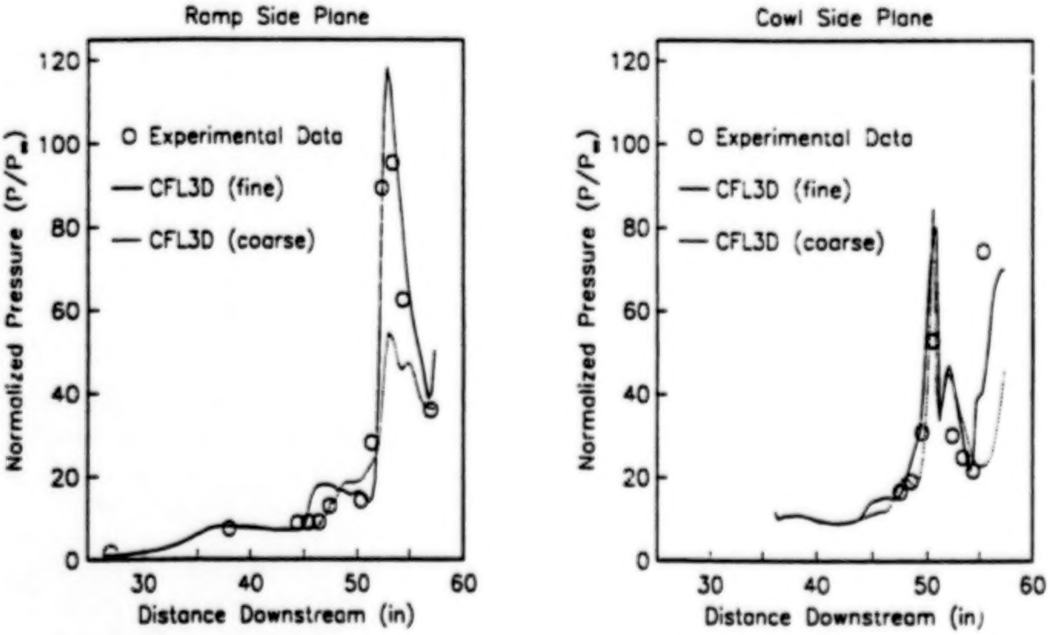

Figure 8. Pressure comparisons between CFL3D and experiment - 2-D Model, ramp side plane and cowl side plane.

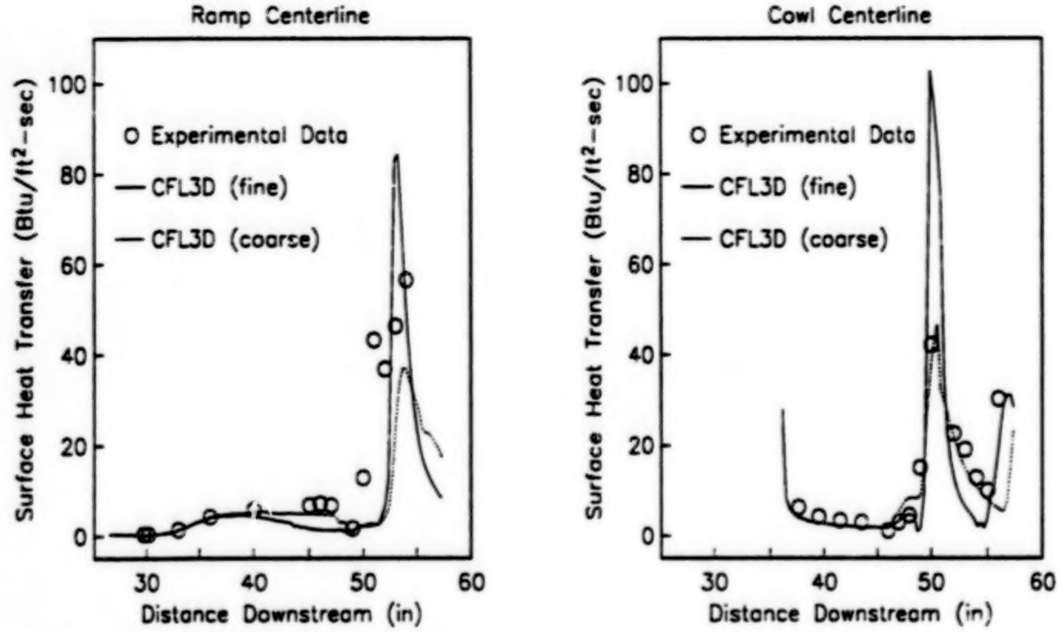

Figure 9. Heat transfer comparisons between CFL3D and experiment - 2-D Model, ramp centerline and cowl centerline.

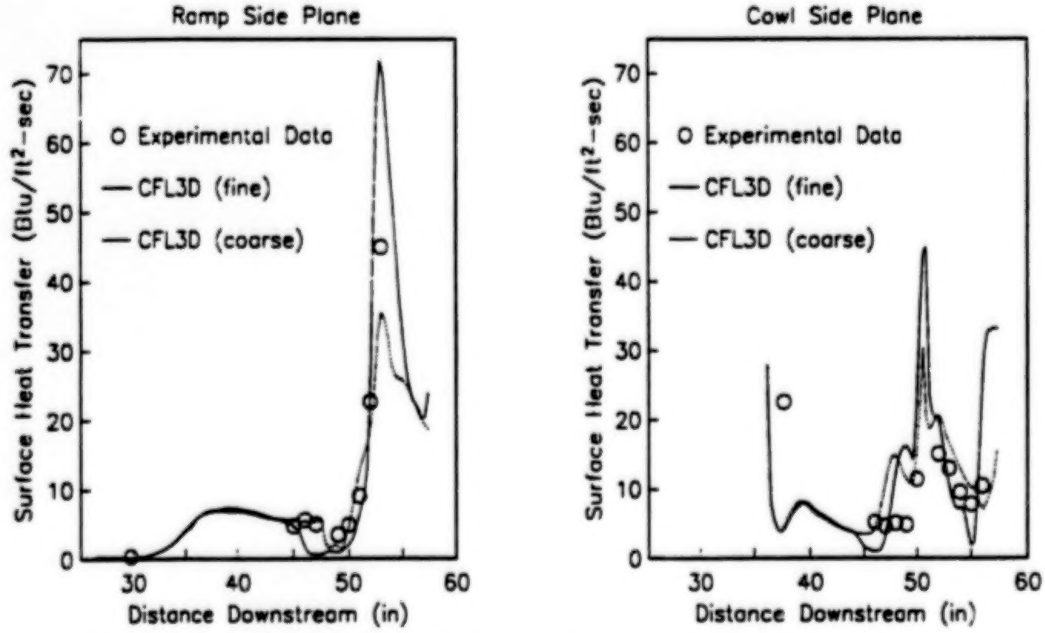

Figure 10. Heat transfer comparisons between CFL3D and experiment - 2-D Model, ramp side plane and cowl side plane.

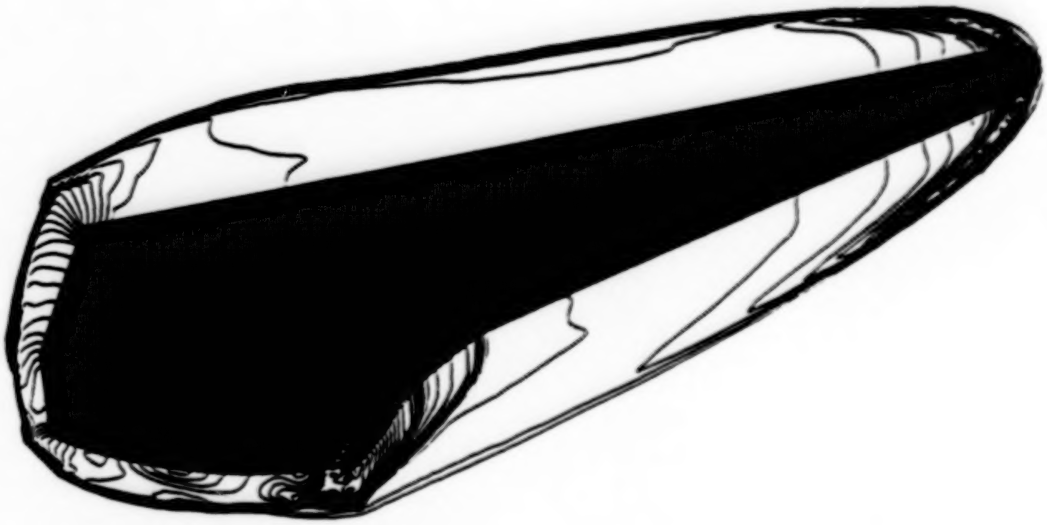

Figure 11. Pressure contours - 3-D Model, symmetry plane, outflow plane, and windward surface.

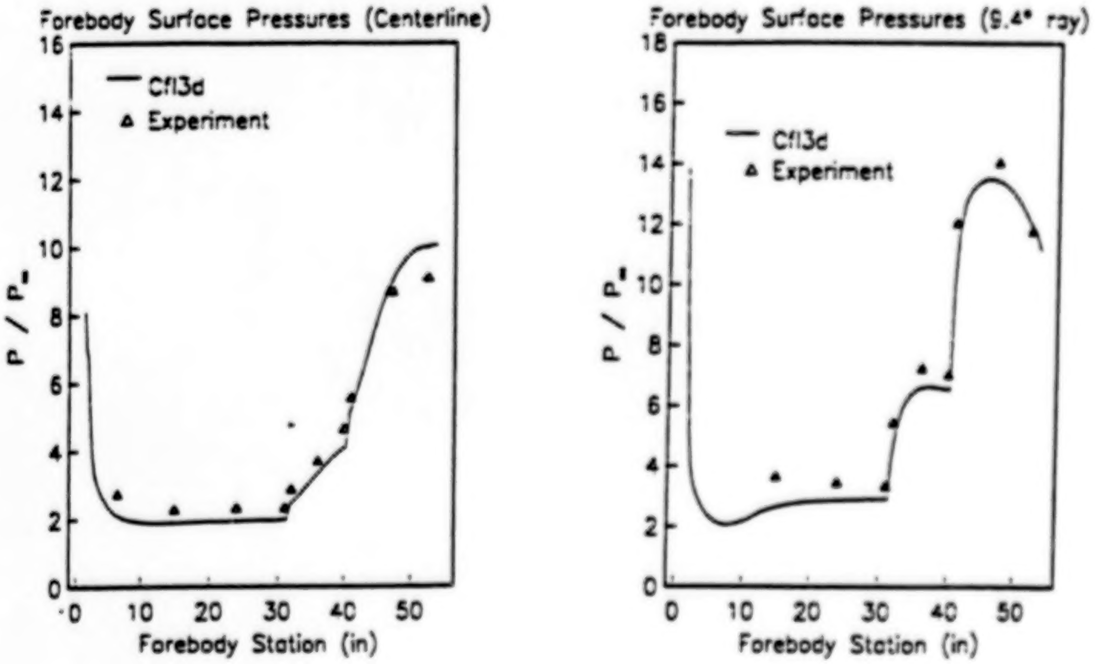

Figure 12. Pressure comparisons between CFL3D and experiment - 3-D Model, lower surface centerline and off-centerline.

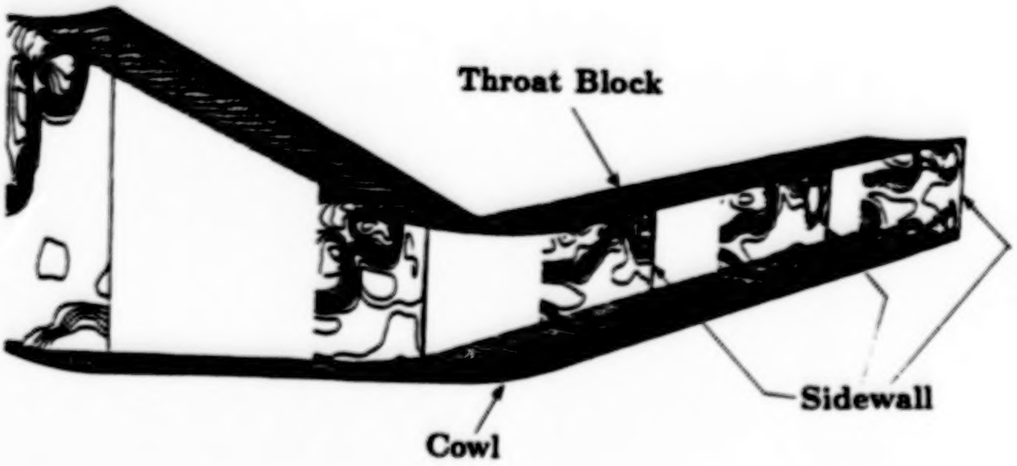

Figure 13. Cross-sectional Mach numbers inside inlet - 3-D Model.

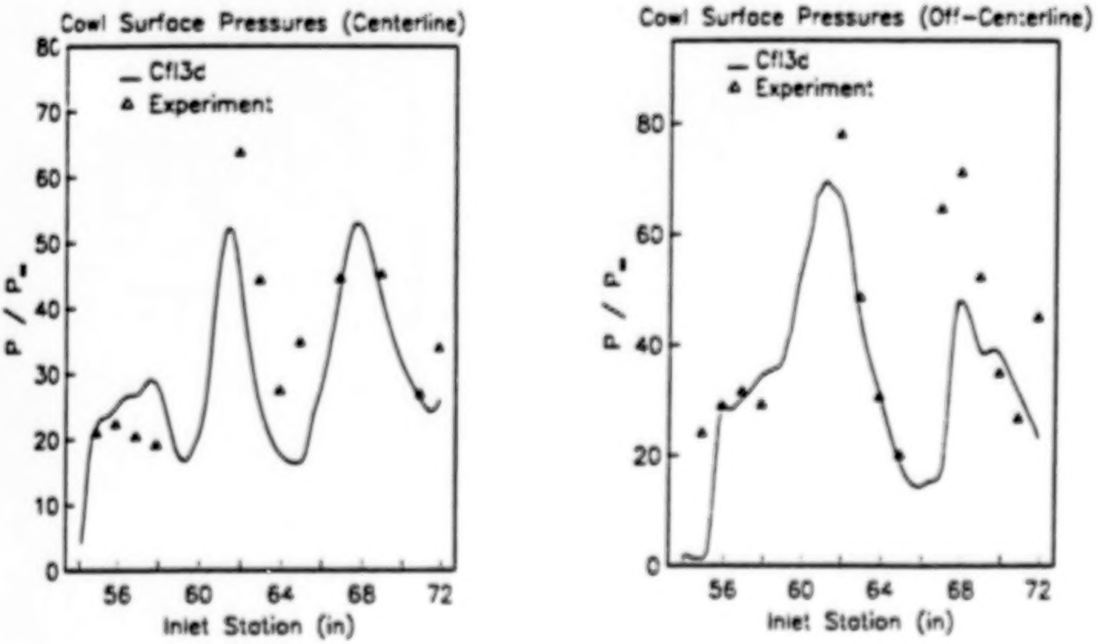

Figure 14. Pressure comparisons between CFL3D and experiment - 3-D Model, cowl surface centerline and off-centerline, inside inlet.

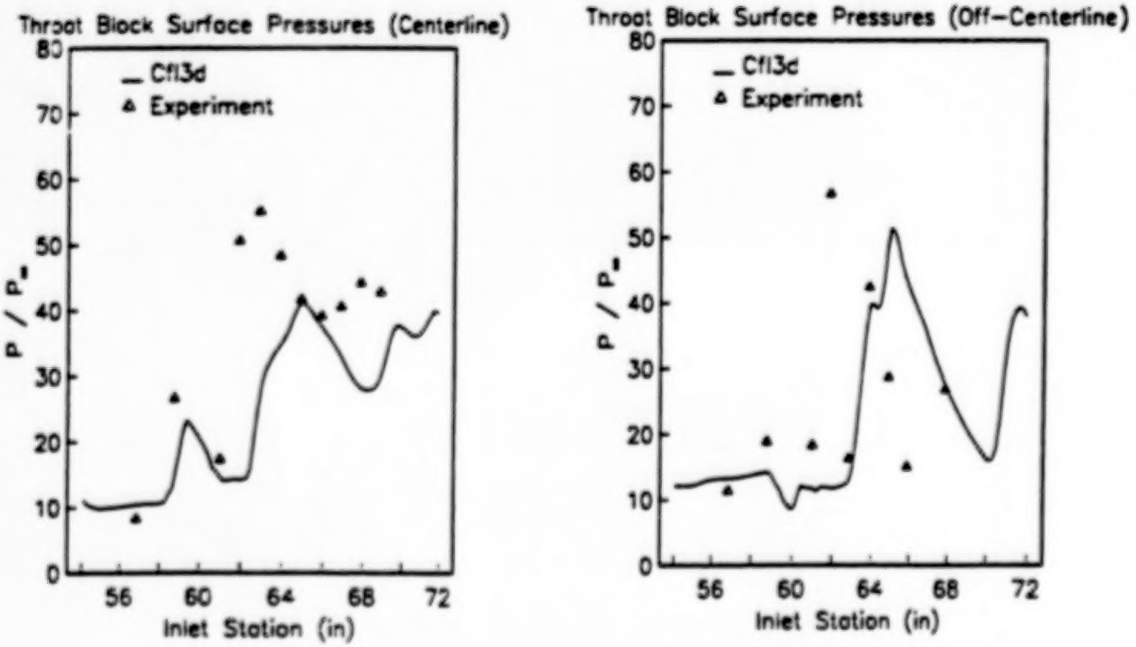

Figure 15. Pressure comparisons between CFL3D and experiment - 3-D Model, throat block surface centerline and off-centerline, inside inlet.

CONCLUSIONS

Using a zonal technique, computational results for two high-speed inlet flows have been obtained and compared with experimental data as part of a code validation study. The ability of the zonal version of CFL3D to supply reasonably accurate flow predictions for simple high-speed inlets is demonstrated by the 2-D Internal Flow Model results. These results indicate the importance of adequate grid refinement in calculating internal flows with shocks. The fine grid results exhibit better agreement with the peak values of the experimental heat transfer and pressure, and have reasonably good agreement overall with the experimental data. However, the agreement for the 3-D Forebody/Inlet Integration Model is not as good for the flow in the inlet. A more refined grid solution for this geometry is currently underway. Based on the 2-D Internal Flow Model results, grid refinement should improve the agreement with the experimental data and demonstrate the forebody/inlet capabilities of the zonal version of CFL3D.

REFERENCES

1. Vatsa, V. N.; Thomas, J. L.; and Wedan, B. W., "Navier-Stokes Computations of Prolate Spheroids at Angle of Attack," AIAA Paper 87-2627-CP (1987).
2. Richardson, P. F.; Parlette, E. B.; Morrison, J. H.; Switzer, G. F.; Dilley, A. D.; and Eppard, W. M., "Heat Transfer and Pressure Comparisons Between Computation and Wind Tunnel For a Research Hypersonic Aircraft," AIAA Paper 89-0029 (1989).
3. Rudy, D. H.; Kumar, A.; Thomas, J. L.; Gnoffo, P. A.; and Chakravarthy, S. U., "A Comparative Study and Validation of Upwind and Central-Difference Navier-Stokes Codes For High Speed Flows," In *Validation of Computational Fluid Dynamics*, AGARD-CP-437, Vol. 1, pp 37-1 to 37-15 (1988).
4. Thomas, J. L.; Rudy, D. H.; Chakravarthy, S. U.; and Walters, R. W., "Patched-Grid Computations of High-Speed Inlet Flows," In *Advances and Applications in Computational Fluid Dynamics*, A.S.M.E., FED-Vol. 66, pp. 11-22 (1988).
5. Rudy, D. H.; Thomas, J. L.; Kumar, A.; Gnoffo, P. A.; and Chakravarthy, S. U., "A Validation Study of Four Navier-Stokes Codes For High Speed Flows," AIAA Paper 89-1838 (1989).
6. "National Aerospace Plane Generic Option #2 Experimental Database/CFD Code Validation," McDonnell Douglas Corporation, Contract F33657-86-C-2126, September 1988.
7. Eriksson, L. E., "Practical Three-Dimensional Mesh Generation Using Transfinite Interpolation," In *SIAM Journal of Science and Statistical Computations*, July 1985, Vol. 6 no. 3, pp 712-741 (1985).
8. Baldwin, B. S. and Lomax, H., "Thin-Layer Approximation and Algebraic Model For Separated Turbulent Flows," AIAA Paper 78-257 (1987).
9. Reddy, D. R.; Smith, G. E.; Liou, M. F.; and Benson, T. J., "Three-Dimensional Viscous Analysis of a Hypersonic Inlet," AIAA Paper 89-0004 (1989).

DYNAMICS OF LOCAL GRID MANIPULATIONS FOR INTERNAL FLOW PROBLEMS

Peter R. Eiseman*
Program Development Corporation
White Plains, New York 10601

Aaron Snyder and Yung K. Choo
NASA Lewis Research Center
Cleveland, Ohio 44135

ABSTRACT

The control point method of algebraic grid generation is briefly reviewed. The review proceeds from the general statement of the method in two dimensions unencumbered by detailed mathematical formulation. The method is supported by an introspective discussion which provides the basis for confidence in the approach. The more complex three-dimensional formulation is then presented as a natural generalization. Application of the method is carried out through two-dimensional examples which demonstrate the technique.

INTRODUCTION

The **Control Point Form (CPF)** of algebraic grid generation (reference 1,2) has recently emerged as a powerful interactive tool for a wide range of geometrical applications. While the basic action comes from the motion of a single control point, various automatic features are evolving for a group of control points. The current implementation of **CPF** is being extended from simple two-dimensional geometries to complex three-dimensional configurations. To keep pace with this trend toward increased problem complexity and the implied increase in required grid points, enhancements to the method are being pursued. A primary method of enhancement which is quite fashionable, in light of the current computer technology, is the development of robust automation procedures. This practical avenue is proceeding along several fronts spurred chiefly by the desire to maintain operational manageability. The benefits derived from increased manageability become more pronounced as the geometrical complexity increases. Self-sustaining strategies to deal with the complexity issue, such as establishing a multi-block environment, do not, in general, directly address the issue as viewed from the **CPF** perspective. However, operating within a multi-block surrounding does provide a natural network supporting numerous automation strategies.

---

* Support given by The U. S. Air Force under AFOSR contract F49620-89-C-0096 and by NASA under Grant NAG 3-877 when author was with Columbia University.

In the current codes, the basic strategy of block interface manipulation has been demonstrated. This is addressed specifically here in the manipulations required to successfully treat periodic boundaries for cascades. This occurs by the periodic tie of two control points and use of free form boundary capability. The potential gain achievable by automating unit operations becomes even more obvious as the number of required points increases.

The actions where it is particularly advantageous to be performed automatically include motion of junctures between blocks, enforcement of boundary orthogonality, and the creation of desired distributions such as uniform or expanding. For example, the objective in implementing automatic boundary orthogonality is the construction of a single command to concurrently reposition all the control points adjacent to a given boundary sector. This would, when chosen, supplant the corresponding tedious interactive option of adjusting each control point successively.

Further features include the dynamic adjustment of the number of control points in each direction and the free form construction of boundaries with more control points than are employed in the given directions within the grid blocks.

Another prominent issue arises when it is necessary to maintain a prescribed boundary geometry while generating a grid for this boundary curve or surface. Enhancements along this line would be particularly welcome and beneficial. Numerical simulations of fluid flow, particularly in the cases where small perturbations in geometry may induce significant changes in the predicted flow field variables, constitute a conspicuous arena where advances in this direction would be highly profitable. Continuing with the subject of fluid flow, the boundary orthogonality procedure alluded to previously can be called upon repeatedly. Through this mechanism, it is possible to extend a simple grid into the interior flow field. This facility requires the automatic movement of bands of control points adjacent to the region of interest.

Since the method is inherently general, the capability exists to advance the automation features to the point where all control points would be determined simultaneously. This brings the stage where solution adaptive techniques could be applied given an arbitrary grid and a reasonable process of attaching a control net to that grid.

OVERVIEW

This section will present the discussion of the following topics: (1) **CPF** methodology and its construction from the transfinite and multisurface techniques; (2) Initialization process which concerns what basic requirements must be established for a control point formulation; and (3) Movement procedures for points once an initial control net is established. The intent of this section is to provide a suitable background to discuss the formulation without relying on lengthy mathematical development. The delivery of concepts will be to initially present them in the particular and next generalize as, for example, first give the significance of a concept in two-dimensions and then expand to three-dimensions. The intent of this paper is to provide appreciation for CPF and its utility. If all goes well, the reader can begin to apply the method with only a modest need to acquire elsewhere greater detail for his particular application.

The CPF Methodology

In the following development, we will be concerned with transformations from some rectangular cartesian coordinate domain which covers the field of interest to a general curvilinear coordinate system. Alternative coordinate domains exist as candidates but rectangular cartesian coordinates provide the most suitable framework for this discussion. Aside from historical convenience, it is also a short step from a general cartesian coordinate domain to the domain of indices where the spacing between them is unity. This, of course, assumes a finite representation in the form of a grid so that grid point indices are definable. Coming from the other direction, it is now a simple conceptual task to mark off an index array which is now in a one-to-one correspondence with grid points. While this can be done in a number of ways, the size of the domain is translation invariant. The result is a mapping relating a simple indexed system to a more complex physical space coordinate system. It is also permissible to rescale the domain to an arbitrary rectangular region. This is convenient in some instances. For computations, however, the index space is usually preferred. With this utilization of rectangular domains, we advance to the subject of transfinite interpolation.

Transfinite interpolation is covered in detail in the literature (reference 3,4). A brief presentation is given here to establish its connection with **CPF**. Transfinite interpolation was so named for its attribute of matching the interpolated function at an infinite set of points. In this procedure, a function on a region is represented in terms of functions on the region boundaries. To see this in terms of our rectangular domains as discussed above, the function would be specified along the boundaries in the curvilinear coordinate system. By blending corresponding boundaries values, an interpolated value can be calculated for any point in the region. The transfinite procedure, by design, interpolates exactly along each boundary. For grid generation procedures, transfinite interpolation takes on the simple abstract form.

$$X(\xi,\eta) = U \oplus V = U + V - UV \qquad (1)$$

Here **X** is the two dimensional coordinate vector of position and ξ, η are curvilinear coordinates. The interpretation of **U** and **V** are explained easily in terms of our above discussion. The variable **U** can be considered as a univariate interpolation in computational coordinate directions of the values of the position coordinate and derivatives (up to some order **n**) of the position coordinate. This interpolation would be carried out over a range of curves in the curvilinear direction of choice, say ξ. Then, likewise, **V** would be another univariate interpolation with respect to the curvilinear variable η. This second interpolation would, of course, interpolate the position vector and its derivatives through order n, but along curves of constant ξ in this instance. It was pointed out that the transfinite procedure interpolates exactly along the boundary. With this in mind, we now discuss the significance of the product term and its sign in the above equation. We have already accounted for the terms **U** and **V** as being separate univariate interpolations in the respective curvilinear directions of ξ and η. It is also clear that these two separate interpolations must have common nodes corresponding to their intersection. At these nodes the interpolation is, in effect, being counted twice. The product term **UV** is equivalent, in the overall interpolation, to the contribution arising from the set of intersection nodes of the separate univariate interpolation curves. It can be stated then that **UV** is the product projection term resulting from the separate univariate operations being applied consecutively. This product projection term must bear a negative sign to provide proper cancellation in the net interpolation, since these points have contributed once in the first interpolation **U** and again in the second interpolation phase **V**. By supplying the product term **UV**, the interpolation at boundaries formed of sets of constant ξ and η curves reduces to the values specified by either **U** or **V** as appropriate. This is the designed nature of the transfinite interpolation procedure and is most easily visualized in the special case where the interpolation is specified only in terms of the bounding curves. The set of points involving the product term **UV** is then merely the four corner points of the region.

We now wish to state a few characteristics that should not be overlooked. First, the transfinite procedure is a Boolean sum procedure and is well defined when the order of carrying out the operation is immaterial. Second, the product projector term is an important interpolator in its own right, but one which interpolates over the set of intersection points. It is often referred to as the Tensor product interpolator. Third, the extension to higher dimensions is conceptually straightforward. Fourth, many variations exist in the specification of the number and choice of curves as well as in the choice of interpolating functions. In continuation, we consider the three-dimensional environment where both curves and surfaces represent the basic construction elements.

Following the above nomenclature, the transfinite interpolation in three dimensions can be compactly expressed as a sum of interpolation operators. Again, in the context of coordinate generation, it is appropriate to express this in terms of the general position vector as follows:

$$\boldsymbol{X}(\xi,\eta,\zeta) = \boldsymbol{U}\oplus\boldsymbol{V}\oplus\boldsymbol{W} = \boldsymbol{U}+\boldsymbol{V}+\boldsymbol{W}-\boldsymbol{UV}-\boldsymbol{UW}-\boldsymbol{VW}+\boldsymbol{UVW} \tag{2}$$

The extra curvilinear coordinate ζ has been introduced as well as the interpolation function **W**. It remains to discuss the significance of the respective terms in the above equation.

To reveal the structure in three-dimensions, it is convenient to take the special case where the interpolation is in terms only of the specified functions on the bounding surfaces. To visualize this, consider a rectangular region with **U**, **V**, and **W** each specified on respective pairs of opposing surfaces. These surfaces comprise the boundary of the rectangular domain. Each pair of opposing surfaces is identified by the variable held separately constant.

With regard to the curvilinear variable ξ, then **U** would be a specified function of η and ζ on one boundary and another function of these two variables on the opposing boundary. This assignment proceeds in a cyclical fashion for the **V** and **W** boundary surfaces which are labeled here by constant η and ζ, respectively. We now examine the origin of each of the terms in the three-dimensional transfinite interpolation expression presented above.

To facilitate this process, let us orient the boundaries such that ξ is directed side-to-side, η top-to-bottom and ζ front-to-back. Then **U** can be the interpolation between side-to-side surfaces, **V** between top-to-bottom surfaces and **W** between front-to-back surfaces. These three interpolations relate to the respective **U**, **V**, **W** terms in the three-dimensional transfinite interpolation equation. The **UV** term arises since the four front-to-back edges formed by the intersection of the side-to-side and top-to-bottom surfaces have each contributed twice, once through **U** and again through **V**. An identical argument holds for the other two sets of four edges corresponding to the product terms **UW**, relating to the top-to-bottom edges; and **VW** relating to the side-to-side edges. Of course, each is fixed with a negative operator. Thus, the three binary product terms are directly related to the three corresponding set of edges as just identified. It now remains to explain the ternary product **UVW**. This is explained by examining the corner points of the region. It can be seen that each corner point contributes once through each of the **U**, **V**, and **W** interpolations and then is subtracted for each of the binary product terms **UV**, **UW**, and **VW**. The effect, so far, is that the eight corner points have not contributed to the overall interpolation. The **UVW** term contains the collective contribution of these points to the interpolation and hence is positive. This establishes the framework to progress to the multi-surface concept and its role in the **CPF** methodology.

We now present a brief description of the multisurface transformation. The geometrical picture in this instance parallels that of the transfinite interpolation procedure laid out above. We will reconstruct the geometry framework so that it will be clear what the connection is between the two procedures.

The multisurface transformation can be viewed as a general technique of connecting coordinates between specified boundaries. In two dimensions, these boundaries can be viewed as distinct curves in space separated by some value of a given curvilinear variable. A second curvilinear variable would vary along these boundary curves. As in the case of transfinite interpolation, the picture easily generalizes to surfaces separated by a constant value of a curvilinear variable. In this instance, it follows that each surface is coincident with a pair of second and third curvilinear variables. Within this framework of an interacting net of families of coordinate lines, the multisurface transformation proceeds by providing for the arbitrary specification of additional curves or surfaces to be used as auxiliary instruments to control grid structure. The discussion will continue with the focus on auxiliary curves with the understanding that this line of argument extends directly to surfaces.

Once a set of auxiliary curves is established, a vector field of smooth tangents is constructed in correspondence with lines connecting the selected auxiliary curves and boundaries. The lines used to construct these tangents are simply defined as vector differences between positions on successive auxiliary curves. The position vector serves as the direct connection between the transfinite and multisurface transformations. The critical differentiation between the two is that, unlike the aforementioned property of the transfinite procedure, the multisurface transformation does not require that the interpolation match any of the auxiliary curves. In the latter case, it is only required that the interpolation match the inner and outer boundaries. In this respect then, the multisurface method described by Eiseman is a very flexible univariate scheme which is similar to Be'zier and B-spline approximation (reference 5), where parameters defining a curve are not necessarily on the curve. The idea of curves extends also to surfaces.

We are now at a point where we can assemble the CPF structure from the transfinite interpolation and multisurface transformation. The result will be a procedure whereby a sparse collection of control points along with the specified boundaries is used to form the transformation and then to generate the grid with any number of desired points. The following discussion will indicate how the transfinite and multisurface concepts lead to a class of coordinate transformations, whereby the interior form of the coordinates can be manipulated in a local fashion and whereby any boundary can be specified or manipulated in a similar fashion.

At the outset, we are given a logically ordered array of control points together with specified boundaries. Because of the intrinsic property of the multisurface constructs, the control points become direct controls over the curvature of the generated curve. The philosophy behind the origin of the net of control points is discussed in the separate initialization section which follows this section.

The specific boundaries are included in the transfinite rather than the tensor product assembly of directions. Recall that the tensor product was introduced above as an interpolation procedure involving a collection of points.

The specific collection of points were the result of either an intersecting net of curves or surfaces. In the present assembly, new constructive elements are introduced by altering the basic parts upon which the multisurface transformation is applied. When the parts are one- or two-dimensional, the first and last elements of each sequence for a multisurface construct are replaced by the specified boundary parts at the corresponding location. This replacement is just a substitution of a specified boundary part for a corresponding part generated by control points. We can review this process by drawing upon our image of the rectangular domain. The assembly proceeds in two dimensions by first taking the sum of the constructs with specified boundaries; by then observing that the sum of a control point curve and a specified curve appears over each domain boundary; and finally, by noting that the specified boundaries can be matched by subtracting the tensor product transformation so that the resultant transformation will match all the boundaries. This represents the Boolean sum process and this assembly is thus transfinite. With some algebraic manipulation, the transfinite form just obtained can be nicely separated into a Tensor product core transformation with four adjustment terms for the boundary blending action. This separation is achieved through the inclusion of on-off factors to switch between specified (transfinite) or free-form (control point) boundaries as the switch values go between one and zero, respectively. In a similar but more complex fashion, this strategy can be established in three-dimensions. In that context, there are now two nontrivial boundary parts represented by faces and edges which can similarly be given on-off switches.

Initialization

Now that the construction of **CPF** has been laid out, it is appropriate to discuss in more detail the initialization procedure. The basic requirements to establish a control point transformation are the specified boundaries, their respective on-off switches, the number of grid points for each direction, the number of control points for each direction and the position of those control points. The last concern is the primary concern since the others are usually introduced as input. Impetus from the desire to be able to automate the process of control point determination and, hence, be free of the tedious manual control is the main guiding force in the following rationale.

The basic automatic control net determination comes from the "attachment" to an existing transformation. The process starts with the existing transformation either in analytical form or in the discrete form of a grid. This allows for considerable flexibility while introducing only a modest constraint. A simple way of giving an analytical form of attachment and perhaps the most efficient is to employ a transfinite interpolation which assembles linear interpolations between all specified opposing boundaries. Of course, as follows from our discussion above, it is a mapping which conforms to all boundaries. Implied mappings exist in the case where a coordinate grid is given. In this instance, it is convenient to index the grid points and thus establish our aforementioned rectangular domain determined by the minimum and maximum index in each direction. As before, the index grid is simply cartesian with unit spacing in each direction. In either the analytical or the discrete case, the common element is the mapping from a given simple domain to the more complicated region of interest. This should sound familiar and it should be of no surprise that in both cases the domain can be assumed to be rectangular. Because of their simplicity, control points can be easily placed in locations that would produce a control point transformation of the rectangle onto itself which would also move no point: that is, we can exactly reproduce the identity map! With this exactness, here, we then consider the more general given map and use it to send the control points from the rectangular domain into the image region of interest. This then automatically defines the control net on the physical region and provides an approximation to the originally given transformation. It turns out in most cases that even with a modest number of points the degree of approximation is quite good. Aside from providing for automatic initialization, we also receive the capability to locally modify virtually any existing transformation be it analytically defined or defined in the form of a grid.

The main part of the initialization concerns the placement of control points in the field. There is also an avenue to specify the boundaries in a control point form with a different number of points. Examine the situation of an increase in the number of control points. For each boundary, the strategy is to attach, as above, to a simply constructed or given boundary and then to move the richer supply of control points about to model the shape into the desired form. The results so obtained can be used either directly or in reparameterized form. In the latter case, the attachment and manipulation process can be employed again, but now in the parameter space.

Movement of Control Points

Once an initial control net is established, a number of strategies exist regarding the movement of these points. Movement can be accomplished through global strategies such as those based on PDE's or more local strategies. In either case, there exists the implicit advantage of dealing with a relatively sparse set of control points rather than a dense set of grid points. Regardless of the choice of movement method, it can also be viewed as an extension of the initialization process.

Several options exist for the use of local controls which can be conducted efficiently in an interactive environment. This set of options includes the free-form modeling of chosen boundaries, the establishment of orthogonality at segments of boundaries or their sum, the inward propagation of such orthogonality, the creation of local grid clusters, and the local embedding of specific coordinate forms. These actions can be executed on a point by point basis or for a section of points. In the event a section of points is to be moved, a single point is usually moved and in response a neighborhood of points similarly move but in a progressive sense. This process is called rubber banding if one direction is involved. The extension of this process is called rubber sheeting. An exception to this type of collective motion is the establishment of local orthogonality where adjacent points along a boundary must be moved as a unit to maintain derivative continuity. A boundary shared by two distinct coordinate systems would require this manner of uniform control. This boundary situation arises naturally in the use of multi-block procedures. The required action to satisfy orthogonality at boundary junctures can clearly be done singly or collectively in the sense of rubber banding or sheeting.

FORMULATION

We are now in a position to present the explicit formulation of **CPF**, the framework being previously outlined in the methodology section. We first present the **CPF** in its two-dimensional version where the elected variables will be ξ and η. In effect, we specialize to a face of our rectangular region which we can take to be either the face $\zeta = \zeta_1$ or $\zeta = \zeta_N$ which bound the domain in that direction. This removes the ζ variable from the general expression and we give the explicit two-dimensional form as

$$\begin{aligned}
\mathbf{X}(\xi,\eta) &= \mathbf{U}(\xi,\eta) + \mathbf{V}(\xi,\eta) - (\mathbf{UV})(\xi,\eta) \\
&= \mathbf{T}(\xi,\eta) + \rho_1\alpha_1(\xi)[\mathbf{X}(\xi_1,\eta) - \mathbf{A}_1(\eta) \\
&\quad + \rho_2\alpha_{L+1}(\xi)[\mathbf{X}(\xi_L,\eta) - \mathbf{A}_{L+1}(\eta)] \\
&\quad + \rho_3\beta_1(\eta)[\mathbf{X}(\xi,\eta_1) - \mathbf{B}_1(\xi)] \\
&\quad + \rho_4\beta_{M+1}(\eta)[\mathbf{X}(\xi,\eta_M) - \mathbf{B}_{M+1}(\xi)]. \qquad (3)
\end{aligned}$$

Here **X** is our position vector and **U** and **V** are the univariate interpolation surfaces in the respective curvilinear directions of ξ and ζ, respectively. We define the remaining quantities as we proceed to explain their significance. The boundary edge curves of the selected face formed from the control point attachment process have been labeled by the minimum and maximum subscript index in each direction and appear as $\mathbf{A}_1$ and $\mathbf{A}_{L+1}$ for the curves of constant ξ and $\mathbf{B}_1$, $\mathbf{B}_{M+1}$ for the curves of constant ζ. The weighting from the continuous distribution of these control point curves is thus evidenced through the last term from each of the four bracketed pairs in this equation. In a similar fashion, the first term in each of these brackets represents the specified boundaries. These specified boundaries are identifiable through the corresponding subscript attached to that coordinate held constant. We now examine the four pairs of coefficients premultiplying each of the bracketed terms. The first factor ρ_i represents the on-off switch which is applied independently to its corresponding boundary curve. With the switches all set to off, the interpolation reduces to the tensor product $\mathbf{T}$ consisting solely of the contribution of the control points in the surface. With each additional switch turned on, the grid is restructured by the control features enabled by that switch. The control mechanism is incorporated essentially in the designed difference between the geometry of the specified curves and that represented by the control point curves. The premultiplying factors yet to be discussed are the quantities α and β which smoothly pass control between the opposing boundaries corresponding to their indicated arguments and subscripts. Taken together, the controls available are then primarily used for boundary conformity and for shaping curves connecting opposing boundaries.

The two-dimensional control point formulation just outlined provides for flexible grid control for arbitrary surfaces. The on-off switches enable adjustments to be made along boundary faces independently. The method provides for a situation where one boundary face is specified and the opposing face is left open for manipulation. Adjustments to this second surface can be made through any of the methods previously discussed.

To supply further support that this method of contrived regulation can be established, it is helpful to quickly review the basic strategy underlying the control point curves in two dimensions. The strategy followed is to construct a transfinite transformation matching all the boundaries. This transfinite transformation can be constructed from the sum along each boundary of a specified curve and a control point curve minus the tensor product transformation used to establish the control point curves. Algebraic manipulation is then used to cast this transfinite transformation into a form where a separate tensor product core is manifested. The remaining part is the controlled adjustment terms representing the deviation from a pure control point representation to one of an exact boundary specification. To make this work out in two dimensions, the corner points of the face are properly accounted for in the adjustment terms in order that they will not contribute twice.

Extending the situation to the case of a three-dimensional rectangular region, we can quickly exploit our understanding of the Boolean sum process provided in the methodology section. Recall that the overall process is to be a Boolean sum which reduces to a tensor product core represented by T along with simple adjustment terms for each face or edge of the grid block. Each adjustment term appears as a blending function times the difference between the specified boundary part and the corresponding control point representation for the same part. Considering a given boundary face, the boundary edge blending terms can be separated from the pure control point dependency by properly accounting for the relevant edges. For the UV tensor product in ξ and η, those edges are the four cube edges varying in ζ. We immediately observe that the remaining faces are treated similarly and the relevant four edges are the edges transverse to the face associated with that product. The end result is a process whereby when a given adjustment term is switched off, the corresponding pair of faces and four edges are dropped in combination. In this way, only those control points effecting a given boundary need be considered when manipulating that boundary. The practical implication is that any combination of specified and free formable boundaries can be employed.

We now present the construction of the three-dimensional **CPF**. This construction is a generalization of the two-dimensional form and consequently new as well as more complex elements must be defined. The three-dimensional construction of the **CPF** can be presented in a step-by-step fashion.

First, define $\mathbf{q}_{ijk}$ as a sparse array of control points with index subscripts as such:

$$(\mathbf{q}_{ijk} : i=1,2,\ldots,L+1,\ j=1,2,\ldots,M+1,\ k=1,2,\ldots,N+1), \tag{4}$$

which establishes three sets of control point sequences whose associated end conditions are (i = 1 or L+1, j = 1 or M+1, k = 1 or N+1) for the three directions ξ, η, and ζ, respectively. It is clear that any normal sequence can be used to generate a curve which connects the first and last control points of the sequence.

Second, define curves connecting the first and last control points. This is done for each of the three families of curves by blending the corresponding control points for each sequence using the summation as follows:

$$\mathbf{a}_{jk}(\xi) = \sum_{i=1}^{L+1} \alpha_i(\xi)\, \mathbf{q}_{ijk}, \tag{5a}$$

$$b_{ik}(\eta) = \sum_{j=1}^{M+1} \beta_j(\eta)\, q_{ijk}, \tag{5b}$$

$$c_{ij}(\zeta) = \sum_{k=1}^{N+1} \gamma_k(\zeta)\, q_{ijk}, \tag{5c}$$

where α and β are the blending functions introduced previously for the two-dimensional construction and γ is the additional function required here.

Third, The curves just defined are used to construct surfaces which match the control points at their corners. The surfaces are generated by three sets of double summations which are given as the following single indexed coefficients:

$$A_i(\eta,\zeta) = \sum_{j=1}^{M+1} \sum_{k=1}^{N+1} \beta_j(\eta)\, \gamma_k(\zeta)\, q_{ijk}, \tag{6a}$$

$$B_j(\xi,\zeta) = \sum_{i=1}^{L+1} \sum_{k=1}^{N+1} \alpha_i(\xi)\, \gamma_k(\zeta)\, q_{ijk}, \tag{6b}$$

$$C_k(\xi,\eta) = \sum_{i=1}^{L+1} \sum_{j=1}^{M+1} \alpha_i(\xi)\, \beta_j(\eta)\, q_{ijk}, \tag{6c}$$

Fourth, the coarse array of control points are used to construct the tensor product core. This is done simply in terms of the blending functions used for the surface construction and is given by

$$T(\xi,\eta,\zeta) = \sum_{i=1}^{L+1} \sum_{j=1}^{M+1} \sum_{k=1}^{N+1} \alpha_i(\xi)\, \beta_j(\eta)\, \gamma_k(\zeta)\, q_{ijk}. \tag{7}$$

This tensor product core corresponds to the UVW term in our three-dimensional Boolean expression for the general position vector $X(\xi,\eta,\zeta)$.

Fifth, we construct the adjustment terms corresponding to the surfaces and edges of the array boundary. The adjustment terms are a generalization of the two-dimensional construction. It can be presented in two steps. Each step is formed around the tensor product core. Thus, for the first adustment associated with the surfaces, the univariate interpolations are given by the following:

$$\mathbf{U}(\xi,\eta,\zeta) = \mathbf{T}(\xi,\eta,\zeta) + \alpha_1(\xi)[\mathbf{X}(\xi_1,\eta,\zeta) - \mathbf{A}_1(\eta,\zeta)] + \alpha_{L+1}(\xi)[\mathbf{X}(\xi_L,\eta,\zeta) - \mathbf{A}_{L+1}(\eta,\zeta)], \tag{8a}$$

$$\mathbf{V}(\xi,\eta,\zeta) = \mathbf{T}(\xi,\eta,\zeta) + \beta_1(\eta)[\mathbf{X}(\xi,\eta_1,\zeta) - \mathbf{B}_1(\xi,\zeta)] + \beta_{M+1}(\eta)[\mathbf{X}(\xi,\eta_M,\zeta) - \mathbf{B}_{M+1}(\xi,\zeta)], \tag{8b}$$

$$\mathbf{W}(\xi,\eta,\zeta) = \mathbf{T}(\xi,\eta,\zeta) + \gamma_1(\zeta)[\mathbf{X}(\xi,\eta,\zeta_1) - \mathbf{C}_1(\xi,\eta)] + \gamma_{N+1}(\zeta)[\mathbf{X}(\xi,\eta,\zeta_N) - \mathbf{C}_{N+1}(\xi,\eta)]. \tag{8c}$$

This establishes the adjustment terms for the boundary surfaces. Notice that the tensor product core appears in each univariate construction. These correspond to the **U**, **V**, and **W** terms in the Boolean expression for the general position vector. To complete the process, the second step deals with the three product terms **UV**, **UW**, and **VW** of the Boolean sum. Again by design, each of these three products are constructed around the tensor product core. To eliminate redundancy, only the **UV** product construction is written out. The remaining two can be achieved by cyclic substitution. This product term takes the following:

$$\mathbf{UV} = \mathbf{T}(\xi,\eta,\zeta) +$$

$$\alpha_1(\xi)\beta_1(\eta)(\mathbf{X}(\xi_1,\eta_1,\zeta) - \mathbf{c}_{1,1}(\zeta)) + \alpha_1(\xi)\beta_{M+1}(\eta)(\mathbf{X}(\xi_1,\eta_M,\zeta) - \mathbf{c}_{1,M+1}(\zeta))$$

$$+ \alpha_{L+1}(\xi)\beta_1(\eta)(\mathbf{X}(\xi_L,\eta_1,\zeta) - \mathbf{c}_{L+1,1}(\zeta)) + \alpha_{L+1}(\xi)\beta_{M+1}(\eta)(\mathbf{X}(\xi_L,\eta_M,\zeta) - \mathbf{c}_{L+1,M+1}(\zeta)). \tag{9}$$

Since each of the three binary product terms appear as negative terms in the Boolean sum, the three tensor product terms arising here collectively cancel those three arising in the **U**, **V**, and **W** constuctions. We are thus left with the single tensor product core due to the **UVW** term and the three pairs of surface adjustments and finally the three sets of corresponding edge adjustments. This completes the construction process.

INTERACTIVE GRID GENERATION EXAMPLES

Figure 1 shows an example of a two-dimensional control point array $(\mathbf{q}_{ij})$. A fundamental part of the **CPF** is the construction of coordinate curves, whose shape and location are controlled by the control points. Construction of a coordinate curve, $\mathbf{E}_2(r)$, is illustrated in the figure. The basic interactive process of generating grids using the **CPF** is illustrated in figure 2 using the basic computer program called CPGRID (reference 1). It starts with the construction of a control net using transfinite interpolation and a surface grid. An initial grid is generated and examined. If desired, the grid can be improved by changing the structure of the control net. In this example a control point is moved to a new position to obtain fine meshes in the middle of the flow domain.

A family of menu-driven interactive grid generation programs (TurboI and TurboT) is being developed using the CPF. Several features of the programs allow the global control net to be conveniently changed by the user. The point by point modification of the control net is then used to make a more precise local change. TurboI (reference 6) generates grids for flow simulations in internal flow passages such as inlets, nozzles, and ducts. TurboT (reference 7) is being tailored for turbomachinery. Both programs run on IRIS 4D workstations.

Figure 3 shows an H-grid generated by using TurboI for a turbine stator vane. In this example, the user used only those basic interactive features (i.e., the point by point control of the control net) which are illustrated in figure 2. Figure 3(a) shows an initial control net; figure 3(b) shows an initial grid. The modified control net and grid are shown in parts (c) and (d) of the figure, respectively. The modified grid is nearly orthogonal to the vane surface and is densely clustered around the leading and trailing edges.

The dynamic nature of the interactive process of TurboI is illustrated in figures 4 through 8 using a grid generation example for a converging/diverging axisymmetric nozzle. After logging on an IRIS 4D workstation, the user should type in TurboI to begin the interactive process of the program. The system then asks for the input filename. When the user types in the input filename, TurboI reads in the data, and displays it as shown in figure 4 with menus. To continue the process, the user selects the option called "RESUME". The workstation mouse is all that is needed to select a menu option. Reference 2 explains about the program TurboI and its interactive features in detail.

Selection of the menu option "RESUME" prompts TurboI to construct initial control net by using a simple linear interpolation. TurboI then proceeds to generate the field grid using the control point form, and displays both the grid and control net on the screen. The "SCROLL VIEW" option allows the user to examine either the grid alone, the control net alone, or the grid and control net together. To examine the grid more closely about a region of interest, the menu option "ZOOM & MOVE" is available. The initial control net and initial grid are shown in parts (a) and (b) of figure 5, respectively. In this example, the initial grid shows that it has a slope discontinuity across the symmetry axis and non-orthogonal grid along the nozzle surface.

For illustration purpose, suppose our objectives of this exercise are (a) to make the grid orthogonal to the nozzle surface and (b) to have slope continuity across the horizontal symmetry axis.

To accomplish the above objectives, the option called "MODIFY CONTROL NET" should be chosen. Then, a set of menus appears on the screen. Selecting the option called "Normalize at TOP (2 level)" is the first step to make the grid orthogonal to the nozzle surface. In order to obtain slope continuity across the symmetry axis, a menu option called "Normalize Bottom (1 level)" is selected. The modified control net at this stage is shown in figure 6(a). Selection of the menu called "Recalculate GRID" will then recompute the grid based on the modified control net. This modified grid shown in figure 6(b), however, does not have slope continuity across the symmetry axis in spite of the orthogonal control net. This is because the grid points on the symmetry axis are not allowed to change (Dirichlet boundary condition is enforced). To modify the grid on the symmetry axis, choose the CN line of that boundary by choosing the menu item "Move j-Net" until the desired boundary CN curve is highlighted in red. Then the menu item called "Free Form Boundary" should be selected to allow movement of grid points along the boundary to conform the orthogonal control net (Neuman boundary condition.) Choosing the option "FREE FORM Boundary" is equivalent to turning off one of the boundary on-off switches (ρ_i) of equation (3). Selecting the option "Recalculate GRID" produces the new grid shown in figure 6(c). This grid meets the objective of this example.

Further improvement (or fine tuning) of mesh structure can easily be done with TurboI. Examination of the internal mesh of figure 6(c) shows that changes in the slope of some coordinate curves are larger than necessary. To cut down on these large changes, a mesh control feature called "SNAP" is used. This allows for smoothing of a CN curve as if a RUBBER BAND were stretched between the current CN point at $\mathbf{q}_{34}$ and a chosen "Hinge Point" in a circular mark at $\mathbf{q}_{32}$ in figure 7(a). On the workstation screen, the current control point is an intersection of two highlighted control-net lines. Selecting the menu option called "SNAP" changes the CN line segment between the hinge point and the current CN point to the one shown in figure 7(b). A user can then move on to the next CN curve and "SNAP" it if desired. At the end of this fine tuning process, the control net has the structure as shown in figure 7(c). Finally, select the option "Recalculate GRID". The new grid calculated from the fine tuned control net is shown in figure 8(a). It is zoomed and shown in figure 8(b).

Many grid generation programs do not allow local mesh control as TurboT does. For TurboT the initial grid may be generated by any program familiar to a user; then an initial control net may be obtained from the grid by attachment to produce a grid structure that is essentially similar to the initial one. The initial control net shown in figure 9(a) was constructed by attachment. Figure 10(a) shows an initial grid of a compressor rotor blade. Once the control net is created, the interactive process to be followed is very similar to the process of TurboI. The control net is modified to the one shown in figure 9(b), and a new grid shown in figure 10(b) is generated from the modified control net. The modified grid is more orthogonal and has slope continuity across the periodic boundary. The shape of the control net can easily be changed by using an interactive process illustrated in figure 11. In part (a) of the figure, a user first chooses a control line to be changed and then picks a hinge point. In part (b), control point 1 is moved to point 2 by moving the mouse of the workstation. Point 1' automatically moves to point 2' while maintaining a pitch with the points 1 and 2, respectively. In part (c), the desired shape of the control line is obtained by choosing a menu option called "SNAP" which makes the control line stretch like a rubberband.

CONCLUSION

Our objective in this work has been to report on a simply structured scheme of algebraic grid generation. This scheme is called **CPF** and a number of grid generation codes now employ it. Several underlying features of **CPF** make it an ideal candidate for existing and emerging applications. These features include the following: the capability of conforming to boundaries; the quality of being easily manipulated by numerous local and global grid distribution strategies, concise structure of its formulation which enables its straightforward implementation, and the inherent quality of being compatible with various complementary or supportive operations. Many of these beneficial features are already being exploited. Their usefulness has been demonstrated here by way of two-dimensional examples illustrating basic interactive features. These examples pertain to flow simulations specific to turbomachinery and internal flow passages such as inlets, nozzles, and ducts. Notwithstanding the restricted range of application considered here, **CPF** is in fact a general procedure with wide-ranging potential for application.

REFERENCES

1. Eiseman, P.R., "A Control Point Form of Algebraic Grid Generation," Intl. J. Numerical Methods in Fluids, Vol. 8, pp. 1165-1181, 1988.

2. Eiseman, P.R., Choo, Y.K., Smith, R.E., "Algebraic Grid Generation with Control Points," Finite Elements in Fluids, Vol. 8, edited by T. J. Chung, Hemisphere Publishing Corporation, to appear in 1990.

3. Gordon, W.J., Thiel, L.C., "Transfinite Mappings and their Application to Grid Generation," Numerical Grid Generation, Edited by J. F. Thompson, North-Holland, 1982, pp. 171-192.

4. Smith, R.E., Eriksson, L.E., "Algebraic Grid Generation," Computer

Methods in Applied Mechanics and Engineering, vol. 64, no. 1-3, Oct. 1987, pp. 285-300.

5. Eiseman, P.R., "Coordinate Generation with Precise Control over Mesh Properties," J. Comp. Phys., Vol. 47, No.3, pp. 331-351, 1982.

6. Choo, Y.K., Reno C., Van Overbeke T., Sosoka, D., "Interactive Grid Generation Using Control Point Form, "Program TurboI for Inlets, Nozzles, and Ducts, version 01.01, to be printed as a NASA TM.

7. Choo, Y.K., Soh, W., Yoon, S., "Application of a Lower-Upper Implicit Scheme and an Interactive Grid Generation for Turbomachinery Flow Field Simulations," ASME Paper 89-GT-20, June 1989.

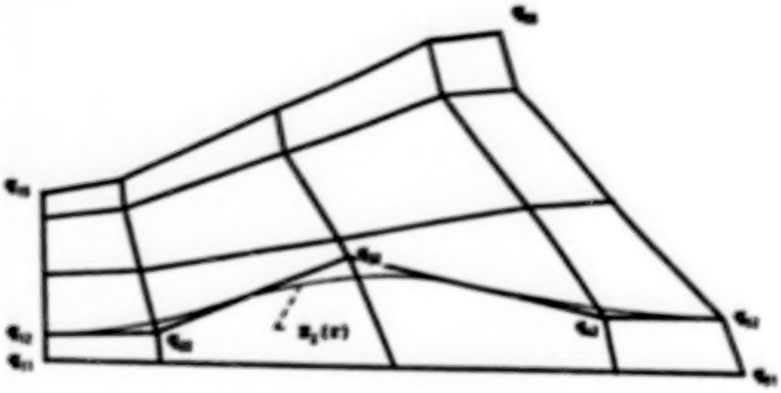

FIGURE 1. CONTROL NET - AN EXAMPLE IN TWO DIMENSIONS

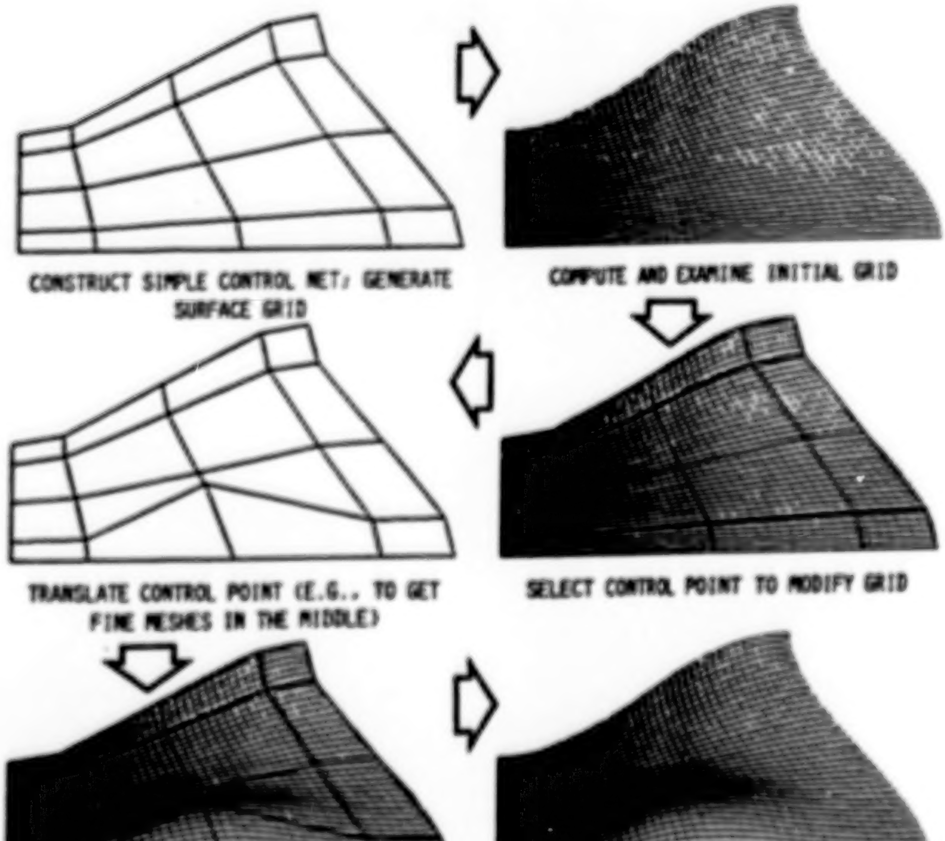

CONSTRUCT SIMPLE CONTROL NET; GENERATE SURFACE GRID

COMPUTE AND EXAMINE INITIAL GRID

SELECT CONTROL POINT TO MODIFY GRID

TRANSLATE CONTROL POINT (E.G., TO GET FINE MESHES IN THE MIDDLE)

RE-COMPUTE

EXAMINE NEW GRID - ACCEPT OR REPEAT PROCESS

FIGURE 2. BASIC INTERACTIVE PROCESS

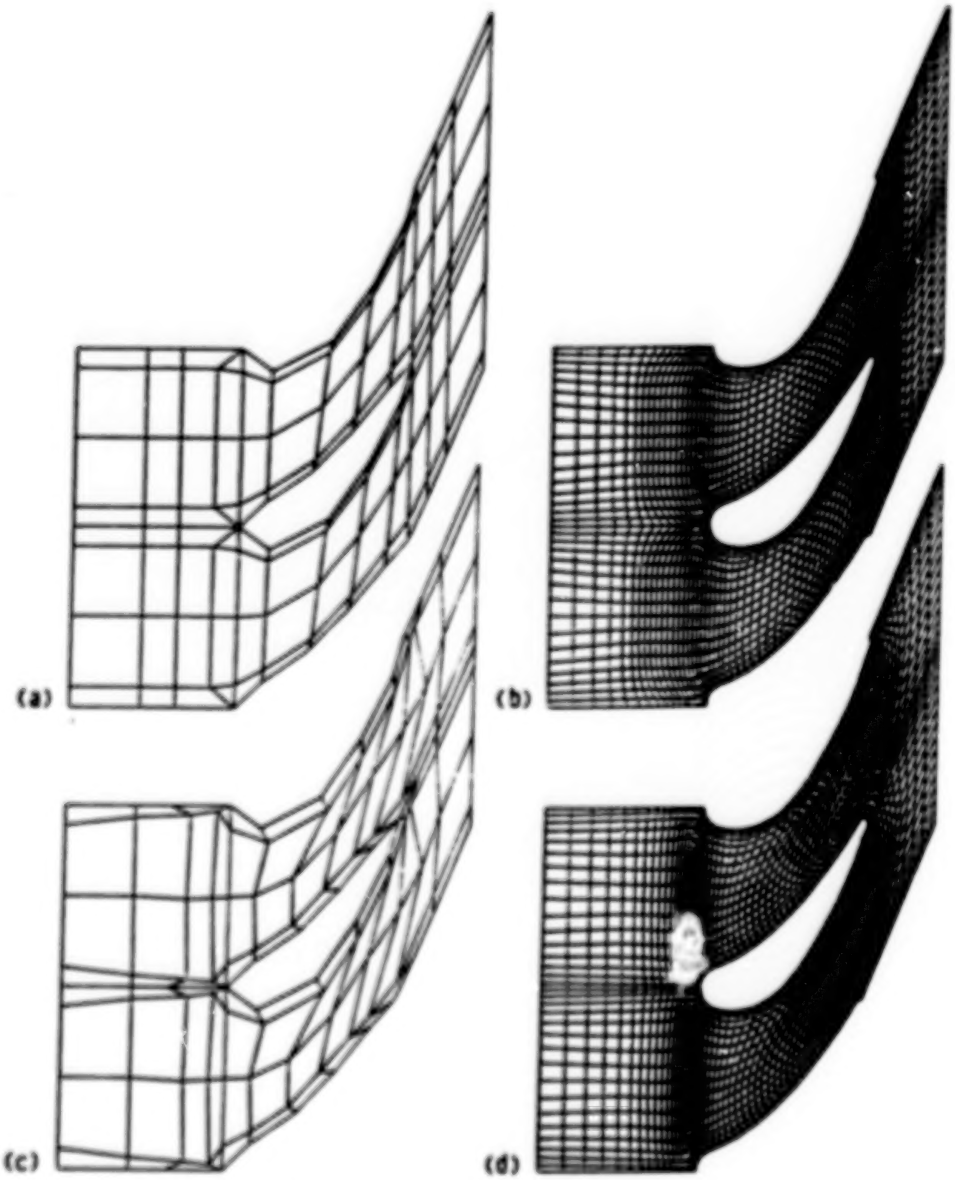

(a) Initial control net.
(c) Modified control net.

(b) Initial grid.
(d) Modified grid.

FIGURE 3. GRID GENERATION FOR A STATOR VANE

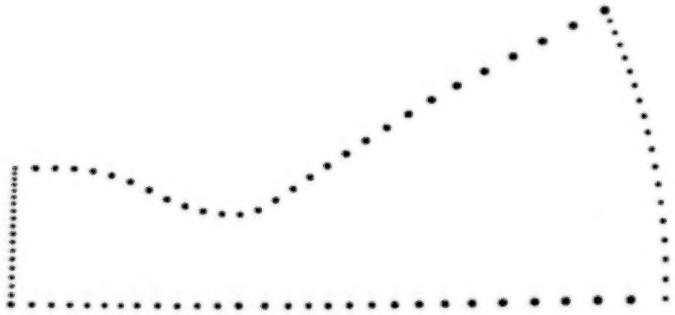

FIGURE 4. BOUNDARY GRID OF A CONVERGING/DIVERGING NOZZLE

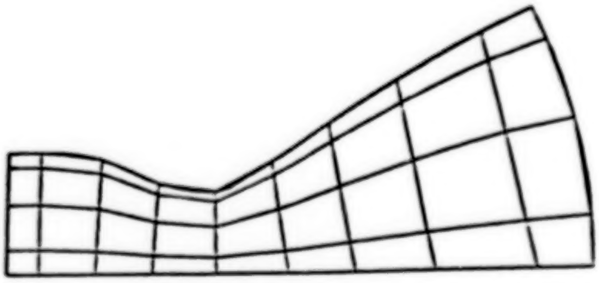

(a) INITIAL CONTROL NET

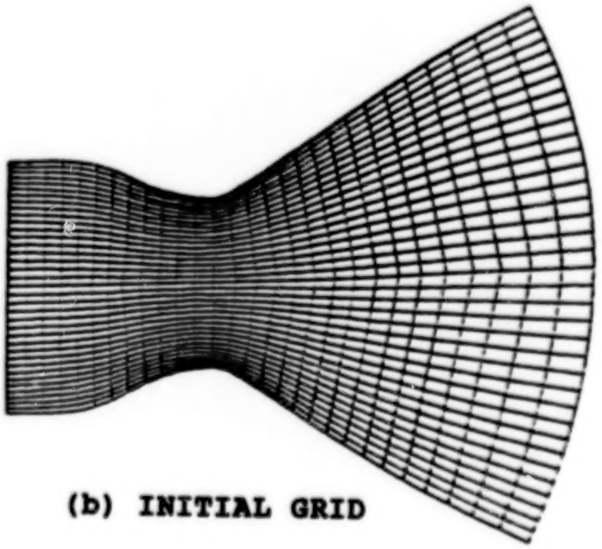

(b) INITIAL GRID

FIGURE 5. INITIAL RESULTS

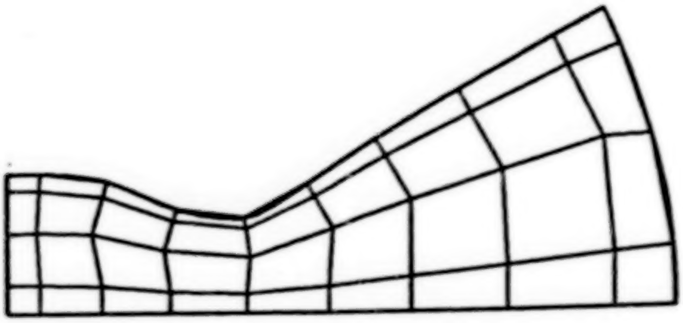

(a) CONTROL NET ORTHOGONAL TO TOP AND BOTTOM BOUNDARIES

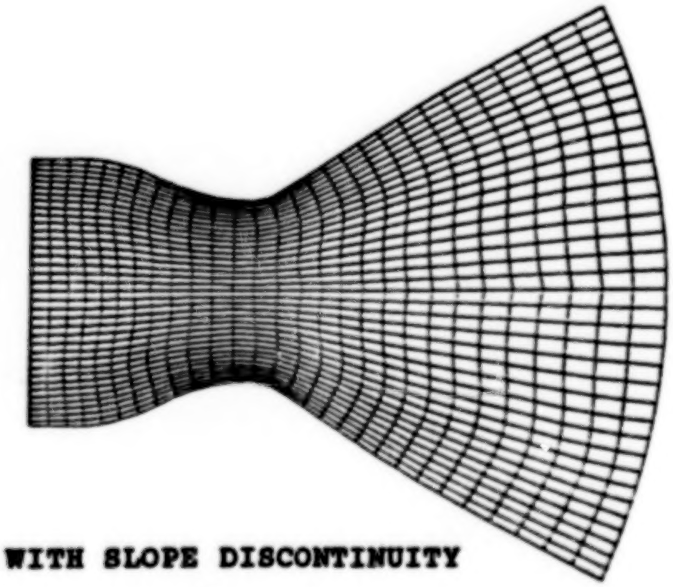

(b) GRID WITH SLOPE DISCONTINUITY
ACROSS THE SYMMETRY AXIS

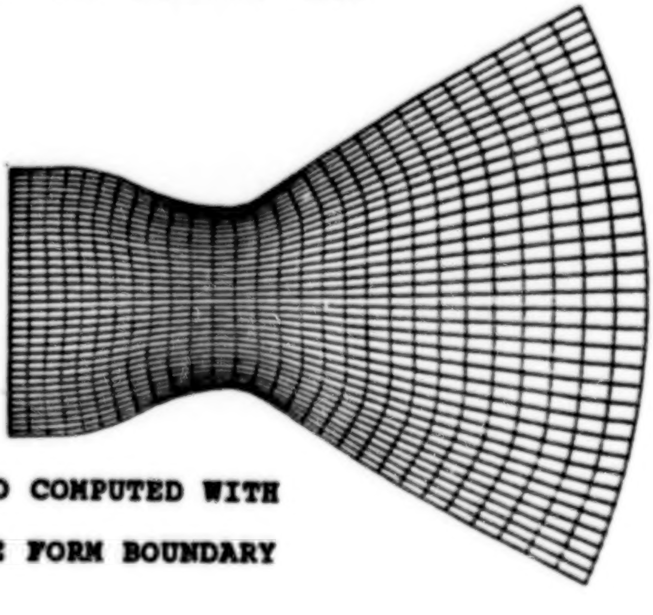

(c) GRID COMPUTED WITH
FREE FORM BOUNDARY

FIGURE 6. INTERACTIVE PROCESS OF GRID MODIFICATION

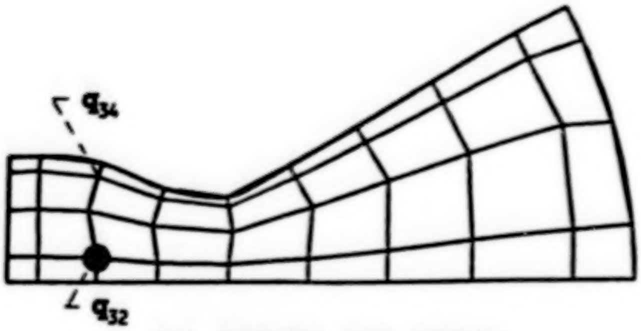

(a) BEFORE THE "SNAP"

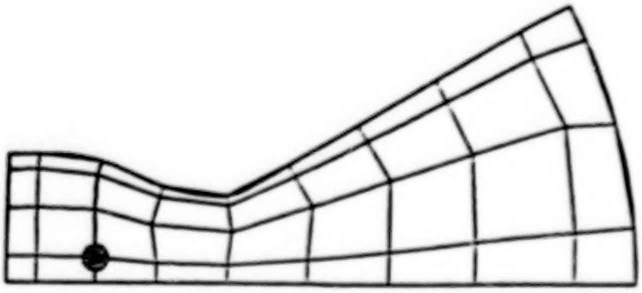

(b) AFTER THE "SNAP"

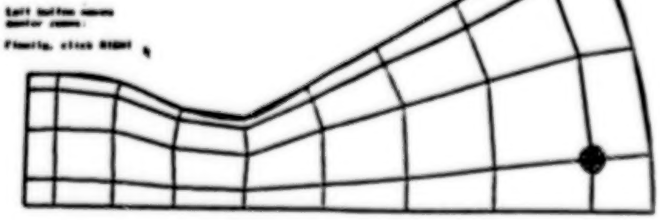

(c) END OF FINE TUNING

FIGURE 7. INTERACTIVE PROCESS FOR FURTHER MODIFICATION

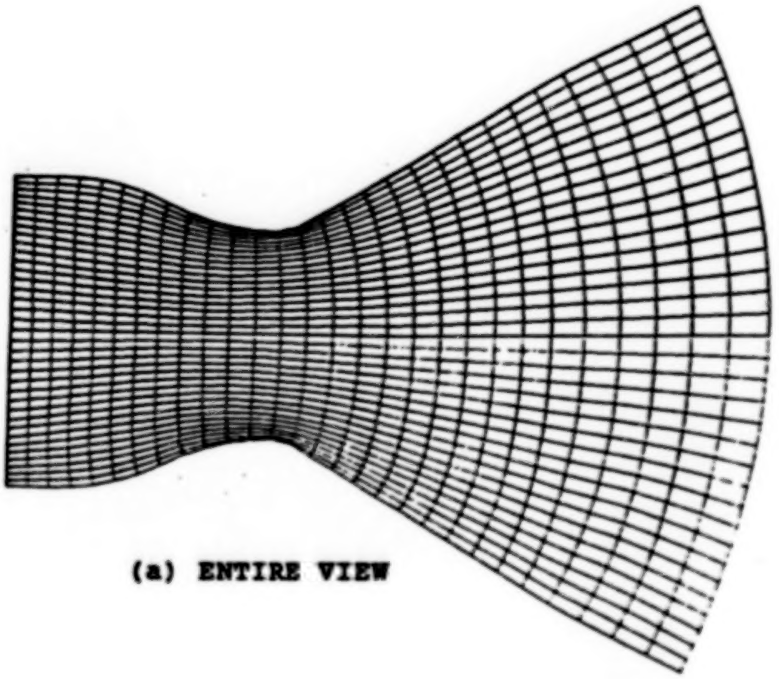

(a) ENTIRE VIEW

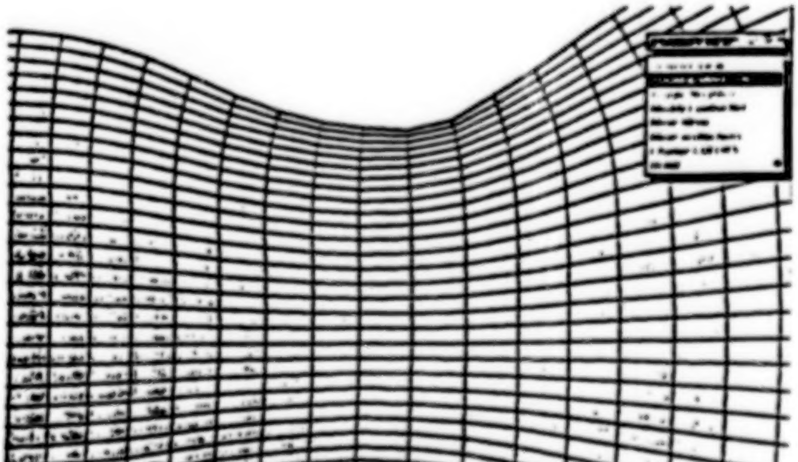

(b) A CLOSER VIEW

FIGURE 8. FINAL MODIFIED GRID

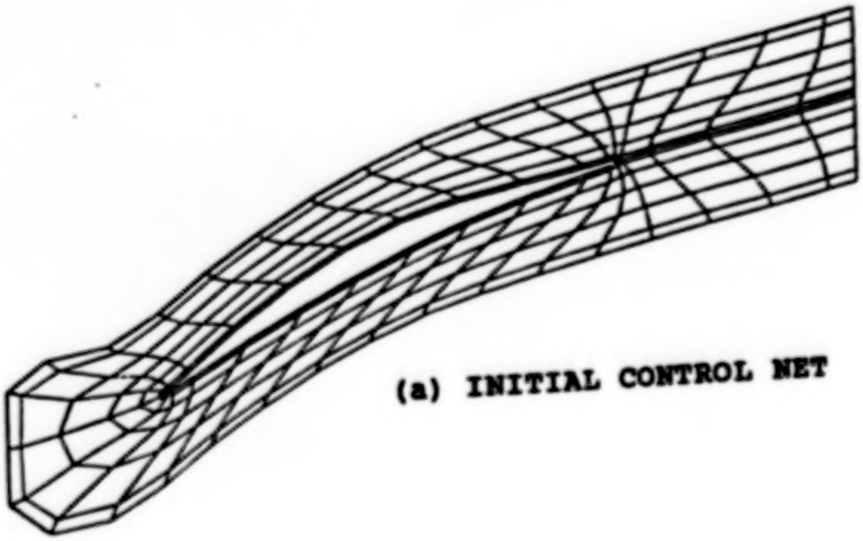

(a) INITIAL CONTROL NET

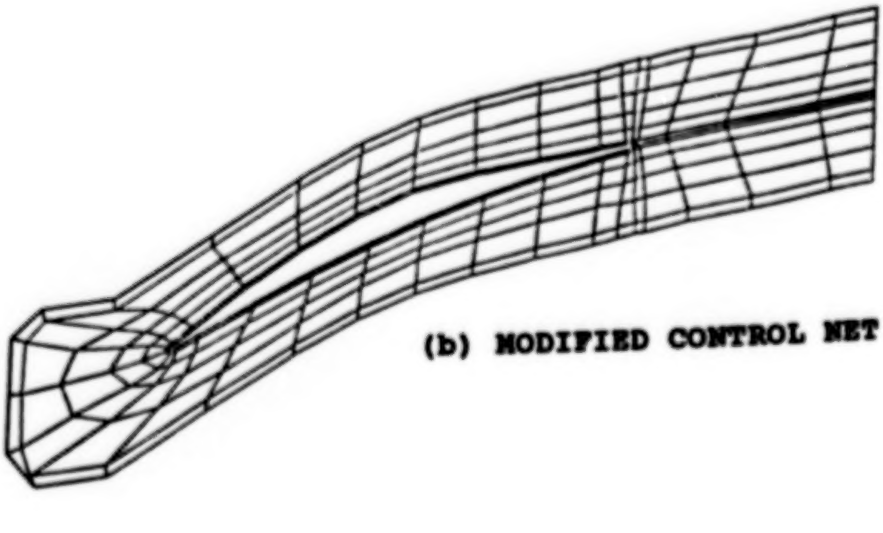

(b) MODIFIED CONTROL NET

FIGURE 9. CONTROL NET FOR A COMPRESSOR ROTOR

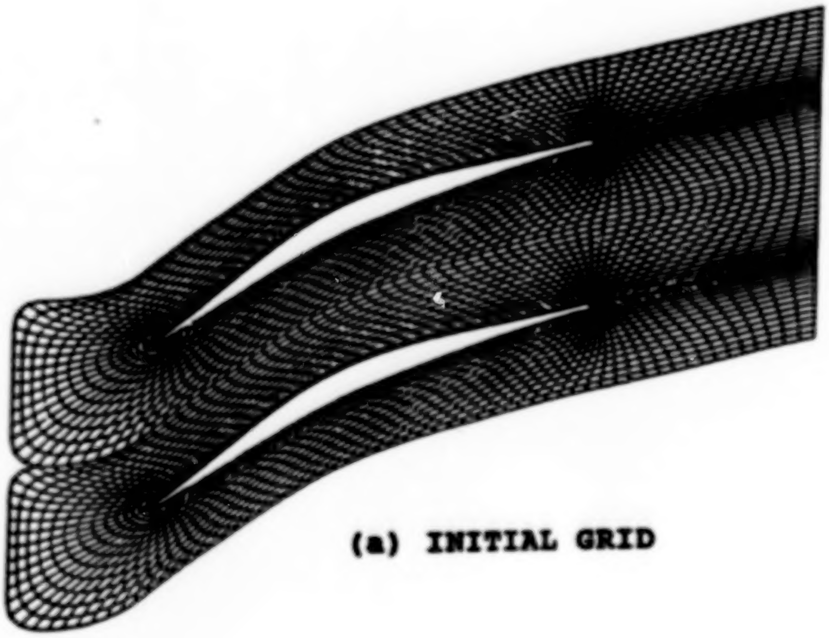

(a) INITIAL GRID

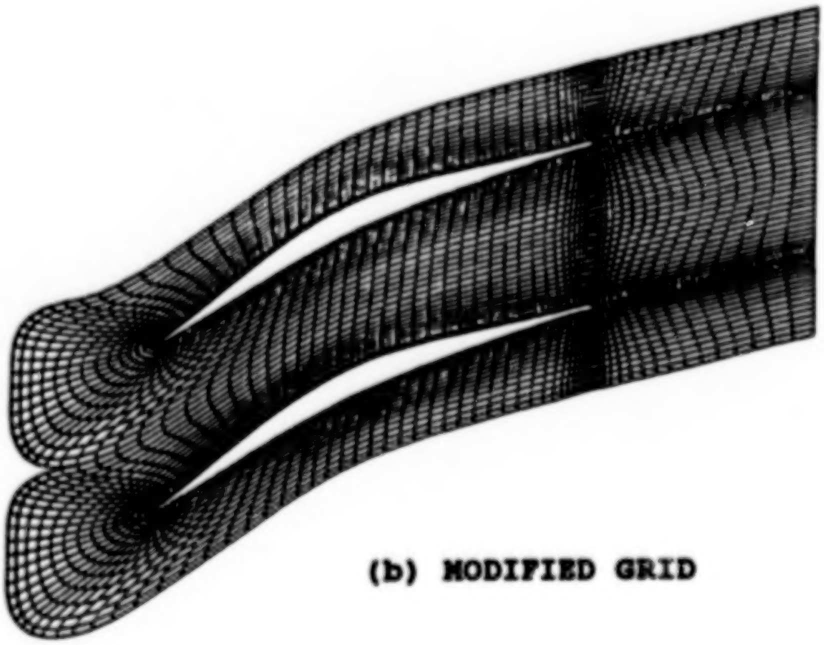

(b) MODIFIED GRID

FIGURE 10. GRID COMPARISON

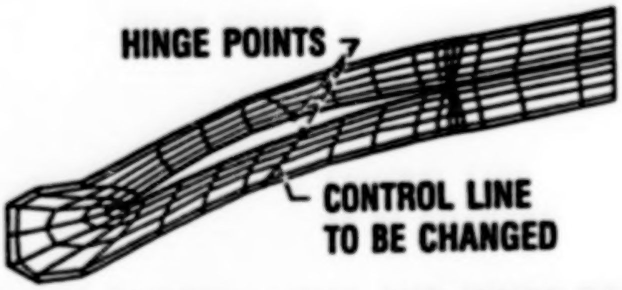

(a) SELECT CONTROL LINES AND HINGE POINTS

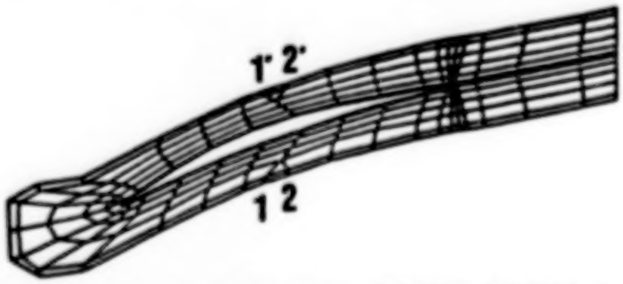

(b) TRANSLATE A CONTROL POINT FROM 1 TO 2

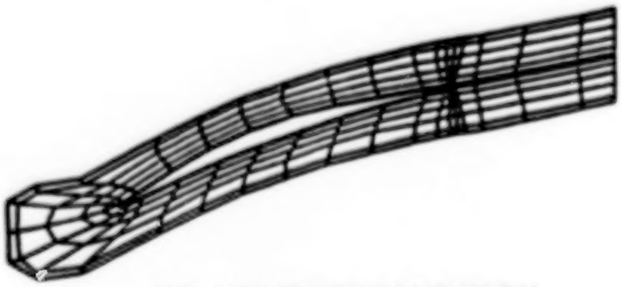

(c) DO "RUBBERBANDING"

FIGURE 11. A CONTROL FEATURE OF TurboT

GRID GENERATION STRATEGIES FOR TURBOMACHINERY CONFIGURATIONS

K. D. Lee* and T. L. Henderson**
University of Illinois
Urbana, IL 61801

ABSTRACT

Turbomachinery flow fields involve unique grid generation issues due to their geometrical and physical characteristics. Several strategic approaches are discussed to generate quality grids. The grid quality is further enhanced through blending and adapting. Grid blending smooths the grids locally through averaging and diffusion operators. Grid adaptation redistributes the grid points based on a grid quality assessment. These methods are demonstrated with several examples.

INTRODUCTION

Providing quality grids is a prerequisite for successful flow calculations. It is well known that most flow codes yield different solutions for the same problem with different grids. Therefore, for accurate solutions, grids should not only resolve geometric details of the configuration, but also accommodate characteristic features of the flow. In addition, grids should be compatible with particular solution algorithms in the flow code. As physical and geometrical complexities increase, it becomes more difficult to generate suitable grids.

Flow fields in propulsion systems often involve complicated geometries and exhibit complex flow phenomena. Internal flow fields are characterized by confined domains which may invoke more restrictive constraints and conflicting requirements in grid generation. Major difficulties involved with grid generation for turbomachinery configurations are attributed to the periodicity of the flow field and the close proximity of configuration elements. Moreover, some grid properties such as grid smoothness, grid orthogonality, and grid-flow alignment become very important in correctly capturing the physics of the flow field. The grid should be tailored to resolve flow features such as large thermal gradients, complicated shocks, and flow separations.

This paper addresses several issues arising in grid generation for turbomachinery configurations and discusses some grid generation strategies which can improve grid quality. Also considered are advantages and disadvantages of multi-block grid topologies and special grid arrangements at the periodic boundary. Then, two approaches which enhance grid quality are presented and demonstrated. One employs a local blending concept that enforces smoothness and continuity in grid properties. The other uses a grid adaptation procedure in which grid points are redistributed according to a grid quality measure. The latter is based on a grid adaptation technique developed to generate adaptive grids with respect to geometry, flow solution, and grid quality [1-3].

---

* Associate Professor, Aeronautical and Astronautical Engineering
** Graduate Research Assistant, Mechanical Engineering

GRID GENERATION ISSUES

The accuracy and efficiency of numerical solutions depend on certain properties of the grid used. Grid density determines the amount of truncation error in the flow calculation. Hence, grid points should be distributed following the flow physics to achieve the best possible accuracy while maintaining the same computational efficiency. This can be accomplished by using fine grids in high gradient regions and relatively coarse grids in slowly varying regions. An additional constraint is that the grid size should be at least the same order of magnitude as the characteristic length scales of the physics to be captured. Other grid properties also affect computational accuracy and economy. The resolution of discontinuities such as shock waves, contact surfaces, and dividing streamlines can best be accomplished with grids that are aligned with the discontinuities. Grid skewness, grid kinking, and grid stretching also affect the order of accuracy in spatial discretizations and strongly influence the convergence rate. In extreme cases, highly distorted grids may cause solution divergence. It is very difficult to generate a grid which is satisfactory in all respects, particularly when complex geometries are involved as in high-speed turbomachinery applications.

The primary difficulty for generating grids for high-speed turbomachinery stems from the confinement and periodicity of the flow domain. The presence of high thermal gradients and complicated shock structures makes the grid generation more difficult. It is desirable to cluster grid points and align grid lines along characteristics of the geometry and the flow in order to improve solution accuracy and numerical efficiency. However, improving one grid property may deteriorate other grid properties and grid enhancement in one region can cause conflicts with grid requirements in other regions. For example, a desirable grid density distribution may require sacrifices in grid properties such as grid orthogonality and smoothness. Grid orthogonality near the blade surface may also increase grid skewness elsewhere. These side effects become more significant when the turbomachinery geometry involves a small pitch angle, high angle of attack, and/or high camber.

Different flow codes impose different requirements on the grid quality. While some flow algorithms are more independent of grid characteristics, others place more stringent restrictions on the quality of the grid. Therefore, a careful balance must be obtained between the grid quality, solution algorithm, and flow physics. When these elements are not properly balanced, numerical errors may destroy important solution details or impair the convergence rate of the flow solver. This may occur to such an extent that the solution may not be useful. For example, many codes prefer that the grid be nearly orthogonal at domain boundaries for accurate implementations of boundary conditions. Another example can be found in the use of the thin-layer Navier-Stokes approximation. The approximation results in better accuracy with grids that have small variations in grid properties. Many higher-order upwind schemes also prefer smooth, well-aligned grids. Such additional restrictions underscore the importance of grid quality.

Since grid quality issues are often subject to conflicting requirements, suitable grids generally cannot be created in a single attempt. Grid generation involves negotiations and compromises between different grid characteristics. Usually grid quality is upgraded through an iterative grid adaptation process using grid quality assessments based on either experience or analysis. However, it is desirable to generate an initial grid that encompasses as many good qualities as possible in order to minimize efforts for improvement. This requires grid generation strategies which can accommodate anticipated flow characteristics and minimize conflicts between grid properties. Then a grid adaptation process can be applied to reduce the remaining deficiencies in grid properties. A systematic means of grid quality assessment can facilitate the grid modification process.

GRID GENERATION STRATEGIES

Three grid topologies are often used to generate grids around airfoil shapes: C-grid, O-grid, and H-grid. Different grid structures create different issues in grid generation and flow calculations. They each have their own advantages and disadvantages. These topologies are also used for turbine and compressor blades, as shown in Figure 1. The O-grid topology requires the least number of grid points to resolve the flow field near the blade surface, but exhibits difficulties in accommodating the confined and periodic features of turbomachinery. It is also difficult to align the grid lines with flow characteristic directions in the upstream and downstream regions. This problem can be resolved in the downstream side by using the C-grid topology. However, difficulties remain in aligning the grid lines with the periodic boundary and the flow direction in the upstream inflow region.

The H-grid structure is an alternative which is well suited to turbomachinery geometries because of its natural alignment with the periodic boundary, but the H-grid introduces other challenges. The H-grid structure raises different issues such as grid kinking across block boundaries and grid singularities at the leading and trailing edges. Figure 2 shows a typical grid for a turbine blade at a high angle of attack using the H-grid topology. Comparatively large cells or kinked grid lines can appear near the leading and trailing edges where rapid flow changes are expected. The grid becomes extremely skewed in the trailing edge region. This happens with all three grid topologies when the angle of attack or camber increases. The grid skewness may deteriorate the accuracy or cause instabilities in flow calculations.

One of the major issues in grid generation for turbomachinery is the grid skewness due to the presence of periodic boundaries. Two approaches are considered to improve grid qualities at the periodic boundary; grid slipping and index off-setting. Figure 3 shows a typical grid generated by allowing the grid lines to slip along the periodic boundary instead of matching them across the boundary. This eliminates the issue of grid skewness and kinkiness. It allows a family of grid lines to float along the boundary until they are orthogonal. Since grid lines no longer match across the periodic boundary, flow solvers should be furnished with an interpolation scheme to communicate across the boundary. The grid orthogonality at the boundary helps prevent losses in accuracy or convergence due to the interpolation. As seen in Figure 3, however, extremely large cells can appear near the periodic boundary when enforcing the orthogonal condition with a highly cambered blade. This presence of large cells can hurt the accuracy of the flow solution.

Another way to reduce grid skewness is to use index off-setting. This is a technique which allows grid lines with different indices to match across the periodic boundary. This allows the grid to be more orthogonal throughout the flow field while maintaining continuity across the periodic boundary. Figure 4 shows a typical example of index off-setting for a grid around a turbine blade. While no interpolation of flow variables is necessary, as in the case with grid line slipping, some additional bookkeeping is required to communicate across the boundary. In addition, a different number of grid points can be used on the leeward and windward sides of the blade. The grid in Figure 4 however uses the same number of grid points on both sides. The index off-setting strategy creates an irregularity at the farfield upstream and downstream boundaries, which may require additional care in handling multiple stage situations.

Grid quality can be further improved by combining different grid topologies. One example is the O-H grid structure. An O-grid is inserted into a H-grid, as shown in Figure 5. This combination can provide the advantages of the O-grid at the near field in accommodating the thermal and viscous boundary layers. It can also provide the flexibility of the H-grid in the upstream and downstream regions. The grid skewness has been reduced by allowing grid lines to slip along the periodic boundary. The grid orthogonality near the blade has been improved, but many grid quality issues are still not resolved. The adoption of different grid strategies accompanies trade-offs. Enhancement of one grid property may cause deterioration in other aspects. All constraints cannot be resolved simultaneously and hence compromises should be reached. Therefore, the next step to improve grid quality is to use grid modifications after the initial grid generation.

GRID IMPROVEMENT BY BLENDING

The basic premise is that good quality grids usually cannot be obtained using a single-block grid structure for complex geometries. The grid quality can be improved by using a multiple block structure where the flow domain is divided into blocks and surface-fitted grids are generated in each block [4]. The H-grid and O-H grid structures in the previous section are examples of a multi-block grid. However, the multi-block structure introduces other concerns with respect to the grid quality. Without communication between blocks, grid lines can be kinked, and grid spacing can change abruptly across block boundaries. Communication between blocks is not always easy. Therefore it would be easier to improve the transition between blocks after the initial grid generation.

A natural approach to smoothing is to use blending. That is, the grid points in the neighborhood of a block boundary are relocated by using a diffusion operator. For example,

$$\overline{X}_t = \mu_1 \overline{X}_{\xi\xi} + \mu_2 \overline{X}_{\eta\eta} \tag{1}$$

where $\overline{X} = (x,y)$ denotes the physical coordinates of a grid point, and (ξ,η) are the grid indices of the computational domain. The parameters μ_1 and μ_2 are diffusion coefficients which determine the degree of blending. The time derivative in the left hand side implies the change of grid positions through blending. The blending can be applied in both implicit and explicit manners.

The blending can be extended into a more general form

$$\overline{X}_t = A_\eta D_\xi \mu_1 D_\xi \overline{X} + A_\xi D_\eta \mu_2 D_\eta \overline{X} \tag{2}$$

where A and D represent averaging and differential operators respectively with their subscripts indicating the direction of operation. Here, the diffusion coefficients μ_1 and μ_2 are no longer constants; they include weighting factors extracted from the initial grids. The weighting is defined to preserve the positive characteristics of the original grids.

The O-H grid shown in Figure 5 includes blending across the block boundaries. Figure 6 compares the grids before and after the blending in the leading and trailing edge regions. The inner O-grid is smoothly blended with the outer H-grid eliminating the grid kinking while maintaining basic grid spacing. The inner O-grid is nearly orthogonal to improve heat transfer and skin friction calculations. Improvements in grid quality can also be seen near the singular points where six cells join together, instead of regular four cells. The blending distributes the vertex angles more evenly and produces smoother grid transitions across block boundaries.

GRID IMPROVEMENT BY ADAPTATION

Grid quality can also be improved by using the adaptive grid generation technique presented in reference 3. In this approach, grid adaptation is achieved by numerically altering the mapping functions between the physical and computational spaces using grid control sources. Depending on how the control sources are defined, grids can be made adaptive to geometry, flow solution, or grid quality. The grid is adapted to grid quality in this work. Source strengths are extracted from the distribution of a grid quality parameter defined on the initial grid.

The grid adaptation procedure begins with a parametric representation of the initial grid which is obtained by normalizing its computational coordinates, or indices, into a unit square. The result is a uniformly discretized domain in parametric coordinates (s,t). This first mapping contains characteristics of the initial grid, which may already include grid controls with respect to geometry and flow solution.

The source strengths for grid control are formulated to reflect local grid characteristics. Two grid control sources are defined in each cell for separate control in each of the parametric directions. First, a monitor function ϕ is chosen which is a measure of some grid property. The source strengths can then be defined as linear combinations of the monitor function and its derivatives in each parametric coordinate. For example,

$$\sigma^s_{kl} = w^s_0\phi + w^s_1\frac{\partial\phi}{\partial s} + w^s_2\frac{\partial^2\phi}{\partial s^2}$$

$$\sigma^t_{kl} = w^t_0\phi + w^t_1\frac{\partial\phi}{\partial t} + w^t_2\frac{\partial^2\phi}{\partial t^2} \qquad (3)$$

where k and l are the indices of the cell containing the source. The w's are input parameters which allow for different weights to be placed on the various derivatives of ϕ. Candidates for the monitor function, or grid quality parameter, include grid skewness, grid kinking, grid stretching, cell aspect ratio, cell volume, etc. A combination of different grid quality parameters can also be used.

A second mapping is obtained by including the influences of the grid control sources. This defines a modified set of parametric coordinates (s',t').

$$s'_{ij} = s_{ij} + \sum_{k,l} K^s_{ijkl}\sigma^s_{kl}$$

$$t'_{ij} = t_{ij} + \sum_{k,l} K^t_{ijkl}\sigma^t_{kl} \qquad (4)$$

where K^s_{ijkl} and K^t_{ijkl} are influence coefficients for the effects of a source (k,l) at a point (i,j). The coefficients are defined as exponentially decaying functions of the distance between the two points.

As a result of the second mapping, grid lines are displaced by the sources. The displacement is greatest in the regions of strong sources. The next step is to rediscretize the modified parametric domain. The physical locations of the new grid points are then obtained by an inverse mapping procedure from the parametric domain to the physical domain. As a result, the grid becomes adapted to the distribution of the chosen grid quality parameter. The adaptation process can be applied successively.

This method provides many desirable features through the use of the parametric mapping and grid control sources. For instance, the basic characteristics of the initial grid can be retained while adapting to grid quality. The grid control sources allow for linear combinations of different controls based on the superposition principle of potential theory. Thus, the grid can be made to adapt to more than one monitor function through a series of mappings. The source formulation also promotes smooth variations of the grid, even with nonsmooth, randomly distributed sources. If satisfactory results are not achieved after a single application, the adaptation process can be repeated in a cyclic manner.

Several examples are presented to demonstrate different applications of the grid adaptation technique. The first example concerns grid kinking at the periodic boundary. Figure 7 shows both the initial and adapted grids. The initial grid contains sharp grid kinking along the periodic boundary. This may create problems for many flow solvers. Large errors or severe stability limitations may occur. Therefore, grid kinking is used as the monitor function for the grid adaptation. Grid lines become smooth across the block boundary in the adapted grid, and the rest of the grid is virtually unchanged.

The second example improves the grid quality along the wake line of the grid shown in Figure 1c. Here, grids at the upper and lower sides of the wake line are generated as separate blocks, hence kinked grid lines appear across the wake. As shown in Figure 8, the adaptation smooths the grid lines across the wake without altering other grid properties.

The final example demonstrates the improvement of boundary orthogonality, as shown in Figure 9 for a H-grid around a cascade configuration. As discussed, boundary behavior of grid lines is especially important in viscous flow calculations for accurate predictions of skin friction and heat transfer rates. Therefore, orthogonal or near-orthogonal grids are sought near the blade. In this case, control sources are defined along the surface based on orthogonality. The adapted grid possesses good orthogonality near the surface and blends smoothly into the rest of the grid.

CONCLUSIONS

Grid generation is not an isolated, single-step process. Instead, an iterative feed-back cycle is required to reach an acceptable balance between different grid properties. Also, the grid should be able to conform to the geometry, to follow the flow characteristics, and be compatible with the specific solution algorithm. The interactions between the grid, flow physics, and solution algorithm will increase as the physical and geometrical complexities of the flow increase.

In this paper, various grid generation issues and grid quality requirements are discussed for high-speed turbomachinery flow calculations. The use of different grid generation strategies provides options for improving grid quality. Two grid modification approaches are presented to systematically correct undesirable grid properties. The examples presented demonstrate how significant improvements can be made through these approaches.

ACKNOWLEDGEMENTS

The authors wish to thank James Loellbach and James Hager of the University of Illinois for their assistance in preparing this paper. The support and encouragement of Dr. Raymond Cosner and Dr. August Verhoff of McDonnell Aircraft Company are also gratefully acknowledged. This work was partially funded by a contract under the Independent Research and Development Program of McDonnell Aircraft Company.

REFERENCES

1. Lee, K. D. and Loellbach, J. M., "Geometry-Adaptive Surface Grid Generation Using a Parametric Projection," *Journal of Aircraft*, 26, 162-167 (1989).

2. Lee, K. D. and Loellbach, J. M., "A Mapping Technique for Solution Adaptive Grid Control," AIAA Paper 89-2178, In *Proc. AIAA 7th Applied Aerodynamics Conference*, Seattle, WA, 129-139 (1989).

3. Lee, K. D., Loellbach, J. M., and Kim, M. S., "Adaptation of Structured Grids for Improved Navier-Stokes Solutions," AIAA Paper 90-0125 (1990).

4. Lee, K. D. and Rubbert, P. R., "Transonic Flow Calculation Using Grid Systems with Block Structure," In *Lecture Notes in Physics* 141, 266-271, Springer-Verlag (1980).

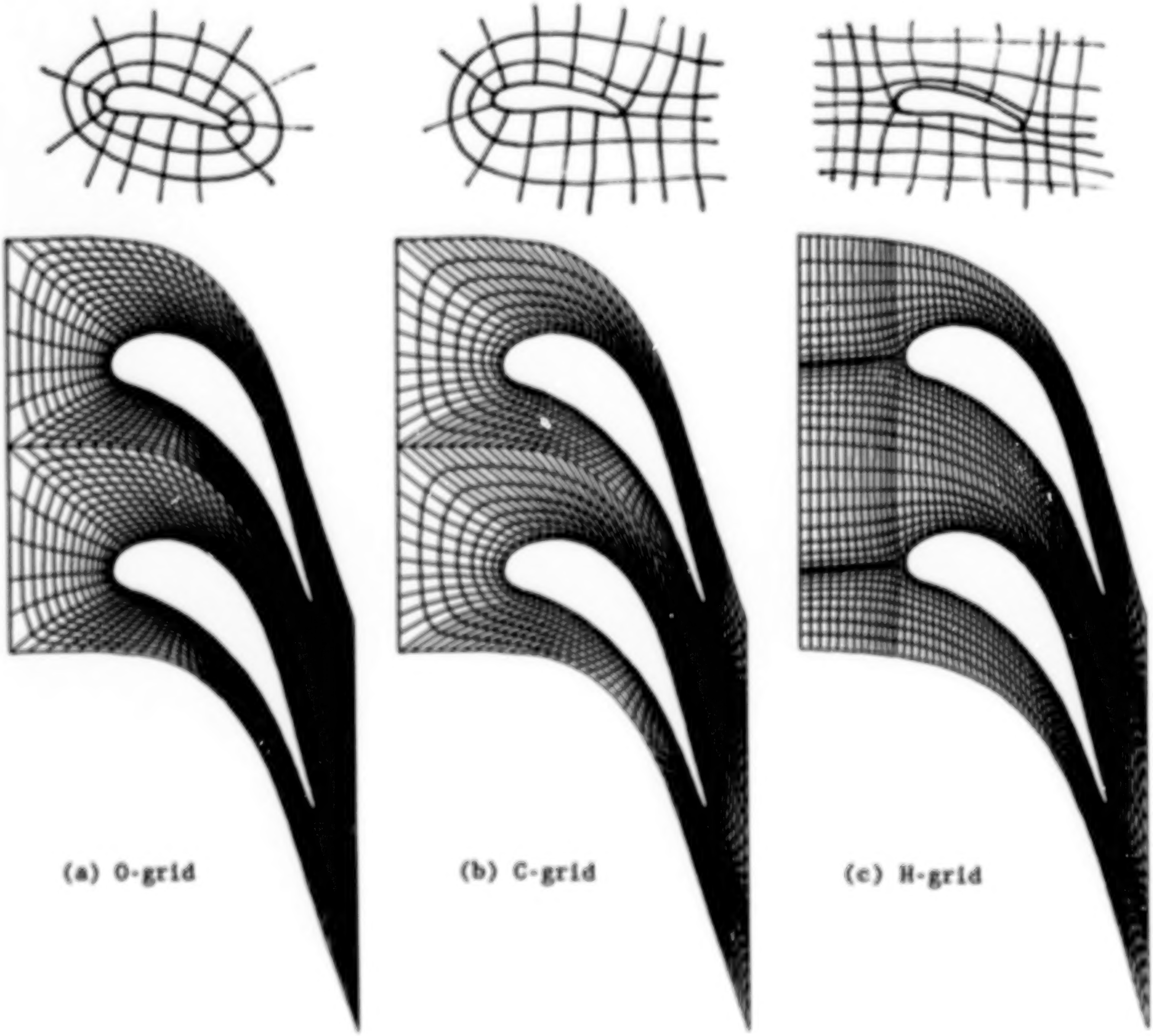

(a) O-grid

(b) C-grid

(c) H-grid

Figure 1. Examples of grid topologies for turbomachinery grids

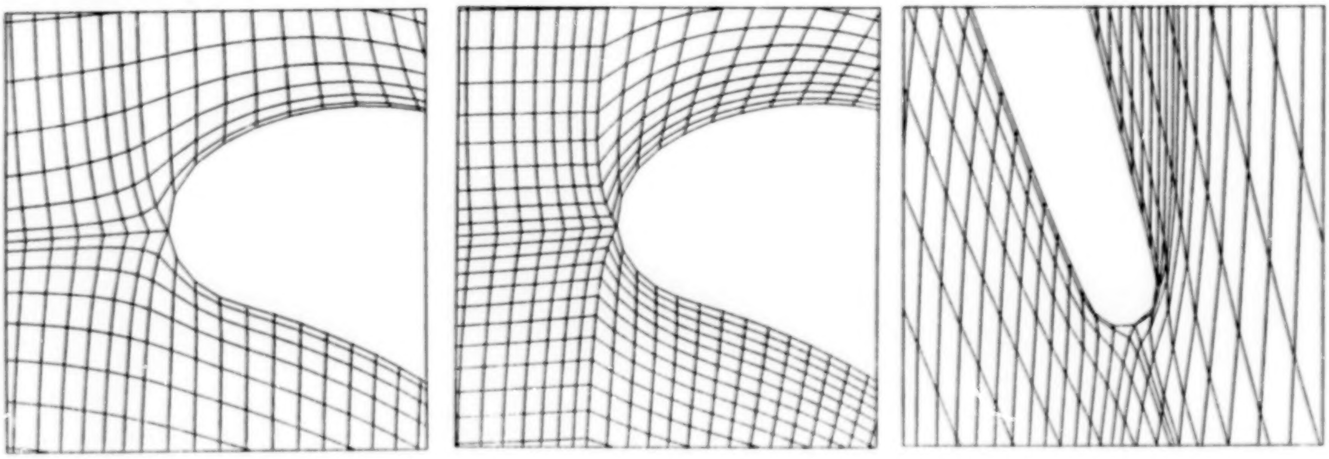

(a) large LE cells (b) patched LE grids (c) skewed TE cells

Figure 2. H-grid details

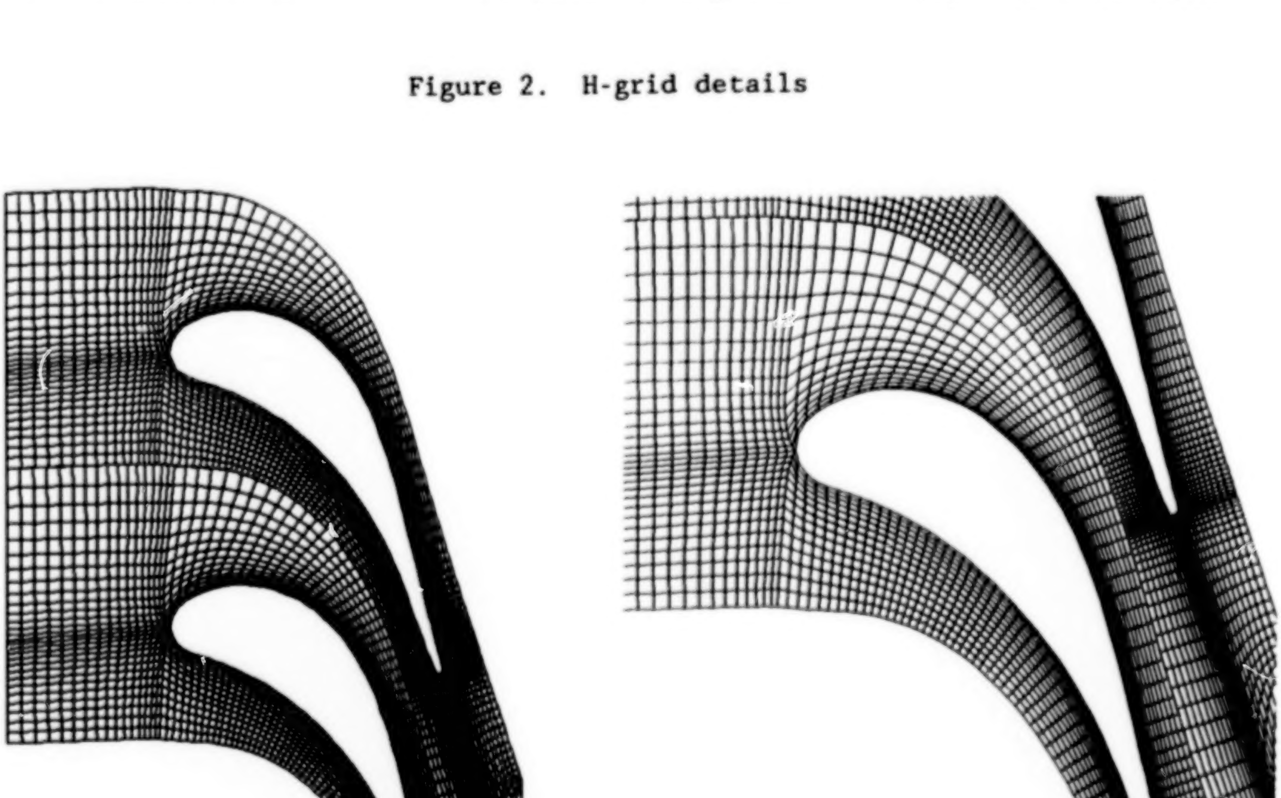

(a) overall grid layout (b) near-field details

Figure 3. Grid line slipping at periodic boundary

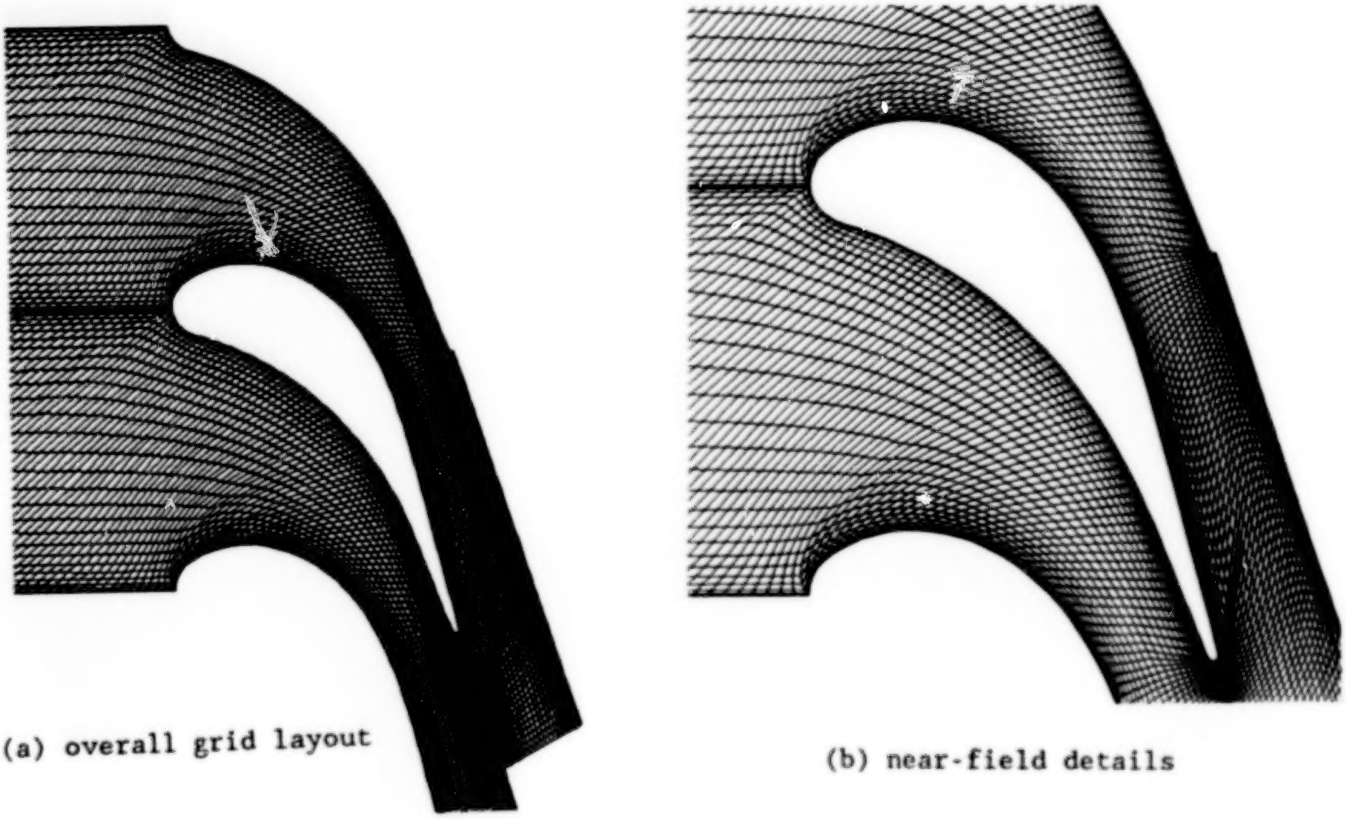

(a) overall grid layout

(b) near-field details

Figure 4. Index off-setting at periodic boundary

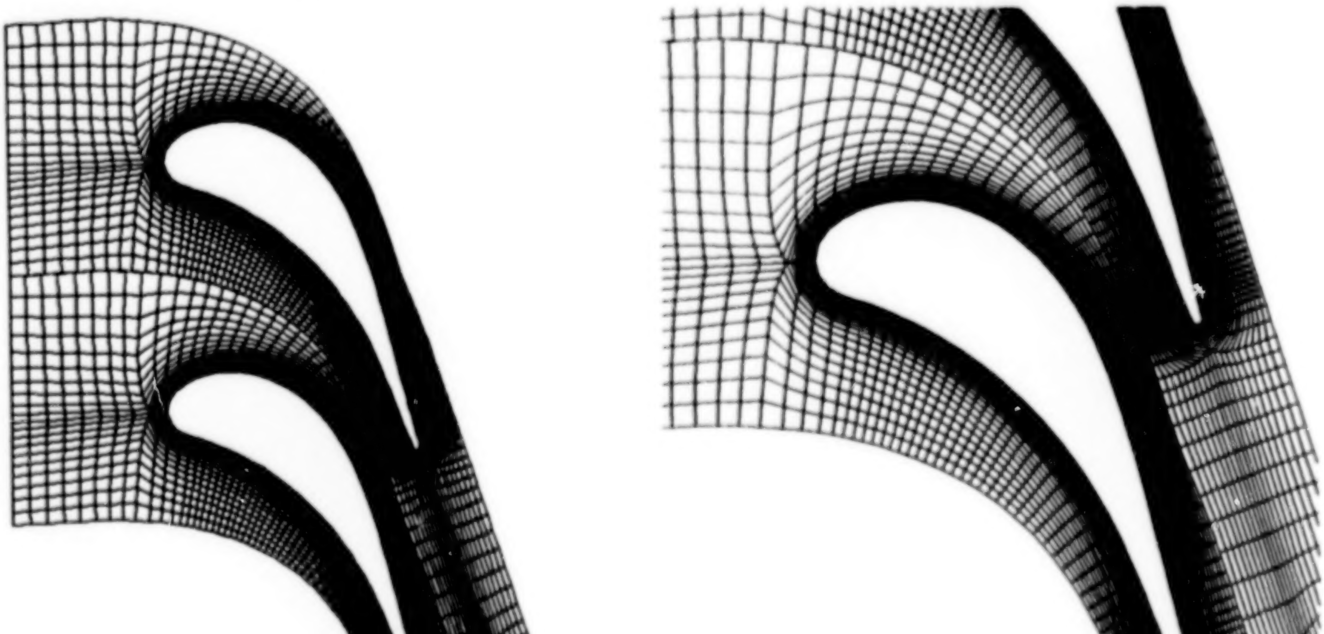

(a) overall grid layout

(b) near-field details

Figure 5. H-grid with O-grid insert

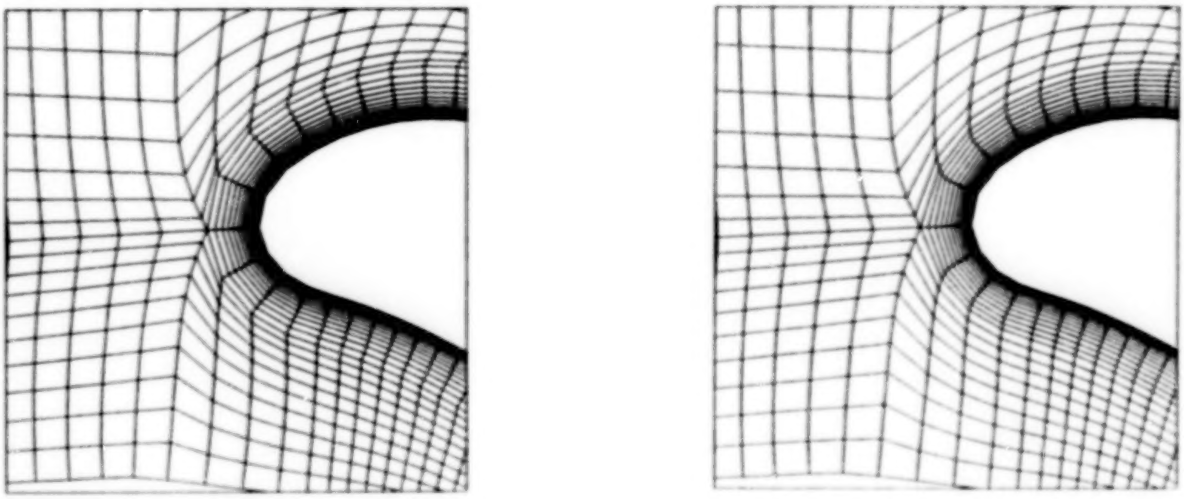

(a) LE grid before blending

(b) LE grid after blending

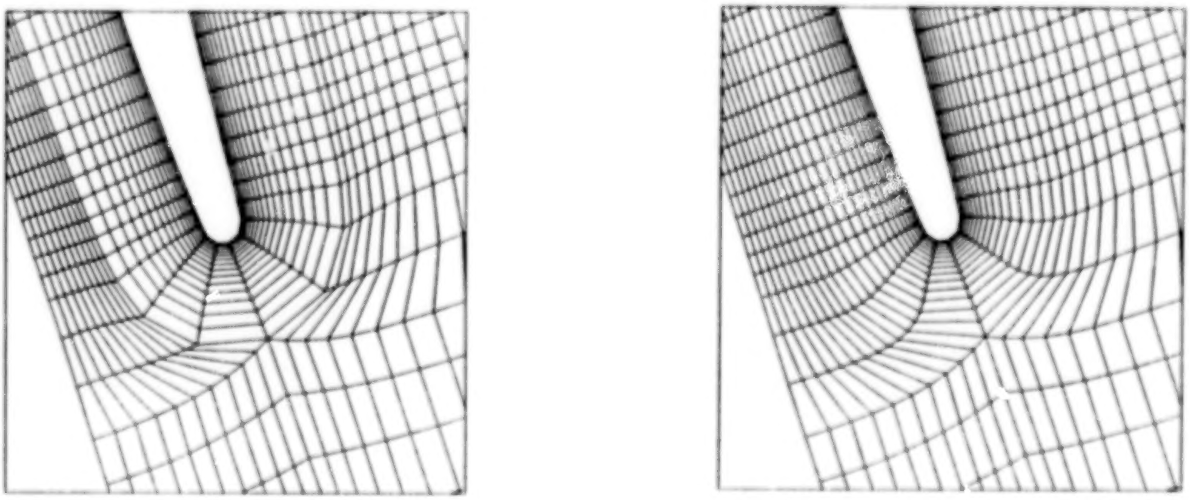

(c) TE grid before blending

(d) TE grid after blending

Figure 6. Blending across block boundaries for a O-H grid

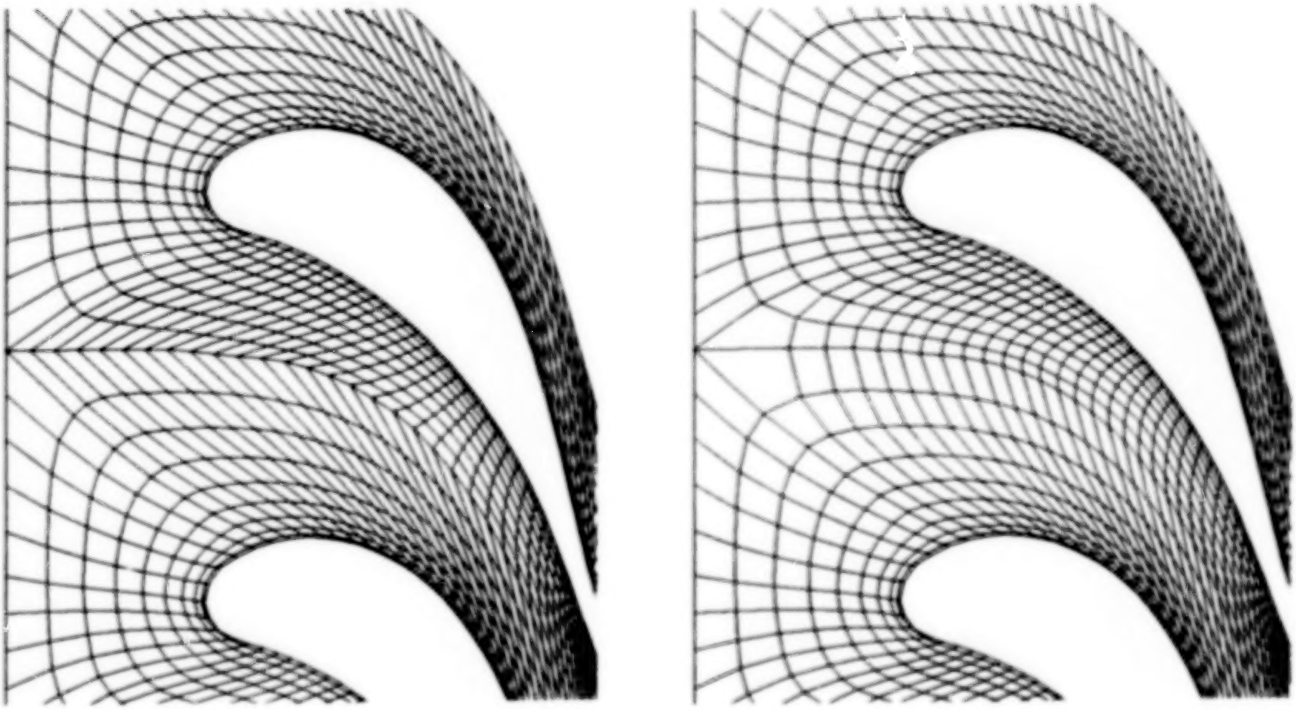

(a) grid before adaptation

(b) grid after adaptation

Figure 7. Grid quality adaptation across periodic boundary - reduction of grid skewness

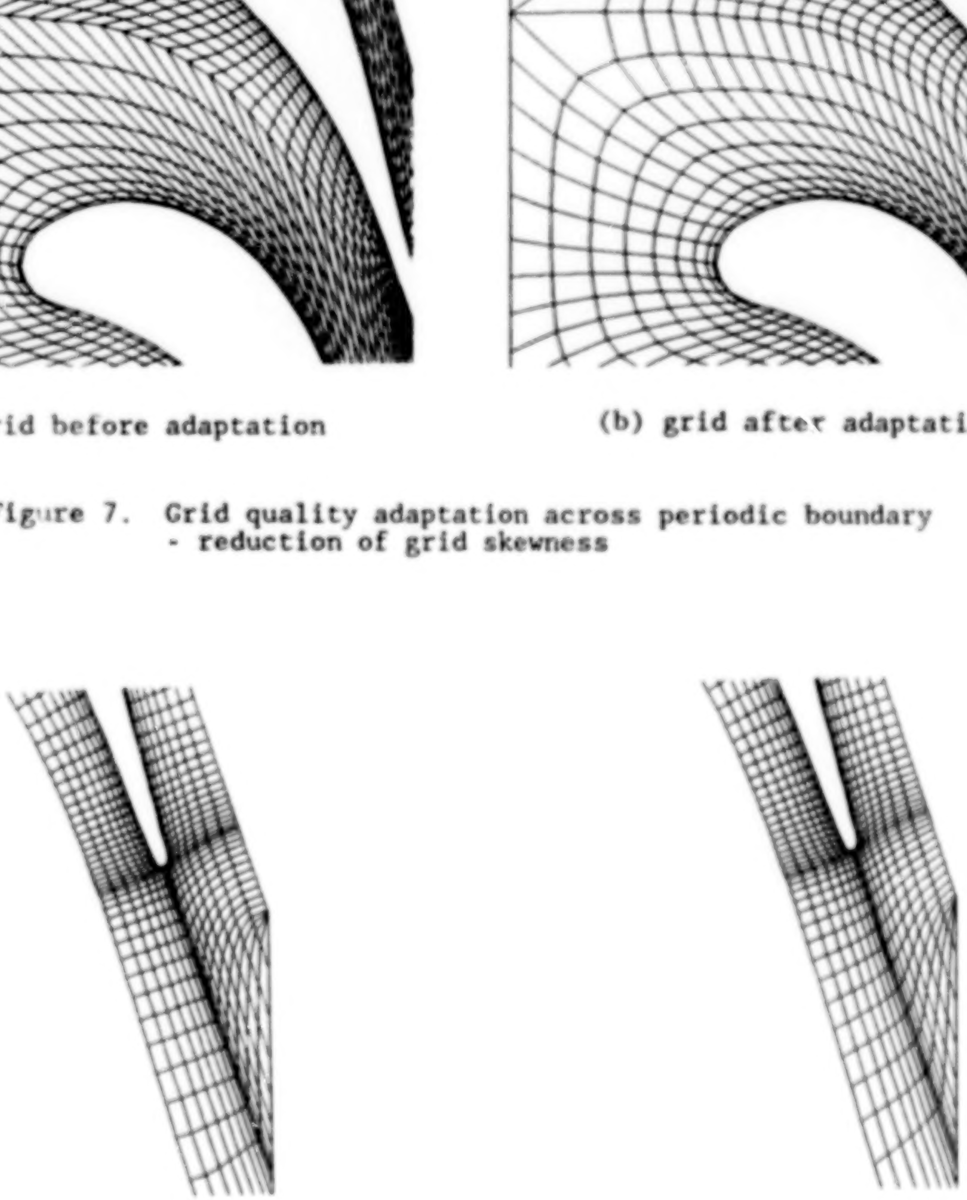

(a) grid before adaptation

(b) grid after adaptation

Figure 8. Grid quality adaptation along wake line - reduction of grid skewness

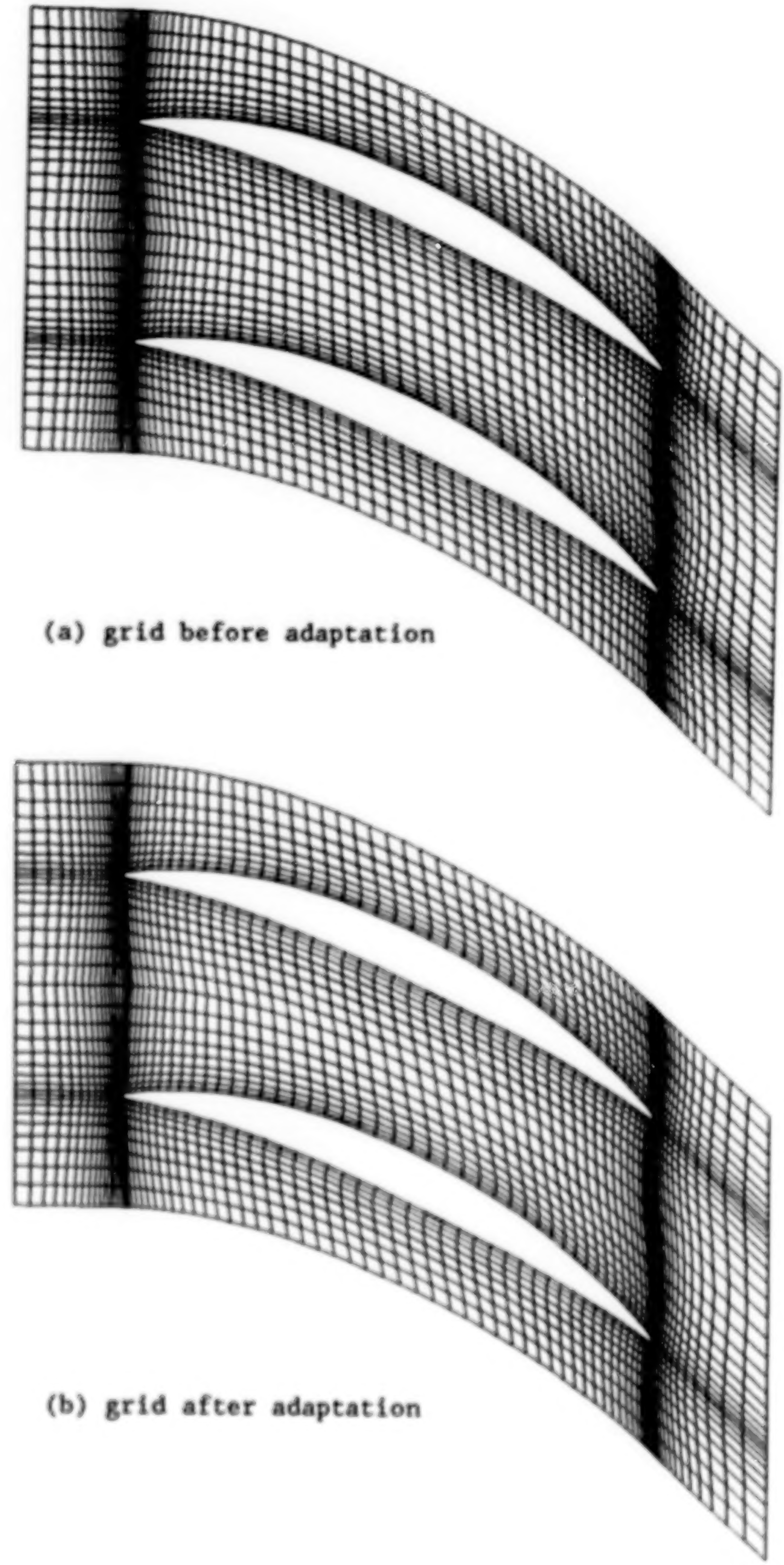

(a) grid before adaptation

(b) grid after adaptation

Figure 9. Grid quality adaptation near blade boundary
- improvement of grid orthogonality

3D COMPUTATION OF SINGLE-EXPANSION-RAMP AND SCRAMJET NOZZLES

H. T. Lai
Sverdrup Technology, Inc.
NASA Lewis Research Center Group
Cleveland, Ohio 44135

ABSTRACT

Description of the computations for three-dimensional nonaxisymmetric nozzles and analysis of the flowfields are presented in this paper. Two different types of nozzles are investigated for compressible flows at high Reynolds numbers. These are the single-expansion-ramp and scramjet nozzles. The computation for the single-expansion-ramp nozzle focuses on the condition of low pressure ratio, which requires the simulation for turbulent flow that is not needed at high pressure ratios. The flowfield contains the external quiescent air, and the internal regions of subsonic and low supersonic flows. The second type is the scramjet nozzle, which typically has a very large area ratio and is designed to operate at high speeds and pressure ratios. The freestream external flow has a Mach number of 6, and the internal flow leaving the combustion chamber is at a Mach number of 1.62. The flowfield is mostly supersonic except in the viscous region near walls. The computed results from both cases are compared with experimental data for the surface pressure distributions.

INTRODUCTION

Numerical flowfields in three dimensions are presented and analyzed for the single-expansion-ramp and scramjet nozzles. These nozzles are nonaxisymmetric because of the geometry of the upper and lower nozzle walls, in which one of the walls is longer than the other. The diverging exit provides the flow an additional external free expansion over the long surface, i.e, an expansion ramp, and allows the exhaust plume behind the nozzle to deflect away from the nozzle axis according to the pressure difference between the internal and ambient flows. The resulting flow structure requires the numerical computation to account for the interaction between the internal flow and the external freestream. This mixing interaction occurs through a free shear layer, which is encountered frequently in the exhaust flows. The shear layers emanating from the short surfaces, i.e., a cowl or a splitter plate, and the nozzle sidewalls, are especially significant. Along with these mixing layers at the edges, expansion fans, compression or shock waves, which are determined by the deflection angles of the shear layers, also emerge and could have large effects on the overall nozzle flowfield. The simulation described here is formulated to include in three dimensions a computational domain that contains the external freestream surrounding the nozzle, in addition to the typical internal converging/diverging section. Consequently, the procedure allows various features of flow interaction to develop. The PARC computer code [1] is employed to model the viscous flowfields for two similar nonaxisymmetric nozzles at high Reynolds numbers. The flowfield for the single-expansion-ramp nozzle consists of regions of internal subsonic/supersonic expansions and an external plume exhausting into a quiescent ambient environment. A substantial flow portion in the quiescent air has very low velocities. This type of nozzle has been investigated experimentally by Re and Leavitt [2] to determine the effects of various geometrical parameters and pressure ratios on nozzle static performance. On the other hand, the scramjet nozzle having large exit-to-throat area ratio is designed to operate at very high speeds and pressure ratios. The flow leaving the combustion chamber has a Mach number of 1.62, whereas the external freestream Mach number is 6. The flowfield is predominantly supersonic at high Mach numbers, except in thin subsonic boundary layers adjacent to the nozzle walls. Experimental work on this scramjet nozzle was performed by Cubbage and Monta [3] to study the flowfield behavior at different geometry and flow conditions. Although air and other simulant gases were used for the experiment, this numerical study considers only air assumed as a perfect gas.

Numerical investigations of the single-expansion-ramp nozzle, the scramjet nozzle, and other nozzles similar to these types have been reported in the litterature [4-7]. Three-dimensional flowfields for the single-expansion-ramp nozzle have been computed for a pressure ratio NPR=10 [4]. Laminar results agreed very well with the experimental data. The simulation includes the exhaust plume which is surrounded by shear layers between the exhaust flow and the external quiescent air. For this class of mixing, in which one of the coflowing streams is quiescent, the flow eventually becomes unsteady downstream because of interaction and momentum transfer. The exhaust flow induces many circulatory vortices in the adjacent quiescent surrounding, as the flow progresses downstream and gradually loses its momentum. This unsteady behavior is characterized by formation of large-scale vortex structures and dissipation. Numerically, the unsteady flow pattern of the plume region can be modelled using a time-accurate procedure, but poses a convergence problem for a time relaxation scheme to obtain steady state solutions, such as the one formulated in the PARC code. However, there is a segment of the exhaust flow upstream near the nozzle exit where the shear layer is stable for a steady state calculation. Through numerical experimentation it has been found that the length of this segment varies depending on the characteristics of the expanding flow inside the nozzle. In general, internal flow at large pressure ratios provides stable shear layers and the unsteadiness takes place at a distance far downstream. This is the case in the previous laminar computation at NPR=10. As the pressure ratio is reduced, the free shear layer becomes unsteady earlier at a very short distance from the nozzle exit. The reason for this pressure ratio dependency is that the flow at large pressure ratios is expanded to a higher Mach number and therefore greater momentum, as compared to the flow at smaller pressure ratios. Consequently, the exhaust flow at high Mach number can penetrate farther into the quiescent surrounding before becoming unsteady. The present study of the single-expansion-ramp nozzle, as a continuation of the previous work, examines the flowfield at a lower pressure ratio of NPR=4. The results presented here are for turbulent flow. This is one of the differences from the previous work where laminar flows were simulated without convergence difficulty. At the present pressure ratio, steady state laminar solution could not be obtained and may not even exist. Further study is required to resolve the issue. Convergence for turbulent flow, however, was obtained but required an extensive amount of computational effort. The present steady state solution indicates a flowfield which contains a three-dimensional internal shock wave on the nozzle walls and a helical streamwise vortex in the exhaust flow, in addition to other similar flow structures observed for laminar results at NPR=10 in the previous investigation.

This paper also presents the results obtained from a three-dimensional computation of a scramjet nozzle. The configuration is similar to that of the single-expansion-ramp nozzle. The difference is in the spanwise geometrical variation that leads to several viscous regions to be resolved. The flow characteristics exhibit very strong expansions in both streamwise and spanwise directions. Because of grid limitation, the exhaust plume behind the body is not modelled in this case. This assumes that the external exhaust flow has a negligible upstream influence at very high Mach numbers. A free shear layer occurs between two supersonic streams and is more stable than the ones encountered in the previous case, even though the relative velocity between the two streams is large. Another physical feature is the vortical flow over the edge of the external expansion surface. This vortex system resembles the structure observed in the flowfield over swept wings, in which the shear layer along the leading edge curls up to form a streamwise vortex. Results are presented for laminar flow, although turbulent solutions can also be obtained. Results calculated in both laminar and turbulent regimes for a two-dimensional test case have indicated no noticeable differences between the two regimes. The apparent stability of the overall scramjet flowfield leads to a minimal computational effort required for convergence.

In order to obtain accurate numerical solutions, a very large number of grid points is needed to resolve all the high gradient regions appearing in the domain. However, grid clustering in such regions is still a difficult problem, except in the case when the location of the sharp gradient regions is known in advance. Effectively resolving the free shear layer, which normally follows an irregularly curved trajectory, becomes quite complex. Although an adaptive grid can concentrate and redistribute grid points in these layers as the computation proceeds, it is not trivial in complex flows to control grid smoothness, distortion and resolution. Though success has been observed in two dimensions, three-dimensional results are still lacking. For this reason, the grid adaptation has not been implemented in the present calculations, and is a subject for future work. Free shear layers and shock waves are then not as accurately defined. Numerical error associated with the lack of resolution appears as an additional artificial diffusion which then smooths out these sharp gradient flows.

NUMERICAL METHOD

The detailed development and some of the recent work related to the PARC computer program can be found in references [1,4,8-9]. Generally, the program solves for steady state solutions of the Euler, full or thin layer Navier-Stokes equations in a generalized curvilinear coordinate system using a time marching finite-difference scheme. This numerical scheme uses standard central differences to approximate the spatial derivatives. The time linearized difference equations in a delta form are solved by the Beam-Warming ADI algorithm with diagonalization of the inviscid terms. Jameson-type artificial dissipation is added for monotonicity and stability. The resulting computational procedure then requires iteration from an initial guess for the flowfield until convergence to a steady state is obtained. Another common feature for a time-like marching technique is the use of spatially variable time steps. This is introduced to achieve faster convergence rates especially in the coarse grid areas where large time steps can be used because of a less severe restriction on stability. In the present calculations, the thin layer Navier-Stokes equations are employed. The thin layer assumption is applied since the flow is in the high Reynolds number range, in which the contribution from the streamwise diffusion terms becomes negligible. In addition, due to computer resource limitations, the grid in the the flow direction cannot adequately resolve the viscous phenomena. The neglect of these diffusion terms then produces considerable decrease in computation time, especially in three dimensions.

In the turbulent calculation, a modified Baldwin-Lomax model is employed for eddy viscosity. A modification to the original model is made to permit multiple Prandtl mixing lengths for the outer wake region, based on the vorticity distribution along individual curvilinear coordinates. This consideration for multiple length scales is particularly important when using algebraic models for flows in the presence of both wall boundary layers and free shear layers, as is the case in this study. In the modified model, each grid line is segmented at the location where the vorticity is minimum. The mixing length is then assumed to be uniform along that segment, and is determined by some ratio of the total velocity and vorticity, see ref. [1]. The wake value of turbulent viscosity is applied throughout the flowfield domain including free shear layers and the outer parts of wall boundary layers without further modification. Numerical work on this modified version, however, has not been documented extensively. The pressure distribution presented here in the region of the shock wave and boundary layer interaction shows an improved prediction of the location and strength of the shock wave as compared to laminar results. Experimental data for the free shear layer in the present investigation are not available for comparison.

For boundary conditions, all are explicitly formulated in an iterative manner. At the inflow or outflow boundaries, the conditions can be either specified or extrapolated according to the local characteristic directions. This kind of boundary treatment works effectively when all characteristics have the same direction, i.e., when boundary points are either all subsonic or supersonic and contain no reversed flow. Difficulty in convergence arises when mixed types of characteristics occur. Extrapolation at every point for boundaries having different characteristics appears to be a more stable treatment, but does not honor the characteristic direction. However, this numerical treatment of extrapolation is implemented here at the outflow boundary. On the nozzle surfaces, no-slip and adiabatic conditions are imposed. In the farfield, the variables are fixed for the external supersonic stream, provided that the boundaries are positioned at a sufficiently large distance from the nozzle/exhaust flows. As for quiescent air, the farfield boundary is treated initially as an inflow boundary because of entrainment into the shear layer, and is then fixed in the later stage of iteration. This dual treatment of the quiescent boundary is considered as a means of relaxation for convergence and can be repeated when necessary. At the entrance of the single-expansion-ramp nozzle, only stagnation pressure and temperature are specified since the flow is subsonic. Other unknowns are computed as inflow conditions using isentropic relations and characteristic variables mentioned above. On the other hand, at the entrance of the scramjet nozzle a uniform profile is assumed, neglecting the incoming boundary layer effects. The variables at this boundary are fixed during the computation process, since the flow is supersonic. For normalization, stagnation quantities at the nozzle entrance are taken as the reference. The nozzle throat height and the speed of sound are the reference length and velocity, respectively. The Reynolds number is computed based on these parameters. For laminar flow, molecular viscosity is obtained from the Sutherland law. The laminar and turbulent Prandtl numbers are assumed to be equal to 0.72 and 0.9 respectively.

GEOMETRY AND GRID

The geometry of the single-expansion-ramp nozzle is illustrated in fig. (1) obtained directly from ref. [2]. In this study, the streamwise, vertical and spanwise directions are labeled as x, y and z respectively. The dimensions shown are in centimeters. The figure depicts the x-y or side view which lies along the streamise direction, showing a converging/diverging nozzle. In addition, there is an extra external section of the upper surface extending from the end of the lower surface. The resulting external expansion provides asymmetric exhaust flowfields and thrust deflections. The upper and lower nozzle walls are flat surfaces having no variation in the spanwise direction that is perpendicular to the x-y plane. Consequently, there is a symmetry plane in this spanwise direction and only half of the nozzle thus needs to be computed. The nozzle width-to-throat ratio is equal to 4, where the throat height is 2.54 cm. The sidewall is also indicated in the figure and is assumed to have a uniform and very small thickness of 0.007 cm. The nozzle exit along the edge of the sidewall is highly skewed as shown. The intersections of the side plate with the nozzle walls occur slightly ahead of the ends of the surfaces. The configuration computed here was labeled as case OT5 in the experiment. For this configuration, one of the intersections is found at the same location as that of the end of the lower surface. The other intersection is measured at 1.708 cm upstream of the end of the upper surface. This detail complicates the simulation only to a small degree.

The overall geometry of the scramjet nozzle is illustrated in fig. (2a). Another view with dimensions is presented in fig. (2b) for the x-y plane. Similar to the single-expansion-ramp nozzle, the model includes a short cowl and a long ramp as the upper and lower surfaces shown in the figure, respectively. In the present computation, the ramp angle is 20 degrees. The interior side of the cowl also has a minor expansion ramp, see fig. (2b), with an angle equal to 12 degrees. In the spanwise direction, the nozzle geometry consists of a reflection plate on one side of the flowfield, and a short sidewall to cortain the internal flow before exiting to expand. The short sidewall has a flat surface facing the internal flow. The sidewall external surface facing the free stream flow is tapered. The sidewall and the cowl therefore both have finite thicknesses with sharp trailing edges. The flow fence connected to the short sidewall, as indicated in the figure, is not simulated in this study. The nozzle width-to-throat ratio is equal to 5, with the throat height of 0.6 inch at the combustor exit. The long ramp surface can be divided into two regions with nearly equal lengths in the spanwise direction. The interior region next to the reflection plate includes the flow between the reflection plate and a streamwise x-y surface containing the sidewall. The exterior region includes the flow between this surface and the freestream. The flow in the exterior region appears to have a simple flow pattern due to just an expansion over a 20-degree ramp. However, because of spanwise expansion outward from the interior side as well as inward from the freestream side, the flow in the exterior region of the ramp surface is a rather complex system characterized by developing streamwise spiral vortices. The computational domain simulated here begins at the combustor exit. The flow effects prior to this location, such as from the action of boundary layers or embedded waves, are ignored for simplicity. This aspect of the boundary effects on the accuracy of the solution will be discussed further in the following section on the numerical results.

The corresponding three-dimensional grid distributions are illustrated in figs. (3a) and (4a) for the single-expansion-ramp and scramjet nozzles respectively. Two-dimensional close-up views on x-y planes are shown in figs. (3b) and (4b). In the figures, some of the grid points have been removed for clarity. These grids were generated by a simple algebraic technique using a hyperbolic tangent for grid clustering in the region near walls. In the spanwise direction, the x-y grids are stacked without variation, i.e., in that the cartesian coordinates, x and y, are not functions of the spanwise transformed curvilinear coordinate. Concentrations in this direction are applied at the sidewalls, as in the middle of the single-expansion-ramp nozzle or along the reflection plate, the short sidewall, and the model edge of the scramjet nozzle. It can be observed that the clustering in the viscous regions near the nozzle walls are extended farther downstream into the wakes behind these surfaces. The clustered regions in the wake become unnecessary since the paths of the shear layer normally do not follow the clustering. This is a typical behavior of structured H-grid distributions, in that the interior grid distribution is affected by the surface grid refinement. However, there are several alternative methods, e.g., simple averaging, which can be employed in the wakes to alter the distribution, but are not pursued in this study. For surface grid coordinates, a cubic spline procedure is used to interpolate between the tabulated data describing the nozzle contours. This interpolation to position grid points is applied for the internal contours of the single-expansion-ramp nozzle. Other surface contours are straight lines which can be easily implemented. Another remark is that the vertical grid lines in the middle section are highly nonorthogonal to the horizontal coordinate, see fig. (3b), but are made to align with the edge of the sidewall in order to simplify the boundary condition application. The grid dimension for the single-expansion-ramp nozzle is 95x90x50, whereas for the scramjet nozzle, the grid has a dimension of 90x90x95. The additional grid used in the scramjet nozzle calculation is needed to resolve four viscous boundary layers in the spanwise direction. In the figures discussed below, the i, j, and k notations denote the grid indices corresponding to the x, y and z directions, respectively.

RESULTS

Single-Expansion-Ramp Nozzle

Numerical results are presented for a turbulent, thin layer Navier-Stokes calculation. Flow through the domain is initiated by a pressure difference between the nozzle entrance, at a total pressure of 405.2 kPa and a total temperature of 300 K, and the quiescent ambient, at a pressure of 101.3 kPa and the same total temperature of 300 K. The stagnation-to-static nozzle pressure ratio, NPR, is therefore equal to 4, and the corresponding Reynolds number obtained for these conditions is 2,251,500.

Starting from a near zero velocity at the entrance, the generated flow becomes sonic at the throat, expands supersonically along the diverging section with the existence of a shock wave, and exhausts supersonically into stationary air. Figures (5a-7c) describe this overall flowfield in terms of Mach number contours, indicating some of the important physical features. The contours cover the entire range of the Mach numbers with an equal increment. Depicted in these figures are the side, top and rear views at various spatial locations. Flow expansion along the streamwise diverging/ converging sections is shown in figs. (5a-c) at three different spanwise locations, moving from the center plane to the sidewall. The pattern consists of a rapid expansion at the throat, and an oblique shock wave with its reflection below the boundary layer on the external section of the upper surface. The lower shear layer acts as a fictitious nozzle wall to complete the diverging section. The shock wave is a result of coalescence of the compression waves formed by the curvature of the lower shear layer. The thickening of the boundary layer behind the shock can be observed. The reflected shock then interacts with the lower shear layer, creating a reflection of expansion waves at the other side of the corner. This lower shear layer gradually diminishes toward the sidewall, resulting from the inward deflection of the vertical shear layer. The maximum Mach number is 1.935 and located in front of the shock near the symmetry plane. The flow behind the shock is nearly sonic, except for a thick subsonic region adjacent to the wall where the shock becomes normal.

Streamwise variations of Mach number can also be seen from the top views in figs. (6a-b). The top boundary is the center line, and the sidewall is in the middle of these figures. The corresponding mixing layers emanate from the sidewall trailing edges. The view in fig. (6a) is at a vertical location near the nozzle center, also showing a rapid expansion at the throat, and compression waves near the sidewall edge. The other view in fig. (6b) is at a vertical location near the upper surface, having a similar pattern except that the compression waves now coalesce into a shock wave which can be seen clearly. This shock wave also interacts with the boundary layer along the sidewall. Another feature present in these figures is the deflection angle of the shear layer from the sidewall. The shear layer in fig. (6a) is deflected toward the internal nozzle region, due to a low pressure from the inside. On the other hand, the shear layer in fig. (6b) is deflected toward the external nozzle region, due to higher pressure behind the shock wave. Therefore, the exhaust flow along the sidewall is both underexpanded and overexpanded in the regions near the lower and upper surfaces, respectively.

Another two-dimensional view of the three-dimensional shock surface can be seen from the rear in figs. (7a-c). These figures illustrate the cross sections at different streamwise locations. It should be noted that the top views, figs. (6a-b), and the rear views, figs. (7a-c), are projections of the curvilinear coordinate planes onto x-z and y-z cartesian planes, see the grid distributions in figs. (3a-b). The symmetry plane is the right boundary in figs.(7a-c). Fig. (7a) is at a streamwise location near the edge of the sidewall, where both nozzle walls are shown. Shock wave and boundary layer interaction can again be seen near the upper surface by the apparent thickening of the viscous regions along the sidewall and the upper surface. Fig. (7b) is located at the external section, showing the initial regions of the vertical and lower shear layers. The reflected shock has moved downward to the middle and becomes diffused. An example of the Mach number contours in the exhaust plume behind the nozzle is depicted in fig. (7c), where only free shear layers are present. The vertical shear layer indicates an irregularly curved sheet of high velocity gradient, as compared to the relatively well-defined upper and lower layers. The lower left-hand intersection of the shear layers is the center area of a helical streamwise vortex.

Typical variations of pressure, density and temperature are presented in figs. (8-11) for the side and top views. Figs. (8-9) show the pressure and density contours near the symmetry plane. There is no variation in pressure and a small gradient in density across the shear layer. These figures indicate a regular pattern of multiple shock cells usually observed in the exhaust flow. In addition to a region of concentrated vorticity, the shear layer in compressible flows also manifests itself through a steep variation of temperature. This associated thermal layer can be seen in the temperature contours in figs. (10a-b) plotted for two vertical locations near the nozzle middle and the upper surface. Similar contour patterns show shock wave, large temperature gradient and deflection of the thermal shear layer. Figs. (11a-b) illustrate the pressure contours for the same view and the same vertical locations as for temperature above. These figures detail the repeated cycles of a shock/compression and expansion wave reflection.

The vortical systems of the exhaust flowfield are demonstrated in the next three figures. The velocity vectors are plotted in fig. (12) for a spanwise cross section located a few stations downstream of the nozzle body. The symmetry plane is now the left boundary, and the dense regions of closely packed vectors arise because of grid clustering along the upper, lower and sidewall surfaces. The pronounced structure clearly identified is the counterclockwise vortex, centered near and inside of the nozzle upper right-hand corner in the figure. The vortex system rotates at higher angular velocities in the sidewall vicinity than in other regions, as suggested by the lengths of the velocity vector. The vortex occupies a large spanwise area of the plume flowfield, and the entire expanding fluid medium exiting from the nozzle, consequently, undergos a streamwise vortical motion. Another smaller vortex having the same sense of rotation also exists, with its center near the lower right-hand corner of the nozzle. The longitudinal view of this streamwise vortex is shown in fig. (13) in three dimensions, illustrating the trajectories of the particles released at the nozzle entrance along the lower, sidewall and upper internal surfaces. The vortex system is represented by the clustered spiral paths of the fluid particles originating behind the nozzle lower corner. Trajectories at the upper corner are deflected downward by the presence of a very small separated bubble. Other trajectories away from the sidewall remain in the regions of shear layers. Another view of the small streamwise vortex with the apex at the nozzle lower corner is illustrated in fig. (14). This is a view looking upstream along the axis of the vortex. Spiraling motion of the fluid particles along the vortex is evident.

Figures (15a-b) compare the computed and measured pressure distributions for the upper and lower surfaces at the symmetry plane. The agreement is very good. The strength and location of the shock wave appearing in the external section of the upper surface are well predicted. The computed discharge coefficient of 0.989 also agrees reasonably with the experimental value of 0.974. In this calculation, the smallest grid size is employed at the walls and is of the order of 0.001. This gives values of y^+ and z^+ in the range of 10 at the first grid point from the wall, and typically 4 subsonic points in the viscous layers.

Convergence is rather difficult to achieve and very sensitive to the time step. The use of a different time step for the energy equation and an underrelaxation for the eddy viscosity somewhat reduces the fluctuating behavior of the residuals. The solution presented here for the single-expansion-ramp nozzle was obtained after a residual reduction of three orders of magnitude in approximately 10,000 iterations. A large number of these iterations was used for the reduction of the last order of magnitude. Further reduction of the residual beyond this level is still possible but becomes prohibitively slow. Each iteration took 16 seconds, and the total computation time required 45 hours on a Cray-2.

Scramjet Nozzle

The solution computed for the scramjet nozzle is obtained from the laminar, thin layer Navier-Stokes equations. The inflow boundary condition at the nozzle entrance is assumed to be a uniform profile at a Mach number of 1.62, a pressure of 3.408 psi and a total temperature of 150 F. The freestream is also assumed fixed and uniform at a Mach number of 6, a pressure of 0.226 psi and a total temperature of 400 F. The static pressure ratio is then equal to 15.09, and the Reynolds number based on this condition is 293,300.

Variations of Mach number of the scramjet nozzle are illustrated in figs. (16a-c) for side views at three spanwise locations. Fig. (16a) shows the contours at a location between the reflection plate and the short sidewall, where the flow is nearly two-dimensional. The internal flowfield is characterized by a strong expansion beginning with two opposite expansion fans emanating at the entrance lower corner and from the upper corner under the cowl surface. The expansion then continues behind the fans over the long ramp, and accelerates the flow to a Mach number of about 5.6 in the ramp rear-end vicinity, a value close to the freestream Mach number. Above the internal expanded flow is a mixing layer emerging from the cowl lip. Even with a large pressure drop behind the expansion fans, the exhaust flow still remains underexpanded. The shear layer consequently turns upward to the external side at the lip, and remains almost horizontal downstream. However, the angle of deflection is small, and the resulting shock wave as well as expansion fan on opposite sides of the shear layer are relatively weak. This shock wave which originates from the cowl lip can be seen clearly in the external flow, but the expansion fan below the shear layer cannot be discerned from other flow features. Along the free shear layer several other waves are also emitted into the external stream, as a result of pressure adjustment to the freestream usually exhibited in supersonic mixing layers. Additionally, an oblique shock wave exists at the cowl leading edge of the upper surface, occurring here solely because of the boundary layer. Fig. (16b) presents the Mach number contours at a spanwise location very close to the short sidewall, depicting a similar structure of the flowfield. The vertical concentration of contours at the cowl lip is an indication of the mixing layer behind the trailing edge of the short sidewall. The internal flow between the entrance and this trailing edge lies within the subsonic region of the sidewall boundary layer, showing an irregular pattern of Mach number contours without the expansion fans observed before. The external region of the ramp surface, fig. (16c), shows simple flow turning over a 20 degree corner with expansion waves at the leading edge. Next to the wall, the flowfield is more complex containing a thick viscous region with embedded streamwise vortices formed by the interaction of internal and external streams. Fig. (17) represents a typical variation of the density contours for a side view located between the reflection plate and the short sidewall. The wave system exhibited here is more discernible than it is illustrated by the Mach number contours. The pressure and temperature contours contain no other significant physics, but have similar patterns as density and Mach number contours, respectively. They are not included here due to space limitation.

Top views for Mach number contours are illustrated in figs. (18a-c) at various vertical locations with the flow from left to right. The sidewall is shown as a thin splitter plate in figs. (18a-b). The flow pattern in fig. (18a) lies within the boundary layer along the ramp surface, illustrating some of the spanwise expansion of the internal flow. It has been found from the solution that the fluid layer nearest to the wall experiences the largest spanwise expansion. The clustering of the contours at the top of the figure is an indication of the viscous effect of the boundary layer along the edge of the model. This effect diminishes when the vertical position is at a higher level as shown in fig. (18b) located near the cowl internal surface. The shear layer emerging behind the sidewall edge is indicated as the horizontal clustering, depicting a small spanwise expansion at this particular vertical location. Another clustering at the bottom of the figure is the boundary layer along the reflection plate. The vertical contour concentration represents the expansion fan due to the deflection of the shear layer originated along the cowl lip. At a higher vertical location far above the cowl, the flow structure becomes very simple as a supersonic flow over a reflection flat plate, and this is illustrated in fig. (18c).

A typical density distribution is presented in fig. (19) for a top view a few stations below the internal cowl surface. The expansion fan centered at the leading edge of the ramp surface is indicated. The solution shows a gradual smearing consisting of several separate contours in front of and behind the fan. It is noted that the top views, figs. (18a-19), are the projections onto an x-z cartesian plan. The rear views are presented in figs. (20a-c) for Mach number contours at different streamwise locations, and in fig. (21) for density distribution located at the middle of the ramp. Fig. (20a) is plotted for a station just behind the trailing edges of the cowl and the short sidewall. This figure shows a thickening region above the viscous layer on the external ramp surface, and the interaction of the vertical shear layer with this region. The interaction continues and enlarges downstream, illustrated in figs. (20b-c), as the lower part of the vertical shear layer near the ramp surface becomes diffused, deflects to the external side, and merges with another shear layer arising from the model edge. This additional shear layer eventually rolls up from the freestream flow to form an external streamwise vortex centered at the corner of the ramp surface and the model edge. Fig. (20c) also shows a thickening region of the boundary layer in the middle of the ramp surface proceeding downstream, indicating the formation of another smaller, flat internal vortex system. The external vortex along the the model edge is illustrated in better detail in fig. (22), showing a projection of the velocity vector on a spanwise plane at the middle of the ramp. The reflection plate here is the left boundary. The main feature in this figure depicts a large vortical structure, comprised of an expansion from the internal flow, and a turning of the external flow. The vortex center at low pressure is located at the model corner, as the fluid from the vicinity is drawn toward it. The concentration of vectors occurs in regions of grid clustering along the cowl, the short sidewall and the model edge, shown near the top, left and right boundaries of the figure.

Trajectories for fluid particles located next to the ramp surface and released from the internal side are shown in three dimensions in fig. (23). The external streamwise vortex along the model edge is represented by the spiral paths of the particles which emerge immediately behind the short sidewall and then follow a very strong spanwise expansion toward the model edge corner, where the particles are deflected into a vortex motion by the high freestream pressure side of the curved shear layer. The other internal vortex forms downstream of the short sidewall near the middle of the ramp, indicated by the clustered wavy trajectories. It can be observed that, adjacent to this vortex in the ramp middle, many even smaller vortices start to develop downstream near the outflow boundary. Another apparent phenomenon present in this figure is the delay of spanwise expansion for the fluid layers near the reflection plate, where the particles follow straight trajectories and only turn inward when they are near the outflow boundary.

Comparisons of the computed and measured pressure are made in figs. (24a-b) for the streamwise ramp-surface at two spanwise stations. Fig. (24a) is at a section near the reflection plate, and demonstrates very good agreement with experimental data, showing the variation from the nozzle entrance to the end of the ramp. A small pressure rise near the entrance is present because of the impingement of the shock wave which originates from the leading edge of the internal cowl surface. In general, the computed pressure near the reflection plate agrees very well with the measurements. It then appears that a uniform internal profile at the entrance does not significantly alter the flowfield downstream.

Computed pressure does not agree well with measurements in the external region of the ramp surface, as illustrated in fig. (24b). The distribution shows a large pressure drop behind the expansion corner at the inflow, and then remains nearly constant without recovering back to freestream pressure, in contrast to the experimental data. As mentioned before, the uniform freestream profile does not account for earlier effects of the incoming flow occuring in front of the inflow boundary. Because of these previous effects, the external Mach number can be lower than the value of 6 employed here, and consequently the pressure drop across the expansion fan then becomes smaller and probably provides a better agreement. The discrepancy observed in the pressure of the external side can, therefore, be attributed to the error inherent in the uniform profile used at the inflow.

In this scramjet computation, the smallest grid size at the walls was of the order of 0.001, giving typically 3 subsonic points in the predominantly supersonic boundary layers. The computation is very stable requiring no special numerical treatment. After an optimum time step was selected by experimentation, convergence was straightforward and fast with no difficulties encountered during the computation. The results presented were obtained after a residual reduction of five orders of magnitude in approximately 3000 iterations. Each iteration for the scramjet simulation took 22 seconds and the total amount required 18 cpu hours on a Cray-2.

CONCLUSIONS

Three-dimensional simulations have been presented for nonaxisymmetric nozzles. Solutions to the thin layer Navier-Stokes equations were obtained with the PARC code. Turbulent calculations were performed for a single-expansion-ramp nozzle with supersonic exhaust flow in a quiescent ambient. Complex interactions between shock/compression or expansion waves and the viscous free shear or boundary layers constituted the fundamental patterns of the flowfield. Another significant structure was the vortical flow associated with two principal vortices in the exhaust plume. One of the vortices was helical with an apex at the exit of the nozzle lower corner. The other larger vortex involved the entire exhaust region behind the nozzle.

Laminar calculations were performed for a scramjet nozzle with supersonic internal and external Mach numbers. The scramjet flowfield was characterized by strong streamwise and spanwise expansions along with a dominant vortical flow. The principal large vortex, formed below the shear layer, spirals along the model edge. Other smaller and flat vortices develop later downstream near the outflow boundary. Computed wall pressure distributions, in general, compare reasonably with the experimental data for both nozzle configurations.

Shock location and strength are correctly predicted for the single-expansion-ramp nozzle. Discrepancy is observed in the external side of the scramjet nozzle, where inflow effects become important such that a uniform inflow profile may not be a good approximation.

ACKNOWLEDGMENTS

This work was supported by the NASA Lewis Research Center under contracts NAS3-24105 and NAS3-25266 with Dr. Meng-Sing Liou as monitor. The author thanks the NAS System Division of NASA Ames Research Center for the Cray-2 time. Appreciation is also expressed to M. Barton, Sverdrup Technology, Inc., for reviewing with many helpful comments.

REFERENCES

1 Cooper, G. K., "The PARC code: Theory and Usage," AEDC-TR-87-24 (1987).

2 Re, R. J., and Leavitt, D. L., "Static Internal Performance of Single- Expansion-Ramp Nozzles with Various Combinations of Internal Geometric Parameters," NASA TM 86270 (1984).

3 Cubbage, J. M., and Monta, W. J., "Surface Pressure Data on a Scramjet External Nozzle Model at Mach 6 Using a Simulant Gas for the Engine Exhaust Flow," NASP CR 1058 (1989).

4 Lai, H., and Nelson, E., "Comparison of 3D Computation and Experiment for Non-Axisymmetric Nozzles," AIAA-89-0007 (1989).

5 Baysal, O., Engelund, W. C., and Tatum, K. E., "2D Navier-Stokes Calculations of Scramjet Afterbody Flowfields," NASP CR 1034 (1988).

6 Bergman, B. K., and Treiber, D. A., "The Application of Euler and Navier- Stokes Methodology to 2D and 3D Nozzle-Afterbody Flowfields," AIAA paper 88-0274 (1988).

7 Peery, K. M., "Non-Axisymmetric Nozzle/Aftbody Flow Field Analysis," AFWAL-TR-81-3406 (1981).

8 Pulliam, T. H., "Euler and Thin Layer Navier-Stokes Codes: ARC2D, ARC3D," Notes for Computational Fluid Dynamics User's Workshop, The University of Tennessee Space Institute, Tullahoma, Tn., UTSI Pub. E02-4005-023-84, pp. 15.1 -15.85 (1984).

9 Beam, R. M., and Warming, R. F., "An Implicit Factored Scheme for the Compressible Navier-Stokes Equations," AIAA Journal, Vol. 16, pp. 393-402 (1978).

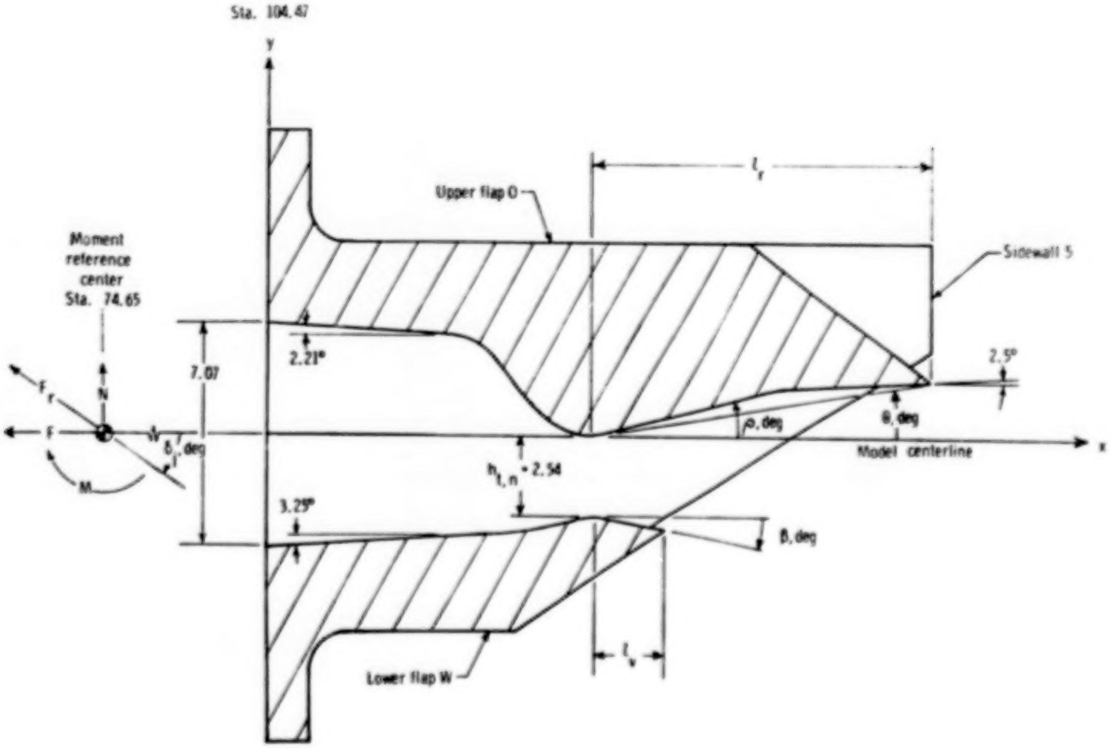

Fig. 1 Geometry of the Single-Expansion-Ramp Nozzle

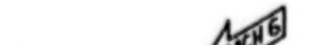

b. Two-Dimensional View

a. Three-Dimensional View

Fig. 2 Geometry of the Scramjet Nozzle

Fig. 3 Grid Distribution

Single-Expansion-Ramp Nozzle

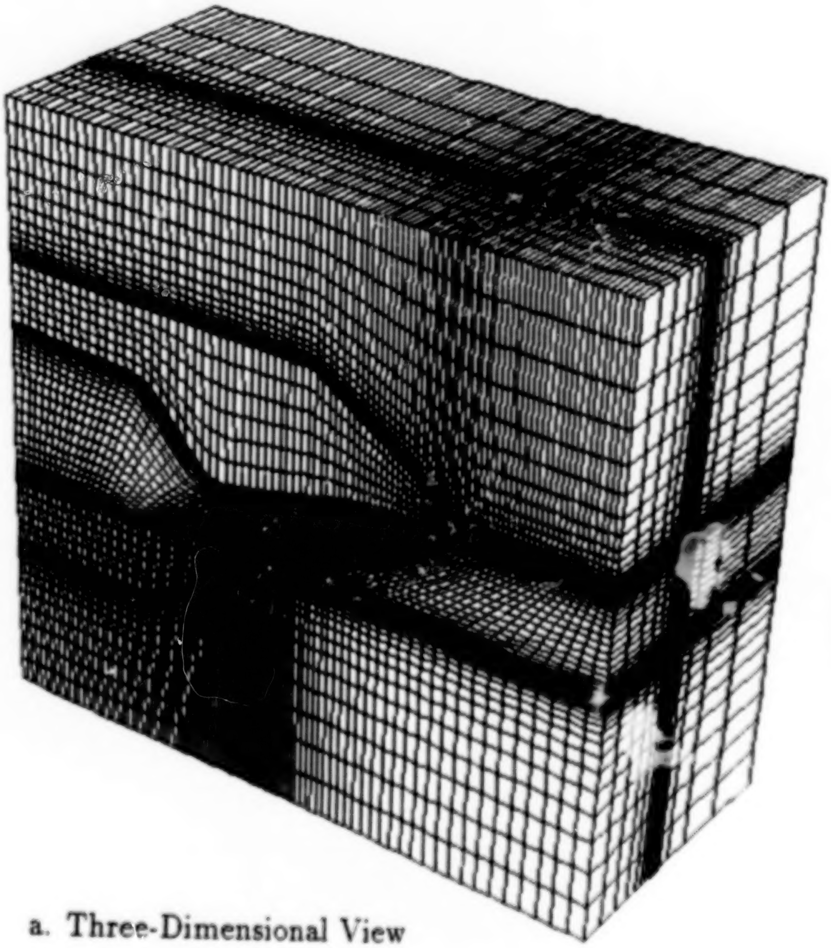

a. Three-Dimensional View

b. Two-Dimensional View

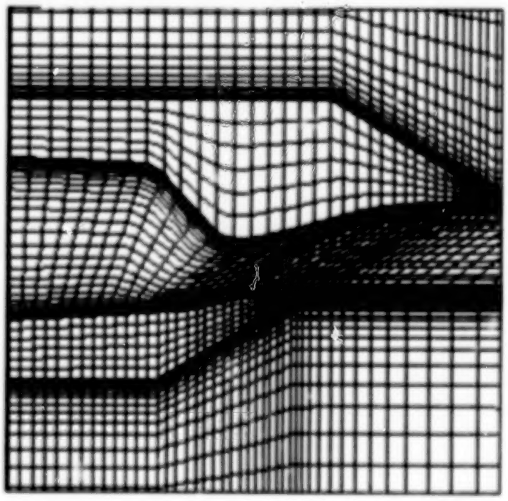

Fig. 4 Grid Distribution

Scramjet Nozzle

a. Surface and Boundary Grid

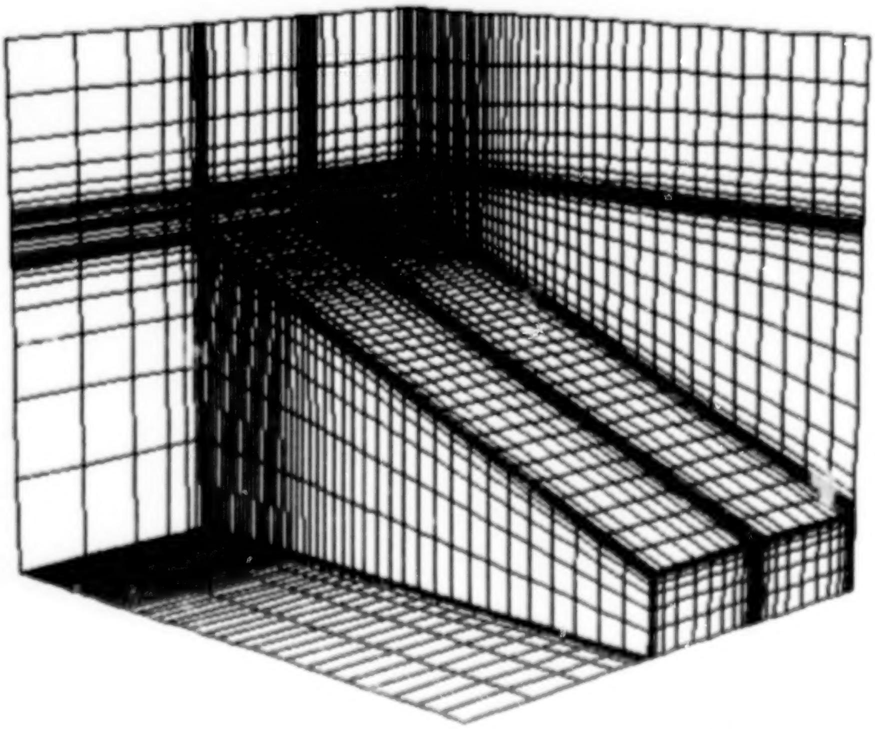

b. Two-Dimensional View

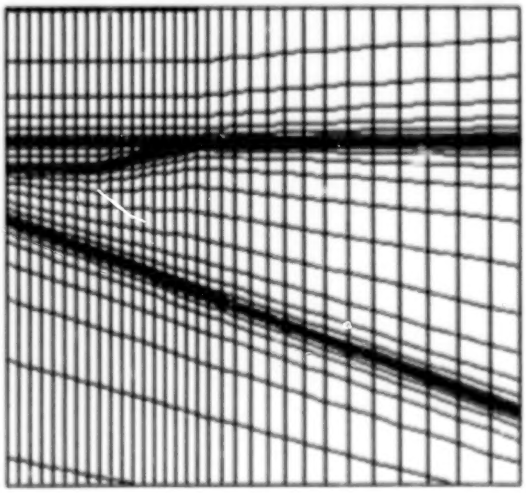

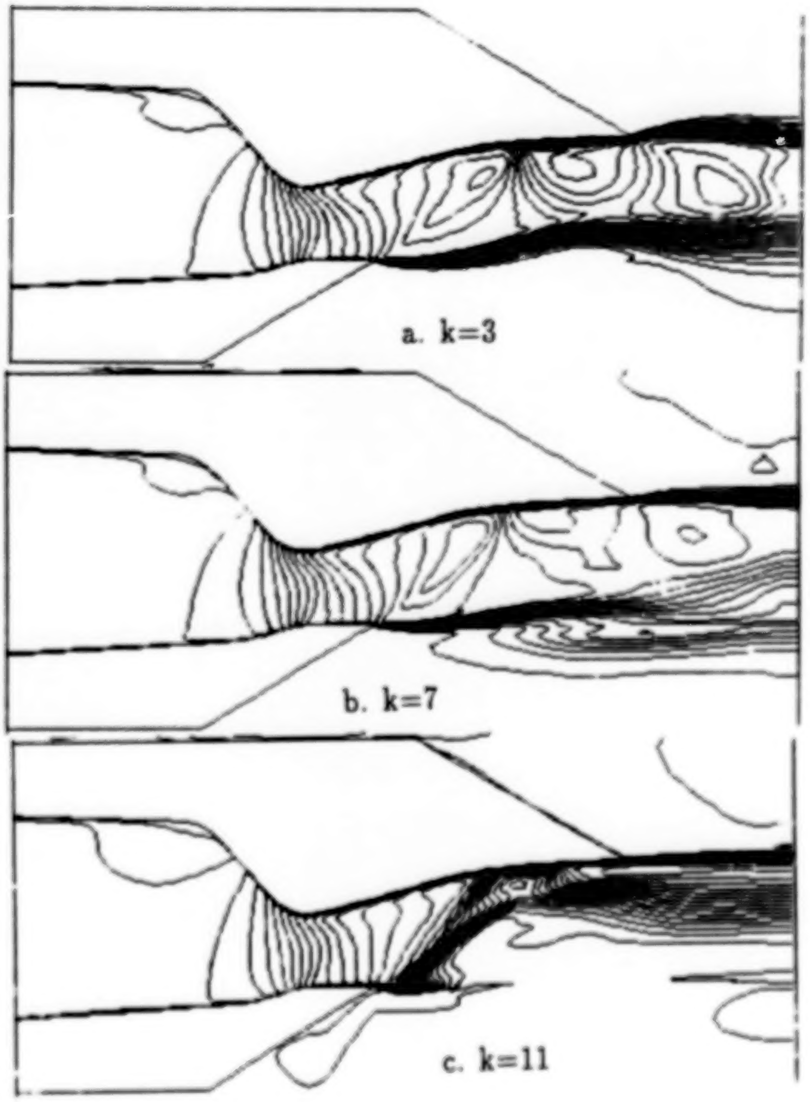

a. k=3

b. k=7

c. k=11

Fig. 5 Mach Number Contours, Side Views

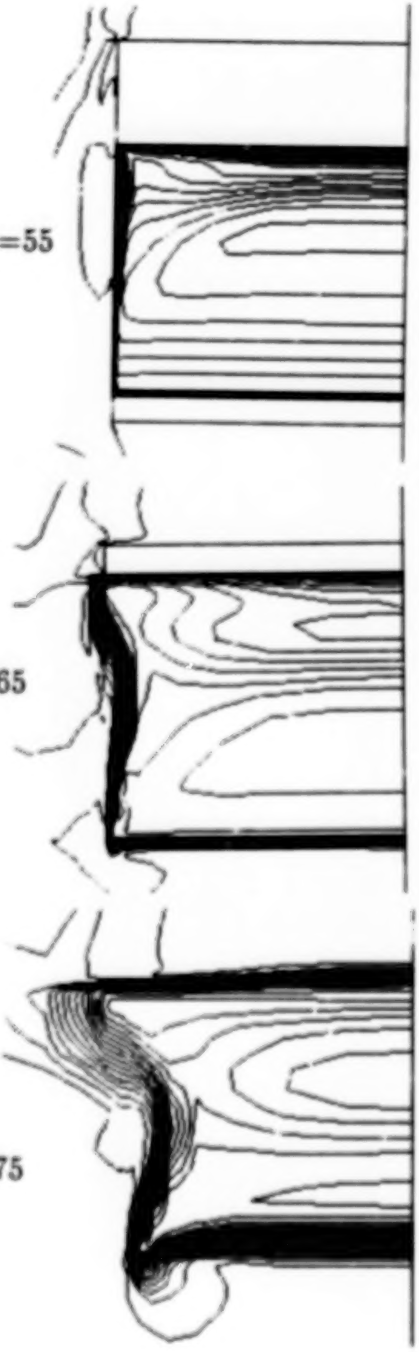

a. i=55

b. i=65

c. i=75

Fig. 7 Mach Number Contours, Rear Views

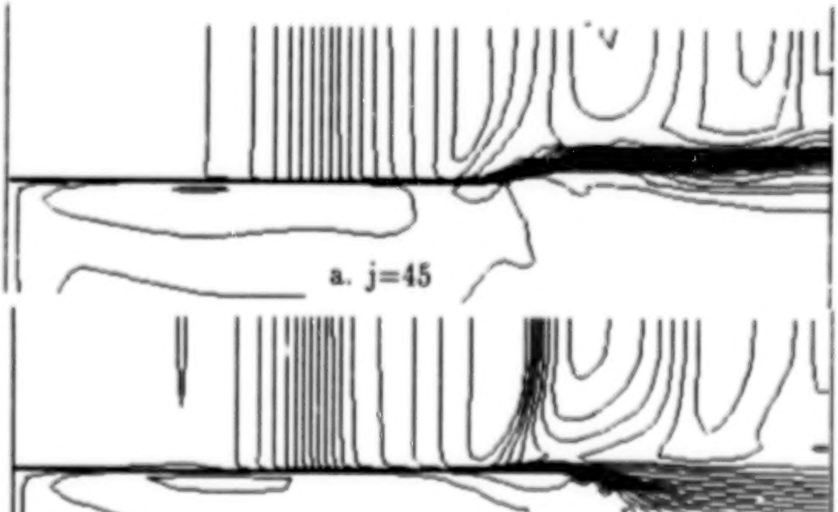

a. j=45

b. j=50

Fig. 6 Mach Number Contours, Top Views

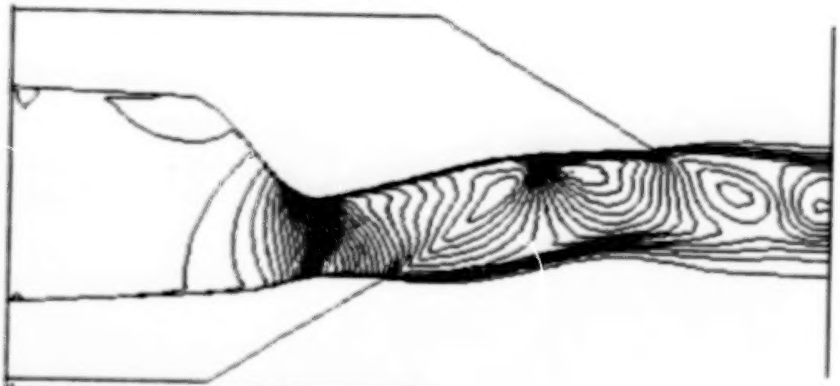

Fig. 8 Density Contours, Side View

k=3

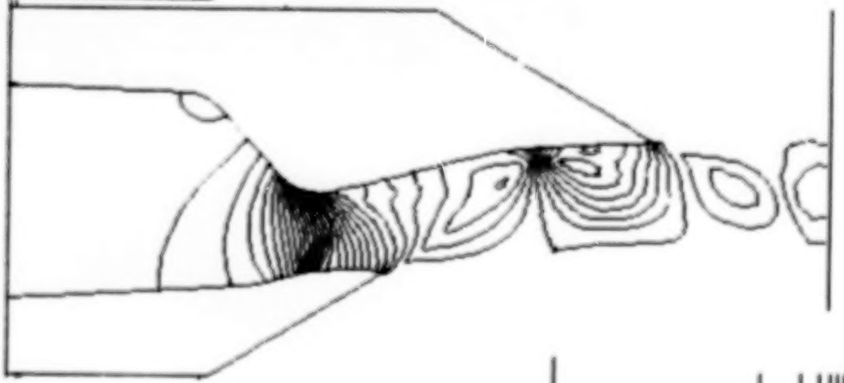

Fig. 9 Pressure Contours, Side View

k=3

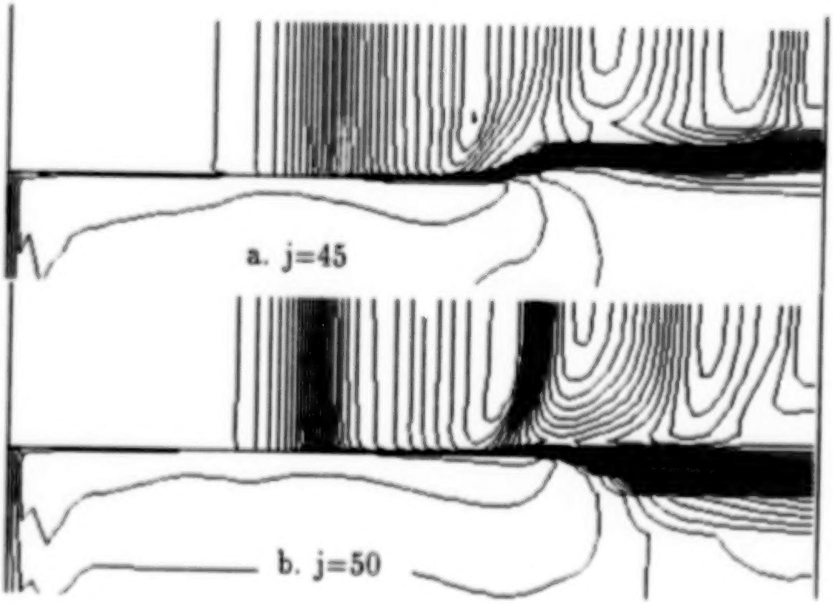

Fig. 10 Temperature Contours, Top Views

a. j=45

b. j=50

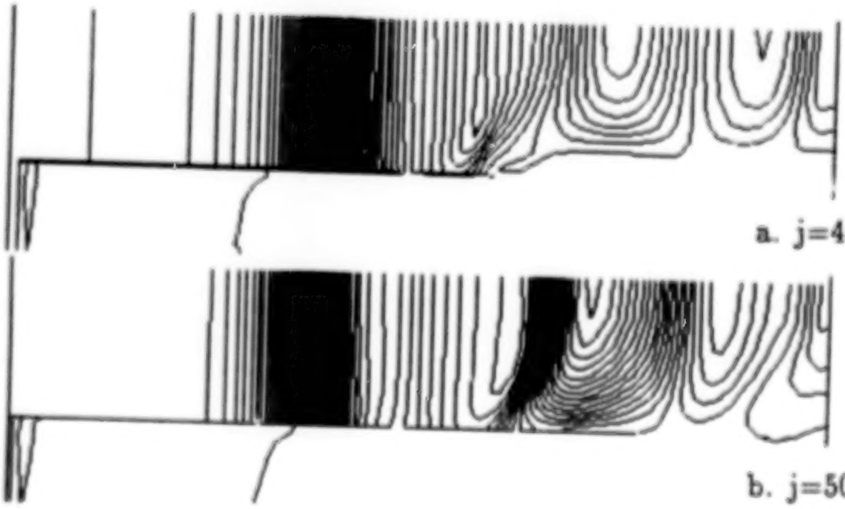

Fig. 11 Pressure Contours, Top Views

a. j=45

b. j=50

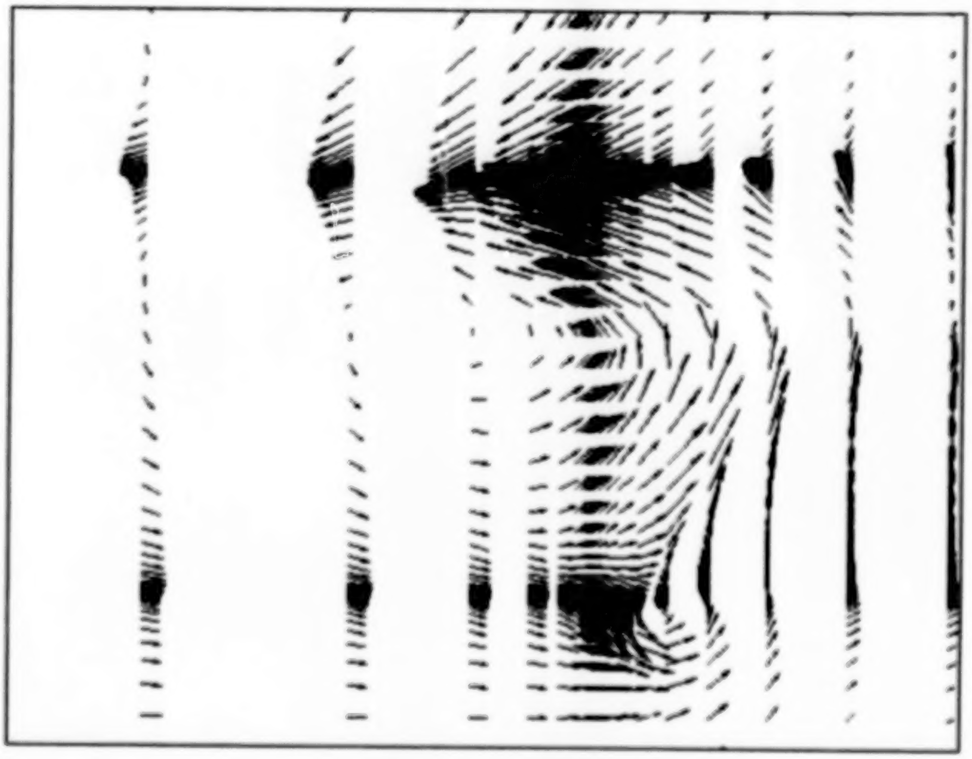

Fig. 12 Spanwise Total Velocities, i=75

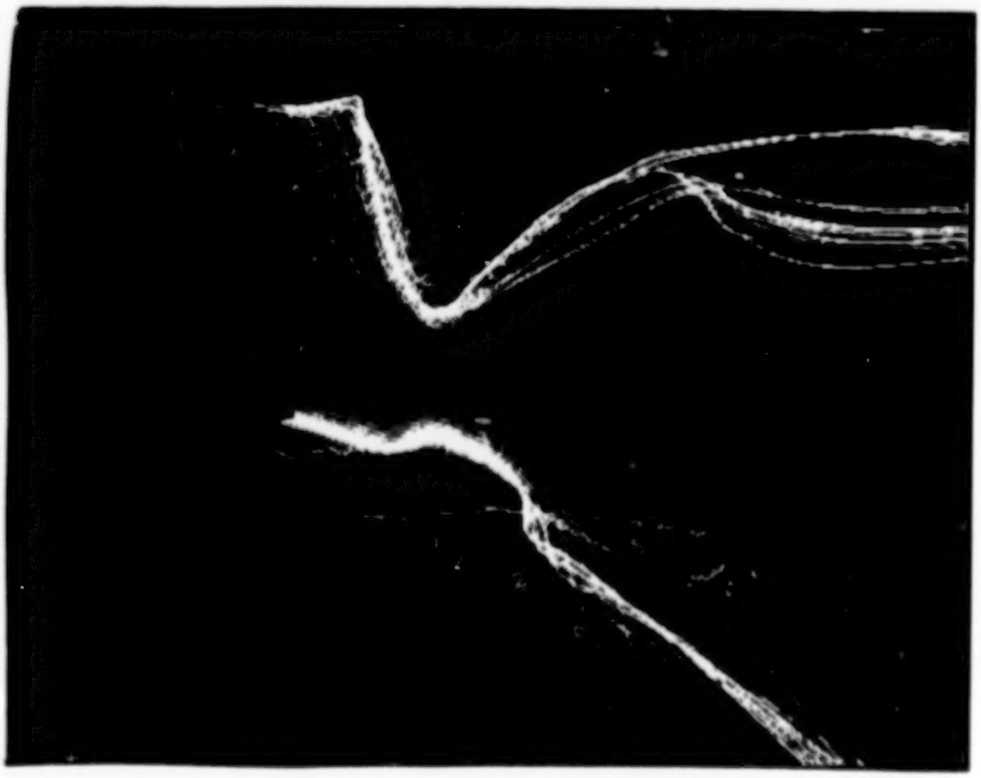

Fig. 13 Particle Trajectories, Side View

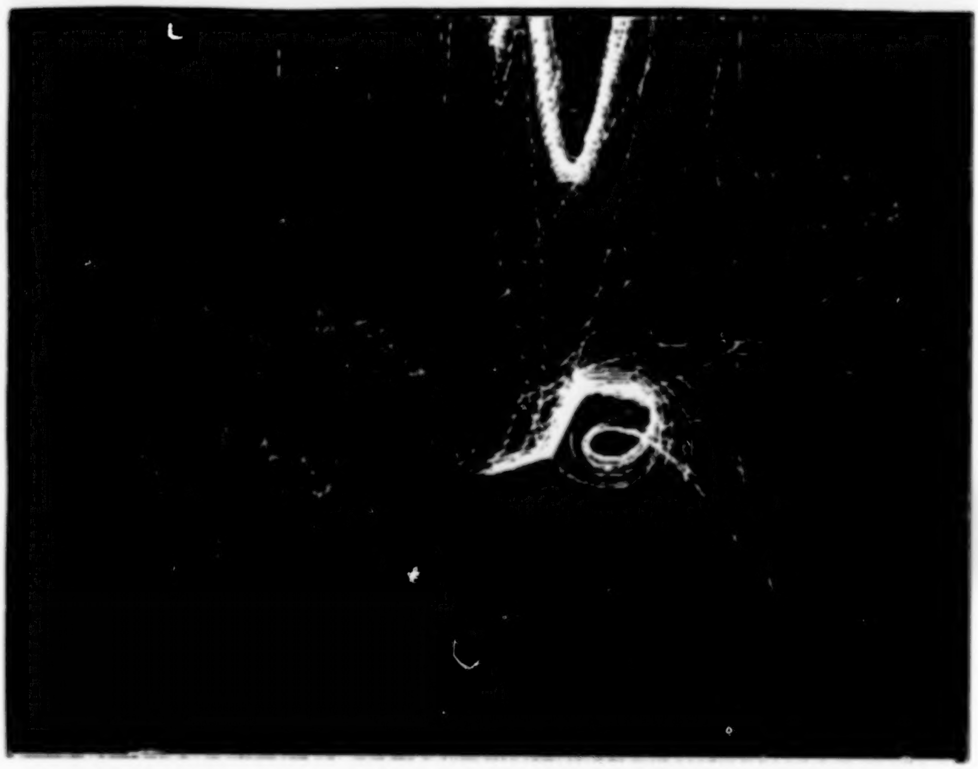

Fig. 14 Particle Trajectories, Rear View

Fig. 15 Wall Pressure Distributions

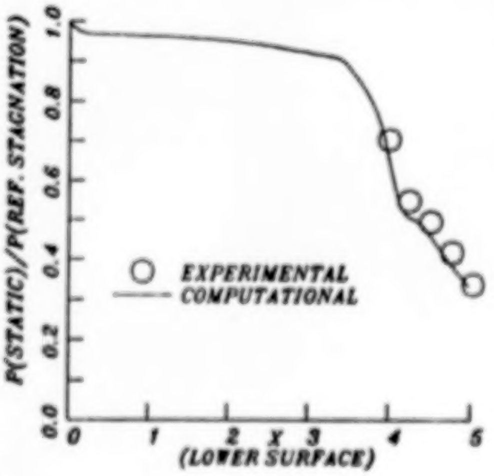

a. Lower Wall

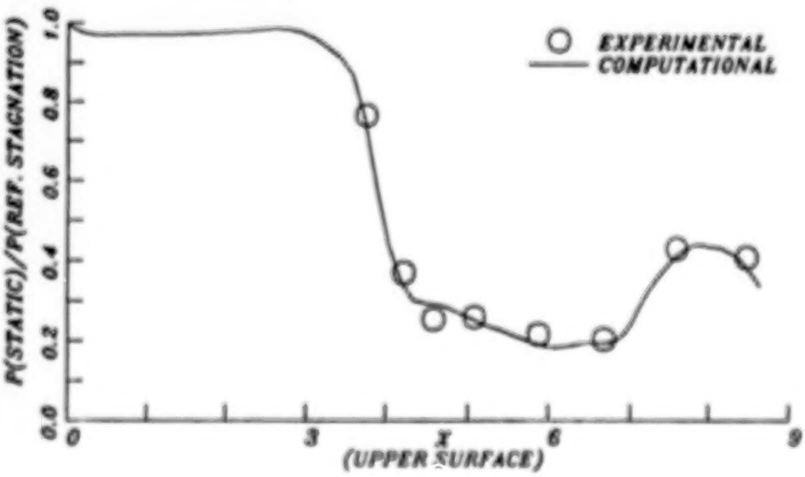

b. Upper Wall

Fig. 16 Mach Contours, Side Views

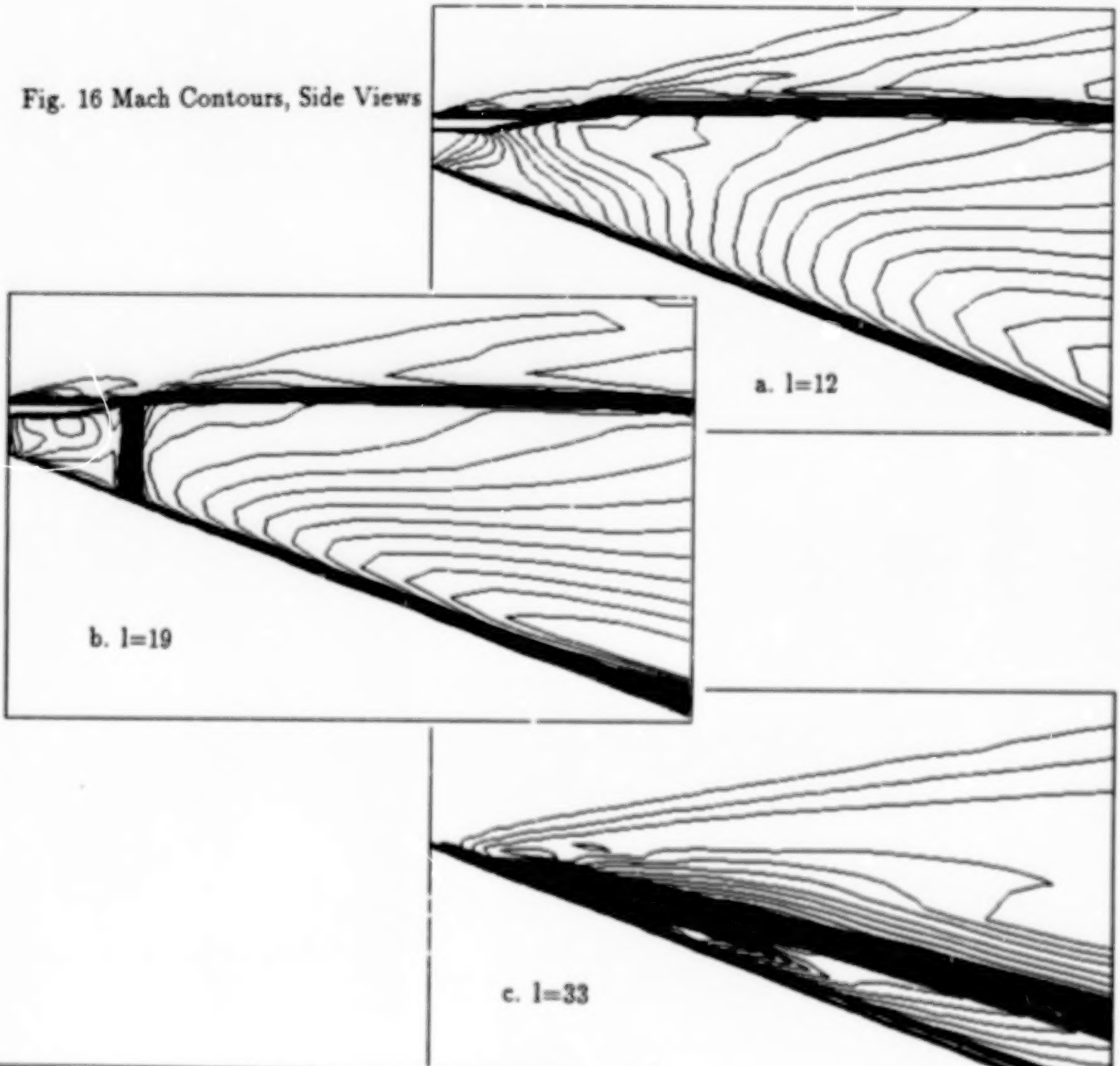

a. l=12

b. l=19

c. l=33

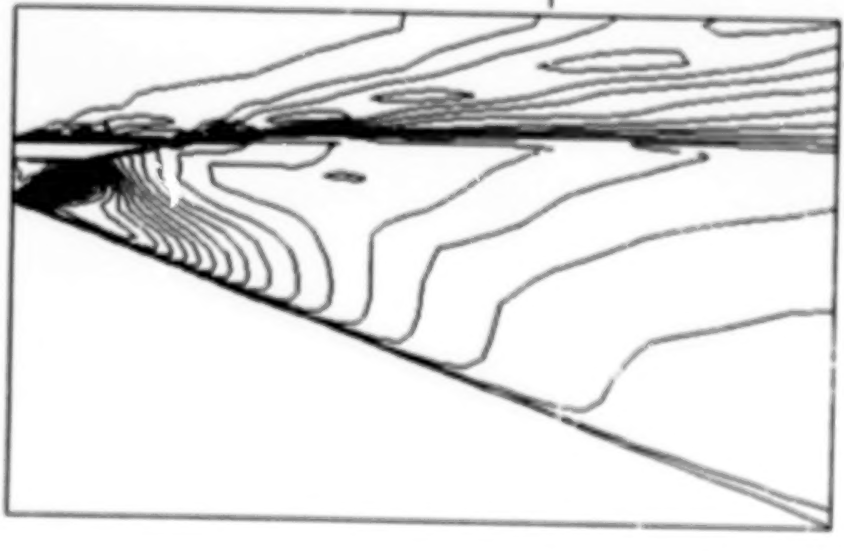

Fig. 17 Density Contours, Side View

l=11

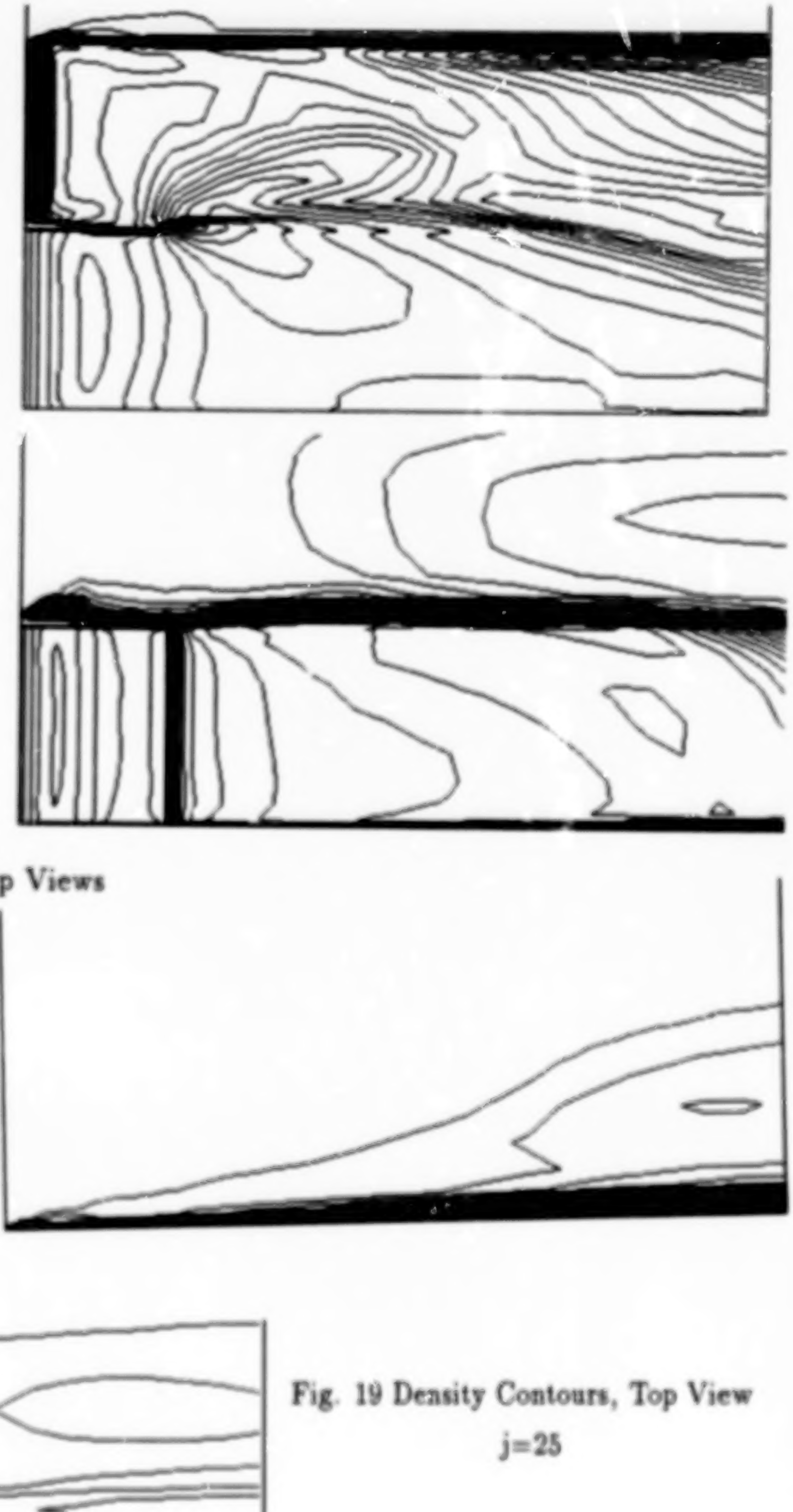

a. j=14

b. j=28

Fig. 18 Mach Number Contours, Top Views

c. j=43

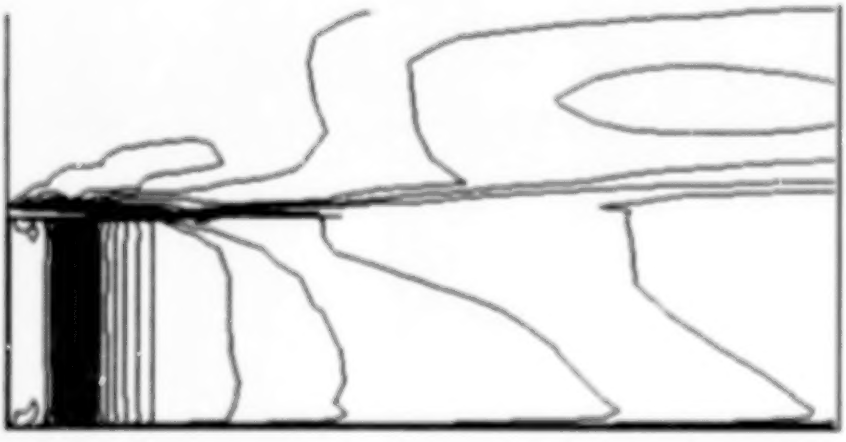

Fig. 19 Density Contours, Top View
j=25

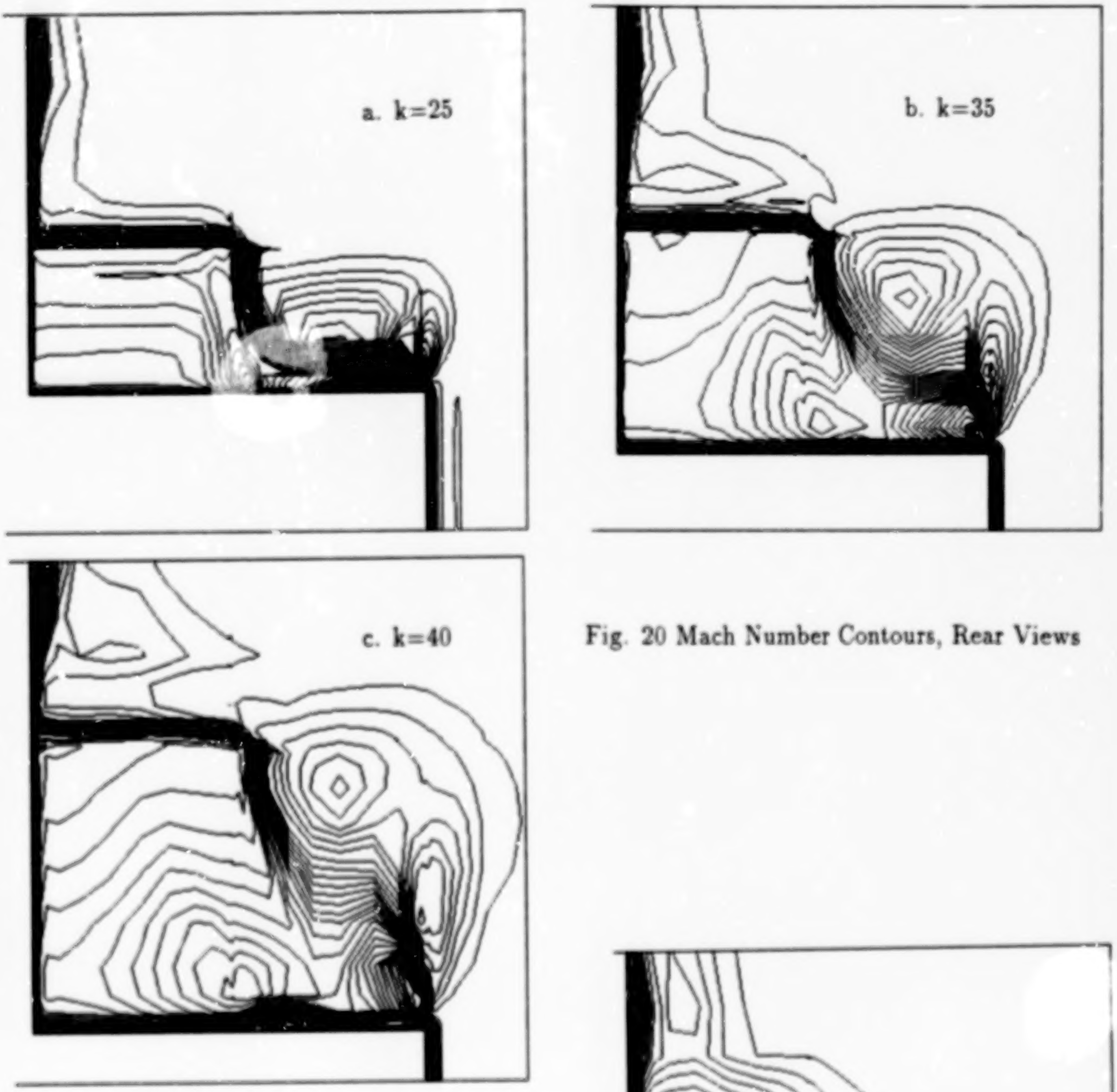

Fig. 20 Mach Number Contours, Rear Views

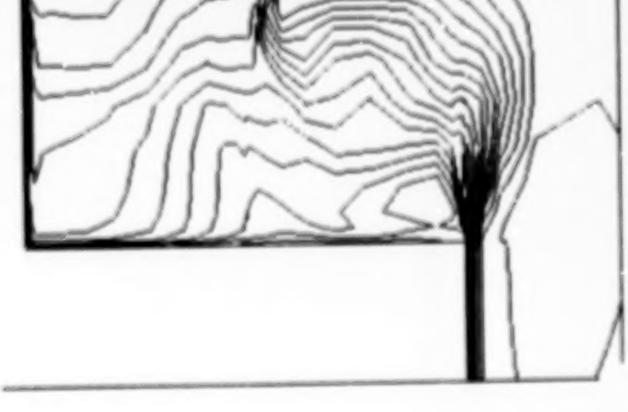

Fig. 21 Density Contours, Rear View
k=35

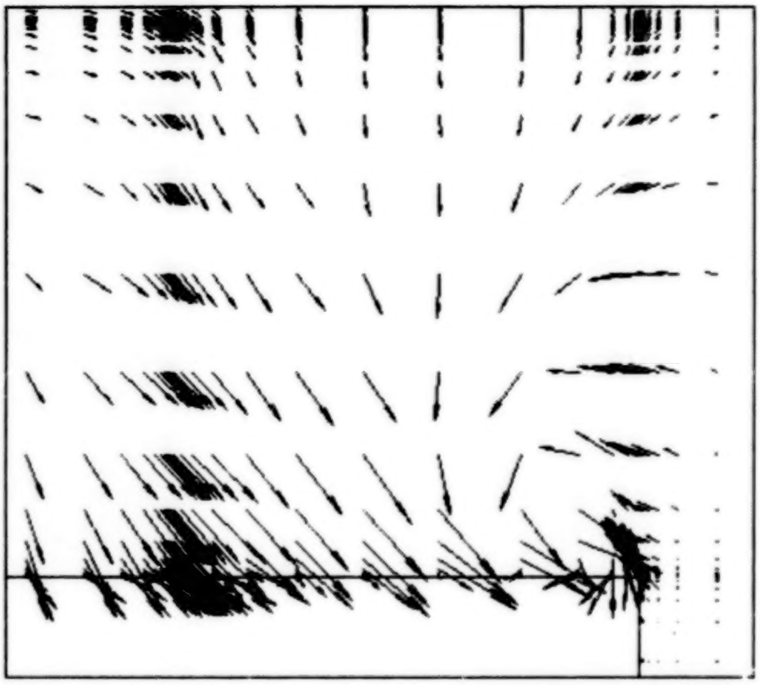

Fig. 22 Spanwise Total Velocities, i=35

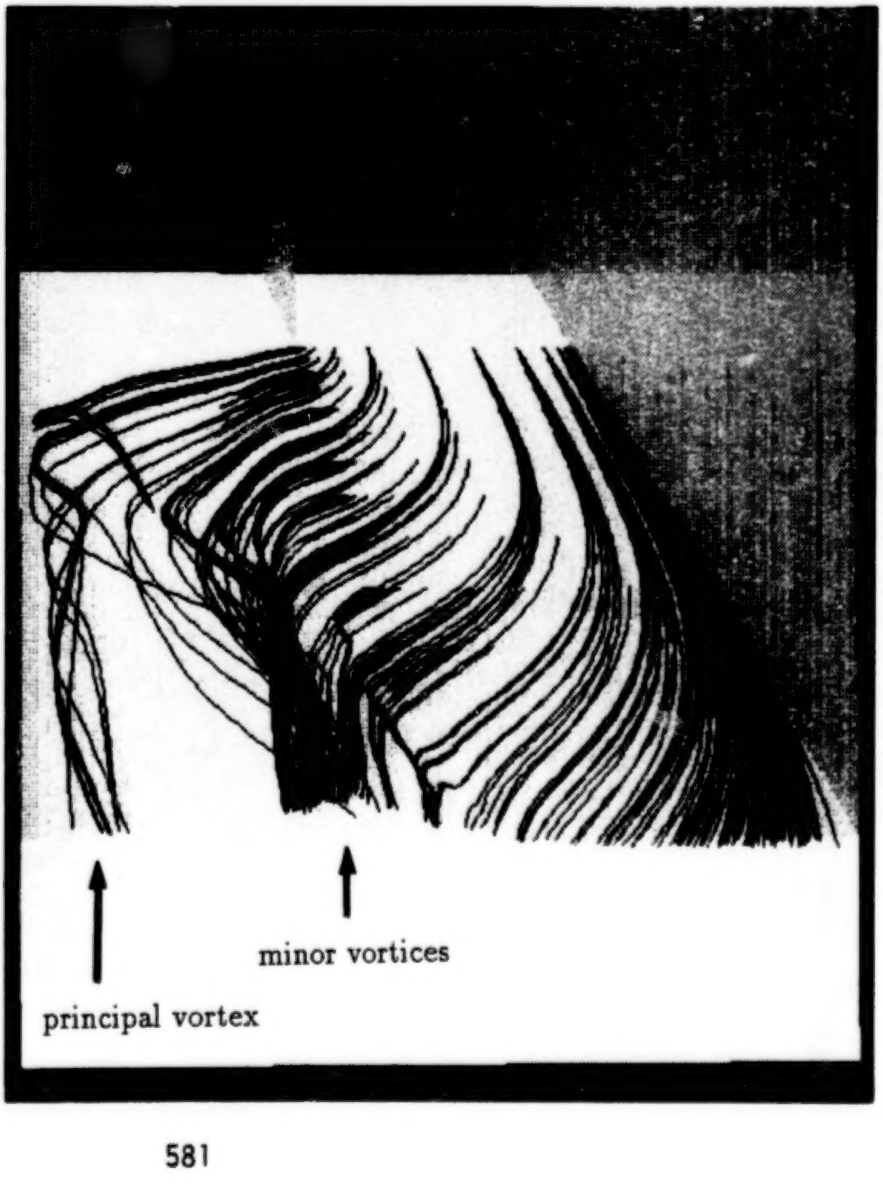

Fig. 23 Particle Trajectories

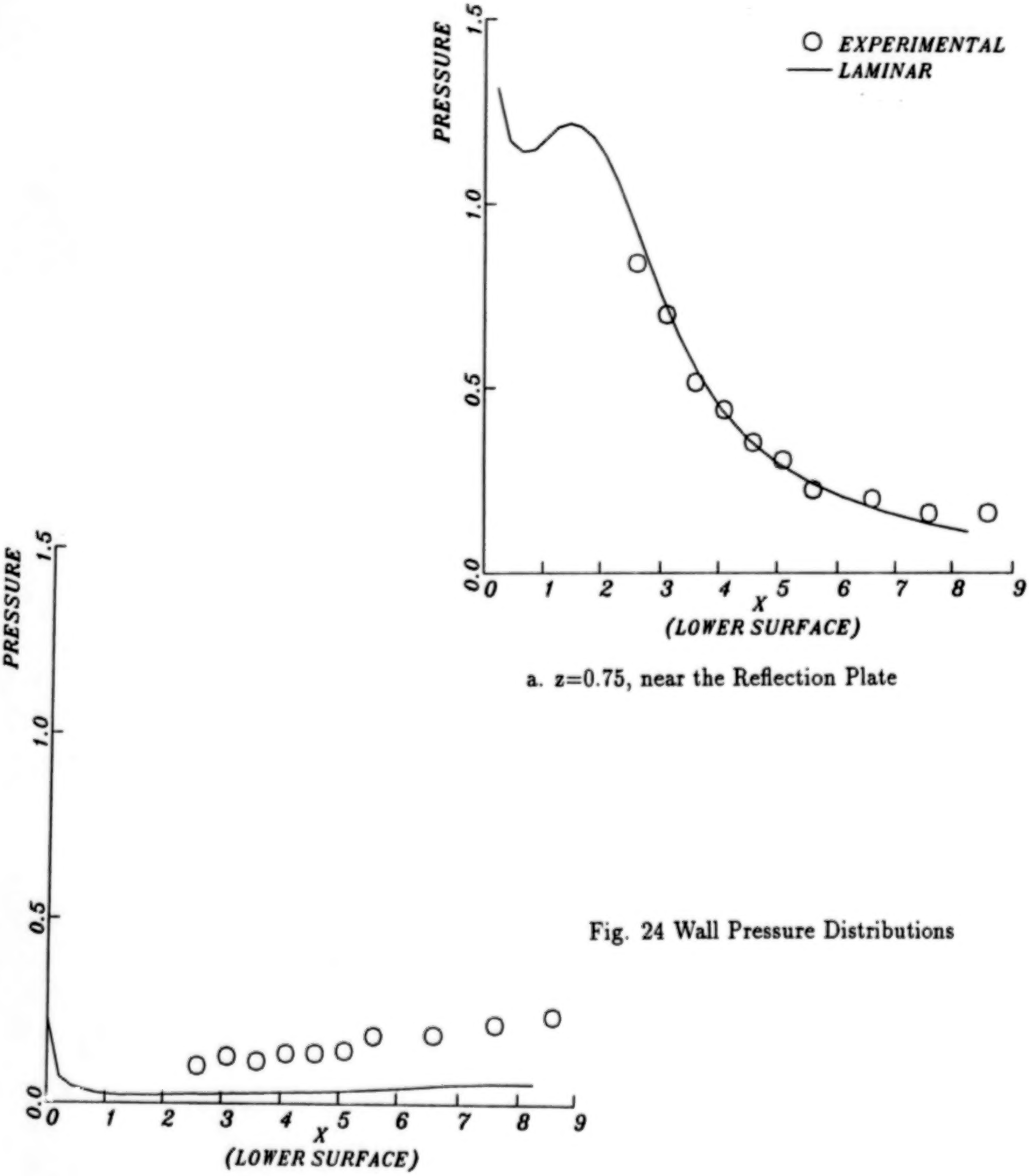

a. z=0.75, near the Reflection Plate

Fig. 24 Wall Pressure Distributions

b. z=4.52, near the Short Sidewall

Solution of Three-Dimensional Afterbody Flow Using Reduced Navier-Stokes Equations

H.M.H. Almahroos, P.K. Khosla and S.G. Rubin
Department of Aerospace Engineering & Eng. Mechanics
University of Cincinnati
Cincinnati, Ohio 45221-0343

ABSTRACT

The flow over afterbody geometries has been investigated using the reduced Navier-Stokes (RNS) approximation. Both pressure velocity flux-split and composite velocity primitive variable formulations have been considered. Pressure or pseudo-potential relaxation procedures are combined with sparse matrix or coupled strongly implicit algorithms to form a 3-D solver for general non-orthogonal coordinates. Three-Dimensional subsonic and transonic viscous/inviscid interacting flows have been evaluated. Solutions with and without regions of recirculation have been obtained.

INTRODUCTION

For a significant class of problems, exhibiting strong viscous-inviscid interaction, the reduced form of the Navier-Stokes (RNS) equations can provide an effective alternative to the full Navier-Stokes (NS) system for large Reynolds (Re) number numerical calculations, in both, two- and, three- dimensions. In a series of papers [1-4], Rubin and Khosla have developed and applied composite velocity primitive variable and pressure velocity formulations for a variety of sub-, trans- and supersonic flow problems. The RNS formulation, which represents a composite of Euler, higher-order boundary-layer triple deck equations, is consistent with all asymptotic large Re strong interaction theories and results in a uniformly valid single set of equations. The RNS system includes all normal and secondary flow diffusion terms in the surface momentum equations, but does not include normal or axial flow diffusion effects in the surface normal momentum equation. This approximation is self consistent for the large Re limit. Crossflow or secondary flow diffusion is retained in all equations as these effects are required to accurately model many three dimensional external and internal flows; see e.g. references [5-11], where it has been shown that explicitly added artificial viscosity can significantly destort secondary flow, heat transfer and surface stress predictions.

In the present paper, both the pressure and composite velocity primitive variable RNS formulations are considered for the computation of three-dimensional afterbody flows. In the pressure velocity formulation, for the velocity ($\bar{q}$) and the pressure (p), the dominant elliptic behavior and associated upstream influence, as manifested through an eigenvalue analysis [12], is associated with acoustic propagation and therefore the discretization requires an appropriate form of pressure velocity flux-split differencing. In the composite velocity formulation, the upstream influence is modelled by considering the velocity as a multiplicative composite of viscous or rotational velocities (U,W), and velocities derived from a pseudo potential (Φ). This representation of velocities is defined in the spirit of matched asymptotic expansions and is such that the resulting system reduces to the potential equation for inviscid irrotational regions. For rotational inviscid flows, a composite form of the Euler equations is recovered and a vorticity (U,W) term appears on the right hand side of the pseudo-potential continuity equation. The composite formulation compliments the two-dimensional vorticity stream function formulation, but is more suitable for three-dimension problems, as the total number of unknowns is does not increase, as would be the case for the three-dimensional vorticity-stream function procedure.

Flux vector splitting [12] is the basis of the discretization for the $(\bar{q},p)$ system and flux biasing with appropriate upwinding [1] is specified for the (U,W,Φ) system. For supersonic flows the both RNS systems reduce to initial value PNS formulations. The $(\bar{q},p)$ system can be solved with a spatial "boundary-layer" type marching relaxation procedure. Since flux biasing is employed for the composite (U,W,Φ) system, supersonic flows are computed by a relaxation process with the Enquist-Osher compressibilty correction applied for the pseudo-potential Φ. It should be emphasized that both formulations are valid throughout the Mach number Reynolds number range, including $M_\infty << 1$ and $M_\infty >> 1$, and do not require the addition of any explicitly added artificial viscosity. The inherent numerical viscosity associated with the discretization is sufficient to capture strong shocks over 3 to 4 mesh points. This numerical error is minimized with fine grids and a multi-grid strategy [1]. In earlier investigations of Rubin and Khosla, both pressure and composite velocity RNS codes have been applied for the computation of incompressible, transonic and supersonic flows with strong viscous-inviscid interaction, flow reversal and shock capturing e.g. see references [1-11]. Furthermore, the omitted diffusion terms have been incorporated directly, or via a deferred corrector approach, to obtain solutions of the complete NS equations. It has been shown that these effects are minimal for the problems considered. These procedures have been tested for the steady flow over an axisymmetric boattail and for the unsteady flow over a Joukowski airfoil. In the steady RNS formulations, outflow boundary conditions are required only for the pressure or pseudo potential and, as such, these are the only variables for which global storage of velocities is required outside of reverse flow regions. This is a significant simplification for steady three dimensional flow computations, and this can also be useful in the computation of complex three-dimensional flows on very fine meshes.

In both RNS formulations, the axial convective terms are first or second-order upwind differenced. The solution procedure takes advantage of the flux split/upwind differencing and results in a boundary-layer type streamwise marching method that is imbedded in a global relaxation process. In certain strong interaction cases a sparse matrix direct solver is applied for the pressure variable cross plan solution; in the composite velocity velocity the coupled strongly implicit ILU inversion is applied.

Subsonic flow past afterbody configurations with elliptic and hyperelliptic cross sections are discussed in this paper. Comparison are given between the pressure and composite velocity solutions. Grid resolutions studies are used to assess the accuracy of the two solution procedures.

GOVERNING RNS SYSTEM AND SOLUTION PROCEDURE

As described in earlier investigations [1-11], the RNS approximation leads to a single composite system that includes the Euler, second-order boundary layer and triple deck equations. The governing RNS system is considered for three-dimensional generalized coordinates and is designed to allow for shock capturing and flow reversal. In nondimensionalized form, the RNS system for low-speed flow is given as

Continuity Equation

$$\frac{\partial}{\partial \xi} (\rho \sqrt{g}\ u) + \frac{\partial}{\partial \eta} (\rho \sqrt{g}\ v) + \frac{\partial}{\partial \zeta} (\rho \sqrt{g}\ w) = 0 \tag{1-a}$$

ξ - Momentum Equation

$$\frac{\partial}{\partial \xi} (\rho \sqrt{g}\ u^2) + \frac{\partial}{\partial \eta} (\rho \sqrt{g}\ vu) + \frac{\partial}{\partial \zeta} (\rho \sqrt{g}\ wu) + \text{curvature terms} =$$

$$- g^{11}\ p_\xi - g^{12}\ p_\eta - g^{13}\ p_\zeta + \text{viscous terms} \tag{1-b}$$

ζ - Momentum Equation

$$\frac{\partial}{\partial \xi} (\rho \sqrt{g}\ wu) + \frac{\partial}{\partial \eta} (\rho \sqrt{g}\ vw) + \frac{\partial}{\partial \zeta} (\rho \sqrt{g}\ w^2) + \text{curvature terms} =$$

$$- g^{31}\ p_\xi - g^{32}\ p_\eta - g^{33}\ p_\zeta + \text{viscous terms} \tag{1-c}$$

η - Momentum Equation

$$\frac{\partial}{\partial \xi} (\rho \sqrt{g}\ uv) + \frac{\partial}{\partial \eta} (\rho \sqrt{g}\ v^2) + \frac{\partial}{\partial \zeta} (\rho \sqrt{g}\ vw) + \text{curvature terms} =$$

$$- g^{21}\ p_\xi - g^{22}\ p_\eta - g^{23}\ p_\zeta \tag{1-d}$$

Energy Equation

$$\sqrt{g}\ u^i \left[\frac{\partial T}{\partial \xi_i} - (\gamma - 1) T \frac{\partial \rho}{\partial \xi_i}\right] = \frac{\gamma}{Re\ Pr} \frac{\partial}{\partial \xi_i} \left[\mu \sqrt{g}\ g^{ij} \frac{\partial T}{\partial \xi_j}\right] \tag{1-e}$$

Equation of State

$$p = \frac{\rho T}{\gamma M_\infty^2} \tag{1-f}$$

where g^{ij} are the contravariant form of the metrics, $\sqrt{g}$ is the Jacobian, ρ, u, v, w, p and T are the density, velocities, pressure and temperature, repectively and γ is the ratio of specific heats. In these equations all variables are non-dimensionalized with respect to their free stream conditions except for the pressure which is normalized with the free stream dynamic pressure.

a) Pressure/Velocity Formulation (P.V.)

The pressure flux vector splitting, as described in reference [12], leads to the following discrete representation of the axial pressure gradient:

$$p_\xi = \omega_{i-1/2}(p_i - p_{i-1}) / \Delta\xi + (1-\omega_{i+1/2})(p_{i+1} - p_i)/\Delta\xi \qquad (2)$$

where

$\omega \le \omega_M = \min[\gamma M /(1+(\gamma-1)M_\xi^2) \; , \; 1 \;]$ for constant stagnation enthalpy

and

$\omega \le \omega_M = \min[M^2 \; , \; 1]$ for the full flux split energy equation.

This pressure gradient splitting and the associated convective upwinding satisfies the major eigenvalue continuity constraints on the fluxes and flux derivatives. For $\omega = \omega_M$, one eigenvalue is alwaya zero so that sharp shocks are obtained. For regions of reverse, flow the condition $\omega=0$ is required. This ensures that the fluxes, flux derivatives and eigenvalues remain continuous throughout the flow. This form of flux splitting is designed to maintain a bias in the direction of convective fluxes and leads to a relaxation procedure that is solely acoustically driven in the subsonic regions.

As described in earlier investigations, the continuity equation is discretized at (i,j-1/2,k). The streamwise (ξ-) and crossflow (ζ-) momentum equations are discretized at (i,j,k) and the normal (η-) momentum equation is discretized at (i,j+1/2,k). This discretization is consistent with the flux eigenvalues and with the appropriate boundary conditions required for u and p . For outflow boundaries without recirculation, only a pressure or pressure gradient condition is required. Far field boundary conditions, with positive outflow, are only required for u, p, and T. Inflow boundary conditions are specified for all flow variables or their gradients. Zero injection is assumed for all solid surface. The resulting algebraic system for the delta form of pressure $\Delta p = p^{n+1} - p^n$ is solved in each cross-plane using a coupled version of a sparse matrix direct solver. Additional details on the solver can be found in references [11,14]

b) Composite Velocity (U,W,Φ) Formulation (C.V.)

In the spirit of matched asymptotic expansions, the contravariant velocities are rewritten as:

$$\begin{aligned} u &= (U+1)\,(\,g^{11}\Phi_\xi + g^{12}\Phi_\eta + g^{13}\Phi_\zeta) = (U+1)u_e \\ v &= (g^{21}\Phi_\xi + g^{22}\Phi_\eta + g^{23}\Phi_\zeta) \qquad (3) \\ w &= (U+1)(g^{13}\Phi_\xi + g^{32}\Phi_\eta + g^{33}\Phi_\zeta) + W \end{aligned}$$

The composite representations for u and w, the axial and cross-flow velocity components, contain two types of terms, e.g. a rotational "pseudo" potential function Φ and viscous velocities U, W. The viscous no-slip boundary conditions are introduced through the velocities U, W. The kinematical boundary conditions are satisfied through the pseudo potential. This is consistent with the potential and boundary-layer approximations. Substitution of equation (3) into equation (1) leads to the RNS composite system. Additional details and the resulting equations are given in references [1-4]. All derivatives are approximated using three point central differences except for the convective U_ξ, W_ξ terms: these are second-order upwinded. Upstream influence in attached flow regions arises solely through $\Phi_{i+1}$and thus an outflow boundary condition on Φ, in lieu of p for the pressure formulation, is required. This leads to boundary-layer like streamwise marching for U, W with global relaxation for Φ . In reversed flow regions, w_ξ is upwind differenced and therefore the relaxation procedure includes both Φ and w, as is the case for p and (u,w) in the pressure split velocity formulation. The resulting algebraic system in each crossplane, for the delta form of Φ, $\nabla\Phi=\Phi^{n+1}-\Phi^{n}$ is solved using a consistent version of the coupled strongly implicit algorithm. This algorithm has previously been described in reference 10.

BOUNDARY CONDITIONS

The boundary conditions used for this investigation are; (i) uniform flow at the inflow; (ii) weak viscous/inviscid interaction at the outflow, thus at $\xi = \xi_m$, $\Phi_{\xi\xi} = 0$ or the negative eigenvalue fluxes are set to zero for the pressure velocity solver; (iii) the no slip and zero injection conditions are specified at the body surface; i.e. $u = U+1 = 0$, $v = v_e = 0$ and $w = W = 0$; (iv) far from the body the flow is assumed to be undisturbed; i.e. $u = 1$, $w = 0$, $\Phi = \Phi_{fs}$, $T = 1$ and the entropy is assumed to be constant.

RESULTS

Afterbody configurations of elliptical (Figure 1a) and hyper-elliptical (Figure 1b) cross-sections have been examined. In view of the geometric symmetry, the calculations have been carried out in one quarter of the flowfield. A body fitted

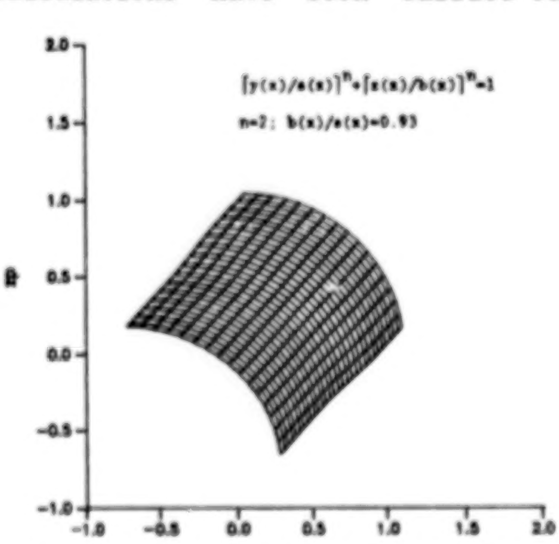

Figure 1-a: Surface grid distribution - ellipse

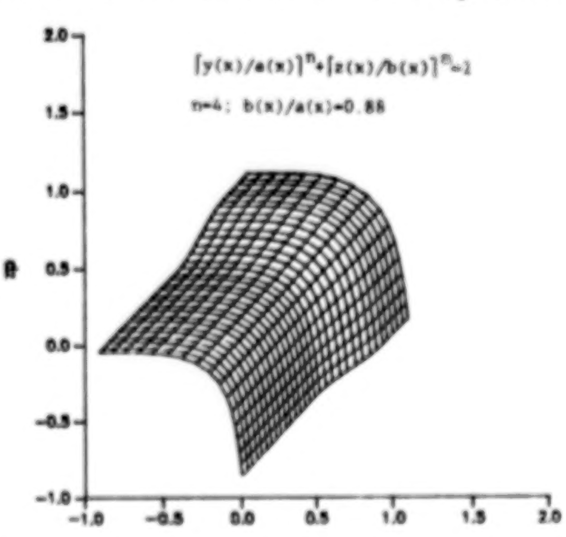

Figure 1-b: Surface grid distribution - hyperellipse

computational grid e.g., see Figure 2 for an elliptic cross-section, was generated

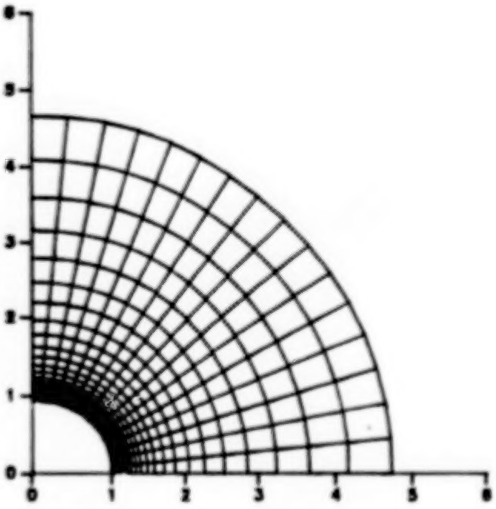

Figure 2:

Ellipse - grid in the cross-plane 71x17

$\Delta\eta_{min} = 0.00175$
variable stretching

by using a shearing transformation. A stretched grid is employed in the normal direction while a uniform spacing is prescribed in the azimuthal direction. The axial boattail is generated by fitting a cubic polynomial between two appropriate cross-sections.

Both laminar and turbulent flows have been investigated using the composite velocity (C.V.) formulation. Only laminar flow computations have been carried out using the pressure velocity (P.V.) formulation. Figure 3a and 3b depict the pressure coefficient and skin friction parameter for a laminar non-separated boattail of elliptical cross-section using both (P.V.) and (C.V.) formulations. The resonable agreement between the two solutions provides a self consistent evaluation of the two formulations. The metrics are calculated analytically for the P.V. solutions and numerically for the C.V. solutions. As the grid is refined the two solutions merge.

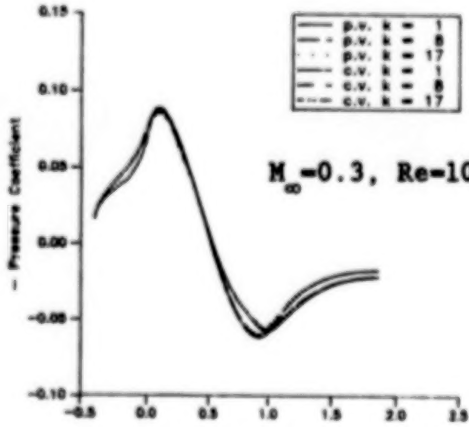

Figure 3-a: Pressure Coefficient - comparison P.V. vs C.V.

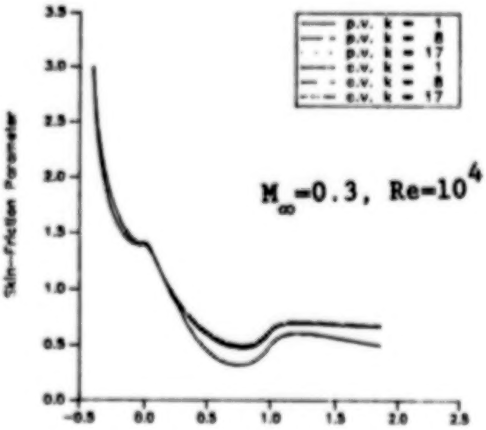

Figure 3-b: Skin-Friction Parameter -comparison P.V. vs C.V.

The pressure coefficient and skin friction parameter for turbulent flow computations for an afterbody of elliptical cross-section at M_∞=0.9 using the (C.V.) formulation are shown in Figures 4-a and 4-b. As seen in the figure, a sharp weak transonic shock has been captured quite well.

The crossplane grid for an afterbody of hyper-ellipse cross-section is depicted in Figure 5. A comparison of the laminar P.V. flow solution for Re=10^4, on two grids 61x79x17 and 121x79x17, is shown in Figures 6a and 6b. The pressure coefficient and skin friction parameter along a symmetry plane and the location of maximum azimuthal curvature are used for this comparison. A region of large recirculation, along the boattail, has been computed by this technique. The sensitivity to grid refinement is quite evident. Further grid refinement in both the axial and azimuthal directions are most likely required to obtain an acceptable level of accuracy. The axial velocity vectors in the recirculation region are depicted in Figures 7a and 7b. The effect of different subsonic Mach numbers is shown in Figures 8a and 8b. The recirculation is slightly increased. This is consistent with previous subsonic calculation on axisymmetric boattails [2].

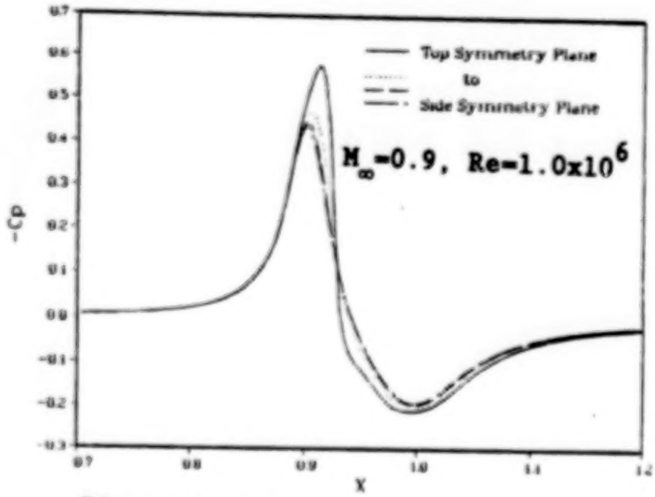

Figure 4-a: Pressure Coefficient - ellipse

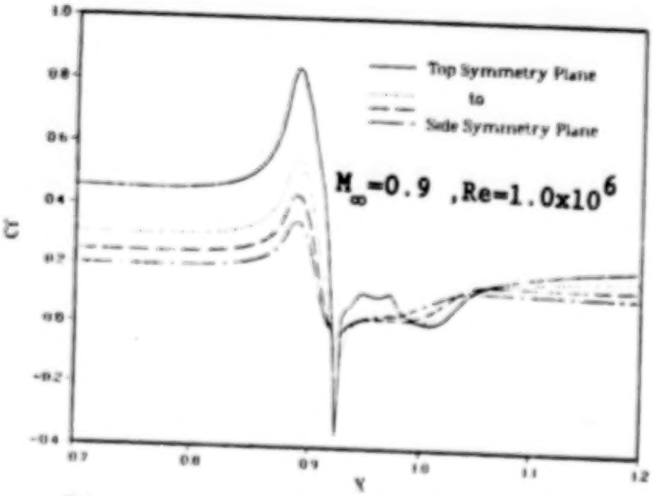

Figure 4-b: Skin-Friction Parameter - ellipse

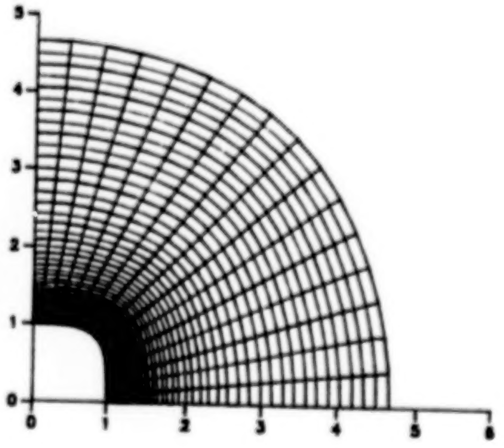

Figure 5: Hyperellipse

- grid in the cross-plane 79x17

$\Delta\eta_{min}$=0.0005

Stretching factor σ=1.09

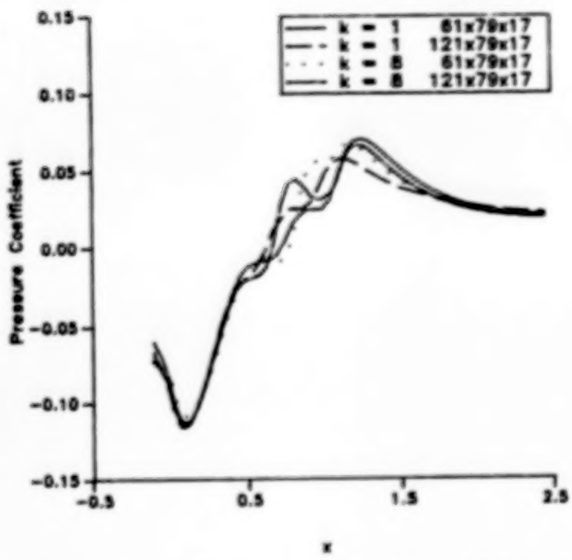

Figure 6-a: Pressure Coefficient for M_∞=0.3, Re=10^4 (hyperellipse) - effect of grid

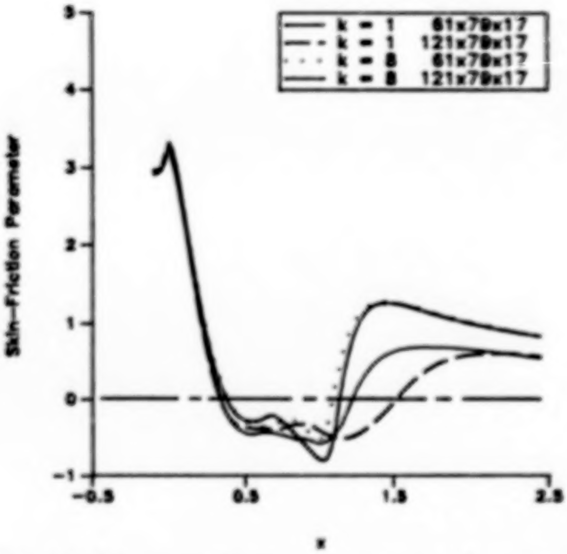

Figure 6-b: Skin-Friction Parameter for M_∞=0.3, Re=10^4 (hyperellipse) - effect of grid

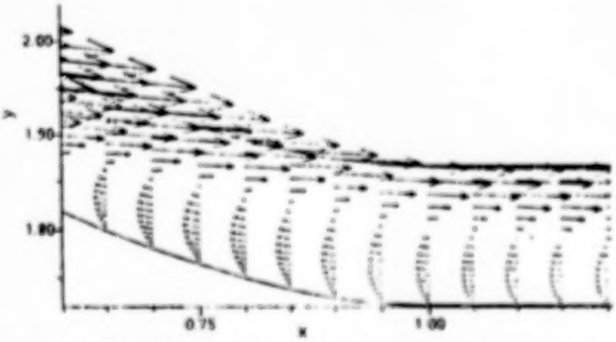

Figure 7-a: Velocity Field in the Separated Region for Hyperellipse M_∞=0.3 , Re=10^4 , k=1

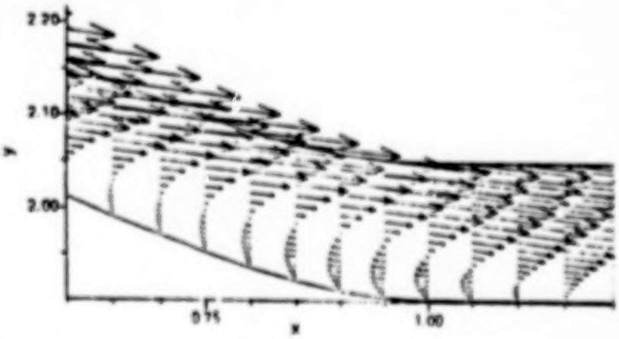

Figure 7-b: Velocity Field in the Separated Region for Hyperellipse M_∞=0.3 , Re=10^4 , k=8

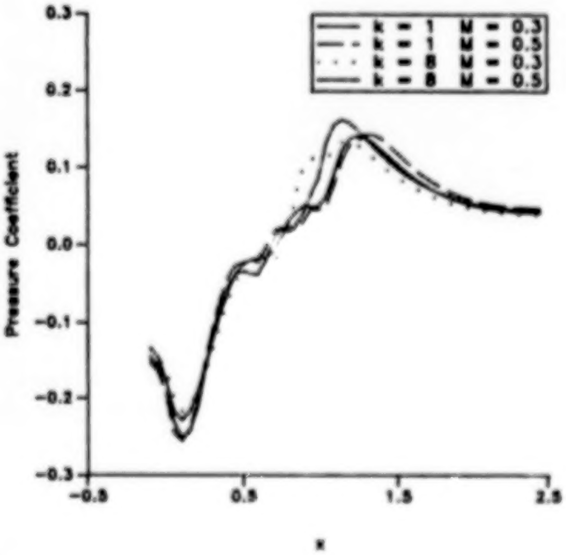

Figure 8-a: Pressure Coefficient for Re=10^4 (hyperellipse) - effect of Mach number

grid: 61x79x17

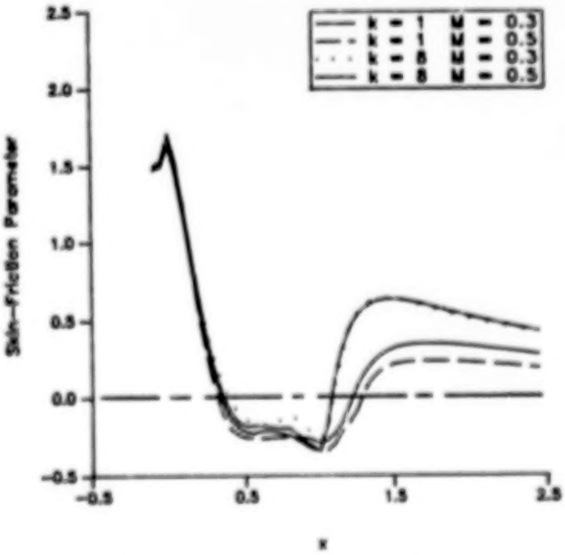

Figure 8-b: Skin-Friction Parameter for Re=10^4 (hyperellipse) - effect of Mach number

grid: 61x79x17

From the above disscusion, it is clear that the present RNS techniques have the ability to compute fairly complex flow fields. The computational cost for the C.V. solution is modest, e.g., with 81923 grid points and 5 coupled unknowns this is of the order of 30 to 60 minutes on the Cray Y-MP. The computational cost of the P.V. solutions, on the other hand, is much greater. This is due of the fact that that sparse matrix direct solver, which requires 8 to 9 times the CPU of the CSIP, is applied for much of the cross plane inversion. Strategies to reduce the overall computational effort by minimizing the need for multiple LU (direct solver) inversions have been investigated. The computational times can be reduced considerably with bach subsitution. Recent studies have provided factors of less than 2 over C.V. computer time . A stabilized version of the consitent coupled strongly implicit algorithm for the P.V. formulation is also currently under investigation. This will result in further reductions in the P.V. CPU time.

CONCLUSION

Two formulations of the three-dimensional RNS equations have been investigated for the computation of laminar/turbulent subsonic, transonic flows with large recirculation regions. The technques are quite efficient in terms of storage and computational times. Future applicaltions to complex internal/external geometries and supersonic free streams are under investigation.

ACKNOWLEDGEMENT

The work has been supported by the AFOSR (L. Sakell, Technical Monitor) under Grant No. AFOSR 90-0096.

The computations have been performed on the Cray Y-MP through a project supported by the Ohio Supercomputer Center.

REFERENCES

1. Gordnier, R.E. and Rubin,S.G., "3-D Composite Velocity Solutions for Subsonic/Transonic Flows over Afterbodies", AIAA paper no. 89-1837, Presented at the 20th Fluid Dynamics, Plasma Dynamics and Lasers Conference, Buffalo, New York, June 12-14, 1989.

2. Swanson, R.C., Rubin, S.G. and Khosla, P.K., "Calculation of Afterbody Flows with a Composite Velocity Formulation", AIAA paper no. 83-1736, Presented at the AIAA 16th Fluid and Plasma Dynamics Conference, Danvers, Massachusetts, July 12-14,1983.

3. Khosla, P.K. and Rubin, S.G., "A Composite Velocity Procedure for the Compressible Navier-Stokes Equations", AIAA Journal, Vol. 21, No. 11, November 1983, pp.1546-1551.

4. Rubin, S.G., Celestina, M. and Khosla, P.K., "Second Order Composite Velocity Solution for Large Reynolds Number Flows", AIAA paper no. 84-0172, Presented at the AIAA 22nd Aerospace Sciences Meeting, Reno, Nevada, January 9-12, 1984.

5. Reddy, D.R. and Rubin, S.G., "Consistent Boundary Conditions for Reduced Navier-Stokes (RNS) Scheme Applied to Three-Dimensional Viscous Flows", Journal of Fluids Engineering, Vol. 110, September 1988, pp. 306-314..

6. Rubin, S.G. and Reddy, D.R., "Analysis of Global Pressure Relaxation for Flows with Strong Interaction and Separation", Computers and Fluids, Vol. 11, 1983, pp. 281-306.

7. Khosla, P.K. and Lai, H.T., "Global PNS Solutions for Transonic Strong Interaction Flows", AIAA 22nd Aerospace Science Meeting, AIAA paper no. 84-0458, January, 1984.

8. Cohen, R. and Khosla, P.K., "Three-Dimensional Reduced Navier Stokes Equations solution for Subsoinc Separated and Non-Separated Flows Using a Global Pressure Relaxation Procedure", International Journal for Numerical Methods in Fluids, Vol. 9, 1989, pp. 1087-1098.

9. Rubin, S.G. and Khosla, P.K., "Navier-Stokes Calculations with a Coupled Strongly Implicit Procedure", Comput. Fluids 9, 1979, pp. 163-180.

10. Khosla, P.K. and Rubin, S.G., "Consistent Strongly Implicit Iterative Procedures for Two-Dimensional Unsteady and Three-Dimensional Space-Marching Flow Calculations", Computers and Fluids, Vol. 15, No. 4, 1987, pp. 361-377.

11. Bender, E.E. and Khosla, P.K., "Two-Dimensional Navier-Stokes Equations using Sparse Matrix Solvers", AIAA paper no. 87-0603, Presented at the 25th Aerospace Sciences Meeting, Reno, Nevada, January 12-15, 1987.

12. Rubin, S.G., "RNS/Euler Pressure Relaxation and Flux Vector Splitting", Technical Note, Computers & Fluids, Vol. 16, No. 4, 1988, pp. 485-490.

13. Pordal, H.S., Khosla, P.K. and Rubin, S.G., "A Flux-Split Solution Procedure for Unsteady Inlet Flows", AIAA paper no. 90-0585, Presented at the 28th Aerospace Sciences Meeting, Reno, Nevada, January 8-11. 1990.

14. Himansu, A., Khosla, P.K. and Rubin, S.G., "Relaxation/Sparse-Matrix Solvers for Three-Dimensional Recirculating Flows", AIAA paper no. 89-0552, Presented at the 27th Aerospace Sciences Meeting, Reno, Nevada, January 9-12, 1989.

Recent Update of the RPLUS2D/3D Codes

Y-L Peter Tsai
Sverdrup Technology, Inc.
NASA Lewis Research Center Group
Cleveland, Ohio 44135

Abstract

The development of the RPLUS2D/3D codes is summarized. These codes utilize LU algorithms to solve chemical non-equilibrium flows in a body-fitted coordinate system. Recent improvements include vectorization method, blocking algorithm for geometric flexibility, out-of-core storage for large-size problems, and an LU-SW/UP combination for CPU-time efficiency and solution quality.

I. Introduction

The technology for hypersonic vehicles has been developed for decades. Back in the sixties, the Air Force and NASA conducted the research on scramjet engines which were proposed for the Aero-Space Plane [1]. This was the prelude of the recent NASP (National Aero-Space Plane) program. Due to lack of powerful computers, early hypersonic scientists relied heavily on experiments. Analysis had to be done on a simplified basis. In the seventies, research on hypersonic planes and scramjet engines became dormant for more than a decade because of the Apollo and Shuttle missions. Recent hypersonic research in the eighties revived in a dramatically different environment in which the capability of computers had grown exponentially since their invention. The methodology in solving flow problems has also advanced significantly, thanks to the research of numerous mathematicians and fluid dynamicists. Three-dimensional, Reynolds-average Navier-Stokes simulations have thus been made feasible. As a result, CFD (Computational Fluid Dynamics) becomes a popular and promising tool for flow-prediction.

As a participant of the NASP program, NASA Lewis Research Center supported the development of the RPLUS2D/3D codes. This task is motivated by the need to numerically predict chemical non-equilibrium flows for the NASP program. Chemical reaction is an important factor for NASP-related flows. For the scramjet combustor, combustion is undoubtedly the vital issue. In the expansion nozzle, recombination of atoms and radicals generated upstream of the nozzle, and possibly some continuous combustion may account for a significant percentage of the thrust. At the NASP surface and inlet where the hypersonic airstream and solid body come in contact, and across the shock waves where the flow speed drastically changes, air-dissociation or even ionization may play important roles. The assumption of chemical-equilibrium may be considered to simplify the problems. However, the chemical-equilibrium assumption may result in poor prediction, thus its application is quite limited. For instance, in an H_2/air combustor, the chemical-equilibrium assumption produces an excessive amount of water vapor, which in turn over-predicts the performance of the combustor. The RPLUS2D/3D codes therefore incorporate chemical non-equilibrium models.

The size of the systems of equations for non-equilibrium chemistry imposes difficulties in obtaining the flow solution. The governing equations include the basic flow equations (continuity, Navier-Stokes, and energy equations) in addition to a number of species transport equations. It is not uncommon for a chemistry model to consider more than ten species, which require the same number of species equations. Multi-dimensional solution of such systems is a major task. It was not until recent advances of computer capability that three-dimensional simulation of chemically non-equilibrium flows has become feasible. Nevertheless, the efficiency of the numerical scheme remains a vital issue.

One of the important features of the RPLUS2D/3D codes is the use of LU algorithms to march in time. In the past, both explicit and implicit algorithms for time-integration have been used for calculating chemical non-equilibrium flows. Among explicit algorithms, the MacCormack [2-5] and Runge-Kutta schemes [4,6] are most notable. The SPARK code [2] developed at NASA Langley center adopts the MacCormack scheme, and more recently, attempted a higher order MacCormack scheme with some success [3]. Shuen and Liou [6] utilized a two-stage Runge-Kutta in conjunction with spatially upwind-differenced method. To alleviate the restrictive limitation on time-step due to stiff source terms, Bussing and Murman [4] proposed implicit treatment for the source terms in these explicit methods. A number of other researchers prefer marching in time implicitly. Candler and MacCormack [7] implemented an implicit Gauss-Siedel line-relaxation technique for ionized flows. Molvik and Merkle [8-9] utilized a three-dimensional AF (Approximate-Factorization) in the inner iteration of a dual time-step procedure specifically for time-accurate calculation. Walters, et al. [10] included in their GASP (General Aerodynamic Simulation Program) code what they called AF/relaxation and LU/relaxation algorithms. Lee and Deiwert [11] extended the implicit flux-vector splitting algorithm of F3D [12] to include non-equilibrium chemistry. In general, implicit time-marching provides more temporal damping than explicit time-marching, and potentially gives better overall efficiency. However, implicit methods must be implemented with caution. The stability characteristics of some approximate factorizations depend strongly on the number of dimensions. An example is the celebrated ADI scheme [13] which has a rather restrictive CFL limit in three dimensions, due to the approximate-factorization error of the order Δt^3. The LU algorithms used by the RPLUS codes are two-factored, regardless of the number of dimensions. The convergence characteristics are therefore similar in one, two, or three dimensions.

The LU algorithm originally adopted by the RPLUS code is the so-called LU-SSOR (Symmetric Successive Over-Relaxation) or LU-SGS (Symmetric Gauss-Siedel) proposed by Yoon and Jameson [14-15]. This scheme was implemented by Shuen and Yoon [16] in the RPLUS2D code, and later extended to RPLUS3D by Yu, Tsai, and Shuen [17]. The implicit operator of the LU-SSOR is constructed by upwind differencing the specially formulated split flux Jacobians. For non-reacting flows, the resulting implicit operator avoids the need for matrix inversion, and is particularly suitable for solving large systems of equations. Even for reacting flows where source terms are treated implicitly, the requirement for matrix inversion is kept at a minimum. Recently, Tsai and Hsieh [18] modified the split flux Jacobians based on a similarity transformation to construct the so-called LU-SW (Steger-Warming). Along with the LU-SW, the right-hand-side calculation was modified from the original central-differencing to the upwind-differencing with Van Leer's flux-vector splitting. The LU-SW does require block-matrix inversion; however, the LU-SW/UP (UPwind-differencing) combination provides much stronger temporal damping. Tsai and Hsieh showed the LU-SW/UP can be more efficient in terms of CPU time than the original LU-SSOR/CD (Central-Differencing) in two dimensions. Since both LU algorithms remain two-factored in any number of dimensions, similar improvement can be expected in three dimensions.

This paper gives an updated summary of the RPLUS development. Besides the algorithm, improvements are made on the capability and flexibility in real application. Most notable improvements are the use of a blocking algorithm and the use of out-of-core storage. The blocking algorithm tremendously broadens the geometry to which the RPLUS codes can be applied. Difficulty in grid generation is also alleviated by the blocking capability. For large scale problems where the required memory storage exceeds the resources available, out-of-core storage is a necessary compromise. This has recently been made available for the RPLUS codes. These new features are addressed in detail.

II. Governing Equations

The governing equations solved by the RPLUS codes are the compressible, Reynolds-averaged Navier-Stokes equations and species transport equations. For completeness, the three-dimensional equations are formulated. Written in a strong conservative form, the governing equations can be expressed as follows:

$$\begin{aligned} \frac{\partial Q}{\partial t} + \frac{\partial}{\partial x}(E - E_v) + \frac{\partial}{\partial y}(F - F_v) & \\ + \frac{\partial}{\partial z}(G - G_v) &= H \end{aligned} \tag{1}$$

Here x, y, and z are Cartesian coordinates, Q is the dependent variable, E, F, and G are the convective flux vectors:

$$\begin{gathered} Q = \begin{pmatrix} \rho \\ \rho u \\ \rho v \\ \rho w \\ \rho e \\ \rho Y_i \end{pmatrix}, \qquad E = \begin{pmatrix} \rho u \\ \rho u^2 + p \\ \rho u v \\ \rho u w \\ u(\rho e + p) \\ \rho u Y_i \end{pmatrix} \\ \\ F = \begin{pmatrix} \rho v \\ \rho u v \\ \rho v^2 + p \\ \rho v w \\ v(\rho e + p) \\ \rho v Y_i \end{pmatrix}, \qquad G = \begin{pmatrix} \rho w \\ \rho u w \\ \rho v w \\ \rho w^2 + p \\ w(\rho e + p) \\ \rho w Y_i \end{pmatrix} \end{gathered} \tag{2}$$

E_v, F_v, and G_v are the viscous flux vectors:

$$\begin{gathered} E_v = \begin{pmatrix} 0 \\ \tau_{xx} \\ \tau_{xy} \\ \tau_{xz} \\ u\tau_{xx} + v\tau_{xy} + w\tau_{xz} - q_x \\ -\rho \hat{u}_i Y_i \end{pmatrix} \\ \\ F_v = \begin{pmatrix} 0 \\ \tau_{yx} \\ \tau_{yy} \\ \tau_{yz} \\ u\tau_{yx} + v\tau_{yy} v + w\tau_{yz} - q_y \\ -\rho \hat{v}_i Y_i \end{pmatrix} \\ \\ G_v = \begin{pmatrix} 0 \\ \tau_{zx} \\ \tau_{zy} \\ \tau_{zz} \\ u\tau_{zx} + v\tau_{zy} v + w\tau_{zz} - q_z \\ -\rho \hat{w}_i Y_i \end{pmatrix} \end{gathered} \tag{3}$$

and H is the source vector:

$$H = \begin{pmatrix} 0 \\ 0 \\ 0 \\ 0 \\ 0 \\ \dot{\omega}_i \end{pmatrix} \tag{4}$$

The specific total energy, e, shear stress components, and heat flux components are given as

$$e = \sum_{i=1}^{N_s} e_i + \frac{1}{2}(u^2 + v^2 + w^2) \tag{5}$$

$$\tau_{xx} = 2\mu\frac{\partial u}{\partial x} - \frac{2}{3}\mu\left(\frac{\partial u}{\partial x} + \frac{\partial v}{\partial y} + \frac{\partial w}{\partial z}\right) \tag{6.a}$$

$$\tau_{yy} = 2\mu\frac{\partial v}{\partial y} - \frac{2}{3}\mu\left(\frac{\partial u}{\partial x} + \frac{\partial v}{\partial y} + \frac{\partial w}{\partial z}\right) \tag{6.b}$$

$$\tau_{zz} = 2\mu\frac{\partial w}{\partial z} - \frac{2}{3}\mu\left(\frac{\partial u}{\partial x} + \frac{\partial v}{\partial y} + \frac{\partial w}{\partial z}\right) \tag{6.c}$$

$$\tau_{xy} = \tau_{yx} = \mu\left(\frac{\partial u}{\partial y} + \frac{\partial v}{\partial x}\right) \tag{7.a}$$

$$\tau_{yz} = \tau_{zy} = \mu\left(\frac{\partial v}{\partial y} + \frac{\partial w}{\partial y}\right) \tag{7.b}$$

$$\tau_{xz} = \tau_{zx} = \mu\left(\frac{\partial u}{\partial z} + \frac{\partial w}{\partial x}\right) \tag{7.c}$$

$$q_x = -k\frac{\partial T}{\partial x} + \rho\sum_{i=1}^{N_s} h_i Y_i \hat{u}_i \tag{8.a}$$

$$q_y = -k\frac{\partial T}{\partial y} + \rho\sum_{i=1}^{N_s} h_i Y_i \hat{v}_i \tag{8.b}$$

$$q_z = -k\frac{\partial T}{\partial z} + \rho\sum_{i=1}^{N_s} h_i Y_i \hat{w}_i \tag{8.c}$$

In the preceding expressions, ρ is the density, u, v, and w are the Cartesian velocity components, p is the pressure, and e is the specific total energy. The subscript i identifies each species, and N_s is the total number of species. For ith species, Y_i, e_i, h_i, and $\dot{\omega}_i$ are its mass fraction, specific internal energy, enthalpy, and production rate, respectively. The enthalpy of species i is obtained by an integration of C_p versus temperature:

$$h_i = \int_0^T C_{pi} dT \tag{9}$$

where C_{pi} is the constant pressure specific heat which is expressed as a fourth order polynomial of temperature:

$$C_{pi} = C_{pi0} + C_{pi1}T + C_{pi2}T^2 + C_{pi3}T^3 + C_{pi4}T^4 \tag{10}$$

The internal energy of species i can be obtained from h_i using the ideal gas assumption which is valid for high temperature:

$$e_i = h_i - R_i T \tag{11}$$

where R_i is the gas constant for species i. The diffusion velocity components, $\hat{u}_i$, $\hat{v}_i$, and $\hat{w}_i$ are calculated by Fick's law [23]:

$$Y_i \hat{u}_i = -D_{im}\frac{\partial Y_i}{\partial x} \tag{12.a}$$

$$Y_i \hat{v}_i = -D_{im} \frac{\partial Y_i}{\partial y} \tag{12.b}$$

and

$$Y_i \hat{w}_i = -D_{im} \frac{\partial Y_i}{\partial z} \tag{12.c}$$

where

$$D_{im} = (1 - X_i) / \sum_{i \neq j} \frac{X_i}{D_{ij}} \tag{13}$$

is the effective binary diffusivity of species i in the gas mixture, and X_i is the mole fraction of species i. Diffusive properties such as viscosity and thermal conductivity are considered as polynomials of temperature, and the diffusive properties of the mixture are calculated based on Wilke's mixing rule [24,25]. The binary mass diffusivities are calculated using Chapman-Enskog theory in conjunction with Lennard-Jones intermolecular potential functions. [25]

The numerical solution of Eq. (1) is performed in a general, body-fitted coordinate system, (ξ, η, ζ). Coordinate transformation of Eq. (1) gives

$$\begin{aligned} \frac{\partial \hat{Q}}{\partial \tau} + \frac{\partial}{\partial \xi}\left(\hat{E} - \hat{E}_v\right) + \frac{\partial}{\partial \eta}\left(\hat{F} - \hat{F}_v\right) & \\ + \frac{\partial}{\partial \zeta}\left(\hat{G} - \hat{G}_v\right) = \hat{H} & \end{aligned} \tag{14}$$

where

$$\hat{Q} = hQ \tag{15.a}$$
$$\hat{E} = h(\xi_x E + \xi_y F + \xi_z G) \tag{15.b}$$
$$\hat{F} = h(\eta_x E + \eta_y F + \eta_z G) \tag{15.c}$$
$$\hat{G} = h(\zeta_x E + \zeta_y F + \zeta_z G) \tag{15.d}$$
$$\hat{E}_v = h(\xi_x E_v + \xi_y F_v + \xi_z G_v) \tag{15.e}$$
$$\hat{F}_v = h(\eta_x E_v + \eta_y F_v + \eta_z G_v) \tag{15.f}$$
$$\hat{G}_v = h(\zeta_x E_v + \zeta_y F_v + \zeta_z G_v) \tag{15.g}$$
$$\hat{H} = hH \tag{15.h}$$

in which h is the cell volume.

III. Recent Advances

The RPLUS2D code was completed in 1987 and extended to RPLUS3D in 1988. During this period of time, the codes remained research-oriented and modification was constantly made for different problems. They were hardly user-friendly due to the lack of user interfaces. From 1989 to present, a series of improvements have been made to render the RPLUS codes user-oriented. Parallel to these efforts, new algorithms for improving efficiency and solution quality were also explored. The details are addressed below.

Program Vectorization

Before a code can be vectorized, the programmer first identifies the operations for which parallel processing is possible. Once this is done, vectorization usually can be achieved with proficiency in programming. In cases when parallel processing is not possible, special hardware is required to accomplish vectorization. The implicit operator of the LU scheme has a recursive property. In the

LU scheme, the ΔQ of the point (i, j, k) requires updated ΔQ at points $(i-1, j, k)$, $(i, j-1, k)$, and $(i, j, k-1)$ in the Lower sweep, and updated values at $(i+1, j, k)$, $(i, j+1, k)$, and $(i, j, k+1)$ in the Upper sweep. At first glance, parallel processing seems to be out of the question. However, the solutions of the points in a plane normal to the sweeping direction are independent and can be parallel-processed. In other words, the points on the planes represented by the equation, $i+j+k =$ constant can be parallel-processed. The schematic of these planes is shown in Fig. 1.

The vectorization of the program is done by reorganizing the indices of the grid points for parallel-processing planes. Before the main iteration begins, mappings between the three-dimensional index, (i, j, k), and two sets of two-dimensional indices, $(ipoint, iplane)$, are generated for the Lower and Upper sweeps. The index *ipoint* identifies the points in a parallel-processing plane, and *iplane* identifies the planes. These mappings are stored as sets of integer arrays which can be invoked by the Lower and Upper sweeps. On CRAY computers, the mapping arrays can be used directly in DO-loops to achieve efficient vectorization. The strategy described does have short-comings. The rather short vector-length near the upper and lower corners makes vectorization somewhat incomplete. Nevertheless, these inefficient vector-processing regions do not constitute a significant efficiency-reduction on the CRAY for two reasons. Firstly, the vector length grows rapidly away from the corners. (The vector length is approximately proportional to square of the distance between the plane and the corner.) Secondly, CRAY's maximum computation speed can almost be reached with a rather short vector-length (e. g., 100). In fact, the CPU time for the implicit operator is reduced by a factor of nearly 10 simply by the described strategy.

The vectorization of the right-hand-side is relatively straightforward. In principle, three-dimensional vectorization is possible for the RHS. However, our experience on CRAY shows very little difference among one-, two-, and three-dimensional vectorization due to its architecture. The program is therefore vectorized in one dimension for better readability of the codes.

Blocking Logic

In order to enhance the capability of the RPLUS codes in handling complex geometries and flows, a blocking algorithm is implemented. The need for blocking is obvious when structured grids are used. Many geometries encountered in practical application, e. g. the nose-to-tail of the NASP, cannot be represented with a single-block grid. In association with the blocking algorithm, a set of flexible boundary conditions is installed, allowing specifying well-posed boundary conditions at grid-cell level. The boundary conditions currently installed include supersonic inflows and outflows, subsonic inflow, no-slip and tangency, freestreams, and interior boundaries (interfaces of blocks).

Blocking the grid does impose difficulty in using the LU algorithm. With the requirement for vectorization, the coding logic can be exceedingly complex. Currently the RPLUS codes use a simplified method in which the LU sweeps are performed independently for each block rather than performed for the whole grid. Figure 2 shows the schematic of this method for a two-dimensional, blocked grid. Notice that at the block interfaces, the boundary conditions for the LU sweeps are the same as any other boundaries. The instability this simplified method may incur is no more than what other boundaries can produce. Actual calculations also confirm that there is no apparent stability problem or deterioration of convergence speed on the interfaces.

The block-RPLUS codes have found many applications since their completion. One example is the study of combustion and mixing phenomenon of the dump combustor in a scramjet engine [19]. The geometry and flow configuration are shown in Fig. 3.a and 3.b. for H_2/air dump combustors with parallel and transverse injectors. The rearward facing step is a common gimmick for enhancing mixing. Grid generation for such geometry can be a major task if only one block is allowed to be used. With two blocks, on the other hand, the grid generation becomes exceedingly simple.

The hydrogen mass fraction and temperature distribution for both cases are shown in Fig. 4 and Fig. 5, respectively. The grid sizes are 41,000 points for the transverse-injection case and 23,700 points for the parallel-injection case. The chemistry model used is a 9-species, 18-step H_2/air reaction model by Brabbs [20]. Each case takes approximately 20 to 30 hours of CPU time on a CRAY-2. Figures 4.a and 4.b show the hydrogen mass fraction for transverse- and parallel-injection cases. Comparing the downstream hydrogen mass fraction shows that the transverse-injection case provides a more complete combustion. This is due to a longer flow residence time and a better mixing mechanism of the transverse jet. The bending of the transverse jet results in a secondary flow which provides an excellent mixing mechanism. The secondary flow can be visualized in Fig. 4.a in which the transverse jet develops into a so-called kidney shape. The advantage of using the parallel jet is the smaller pressure loss as opposed to the transverse jet. The corresponding temperature distributions are shown in Figs. 5.a and 5.b. In both cases the recirculation zones generated by the steps have low subsonic speed and high temperature. The temperature distributions show that the mixing pattern in the parallel injection is somewhat different from that in the transverse injection. In the parallel injection case, the jets tend to recirculate sideways into the corner, while the transverse injection tends to mix the jets with the upstream air.

Out-of-Core Storage

While there is a growing demand for large-scale, three-dimensional computations, sufficient resources for core memory may not always be available. An alternative for such a dilemma is the use of secondary storage. Recently the possibility of utilizing secondary storage for the RPLUS3D code has been assessed. An experimental RPLUS version that requires a much smaller core memory has been developed. This version has been tested for a typically large grid of 360,000 (100 × 60 × 60) points. It requires only 5.7 Megawords for solving a nine-species chemical system, as opposed to 50 Megawords for the original version. For the secondary storage, the SSD (Solid-state Storage Device) currently available to CRAY-XMP and YMP appears to be the best candidate. Although using magnetic disks is also possible, the waiting time for the mechanical movement may result in a long lapse time for a small amount of CPU time.

The idea of out-of-core storage is stocking the major portion of data while operating on a minor portion of the data. For a three-dimensional problem at least two strategies can be considered. The first strategy is dividing the three-dimensional domain into much smaller subdomains. The data for each subdomain are stored in the secondary storage ordered on direct-access records. Operations are then done for one subdomain at a time, and updated data are written to the proper records when the operations are finished. The second strategy is storing the data based on two-dimensional planes. At any given time, data for a number of planes may be required to appear on the stage. The updated data are stored back to the designated records after required operations are done. The I/O efficiency of a strategy depends not only on the frequency of accessing but also on the manner that the data are stored. For direct-access storage, longer records give more efficient access. If both strategies give identical results, the first strategy seems to be more attractive since it gives the freedom of controlling the record-length. For implicit schemes, however, the first strategy requires using explicit boundary conditions on the interfaces of the subdomains. The RPLUS3D therefore chooses the second strategy.

The programming logic currently used by the RPLUS3D for storing the two-dimensional planes is by no means the most efficient one. Due to vectorization considerations, the planes whose data are stored in records are of constant-I, -J, -K for RHS calculation and of constant-I+J+K for LHS. In each iteration, the data files have to be reorganized four times to ensure efficient retrieve. This demands a tremendous amount of I/O. A more efficient way is to vectorize the RHS calculation for constant-I+J+K planes, the same as for the LHS calculation. This can avoid the need to reorganize the data files. The experimental version of RPLUS3D is currently modified to adopt this strategy.

LU-SW and Upwind-differencing

The RPLUS codes are originally designed to use LU-SSOR/CD. The efficiency and solution quality of this algorithm have recently been re-assessed, and other possible algorithms have been explored [6,18]. Among them, the LU-SW/UP has been identified as a promising algorithm. This algorithm has been added to the RPLUS2D.

The finite-difference equations for the LU-SSOR and LU-SW have the same generic form. In two dimensions, both can be expressed by

$$\begin{aligned}&\left[\mathbf{I}+\Delta t\left(D_\xi^-\hat{\mathbf{A}}^+ + D_\eta^-\hat{\mathbf{B}}^+ - \frac{\hat{\mathbf{A}}^-}{\Delta\xi} - \frac{\hat{\mathbf{B}}^-}{\Delta\eta} - \hat{\mathbf{D}}\right)\right] \\ &\left(\mathbf{I}+\frac{\Delta t}{\Delta\xi}(\hat{\mathbf{A}}^+ - \hat{\mathbf{A}}^-)+\frac{\Delta t}{\Delta\eta}(\hat{\mathbf{B}}^+ - \hat{\mathbf{B}}^-)\right)^{-1} \\ &\left[\mathbf{I}+\Delta t\left(D_\xi^+\hat{\mathbf{A}}^- + D_\eta^+\hat{\mathbf{B}}^- + \frac{\hat{\mathbf{A}}^+}{\Delta\xi} + \frac{\hat{\mathbf{B}}^+}{\Delta\eta}\right)\right]\Delta\hat{\mathbf{Q}} \\ &= \Delta t RHS\end{aligned} \tag{16}$$

The two LU algorithms have different ways in constructing the split flux-Jacobians. For LU-SSOR, the split flux Jacobians are defined as

$$\hat{\mathbf{A}}^+ = 0.5(\hat{\mathbf{A}} + \gamma_{\hat{\mathbf{A}}}\mathbf{I}) \tag{17.a}$$

$$\hat{\mathbf{A}}^- = 0.5(\hat{\mathbf{A}} - \gamma_{\hat{\mathbf{A}}}\mathbf{I}) \tag{17.b}$$

$$\hat{\mathbf{B}}^+ = 0.5(\hat{\mathbf{B}} + \gamma_{\hat{\mathbf{B}}}\mathbf{I}) \tag{17.c}$$

$$\hat{\mathbf{B}}^- = 0.5(\hat{\mathbf{B}} - \gamma_{\hat{\mathbf{B}}}\mathbf{I}) \tag{17.d}$$

where $\gamma_{\hat{\mathbf{A}}}$ and $\gamma_{\hat{\mathbf{B}}}$ are greater than the spectral radii of the associated flux Jacobians :

$$\gamma_{\hat{\mathbf{A}}} \geq \max(|\lambda_{\hat{\mathbf{A}}}|) \tag{18.a}$$

$$\gamma_{\hat{\mathbf{B}}} \geq \max(|\lambda_{\hat{\mathbf{B}}}|) \tag{18.b}$$

For the LU-SW, the split flux Jacobians are defined as

$$\hat{\mathbf{A}}^+ = \hat{\mathbf{M}}_\xi \Lambda_\xi^+ \hat{\mathbf{M}}_\xi^{-1} \tag{19.a}$$

$$\hat{\mathbf{A}}^- = \hat{\mathbf{M}}_\xi \Lambda_\xi^- \hat{\mathbf{M}}_\xi^{-1} \tag{19.b}$$

$$\hat{\mathbf{B}}^+ = \hat{\mathbf{M}}_\eta \Lambda_\eta^+ \hat{\mathbf{M}}_\eta^{-1} \tag{19.c}$$

$$\hat{\mathbf{B}}^- = \hat{\mathbf{M}}_\eta \Lambda_\eta^- \hat{\mathbf{M}}_\eta^{-1} \tag{19.d}$$

in which Λ_ξ^+, etc., are the diagonal eigenvalue matrices, and $\hat{\mathbf{M}}_\xi$, etc., are the right eigenmatrices.

In the LU-SSOR, the flux Jacobians are split in such a fashion that the block-matrix inversion is avoided. The eigenvalues of the resulting split flux-Jacobians are inconsistent with the characteristic speeds of the flow. Because of this inconsistency, relatively slow convergence is usually observed using this scheme. The LU-SW, on the other hand, requires block-matrix inversion and each iteration is more expensive. However, because the LU-SW scheme uses split Jacobians whose eigenvalues are consistent with the characteristic speeds of the flow, it is apt to give a convergence rate faster than the LU-SSOR in terms of number of iterations.

The efficiency of the LU-SSOR and LU-SW schemes are strongly affected by the method of the right-hand-side discretization, which can be central or upwind. The flux-vector splitting by Van Leer [21] is selected for upwind-differencing. Higher order accuracy is achieved by the MUSCL procedure [22]. The two LU schemes and two methods for right-hand-side discretization result in four combinations, namely, LU-SSOR/CD, LU-SSOR/UP, LU-SW/CD, and LU-SW/UP. Among these combinations, the LU-SW/CD can be shown to be unstable by a stability analysis [18]. The efficiency of the other three combinations is tested by three cases : (1) 15° ramp, (2) 20° ramp with expansion, and (3) jet in crossflow.

Figures 6.a, 7.a, and 8.a show the geometry and flow conditions for the three test cases. In cases 1 and 2, a premixed H_2/air flow passes through a ramp. Chemical reaction is activated by the high temperature induced by oblique shocks, boundary layers, and their interaction. Case 3 simulates the combustion process in a hydrogen combustor. In all three cases, the optimum CFL number is infinity for the LU-SSOR and approximately 1.5 for the LU-SW. The flows are assumed to be laminar. Figures 6.b, 7.b, and 8.b. show the corresponding convergence histories. The CPU seconds required by each scheme for reducing the residual by one order are tabulated in Table. 1. It clearly shows that the LU-SW/UP scheme is the most efficient among the three.

	Case 1	Case 2	Case 3
LU-SSOR/CD	675	-	1500
LU-SSOR/UP	477	1908	-
LU-SW/UP	225	1620	900

Table 1. CPU Seconds for Reducing Residual by One Order.

Other Improvements

The most updated versions of the RPLUS codes are designed to cope with a variety of flows. They are able to compute perfect-gas or real-gas, single-species or multiple-species, inviscid or viscous, non-reacting or reacting flows. All these options can be used conveniently without modifying the codes. For chemistry models, a 9-species, 18-step H_2/air combustion model is stored internally as one of the default options. Suitable chemistry models will be installed in the future. Any other chemistry models can be defined through an input file. In addition to the H_2/air combustion model, real-gas properties such as the specific heats, viscosity and thermal conductivity of a number of species are also stored internally for convenient usage. All these features make the RPLUS codes extremely flexible and useful.

IV. Conclusion

Continuous effort at NASA Lewis has improved the RPLUS codes significantly. The updated RPLUS codes have included a number of new features for practical application. To handle complex geometry and simplify grid generation, a blocking logic is incorporated. Out-of-core storage shows potential in calculating large size problems with limited core-memory. The LU-SW/UP algorithm improves the overall efficiency as well as solution quality. These improvements not only make the RPLUS codes more ready for use, but also impose an impact on their future development. Future work includes advance turbulence modelling such as the $k - \epsilon$ modelling and PDF (Probability Density Function) modelling. For geometry flexibility, an algorithm for multiple, mismatched grid with global conservation law will be explored.

Acknowledgement

This work was supported by NASA Lewis Research Center under contract NAS3-25266. The computer time is provided by the Numerical Aerodynamic Simulation Program (NAS). The support is gratefully acknowledged.

References

1. Rubert, K. F., "Aero-Space Plane," Joint Meeting of the Bumblebee Aerodynamic Composite Design and Propulsion Panels, Silver Spring, Maryland, November 15-16, 1961.

2. Drummond, J. P., Rogers, R. C., and Hussaini, M. Y., "A Detailed Numerical Model of

a Supersonic Reacting Mixing Layer," AIAA paper 86-1427, AIAA/ASME/SAE/ASEE 22nd Joint Propulsion Conference, 1986.

3. Uenishi, K., Rogers, R.C., and Northam, G.B., "Three Dimensional Computations of Transverse Hydrogen Jet Combustion in a Supersonic Airstream," AIAA Paper 87-0089, AIAA 25th Aerospace Sciences Meeting, Jan. 12-15, 1987, Reno, Nevada.

4. Bussing, T.R.A, and Murman, E.M., "A Finite Volume for the Calculation of Compressible Chemically Reacting Flows," AIAA Paper 85-0331, AIAA 23th Aerospace Sciences Meeting, Jan. 14-17, 1985, Reno, Nevada.

5. Carpenter, M. H., "Three-Dimensional Computations of Cross-Flow Injection and Combustion in a Supersonic Flow," AIAA Paper 89-1870, AIAA 20th Fluid Dynamics, Plasma Dynamics and Lasers Conference, Buffalo, NY, June 12-14, 1989.

6. Shuen, J.-S., Liou, M.-S., "Flux Splitting Algorithms for Two-Dimensional Viscous Flows with Finite-Rate Chemistry," AIAA Paper 89-0388, AIAA 27th Aerospace Sciences Meeting, Jan. 9-12, 1989, Reno, Nevada.

7. Candler, G. V., and MacCormack, R. W., "The Computation of Hypersonic Ionized Flows in Chemical and Thermal Non-Equilibrium," AIAA Paper 88-0511, AIAA 26th Aerospace Sciences Meeting, Jan. 11-14, 1988, Reno, Nevada.

8. Molvik, G. A., and Merkle, C. L., "A Set of Strongly Coupled, Upwind Algorithms for Computing Flows in Chemical Non-Equilibrium," AIAA Paper 89-0199, AIAA 27th Aerospace Sciences Meeting, Jan. 9-12, 1989, Reno, Nevada.

9. Molvik, G. A., "Computation of Viscous Blast Wave Solutions with an Upwind, Finite-Volume Method," AIAA Paper 87-1290, June 1987.

10. Walters, R. W., Cinnella, P., Slack, D. C., and Halt, D., "Characteristic-Based Algorithms for Flows in Thermo-Chemical Non-Equilibrium," AIAA Paper 90-0393, AIAA 28th Aerospace Sciences Meeting, Jan. 8-11, 1990, Reno, Nevada.

11. Lee, S.-H., and Deiwert, G. S., "Calculation of Non-equilibrium Hydrogen-Air Reactions with Implicit Flux Vector Splitting Method," AIAA Paper 89-1700, AIAA 24th Thermophysics Conference, June 12-14, 1989, Buffalo, NY.

12. Ying, S. X., "Three-Dimensional Implicit Approximately Factored Schemes for the Equations of Gasdynamics," Ph. D. Thesis, Stanford University, Jun. 1986.

13. Pulliam, T. H., and Steger, J. L., "Implicit Finite-Difference Simulations of Three Dimensional Compressible Flow," *AIAA Journal*, Vol. 18, 1980, pp. 159.

14. Yoon, S., and Jameson, A., "An LU-SSOR Scheme for the Euler and Navier-Stokes Equations," AIAA Paper 87-0600, Jan., 1987.

15. Jameson, A., and Yoon, S., "Lower-Upper Implicit Schemes with Multiple Grids for the Euler Equations," *AIAA Journal*, Vol. 25, No. 7, July 1987, pp. 929-935.

16. Shuen, J. S. and Yoon, S., "Numerical Study of Chemically Reacting Flows Using an LU Scheme," AIAA paper 88-0436, Jan., 1988.

17. Yu, S-T, Tsai, Y-L P., and Shuen, J-S, "Three-Dimensional Calculation of Supersonic Reacting Flows Using an LU Scheme," AIAA paper 89-0391, 27th Aerospace Sciences Meeting, Jan. 9-12, 1989, Reno, Nevada.

18. Tsai, Y.-L. P., and Hsieh, K.-C., "Comparative Study of Computational Efficiency of Two LU Schemes for Non-Equilibrium Reacting Flows," AIAA paper 90-0396, 28th Aerospace Sciences Meeting, Jan. 8-11, 1990, Reno, Nevada.

19. Tsai, Y-L P., Yu, S-T, "Further Development of the RPLUS3D Code," Paper 8, 7th National Aero-Space Plane Symposium, Cleveland, Ohio, Oct. 23-27, 1989.

20. Brabbs, T. A., personal communication.

21. Van Leer, B., "Flux-Vector Splitting for the Euler Equations," Lecture Notes in Physics, Vol. 170, 1982, pp. 507-512.

22. Van Leer, B., "Towards the Ultimate Conservative Difference Scheme V. A Second-Order Sequel to Gudonov's Method," *J. Comput. Phys.*, vol. 32, 1979, pp. 101-136.

23. Kuo, K. K., (1986). *Principles of Combustion*, p. 165. John Wiley & Sons, Inc., New York.

24. Wilke, C. R., "A Viscosity Equation for Gas Mixture," *J. Chem. Phys.*, Vol. 18, No. 4, Apr. 1950, p. 517.

25. Reid, R. C., Prausnitz, J. M., and Sherwood, T. K., (1977), *The Properties of Gases and Liquids*, 3rd Ed., McGraw-Hill, New York.

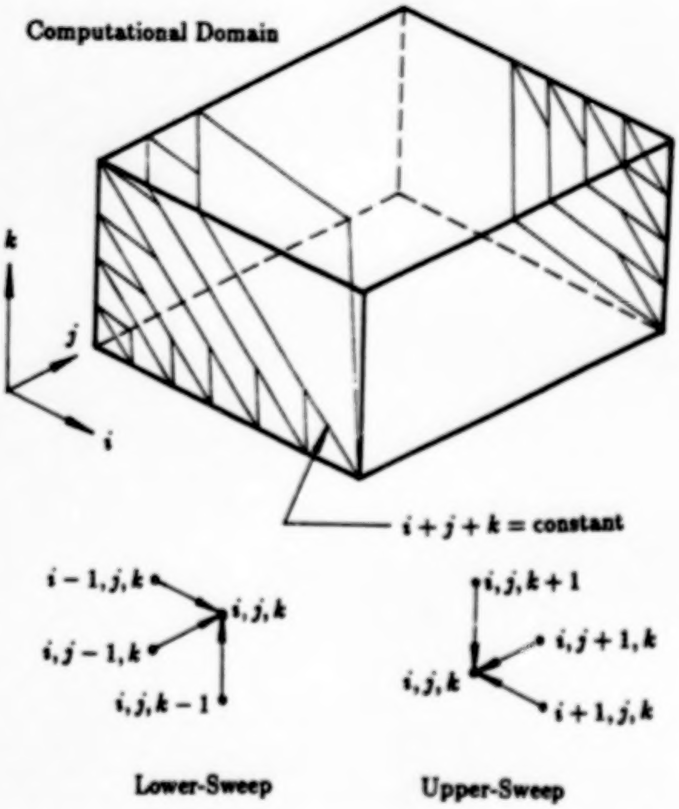

Fig. 1 Schematic of Program Vectorization.

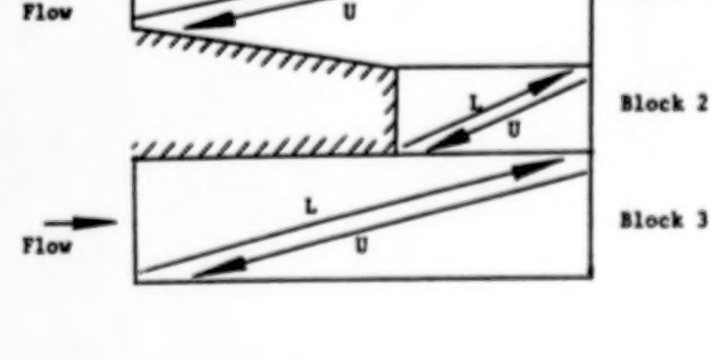

Fig. 2 Schematic of LU Sweeps in a Multi-Block Grid.

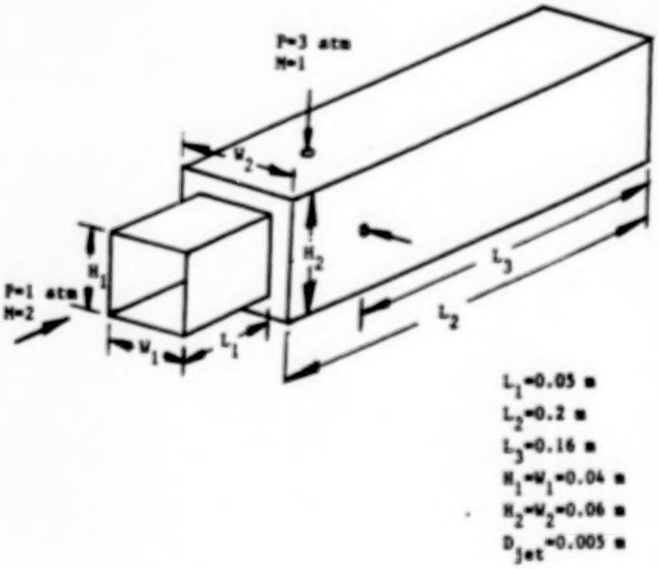

Fig. 3.a Geometry and Flow Conditions for Dump Combustor with Transverse Injection.

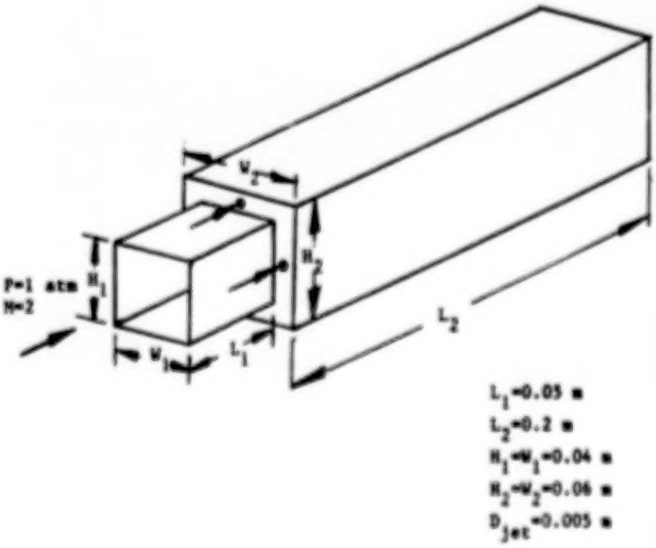

Fig. 3.b Geometry and Flow Conditions for Dump Combustor with Parallel Injection.

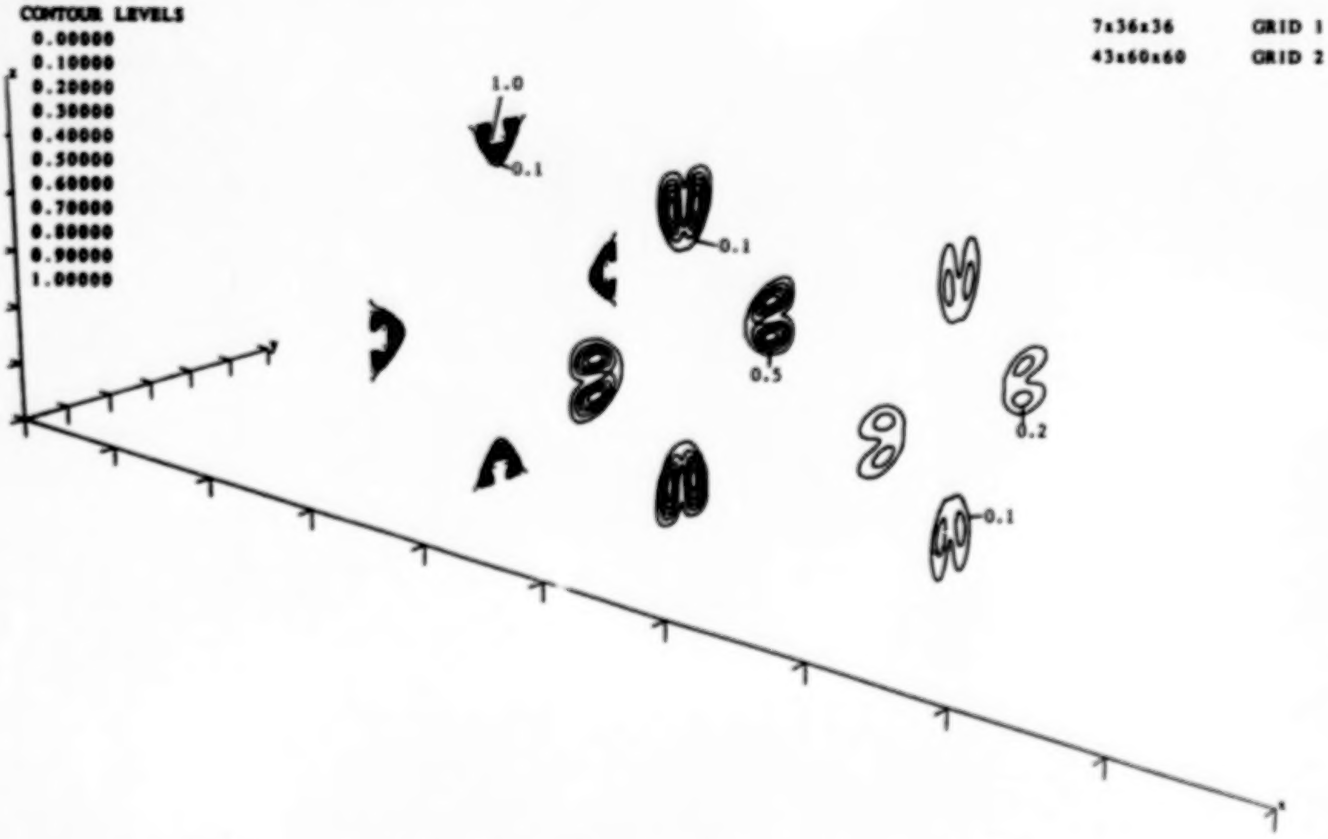

Fig. 4.a Hydrogen Mass Fraction for Dump Combustor with Transverse Injection.

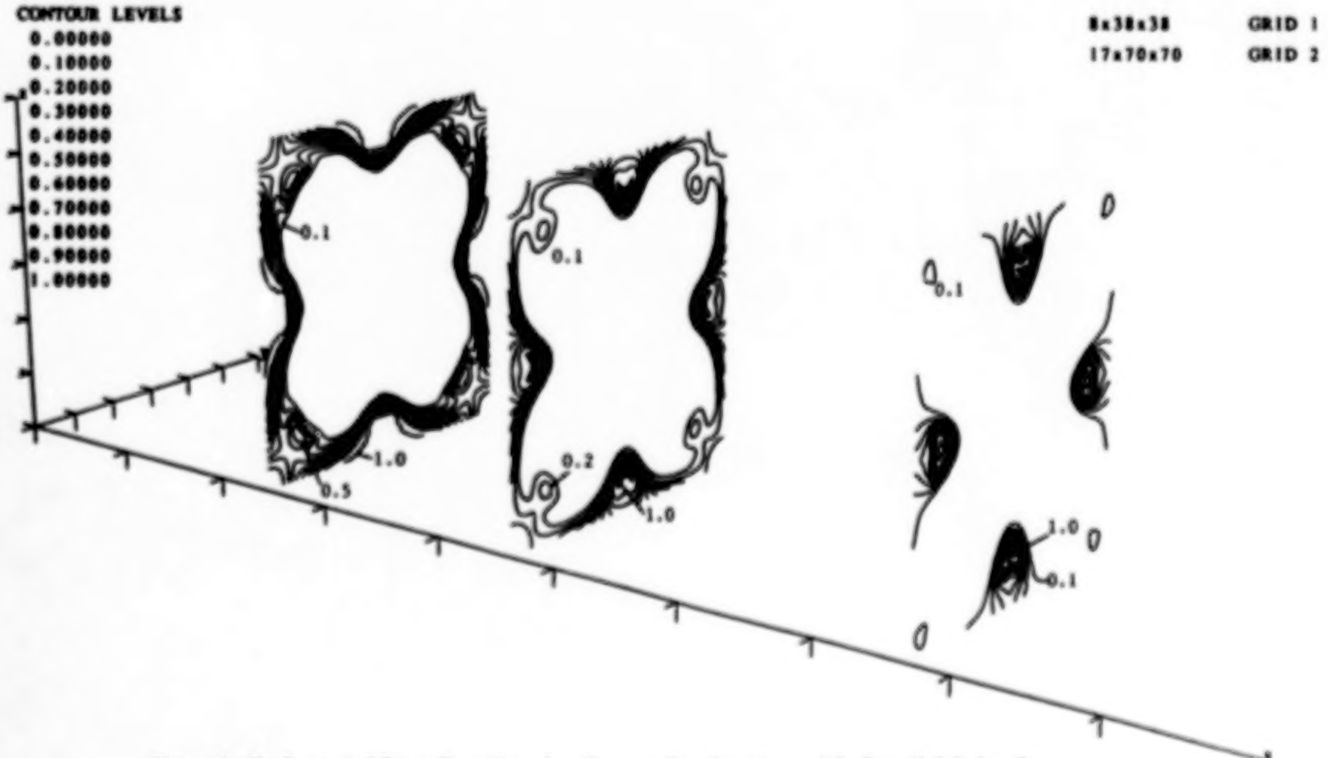

Fig. 4.b Hydrogen Mass Fraction for Dump Combustor with Parallel Injection.

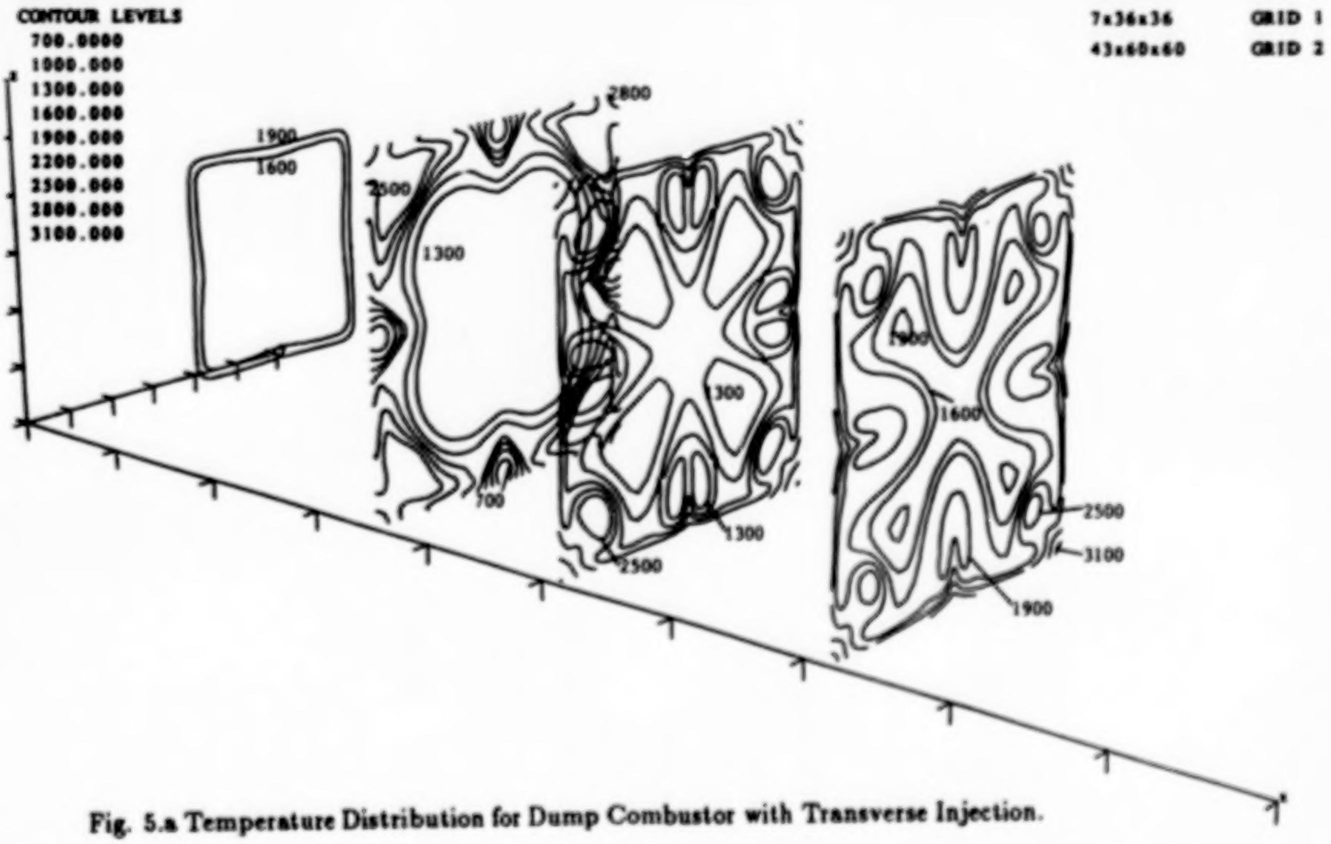

Fig. 5.a Temperature Distribution for Dump Combustor with Transverse Injection.

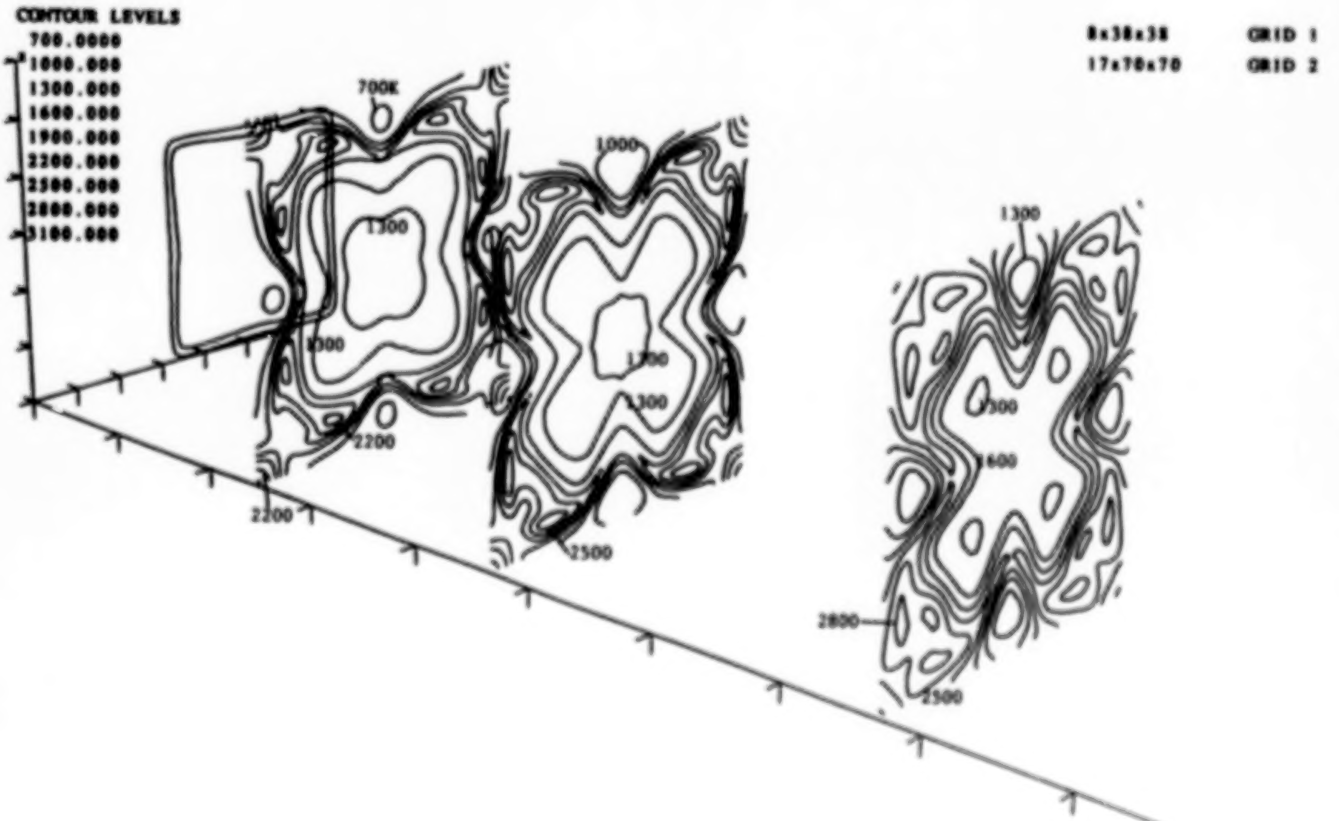

Fig. 5.b Temperature Distribution for Dump Combustor with Parallel Injection.

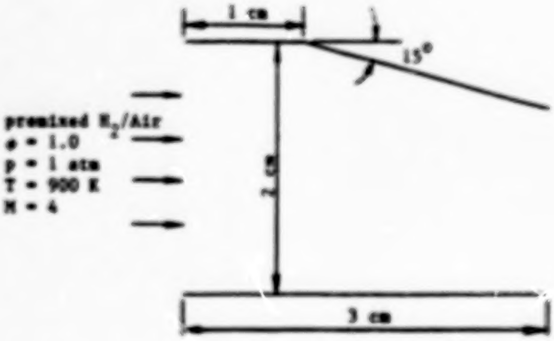

Fig. 6.a Geometry and Flow Conditions of 15° Ramp.

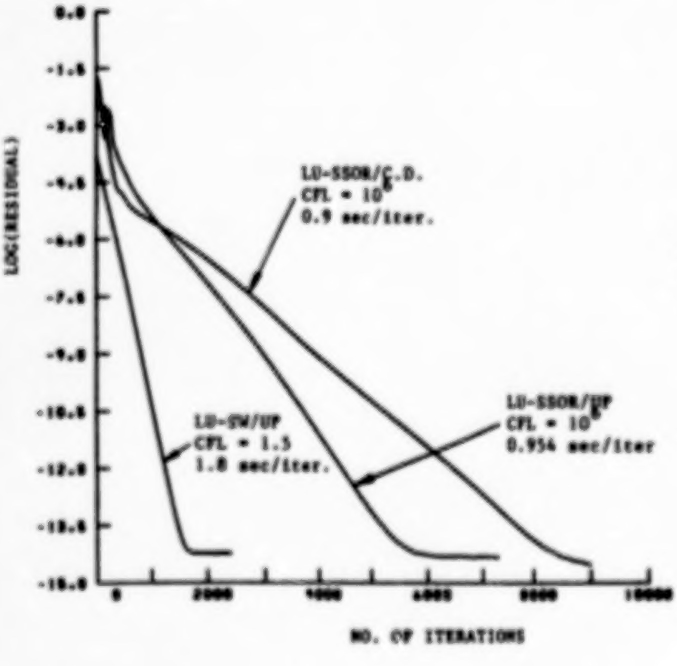

Fig. 6.b Convergence Rate for 15° Ramp.

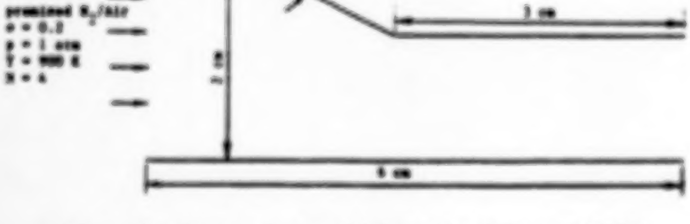

Fig. 7.a Geometry and Flow Conditions of 20° Ramp with expansion.

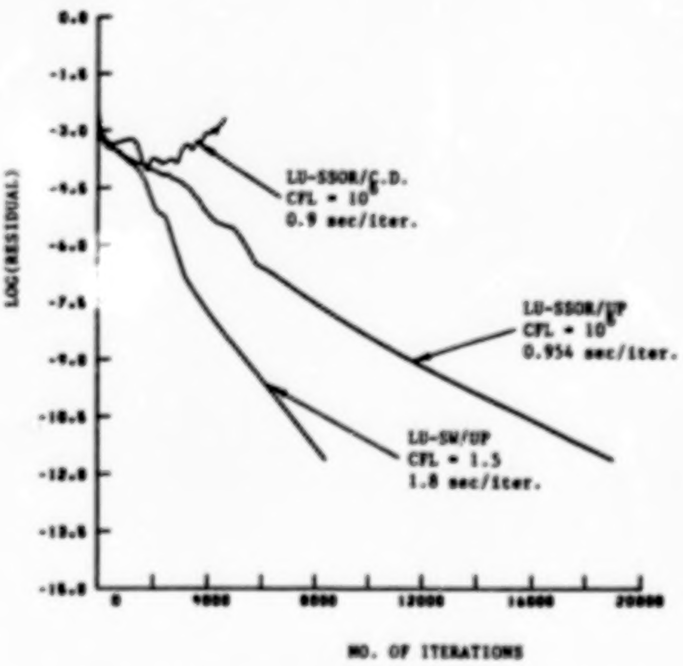

Fig. 7.b Convergence Rate for 20° Ramp with expansion.

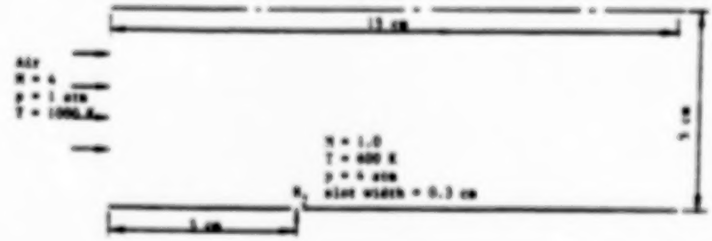

Fig. 8.a Geometry and Flow Conditions of Jet in Crossflow.

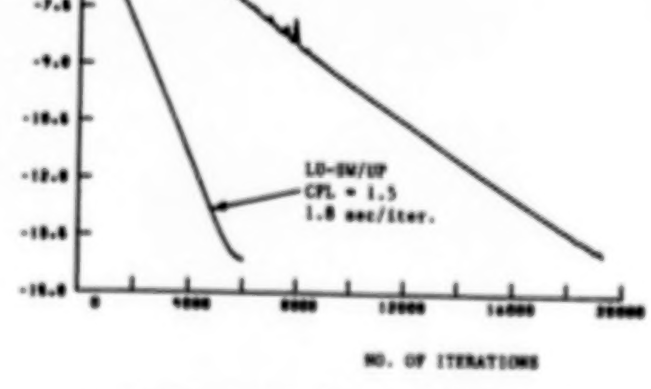

Fig. 8.b Convergence Rate for Jet in Crossflow.

THE DIRECT SIMULATION OF HIGH-SPEED MIXING-LAYERS WITHOUT AND WITH CHEMICAL HEAT RELEASE

B. Sekar[*], H.S. Mukunda[†], M.H. Carpenter[‡]

ABSTRACT

This computational study is a direct numerical simulation of high speed reacting and non-reacting flows for H_2-air systems. The calculations are made for a convective Mach number of 0.38 with hyperbolic tangent initial profile and finite rate chemical reactions. A higher-order numerical method is used in time accurate mode to time advance the solution to a statistical steady state. About 600 time slices of all the variables are then stored for statistical analysis.

It is shown that most of the problems of high-speed combustion with air are characterized by relatively weak heat release. The present study shows that (i) the convective speed is reduced by heat release by about 10 % at this convective Mach number $M_c = 0.38$, (ii) the variation of the mean and rms fluctuation of temperature can be explained on the basis of temperature fluctuation between the flame temperature and the ambient, (iii) the growth rate with heat release is reduced by 7 %, (iv) and the entrainment is reduced by 25 % with heat release. These differences are small in comparison with incompressible flow dynamics, and are argued to be due to the reduced importance of heat release in comparison with the large enthalpy gradients resulting from the large-scale vortex dynamics. It is finally suggested that the problems of reduced mixing in high-speed flows are not severely complicated by heat release.

NOMENCLATURE

M	Mach number	M_c	Convective Mach number
p	Pressure	Re	Reynolds number
T	Temperature	T'	Root mean square fluctuation of T
t	Time	$tanh$	Tanhyperbolic
u	Streamwise velocity	u'	Root mean square fluctuation of u
u_∞	Primary stream velocity	$u_{-\infty}$	Secondary stream velocity
u_c	Convective velocity	v	Transverse velocity
x	Streamwise coordinate	x_m	Maximum extent of x field
y	Transverse coordinate	y_m	Maximum extent of y field
δ	Mixing-layer thickness	ρ	Density
Ω	Vorticity	μ	Laminar viscosity

INTRODUCTION

Non-reacting and reacting incompressible mixing-layers have been extensively explored both experimentally (ref. 1-3) and computationally (ref. 4,5). Laboratory experiments have shown that the growth of the mixing-layer is dominated by large-scale quasi-two-dimensional vortices and their pairing in the early stages. A non-reacting spatial simulation of the incompressible mixing-layer carried out by McInville et al. (ref. 4), found that the growth of the layer with axial distance shows an occasional decrease to an extent of 10 %. This has been argued to be due to the phase relationships between the initial disturbance and the evolution of the roll up of the vortical structure downstream. Under suitable phase conditions the energy of the fluctuating part is drawn away into the mean flow thus decreasing the growth of the layer.

---

[*] Research Scientist, Vigyan Research Associates, Hampton, VA. Research funded under contract NAS1-18585 from NASA Langley.

[†] Professor, Indian Institute of Science, Bangalor, India. Work performed while in residence at NASA Langley as NRC fellow.

[‡] Aerospace Engineer, Theoretical Flow Physics Branch, Fluid Mechanics Division, NASA Langley Research Center, Hampton, VA.

For reacting mixing-layers, the results of Hermanson and Dimotakis (ref. 2), also quoted in McMurtry et al. (ref. 5) for their experiments classified as "weak heat release" cases with the peak to initial temperature ratio being 2.3 and 4 respectively, show that heat release results in a slightly reduced growth of the shear-layer (of the order of 10 - 15 %). This result has been related to the reduction in turbulent shear stresses in the layer. Though the spacing of the cores of vortical structures has been shown not to be affected by heat release (p.11, ref.5), this result seems to have been accepted with reservation. McMurtry et al. (ref. 5) have conducted accurate temporal simulations of low Mach number flows without and with heat release. These have confirmed the experimental findings regarding the slower growth of the layer with heat release. Analysis seems to indicate the important role of thermal expansion and baroclinic torque in reducing the peak vorticity generation within the layer, thereby reducing the molecular diffusion.

All the results noted above are for near incompressible flows. Supersonic mixing-layers have been explored experimentally by Papamoschou and Roshko (ref. 6) who showed that the growth rate decreases with an increase in the convective Mach number (M_c); M_c is the ratio of the difference in the velocities of the two streams to the sum of the acoustic speeds in the upper and lower streams. The reduction in the growth rate is shown to be related to the reduced amplification of the disturbances in supersonic flows (ref. 7). Lele (ref. 8) made direct simulation calculations of supersonic flows using higher-order finite difference methods and validated the concept of M_c. Mukunda et al. (ref. 9) made similar calculations for non-reacting flows first establishing the results of Papamoschou and Roshko (ref. 6) and then exploring the influence of initial profile (hyperbolic tangent and wake like profiles), the disturbance level and nature on the development of the mixing-layer. All these studies were restricted to non-reacting flows. The present work aims at elucidating the effects of chemical heat release in high-speed flows.

MOTIVATION

The origin of the present problem lies in the recent interest in the development of the propulsion system for the national aerospace plane. The typical flight Mach numbers can be as high as 21 and in the combustor up to 7. The combustor inlet temperatures are 1500-2500 K and pressures are 0.05 to 0.15 MPa. At these conditions the reaction rates are very high and the steady combustion will be limited by mixing. The findings of reduced mixing in shear flows (i) due to high M_c (ref. 6) and (ii) due to heat release in incompressible flows (ref. 2,3) have caused concern in the development of combustors for high-speed flows and need for a basic examination of reacting high-speed flows. The present contribution considers a typical case (ref. 10) of a high-speed mixing-layer.

The fuel-oxidiser combination used is N_2 diluted H_2-air. In the present study, the case with 10 % (mass) H_2 in N_2 is treated in continuation with the earlier studies by Drummond and Mukunda (ref. 10). The relevance of a study with a low fraction of hydrogen can be justified by analysing the importance of the extent of heat release. In incompressible flows, one would obtain substantial variation in adiabatic flame temperature, T_{ad} (a good estimate of possible peak temperatures in the flame) by adjusting the hydrogen mass fraction Y_{H_2} in the N_2 stream. The ratio s ($= T_{ad} / T_{in}$, where T_{in} is the initial temperature) for $T_{in} = 300$ K would be about 8 for pure H_2 and about 7 for $Y_{H_2} = 0.1$. For high-speed applications, the magnitude of this trend is greatly reduced. Computation of T_{ad} shows that with $T_{in} = 2000$ K, $s = 1.6$ for pure H_2 and 1.57 for $Y_{H_2} = 0.1$. Two important facts from these values are that (i) the T_{ad} is virtually the same for pure and diluted H_2, and (ii) the temperature ratio is not large. In fact, it is lower than the values used for the case of weak heat release in the experiments (see ref. 5). The reason "s" does not differ greatly between $Y_{H_2} = 1.0$ and 0.1 is that most of the energy input goes into the dissociation of the species including N_2 and the formation of energy absorbing NO. Though the present work treats N_2 as an inert, the use of a reversible reaction limits the peak temperature to $s = 1.575$, a value close to that from full chemistry.

THE COMPUTATIONAL ASPECTS

The geometry considered here is shown in figure (1). The computational box ABCD has an x and y dimension of x_m and y_m, respectively. The inflow boundary profile (A-D) is divided into two domains at the point $y = y_m/2$. The top section is the fuel region and the bottom, air. The inflow velocity is the hyperbolic tangent profile conventionally used in mixing-layer studies given by $u_m = \frac{1}{2}[(u_\infty + u_{-\infty}) + (u_\infty - u_{-\infty}) tanh\ ky]$ with the constant k taken here as 1800 m^{-1}. This results in an effective boundary-layer thickness of two millimeters, based on a 99 % freestream criterion.

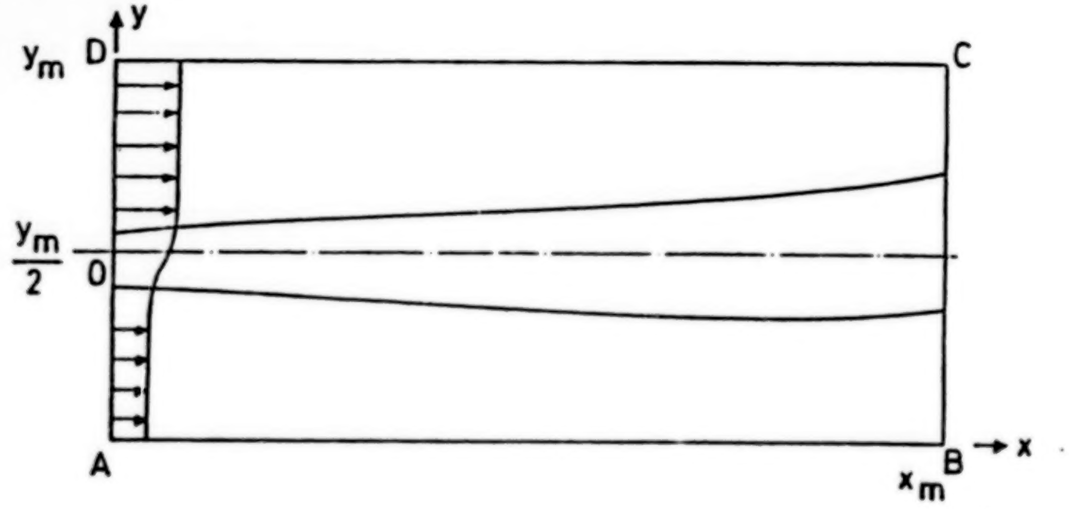

Figure 1: Schematic of mixing-layer.

Table 1 shows the parameters relevant to the cases considered. The velocity of the air stream is lower than that of the fuel in the case $M_c = 0.38$. The momentum ratios indicate that the momenta are balanced for $M_c = 0.38$. This causes the shear-layer to remain roughly in alignment with the central axis. The momentum defect thickness (θ) is 1.54 mm. This implies that for the x grid length of 100 mm, the axial span is about 64 θ. The Re_δ based on the average properties is 3500. If the reference speed is the difference in speeds between the streams, then Re is 250. These values are considered low enough to obtain realistic results using direct simulations with the current day computational resources for non-reacting flows. It is for this range of values that Lele (ref. 8) has made direct simulation computations. Chemical reactions will certainly introduce scales which are smaller than those present in non-reacting flows. It is hoped that the essential features of the reaction will still be resolved.

Disturbances are provided on the axial and lateral velocities (u_d and v_d)at x = 0 to excite the layer. The disturbance is composed of a linear combination of several harmonic components of frequency determined from a spectral analysis of the flow field (at a downstream region) computed without any initial disturbances. The initial rms "u" fluctuation is about 3.68 %. The boundary conditions on (A-D) would be u= u_m +u_d, v=v_d, p=0.101325 MPa, T= 2000 K and

$$Y_{H_2} = 0.1,\ Y_{O_2} = \ Y_{H_2O} = 0.0,\ Y_{N_2} = 0.9, (y_m > y > y_m/2) \qquad (1)$$
$$Y_{O_2} = 0.232, Y_{H_2} = \ Y_{H_2O} = 0.0,\ Y_{N_2} = 0.768, (y_m/2 > y > 0)$$

At x = x_m, third order extrapolation of the primitive variables is used. At y = 0 and y_m, characteristic boundary conditions are used to obtain the extrapolated primative variables.

After a detailed study (ref. 9), the region of calculation was chosen as 100 mm × 50 mm. In order to capture most scales of importance, the grid distribution is chosen by considerations outlined in reference 9 and partly based on the discussion of Reynolds (ref. 11). The number of gridpoints used in the y direction is 125 or 151 for a region of 50 mm and are concentrated near the center of the layer. The x direction (100 mm) is embedded with 201 or 251 equi-spaced gridpoints resulting in a axial spacing of 0.5 - 0.4 mm. Calculations have been made to ensure grid independence of several details of the flow (ref. 9).

The code used in the present calculations is the SPARK2D combustion code developed at NASA Langley over

Table 1: INFLOW PARAMETERS

composition	quantity	case 1
Fuel $0.1H_2 + 0.9N_2$	ρ, kg/m^3	0.075
	u, m/s	2670.0
	M	2.0
	γ	1.3133
	sound speed, m/s	1336.0
	δ, mm	1.0
	μ, kg/m.s	5.5 $\times 10^{-5}$
Oxidant $0.232O_2 + 0.768N_2$	ρ, kg/m^3	0.175
	u, m/s	1814.0 .0
	M	2.1
	γ	1.296
	sound speed, m/s	864.3
	δ, mm	1.0
	μ, kg/m.s	6.2 $\times 10^{-5}$
	u_c, m/s	2150.0
	M_c	0.385

T = 2000 K, p = 0.101325 MPa, θ = 1.54 mm

the past four years by Drummond and Carpenter(see refs 10, 12 and 13). In the latest version (ref. 12), it uses either a third-order upwind biased or a dissipative compact fourth-order central difference algorithm (DCPS) for the streamwise direction, and the DCPS (ref. 13) for the cross-stream direction. The temporal accuracy is second order. This choice represents a compromise between the accuracy of higher-order numerical algorithms and the robustness and efficiency of lower-order methods.

In addition to full finite rate chemical kinetics, two simplified reaction models were used in this study. The purpose was to evaluate the validity of the simplified reaction models at these flow conditions with respect to the more general full chemistry model. The first is $2H_2 + O_2 \rightleftharpoons 2H_2O$, and the reaction rate is given by

$$\dot{\omega}''' = A_f p^2 Y_{H_2}^2 Y_{O_2} e^{-E_f/RT} - A_b p Y_{H_2O}^2 e^{-E_b/RT} \tag{2}$$

Here the backward rate constant in the above equation is chosen to be consistent with the equilibrium constant. The parameters of the forward rate constant are taken as $A_f = 1.1 \times 10^{19}$, and an activation energy, $E_f = 16$ kcal / mole. These values were obtained by requiring that the flame speed of the single step kinetics match with those from full chemistry. The second reaction model chosen is a seven species, seven reaction path model involving $H_2, O_2, H_2O, OH, H, O,$ and passive N_2. This model is the reaction system given by Drummond (ref. 10) abridged to the major species at these temperatures. The species and their reactions usually included to predict ignition onset (HO_2 and H_2O_2) are neglected for computational efficiency. A binary diffusion model was used for all calculations with a single representative Schmidt number of 0.22, the value generally used for the diffusion of H_2. This has been taken so as to obtain a reference case for comparison with subsequent calculations on the effect of multi-component diffusion of various species.

In order to ensure that the flow attains a statistical steady state before sampling is performed, the computations were performed for each case for a duration of about three sweeps of the flow. Each sweep takes a time given by x_m/u_c. This is about 50 μs for the $M_c = 0.38$ case. The time step is typically 0.005 μs and, therefore, takes 20000 - 30000 time steps before statistical steady state is achieved. After this, a total of about 600 time samples of all the flow field variables at specific x and y stations are stored at equal time intervals. These are subsequently analyzed by a separate statistical package. The results from this package include the mean and correlation quantities. The shear-layer thickness was obtained for "u", ρ, Y_{H_2}, Ω, and Y_{H_2O}. Of these, Y_{H_2O} and Ω tend to zero at y → $\pm\infty$;

the others tend to nonsero finite values. In view of these features, the thicknesses are defined by

$$\delta_{\psi} = \frac{(\psi_{\infty} - \psi_{-\infty})}{(\partial \psi_{mean} / \partial y)_{max}} \tag{3}$$

where ψ stands for any of the first three quantities. For Y_{H_2O} and Ω, $\delta_{\psi} = \int_{-\infty}^{\infty} \psi dy \,/\, \psi_{max}$.

The speed of vortical structures expected to be at the convective speed (u_c) is obtained by making instantaneous p vs x plots at some value of y near the center of the mixing-layer. These plots are made at a few times sufficiently spaced apart. The rate of movement of the point of peak pressure along x gives the convective speed. The convective speed is also calculated by using the formula (ref. 6),

$$u_c = \frac{\sqrt{\rho_{-\infty}} u_{-\infty} + \sqrt{\rho_{\infty}} u_{\infty}}{(\sqrt{\rho_{\infty}} + \sqrt{\rho_{-\infty}})} \tag{4}$$

CODE VALIDATION

The first step in validating the code was to determine if the numerical methods used in the SPARK2D code are capable of resolving the linear growth of the two-dimensional mixing-layer. It is essential that for grids comparable to those used in this study, all the aspects of the linear regime of the mixing-layer be well resolved, before addressing the far more difficult non-linear problem of vortex role-up and chemical reaction. Linear stability theory predicts that the temporally developing compressible 2-D mixing-layer (air into air, in this case), is unstable to a velocity profile which is initially specified as a hyperbolic tangent axial velocity distribution. In the initial stages of the instability (the linear regime), the growth of the unstable modes is exponential. For these calculations, accurate eigenmodes were provided from a spectral linear stability code developed by Macaraeg (ref. 14). From these eigenmodes, nondimensional growth rates and characteristic frequencies were calculated. This non-dimensional growth rate provided a reliable measure of the accuracy of the finite-difference algorithm being tested.

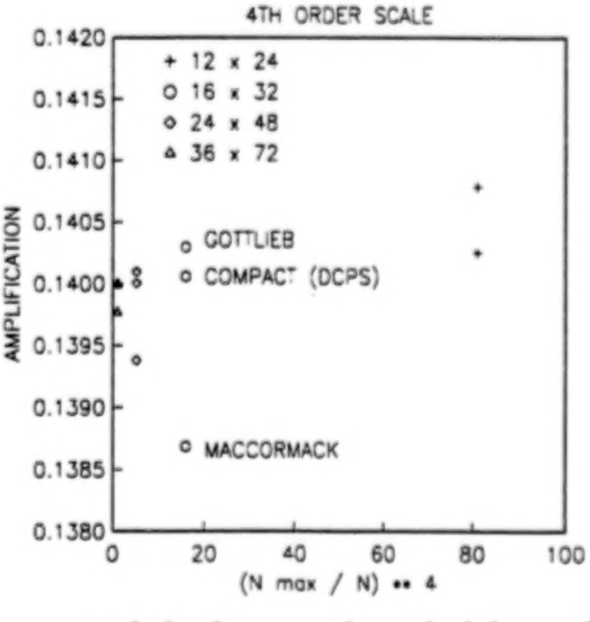

Figure 2: Grid convergence study for the temporal growth of the two-dimensional mixing-layer.

The temporal growth of the two-dimensional mixing-layer is simulated by assuming the flow to be periodic in the stream-wise direction. The period corresponds to a wavelength of x = 0.6283mm (the mode which grows most rapidly, as determined from the linear analysis). The initial velocity distribution is specified as $U(x, y, 0) = u_{\infty} \tanh(\frac{y}{\delta})$, v(x,y,0) = 0.0, T(x,y,0) = $293^o k$, p(x,y,0) = 0.101325 MPa. Source terms were added to the Navier-Stokes equations so that the momentum and energy equations would preserve free-stream. The resulting Reynolds number of the flow is 187, based on the layer thickness, where $U_\infty = 100$ m/s. The Mach number is 0.30. The width of the half-layer D is specified to be $2.5x10^{-2}$mm and the half-width of the domain is 100 times the layer thickness. The grid in the stream-wise direction is uniform, while the grid in the cross-stream direction is highly stretched. The transformation of the grid ensures that about one half of all the y grid-points are located within the initial mixing-layer width.

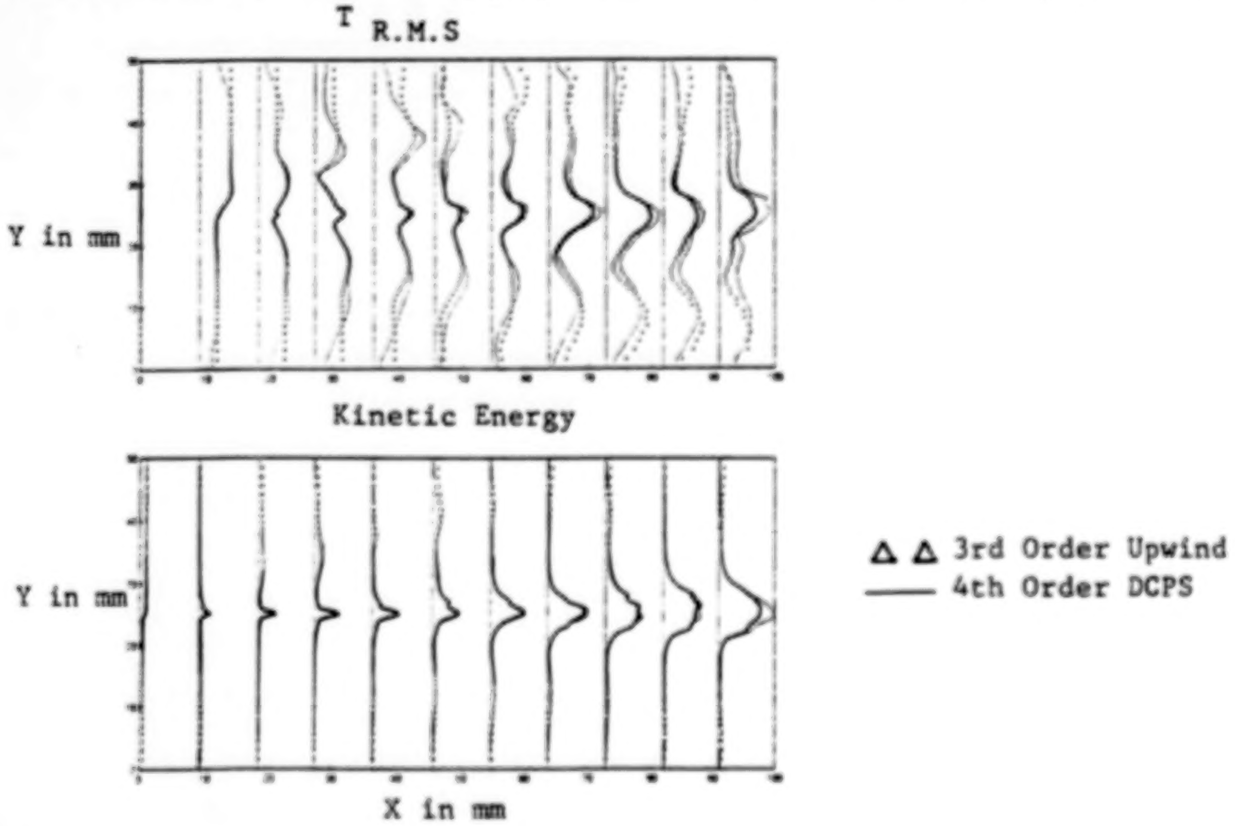

Figure 3: Comparison of a) r.m.s temperature profiles and b) Kinetic energy fluctuating statistics calculated with third and fourth-order numerical methods.

For these studies the unstable modes in the layer were allowed to grow from the numerical instabilities produced by machine roundoff errors. Exponential growth of these modes was seen in all cases after an initial transient period. The "linear" regime was characterised by the growth period during which the product of perturbation quantities was still negligible. For these tests this period was arbitrarily chosen between the physical times of $2.5x10^{-5}$ and $2.75x10^{-5}$ seconds, and corresponded to disturbance amplitudes three to five orders larger than machine roundoff errors. A grid convergence history of the numerical method was used to determine its formal accuracy, and to ascertain the grids necessary to resolve this fundamental phenomena.

The most unstable mode in this problem grows at an exponential growth rate with an exponent determined from linear stability theory to be 0.14000 in non-dimensional units. This rate was used as the "exact" growth rate for these conditions. A series of four grids was then defined, each having a grid density which was a constant multiple of the previous grid. Three algorithms: 1) MacCormack at a CFL of 1.0, 2) Gottlieb-Turkel (ref. 15) at a CFL of 0.5, and 3) DCPS at a CFL of 0.5, were then run on identical grids and the non-dimensional amplification rate was determined from an integration of the energy spectrum. (The integral of the fundamental mode over the entire domain was monitored in time. The change with respect to time yields the amplification rate).

In figure (2) the amplification rates of the three methods are plotted against $(\frac{N_{max}}{N})^4$ (where N_{max} and N are the maximum number of gridpoints used in the study and the number used on a particular coarser grid, respectively) to show quartic accuracy. Here, the fourth-order spatial accuracy of the spatial derivatives from each method is indicated by the linear convergence of the solution to the predetermined amplification rate. The Gottlieb-Turkel scheme and the DCPS both converge with fourth-order accuracy. (This indicates that the coefficients multiplying the temporal terms of $O(\Delta t^2)$ and $O(\Delta t \Delta x^2)$ in the methods, are small compared with the spatial truncation terms). A direct comparison of the accuracy of the two fourth-order methods can be drawn, since the only variable in this study was the method used. The DCPS appears to be about twice as accurate as the the Gottlieb-Turkel scheme for this problem. From these results it is apparent that, even for coarse grids (10 grid-points per wavelength), the fundamental features of the linear growth of the mixing-layer are resolved. There should be no question that the grids used in these studies are sufficient to resolve the linear regime of the two-dimensional mixing-layer.

Showing appropriate grid resolution for the non-linear case is far more difficult. In addition to grid convergence studies for a representative flow, a direct comparison of two numerical methods was used to measure the grid independence of the solutions. The similarity of solutions obtained on the same grid from numerical methods having different truncation errors, provides a measure of the solution convergence on that grid (for the methods being used). In this vein, a third-order upwind-biased method was compared with the fourth-order DCPS central difference scheme on a 201 x 151 grid. Both were run to the same physical time and statistics of the flow were gathered for each case. The mean profiles calculated with each method do not show any appreciable differences. However, small changes in the fluctuating quantities are present. Figure (3a) shows the r.m.s temperature profiles for the flow as calculated with each method. Figure (3b) shows a comparison of the kinetic energy statistics gathered from each simulation. While the qualitative features of the statistics are reproduced with each method, they are not quantitatively the same. (The dissipative nature of the third-order method is apparent in these comparisons). They are however, accurate enough to draw qualitative conclusions about the effects of heat release on the growth of the two-dimensional mixing-layer, and other global features.

The final calibration of the code involves the overall validity of the chemistry models used in these studies. The full finite rate chemical kinetics model used previously by Drummond (ref. 10) was used as the standard for all comparisons. This model incorporates nine chemical species and eighteen reaction paths, with N_2 passive. The one-step chemistry model is nearly five times more efficient than the full chemistry model used for complete hydrogen-air combustion, and the abridged model is about twice as fast. The chemically reacting mixing-layer at a $M_c = 0.38$ between air and hydrogen seeded (10% mass) nitrogen was used to compare the models. The calculations were run to identical times on the same grid with the DCPS numerical method. Figures (4a-4e) show the spread of the layer based on the mean profiles as a function of spatial distance for five different quantities as calculated with each chemistry model: they are the 1) u velocity, 2) vorticity, 3) density, 4) H_2 mass fraction, and the 5) H_2O mass fraction. The global features of the velocity, vorticity and H_2O are both qualitatively and quantitatively similar. That the H_2O profiles compare so favorably is somewhat deceiving in these calculations. In comparing the ρ and H_2 mass fraction profiles, it is apparent that the one-step model is missing some of the more subtle features of the chemistry, and that the abridged reaction system is nearly identical to that of the full chemistry. Figure (4f) shows a comparison of the r.m.s. temperature profiles as calculated with each of the reaction models. Here it is apparent that the one-step model vastly overpredicts the temperature peaks in the system. The reasons for this are most likely a chemistry timescale which is too short and the inability of the one-step model to properly account for the endothermic molecular dissociation occurring in the reaction. Again, the abridged model is nearly identical with that of the full chemistry. It must be concluded from this study that the one-step model is only appropriate in representing global hydrodynamic features of the flow. The heat release and water production predicted by the model will only be qualitative. For calculations where the more subtle chemistry features of the flow are desired, then at least the abridged model must be used. In further calculations the one-step model was used when only heat release was important. For more detailed comparisons between non-reacting and reacting flows, the 7-7 model was used.

RESULTS AND DISCUSSION

The results presented here are for $M_c = 0.38$. The non-reacting case will be referred to as "n" and the reacting case as "r". Figure (5) shows the vorticity contour plot for both the cases "n" and "r". A direct comparison of the two cases shows that the early role-up of the layer occurring from x = 30mm to x = 50mm, is suppressed by the reaction. Further downstream, the length scale of the reacting case appears to be larger but the number and magnitude of vortical structures appear to be fewer than in the non-reacting case. Figure (6) shows the plots of the mean velocity and temperature, and their rms fluctuations. The growth of the layer is shown by the dotted lines. One can notice the distinct change of growth rate with distance. Recognizing that the first part of the growth is laminar, and the subsequent part transitional, similarity plots on the basis of the laminar and transitional similarity coordinates have been established (ref. 9).

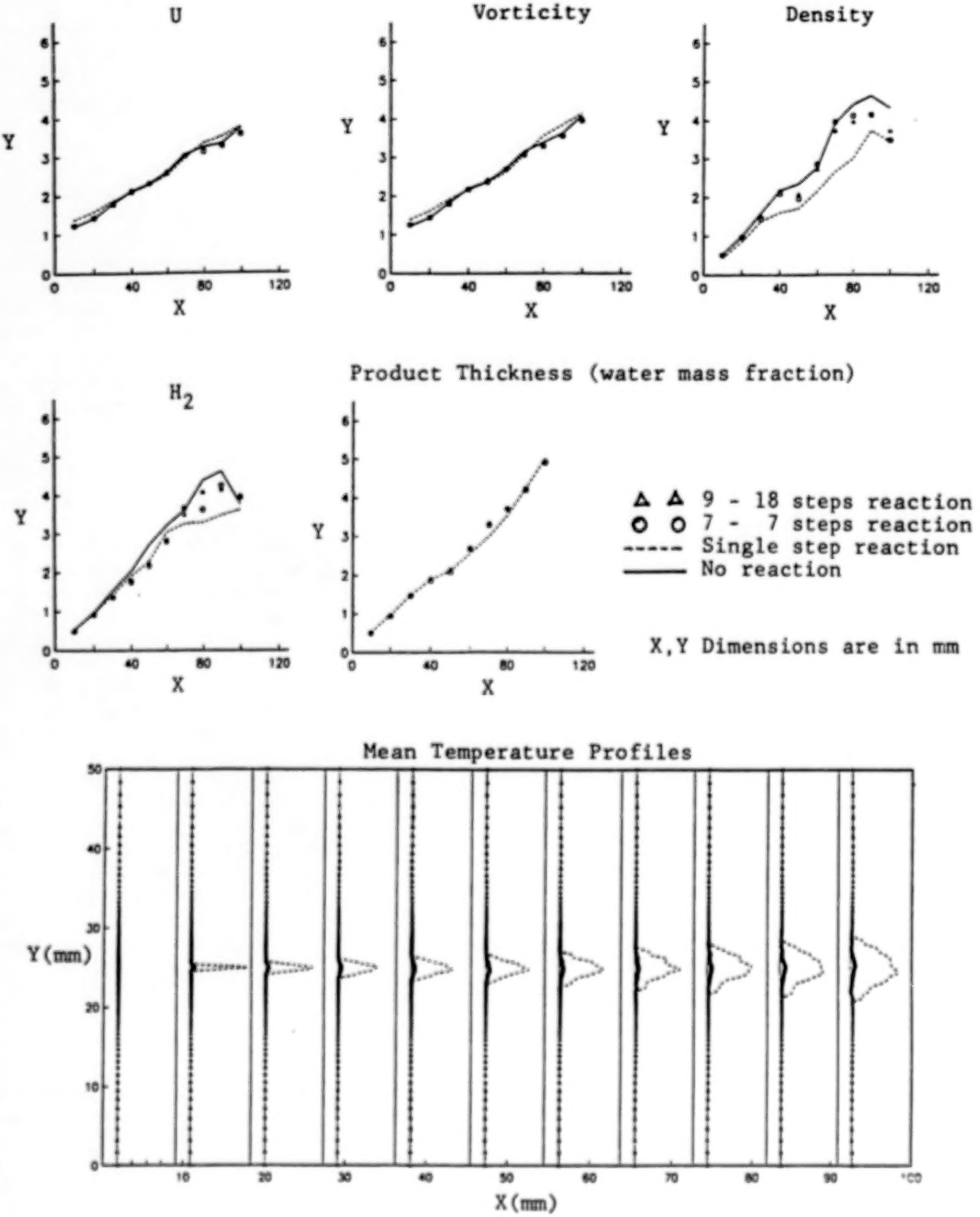

Figure 4: Comparison of the mean growth of (a) velocity, (b) vorticity, (c) density, (d) H_2, (e) H_2O and the (f) mean temperature profiles as calculated with the one-step, the abridged and full finite rate chemistry models.

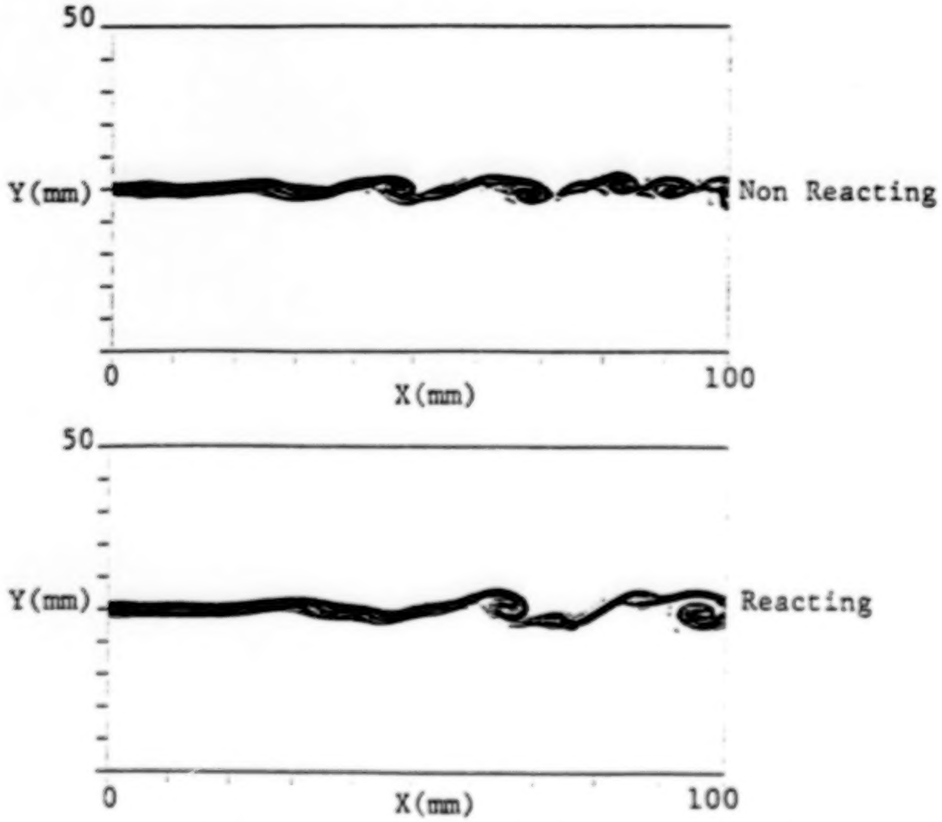

Figure 5: Comparison of vorticity contours for the a) "n" = no reaction, b) "r" = reaction.

The rms "u" fluctuations are shown in figure (6b) indicate that the maximum is about 6 %. There seems to be little difference in the location or magnitude of the fluctuations between the "n" and "r" cases. The development of the mean temperature profile shows that it peaks at about 2100 K and broadens with increasing x. The peak fluctuation goes to as high as 10 % of the mean for the case "r" and about 4 % for the case "n". The fluctuating values tend to grow with increasing distance in x, but are fairly uniform laterally across the layer. It is the large fluctuation with chemistry that produces a mean temperature which is low compared with the flame temperature. An examination of the temperature history at any x location shows that it is essentially at either the peak temperature of 2500 K (about half the theoretical increase predicted by an stiochiometric adiabatic flame temperature argument.) and the ambient of 2000 K with sharp transition. This picture is consistent with reaction being fast compared to flow times.

To help quantify this observation the concept of fractional residence time (α) is introduced. The mean temperature at any point is given in terms of the two temperatures, T_1 and T_0 by, $T_m = \alpha T_1 + (1-\alpha)T_0$. The root mean square fluctuation of temperature (T') is given by $T' = \sqrt{\alpha(T_1 - T_m)^2 + (1-\alpha)(T_m - T_0)^2} / T_m$. Examination of the data showed that the (α) at 2500 K remains at about 0.2 to 0.3 depending on the axial location. For the reacting case, $T_1 = 2500$ K, $T_0 = 2000$ K, $\alpha = 0.20$, one gets $T_m = 2100$ K and $T' = 0.10$. These are the peak values of T_m and T' seen in the figure (6d), particularly in the downstream region. This model is consistent with the observation that mixing is centered around interfacial sheets within the vortical structures of the layer, and occupy a small fraction of the total mean width of the layer. By the same kind of arguments, for the nonreacting case for which $T_1 = 1900$ K, $T_0 = 2000$ K, $\alpha = 0.6$, one obtains $T_m = 1940$ K and $T' = 0.027$. T_1 is taken as 1900 K because it is seen that in this case the local static temperature goes down to 1900 K due to gas dynamic expansion of the fluid locally. These results are also consistent with those seen in figure (6d) where the non-reacting flow shows the peak T' to be about 0.03.

A plot of the instantaneous p vs x at a specific y station for the $M_c = 0.38$ case is shown in figure (7a). Firstly, it can be noticed from this plot that the change in pressure is by no means insignificant. This results from both the initial perturbations and the large vortical forces in the layer. It changes from 0.07 to 0.14 MPa along x (as also along y through the shear layer). The plots of p vs x with reaction also show similar changes in pressure, without any other qualitative difference. The local Mach number plot with x shown in figure (7b) indicates that reaction reduces Mach number on an average. This is largely due to raise in acoustic speed due to increase in static temperature.

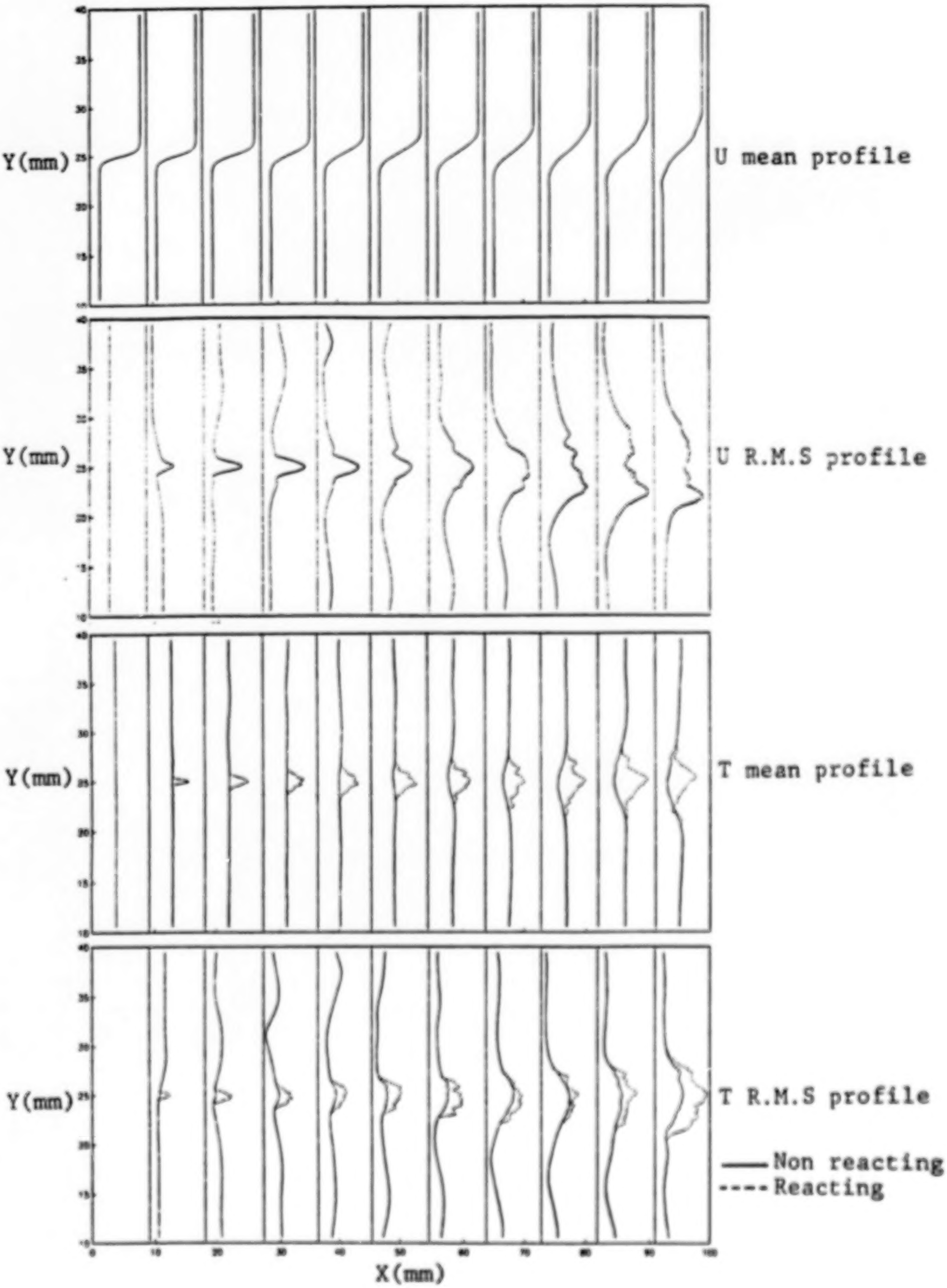

Figure 6: The plots of (a) u_m vs y , (b) rms u vs y, (c) T_m vs y, (d) rms T at various x stations.

The instantaneous pressure plots, at different times are used to obtain the convective speeds as discussed earlier. The results for the two cases at $M_c = 0.38$ are 1) "n", $u_c = 2260 \pm 50$ m/s and 2) "r", $u_c = 2083 \pm 50$ m/s. The theoretical speed calculated by equation (4) is 2150 m/s. The convective speed obtained here seems to be higher than that given by the formula by about 100 m/s at $M_c = 0.38$ The p-x curves have the same shape at different times, thus reflecting the truly constant speed of the structure. As reported by Mukunda et al. (ref. 9) and found in preliminary results here, for $M_c = 0.76$, the p-x curves change their shape even with in the characteristic sweep time. In addition, there is a variation in the speed of the structures computed at different times. It may well be that the concept of convective speed cannot be directly used to characterise the flow because the structures undergo dilatation to a large extent. Reaction seems to reduce the convective speed of the structures substantially - a 8.5 % (180 m/s) decrease at $M_c = 0.38$. This is expected to be a function of M_c. Again from preliminary calculations where the one-step chemistry model was used (with reservation) on $M_c = 0.76$, the heat release had a greatly reduced effect in lowering the convective speeds of the structures. This is not surprising since the increase in enthalpy is a much smaller percentage of the total enthalpy in the flow under the higher M_c conditions. At $M_c = 0.38$, the fractional increase in the instantaneous temperature is as much as 0.15 T_o and at $M_c = 0.76$, it is 0.25 T_o, whereas that due to combustion is 0.25 T_0. Thus as Mach number increases, changes due to gas dynamics become more relevant compared to those due to heat release.

Figure (7c) shows the variation of density (ρ) in the field. Firstly, it can be seen that the decrease in mean ρ is about 10 % due to heat release. This decrease in ρ is composed of that due to temperature, pressure and species mass fractions. In the experiments and analysis conducted elsewhere (ref. 2-5) on low Mach number flows with reaction, the free stream pressure of the two fluids is not significantly different while the local temperature rise is large compared with the ambient temperature. In these cases, the fractional change in ρ goes up to 0.4. In the present case, it is about 0.10 at the maximum.

Referring again to figures (4a-4e), plots of the thickness of the mixing-layer for the "n" and "r" cases are shown. In both cases, the growth of δ_u δ_ρ and δ_ω are around 4mm in 100mm. The mass fraction profiles grow from zero thickness and being passive scalars begin to acquire profiles similar to that of "u" at smaller x, and display an effective higher growth of 5mm in 100mm. The heat release seems to decrease the growth rate marginally. No appreciable difference between the "u" and vorticity growths are present. The Y_{H_2} growth shows a decrease of at least 10 %, but this is likely due to the consumption of H_2 by the reaction. The growth in the early stages is uniform but near the outflow plane, a drop in width occurs. These are due to coupling of the downstream region with initial disturbance pattern discussed earlier and also found in earlier work (ref. 5). From the ρ growth profiles it is seen that marginal reduction of the growth results from the chemical reaction (perhaps 10 %). It too shows spurious growth with axial distance due to the coupling effects of the inflow disturbance field. Figure (7d) shows the plot of Reynolds shear stress in the field. The Reynolds stresses with heat release are generally smaller than those without heat release. This contribution most likely comes from reduction in ρ. The decrease in the Reynolds stresses in the flow field due to heat release has been argued to be the cause of reduced growth of the shear-layer in incompressible flows. It seems unlikely that this could be the case in these calculations, due to the similarity between the "n" and "r" profiles.

In addition to the above, the time and space spectra of "u" fluctuations, kinetic energy of fluctuations, and vorticity fluctuations were examined for the "n" and "r" cases. The kinetic energy of fluctuations showed a 5 % decrease with the heat release, time and space spectra of "u" showed no discernible trends, and the vorticity distribution showed a marginal change.

It is appropriate now to discuss the present results in the light of earlier work. There are no experimental studies in supersonic reacting flows for comparison. However, there are many studies in incompressible flows referred to earlier. The principal conclusions of the work of Hermanson, Dimotakis (ref. 2,3) and McMurty et al. (ref. 5) are that the growth rate of the shear-layer decreases with the extent of heat release. A careful examination of the data indicates that the scatter in the data is not small though it may not invalidate the result that the layer thickness decreases with heat release. While most of their discussion centers around the growth variation with decrease in ρ due to heat release, some results of the growth rate variation with increase in the peak temperature is plotted. It is argued that the decrease in ρ causes dilatation and one would have to expect increase in growth rate. That the observed growth rate decreases - up to 10 % in the incompressible case and to a slightly lower extent in the present case at the same peak increment in temperature - is taken to indicate a decrease in entrainment of the fluid, to a larger extent (20-25 %).

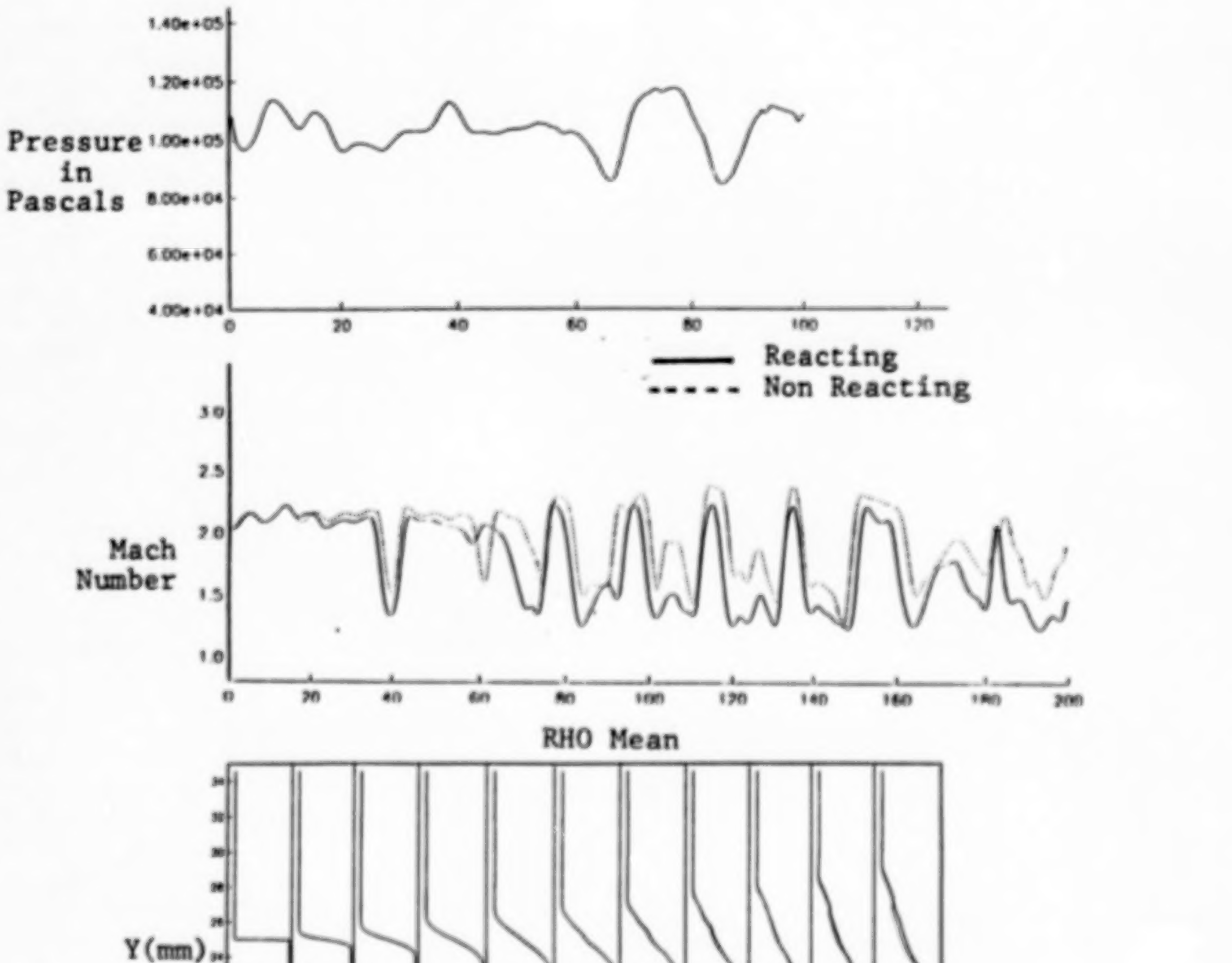

Figure 7: The variation of (a) static pressure with x ($y = y_m/2$), (b) Mach number with x ($y = y_m/2$), (c) ρ_m vs y at various x, (d) Reynolds stresses vs y at various x.

In the present case, the overall decrease in entrainment is estimated from the mass flux profiles to be 18 % at $M_c = 0.38$. The vortex core spacing in the case of non-reacting flow is about three times the layer thickness. This should be compared with values of about 1.5 in incompressible flows and 2-3 in high-speed flows (ref. 6). The enhanced core spacing in high-speed flows is argued to be due to a decreased rate of amplification of disturbances. This decreased rate causes the process of roll up to occur at a slower rate. Heat release causes a slight reduction in the vortex spacing (to about 2.5 δ) and causes the distinction between the vortical structures to be less clear (see figure (5)). Both these features have been discussed in incompressible flows (ref. 2).

CONCLUSIONS

In summary, high-speed reacting mixing-layers are characterized by a 'weak heat release' situation where gas dynamic interactions play a more substantial role in affecting the growth of the layer compared to incompressible flows. Specifically,

(1) The significant role of heat release is to reduce the growth rate of the mixing-layer by about 5-7 % and to reduce the convective speed of the structures by about 10 % at $M_c = 0.38$. Preliminary results indicate that increasing the convective Mach number will further reduce the effect of heat release.

(2) The density changes in the flow are caused by composition, pressure and temperature in the compressible case, unlike those in incompressible flows where temperature is the dominating factor. The reduction of entrainment in high-speed flows due to density changes is much less than in incompressible flows.

(3) Many phenomena like the reduction in Reynolds stresses, and kinetic energy of fluctuations due to heat release are akin to those in incompressible flows, but to a much lesser extent.

In view of the weaker role of heat release in affecting the dynamics of mixing-layers in high-speed flows, it is reasonable to conclude that it is useful to concentrate on non-reacting flows for the mixing related issues like enhanced mixing concepts. For many flows, heat release is likely to provide only a small perturbation to the non-reacting flow, and need not be a matter of major concern. Certainly, flow conditions exist where these conclusions may not be totally valid, and more work is needed in the area of three-dimensional chemically reacting flows. It is, however, believed that this work provides some useful guidelines on the behavior of high-speed chemically reacting mixing-layers.

REFERENCES

1. Brown, G.L. and Roshko, A., "On Density Effects and Large Structure in Turbulent Mixing Layers," *J.Fluid Mech.*, Vol. **91**, 319 - 335, (1974).
2. Hermanson, J.C. and Dimotakis, P.E., "Effects of Heat Release in a Turbulent, Reacting Shear Layer," *J.Fluid Mech.*, Vol. **199**, 333 - 375, (1989).
3. Dimotakis, P. E., "Turbulent Free Shear Layer Mixing," 27th Aerospace Sciences meeting, AIAA 89 - 0269, (1989).
4. McInville, R. M., Gatski. T. B., and Hassan. H, A., "Analysis of Large Vortical Structures in Shear Layers," *AIAAJ.*, Vol. **23**, 1165 -1171, (1985).
5. McMurtry, P.A., Riley, J.J. and Metcalfe, R.W. "Effects of Heat Release on the Large Scale Structures in a Turbulent Reacting Mixing Layer," *J.FluidMech*, Vol. **199**, 297 - 332, (1989).
6. Papamoschou, D and Roshko, A, "The Compressible turbulent Shear Layer," *J.FluidMech.*, Vol. **197**, 453-477 (1988); also see Papamoschou, D, "Structure of the Compressible Turbulent Shear Layer," AIAA Paper 89-0126, 27th Aerospace Sciences meeting, (1989).
7. Sandham, N and Reynolds, W., "The Compressible Mixing Layer: Linear Theory and Direct Simulation," 27th Aerospace Sciences meeting, AIAA 89-0371, (1989).

8. Lele, S,K., "Numerical Simulation of Compressible Free Shear Layer Flows," 27th Aerospace Sciences meeting, AIAA 89-0374, (1989).

9. Mukunda, H.S., Sekar, B., Carpenter, M., Drummond, J.P. and Kumar, A., Studies in the direct numerical simulation of high-speed mixing layers, NASA TP, to be released (1990).

10. Drummond, J.P. and Mukunda, H.S., Mixing enhancement in two-dimensional shear layers, NASA TM 1033, (1988).

11. Reynolds, W, C., "The Potential and Limitations of Direct and Large Eddy Simulations," Whither turbulence conference, Cornell Uni., March (1989).

12. Carpenter, M.H., "A Comparative Study of High Order, and Compact Numerical Algorithms with Existing Central and Upwind Algorithms," NASA TR in progress (1990).

13. Carpenter, M.H., "A Family of Compact Dissipative Two-Four Schemes," Submitted to the Journal of Computational Physics (1990).

14. Macaraeg, M.G., Streett, C.L., and Hussaini, M.Y., "A Spectral Collocation Solution to the Compressible Stability Eigenvalue Problem," NASA Technical Paper 2858, December (1988).

15. Gottlieb, and D. Turkel, E., "Dissipative Two-Four Methods for Time-Dependent Problems," *Mathematics of Computation*, Vol. 30, No. 136, October, 703-723 (1976).

COMPUTATIONAL MODELLING OF DUMP COMBUSTORS FLOWFIELD

D. Lentini
Dipartimento di Meccanica e Aeronautica
Universita' degli Studi di Roma "La Sapienza"
00184 Rome, Italy

W.P. Jones
Department of Chemical Engineering and Chemical Technology
Imperial College of Science, Technology and Medicine
London SW7 2BY, United Kingdom

ABSTRACT

A computational model aimed at predicting the flowfield of dump combustors is presented. The turbulent combustion model is based on the conserved scalar approach and on a convenient specification of its probability density function, which reduces the computation of the mean density to a closed form. Turbulence is modelled by means of the k-ϵ model. The averaged conservation equations are solved by a technique based on a staggered grid and on the SIMPLE solver.

The computational model is applied to a simple dump combustor to assess the computer time requirements and accuracy. The turbulent combustion model here introduced is shown to reduce the computer time by an order of magnitude when compared to evaluating the mean density by numerical quadrature.

NOMENCLATURE

a, b	exponents of the beta-function
c_j	coefficients of polynomial approximation of $F(f)$
C	normalization constant of the beta function
C_{g1}, C_{g2}	constants in the equation for the variance of the conserved scalar
$C_{\epsilon1}$, $C_{\epsilon2}$	constants in the equation for the viscous dissipation rate
C_{μ}	constant in the expression for the turbulent viscosity
f	conserved scalar
$F(f)$	quantity defined by eq. (4)
k	turbulent kinetic energy
$h_k(\tilde{f}, \widetilde{f''^2})$	factor defined by eq. (14)
$H(\tilde{f}, \widetilde{f''^2})$	function defined by eq. (13)
I_j	integral defined by eq. (11)
J	order of the polynomial approximation of $F(f)$
p	pressure
$\bar{p}^*$	quantity defined by eq. (2)
$P(f)$	probability density function of the conserved scalar

P_g, P_k	production terms defined by eqs. (3)
r	radial coordinate
R^0	universal gas constant
T	temperature
u, v	velocity components in x and r
$\bar{W}$	mixture mean molecular weight
x	axial coordinate
ϵ	viscous dissipation rate
Φ	generic quantity
μ	molecular viscosity
μ_t	turbulent viscosity
ρ	density
ρ_{ref}	reference density
σ	molecular Prandtl number
σ_f, σ_g, σ_k, σ_ϵ	effective turbulent Prandtl numbers

Subscripts

$(\ )_r$	derivative with respect to r
$(\ )_x$	derivative with respect to x

Superscripts

$(\bar{\ })$	conventional average
$(\tilde{\ })$	Favre average
$(\ )'$	fluctuation about conventional average
$(\ )''$	fluctuation about Favre average

1. INTRODUCTION

Flameholding in subsonic combustion ramjets is achieved by using dump combustors, in which the flame is anchored to the chamber by a large region of recirculation. The ensuing elliptic character of the flow imposes however a considerable stress on the numerical simulation of such flowfields. Special grid arrangements and computational techniques must therefore be used, and the computational requirements are demanding. The problem is compounded with that of providing an adequate representation of the effects of turbulent fluctuations on combustion. For nonpremixed flames the most popular approach is that making use of a presumed probability density function (pdf) of a conserved scalar quantity (ref. 1). The effect of turbulent fluctuations is thus restricted to the mean density $\bar{\rho}$, which is computed via an appropriate integral. The accurate evaluation of such integrals, which must be computed at each node point and at each computational step, requires a large number of intervals and takes therefore the largest share of the overall computing time.

Three examples of previous applications of computer codes to the solution of dump combustor flowfields in subsonic combustion ramjets are worthy of note. Harsha et al. (ref. 2) reduced the computer time to an acceptable level (4 to 15 minutes on a CDC 7600) by separating the computation of the directed flow from that of the recirculation region: this requires an a priori knowledge of the reattachment length, so that this code cannot be considered to be a truly predictive tool. Further, no account was taken of the effect of fluctuations on combustion. Drummond (ref. 3) performed a unified calculation of the combustor flowfield, but the computer time was exceedingly high, even for nonreacting computations, in which 150000 steps and 4.6 hours on a CYBER 203 were needed. When reacting flowfields were considered the number of iterations rose to 200000, and the convergence of the solution was poor; the computer time is not reported. Also the combustion model did not account for the effects of fluctuations. The difficulty in obtaining a converged solution might be ascribed to the grid arrangement and the algebraic eddy viscosity model used, which appears not be suited to recirculating flows. A sounder computational model was presented by Vanka et al. (ref. 4) for ducted rockets, a ramjet variant. They correctly account for the effects of fluctuations by specifying the conserved scalar pdf as a battlement shaped function. The inherently three-dimensional character of the flowfield in this case requires using a rather coarse mesh (24 × 11 × 11) to limit the computing time to 25 minutes on an IBM 3033.

The intent of the present paper is to show that, by introducing suitable assumptions to effect the thermochemical closure of the model, a very large reduction in computer time can be achieved. This is substantiated by applying the present model to a simple hydrogen-air dump combustor. In the following Section the describing equations are introduced, and then in Sec. 3 the proposed model for the thermochemical closure of such equations is presented.

2. CONSERVATION EQUATIONS

The bases of the analysis of the flowfield of nonpremixed turbulent combustion are the averaged conservation equations for mass, momentum and a scalar quantity f. The latter represents either a normalized enthalpy or atomic mass fraction: in fact, with the assumption that the kinetic energy is neglegible in the energy equation (implying relatively low-speed flow), that the diffusion can be represented in terms of a single coefficient, and that the Lewis number is unity, the equations for the above mentioned scalar quantities assume the same form, free of source terms. Favre-averaging (see e.g. ref. 5) is used to account for the effects of variable density: for a generic quantity Φ, it gives

$$\tilde{\Phi} = \frac{\overline{\rho\Phi}}{\bar{\rho}} \qquad\qquad \Phi'' = \Phi - \tilde{\Phi}$$

where the tilde denotes the Favre mean, the overbar a conventional average, and the double prime the fluctuation about the Favre mean. Conventional averages are retained for the mean pressure $\bar{p}$ and density $\bar{\rho}$. Turbulence is modeled according to the k-ϵ model, which is generally accepted as the most reliable compromise between rather crude algebraic eddy viscosity models and second-order closure models. The latter are rather complicated and still not fully tested (see ref. 6, although considerable progress has been recently reported by Jones and Pascau, ref. 7). To complete the model equations for the mean $\tilde{f}$ and the variance $\widetilde{f''^2}$ of the conserved scalar (ref. 1) are included in the formalism. Molecular diffusion terms are retained for completeness to account for near-wall and possible low Reynolds number effects (ref. 8), in particular at the inlet. As they are relatively important only in regions where the intensity of the fluctuations is low, such fluctuations are neglected in their evaluation. The steady, axisymmetric form of the conservation equations is considered.

Thus, the averaged equations for mass, axial and normal momentum, turbulent kinetic energy $\tilde{k}$, viscous dissipation rate $\tilde{\epsilon}$, and for the mean and the variance of the conserved scalar are

$$\left(\bar{\rho}\tilde{u}\right)_x + \frac{1}{r}\left(r\bar{\rho}\tilde{v}\right)_r = 0 \tag{1a}$$

$$\bar{\rho}\tilde{u}\tilde{u}_x + \bar{\rho}\tilde{v}\tilde{u}_r = \left[2\ (\mu + \mu_t)\ \tilde{u}_x\right]_x + \frac{1}{r}\left[r\ (\mu + \mu_t)\ (\tilde{u}_r + \tilde{v}_x)\right]_r - \bar{p}^*_x \tag{1b}$$

$$\bar{\rho}\tilde{u}\tilde{v}_x + \bar{\rho}\tilde{v}\tilde{v}_r = \left[(\mu + \mu_t)\ (\tilde{v}_x + \tilde{u}_r)\right]_x + \frac{1}{r}\left[2r\ (\mu + \mu_t)\ \tilde{v}_r\right]_r - \bar{p}^*_r \tag{1c}$$

$$\bar{\rho}\tilde{u}\tilde{f}_x + \bar{\rho}\tilde{v}\tilde{f}_r = \left[(\frac{\mu}{\sigma} + \frac{\mu_t}{\sigma_f})\ \tilde{f}_x\right]_x + \frac{1}{r}\left[r\ (\frac{\mu}{\sigma} + \frac{\mu_t}{\sigma_f})\ \tilde{f}_r\right]_r \tag{1d}$$

$$\bar{\rho}\tilde{u}\tilde{k}_x + \bar{\rho}\tilde{v}\tilde{k}_r = \left[(\mu + \frac{\mu_t}{\sigma_k})\ \tilde{k}_x\right]_x + \frac{1}{r}\left[r\ (\mu + \frac{\mu_t}{\sigma_k})\ \tilde{k}_r\right]_r + P_k - \bar{\rho}\tilde{\epsilon} \tag{1e}$$

$$\bar{\rho}\tilde{u}\tilde{\epsilon}_x + \bar{\rho}\tilde{v}\tilde{\epsilon}_r = \left[(\mu + \frac{\mu_t}{\sigma_\epsilon})\ \tilde{\epsilon}_x\right]_x + \frac{1}{r}\left[r\ (\mu + \frac{\mu_t}{\sigma_\epsilon})\ \tilde{\epsilon}_r\right]_r + C_{\epsilon 1}\frac{\tilde{\epsilon}}{\tilde{k}}P_k - C_{\epsilon 2}\frac{\bar{\rho}\tilde{\epsilon}^2}{\tilde{k}} \tag{1f}$$

$$\bar{\rho}\tilde{u}\widetilde{f''^2}_x + \bar{\rho}\tilde{v}\widetilde{f''^2}_r = \left[(\frac{\mu}{\sigma} + \frac{\mu_t}{\sigma_g})\ \widetilde{f''^2}_x\right]_x + \frac{1}{r}\left[r\ (\frac{\mu}{\sigma} + \frac{\mu_t}{\sigma_g})\ \widetilde{f''^2}_r\right]_r + C_{g1}\ P_g - C_{g2}\frac{\bar{\rho}\tilde{\epsilon}\widetilde{f''^2}}{\tilde{k}} \tag{1g}$$

$\bar{p}^*$ is defined as

$$\bar{p}^* = \bar{p} - \frac{2}{3}\left\{(\mu + \mu_t)\ [\tilde{u}_x + \frac{1}{r}\ (r\ \tilde{v})_r] + \bar{\rho}\ \tilde{k}\right\} \tag{2}$$

and the production rates are given by

$$P_k = \mu_t\left[\ \tilde{v}_x^{\ 2} + \tilde{u}_r^{\ 2} + 2\left(\tilde{u}_x^{\ 2} + \tilde{v}_r^{\ 2} + \tilde{v}_x\ \tilde{u}_r\right)\right] \tag{3a}$$

$$P_g = \mu_t\left(\ \tilde{f}_x^{\ 2} + \tilde{f}_r^{\ 2}\ \right) \tag{3b}$$

The turbulent viscosity is given as

$$\mu_t = C_\mu\ \bar{\rho}\ \frac{\tilde{k}^2}{\tilde{\epsilon}}$$

σ has the meaning of a molecular Prandtl number. The model constants are taken as (refs. 9 and 6)

$\sigma_f = 0.7$	$\sigma_k = 1$	$\sigma_\epsilon = 1.3$	$\sigma_g = \sigma_f$
$C_{\epsilon 1} = 1.44$	$C_{\epsilon 2} = 1.92$	$C_{g1} = \frac{2}{\sigma_f}$	$C_{g2} = 2$

$C_\mu = 0.09$

Eqs. (1) represent a set of seven differential equations for the variables $\tilde{u}$, $\tilde{v}$, $\bar{p}^*$, $\tilde{f}$, $\tilde{k}$, $\tilde{\epsilon}$, $\widetilde{f''^2}$.

In order to close this set, the mean density $\bar{\rho}$ must be expressed as a function of the state variables considered.

3. THERMOCHEMICAL CLOSURE

Following the conserved scalar approach, all state quantities can be determined as a function of a single scalar quantity f, which is taken here as the elemental mass fraction of hydrogen. In fact, with the assumption that the pressure is thermochemically constant, the mixture composition and temperature (as well as any further state variable) are determined by chemical equilibrium computations, as a function of f alone. Thus from the equation of state:

$$\rho = \frac{P}{\frac{R^0}{\bar{W}} T}$$

where R^0 is the universal gas constant and $\bar{W}$ is the mixture average molecular weight, the density too turns out to be a function of f alone. The above equation can be rewritten for convenience as

$$\rho = \frac{\rho_{ref}}{F(f)} \tag{4}$$

where F(f) is a function of f determined by equilibrium computations; ρ_{ref} is a reference density, introduced to make this function dimensionless.

In order to evaluate the mean density, a probability density function (pdf) for the conserved scalar must be introduced, such that P(f) df is the fraction of time the conserved scalar is bounded between the values f and f+df. The mean density is then obtained from:

$$\bar{\rho} = \rho_{ref} \int_0^1 \frac{P(f)}{F(f)}\, df \tag{5}$$

The pdf shape is assigned a priori, since it can be shown (ref. 1) that the result is relatively insensitive to the specific pdf assumed. Its parameters are determined on the basis of the mean $\tilde{f}$ and the variance $\widetilde{f''^2}$ of the conserved scalar, for which appropriately modelled differential equations are solved. In the present model (refs. 10, 11), developed after a suggestion by Libby (ref. 12), F(f) is approximated by a J-th order polynomial fit

$$F(f) \cong \sum_{j=0}^{J} c_j\, f^j \tag{6}$$

and a pdf is specified for the whole ratio P(f)/F(f) as a beta-function

$$\frac{P(f)}{F(f)} = C\, f^{a-1}(1-f)^{b-1} \tag{7}$$

where C is a normalization constant and the exponents a and b of the beta-function are related to the mean and the intensity of the conserved scalar through the expressions (ref. 13)

$$a = \frac{\tilde{f}^2\,(1-\tilde{f})}{\widetilde{f''^2}} - \tilde{f}$$

$$b = \frac{\tilde{f}\,(1-\tilde{f})^2}{\widetilde{f''^2}} - (1-\tilde{f}) \qquad (8)$$

Intermittency at the edges of the mixing layer is not accounted for explicitly in the present model. In any case, the beta-function itself accounts for intermittency to some extent, by giving a finite probability to the states $f = 0$ (if $a < 1$) and $f = 1$ (if $b < 1$).

To determine the parameter C, the normalization condition

$$\int_0^1 P(f)\,df = 1$$

is enforced. Its left-hand side can be written as

$$C \int_0^1 f^{a-1}(1-f)^{b-1}F(f)df \cong C \sum_{j=0}^{J} c_j I_j(a,b) \qquad (10)$$

where use has been made of approximation (6); the integrals I_j ($j=0,1,\ldots,J$), defined as

$$I_j(a,b) = \int_0^1 f^{a-1+j}(1-f)^{b-1}df \qquad (11)$$

are expressed through the relation (derived after ref. 14)

$$I_j(a,b) = \frac{\Gamma(a+j)\Gamma(b)}{\Gamma(a+b+j)}$$

Thanks to properties of the gamma-function, the summation appearing in (10) can be expressed as

$$\sum_{j=0}^{J} c_j I_j(a,b) = I_0(a,b) \sum_{j=0}^{J} c_j \prod_{k=1}^{j} \frac{a+k-1}{a+b+k-1}$$

This allows C to be determined. Upon substitution in (7) and then in (5), the mean density is obtained as

$$\bar{\rho} = \frac{\rho_{ref}}{H(\tilde{f},\widetilde{f''^2})} \qquad (12)$$

with

$$H(\tilde{f},\widetilde{f''^2}) = \sum_{j=0}^{J} c_j \prod_{k=1}^{j} h_k(\tilde{f},\widetilde{f''^2}) \qquad (13)$$

and ($k = 1,2,\ldots,J$)

$$h_k(\tilde{f},\widetilde{f''^2}) = \qquad (14)$$

$$= \tilde{f} + \frac{(k-1)\,(1-\tilde{f})}{k - 2 + \dfrac{\tilde{f}\,(1-\tilde{f})}{\widetilde{f''^2}}} \qquad \text{for } 0 < \tilde{f} < 1$$

$$= \tilde{f} \qquad \text{for } \tilde{f} = 0,\ 1$$

where use has been made of (8).

This formulation has the advantage of reducing the integral appearing in (5) to a closed form. Further, the probability density function here introduced has been shown to give results fully consistent with experimental data (ref. 11).

4. NUMERICAL ALGORITHM

The present model for the mean density $\bar{\rho}$ has been introduced into the computer program JETFLO (ref. 15). This code is based on use of a staggered grid (ref. 16) and SIMPLE solver. The converged solution is obtained by iteration. Synthetic wall boundary conditions are enforced to avoid resolving the boundary layer, which would otherwise take the largest share of computing time.

F(f) is approximated by a 12th order polynomial fit. The equilibrium conditions for the hydrogen-air flow considered here are computed by means of the equilibrium chemistry program STANJAN (ref. 17); the included species are Ar, H, H_2, H_2O, N, N_2, NO, NO_2, O, O_2, OH.

5. TEST CASE

The present model is here applied to a simple cylindrical dump combustor. The main aim of this test case is to quantify the reduction of computing time achieved with the present turbulent combustion model, rather than to present an accurate computation of a practical combustor. Some limitations of the configuration being considered (i.e., the quite low Mach number and equivalence ratio) and of the computational implementations (i.e., the rather coarse mesh and the approximate specification of the inlet conditions) must be viewed in this perspective; they are introduced only for the sake of computational convenience and to limit the CPU time to an amount convenient for initial testing. The test case is computed with four different options, labelled 1 to 4:

1) 28 × 28 grid, $\bar{\rho}$ given by the present model
2) 15 × 15 grid, $\bar{\rho}$ given by the present model
3) 15 × 15 grid, $\bar{\rho}$ computed by numerical quadrature over 200 intervals
4) 15 × 15 grid, $\bar{\rho}$ computed by numerical quadrature over 100 intervals

In runs 3 and 4 the probability density function P(f) of the conserved scalar is taken as a beta-function.

The results of run 1 are presented in detail as the most accurate ones. A comparison of the results of runs 1 and 2 is used to give some indications as to what an extent the solution may be considered grid independent. The comparison of CPU time of runs 2 and 3 is used to quantify the reduction achieved by the present model, as compared to evaluating $\bar{\rho}$ by numerical quadrature over 200 intervals. In order to assess whether 200 intervals are adequate for estimating $\bar{\rho}$, a comparison of the results of runs 3 and 4 is used.

The dump combustor considered in this test case is fed with hydrogen, injected through the central pipe (0.0077 m internal radius, 0.0154 m outer radius) at 1 m/s, and air, supplied through a 0.0115 m wide annulus at 10 m/s. The combustor internal radius is 0.05 m, resulting in a rearward facing step 0.0231 m high at the inlet; its length is 0.3 m. The velocity profiles at the inlet are assumed to be flat for each stream for simplicity. In any event this oversimplified assumption is unlikely to affect the overall flowfield to a significant extent in elliptic flows and, moreover, the definition of the initial conditions for the test case being considered involves much larger incertainties, as will be apparent in the following paragraph.

Figure 1 reports the main features of the combustor flowfield, as computed in run 1. In particular, Fig. 1a reports stream function isolines, i.e., streamlines. A recirculation zone appears downstream of the dump plane and ensures flame stabilization. Due to the very low density of hydrogen, as well as to its low inlet velocity in this test case, such isolines are widely separated near the centerline, thus giving a rather poor representation of the flowfield. It is possible however to identify a smaller region of local recirculation near the hydrogen inlet, due to its inlet velocity being substantially lower than the other stream. It appears likely that such a recirculation spot reaches into the hydrogen supply pipe, thus invalidating the assumption of fully developed flow used at the inlet for computational purposes. This should however only affect the flowfield in the immediate neighbourhood of the hydrogen inlet, and have limited effects on the overall flow pattern. However this does suggest that a specification of the initial velocity profiles more accurate than that hypothesized above is unwarranted, at least in this case. The solution would be to extend the computational domain upstream into the hydrogen supply pipe. In Fig. 1b the isolines of the logarithm of the mean value of the conserved scalar are shown. A rapid mixing is observed close to the plate separating the hydrogen and air streams. The stoichiometric combustion of hydrogen and air corresponds to $f = 0.0284$, so that the isoline -1.5 is very close to the mean location of the stoichiometric contour, albeit somewhat on the rich side. Of course, due to the fluctuations, such a front is highly oscillating. An estimate of the intensity of such oscillations can be obtained from Fig. 1c which shows the isolines of the logarithm of the variance of the conserved scalar. The intensity of the fluctuations appears to be maximum close to the flame front.

Figure 2 displays (for run 1) the isolines of the mean and the intensity of state quantities which are recovered from the mean and the variance of the conserved scalar via its assumed probability density function. For the mean density $\bar{\rho}$, the form (12) is used. For any other state quantity (but the pressure) Φ, both conventional and Favre averages can be recovered as

$$\bar{\Phi} = \int_0^1 \Phi(f)\ P(f)\ df$$

$$\tilde{\Phi} = \frac{\overline{\rho\Phi}}{\bar{\rho}} = \frac{1}{\bar{\rho}} \int_0^1 \rho(f)\ \Phi(f)\ P(f)\ df$$

Further, the intensity of the fluctuations can be obtained as

$$\overline{\Phi'^2} = \int_0^1 [\Phi(f)-\bar{\Phi}]^2\ P(f)\ df$$

and similarly for $\widetilde{\Phi''^2}$.

In these expressions, $\Phi(f)$ denotes the equilibrium value of Φ as a function of the conserved scalar. The evaluation of such integrals was achieved by numerical quadrature. However the contribution to the overall computing time is negligible as they need only be computed at the last iteration. The computation is further expedited by limiting the integration range to the domain

$$[\max(\ 0,\ \tilde{f}-6\sqrt{\widetilde{f''^2}}),\ \min(\ 1,\ \tilde{f}+6\sqrt{\widetilde{f''^2}})]$$

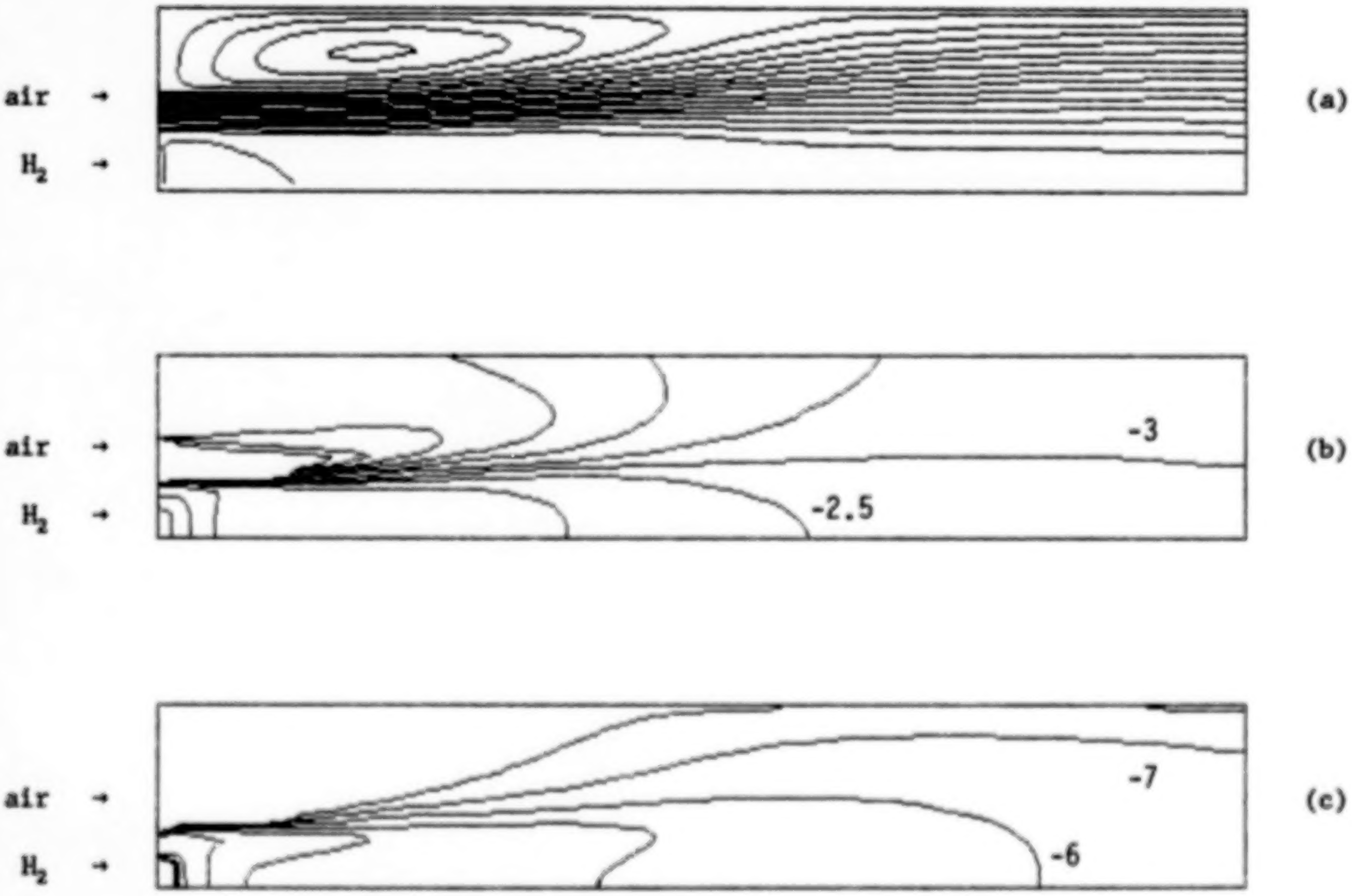

Fig. 1. Isoline plots: a) stream function (streamlines), b) logarithm of the mean of the conserved scalar, c) logarithm of the variance of the conserved scalar.

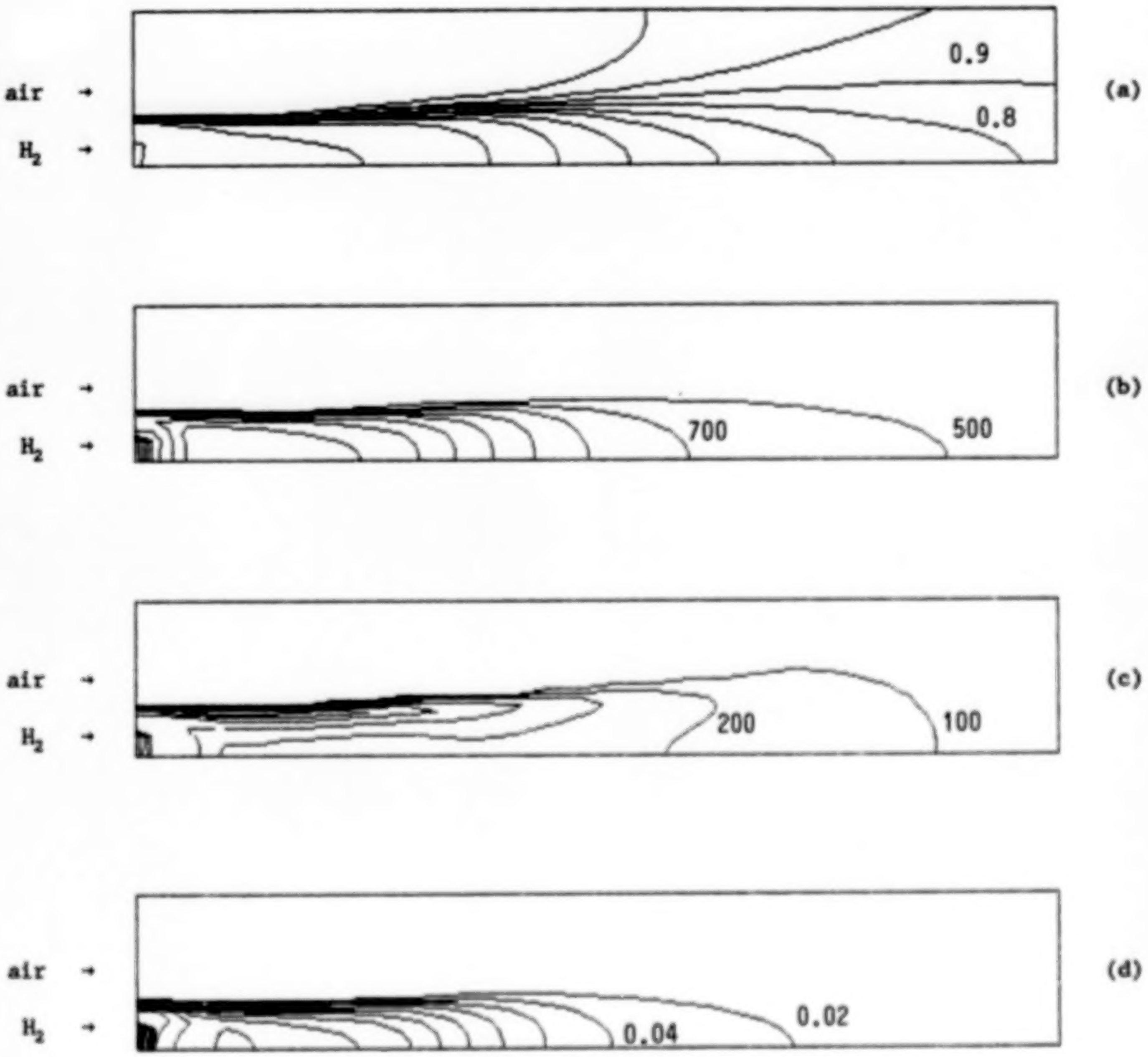

Fig. 2. Isoline plots: a) mean density (kg/m^3), b) mean temperature ($^\circ$K), c) rms of temperature fluctuations ($^\circ$K), d) mean water vapour mass fraction.

rather than [0,1].

Figures 2a through 2d show isolines of the average density, average temperature, rms of temperature fluctuations and average water vapour mass fraction, respectively. Conventional averages are reported for temperature as measurements by thermocouples give unweighted means, whereas Favre-averaging is used for the mass fraction as probe sampling results in close to density-weighted concentrations. It can be seen that the temperature at the exit of the combustor is rather low due to the large excess air involved in this particular test case. Mean temperatures about 2100 °K are predicted near the flame zone, with accompanying rms of fluctuations in excess of 770 °K. The mean water vapour mass fraction at the exit is rather low as well.

We will now briefly compare the results of the different runs in terms of accuracy and CPU time.

By comparing runs 1 and 2, it can be seen that the mean axial velocity component computed with the coaser grid (step size doubled in both directions) exhibits a maximum difference of 25% of the maximum velocity with respect to that computed with the finer grid. Although this may not represent a sufficiently grid-converged solution for most purposes, it is believed that the 28 × 28 grid gives results at least indicative of the overall flowfield configuration. Run 1 requires 443 iterations and 50.16 s CPU time on an IBM 3090/600 processor; the computation is assumed to be converged when the residuals of all quantities are less than 10^{-4}.

The comparison of the CPU time requirements of the present model ($\bar{\rho}$ in closed form) and of a more conventional approach ($\bar{\rho}$ evaluated by numerical quadrature) is performed on a 15 × 15 points grid, because the latter model involves very long computer runs. By comparing runs 2 (196 iterations and 6.11 s CPU time) and 3 (375 iterations and 62.22 s), it can be seen that the present model cuts the CPU time by a factor ten when compared to a numerical quadrature over 200 intervals.

The question remain to be addressed whether 200 intervals are enough to ensure an accurate evaluation of $\bar{\rho}$. To this ends, the results of run 3 can be compared to those of run 4 (numerical quadrature over 100 intervals). The relative difference between the values of $\bar{\rho}$ computed with the two runs reaches a maximum of about 4%. This seems to indicate that the 200 intervals considered in run 3 might be adequate for a reasonably accurate computation, but 100 intervals might not.

6. CONCLUSIONS

The present model defines a soundly based treatment for nonpremixed turbulent combustion and, thanks to an appropriate assumption for the conserved scalar pdf, reduces the computer time requirements by about an order of magnitude in elliptic flows.

REFERENCES

1. Bilger, R.W., "Turbulent flows with nonpremixed reactants", in *Turbulent reacting flows* (eds. P.A. Libby and F.A. Williams), Topics in applied physics 44, 65-113, Springer-Verlag, Berlin (1980).

2. Harsha, P.T., Edelman, R.B., Schmotolocha, S.N. and Pederson, R.J., "Combustor modeling for ramjet development programs", in *AGARD CP 307* (1981).

3. Drummond, J.P., "Numerical study of a ramjet dump combustor flowfield", *AIAA J.*, 23, 604-611 (1985).

4. Vanka, S.P., Craig, R.R. and Stull, F.D., "Mixing, chemical reaction and flowfield development in ducted rockets", *J. Prop. P.*, 2, 331-338 (1986).

5. Libby, P.A. and Williams, F.A., "Fundamental aspects", in *Turbulent reacting flows* (eds. P.A. Libby and F.A. Williams), Topics in applied physics 44, 1-43, Springer-Verlag, Berlin (1980).

6. Jones, W.P. and Whitelaw, J.H., "Calculation methods for turbulent reacting flows: a review", *Comb. Flame*, 48, 1-26 (1982).

7. Jones, W.P. and Pascau, A., "Calculation of confined swirling flows with a second moment closure", *J. Fluids Engineering, Trans. ASME*, 111, 248-255 (1989).

8. Patel, V.C., Rodi, W. and Scheurer, G., "Turbulence model for near-wall and low Reynolds number flows: a review", *AIAA J.*, 23, 1308-1319 (1985).

9. Rodi, W., *Turbulence models and their application to hydraulics - a state of the art review*. Int. Ass. Hydraulic Research, Delft (1980).

10. Lentini, D., "Modelling and simulation of nonpremixed turbulent flames", *IV Conv. It. Mecc. Comp.*, Padova (1989). Also submitted to *Meccanica*.

11. Lentini, D., "Numerical prediction of nonpremixed turbulent flames", AIAA paper 90-0730 (1990).

12. Libby, P.A., Private communication (1988).

13. Jones, W.P., "Models for turbulent flows with variable density and combustion", in *Prediction models for turbulent flows*, (ed. W. Kollmann), 380-421, Hemisphere Publ. Co., Washington (1980).

14. Abramowitz, M. and Stegun, I.A., *Handbook of mathematical functions*, National Bureau of Standards, Washington (1964).

15. Jones, W.P. and McGuirk, J.J., "Computational fluid dynamics of turbulent flows", Short course lecture notes, Univ. Zaragoza (1984).

16. Harlow, F.H. and Welch, J.E., "Numerical calculation of time-dependent viscous incompressible flow of fluids with free surface", *Phys. Fluids*, 8, 2182-2189 (1965).

17. Reynolds, W.C., STANJAN, Stanford Univ. (1981).

NUMERICAL SIMULATION OF TRANSVERSE FUEL INJECTION

Marlon Mao and David W. Riggins,
Analytical Services and Materials, Inc.
Hampton, VA 23666

Charles R. McClinton
NASA Langley Research Center
Hampton, VA 23665

ABSTRACT

This paper presents a review of recent work at NASA-LaRC to compare the predictions of transverse fuel injector flow fields and mixing performance with experimental results. Various "cold" (non-reactive) mixing studies have been selected for code calibration; these include the effects of boundary layer thickness and injection angle for sonic hydrogen injection into supersonic air. Angled injection of helium is also included. This study was performed using both the three-dimensional elliptic and the parabolized Navier-Stokes (PNS) versions of SPARK. Axial solution planes were passed from PNS to elliptic and elliptic to PNS in order to efficiently generate solutions. The PNS version is used both upstream and far downstream of the injector where the flow can be considered parabolic in nature. The comparisons are used to identify experimental deficiencies and computational procedures to improve agreement.

NOMENCLATURE

$A_{\alpha=0}$	area enclosed by the $\alpha = 0$ curve
D	injector diameter
$\dot{m}_{H_2,inj}$	mass flow rate of injected H_2
$\dot{m}_{H_2,mix}$	mass flow rate of mixed H_2
$\dot{m}_{H_2,total}$	total H_2 mass flow rate from flow field integration
M	Mach number
p	pressure
p_t	total pressure
P	penetration to outer edge of mixing region (height of $\alpha_{H_2} = .00035$ or $x_{He} = .005$ contour)
$\bar{q}$	jet-to-air dynamic pressure ratio
Re	Reynolds number
Sc_t	turbulent Schmidt number
T	temperature
T_t	total temperature
T_w	plate temperature
u	axial velocity
W	width
x or X	axial coordinate
x_{He}	helium mole fraction

y or Y	lateral coordinate
z or Z	coordinate normal to plate
Z_m	height of α_{max} contour
α	mass fraction
α_{max}	maximum mass fraction
α_R	mass fraction defined by Eqn. 1
α_s	stochiometric hydrogen mass fraction (0.0285)
β	air mass fraction $(1-\alpha)$
δ	boundary layer thickness
η_m	mixing efficiency
$\eta_m^{\prime}$	mixing efficiency with $\alpha_s = 0.01425$
$(\eta_m^{\prime})_{adj}$	mixing efficiency with $\alpha_s = 0.01425$ and assuming missing fuel to be unmixed
ρ	density
θ_{inj}	injection angle

INTRODUCTION

Efficient hypersonic flight at speeds above Mach 6 require the use of supersonic combustion ramjet or scramjet engines. Research efforts to establish a technology base for scramjet engine components have been underway at NASA Langley Research Center (LaRC) since the mid 1960's. This research was focused on the Mach 4 to 7 speed range, the range within the enthalpy limits of combustion heated or arc heated facilities, and directed toward the inlet and combustor components of the engine. Combustor technology development[Ref. 1] was directed at understanding the requirements for and performance of fuel injection, mixing and reaction (ignition and flame holding) in the scramjet combustor environment, and incorporated a dual approach of experimental and computational technology development.

Experimental combustor technology development started with single[2-4] and multiple[5-7] fuel injector studies in cold flow to characterize fuel mixing, followed by reacting coaxial flow configurations[8,9] to characterize the supersonic combustion phenomena. Direct connect combustor experiments[10-16] were used to verify empirical models[17] for the mixing limited supersonic combustion process developed from the early mixing studies. Finally, the empirical combustor models were integrated into a complete subscale engine design and tested[18] over the Mach 4 to 7 speed range in two engine test facilities.

Computational fluid dynamics (CFD) technology development started with codes which contained the physical modeling necessary to predict the supersonic, chemically reacting flow encountered in a scramjet combustor[19]. Because of computer memory limitations, these codes were limited to two-dimensional or axisymmetric cases until the mid 1980's. The two-dimensional codes were calibrated to appropriate data for non-reacting fuel injection and mixing[20], and reacting fuel injection and mixing[21,22] in ducted flows. Various finite-rate chemistry models were developed and applied for hydrogen fuel[19,23] and silane-hydrogen-air mixtures[24]. Recent code applications have evaluated non-reactive three-dimensional fuel mixing[25] and reactive fuel mixing in confined simulated combustor flows[25-29]. Even though they have provided significant insight into these highly complex flow fields, these studies have not provided the essential features of code calibration for scramjet fuel mixing.

The objective of this paper is to present comparisons of numerical predictions with experimental measurements for non-reacting fuel injection into a supersonic freestream and to document efforts to improve the agreement. This study will look at a large data set with the intent of identifying experimental limitations and correct procedures to use when exercising the codes. The primary index of agreement is overall mixing efficiency of the fuel or simulated fuel. In the absence of experimental mixing efficiency, the index defaults to fuel mass or mole fraction distributions. Secondary values of interest include fuel penetration and spreading, wall pressure, and any other measured data available.

A brief description of the experimental tests chosen for this paper is followed by a brief description of the SPARK codes. The computational method used to solve the injection problems is discussed along with convergence criteria for the elliptic region. The grid and boundary conditions are also given. Results from the calculations are then compared with data in order to demonstrate the accuracy of the numerical modeling.

EXPERIMENTAL CONFIGURATION

Details of the flat plate non-reacting injection cases modeled are provided in Table 1. Variables in the table include the jet-to-air dynamic pressure ratio, $\bar{q}$; the freestream Mach number, M_{air}; freestream Reynolds number, Re; downstream injection angle, θ_{inj}, measured from the plate surface; the boundary-layer thickness upstream of the injector normalized by jet diameter, δ/D; and the jet diameter in centimeters, D.

Table 1. Summary of Conditions

Case	Injectant	$\bar{q}$	M_{air}	$\mathrm{Re}(m^{-1})$	θ_{inj}	δ/D	D(cm)	Ref.
1	hydrogen	1.0	4.05	$8.3\text{x}10^8$	90^o	1.25	0.2540	4
2	hydrogen	1.0	4.05	$6.19\text{x}10^7$	90^o	2.51	0.1016	3
3	hydrogen	1.0	4.05	$8.0\text{x}10^8$	90^o	6.25	0.0508	4
4	hydrogen	1.0	4.05	$6.19\text{x}10^7$	30^o	3.40	0.1016	7
5	helium	0.6	3.00	$5.2\text{x}10^7$	30^o	2.20	0.3175	30
6	helium	3.1	3.00	$5.2\text{x}10^7$	30^o	2.20	0.3175	30
7	helium	0.27	3.00	$5.2\text{x}10^7$	15^o	2.20	0.3175	30

Table 2. Experimental Flow Properties

	Air			Injectant			
Case	p_t(MPa)	T_t(K)	Mach	Gas	p_t(MPa)	T_t(K)	Mach
1	1.72	295	4.05	H_2	0.33	289	1.0
2	1.38	294	4.05	H_2	0.27	294	1.0
3	1.72	303	4.05	H_2	0.32	298	1.0
4	1.38	300	4.05	H_2	0.27	295	1.0
5	.655	290	3.00	He	0.17	295	1.0
6	.655	290	3.00	He	0.86	295	1.0
7	.655	290	3.00	He	0.076	295	1.0

Cases 1-4 are from tests performed on a flat plate model (Fig. 1) in a Mach 4.05, 23x23 cm blow down tunnel. Table 2 presents nominal test conditions for the cold air and sonic

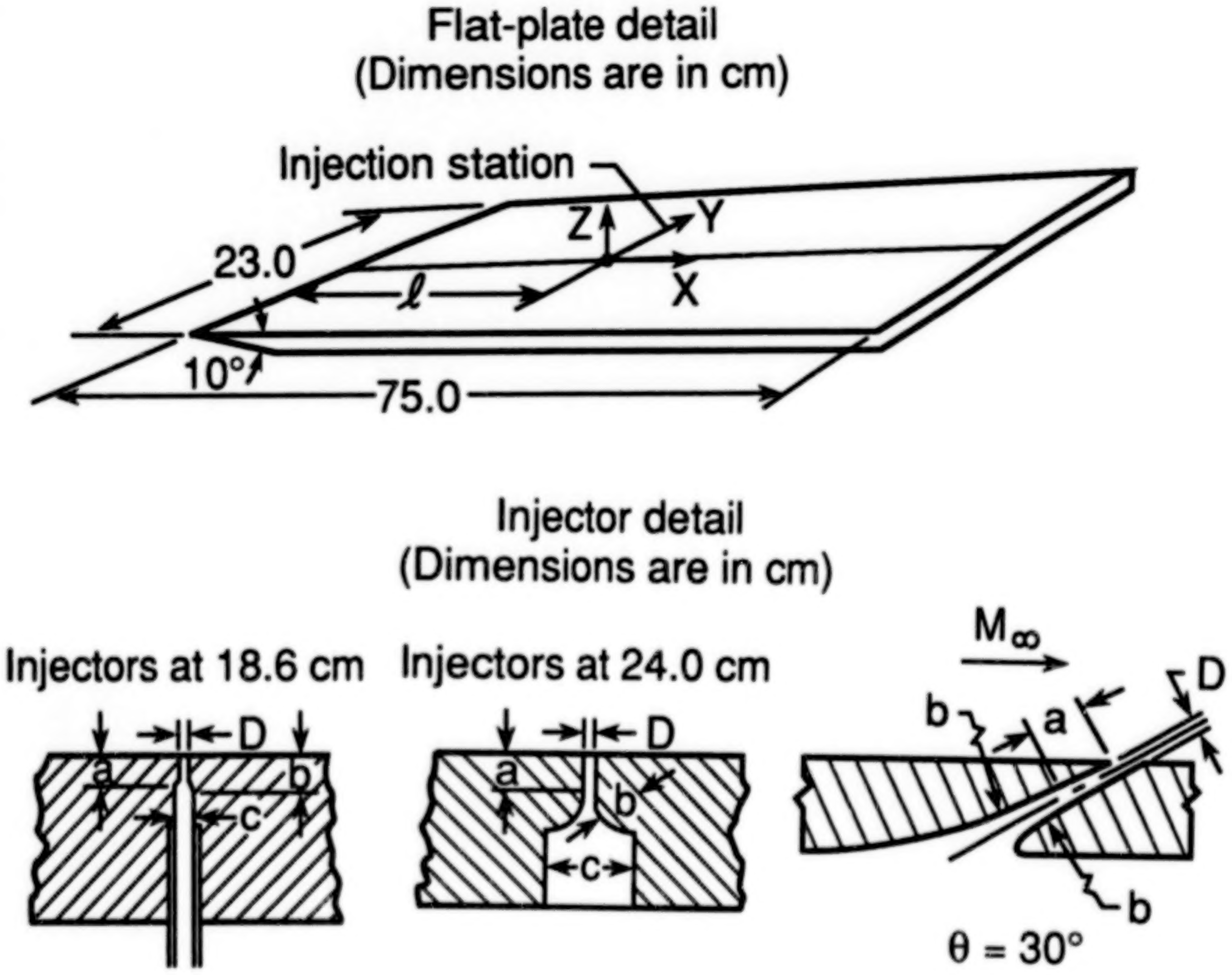

Case	ℓ	a	b	c	D	C_D
1 ref. 4	24.0	0.635	0.578	1.41	0.254	0.830
2 ref. 3	18.6	0.317	0.397	0.15	0.102	0.76
3 ref. 4	24.0	0.152	0.680	1.41	0.051	0.754
4 ref. 7	27.1	0.303	3.12	-	0.102	0.76

Figure 1. Experimental Model

hydrogen injectors. The facility was operated at stagnation pressures of either 1.38 or 1.72 MPa, but the four cases selected all operated with unity jet-to-freestream dynamic pressure ratio (see Table 1). Instrumentation was provided to measure the stagnation pressures and temperatures of hydrogen and air, plate-surface static pressures and hydrogen concentrations. In addition, the H_2 mass flow rate was measured using a sharp-edge orifice meter. Plate static-pressure orifices of 0.051 cm diameter were located on the longitudinal center line from 30D ahead of the injector station to 150D downstream for Case 4. In-stream measurements were made using a 0.038 cm ID pitot and a 0.102 cm OD conventional static probe. Gas samples were taken from the mixing region by the pitot probe and were analyzed with an on-line process gas chromatograph having a cycle time of 60 seconds.

Historically, mixing efficiency, η_m, is defined as that fraction of the least available reactant (i.e. O_2 or fuel) which would react if the fuel-air mixture were brought to chemical equilibrium without additional local or global mixing. Thus in fuel rich regions, all of the local oxygen is considered "mixed," while in fuel lean regions all of the fuel is mixed. Two definitions of mixing efficiency are required--one for flows which are globally fuel rich, and one for flows which are lean. For fuel lean flows, as those reported here,

$$\eta_m = \frac{\dot{m}_{H_2,mix}}{\dot{m}_{H_2,total}} = \frac{\int_{A_{\alpha=0}} \alpha_R \rho u dA}{\int_{A_{\alpha=0}} \alpha \rho u dA} \tag{1}$$

where: α is hydrogen (fuel) mass fraction

$$\alpha_R = \begin{cases} \alpha & where\, \alpha \le \alpha_s \\ (\frac{1-\alpha}{1-\alpha_s})\alpha_s & where\, \alpha > \alpha_s \end{cases}$$

α_s is H_2 stochiometric mass fraction (0.0285)
$A_{\alpha=0}$ is the area enclosed by zero H_2 contour defining the extent of the mixing region
$\dot{m}_{H_2,mix}$ is mixed H_2 mass flow rate
$\dot{m}_{H_2,total}$ is total H_2 mass flow rate from flow field integration.
When $\alpha_{max} < \alpha_s$, η_m equals 1.0.

Experimental mixing efficiencies for the data from Ref. 3, 4 and 7 are determined by integration of the hydrogen and airflow contours as illustrated in Fig. 2. Overlaying the stochiometric fuel-air contour (α_s = 0.0285) on the H_2 and air flow contours to provide integration limits, the total hydrogen mixed and mixing efficiency are determined by the integration procedure of Eqn. 1. Total hydrogen mixed in the fuel lean region is determined by integration of hydrogen flow rate in that region (Fig. 2b), while hydrogen mixed in the fuel rich region is determined by integration of the air flow rate within the fuel rich region (Fig. 2c).

As discussed in Ref. 3, one indication of the overall accuracy of the profile data is comparison of the integrated hydrogen mass flow rate with the metered hydrogen mass flow supplied to the jet. Figure 3 illustrates this comparison for all data in Ref. 3. Agreement of the integrated and metered mass flows improves as X/D increases and $\bar{q}$ decreases. This improvement is probably due to the smaller gradients in the concentration and velocity which are associated with the local turbulence level at the downstream stations and lower values of $\bar{q}$. It has also been suggested that selective sampling by the subcritical pitot probe produces the low indicated hydrogen composition[30].

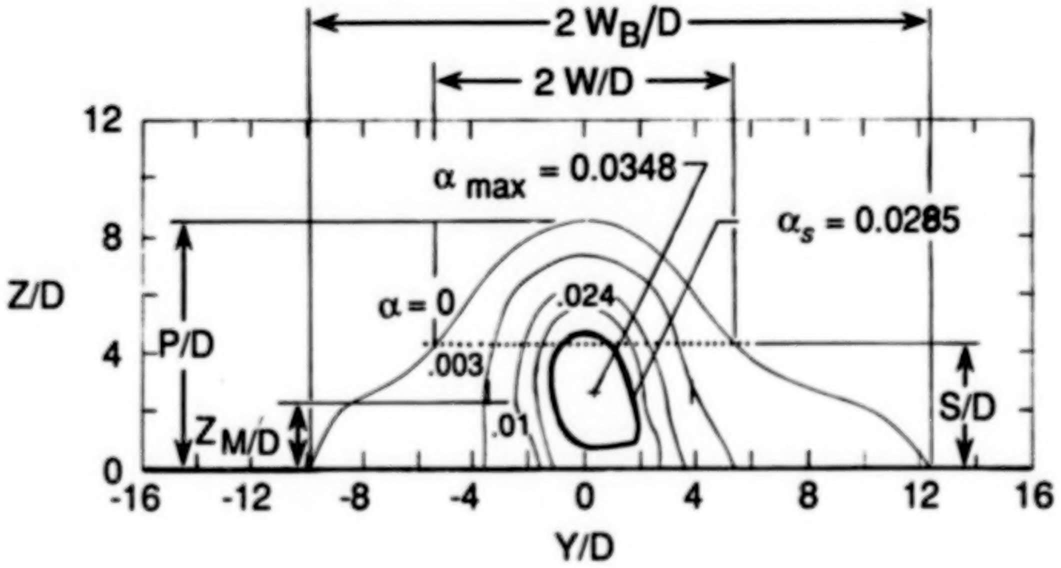

Hydrogen concentration contour

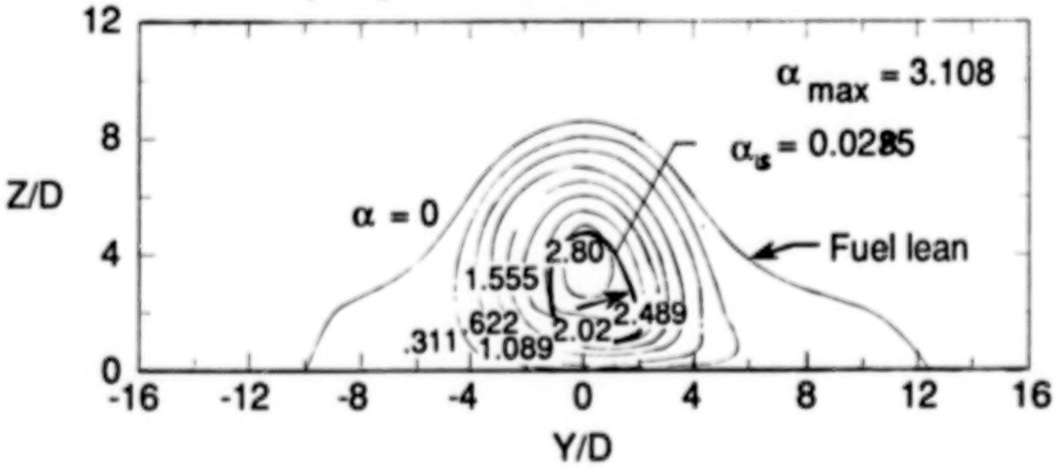

Hydrogen flow rate contours in kg/m²-sec

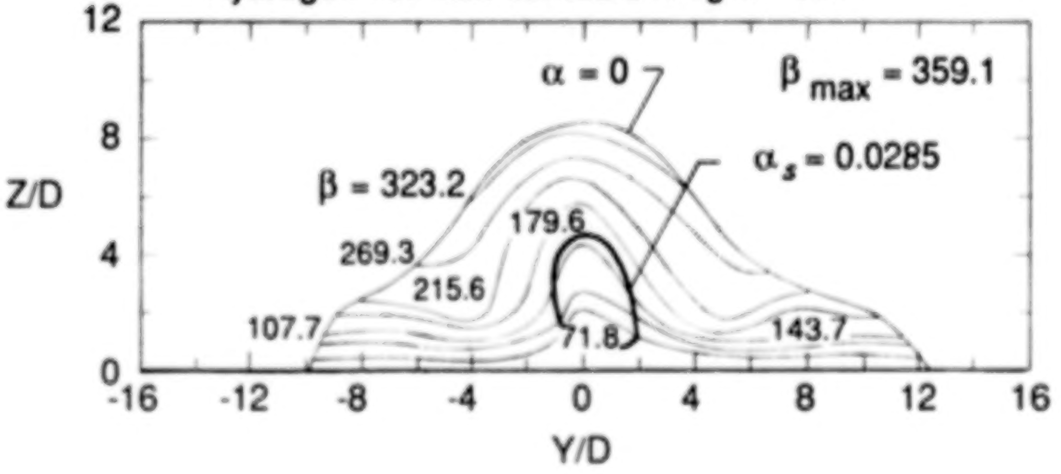

Airflow rate contours in kg/m²-sec

Figure 2. Experimental Determination of Mixing Efficiency.

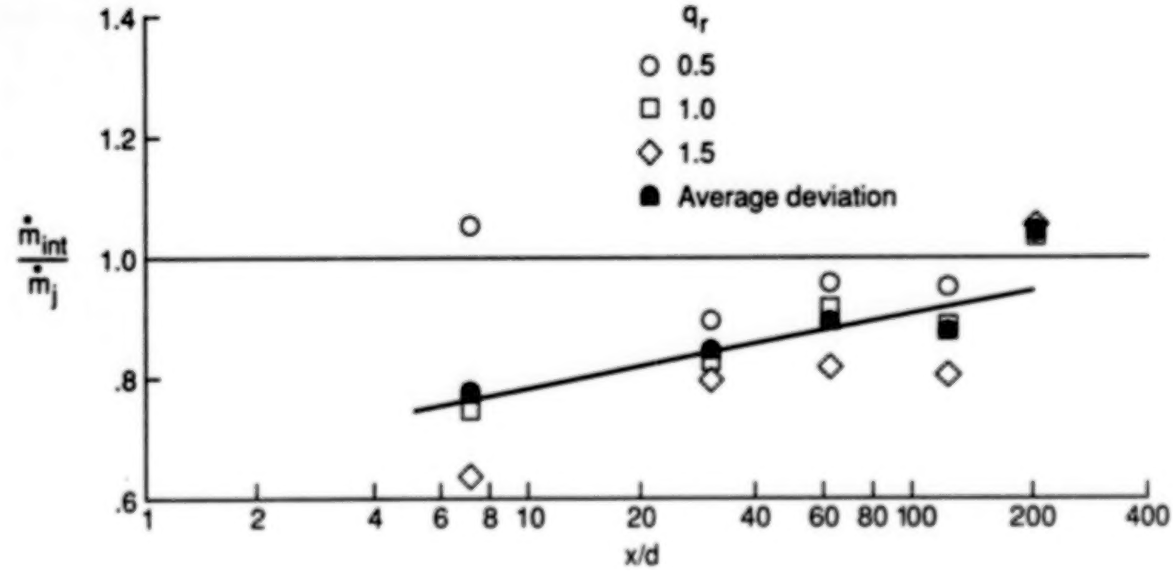

Figure 3. Results of Fuel Mass Flow Contour Integration [Ref. 3].

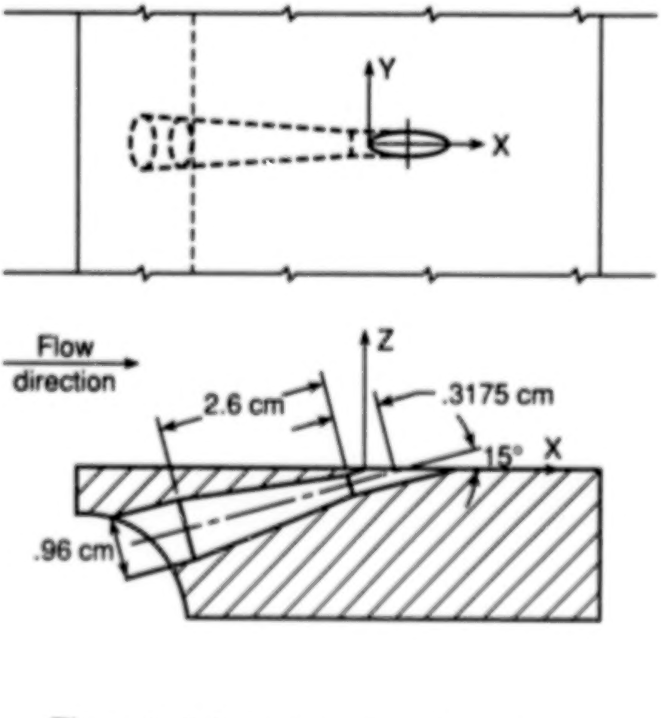

Figure 4. Schematic of 15° Nozzle Design.

Cases 5-7 represent low-angled helium injection experiments performed in a Mach 3, 11x23 cm blow down tunnel at Virginia Tech[30] with injection from the lower tunnel wall. Boundary layer thickness at the fuel injector is about two jet diameters. Geometric details of the 15° injector presented in Fig. 4 illustrate the converging and short 1-d constant diameter section used to provide the sonic helium jet. Nominal test conditions for the cold air and sonic helium injector are presented in Table 2. The facility is operated at a total pressure and temperature of 0.655±.02 MPa and 290 K respectively and helium is injected either at matched or underexpanded pressure. Instream measurements of fuel concentration, flow temperature, pitot and static pressure were obtained at axial stations of 20, 40 and 90 jet diameters downstream of the injector on the jet centerline. Additional surveys of fuel concentration were obtained at off jet centerline locations. The gas sampling probe[31] utilizes a very small internal expansion tip with an internal diameter of 0.028 cm (one tenth the injector diameter), which has sufficient internal expansion and flow suction to swallow the tip shock wave.

DESCRIPTION OF CODES

The LaRC SPARK family of CFD codes was used in this study. The two-dimensional Navier-Stokes code was originally developed and extensively validated for chemically reacting and mixing flows by Drummond[32] and has been expanded to three dimensions and validated by Carpenter[33]; this three-dimensional version has additionally been developed into a parabolized Navier-Stokes (PNS) version by Kamath[34]. The elliptic SPARK code can use either a temporally explicit second-order accurate MacCormack-based finite-difference technique to solve the mass, momentum, and energy conservation equations or a fourth-order compact spatial scheme[33] which provides high spatial accuracy and a convenient method for marching to the steady state. In addition, the code has the fourth-order time accurate Gottlieb scheme[33]. For mixing results, the source terms in the species continuity equations are set to zero.

At the time of this work, the SPARK codes contained only the Baldwin-Lomax algebraic turbulence model. The formulation used contained the constants as presented in the original paper[35] for a thin layer on a flat plate. Freestream turbulence in the tunnel was ignored. For Cases 5-7, the turbulent viscosity was limited to 1000 times the laminar viscosity. It was found in this investigation that the use of $Sc_t < 1.0$ enabled better agreement between numerical results and experimental data. There is both experimental and computational justification for the use of turbulent Schmidt numbers less than unity for flows such as that examined in this work[36,37].

SOLUTION METHODOLOGY

Due to limited computational resources, the solutions were performed in a piece-wise elliptic/PNS fashion. The flowfield upstream of the elliptic injection region is modeled using the SPARKPNS code in 2-d mode. The injection nearfield region, which is highly three-dimensional and characterized by such features as large-scale vorticity, separation ahead of and behind the injector, strong shocks and expansions, was computed with the 3-d elliptic version of the SPARK code. The injection region extended from six to ten jet diameters ahead of the injector to ten to forty jet diameters downstream of the injector, depending on the case. The 3-d SPARKPNS code was used in the farfield with the outflow plane from the elliptic code passed as a fixed inflow into the PNS code. A small inconsistency is inherent in this strategy which is illustrated in Fig. 5, since the character of the governing equations is changed discontinuously from the full Navier-Stokes (FNS) to that of the parabolized approximation. However, this was considered an acceptable compromise to achieve computational efficiency, and the inconsistency involved in the passing of a plane from the full Navier-Stokes elliptic domain to the parabolized version of these equations are believed to be small in

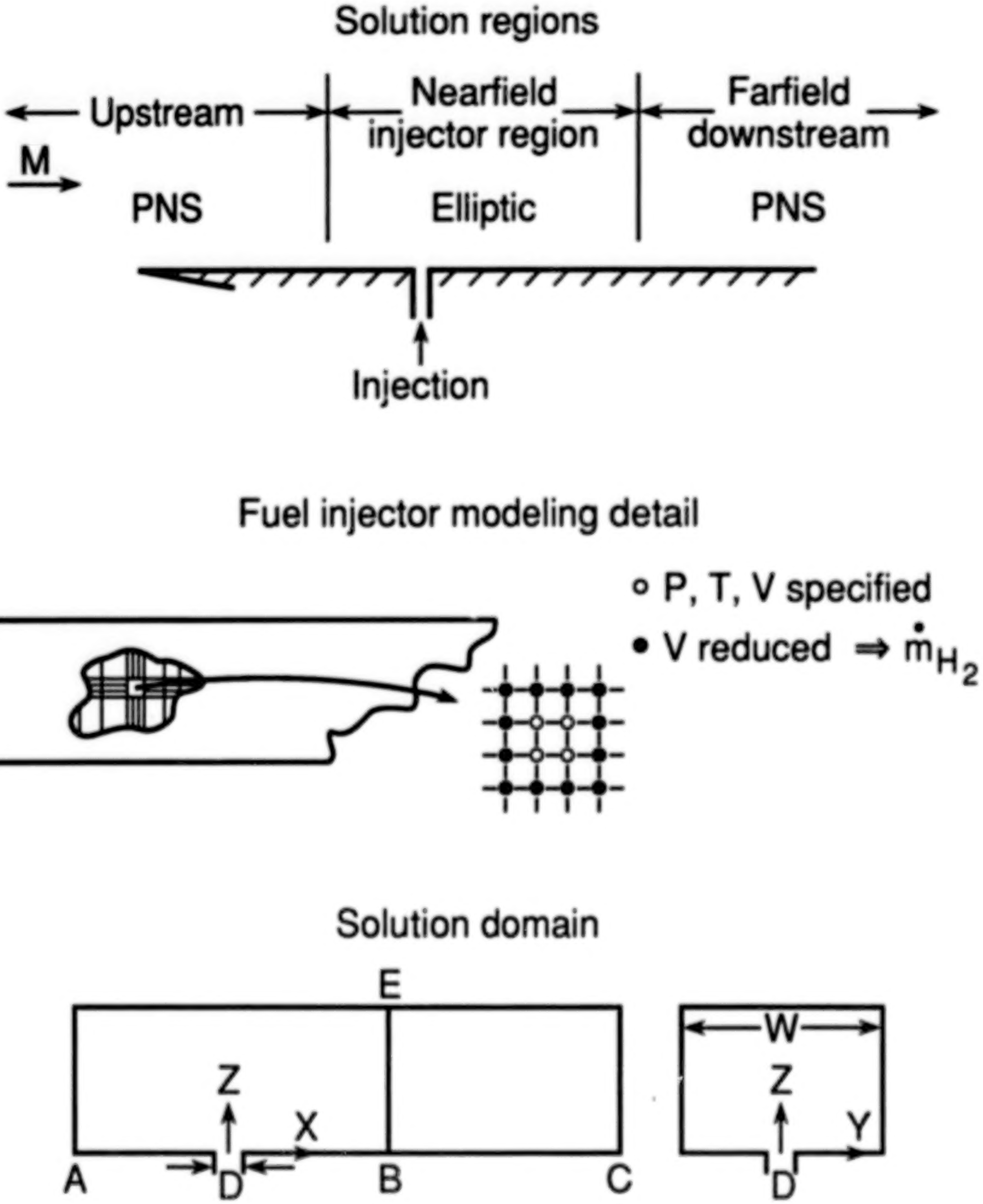

Solution regions

Fuel injector modeling detail

Solution domain

Figure 5. Solution Methodology

relation to turbulence and grid issues.

The computations presented here were performed on the Cray supercomputers of the Numerical Aerodynamic Simulation (NAS) at NASA Ames and the Cray 2 at LaRC. The mixing studies each took about 2-10 hours of CPU time. Convergence as defined in the next section occurred at about 10000 iterations. The parabolized computations in this study comprised about 15% of the CPU time used and a fraction of the memory.

CONVERGENCE REQUIREMENTS

Due to the swirling nature of the flow around and behind the injectors, the flow is at best quasi-steady, and there is some small fluctuation of pressure in the elliptic region as well as for flow parameters in the outflow plane passed to the parabolized code. Claimed convergence for an elliptic solution of this nature must be limited in its scope to the unchanging mean or averaged values of the parameters of interest such as density ($(\Delta\rho)_{max} < 5\%$) and the conservation (within 10%) of total fuel for all axial planes.

GRID AND BOUNDARY CONDITIONS

Grids for each solution discussed herein are summarized in Table 3. All cases used a rectangular grid for both the parabolic and elliptic regions with the downstream parabolic region having the same cross-sectional grid as in the elliptic. All meshes were clustered near the injector and near the plate. Grid domain represents the number of nodes in the axial, lateral and vertical directions. The last 5 columns in the table deal with grid dimensions in terms of jet diameter with the origin at the injector center (Fig. 5).

All inflow boundary values were fixed. No-slip boundary conditions were applied to the flat plate, which was either at a constant temperature or adiabatic. All of the circular injectors were modeled as rectangles on the mesh lower boundary (the plate). The nodes within the orifice had their properties set to the jet properties calculated from the stagnation properties listed in Table 2. The computational injector was modeled to match the injector area. The computational area and/or the velocity on the jet edge nodes were then reduced to match the metered injectant mass flow, thereby simulating a discharge coefficient due to losses near the injector walls. All other boundary planes were set as outflow planes, except for those of Case 4 which had multiple injectors and thus two symmetry planes. (Table 3 also lists the number of nodes used to model an injector. At each such node, the jet conditions were applied.)

Table 3. Grid and Solution Details

Case	Domain	Injector	Sc_t	T_w	A/D	B/D	C/D	E/D	W/D
1	41x61x41	25	0.2,0.5	250.	-6	10	120	16	32
	41x51x51	20	0.2	250.	-6	10	120	16	16
2	51x31x41	25	0.2,0.5,1.0	300.	-16	33	120	49	49
	51x31x21	25	0.2,0.5,1.0	300.	-16	33	120	49	49
	41x25x21	9	0.2,0.5,1.0	300.	-16	33	120	49	49
3	41x61x41	25	0.2	250.	-6	10	120	16	32
4	41x31x41	25	0.2	300.	-6	10	120	14	6.25
5	51x41x41	35	0.5	adia.	-6	10	90	16	16
6	51x41x41	35	0.5	adia.	-6	10	90	16	16
7	51x41x41	55	0.5	adia.	-6	10	90	16	16

RESULTS

This section presents computational results and comparisons with experimental data for the seven cases. The computational analysis was performed with several values of turbulent Schmidt number, and one case was evaluated using several mesh densities. Details of these variations are highlighted. The following section will discuss the implications of these findings and give recommendations on applying the SPARK or equivalent CFD codes to fuel injector problems.

Case 1

Computational results for Case 1 are presented in Figs. 6-9. Two different solutions were obtained: one with $Sc_t = 0.2$ and one with $Sc_t = 0.5$. Hydrogen concentration contours in the vertical X-Z plane through the jet centerline are given in Fig. 6 for the solution with $Sc_t = 0.2$. These results illustrate fuel feeding upstream into a region of boundary layer separation, the penetration and dispersion of the hydrogen core in the nearfield, and penetration of the outer edge of the fuel. Note that the $\alpha = 0.10$ contour (3.5 times stochiometric) extends about 3 jet diameters upstream of the injector centerline, and the .005 contour extends to about 4 jet diameters upstream. The hydrogen core (i.e. the region of highest concentration extending downstream from the initial jet, indicated by the dashed line in Fig. 6a) penetrates to about 1.2 jet diameters above the flat plate and the 0.40 contour (an arbitrarily selected indicator of core breakup) persists about 6.5D downstream. The peak hydrogen concentration moves back toward the plate and lies along the surface for axial stations past 10 diameters. Fig. 6b shows combined FNS and PNS results and indicates complete mixing by 80D downstream ($\alpha < \alpha_s$ everywhere).

Computational and experimental results are compared in Fig. 7 by lateral Y-Z plane hydrogen mass fraction contours at the 120D station. The outer edge of the fueled region is represented here by the 0.003 H_2 mass fraction contour. The computational results have greater penetration P/D (see Fig. 2a) and lateral spreading than experimental results with the spreading near the plate W_b/D nearly double that of the experiment. However, the computed 0.010 hydrogen mass fraction contour illustrates slightly (≈20%) lower penetration and slightly (≈25%) greater spreading than the experimental contour.

Computed vertical jet centerline profiles ($Sc_t = 0.2$) at the 120 jet diameter station are presented in Fig. 8 and compared with measured H_2 mass fraction, static pressure, static temperature and velocity. The profiles are in reasonable agreement, except for the location of the peak hydrogen concentration. The dashed curve represents results from a solution with $Sc_t = 0.5$ in both elliptic and parabolized solutions. Again, the peak concentration is adjacent to the wall, but the peak value is nearly double that measured because of reduced mass transport. However, penetration to the outer edge of the mixing region is not significantly affected by the value of Sc_t

Longitudinal variation in predicted fuel mixing efficiency is presented in Fig. 9 for both solutions discussed above. Mixing efficiency presented in this figure is **NOT** as defined in Eqn. 1. because of an error in the CFD code used for this and the other hydrogen cases. Mixing efficiency, η_m', for Fig. 9 is defined by Eqn. 1, but with

$$\alpha_s = 0.01425 \tag{2}$$

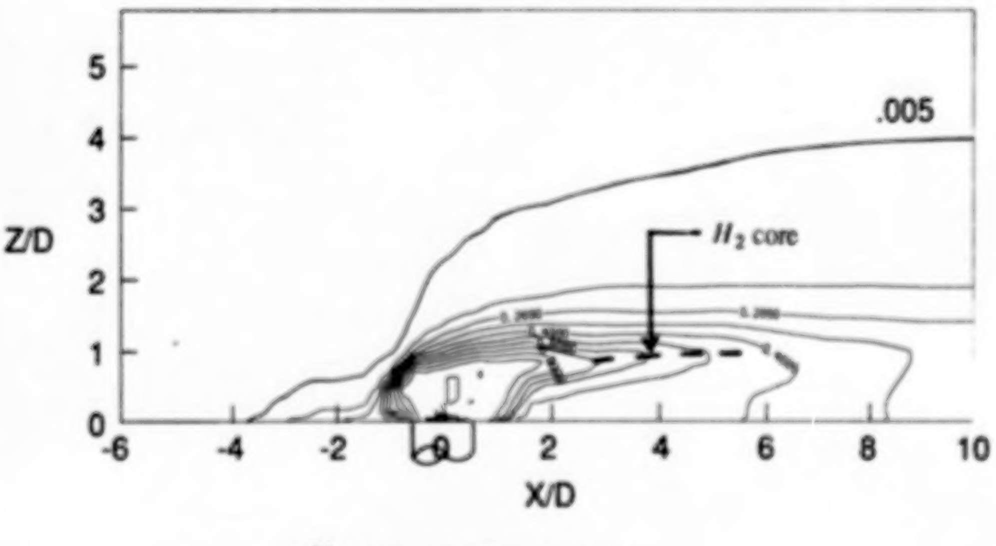

a) H_2 contours, elliptic region.

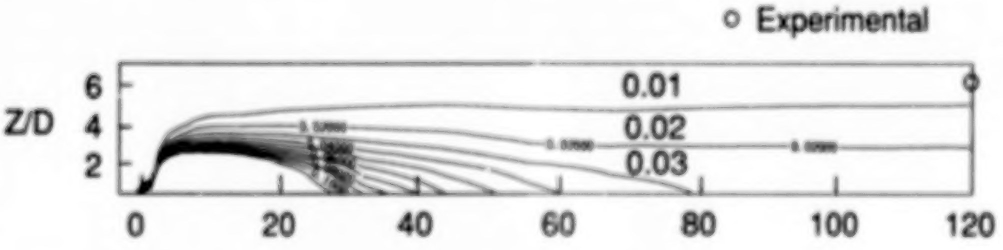

b) H_2 contours, elliptic plus PNS region.

Figure 6. Longitudinal Hydrogen Mass Fraction Contours; Case 1, $Sc_t = 0.2$.

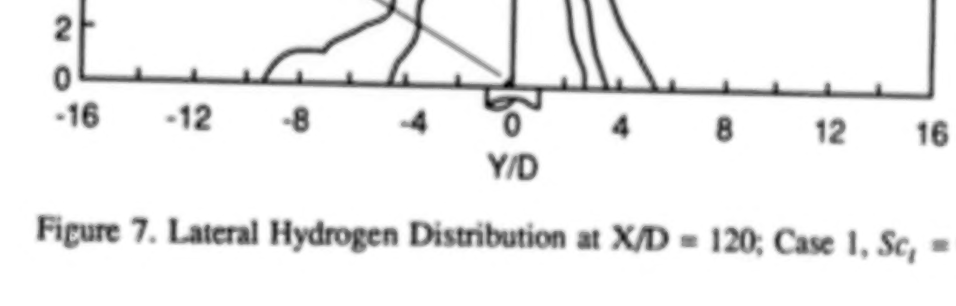

Figure 7. Lateral Hydrogen Distribution at X/D = 120; Case 1, $Sc_t = 0.2$.

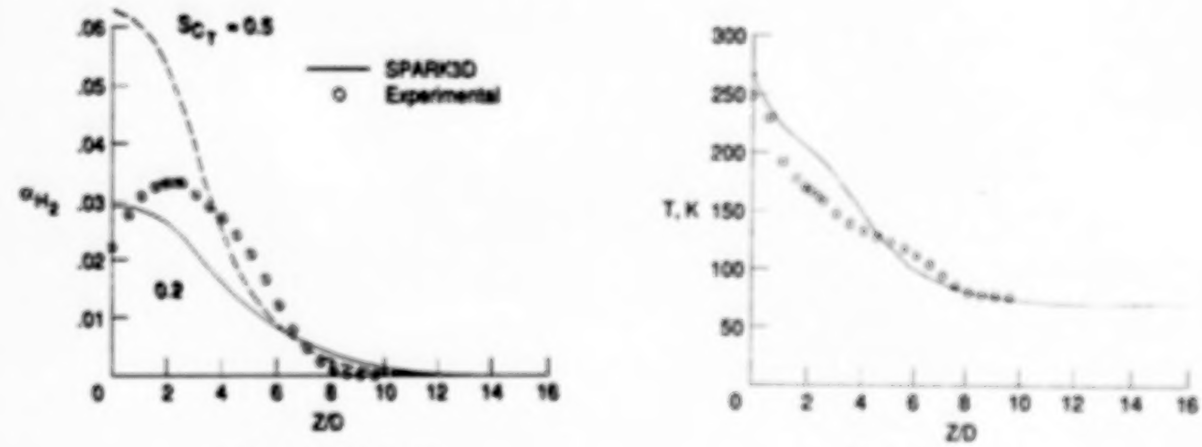

a) H_2 Mass Fraction

b) Temperature

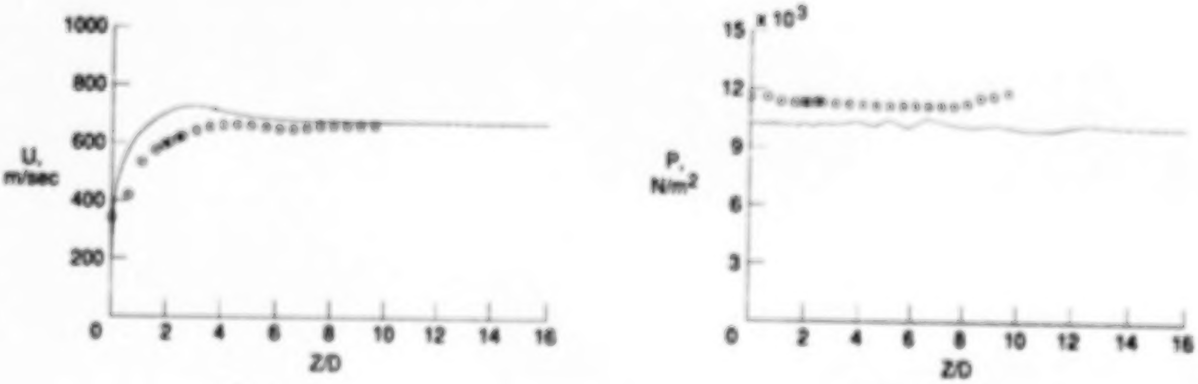

c) Velocity

d) Pressure

Figure 8. Vertical Centerline Profiles at X/D =120; Case 1, $Sc_t = 0.2$.

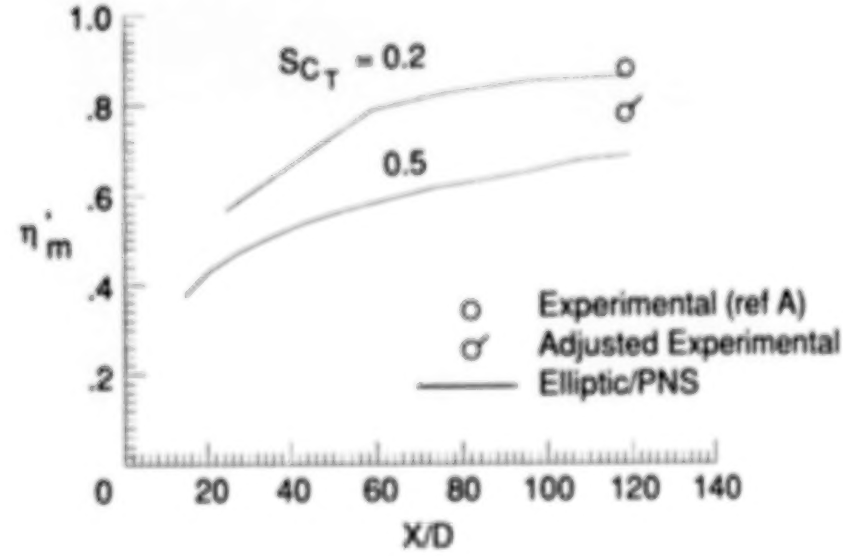

Figure 9. Fuel Mixing Efficiency Distribution; Case 1.

Experimental η'_m determined by integration of Ref. 4 contours at X/D = 120 is presented by unflagged symbol. Although this is not the standard definition, the comparison of experimental and computational results using this method provides a reasonable percent error in modeling mixing efficiency. For this case, between 10% to 20% of the injected fuel was not accounted for in the experimental downstream survey. The flagged symbol represents the mixing efficiency if all of the missing fuel is assumed to be unmixed; i.e.:

$$(\eta'_m)_{adj} = \int_{A_{\alpha\neq 0}} \frac{\alpha_R \rho u dA}{\dot{m}_{H_2,inj}} \tag{3}$$

where α_R is defined by Eqn. 2. Computational results are in good agreement with experimental results when performed using Sc_t = 0.2 and with the adjusted experimental result when using Sc_t = 0.5. At the 120 diameter station, the calculated mixing efficiency for Sc_t = 0.5 is only 20% lower than for Sc_t = 0.2, whereas α_{max} is more than double for the Sc_t = 0.2 case. The use of an adjusted mixing efficiency results from concern about quality of this older data in light of good agreement with the newer He injection data for Cases 5-7. This adjusted mixing efficiency represents the lowest bound of experimental scatter conceivable to account for limitations.

Case 2

Ten computational solutions were obtained for Case 2 for three different values of the turbulent Schmidt number on three different density grids plus one laminar fine grid solution. Figures 10-13 illustrate flow details obtained with a fine grid and Sc_t of either 0.2 or 0.5. Figures 14-15 illustrate the sensitivity of mixing efficiency to various grids and Sc_t plus one laminar solution.

Hydrogen contours (Sc_t = 0.5) presented in Figs. 10a,b illustrate fuel penetration, decay of the core and details of the upstream flow separation. The 0.10 contour (3 times stochiometric) extends less than 1.5 jet diameters upstream of the jet centerline, and the .005 contour extends about 3.5 diameters upstream. The H_2 core penetrates about 2D, and the 0.40 contour persists about 6.2D downstream. Peak concentration moves back to the wall at about X/D = 25 (not shown). Comparison with experimental penetration of the 0.010 hydrogen mass fraction contour are within 10% at X/D = 7, 30, 60 and 120 (Fig. 10b).

Hydrogen contours (Sc_t = 0.5) presented in Fig. 10c illustrate fuel penetration, decay of the core and details of the upstream flow separation for the same jet with the same inflow plane including boundary layer profile, but with no turbulence in the elliptic region. As expected for a disturbed laminar flow, the upstream separation region has become quite extensive (It should be noted that this solution is not completely converged). The H_2 core penetrates about 2.3D, and the 0.40 contour persists about 8D downstream. Both of these values are slightly greater than for the turbulent solution.

Computed lateral spreading of the fuel at X/D at 120D is illustrated in Fig. 11 for each value of Sc_t for the fine mesh. At Z/D = 4.0, lateral spreading W/D (see Fig. 4) of all computational contours is greater than experimental values, and higher Sc_t produces less spreading. At Z/D = 0, lateral spreading W_b/D of all computational contours is in reasonable agreement with the experimental results. Fuel penetration (P/D) increases for the lowest value of Sc_t, but all cases exceed experimental results.

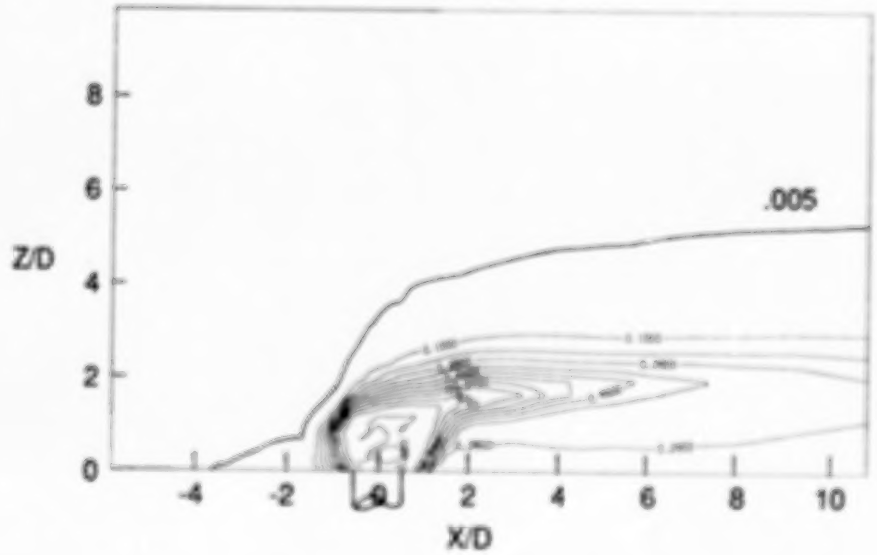

a) H_2 contours, elliptic region.

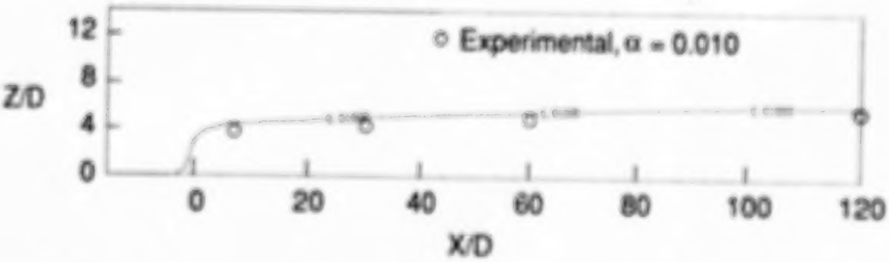

b) H_2 contours, elliptic plus PNS region.

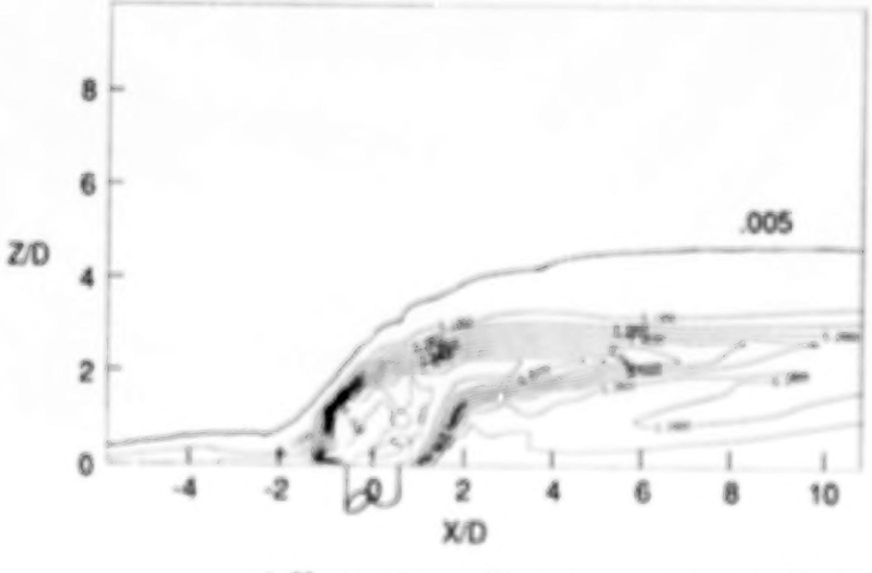

c) H_2 contours, elliptic region, Laminar Flow.

Figure 10. Longitudinal Hydrogen Mass Fraction Contours; Case 2, $Sc_t = 0.5$.

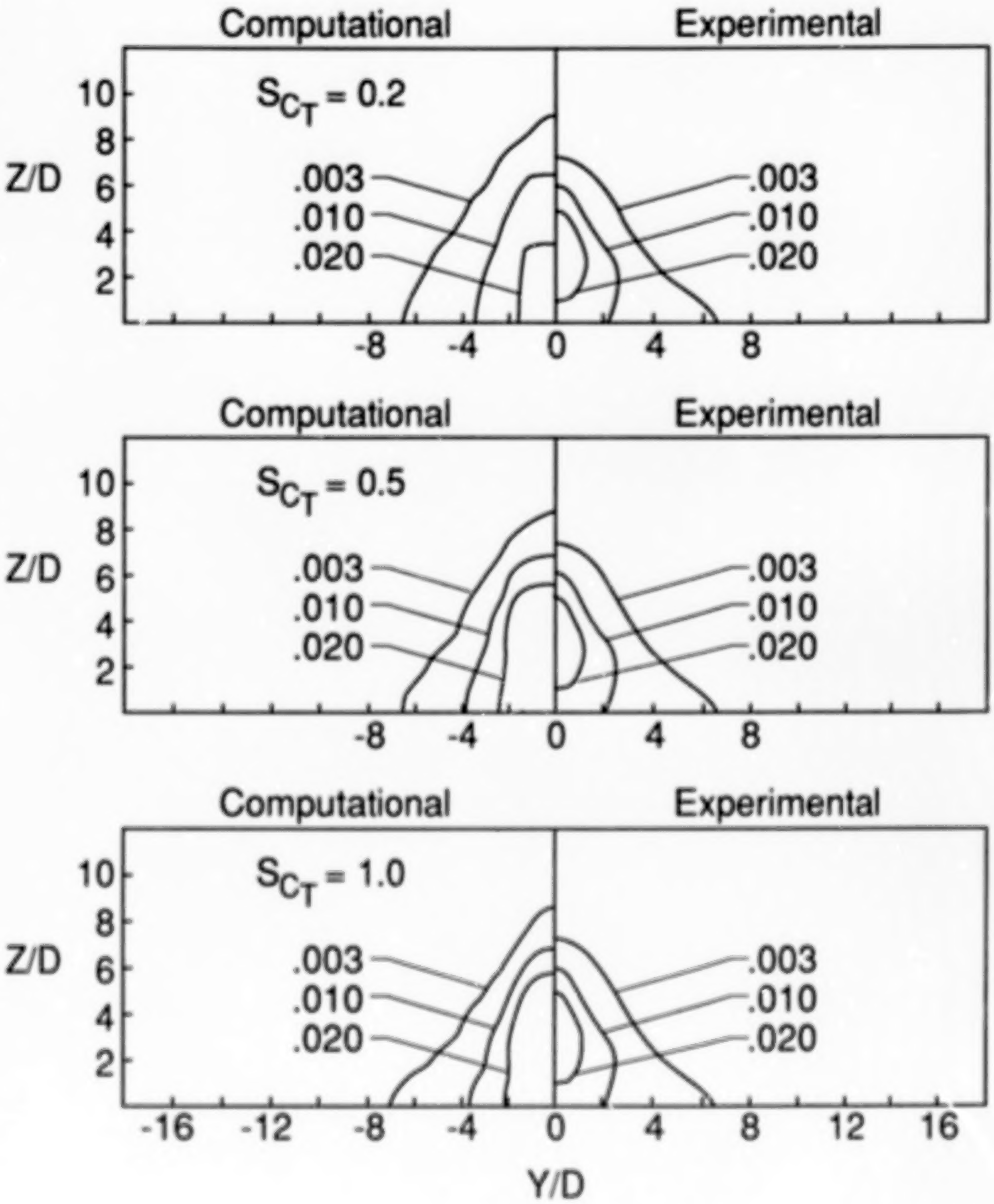

Figure 11. Lateral Hydrogen Distribution at X/D = 120; Case 2.

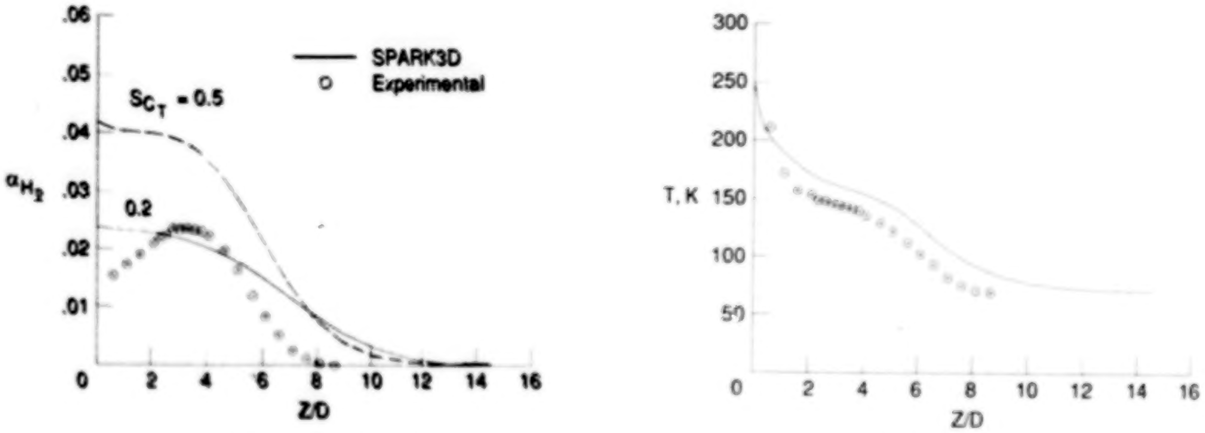

a) H_2 Mass Fraction

b) Temperature

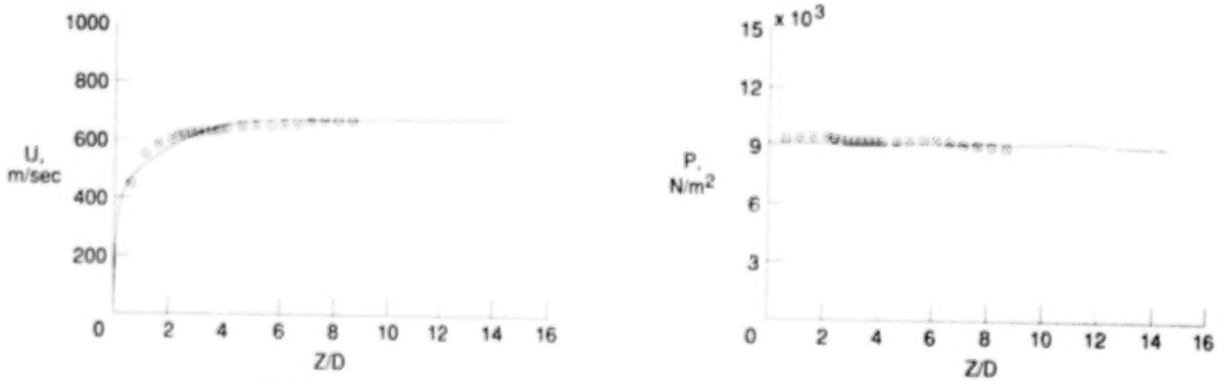

c) Velocity

d) Pressure

Figure 12. Vertical Centerline Profiles at X/D =120; Case 2, Sc_t = 0.2.

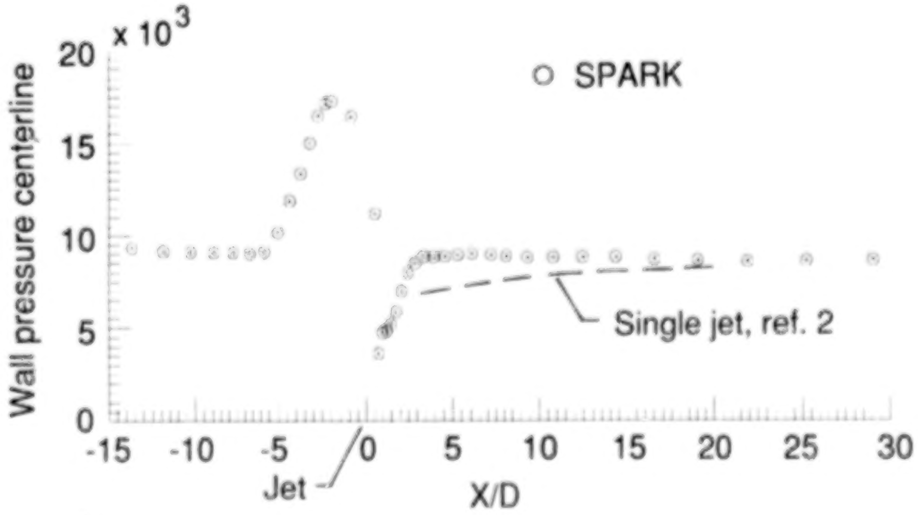

Figure 13. Longitudinal Centerline Wall Pressure; Case 2, Sc_t = 0.5.

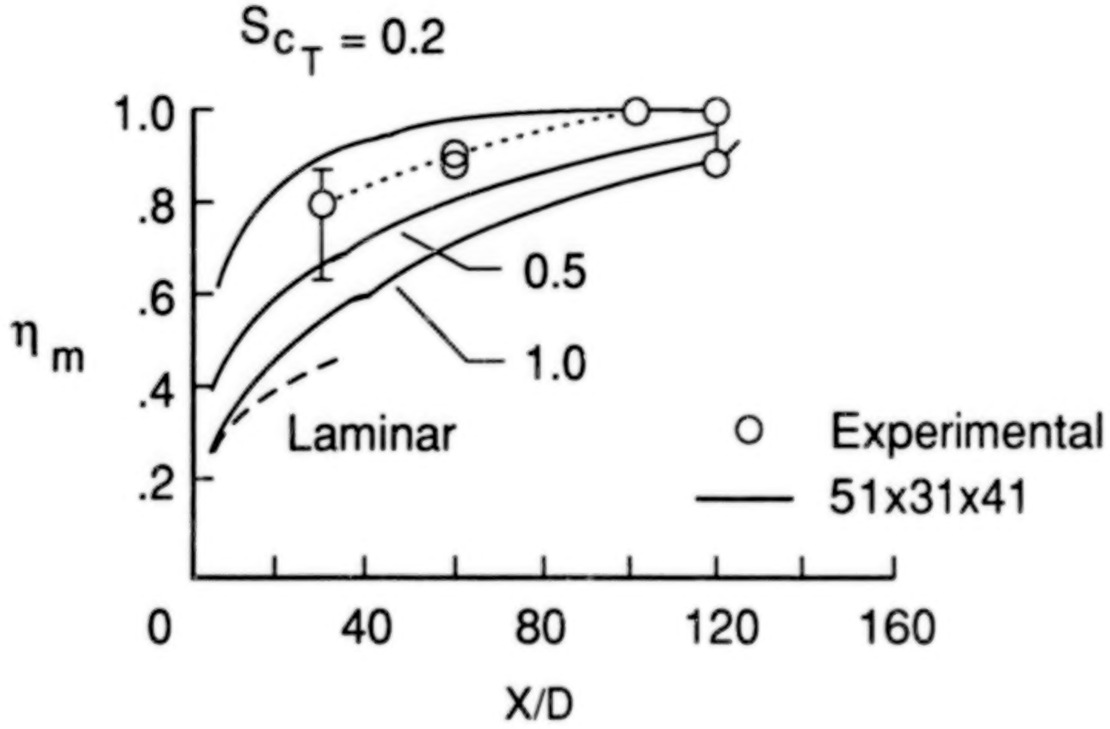

Figure 14. Fuel Mixing Efficiency Distribution; Case 2.

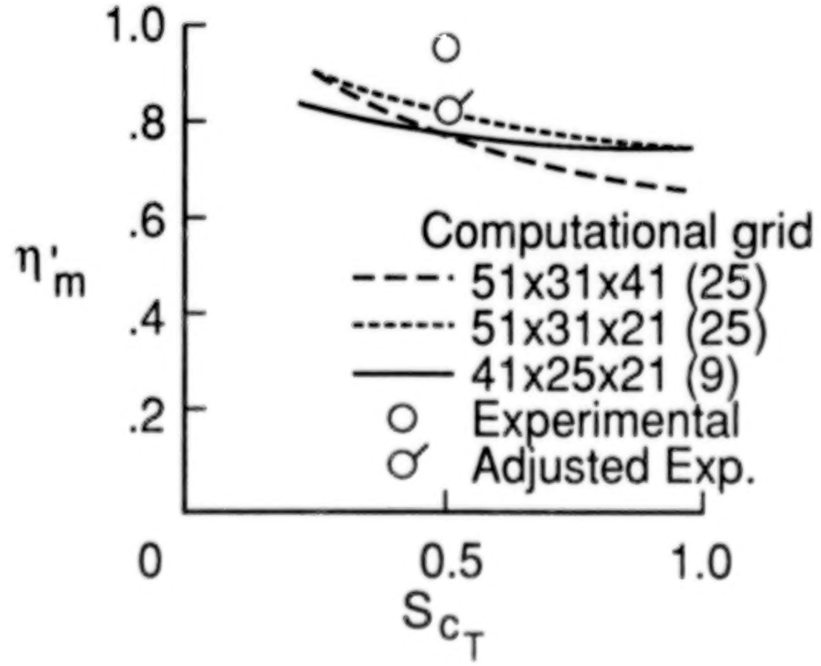

Figure 15. Fuel Mixing Efficiency at X/D = 120; Case 2.

Computed vertical jet centerline profiles (Sc_t = 0.2) at the 120D station are presented in Fig. 12 and compared with measured hydrogen mass fraction, static pressure, static temperature and velocity. Computed profiles are in excellent agreement with experimental results except for the fuel concentration. The magnitude of the peak computed hydrogen concentration is in excellent agreement with data but is offset to the wall. The dashed curve illustrates the computed H_2 mass fraction using Sc_t = 0.5. Peak concentration is about 80% higher than for the Sc_t = 0.2 solution.

Longitudinal jet centerline wall pressure distribution (Sc_t = 0.5) in the nearfield is illustrated in Fig. 13. These results show the extent of jet disturbance on upstream flow, recovery pressure in the upstream recirculation region, and low pressure in the wake downstream of the injector. Note that the pressure rise extends to 5.5D ahead of the injector, which is significantly greater than the "zero" hydrogen contour (α = .005) presented in Fig. 10a. Downstream pressure is in reasonable agreement with wall pressure data scaled from experiments in Ref. 2. Calculated results presented are closer to the injector than could be measured experimentally.

Calculated longitudinal distributions of mixing efficiency for Case 2 are illustrated in Fig. 14 for fine mesh solutions using Sc_t = 0.2, 0.5 and 1.0; and in Fig. 15 for all solutions at X/D = 120. Mixing efficiency presented in Fig. 14 is as defined by Eqn. 1; whereas the mixing efficiency presented in Fig. 15 was calculated using the incorrect value of stochiometric mass fraction presented by Eqn. 2. Experimental data presented on each figure have been adjusted to the appropriate definition. Fig. 14 illustrates the effect of turbulence on the mixing efficiency distribution. A laminar solution (Sc_t = 0.5) in the elliptic region illustrates that turbulence modeling is not an issue for the first 4 jet diameters downstream of the jet, as both the laminar and turbulent solutions have identical mixing efficiencies. However, Sc_t has a large impact in the downstream mixing, because it is used to determine the turbulent mass diffusivity from the turbulent viscosity. For Sc_t = 0.2, fuel mixing is complete (η_m = 1.0) at about X/D = 80, whereas experimental measurements indicate η_m reaches unity at about X/D = 100. Using Eqn. 3 to adjust mixing to account for all hydrogen injected produces flagged data points which are in better agreement with the Sc_t = 0.5 computational results. Between X/D = 5 and 30, turbulent mixing is about 50% higher than laminar mixing.

Figure 15 illustrates the effect of mesh density and turbulent Schmidt number on the fuel mixing efficiency $\eta_m^{/}$ at X/D = 120. Experimental points were obtained using Eqn. 1 and 2 to integrate data from Ref. 3. Adjusted data is from Eqn. 2 and 3 using data from Fig. 3 to determine the ratio of integrated total fuel to metered fuel flow rate. Fig. 15 illustrates the large impact of reduced turbulent Schmidt number on $\eta_m^{/}$ for fine grid solutions. Mixing efficiency is seen to increase from about 65% with Sc_t = 1.0 to 92% with Sc_t = 0.2. Coarse grids do not have as large a sensitivity to turbulent Schmidt number. Changing vertical mesh from 41 to 21 results in increased predicted mixing for Sc_t = 1.0 from 65% to 75% and no change for Sc_t = 0.2. The 41x25x21 mesh is coaser both in the x and y directions, as well as having the injector defined by 9 nodes versus 25 for the other cases, and the solutions are even less sensitive to Sc_t than other grids. Note that all solutions with Sc_t = 0.5 predict η_m = 0.79±0.04. Note also that the data is in the best agreement with fine grid solutions with Sc_t = 0.2 for this case.

Case 3

Only one computational solution was performed for the smallest normal jet, and results from that case are illustrated in Figures 16-18. The solution utilized a turbulent Schmidt

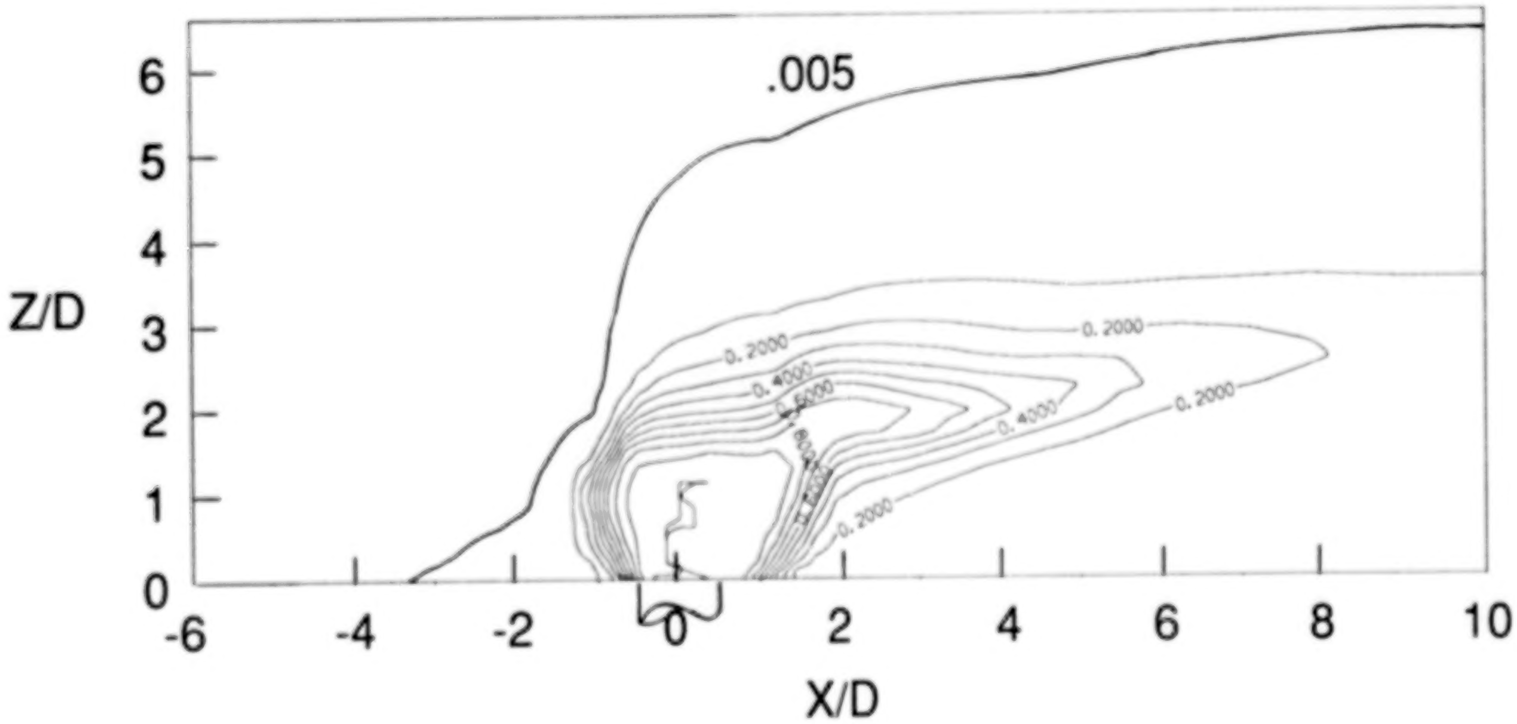

Figure 16. Longitudinal Hydrogen Mass Fraction Contours; Case 3, $Sc_t = 0.2$.

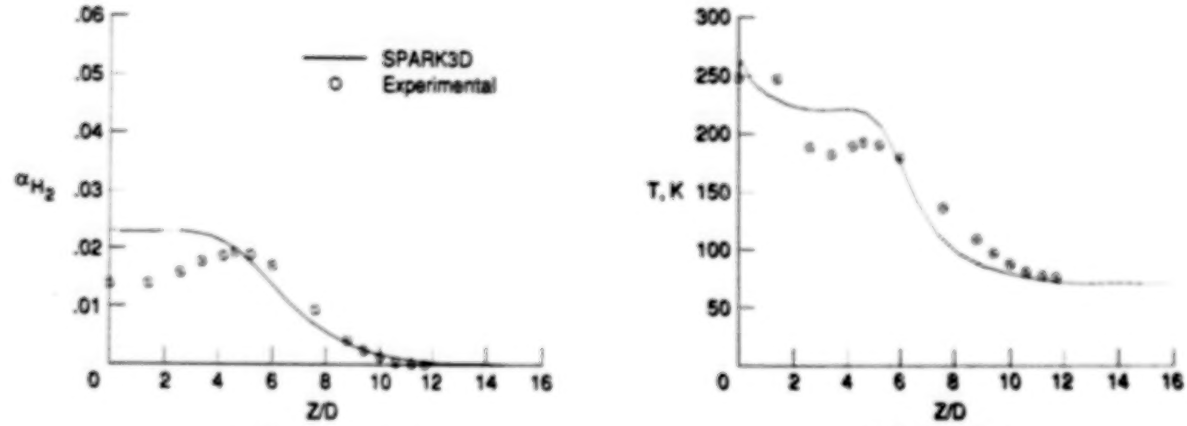

a) H_2 Mass Fraction

b) Temperature

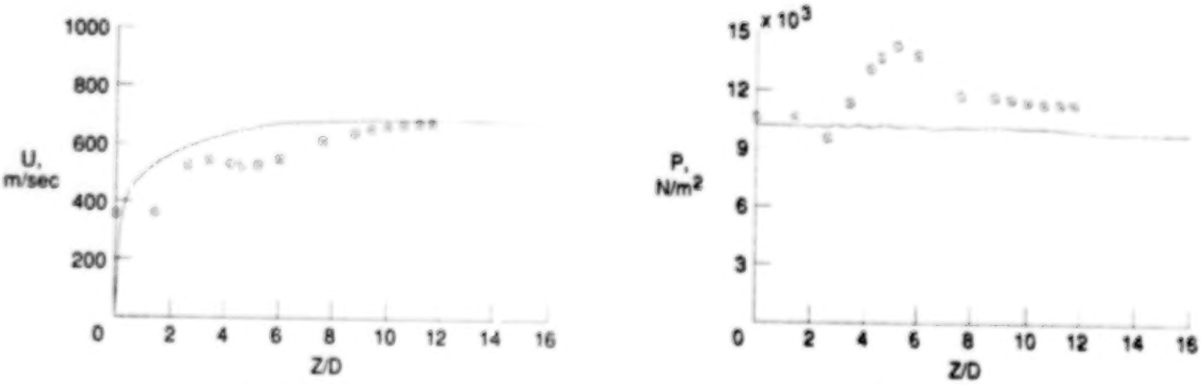

c) Velocity

d) Pressure

Figure 17. Vertical Centerline Profiles at X/D =120; Case 3, Sc_t = 0.2.

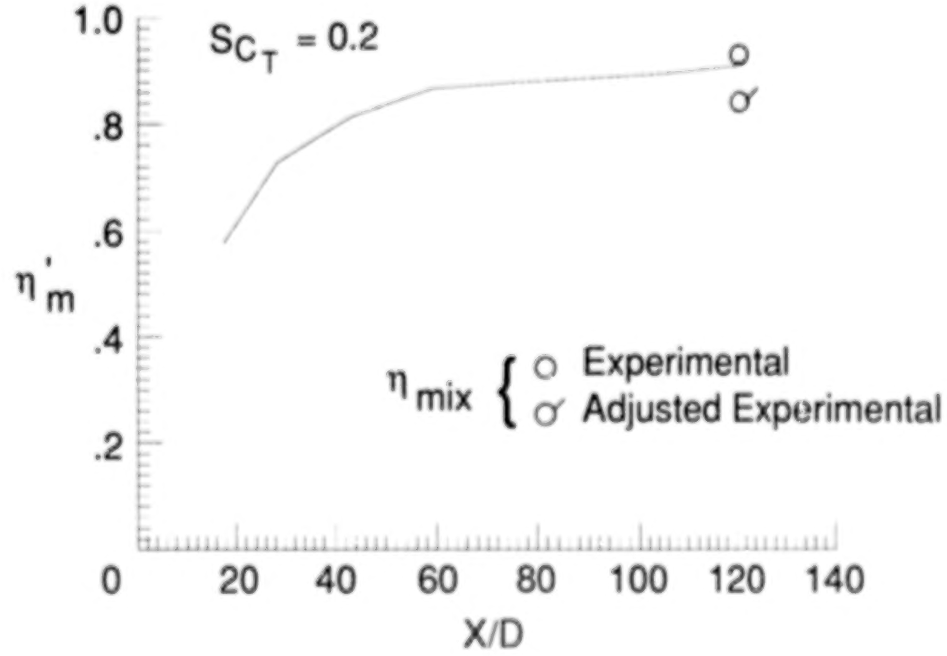

Figure 18. Fuel Mixing Efficiency Distribution; Case 3, Sc_t = 0.2.

number of 0.2.

Hydrogen contours presented in Fig. 16 illustrate fuel penetration, decay of the hydrogen core, and details of the upstream flow separation region. The 0.10 contour extends only about 1.1D upstream of the jet center, and the .005 contour extends about 3.2D upstream. The hydrogen core penetrates about 2.5D, and the 0.40 H_2 concentration persists only 5 jet diameters before dispersing.

Vertical jet centerline profiles at the 120D station are compared in Fig. 17 to experimentally measured values. In addition to the high fuel concentration at the wall for the computational results, the major differences arise from the variation in experimentally measured static pressure between 2 and 5 diameters from the wall. Because of the relative uniformity of the pressure for the other hydrogen cases, the pressure variations in the experimental data here are suspect. Notice the reasonable although slightly overpredicted maximum H_2 concentration and the extremely accurate agreement in the penetration of the .005 contour.

Computational mixing efficiency, η_m' defined in the nonstandard way discussed above (Eqn. 1 and 2) for Case 3 is compared with experimental results in Fig. 18. Whereas the correctly defined mixing efficiency is 100%, this nonstandard mixing efficiency actually allows quantitative comparison of two fully mixed results. Computational results using $Sc_t = 0.2$ underpredict the experimental mixing efficiency by 4% and over predict the adjusted mixing efficiency by 8%, consistent with predictions for Case 1 which had the thin boundary layer.

Case 4

Only one computational solution was obtained for the 30° multiple hydrogen jets. The solution utilized a turbulent Schmidt number of 0.2, and results from that case are illustrated in Figures 19-21.

Hydrogen contours presented in Fig. 19 illustrate fuel penetration, decay of the hydrogen core, and details of the upstream flow separation region. The 0.10 contour extends about 2.0D upstream of the jet center, and the .005 contour extends about 2.5D upstream. The core penetrates about 2.0D, and the 0.40 H_2 concentration persists only 5.4 jet diameters before dispersing.

Vertical jet centerline profiles at the 120D station are compared in Fig. 20 to experimentally measured values. As with the cases from Ref. 4, the computed pressure underpredicts experimental values at the 120D station. Small differences in predicted and measured temperature and velocity are believed associated with boundary layer energization by the downstream angled fuel. Note that at $Z/D = 2$ the velocity is higher than the freestream value. Peak hydrogen mass fraction occurs at the wall for the computed flow, compared to about 3D above the wall for the data. The computed α_{max} is about 33% higher than experimental measurements. Based on results for Cases 1-3, this difference suggests that the predicted mixing efficiency for $Sc_t = 0.2$ is about 6% lower than the experimental values.

Longitudinal jet centerline wall pressure distribution in the nearfield is illustrated in Fig. 21. These results show the extent of the flow disturbance upstream of the injector and a very small low pressure region downstream of the injector. The pressure rise extends about 1D farther upstream than the .005 H_2 mass fraction contour. Unlike the Case 2 results, the downstream pressure increases following a low pressure region. This rise in pressure is believed to be associated with the multiple jet interacting bow shocks. Data at 3D on the jet centerline is

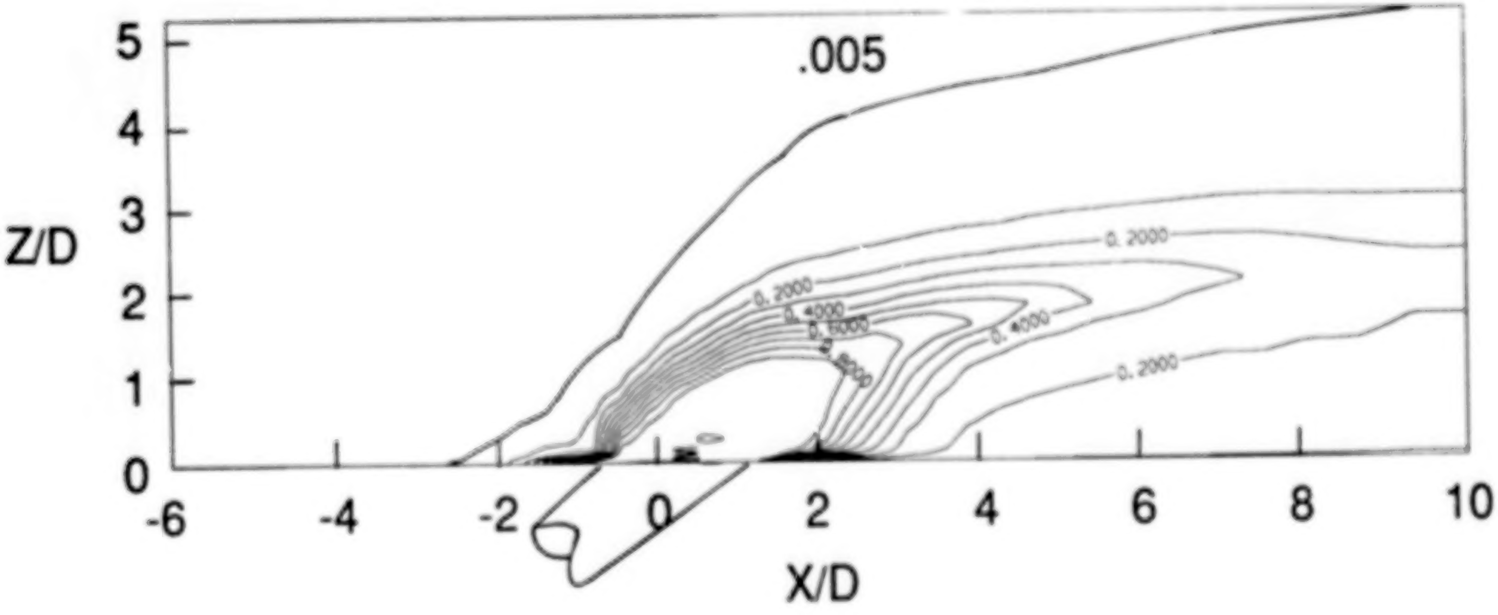

Figure 19. Longitudinal Hydrogen Mass Fraction Contours; Case 4, $Sc_t = 0.2$.

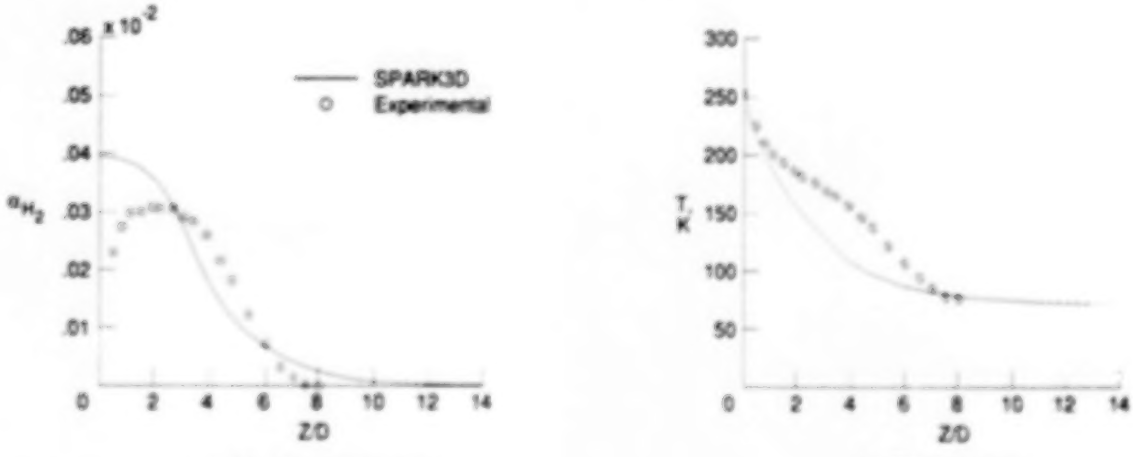

a) H_2 Mass Fraction

b) Temperature

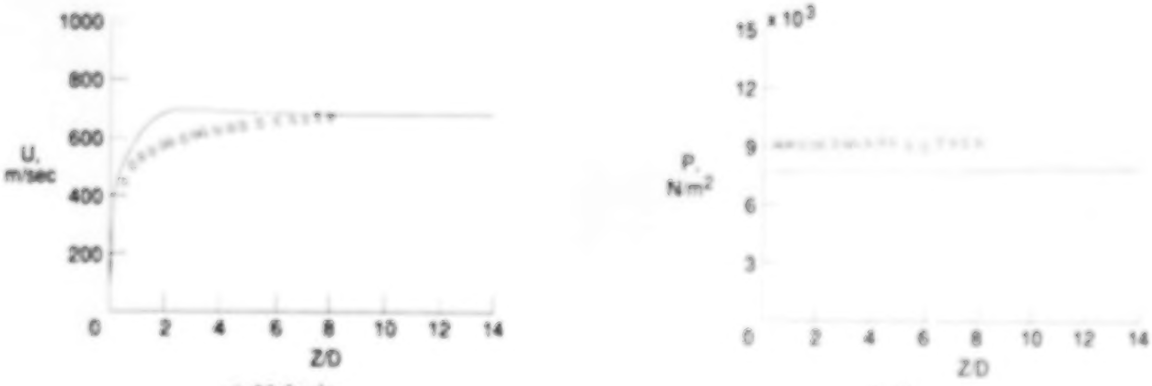

c) Velocity

d) Pressure

Figure 20. Vertical Centerline Profiles at X/D =120; Case 4, Sc_t = 0.2.

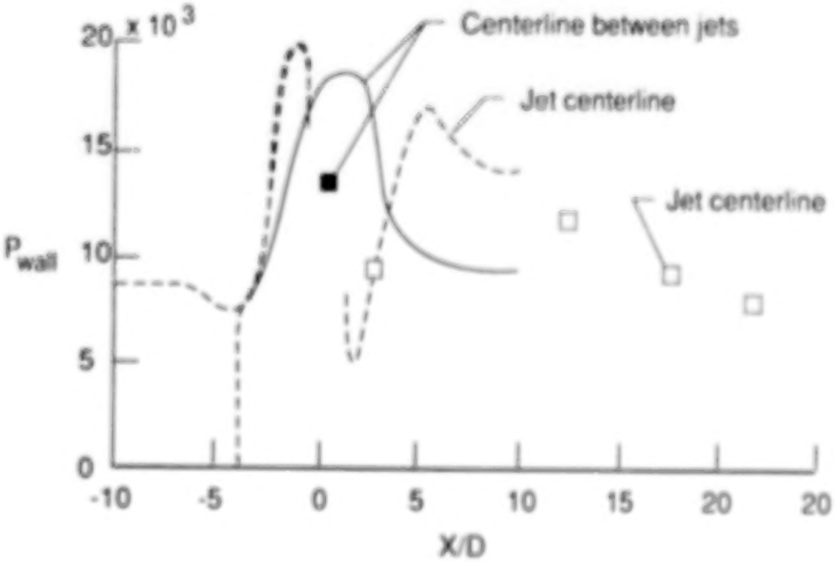

Figure 21. Longitudinal Centerline Wall Pressure; Case 4, Sc_t = 0.2.

in good agreement with prediction, however the data between jets is not.

Case 5

Only one computational solution was obtained for each of Cases 5 through 7. These solutions used $Sc_t = 0.5$, because that value provided excellent agreement with the experimental data. Comparisons of computational and experimental results for Case 5, 30° matched static pressure helium injection, are presented in Figures 22-24.

Helium contours presented in Fig. 22 illustrate fuel penetration, decay of the core and details of the upstream flow separation. The .005 contour extends upstream only about 0.5D from the edge of the highly elongated angled injector. The He core penetrates about 1D off the wall, and the 0.40 contour extends downstream about 8D. Basically, the helium does not penetrate out of the boundary layer because of the low jet-to-freestream dynamic pressure ratio. Case 5 had a $\bar{q}$ of 0.6 versus 1.0 for the the 30° injection of hydrogen in Case 4.

Vertical jet centerline mole fraction profiles at 20, 40 and 90 jet diameters are compared with experimentally measured values in Fig. 23. The nearfield core penetrates about 1.5D off the plate, but the outer edge of the mixing region remains within 4D, about half as high as data. In the farfield, a weak peak remains about 2D off the plate, unlike the H_2 cases. Peak concentration are in good agreement with data throughout.

Figure 24 presents longitudinal distributions of maximum helium mass fraction and penetration. Excellent agreement in the peak He concentration is illustrated in Fig. 24a, which was shown by the hydrogen cases to be a good indication that mixing efficiency is accurately predicted. Predicted helium penetration is quite low compared to data. Fig. 24b illustrates computed and experimental measurements of He penetration to the outer edge of the jet ($x_{He} = 0.$) and the to the location of peak concentration. Measured penetration of the edge is twice the computed value for the nearfield and about 25% higher than computed for the 90D station. However, the peak penetration is accurately modeled in the nearfield and only about 30% underpredicted at the 90D station.

Case 6

Comparisons of computational and experimental results for Case 6, 30° underexpanded helium injection, are presented in Figures 25-27. This solution also utilized a Sc_t of 0.5.

Helium contours presented in Fig. 25 illustrate fuel penetration, decay of the core and details of the upstream flow separation. The .005 contour extends upstream about 1D from the edge of the highly elongated angled injector. The He core penetrates about 2.5D off the wall, and the 40% contour extends downstream past the end of the elliptic solution (>10D). Comparing Fig. 25 with Fig. 22, the underexpanded jet has much higher penetration, consistent with the fivefold increase in helium pressure and mass flow rate.

Vertical jet centerline mole fraction profiles at 20, 40 and 90 diameters are compared with experimentally measured values in Fig. 26. This high pressure jet penetrates about 4D off the plate in the nearfield, and the computational profile maintains a peak concentration 6D off the plate at the 90D station. Shape and magnitude of the x_{He} contours are in excellent agreement with experimental measurements at all three stations. The only noticible discrepancy is near the wall, where the experimental profile drops off more rapidly than the computational results.

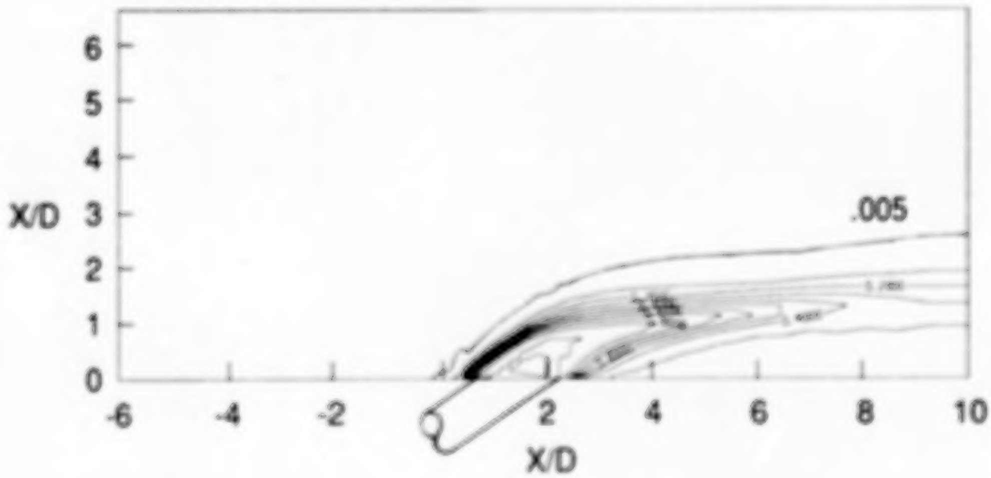

Figure 22. Longitudinal Helium Mass Fraction Contours; Case 5, $\theta = 30°$, $\bar{q} = 0.6$.

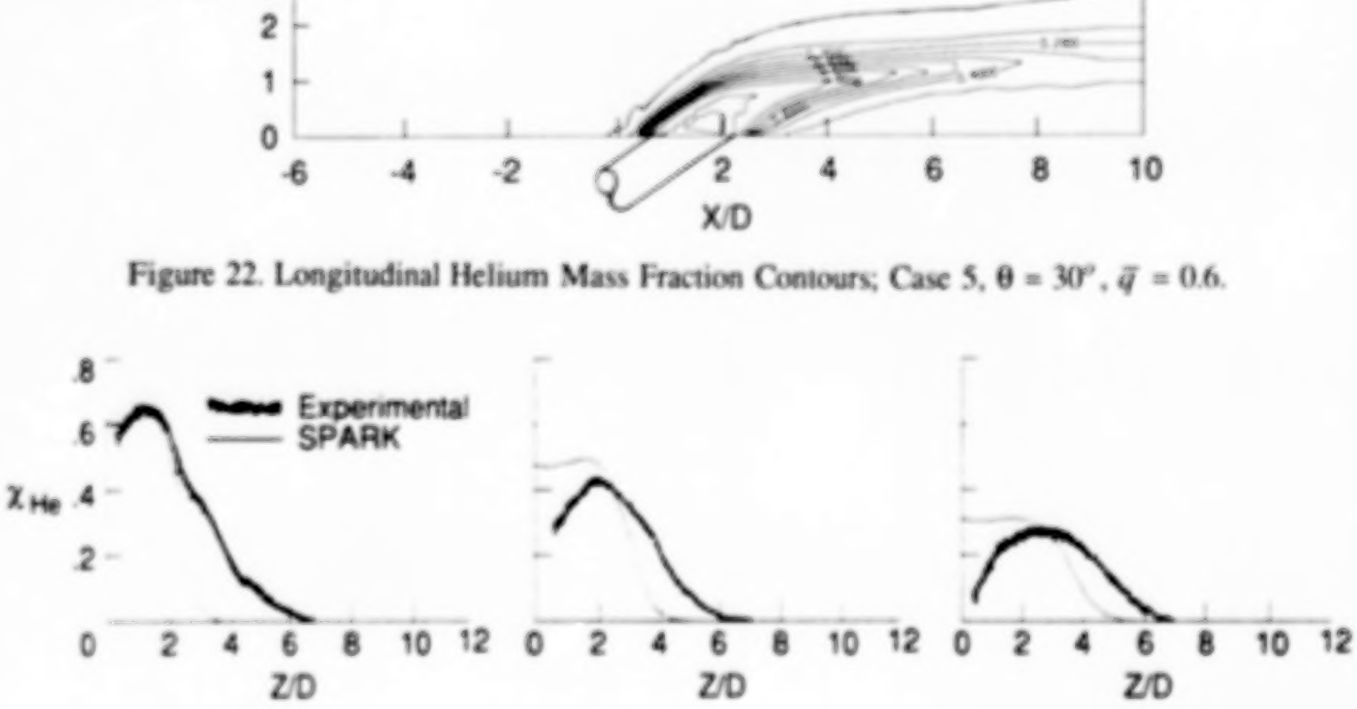

a) X/D = 20

b) X/D = 40

c) X/D = 90

Figure 23. Vertical Centerline Helium Mole Fraction Profiles; Case 5, $\theta = 30°$, $\bar{q} = 0.6$.

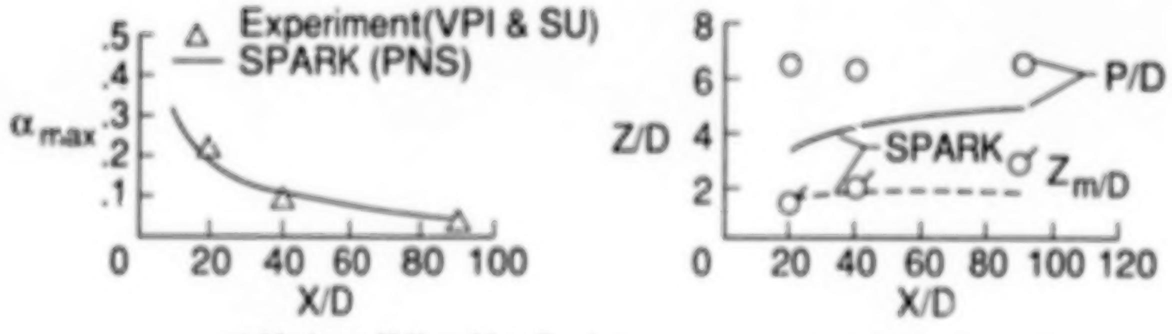

a) Maximum Helium Mass Fraction

b) Helium Penetration

Figure 24. Longitudinal Distributions; Case 5, $\theta = 30°$, $\bar{q} = 0.6$.

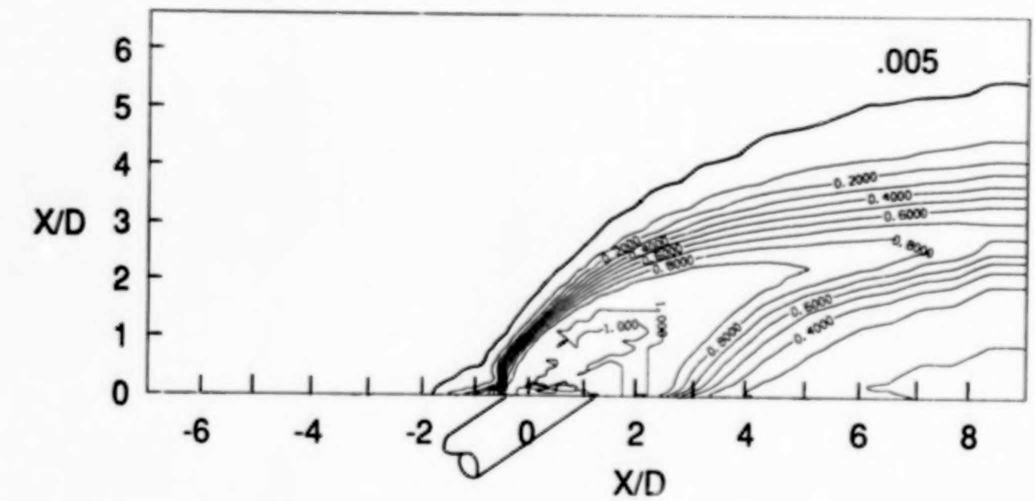

Figure 25. Longitudinal Helium Mass Fraction Contours; Case 6, $\theta = 30^o$, $\bar{q} = 3.1$.

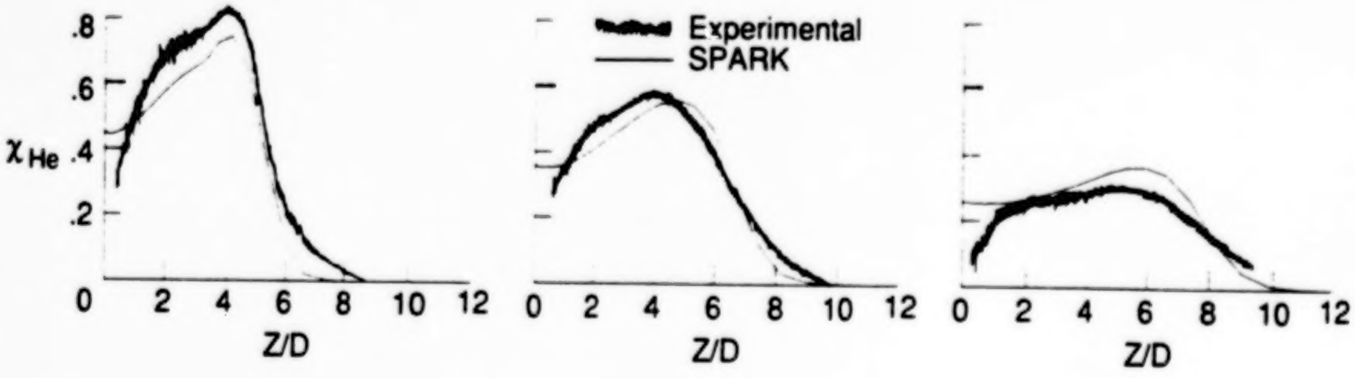

a) X/D = 20

b) X/D = 40

c) X/D = 90

Figure 26. Vertical Centerline Helium Mole Fraction Profiles; Case 6, $\theta = 30^o$, $\bar{q} = 3.1$.

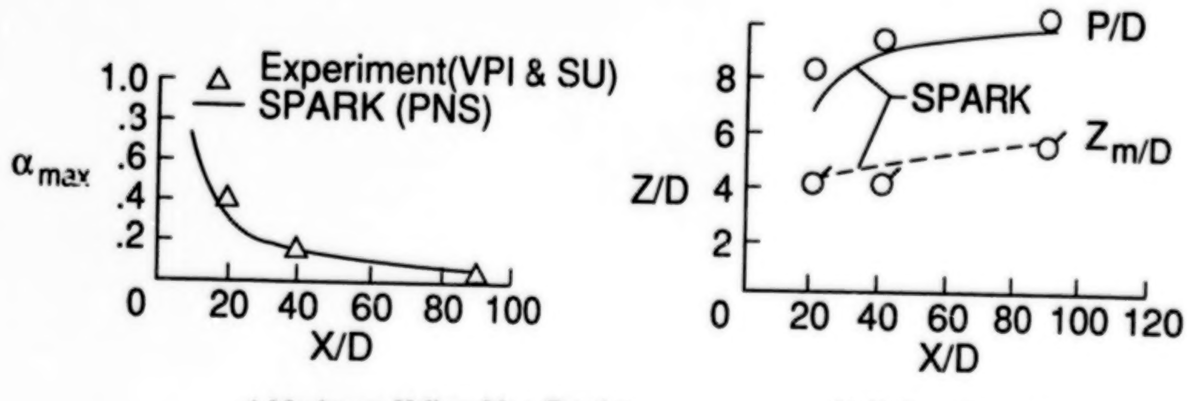

a) Maximum Helium Mass Fraction

b) Helium Penetration

Figure 27. Longitudinal Distributions; Case 6, $\theta = 30^o$, $\bar{q} = 3.1$.

Figure 27 presents longitudinal distribution of maximum helium mass fraction α_{max} and penetration P/D. The excellent agreement in Fig. 27a indicates that mixing efficiency is accurately predicted. Computed helium penetration, both core and outer edge of mixing region, are compared to experimental results in Fig. 27b and show excellent agreement. The largest discrepancy is the 15% underpredicted penetration of the edge at X/D = 20.

Case 7

Comparisons of computational (Sc_t = 0.5) and experimental results for Case 7, 15° matched static pressure injection, are presented in Figures 28-30.

Helium contours presented in Fig. 28 illustrate fuel penetration, decay of the core and details of the upstream flow separation. The .005 contour extends upstream about 0.5D from the edge of the highly elongated angled injector. The He core penetrates about 0.5D off the wall, and the 40% contour extends downstream about 10D.

The low pressure, low angle injector produces a mixing region characterized by the highest He concentration and core on the wall by the first survey station, X/D =20, as illustrated by the vertical profiles in Fig. 29. The computational results indicate that a core exists off the wall in the nearfield, but returns to the wall by the 20D station. Shape and magnitude of the predicted mole fraction contours are in good agreement with experimental contours. However, the underprediction of the peak x_{He} by about 40% at the 90D station suggests that a slightly lower value of Sc_t may be appropriate for this case. However, this is inconclusive, since the experimental data for this case showed an unexplained asymmetry.

Figure 30 presents longitudinal distribution of maximum helium mass fraction α_{max} and penetration P/D. Fig. 30a illustrates good agreement between calculated and measured peak helium mass fraction, suggesting that the computational results accurately predict mixing efficiency. Predicted helium penetration to the outer edge of the mixing region is compared to the experimental data in Fig. 30b, illustrating slight underprediction at 20 and 40 X/D, but excellent agreement at the 90D station.

DISCUSSION OF RESULTS

Qualitatively, the computations are good in that computational trends are consistent with experimental observations. The results show that increasing δ/D increases penetration, both of the outer edge of the mixing region and of the point of maximum concentration, which was a conclusion of Ref. 4. Pressure plots (not included) reveal bow shocks which are naturally stronger for the normal injection and underexpanded injection. Velocity vector plots (also not included) reveal the horseshoe vortex system characteristic of injection flow fields. These and other observations and details of the flow solutions are beyond the scope of this presentation, but will be addressed in the future.

Accuracy

Table 4 summarizes observed differences between computed and experimental measurements for jet penetration (P/D and Z_m/D), spreading (W/D and W_B/D), maximum H_2 concentration (α_{max}), and mixing efficiency, η_m.

Where available, solutions using Sc_t = 0.5 as recommended above are included in the table. Because of the recognized errors in the hydrogen data, the Sc_t = 0.2 solutions are used

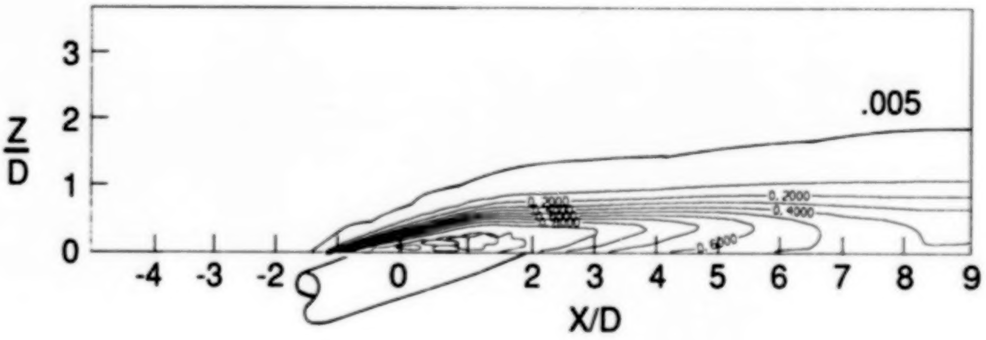

Figure 28. Longitudinal Helium Mass Fraction Contours; Case 7, $\theta = 15^o$, $\bar{q} = 0.27$.

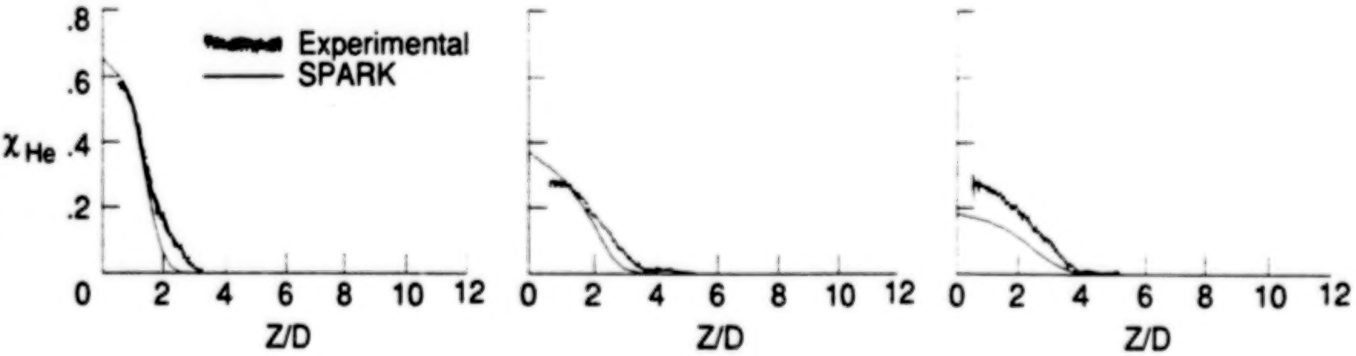

a) X/D = 20

b) X/D = 40

c) X/D = 90

Figure 29. Vertical Centerline Helium Mole Fraction Profiles; Case 7, $\theta = 15^o$, $\bar{q} = 0.27$.

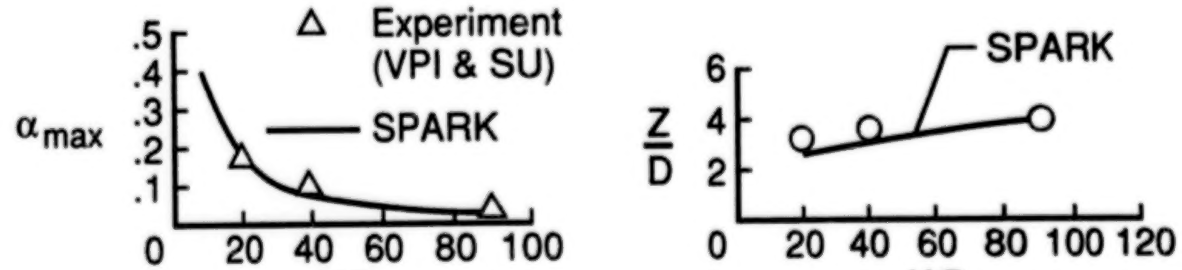

a) Maximum Helium Mass Fraction

b) Helium Penetration

Figure 30. Longitudinal Distributions; Case 7, $\theta = 15^o$, $\bar{q} = 0.27$.

when comparing peak hydrogen mass fraction and mixing efficiency. Mean deviation is summarized in the last column.

The codes consistently underpredicted penetration of the maximum concentration (Z_m/D) in the farfield, generally leaving the peak along the wall. Penetration to the outer edge of the mixing layer is generally predicted within ±1.6 diameters, or to within about ±7%.

Lateral spreading is slightly overpredicted in the freestream and generally significantly overpredicted in the boundary layer. Comparisons available are insufficient to provide reliable estimates, but the range is about 1D for W and -2D for W_B.

Peak injectant concentration in the farfield is over or underpredicted by about ±17%, while the unadjusted fuel mixing efficiency has an average deviation of 5% (universally underpredicted). Confidence in this mixing efficiency accuracy will be significantly enhanced by additional data and integration of the available helium data.

Table 4. Accuracy Summary

Case no.

	1	2	3	4	5	6	7	M.D.
X/D	120	120	120	120	90	90	90	
Sc_t	0.2	0.5	0.2	0.2	0.5	0.5	0.5	
P/D	2.0	4.0	0.0	3.0	-1.8	-0.5	0	1.6
Z_m/D	-2.5	-3.0	-2.5	-2.5	-1.5	0.2	0	1.7
W/D	1.25	.70	--	--	--	--	--	.98
W_B/D	4.0	0.2	--	--	--	--	--	2.1
α_{max}	-14%	0%*	20%	30%	10%	12%	-30%	17%
η_m	-.09	–.05*	-.03	--	--	--	--	.05

*Sc_t = 0.2

Recommendations

There are obvious differences between the hydrogen and helium cases in the application of the code to achieve acceptable code vs. experiment agreement. For the H_2 cases, better agreement was obtained using Sc_t = 0.2, whereas for the He cases, better agreement was obtained with Sc_t = 0.5. Because of the superior experimental measurement capability of the recent helium tests reported in Ref. 30 and documented uncertainties of the older hydrogen data[3,4 and 7], it is prudent to recommend solution techniques used for Cases 5-7. Therefore, when using a fine grid and the Baldwin-Lomax turbulence model, results indicate that mixing of transverse injectors with injection angles, between 15 and 90 degrees should be modeled using $Sc_t \approx 0.5$. However, when performing a complete combustor analysis requiring a coarse grid with multiple fuel injectors, a more realistic prediction of fuel mixing may be achieved using Sc_t = 1.0[28]. It would also be advisable to compare grid density used for such solutions to the injection cases (preferably He) presented in this paper.

Fuel mixing efficiency is relatively insensitive to maximum fuel concentration (Cases 1 and 2). If the decay of peak fuel concentration is accurately predicted, then the mixing efficiency will be accurate, but not vice versa.

Turbulent diffusivity (Schmidt number) has been shown to vary across a boundary layer[37] and that trend appears in Table 4. Lateral spreading within and spreading out of a boundary layer are not correctly predicted when using a single value of Sc_t over the entire flow. This observation suggests that improved turbulence modeling to account for the nonuniform turbulent diffusivity is in order.

CONCLUSIONS

The SPARK family of Navier Stokes codes were validated for fuel mixing in a supersonic flow, using experimental data for discrete circular injectors angled at 15^o (downstream) to 90^o (normal) for air flow boundary layer thicknesses ranging from 1.25 to 6.25 injector diameters. Details of the physical model, solution methodology, boundary conditions and turbulence model are presented in sufficient detail such that recreation of the solutions is possible. Results presented demonstrate that "grid converged" solutions for one injector were not attained but that mixing efficiency sensitivity is acceptable. Mixing efficiency is also relatively insensitive to peak fuel concentrations. Recommendations are presented for modeling the fuel injector problem. These recommendations are different depending on the grid density around each injector. Coarse grids require damped turbulence (achieved with a turbulent Schmidt number of unity). This type of grid is representative of large scale combustor solutions with many fuel injectors. Fine grids require a reduced turbulent Schmidt number on the order of 0.5, which are in agreement with experimentally observed values for similar flows. The turbulent Schmidt number is not constant across the entire flow domain; a distribution may enhance fuel injection modeling.

REFERENCES

1 Northam, G.B. and Anderson, G.Y., "Supersonic Combustion Ramjet Research at Langley," AIAA Paper 86-0159, presented at 24th Aerospace Sciences Meeting, Reno, NV.

2 Torrence, M.G., "Concentration Measurements of an Injected Gas in a Supersonic Stream," NASA TN D-3860, 1967.

3 Rogers, R.C., "A Study of the Mixing of Hydrogen Injected Normal to a Supersonic Airstream," NASA TN D-6114, 1971.

4 McClinton, C.R., "Effect of Ratio of Wall Boundary-Layer Thickness to Jet Diameter on Mixing of a Normal Hydrogen Jet in a Supersonic Stream," NASA TM X-3030, 1974.

5 Orth, R.C., Schetz, J.A. and Billig, F.S., "The Interaction and Penetration of Gaseous Jets in Supersonic Flow," NASA CR-186, 1969.

6 Rogers, R.C., "Mixing of Hydrogen Injected From Multiple Injectors Normal to a Supersonic Airstream," NASA TN D-6476, 1971.

7 McClinton, C.R., "The Effect of Injection Angle on the Interaction Between Sonic Secondary Jets and a Supersonic Free Stream," NASA TN D-6669, Feb. 1972.

8 Anderson, G.Y. and Vick, A.R., "An Experimental Study of Flame Propagation in Supersonic Premixed Flows of Hydrogen and Air," NASA TN D-4631, June 1968.

9 Beach, H.L., Jr., "Supersonic Mixing and Combustion of a Hydrogen Jet in a Coaxial High-Temperature Test Gas," AIAA Paper 72-1179, Nov.-Dec. 1972.

10 Rogers, R.C. and Eggers, J.M., "Supersonic Combustion of Hydrogen Injected Perpendicular to a Ducted Vitiated Airstream," AIAA Paper 73-1322, Nov. 1973.

11 Anderson, G.Y. and Gooderum, P.B., "Exploratory Tests of Two Strut Fuel Injectors for Supersonic Combustion," NASA TN D-7581, 1974.

12 Rogers, R.C., "Influence of Fuel Temperature on Supersonic Mixing and Combustion of Hydrogen," AIAA Paper 77-17, 1977.

13 Eggars, J.M., Reagon, P.G. and Gooderum, P.B., "Combustion of Hydrogen in a Two-Dimensional Duct With Step Fuel Injectors," NASA TP-1159, 1978.

14 McClinton, C.R. and Gooderum, P.B., "Direct-Connect Test of a Hydrogen-Fueled Three-Strut Injector for an Integrated Modular Scramjet Engine," 14th JANNAF Combustion Meeting, Vol. II, CPIA Publ. 292, 489-505, Dec. 1977.

15 McClinton, C.R., "Interaction Between Step Fuel Injectors on Opposite Walls in a Supersonic Combustor Model," NASA TP-1174, 1978.

16 Northam, G.B., Trexler, C.A. and Anderson, G.Y., "Characterization of a Swept-Strut Hydrogen Fuel-Injector for Scramjet Applications," 15th JANNAF Combustion Meeting, Vol. III, CPIA Publ. 297, 393-410, Feb. 1979.

17 Anderson, G.Y. and Rogers, R.C., "A Comparison of Experimental Supersonic Combustor Performance with an Empirical Correlation of Nonreactive Mixing Results," NASA TM X-2429, Oct. 1971.

18 Guy, R.W. and Mackley, E.A., "Initial Wind Tunnel Tests at Mach 4 and 7 of a Hydrogen-Burning, Airframe-Integrated Scramjet," NASA Paper 79-8045, presented at the 4th International Symposium on Air Breathing Engines (Lake Buena Vista, FL), Apr. 1979.

19 Drummond, J.P., Rogers, R.C. and Evans, J.S., "Combustor Modeling For Scramjet Engines," AGARD 54th (B) Specialists Meeting On Combustor Modeling, Propulsion, and Energetics Panel, Cologne, Germany, Oct. 1979.

20 Pan, Y.S., Drummond, J.P. and McClinton, C.R., "Comparison of Two Computer Programs by Predicting Turbulent Mixing of Helium in a Ducted Supersonic Airstream," NASA TP-1166, May 1978.

21 Evans, J.S., Schexnayder, C.J., Jr. and Beach, H.L., Jr., "Application of a Two-Dimensional Parabolic Computer Program to Prediction of Turbulent Reacting Flows," NASA TP-1169, Mar. 1978.

22 Rogers, R.C. and Weidner, E.H., "Analysis of Hydrogen Combustion in High Enthalpy Supersonic Air Flows From a Shock Tunnel," 23rd JANNAF Combustion Meeting, Vol. III, CPIA Publ. 457, Oct. 1986.

23 Rogers, R.C. and Chinitz, W., "On the Use of a Global Hydrogen-Air Combustion Model in the Calculation of Turbulent Reacting Flows," AIAA Paper 82-0112, Jan. 1982.

24 Chinitz, W., "Theoretical Studies of the Ignition and Combustion of Silane-Hydrogen-Air Mixtures," NASA CR-3876, Feb. 1985.

25 Uenishi, K. and Rogers, R.C., "Three-Dimensional Computations of Mixing of Transverse Injector in a Ducted Supersonic Airstream," AIAA Paper 86-1423, Huntsville, AL, June 1986.

26 Uenishi, K., Rogers, R.C., and Northam G.B., "Three-Dimensional Computation of Transverse Hydrogen Jet Combustion in a Supersonic Airstream," AIAA Paper 87-0089, Reno, NV, Jan. 1989.

27 Chitsomboon, T., Northam, G.B., Rogers, R.C. and Diskin, G.S., "CFD Prediction of the Reacting Flowfield Inside a Subscale Scramjet Combustor," AIAA Paper 88-3259, Boston, MA, July 1988.

28 Srinivasan, S., Kamath, P. and McClinton, C.R., "Numerical Simulation of Flow Through the Langley Parametric Scramjet Engine," SAE Paper 892314, Los Angeles, CA, Sept. 1989.

29 Riggins, D.W., Mekkes, G.L., McClinton, C.R. and Drummond, J.P., "A Numerical Study of Mixing Enhancement in a Supersonic Combustor," AIAA Paper 90-0203, Jan. 1990.

30 Mays, R.B., Thomas, R.H. and Schetz, J.A., "Low Angle Injection Into a Supersonic Flow," AIAA Paper 89-2461, Monterey, CA, July 1989.

31 Ng. W.F., Kwok, F.T. and Ninnemann, T.A., "A Concentration Probe for the Study of Mixing in Supersonic Shear Flows," AIAA 89-2459, Monterey, CA, July 1989.

32 Drummond, J.P., Rogers, R.C. and Hussaini, M.Y., "A Detailed Numerical Model of a Supersonic Reacting Mixing Layer," AIAA Paper 86-1427, June 1986.

33 Carpenter, M.H., "Three-Dimensional Computations of Cross-Flow Injection and Combustion in a Supersonic Flow," AIAA Paper 89-1870, June 1989.

34 Kamath, H., "Parabolized Navier-Stokes Algorithm for Chemically Reacting Flows," AIAA Paper 89-0386, Jan. 1989.

35 Baldwin, B. and Lomax, H., "Thin Layer Approximation and Algebraic Model for Separated Turbulent Flows," AIAA Paper 78-257, 1978.

36 Sturgess, G.J. and McManus, K.R., "Calculations of Turbulent Mass Transport in a Bluff-Body Diffusion-Flame Combustor," AIAA Paper 84-0372, Jan. 1984.

37 Launder, B.E. and Spaulding, D.B., *Mathematic Models of Turbulence*, Academic Press, 1972, p. 49.

A HIGHLY EFFICIENT ENGINEERING TOOL FOR THREE-DIMENSIONAL SCRAMJET FLOWFIELD AND HEAT TRANSFER COMPUTATIONS

Pradeep S. Kamath
Analytical Services and Materials Inc.
Hampton, Virginia

Richard W. Hawkins
Analytical Services and Materials Inc.
Hampton, Virginia

Nathaniel R. Baker
Lockheed Engineering and Sciences Company
Hampton, Virginia

Charles R. McClinton
NASA Langley Research Center
Hampton, Virginia

ABSTRACT

The SIMPLE-based parabolic flow code, SHIP3D has been under development for use as a parametric design and analysis tool for scramjets. This paper demonstrates some capabilities and applications of the code and is also a report on its current status. The focus is on the combustor for which the code has been mostly used. Recently, it has also been applied to nozzle flows. Code validation results are presented for combustor unit problems involving film cooling and transverse fuel injection, and for a nozzle test. A parametric study of a film cooled or transpiration cooled Mach 16 combustor is also conducted to illustrate the application of the code to a design problem.

INTRODUCTION

There is currently great interest in the development of computer codes to predict the performance of hypersonic, air-breathing propulsion systems at flight speeds that are beyond ground test capabilities. Of particular interest among air-breathing power plants for hypersonic flight is the hydrogen-fueled, airframe-integrated scramjet, a schematic sketch of which is shown in Figure 1. In this

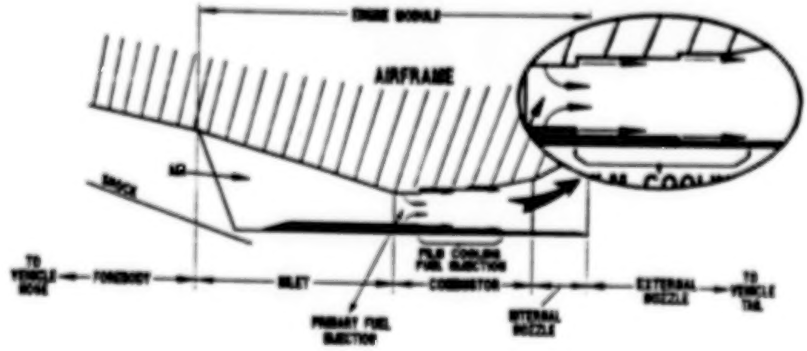

Figure 1. Schematic of Airframe-Integrated Scramjet

design, modular engines mounted on the lower surface of the fuselage process most of the compressed air mass contained within the envelope of the vehicle forebody bow shock [1]. Each module is a duct of rectangular cross-section consisting of an inlet, a combustor and an internal nozzle. The exhaust from these engines expands against and pressurizes the rear end of the vehicle, thus generating thrust.

The performance of these engines have heretofore been analyzed using one-dimensional cycle codes into which are empirically incorporated, most of the knowledge gained of the individual components in the propulsion flowpath, by testing at low Mach numbers. Although CFD has recently been used to analyze portions of the propulsion flowpath in greater detail [2], the overall vehicle performance is still computed using cycle codes. It has become clear that even this limited use of CFD involves an expense that borders on being prohibitive. This is particularly true for the combustor where the conventional solution method of time-marching the Navier-Stokes equations to convergence requires in excess of one hundred Cray-2 CPU hours, on a grid just fine enough to get an adequate estimate of the combustion efficiency but not of heat transfer and skin friction.

The need to bridge the gap between these two approaches is critical if CFD is to be used for design and parametric studies. Key to achieving this is to use methods that fully exploit the efficiencies inherent in these flows, one of which is the largely parabolic nature of the flow over most of the propulsion flowpath at hypersonic speeds. Thus, one approach is to treat locally elliptic regions in a parabolic manner while ensuring the global conservation of mass, momentum and energy. In the combustor, this mainly requires the parabolic treatment of fuel injection since regions of elliptic flow are usually around the injectors. Depending on its design, a primary fuel injector may be, a discrete hole flush with the wall for sonic, transverse injection, or a ramped strut or wedge-shaped protrusion into the flow for supersonic, parallel injection. A parallel injection slot is also placed at the bottom of a backward-facing step at one or more axial stations on each wall for film cooling. In addition, portions of the combustor wall may be transpiration cooled with fuel.

The topic of the first portion of the paper is film cooling. The methodology for the parabolic computation of parallel injection from a step is outlined and validated for a classic, hydrogen-cooled combustor film cooling case. Next follows a similar discussion on transverse injection and its validation against mixing data. The practical use of these capabilities is then demonstrated by a parametric analysis of a conceptual combustor with transverse fuel injection and film cooling or transpiration cooling. The parabolic treatment of fuel injection from ramp and strut injectors that protrude into the flow is currently under development and is not discussed here. Finally, a nozzle computation and comparison with test data is shown.

FILM COOLING

Film cooling in a scramjet combustor involves the injection of a portion of the hydrogen fuel parallel to and alongside the planar walls of the combustor to lower the heat load on the wall. Ignoring regenerative cooling and the effect of film cooling on engine performance, which are discussed in the parametric study later in the paper, the task reduces to the computation of the wall heat flux and shear stress in a turbulent, reacting flow. A representative unit problem is shown in Figure 2, which is a schematic of a test conducted in the Calspan 48-inch shock tunnel. The bottom wall of the model represents the body side of the vehicle and the top wall, the cowl side (see Figure 1). Both walls are film cooled in the test, with 59 percent of the fuel used on the bottom wall and 41

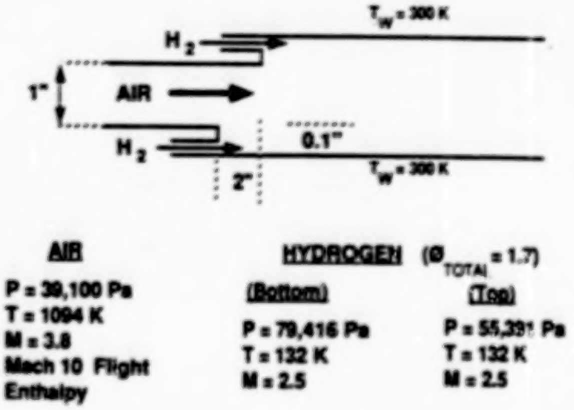

Figure 2. GASL/Calspan Run 41 Film Cooling Test Setup

percent on the top wall. The step on the top wall is 2 inches downstream of that on the bottom wall. Air at Mach 10 flight enthalpy enters the combustor with a 0.4 inch turbulent boundary layer on the bottom wall. Hydrogen is injected at Mach 2.5. The hydrogen and air mass flow rates are such that the equivalence ratio, defined as:

$$\phi = m_f/(m_a \times 0.0293) \ldots\ldots\ldots\ldots\ldots (1)$$

where 0.0293 is the stoichiometric fuel-to-air mass flow rate ratio, is 1.7. Both walls are maintained at the fuel total temperature of 300 degrees K to represent a thermally balanced system.

The parabolic computation is started at the axial location of the bottom slot where the profiles of air velocity and temperature in the central 1 inch section of the duct are first specified. Pressure is assumed to be uniform and the vertical velocity is set to zero. Given the initial velocity profile, the turbulent kinetic energy, k and the dissipation rate, ε for the $k-\varepsilon$ turbulence model are initialized in the turbulent boundary layer according to the following rationale:

1. In a fully developed turbulent boundary layer, the generation and dissipation of turbulence are in balance. The transport equation for k then reduces to the following simple form [3]:

$$\tau = \rho \, k C_D^{1/2} \ldots\ldots\ldots\ldots\ldots\ldots\ldots\ldots (2)$$

where C_D, one of the constants in the k-ε model is equal to 0.09. The symbols τ and ρ are the density and the wall shear stress.

2. From the mixing length hypothesis,

$$\tau = \rho l_m^2 (\partial w/\partial y)^2 \ldots\ldots\ldots\ldots\ldots\ldots (3)$$

3. From turbulence measurements near walls [3], the variation of the mixing length in the boundary layer is known to be,

$$l_m = \kappa y, \text{ if } y < \lambda \delta/\kappa$$

$$= \lambda \delta, \text{ if } y > \lambda \delta/\kappa$$

or,

$$l_m(y) = \min(\kappa y, \lambda\delta) \quad \ldots\ldots\ldots\ldots\ldots \quad (4)$$

where δ is the boundary layer thickness, κ is one of the logarithmic law-of-the-wall constants (0.42) and λ has a value of 0.09.

4. The equation for the initial turbulent kinetic energy in the boundary layer is thus obtained by combining Equations (2), (3) and (4),

$$k = [\min(\kappa y, \lambda\delta)/C_D^{1/4} \quad \partial w/\partial y]^2 \quad \ldots\ldots \quad (5)$$

Note that k is proportional to the square of the velocity gradient. Outside the boundary layer, k is set so that the freestream turbulence intensity k^2 is 0.05 percent.

5. The dissipation rate, ε is related to k and the turbulence length scale, l by definition as,

$$\varepsilon = C_D k^{3/2}/l \quad \ldots\ldots\ldots\ldots\ldots\ldots\ldots\ldots \quad (6)$$

where the length scale is related to the mixing length as,

$$l = C_D^{1/4} l_m \quad \ldots\ldots\ldots\ldots\ldots\ldots\ldots\ldots \quad (7)$$

Equation (6) along with (5), (7) and (4) are used to compute the initial profile of ε.

The flowfield at z=0.0 is thus completely specified on a grid that covers the central 1 inch portion of the duct. Before initiating space marching, the bottom boundary of the domain is extended downwards to accomodate the step. This extended domain is then regridded without changing the total number of grid points. The main flow is then conservatively patched onto the new grid as are the slot and lip flows. The same procedure is used at the second step. To suppress recirculation, the lip flow is given a small streamwise velocity (one percent of the freestream velocity), a pressure equal to the theoretical base pressure [4]

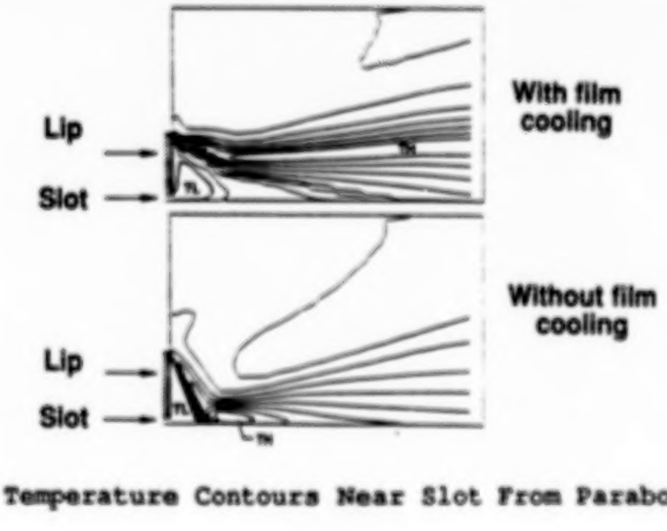

Figure 3. Temperature Contours Near Slot From Parabolic Computation

and a temperature that is the average of the slot and lip temperatures. For cases without film cooling, the entire step is treated as a lip. The above treatment of the elliptic region at the lip causes little numerical difficulty because the pressure is treated so as to render the equations parabolic in the streamwise direction in subsonic regions [5]. Computed flowfields near the slot and lip region for a generic case with and without film cooling are shown in Figure 3, where the regions of high (freestream) and low (slot) temperatures are demarcated. The CPU time for the GASL-Calspan Run 41 analyzed here is 2 minutes on a Cray-2, using 81 grid points wall-to-wall and a minimum grid spacing of 10 microns at the walls.

The computed heat flux and pressure on the bottom wall are compared to the measured data in Figures 4 and 5. In this test, a sharp increase in the heat flux at any location on the combustor walls is attributed largely to the degradation of the film by mixing and combustion, and not to shocks. This is because the test appraratus did not have strong shock generators such as fuel injectors or coverging walls. Thus, the rapid rise in both, heat flux and pressure data after 60 cm. indicates that ignition did not occur before 60 cm. The combustion downstream is not mixing-limited because, as seen from Figure 6, the computation shows an almost fully mixed condition at 60 cm. Thus, the finite slope of the rise in the heat flux and the pressure after 60 cm. must be attributed to kinetics, as is the ignition delay up to 60 cm. Lacking the capability to treat

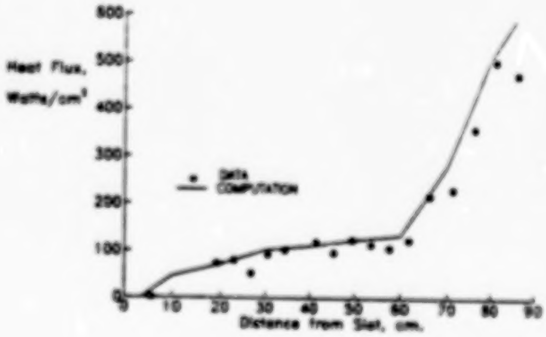

Figure 4. Comparison of Ship Computation vs Heat Flux Data

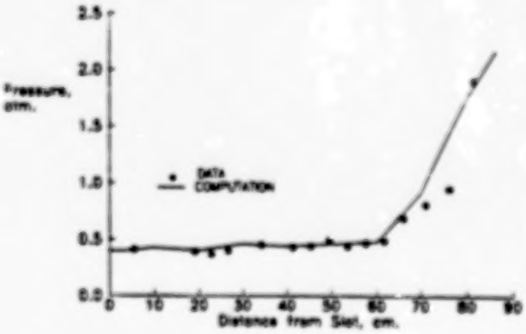

Figure 5. Comparison of SHIP Computation vs Pressure Data

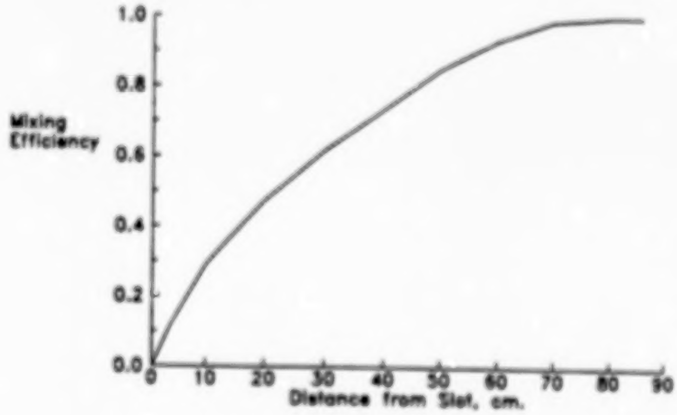

Figure 6. Mixing Efficiency Computed by SHIP

chemical kinetics in SHIP at present, the computation was performed assuming no reaction until 60 cm. downstream of which a non-kinetic, ramped reaction model was used. Thus, the predictive capability of SHIP for such relatively low enthalpy flows is, at present limited. However at the higher end of the hypersonic flight regime (Mach 16 to 25), where film cooling is expected to be used most, the assumption of mixing-limited combustion is quite valid and the existing capability is satisfactory.

TRANSVERSE INJECTION

In some supersonic combustor designs, fuel is injected transverse to the main flow to achieve a higher rate of mixing than parallel injection from a step. The flowfield in the vicinity of these injectors is elliptic due to the streamwise recirculation regions both upstream and downstream of injection. Parabolic treatment of transverse injection circumvents the need for an elliptic solution, which typically requires from 2 to 5 hours of CPU time on a Cray-class machine to solve just the region near a single injector. Such a procedure has recently been implemented in the SHIP3D code. In contrast to methods that use correlations or an equivalent body, the procedure involves the actual imposition of the injection boundary conditions during space-marching. Thus, it would allow the computation, not only of the combustion efficiency but also of the flow losses from which a performance parameter such as the combustor effectiveness can be obtained.

At present the procedure gives excellent mass conservation and good agreement with the mixing measurements, of Rogers [6]. The test setup and comparisons are shown in Figures 7 and 8. In that experiment, cold hydrogen was injected sonically through five injectors on a flat plate normal to a Mach 4

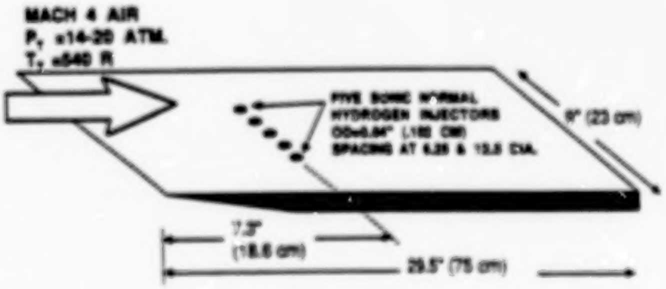
MACH 4 AIR
P_T ≈14-20 ATM.
T_T ≈540 R
FIVE SONIC NORMAL HYDROGEN INJECTORS OD=0.04" (.102 CM) SPACING AT 6.25 & 12.5 DIA.
9" (23 cm)
7.3" (18.6 cm)
29.5" (75 cm)

Figure 7. Setup for Rogers Cold Flow Mixing Experiment

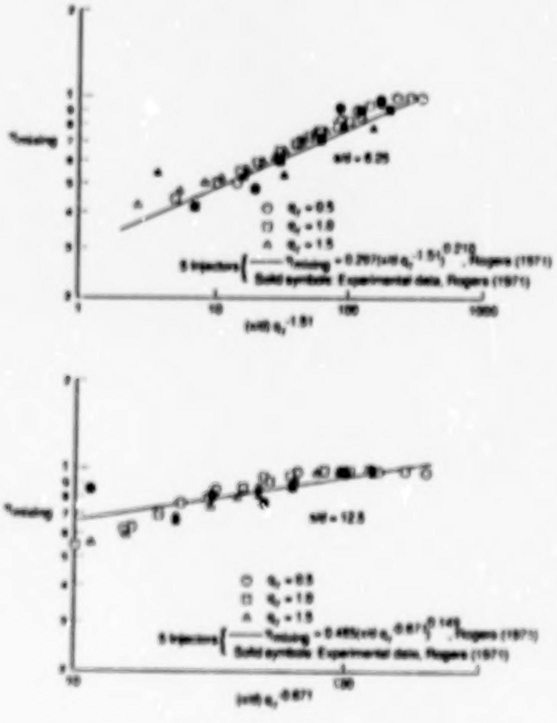

Figure 8. Parabolic Normal Injection vs Rogers Data

airstream. The dynamic pressure ratio was changed by varying the total pressure of the tunnel air and that of injection. Mass fraction surveys were conducted at distances up to 120 injector diameters downstream. These were integrated over the area fueled by the central injector to obtain the mixing efficiencies shown in Figure 8. For each case shown in Figure 8, the CPU time for a SHIP run using a 31 X 61 grid with a 100 micron minimum grid spacing is 3.5 minutes on a Cray-2. The standard values of the κ-ε model constants [5] were used in the computations. The domain covers the entire length of the flat plate and extends to the roof of the tunnel some 4.5 inches above the plate.

Although the predicted mixing efficiency is in agreement with data, the computed pressures downstream of the injector (not shown here) are high. Among the possible reasons for this behaviour, initialization of the flowfield upstream of injection, rather than the injection procedure itself, has been identified as the main cause. Validation using pitot pressure measurements close to the injectors is currently in progress.

PARAMETRIC ANALYSIS OF AN ACTIVELY COOLED SCRAMJET COMBUSTOR

Adequate cooling of the scramjet combustor walls at the upper end of the hypersonic flight regime is a critical design issue. It is estimated that a stoichiometric flow rate of the cryogenic hydrogen fuel is sufficient to regeneratively cool the engine upto a flight Mach number of 10. At higher speeds, film cooling and transpiration cooling are being considered to lower the wall heat load and thus, the fuel mass flow rate required for regenerative cooling. The analysis presented here covers both film and transpiration cooling in conjunction with regenerative cooling. One advantage of film cooling over transpiration cooling is that, at these high Mach numbers the streamwise momentum of the fuel makes a significant contribution to the thrust [7]. Both cooling methods however, degrade performance to some extent due to the poorer mixing and combustion associated with fuel injection close to the wall.

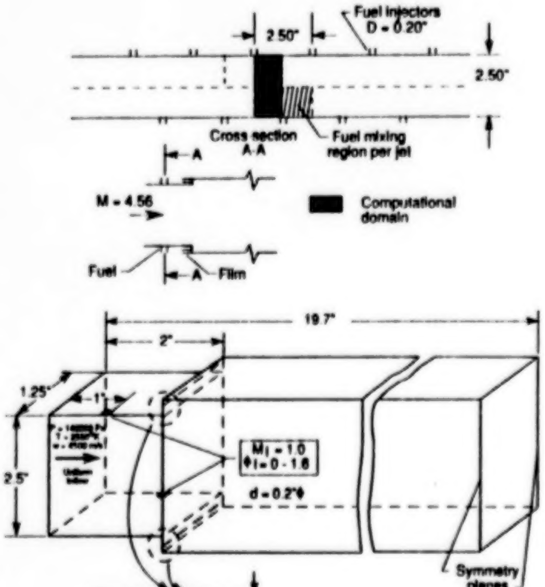

Figure 9. Conceptual Combustor for Parametric Analysis

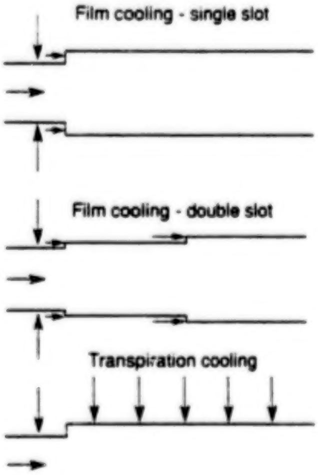

Figure 10. Combustor Configurations for Film Cooling and Transpiration Cooling

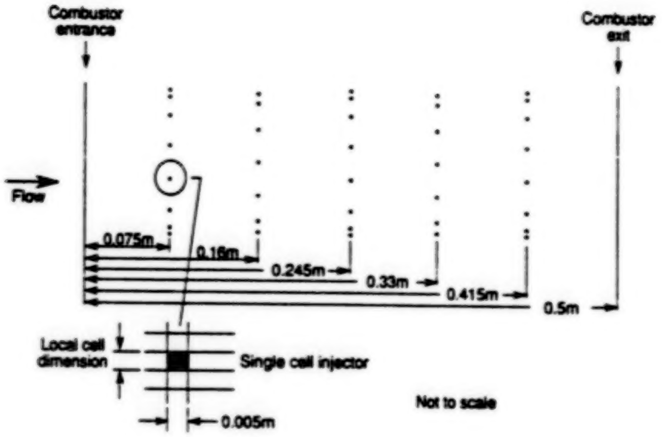

Figure 11. Transpiration Cooling Injector Locations

In this study, the relative magnitudes of these effects and the overall influence on engine performance at Mach 16 flight is assessed on a hypothetical vehicle with a conceptual combustor, shown in Figure 9. The three cooling designs in Figure 10, two using film cooling and one using transpiration cooling are analyzed. The transpiration cooling injector locations on each combustor wall are shown in Figure 11. The porosity of the walls is chosen to be low solely to keep the run times affordable. The rest of the propulsion flowpath was specified in sufficient detail for cycle analysis. The parametric analysis involved a series of three-dimensional, turbulent, reacting SHIP3D runs for the combustor with different proportions of the fuel used for cooling while keeping the total fuel and air flow rates constant. Thus, the equivalence ratio, defined in Equation (1) is kept constant at 1.6, a value considered typical at Mach 16 flight. The CPU time for each film cooling run was 30 minutes on a Cray 2. Each transpiration cooling run however, required 5 hours because of transverse injection from each cooling orifice into a finely resolved grid with a 5 micron grid spacing at the walls.

The computed quantities of interest are the longitudinal distribution of mixing efficiency, wall heat flux and shear stress. Using these results, the tip-to-tail engine specific impulse is obtained using a cycle code. Additional details of the methodology are given in reference [8]. In the following discussion, the equivalence ratio is referred to as ø. For the cases with high normal ø, the regions around the injectors and the steps are subject to severe heating due to the glancing and impinging shocks from injectors on both walls. Figure 12 shows

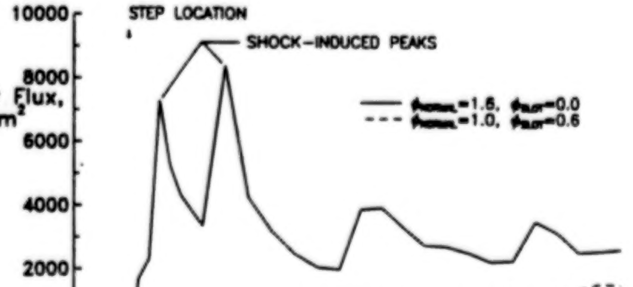

Figure 12. Laterally-Averaged Heat Flux vs Distance

the laterally-averaged heat flux on the top wall, where the shock-induced peaks for the case without cooling are evident. For the case with a film cooling ø of 0.6, both shock induced peaks are absent and the heat flux is generally lower.

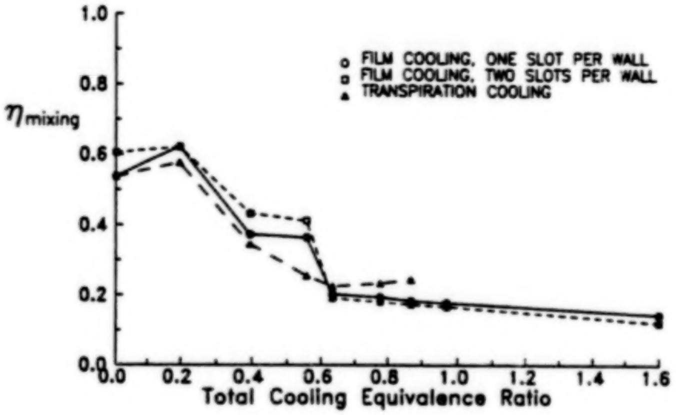

Figure 13. Mixing Efficiency at Combustor Exit

Figure 13 shows the variation in mixing efficiency at the combustion exit with the cooling ø. In this figure, an increase in the cooling ø implies an equal decrease in the normal ø. For purely normal injection, the mixing efficiency is 0.537 while for a slot ø of 0.2, it increases to 0.622. The latter is close to a fully mixed condition for this confined flow at a total ø of 1.6. The reason for this unexpected increase in mixing with a decrease in the transverse ø is that when all the fuel is injected normal to the flow, the fuel jets penetrate deep into the flow but do not adequately fuel the region near the wall. Thus, diversion of a small portion of the fuel to the slots improves mixing. For the same reason, the average wall heat flux at a cooling ø of 0.2 is higher than that without cooling as shown in Figure 14. For the configuration with two film cooling slots

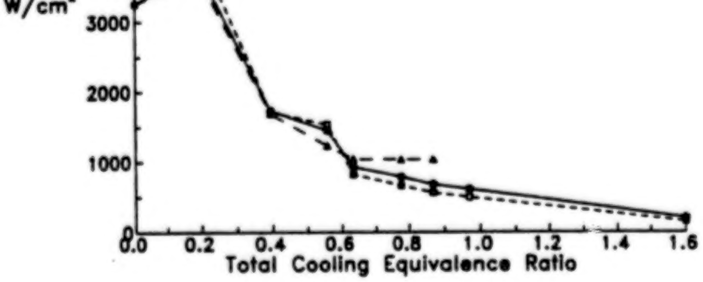

Figure 14. Average Combustor Wall Heat Flux

per wall, the higher average heat flux at low cooling ø is attributed to the higher average pressure in the combustor caused by the smaller steps.

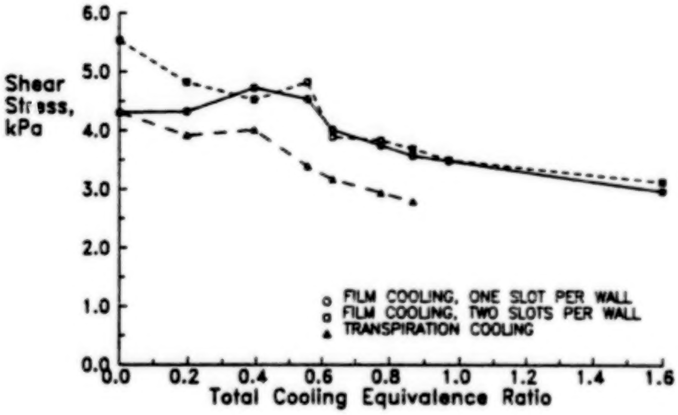

Figure 15. Average Wall Shear Stress

The average shear stress on the wall is shown in Figure 15. For film cooling, it follows the trend in the average heat flux (Figure 14) at only high cooling ø, where the behaviour is in agreement with Reynolds analogy. For transpiration cooling, the shear stress is consistently lower, indicative of the lower velocity gradients at the wall. Figures 13, 14 and 15 show that the greatest gain in cooling effectiveness is achieved when the cooling ø is increased from 0.2 to 0.6, with little change in wall shear, but accompanied by a drop in the mixing efficiency from 0.622 to 0.2. Not evident in these figures, however, is the contribution of the fuel momentum to thrust, which is the major advantage that film cooling has over transpiration cooling. For this, the results of cycle analysis are now examined.

The specific impulse, defined as the net thrust per unit fuel flow rate, is obtained from cycle analysis for each of the parametric SHIP3D combustor runs. The results, shown in Figure 16, indicate that the penalty in performance

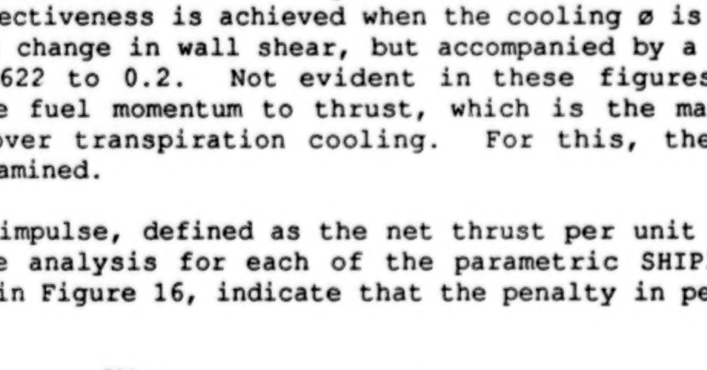

Figure 16. Tip-to-Tail Engine Specific Impulse

associated with film cooling is low for cooling ϕ up to 0.556, below which the contribution of the fuel momentum to thrust compensates for the drop in mixing. The balance is tipped at a film cooling ϕ of 0.556 above which the specific impulse drops sharply. This threshold value of the film cooling ϕ determines how effectively the combustor can be film cooled without a large penalty in performance.

For transpiration cooling, Figure 16 shows that this threshold value of the cooling ϕ is a low 0.2, at which the mixing efficiency also peaks (Figure 13). Since the momentum of the fuel used for transpiration cooling makes no contribution to the thrust, the specific impulse for transpiration cooling follows the decline in the mixing efficiency (Figure 13) with increasing cooling ϕ.

NOZZLES

Expansion of the combustor exhaust against the lower rear portion of the fuselage, which serves as a nozzle, is the main thrust generating mechanism in an airframe-integrated scramjet. Thus the nozzle problem requires the computation of the pressure on the entire, contoured nozzle wall. Figure 17 shows the sideview of a nozle that was tested using high pressure air [9]. The nozzle block sets up a Mach 4-5 flow, which simulates a scramjet combustor exhaust at Mach 20-25 flight. This flow is then expanded in the internal nozzle model, the bottom wall of which represents a cowl. Measurements of wall pressure and heat flux, the overall thrust and boundary layer surveys were taken to provide data to validate codes for the two key nozzle unit problems, expansion and boundary layer development.

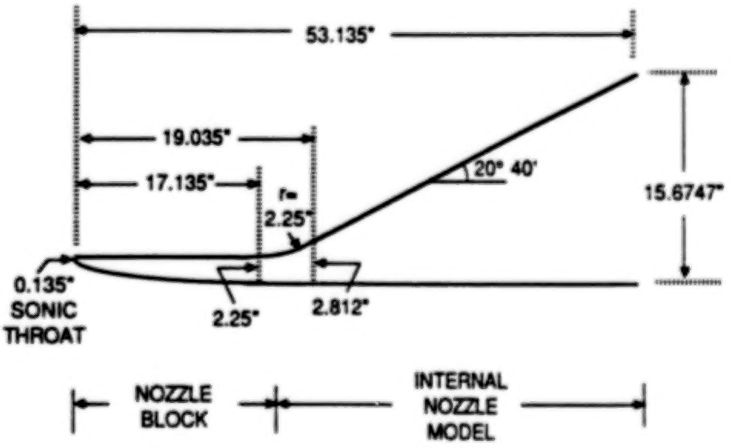

Figure 17. Sideview of Nozzle Block and Internal Nozzle Model

The parabolic computation of this air-only case was run from the sonic throat all the way to the exit. Forty-one grid points are used from wall-to-wall and the minimum grid spacing at the throat is 30 microns. The grid is expanded proportionately to the expansion of the duct as the computation proceeds downstream. The CPU time for this case is 4 minutes on a Cray-2.

The computed and measured pressures are compared in Figures 18 and 19 for the nozzle block and internal nozzle model. The increase in the computed lower wall pressure between 0.3 and 0.43 m is slightly in excess of that shown by the data. For the top wall of the internal nozzle (Figure 19), the computation and

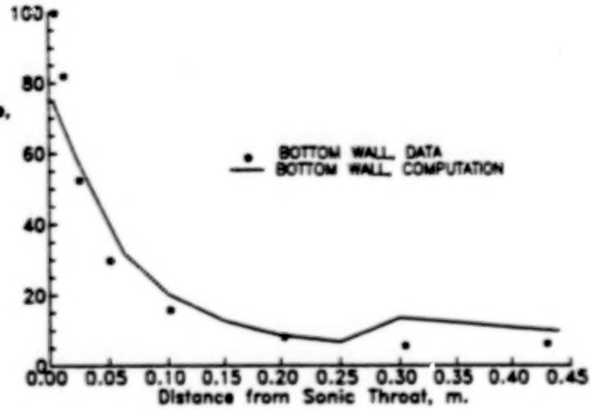

Figure 18. Wall Pressure for Nozzle Block

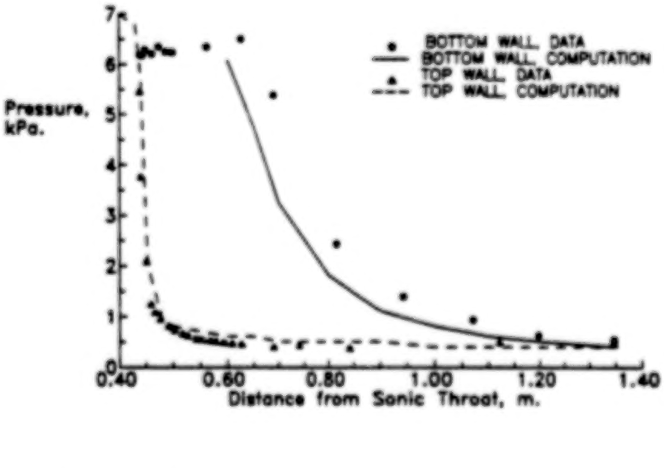

Figure 19. Wall Pressure for Internal Nozzle Model

test data are in good agreement. For this wall, the computed thrust is higher than that obtained by integrating the measured presures by 4.3 percent.

Because of the quasi-orthogonal metrics used in SHIP [5], a sudden change in the slope of the wall causes some locally oscillatory behaviour in the pressure which however, quickly recovers to the correct value. Work on a more realistic coordinate transformation is currently in progress.

SUMMARY

The SIMPLE-based three-dimensional parabolic flow code, SHIP3D is shown to be a highly efficient code for scramjet combustor and nozzle computations. The capability to accurately compute the heat transfer in a turbulent, reacting flowfield makes it particularly suitable for combustor film cooling studies. This along with recently implemented methods for the parabolic treatment of fuel injection, makes it possible to conduct parametric studies of realistic combustor configurations. One such study is included in this paper.

A simulated scramjet nozzle flow at flight Mach 20 to 25 is computed. For this preliminary analysis, the agreement with the pressure force, obtained by integration of the measured pressures, is within 4.3 percent.

For those computations not involving heat transfer, where a minimum grid spacing of the order of 50 to 100 microns suffices, 1 to 5 CPU minutes is the typical run time on a Cray-2. The memory required is usually less than 1 million words. Thus, the SHIP code could be run productively on a machine as small as a personal computer.

REFERENCES

1. Northam, G. B. and Anderson, G. Y.: "Supersonic Combustion Ramjet Research at Langley," AIAA Paper No. 86-0159, 1986.

2. Srinivasan, S., McClinton, C. R. and Kamath, P. S.: "Numerical Simulation of Flow Through the Langley Parametric Scramjet," SAE Paper 892314, Aerospace Technology Conference and Exposition, Anaheim, California, September 25-28, 1989.

3. Ng, K. H. and Spalding, D. B.: "Turbulence Model for Boundary Layers Near Walls," The Physics of Fluids, v15, n1, pp 20-30, January 1972.

4. Love, E. S.: "Base Pressure at Supersonic Speeds on Two-dimensional Airfoils and on Bodies of Revolution With and Without Fins Having Turbulent Boundary Layers," NACA TN-3819, 1957 (supersedes NACA RM L53C02).

5. Markatos, N. C., Spalding, D. B. and Tatchell, D. G.: "Combustion of Hydrogen Injected into a Supersonic Airstream (The SHIP Computer Program)," NASA CR-2802, April 1977.

6. Rogers, R.C.: "Mixing of Hydrogen Injected from Multiple Injectors Normal to a Supersonic Airstream," NASA TN-D-6476, 1971.

7. Kamath, P.S., Baker, N.R. and McCLinton, C. R,: "Film Cooling vs Transpiration Cooling for Scramjet Combustors - A Computational Study," Paper No. 96, Seventh NASP Technology Symposium, October 23-27, 1989.

8. Kamath, P.S., Baker, N. R., and McClinton, C. R.: "A Computational Design Tool for Scramjet Combustor Film Cooling and Fuel Mixing Predictions, AIAA Paper No. 90-0645.

9. Seifertt, T.:"Generic Option No. 2 Validation/Experimental Database Development Hypersonic Nozzle Test Program," Paper No. 85, Seventh NASP Technology Symposium, October 23-27, 1989.

NASA
National Aeronautics and Space Administration

Report Documentation Page

1. Report No. NASA CP-3078	2. Government Accession No.	3. Recipient's Catalog No.

4. Title and Subtitle

Computational Fluid Dynamics Symposium on Aeropropulsion

5. Report Date

January 1991

6. Performing Organization Code

7. Author(s)

8. Performing Organization Report No.

E-5296

10. Work Unit No.

505-62-21

9. Performing Organization Name and Address

National Aeronautics and Space Administration
Lewis Research Center
Cleveland, Ohio 44135-3191

11. Contract or Grant No.

13. Type of Report and Period Covered

Conference Publication

12. Sponsoring Agency Name and Address

National Aeronautics and Space Administration
Washington, D.C. 20546-0001

14. Sponsoring Agency Code

15. Supplementary Notes

This publication supercedes NASA CP-10045. It contains six papers that were not included in the preprint.

16. Abstract

Recognizing the considerable advances that have been made in computational fluid dynamics, the Internal Fluid Mechanics Division of NASA Lewis Research Center sponsored the Computational Fluid Dynamics Symposium on Aeropropulsion at Lewis Research Center, Cleveland, Ohio, on April 24-26, 1990. The objective of the symposium was to provide a forum for exchanging information regarding recent developments in numerical methods, physical and chemical modeling, and applications. This conference publication is a compilation of 4 invited and 34 contributed papers presented in six sessions: Algorithms I and II, Turbomachinery, Turbulence, Components Application, and Combustors. Topics include numerical methods, grid generation, chemically reacting flows, turbulence modeling, turbomachinery, inlets, nozzles, and unsteady flows.

17. Key Words (Suggested by Author(s)) CFD Aeropropulsion Computational fluid dynamics	18. Distribution Statement Unclassified – Unlimited Subject Category 02

19. Security Classif. (of this report)	20. Security Classif. (of this page)	21. No. of pages	22. Price*
Unclassified	Unclassified	692	A99

NASA FORM 1626 OCT 86

*For sale by the National Technical Information Service, Springfield, Virginia 22161

682